WOMEN IN SCIENCE: MATERIALS

EDITED BY: Maria Chiara Bignozzi, Patricia Krawczak, Emilia Morallon, Ming Xu and Jacqueline Anne Johnson

PUBLISHED IN: Frontiers in Materials and Frontiers in Bioengineering and Biotechnology

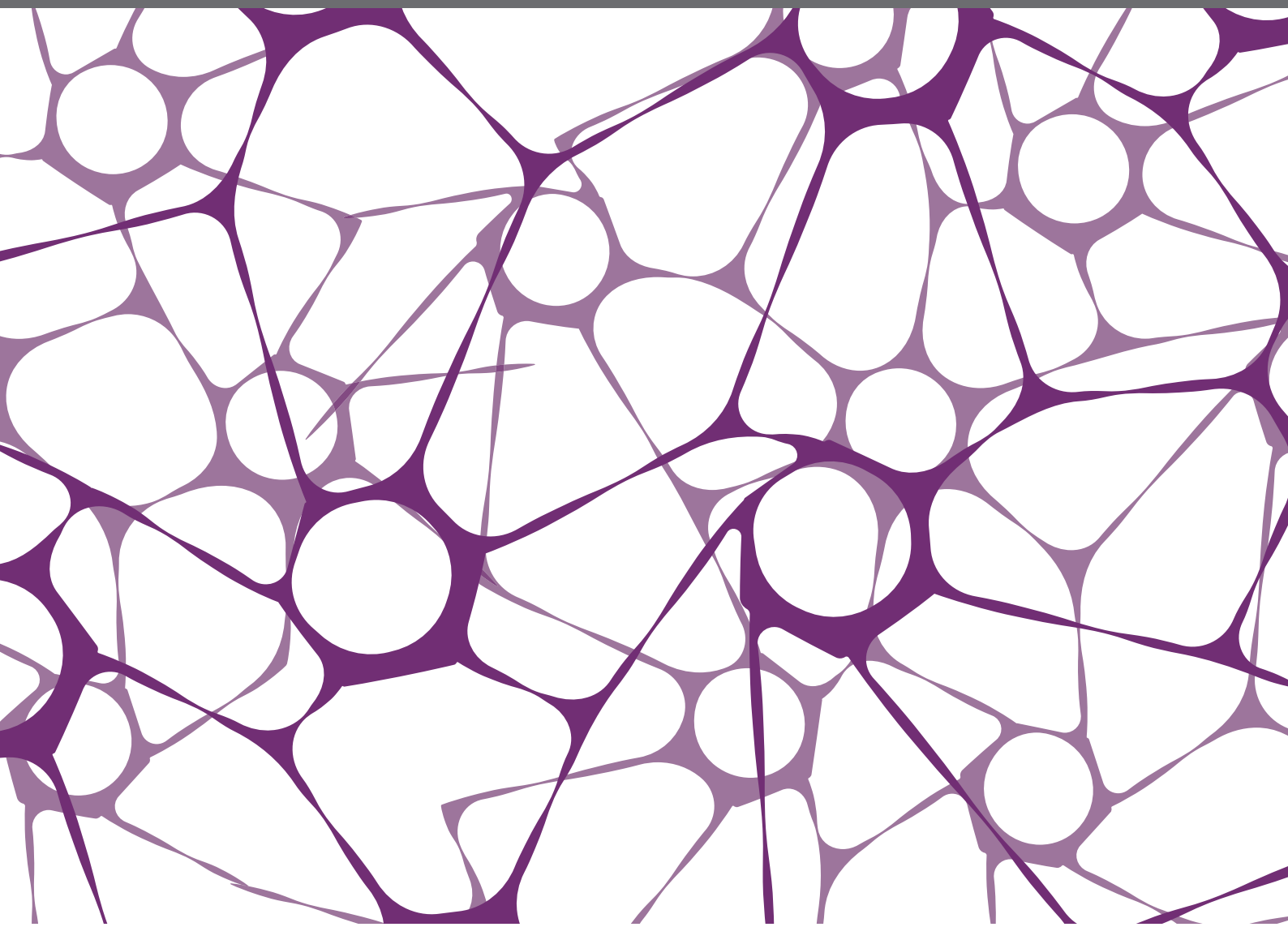

frontiers Research Topics

ISSN 1664-8714
ISBN 978-2-88966-951-6
DOI 10.3389/978-2-88966-951-6

About Frontiers

Frontiers is more than just an open-access publisher of scholarly articles: it is a pioneering approach to the world of academia, radically improving the way scholarly research is managed. The grand vision of Frontiers is a world where all people have an equal opportunity to seek, share and generate knowledge. Frontiers provides immediate and permanent online open access to all its publications, but this alone is not enough to realize our grand goals.

Frontiers Journal Series

The Frontiers Journal Series is a multi-tier and interdisciplinary set of open-access, online journals, promising a paradigm shift from the current review, selection and dissemination processes in academic publishing. All Frontiers journals are driven by researchers for researchers; therefore, they constitute a service to the scholarly community. At the same time, the Frontiers Journal Series operates on a revolutionary invention, the tiered publishing system, initially addressing specific communities of scholars, and gradually climbing up to broader public understanding, thus serving the interests of the lay society, too.

Dedication to Quality

Each Frontiers article is a landmark of the highest quality, thanks to genuinely collaborative interactions between authors and review editors, who include some of the world's best academicians. Research must be certified by peers before entering a stream of knowledge that may eventually reach the public - and shape society; therefore, Frontiers only applies the most rigorous and unbiased reviews.
Frontiers revolutionizes research publishing by freely delivering the most outstanding research, evaluated with no bias from both the academic and social point of view. By applying the most advanced information technologies, Frontiers is catapulting scholarly publishing into a new generation.

What are Frontiers Research Topics?

Frontiers Research Topics are very popular trademarks of the Frontiers Journals Series: they are collections of at least ten articles, all centered on a particular subject. With their unique mix of varied contributions from Original Research to Review Articles, Frontiers Research Topics unify the most influential researchers, the latest key findings and historical advances in a hot research area! Find out more on how to host your own Frontiers Research Topic or contribute to one as an author by contacting the Frontiers Editorial Office: frontiersin.org/about/contact

WOMEN IN SCIENCE: MATERIALS

Topic Editors:
Maria Chiara Bignozzi, University of Bologna, Italy
Patricia Krawczak, IMT Lille Douai, France
Emilia Morallon, University of Alicante, Spain
Ming Xu, Huazhong University of Science and Technology, China
Jacqueline Anne Johnson, University of Tennessee Space Institute (UTSI), United States

The *Frontiers in Materials* Editorial Office team are delighted to present the inaugural "Women in Science: Materials" article collection, showcasing the high-quality work of women in science across the breadth of materials science and engineering.

All researchers featured within this collection were individually nominated by the Topic Editors in recognition of their status as leading academics who have great potential to influence the future directions of their respective fields. The work presented here highlights the diversity of research performed across the entire breadth of the materials science and engineering field and presents advances in theory, experimentation, and methodology with applications for solving compelling problems.

This Editorial features the corresponding author(s) of each paper published within this important collection, ordered by section alphabetically, highlighting them as the great researchers of the future.

The *Frontiers in Materials* Editorial Office team would like to thank each researcher who contributed their work to this collection. We would also like to personally thank the Topic Editors for their exemplary leadership of this article collection; their strong support and passion for this important, community-driven collection has ensured its success and global impact.

Emily Young

Journal Development Manager

Topic Editors

Maria Chiara Bignozzi

Prof. Maria Chiara Bignozzi (MCB) is an associate professor in Materials Science and Technology at the School of Engineering and Architecture, Alma Mater Studiorum University of Bologna, Italy, and director of Centro Ceramico (www.centroceramico.it). She is also involved in European and international standards, being a Convener of WG1 "Test methods" for ISO TC 189 and CEN TC 67 "Ceramic tiles". Her research activity is mainly concerned with building materials (ceramic tiles, geopolymers/alkali-activated materials, concrete, cement, etc.) and their physical-mechanical performances, durability, and sustainability features.

Patricia Krawczak

Prof. Patricia Krawczak is a Full Professor of Materials Science and Engineering at Ecole Nationale Supérieure Mines-Télécom Lille Douai, France. After being the director of the "Polymers and Composites Technology & Mechanical Engineering" department of this graduate school for 20 years, she has been the strategic program manager of "Technological Platforms" at the Institut Mines-Télécom since 2019. Her research expertise focuses on the advanced manufacturing, physics, and mechanics of plastics and composites. She has authored over 400 journal or conference publications and book chapters. She is a member of the Executive Board of the French society of plastics engineers and the Board of Directors of the French Industrial Technical Centre for polymer processing and composites. She is the recipient of the Légion d'Honneur national award.

Emilia Morallon

Prof. Emilia Morallon is a Full Professor of Physical Chemistry at the University of Alicante, Spain, has been the Head of Electrocatalysis and Polymer Electrochemistry Research Group since 2008, and is a member of the Materials Institute of the University of Alicante. She has authored 240 papers and book

chapters and has supervised more than 20 Ph.D. theses. She has several research interests: preparation and characterization of conducting polymers, preparation and characterization of hybrid compounds, synthesis and characterization of metal oxides for use in environmental and energy applications, electrochemical characterization and electrochemical functionalization of carbon materials, and environmental and energy applications, such as fuel cells, supercapacitors, and the removal of pollutants.

Ming Xu

Prof. Ming Xu is a Full Professor of Huazhong University of Science and Technology (HUST), China, and the head of the lab of Carbon Nanomaterials of HUST (www.nanocarbon-hust.cn). Her research interests include synthesis and functionalization of carbon nanomaterials for dry adhesion, sensoring, energy storage and harvesting, processing of composite materials based on carbon nanomaterials, and a focus on the development of carbon nanomaterials application in extreme environments. She won the 7th Iijima Prize, which is recognized as one of the most distinguished honors in the field of carbon nanomaterial research.

Jacqueline Anne Johnson

Dr. Johnson completed her doctorate in solid-state physics in the research area of magnetic phase transitions at the University of Liverpool in 1985. She transitioned to working on glass materials after being approached by Pilkington Glass to solve technical problems. She was a Professor in Liverpool until 1995 when she joined Argonne National Laboratory in the United States. Here, she was introduced to solving the structure of amorphous materials using neutron scattering. After a 2-year period in administration, she returned to research to develop a new mammography system using a glass-ceramic plate. In 2007, Dr. Johnson returned to academia at the University of Tennessee Space Institute, and she continues to synthesize and characterize glasses, glass ceramics, and nanomaterials pertaining to medical devices, non-destructive evaluation, and image enhancement.

Citation: Bignozzi, M. C., Krawczak, P., Morallon, E., Xu, M., Johnson, J. A., eds. (2021). Women in Science: Materials. Lausanne: Frontiers Media SA.
doi: 10.3389/978-2-88966-951-6

Table of Contents

09 ***Editorial: Women in Science: Materials***
Maria Chiara Bignozzi, Jacqueline Anne Johnson, Patricia Krawczak, Emilia Morallon and Ming Xu

BIOMATERIALS

13 ***Surface Triggered Self-Assembly of Fmoc-Tripeptide as an Antibacterial Coating***
Miryam Criado-Gonzalez, Muhammad Haseeb Iqbal, Alain Carvalho, Marc Schmutz, Loïc Jierry, Pierre Schaaf and Fouzia Boulmedais

22 ***Evaluating the Toxicity of Ionic Liquids on* Shewanella *sp. for Designing Sustainable Bioprocesses***
Hakima Kebaili, Antonia Pérez de los Ríos, María José Salar-García, Víctor Manuel Ortiz-Martínez, Mostefa Kameche, Jesús Hernández-Fernández and Francisco J. Hernández-Fernández

CARBON-BASED MATERIALS

43 ***Thermal Properties Enhancement of Vertically Aligned Carbon Nanotubes-Based Metal Nanocomposites as Thermal Interface Materials***
Qiuhong Zhang, Brian A. Calderon, Charles R. Ebbing, Levi J. Elston, Larry W. Byrd and Bang-Hung Tsao

55 ***Direct Graphene Synthesis on Lithium Niobate Substrate by Carbon Ion Implantation***
Yuhang Xu, Fei Lu, Kaijing Liu and Changdong Ma

64 ***Effect of Co-solution of Carbon Precursor and Activating Agent on the Textural Properties of Highly Porous Activated Carbon Obtained by Chemical Activation of Lignin With H_3PO_4***
Imane Moulefera, Francisco J. García-Mateos, Abdelghani Benyoucef, Juana M. Rosas, José Rodríguez-Mirasol and Tomás Cordero

78 ***Mechanically Robust Free-Standing Single-Walled Carbon Nanotube Thin Films With Uniform Mesh-Structure by Blade Coating***
Yuichi Kato, Atsuko Sekiguchi, Kazufumi Kobashi, Rajyashree Sundaram, Takeo Yamada and Kenji Hata

CERAMICS AND GLASS

87 ***Multifunctional Lightweight Mortars for Indoor Applications to Improve Comfort and Health of Occupants: Thermal Properties and Photocatalytic Efficiency***
Chiara Giosuè, Mattia Pierpaoli, Alessandra Mobili, Maria Letizia Ruello and Francesca Tittarelli

COLLOIDAL MATERIALS AND INTERFACES

99 ***Advances in Microtechnology for Improved Cytotoxicity Assessment***
Maite Garcia-Hernando, Fernando Benito-Lopez and Lourdes Basabe-Desmonts

116 ***Dynamic Wetting of Molten Polymers on Cellulosic Substrates: Model Prediction for Total and Partial Wetting***
Monica Francesca Pucci, Benoît Duchemin, Moussa Gomina and Joël Bréard

ENERGY MATERIALS

129 ***Energy Storage in Supercapacitors: Focus on Tannin-Derived Carbon Electrodes***
Jimena Castro-Gutiérrez, Alain Celzard and Vanessa Fierro

154 ***Non-precious Melamine/Chitosan Composites for the Oxygen Reduction Reaction: Effect of the Transition Metal***
B. Aghabarari, M. V. Martínez-Huerta, M. C. Capel-Sánchez and M. J. Lázaro

ENVIRONMENTAL MATERIALS

164 ***Experimental Study on an Innovative Biopolymeric Treatment Against Salt Deterioration of Materials in Cultural Heritage***
Mattia Bassi, Enrico Sassoni and Elisa Franzoni

MECHANICS OF MATERIALS

188 ***A Contribution to the Study of the Forming of Dry Unidirectional HiTape® Reinforcements for Primary Aircraft Structures***
Laure Bouquerel, Nicolas Moulin and Sylvain Drapier

205 ***An Incremental Cohesive Law for Delamination Under a Mixed Mode Loading***
Man Zhu, Larissa Gorbatikh and Stepan V. Lomov

217 ***Characterization of Surface Fatigue Crack Nucleation and Microstructurally Small Crack Growth in High Strength Aluminum Alloys***
Robert Fleishel, Cole Cauthen, Steven Daniewicz, Andrew Baker, J. Brian Jordon and Stephanie TerMaath

233 ***Changing Compliance of Poly(Vinyl Alcohol) Tubular Scaffold for Vascular Graft Applications Through Modifying Interlayer Adhesion and Crosslinking Density***
YeJin Jeong, Yuan Yao, Tizazu H. Mekonnen and Evelyn K. F. Yim

POLYMERIC AND COMPOSITE MATERIALS

253 ***Use of Flow Modeling to Optimize the Twin-Screw Extrusion Process for the Preparation of Lignocellulosic Fiber-Based Composites***
Françoise Berzin, Chantal David and Bruno Vergnes

260 ***Roles of Size, Shape, Amount, and Functionalization of Nanoparticles of Titania in Controlling the Tribo-Performance of UHMWPE Composites***
Meghashree Padhan, Gourab Paul and Jayashree Bijwe

275 ***Hollow Section Fibers Characterization for Seats Covers Fabric Application***
Valentina Brunella, Giulia Albini, Vito Guido Lambertini and Bartolomeo Placenza

285 ***Under Glass Weathering of Hemp Fibers Reinforced Polypropylene Biocomposites: Degradation Mechanisms Based on Emitted Volatile Organic Compounds***
Célia Badji, Jean-Marc Sotiropoulos, Joana Beigbeder, Hélène Garay, Anne Bergeret, Jean-Charles Bénézet and Valérie Desauziers

297 ***Corrigendum: Under Glass Weathering of Hemp Fibers Reinforced Polypropylene Biocomposites: Degradation Mechanisms Based on Emitted Volatile Organic Compounds***
Célia Badji, Jean-Marc Sotiropoulos, Joana Beigbeder, Hélène Garay, Anne Bergeret, Jean-Charles Bénézet and Valérie Desauziers

298 ***Fiber Orientation Distribution Predictions for an Injection Molded Venturi-Shaped Part Validated Against Experimental Micro-Computed Tomography Characterization***
María C. Quintana, Patricia M. Frontini, Aitor Arriaga, Bernhard Plank and Zoltan Major

311 ***Processing–Structure–Properties of Cork Polymer Composites***
Carla I. Martins and Vitória Gil

323 ***Statistical Fatigue Investigation and Failure Prediction of a Healable Composite System***
Nathan Hostettler, Amaël Cohades and Véronique Michaud

332 ***Supramolecular Structure and Mechanical Properties of Wet-Spun Polyacrylonitrile/Carbon Nanotube Composite Fibers Influenced by Stretching Forces***
Hamideh Mirbaha, Paolo Scardi, Mirco D'Incau, Shahram Arbab, Parviz Nourpanah and Nicola M. Pugno

345 ***Role of Compatibilizer in Improving the Properties of PLA/PA12 Blends***
Amulya Raj, Cedric Samuel and Kalappa Prashantha

357 **In-situ *Monitoring of the Out-Of-Autoclave Consolidation of Carbon/Poly-Ether-Ketone-Ketone Prepreg Laminate***
Florence Saffar, Camille Sonnenfeld, Pierre Beauchêne and Chung Hae Park

SMART MATERIALS

370 ***Hydrogen Sulfide Detection by Sensors Based on Conductive Polymers: A Review***
Caroline Duc, Mohamed-Lamine Boukhenane, Jean-Luc Wojkiewicz and Nathalie Redon

STRUCTURAL MATERIALS

383 ***Gender Balance in Construction Material Research: The Analysis of Alkali-Activated Materials by a Bibliometric Study Using Scopus Database***
Giulia Masi, Stefania Manzi and Maria Chiara Bignozzi

394 ***A Case Study of Industrial Symbiosis to Reduce GHG Emissions: Performance Analysis and LCA of Asphalt Concretes Made With RAP Aggregates and Steel Slags***
Alessandra Bonoli, Anna Degli Esposti and Chiara Magrini

408 ***3D-Extrusion Manufacturing of a Kaolinite Dough Taken in Its Pristine State***
Séverine A. E. Boyer, Lucie Jandet and Alain Burr

420 ***Characterization of Fly Ash Alkali Activated Foams Obtained Using Sodium Perborate Monohydrate as a Foaming Agent at Room and Elevated Temperatures***
Lidija Korat and Vilma Ducman

435 ***Alkali-Activated Binders From Waste Incinerator Bottom Ashes and Metakaolin Reinforced by Recycled Carbon Fiber Composites***
Stefania Manzi, Isabella Lancellotti, Giulia Masi and Andrea Saccani

frontiers in Materials

EDITORIAL
published: 23 April 2021
doi: 10.3389/fmats.2021.668092

Editorial: Women in Science: Materials

Maria Chiara Bignozzi[1]*, *Jacqueline Anne Johnson*[2]*, *Patricia Krawczak*[3]*, *Emilia Morallon*[4]* and *Ming Xu*[5]*

[1] Department of Civil, Chemical, Environmental and Materials Engineering, University of Bologna, Bologna, Italy, [2] University of Tennessee, Space Institute, Tullahoma, TN, United States, [3] IMT Lille Douai, Institut Mines-Télécom, Univ. Lille, Centre for Materials and Processes, Douai, France, [4] Physical Chemistry Department, Institute of Materials Science, University of Alicante, Alicante, Spain, [5] School of Materials Science and Engineering, Huazhong University of Science and Technology, Wuhan, China

Keywords: women in STEM, women in science and engineering, materials engineering, materials science, gender equality

OPEN ACCESS

Edited and reviewed by:
Alberto Corigliano,
Politecnico di Milano, Italy

***Correspondence:**
Maria Chiara Bignozzi
maria.bignozzi@unibo.it
Jacqueline Anne Johnson
jjohnson@utsi.edu
Patricia Krawczak
patricia.krawczak@imt-lille-douai.fr
Emilia Morallon
morallon@ua.es
Ming Xu
ming.xu@hust.edu.cn

Specialty section:
This article was submitted to Mechanics of Materials, a section of the journal Frontiers in Materials

Received: *15 February 2021*
Accepted: *25 February 2021*
Published: *23 April 2021*

Citation:
Bignozzi MC, Johnson JA, Krawczak P, Morallon E and Xu M (2021) Editorial: Women in Science: Materials. Front. Mater. 8:668092. doi: 10.3389/fmats.2021.668092

Editorial on the Research Topic

Women in Science: Materials

According to UNESCO Institute for Statistics (UIS) data (2019), <30% of researchers worldwide are women. Long-standing biases and gender stereotypes are discouraging girls and women away from science-related fields. In particular, STEM (science, technology, engineering, and mathematics) research is traditionally male dominated and women remain underrepresented. As UNESCO has highlighted, both science and gender equality are, however, essential to ensuring sustainable development. To change traditional mindsets, gender equality must be promoted, stereotypes defeated, and girls and women should be encouraged to pursue careers in STEM.

Throughout history, the contributions of female researchers to scientific progress have been extremely important. Yet, whereas the extraordinarily talented Nobel laureate Marie Skłodowska-Curie is often mentioned as a role model, it is nowadays well-established that countless women such as Lise Meitner have received less recognition and acknowledgment for their research findings than their male counterparts [so-called Matilda effect (Rossiter, 1993)].

Also, women traditionally publish less than men according to the European Commission She Figures, the ratio of women to men among authors of scientific publications in the EU being on the average one to two (European Union, 2019), and recent surveys are highlighting a further drop in academic submissions from female scientists since the start of the Covid-19 pandemic early 2020.

Role models are definitely extremely important to show to younger generations the growing impact of female researchers to science. Therefore, continuing the spirit of the International Day of Women and Girls in Science, *Frontiers in Materials* is proud to offer this platform to promote the work of female scientists across the breadth of materials science and engineering.

This inaugural "Women in Science: Materials" collection (**Figure 1**) aims to highlight the impact of women researchers working in materials science and engineering. It gathers a selection of original articles with the lead author and/or corresponding author being a woman.

A total of 32 contributions (three reviews, one brief research report, and 28 original research articles) present advances in theory, experiment, and methodology with applications to compelling problems, across almost all sections of the journal:

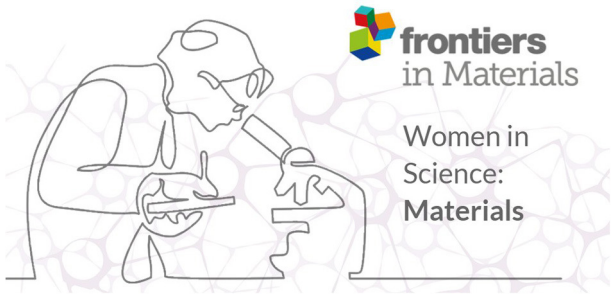

FIGURE 1 | "Women in Science: Materials" collection in *Frontiers in Materials*.

- Mechanics of materials (Bouquerel et al.; Jeong et al., TerMaath et al.; Zhu et al.)
- Smart materials (Duc et al.)
- Polymeric and composite materials (Badji et al.; Berzin et al.; Brunella et al.; Hostettler et al.; Martins and Gil; Mirbaha et al.; Padhan et al.; Quintana et al., Raj et al.; Saffar et al.)
- Carbon-based materials (Kato et al.; Moulefera et al.; Xu et al., Zhang et al.)
- Structural materials (Bonoli et al.; Boyer et al.; Korat and Ducman; Manzi et al., Masi et al.)
- Colloidal materials and interfaces (Garcia-Hernando et al.; Pucci et al.)
- Energy materials (Castro-Gutiérrez et al.)
- Ceramics and glass (Giosuè et al.)
- Environmental materials (Bassi et al.)
- Biomaterials (Criado-Gonzalez et al.; Kebaili et al.)

The Guest Editorial team hope that this collection of papers will be the foundation of an international network of women researchers working in materials science and engineering, and a starting point for future collaborations and discussions.

AUTHOR CONTRIBUTIONS

This Editorial was jointly written by all co-authors who also served as Guest Editors for the Research Topic. All authors contributed to the article and approved the submitted version.

REFERENCES

European Union (2019). *European Commission She Figures 2018*. Publications Office of the European Union, Luxembourg. doi: 10.2777/936

Rossiter, M.W. (1993). The Matthew Matilda effect in science. *Soc. Stud. Sci.* 23, 325–341. doi: 10.1177/030631293023002004

UNESCO Institute for Statistics (2019). *Women in Science (n°55)* [Fact sheet], UIS/FS/2019/SCI/55, UIS Publ., Montreal, QC, Canada. Available online at: https://unesdoc.unesco.org/ark:/48223/pf0000370742

Conflict of Interest: The authors declare that the research was conducted in the absence of any commercial or financial relationships that could be construed as a potential conflict of interest.

Biomaterials

Fouzia Boulmedais

Dr. Fouzia Boulmedais is a physical chemist with a CNRS position at Institut Charles Sadron, Strasbourg; here, she develops biopolymer films as biomaterial coatings and electrodeposited polymeric films for biosensing. She graduated from University Louis Pasteur, Strasbourg, where she received her Ph.D. in chemistry and physical chemistry in 2003. In 2004, she worked as a post-doc with Prof. Marcus Textor at ETH Zurich, Switzerland, and with Prof. Gleb Sukhorukhov at Max Planck Institute, Germany, on electrodissolution of polyelectrolytes multilayers. As of 2006, she has been a co-author of 109 publications and four patents.

Miryam Criado-Gonzalez

Dr. Miryam Criado-Gonzalez studied Chemical Engineering (2011) at the University of Salamanca, Spain, where she also pursued a Master of Chemical Engineering (2013). Then, she studied for a Master of Polymer Science (2014) at the Institute of Polymer Science and Technology (ICTP-CSIC) in Madrid, Spain, where she also obtained her Ph.D. (2017). She held a postdoctoral position at Institut Charles Sadron (CNRS) in collaboration with INSERM (Strasbourg, France) in 2017. From June 2020, she worked as a postdoctoral researcher on a collaborative project CSIC-CNRS at ICTP, Madrid, Spain. In March 2021, she joined the Innovative Polymers Group at POLYMAT, Spain. Her research interests include the layer-by-layer assembly of biopolymers, supramolecular peptide/polymer hydrogels, and additive manufacturing of conducting polymers.

María José Salar

Dr. María José Salar is an assistant professor at the Technical University of Cartagena, Spain. She got her BSc (2010) and MSc (2011) in Chemical Engineering and Molecular Chemistry, respectively, at the University of Murcia, Spain. Following a move to the Technical University of Cartagena in 2012, she obtained her Ph.D. and the extraordinary Ph.D. award in 2016. After her Ph.D., she was funded by the Seneca Foundation to conduct her research at the Bristol BioEnergy Centre, United Kingdom. Her research field focuses on the design and optimization of microbial fuel cells as well as the use of green solvents, such as ionic liquids, in membrane technology. These research lines have resulted in more than 45 scientific publications (h-index: 17) and nine book chapters.

frontiers in Bioengineering and Biotechnology

BRIEF RESEARCH REPORT
published: 07 August 2020
doi: 10.3389/fbioe.2020.00938

Surface Triggered Self-Assembly of Fmoc-Tripeptide as an Antibacterial Coating

Miryam Criado-Gonzalez[1,2], Muhammad Haseeb Iqbal[1,2], Alain Carvalho[1], Marc Schmutz[1], Loïc Jierry[1], Pierre Schaaf[1,2,3] and Fouzia Boulmedais[1]**

[1] Université de Strasbourg, CNRS, Institut Charles Sadron UPR 22, Strasbourg, France, [2] Institut National de la Santé et de la Recherche Médicale, UMR-S 1121, "Biomatériaux et Bioingénierie", Strasbourg, France, [3] Faculté de Chirurgie Dentaire, Fédération de Médecine Translationnelle de Strasbourg and Fédération des Matériaux et Nanoscience d'Alsace, Université de Strasbourg, Strasbourg, France

In western countries, one patient on twenty will develop a nosocomial infection during his hospitalization at health care facilities. Classical antibiotics being less and less effective, this phenomenon is expanding year after year. Prevention of bacteria colonization of implantable medical devices constitutes a major medical and financial issue. In this study, we developed an antibacterial coating based on self-assembled Fmoc-tripeptide. Fmoc-FFpY peptides (F: phenylalanine; Y: tyrosine; p: PO_4^{2-}) are dephosphorylated enzymatically into Fmoc-FFY by action of alkaline phosphatase functionalized silica nanoparticles (NPs@AP), previously deposited on a surface. Fmoc-FFY peptides then self-assemble through π–π stacking interactions, hydrogen bonds and hydrophobic interactions adopting β-sheets secondary structures. The obtained hydrogel coatings show fibrillary structures observed by cryo-scanning electron microscopy with a thickness of few micrometers. At low concentration (≤0.5 mg.mL^{-1}), self-assembled Fmoc-FFY has a superior antibacterial activity than Fmoc-FFpY peptide in solution. After 24 h of incubation, Fmoc-FFY hydrogel coatings fully inhibit the development of Gram-positive *Staphylococcus aureus (S. aureus)*. The antibacterial effect is maintained on an *in vitro* model of repetitive infection in the case of *S. aureus*. This coating could serve in infections were Gram positive bacteria are prevalent, e.g., intravascular catheter infections. This work gives new insights toward the design of an alternative antimicrobial coating.

Keywords: peptides, hydrogels, antimicrobial, enzyme-assisted self-assembly, nanoparticles

OPEN ACCESS

Edited by:
Patricia Krawczak, IMT Lille Douai, France

Reviewed by:
Garry Laverty, Queen's University Belfast, United Kingdom
Bing Xu, Brandeis University, United States

****Correspondence:***
Miryam Criado-Gonzalez
miryamcg22@gmail.com
Fouzia Boulmedais
fouzia.boulmedais@ics-cnrs.unistra.fr

Specialty section:
This article was submitted to Biomaterials, a section of the journal Frontiers in Bioengineering and Biotechnology

Received: *13 May 2020*
Accepted: *20 July 2020*
Published: *07 August 2020*

Citation:
Criado-Gonzalez M, Iqbal MH, Carvalho A, Schmutz M, Jierry L, Schaaf P and Boulmedais F (2020) Surface Triggered Self-Assembly of Fmoc-Tripeptide as an Antibacterial Coating. Front. Bioeng. Biotechnol. 8:938. doi: 10.3389/fbioe.2020.00938

INTRODUCTION

Biomedical implants, i.e., prosthetics, catheters or intraocular lenses, are indispensable in medicine and gain increasing attention over the years (Lombardi et al., 2019). However, the direct contact of their surfaces with biological fluids becomes susceptible to bacterial colonization and biofilm formation leading to a major medical and financial issue (McCloskey et al., 2014). Implant-associated infections increase the probability of implant failure and may result, if untreated, in chronic microbial infection, inflammation, tissue necrosis, and even morbidity (McCloskey et al., 2014). In western countries one patient on twenty will develop a nosocomial infection during

his hospitalization at health care facilities (Cassini et al., 2016). These infections are mostly due to *Staphylococcus epidermidis*, in the case of intravascular catheter-associated infections (Rupp and Archer, 1994), and *Staphylococcus aureus* (*S. aureus*) in the case of metallic implants (Barth et al., 1989). Biofilm formation contributes to the resistance to antibiotic treatments, it protects the bacterial colonies from host defense systems and bactericidal agents (Kaplan, 2011). This leads to the chemotherapeutic failure which often results in an increase of the resistance mechanism adopted by many bacterial strains, particularly those involving *S. aureus* (Darouiche, 2004). In this scenario, the development of antimicrobial coatings to protect against such infections has become a major field of scientific and technological research (Séon et al., 2015). As alternative to antibiotics, antimicrobial peptides are promising candidates to overcome pathogen resistance and for clinical exploitation (Lombardi et al., 2019). Self-assembly of peptides, with a sequenced-defined chemical structure, can give hydrogels with a desired functionality which becomes increasingly attractive in the development of therapeutics materials (Makam and Gazit, 2018; Criado-Gonzalez et al., 2020a).

In the last decade, low molecular weight hydrogelators (LMWH) fabricated from natural biomolecules such as amino acids got great interest due to their ease and powerful bottom-up fabrication. They self-assemble into supramolecular hydrogels by non-covalent interactions, i.e., electrostatic, van der Waals forces, hydrogen bonding and π-π stacking (McCloskey et al., 2014), in response to external stimuli, such as temperature change (Collier et al., 2001), pH switch (Aggeli et al., 2003; Chen et al., 2011), solvent change (Mahler et al., 2006), electrostatic interactions (Criado-Gonzalez et al., 2020b), chemical (Bowerman and Nilsson, 2010; Zhao et al., 2011) or enzymatic reactions (Yang et al., 2004; Yang and Xu, 2006; Criado-Gonzalez et al., 2019b). Ultrashort peptides, up to 7 amino acids in length, are an emerging class of LMWH of increasing interest due to their versatility in molecular design, ease synthesis, and costs reduction. Few studies have been carried out on the development of self-assembling materials with antibacterial properties using short peptides. Based on the pioneering work of Moir and coll. (Soscia et al., 2010; Kumar et al., 2016) which demonstrated the antimicrobial activity of an amyloid-β peptide, Schnaider et al. (2017) proved the antibacterial activity of a self-assembled dipeptide, diphenylalanine (FF), against *Escherichia Coli* (*E. coli*). In this work, FF moiety was identified as the central recognition module of amyloid, as well as the fundamental self-assembly motif proving the efficiency of this unit for the development of self-assembling antimicrobial hydrogels. Fluorenylmethyloxycarbonyl-FF (Fmoc-FF) derived peptides were shown to possess excellent activity against the most antibiotic resistant biofilm phenotype of both Gram-positive and Gram-negative bacteria (McCloskey et al., 2017). Fmoc-FF self-assemblies were employed as host hydrogels to incorporate silver nanoparticles to improve the antimicrobial response (Paladini et al., 2013). The backbone of this dipeptide was modified incorporating an urea moiety to inhibit the *E. coli* bacterial adhesion (Basavalingappa et al., 2019).

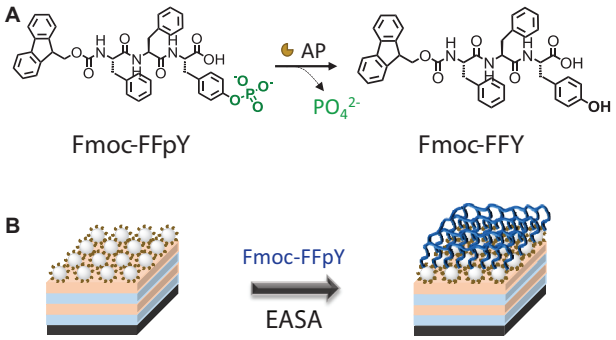

SCHEME 1 | Schematic representation of Fmoc-FFY hydrogel coating: **(A)** Enzyme-assisted self-assembly (EASA) of Fmoc-FFY by Fmoc-FFpY dephosphorylation **(B)** obtained on the surface of NPs@AP coating deposited on polyelectrolyte multilayer film.

Poorly soluble in water, Fmoc-FF peptide self-assembly is induced by dissolution in DMSO followed by a dilution step in water (Basavalingappa et al., 2019), by change of pH (Paladini et al., 2013), or by heating the solution, up to 90°C for solubilization, followed by a cooling step (Kumar et al., 2016). To overcome these tedious processes, the enzyme assisted self-assembly (EASA) of peptides was introduced by Xu and co-workers (Yang et al., 2004; Yang and Xu, 2006). Soluble at room temperature in aqueous solution, phosphorylated peptides were transformed into gelators by alkaline phosphatase (AP) catalyzing the removal of the phosphate groups. Later, we introduced the use of non-self-assembling Fmoc-FFpY peptide (Y: tyrosine; p: PO_4^{2-}), which is transformed into the hydrogelator Fmoc-FFY by AP. The enzymatic assisted self-assembly of Fmoc-FFpY was localized on a planar substrate (Vigier-Carrière et al., 2017) or on silica nanoparticles (Criado-Gonzalez et al., 2019a) thanks to the functionalization of their surfaces by AP. In contrast to the pH triggered self-assembly (Jayawarna et al., 2006; Raeburn et al., 2012), the EASA allows to use a more water-soluble peptide as a precursor and to obtain, by simple contact with the peptide solution, a fast and localized self-assembly on the surface of a substrate, previously functionalized by the enzyme.

Integrating self-assembling peptides with antimicrobial property on the surface of a biomaterial is an innovative design for the development of antibacterial materials. Herein, we report an antibacterial coating based on Fmoc-FFY hydrogel self-assembled by enzymatic dephosphorylation. To this aim, AP functionalized silica nanoparticles (NPs@AP) were first deposited on the surface of a material using the layer-by-layer method and then put in contact with Fmoc-FFpY solution to obtain the Fmoc-FFY hydrogel coating (**Scheme 1**). NPs@AP allowed to immobilize a higher quantity of enzyme on the surface than AP monolayer. The antimicrobial property was tested against *S. aureus*, Gram-positive strain which is one of the most virulent bacteria leading to high rates of device-related systemic infections and mortality and *E. coli*, a Gram-negative strain mainly found on the surface of urinary catheters.

MATERIALS AND METHODS

Materials

Poly(ethylene imine) (PEI, Mw = 250 000 g.mol^{-1}), Poly(allylamine hydrochloride) (PAH, M_w = 58 000 g.mol^{-1}), Alkaline Phosphatase (AP, 10 DEA units.mg protein^{-1}) from bovine intestinal mucosa, Poly(sodium 4-styrenesulfonate) (PSS, M_w = 70 000 g.mol^{-1}), Tetraethyl orthosilicate (TEOS), (3-glycidyloxypropyl) trimethoxysilane (GPMS) were from Sigma Aldrich. *p*-Nitrophenyl phosphate (PNP) was from ThermoFisher Scientific. Sodium tetra-borate anhydrous (borax) and dry toluene were supplied by Acros Organics. Fmoc-FFpY was purchased by PepMic, ammonium hydroxide by Carlo Erba and ethanol by VWR. Mueller Hinton (MH) broth was purchased from Merck (Germany).

Synthesis and Functionalization of Silica Nanoparticles

The synthesis of silica nanoparticles (NP) and their functionalization with AP were carried out following the procedure described previously (Criado-Gonzalez et al., 2019a). After their synthesis, NPs were functionalized covalently by AP using an epoxy silane coupling agent, giving rise to NPs@AP (**Supplementary Data**). The catalytic activity of NPs@AP suspensions was determined employing PNP, a substrate which is transformed in *para*-nitrophenol (λ_{max} = 405 nm) by action of AP.

Multilayer Film Preparation and Fmoc-FFpY Self-Assembly

All solutions were prepared in 25 mM borax buffer pH 9.5. Multilayer films were built on glass slides of 12 mm diameter (Marienfeld) or silicon slides of 10 × 10 mm (Sil'tronix Silicon Technologies). As the substrates are negatively charged, a precursor layer of branched PEI (1 mg.mL^{-1}) was deposited to achieve a homogeneous distribution of positive charges over the surface allowing an efficient deposition of the coating. For that, substrates were immersed in a solution of PEI for 5 min followed by a rinsing step with borax buffer for 2 min. After that, the multilayer film was built up through sequential contact of the substrate with 400 μL of PSS (1 mg.mL^{-1}) (polyanion) or PAH (1 mg.mL^{-1}) (polycation) solutions for 5 min with a rinsing step in borax buffer of 2 min after each polyelectrolyte deposition. This cycle was repeated two times and samples were denoted as polyelectrolyte multilayer (PEM). Then the substrate was put in contact with 400 μL of NPs@AP (1.25% w/v in borax buffer) suspension for 60 min followed by three rinsing steps of 2 min in borax buffer. Samples were denoted as NPs@AP coatings. Subsequently, 400 μL Fmoc-FFpY (1 mg.mL^{-1}) solution was brought in contact with NPs@AP coating for 16 h.

Quartz Crystal Microbalance With Dissipation Monitoring (QCM-D)

Quartz crystal microbalance with dissipation monitoring experiments were performed in a QCM-D cell on a Q-Sense E1 apparatus (Q-Sense AB, Gothenburg, Sweden) at 22°C using an open cell. The resonance frequencies of a gold coated crystal and the dissipation factors at the fundamental frequency at 5 MHz (ν = 1) were monitored during the deposition of NPs@AP and the Fmoc-FFY self-assembly. The perturbation due to the pipetting of the solutions at each deposition steps were removed from the plot.

Atomic Force Microscopy (AFM)

Atomic force microscopy Multimode Nanoscope IV (Bruker, Palaiseau, France) was used to analyze the surface topography of the coatings. Micrographs were recorded in Peak Force Tapping (ScanAsyst) mode by using silicon tips from Bruker (Model: ScanAsyst-Air) mounted on aluminum coated silicon nitride cantilevers. All samples were observed in dry state with triangular cantilevers having a spring constant of around 0.4 N.m^{-1} and a nominal tip radius of 2 nm. Selected AFM images were treated with the NanoScope Analysis Software (version 1.7). Samples were prepared on silicon substrates and air dried before analysis. Prior to the sample preparation, the silicon wafers were incubated in ethanol/water (50% by vol) mixture for 15 min and activated using plasma treatment for 3 min.

Circular Dichroism (CD)

Circular dichroism (CD) spectra were recorded between 190 and 320 nm using a Jasco J-1100 spectropolarimeter with a data pitch of 1 nm on the light wavelength. Samples were built up on a quartz slide of 1 mm thickness.

Fluorescence Spectroscopy

Fluorescence spectra were recorded between 300 and 355 nm using a Fluoromax-4 (Horiba Jobin Yvon – Edison, NJ, United States) at an excitation wavelength of 290 nm using a quartz slide of 1 mm thickness to build up the samples.

Scanning Electron Microscopy (SEM) and Cryo-SEM

The Fmoc-FFY hydrogel coating on a Silicon wafer was placed on a home-made cryo-holder (Vigier-Carrière et al., 2017) to be quickly plunged into an ethane slush. As the sample is free standing over the holder, the sample is rapidly frozen during the plunging by direct contact with the liquid ethane. Subsequently, the sample is transferred into the Quorum PT 3010 chamber attached to the microscope. There, the frozen sample is fractured with a razor blade. A slight etching at −90°C may be performed to render the fibers more visible. The sample is eventually transferred in the FEG-cryo SEM (Hitachi SU8010) and observed at 1 kV at −150°C.

Inverted Tube Tests

All solutions were prepared in 25 mM borax buffer pH = 9.5. 150 μL of Fmoc-FFpY (1 mg.mL^{-1}) was mixed with 50 μL of NPs@AP (5% w/v) in vials. After 24 h, inverted tube tests were carried out to determine the hydrogel formation. Then, 400 μL of bacteria culture medium (MH) was added and the stability was checked up to 9 days.

Antibacterial Activity

Antibacterial tests were carried out employing one strain Gram-positive bacteria, *Staphylococcus aureus* (*S. aureus*, ATCC 25923) and another strain Gram-negative bacteria, *Escherichia coli* (*E. coli*, ATCC 25922). *S. aureus* and *E. coli* were precultured separately in aerobic conditions at 37°C in a MH broth medium (Merck, Germany), pH 7.4. One colony from previously prepared agar plates by bacteria streaking protocol was transferred to 7 mL of MH medium and incubated in an agitator overnight at 37°C. To obtain bacteria in their mid-logarithmic phase of growth, the absorbance at 620 nm (OD_{620}) of overnight cultures was adjusted to 0.001 by diluting in MH, corresponding to a final cell density of approximately 8×10^5 CFU.mL^{-1}. Cultures growing in the presence of antibiotics (Tetracycline and Cefotaxime) were taken as positive control. Bacteria quantification (in colony forming unit per mL, CFU.mL^{-1}) was performed at time zero and 24 h after the incubation with the samples. This was determined by plating 100 μL of the supernatant, after serial dilution, on nutrient agar plates at 37°C overnight, then the viable cell colonies were counted and represented as $\log_{10}$ reduction (CFU.mL^{-1}). To determine the Minimum Inhibitory Concentration (MIC) value of Fmoc-FFpY and Fmoc-FFY hydrogel, the peptide was dissolved in RPMI medium at 2 mg.mL^{-1} and at lower concentrations by serial dilution in RPMI. *S. aureus* was pre-cultured overnight in MH medium, and diluted in RPMI medium. MIC value of Fmoc-FFpY was determined by mixing 100 μL of the peptide solution and 100 μL of *S. aureus* suspension with a final optical density of OD = 0.001. To form the Fmoc-FFY hydrogel, 100 μL of the peptide solution (at different concentrations) was mixed with 100 μL of AP solution (1.4 μg.mL^{-1}) and left 24 h at 22°C. MIC value of Fmoc-FFY hydrogel was determined by adding to the hydrogel 200 μL of *S. aureus* inoculation with a final optical density of OD_{620} = 0.001. Fmoc-FFY hydrogel coating samples were built up on glass substrates of 12 mm diameter, placed in 24-well plates and sterilized for 20 min by UV light. 400 μL of *S. aureus* or *E. coli* inoculation (OD_{620} = 0.001) were added to each well and incubated at 37°C for 24 h. In repetitive culture experiments, the supernatant was totally removed and replaced by 400 μL of freshly prepared *S. aureus* or *E. coli* inoculation (OD_{620} = 0.001). Regarding the statistical analysis, all experiments were carried out independently in triplicate and three analyses per replication at least were done. The significant differences in the experimental data were analyzed using the ANOVA procedure (SAS Institute Inc., Cary, NC, United States) at $p < 0.01$ with mean separation determined by Tukey's multiple range tests.

Cell Cytotoxicity Test

Cytotoxicity assays were carried out by incubating the gels with 1 mL of DMEM at 37°C. After 24 and 48 h, the extracts were removed under sterile conditions. Separately, NIH 3T3 mouse embryonic fibroblasts cells were seeded at a density of 1×10^5 cells.mL^{-1} in complete medium in a sterile 24 well culture plate and incubated to confluence. After 24 and 48 h of incubation, the medium was replaced with the corresponding extracts and incubated at 37°C in humidified air with 5% CO_2 for 24 h and 48 h. Subsequently, plates were incubated with 500 μL per well of a MTT solution (0.1% w/v 3-(4,5-dimethylthiozol-2-yl)-2,5-diphenyltetrazolium bromide in Phosphate Buffer Saline) and incubated for 180 min at 37°C. Medium was displaced by 500 μL of DMSO. Optical Density (OD) was measured at 570 nm. The cell viability was calculated from Eq. (1):

$$Cell\ viability\ (\%) = \frac{OD_S - OD_B}{OD_C - OD_B} \cdot 100 \quad (1)$$

where OD_S, OD_B, and OD_C are the optical density for the sample (S), blank (culture medium) (B), and control (glass) (C), respectively.

RESULTS AND DISCUSSION

Physico-Chemical Characterization of Fmoc-FFY Hydrogel Coating

Alkaline phosphatase functionalized silica nanoparticles suspensions were obtained with a solid content of 5% (w/v) and had an average diameter of 132 ± 10 nm (**Supplementary Figure S1**). The suspension showed an activity equivalent to 30 units.mL^{-1} determined using PNP, a model substrate of AP, with a calibration curve (**Supplementary Figure S2**). To immobilize NPs@AP on a planar surface, a PEI-$(PSS/PAH)_2$ polyelectrolyte multilayer film (PEM) was first deposited as precursor film. When NPs@AP suspension is put in contact with the PEM precursor film, a high increase of the normalized frequency shift is observed by QCM-D reaching about 700 Hz after the rinsing steps (**Figure 1A**).

The obtained NPs@AP coating has a catalytic activity equivalent to 0.6 μg.mL^{-1} of AP in solution, corresponding to 0.08 μg.cm^{-2} of active enzyme. AFM images of NPs@AP coating showed round shape NPs all over the surface (**Supplementary Figure S3**). The section profile of the AFM images provides an average diameter of the deposited NPs of 140 nm (**Supplementary Figure S3C**) in agreement with SEM observations (**Supplementary Figure S1**). The NPs@AP coating was then employed as catalytic support for the localized growth of supramolecular peptide by putting it in contact with Fmoc-FFpY solution (1 mg.mL^{-1}) (**Scheme 1**). The Fmoc-FFY self-assembly induced an increase of the frequency shift of about 230 Hz after 3.5 h (**Figure 1A**). The dissipation value reached 400×10^{-6} which is the signature of highly hydrated films (**Figure 1B**). In contrast, NPs@AP coating had a dissipation value of 130×10^{-6}. By decreasing Fmoc-FFpY concentration of the solution in contact with NPs@AP coating, the final frequency shift decreased reaching 100 Hz at 0.5 and 0.25 mg.mL^{-1} and 50 Hz at 0.1 mg.mL^{-1}. This was corroborated by the decrease of the dissipation value (**Supplementary Figures S4A,B**). As a control experiment, the contact of a non-self-assembling peptide, Fmoc-G-OH (1 mg.mL^{-1}), with the NPs@AP coating induces an increase of 43 Hz of the frequency shift (**Supplementary Figures S4C,D**). Fmoc-G-OH peptide is probably physisorbed on the surface such as Fmoc-FFpY when the concentration is lower than 0.1 mg.mL^{-1}.

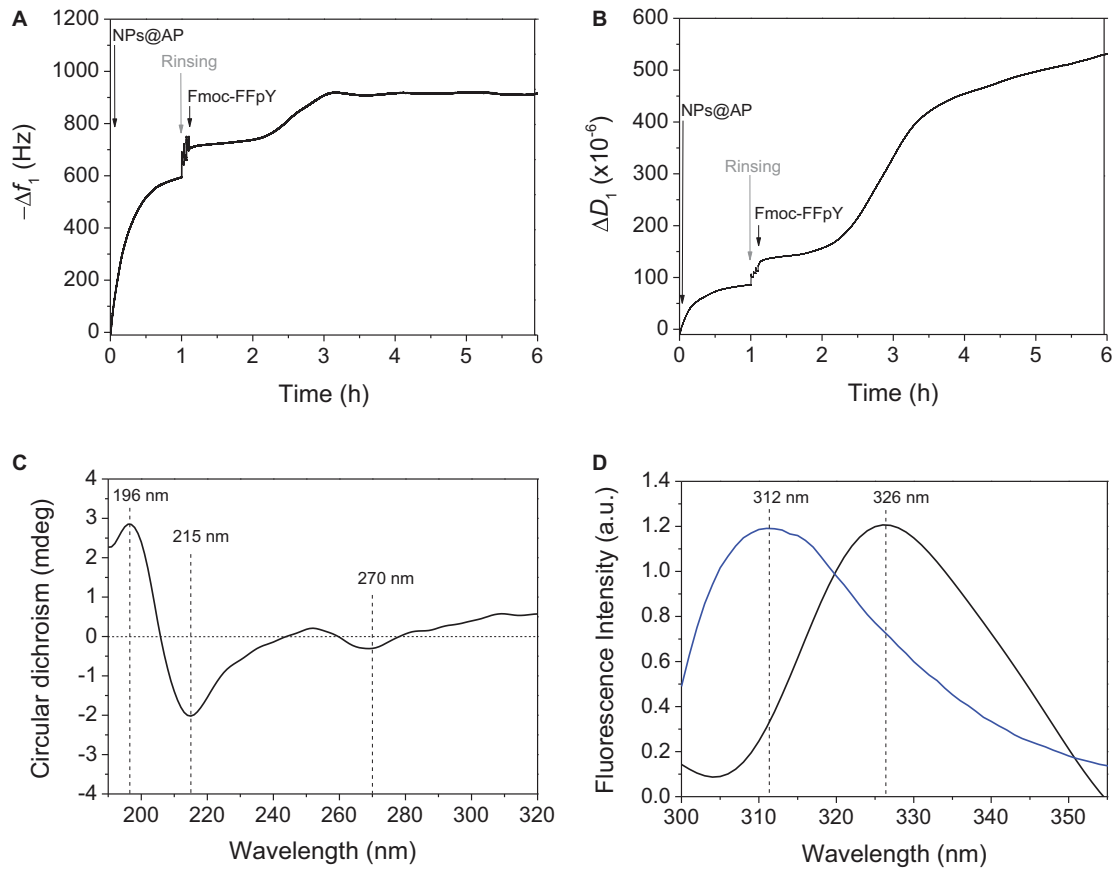

FIGURE 1 | Evolution of the **(A)** fundamental frequency shift and **(B)** dissipation value, measured by QCM-D at 5 MHz, during the deposition of NPs@AP on PEM precursor film, leading to NPs@AP coating, followed by the contact with Fmoc-FFpY solution leading to the Fmoc-FFY hydrogel coating. **(C)** Circular Dichroism and **(D)** Fluorescence emission (λ_{ex} = 290 nm) spectra of Fmoc-FFY hydrogel coating (black curve) and Fmoc-FFpY solution (blue curve).

The structural organization of Fmoc-FFY self-assembled on NPs@AP coating, named Fmoc-FFY hydrogel coating, was investigated by CD (**Figure 1C** and **Supplementary Figure S5**). The CD spectrum shows a positive band at 196 nm and a strong negative band at 215 nm characteristics of β-sheets structures (Smith et al., 2008). The presence of a negative band at 270 nm is assigned to offset face-to-face stacking of the Fmoc moieties which is not observed in the case of non-self-assembling Fmoc-FFpY in solution (Ryan et al., 2010). The excimer formation of Fmoc moieties was checked after Fmoc-FFY self-assembly by fluorescence spectroscopy (Tang et al., 2011; Criado-Gonzalez et al., 2019b). When excited at 290 nm, Fmoc-FFpY solution have a fluorescence emission peak at 312 nm due to fluorenyl moieties (**Figure 1D**). The self-assembly of Fmoc-FFY on NPs@AP coating induced a shift of this peak up to 326 nm, due to fluorenyl excimers.

Morphological Characterization of Fmoc-FFY Deposited Hydrogel

The morphology of the Fmoc-FFY hydrogel coating was visualized by Cryo-SEM (**Figure 2**). The cross-section of the coating showed three different areas. The magnification of the bottom part allowed to distinguish monolayer and multilayers of round shape NPs@AP, with a size of ∼ 120 nm determined using ImageJ, on the surface of the glass slide (**Figure 2B**). It can be noticed that there is no diffusion of NPs@AP throughout the whole Fmoc-FFY hydrogel after 16 h in contact (dashed line in **Figure 2B**). Fmoc-FFY fibers grow from the NPs@AP giving rise to a hydrogel coating with a thickness of ∼ 5 μm. A gradient of organic matter is observed in the self-assembled Fmoc-FFY hydrogel with two different areas (**Figure 2A**). Higher density of fibers is close to the bottom, in direct contact NPs@AP, and a lower density on the upper part of the Fmoc-FFY hydrogel. A magnification of the upper part allows to distinguish long fibers of micrometer length oriented in the vertical direction perpendicular to the substrate (**Figure 2C**). Fmoc-FFY fibers have a diameter ranging from 13 to 40 nm (red arrows in **Figure 2C**).

Antimicrobial Properties of Fmoc-FFY Hydrogel Coating

Before to study the antibacterial properties of the Fmoc-FFY hydrogel coating, the stability of the hydrogel was tested in contact with bacteria culture medium. For that purpose,

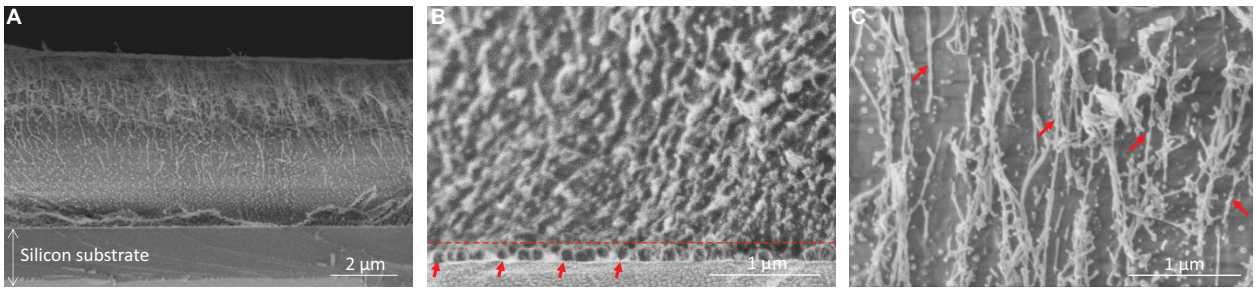

FIGURE 2 | Cryo-SEM images of **(A)** Fmoc-FFY hydrogel self-assembled on NPs@AP coating, **(B)** zoom-in of the bottom area to show the localization of the NPs@AP delimited with a dashed line and highlighted with red arrows and **(C)** zoom-in of the upper part showing Fmoc-FFY fibers (red arrows).

Fmoc-FFY hydrogel was formed in a vial by mixing Fmoc-FFpY solution and NPs@AP suspension. The inverted tube test indicated the formation of a gel after 24 h (**Supplementary Figure S6**). The hydrogel remains stable up to 9 days in contact with MH culture medium. To underline the necessity of the enzymatic dephosphorylation of the peptide, the antibacterial properties of Fmoc-FFpY and Fmoc-FFY hydrogel were studied against Gram-positive *S. aureus* in RPMI media at different concentrations in peptide (**Figure 3A**). Bacteria quantification (in colony forming unit per mL, CFU.mL^{-1}) was performed at time zero and 24 h after the incubation with the samples and presented in $\log_{10}$ reduction. At 1 mg.mL^{-1}, 3-$\log_{10}$ (99%) reduction bacterial load against *S. aureus* is obtained for Fmoc-FFpY peptide, whereas 4-$\log_{10}$ (99.99%) reduction were achieved with Fmoc-FFY hydrogel, obtained by dephosphorylation of the peptide. At lower peptide concentrations ($\leq$0.5 mg.mL^{-1}), the antibacterial property of Fmoc-FFpY is lost whereas Fmoc-FFY hydrogel showed 3-$\log_{10}$ (99%) reduction of *S. aureus* suspension up to 0.1 mg.mL^{-1} of peptide. The self-assembly of the peptide ensure the antibacterial effect at low concentration. Bare NPs@AP coatings did not prevent the proliferation of the bacteria (**Supplementary Figure S7**). The antibacterial effect of the Fmoc-FFY hydrogel coating, self-assembled on NPs@AP at different concentrations in Fmoc-FFpY, was tested against *S. aureus* (**Figure 3B**). After 24 h of contact, Fmoc-FFY hydrogel coatings demonstrated efficacy of more than 4-$\log_{10}$ (99.99%) reduction of bacterial load against *S. aureus* whatever the concentration of peptide used for their self-assembly up to 0.1 mg.mL^{-1}. To mimic the worst conditions of repetitive bacterial infections, for example in the case of urinary or venous catheter-associated infections, the bacterial inoculation in contact with the hydrogel coating was completely renewed every 24 h. At least 3-$\log_{10}$ (99%) reduction of *S. aureus* was observed for the second culture in contact with Fmoc-FFY hydrogel coating self-assembled with 1 mg.mL^{-1} Fmoc-FFpY. At lower concentration in peptide, the second culture with *S. aureus* showed between 2 and 1-$\log_{10}$ (90%) reduction. In the following culture, a significant decrease in efficiency is detectable with 1-log reduction only with 1 mg.mL^{-1}. Fmoc-FFY hydrogel coating, self-assembled with 1 mg.mL^{-1} Fmoc-FFpY, showed only 1-log reduction of bacterial load against Gram-negative *E. coli* after 24 h with no significant inhibition at the second culture (**Figure 3C**). A selective antibacterial effect of Fmoc-FFY hydrogel coating was observed against *S. aureus* Gram-positive bacteria in contrast to *E. coli* Gram-negative bacteria.

The mechanism of action of Fmoc-FFY hydrogels could be attributed to a combination of two factors: the fibrillary β-sheet structure of the self-assembly and the peptide hydrophobicity as it was reported for β-amyloid peptides (Kagan et al., 2012; Last and Miranker, 2013). Pioneering works of Moir and coll. demonstrated the antimicrobial activity of Alzheimer's β-amyloid peptides *in vitro* and *in vivo* (Soscia et al., 2010; Kumar et al., 2016). Diphenylalanine moieties (FF), identified as the core recognition motif of β-amyloid peptides, were reported to self-assemble in discrete and stiff nanotubes adopting β-sheet structures (Reches and Gazit, 2003). Self-assembled FF peptides have the ability to bind to the surface of bacterial membrane, to aggregate and to orient themselves to optimize hydrophilic/hydrophobic interactions, inducing a surface tension leading to membrane depolarization, pore formation and release of cellular content (Schnaider et al., 2017). Moreover, FF peptides also induce upregulation of stress response regulons at sub-lethal concentration causing severe damage to bacterial morphology. Recently, the antibacterial activity of self-assembled Fmoc-F was attributed to the peptide release from the hydrogel inducing oxidative and osmotic stress as well as altering bacterial membrane integrity (Gahane et al., 2018). The comparison of Fmoc-FF cationic peptide, designed with a pyridinium moiety at the C-terminal, with other Fmoc-cationic peptides showed that the proximity of fluorenyl and phenyl moieties achieves an optimum hydrophobicity environment improving the antibacterial activity (Debnath et al., 2010). In summary, the antibacterial property of the Fmoc-FFY hydrogel coating could be explained by the ability of the β-sheet self-assembled nanofibers to bind and aggregate on the surface of the bacterial membrane, altering the membrane integrity and also to oxidative and osmotic stresses leading to the death of the bacteria. This mechanism is confirmed by the efficiency of peptide self-assembly at low concentration in comparison to the non-self-assembled peptide. In contrast to Gram-positive, Gram-negative bacteria have an additional outer bilayer membrane, formed by lipopolysaccharides and phospholipids, that makes difficult the diffusion of molecules across the membrane and renders them more resistant to break (Haldar et al., 2005). The cytotoxicity of the Fmoc-FFY gel was determined *in vitro*, through a MTT indirect test, employing NIH 3T3 mouse embryonic fibroblasts

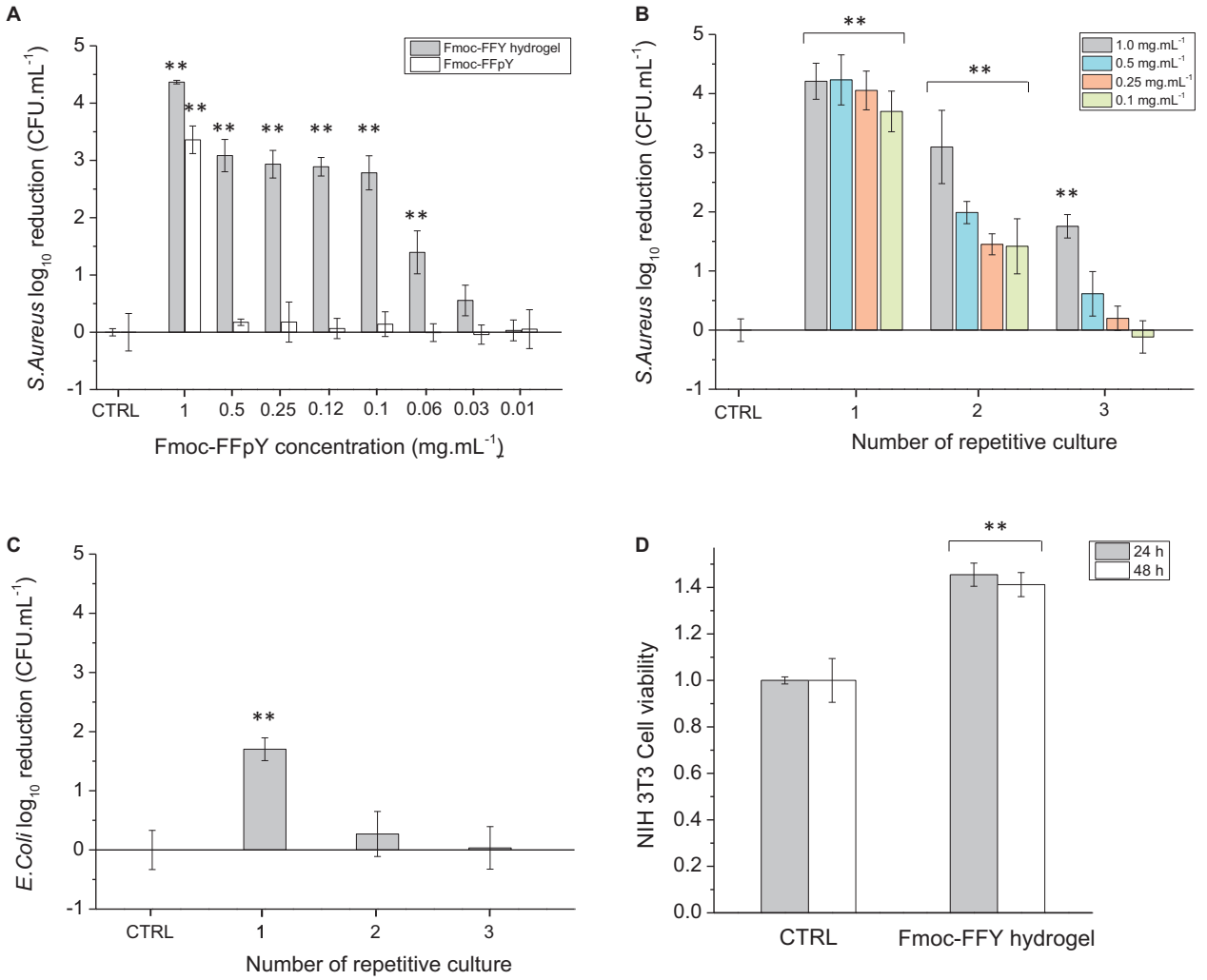

FIGURE 3 | Colony-forming unit (CFU) $\log_{10}$ reduction on planktonic **(A)** *S. aureus* cells incubated in the presence of different concentrations of Fmoc-FFpY and of Fmoc-FFY hydrogel, self-assembled with different concentrations of Fmoc-FFpY, **(B)** *S. aureus* cells incubated on Fmoc-FFY hydrogel coatings, self-assembled with different concentrations of Fmoc-FFpY on NPs@AP coating and **(C)** *E. coli* cells incubated on Fmoc-FFY hydrogel coating, self-assembled with 1 $mg.mL^{-1}$ Fmoc-FFpY solution on NPs@AP coating, as a function of the number of repetitive culture. The coating was brought in contact with a fresh pathogen suspension for 24 h. In repetitive culture experiments, the supernatant was removed and replaced every 24 h by a fresh suspension. **(D)** Cytotoxicity assay of Fmoc-FFY gel through MTT indirect test using NIH 3T3 mouse embryonic fibroblasts cells. Uncoated glass substrates were employed as controls (CTRL). Diagrams include the results from three independent experiments in triplicate and results are shown as mean ± s.e.m. and the ANOVA results at a significance level of $^{**}p < 0.01$ vs. uncoated glass (negative control, CTRL).

cells (**Figure 3D**). NIH 3T3 cell viability do not show any decrease of up to 48 h proving that Fmoc-FFY gel is not cytotoxic. This result confirmed the absence of toxicity of Fmoc-FF peptides when they are in self-assembled form (Truong et al., 2015). Besides, Fmoc-FF peptides have been used as 3-D cell culture scaffolds for chondrocytes (Jayawarna et al., 2006) or astrocytes (Liebmann et al., 2007).

CONCLUSION

In this work a phosphorylated peptide, Fmoc-FFpY, able to be solubilized in water at room temperature, was transformed in Fmoc-FFY hydrogelator by action of NPs@AP immobilized on a surface. The hydrogel coating, based on fibers homogeneously distributed all around the sample, was efficient to prevent *S. aureus* growth with 4-$\log_{10}$ of viable bacteria. This coating could serve in infections were Gram positive bacteria are prevalent, e.g., intravascular catheter infections. This kind of antibacterial self-assembled hydrogel represents a very simple and efficient method to coat biomaterial surfaces for protection against bacteria proliferation. In clinical practice to ensure the integrity of the hydrogel coating, one idea would be to trigger the peptide self-assembly *in situ* after implantation of the medical device by addition of the peptide solution near the enzyme functionalized implant surface. With the prospect of

long-term use of the antibacterial coating, the surface triggered self-assembly of peptide could be done on porous surfaces or even inside the pores of foams. The high surface of coverage, obtained on rough or porous implants, could lead to sustained antibacterial property as the coating maintained its property even after being in contact several times with fresh inoculated *S. aureus* suspension. Moreover in a curative strategy, the peptide self-assembly could be triggered by using enzymes naturally secreted by bacteria to obtain the antibacterial gel either inside the cells or at their surface using overexpression of phosphatase by bacteria (Yang et al., 2007) or by mammalian cancer cells (Pires et al., 2015).

DATA AVAILABILITY STATEMENT

All datasets presented in this study are included in the article/**Supplementary Material**.

AUTHOR CONTRIBUTIONS

PS and FB conceived the project. MC-G, LJ, PS, and FB designed the experiments. MC-G carried out the preparation of all samples under study, QCM-D analyses, gelation tests, circular dichroism, and fluorescence spectroscopy characterization. MI performed the AFM characterization and bacteria tests. MC-G, MI, and FB contributed to the interpretation of the results. AC and MS carried out the SEM and cryo-SEM experiments. All authors contributed to the article and approved the submitted version.

FUNDING

MI thanks the Higher Education Commission (HEC) Pakistan for his Ph.D. scholarship. We gratefully acknowledge the financial support from the Agence Nationale de la Recherche (EASA, ANR-18-CE06-0025-03).

ACKNOWLEDGMENTS

ICS microscopy and characterization platforms are acknowledged for the use of the SEM and the fluorescence spectroscopy, respectively.

SUPPLEMENTARY MATERIAL

The Supplementary Material for this article can be found online at: https://www.frontiersin.org/articles/10.3389/fbioe.2020.00938/full#supplementary-material

REFERENCES

Aggeli, A., Bell, M., Carrick, L. M., Fishwick, C. W. G., Harding, R., Mawer, P. J., et al. (2003). pH as a trigger of peptide β-Sheet self-assembly and reversible switching between nematic and isotropic phases. *J. Am. Chem. Soc.* 125, 9619–9628. doi: 10.1021/ja021047i

Barth, E., Myrvik, Q. M., Wagner, W., and Gristina, A. G. (1989). In vitro and in vivo comparative colonization of *Staphylococcus aureus* and *Staphylococcus epidermidis* on orthopaedic implant materials. *Biomaterials* 10, 325–328. doi: 10.1016/0142-9612(89)90073-2

Basavalingappa, V., Guterman, T., Tang, Y., Nir, S., Lei, J., Chakraborty, P., et al. (2019). Expanding the functional scope of the fmoc-diphenylalanine hydrogelator by introducing a rigidifying and chemically active urea backbone modification. *Adv. Sci.* 6:1900218. doi: 10.1002/advs.201900218

Bowerman, C. J., and Nilsson, B. L. (2010). A reductive trigger for peptide self-assembly and hydrogelation. *J. Am. Chem. Soc.* 132, 9526–9527. doi: 10.1021/ja1025535

Cassini, A., Plachouras, D., Eckmanns, T., Abu Sin, M., Blank, H.-P., Ducomble, T., et al. (2016). Burden of six healthcare-associated infections on european population health: estimating incidence-based disability-adjusted life years through a population prevalence-based modelling study. *PLoS Med.* 13:e1002150. doi: 10.1371/journal.pmed.1002150

Chen, L., Pont, G., Morris, K., Lotze, G., Squires, A., Serpell, L. C., et al. (2011). Salt-induced hydrogelation of functionalised-dipeptides at high pH. *Chem. Commun.* 47, 12071–12073.

Collier, J. H., Hu, B. H., Ruberti, J. W., Zhang, J., Shum, P., Thompson, D. H., et al. (2001). Thermally and photochemically triggered self-assembly of peptide hydrogels. *J. Am. Chem. Soc.* 123, 9463–9464. doi: 10.1021/ja011535a

Criado-Gonzalez, M., Fores, J. R., Carvalho, A., Blanck, C., Schmutz, M., Kocgozlu, L., et al. (2019a). Phase separation in supramolecular hydrogels based on peptide self-assembly from enzyme-coated nanoparticles. *Langmuir* 35, 10838–10845. doi: 10.1021/acs.langmuir.9b01420

Criado-Gonzalez, M., Rodon Fores, J., Wagner, D., Schröder, A. P., Carvalho, A., Schmutz, M., et al. (2019b). Enzyme-assisted self-assembly within a hydrogel induced by peptide diffusion. *Chem. Commun.* 55, 1156–1159. doi: 10.1039/c8cc09437c

Criado-Gonzalez, M., Loftin, B., Rodon Fores, J., Vautier, D., Kocgozlu, L., Jierry, L., et al. (2020a). Enzyme assisted peptide self-assemblies trigger cell adhesion in high density oxime based host gels. *J. Mater. Chem. B* 8, 4419–4427. doi: 10.1039/d0tb00456a

Criado-Gonzalez, M., Wagner, D., Rodon Fores, J., Blanck, C., Schmutz, M., Chaumont, A., et al. (2020b). Supramolecular hydrogel induced by electrostatic interactions between polycation and phosphorylated-fmoc-tripeptide. *Chem. Mater.* 32, 1946–1956. doi: 10.1021/acs.chemmater.9b04823

Darouiche, R. O. (2004). Treatment of infections associated with surgical implants. *N. Engl. J. Med.* 350, 1422–1429. doi: 10.1056/nejmra035415

Debnath, S., Shome, A., Das, D., and Das, P. K. (2010). Hydrogelation through self-assembly of fmoc-peptide functionalized cationic amphiphiles: potent antibacterial agent. *J. Phys. Chem. B* 114, 4407–4415. doi: 10.1021/jp909520w

Gahane, A. Y., Ranjan, P., Singh, V., Sharma, R. K., Sinha, N., Sharma, M., et al. (2018). Fmoc-phenylalanine displays antibacterial activity against Gram-positive bacteria in gel and solution phases. *Soft Matter.* 14, 2234–2244. doi: 10.1039/c7sm02317k

Haldar, J., Kondaiah, P., and Bhattacharya, S. (2005). Synthesis and antibacterial properties of novel hydrolyzable cationic amphiphiles. incorporation of multiple head groups leads to impressive antibacterial activity. *J. Med. Chem.* 48, 3823–3831. doi: 10.1021/jm049106l

Jayawarna, V., Ali, M., Jowitt, T. A., Miller, A. F., Saiani, A., Gough, J. E., et al. (2006). Nanostructured hydrogels for three-dimensional cell culture through self-assembly of fluorenylmethoxycarbonyl-dipeptides. *Adv. Mater.* 18, 611–614. doi: 10.1002/adma.200501522

Kagan, B. L., Jang, H., Capone, R., Teran Arce, F., Ramachandran, S., Lal, R., et al. (2012). Antimicrobial properties of amyloid peptides. *Mol. Pharm.* 9, 708–717. doi: 10.1021/mp200419b

Kaplan, J. B. (2011). Antibiotic-induced biofilm formation. *Int. J. Artif. Organs* 34, 737–751. doi: 10.5301/ijao.5000027

Kumar, D. K. V., Choi, S. H., Washicosky, K. J., Eimer, W. A., Tucker, S., Ghofrani, J., et al. (2016). Amyloid-β peptide protects against microbial infection in mouse and worm models of Alzheimer's disease. *Sci. Transl. Med.* 8, 1–15.

Last, N. B., and Miranker, A. D. (2013). Common mechanism unites membrane poration by amyloid and antimicrobial peptides. *Proc. Natl. Acad. Sci. U.S.A.* 110:6382. doi: 10.1073/pnas.1219059110

Liebmann, T., Rydholm, S., Akpe, V., and Brismar, H. (2007). Self-assembling Fmoc dipeptide hydrogel for in situ 3D cell culturing. *BMC Biotechnol.* 7:88. doi: 10.1186/1472-6750-7-88

Lombardi, L., Falanga, A., Del Genio, V., and Galdiero, S. (2019). A new hope: self-assembling peptides with antimicrobial activity. *Pharmaceutics* 11:166. doi: 10.3390/pharmaceutics11040166

Mahler, A., Reches, M., Rechter, M., Cohen, S., and Gazit, E. (2006). Rigid, self-assembled hydrogel composed of a modified aromatic dipeptide. *Adv. Mater.* 18, 1365–1370. doi: 10.1002/adma.200501765

Makam, P., and Gazit, E. (2018). Minimalistic peptide supramolecular co-assembly: expanding the conformational space for nanotechnology. *Chem. Soc. Rev.* 47, 3406–3420. doi: 10.1039/c7cs00827a

McCloskey, A. P., Draper, E. R., Gilmore, B. F., and Laverty, G. (2017). Ultrashort self-assembling Fmoc-peptide gelators for anti-infective biomaterial applications. *J. Pept. Sci.* 23, 131–140. doi: 10.1002/psc.2951

McCloskey, A. P., Gilmore, B. F., and Laverty, G. (2014). Evolution of antimicrobial peptides to self-assembled peptides for biomaterial applications. *Pathogens* 3, 791–821. doi: 10.3390/pathogens3040791

Paladini, F., Meikle, S. T., Cooper, I. R., Lacey, J., Perugini, V., and Santin, M. (2013). Silver-doped self-assembling di-phenylalanine hydrogels as wound dressing biomaterials. *ı J. Mater. Sci. Mater. Med.* 24, 2461–2472. doi: 10.1007/s10856-013-4986-2

Pires, R. A., Abul-Haija, Y. M., Costa, D. S., Novoa-Carballal, R., Reis, R. L., Ulijn, R. V., et al. (2015). Controlling cancer cell fate using localized biocatalytic self-assembly of an aromatic carbohydrate amphiphile. *J. Am. Chem. Soc.* 137, 576–579. doi: 10.1021/ja5111893

Raeburn, J., Pont, G., Chen, L., Cesbron, Y., Lévy, R., and Adams, D. J. (2012). Fmoc-diphenylalanine hydrogels: understanding the variability in reported mechanical properties. *Soft Matter.* 8, 1168–1174. doi: 10.1039/c1sm06929b

Reches, M., and Gazit, E. (2003). Casting metal nanowires within discrete self-assembled peptide nanotubes. *Science* 300:625. doi: 10.1126/science.1082387

Rupp, M. E., and Archer, G. L. (1994). Coagulase-negative *Staphylococci*: pathogens associated with medical progress. *Clin. Infect. Dis.* 19, 231–245. doi: 10.1093/clinids/19.2.231

Ryan, D. M., Anderson, S. B., Senguen, F. T., Youngman, R. E., and Nilsson, B. L. (2010). Self-assembly and hydrogelation promoted by F5-phenylalanine. *Soft Matter.* 6, 475–479. doi: 10.1039/b916738b

Schnaider, L., Brahmachari, S., Schmidt, N. W., Mensa, B., Shaham-Niv, S., Bychenko, D., et al. (2017). Self-assembling dipeptide antibacterial nanostructures with membrane disrupting activity. *Nat. Commun.* 8: 1365.

Séon, L., Lavalle, P., Schaaf, P., and Boulmedais, F. (2015). Polyelectrolyte multilayers: a versatile tool for preparing antimicrobial coatings. *Langmuir* 31, 12856–12872. doi: 10.1021/acs.langmuir.5b02768

Smith, A. M., Williams, R. J., Tang, C., Coppo, P., Collins, R. F., Turner, M. L., et al. (2008). Fmoc-Diphenylalanine Self assembles to a hydrogel via a novel architecture based on π-π interlocked β-sheets. *Adv. Mater.* 20, 37–41. doi: 10.1002/adma.200701221

Soscia, S. J., Kirby, J. E., Washicosky, K. J., Tucker, S. M., Ingelsson, M., Hyman, B., et al. (2010). The Alzheimer's disease-associated amyloid β-protein is an antimicrobial peptide. *PLoS One* 5:e9505. doi: 10.1371/journal.pmed.1009505

Tang, C., Ulijn, R. V., and Saiani, A. (2011). Effect of glycine substitution on fmoc-diphenylalanine self-assembly and gelation properties. *Langmuir* 27, 14438–14449. doi: 10.1021/la202113j

Truong, W. T., Su, Y., Gloria, D., Braet, F., and Thordarson, P. (2015). Dissolution and degradation of Fmoc-diphenylalanine self-assembled gels results in necrosis at high concentrations in vitro. *Biomater. Sci.* 3, 298–307. doi: 10.1039/c4bm00244j

Vigier-Carrière, C., Wagner, D., Chaumont, A., Durr, B., Lupattelli, P., Lambour, C., et al. (2017). Control of surface-localized, enzyme-assisted self-assembly of peptides through catalyzed oligomerization. *Langmuir* 33, 8267–8276. doi: 10.1021/acs.langmuir.7b01532

Yang, Z., Gu, H., Fu, D., Gao, P., Lam, J. K., and Xu, B. (2004). Enzymatic formation of supramolecular hydrogels. *Adv. Mater.* 16, 1440–1444. doi: 10.1002/adma.200400340

Yang, Z., Liang, G., Guo, Z., Guo, Z., and Xu, B. (2007). Intracellular hydrogelation of small molecules inhibits bacterial growth. *Angew. Chem. Int. Edn.* 46, 8216–8219. doi: 10.1002/anie.200701697

Yang, Z., and Xu, B. (2006). Using enzymes to control molecular hydrogelation. *Adv. Mater.* 18, 3043–3046. doi: 10.1002/adma.200600400

Zhao, F., Gao, Y., Shi, J., Browdy, H. M., and Xu, B. (2011). Novel anisotropic supramolecular hydrogel with high stability over a wide pH range. *Langmuir* 27, 1510–1512. doi: 10.1021/la103982e

Conflict of Interest: The authors declare that the research was conducted in the absence of any commercial or financial relationships that could be construed as a potential conflict of interest.

frontiers in Materials

ORIGINAL RESEARCH
published: 27 November 2020
doi: 10.3389/fmats.2020.578411

Evaluating the Toxicity of Ionic Liquids on *Shewanella* sp. for Designing Sustainable Bioprocesses

Hakima Kebaili[1,2], Antonia Pérez de los Ríos[1], María José Salar-García[3]*, Víctor Manuel Ortiz-Martínez[3]*, Mostefa Kameche[2], Jesús Hernández-Fernández[1] and Francisco J. Hernández-Fernández[1]**

[1]Department of Chemical Engineering, Faculty of Chemistry, University of Murcia (UMU), Murcia, Spain, [2]Laboratory of Physico-Chemistry of Materials, Catalysis and Environment, Faculty of Chemistry, University of Sciences and Technology of Oran-Mohamed Boudiaf, Oran, Algeria, [3]Department of Chemical and Environmental Engineering, Technical University of Cartagena (UPCT), Campus La Muralla, Cartagena, Spain

OPEN ACCESS

Edited by:
Emilia Morallon,
University of Alicante, Spain

Reviewed by:
Adil Denizli,
Hacettepe University, Turkey
Guillermo Díaz-Sainz,
University of Cantabria, Spain

***Correspondence:**
María José Salar-García
mariajose.salar@upct.es
Francisco J. Hernández-Fernández
fjhernan@um.es
Hakima Kebaili
kebailihakima@gmail.com
Víctor Manuel Ortiz-Martínez
victor.ortiz@upct.es

Specialty section:
This article was submitted to Biomaterials, a section of the journal Frontiers in Materials

Received: 01 July 2020
Accepted: 13 October 2020
Published: 27 November 2020

Citation:
Kebaili H, Pérez de los Ríos A, Salar-García MJ, Ortiz-Martínez VM, Kameche M, Hernández-Fernández J and Hernández-Fernández FJ (2020) Evaluating the Toxicity of Ionic Liquids on Shewanella sp. for Designing Sustainable Bioprocesses. Front. Mater. 7:578411. doi: 10.3389/fmats.2020.578411

Ionic liquids (ILs) are widely used as reaction and separation media in many technologies due to their unique and advantageous physicochemical properties. Thus, further studies approaching the study of the toxicity of these materials are required. Moreover, they are utilized in devices in which microorganisms such as *Shewanella* sp. act as biocatalysts. Thus, in this work, the toxicity of 69 ILs on the marine bacterium *Shewanella* sp. was tested. Specifically, the ILs analyzed were based on the cations imidazolium, pyridinium, pyrrolidinium, piperidinium, morpholinium, oxazolinium, phosphonium, ammonium, and sulfonium, in combination with different anions. The toxicities of this wide group of ILs on *Shewanella* sp. were determined using two methods: 1) the agar disk-diffusion test and 2) the growth inhibition test in liquid media. The relationship between toxicity and IL chemical structure was elucidated. A decrease in the hydrophobicity of the alkyl chain length was found to be a key factor to reduce IL toxicity. On the other hand, phosphonium-based ILs containing long alkyl chains were shown to be largely incompatible with *Shewanella* sp.

Keywords: ionic liquids, toxicity, *Shewanella* sp, sustainable materials, biocompatibility

HIGHLIGHTS

- ILs as clean and green alternatives to organic solvents in bioprocesses
- Screening IL toxicity toward *Shewanella* sp. for bioprocess applications
- Analysis of chemical structure contributions to IL toxicity toward *Shewanella* sp.
- Tool for the adequate cation/anion combination to synthesis nontoxic ILs

INTRODUCTION

The genus *Shewanella* was first described in 1931. This microorganism responsible for butter putrefaction was initially named as *Achromobacter putrefaciens* but after further studies and biochemical characterizations, the species isolated in 1931 was then reclassified into a new genus, *Shewanella* (Derby and Hammer, 1931; MacDonell and Colwell, 1985). So far, all members belonging to this genus are facultatively anaerobic, which allows them to survive in a wide variety of environments, although they are usually found in aquatic or marine habitats (Hau

and Gralnick, 2007). One of the main characteristics of the *Shewanella* genus is its capability to grow at low temperatures. Although most of the strains are psychrotolerant with optimum growth temperature above 16°C, many strains are psychrophilic and can easily grow below this temperature (Hau and Gralnick, 2007). The capability of *Shewanella* to use several external electron acceptors to respire, which enables this genus to live in extreme conditions, as well as the possibility of being genetically modified, has boosted its application in a wide variety of technological fields (Hau and Gralnick, 2007; Marsili et al., 2008; Zou et al., 2019), from bioremediation of polluted environments (Varia et al., 2014; Zhang et al., 2018) and biosensing (Webster et al., 2014) to bioenergy production in microbial fuel cell technology (Jorge and Hazael, 2016; Kumar et al., 2016).

Ionic liquids (ILs) are combinations of cations (i.e., imidazolium, pyridinium, and ammonium) and anions (i.e., hexafluorophosphate, tetrafluoroborate, and bis [(trifluoromethyl)sulfonyl]imide) that remain liquid at temperatures below 100°C. In recent years, these compounds have drawn the attention of the scientific community due to their unique properties such as negligible vapor pressure, chemical and thermal stability, nonflammability, high ionic conductivity, wide electrochemical potential window, and solvation ability, among other features (Ventura et al., 2012b). ILs are also considered clean and green alternatives to organic solvents mainly due to their low vapor pressure, which prevents their release into the atmosphere. Besides, their physical and chemical properties can be adapted to specific applications by the fine-tuning of the cation structure and by selecting proper cation-anion combinations. Since a wide variety of ion combinations are possible, it is of the highest importance to outline rational guidelines to develop technologically suitable but also environmentally harmless ILs (Latała et al., 2009).

The emergence of ILs as solvents has instigated several new and exciting areas of scientific research including organic synthesis (Welton, 1999; Earle et al., 2008), catalysis (Welton, 1999; Pârvulescu and Hardacre, 2007), electrodeposition (Endres, 2002; Zein El Abedin et al., 2006; El Abedin and Endres, 2007), dye-sensitized solar cells (Gorlov and Kloo, 2008), and lubrication (Ye et al., 2001). Moreover, within the field of nanotechnology, ILs have been synthesized with finely tuned nanoscopic structures for the preparation of polymers (Haddleton et al., 2008; Kim et al., 2008), nanoparticles (Dupont et al., 2002; Schrekker et al., 2007), nanotubes (Barisci et al., 2004; Shim and Kim, 2009), and microemulsions (Eastoe et al., 2005; Qiu and Texter, 2008). ILs are currently being investigated worldwide for cutting edge applications, especially for electrochemical devices and energy production such as lithium batteries (Sakaebe et al., 2005; Ishikawa et al., 2006), electrochemical capacitors (Balducci et al., 2005), electrochemical actuators (Ding et al., 2003), and light-emitting electrochemical cells (Yang et al., 2003). In the field of biocatalysis, ILs have been used free of solvent (Toral et al., 2007; de los Ríos et al., 2012; Lee et al., 2015), adsorbed (Hernández et al., 2006; Lee et al., 2007; Jiang et al., 2009; Zou et al., 2014), and covalently linked to particles enzymes (Lozano et al., 2010; Suo et al., 2018; Xiang et al., 2018) or as polymeric ILs (Nakashima et al., 2009) in enzyme particles, in all cases to create an adequate enzyme microenvironment and improve the catalytic efficiency (Hernández et al., 2006; Toral et al., 2007; Lozano et al., 2010; de los Ríos et al., 2012; Lee et al., 2015). ILs and *Shewanella* sp. have been recently used together in microbial fuel cell technology for bioenergy production (Zhao et al., 2013; Wei et al., 2016) and the biofabrication of nanoparticles (Wang et al., 2018). Due to the enormous range of IL application and the multiple benefits of including bacteria in certain types of bioprocesses, it is crucial to address the biocompatibility of IL-based materials for progress in the design of sustainable processes.

In this context, this work investigates the biocompatibility of ILs containing different cation and anion structures toward *Shewanella* sp. Thus, the toxicity of a total number of 69 ILs based on imidazolium, pyridinium, pyrrolidinium, piperidinium, morpholinium, oxazolinium, phosphonium, ammonium, and sulfonium combined with different anions has been analyzed in solid and liquid media. The results obtained are in-depth discussed and related to the structural characteristic of the ILs, which enables identifying key factors for the design of environmentally friendly ILs with lower ecotoxicological risks than conventional organic solvents.

MATERIALS AND METHODS

Ionic Liquids

The ILs investigated in the current work are grouped according to the type of cation present in their structure. **Tables 1–8** include the name of each IL analyzed, together with its structure and water solubility. These tables also include the nomenclature used for each IL (abbreviation name). All ILs were supplied by IoLiTec (Ionic Liquids Technologies).

Culture of *Shewanella* sp.

The strain of *Shewanella* sp. was provided by the Aquatic Ecology Laboratory (University of Murcia, Spain) and kept on Luria-Bertani Agar (LB). A single colony was used to grow the inoculum on LB broth at 25°C with shaking at 200 rpm. All chemicals and media reagents were purchased from Sigma-Aldrich.

Toxicity Analysis

The toxicity of 69 ILs toward *Shewanella* sp. was analyzed by using two different methods: 1) agar disk-diffusion test and 2) toxicity in liquid media. Both methods are described below.

Agar Disk-Diffusion Test

The agar disk-diffusion method was used for the first time in 1940 by Heatley (Heatley, 1944) being now the most common technique for determining the antimicrobial properties of many compounds (Balouiri et al., 2016). So far, a wide variety of bacteria has been successfully tested by this method by varying the culture media and the incubation conditions as well as the evaluation criteria for the inhibition zones (Clinical and Laboratory Standards Institute, 2015). This method consists of

TABLE 1 | Imidazolium-based ionic liquids.

Full name	Abbreviation name	Structure	Water miscibility	State 25 °C	Ref.	Inhibition zone/cm	μ/% in LB broth
1-(2-Hydroxypropyl)-methylimidazolium chloride	[HOPmim$^+$][Cl$^-$]	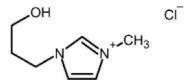	Soluble	Liquid	Pérez De Los Ríos et al., 2017	0	73.65 ± 2.69
1-Butyl-3-methylimidazolium chloride	[Bmim$^+$][Cl$^-$]	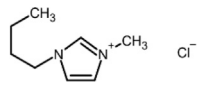	Soluble	Solid	Dharaskar et al., 2013	0	30.51 ± 1.29
1-Hexyl-3-methylimidazolium chloride	[Hmim$^+$][Cl$^-$]	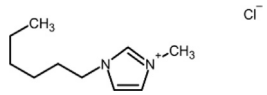	Soluble	Liquid	Pérez De Los Ríos et al., 2017	0	272.95 ± 9.93
1-Ethyl-3-methylimidazolium tetrafluoroborate	[Emim$^+$][BF$_4^-$]	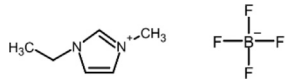	Soluble	Liquid	Pérez De Los Ríos et al., 2017	0	40.30 ± 16.53
1-Butyl-3-methylimidazolium tetrafluoroborate	[Bmim$^+$][BF$_4^-$]	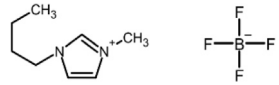	Soluble	Liquid	Dharaskar et al., 2016b	0.7 ± 0.6	0
1-Methyl-3-octylimidazolium tetrafluoroborate	[Moim$^+$][BF$_4^-$]	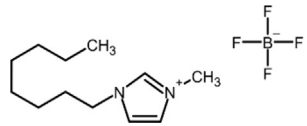	Insoluble decomposition in the presence of water	Liquid	Freire et al., 2007; Galai et al., 2015	2.6 ± 0.1	0
1-Butyl-2,3-dimethylimidazolium tetrafluoroborate	[BDImim$^+$][BF$_4^-$]	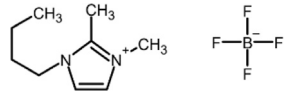	Soluble	Liquid	Pérez De Los Ríos et al., 2017	0	64.20 ± 4.59
1-Methoxymethyl-3-methylimidazolium tetrafluoroborate	[MOMmim$^+$][BF$_4^-$]	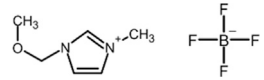	Soluble	Liquid	Pérez De Los Ríos et al., 2017	0	263.74% ± 6.85
1-Methoxyethyl-3-methylimidazolium tetrafluoroborate	[MOEmim$^+$][BF$_4^-$]	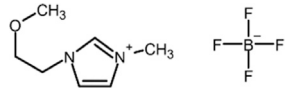	Insoluble	Liquid	Pérez De Los Ríos et al., 2017	0	34.74 ± 18.82
1-Butyl-3-methylimidazolium hexafluorophosphate	[Bmim$^+$][PF$_6^-$]	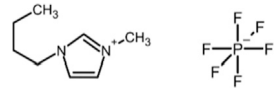	Insoluble	Liquid	Carda–Broch et al., 2003	2.9 ± 0.1	0 (RWM)

(Continued on following page)

TABLE 1 | (*Continued*) Imidazolium-based ionic liquids.

Full name	Abbreviation name	Structure	Water miscibility	State 25 °C	Ref.	Inhibition zone/cm	μ/% in LB broth
1-Methyl-3-octylimidazolium hexafluorophosphate	[Omim$^+$][PF_6^-]	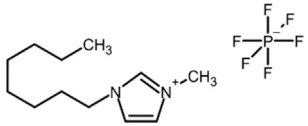	Insoluble decomposition in the presence of water	Liquid	Freire et al., 2007; Iolitec, 2014; Galai et al., 2015	2.6 ± 0.2	24.19% ± 6.25
1-Methoxymethyl-3-methylimidazolium hexafluorophosphate	[MOMmim$^+$][PF_6^-]	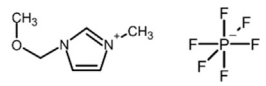	Soluble	Solid	Galai et al., 2015	1.5 ± 0.0	24.16 ± 4.37
1-(Ethoxyethyl)-3-methylimidazolium hexafluorophosphate	[EOEmim$^+$][PF_6^-]	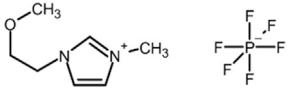	Soluble	Solid	Pérez De Los Ríos et al., 2017	2.0 ± 0.4	45.92 ± 14.12
1-Butyl-3-methylimidazolium nitrate	[Bmim$^+$][NO_3^-]	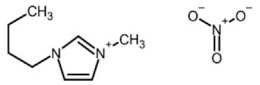	Soluble	Liquid	Pérez De Los Ríos et al., 2017	0	102.80 ± 3.46
1-(2-Hydroxypropyl)-3-methylimidazolium nitrate	[HOPmim$^+$][NO_3^-]	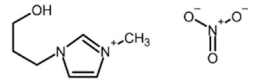	Soluble	Liquid	Pérez De Los Ríos et al., 2017	0.5 ± 0.0	0
1-Butyl-3-methylimidazolium acetate	[Bmim$^+$][CH_3COO^-]	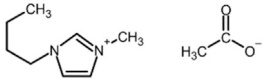	Soluble	Liquid	Pérez De Los Ríos et al., 2017	0.8 ± 0.0	0
1-Butyl-3-methylimidazolium glycolate	[Bmim$^+$][CH_2OHCOO^-]	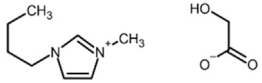	Soluble	Liquid	Pérez De Los Ríos et al., 2017	0.5 ± 0.0	30.17 ± 8.57
1-Butyl-3-methylimidazolium methylcarbonate	[Bmim$^+$][$MeCOO_2^-$]	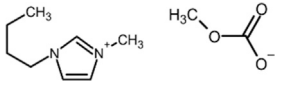	Soluble	Liquid	Galai et al., 2015	1.5 ± 0.4	0
1-Butyl-3-methylimidazolium thiocyanate	[Bmim$^+$][SCN^-]	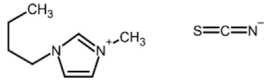	Insoluble	Liquid	Dharaskar et al., 2016a	1.5 ± 0.0	0
1-Ethyl-3-methylimidazolium dicyanamide	[Emim $^+$][dca$^-$]	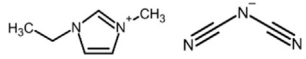	Soluble	Liquid	Pérez De Los Ríos et al., 2017	0	24.13 ± 11.44

(Continued on following page)

TABLE 1 | (*Continued*) Imidazolium-based ionic liquids.

Full name	Abbreviation name	Structure	Water miscibility	State 25 °C	Ref.	Inhibition zone/cm	μ/% in LB broth
1-Butyl-3-methylimidazolium dicyanamide	[Bmim$^+$][dca$^-$]	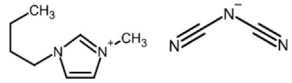	Soluble	Liquid	(Papaiconomou et al., 2006)	1.6 ± 0.2	0
1-Hexyl-3-methylimidazolium dicyanamide	[Hmim$^+$][dca$^-$]	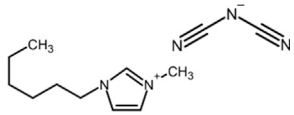	Soluble	Liquid	Pérez De Los Ríos et al., 2017	3.0 ± 0.0	0
1-Methyl-3-octylimidazolium dicyanamide	[Omim$^+$][dca$^-$]	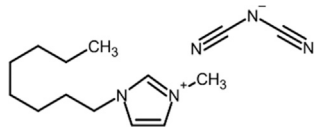	Soluble	Liquid	Papaiconomou et al., 2006	3.9 ± 0.1	0
1-Methoxymethyl-3-methylimidazolium dicyanamide	[MOMmim$^+$][dca$^-$]	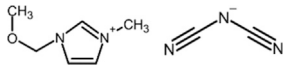	Soluble	Liquid	Galai et al., 2015	0	309.75 ± 0.78
1-Methoxyethyl-3-methylimidazolium dicyanamide	[MOEmim$^+$][dca$^-$]	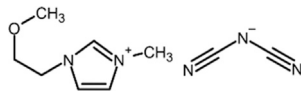	Soluble	Liquid	Galai et al., 2015	1.5 ± 0.0	0
1-Butyl-3-methylimidazolium hydrogen sulfate	[Bmim$^+$][HSO_4^-]	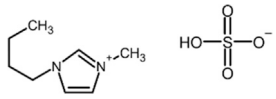	Soluble	Liquid	Galai et al., 2015	0.9 ± 0.0	0
1,2,3-Trimethylimidazolium methylsulfate	[$(CH_3)_3IM^+$][$CH_3SO_4^-$]	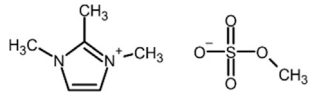	Partly soluble	Solid	Santa Cruz Biotechnology, Inc., 2012	0.7 ± 1.0	116.19 ± 24.70
1-(Ethoxyethyl)-3-methylimidazolium trifluoromethanesulfonate (triflate)	[EOEmim$^+$][$CF_3SO_3^-$]	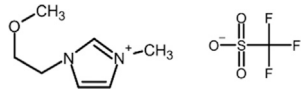	Soluble	Liquid	Missoun et al., 2020	3.5 ± 0.7	0
1-Butyl-3-methylimidazolium 1,1,2,2-tetrafluoroethanesulfonate	[Bmim$^+$][TFES$^-$]	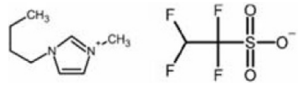	Soluble	Liquid	Zhang et al., 2016	0.7 ± 0.0	13.58 ± 1.93

(Continued on following page)

TABLE 1 | (*Continued*) Imidazolium-based ionic liquids.

Full name	Abbreviation name	Structure	Water miscibility	State 25 °C	Ref.	Inhibition zone/cm	μ/% in LB broth
1-Ethyl-3-methylimidazolium bis[(trifluoromethyl) sulfonyl]imide	[Emim$^+$][NTf$_2^-$]	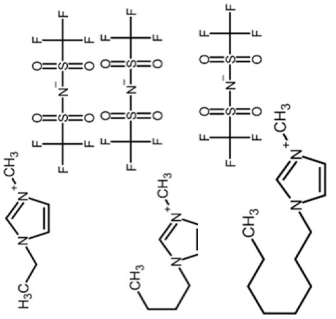	Insoluble	Liquid	Zhou et al., 2012	0.7 ± 0.3	0
1-Butyl-3-methylimidazolium bis[(trifluoromethyl) sulfonyl]imide	[Bmim$^+$][NTf$_2^-$]		Insoluble	Liquid	Papaiconomou et al., 2006	1.0 ± 0.1	0
1-Methyl-3-octylimidazolium bis[(trifluoromethyl) sulfonyl]imide	[Omim$^+$][NTf$_2^-$]		Insoluble	Liquid	Papaiconomou et al., 2006	2.3 ± 0.4	0

inoculating agar plates with a standardized inoculum of a specific microorganism. Then, the test compound embedded in small pieces of filter paper was placed on the agar surface and the Petri dishes were incubated under suitable conditions for the growth of the microorganisms. Finally, the antimicrobial activity of the test compound was evaluated according to the diameter of the inhibition growth zone. Although this method is not entirely satisfactory to determine the minimum inhibitory concentration (MIC), it brings many advantages over other techniques such as its simplicity and suitability to assess the compatibility between a wide variety of compounds and microorganisms as well as its low cost (Balouiri et al., 2016).

Due to the great interest of the scientific community in the search for new and safe applications of ILs, the agar disk-diffusion method has also been used to determine the biocompatibility of these green solvents (Rebros et al., 2009; Ventura et al., 2012a). Thus, this procedure was selected to evaluate the inhibitory capacity of a wide variety of ILs on the growth of *Shewanella* sp. To this end, 100 μl of *Shewanella* sp. culture incubated overnight was spread on an LB agar plate. Each IL was added to sterile, preweighted disks of filter paper (around 6 mm of diameter), and then placed on the surface of the Petri agar dish. ILs in solid-state were weighed and then sterile-distilled water was added dropwise until the salt was completely dissolved. An aliquot of 5 μl of the salt solution was added to the disk of filter paper and the amount embedded ranged between 0.004 and 0.0125 g. All Petri dishes were incubated overnight in a static incubator at 25°C, and the radius of the inhibition zone around the filter paper was measured according to Rebros et al. (2009). Each IL was tested in triplicate and the inhibition zones reported in the present work are the average of the three replicates unless otherwise stated.

Toxicity in Liquid Media

To delve into the biocompatibility of the ILs with *Shewanella* sp., an alternative method based on measuring the growth rates in LB broth medium containing yeast extract, peptone, glucose, and NaCl in the presence and absence of IL was used. In order to decrease the viscosity, water-miscible ILs were weighed and mixed with sterile-distilled water to produce a stock solution (95% w/v). Viscous ILs along with those with unusual phase behavior were also prepared in the same way. The stock solutions were vortexed before adding an aliquot of 40 μl to the microcultures up to a final concentration of 2% (v/v). Nonviscous water-immiscible ILs were added directly to the cultures by volumetric measurement to produce a biphasic system 2% v/v. The cultures were inoculated with 100 μl from an overnight culture of *Shewanella* sp. grown in the same medium. The flasks were incubated for 24 h at 25°C with continuous and intensive shaking.

The optical density (OD) of each culture was measured every 2 h and the growth curve was determined for each case. The specific growth rate (μ, h^{-1}) was calculated by selecting two points at times t_1 and t_2 in the exponential growth phase and applying the following equation:

$$\mu = \frac{\ln\,(OD_2/OD_1)}{t_1 - t_2}.$$

TABLE 2 | Pyridinium-based ionic liquids.

Full name	Abbreviation name	Structure	Water miscibility	State 25°C	Ref.	Inhibition zone/cm	μ/% in LB broth
1-Butyl-3-methylpyridinium tetrafluoroborate	[$BMPy^+$][BF_4^-]	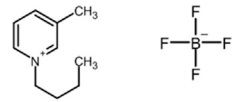	Soluble	Liquid	Ortega et al., 2007; Galai et al., 2015	0	232.69 ± 4.22
1-Butyl-3-methylpyridinium dicyanamide	[$BMPy^+$][dca^-]	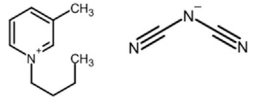	Soluble	Liquid	Bandrés et al. 2008; Kalčíková et al., 2012; Galai et al., 2015	1.0 ± 0.0	155.18 ± 34.40
1-Methyl-3-octylpyridinium dicyanamide	[$MOPy^+$][dca^-]	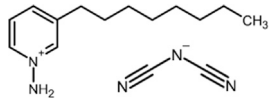	Insoluble	Liquid	Galai et al., 2015	1.1 ± 0.0	0
1-Methylpyridinium methylsulfate	[MPy^+][$MeSO_4^-$]	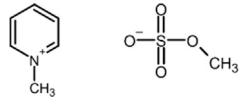	Soluble	Solid	Galai et al., 2015	0	170.77 ± 9.85
1,4 dimethyl pyridinium methylsulfate	[$MMPy^+$][Me SO_4^-]	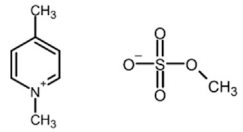	Soluble	Solid	Galai et al., 2015	1.8 ± 0.4	317.77 ± 9.99
1-Ethylpyridinium ethyl sulfate	[EPy^+][$EtSO_4^-$]	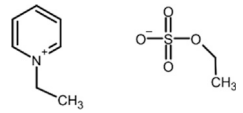	Soluble	Liquid	Benito et al., 2014; Galai et al., 2015	0	286.16 ± 10.19
1-Ethylpyridinium bis [(trifluoromethyl)sulfonyl]imide	[EPy^+][NTf_2^-]	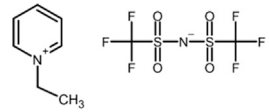	Insoluble	Liquid	Benito et al., 2014; Galai et al., 2015; Iolitec, 2015b	0.9 ± 0.0	19.68 ± 5.83

TABLE 3 | Pyrrolidinium-based ionic liquids.

Full name	Abbreviation name	Structure	Water miscibility	State 25 °C	Ref.	Inhibition zone/cm	μ/% in LB broth
1-Butyl-1-methyl pyrrolidinium chloride	[$BMPyr^+$][Cl^-]	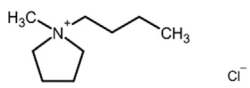	Soluble	Solid	Galai et al., 2015; Iolitec, 2015a	0.9 ± 0.0	0
1-Butyl-1-methyl pyrrolidinium hexafluorophosphate	[$BMPyr^+$][PF_6^-]	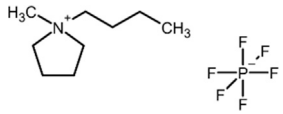	Insoluble	Solid	Iolitec, 2011c; Ventura et al., 2013	0.8 ± 0.0	0
1-Butyl-1-methyl pyrrolidinium dicyanamide	[$BMPyr^+$][dca^-]	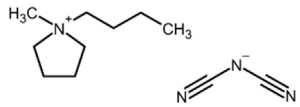	Soluble	Liquid	Iolitec, 2011b; Cumicheo et al., 2015	0	88.78 ± 14.74
1-Butyl-1-methyl pyrrolidinium triflate	[$BMPyr^+$][TFO^-]	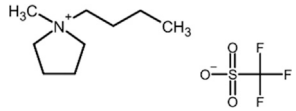	Soluble	Liquid	Iolitec, 2012b; Fadeeva et al., 2015	0	106.33 ± 4.44
1-Ethyl-1-methyl pyrrolidinium bis[(trifluoromethyl)sulfonyl]imide	[$EMPyr^+$][NTf_2^-]	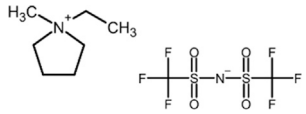	Insoluble	Solid	Galai et al., 2015; Iolitect, 2011	1.3 ± 0.3	0
1-Butyl-1-methyl pyrrolidinium bis[(trifluoromethyl)sulfonyl]imide	[$BMPyr^+$][NTf_2^-]	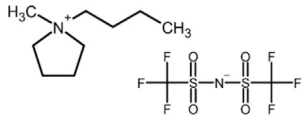	Insoluble	Liquid	Iolitec, 2011a; Fadeeva et al., 2015	2.2 ± 1.2	14.33 ± 6.31

TABLE 4 | Piperidinium-based ionic liquids.

Full name	Abbreviation name	Structure	Water miscibility	State at 25 ˚C	Ref.	Inhibition zone/cm	μ/% in LB broth
1-Butyl-1-methylpiperidinium bis[(trifluoromethyl)sulfonyl] imide	[$BMPi^+$][NTf_2^-]	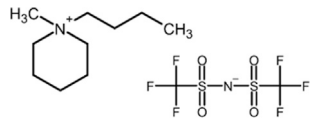	Insoluble	Liquid	Iolitec, 2012a; Galai et al., 2015	1.6 ± 0.1	0

TABLE 5 | Morpholinium-based ionic liquids.

Full name	Abbreviation name	Structure	Water miscibility	State at 25 ˚C	Ref.	Inhibition zone/cm	μ/% in LB broth
Ethyl methyl morpholinium dicyanamide	[$EMMOR^+$][dca^-]	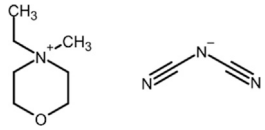	Soluble	Liquid	Russina et al., 2013; Peréz de los Ríos et al., 2017	0	3.95 ± 1.72

TABLE 6 | Oxazolinium-based ionic liquids.

Full name	Abbreviation name	Structure	Water miscibility	State at 25 ˚C	Ref.	Inhibition zone/cm	μ/% in LB broth
Methyloxazolinium methylsulfate	[$Moxa^+$][$MeSO_4^-$]	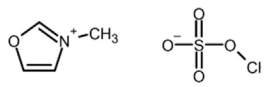	Soluble	Liquid	Galai et al., 2015; Peréz de los Ríos et al., 2017	1.1 ± 0.3	25.35 ± 2.79

TABLE 7 | Ammonium-based ionic liquids.

Full name	Abbreviation name	Structure	Water miscibility	State at 25 °C	Ref.	Inhibition zone/cm	μ/% in LB broth
Methyltrioctylammonium chloride	$[N_{8,8,8,1}^{+}][Cl^{-}]$	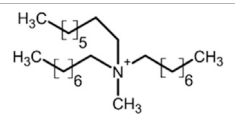	Insoluble	Liquid	Sigma Aldrich, 2006; Galai et al., 2015	3.0 ± 0.7	0
Choline dihydrogen phosphate	$[Chol^{+}][H_2PO_4^{-}]$	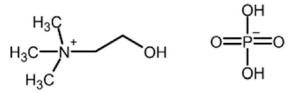	Soluble	Solid	Iolitec, 2012c; Galai et al., 2015	0	146 ± 0.15
N,N-dimethylbutylammonium 2-hexyldecanoate	$[N_{4,1,1,0}^{+}]$ $[C_8C_6CHCOO^{-}]$	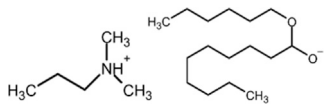	Soluble	Liquid	Walker, 2009	0.5 ± 0.7	0
Methyltrioctylammonium trifluoromethanesulfonate	$[N_{\mathbf{8,8,8,1}}^{+}]$ $[CF_3SO_3^{-}]$	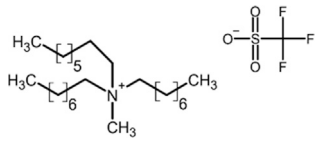	Insoluble	Solid	Iolitec, 2012d; Galai et al., 2015	1.4 ± 0.5	179.23 ± 6.72
Cocosalkylpentaethoximethylammonium methylsulfate	[C1EG]	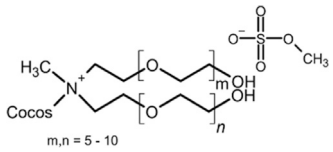	Soluble	Liquid	Galai et al., 2015; Iolitec, 2015d	3.5 ± 0.7	0
Tallowsalkylpentaethoximethylammonium methylsulfate	[C1EG1]	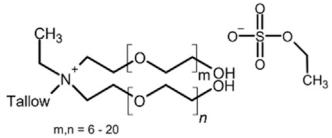	Insoluble	Liquid	Iolitec, 2010; Galai et al., 2015	2.8 ± 0.1	0
TEGO®-IL-P9	[221PG]	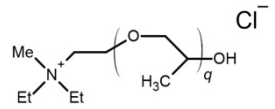	Soluble	Liquid	Galai et al., 2015; Iolitec, 2015c	0	39.12 ± 3.16
Choline bis[(trifluoromethyl)sulfonyl]imide	$[Chol^{+}][NTf_2^{-}]$	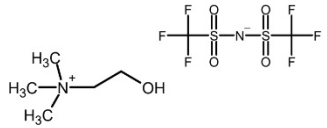	Insoluble	Liquid	Nockemann et al., 2009; Galai et al., 2015; Iolitec, 2016	1.2 ± 0.7	36 ± 18

TABLE 8 | Phosphonium-based ionic liquids.

Full name	Abbreviation name	Structure	Water miscibility	State at 25 °C	Ref.	Inhibition zone/cm	μ/% in LB broth
Tetradecyl(trihexyl)phosphonium chloride	$[P_{6,6,6,14}^{+}][Cl^{-}]$	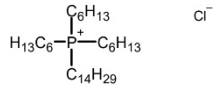	Insoluble	Liquid	Iolitec, 2011g; Galai et al., 2015	1.0 ± 0.0	27.72 ± 3.06
Tetradecyl(trihexyl)phosphonium bromide	$[P_{\mathbf{6,6,6,14}}^{+}][Br^{-}]$	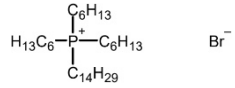	Insoluble	Liquid	Iolitec, 2011f; Galai et al., 2015	5.5 ± 2.8	0
Tetraoctylphosphonium bromide	$[P_{\mathbf{8,8,8,8}}^{+}][Br^{-}]$	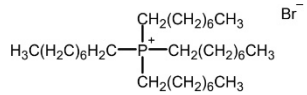	Insoluble	Solid	Galai et al., 2015; Iolitec, 2015e	1.0 ± 0.0	0
Tetradecyl(trihexyl)phosphonium tetrafluoroborate	$[P_{14,\ 6,6,6}^{+}][BF_4^{-}]$	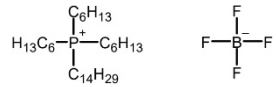	Insoluble	Liquid	Åkerstedt et al., 2013; Galai et al., 2015	1.8 ± 0.4	108.30 ± 20.08
Tetrabutylphosphonium dibutyl phosphate	$[P_{4,4,4,4}^{+}][\ Bu_2Phos^{-}]$	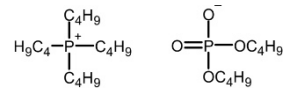	Soluble	Solid	Zhou et al., 2002; Galai et al., 2015	0.9 ± 0.2	75.94 ± 7.29
Trihexyl(tetradecyl)phosphonium bis-2,4,4-(trimethylpentyl)phosphinate	$[P_{6,6,6,14}^{+}][TMPPhos^{-}]$	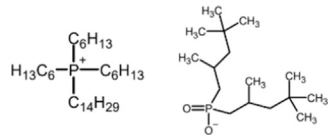	Insoluble	Liquid	Galai et al., 2015; Iolitec, 2018	2.6 ± 0.1	0
Trihexyl (tetradecyl)phosphonium decanoate	$[P_{6,6,6,14}^{+}][C_9COO^{-}]$	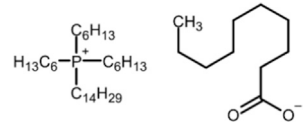	Insoluble	Liquid	Iolitec, 2013b; Galai et al., 2015	1.5 ± 0.2	0
Tetradecyl (trihexyl)phosphonium dicyanamide	$[P_{6,6,6,14}^{+}][dca^{-}]$	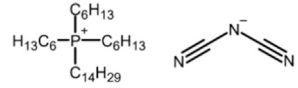	Insoluble	Liquid	Iolitec, 2011h; Galai et al., 2015	0.8 ± 0.1	32.28 ± 1.92
Tributylmethylphosphonium methylsulphate	$[P_{4,4,4,1}^{+}][CH_3SO_4^{-}]$	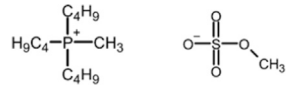	Soluble	Solid	Iolitec, 2013a; Galai et al., 2015	1.0 ± 0.0	0
Trihexyl (tetradecyl)phosphonium bis [trifluoromethyl) sulfonyl]imide	$[P_{6,6,6,14}^{+}][NTf_2^{-}]$	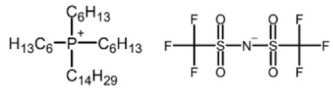	Insoluble	Liquid	Iolitec, 2011e; Galai et al., 2015	1.2 ± 0.2	0

(Continued on following page)

TABLE 8 | (*Continued*) Phosphonium-based ionic liquids.

Full name	Abbreviation name	Structure	Water miscibility	State at 25 °C	Ref.	Inhibition zone/cm	μ/% in LB broth
Trisobutyl (methyl)phosphonium tosylate	$[P_{(4,4,4)1}^{+}][TOS^{-}]$	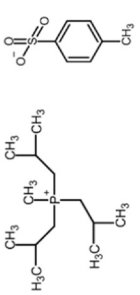	Soluble	Liquid	Iolitec, 2011i; Galai et al., 2015	1.0 ± 0.1	0
Tributyltetradecylphosphonium dodecylbenzenesulfonate	$[(C_4H_9)3(C_{14}H_{29})P^{+}]$ $[C_{12}H_{25}C_6H_4SO_3^{-}]$	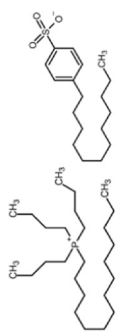	Insoluble	Liquid	Iolitec, 2011d; Galai et al., 2015	2.3 ± 0.4	0

This parameter is shown as a percentage of the growth rate in control cultures without ILs. The specific growth rates in % (μ) are reported as a percentage of the growth rate in control cultures grown without ILs (μ_0 = 0.13 h^{-1}) applying the following equation:

$$\mu(\%) = (\mu^{*}100)/\mu_0.$$

The specific growth rates reported are the mean of triplicate, unless otherwise stated.

RESULTS AND DISCUSSION

As preliminary information, three types of inhibition were observed in the presence of ILs. The first type corresponds to symmetric inhibition when the IL diffused correctly in the agar-agar (**Figure 1A**). In other cases, the asymmetric inhibition zones offer a variable zone of clearance, rather than a uniform circle around the filter paper, which can be attributed to nonuniform diffusion (**Figure 1B**) (Rebros et al., 2009). Finally, there are several ILs that do not form an inhibition zone (**Figure 1C**). The results obtained with the agar diffusion test were compared with the toxicity test in liquid media. As an example, **Figure 2** shows the effect of different ILs on the growth of *Shewanella* sp. The strain was grown in LB broth with and without the respective ILs (2% v/v). The results show that the three ILs displayed $[Chol^{+}][H_2PO_4^{-}]$, $[Bmim^{+}][Cl^{-}]$, and $[BMPyr^{+}][TFO^{-}]$ are not toxic toward the strain. Moreover, stimulation of bacterial growth (the bacteria utilize the ILs as growth factor) can be obtained. Uninoculated controls with IL are also presented. The means of three replicates are shown with standard deviation error bars.

The effect of the ILs on pH change was checked in cultures and inoculated controls using a universal indicator (20 ml) added before and after growth. In general, the influence on pH was small (changes of < 0.5 pH units). On the other hand, as can be expected, the toxicity effect is variable and greatly depends on the chemical structure of each IL. **Tables 1–8** include the ILs studied and are organized by type of cation. The structure of the IL and its water solubility, the inhibition zone, and the specific growth rate (μ, h^{-1}) are also presented. The influence of the alkyl substituent of the cation and the type of the cation and anion are systematically analyzed below with the aim to establish toxicity-structure relationships.

Influence of the Alkyl Substituent of the Cation of Ionic Liquid on Toxicity Toward *Shewanella* sp.

Although there are no data available in the literature related to the toxicity of ILs toward *Shewanella* sp., several works have shown that, for other microorganisms, the toxicity is directly correlated with the chain length of the alkyl substituent in the cation (Couling et al., 2006; Luis et al., 2007; Romero et al., 2008; Pretti et al., 2009; Pérez De Los Ríos et al., 2017). The influence of an increasing chain length of R1 or R2 in the imidazolium cation moiety on the cytotoxicity in marine bacteria and two types of

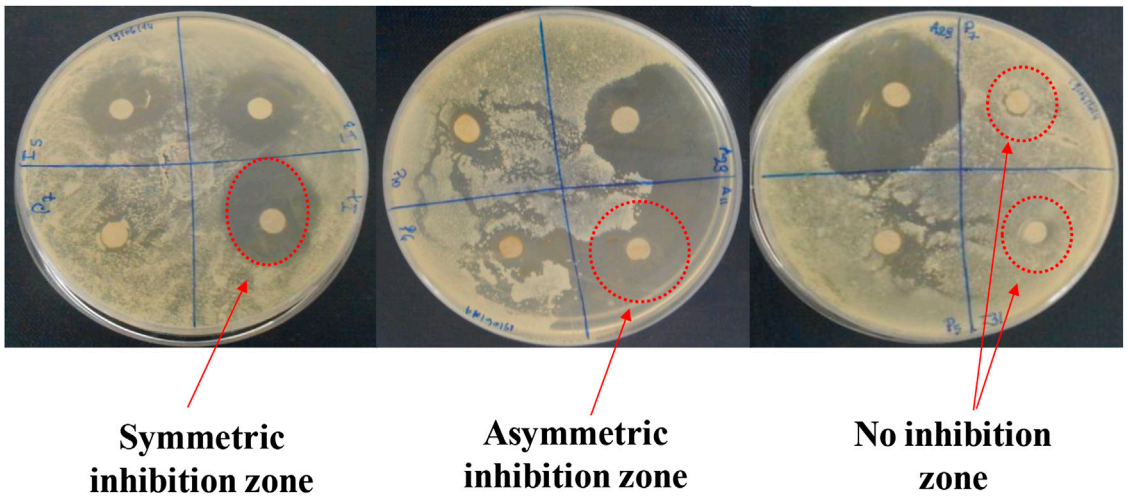

FIGURE 1 | (A) Symmetric inhibition ([C_4mim^+][PF_6^-]), **(B)** asymmetric inhibition ([$N_{8,8,8,1}^+$] [NTf_2^-]), and **(C)** no inhibition zone ([C_2mim^+] [NTf_2^-]) in the agar diffusion test.

mammalian cell cultures was also evident in HeLa cells (Stepnowski et al., 2004; Ranke et al., 2007). This effect is currently known as "side-chain effect" (Matzke et al., 2010). For highly lipophilic cations, cytotoxicity does not significantly increase with lipophilicity anymore. It is well known that lipophilicity relationships with biological activity are only linear over a restricted range (Pernak et al., 2003). For *Shewanella* sp., we also found that behavior. In the case of imidazolium cation combined with dicyanamide, a decrease of the specific growth rate and/or an increase in the inhibition radius was found for the series [$Emim^+$][dca^-], [$Bmim^+$][dca^-], [$Hmim^+$][dca^-], and [$Omim^+$][dca^-] and furthermore from [$MOMmim^+$][dca^-] to [$MOEmim^+$][dca^-]. Increasing inhibition radii as alkyl chain length rises were also obtained in the series [$Emim^+$][NTf_2^-], [$Bmim^+$][NTf_2^-], and [$Hmim^+$][NTf_2^-]. Decreasing specific growth rates with the alkyl chain length was observed from [$MOMmim^+$][BF_4^-] to [$MOEmim^+$][BF_4^-]. For this anion, increasing inhibition radii were found from [$Bmim^+$][BF_4^-] to [$Omim^+$][BF_4^-]. According to these results, a higher hydrophobic character in ILs would increase the possibility of their interaction with cell membrane phospholipid bilayers and the hydrophobic domains of the membrane proteins, leading to the disruption of the membrane physiological functions and, consequently, to cell death (Stepnowski et al., 2004; Latała et al., 2005; Ranke et al., 2007; Hernández-Fernández et al., 2015).

In some cases, the toxicity of ILs shows a slight decrease with the increase in alkyl chain length, for instance, from [$Bmim^+$][Cl^-] to [$Hmim^+$][Cl^-] (considering the specific growth rate) and from [$Bmim^+$][PF_6^-] to [$Omim^+$][PF_6^-] (considering both the inhibition radius and the specific growth rate). In this case, an increase in the alkyl chain length also involves a decrease in water media solubility, reducing the effective concentration of the IL in the medium. Besides, the toxic effect of the ILs could depend on the synergy effect of the combined anion and cation and not exclusively on the cation.

As can be observed from **Table 1**, the inclusion of an oxygen atom in the alkyl substituent of the imidazolium ring can significantly decrease the toxicity of imidazolium-based ILs. In fact, it has been observed that [$HOPmim^+$][Cl^-] (μ = 73.5%) displayed much lower toxic effects than [$Bmim^+$][Cl^-] (μ = 30.5%) and also the toxic effect of [$MOEmim^+$][BF_4^-] (μ = 34.7%) on *Shewanella* was lower than that of [Bmim][BF_4^-] (μ = 0%). This behavior is in agreement with the work by Álvarez-Guerra and Irabien (Alvarez-Guerra and Irabien, 2011), who reported that the presence of oxygenated groups in the structure of cations can lead to a decrease in the ecotoxicity of the IL. In this sense, the presence of oxygen makes the IL more hydrophilic, and therefore, less toxic. On the contrary, the toxicity of [$Bmim^+$][NO_3^-] was higher than the toxicity of [HOPmim][NO_3^-]. The higher water solubility of [$HOPmim^+$][NO_3^-] and consequently the higher effective concentration in water medium might explain this fact.

Effect of the Ionic Liquid Cation on Toxicity Toward *Shewanella* sp.

In order to study the effect of the cation, ILs with the same anion and different cation will be compared. This is the best way to systematically study the toxicity of ILs; however, it is important to point out that toxicity synergy effects could occur between anions and cations, and consequently the sequence of toxicity could be modified for different anion families. In this case, it is difficult to separate individual anion and cation contributions to toxicity. In general and in terms of cation toxicity for other microorganisms, ILs containing aromatic cations, such as imidazolium and pyridinium cations, have shown higher levels of toxicity in comparison to those including nonaromatic cations like pyrrolidinium. A higher hydrophobic character of aromatic cations could increase the possibility of interaction with the cell membrane (Stepnowski et al., 2004; Latała et al., 2005; Ranke et al., 2007). Furthermore, the planarity of the cation

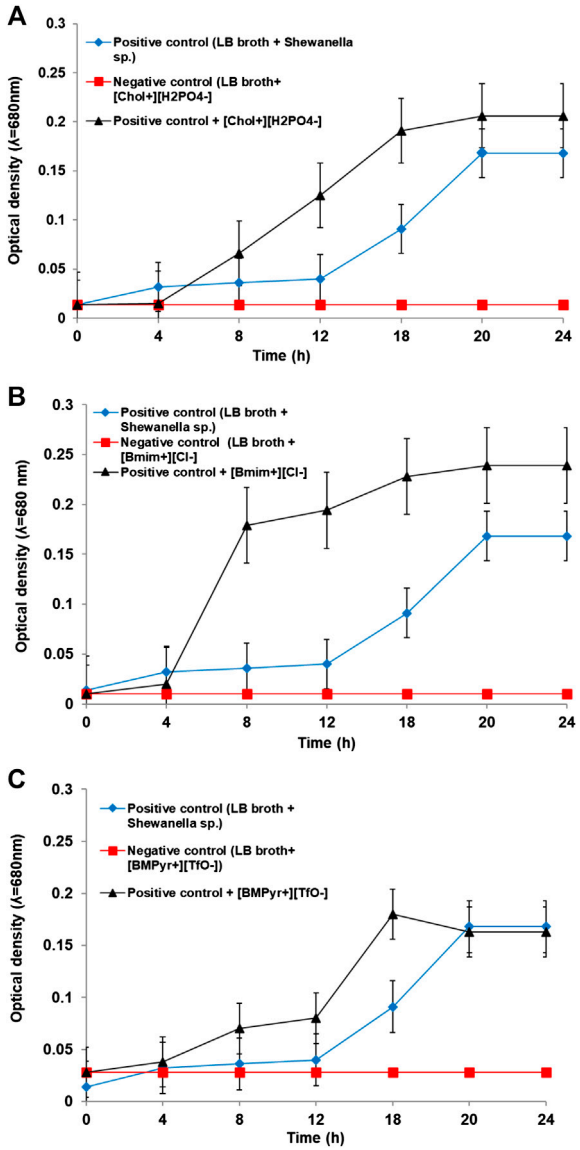

FIGURE 2 | (A) Growth profile of *Shewanella* sp. in LB broth. (■) Negative control (LB+ [Chol$^+$][$H_2PO_4^-$] 2%v/v). (◆) Positive control LB + *Shewanella* sp. (▲) Positive control + [Chol$^+$][$H_2PO_4^-$]. **(B)** Growth profile of *Shewanella* sp. in LB broth. (■) Negative control (LB+ [Bmim$^+$][Cl$^-$] 2%v/v). (◆) Positive control LB + *Shewanella* sp. (▲) Positive control + [Bmim$^+$][Cl$^-$]. **(C)** Growth profile of *Shewanella* sp. in LB broth. (■) Negative control (LB+ [BMPyr$^+$][TFO$^-$] 2%v/v). (◆) Positive control LB + *Shewanella* sp. (▲) Positive control +[BMPyr$^+$][TFO$^-$].

ring in imidazolium and pyridinium appeared to be also a relevant parameter for increasing IL toxicity, as reported in (Viboud et al., 2012). This fact could be due to the lower steric hindrance of the aromatic cation, which may favor the interactions with the lipid membrane to a greater extent.

For *Shewanella* sp., higher toxicity was found for imidazolium cations compared with pyrrolidinium cations in the case of [Bmim$^+$][PF_6^-] vs. [BMPyr$^+$][PF_6^-] (inhibition radius 2.9 vs. 0.8 cm, respectively), [Bmim$^+$][dca$^-$] vs. [BMPyr$^+$][dca$^-$], and [Bmim][NTf_2^-] vs. [BMPyr$^+$][NTf_2^-]. No significant differences were found between [Emim$^+$][NTf_2^-] and [EMPyr$^+$][NTf_2^-]. On the contrary, the toxicity of [Bmim$^+$][NTf_2^-] was lower than the toxicity of [BMPyr$^+$][NTf_2^-]. It is also important to remark the higher toxicity observed for [Bmim$^+$][BF_4^-] compared to the toxicity of [BDImim$^+$][BF_4^-]. The inclusion of the methyl substituent in the R2 position of the imidazolium ring could reduce the acid proton in 2, so lowering the toxicity of the IL.

The effect of pyridinium cations was studied by comparison of imidazolium-based ILs with equal alkyl chain length and anions. In all cases, a higher toxicity was found for the imidazolium cation with respect to the pyridinium cation by comparing [Bmim$^-$][BF_4^+] vs. [BMPy$^+$][BF_4^-], [Bmim$^+$][dca$^-$] vs. [BMPy$^+$][dca$^-$], and [Omim$^+$][dca$^-$] vs. [OMPy$^+$][dca$^-$]. Regarding the piperidinium-based IL studied, [BMPi$^+$][NTf_2^-], there were no significant differences with their homologous imidazolium and pyrrolidinium ones ([Bmim$^+$][NTf_2^-] vs. [BMPyr$^+$][NTf_2^-]. The morpholinium cation in [EMMOR$^+$][dca$^-$] can be compared with [Emin$^+$][dca$^-$]. In both cases, the inhibition radius was zero and the growth rate was higher for the imidazolium-based IL. Matzke et al. (2008) studied the morpholinium compound founding that it only exhibited a moderate effect on the aquatic plant *Lemna minor* and the algae *Scenedesmus vacuolatus*. The oxazolinium cation in [Moxa$^+$][$MeSO_4^-$] can be compared with the pyridinium cation in [MPy$^+$][$MeSO_4^-$]; in this case, the toxicity of the pyridinium cation was lower than that of the [Moxa$^+$] cation, considering both the inhibition radius (0 vs. 1.1 cm, respectively) and the growth rate (170.7 vs. 25.4%, respectively).

For ILs based on the ammonium cation, different toxicity values were found depending on the alkyl chain length of the cation and the type of the anion. The toxicity values ranged from the highest toxicity for C1EG, C1EG1, and [N_{8881}^+][Cl$^-$] (inhibition radius of 3 cm and 0% growth rate) to the lowest toxicity for [N_{8881}^+][$CF_3SO_3^-$] (1.4 cm of inhibition radius and 179% of growth rate). Wood and Stephens (2010) found that quaternary ammonium salts were generally toxic to *E. coli*. However, it was evidenced that decreasing alkyl chain lengths reduced the toxicity. Our experiment reveals that quaternary ammonium salts are generally toxic, maybe due to their high lipophilic character. However, [Chol$^+$][$H_2PO_4^-$] and [221PG] (TEGO®-IL-P9) displayed low toxicity toward the strain tested, not inhibiting the bacterial growth in the agar diffusion test. In these cases, the cation contains heteroatoms and short alkyl chains.

Phosphonium-based ILs have been less frequently studied in comparison to other groups despite their high industrial interest (for example, in biotransformation processes such as xenobiotics degradation) (Cieniecka-Rosłonkiewicz et al., 2005). The toxicity results obtained for the phosphonium family suggest that long alkyl chains promote higher toxic effects toward the bacterium (Matzke et al., 2010). The same result was found by Stolte et al. (2008) for phosphonium cations with longer chains (C12, C16, and C18), with a strong inhibitory potential to the used inoculum. The high toxicity of phosphonium halides against *Vibrio fischeri* was also proved (Couling et al., 2006). However, there are possibilities to decrease the antimicrobial activity using long

alkyl chains, e.g., phosphonium based on alkyl chains of 8 and 14 carbons conjugated with the chloride anion. The exchange of the halide by other anions resulted in a loss of antimicrobial activity (Cieniecka-Rosłonkiewicz et al., 2005). In this study, we found that 9 out of 12 phosphonium ILs were very toxic toward *Shewanella* sp. (large radii of inhibition zone and μ of 0% for the bacterial growth in liquid phase). In the case of phosphonium-based IL, the toxicity values ranged from 5.5 cm of inhibition radius and 0% growth rate ($[P_{14,6,6,6}^+][Br^-]$) to 1.8 cm of inhibition rate and 108.3% of growth rate ($[P_{14,6,6,6}^+][BF_4^-]$). For sulfonium-based ILs, only one compound was assayed, offering high toxicity since no growth of *Shewanella* was observed and the inhibition radius was 1.5 cm.

Effect of the Ionic Liquid Anion on Toxicity toward *Shewanella* sp.

The effect of the anion composition on the toxicity was analyzed by comparing ILs with different anions and the same cation. As commented above, synergy effects between anion and cation can occur, which makes it difficult to completely isolate individual anion and cation contributions. Several authors have reported that the toxicity is directly correlated to the cation nature, while the anion seems to modulate the toxicity to some extent and in specific cases (Ranke et al., 2004; Couling et al., 2006; Luis et al., 2007; Romero et al., 2008; Pretti et al., 2009). We observed this behavior in several ILs in which the toxicity values were similar when sharing the same cation but containing different anions. For example, for the $[Bmim^+]$ family, zero growth rate was obtained for the anions $[PF_6^-]$, $[dca^-]$, $[SCN^-]$, $[MeCOO_2^-]$, $[NTf_2^-]$, $[HSO_4^-]$, $[CH_3COO^-]$, and $[BF_4^-]$ with inhibition radii ranging from 2.9 to 0.7 cm. Stolte et al. (2007a) showed that anions with lipophilicity or susceptible to hydrolysis could offer partially drastic effects. In this group, $[PF_6^-]$ could be included since it can be hydrolyzed in the presence of water, consequently delivering HF to the medium; $[NTf_2^-]$ could be also included due to its hydrophobicity. Growth rate values higher than zero were obtained for $[TFES^-]$, $[Cl^-]$, $[CH_2OHCOO^-]$, and $[NO_3^-]$ (13.6, 30.5, 30, and 102.8, respectively). The $[Cl^-]$ anion yielded low toxicity when combined with other imidazolium cations such as $[HOPmim^-]$ and $[Hmim^-]$. Wood et al. (2011) tested the toxicity of imidazolium cations combined with halides ($[Cl^-]$ $[Br^-]$) toward *E. coli*. The $[Emim^+]$ and $[Bmim^+]$ chlorides and bromides did not produce inhibition zones in the agar diffusion test; however, inhibition zones were observed when the alkyl chain was increased up to six and eight carbons. Short-chained imidazolium salts [EMIM] and [BMIM] with a chloride anion proved weak antimicrobial activity (Łuczak et al., 2010). Therefore, for longer alkyl chain derivatives, the toxicity of the anion can be neglected in comparison to the effects caused by the corresponding cation. On the other hand, for $[Cl^-]$ combined with pyrrolidinium ($[BMPyr^+]$) and ammonium ($[N_{8,8,8,1}^+]$), high toxicity was found. Cornmell et al. (2008) reported that the IL $[N_{1,8,8,8}^+][Cl^-]$ did not allow any growth for *E. coli*. The $[BF_4^-]$ anion gave rate growth values over 30% for $[Emim^+]$ $[MOEmim^+]$, over 100% for $[P_{6,6,6,14}^+]$, and even over 200% for $[MOMmim^+]$ and $[BMPy^+]$; however, nongrowth of *Shewanella* was observed in $[Bmim^+][BF_4^-]$. For other frequent anions such as $[dca^-]$, $[PF_6^-]$, and $[NTf_2^-]$, a wide variety of toxicity values was found, depending on the paired cation. For instance $[dca^-]$ combined with $[Bmim^+]$, $[Emim^+]$, $[Hmim^+]$, $[MOMmim^+]$, $[MOEmim^+]$, $[Omim^+]$, $[BMPy^+]$, $[BMPyr^+]$, or $[P_{6,6,6,14}^+]$ yielded growth rates from 0 to 155%. This fact could be attributed to the dependency of the toxicity values on the IL cation and the possible synergy toxicity effects between the cation and anion.

Choosing the Less Toxic Ionic Liquids for *Shewanella* sp. Applications

Two general possibilities for the joint application of ILs and *Shewanella* sp. in chemical processes are 1) the use of ILs as reaction media in biotechnological processes or 2) the use of ILs as extractants in biphasic systems with *Shewanella* sp. in an aqueous phase. For the first scenario, the key aspect is to find an IL compatible with this bacterium. The results obtained in this study in terms of biocompatibility have been obtained from a wide range of compounds, but they can also help us to qualitatively predict the toxicity of other nonanalyzed ILs. From this work, we can know that several ILs could serve as a medium for *Shewanella* sp. or could be used in different applications such as microbial fuel cells, in which *Shewanella* sp. act as biocatalysts and ILs are used for membrane preparation. Between the biocompatible ILs, we have found the following: $[Hmim^+][Cl^-]$, $[MOMmim^+][BF_4^-]$, $[MOMmim^+][dca^-]$, $[BMPy^+][BF_4^-]$, and $[EPy^+][ETSO_4^-]$. These selected ILs have a growth rate higher than 150% and an inhibition radius equal to zero. It is important to remark that in all cases these ILs were water-soluble, which relates the idea of water solubility to biocompatibility. This is highlighted by the fact that 19 out of 29 insoluble ILs allowed no growth, while only 17 out of 40 water-soluble ILs showed no growth for *Shewanella* sp. Furthermore, only two water-insoluble ILs provided growth rates over 100%, $[N_{8,8,8,1}^+][CF_3SO_3^-]$ and $[P_{6,6,6,14}^+][BF_4^-]$, and in both cases, the inhibition radius was higher than 1.4 cm.

It is important to note that it is hard to find conventional organic solvents that extract polar compounds from the water with high efficiency since they would need to be water-insoluble and polar, two properties barely possible in conventional organic solvents. These limitations can be overcome in the case of using ILs as extractant medium from water solutions. Furthermore, the ILs would have to be biocompatible with *Shewanella* sp. In this case, the two ILs, $[N_{8,8,8,1}^+][CF_3SO_3^-]$ and $[P_{6,6,6,14}^+][BF_4^-]$, could meet both conditions.

Mechanisms of Ionic Liquid Toxicity

Relatively, few mechanisms have been suggested to explain the toxicity of ILs toward marine bacteria, but membrane disruption is considered the most common. ILs at concentrations several orders of magnitude higher than those used in our study have been shown to disrupt synthetic membranes (Sena et al., 2010). In aquatic systems, the side-chain effect could be observed even with the shorter side chains, e.g., IM12 (1-ethyl-3-methyl-imidazolium) and IM14 (1-butyl-3-methyl-imidazolium), which means that the EC50 values for IM12 are higher than

for IM14 (Stolte et al., 2007a; Stolte et al., 2007b). Our results support the membrane disruption mechanism by toxic ILs since, in general, increasing toxicity is observed with increasing IL hydrophobicity and alkyl chain length in the cation (which also contributes to IL hydrophobicity). Furthermore, the inclusion of a heteroatom such as oxygen leads to reducing hydrophobicity and thus toxicity. Nevertheless, other molecular mechanisms cannot be excluded when explaining the toxicity of ILs.

CONCLUSIONS

This work assesses the toxicity of a high number of ILs toward *Shewanella* sp. in order to analyze their biocompatibility and possible joint application for bioprocess implementation. We observed that the adequate combination of cations and anions can make the whole molecule safe for alive bacterial cells in bioprocess devices. Different and wide ion combinations are possible, by selecting cation-anion combinations suitable to specific applications, which highlights the necessity of screening IL toxicity toward the design of biocompatible compounds.

The results obtained allowed establishing several toxicity-structure relationships. According to the results obtained, the immiscibility of ILs in water has an important effect on the toxicity behavior of the ILs since 66% of the water-immiscible ILs tested were highly toxic, whereas only 42% of immiscible ILs were highly toxic. Furthermore, it was observed that the length of the alkyl chain of the cation presented an important impact on IL toxicity. As a general trend, an increase in the alkyl chain length, which involves an increase in the hydrophobicity, contributes to rising IL toxicity.

It was also determined that several ILs could be used as reaction media in the presence of *Shewanella* sp. based on their biocompatibility and water miscibility, specifically $[Hmim^+][Cl^-]$, $[MOMmim^+][BF_4^-]$, $[MOMmim^+][dca^-]$, $[BMPy^+][BF_4^-]$, and $[EPy^+][ETSO_4^-]$. In the case of water-insoluble ILs, $[N_{8,8,8,1}{}^+][CF_3SO_3^-]$ and $[P_{6,6,6,14}{}^+][BF_4^-]$ showed to be suitable ILs for their use as extractant medium for *Shewanella* sp. This work demonstrates the potential combination of IL technology and *Shewanella* sp. The results of this study are encouraging and also suggest that new fields could be explored with *Shewanella* sp. and IL materials.

DATA AVAILABILITY STATEMENT

The original contributions presented in the study are included in the article/supplementary material; further inquiries can be directed to the corresponding authors.

AUTHOR CONTRIBUTIONS

HK: Data curation, formal analysis, investigation, methodology, writing–original draft. AR: conceptualization, resources, funding acquisition, supervision, writing–review and editing. MS and VO: data curation, formal analysis, writing–original draft, writing–review and editing. MK: funding acquisition, supervision. JH: writing–review and editing. FH: conceptualization, funding acquisition, project administration, resources, supervision, writing–original draft, writing–review and editing.

FUNDING

This work has been funded by the Spanish Ministry of Economy and Competitiveness (MINECO) (Grant number: RTI2018-099011-B-I00) and Séneca Foundation (Grant number: 20957/PI/18).

ACKNOWLEDGMENTS

H. Kebaili thanks Erasmus Mundus Program for the fellowship for students' exchange received.

REFERENCES

Åkerstedt, J., Gorlov, M., and Kloo, L. (2013). Room-temperature synthesis of the Bi5[GaCl4]3 salt from three different classes of ionic liquids. *J. Cluster Sci.* 24, 157–164. doi:10.1007/s10876-012-0526-3

Alvarez-Guerra, M., and Irabien, A. (2011). Design of ionic liquids: an ecotoxicity (Vibrio fischeri) discrimination approach. *Green Chem.* 13, 1507–1516. doi:10.1039/c0gc00921k

Balducci, A., Henderson, W. A., Mastragostino, M., Passerini, S., Simon, P., and Soavi, F. (2005). Cycling stability of a hybrid activated carbon//poly(3-methylthiophene) supercapacitor with N-butyl-N-methylpyrrolidinium bis(trifluoromethanesulfonyl) imide ionic liquid as electrolyte. *Electrochim. Acta.* 50, 2233–2237. doi:10.1016/j.electacta.2004.10.006

Balouiri, M., Sadiki, M., and Ibnsouda, S. K. (2016). Methods for *in vitro* evaluating antimicrobial activity: a review. *J. Pharm. Anal.* 6, 71–79. doi:10.1016/j.jpha.2015.11.005

Bandrés, I., Giner, B., Gascón, I., Castro, M., and Lafuente, C. (2008). Physicochemical characterization of n-Butyl-3-methylpyridinium dicyanamide ionic liquid. *J. Phys. Chem. B.* 39, 12461–12467. doi:10.1021/jp805816x.

Barisci, J. N., Wallace, G. G., MacFarlane, D. R., and Baughman, R. H. (2004). Investigation of ionic liquids as electrolytes for carbon nanotube electrodes. *Electrochem. Commun.* 6, 22–27. doi:10.1016/j.elecom.2003.09.015

Benito, J., García-Mardones, M., Pérez-Gregorio, V., Gascón, I., and Lafuente, C. (2014). Physicochemical study of n-ethylpyridinium bis(trifluoromethylsulfonyl) imide ionic liquid. *J. Solut. Chem.* 43, 696–710. doi:10.1007/s10953-014-0156-5

Carda–Broch, S., Berthod, A., and Armstrong, D. W. (2003). Solvent properties of the 1-butyl-3-methylimidazolium hexafluorophosphate ionic liquid. *Anal. Bioanal. Chem.* 375, 191–199. doi:10.1007/s00216-002-1684-1

Cieniecka-Rosłonkiewicz, A., Pernak, J., Kubis-Feder, J., Ramani, A., Robertson, A. J., and Seddon, K. R. (2005). Synthesis, anti-microbial activities and anti-electrostatic properties of phosphonium-based ionic liquids. *Green Chem.* 7, 855–862. doi:10.1039/b508499g

Clinical and Laboratory Standards Institute (2015). *M02-A12 performance standards for antimicrobial disk susceptibility tests; approved standard-twelfth edition*. Wayne, PA: Clinical and Laboratory Standards Institute.

Cornmell, R. J., Winder, C. L., Tiddy, G. J. T., Goodacre, R., and Stephens, G. (2008). Accumulation of ionic liquids in Escherichia coli cells. *Green Chem.* 10, 836–884. doi:10.1039/b807214k

Couling, D. J., Bernot, R. J., Docherty, K. M., Dixon, J. N. K., and Maginn, E. J. (2006). Assessing the factors responsible for ionic liquid toxicity to aquatic organisms via quantitative structure–property relationship modeling. *Green Chem.* 8, 82–90. doi:10.1039/b511333d

Cumicheo, M. C., Nobre, L. C. S., Santos, A. F., Lampreia, I. M. S., Santos, M. S. C. S., Santos, F. J. V., et al. (2015). Thermophysical properties of 1-Butyl-1-methylpyrrolidinium dicyanamide + H2O mixtures. *J. Chem. Eng. Data.* 60, 3766–3775. doi:10.1021/acs.jced.5b00944

de los Ríos, A. P., van Rantwijk, F., and Sheldon, R. A. (2012). Effective resolution of 1-phenyl ethanol by Candida Antarctica lipase B catalysed acylation with vinyl acetate in protic ionic liquids (PILs). *Green Chem.* 14, 1584–1588. doi:10.1039/c2gc35196j

Derby, H. A., and Hammer, B. W. (1931). Bacteriology of butter IV. Bacteriological studies on surface taint butter. *Iowa Agric. Home Econ. Exp. Stn. Res. Bull.* 145, 387–416.

Dharaskar, S. A., Varma, M. N., Shende, D. Z., Yoo, C. K., and Wasewar, K. L. (2013). Synthesis, characterization and application of 1-butyl-3 methylimidazolium chloride as green material for extractive desulfurization of liquid fuel. *Sci. World J.* 2013, 395274. doi:10.1155/2013/395274

Dharaskar, S. A., Wasewar, K. L., Varma, M. N., and Shende, D. Z. (2016a). Synthesis, characterization, and application of 1-butyl-3-methylimidazolium thiocyanate for extractive desulfurization of liquid fuel. *Environ. Sci. Pollut. Res.* 23, 9284–9294. doi:10.1007/s11356-015-4945-1

Dharaskar, S. A., Wasewar, K. L., Varma, M. N., Shende, D. Z., and Yoo, C. K. (2016b). Synthesis, characterization and application of 1-butyl-3-methylimidazolium tetrafluoroborate for extractive desulfurization of liquid fuel. *Arab. J. Chem.* 9, 578–587. doi:10.1016/j.arabjc.2013.09.034

Ding, J., Zhou, D., Spinks, G., Wallace, G., Forsyth, S., Forsyth, M., et al. (2003). Use of ionic liquids as electrolytes in electromechanical actuator systems based on inherently conducting polymers. *Chem. Mater.* 15, 2392–2398. doi:10.1021/cm020918k

Dupont, J., Fonseca, G. S., Umpierre, A. P., Fichtner, P. F. P., and Teixeira, S. R. (2002). Transition-metal nanoparticles in imidazolium ionic liquids: recycable catalysts for biphasic hydrogenation reactions. *J. Am. Chem. Soc.* 124, 4228–4229. doi:10.1021/ja025818u

Earle, M., Wasserscheid, P., Schulz, P., Olivier-Bourbigou, H., Favre, F., Vaultier, M., et al. (2008). "Organic synthesis," in *Ionic liquids in synthesis*. Weinheim, Germany: Wiley-VCH Verlag GmbH & Co. KGaA, 265–568. doi:10.1002/9783527621194.ch5

Eastoe, J., Gold, S., Rogers, S. E., Paul, A., Welton, T., Heenan, R. K., et al. (2005). Ionic liquid-in-oil microemulsions. *J. Am. Chem. Soc.* 127, 7302–7303. doi:10.1021/ja051155f

El Abedin, S. Z., and Endres, F. (2007). Ionic liquids: the link to high-temperature molten salts? *Acc. Chem. Res.* 40, 1106–1113. doi:10.1021/ar700049w

Endres, F. (2002). Ionic liquids: solvents for the electrodeposition of metals and semiconductors. *ChemPhysChem.* 3, 145–154. doi:10.1002/1439-7641(20020215)3:2<144::aid-cphc144>3.0.co;2-#

Fadeeva, T. A., Husson, P., Devine, J. A., Costa Gomes, M. F., Greenbaum, S. G., and Castner, E. W. (2015). Interactions between water and 1-butyl-1-methylpyrrolidinium ionic liquids. *J. Chem. Phys.* 143, 064503. doi:10.1063/1.4928065

Freire, M. G., Santos, L. M. N. B. F., Fernandes, A. M., Coutinho, J. A. P., and Marrucho, I. M. (2007). An overview of the mutual solubilities of water-imidazolium-based ionic liquids systems. *Fluid Phase Equil.* 261, 449–454. doi:10.1016/j.fluid.2007.07.033

Galai, S., De Los Ríos, A. P., Hernández-Fernández, F. J., Haj Kacem, S., and Tomas-Alonso, F. (2015). Over-activity and stability of laccase using ionic liquids: screening and application in dye decolorization. *RSC Adv.* 5, 16173–16189. doi:10.1039/c4ra07351g

Gorlov, M., and Kloo, L. (2008). Ionic liquid electrolytes for dye-sensitized solar cells. *J. Chem. Soc., Dalton Trans.* 2655–2666. doi:10.1039/b716419j

Haddleton, D. M., Welton, T., and Carmichael, A. J. (2008). "Polymer synthesis in ionic liquids," in *Ionic liquids in synthesis*. Weinheim, Germany: Wiley-VCH Verlag GmbH & Co. KGaA, 619–640. doi:10.1002/9783527621194.ch7

Hau, H. H., and Gralnick, J. A. (2007). Ecology and biotechnology of the genus shewanella. *Annu. Rev. Microbiol.* 61, 237–258. doi:10.1146/annurev.micro.61.080706.093257

Heatley, N. G. (1944). A method for the assay of penicillin. *Biochem. J.* 38, 61–65. doi:10.1042/bj0380061

Hernández, F. J., de los Ríos, A. P., Gómez, D., Rubio, M., and Víllora, G. (2006). A new recirculating enzymatic membrane reactor for ester synthesis in ionic liquid/supercritical carbon dioxide biphasic systems. *Appl. Catal. B Environ.* 67, 121–126. doi:10.1016/j.apcatb.2006.04.009

Hernández-Fernández, F. J., Bayo, J., Pérez de los Ríos, A., Vicente, M. A., Bernal, F. J., and Quesada-Medina, J. (2015). Discovering less toxic ionic liquids by using the Microtox® toxicity test. *Ecotoxicol. Environ. Saf.* 116, 29–33. doi:10.1016/j.ecoenv.2015.02.034

Iolitec (2010). *Safety data sheet IoLiLyte T2EG.*

Iolitec (2011a). *Technical data sheet 1-Butyl-1-methylpyrrolidinium bis(trifluoromethylsulfonyl)imide.*

Iolitec (2011b). *Technical data sheet 1-Butyl-1-methylpyrrolidinium dicyanamide.*

Iolitec (2011c). *Technical data sheet 1-Butyl-1-methylpyrrolidinium hexafluorophosphate.*

Iolitec (2011d). *Technical data sheet tributyltetradecylphosphonium dodecylbenzenefulfonate.*

Iolitec (2011e). *Technical data sheet trihexyltetradecylphosphonium bis(trifluoromethylsulfonyl)imide.*

Iolitec (2011f). *Technical data sheet trihexyltetradecylphosphonium bromide.*

Iolitec (2011g). *Technical data sheet trihexyltetradecylphosphonium chloride.*

Iolitec (2011h). *Technical data sheet trihexyltetradecylphosphonium dicyanamide.*

Iolitec (2011i). *Technical data sheet triisobutylmethylphosphonium tosylate.*

Iolitec (2012a). *Technical data sheet 1-Butyl-1-methylpiperidinium bis(trifluoromethylsulfonyl)imide.*

Iolitec (2012b). *Technical data sheet 1-butyl-1-methylpyrrolidinium trifluoromethanesulfonate.*

Iolitec (2012c). *Technical data sheet choline dihydrogenphosphate.*

Iolitec (2012d). *Technical data sheet methyltrioctylammonium triflate.*

Iolitec (2013a). *Technical data sheet tributylmethylphosphonium methyl sulfate (CYPHOS IL-108).*

Iolitec (2013b). *Technical data sheet trihexyl(tetradecyl)phosphonium decanoate.*

Iolitec (2014). Technical data sheet 1-methyl-3-octylimidazolim hexafluorophosphate.

Iolitec (2015a). *Safety data sheet 1-Butyl-1-methylpyrrolidinium chloride.*

Iolitec (2015b). *Safety data sheet 1-Ethylpyridinium bis(trifluoromethylsulfonyl) imde.*

Iolitec (2015c). *Safety data sheet IoLiLyte 221PG.*

Iolitec (2015d). *Safety data sheet IoLiLyte C1EG.*

Iolitec (2015e). *Safety data sheet tetraoctylphosphonium bromide (CYPHOS IL-166).*

Iolitec (2016). *Technical data sheet choline bis(trifluoromethylsulfonyl)imide.*

Iolitec (2018). *Technical data sheet trihexyltetradecylphosphonium bis(2,4,4-trimethylpentyl)phosphinate.*

Iolitect (2011). *Technical data sheet 1-Ethyl-1-methylpyrrolidinium bis(trifluoromethylsulfonyl)imide.*

Ishikawa, M., Sugimoto, T., Kikuta, M., Ishiko, E., and Kono, M. (2006). Pure ionic liquid electrolytes compatible with a graphitized carbon negative electrode in rechargeable lithium-ion batteries. *J. Power Sources.* 162, 658–662. doi:10.1016/j.jpowsour.2006.02.077

Jiang, Y., Guo, C., Xia, H., Mahmood, I., Liu, C., and Liu, H. (2009). Magnetic nanoparticles supported ionic liquids for lipase immobilization: enzyme activity in catalyzing esterification. *J. Mol. Catal. B Enzym.* 58, 103–109. doi:10.1016/j.molcatb.2008.12.001

Jorge, A. B., and Hazael, R. (2016). Use of *Shewanella oneidensis* for energy conversion in microbial fuel cells. *Macromol. Chem. Phys.* 217, 1431–1438. doi:10.1002/macp.201500477

Kalčíková, G., Zagorc-Končan, J., Žnidaršič-Plazl, P., and Gotvajn, A. Ž. (2012). Assessment of environmental impact of pyridinium-based ionic liquid. *Fresenius Environ. Bull.* 21, 2320–2325.

Kim, J. Y., Kim, J. T., Song, E. A., Min, Y. K., and Hamaguchi, H. O. (2008). Polypyrrole nanostructures self-assembled in magnetic ionic liquid as a template. *Macromolecules.* 41, 2886–2889. doi:10.1021/ma071333k

Kumar, R., Singh, L., and Zularisam, A. W. (2016). Exoelectrogens: recent advances in molecular drivers involved in extracellular electron transfer and strategies

used to improve it for microbial fuel cell applications. *Renew. Sustain. Energy Rev.* 56, 1322–1336. doi:10.1016/j.rser.2015.12.029

Latała, A., Nędzi, M., and Stepnowski, P. (2009). Toxicity of imidazolium and pyridinium based ionic liquids towards algae. Bacillaria paxillifer (a microphytobenthic diatom) and Geitlerinema amphibium (a microphytobenthic blue green alga). *Green Chem.* 11, 1371–1376. doi:10.1039/b901887e

Latała, A., Stepnowski, P., Nędzi, M., and Mrozik, W. (2005). Marine toxicity assessment of imidazolium ionic liquids: acute effects on the Baltic algae Oocystis submarina and Cyclotella meneghiniana. *Aquat. Toxicol.* 73, 91–98. doi:10.1016/j.aquatox.2005.03.008

Lee, S. H., Doan, T. T. N., Ha, S. H., and Koo, Y. M. (2007). Using ionic liquids to stabilize lipase within sol-gel derived silica. *J. Mol. Catal. B Enzym.* 45, 57–61. doi:10.1016/j.molcatb.2006.11.008

Lee, S. Y., Vicente, F. A., E Silva, F. A., Sintra, T. E., Taha, M., Khoiroh, I., et al. (2015). Evaluating self-buffering ionic liquids for Biotechnological applications. *ACS Sustain. Chem. Eng.* 3, 3420–3428. doi:10.1021/acssuschemeng.5b01155

Lozano, P., García-Verdugo, E., Karbass, N., Montague, K., De Diego, T., Burguete, M. I., et al. (2010). Supported ionic liquid-like phases (SILLPs) for enzymatic processes: continuous KR and DKR in SILLP–scCO2 systems. *Green Chem.* 12, 1803–1810. doi:10.1039/c0gc00076k

Łuczak, J., Jungnickel, C., Łącka, I., Stolte, S., and Hupka, J. (2010). Antimicrobial and surface activity of 1-alkyl-3-methylimidazolium derivatives. *Green Chem.* 12, 593–660. doi:10.1039/b921805j

Luis, P., Ortiz, I., Aldaco, R., and Irabien, A. (2007). A novel group contribution method in the development of a QSAR for predicting the toxicity (Vibrio fischeri EC50) of ionic liquids. *Ecotoxicol. Environ. Saf.* 67, 423–429. doi:10.1016/j.ecoenv.2006.06.010

MacDonell, M. T., and Colwell, R. R. (1985). Phylogeny of the vibrionaceae, and recommendation for two new genera, listonella and shewanella. *Syst. Appl. Microbiol.* 6, 171–182. doi:10.1016/S0723-2020(85)80051-5

Marsili, E., Baron, D. B., Shikhare, I. D., Coursolle, D., Gralnick, J. A., and Bond, D. R. (2008). Shewanella secretes flavins that mediate extracellular electron transfer. *Proc. Natl. Acad. Sci. U. S. A.* 105, 3968–3973. doi:10.1073/pnas.0710525105

Matzke, M., Arning, J., Ranke, J., Jastorff, B., and Stolte, S. (2010). "Design of inherently safer ionic liquids: toxicology and biodegradation," in *Handbook of green chemistry*. Weinheim, Germany: Wiley-VCH Verlag GmbH & Co. KGaA, 233–298. doi:10.1002/9783527628698.hgc069

Matzke, M., Stolte, S., Arning, J., Uebers, U., and Filser, J. (2008). Imidazolium based ionic liquids in soils: effects of the side chain length on wheat (Triticum aestivum) and cress (Lepidium sativum) as affected by different clays and organic matter. *Green Chem.* 10, 584–659. doi:10.1039/b717811e

Missoun, F., Pérez de los Ríos, A., Ortiz-Martínez, V. M., Salar-García, M. J., Hernández-Fernández, J., and Hernández-Fernández, F. J. (2020). Discovering low toxicity ionic liquids for Sacharomyces cerevisiae by using the agar well diffusion test. *Processes*. 8 (9), 1163. doi:10.3390/pr8091163

Nakashima, K., Kamiya, N., Koda, D., Maruyama, T., and Goto, M. (2009). Enzyme encapsulation in microparticles composed of polymerized ionic liquids for highly active and reusable biocatalysts. *Org. Biomol. Chem.* 7, 2353–2358. doi:10.1039/b823064a.

Nockemann, P., Binnemans, K., Thijs, B., Parac-Vogt, T. N., Merz, K., Mudring, A. V., et al. (2009). Temperature-driven mixing-demixing behavior of binary mixtures of the ionic liquid choline bis(trifluoromethylsulfonyl)imide and water. *J. Phys. Chem. B.* 113, 1429–1437. doi:10.1021/jp808993t.

Ortega, J., Vreekamp, R., Marrero, E., and Penco, E. (2007). Thermodynamic properties of 1-butyl-3-methylpyridinium tetrafluoroborate and its mixtures with water and alkanols. *J. Chem. Eng. Data.* 52, 2269–2276. doi:10.1021/je700294p

Papaiconomou, N., Yakelis, N., Salminen, J., Bergman, R., and Prausnitz, J. M. (2006). Synthesis and properties of seven ionic liquids containing 1-methyl-3-octylimidazolium or 1-butyl-4-methylpyridinium cations. *J. Chem. Eng. Data.* 52, 319. doi:10.1021/je060096y

Pârvulescu, V. I., and Hardacre, C. (2007). Catalysis in ionic liquids. *Chem. Rev.* 107, 2615–2665. doi:10.1021/cr050948h

Pérez De Los Ríos, A., Hernández-Fernández, F. J., Zapata Henríquez, P. A., Missoun, F., Hernández-Fernández, J., Ortiz-Martínez, V., et al. (2017). Keys for Bioethanol production processes by fermentation and ionic liquid extraction. *ACS Sustain. Chem. Eng.* 5, 6986–6993. doi:10.1021/acssuschemeng.7b01170

Pernak, J., Sobaszkiewicz, K., and Mirska, I. (2003). Anti-microbial activities of ionic liquids. *Green Chem.* 5, 52–56. doi:10.1039/b207543c

Pretti, C., Chiappe, C., Baldetti, I., Brunini, S., Monni, G., and Intorre, L. (2009). Acute toxicity of ionic liquids for three freshwater organisms: pseudokirchneriella subcapitata, Daphnia magna and *Danio rerio*. *Ecotoxicol. Environ. Saf.* 72, 1170–1176. doi:10.1016/j.ecoenv.2008.09.010

Qiu, Z., and Texter, J. (2008). Ionic liquids in microemulsions. *Curr. Opin. Colloid Interface Sci.* 13, 252–262. doi:10.1016/j.cocis.2007.10.005

Ranke, J., Mölter, K., Stock, F., Bottin-Weber, U., Poczobutt, J., Hoffmann, J., et al. (2004). Biological effects of imidazolium ionic liquids with varying chain lengths in acute Vibrio fischeri and WST-1 cell viability assays. *Ecotoxicol. Environ. Saf.* 58, 396–404. doi:10.1016/S0147-6513(03)00105-2

Ranke, J., Müller, A., Bottin-Weber, U., Stock, F., Stolte, S., Arning, J., et al. (2007). Lipophilicity parameters for ionic liquid cations and their correlation to *in vitro* cytotoxicity. *Ecotoxicol. Environ. Saf.* 67, 430–438. doi:10.1016/j.ecoenv.2006.08.008

Rebros, M., Gunaratne, H. Q. N., Ferguson, J., Seddon, K. R., and Stephens, G. (2009). A high throughput screen to test the biocompatibility of water-miscible ionic liquids. *Green Chem.* 11, 402–440. doi:10.1039/b815951c

Romero, A., Santos, A., Tojo, J., and Rodríguez, A. (2008). Toxicity and biodegradability of imidazolium ionic liquids. *J. Hazard Mater.* 151, 268–273. doi:10.1016/j.jhazmat.2007.10.079

Russina, O., Caminiti, R., Triolo, A., Rajamani, S., Melai, B., Bertoli, A., et al. (2013). Physico-chemical properties and nanoscale morphology in N-alkyl-N-methylmorpholinium dicyanamide room temperature ionic liquids. *J. Mol. Liq.* 187, 252–259. doi:10.1016/j.molliq.2013.08.002

Sakaebe, H., Matsumoto, H., and Tatsumi, K. (2005). Discharge-charge properties of Li/LiCoO2 cell using room temperature ionic liquids (RTILs) based on quaternary ammonium cation - effect of the structure. *J. power sources.* 146, 693–697. doi:10.1016/j.jpowsour.2005.03.071

Santa Cruz Biotechnology, Inc. (2012). 1,2,3-Trimethylimidazolium methyl sulfate. Tech. Data Sheet.

Schrekker, H. S., Gelesky, M. A., Stracke, M. P., Schrekker, C. M. L., Machado, G., Teixeira, S. R., et al. (2007). Disclosure of the imidazolium cation coordination and stabilization mode in ionic liquid stabilized gold(0) nanoparticles. *J. Colloid Interface Sci.* 316, 189–195. doi:10.1016/j.jcis.2007.08.018

Sena, D. W., Kulacki, K. J., Chaloner, D. T., and Lamberti, G. A. (2010). The role of the cell wall in the toxicity of ionic liquids to the alga Chlamydomonas reinhardtii. *Green Chem.* 12, 1066–1071. doi:10.1039/c000899k

Shim, Y., and Kim, H. J. (2009). Solvation of carbon nanotubes in a room-temperature ionic liquid. *ACS Nano*. 3, 1693–1702. doi:10.1021/nn900195b

Sigma Aldrich (2006). *Safety data sheet methyltrioctylammonium chloride*. St. Louis, MO: Sigma Aldrich.

Stepnowski, P., Składanowski, A. C., Ludwiczak, A., and Łaczyńska, E. (2004). Evaluating the cytotoxicity of ionic liquids using human cell line HeLa. *Hum. Exp. Toxicol.* 23, 513–517. doi:10.1191/0960327104ht480oa

Stolte, S., Abdulkarim, S., Arning, J., Blomeyer-Nienstedt, A. K., Bottin-Weber, U., Matzke, M., et al. (2008). Primary biodegradation of ionic liquid cations, identification of degradation products of 1-methyl-3-octylimidazolium chloride and electrochemical wastewater treatment of poorly biodegradable compounds. *Green Chem.* 10, 214–222. doi:10.1039/b713095c

Stolte, S., Arning, J., Bottin-Weber, U., Müller, A., Pitner, W. R., Welz-Biermann, U., et al. (2007a). Effects of different head groups and functionalised side chains on the cytotoxicity of ionic liquids. *Green Chem.* 9, 760–776. doi:10.1039/b615326g

Stolte, S., Matzke, M., Arning, J., Böschen, A., Pitner, W. R., Welz-Biermann, U., et al. (2007b). Effects of different head groups and functionalised side chains on the aquatic toxicity of ionic liquids. *Green Chem.* 9, 1170–1179. doi:10.1039/b711119c.

Suo, H., Xu, L., Xu, C., Chen, H., Yu, D., Gao, Z., et al. (2018). Enhancement of catalytic performance of porcine pancreatic lipase immobilized on functional ionic liquid modified Fe3O4-Chitosan nanocomposites. *Int. J. Biol. Macromol.* 119, 624–632. doi:10.1016/j.ijbiomac.2018.07.187

Toral, A. R., de los Ríos, A. P., Hernández, F. J., Janssen, M. H. A., Schoevaart, R., van Rantwijk, F., et al. (2007). Cross-linked Candida Antarctica lipase B is active

in denaturing ionic liquids. *Enzym. Microb. Technol.* 40, 1095–1099. doi:10.1016/J.ENZMICTEC.2006.08.027

Varia, J., Zegeye, A., Roy, S., Yahaya, S., and Bull, S. (2014). Shewanella putrefaciens for the remediation of Au3+, Co2+ and Fe3+ metal ions from aqueous systems. *Biochem. Eng. J.* 85, 101–109. doi:10.1016/j.bej.2014.02.002

Ventura, S. P. M., de Barros, R. L. F., Sintra, T., Soares, C. M. F., Lima, Á. S., and Coutinho, J. A. P. (2012a). Simple screening method to identify toxic/non-toxic ionic liquids: agar diffusion test adaptation. *Ecotoxicol. Environ. Saf.* 83, 55–62. doi:10.1016/j.ecoenv.2012.06.002

Ventura, S. P. M., Marques, C. S., Rosatella, A. A., Afonso, C. A. M., Gonçalves, F., and Coutinho, J. A. P. (2012b). Toxicity assessment of various ionic liquid families towards Vibrio fischeri marine bacteria. *Ecotoxicol. Environ. Saf.* 76, 162–168. doi:10.1016/j.ecoenv.2011.10.006

Ventura, S. P. M., Gonçalves, A. M. M., Sintra, T., Pereira, J. L., Gonçalves, F., and Coutinho, J. A. P. (2013). Designing ionic liquids: the chemical structure role in the toxicity. *Ecotoxicology.* 22, 1–12. doi:10.1007/s10646-012-0997-x

Viboud, S., Papaiconomou, N., Cortesi, A., Chatel, G., Draye, M., and Fontvieille, D. (2012). Correlating the structure and composition of ionic liquids with their toxicity on Vibrio fischeri: a systematic study. *J. Hazard Mater.* 215–216, 40–48. doi:10.1016/j.jhazmat.2012.02.019

Walker, A. (2009). *Solvents*. International publication number WO2009034329A1.

Wang, L., Chen, S., Ding, Y., Zhu, Q., Zhang, N., and Yu, S. (2018). Biofabrication of morphology improved cadmium sulfide nanoparticles using Shewanella oneidensis bacterial cells and ionic liquid: for toxicity against brain cancer cell lines. *J. Photochem. Photobiol. B Biol.* 178, 424–427. doi:10.1016/j.jphotobiol.2017.11.007

Webster, D. P., TerAvest, M. A., Doud, D. F. R., Chakravorty, A., Holmes, E. C., Radens, C. M., et al. (2014). An arsenic-specific biosensor with genetically engineered Shewanella oneidensis in a bioelectrochemical system. *Biosens. Bioelectron.* 62, 320–324. doi:10.1016/j.bios.2014.07.003

Wei, H., Wu, X. S., Zou, L., Wen, G. Y., Liu, D. Y., and Qiao, Y. (2016). Amine-terminated ionic liquid functionalized carbon nanotubes for enhanced interfacial electron transfer of Shewanella putrefaciens anode in microbial fuel cells. *J. Power Sources.* 315, 192–198. doi:10.1016/j.jpowsour.2016.03.033

Welton, T. (1999). Room-temperature ionic liquids. Solvents for synthesis and catalysis. *Chem. Rev.* 99, 2071–2084. doi:10.1021/cr980032t

Wood, N., Ferguson, J. L., Gunaratne, H. Q. N., Seddon, K. R., Goodacre, R., and Stephens, G. M. (2011). Screening ionic liquids for use in biotransformations with whole microbial cells. *Green Chem.* 13, 1843–1851. doi:10.1039/c0gc00579g

Wood, N., and Stephens, G. (2010). Accelerating the discovery of biocompatible ionic liquids. *Phys. Chem. Chem. Phys.* 12, 1670–1674. doi:10.1039/b923429b.

Xiang, X., Suo, H., Xu, C., and Hu, Y. (2018). Covalent immobilization of lipase onto chitosan-mesoporous silica hybrid nanomaterials by carboxyl functionalized ionic liquids as the coupling agent. *Colloids Surf. B Biointerfaces.* 165, 262–269. doi:10.1016/j.colsurfb.2018.02.033

Yang, C., Sun, Q., Qiao, T., and Li, Y. (2003). Ionic liquid doped polymer light-emitting electrochemical cells. *J. Phys. Chem. B.* 107, 12981–12988. doi:10.1021/jp034818t

Ye, C., Liu, W., Chen, Y., and Yu, L. (2001). Room-temperature ionic liquids: a novel versatile lubricant. *Chem. Commun.* 21, 2244–2245. doi:10.1039/b106935g

Zein El Abedin, S., Moustafa, E. M., Hempelmann, R., Natter, H., and Endres, F. (2006). Electrodeposition of nano- and macrocrystalline aluminium in three different air and water stable ionic liquids. *ChemPhysChem.* 7, 1535–1543. doi:10.1002/cphc.200600095

Zhang, C. L., Yu, Y. Y., Fang, Z., Naraginti, S., Zhang, Y., and Yong, Y. C. (2018). Recent advances in nitroaromatic pollutants bioreduction by electroactive bacteria. *Process Biochem.* 70, 129–135. doi:10.1016/j.procbio.2018.04.019

Zhang, S., Zhou, Q., Lu, X., Song, Y., and Wang, X. (2016). "Solubility and diffusivity of 1-butyl-3-methylimidazolium 1,1,2,2-tetrafluoroethanesulfonate mixtures," in *Physicochemical Properties of ionic liquid mixtures*. Dordrecht, Netherlands: Springer, 588–599. doi:10.1007/978-94-017-7573-1_46

Zhao, C., Wang, Y., Shi, F., Zhang, J., and Zhu, J. J. (2013). High biocurrent generation in shewanella-inoculated microbial fuel cells using ionic liquid functionalized graphene nanosheets as an anode. *Chem. Commun.* 49, 6668–6670. doi:10.1039/c3cc42068j

Zhou, T., Chen, L., Ye, Y., Chen, L., Qi, Z., Freund, H., et al. (2012). An overview of mutual solubility of ionic liquids and water predicted by COSMO-RS. in *Industrial and engineering chemistry research*. Washington, D.C: American Chemical Society, 6256–6264. doi:10.1021/ie202719z

Zhou, Y., Roberson, A. J., and Hillhouse, H. H, B. D. (2002). *US7638636B2 - phosphonium and imidazolium salts and methods of their preparation*. Google Patents.

Zou, B., Song, C., Xu, X., Xia, J., Huo, S., and Cui, F. (2014). Enhancing stabilities of lipase by enzyme aggregate coating immobilized onto ionic liquid modified mesoporous materials. *Appl. Surf. Sci.* 311, 62–67. doi:10.1016/j.apsusc.2014.04.210

Zou, L., Huang, Y., Long, Z., and Qiao, Y. (2019). On-going applications of Shewanella species in microbial electrochemical system for bioenergy, bioremediation and biosensing. *World J. Microbiol. Biotechnol.* 35, 9. doi:10.1007/s11274-018-2576-7

Conflict of Interest: The authors declare that the research was conducted in the absence of any commercial or financial relationships that could be construed as a potential conflict of interest.

Carbon-Based Materials

Qiuhong Zhang

Dr. Qiuhong Zhang is a senior scientist at the University of Dayton Research Institute. She has more than 30 years of R&D experience in the fields of nanomaterials, high-temperature polymers, and advanced composite materials. Her main research areas include CNT synthesis, characterization, and application; modification, processing, and manufacturing of advanced nanocomposites based on CNTs; and design, processing, and failure analysis of high-temperature polymer composites. Currently, Dr. Zhang's research focuses on combining high-energy-density carbon-based cathode active materials with high-conductivity carbon nanostructures for high-energy stable lithium-based batteries. Ultimately, efforts are directed toward the development of prototype 3D batteries and scalable technologies.

Fei Lu

Dr. Fei Lu graduated from the Department of Optics, Shandong University, in 1985, receiving a doctorate in the science of condensed matter physics in 1997. From 2000 to 2002, as a Hongbao scholar, he worked on rare-earth ion-doped semiconductor light-emitting devices at the Juelich Research Center in Germany. He presided over and undertook the National Natural Science Foundation of China: "Research on New Methods of Ion Implantation in Optical Waveguides", the Ministry of Education's Doctoral Program Fund "Ion Implantation on the Modulation of Ion Exchange KTP Periodic Waveguides", and a number of key projects from the Open Laboratory of Peking University. As the main finisher, he successively participated in one of the key projects of the National Natural Science Foundation of China, three projects of the Natural Science Foundation of China, and one of the doctoral programs of the Ministry of Education. As the main performer, he has won the second prize of National Natural Science, the first prize of Natural Science of Chinese Universities of the Ministry of Education, and the second prize of the Shandong Science and Technology Progress Award. He has undertaken and participated in the declaration of two national invention patents. He has published more than 100 articles.

Juana Maria Rosas Martínez

Dr. Juana María Rosas Martínez, a Chemical Engineer at Málaga University since 2003, got her Ph.D. at the same university in 2009. From 2020 to 2015, she has had two postdoctoral contracts at the Complutense University of Madrid and the University of Alicante. After this date, she has worked as Associate Professor at Málaga University. Her main research areas are lignocellulosic waste valorization through thermochemical processes and its application in adsorption and catalytic processes with the aim to reduce or eliminate pollutants in flue gas and to get biofuels and industrial chemicals within a biorefinery context. Besides, she has analyzed the use of electrospray/electrospinning in inorganic catalysts preparation for catalytic applications.

Atsuko Sekiguchi

Dr. Atsuko Sekiguchi has been a Senior Researcher at the National Institute of Advanced Industrial Science and Technology since 2015 and is currently a member of the CNT-Application Research Center. She has been a Review Editor for Frontiers in Materials' Carbon-based Materials section since 2016.

frontiers in Materials

ORIGINAL RESEARCH
published: 28 October 2020
doi: 10.3389/fmats.2020.572956

Thermal Properties Enhancement of Vertically Aligned Carbon Nanotubes-Based Metal Nanocomposites as Thermal Interface Materials

Qiuhong Zhang[1], Brian A. Calderon[1], Charles R. Ebbing[1], Levi J. Elston[2], Larry W. Byrd[2] and Bang-Hung Tsao[2]*

[1]University of Dayton Research Institute (UDRI), Dayton, OH, United States, [2]Air Force Research Laboratory (AFRL), WPAFB, Dayton, OH, United States

Increasing power densities in high-power electronic packages require advanced heat transmission from their respective thermal interface materials (TIMs). Modern TIMs do not accommodate both thermal performance and mechanical compliance with increasing device power density. Vertically aligned carbon nanotubes (VACNT) are advantageous in that their intrinsic properties promote both high thermal conductivity while maintaining a mechanically flexible/compliant interface. Therefore, it is a promising approach to use carbon nanotubes (CNTs), specialty VACNTs, to make a novel interface heat transfer material. However, the high thermal contact resistance between VACNTs and substrate(s) has been a big issue to limit its application. In this study, the effect of post-processing techniques such as plasma treatment and surface metallization of VACNT layer (directly grown on Cu substrate) on interfacial properties of CNTs with matching substrate were explored. Thermal properties were evaluated via a Laser Flash testing system. Thermal test results demonstrated that modifying the surface of the VACNT layer is effective method to improve interfacial attachment between CNTs and matching substrate. Results indicated that, among different VACNT surface modification methods, the plasma treated VACNT layer surface promote the best thermal properties of VACNT-based metal nanocomposite as a TIM. Compared to the unmodified VACNT layer, in this study, the interphase thermal resistance of the Cu/VACNT/matched substrate sample made from the plasma treated VACNT layer was reduced approximately 80%.

Keywords: vertical aligned carbon nanotubes, plasma, sputtering, metallization, thermal resistance, metal nanocomposite, laser flash testing

OPEN ACCESS

Edited by:
Ruixin Zhu,
Tongji University, China

Reviewed by:
Che Azurahanim Che Abdullah,
Putra Malaysia University, Malaysia
Imad Arfaoui,
Université Pierre et Marie Curie, France

****Correspondence:***
Qiuhong Zhang
qiuhong.zhang.3.ctr@us.af.mil

Specialty section:
This article was submitted to Carbon-Based Materials, a section of the journal Frontiers in Materials

Received: *15 June 2020*
Accepted: *28 September 2020*
Published: *28 October 2020*

Citation:
Zhang Q, A. Calderon B, R. Ebbing C, J. Elston L, W. Byrd L and Tsao B-H (2020) Thermal Properties Enhancement of Vertically Aligned Carbon Nanotubes-Based Metal Nanocomposites as Thermal Interface Materials. Front. Mater. 7:572956.

INTRODUCTION

Long-term electronic device failures are often due to thermally induced stress/fatigue that shows up as interfacial delamination. This problem increases the component thermal resistance, which causes increased operational temperature. After enough cycles, this problem propagates into severe delamination that eventually causes the device to overheat, reducing its breakdown voltage within the limits of operation, causing catastrophic failure. Improved thermal management

materials, namely thermal interface materials (TIMs) that can maintain a low thermal resistance but extend the device fatigue life, will increase component reliability and reduce operational failures. Thus, TIMs play a key role in thermal management of power modules in high-performance electronic packages. Some major issues with current TIMs such as fatigue failure (solder), low thermal conductivity (phase change materials), and dry out/pump out (grease) have lead researchers to develop advanced nano-engineered materials to make more efficient thermal interfaces in high power density device. Among the many nano-materials available, carbon nanotubes (CNTs), with their unique thermal, electrical, and mechanical properties, are a very attractive candidate for advanced TIMs (Berber et al., 2000; Che et al., 2000; Kim et al., 2001), and have been widely investigated (Ganguli et al., 2012; Ganguli et al., 2013). It has been reported that taking full advantage of the positive influence of CNTs on the effective thermal conductivity of nanocomposites is a challenge due to difficulties in homogeneous distribution of nanotubes in the matrix phase and proper orientation/alignment for an optimum thermal path (Chu et al., 2010; Firkowska et al., 2011). Therefore, to overcome this problem, significant attention has shifted to using vertically aligned CNT arrays (VACNT) as a promising TIM structure.

An aligned CNT configuration possesses a synergistic combination of mechanical compliance, extraordinarily high axial thermal conductivity (3,000 W/m-K for individual MWCNT), small coefficient of thermal expansion, and high thermal and chemical stability (Berber et al., 2000; Che et al., 2000; Yang et al., 2002; Hu et al., 2006). The elasticity/conformability feature is particularly advantageous in addressing mismatches in coefficients of thermal expansion that can cause TIM delamination and device failure. In the past several years, VACNT arrays have been widely investigated with successful results from synthesis to characterization (Huang et al., 2005; Xu and Fisher, 2006; Cola et al., 2007; Tong et al., 2007). However, practical implementation of CNTs as TIMs in an electronic package configuration is not a trivial endeavor. A large interfacial thermal resistance has been found between CNTs and the contact substrates, which erects a significant barrier against applying CNTs as TIMs. This resistance is primarily caused by the small percentage of CNTs in contact with the substrate surface and weak interfacial adhesion at each matching surface (Panzer et al., 2008; Son et al., 2008; Lin et al., 2009). Therefore, based on investigation of VACNTs and characterizing the influence on their thermal properties (Wang et al., 2007; Yin et al., 2008; Chen et al., 2010), the fundamental studies on managing the VACNTs/substrate interfaces to effectively reduce the thermal contact resistance and simultaneously improve the interfacial adhesion is necessary and very important. A few groups have explored techniques to enhance the contact area at the CNT-substrate bond line, particularly at the free CNT end (Cola et al., 2008; Cross et al., 2010; Barako et al., 2012). However, the total thermal resistance does not decrease sufficiently due to the material's low intrinsic thermal conductivity (grease), weak bonding (metal), as well as infiltration issues with CNT array. To overcome these problems, the proper surface modification of VACNTs combined with a high conductivity matrix fill material is a promising approach. Compared to nonaligned CNTs, vertical aligned CNT forest surface modification continues to be a challenge. The difficulties lie in controlling the nanotube length being modified and restricting the nanotube bundling due to the capillary force and van der Waal force between the tubes (entanglements). Among the different methods available to modify/functionalize VACNTs, plasma technique can not only be used to produce a cleaned VACNTs surface (remove amorphous carbon on as-received CNT layer), but can also functionalize CNTs by opening the top end caps or making side wall defects to improve wettability. Using sputter coating techniques, the selected single or multi thin metal layer can be coated on the CNTs surfaces. This suitable thin layer will enhance CNT and metal matrix interfacial properties. On the other hand, compared to pure CNTs, metal coated CNTs with increased mechanical properties and reduced interfacial Van de Waals forces will benefit by maintaining CNT alignment during matrix filtration processing.

Previous work by this group demonstrated that a uniform VACNT layer can be grown directly on a conductive substrate (Cu, Carbon, etc.) when a suitable thin buffer layer was coated on the surface (Zhang et al., 2004). In order to improve the interface connection between the CNTs and the matching substrate, this study focused on the surface modification of the VACNT array grown on the Cu foil substrate (as CNT/Cu), followed by optimum CNT-surface solder filtration processing to form a VACNT-based metal nanocomposite (MNC) structure. This procedure not only increases the VACNT layer to solder/substrate contact, but it also can introduce high thermal conductivity material on the CNTs surface as a bridge to enhance adhesion of VACNTs to a matching substrate surface (ceramic). Furthermore, given the excellent thermal properties of VACNTs in combination with the high electrical and thermal conductivities of metals, VACNT-based MNCs can meet the increasing demands for tailorable performance thermal management materials for use in heat sinks and advanced electronic packages in the aerospace, automotive, and electronics markets.

MATERIALS AND METHODS

Sample Preparation

Synthesis of Vertically Aligned Carbon Nanotubes Layer on Cu Foil Substrate

The VACNT layer were synthesized directly on a 10 mm × 10 mm × 2.35 mm copper (Cu) substrate (purchased from Online metals) via a FCCVD (Floating Catalyst CVD) method (Zhang et al., 2004). Before the CNT growth process was initiated, an optimized 10–15 nm aluminum (Al) buffer layer was applied to the pre-cleaned Cu substrate surface using a sputter coating technique. The growth process/conditions of CNTs by FCCVD is the same as previously reported (Zhang et al., 2004). The density and length of VACNT layer on Cu foil was controlled by growth time under the same growth conditions (Zhang et al., 2004). In this study, VACNT/Cu samples, with a VACNT layer thickness between

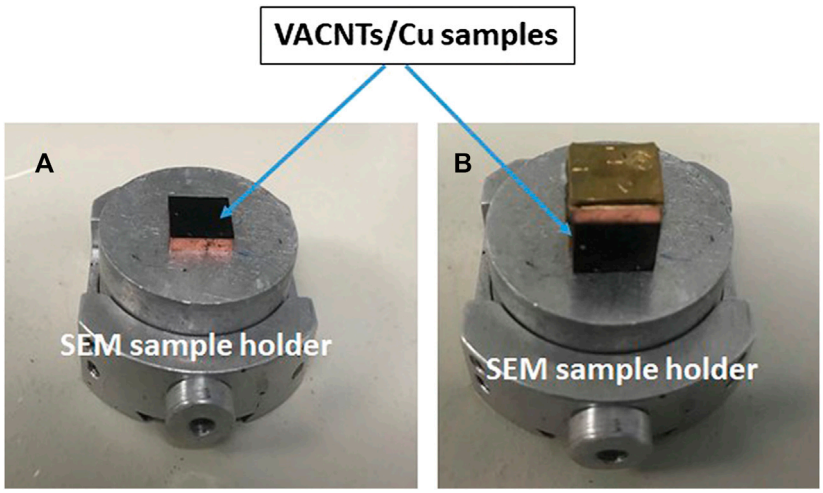

FIGURE 1 | (A) Top view setup for VACNT layer surface morphology. **(B)** Side view setup for VACNT layer thickness.

80 and 100 μm, were selected to prepare a series of three-layer (sandwich) samples. SEM (JEOL JSM6060 Scanning electron microscope) was employed to characterize the morphology/structure of VACNT layer. An example setup is shown in **Figure 1**.

Vertically Aligned Carbon Nanotubes Layer Surface Modification

Owing to its intrinsic structure and the high packing density of the VACNT layer, the main issue faced in the fabrication of VACNT-based MNC is the low wettability of CNTs with the molten metal matrix fill. To overcome this problem, in this study, the surface modification techniques were introduced for the objective of enhancing overall attachment between the VACNT layer and matching substrate. The different methods including plasma (South bay Technologies RIE-2000), sputter coating (Denton DV502A), and a combination of plasma and sputter coating were selected to modify the VACNT layer surface to improve CNT surface wettability while maintaining the alignment of VACNTs. The time of plasma treatment and the thickness of the metal layer were varied to find the optimum conditions for surface modification of the VACNT layer. Before and after surface modification, the VACNT layer surface morphology/structure was characterized by SEM. The results will be discussed in the next section.

Fabrication of Vertically Aligned Carbon Nanotubes-Based Metal Nanocomposite as Thermal Interface Material

Based on VACNT/Cu sample, a three-layer "sandwich" structure (Cu/TIM/Substrate) was created to make the VACNT-based MNC as TIM and processing scheme can be seen in **Figure 2**. The material and size/thickness of each layer on sandwich sample was shown in **Table 1**.

To reach the aforementioned goal, a new soldering setup was developed by converting a Thermo-Electric Generator (TEG) test stand into a Heated Compression System shown in **Figure 3**. A sandwich sample, produced by attaching a thin ceramic (0.64 mm) substrate (coated with a 20 nm nickel and 50 nm gold bi-layer) to a VACNT/Cu sample using selected 241 solder (10 × 10 mm), was first placed into a custom Macor sample holder (see **Figure 3**) and then delivered the holder to the HCS. A developed optimum processing, as **Table 2** shown, was used to fabricate the

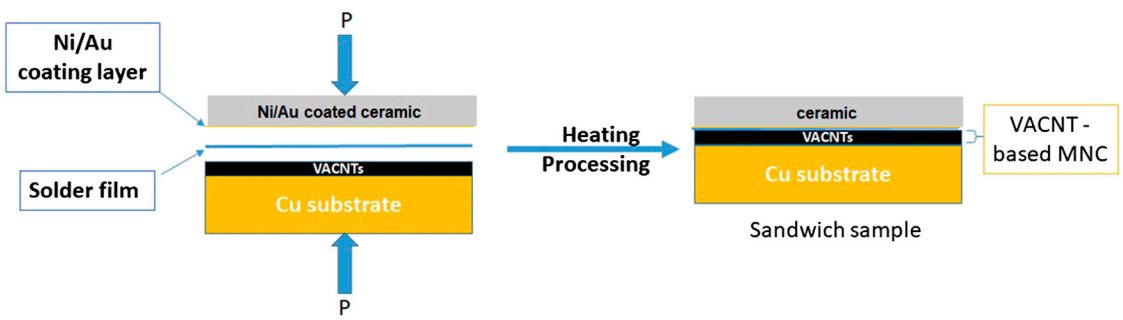

FIGURE 2 | Sandwich sample fabrication process and configuration.

TABLE 1 | Sample preparation materials.

Layer	Material	Size/Thickness (mm)	Surface modification/Treatment
Target substrate	Al_3O_2 Ceramic (Stellar Ceramics)	10 × 10 × 0.64	Coated with Ni (20 nm) and Au (50 nm)
Interphase layer (MNC)	Solder #241 (95.5 Sn/3.5 Ag/0.7 Cu) (Indium Corp)	10 × 10 × 0.05 (as received)	n/a
	VACNT layer	10 × 10 × 0.08–0.10 (as received)	None/plasma/Ni/Ti metallization
Growth substrate	Cu	10 × 10 × 2.35	As-received, coated with Al buffer layer (15 nm)

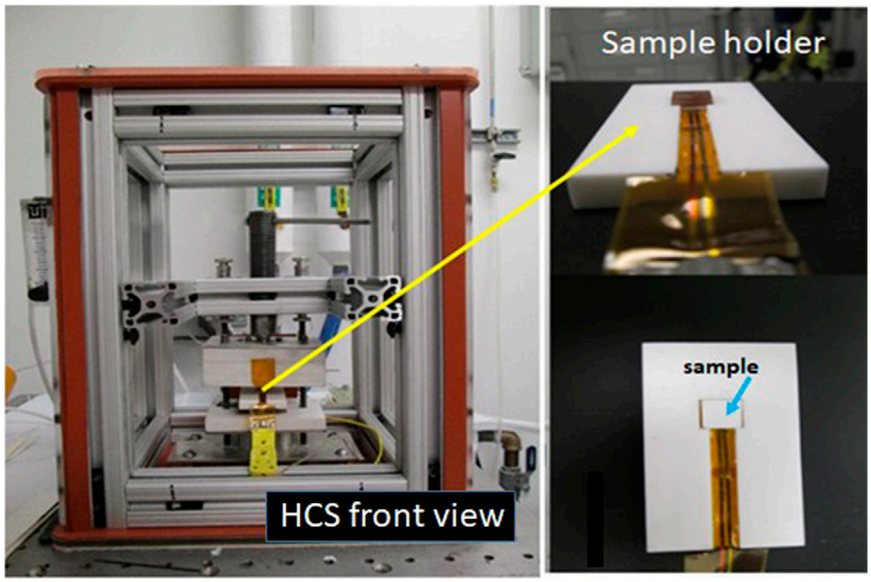

FIGURE 3 | Heated Compression System (HCS) for "sandwich" structure MNC fabrication and sample holder with sample in-place **(Right bottom)**.

VACNT based MNC interphase in a three-layer "sandwich" sample. The desired temperatures and load pressures are monitored/controlled using a custom LabVIEW program; a nitrogen purge capability was added to ensure the copper does not oxidize at high temperatures. Using metal coated ceramic substrates, solder241 and VACNT/Cu samples (with/without VACNT layer surface modification), a series of sandwich samples were produced by HCS (**Figure 3**) under the optimized processing conditions (**Table 2**). The structure of sandwich and morphology of interphase (MNC) in sandwich sample was characterized by SEM and will be discussed in next section.

Vertically Aligned Carbon Nanotubes/ Solder Interphase (Metal Nanocomposite) Thermal Analysis and Stability Testing

The thermal diffusivity of the VACNT/solder nanocomposite interphase layer was conducted by utilizing the Netzch Laser Flash Apparatus 457 (LFA) with the goal of characterizing thermal properties and evaluating thermal performance/ stability. In this study, a series of three-layer sandwich samples, made with different treatments on the surface of the VACNT layer (plasma, sputtering, etc.), were tested. Each sample was tested at least three times in alternating tray positions with a one-dimensional heat flux at temperature steps of 25, 50, 100, and 150°C. For three-layer structure samples, the Cu (bottom) and ceramic (top) substrates are programmed as known layers with a constant thickness and density; as the unknown layer, the thickness of VACNT based MNC was measured with SEM. The standard heat-loss (minus contact resistance) correction model was selected as the best match to determine the correct diffusivity (Firkowska et al., 2011).

The reliability of the VACNT based MNC were evaluated by a custom designed Rapid Thermal Cycling System. All three-layer (Cu/MNC/Ceramic) samples which were already measured in the LFA, were tested. To simulate the conditions that TIMs undergo in the field, the experimental conditions were selected, seen in **Table 3**. Thermal properties of tested samples were measured/ calculated by LFA system again after each set of 50 thermal cycles from −25 to 125°C up to 150 cycles. The thermal stability of interphase was assessed by a percentage increase in the thermal resistance of MNC after thermal cycles. According to a standard approach to testing device failure in electronics, a 50% increase in

TABLE 2 | Optimized parameters for VACNT based MNC fabrication (HCS).

Pressure (load force)	0.9 MPa (20–40 lbs)
Temperature	~20°C above solder melting point
Duration of hold	3–5 min
Sample set-up	Hot side: Cu/Cold side: ceramic

TABLE 3 | Parameters of thermal reliability testing (rapid thermal cycling machine).

Temperature range	−25 to 125°C
Temperature ramp rate	3.3°C/min (low ramp rate)
Soak time (per set point)	3 min
Number of cycles per run	50 cycles

the thermal resistance of the MNC indicates failure of the sample because this can lead to further degradation of the interface and thermal runaway as the mismatch in thermal expansion becomes worse.

RESULTS AND DISCUSSION

The Morphology of Vertically Aligned Carbon Nanotubes Layer Before and After Surface Modification

As a TIM, the CNT layer structure plays an important role on its thermal and mechanical properties. The VACNT layer with high packing density will increase interface contact area and resulted a good thermal and mechanical performance. SEM images of CNT array synthesized on Cu substrate are shown in **Figure 4**. The result indicated that, using FCCVD method, a uniform and high dense vertical aligned CNT layer was successfully grown on buffer layer coated Cu foil surface. After plasma or/and sputtering metallization treatment, the surface of VACNT layer has undergone significant changes.

Vertically Aligned Carbon Nanotubes Layer Surface Plasma Etching

Several CNT/Cu samples were subjected to plasma treatment (H_2 as sources) with 5, 10, or 15 min of treating times. The changes on VACNT layer surface morphology before and after treatment as well as the effect of treated time were monitored with SEM, and the results are shown in **Figures 5 and 6**. Comparing the SEM images before and after plasma etching, in **Figure 5**, the surface morphology of the VACNT layer obvious changed as expected; when the treatment duration was increased from 5 to 15 min, more "open space" at the top became exposed. There was a visible difference between the 10 and 15 min plasma treatment (see **Figure 6**): the 10 min treatment tops off between 1 and 2 microns from the surface whereas the 15 min treatment shreds through 2–3 microns from the surface, leaving a much lower density of VACNT layer packing and thus further increasing the solder infiltration surface. This result indicated that the surface morphology of the treated VACNT layer was determined by the time of plasma treatment. There was more open space on the top of the VACNT layer after a long-time processing, which will result in the improved wettability of the CNT array.

Vertically Aligned Carbon Nanotubes Layer Surface Metallization

The metallization of both substrate and VACNT layer surface is a promising approach to reduce the thermal contact resistance and simultaneously improve the interfacial adhesion of CNTs/matching substrate. In this study, Ti (Titanium)) and Ni (Nickel) were selected to metalize/modify the VACNT layer surface of VACNT/Cu samples due to their excellent physical properties and good adhesion with CNT (Ti as first layer) and solder (Ni as second layer). The Ti/Ni bi-metal thin layer with different thickness and Ti/Ni ratio were sputter coated on VACNT layer surface of VACNT/Cu samples. SEM images of the VACNT layer surface, before and after metal coating, can be found in **Figure 7**. These images show that a thin metal layer was evenly covered on the surface of the VACNT layer, which will result in a strong interfacial adhesion between the CNT array and the solder. The sputtering method was also used to coat a Ni/Au (20 nm/50 nm) double-layer thin film onto the surface of ceramic matching substrate to enhance interface properties between VACNT layer and substrate.

Vertically Aligned Carbon Nanotubes Layer Surface Plasma Treatment and Metallization

Surface metallization and plasma treatment are the two methods of surface modification pursued in this study. Ideally, plasma treatment will promote wettability/solder infiltration and surface metallization will improve surface attachment. Therefore, if these two methods are combined for VACNT layer surface treatment, the best interface performance should be produced. Based on this consideration, the sample processing was performed by coating different thicknesses of Ti/Ni bi-metal layer on the plasma-treated (via H_2 for 10 or

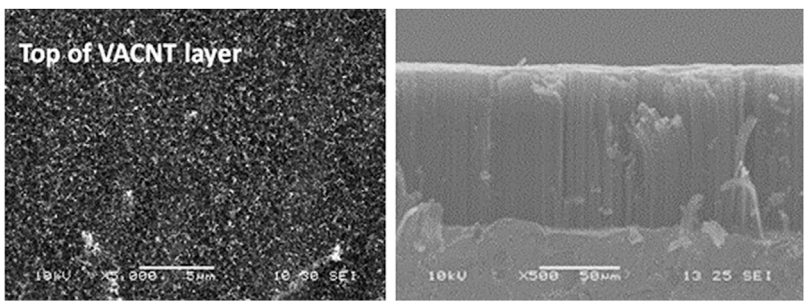

FIGURE 4 | SEM images of VACNTs grown on 15 nm Al coated Cu foil substrate. Top view (Left, scale bar = 5 μm) and side view (Right, scale bar = 50 μm).

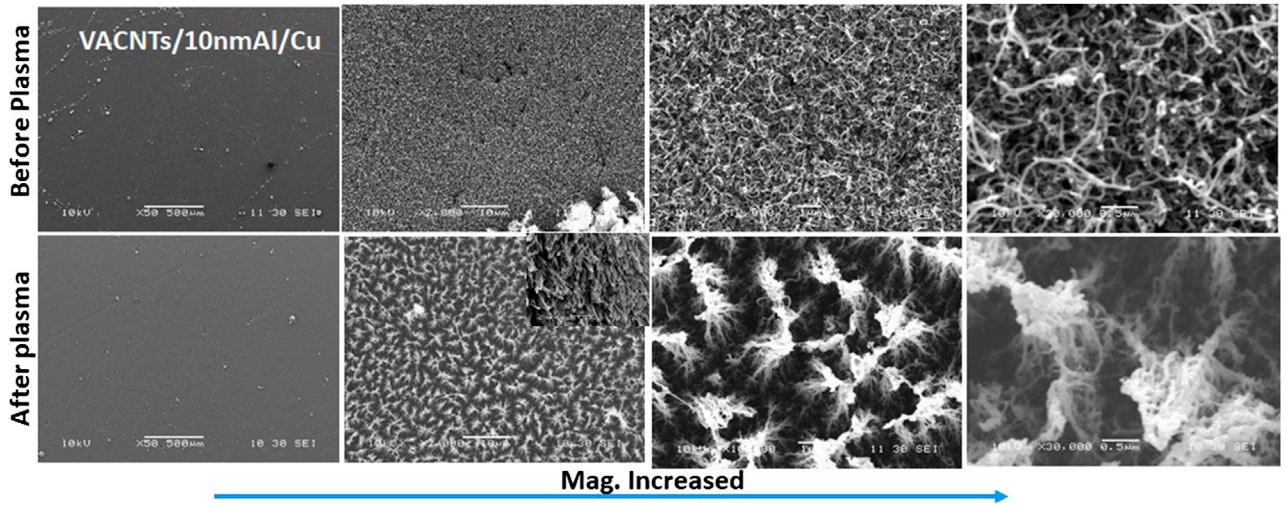

FIGURE 5 | Top view SEM images of VACNT layer: before and after 15 min plasma treatment. (Scale bar from left to right = 500, 10, 1.0, 0.5 μm.)

15 min) VACNT layer surface. The SEM images of the combined surface treatment samples can be found in **Figure 8**. The SEM images depict the expected results: open areas on the surface of VACT layer for solder infiltration are covered with a layer of metallic particles.

Structure of Three-Layer "Sandwich" Sample with Vertically Aligned Carbon Nanotubes-Based Metal Nanocomposite

The structure of sandwich and morphology of interphase (MNC) in sandwich sample was characterized by SEM and shown in **Figure 9**. SEM images shown a good interface connection between the MNC and the two substrates (ceramic and Cu). The results demonstrated that, with a suitable solder material, the fabrication process of sandwich sample can not only completely attach the matching substrate to the surface of the VACNT layer, but also maintain the interface adhesion of VACNT/Cu (No CNTs peeled from Cu foil). Due to the elastic properties of the VACNT array, the deformation of the VACNT layer can be clearly observed in the SEM image of **Figure 9**. As a TIM, this deformation should bring MNC good thermal and mechanical performance, especially in terms of thermal reliability.

Thermal Property of Vertically Aligned Carbon Nanotubes-Based Metal Nanocomposite in Sandwich Sample

Thermal property analysis for the MNC interphase of Cu/MNC/Ceramic samples focused on LFA testing to calculate the thermal

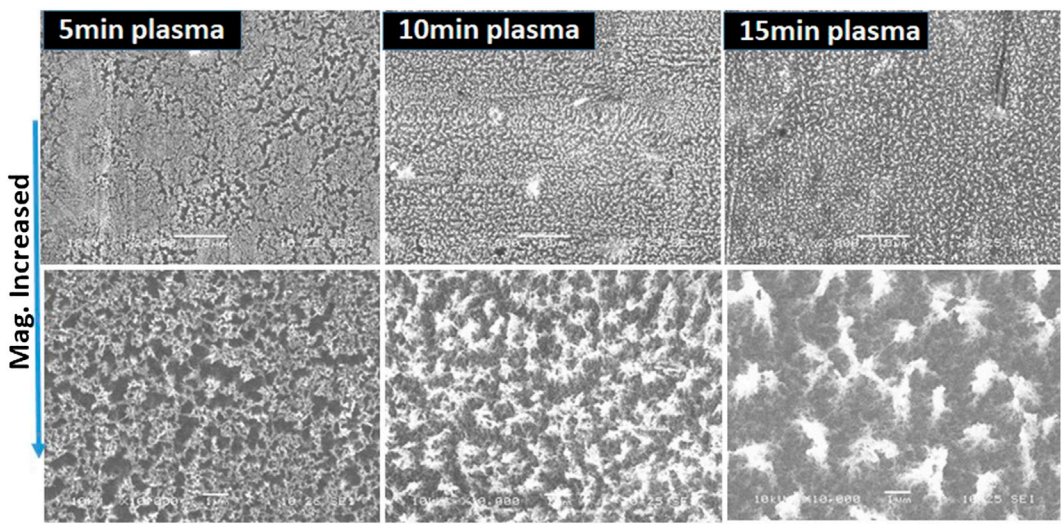

FIGURE 6 | Top view SEM images of VACNT layer: comparison of plasma treatment durations. (Scale bar on top = 10 μm; Scale bar on bottom = 1.0 μm).

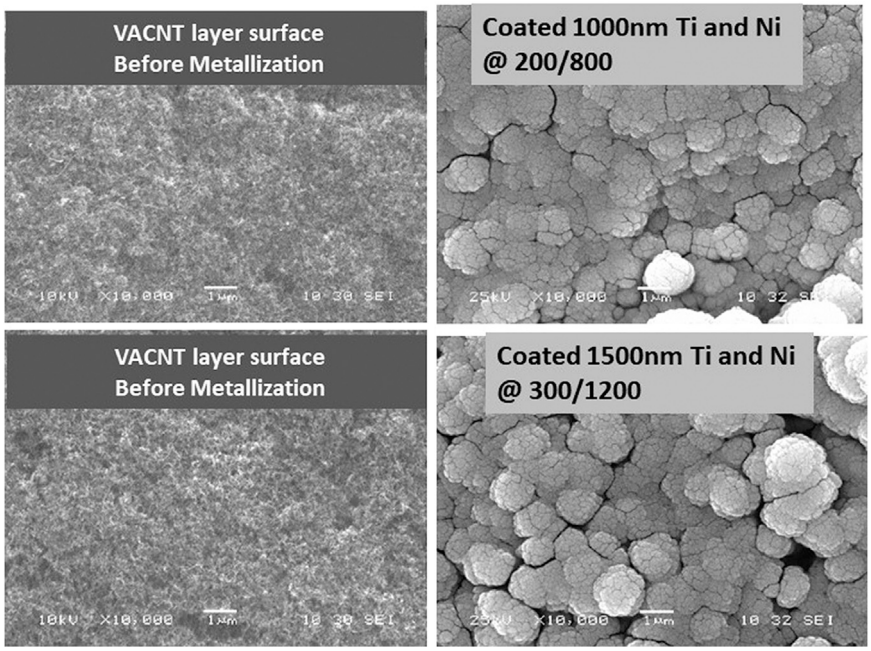

FIGURE 7 | Top view of SEM images: the metalized VACNTs surface by Ti/Ni bi-metal layer. (Scale bar = 1.0 μm)

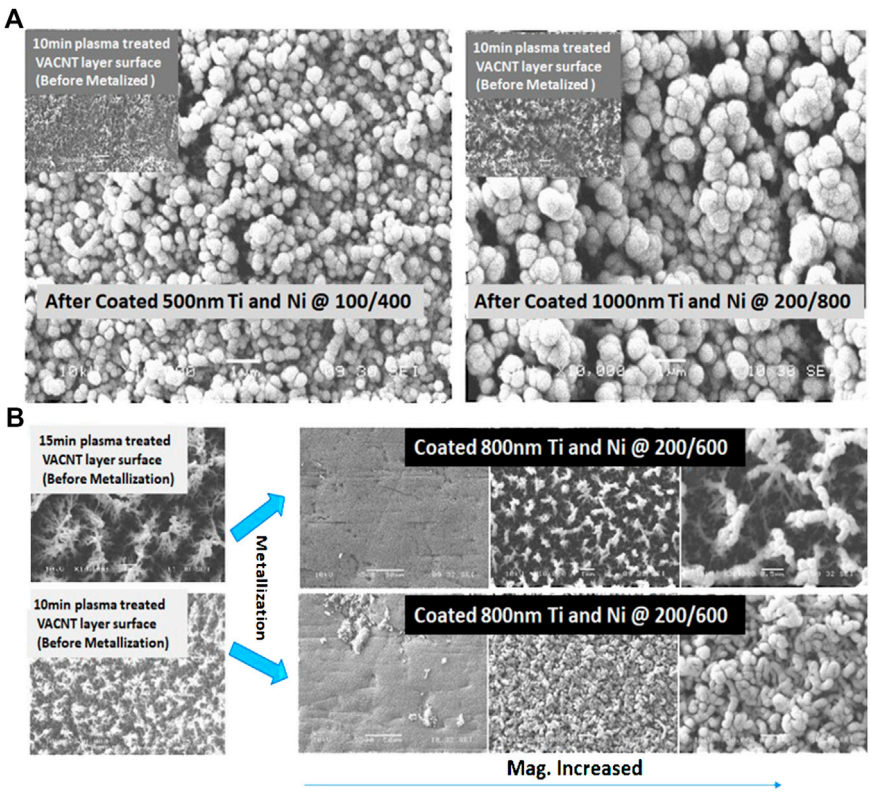

FIGURE 8 | Top view SEM Images. **(A)** The bi-metal layer with different thickness coated on Plasma treated VACNTs surface (10 min). **(B)** The bi-metal layer coated on Plasma treated (10 and 15 min) VACNTs surface. Scale bar = 1 μm **(A)**; Scale bar (from left to right) = 1, 50, 1.0, 0.5 μm **(B)**.

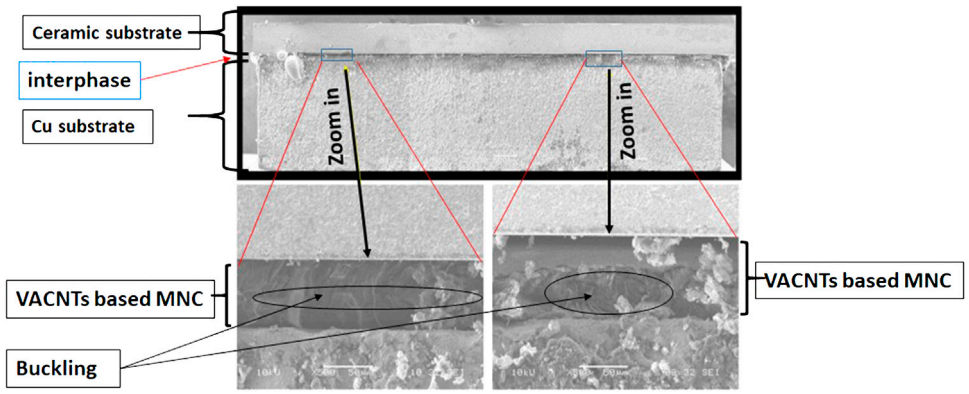

FIGURE 9 | Side view of fabricated sandwich sample **(top)** and MNC interphase **(bottom)**. (Top scale bar = 500 μm; Bottom scale bar = 50 μm).

resistance of the VACNT/solder interphase layer. All qualified three-layer sandwich samples, including with and without VACNT layer surface modification, were tested. Thus, the following results and discussion section focused on how the thermal properties of the MNC interphase were influenced by the method of VACNT layer surface treatment. Specifically, the thermal resistance was calculated based on the thermal diffusivity measured at 100°C by **Eq. 1**, where L is the VACNT layer thickness, α is the measured diffusivity, ρ is the VACNT layer density and C_p is the specific heat of the CNTs set to a constant of $C_p = 0.8$.

$$R = \frac{L}{\alpha \rho C_p} \tag{1}$$

To minimize error, numerous samples (grouped by VACNT layer surface treatment method) were tested. The average thermal resistance of each group samples, with standard deviation, can be found in **Figure 10**. These results will be discussed based on the VACANT layer surface treatment method.

From test results in **Figure 10**, the following conclusions about the effect of VACNT layer surface modification on the thermal resistance of the interphase (Cu/VACNT-solder/Ceramic sample) were drawn:

(1) The thermal resistance of MNC interphase was clearly influenced by surface treatment of VACNT layer. The changes of interface contact area, infiltration space and CNT surface wettability after surface treatment are the main reasons for this result.
(2) The thermal resistance of all samples made of untreated VACNT layers varied greatly (a large standard deviation). The main reason is most likely due to the uncertainty of the surface structure (morphology/purity, etc.) with untreated VACNT layer (as received). These variations will cause actual the interface contact area between the VACNT layer and matching substrate to be different varying for each untreated sample, thereby resulting in different thermal resistance values.

Compared to surface modified VACNT layer, the sample made with surface unmodified VACNT Layer had the highest thermal resistance value (see **Figure 10**). Namely, without VACNT layer surface modification, there is a large interface resistance between VACNT layer and matching substrate although fabrication techniques were optimized. This issue is primarily caused by the lack of solder infiltration within the VACNT layer during fabrication processing due to the CNTs low wettability and dense surface (non-aligned) of VACNT layer.

Surface metallization promotes improved adhesion (wettability) for contact between the CNT array tips and solder. Improved interfacial adhesion, where the thickness of metallization layer plays an important role, establishes a better connection, and thus resulted in improved thermal and mechanical properties. In this study, the interfacial mechanical properties (including the tensile strength and shear strength) of sandwich samples were explored by pull-off (tensile) and shear test. The results indicated that, when an 800 nm bi-metal thin layer (200 nm Ti layer and then 600 nm Ni layer) was coated on VACNT layer surface, a strong tensile strength was produced in the interface between VACNT layer and matching substrate. Therefrom, the 800 nm bi-metal layer was applied for all VACNT layer surfaces metallization. It can be clearly seen in **Figure 10** that MNC interphase thermal resistance was reduced by VACNT surface metallization. Adding conducting film/particles to the VACNT layer surface to enhance adhesion between CNT-solder are main reason for this improvement. However, an average thermal resistance of 66 mm^2-K/W means that surface metallization does not significantly improve the interphase thermal resistance. This is most likely due to the small penetration space for solder on the surface of the metalized VACNT layer.

VACNT layer surface plasma treatment was applied to improve the overall wettability of the CNT surface and opened space to enhance solder infiltration during MNC fabrication. Compared to the reference of VACNT based MNC (untreated) thermal resistance, the results as shown in **Figure 10** demonstrated a significantly lower thermal resistance with surface plasma modified VACNT/solder interphase (between two substrates). Specifically, samples which were treated by 15 min H_2 plasma had the lowest thermal resistances with a small standard deviation, as well as a greater improvement compared to sample made of 10 min H_2 plasma treated

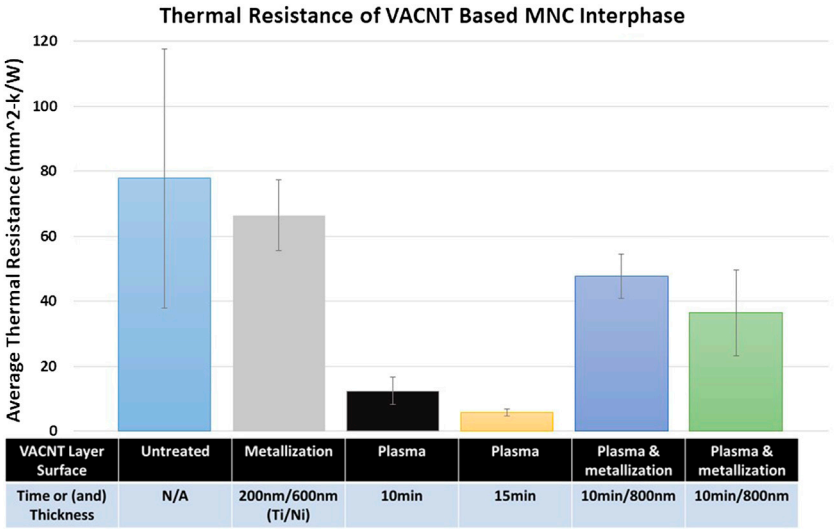

FIGURE 10 | Thermal resistance of MNC sandwich samples, per category of surface modification.

VACNT layer. The reasonable explanation for this result is that the longer treatment time can create more space on VACNT layer surface as shown in **Figure 6**, and this would allow more solder to infiltrate into the VACNT array during three layer sample fabrication to produce a stable MNC interface.

VACNT layer surface plasma treatment followed by surface metallization processing were expected to enhance the interfacial adhesion of CNT tip and solder while providing more infiltration space to improve thermal properties and reliability of the VACNT based MNC as TIM. The experimental results in **Figure 10** indicated that the surface modification of the VACNT layer by a combination technique (plasma and metallization) did reduce the thermal resistance of the VACNT based MNC interphase compared to the original (untreated samples). The pull-off testing results also show a strong interfacial adhesion between the modified VACNT surfaces and matching substrate. Under the same metallization conditions (metal layer Ti/Ni = 200 nm/600 nm), the VACNT surface after 15 min of H_2 plasma treatment produced a lower MNC interphase thermal resistance than that with 10 min of H_2 plasma treatment. However, this value is much higher than that of samples made with VACNT layer treated by plasma only. This is because the metal layer/particles coated on plasma treated VACNT surface (see **Figure 8**) may prevent solder infiltrating into the VACNT layer during MNC fabrication processing.

Thermal Performance/Reliability of Vertically Aligned Carbon Nanotubes-Based Metal Nanocomposite in Sandwich Sample

Although reducing the overall thermal resistance is a primary goal of this study, practical applications will cause periodic thermal stresses during normal operations. Thus, reliability

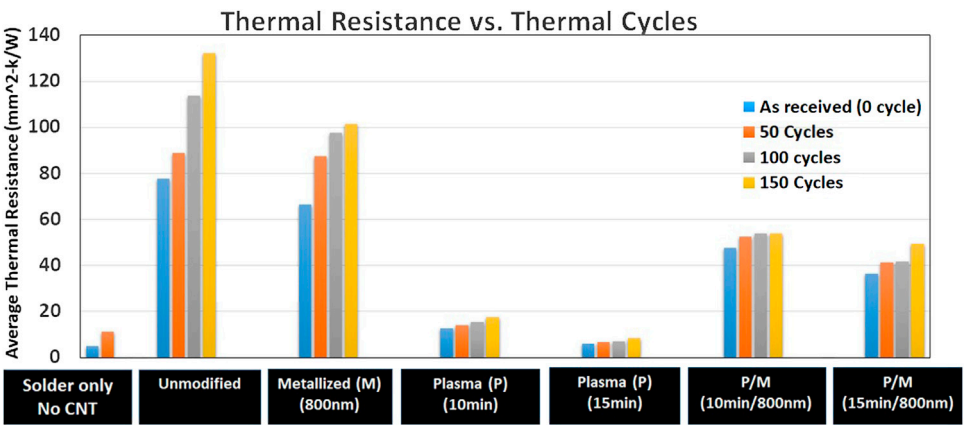

FIGURE 11 | Thermal cycles vs. thermal resistance of VACNT-based MNC as thermal interphase.

TABLE 4 | The effect of thermal cycles on thermal resistance (average) of TIM.

interphase //Resistance mm^2-K/W	Solder only (no VACNT layer)	Untreated VACNT layer	Metallized VACNT layer (800 nm)	Plasma (P)(10 min) VACNT layer	Plasma(P)(15 min) VACNT layer	P/M (10 min/800 nm) VACNT layer	P/M (15 min/800 nm) VACNT layer
R_0 (0 cycles)	4.95	77.81	66.35	12.45	5.90	47.70	36.40
R50 (50 cycles)	11.05	88.95	87.3	14.15	6.65	52.40	41.30
$\Delta R(R - R_0)$	6.1	11.14	20.95	1.7	0.75	4.7	4.9
$\Delta R/R_0$% increase	**123%**	**14.3%**	**31.57%**	**13.65%**	**12.71%**	**9.90%**	**13.46%**
R100 (100 cycles)	—	113.62	77.75	15.56	7.14	53.80	43.67
$\Delta R(R - R_0)$	—	35.81	11.4	3.11	1.24	6.10	7.27
$\Delta R/R_0$% increase	—	**46.00%**	**47.32%**	**24.98%**	**20.93%**	**12.79%**	**14.48%**
R150 (150 cycles)	—	132.20	101.30	17.60	8.28	53.8	49.4
$\Delta R(R - R_0)$	—	54.39	34.95	5.15	2.38	6.10	13.00
$\Delta R/R_0$% increase	—	**66.90%**	**52.67%**	**41.37%**	**40.25%**	**12.79%**	**35.71%**

Bold entries show the increased percentage of MNC interphase thermal resistance after thermal cycling and italic entries show the increased thermal resistance of MNC interphase after thermal cycling.

testing is necessary to characterize the thermal and mechanical performance of three-layer samples being created with VACNTs based nanocomposite (as TIM). In this study, the reliability of the VACNT-based MNC was evaluated as the percent increase in VACNTs/solder interphase thermal resistance from the original value through nominally induced thermal stress (thermal cycling). Using the aforementioned procedure and equipment related to reliability testing, all three-layer samples were subjected to 150 thermal cycles from −25 to 125°C. The thermal performance of the samples was retested by LFA after each set of 50 thermal cycles. The thermal resistance (including the results before and after the thermal cycle) and the nominal percentage increase (original value as reference) in thermal resistance after each set of 50 thermal cycles were illustrated in **Figure 11** and **Table 4**, respectively, by surface treatment category as below.

To compare the thermal properties of VACNT-based MNC and conventional TIM (solder), the Cu/Solder/Ceramic three-layer sandwich samples were prepared and tested. As expected, the solder-only TIM produced the lowest value of thermal resistance (good thermal conductivity) but quickly loses its reliability (very poor interfacial tensile strength) after only 50 thermal cycles, and the thermal resistance was significantly increased by more than 100% as shown in **Figure 11** and **Table 4**. As compared, the sandwich samples made of unmodified VACNT layer produced a more reliable VACNT-based TIM, which showed the lower rate of increase in thermal resistance after thermal cycles as seen in **Figure 11** and **Table 4**. However, the overall performance of these samples was not satisfactory due to their high thermal resistance.

Related to reliability during thermal cycling, all sandwich samples made with surface modified VACNT layer were tested. As expected, thermal resistance of MNC interphase for all tested samples increased after each thermal cycling test. However, the samples which have the VACNT surface modified, except for the samples with surface metallization treatment, showed modest increases in thermal resistance when compared to samples which have not, especially after 100 cycles. Except the surface metallized samples, all samples made with surface modified VACNT layer demonstrated improved interphase thermal stability, resulting in the thermal resistance increased by less than 50% (failure point) even after 150 thermal cycles. Moreover, the samples made with both plasma treated and metalized VACNT layer demonstrated the best thermal stability by showing a 12.79% increase on thermal resistance after 150 thermal cycles. The good thermomechanical performance under continued stresses was attributed to 1) opened veins/space (plasma treatment) on the VACNT array for solder infiltration; 2) metal particles (metallization) to promote the wettability of CNT tips to form a strong interfacial adhesion of VACNT layer and solder.

CONCLUSION

In this study, a VACNT layer was synthesized directly onto Cu foil substrate by FCCVD method. In order to achieve better interfacial adhesion of VACNT-based MNC (as TIM), a VACNT layer surface post-processing procedure (including plasma treatment and

metallization) was developed to improve the solder infiltration onto VACNT layer and thereby improve the overall thermal performance of interphase. The effect of different post-processing techniques on VACNT layer surface and interfacial properties of VACNTs/matching substrate were explored. The thermal performance of MNC were evaluated via Laser Flash system and Rapid Thermal Cycling System. Overall experimental results demonstrated:

(1) The VACNT layer surface modification is an effective method to improve thermal properties of VACNT based MNC as TIM. Compared with surface untreated VACNT layer, all the surface modified VACNT layer (as TIM) showed lower thermal resistance and higher thermal stability in tested sandwich samples.
(2) Among different VACNT surface modification methods, the plasma treated (especially with 15 min) VACNT layer surface promoted the best thermal properties of MNC, which was manifested by the lowest thermal resistance (5.90 mm^2-k/W, close to tested solder value 4.95 mm^2-k/W) and high thermal reliability under the thermal cycling test.
(3) Compared with the untreated VACNT layer, the 15 min plasma treated VACNT layer can reduce the thermal resistance of VACNT-based MNC by more than 80%. This finding indicated that CNT surface plasma treatment is a promising technique to enhance interfacial connection between CNT layer and solder to produce a good performance of VACNT based MNC as TIM.
(4) The sample, made with a VACNT layer surface treated by both plasma and metallization, showed an improved thermomechanical performance under thermal cycling. This is because the improved infiltration and wettability of solder by opened veins/holes and coated particles on VACNT array which promote interfacial adhesion and thermal conductivity, thereby maintaining the thermal performance under continued stresses.

DATA AVAILABILITY STATEMENT

The raw data supporting the conclusions of this article will be made available by the authors, without undue reservation.

AUTHOR CONTRIBUTIONS

QZ is a main author, all others are equal. All authors contributed to manuscript revision, read, and approved the submitted version.

FUNDING

Air Force Office of Scientific Research for funding support.

ACKNOWLEDGMENTS

The authors would like to thank the Air Force Office of Scientific Research for funding support, the Air Force Research Laboratory/RQQM, and following people for their help on this project: John Murphy, Jacob Lawson, Ammon Williams, James Scofield, William Lanter, and Joseph Merrett.

REFERENCES

Barako, M., Yuan, G., Marconnet, A., Asheghi, M., and Goodson, K. (2012). "Solder-bonded carbon nanotube thermal interface materials," in Proceedings of 13th IEEE intersociety conference: thermal and thermomechanical phenomena in electronic systems (iTherm), San Diego, CA, May 30–June 1, 2012, 1225–1233. doi:10.1109/ITherm18282.2012

Berber, S., Kwon, Y.-K., and Tománek, D. (2000). Unusually high thermal conductivity of carbon nanotubes. *Phys. Rev. Lett.* 84, 4613–4616. doi:10.1103/physrevlett.84.4613

Che, J., Çagin, T., and Goddard, W. A. (2000). Thermal conductivity of carbon nanotubes. *Nanotechnology* 11, 65–69. doi:10.1088/0957-4484/11/2/305

Chen, H., Roy, A., Baek, J.-B., Zhu, L., Qu, J., and Dai, L. (2010). Controlled growth and modification of vertically-aligned carbon nanotubes for multifunctional applications. *Mater. Sci. Eng. R Rep.* 70, 63–91. doi:10.1016/j.mser.2010.06.003

Chu, K., Guo, H., Jia, C., Yin, F., Zhang, X., Liang, X., et al. (2010). Thermal properties of carbon nanotube-copper composites for thermal management applications. *Nanoscale Res. Lett.* 5, 868–874. doi:10.1007/s11671-010-9577-2

Cola, B., Hodson, S., Xu, X., and Fisher, T. (2008). "Carbon nanotube array thermal interface enhanced with paraffin wax," in Proceedings of the ASME summer heat transfer conference, August 10–14, 2008, Jacksonville, FL, HT2008–56483.

Cola, B. A., Xu, J., Cheng, C., Xu, X., Fisher, T., Fisher, T. S., et al. (2007). Photoacoustic characterization of carbon nanotube array thermal interfaces. *J. Appl. Phys.* 101 (5), 054313. doi:10.1063/1.2510998

Cross, R., Cola, B. A., Fisher, T., Xu, X., Gall, K., and Graham, S. (2010). A metallization and bonding approach for high performance carbon nanotube thermal interface materials. *Nanotechnology* 21, 445705. doi:10.1088/0957-4484/21/44/445705

Firkowska, I., Boden, A., Vogt, A.-M., and Reich, S. (2011). Effect of carbon nanotube surface modification on thermal properties of copper-CNT composites. *J. Mater. Chem.* 21 (43), 17541–17546. doi:10.1039/c1jm12671g

Ganguli, S., Reed, A., Jayasinghe, C., Sprengard, J., Roy, A. K., Voevodin, A. A., et al. (2013). A simultaneous increase in the thermal and electrical transport in carbon nanotube yarns induced by inter-tube metallic welding. *Carbon* 59, 479–486. doi:10.1016/j.carbon.2013.03.042

Ganguli, S., Roy, A. K., Wheeler, R., Varshney, V., Du, F., and Dai, L. (2012). Superior thermal interface via vertically aligned carbon nanotubes grown on graphite foils. *J. Mater. Res.* 28, 933. doi:10.1557/jmr.2012.401

Hu, X. J., Padilla, A. A., Xu, J., Fisher, T. S., and Goodson, K. E. (2006). 3-Omega measurements of vertically oriented carbon nanotubes on silicon. *ASME J. Heat Transfer.* 128, 1109–1113. doi:10.1115/1.2352778

Huang, H., Liu, C. H., Wu, Y., and Fan, S. (2005). Aligned carbon nanotube composite films for thermal management. *Adv. Mater.* 17, 1652–1656. doi:10.1002/adma.200500467

Kim, P., Shi, L., Majumdar, A., and McEuen, P. (2001). Thermal transport measurements of individual multiwalled nanotubes. *Phys. Rev. Lett.* 87, 2155021. doi:10.1103/physrevlett.87.215502

Lin, W., Olivares, V., Liang, Q., Zhang, R., Moon, K., and Wang, C. (2009). "Vertically aligned carbon nanotubes on copper substrates for applications as thermal interface materials: from synthesis to assembly," in 9th IEEE conference on nanotechnology, Genoa, Italy, July 26–30, 2009. doi:10.1109/ectc.2009.5074051

Panzer, M., Zhang, G., Mann, D., Hu, X., Pop, E., Dai, H., et al. (2008). Thermal properties of metal-coated vertically-aligned single-wall nanotube arrays. *J. Heat Transfer.* 130, 052401, 2008. doi:10.1115/1.2885159

Son, Y., Pal, S., Borca-Tasciuc, T., Ajayan, P., and Siegel, R. (2008). Thermal resistance of the native interface between vertically aligned multiwalled carbon nanotube arrays and their SiO_2/SiSiO_2/Si substrate. *J. Appl. Phys.* 103, 024911. doi:10.1063/1.2832405

Tong, T., Zhao, Y., Delzeit, L., Kashani, A., Meyyappan, M., and Majumdar, A. (2007). Dense vertically aligned multiwalled carbon nanotube arrays as thermal

interface materials. *IEEE Trans. Comp. Packag. Technol.* 30, 92–100. doi:10.1109/TCAPT.2007.892079

Wang, H., Feng, J., Hu, X., and Ng, K. M. (2007). Synthesis of aligned carbon nanotubes on double-sided metallic substrate by chemical vapor deposition. *J. Phys. Chem. C* 111, 12617–12624. doi:10.1021/jp0730848

Xu, J., and Fisher, T. S. (2006). Enhancement of thermal interface materials with carbon nanotube Arrays. *Int. J. Heat Mass Tran.* 49, 1658–1666. doi:10.1016/j.ijheatmasstransfer.2005.09.039

Yang, D., Zhang, Q., Chen, G., Yoon, S., Ahn, J., Wang, S., et al. (2002). Thermal conductivity of multiwalled carbon nanotubes. *Phys. Rev. B* 66, 165440. doi:10.1103/physrevb.66.165440

Yin, X., Wang, Q., Lou, C., Zhang, X., and Lei, W. (2008). Growth of multi-walled CNTs emitters on an oxygen-free copper substrate by chemical-vapor deposition. *Appl. Surf. Sci.* 254 (20), 6633–6636. doi:10.1016/j.apsusc.2008.04.040

Zhang, Q., Quinton, B., Scofield, J., Merrett, J., Lawson, J., Tsao, B., et al. (2004). "Growth and characterization of uniform carbon nanotube arrays on active substrates," in Proceedings of materials research society 2004 fall meeting, Boston, MA, November 28–December 3, 2004.

Conflict of Interest: The authors declare that the research was conducted in the absence of any commercial or financial relationships that could be construed as a potential conflict of interest.

frontiers in Materials

ORIGINAL RESEARCH
published: 10 November 2020
doi: 10.3389/fmats.2020.572280

Direct Graphene Synthesis on Lithium Niobate Substrate by Carbon Ion Implantation

Yuhang Xu[1], *Fei Lu*[1]*, *Kaijing Liu*[1] *and Changdong Ma*[2]

[1]School of Information Science and Engineering, Shandong University, Qingdao, China, [2]Department of Radiation Oncology, Qilu Hospital of Shandong University, Jinan, China

For this study, a dozen-micron-scale four to seven layers of graphene were synthesized directly onto Lithium Niobate ($LiNbO_3$, LN) by carbon implantation in a nickel covered $LiNbO_3$ film. The 1.52E16 ions·cm^{-2} carbon ions of 80 keV were implanted into the nickel film to a depth of 100 nm, which is close to the interface between the nickel film and the $LiNbO_3$. The implanted carbon atoms dissolved in nickel at an elevated temperature and diffused towards the interface between the nickel film and $LiNbO_3$ during annealing. After the nickel film fell off, the graphene material was found by Raman spectroscopy and confirmed by the Atomic Force Microscope topographic image. This implantation combined with patterned metal film suggests possibilities for engineering two-dimensional graphene with special confinement. It also provides a valuable and novel way for integrating graphene-wafer structure for other available substrate wafer in microelectronics and photonics devices.

Keywords: graphene, direct synthesis, lithium niobate substrate, carbon ion implantation, nickel film, annealing

OPEN ACCESS

Edited by:
Ming Xu,
Huazhong University of Science and Technology, China

Reviewed by:
Jiangtao Di,
Suzhou Institute of Nano-Tech and Nano-Bionics (CAS), China
Horacio Javier Salavagione,
Consejo Superior de Investigaciones Científicas (CSIC), Spain

***Correspondence:**
Fei Lu
lufei@sdu.edu.cn

Specialty section:
This article was submitted to Carbon-Based Materials, a section of the journal Frontiers in Materials

Received: *13 June 2020*
Accepted: *28 August 2020*
Published: *10 November 2020*

Citation:
Xu Y, Lu F, Liu K and Ma C (2020) Direct Graphene Synthesis on Lithium Niobate Substrate by Carbon Ion Implantation. Front. Mater. 7:572280. doi: 10.3389/fmats.2020.572280

INTRODUCTION

Graphene has received increasing attention since the successful preparation of it in 2004 (Novoselov et al., 2004). Single-layer graphene is a two-dimensional honeycomb lattice structure composed of a single layer of carbon atoms, and each carbon atom is bonded to the surrounding carbon atoms through SP^2 hybridization (Xu et al., 2013). This structure has excellent conductivity. The electron mobility of graphene is higher than that of carbon nanotubes or silicon crystals. At room temperature, it can reach 15000 cm^2 ($V^{-1}{\cdot}s^{-1}$), while the resistivity is as low as about $10^{-6}\,\Omega$ cm (Chen, 2015). Graphene also has high transmittance to light. The graphene monolayer absorbs only 2.3% of visible light, that is, it has a high transmittance (97.7%) in a wide spectral range from visible to infrared (Zhu et al., 2010). Graphene also has exceptionable mechanical properties, due to an elastic modulus of 1.0 TPa, its inherent tensile strength of 130 GPa and a two-dimensional ultimate plane strength of 42 N·m^{-1} (Lee et al., 2008). As a material, graphene has excellent thermal conductivity (up to 5500 W ($m^{-1}k^{-1}$)) and high specific surface area (up to 2630 m^2g^{-1}) (Wang et al., 2017). Due to this special structure, outstanding thermal conductivity and mechanical properties, graphene has aroused great interest from the scientific community in recent years (Geim and Novoselov, 2007; Geim, 2009; Ma et al., 2018; Martín-García et al., 2018), and is expected to trigger a revolution in the field of modern optoelectronic technology.

The preparation and application of graphene have been explored in many studies over the past decade. Common preparation technologies include micro-mechanical peeling (Novoselov et al., 2004), pyrolysis of silicon carbide (Juang et al., 2009), Chemical Vapor Deposition(CVD) (Li et al.,

2009) and reduction of graphene oxide (Yin et al., 2011). The CVD method allows for the production of wafer-scale graphene layers, which has become the most popular technology. In recent years, a physical process has been proposed to synthesize graphene that involves the ion implantation of carbon into metal film and post-implantation annealing. Compared with a CVD method, ion implantation is a non-thermal equilibrium process, and has no requirements in terms of the carbon solubility of the material being implanted. The ability to control the number of layers of synthetic graphene may be possible by precisely adjusting the implantation dose (Garaj et al., 2010; Zhang et al., 2013). At present, transition metal nickel or copper are usually used to form graphene by carbon implantation (Garaj et al., 2010; Baraton et al., 2011a; Mun et al., 2012; Wang et al., 2013; Zhang et al., 2013; Lee et al., 2014; Kim et al., 2015; Wang et al., 2016). As the solubility of carbon in nickel decreases significantly with the decline of temperature, the carbon dissolved in nickel at high temperature will become saturated with the decrease of annealing temperature, and with the progress of thermal diffusion, they will eventually spread to the surface of the metal to form a single-layer or multi-layer graphene (Lander et al., 1952; Berry, 1973; Baraton et al., 2011b).

The application of graphene must be based on the graphene/substrate structure, and a lot of research has been conducted in recent years, but these studies are mainly focused on graphene/$Si(SiO_2)$ structure (Yoon et al., 2009; Garaj et al., 2010; Baraton et al., 2011b; Wang et al., 2011; Kumari et al., 2014; Lee et al., 2014; Dong et al., 2016; Onishi et al., 2017; Zuppella et al., 2017; Faggio et al., 2019; Ma et al., 2020). Few studies have focused on graphene/optical crystal, but among those that have , the combination of graphene and Lithium Niobate ($LiNbO_3$, LN) is one of the most promising structures for development. LN is a nearly all-around artificial crystal, it has ferroelectric, piezoelectric, pyroelectric, photovoltaic, photoelastic, photorefractive and other properties, and has a wide range of applications unmatched by other crystals, known as "silicon materials in the optical field" (Graca et al., 2012; Boes et al., 2018; He et al., 2019; Kong et al., 2019). Its combination with graphene may have an impact on the quantum properties of two-dimensional materials, resulting in new photoelectric properties, which will inevitably have a wide range of potential applications (Jin et al., 2013; Baeumer et al., 2015; Salas et al., 2017a; Salas et al., 2018). For example, some studies have theoretically explored the interfacial properties of the combination of graphene and LN crystals (Wang et al., 2015; Salas et al., 2017b). One typical example is the modulation of carrier doping of graphene via LN polarization properties. The results show that by adjusting the carrier doping in graphene in the graphene/LN structure, the formation and propagation of surface plasmons polaritons can be controlled.

Previously, graphene bonding to substrates was mostly based on the graphene transfer method. However, the resulting graphene/LN or Si (SiO_2) structures often suffer from graphene defects caused by the transfer process which leads to additional graphene degradation. Therefore, it's necessary to study the direct synthesis of graphene/LN structure. The formation of graphene on the LN surface using direct carbon implantation of LN has been reported in our previous study (Liu et al., 2019), which found that the carbon implanted into the LN can accumulate on the crystal surface by out-diffusion at a moderate temperature and eventually form graphene. The carbon diffusion pathways, on the other hand, is related to the distribution of damage of LN lattice induced by carbon implantation. However, in this experiment only turbostratic graphene was demonstrated on the LN surface. LN has a complex structure, the solubility and diffusion behavior of carbon in LN is still unclear.

In this article, we report the direct synthesis of graphene on the surface of LN by annealing the post-carbon-implantation sample consisting of surface transition metal film and LN substrate. In the present experiment the carbon ions were implanted into the metal film covering the surface of the crystal rather than into the LN itself. This approch used the nickel as a catalyst, and graphene growth was based on the large solubility change of carbon ions in nickel films at different temperatures. Graphene was synthesized at the interface of nickel/LN, and the realization of immediate contact between graphene and LN omits the conventional intermediate process of graphene transfer. Our research provides a new method of preparation for applying graphene on substrates without transfer. Importantly, it provides a new approch that enables the direct synthesis of graphene that can create specific shapes and sizes on any substrates, which is often emphasized in photoelectric crystals such as LN.

MATERIALS AND METHODS

A schematic diagram of the experimental method used in this study is shown in **Figure 1**. The substrate was Z-cut $10 \times 10 \times 0.5\ mm^3$ bulk LN with Chemical Mechanical Polishing on one $10 \times 10\ mm^2$ surface for the following nickel coating. First, a layer of nickel foil is deposited on this surface as an overlay, and then the deposited sample is implanted with carbon ion. During the annealing process, the implanted carbon moves to the interface between the nickel foil and LN crystal. Ideally, a few layers of graphene will be formed, and finally, the nickel foil is removed to gain the graphene/LN structure.

The thin layer of nickel was deposited on the surface of LN by resistance heating evaporation. As shown in **Figure 2A**, the thickness of the nickel foil measured by Atomic Force Microscope (AFM) is around 134 nm. The dose of carbon ion implantation we used is 1.52E16 ions·cm^{-2}, which is selected to match the carbon content of four-layer graphene, and the ion energy of 80 keV ensures that the implanted carbons distribute near the interface between the nickel foil and LN crystal. **Figure 2B** shows the carbon ion distribution along the depth profiles simulated by Stopping and Range of Ion in Matter (SRIM) in the nickel/LN sample. According to SRIM simulation, the peak of carbon concentration is at roughly 100 nm below the surface of nickel film and is close to the interface between nickel and LN. The variation of the carbon concentration with the depth of implantation approximately follows the Gaussian distribution and the nickel film holds more than 80% in all implanted carbon. Subsequently, the as-

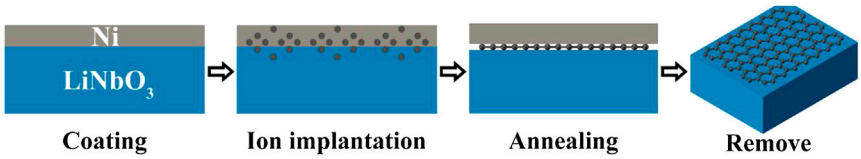

FIGURE 1 | A schematic diagram of the steps of the experiment.

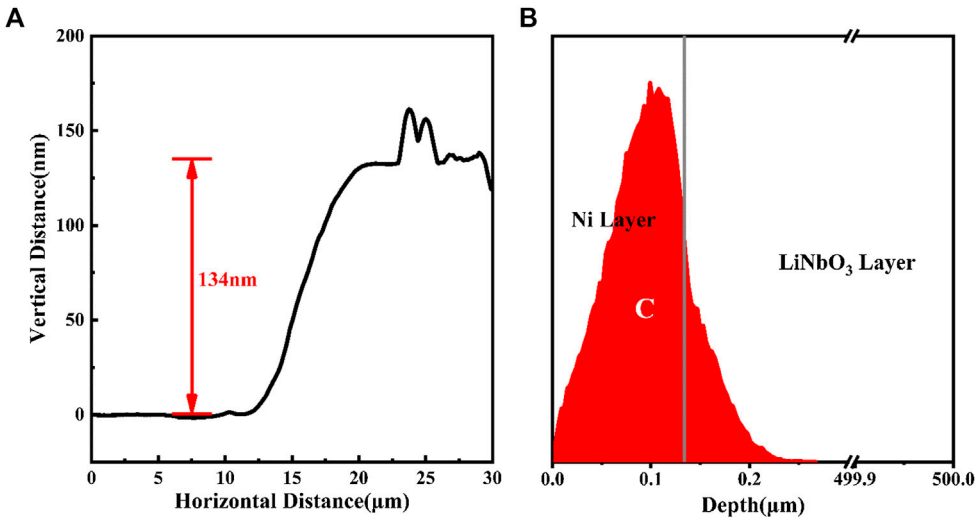

FIGURE 2 | (A) AFM height profiles along the straight line from uncoated notch to the coated area **(B)** Structural schematic diagram of the coated bulk LN crystal with the distribution of carbon ions along with the depth profiles, simulated by SRIM.

implanted sample was annealed in the furnace. It was first heated to 900 °C at a rate of 10 °C·min^{-1}, an kept at this temperature for 30 min, then allowed to naturally cooled to room temperature. The entire annealing process was carried out in N2 ambient, with a gas flow rate of 100 sccm (standard-state cubic centimeter per minute) and pressure of 6E4Pa.

RESULTS AND DISCUSSIONS

The sample was first observed with an optical microscope, the images of the sample before and after annealing were shown in **Figures 3A,B**, respectively. Wrinkles appeared on the surface of the annealed sample. This phenomenon occurs on the one hand, because of the poor adhesion between the deposited metal film and the LN substrate, and on the other, due to the different thermal expansion properties of the two materials. **Figure 3C** shows the enlarged two-dimensional AFM image of the wrinkles on the surface of the sample, and **Figures 3D, E** are the respective height profiles along the solid red line one and line two marked in **Figure 3C**, respectively. As revealed by these images, the average height of the folds is around 0.7–1.8 μm and the width is about 10 μm. To determine the cause of the wrinkles, another two kinds of samples (one without carbon ion implantation and the other with carbon ion implantation) of the same coating treatment were annealed under the same conditions. It was found that both samples had similar wrinkles. This shows that the occurrence of wrinkles on the surface of this sample depends on the surface nickel film and the LN substrate themselves, and has nothing to do with carbon ion implantation.

No information of carbon material was detected by Raman spectroscopy on the upper surface of the nickel film, which excludes the case where carbon is precipitated from the nickel surface. The existence of wrinkles makes the nickel film easy to peel off. After the nickel film fell off, the LN surface was observed with a scanning electron microscope (SEM). A strong carbon signal was detected, indicating that the implanted carbon was mainly deposited at the interface between nickel and LN after annealing. Some carbon atoms converge into large clusters, which are distributed on the surface of LN. **Figures 4A, B** show the SEM image and its Energy Dispersive Spectrometer (EDS) mapping distribution of carbon from one of the clusters respectively. The highlights of the carbon distribution seen in **Figure 4B** fit well with the material distribution profile, and the Raman Spectra with the excitation wavelength at 532 nm from three, positions marked in **Figure 4A**, also confirmed that the aggregated carbon exhibits an amorphous structure. As can be seen in **Figure 4C**, the Raman curves at three locations show similar profiles. The D and G peaks

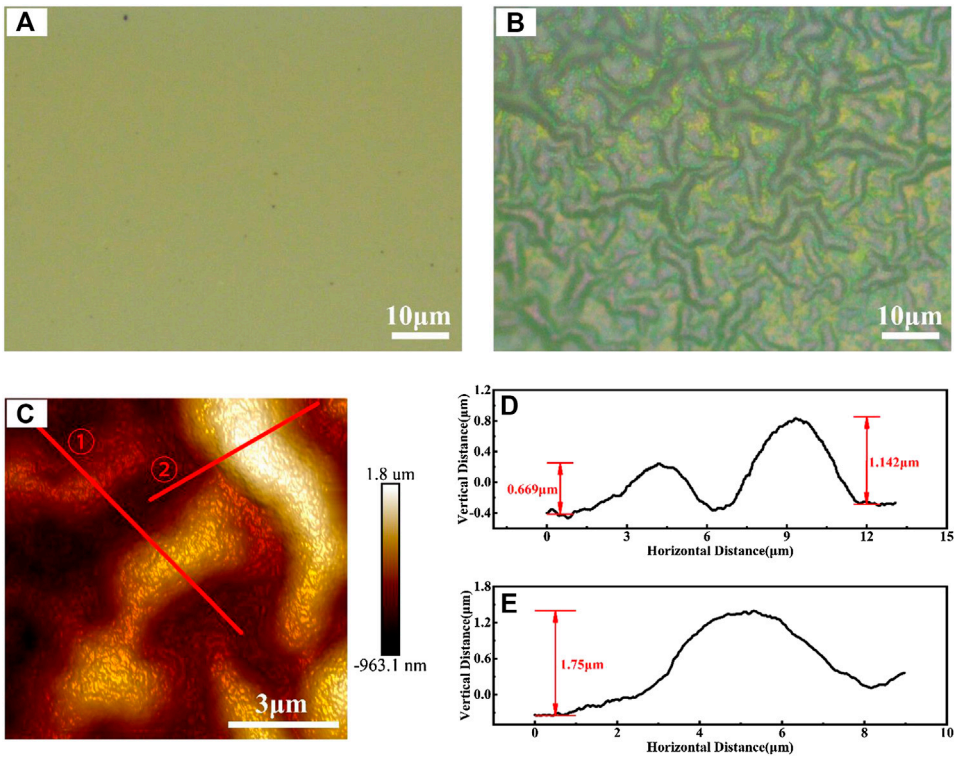

FIGURE 3 | (A, B) The optical microscope images of the surface of the bulk LN crystal with nickel film before **(A)** and after annealing **(B) (C)** AFM topographic image of the wrinkles, and **(D)**–**(E)** AFM height profiles along the solid red line one and line two in **(C)**.

are merged into one peak, while the 2D peak shows a very gentle and wide span distribution. This characteristic indicates that the carbon here is amorphous carbon with poor crystallinity (Shimodaira and Masui, 2002; Kaniyoor and Ramaprabhu, 2012; Sathish-Kumar et al., 2012). **Figures 4D,E** indicate the AFM of this cluster and its height profiles along marked red solid lines respectively. The height of the carbon material is about 1 μm, which is consistent with the height of the bulge in the wrinkled nickel film in **Figure 3**, which is around 0.7–1.8 μm. It is reasonable to suppose that the amorphous carbon material gathered and developed in wrinkled bumps and that the bulged nickel film provides space for holding these carbon materials. Improving the deposit of nickel film and its adhesion to LN is one of the key factors for ensuring the uniformity of carbon distribution.

We also found other forms of carbon structures on the surface of the LN, as shown in **Figure 5A** is the SEM image from part of the sample surface, and **Figures 5(B)–(D)** are the corresponding EDS mapping diagrams of Nb, C and O elements at the same area, respectively. It can be seen that the elements Nb and O, which come from the LN substrate, are distributed uniformly. While the distribution of element C seen in **Figure 5C** is consistent with the morphology of **Figure 5A**, indicating that the spots on the surface are carbon materials. Subsequently, Raman spectra with 532 nm excitation wavelength for the five marked positions one to five in **Figures 5A,C**, which correspond to exactly the same positions, were obtained, as shown in **Figure 6**.

The Raman spectra at positions one and two are similar, revealing spectral features and uniquely characteristic of graphene films: a G peak (1,580 cm^{-1}) associated with sp^2 carbon bond stretching, a D peak (1,345 cm^{-1}) arising from symmetry-breaking features, such as graphene defects and domain boundaries, and a 2D peak (2,690 cm^{-1}) sensitive to the graphene inter layer interactions (Garaj et al., 2010; Han et al., 2011; Mun et al., 2012; Lee et al., 2014). The ratios of I_D to I_G (a measure of disorder) and I_{2D} to I_G (determined by the number of stacked graphene layers) are very similar, and are often used as the main parameters to judge the structural defects and the number of layers of graphene (Garaj et al., 2010; Lee et al., 2014). The corresponding ratio values of 1.1 and ~0.5 indicate that the number of graphene layers is four to seven layers (Yu et al., 2008; Wang et al., 2013; Zhang et al., 2013). At the same time, the ratios of I_D to I_G are also higher at positions one and two, indicating that the graphene is defective. The graphene we obtained had many defects, including the mixing of multiple structures, graphene fragmentation, folding and structural distortion. This is the main reason for the larger I_D/I_G ratio. The spectra at positions three to five are shown in **Figure 6B**, where three distinct Raman peaks of D, G, and 2D are also visible. However, the ratio of I_{2D} to I_G is much lower than those of

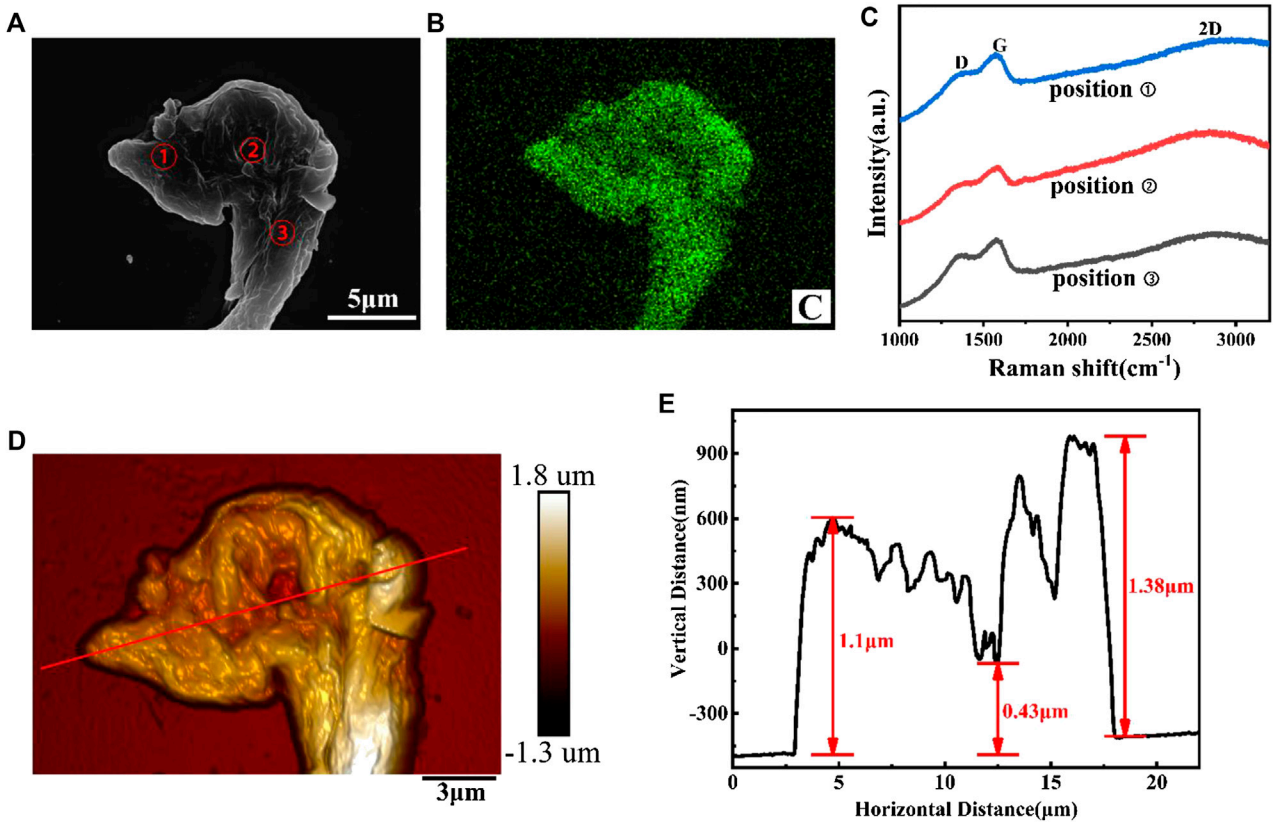

FIGURE 4 | (A) SEM image of the amorphous carbon material on LN **(B)** EDS mapping for C element in the region shown in **(A)** **(C)** Raman Spectra of three positions shown in **(A)** **(D)** AFM topographic image of the amorphous carbon material, and **(E)** AFM height profiles along the solid red line in **(D)**.

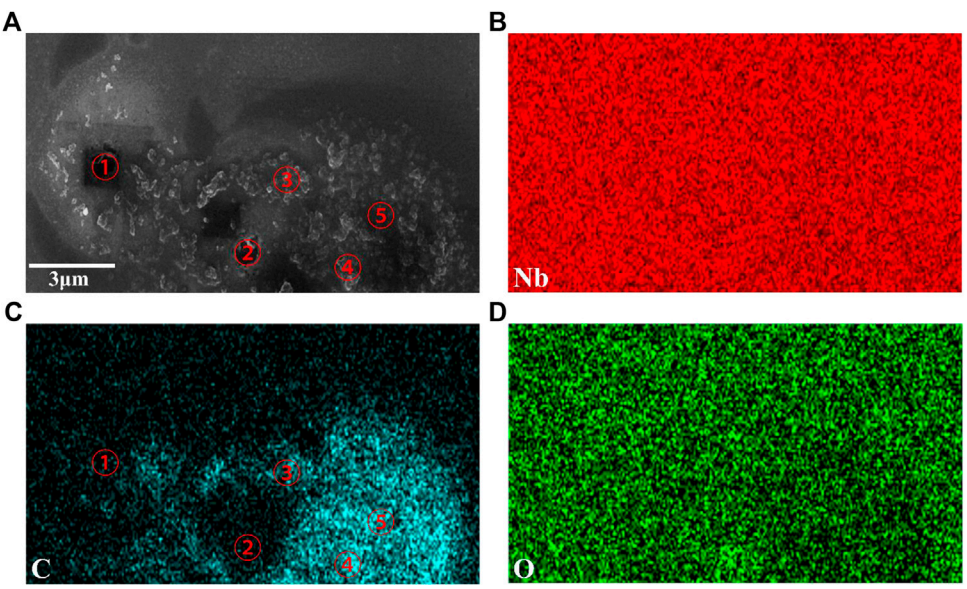

FIGURE 5 | (A) SEM image of graphene on LN **(B)**–**(D)** EDS mapping for Nb, C, and O elements in the region shown in **(A)**.

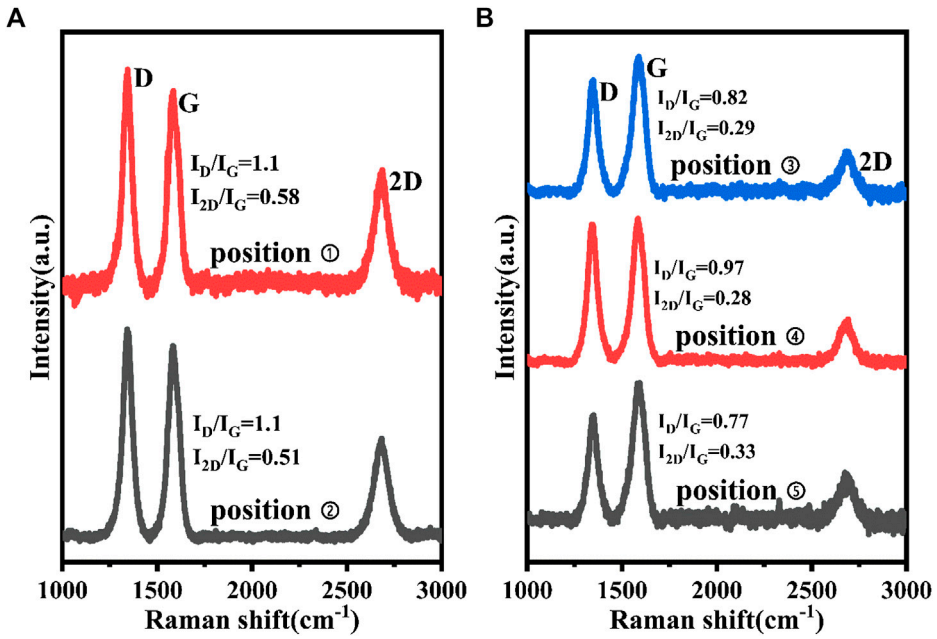

FIGURE 6 | Raman Spectra of **(A)** positions one and two, **(B)** positions three, four, and five in **Figure 5**.

positions one and two, which is only around 0.3, suggesting that the graphene here could be a stacked multilayer structure. This result indicates that the carbon materials at these positions have the structural characteristics of turbostratic graphene (Garlow et al., 2016; Liu et al., 2019). Turbostratic graphene is a multilayer structure with a disordered arrangement, and its properties are significantly different from the structured two-dimensional multilayer graphene. Since our research focus is to obtain a two-dimensional multilayer graphene structure on LN, the results of positions one and two are of particular note.

The SEM image around position one in **Figure 5** is shown in **Figure 7A**, some layered structures were observed. Subsequently, we conducted AFM scanning around positions one and two in **Figure 5**, and the results are shown in **Figures 7B–E**. A depression in the dark spot can be found at the test center point due to the loss of graphene caused by multiple Raman spectroscopy measurements. The height difference between the depression and the surrounding area represents the thickness of the multilayer graphene here. **Figures 7B,C** are the AFM topographic image around locations one and two, and **Figures 7D,E** are the profiles along the three different solid yellow lines in **Figures 7B,C**, respectively. It can be seen that there is a downward hollow in **Figures 7D,E**, which is the edge depression of a few layers of graphene. Although the three height change curves of each set in the figure are slightly different, on average, the depth of the depression at position one and two are about 46 and 70 nm respectively. These results are consistent with the estimations from our Raman results, an I_{2D}/I_G ratio of 0.58 in position one representing four to six layers of graphene, while 0.51 in position two represents five to seven layers of graphene. They also all correspond to the thickness values of four to six layers and five to seven layers multilayer graphene measured with AFM in references (Wu et al., 2009; Lee et al., 2014).

The direct two-dimensional synthesis of graphene on the surface of LN by carbon implantation has been proved to be feasible in our experimental scheme, although there are still many areas that need improvement. The current experimental results show that as a host for carbon ions, the quality of the nickel film and the uniform adhesion between the nickel and the LN substrate are important factors that affect the formation and structure of graphene. One of the improvements to the current experimental method is to use magnetron sputtering instead of vacuum evaporation to grow nickel thin films, which will increase the uniformity of nickel and the adhesion to the substrate.

The control of the annealing process is also an important factor, because proper annealing may reduce the thermal mismatch between the two materials during expansion and contraction. Thermal annealing is the only way to form graphene through carbon precipitation. The sample is firstly annealed at high temperature to accommodate more carbon and then cooled down so that the carbon becomes saturated in nickel as the temperature decreases, and the graphene is formed when the carbon overflows to the interface between nickel and LN with thermal diffusion. Since the diffusion property of carbon depends on several variables, such as the concentration gradient of carbon, the distance from carbon to the nickel/LN interface, the temperature range and temperature rise and fall speed, and ambient gas, etc., make the determination of annealing conditions particularly difficult. Therefore, the establishment of appropriate annealing conditions requires

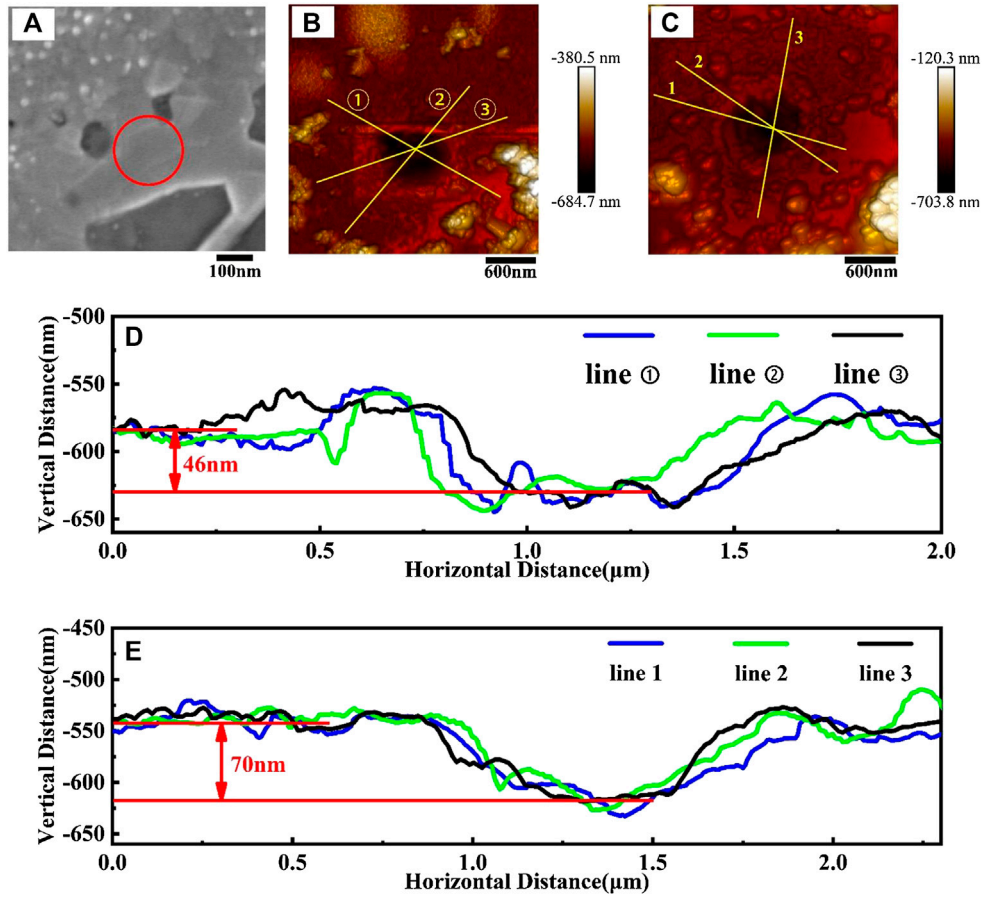

FIGURE 7 | (A) SEM image around position one in **Figure 5**, **(B,C)** are the AFM topographic image around locations one and two in **Figure 5**, **(D,E)** are the profiles along the three different solid yellow lines in figure **(B)** and figure **(C)**.

repeated adjustments, improvements, and measurements, which are currently being carried out in our research.

CONCLUSION

In our experiment, the 1.52E16 ions·cm^{-2} carbon ions of 80 keV were implanted to the nickel/LN substrate, which consists of an LN crystal covered with a layer of 134 nm thick nickel metal film. The implantation depth was 100 nm according to simulation by SRIM, which is close to the interface between the nickel film and LN. During post-implanted annealing, the sample was heated to 900°C and held for 30 min, then cooled down naturally *in situ*. After annealing, the nickel film on the surface of LN was wrinkled and easy to fall off. This can be attributed to the weak bonding between the nickel film and LN substrate and their mismatch thermal expansion coefficients. No signal of carbon material was detected by Raman spectroscopy from the upper surface of the nickel film, which excludes a result of carbon precipitation from the upper surface of the nickel film. After the nickel film fell off, two kinds of carbon structures were found on the surface of the LN substrate by SEM, EDS, and Raman spectroscopy. First, amorphous carbon with poor crystallinity gathered and developed under the bulge of the wrinkled nickel film. Second, the graphene structure with an uneven number of layers mixed with turbostratic graphene and four to seven layers of two-dimensional graphene, as confirmed by AFM topographic image. The direct synthesis of two-dimensional graphene on the surface of LN was proved in our experimental scheme, which draws on the experiences of predecessors in the synthesis of graphene by carbon ion implantation of nickel, but our experiment omitted the process of film transfer. In particular, implantation combined with patterned metal film suggests the possibility of engineering two-dimensional graphene with special confinement, which is often emphasized in photoelectric crystals such as LN. The flexibility of photolithography technology in the metal pattern may makes it achievable to potentially form an air-graphene-wafer system with

special nanostructure, such as graphene nano-disk. Direct synthesis of graphene with patterned and even distribution on the LN is our next research goal, and further experiments are in progress.

DATA AVAILABILITY STATEMENT

The raw data supporting the conclusions of this article will be made available by the authors, without undue reservation.

AUTHOR CONTRIBUTIONS

YX, and FL: conceptualization, data curation, formal analysis, methodology, and writing - review and editing. FL: funding acquisition, supervision and validation. YX, FL, and KL: investigation. YX, KL, and CM: project administration. YX: visualization and writing - original draft.

FUNDING

This study was funded by the National Natural Science Foundation of China (Grant Number 61975094).

ACKNOWLEDGMENTS

We would like to thank Dr Mingsheng Xu, School of Microelectronics, Shandong University for the use of his equipment.

REFERENCES

Baeumer, C., Saldana-Greco, D., Martirez, J. M. P., Rappe, A. M., Shim, M., and Martin, L. W. (2015). Ferroelectrically driven spatial carrier density modulation in graphene. *Nat. Commun.* 6, 6136. doi:10.1038/ncomms7136

Baraton, L., He, Z. B., Lee, C. S., Cojocaru, C. S., Châtelet, M., Maurice, J.-L., et al. (2011a). On the mechanisms of precipitation of graphene on nickel thin films. *Epl* 96, 46003. doi:10.1209/0295-5075/96/46003

Baraton, L., He, Z., Lee, C. S., Maurice, J.-L., Cojocaru, C. S., Gourgues-Lorenzon, A.-F., et al. (2011b). Synthesis of few-layered graphene by ion implantation of carbon in nickel thin films. *Nanotechnology* 22, 085601. doi:10.1088/0957-4484/22/8/085601

Berry, B. S. (1973). Diffusion of carbon in nickel. *J. Appl. Phys.* 44, 3792–3793. doi:10.1063/1.1662846

Boes, A., Corcoran, B., Chang, L., Bowers, J., and Mitchell, A. (2018). Status and potential of lithium niobate on insulator (LNOI) for photonic integrated circuits. *Laser Photon. Rev.* 12, 1700256. doi:10.1002/lpor.201700256

Chen, C.-M. (2015). Surface chemistry and macroscopic assembly of graphene for application in energy storage. PhD thesis. Beijing (China): University of Chinese Academy of Sciences.

Dong, T., Sparkes, M., Durkan, C., and O'Neill, W. (2016). Evaluating femtosecond laser ablation of graphene on SiO_2/Si substrate. *J. Laser Appl.* 28, 022202. doi:10.2351/1.4944510

Faggio, G., Gnisci, A., Messina, G., Lisi, N., Capasso, A., Lee, G. H., et al. (2019). Carbon dots dispersed on graphene/SiO_2/Si: a morphological study. *Phys. Status Solidi.* 216, 1800559. doi:10.1002/pssa.201800559

Garaj, S., Hubbard, W., and Golovchenko, J. A. (2010). Graphene synthesis by ion implantation. *Appl. Phys. Lett.* 97, 183103. doi:10.1063/1.3507287

Garlow, J. A., Barrett, L. K., Wu, L., Kisslinger, K., Zhu, Y., and Pulecio, J. F. (2016). Large-area growth of turbostratic graphene on Ni(111) via physical vapor deposition. *Sci. Rep.* 6, 19804. doi:10.1038/srep19804

Geim, A. K. (2009). Graphene: status and prospects. *Science* 324, 1530–1534. doi:10.1126/science.1158877

Geim, A. K., and Novoselov, K. S. (2007). The rise of graphene. *Nat. Mater.* 6, 183–191. doi:10.1038/nmat1849

Graca, M. P. F., Prezas, P. R., Costa, M. M., and Valente, M. A. (2012). Structural and dielectric characterization of $LiNbO_3$ nano-size powders obtained by Pechini method. *J. Sol. Gel Sci. Technol.* 64, 78–85. doi:10.1007/s10971-012-2829-0

Han, G. H., Güneş, F., Bae, J. J., Kim, E. S., Chae, S. J., Shin, H.-J., et al. (2011). Influence of copper morphology in forming nucleation seeds for graphene growth. *Nano Lett.* 11, 4144–4148. doi:10.1021/nl201980p

He, M., Xu, M., Ren, Y., Jian, J., Ruan, Z., Xu, Y., et al. (2019). High-performance hybrid silicon and lithium niobate Mach-Zehnder modulators for 100 Gbit s^{-1} and beyond. *Nat. Photon.* 13, 359–364. doi:10.1038/s41566-019-0378-6

Jin, D., Kumar, A., Hung Fung, K., Xu, J., and Fang, N. X. (2013). Terahertz plasmonics in ferroelectric-gated graphene. *Appl. Phys. Lett.* 102, 201118. doi:10.1063/1.4807762

Juang, Z.-Y., Wu, C.-Y., Lo, C.-W., Chen, W.-Y., Huang, C.-F., Hwang, J.-C., et al. (2009). Synthesis of graphene on silicon carbide substrates at low temperature. *Carbon* 47, 2026–2031. doi:10.1016/j.carbon.2009.03.051

Kaniyoor, A., and Ramaprabhu, S. (2012). A Raman spectroscopic investigation of graphite oxide derived graphene. *AIP Adv.* 2, 032183. doi:10.1063/1.4756995

Kim, J., Lee, G., and Kim, J. (2015). Wafer-scale synthesis of multi-layer graphene by high-temperature carbon ion implantation. *Appl. Phys. Lett.* 107, 033104. doi:10.1063/1.4926605

Kong, Y., Bo, F., Wang, W., Zheng, D., Liu, H., Zhang, G., et al. (2019). Recent progress in lithium niobate: optical damage, defect simulation, and on-chip devices. *Adv. Mater.* 32, 1806452. doi:10.1002/adma.201806452

Kumari, A., Prasad, N., Bhatnagar, P. K., Mathur, P. C., Yadav, A. K., Tomy, C. V., et al. (2014). Electrical transport properties of polycrystalline CVD graphene on SiO2/Si substrate. *Diam. Relat. Mater.* 45, 28–33. doi:10.1016/j.diamond.2014.03.003

Lander, J. J., Kern, H. E., and Beach, A. L. (1952). Solubility and diffusion coefficient of carbon in nickel: reaction rates of nickel-carbon alloys with barium oxide. *J. Appl. Phys.* 23, 1305–1309. doi:10.1063/1.1702064

Lee, C., Wei, X., Kysar, J. W., and Hone, J. (2008). Measurement of the elastic properties and intrinsic strength of monolayer graphene. *Science* 321, 385–388. doi:10.1126/science.1157996

Lee, J. S., Jang, C. W., Kim, J. M., Shin, D. H., Kim, S., Choi, S.-H., et al. (2014). Graphene synthesis by C implantation into Cu foils. *Carbon* 66, 267–271. doi:10.1016/j.carbon.2013.08.066

Li, X., Cai, W., An, J., Kim, S., Nah, J., Yang, D., et al. (2009). Large-area synthesis of high-quality and uniform graphene films on copper foils. *Science* 324, 1312–1314. doi:10.1126/science.1171245

Liu, K., Lu, F., Li, K., Xu, Y., and Ma, C. (2019). Synthesis of turbostratic graphene by direct carbon ions implantation on LiNbO3. *Appl. Surf. Sci.* 493, 1255–1259. doi:10.1016/j.apsusc.2019.07.105

Ma, R.-S., Ma, J., Yan, J., Wu, L., Guo, W., Wang, S., et al. (2020). Wrinkle-induced highly conductive channels in graphene on SiO2/Si substrates. *Nanoscale* 12, 12038. doi:10.1039/d0nr01406k

Ma, X., Liu, Y., Liu, H., Zhang, L., Xu, B., and Xiao, F. (2018). Fabrication of novel slurry containing graphene oxide-modified microencapsulated phase change material for direct absorption solar collector. *Sol. Energy Mater. Sol. Cell.* 188, 73–80. doi:10.1016/j.solmat.2018.08.021

Martín-García, B., Bi, Y., Prato, M., Spirito, D., Krahne, R., Konstantatos, G., et al. (2018). Reduction of moisture sensitivity of PbS quantum dot solar cells by incorporation of reduced graphene oxide. *Sol. Energy Mater. Sol. Cell.* 183, 1–7. doi:10.1016/j.solmat.2018.04.005

Mun, J. H., Lim, S. K., and Cho, B. J. (2012). Local growth of graphene by ion implantation of carbon in a nickel thin film followed by rapid thermal annealing. *J. Electrochem. Soc.* 159, G89–G92. doi:10.1149/2.059206jes

Novoselov, K. S., Geim, A. K., Morozov, S. V., Jiang, D., Zhang, Y., Dubonos, S. V., et al. (2004). Electric field effect in atomically thin carbon films. *Science* 306, 666–669. doi:10.1126/science.1102896

Onishi, K., Kirimoto, K., and Sun, Y. (2017). Coupling behaviors of graphene/SiO_2/Si structure with external electric field. *AIP Adv.* 7, 025113. doi:10.1063/1.4975150

Salas, O., Garcés, E., Castillo, F. L., and Magaña, L. F. (2017a). Absorption and reflectivity of the lithium niobate surface masked with a graphene layer. *AIP Adv.* 7, 015305. doi:10.1063/1.4974745

Salas, O., Garcés, E., Castillo, F. L., and Magaña, L. F. (2017b). Changes in the reflectivity of a lithium niobate crystal decorated with a graphene layer. *J. Phys.: Conf. Ser.* 792, 012069. doi:10.1088/1742-6596/792/1/012069

Salas, O., Garces, E., and Magana, L. (2018). Optical absorption and reflectivity of a molecular cluster of lithium niobate adsorbed on a graphene layer. *Crystals* 8, 208. doi:10.3390/cryst8050208

Sathish-Kumar, K., Vázquez-Huerta, G., Rodríguez-Castellanos, A., Poggi-Varaldo, H. M., and Solorza-Feria, O. (2012). Microwave assisted synthesis and characterizations of decorated activated carbon. *Int. J. Electrochem. Sci.* 7, 5484–5494.

Shimodaira, N., and Masui, A. (2002). Raman spectroscopic investigations of activated carbon materials. *J. Appl. Phys.* 92, 902–909. doi:10.1063/1.1487434

Wang, G., Ding, G., Zhu, Y., Chen, D., Ye, L., Zheng, L., et al. (2013). Growth of controlled thickness graphene by ion implantation for field-effect transistor. *Mater. Lett.* 107, 170–173. doi:10.1016/j.matlet.2013.06.013

Wang, H., Zhao, H., Hu, G., Li, S., Su, H., and Zhang, J. (2015). Graphene based surface plasmon polariton modulator controlled by ferroelectric domains in lithium niobate. *Sci. Rep.* 5, 18258. doi:10.1038/srep18258

Wang, J., Ma, F., and Sun, M. (2017). Graphene, hexagonal boron nitride, and their heterostructures: properties and applications. *RSC Adv.* 7, 16801–16822. doi:10.1039/c7ra00260b

Wang, X., Berke, K., Rudawski, N. G., Venkatachalam, D. K., Elliman, R. G., Fridmann, J., et al. (2016). Synthesis of graphene and graphene nanostructures by ion implantation and pulsed laser annealing. *J. Appl. Phys.* 120, 025105. doi:10.1063/1.4955137

Wang, X., Xu, J.-B., Wang, C., Du, J., and Xie, W. (2011). High-performance graphene devices on SiO2/Si substrate modified by highly ordered self-assembled monolayers. *Adv. Mater.* 23, 2464–2468. doi:10.1002/adma.201100476

Wu, Z.-S., Ren, W., Gao, L., Liu, B., Jiang, C., and Cheng, H.-M. (2009). Synthesis of high-quality graphene with a pre-determined number of layers. *Carbon* 47, 493–499. doi:10.1016/j.carbon.2008.10.031

Xu, M., Liang, T., Shi, M., and Chen, H. (2013). Graphene-like two-dimensional materials. *Chem. Rev.* 113, 3766–3798. doi:10.1021/cr300263a

Yin, K., Li, H., Xia, Y., Bi, H., Sun, J., Liu, Z., et al. (2011). Thermodynamic and kinetic analysis of lowtemperature thermal reduction of graphene oxide. *Nano-Micro Lett.* 3, 51–55. doi:10.1007/BF03353652

Yoon, D., Moon, H., Son, Y.-W., Choi, J. S., Park, B. H., Cha, Y. H., et al. (2009). Interference effect on Raman spectrum of graphene onSiO2/Si. *Phys. Rev. B* 80, 125422. doi:10.1103/PhysRevB.80.125422

Yu, Q., Lian, J., Siriponglert, S., Li, H., Chen, Y. P., and Pei, S.-S. (2008). Graphene segregated on Ni surfaces and transferred to insulators. *Appl. Phys. Lett.* 93, 113103. doi:10.1063/1.2982585

Zhang, R., Wang, Z. S., Zhang, Z. D., Dai, Z. G., Wang, L. L., Li, H., et al. (2013). Direct graphene synthesis on SiO2/Si substrate by ion implantation. *Appl. Phys. Lett.* 102, 193102. doi:10.1063/1.4804982

Zhu, Y., Murali, S., Cai, W., Li, X., Suk, J. W., Potts, J. R., et al. (2010). Graphene and graphene oxide: synthesis, properties, and applications. *Adv. Mater.* 22, 3906–3924. doi:10.1002/adma.201001068

Zuppella, P., Gerlin, F., and Pelizzo, M. G. (2017). Angular reflectance of graphene/SiO 2/Si in UV spectral range: a study for potential applications. *Opt. Mater.* 67, 132–138. doi:10.1016/j.optmat.2017.03.042

Conflict of Interest: The authors declare that the research was conducted in the absence of any commercial or financial relationships that could be construed as a potential conflict of interest.

frontiers in Materials

ORIGINAL RESEARCH
published: 21 May 2020
doi: 10.3389/fmats.2020.00153

Effect of Co-solution of Carbon Precursor and Activating Agent on the Textural Properties of Highly Porous Activated Carbon Obtained by Chemical Activation of Lignin With H_3PO_4

Imane Moulefera[1,2], Francisco J. García-Mateos[1], Abdelghani Benyoucef[2], Juana M. Rosas[1], José Rodríguez-Mirasol[1] and Tomás Cordero[1]*

[1] Departamento de Ingeniería Química, Facultad de Ciencias, Universidad de Málaga, Andalucía TECH, Málaga, Spain,
[2] Laboratory of Technique and Sciences of Water, Mustapha Stambouli University of Mascara, Mascara, Algeria

OPEN ACCESS

Edited by:
Maria Chiara Bignozzi, University of Bologna, Italy

Reviewed by:
Francisco Carrasco-Marín, University of Granada, Spain
Alexander M. Puziy, National Academy of Sciences of Ukraine (NAN Ukraine), Ukraine

***Correspondence:**
Juana M. Rosas
jmrosas@uma.es

Specialty section:
This article was submitted to Carbon-Based Materials, a section of the journal Frontiers in Materials

Received: *05 March 2020*
Accepted: *29 April 2020*
Published: *21 May 2020*

Citation:
Moulefera I, García-Mateos FJ, Benyoucef A, Rosas JM, Rodríguez-Mirasol J and Cordero T (2020) Effect of Co-solution of Carbon Precursor and Activating Agent on the Textural Properties of Highly Porous Activated Carbon Obtained by Chemical Activation of Lignin With H_3PO_4. Front. Mater. 7:153. doi: 10.3389/fmats.2020.00153

This work analyzes the effect of co-solution of carbon precursor and activating agent on the textural and surface chemistry properties of highly nanoporous activated carbons obtained by chemical activation of Alcell lignin with phosphoric acid. The success of this methodology highlights the possibility of directly using the liquors produced in organosolv process (Alcell) to prepare activated carbons by chemical activation with phosphoric acid. Co-solutions of lignin and phosphoric acid were submitted to a two steps thermal treatment, which consisted of a first oxidative treatment in air at 200°C, followed by a thermal treatment in N_2 at 400°C, where activation of the oxidized lignin with phosphoric acid took place. A lignin-derived activated carbon with very high apparent surface area (2550 m^2/g) and pore volume (1.30 cm^3/g) was obtained with an initial phosphoric acid to lignin mass ratio of 2. Up to now, this is one of the highest values of apparent surface area reported not only for activated carbons prepared from lignin, but even for porous carbons prepared by chemical activation of other lignocellulosic materials with phosphoric acid. The use of lignin and phosphoric acid co-solution provided larger and more homogeneous effective interactions between the carbon precursor and the activating agent, by the formation of phosphate esters in the lignin matrix, which seems to be a key factor in the subsequent treatments: promoting crosslinking reactions in the carbonaceous matrix during the oxidative treatment in air at 200°C and enhancing the development of a wide porosity during the following activation thermal treatment.

Keywords: Alcell lignin, chemical activation, phosphoric acid, co-solution, activated carbon, phosphate esters, high surface areas

INTRODUCTION

Within a biorefinery scheme, the conversion of the major components of lignocellulosic biomass (cellulose, hemicellulose, and lignin) into energy and chemicals is essential. However, lignin has been used, up to date, mainly, as a fuel to recover energy and chemical reactants in the pulp and paper industry and only a 2% of the produced lignin is currently commercialized (Higson and Smith, 2011; Smolarski, 2012; Laurichesse and Avérous, 2014; Rosas et al., 2014). There are different pretreatments to fractionate lignocellulosic biomass into their main components, but Organosolv process becomes an ideal candidate in the biorefinery context, given the need of using environmentally friendly treatments. During Organosolv process, lignin is fractionated into smaller parts, dissolved from the lignocellulosic biomass with organic compounds and separated in the form of a liquor rich in phenolic compounds (Xu et al., 2006; Ruiz et al., 2011; Espinoza-Acosta et al., 2014). The next step consists of lignin precipitation from the liquors by partially evaporating the organic solvent, lowering the temperature or a combination of those, followed by a separation step through centrifugation, filtration, etc. The lignin derived from this method presents lower molecular weight and higher purity than others obtained by other processes, such as Kraft one. All these properties make this type of lignin an ideal precursor for the preparation of activated carbon, an added-value material, whose production process would imply both economic and environmental advantages.

Chemical activation with phosphoric acid is a well-known method to prepare activated carbons from different biomass precursors (Jagtoyen and Derbyshire, 1998; Kennedy et al., 2004; Montané et al., 2005; Sych et al., 2012). Many papers have been reported dealing with the optimization of the preparation conditions in order to obtain activated carbons with a high development of the porous texture. The influence of the impregnation ratio and the activation temperature on the textural properties of activated carbons prepared from different biomassic waste has been deeply analyzed (Jagtoyen et al., 1993; Hayashi et al., 2000; Molina-Sabio and Rodríguez-Reinoso, 2004; Rosas et al., 2009; Puziy et al., 2020). However, the effect of the gas atmosphere during the activation step on these properties is not so clear and some contradictions have appeared in this respect in the literature. Generally, activation takes place under inert atmosphere, although some authors have proposed the preparation of activated carbons by chemical activation with phosphoric acid under air atmosphere in order to enhance the textural properties (increase apparent surface area, A_{BET}) (Laine et al., 1989). However, (Benaddi et al., 1998) reported no significant influence of the atmosphere on the textural characteristics of activated carbons prepared by chemical activation of wood with phosphoric acid. They obtained values of apparent surface area of approximately 2100 m^2/g, independently of the use of air or nitrogen as activation atmosphere. In contrast, Moreno Castilla et al. reported the preparation of activated carbons from olive-mill waste with similar A_{BET} ($\sim$ 400 m^2/g), using either nitrogen, CO_2 or H_2O atmospheres (Moreno-Castilla et al., 2001), but the A_{BET} value decreased ($\sim$ 180 m^2/g) when they used air as gas atmosphere.

With regard to lignin, activated carbons with very high A_{BET} values (around 3000 m^2/g) by chemical activation of Kraft lignin with KOH has been reported (Fierro et al., 2007a), but these carbon materials presented a very narrow microporosity. Chemical activation of Kraft lignin with zinc chloride and phosphoric acid gave rise to activated carbons with a much wider porosity, depending on the activation temperature and impregnation ratio, but with A_{BET} values lower than 1800 m^2/g (Gonzalez-Serrano et al., 1997, 2004; Guillén et al., 2009). However, no much information can be found in the literature regarding the preparation of activated carbons from Alcell lignin (Bedia et al., 2009; Rosas et al., 2012), a co-product that appears dissolved in the liquors produced in one of the most important Organosolv process.

Thus, the objective of this work was to analyze the effect of co-solution of carbon precursor and activating agent on the textural and surface chemistry properties of activated carbons obtained by chemical activation of Alcell lignin with phosphoric acid, in order to assess the possibility of directly using the liquors produced in the Organosolv process (Alcell), which would avoid the lignin precipitation and separation steps in this process. The influence of the use of a low temperature oxidative thermal treatment, previous to the activation process, on the surface chemistry and textural properties of the final lignin-derived carbons obtained was also studied.

EXPERIMENTAL SECTION

Activated Carbons Preparation

Alcell lignin (supplied by Repap Technologies Inc., Co.) was used as raw material for the activated carbons preparation. Different procedures were used for the preparation of activated carbons from lignin. Alcell lignin was dissolved in ethanol to simulate the composition of dissolved lignin in the Organosolv liquors. Solid Alcell lignin was directly impregnated with aqueous H_3PO_4 85% (w/w) at room temperature. Co-solution of lignin and the activating agent, H_3PO_4 85% (w/w), was also prepared at room temperature and the ethanol/lignin/H_3PO_4 solution was stirred until evaporation of the ethanol (which could be recovered). Both the impregnated lignin and the solid derived from the co-solution of lignin and H_3PO_4 were dried for 24 h at 60°C in a vacuum dryer. The amounts of lignin and H_3PO_4 used in both cases were those to obtain a final H_3PO_4/lignin mass ratio of 2. The as-received lignin and that dissolved in ethanol were denoted by L and LE, respectively. H_3PO_4 impregnated lignin and the solid derived from the lignin/ethanol/H_3PO_4 solution once dried were denoted as L2P and LE2P, respectively. These two samples were subsequently submitted to a low temperature oxidative treatment at 200°C in air atmosphere for 1.5 h, followed by an activation treatment under inert atmosphere at 400°C, both inside a laboratory horizontal tubular furnace. The heating rate to reach the oxidative and the activation temperature was 3 and 10°C/min, respectively. Once the activation temperature was reached the samples were cooled inside the furnace under inert atmosphere and then washed with distilled water at 60°C until neutral pH. The resulting activated carbons were dried at 60°C.

L2P and LE2P submitted to the oxidative treatment in air at 200°C for 1.5 h were denoted by adding the letter S to the corresponding names (L2PS and LE2PS, respectively). The final activated carbons obtained at 400°C in inert atmosphere were denoted by adding 400 to the respective notations (L2PS400 and LE2PS400, respectively). In case of oxidative treatments at different temperatures, the activated carbons notation will include at the end of the name the temperature of the treatment. For the sake of comparison, some samples were directly activated at 400°C under air atmosphere without being subjected to the previous oxidative low temperature treatment. In these cases, the letter S was not included in their corresponding notations (L2P400 and LE2P400) and the letter A was added at the end of its corresponding name. In order to also evaluate the influence of the gas atmosphere during the low temperature treatment, a sample was treated under inert atmosphere at 200°C for 1.5 h and was denoted by adding the letter N to its corresponding notation.

Activated Carbons Characterization

The porosity of the samples was characterized by N_2 adsorption–desorption and CO_2 adsorption at −196 and 0°C, respectively, using a micromeritics instrument (ASAP 2020 model). The samples were previously outgassed for at least 8 h at 150°C. From the N_2 isotherm, the apparent surface area (A_{BET}) was determined by applying the BET equation (Brunauer et al., 1938); micropore volume (V_t) and external surface area (A_t) were calculated using the *t*-method (Lippens and de Boer, 1965); mesopore volume (V_{mes}) was determined as the difference between the maximum adsorbed volume of N_2 (V_p) at a relative pressure of 0.99 and the micropore volume (V_t) (Rodríguez-Reinoso et al., 1995). From the CO_2 adsorption data, the narrow micropore volumen (V_{DR}) and surface area (A_{DR}) were calculated using the Dubinin–Radushkevich equation (Dubinin et al., 1947). Pore size distributions were obtaining by applying the 2D-NLDFT heterogeneous surface model from N_2 adsorption isotherm (Jagiello and Olivier, 2013).

Thermal treatments of different samples were carried out in a gravimetric thermobalance system, CI electronics. The thermobalance automatically measures the weight of the sample and the temperature as a function of time. Experiments were carried out in inert atmosphere (N_2) and in air atmosphere, for a total flow rate of 150 cm^3 (STP)/min, employing sample mass of approximately 10 mg. The sample temperature was increased at a heating rate of 10°C/min. Differential scanning calorimetry (DSC) experiments were also obtained by a thermal analyzer (Mettler Toledo equipment) coupled to a Mass Spectrometer (Pfeiffer Vacuum model ThermoStar TM GSD 320).

The FTIR spectra of lignin and lignin-derived samples were recorded in a Bruker Optics Vertex 70 FTIR spectrometer, in the 500–4000 cm^{-1} range, in KBr disks [ca. 1% (w/w)]. A KBr beam splitter and a Golden gate single reflection diamond ATR system detector were used. The spectra were collected for 2 min, with 4 cm^{-1} resolution.

Solid-state ^{13}C and ^{31}P-NMR spectra of lignin and lignin-derived samples were recorded, as well, with a NMR spectrometer (400 WB Plus model from Bruker) using the Cross Polarization Magic Angle Spinning (CPMAS) and high power decoupling (HPDEC) techniques and a 3.2 mm MAS triple-channel probe at a spinning frequency of 15 kH, with SPINAL-64 ^1H decoupling conditions.

X-ray photoelectron spectroscopy (XPS) analyses of the samples were carried out in a PHI 5700C model Physical Electronics apparatus, with MgKα radiation (1253.6 eV). For the analysis of the XPS peaks, the C1s peak position was set at 284.5 eV and used as reference to position the other peaks. For the deconvolution of the peaks, Gaussian–Lorentzian curves were used. The deconvolution of the phosphorus spectrum was carried out by using two doublet peaks with an area ratio of 0.5 and a separation between peaks of 0.84 eV for each phosphorus groups. TPD experiments were carried out in a customized quartz fixed-bed reactor placed inside an electrical furnace. CO and CO_2, as output gases, were measured by a non-dispersive infrared (NDIR) gas analyzer, Siemens ULTRAMAT 22 (Siemens AG, Munich, Germany). Eighty mg of dried carbon sample was heated from room temperature to 930°C at a heating rate of 10°C/min under N_2 flow (200 cm^3/min).

RESULTS AND DISCUSSION

Surface Chemistry Characterization of As-Received and Ethanol-Dissolved Lignin

Alcell lignin is a type of lignin derived from Organosolv process, a pulping technique that uses an organic solvent to solubilize lignin and hemicellulose. This type of lignin contains very small amounts of inorganic compounds (Kubo and Kadla, 2004). Delignification is mostly the result of high-temperature uncatalyzed hydrolysis of lignin ether linkages by water. The solvent in the system mainly serves to dissolve the lignin fragments (Girard and van Heiningen, 2000). One of the most used solvents in the Organosolv process is ethanol, which has been the solvent selected in this work to dissolve lignin.

Figure 1A shows the normalized CPMAS ^{13}C NMR spectra of the as-received Alcell lignin and that dissolved in ethanol. Some differences can be observed, which suggest modifications of the lignin structure by its solution in ethanol. The main difference of both spectra is observed in the range of 15–27 ppm, which can be associated to terminal CH_3 groups. The increase of this signal suggests the accumulation of saturated alkyl structures after dissolving the lignin with ethanol. The predominant signal around 62–68 ppm, which remains practically the same after dissolving the lignin in ethanol, can be assigned to C_5 in xylose internal unit and C_γ, in β-O-4-linked unit; C_4 in xylose non-reducing end and C_γ, in β-O-4-linked unit with C = O. However, the signal around 144–148 ppm slightly increases after solution with ethanol, which can be associated to an increase of C_3 and C_4 in etherified guaiacyl; C_4 and $C_{4'}$ in etherified 5-5′ units and C_α, in cinnamic acid and ester (Almendros et al., 1992), and maybe related to the interaction of -OH groups of ethanol with those of lignin, which would also explain the increase of the signal between 15 and 27 ppm.

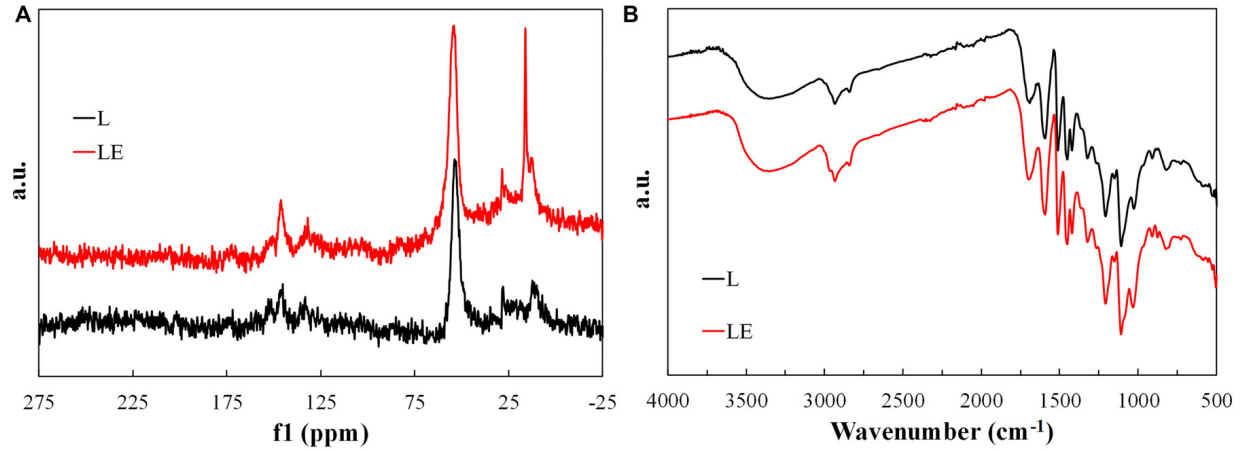

FIGURE 1 | Normalized CPMAS ^{13}C NMR spectra **(A)** and FTIR spectra **(B)** of as-received Alcell lignin and that dissolved in ethanol.

Figure 1B represents the corresponding FTIR spectra of both samples. The spectrum of lignin is complicated and most of the bands observed are produced by contribution of various types of vibrations of different functional groups. Therefore, assignment of the bands is possible only in the approximation of the predominant contribution of certain atomic groups (Fiţigău et al., 2013). Alcell lignin shows a broad band at 3410–3460 cm^{-1}, attributed to the hydroxyl groups in phenolic and aliphatic structures, which remains the same after dissolving with ethanol. The bands centered around 2935 and 2840 cm^{-1} can be predominantly associated to CH stretching in aromatic methoxyl groups and in methyl and methylene groups of side chains. In the LE sample also appears a band around 2965 cm^{-1} related to stretching vibration of aliphatic C-H. This appearance is in concordance to the accumulation of saturated alkyl structures, suggested by CPMAS ^{13}C NMR spectra, after dissolving lignin with ethanol. In the carbonyl/carboxyl region, a band around 1700 cm^{-1} is found, originating from unconjugated carbonyl/carboxyl stretching, which is more intense in the case of the sample LE. Typical bands of lignin are those at 1600, 1515, and 1425 cm^{-1} related to aromatic skeleton vibrations and at 1460 cm^{-1} associated to the C–H deformation combined with aromatic ring vibration (Vallejos et al., 2011; Fiţigău et al., 2013), which are practically the same in both samples.

The samples show the characteristic vibrations for the guaiacyl unit (G ring and C = O stretch at around 1260 cm^{-1}; CH in-plane deformation at 1150 cm^{-1}; and C–H out-of plane vibrations in position 2, 5, and 6 of guaiacyl units at 830 and 915 cm^{-1}). Syringyl (S) and guaiacyl (G) units are detected by aromatic skeleton vibrations at 1600 and 1325 cm^{-1} (S), 1515 and 1260 cm^{-1} (G), and aromatic in plane C-H vibrations at 1110 (S) and 1030 cm^{-1} (G). This last band is more intense in case of the LE sample (Vallejos et al., 2011; Fiţigău et al., 2013). Another band at 880 cm^{-1}, related to C-C asymmetrical stretching mode, is more accused in sample LE, which also evidences the modification of the chemical structure of lignin after dissolving it with ethanol.

Finally, both samples also contain a weak band at 1370–1375 cm^{-1} originating from phenolic OH and aliphatic C–H in methyl groups and a strong vibration at 1215–1220 cm^{-1} that can be associated with C–C, C–O, and/or C = O stretching. The aromatic C–H deformation at 1030 cm^{-1} appears as a complex vibration associated with the C–O, C–C stretching and C–OH bending in polysaccharides (Vallejos et al., 2011; Fiţigău et al., 2013).

Effect of H_3PO_4 and Low Temperature Oxidative Treatment on Lignin Surface Chemistry

Figure 2 shows the corresponding FTIR spectra of the H_3PO_4 impregnated lignin and the solid derived from the lignin/ethanol/H_3PO_4 solution, L2P and LE2P, respectively. Most of the absorption peaks corresponding to functional groups for these two samples were diminished compared to those corresponding to the samples L and LE. Spectra of samples L2P and LE2P are very similar, showing an important decrease of the intensity in the bands associated to the presence of O-H stretching of hydroxyl functional groups (3500 to 3300 cm^{-1}). This reduction is due to the presence of phosphoric acid, which acts as dehydrating agent immediately after impregnation, even at room temperature. The band around 2965 cm^{-1} related to stretching vibration of aliphatic C-H is also substantially reduced due to the increase of aromaticity (conversion of aliphatic to aromatic compounds). This loss of aliphatic character takes place at low temperatures and is caused by the cleavage of aliphatic side chains. Jagtoyen and Derbyshire also reported that the primary effects of acid attack are to cleave aryl ether bonds in lignin, accompanied by dehydration, degradation and condensation reactions (Jagtoyen and Derbyshire, 1998), which are the responsible of the decrease observed at 1600, 1515, and 1425 cm^{-1},related to aromatic skeleton vibrations of phenyl skeletons and, at 1460 cm^{-1}, associated to the C–H deformation, combined with aromatic ring vibration.

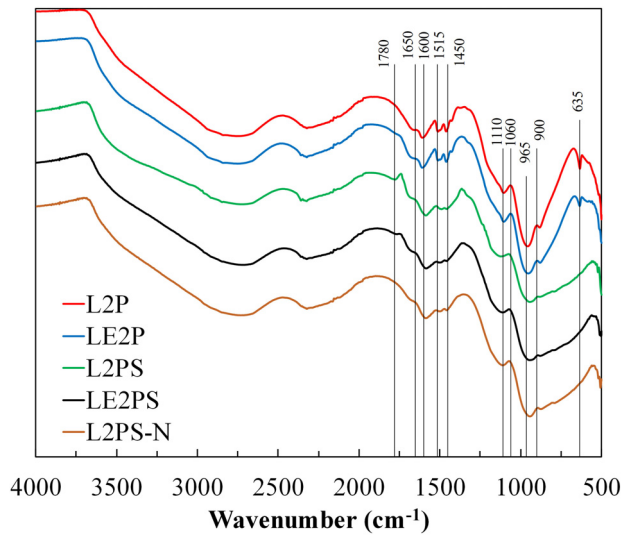

FIGURE 2 | FTIR spectra of the different H_3PO_4-lignin derived samples.

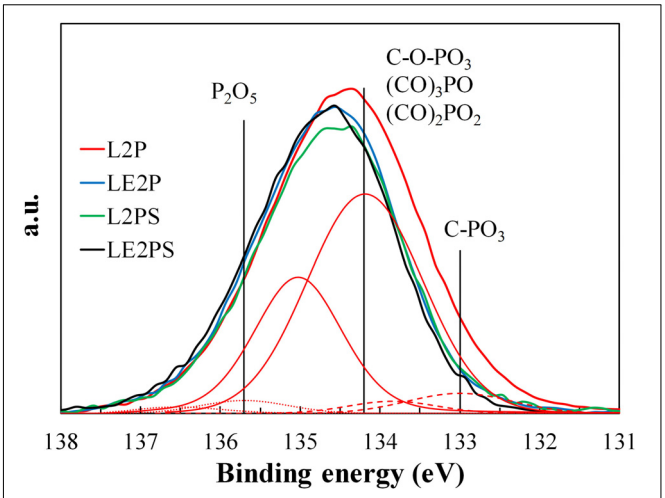

FIGURE 3 | XPS P2p spectra of the different H_3PO_4-lignin derived samples and deconvolution of LE2PS sample (C-O-P groups: continuous line, P_2O_5: dotted line and C-PO_3: dashed line).

Furthermore, the acid-catalyzed hydrolysis of ether linkages in lignin can lead to the formation of ketones, as can be observed in the characteristic band that appears at 1685 cm^{-1}.

The typical bands for guaiacyl unit are also significantly reduced, those at 1215–1220 cm^{-1} and at 1030 cm^{-1}, associated to C–C, C–O, and/or C = O stretching and C–O, C–C stretching and C–OH bending in polysaccharides, respectively. However, the appearance of other bands probably related to phosphorus compounds is also observed. In this sense, the broad band at 965 cm^{-1} and the intense peak at 635 cm^{-1} could be initially associated to P-O-P and P-C bending of aromatic compounds, respectively, although the peak at 635 cm^{-1} can be also related to C ≡ CH bonds (Labruquère et al., 1998). In addition, disappearance of this band, at 635 cm^{-1}, is observed for samples submitted to the oxidative treatment in air at 200°C (L2PS and LE2PS), which can be related to the formation of more oxidized species of phosphorus or to decomposition of non-stable species. Furthermore, a decrease of the intensity of the bands at 1600, 1515, 1460, and 1425 cm^{-1} was also detected after this low temperature treatment in air.

In order to analyze if phosphoric acid can act as an oxygen donor to the lignin matrix at this low temperature, sample L2P was treated at 200°C for 1.5 h, but under inert (N_2) atmosphere (L2PS-N). The FTIR results for L2PS-N are also shown in **Figure 2**. As it can be seen, all the bands already mentioned were also reduced for L2PS-N, which suggests that the presence of oxygen coming from the H_3PO_4 is more than enough to produce crosslinking reactions (García-Mateos et al., 2018). In this sense, phosphoric species could be combined with organic species to form phosphate linkages that can serve to connect and crosslink lignin fragments (Jagtoyen and Derbyshire, 1998). These reactions are probably responsible for the reduction of these typical bands of lignin.

The results obtained from XPS analysis confirmed the presence of phosphorus groups on the surface of L2P, LE2P, L2PS, and LE2PS samples (see **Figure 3**). The XPS P2p spectrum for L2P showed a broad band with a main peak at a binding energy around 134.3 eV, characteristic of pentavalent tetracoordinated phosphorus, as in phosphates and/or polyphosphates (Wu and Radovic, 2006). The obtained P2p broad band indicated the presence of different surface phosphorus species. Lower binding energies (around 133 eV) are characteristic of C-P bonding, as in C-PO_3 surface groups, which seem to be practically negligible in these samples (see **Table 1**); whereas higher values (134.2 eV) are ascribed to more oxidized phosphorus species, with C-O-P type bonds, as those in C-O-PO_3 surface groups (Wu and Radovic, 2006; Puziy et al., 2008). The contribution of these species was higher than 85%, suggesting that all phosphorus was mainly present in form of C-O-PO_3 surface groups. However, due to these samples were not yet activated, the presence of even more oxidized phosphorus species as P_2O_5 (135.7 eV) cannot be disregarded. It seems clear that co-solution of lignin with phosphoric acid generated a higher contribution of oxidized P surface groups to the total P surface groups than the traditional impregnation process (LE2P vs. L2P). On the other hand, the lower P content value observed for LE2P, when compared with that for L2P (see **Table 1**), suggests that this sample presents more P in the inner part of the lignin matrix, due probably to a better dispersion and to a more homogeneous distribution of P through the entire lignin matrix obtained by co-solution of the activating agent, phosphoric acid, and the carbon precursor, lignin. After the low temperature oxidative treatment both samples, L2PS and LE2PS, presented a similar surface P content value. However, the amount of surface O was significantly higher for the sample prepared by co-solution of lignin and H_3PO_4, LE2PS, which suggests that this preparation procedure enhances the lignin oxidation process at low temperature.

Thermal decomposition of the different lignin-derived samples was studied by TG analyses. **Figure 4A** represents the weight loss of the different lignin-derived samples as a

TABLE 1 | Mass surface concentration of the different H_3PO_4-lignin derived samples and the corresponding contribution of different phosphorus surface group obtained by XPS analyses.

Sample	Surface concentration by XPS			Phosphorus surface groups		
	C (%)	O (%)	P (%)	P_2O_5 (%)	C-O-P (%)	C-PO_3 (%)
L2P	30.7	45.3	24	3.9	89.05	7.05
LE2P	40.1	39	20.9	9.9	89.6	0.5
L2PS	48.8	31.3	19.9	5.85	93.7	0.45
LE2PS	42.9	36.5	20.6	9.24	89.59	1.17

function of temperature, under inert atmosphere and at a heating rate of 10°C/min. In general, three different ranges can be observed in all the samples. First, there is a small weight loss at temperatures lower than 200°C that can be partially attributed to release of water. Water can come from the phosphoric acid solution and produced by the reaction between phosphoric acid and lignin. As abovementioned, phosphoric acid cleaves aryl ether bonds in lignin, producing many transformations that include dehydration, degradation, and condensation (Jagtoyen and Derbyshire, 1998). At temperatures lower than 150°C, the acid catalyzes the hydrolysis of ether linkages, leading to the formation of ketones. These and other bond cleavage reactions that proceed through ionic mechanism promotes the release of H_2O, CO, CO_2, and CH_4 at these low temperatures, and can contribute to the corresponding weight loss observed in **Figure 4A**.

Between 200 and 500°C a further decrease of mass is observed associated to the release of light compounds from lignin degradation. In this temperature range, crosslinking reactions dominate over bond cleavage and de-polimerization reactions. At 250°C the structures are considered to be small polyaromatic units connected mainly by phosphate and polyphosphate bridges, including polyethylene linkages. As the temperature increases, cyclization and condensation reactions lead to increases in aromaticity and size of the poliaromatic units, enabled by the scission of P-O-C bonds (Jagtoyen and Derbyshire, 1998).

A change in the slope of the weight-loss curve can be also observed at temperatures higher than 500°C, probably associated to volatilization of carbon–oxygen complexes generated by the activation process, and to a lesser extent, to decomposition of phosphorous-compounds (as P_2O_5), produced by the reaction of phosphoric acid with the carbon matrix (Montané et al., 2005).

The profiles of L2P and LE2P are very similar, suggesting the low impact of using dissolved lignin in ethanol in the thermal decomposition reactions. However, the weight loss curves of the samples treated with air (L2PS and LE2PS) are above those of L2P and LE2P samples. If the difference between the weight loss for a specific temperature of the non-treated and treated samples is represented as a function of temperature (**Figure 4B**), an important weight loss deviation around 700°C can be noticed for both curves, suggesting that the treatment with air generates significant differences to the samples treated with phosphoric acid. Montané et al. (2005) proposed that the peak observed at 650°C in the DTG curves was attributed to the volatilization of P_2O_5. On the other hand, Martínez De Yuso et al. (2014) found a band around 800°C, which they associated to the more important crosslinking reactions to produce aromatic units. Therefore, the treatment with air seems to stabilize or increase the number of phosphate and polyphosphate bridges, and/or to increase other crosslinking reactions. With this regard, although the weight loss percentage from 800°C is the same for the samples L2PS and LE2PS (around 10%), the remaining weight is not equal, due to a higher weight loss between 750 and 800°C. The weight loss observed in this range temperature coincides with the higher CO evolution observed in the TPD analysis for the LE2PS400 sample, and it is associated to the higher presence of C-O-PO_3 surface groups (Bedia et al., 2009).

Differential scanning calorimetry (DSC) scans of all the lignin-derived samples are shown in **Figure 5**. **Figure 5A** shows a broad endothermic peak near 80°C from absorbed moisture for all the impregnated samples. The impregnated lignin L2P also presents

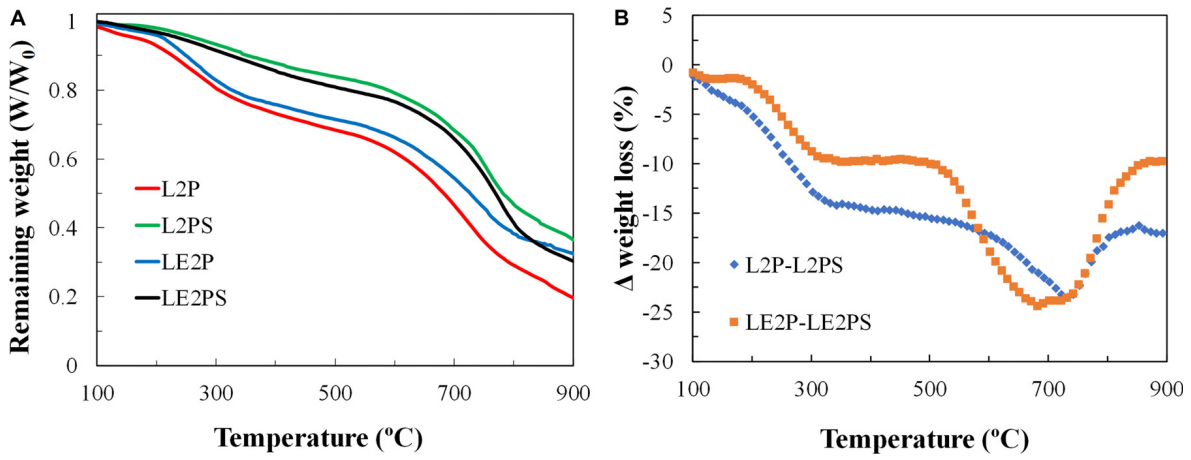

FIGURE 4 | (A) Thermogravimetric analysis in inert atmosphere for different lignin-derived samples; **(B)** Weight loss differences during TG analyses between the non-treated and low temperature oxidized (air) treated samples.

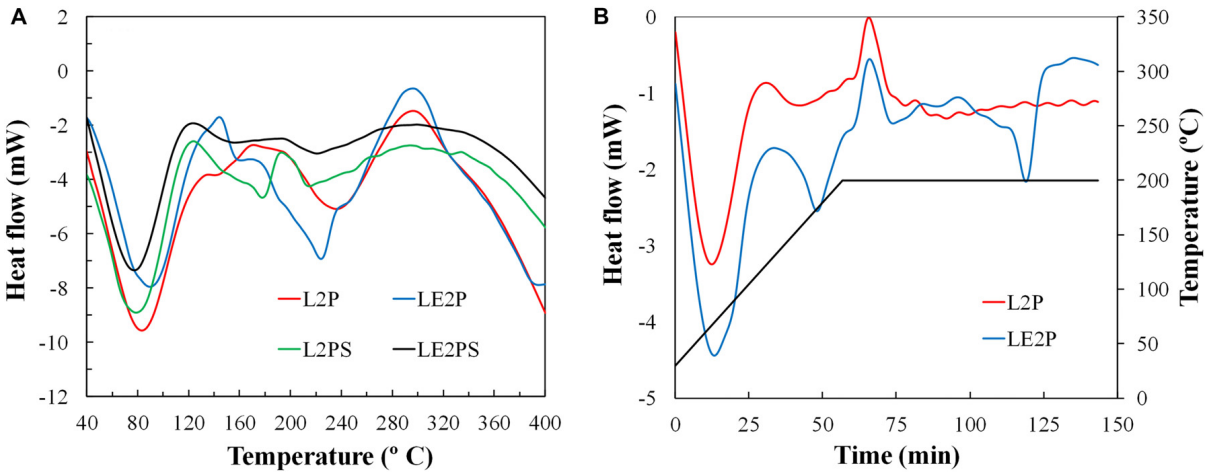

FIGURE 5 | (A) DSC curves during pyrolysis of different lignin-derived samples and **(B)** DSC curves during treatment of L2P and LE2P with air at 200°C.

a broad endotherm peak around 235°C, which can be associated to the decomposition and depolymerization reactions of lignin. Similarly, Karacan and Soy (2013) related an endothermic peak around 214°C to decomposition and depolymerization reactions of cellulose. Another exothermic peak was observed around 300°C. This peak coincides with a maximum in the CO and CO_2 evolution and is due mainly to the crosslinking reactions taking place during the decomposition process (Jagtoyen and Derbyshire, 1998), which could be softened by the endothermic polymerization and condensation reactions that take also place at this temperature range (Zhu et al., 2016). The scan of LE2P is very similar to that of L2P, but a shift of the endothermic peak is observed to 225°C, which suggests an earlier beginning of the decomposition and depolymerization reactions of lignin. In the case of the L2PS and LE2PS samples, the treatment with air results in the reduction of the endothermic peak, probably because the endothermic reaction has already taken place during the treatment with air (at 200°C for 1.5 h). From this temperature, a broad but much less intense exothermic peak can be observed centered on 300°C.

A further experiment was carried out trying to simulate the oxidative treatment at 200°C. The corresponding DSC curves are shown in **Figure 5B**. As can be seen, a sharp exothermic peak appears once the temperature is reached. This exothermic peak could be related to that shown in **Figure 5A** at 300°C in samples L2P and LE2P, due to different exothermic crosslinking reactions. In this sense, Jagtoyen and Derbyshire (1998) proposed that crosslinking reactions begin to dominate over depolymerization reactions from 200°C. Therefore, if enough time is provided, the reactions could take place at lower temperatures. Another important aspect is the presence of two endothermic peaks only in the sample LE2P. These two peaks could be related to the splitting of the endothermic peak that appears in **Figure 5A** around 220°C, caused by the superposition of several depolymerization and condensation reactions with different kinetic rates. In this sense, (Montané et al., 2005) already observed with isothermal experiments the existence of several reactions which appears overlapped during DTG analyses of impregnated samples.

Characterization of Activated Carbons

Table 2 shows the yield values of each treatment step and the total yield values for the different prepared activated carbons. As it is well known, phosphoric acid limits the formation of tars during the carbonization treatment, increasing the yield of the remaining solid product (Jagtoyen and Derbyshire, 1998). In this case, the yield of the treatment with air at 200°C is, approximately, 90% for both samples derived from co-solution of lignin and phosphoric acid and impregnated with phosphoric acid. The yield of the activation step (mass of activated sample/mass of impregnated or treated with air sample) was around 75% for samples non-treated with air, and about 85% for samples treated with air. There was approximately a difference of 10%, which practically corresponded to the loss of light hydrocarbons from the lignin degradation that was previously observed during the treatment with air at 200°C. The washing yield (mass of washed sample/mass of activated sample) was around 25%, very similar in all cases, and a total yield of around 60% was obtained for all the activated carbons, with no significant differences observed when lignin was co-dissolved or not with the activated agent and/or when the oxidative stabilization step was or was not performed. The total yield values (mass of activated carbon/mass of lignin) are considerably higher than others reported in the literature for lignin and other lignocellulosic materials (Montané et al., 2005; Puziy et al., 2005; Rosas et al., 2008).

Figure 6 shows the N_2 adsorption-desorption isotherms at −196°C of the different activated carbons, prepared at 400°C and with an H_3PO_4 to lignin mass ratio of 2. The isotherm of the activated carbon L2P400 is a type I isotherm, characteristic of a typical microporous solid, which adsorbs almost all N_2 at low relative pressures. No significant changes in the N_2 isotherm were observed when lignin was co-dissolved with the activating agent. However, the treatment with air at 200°C produced solids with a remarkable increased N_2 adsorbed volume up to 0.4 of

TABLE 2 | Yield values of the lignin activated carbons.

Activated carbon	Oxidative treatment yield (%)	Activation yield (%)	Washing yield (%)	Total yield (%)
L2P400	–	75.9	28.0	63.8
LE2P400	–	75.9	25.9	59.2
L2PS400	87.3	87.8	27.3	62.9
LE2PS400	90.7	81.6	25.2	63.3

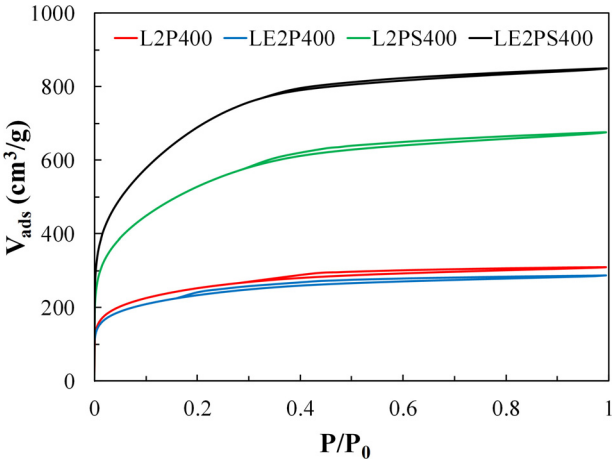

FIGURE 6 | N_2 adsorption-desorption isotherms obtained at −196°C of the different activated carbons obtained at 400°C and with H_3PO_4 to lignin mass ratio of 2.

relative pressure, which indicated a larger presence of wider microporosity in these carbonaceous solids. This N_2 adsorption volume increase was significantly more pronounced when co-solution of lignin and phosphoric acid was carried out previously to the oxidative stabilization step (air at 200°C). The small hysteresis cycle at medium relative pressures shown by the N_2 adsorption isotherms indicates the presence (to a lesser extent) of narrow mesopores.

The textural properties obtained from the N_2 and CO_2 isotherms of the different activated carbons are summarized in **Table 3**. The differences between the micropore volumes obtained from N_2 (V_t) and CO_2 (V_{DR}) isotherms, with higher values for those from N_2 ones, confirmed the presence of a wide microporosity for the lignin-derived activated carbons. However, the mesopore volumes are quite low in all the samples.

The apparent surface area (A_{BET}) values increased considerably from 912 m^2/g for L2P400 to 1937 m^2/g for L2PS400, and to 2551 m^2/g for LE2PS400. This last value is much higher than others reported in the literature for lignin-derived activated carbons using other activation methods (Rodríguez-Mirasol et al., 1993a,b; Gonzalez-Serrano et al., 1997; Hayashi et al., 2000; Cotoruelo et al., 2007; Babeł and Jurewicz, 2008; Carrott et al., 2008; Sun et al., 2010; Al-Lagtah et al., 2016; Kim et al., 2017; Lin et al., 2019; Rowlandson et al., 2020), including the same activating agent (H_3PO_4), at similar temperatures and impregnation ratios (Gonzalez-Serrano et al., 2004; Guo and Rockstraw, 2006; Fierro et al., 2007b; Bedia et al., 2010; Rosas et al., 2012). Only a few works reported the preparation of activated carbons from lignin with higher apparent surface areas (∼3000 m^2/g) by using KOH activation, but at much higher activation temperatures than those used in this work (Zou and Han, 2001; Fierro et al., 2007a; Li et al., 2014; Fernandez-Ruiz et al., 2018; Han et al., 2019). In the method here proposed, the use of lower activation temperatures would substantially decrease the cost of the obtained activated carbons, without compromising the high development of porosity.

Figure 7 collects the micropore size distribution of the different activated carbons obtained at 400°C and H_3PO_4 to lignin mass ratio of 2. The activated carbon prepared by direct impregnation of lignin shows a bimodal micropore size distribution, with a main band with a maximum at around 6.7 Å and a second one (shoulder), less intense, with a maximum at around 16 Å, ending at a pore size value of about 40 Å, indicating the presence of narrow mesopores. The micropore size distribution of the activated carbon when lignin was co-dissolved with the activating agent is practically the same as that of the activated carbon prepared by direct impregnation of lignin. However, the treatment with air at 200°C produces a clear change in the bimodal micropore size distribution. This treatment produced an increase of both bands, with the maximum of the first one slightly shifting to higher micropore sizes (from 6.7 to approximately 8.5 Å). However, the increase of the band corresponding to micropores of about 16 Å was proportionally higher than that corresponding to the lower micropore sizes (6.7 to 8.5 Å), even surpassing it in the case of LE2PS400. These results suggest that the treatment with air at 200°C increased the volume of micropores, especially that of the largest pore size (16 Å), and this effect was clearly enhanced by the co-solution of lignin and phosphoric acid. However, this treatment does not appear to greatly affect the micropore (or mesopore) size of the obtained activated carbons.

TABLE 3 | Textural properties of the different lignin derived activated carbons obtained from the N_2 and CO_2 isotherms.

	N_2 Isotherm					CO_2 Isotherm	
	A_{BET} (m^2/g)	A_t (m^2/g)	V_t (cm^3/g)	V_p (cm^3/g)	V_{mes} (cm^3/g)	A_{DR} (m^2/g)	V_{DR} (cm^3/g)
L2P400	912	55	0.412	0.477	0.063	438	0.176
LE2P400	845	36	0.395	0.444	0.054	407	0.163
L2PS400	1937	131	0.892	1.044	0.146	673	0.270
LE2PS400	2551	143	1.158	1.313	0.152	859	0.344

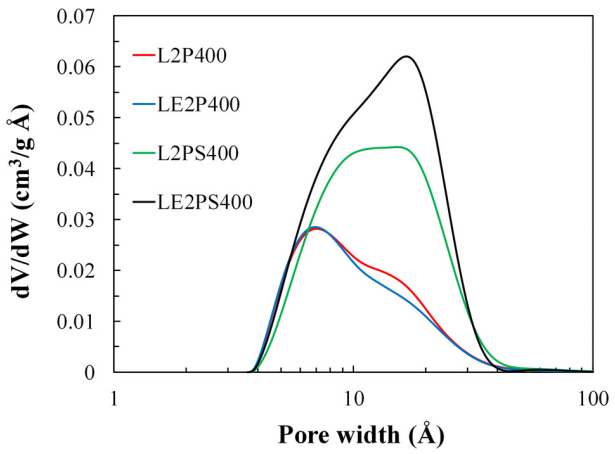

FIGURE 7 | Micropore size distribution of the different activated carbons obtained at 400°C and with H_3PO_4 to lignin mass ratio of 2.

The present results indicate that the use of co-solution of lignin with phosphoric acid in combination with an oxidative treatment at 200°C provides activated carbons with extremely high specific surface area and a large and wide microporosity. These significant differences in the porous texture seem to be the result of larger and more homogeneous interactions between lignin and the activating agent when they are co-dissolved that may increase the formation of effective phosphate esters, which are the responsible of the cross-linking reactions in the carbonaceous matrix during the oxidative stabilization process (Puziy et al., 2005). To support this hypothesis, TPD (**Figure 8**) and XPS (not shown) analyses were carried out for the different activated carbons. As it was observed in previous works, activated carbons prepared by chemical activation with phosphoric acid presented most of CO evolution at temperatures higher than 700°C, due to the presence of oxygen-containing P surface groups, which include metaphosphates, mainly as C-O-PO_3 groups and C-PO_3 groups, which decompose as gaseous CO, producing C-P type surface groups (Bedia et al., 2009; Rosas et al., 2009). In addition, XPS P2p spectra of the different activated carbons, which were very similar to those of the corresponding lignin-derived samples (**Figure 3**), also evidence the presence of, mainly, C-O-P ones (CO-$PO(OH)_2$ and $(C\text{-}O)_3PO$) at 134.2 eV and C-P-O groups (such as C-$PO(OH)_2$ or C_2-PO(OH)) at 133 eV. The similarity among the spectra indicated that the contribution of this kind of groups is very similar in the different obtained activated carbons, independently of the preparation method used. In this sense, a similar P surface concentration value of 1.6%wt was obtained for L2P400, L2PS400, and LE2P400. However, the combined effect of the co-solution of lignin and phosphoric acid and the oxidative treatment at low temperature increased this value to 2.4%wt.

TPD CO profiles for the activated carbon prepared from dissolved and not-dissolved lignin are very similar, showing most of their CO release between 700 and 900°C (**Figure 8**). However, the treatment with air at 200°C and the combined use of this treatment with co-solution of lignin and the activating agent provided a higher release of CO, even at temperatures lower than 700°C. This CO evolution at lower temperatures can be associated to decomposition of mainly phenol and ether surface groups and, to a lesser extent, to anhydride surface groups. As decomposition of this last group also should produce CO_2 evolution, the low CO_2 evolution for these activated carbons at this temperature range provided evidences of the low presence of anhydride surface groups on those samples. On the other hand, the sample LE2PS400 presented the highest CO evolution between 700 and 800°C, which suggests a higher presence of metaphosphates (C-O-PO_3 and/or C-PO_3 type) surface groups on this sample (Bedia et al., 2009). These P surface groups, with C-O-P bonds, decompose to gas CO and P surface groups of C-P bond type at these temperatures (Wu and Radovic, 2006). The larger evolution of CO observed in the TPD for LE2PS400 can be associated to a higher generation of phosphate esters during the preparation process, as it was evidenced by FTIR analyses (**Figure 2**) and by the higher surface P content (2.4%wt) of this activated carbon, revealed by XPS results.

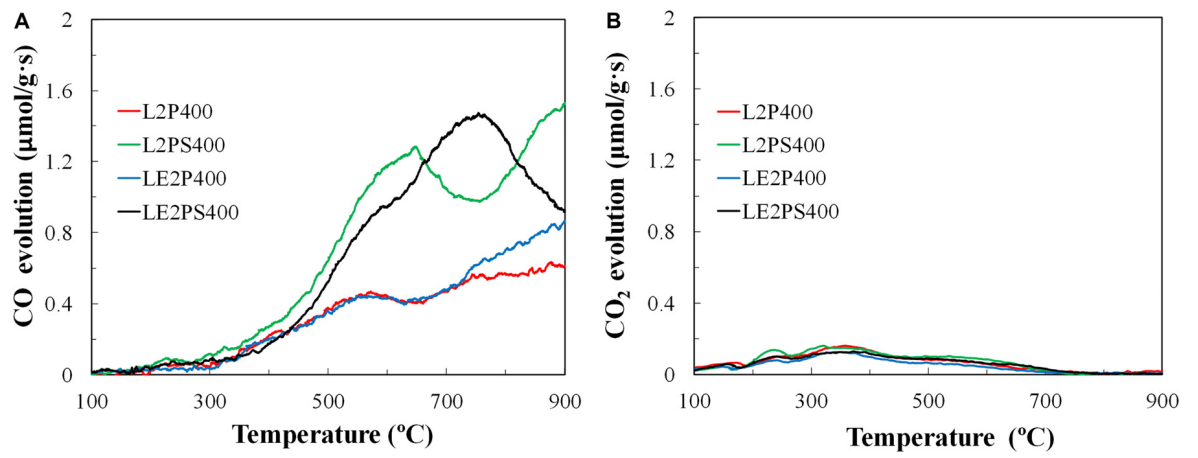

FIGURE 8 | (A) CO and **(B)** CO_2 evolution of the different activated carbons.

Effect of Temperature of the Oxidative Treatment

Although to our best knowledge the co-solution of the carbon precursor and the activating agent has not been previously reported, some authors have already proposed the activation in two different steps. Toles et al. (1998) analyzed different approaches of acid-activation/oxidation to produce activated carbons with high metals and organics compounds adsorption uptakes. They observed no significant differences on the porosity of samples directly activated in air at 450°C and compared with samples prepared with a further intermediate step at 170°C, obtaining a maximum apparent surface area of A_{BET} = 1662 m^2/g. They suggested that the intermediate step was not necessary because the time spent during the ramping stage (averaging approximately 0.8 h) to 450°C was sufficient to allow penetration of the activating agent (phosphoric acid) and any preliminary reactions to take place. Dastgheib and Rockstraw (2001) proposed also a two steps activation process, both of them in air, with the first one up to 215°C, temperature from which ortho-phosphoric acid dehydrates, losing half a molecule of water and forming pyrophosphoric acid, but they do not compare the porosity of activated carbons prepared in other gas atmospheres.

In order to deep in the role of this oxidative treatment, further oxidative treatments were carried out at different temperatures. **Table 4** shows the yield values of the lignin derived activated carbons obtained at 400°C and H_3PO_4/lignin mass ratio of 2, but previously treated at different temperatures under air atmosphere. As can be seen, the yield of the treatment in air decreases as the temperatures increases, due to a higher release of light hydrocarbons and water. The activation and washing yields remain approximately the same regardless of the treatment previously carried out, since the impregnation ratio and the activation temperature is the same in all the samples. Therefore, the total yield values follow the same sequence found for the treatments with air.

Figure 9 shows the N_2 adsorption-desorption isotherms at −196°C of the different activated carbons prepared at 400°C and H_3PO_4/lignin mass ratio of 2, treated at different oxidative temperatures. The isotherms of the series are all of them type I isotherms. The results indicate that the oxidative treatment at 100°C did not generate large porosity development compared to that of the sample without any oxidative treatment. The highest amount of N_2 adsorbed volume was observed for the sample treated at 200°C. An increase of this temperature to 300°C slightly reduced the N_2 adsorbed volumes. **Table 5** collects the textural properties derived from the N_2 and CO_2 isotherms of the different lignin derived activated carbons obtained at 400°C, a H_3PO_4/lignin mass ratio of 2 and treated at different oxidative temperatures. As can be seen, the textural properties of the sample treated at 100°C are very similar to those reported in **Table 3** for the sample L2P400, which was not submitted to any oxidative treatment. It can also be observed that maximum pore volume (1.31 cm^3/g) and apparent surface area (2551 m^2/g) were obtained with an oxidative treatment at 200°C, while a relative decrease in the apparent surface area to 2128 m^2/g was noticed when the oxidative treatment was performed at 300°C.

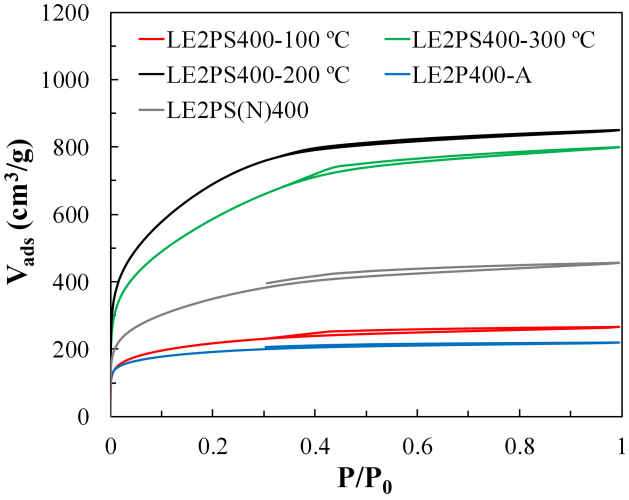

FIGURE 9 | N_2 adsorption-desorption isotherms obtained at –196°C of the different activated carbons obtained at 400°C and H_3PO_4/lignin mass ratio of 2, treated at different temperatures.

TABLE 4 | Yield values of the lignin-derived activated carbons obtained at 400°C and H_3PO_4/lignin mass ratio of 2, treated at different temperatures.

Sample	Oxidative treatment yield (%)	Activation yield (%)	Washing yield (%)	Total yield (%)
LE2PS400-100°C	98.1	85.8	25.7	65.0
LE2PS400-200°C	90.7	81.6	22.2	63.3
LE2PS400-300°C	87.7	88.7	24.0	56.0
LE2P400-A	–	80.1	27.2	64.9
LE2PS(N)400	88.8	87.3	26.2	60.9

The treatment in air at low temperature seems to enhance the formation of phosphate and polyphosphate bridges, which are responsible for connecting and crosslinking the lignin fragments. These phosphorus groups are inserted in the carbon matrix, separating the organic species. These groups generate an expansional process that, after removal of the acid, leaves the matrix in an expanded state, with a high pore development structure. In this case, the highest porosity development is observed when the oxidative treatment is performed at intermediate temperatures (200°C). The treatment at 100°C does not produce any enhancement in the porosity, and at 300°C some reduction begins to be noticed. These differences can be explained, according to the findings of Jagtoyen and Derbyshire (1998) by the fact that bond cleavage reactions that proceed through ionic mechanisms are taking place at low temperature and cross-linking reaction dominates over bond cleavage and de-polymerization reactions from 150°C. Therefore, the results seem to indicate that the presence of oxygen promotes preferentially the cross-linking reactions around 200°C and from this temperature some over-oxidation could take place.

TABLE 5 | Textural properties of the different lignin activated carbons obtained at 400°C and H_3PO_4/lignin mass ratio of 2, treated at different temperatures under air atmosphere, obtained from the N_2 and CO_2 isotherms.

Sample	N_2 isotherm					CO_2 isotherm	
	A_{BET} (m^2/g)	A_t (m^2/g)	V_t(cm^3/g)	V_p(cm^3/g)	V_{mes} (cm^3/g)	A_{DR}(m^2/g)	V_{DR}(cm^3/g)
LE2PS400-100°C	877	61	0.386	0.459	0.066	420	0.168
LE2PS400-200°C	2551	143	1.158	1.313	0.152	859	0.344
LE2PS400-300°C	2128	181	1.036	1.237	0.175	570	0.228
LE2P400-A	707	26	0.306	0.339	0.031	501	0.201
LE2PS(N)400	1263	111	0.575	0.706	0.127	483	0.194

In addition, other experiment was carried out but treating the lignin/H_3PO_4 samples at 200°C under inert (N_2) atmosphere (instead of air), followed by activation also in N_2 at 400°C (LE2PS(N)400). The amount of N_2 adsorbed volume over the entire range of relative pressure for the sample thus obtained was significantly higher than that observed for the LE2P400 sample, evidencing the presence of larger and wider microporosity. These results suggest that some reactions are being promoted at 200°C even under inert atmosphere, when sufficient time is provided. According to DSC results, it must be related to crosslinking reactions taking place during the decomposition process (Karacan and Soy, 2013) and/or to the polymerization and condensation reaction with H_3PO_4 (Zhu et al., 2016). Based on these results, it seems that, in agreement with the hypothesis of Toles et al. (1998) there are some kinetic limitations, as can be deduced from the increase of the microporosity with the treatment at 200°C under inert atmosphere, mainly associated to some crosslinking reactions. However, the use of an oxidative atmosphere becomes necessary to boost the porosity development, as pointed out by Dastgheib and Rockstraw (2001), but at adequate experimental conditions, as those previously observed.

In order to provide evidences of a possible over-oxidation of the activated carbon, which avoids the porosity development, a further activation of the LE2P sample at 400°C but directly in air was carried out. The isotherm of the corresponding activated carbon, LE2P400-A, (shown in **Figure 9**) presented lower N_2 adsorption volumes than the ones for the corresponding carbon materials obtained by activation under inert atmosphere. The same tendency was found for the sample L2P also activated in air at 400°C (not shown). In particular, a reduction in the apparent surface area of almost 200 m^2/g (**Table 5**) was observed, suggesting that some over-oxidation has occurred, causing some pores to collapse (Wang et al., 2014). In this line, several authors prepared activated carbons under different gas atmospheres in order to analyze their influence on the porous texture development. However, some discrepancies can be found in these works. Laine et al. (1989) observed an increase of the surface area of activated carbons from coconut shell at 400°C, when forced air was used, varying from 180 (in N_2) to 860 (in air) m^2/g. Molina-Sabio et al. (1995) suggested that the presence of oxygen at 450°C, at low impregnation ratios ($R < 0.32$), inhibits the aromatization process, thus reducing the influence of the phosphoric acid in both promoting the development of porosity and reducing the extent of contraction produced during the heat treatment of peach stones. At higher impregnation ratios ($R > 0.32$), they proposed that the access of air will be more restricted and will have smaller effect on the process. Benaddi et al. (1998) reported very similar micropores volumes and surface areas independently of the gas atmosphere (O_2 or N_2) used to prepare activated carbons from wood at 480°C. Puziy et al. (2003) associated a maximum of porosity in activated carbons prepared from a styrene–divinylbenzene copolymer in air, at 900°C, to a further air gasification. Wang et al. (2014) mixed ammonium persulfate with phosphoric acid. They proposed that the oxygen generated from decomposition of ammonium persulfate enhanced both the formation of phosphate esters and the formation of CO and CO_2 by gasification. At low oxygen dosages, the formation of phosphate esters predominated, hence promoting the crosslinking between phosphoric acid and lignin. They also pointed out that lignin presents higher carbon content than wood and can thus produce more phosphate esters. However, the excessive amount of persulfate leads to over-oxidation and carbon deletion. Furthermore, the over-oxidation also can cause some pores to collapse (Wang et al., 2014).

Based on our results and taking into account the statements of all these authors, it seems that in our experimental conditions, the presence of oxygen at intermediate temperatures, where cross-linking reactions dominate, promote the porosity development due to the creation of more phosphate esters, but at higher temperatures, where the aromatization process preferentially takes place, an excess of oxygen was counter-productive, generating an over-oxidation that would inhibit the increase of the porosity.

This new methodology can be an interesting alternative for the valorization of Alcell lignin into highly porous activated carbons. The high apparent surface area obtained and the presence of surface phosphorus functional groups, which provides to the activated carbons with surface acid character (Valero-Romero et al., 2017) and oxidation resistance (Rosas et al., 2012), open the possibilities for different applications (Puziy et al., 2020). Specifically, these activated carbons can be used in adsorption processes (gas and liquid phases), like adsorbent for basic compounds (Guo et al., 2005; László, 2005; Suhas et al., 2007), in heterogeneous catalytic processes, like catalyst or catalytic support (Bedia et al., 2009, 2010) and even in electrochemistry applications (Hulicova-Jurcakova et al., 2009).

CONCLUSION

This work analyzes the effect of co-solution of carbon precursor and activating agent on the textural and surface chemistry properties of highly nanoporous activated carbons obtained by chemical activation of Alcell lignin with phosphoric acid. The success of this methodology highlights the possibility of directly using the liquors produced in organosolv process (Alcell) to prepare activated carbons by chemical activation with phosphoric acid. Co-solutions of lignin and phosphoric acid were submitted to a two steps thermal treatment, which consisted of a first oxidative stabilization in air at 200°C, followed by a thermal treatment in N_2 at 400°C, where activation of the oxidized lignin with phosphoric acid took place. A lignin-derived activated carbon with very high apparent surface area (2550 m^2/g) and pore volume (1.30 cm^3/g) was obtained with an initial phosphoric acid to lignin mass ratio of 2. Up to now, this is one of the highest values of apparent surface area reported not only for activated carbons prepared from lignin, but even for porous carbons prepared by chemical activation of other lignocellulosic materials with phosphoric acid. The use of lignin and phosphoric acid solutions provided more homogeneous and effective interactions between the carbon precursor and the activating agent, by the formation of phosphate esters in the lignin matrix, which seems to be a key factor in the subsequent treatments: promoting crosslinking reactions in the carbonaceous matrix during the oxidative treatment in air at 200°C and enhancing the development of a wide porosity during the followed activation thermal treatment.

DATA AVAILABILITY STATEMENT

All datasets generated for this study are included in the article/supplementary material.

AUTHOR CONTRIBUTIONS

IM and FG-M prepared the activated carbons. IM, FG-M, and JR performed the characterization of the samples and prepared the manuscript. JR, AB, JR-M, and TC developed the synthesis concept and planned the experiments. All authors discussed the result and commented on the manuscript.

FUNDING

We gratefully thank MICINN and FEDER (Project RTI2018-097555-B-I00) and Junta de Andalucía (Project UMA18-FEDERJA-110) for financial support.

REFERENCES

Al-Lagtah, N. M. A., Al-Muhtaseb, A. H., Ahmad, M. N. M., and Salameh, Y. (2016). Chemical and physical characteristics of optimal synthesised activated carbons from grass-derived sulfonated lignin versus commercial activated carbons. *Microporous Mesoporous Mater.* 225, 504–514. doi: 10.1016/j.micromeso.2016.01.043

Almendros, G., Martínez, A. T., González, A. E., González-Vila, F. J., Fründ, R., and Lúdemann, H. D. (1992). CPMAS 13C NMR study of lignin preparations from wheat straw transformed by five lignocellulose-degrading fungi. *J. Agric. Food Chem.* 40, 1297–1302. doi: 10.1021/jf00019a043

Babeł, K., and Jurewicz, K. (2008). KOH activated lignin based nanostructured carbon exhibiting high hydrogen electrosorption. *Carbon* 46, 1948–1956. doi: 10.1016/j.carbon.2008.08.005

Bedia, J., Rosas, J. M., Márquez, J., Rodríguez-Mirasol, J., and Cordero, T. (2009). Preparation and characterization of carbon based acid catalysts for the dehydration of 2-propanol. *Carbon* 47, 286–294. doi: 10.1016/j.carbon.2008.10.008

Bedia, J., Rosas, J. M., Rodríguez-Mirasol, J., and Cordero, T. (2010). Pd supported on mesoporous activated carbons with high oxidation resistance as catalysts for toluene oxidation. *Appl. Catal. B Environ.* 94, 8–18. doi: 10.1016/j.apcatb.2009.10.015

Benaddi, H., Legras, D., Rouzaud, J. N., and Beguin, F. (1998). Influence of the atmosphere in the chemical activation of wood by phosphoric acid. *Carbon* 36, 306–309. doi: 10.1016/S0008-6223(98)80123-1

Brunauer, S., Emmett, P. H., and Teller, E. (1938). Adsorption of gases in multimolecular layers. *J. Am. Chem. Soc.* 60, 309–319. doi: 10.1016/j.jhazmat.2010.01.120

Carrott, P. J. M., Suhas, Ribeiro Carrott, M. M. L., Guerrero, C. I., and Delgado, L. A. (2008). Reactivity and porosity development during pyrolysis and physical activation in CO2 or steam of kraft and hydrolytic lignins. *J. Anal. Appl. Pyrolysis* 82, 264–271. doi: 10.1016/j.jaap.2008.04.004

Cotoruelo, L. M., Marqués, M. D., Díaz, F. J., Rodríguez-Mirasol, J., Cordero, T., and Rodríguez, J. J. (2007). Activated carbons from lignin: their application in liquid phase adsorption. *Sep. Sci. Technol.* 42, 3363–3389. doi: 10.1080/01496390701626800

Dastgheib, S. A., and Rockstraw, D. A. (2001). Pecan shell activated carbon: synthesis, characterization, and application for the removal of copper from aqueous solution. *Carbon* 39, 1849–1855. doi: 10.1016/S0008-6223(00)00315-8

Dubinin, M. M., Zaverina, E. D., and Radushkevich, L. V. (1947). Sorption and structure of active carbons I. Adsorption of organic vapors. *Zhurnal Fizicheskoi Khimii.* 21, 1351–1362.

Espinoza-Acosta, J. L., Torres-Chávez, P. I., Carvajal-Millán, E., Ramírez-Wong, B., Bello-Pérez, L. A., and Montaño-Leyva, B. (2014). Ionic liquids and organic solvents for recovering lignin from lignocellulosic biomass. *Bioresources* 9, 3660–3687. doi: 10.15376/biores.9.2.3660-3687

Fernandez-Ruiz, C., Bedia, J., Bonal, P., Rodriguez, J. J., and Gómez-Sainero, L. M. (2018). Chloroform conversion into ethane and propane by catalytic hydrodechlorination with Pd supported on activated carbons from lignin. *Catal. Sci. Technol.* 8, 3926–3935. doi: 10.1039/c8cy00461g

Fierro, V., Torné-Fernández, V., and Celzard, A. (2007a). Methodical study of the chemical activation of Kraft lignin with KOH and NaOH. *Microporous Mesoporous Mater.* 101, 419–431. doi: 10.1016/j.micromeso.2006.12.004

Fierro, V., Torné-Fernández, V., Celzard, A., and Montané, D. (2007b). Influence of the demineralisation on the chemical activation of Kraft lignin with orthophosphoric acid. *J. Hazard. Mater.* 149, 126–133. doi: 10.1016/j.jhazmat.2007.03.056

Fiţigău, I. F., Peter, F., and Boeriu, C. G. (2013). Structural analysis of lignins from different sources. *World Acad. Sci. Eng. Technol.* 7, 98–103.

García-Mateos, F. J., Berenguer, R., Valero-Romero, M. J., Rodríguez-Mirasol, J., and Cordero, T. (2018). Phosphorus functionalization for the rapid preparation of highly nanoporous submicron-diameter carbon fibers by electrospinning of lignin solutions. *J. Mater. Chem. A* 6, 1219–1233. doi: 10.1039/c7ta08788h

Girard, R. D., and van Heiningen, A. (2000). Delignification rate of White birch chips during etanol-water cooking in a stirred batch reactor with rapid liquor displacement. *J. Pulp Pap. Sci.* 26, 1–7.

Gonzalez-Serrano, E., Cordero, T., Rodriguez-Mirasol, J., Cotoruelo, L., and Rodriguez, J. J. (2004). Removal of water pollutants with activated carbons

prepared from H3PO4 activation of lignin from kraft black liquors. *Water Res.* 38, 3043–3050. doi: 10.1016/j.watres.2004.04.048

Gonzalez-Serrano, E., Cordero, T., Rodríguez-Mirasol, J., and Rodríguez, J. J. (1997). Development of porosity upon chemical activation of kraft lignin with ZnCl 2. *Ind. Eng. Chem. Res.* 36, 4832–4838. doi: 10.1021/ie970261q

Guillén, E., Rico, R., López-Romero, J. M., Bedia, J., Rosas, J. M., Rodríguez-Mirasol, J., et al. (2009). Pd-activated carbon catalysts for hydrogenation and Suzuki reactions. *Appl. Catal. A Gen.* 368, 113–120. doi: 10.1016/j.apcata.2009.08.016

Guo, J., Xu, W. S., Chen, Y. L., and Lua, A. C. (2005). Adsorption of NH 3 onto activated carbon prepared from palm shells impregnated with H 2SO 4. *J. Colloid Interface Sci.* 281, 285–290. doi: 10.1016/j.jcis.2004.08.101

Guo, Y., and Rockstraw, D. A. (2006). Physical and chemical properties of carbons synthesized from xylan, cellulose, and Kraft lignin by H3PO4 activation. *Carbon* 44, 1464–1475. doi: 10.1016/j.carbon.2005.12.002

Han, J., Jeong, S. Y., Lee, J. H., Choi, J. W., Lee, J. W., and Roh, K. C. (2019). Structural and electrochemical characteristics of activated carbon derived from lignin-rich residue. *ACS Sustain. Chem. Eng.* 7, 2471–2482. doi: 10.1021/acssuschemeng.8b05351

Hayashi, J., Kazehaya, A., Muroyama, K., and Watkinson, A. P. (2000). Preparation of activated carbon from lignin by chemical activation. *Carbon* 38, 1873–1878. doi: 10.1016/S0008-6223(00)00027-0

Higson, A., and Smith, C. (2011). *Lignin*. York: NNFCC Renewable Chemicals Factsheet The National Non-Food Crops Centre.

Hulicova-Jurcakova, D., Seredych, M., Lu, G. Q., Kodiweera, N. K. A. C., Stallworth, P. E., Greenbaum, S., et al. (2009). Effect of surface phosphorus functionalities of activated carbons containing oxygen and nitrogen on electrochemical capacitance. *Carbon* 47, 1576–1584. doi: 10.1016/j.carbon.2009.02.006

Jagiello, J., and Olivier, J. P. (2013). 2D-NLDFT adsorption models for carbon slit-shaped pores with surface energetical heterogeneity and geometrical corrugation. *Carbon* 55, 70–80. doi: 10.1016/j.carbon.2012.12.011

Jagtoyen, M., and Derbyshire, F. (1998). Activated carbons from yellow poplar and white oak by H3PO4 activation. *Carbon* 36, 1085–1097. doi: 10.1016/S0008-6223(98)00082-7

Jagtoyen, M., Groppo, J., and Derbyshire, F. (1993). Activated carbons from bituminous coals by reaction with H3PO4: the influence of coal cleaning. *Fuel Process. Technol.* 34, 85–96. doi: 10.1016/0378-3820(93)90093-J

Karacan, I., and Soy, T. (2013). Structure and properties of oxidatively stabilized viscose rayon fibers impregnated with boric acid and phosphoric acid prior to carbonization and activation steps. *J. Mater. Sci.* 48, 2009–2021. doi: 10.1007/s10853-012-6970-5

Kennedy, L. J., Vijaya, J. J., and Sekaran, G. (2004). Effect of two-stage process on the preparation and characterization of porous carbon composite from rice husk by phosphoric acid activation. *Ind. Eng. Chem. Res.* 43, 1832–1838. doi: 10.1021/ie034093f

Kim, D., Cheon, J., Kim, J., Hwang, D., Hong, I., Kwon, O. H., et al. (2017). Extraction and characterization of lignin from black liquor and preparation of biomass-based activated carbon therefrom. *Carbon Lett.* 22, 81–88. doi: 10.5714/CL.2017.22.081

Kubo, S., and Kadla, J. F. (2004). Poly(ethylene oxide)/organosolv lignin blends: relationship between thermal properties, chemical structure, and blend behavior. *Macromolecules* 37, 6904–6911. doi: 10.1021/ma0490552

Labruquère, S., Pailler, R., Naslain, R., and Desbat, B. (1998). Oxidation inhibition of carbon fibre preforms and C/C composites by H3PO4. *J. Eur. Ceram. Soc.* 18, 1953–1960. doi: 10.1016/S0955-2219(98)00135-6

Laine, J., Calafat, A., and Labady, M. (1989). Preparation and characterization of activated carbons from coconut shell impregnated with phosphoric acid. *Carbon* 27, 191–195. doi: 10.1016/0008-6223(89)90123-1

László, K. (2005). Adsorption from aqueous phenol and aniline solutions on activated carbons with different surface chemistry. *Colloids Surf. A Physicochem. Eng. Asp.* 265, 32–39. doi: 10.1016/j.colsurfa.2004.11.051

Laurichesse, S., and Avérous, L. (2014). Chemical modification of lignins: towards biobased polymers. *Prog. Polym. Sci.* 39, 1266–1290. doi: 10.1016/j.progpolymsci.2013.11.004

Li, X.-F., Xu, Q., Fu, Y., and Guo, Q.-X. (2014). Preparation and characterization of activated carbon from kraft lignin via KOH activation. *Environ. Prog. Sustain. Energy* 33, 519–526. doi: 10.1002/ep

Lin, J., Xue, F., and Zhao, G. (2019). Soda lignin-based activated carbon and its adsorption properties. *Bioresources* 14, 376–386. doi: 10.15376/biores.14.1.376-386

Lippens, B. C., and de Boer, J. H. (1965). Studies on pore systems in catalysts. V. The t method. *J. Catal.* 4, 319–323. doi: 10.1016/0021-9517(65)90307-6

Martínez De Yuso, A., Rubio, B., and Izquierdo, M. T. (2014). Influence of activation atmosphere used in the chemical activation of almond shell on the characteristics and adsorption performance of activated carbons. *Fuel Process. Technol.* 119, 74–80. doi: 10.1016/j.fuproc.2013.10.024

Molina-Sabio, M., Caturla, F., and Rodriguez-Reinoso, F. (1995). Influence of the atmosphere used in the carbonization of phosphoric acid impregnated peach stones. *Carbon* 33, 1180–1182. doi: 10.1016/0008-6223(95)91248-6

Molina-Sabio, M., and Rodríguez-Reinoso, F. (2004). Role of chemical activation in the development of carbon porosity. *Colloids Surf. A Physicochem. Eng. Asp.* 241, 15–25. doi: 10.1016/j.colsurfa.2004.04.007

Montané, D., Torné-Fernández, V., and Fierro, V. (2005). Activated carbons from lignin: kinetic modeling of the pyrolysis of Kraft lignin activated with phosphoric acid. *Chem. Eng. J.* 106, 1–12. doi: 10.1016/j.cej.2004.11.001

Moreno-Castilla, C., Carrasco-Marín, F., López-Ramón, M. V., and Alvarez-Merino, M. A. (2001). Chemical and physical activation of olive-mill waste water to produce activated carbons. *Carbon* 39, 1415–1420. doi: 10.1016/S0008-6223(00)00268-2

Puziy, A. M., Poddubnaya, O. I., Gawdzik, B., and Tascón, J. M. D. (2020). Phosphorus-containing carbons: preparation, properties and utilization. *Carbon* 157, 796–846. doi: 10.1016/j.carbon.2019.10.018

Puziy, A. M., Poddubnaya, O. I., Martínez-Alonso, A., Suárez-García, F., and Tascón, J. M. D. (2003). Synthetic carbons activated with phosphoric acid III. Carbons prepared in air. *Carbon* 41, 1181–1191. doi: 10.1016/S0008-6223(03)00031-9

Puziy, A. M., Poddubnaya, O. I., Martínez-Alonso, A., Suárez-García, F., and Tascón, J. M. D. (2005). Surface chemistry of phosphorus-containing carbons of lignocellulosic origin. *Carbon* 43, 2857–2868. doi: 10.1016/j.carbon.2005.06.014

Puziy, A. M., Poddubnaya, O. I., Socha, R. P., Gurgul, J., and Wisniewski, M. (2008). XPS and NMR studies of phosphoric acid activated carbons. *Carbon* 46, 2113–2123. doi: 10.1016/j.carbon.2008.09.010

Rodríguez-Mirasol, J., Cordero, T., and Rodríguez, J. J. (1993a). Activated carbons from CO2 partial gasification of eucalyptus kraft lignin. *Energy and Fuels* 7, 133–138. doi: 10.1021/ef00037a021

Rodríguez-Mirasol, J., Cordero, T., and Rodríguez, J. J. (1993b). Preparation and characterization of activated carbons from eucalyptus kraft lignin. *Carbon* 31, 87–95. doi: 10.1016/0008-6223(93)90160-C

Rodríguez-Reinoso, F., Molina-Sabio, M., and González, M. T. (1995). The use of steam and CO2 as activating agents in the preparation of activated carbons. *Carbon* 33, 15–23. doi: 10.1016/0008-6223(94)00100-E

Rosas, J. M., Bedia, J., Rodríguez-Mirasol, J., and Cordero, T. (2008). Preparation of hemp-derived activated carbon monoliths. Adsorption of water vapor. *Ind. Eng. Chem. Res.* 47, 1288–1296. doi: 10.1021/ie070924w

Rosas, J. M., Bedia, J., Rodríguez-Mirasol, J., and Cordero, T. (2009). HEMP-derived activated carbon fibers by chemical activation with phosphoric acid. *Fuel* 88, 19–26. doi: 10.1016/j.fuel.2008.08.004

Rosas, J. M., Berenguer, R., Valero-Romero, M. J., Rodríguez-Mirasol, J., and Cordero, T. (2014). Preparation of different carbon materials by thermochemical conversion of lignin. *Front. Mater.* 1:1. doi: 10.3389/fmats.2014.00029

Rosas, J. M., Ruiz-Rosas, R., Rodríguez-Mirasol, J., and Cordero, T. (2012). Kinetic study of the oxidation resistance of phosphorus-containing activated carbons. *Carbon* 50, 1523–1537. doi: 10.1016/j.carbon.2011.11.030

Rowlandson, J. L., Edler, K. J., Tian, M., and Ting, V. P. (2020). Toward process-resilient lignin-derived activated carbons for hydrogen storage applications. *ACS Sustain. Chem. Eng.* 8, 2186–2195. doi: 10.1021/acssuschemeng.9b05869

Ruiz, H. A., Ruzene, D. S., Silva, D. P., Da Silva, F. F. M. I., Vicente, A. A., and Teixeira, J. A. (2011). Development and characterization of an environmentally friendly process sequence (autohydrolysis and organosolv) for wheat straw delignification. *Appl. Biochem. Biotechnol.* 164, 629–641. doi: 10.1007/s12010-011-9163-9

Smolarski, N. (2012). *High-Value Opportunities for Lignin: Unlocking its Potential Lignin potential*. Paris: Frost & Sullivan.

Suhas, Carrott, P. J. M., and Ribeiro Carrott, M. M. L. (2007). Lignin–from natural adsorbent to activated carbon: a review. *Bioresour. Technol.* 98, 2301–2312. doi: 10.1016/j.biortech.2006.08.008

Sun, Y., Wei, J., Wang, Y. S., Yang, G., and Zhang, J. P. (2010). Production of activated carbon by K2CO3activation treatment of cornstalk lignin and its performance in removing phenol and subsequent bioregeneration. *Environ. Technol.* 31, 53–61. doi: 10.1080/09593330903338411

Sych, N. V., Trofymenko, S. I., Poddubnaya, O. I., Tsyba, M. M., Sapsay, V. I., Klymchuk, D. O., et al. (2012). Porous structure and surface chemistry of phosphoric acid activated carbon from corncob. *Appl. Surf. Sci.* 261, 75–82. doi: 10.1016/j.apsusc.2012.07.084

Toles, C. A., Marshall, W. E., and Johns, M. M. (1998). Phosphoric acid activation of nutshells for metals and organic remediation: process optimization. *J. Chem. Technol. Biotechnol.* 72, 255–263. doi: 10.1002/(SICI)1097-4660(199807)72:3<255::AID-JCTB890<3.0.CO;2-P

Valero-Romero, M. J., García-Mateos, F. J., Rodríguez-Mirasol, J., and Cordero, T. (2017). Role of surface phosphorus complexes on the oxidation of porous carbons. *Fuel Process. Technol.* 157, 116–126. doi: 10.1016/j.fuproc.2016.11.014

Vallejos, M. E., Felissia, F. E., Curvelo, A. A. S., Zambon, M. D., Ramos, L., and Area, M. C. (2011). Chemical and physico-chemical characterization of lignins obtained from ethanol-water fractionation of bagasse. *Bioresources* 6, 1158–1171.

Wang, Y., Zuo, S., Zhu, Y., Shao, Q., and Ni, Y. (2014). Role of oxidant during phosphoric acid activation of lignocellulosic material. *Carbon* 66, 734–737. doi: 10.1016/j.carbon.2013.09.048

Wu, X., and Radovic, L. R. (2006). Inhibition of catalytic oxidation of carbon/carbon composites by phosphorus. *Carbon* 44, 141–151. doi: 10.1016/j.carbon.2005.06.038

Xu, F., Sun, J. X., Sun, R., Fowler, P., and Baird, M. S. (2006). Comparative study of organosolv lignins from wheat straw. *Ind. Crops Prod.* 23, 180–193. doi: 10.1016/j.indcrop.2005.05.008

Zhu, G. Z., Deng, X. L., Hou, M., Sun, K., Zhang, Y. P., Li, P., et al. (2016). Comparative study on characterization and adsorption properties of activated carbons by phosphoric acid activation from corncob and its acid and alkaline hydrolysis residues. *Fuel Process. Technol.* 144, 255–261. doi: 10.1016/j.fuproc.2016.01.007

Zou, Y., and Han, B. X. (2001). Preparation of activated carbons from Chinese coal and hydrolysis lignin. *Adsorpt. Sci. Technol.* 19, 59–72. doi: 10.1260/0263617011493971

Conflict of Interest: The authors declare that the research was conducted in the absence of any commercial or financial relationships that could be construed as a potential conflict of interest.

frontiers in Materials

ORIGINAL RESEARCH
published: 08 October 2020
doi: 10.3389/fmats.2020.562455

Mechanically Robust Free-Standing Single-Walled Carbon Nanotube Thin Films With Uniform Mesh-Structure by Blade Coating

Yuichi Kato, Atsuko Sekiguchi, Kazufumi Kobashi, Rajyashree Sundaram, Takeo Yamada and Kenji Hata*

National Institute of Advanced Industrial Science and Technology (AIST), Tsukuba, Japan

Carbon nanotubes (CNTs) have garnered tremendous attention as building blocks for self-supporting membranes owing to remarkable developments in the manufacturing technology of high-quality CNT films. CNT films are expected to be applied in a wide range of applications, such as ultrafiltration membranes and as switching or sensing elements in microelectromechanical systems. However, the main challenge has been in fabricating CNT films by versatile and scalable processes suitable for industrial production while retaining lab-scale high performance. In this work, we succeed in fabricating macroscale (10 cm^2) free-standing CNT films with thicknesses as low as 200 nm showing tensile strengths of ∼166 MPa by simple, versatile, and scalable blade-coating of CNT suspensions. Our study demonstrates that it is possible to control CNT film bundle size distribution and pore structure by controlling the CNT dispersibility and entanglement in the suspensions. We find that controlling bundle size distribution, pore structure uniformity, and packing can lead to five-fold, four-fold, and three-fold higher tensile strengths, fracture strain, and Young's modulus, respectively, compared to films with poorer uniformity and packing.

Keywords: carbon nanotube, free-standing film, tensile strength, fracture strain, bundle thickness, pore size

OPEN ACCESS

Edited by:
Ming Xu,
Huazhong University of Science and Technology, China

Reviewed by:
Qingwen Li,
Suzhou Institute of Nano-Tech and Nano-Bionics (CAS), China
Renyuan Zhang,
Tongji University, China

****Correspondence:***
Atsuko Sekiguchi
atsuko-sekiguchi@aist.go.jp

Specialty section:
This article was submitted to Carbon-Based Materials, a section of the journal Frontiers in Materials

Received: *15 May 2020*
Accepted: *14 August 2020*
Published: *08 October 2020*

Citation:
Kato Y, Sekiguchi A, Kobashi K, Sundaram R, Yamada T and Hata K (2020) Mechanically Robust Free-Standing Single-Walled Carbon Nanotube Thin Films With Uniform Mesh-Structure by Blade Coating. Front. Mater. 7:562455. doi: 10.3389/fmats.2020.562455

INTRODUCTION

Thin and robust carbon nanotube (CNT)-based free-standing films are in high demand as switching or sensing elements in microelectromechanical systems (MEMS), ultrafiltration membranes, or liquid film supports for water purification, metal ion refinement, etc. For sensing/switching elements in MEMS, sufficiently thin substrate-free films are necessary to be sensitive and rapidly respond to external stimuli, such as fluid pressure, static electricity by elastic deformation, etc. Ultrafiltration membranes and liquid film supports (Parhi, 2013) require free-standing films that readily allow liquid passage while being mechanically strong to withstand liquid influx backpressure. Such robust and thin ultrafiltration membranes obviate the need for support films and save space in liquid separation modules, increasing filtration efficiency and throughput. Thinner films increase permeation flow velocity, which could also result in enhanced separation efficiencies of liquid film supports. Among the various materials developed for self-supporting films (such as polymer-based, organic-inorganic hybrids), CNTs offer the advantages of high

thermal and chemical stability and mechanical strength as well as easy formation of mesh-like structures with high surface areas (Narisawa, 1982; Hecht et al., 2011; Jiang et al., 2011; Kobashi et al., 2013; Janas and Koziol, 2014).

Two broad strategies have evolved to fabricate thin and robust CNT free-standing films: (i) dry process and (ii) wet process. Dry process involves either spinning from vertically aligned nanotube arrays or depositing directly from a floating catalyst chemical vapor deposition reactor (Jiang et al., 2011; Nasibulin et al., 2011). In general, spinning from vertically aligned nanotube arrays yields an oriented CNT film. On the other hand, depositing directly from a floating catalyst chemical vapor deposition reactor leads to randomly aligned CNT films. With appropriate CNT synthesis methods, nanotube structure and entanglement can be controlled, leading to $\leq$ 200-nm-thick free-standing films with tensile strengths of ∼65–360 MPa (Zhang et al., 2005; Ma et al., 2007; Liu et al., 2011; Nasibulin et al., 2011; Zhou et al., 2012). Dry-processed freestanding thin films have even been mass produced and are available commercially. Wet processing, the second route to fabricate free-standing CNT films, involves dispersing and debundling CNTs in a liquid medium to form suspensions that are subsequently converted into films (Hu et al., 2010; Hecht et al., 2011; Kobashi et al., 2013; Janas and Koziol, 2014; Wang and Bao, 2015). To make the CNT suspension, ultrasonic cavitation, shearing, or turbulence force are applied to CNT powders suspended in a liquid medium to enable nanotube de-bundling. The CNT suspensions are converted into films by methods such as spin-coating, blade-coating, dip-coating, vacuum filtration, etc. The primary advantage of wet process is fabrication and structural control flexibility. CNTs (including commercial samples) with regulated structures (wall number, diameters, lengths, crystallinity, chirality) and purity can be chosen for wet-process film fabrication (Hu et al., 2010; Wang and Bao, 2015). In contrast, in dry process, CNT structural and purity control have to be exercised at the synthesis stage.

Fabricating free-standing CNT films with thicknesses $\leq$ 200 nm by wet process is a major challenge (Sreekumar et al., 2003; Gu and Swager, 2008; Jo et al., 2010; Liu et al., 2010; Shi et al., 2011; Janas and Koziol, 2014; Ibañez et al., 2016; Janas et al., 2017). Achieving thinness in combination with high strength by wet process with minimal CNT damage during the dispersion step have been widely investigated. Shi et al. show promising results on wet-processed CNT films (Shi et al., 2011). They obtain 20-nm-thick free-standing films with tensile strength and Young's modulus of 860 MPa and 36 GPa, respectively, from suspensions of ultralong CNTs. In their process, the CNT films are fabricated by CNT suspension filtration. Shi et al. (2011) claim their filtration process to be scalable as the process is used in commercial paper production. However, the filter material needs to have appropriate porous structure, and solvents for the suspension need to be designed to have good permeability for the filtering process. Therefore, there are still unresolved issues in devising versatile and industrially compatible CNT film fabrication methods by wet processing to enable utility in a wide range of applications.

Here, we report macroscale (10-cm-square) freestanding CNT films with thicknesses ∼200 nm and tensile strengths of ∼166 MPa fabricated by wet process involving simple and scalable blade-coating of nanotube suspensions. In addition, we demonstrate the possibility of controlling the pore and bundle size in the CNT film mesh structure by regulating CNT dispersibility and entanglement in the suspensions. Further, we find this control in bundle and pore structure to be critical for achieving high CNT film tensile strengths, fracture strain, and Young's moduli.

MATERIALS AND METHODS

Our film fabrication protocol by wet process involves suspending CNT powders in a liquid medium aided by ultrasonication and blade-coating the suspensions into films. For fabricating 200-nm-thin free-standing CNT film, we peeled off the CNT film by dissolving the Al sacrificial layer and scooped up the film by a photo flame.

The CNTs we used in this study were synthesized by water-assisted chemical vapor deposition ("Super Growth"). The CNTs were grown as a vertical array on a Si substrate using iron nanoparticles as catalyst and C_2H_4 as carbon source with water vapor as growth enhancer (Hata et al., 2004). The as-grown CNTs were removed from the substrate to obtain powders, which were used as starting materials for film preparation.

We prepared four types of CNT suspensions for film fabrication using four types of liquid media (**Table 1** and **Supplementary Table S1**). In suspension 1, we used 10-dodecyl-7,8-dimethyl-10H-benzo[g]pteridine-2,4-dione (Flavin) (Ju et al., 2009; Kato et al., 2015). as the surfactant and toluene as the solvent to debundle the CNT powders. In suspension 2, we used sodium deoxycholate (SDOC) as the surfactant in aqueous solution. In suspension 3 and 4, N-methylpyrrolidone (NMP) and propylene glycol (PG) were used as the solvents, respectively (without any surfactant). The CNT and surfactant concentrations were optimized to make suspensions suitable for blade-coating. We made the CNT suspensions according to procedures reported elsewhere (Sakurai et al., 2018).

Details of the procedures we used for CNT film characterization—tensile testing, scanning electron microscopy (SEM), sheet resistance measurement, mercury porosimetry, gas adsorption, CNT film thickness measurement, Raman spectroscopy, thermogravimetric analysis (TGA), and CNT suspension characterization (by flow image analysis) are provided in the **Supplementary Material**.

RESULTS AND DISCUSSION

Manufacturing of Free-Standing CNT Films and Mechanical Properties

Our fabrication process is designed to be scalable, easy, and versatile, showing compatibility to various types of substrates and solvents. We fabricated our suspension blade-coated CNT films on 4-inch wafer scale (**Figures 1A,B**) and as 10-cm-square free-standing samples with <200 nm thickness (**Figures 1C,D**). As shown in **Figure 1D**, our free-standing films are translucent and

TABLE 1 | Four types of CNT films prepared using four types of suspensions and their mechanical properties by tensile test – tensile strength, fracture strain, and Young's modulus.

Sample name	Suspension		Mechanical properties		
	Solvent	Surfactant	Tensile strength [MPa]	Fracture strain [%]	Young's modulus [GPa]
Film 1	Toluene	Flavin	166	2.4	7.6
Film 2	Water	SDOC	71	2.2	2.9
Film 3	NMP	No surfactant	55	1.5	8.4
Film 4	PG	No surfactant	33	0.6	2.4

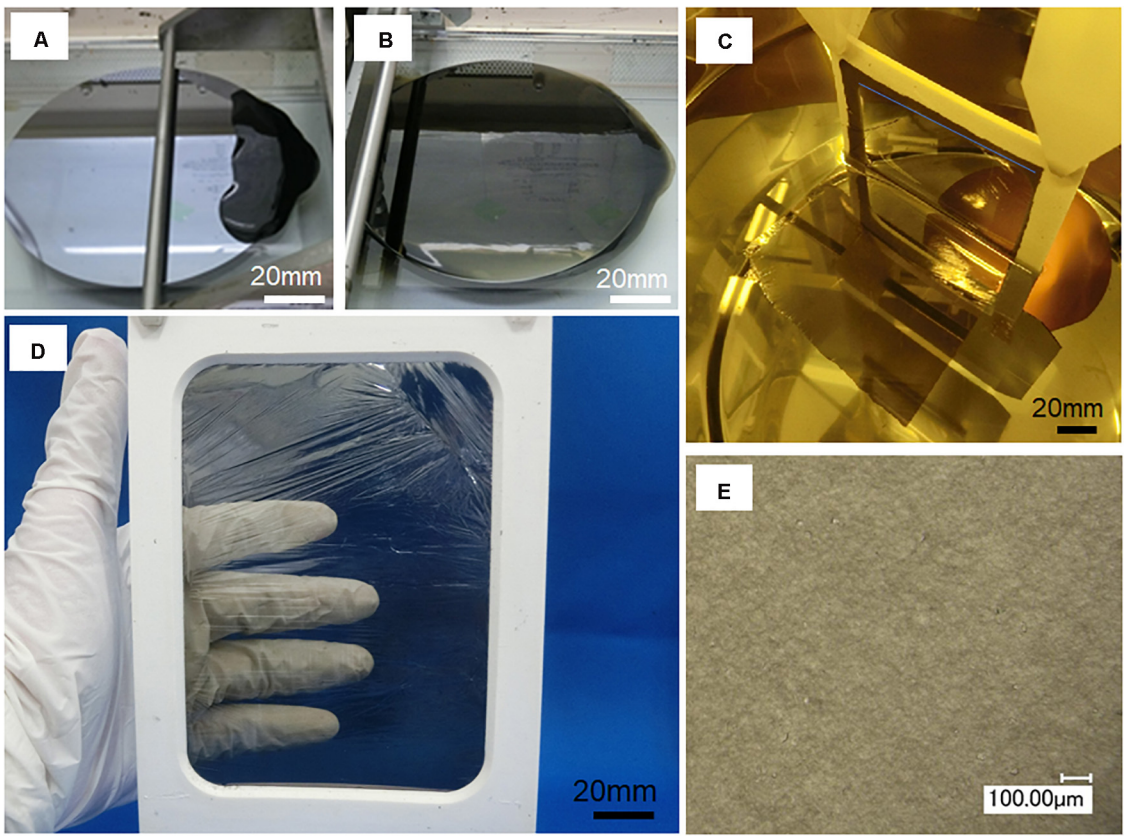

FIGURE 1 | (A,B) Photograph of the CNT suspension blade-coating process, **(C)** photograph of the CNT film transfer process, and **(D,E)** photograph and optical micrograph of a free-standing CNT film.

uniform in appearance without agglomerates over the entire span of the membrane. Optical microscopy images of the freestanding films also suggest that the film is uniform at the microscale (**Figure 1E**). Among the 4 types of samples prepared (**Table 1**), free-standing films with submicrometer thickness and >10 cm in size could only be obtained from CNT/flavin/toluene suspensions (film 1). Samples other than film 1 ruptured during the transfer process, suggesting that film 1 is more suitable for applications requiring free-standing films, such as switching/sensing elements in MEMS or ultrafiltration membranes.

Differences in transferability observed for the four types of samples stem from differences in the CNT film mechanical properties. It should be noted that film 1 showed markedly better mechanical properties than the other samples (films 2–4). **Figure 2**, which shows the stress-strain curves of the CNT films, indicates that film 1 shows the highest tensile strength (166 MPa), fracture strain (∼2.4%), and Young's modulus (7.6 GPa) among the four samples. The tensile strength, fracture strain, and Young's modulus of each sample calculated from the stress-strain curve (summarized in **Table 1**) show distinct differences in mechanical performances of the four samples. Film 1 shows nearly three times higher tensile strength than the other three samples (films 2–4). With regard to fracture strains, films 1 and 2 show similar values - nearly 1.5 times the values shown by the other two samples (films 3 and 4). In terms of Young's modulus, films 1 and 3 show similar values, which are more than twice the values shown by the other two films (films 2 and 4). We think the different mechanical properties observed are

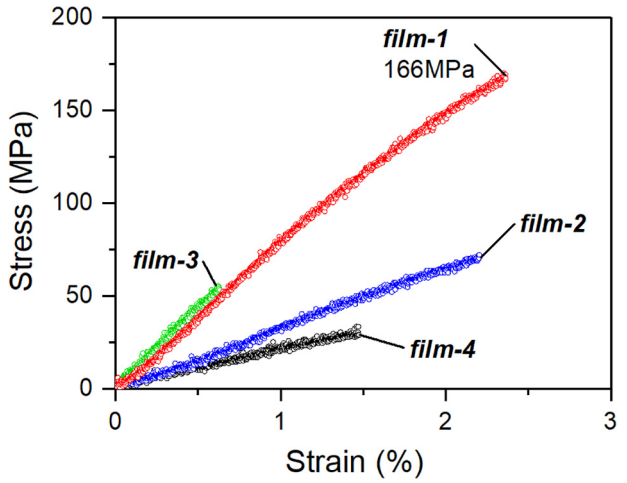

FIGURE 2 | Tensile stress-strain curves of the CNT films.

related to differences in the bundle and pore structures of each sample. Therefore, we systematically characterized and studied the influence of these structural factors. The results of the film structure characterization and their correlation to the mechanical performances are presented below.

We note that the tensile strength of film 1 (166 MPa) is comparable to thin free-standing films obtained by dry process (Zhang et al., 2005; Ma et al., 2007; Liu et al., 2011; Nasibulin et al., 2011; Zhou et al., 2012). The mechanical robustness of film 1 contributes to free-standing film fabrication in two ways.

1. It helps the film support its own weight, making free-standing submicrometer-thick samples possible.
2. It maintains film integrity during lift-off in the wet-process protocol.

We also measured film sheet resistances (film 1: 18.2 ± 1.9Ω, film 2: 18.3 ± 0.4Ω, film 3: 14.6 ± 1.1Ω, and film 4: 18.1 ± 1.7Ω). Since the values are similar and do not show a clear correlation with the film structure, we focused only on the mechanical properties.

Characterization of the CNT Film Mesh Structure

As reported in previous papers (Sakurai et al., 2018), bundled CNTs entangle in blade-coated CNT films, forming a mesh structure. Two factors could affect the film strength: (A) mesh structure of CNT bundles constituting the film (including attributes such as bundle thickness and inter- and intra-bundle pore sizes) and (B) characteristics of the CNTs themselves (such as length, diameter, wall number, crystallinity, functionalization level, etc.). In this paper, we fixed factor (B) by using identical CNT starting materials and processing methodology (sonication-based dispersion and blade-coating) for fabricating all our film samples. Our CNTs are typically single-walled nanotubes (average wall number ∼1.2), 100–300 μm in length, and 1–5 nm in diameter (average ∼3.7 nm) (Kobashi et al., 2019). Therefore, we assume that CNT attributes in our samples are comparable, which is supported by the similar Raman G/D ratios of our films (0.9, 1.9, 2.2, and 2.3, respectively, for films 1–4). Hence, we have attempted to explain the exceptional tensile strength of film 1 compared to the rest of the samples based on differences in the CNT bundle mesh structure. We characterize the mesh structure of the four films through relative standard deviation (RSD) of bundle thicknesses measured by SEM, Brunauer-Emmett-Teller (BET)-specific surface area (SSA) by gas adsorption analysis, bulk density, and G/D ratio by Raman spectroscopy (summarized in **Table 2**).

Our analysis of the mesh structure indicates that film 1 shows narrower bundle thickness and pore-size distributions than the other samples, which could contribute to the high mechanical strengths observed. **Figure 3** compares the mesh structure uniformity of the strongest and weakest CNT films (films 1 and 4, respectively) in terms of SEM images and bundle thickness distribution. The CNTs are randomly aligned in both samples, which is typical for CNTs in films prepared by wet process. However, film 1 shows smaller bundles with a narrower thickness distribution (bundle thickness 10–90th percentiles: 7–11 nm, RSD: 20%) than film 4 (bundle thickness 10–90th percentiles: 19–109 nm, RSD: 77%). Consequently, film 1 contains CNT bundles of similar thicknesses forming a dense mesh with similar-sized small pores distributed uniformly throughout (**Figure 3a**). This narrow bundle thickness distribution of film 1 is a key feature contributing to its structural uniformity and, hence, high strength. In contrast, in film 4 (**Figure 3b**), bundles of various sizes entangle to result in pores of different dimensions. The presence of bundles of various thicknesses usually leads to the formation of macropores, which reduces structural uniformity and thereby lowers film mechanical strength as observed in film 4.

Quantitative pore size distributions obtained by mercury porosimetry support SEM results on the presence of smaller pores with more size uniformity in film 1 compared to film 4 (**Figure 4**). **Figure 4**, which plots pore volume (normalized by sample weight) versus pore diameter, shows that film 1 contains fewer pores of sizes >300 nm compared to film 4. The widths of the pore volume versus diameter plots can be used as a measure of the pore-size distribution and uniformity. Film 1 shows a smaller pore volume versus diameter plot width than film 4, indicating higher pore-size uniformity in film 1 than film 4. The overall structural uniformity of film 1 (arising from similarly sized pores and bundles) enables even stress distribution, precluding stress concentration, leading to high tensile strength.

In addition to structural uniformity, bulk density is a well-known factor affecting mechanical strength: the higher the density, the better the CNT packing and stress transfer and the higher the tensile properties (Ma et al., 2007; Jiang et al., 2011; Zhou et al., 2012). In addition to better structural uniformity, film 1 also has a higher bulk density (0.84 ± 0.06 g/cm^3) than film 4 (0.47 ± 0.14 g/cm^3), which additionally contributes to the higher strength values observed. We emphasize that the

TABLE 2 | RSD of bundle thickness measured by SEM, SSA by gas adsorption analysis, bulk density, and G/D ratio by Raman spectroscopy of the four types of CNT films prepared using four types of suspensions.

Sample name	G/D ratio	Bundle thickness (RSD) [%]	Bulk density [g/cm^3]	SSA [m^2/g]
Film 1	0.9	20	0.84	766
Film 2	1.9	35	0.69	595
Film 3	2.2	71	0.82	500
Film 4	2.3	77	0.47	1130

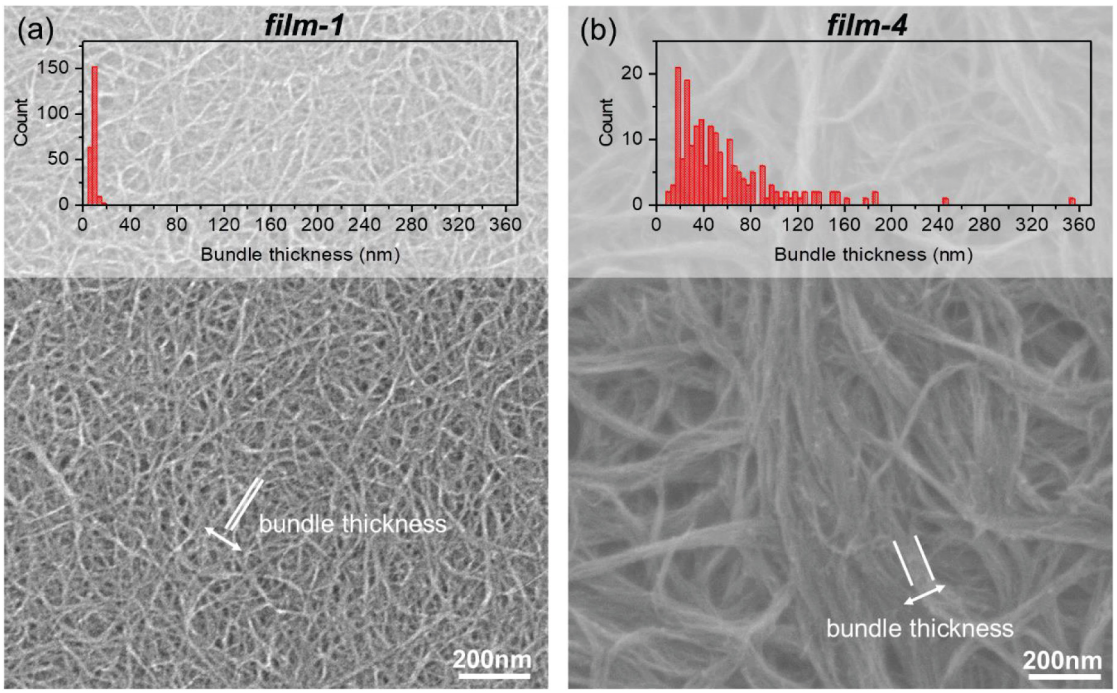

FIGURE 3 | SEM image and CNT bundle thickness distribution of **(a)** film 1, **(b)** film 4.

mesh structure uniformity in terms of bundle thickness and pore-size uniformity more profoundly affects film mechanical strength than the bulk density. The sample with high bulk density (film 3, 0.82 ± 0.12 g/cm^3) shows a much lower mechanical strength than film 1. We attribute this to the mesh structure of film 3, which, similar to film 4, is non-uniform with diverse bundle thicknesses and pore sizes (bundle thickness 10–90th percentiles: 19–111 nm, RSD: 71%) (see **Supplementary Figure S1**).

The structure and performance of film–2 also support that structural uniformity is important for film robustness. Film–2 shows similar mesh–structures as film 1 (see **Supplementary Figure S1**). The bundle thickness distribution for film 2 (bundle thickness 10–90th percentiles: 8–19 nm, RSD: 35%) is comparable to that for film 1 (bundle thickness 10–90th percentiles: 7–11 nm, RSD: 20%). Although film 2 (strength: 71 MPa) is weaker than film 1 (strength: 166 MPa), film 2 is stronger than film 4 (strength: 33 MPa) and film 3 (strength: 55 MPa). The discrepancy in the film strengths between films 1 and 2 indicates other factors are in play, affecting mechanical robustness. The poor tensile performance of film 2 can be explained based on two factors. First, film 2 shows a smaller bulk density (0.69 ± 0.10 g/cm^3) than film 1 (0.84 ± 0.06 g/cm^3), which translates to poorer CNT packing and stress transfer. Second, film 2 might contain a higher amount of residual surfactant (SDOC), which essentially acts as defects and, therefore, stress centers, undermining the tensile performance of the sample. We observed 8.6 wt% of TGA (air) residue for film 2 (see **Supplementary Figure S2**). On the other hand, very little residual flavin is left as residue in film 1. We recovered and detected at least 99% of flavin in rinsing solutions, as confirmed by ultraviolet-visible spectrophotometery (see **Supplementary Figure S3**). In addition, the virtual absence of residual surfactant may also be attributed to the higher (more than two times) Young's modulus of film 1 compared to film 2. However, it should be also noted that Young's modulus is different between film 3 and film 4 by more than two times despite similar mesh structures and being unaffected by surfactant residues. This suggests that CNT packing is more important for Young's modulus than uniformity. In fact, gas adsorption/desorption isotherm analyses (see **Supplementary Figure S4** and **Table 2**) indicate that film 4 contains more micropores and shows higher SSA compared to film 3, suggesting

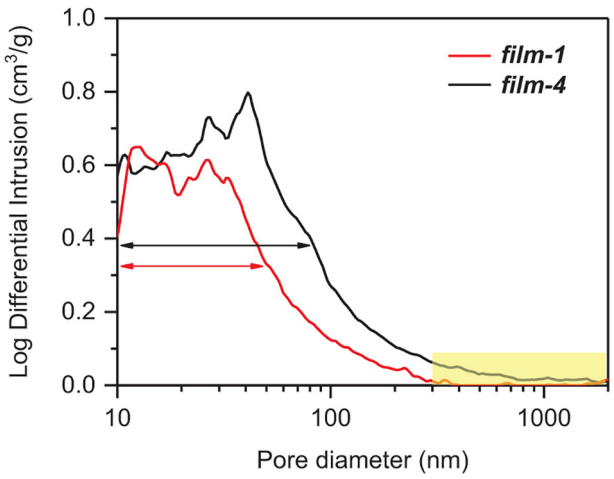

FIGURE 4 | Pore-size distribution of films 1 (red) and 4 (black) measured by mercury porosimetery.

that the existence of inter- or intra-bundle pores is an important factor affecting the Young's modulus of the CNT films.

Finally, the correlation of CNT film mechanical properties with mesh-structure uniformity and CNT packing is summarized in **Figure 5**. **Figure 5** plots the tensile strength, fracture strain, Young's modulus versus bundle size distribution and bulk density for the four types of samples. These figures show a clear dependence of tensile strength and fracture strain on bundle size distribution, which represents network structure uniformity. This suggests that controlling bundle size and, therefore, bundle and pore structures leads to five-fold and four-fold higher tensile strengths and fracture strains, respectively, compared to films with more bundle size variation. On the other hand, Young's modulus depends more on bulk density, which represents the number of pores and degree of CNT packing. Therefore, films with higher bulk density with better CNT packing show three-fold higher Young's modulus than those with the least packing (and, therefore, bulk density).

We believe that the differences in film mesh structures observed are related to differences in the CNT aggregate sizes and their distributions in the parent suspensions. Suspending CNTs in a liquid medium by ultrasonication is typically known to result in nanotube bundle agglomerations of sizes ranging to tens of microns (Kobashi et al., 2013; Sakurai et al., 2018). These aggregates, in turn, form higher order structures, (Kobashi et al., 2013) such as our films, when suspensions are processed by techniques such as blade-coating, drop-casting, etc. We observe clear differences in CNT aggregate size distributions of the different suspensions we made for film fabrication as seen in the number frequency versus aggregate size plots (**Figure 6**). The parent suspensions of films 1 and 2 show a noticeably higher number fraction (>95%) of smaller aggregates (<10-micron-diameter) than that observed in the parent suspensions of films 3 and 4 (78.1 and 54.5%, respectively). The higher fraction of smaller aggregates in parent suspension 1 and 2 is indicative of superior nanotube

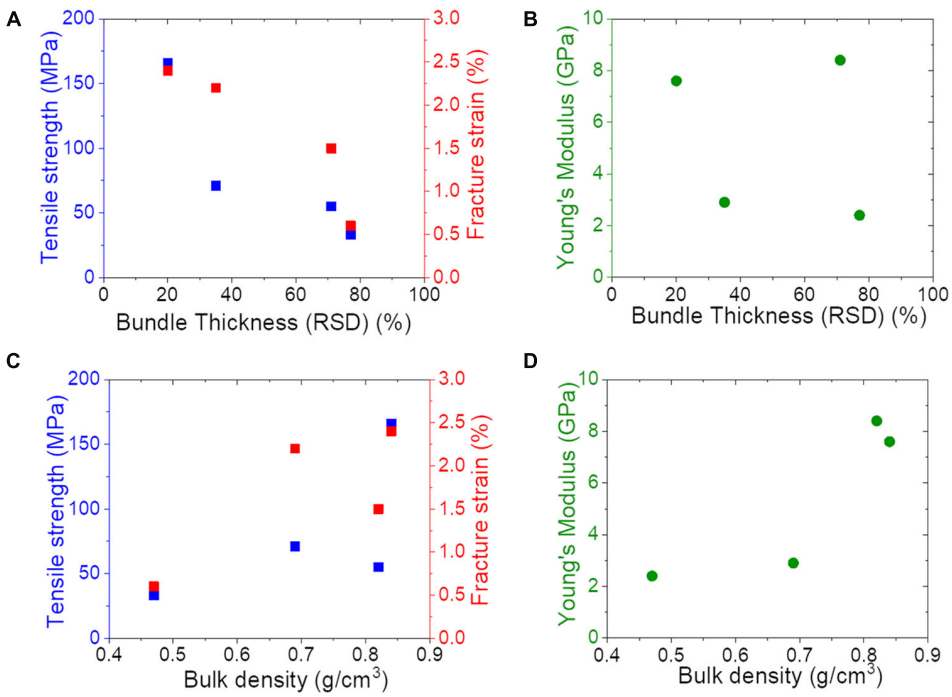

FIGURE 5 | Plots correlating mechanical strength and bundle network structure. **(A,C)** Tensile strength (blue), fracture strain (red), and **(B,D)** Young's modulus (green) versus bundle thickness distribution and bulk density of the CNT films.

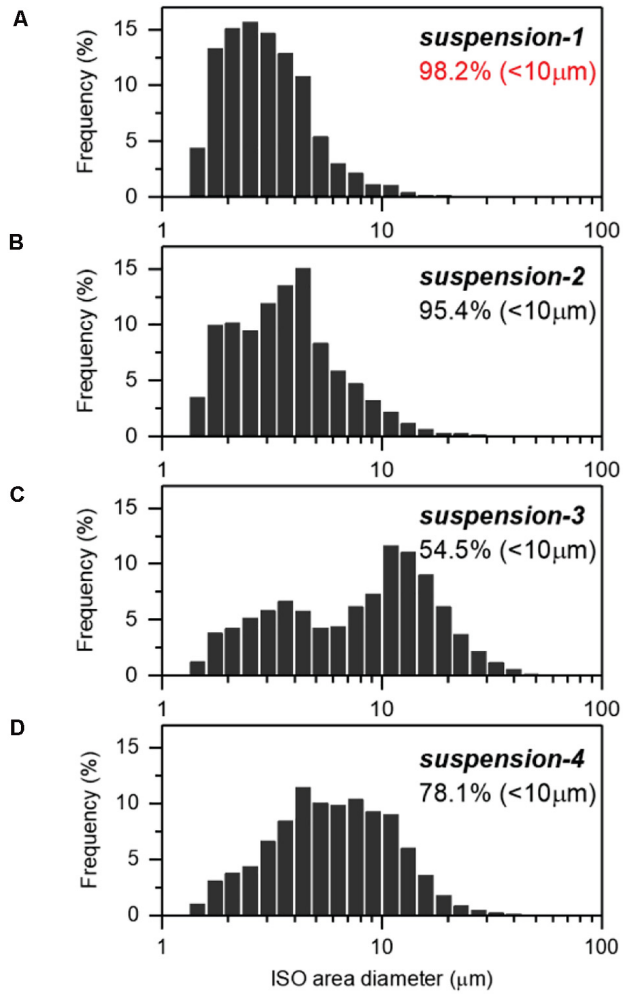

FIGURE 6 | Size distribution of CNT aggregates measured by flow image analyzer of **(A)**, suspension 1, **(B)** suspension 2, **(C)** suspension 3, **(D)** suspension 4.

debundling during the dispersion process, which leads to smaller and uniform-sized CNT bundles that ultimately result in the uniform mesh-structured films 1 and 2. The superior debundling of suspensions 1 and 2 can be attributed to the presence of a surfactant, i.e., flavin and SDOC, respectively, that are known to stabilize CNT aggregates and prevent their agglomeration by strong steric/electrostatic repulsions. In contrast, suspensions 3 and 4 are made without a surfactant by sonicating CNT powders in a neat solvent (i.e., PG and NMP, respectively) that stabilize the aggregates only by weak solvation effects. To sum up, well-stabilized CNT suspensions with a large fraction of small aggregates are key to making films with highly uniform mesh structures, in turn, vital to achieving high film mechanical strengths. Therefore, our study draws a holistic connection between the suspension quality, mesh structure of the films obtained, and their mechanical performances. We believe this bottom-up tailoring of robust free-standing ultrathin CNT films by wet-process blade-coating demonstrated here provides a pathway to the nanocarbon community for custom-building free-standing high-performance films of required properties. For instance, our work could be extended to CNTs with any predefined set of attributes (wall numbers, diameters, chirality, lengths, etc.) to improve electrical performances, optical properties, and so on because the suspension technique and bladed-coating can be adapted to various CNTs easily.

CONCLUSION

In summary, we fabricated large (10-cm-square) 200-nm-thick free-standing robust CNT films by a scalable, wet process involving blade-coating of CNT/surfactant suspensions. We demonstrate that a uniform mesh structure with narrow bundle and pore size distribution is vital to achieving robust thin films with strengths as high as 166 MPa. Further, we correlate the mesh structure with CNT aggregate sizes (and its distribution) in the parent suspension. We find that well-stabilized suspensions using surfactants with higher fractions of smaller aggregates lead to CNT films with uniform mesh structures that exhibit high mechanical performances. Our work presents a bottom-up approach of tailoring robust ultrathin free-standing CNT films by wet process through a versatile and potentially scalable fabrication methodology.

DATA AVAILABILITY STATEMENT

The raw data supporting the conclusions of this article will be made available by the authors, without undue reservation.

AUTHOR CONTRIBUTIONS

YK performed sample preparation, measurement, and analysis. YK and AS conceived the idea and designed the experiments. KK contributed to flow image analysis. YK, AS, and RS prepared the draft of the manuscript. TY and KH conceived the idea and supervised the project. All authors contributed to the article and approved the submitted version.

ACKNOWLEDGMENTS

We thank Dr. T. Morimoto and Dr. T. Okazaki for useful discussion. M. Nishimura, R. Shiina, F. Kamada, K. Miura, M. Fujii, and S. Nemoto are acknowledged for their technical support.

SUPPLEMENTARY MATERIAL

The Supplementary Material for this article can be found online at: https://www.frontiersin.org/articles/10.3389/fmats.2020.562455/full#supplementary-material

REFERENCES

Gu, H., and Swager, T. M. (2008). Fabrication of free-standing, conductive, and transparent carbon nanotube films. *Adv. Mater.* 20, 4433–4437. doi: 10.1002/adma.200801062

Hata, K., Futaba, D. N., Mizuno, K., Namai, T., Yumura, M., and Iijima, S. (2004). Water-assisted highly efficient synthesis of impurity-free single-walled carbon nanotubes. *Science* 306, 1362–1364. doi: 10.1126/science.1104962

Hecht, D. S., Hu, L., and Irvin, G. (2011). Emerging transparent electrodes based on thin films of carbon nanotubes, graphene, and metallic nanostructures. *Adv. Mater.* 23, 1482–1513. doi: 10.1002/adma.201003188

Hu, L., Hecht, D. S., and Grüner, G. (2010). Carbon nanotube thin films: fabrication, properties, and applications. *Chem. Rev.* 110, 5790–5844. doi: 10.1021/cr9002962

Ibañez, D., Garoz-Ruiz, J., Plana, D., Heras, A., Fermín, D. J., and Colina, A. (2016). Spectroelectrochemistry at free-standing carbon nanotubes electrodes. *Electrochim. Acta* 217, 262–268. doi: 10.1016/j.electacta.2016.09.074

Janas, D., and Koziol, K. K. (2014). A review of production methods of carbon nanotube and graphene thin films for electrothermal applications. *Nanoscale* 6, 3037–3045. doi: 10.1039/c3nr05636h

Janas, D., Rdest, M., and Koziol, K. K. (2017). Free-standing films from chirality-controlled carbon nanotubes. *Mater. Des.* 121, 119–125. doi: 10.1016/j.matdes.2017.02.062

Jiang, K., Wang, J., Li, Q., Liu, L., Liu, C., and Fan, S. (2011). Superaligned carbon nanotube arrays, films, and yarns: a road to applications. *Adv. Mater.* 23, 1154–1161. doi: 10.1002/adma.201003989

Jo, J. W., Jung, J. W., Lee, J. U., and Jo, W. H. (2010). Fabrication of highly conductive and transparent thin films from single-walled carbon nanotubes using a new non-ionic surfactant via spin coating. *ACS Nano* 4, 5382–5388. doi: 10.1021/nn1009837

Ju, S.-Y., Kopcha, W. P., and Papadimitrakopoulos, F. (2009). Brightly fluorescent single-walled carbon nanotubes via an oxygen-excluding surfactant organization. *Science* 323, 1319–1323. doi: 10.1126/science.1166265

Kato, Y., Fukuzawa, M., Toshimitsu, F., and Nakashima, N. (2015). Separation of semiconducting single-walled carbon nanotubes using a flavin compound. *Chem. Lett.* 44, 566–567. doi: 10.1246/cl.141193

Kobashi, K., Ata, S., Yamada, T., Futaba, D. N., Okazaki, T., and Hata, K. (2019). Classification of commercialized carbon nanotubes into three general categories as a guide for applications. *ACS Appl. Nano Mater.* 2, 4043–4047. doi: 10.1021/acsanm.9b00941

Kobashi, K., Ata, S., Yamada, T., Futaba, D. N., Yumura, M., and Hata, K. (2013). A dispersion strategy: dendritic carbon nanotube network dispersion for advanced composites. *Chem. Sci.* 4, 727–733. doi: 10.1039/C2SC21266H

Liu, K., Sun, Y., Liu, P., Lin, X., Fan, S., and Jiang, K. (2011). Cross-stacked superaligned carbon nanotube films for transparent and stretchable conductors. *Adv. Funct. Mater.* 21, 2721–2728. doi: 10.1002/adfm.201100306

Liu, Q., Fujigaya, T., Cheng, H.-M., and Nakashima, N. (2010). Free-standing highly conductive transparent ultrathin single-walled carbon nanotube films. *J. Am. Chem. Soc.* 132, 16581–16586. doi: 10.1021/ja1067367

Ma, W., Song, L., Yang, R., Zhang, T., Zhao, Y., Sun, L., et al. (2007). Directly synthesized strong, highly conducting, transparent single-walled carbon nanotube films. *Nano Lett.* 7, 2307–2311. doi: 10.1021/nl070915c

Narisawa, I. (1982). *Polymer Material Strength*. Tokyo: Ohmsha Ltd.

Nasibulin, A. G., Kaskela, A., Mustonen, K., Anisimov, A. S., Ruiz, V., Kivistö, S., et al. (2011). Multifunctional free-standing single-walled carbon nanotube films. *ACS Nano* 5, 3214–3221. doi: 10.1021/nn200338r

Parhi, P. K. (2013). Supported liquid membrane principle and its practices: a short review. *J. Chem.* 2013, 1–11. doi: 10.1155/2013/618236

Sakurai, S., Kamada, F., Kobashi, K., Futaba, D. N., and Hata, K. (2018). A new, general strategy for fabricating highly concentrated and viscoplastic suspensions based on a structural approach to modulate interparticle interaction. *J. Am. Chem. Soc.* 140, 1098–1104. doi: 10.1021/jacs.7b11305

Shi, Z., Chen, X., Wang, X., Zhang, T., and Jin, J. (2011). Fabrication of superstrong ultrathin free-standing single-walled carbon nanotube films via a wet process. *Adv. Funct. Mater.* 21, 4358–4363. doi: 10.1002/adfm.201101298

Sreekumar, T. V., Liu, T., Kumar, S., Ericson, L. M., Hauge, R. H., and Smalley, R. E. (2003). Single-wall carbon nanotube films. *Chem. Mater.* 15, 175–178. doi: 10.1021/cm020367y

Wang, H., and Bao, Z. (2015). Conjugated polymer sorting of semiconducting carbon nanotubes and their electronic applications. *Nano Today* 10, 737–758. doi: 10.1016/j.nantod.2015.11.008

Zhang, M., Fang, S., Zakhidov, A. A., Lee, S. B., Aliev, A. E., Williams, C. D., et al. (2005). Strong, transparent, multifunctional, carbon nanotube sheets. *Science* 309, 1215–1219. doi: 10.1126/science.1115311

Zhou, W., Ma, W., Niu, Z., Song, L., and Xie, S. (2012). Freestanding single-walled carbon nanotube bundle networks: fabrication, properties and composites. *Chin. Sci. Bull.* 57, 205–224. doi: 10.1007/s11434-011-4878-0

Conflict of Interest: The authors declare that the research was conducted in the absence of any commercial or financial relationships that could be construed as a potential conflict of interest.

Ceramics and Glass

Francesca Tittarelli

Prof. Francesca Tittarelli has a Ms. Degree in Chemistry, a Ph.D. in Materials Engineering, and is an Associate Professor in Materials Science and Technology at Università Politecnica delle Marche (UNIVPM) for the "Civil and Environmental Engineering" and "Building Engineering and Architecture" courses. She is a member of the RILEM Technical Committee HDB "Hygrothermal behaviour and Durability of Bio-aggregate based building materials" and of the Directive Board of the National Interuniversity Consortium of Materials Science and Technology (INSTM). She is the author of more than 220 papers about the development, characterization, durability, and sustainability of building materials and the co-inventor of two national patents.

Chiara Giosuè

Dr. Chiara Giosuè, Eng, Ph.D., is a Research Fellow at the SIMAU department (UNIVPM). Her research focuses on the interaction between environment and materials, such as waste valorization in sustainable construction and depolluting materials, alternative binders/aggregates for the construction industry, functionalization of materials to improve indoor air quality, material characterization and materials for conservation of cultural heritage, and the management and optimization of critical raw materials in the context of a circular economy. She is involved in teaching activities in Materials Science and Technology as a supervisor/co-supervisor of Bachelor's and Master's theses, the author/co-author of more than 40 scientific publications in international journals, and a reviewer of several of those same journals.

frontiers in Materials

ORIGINAL RESEARCH
published: 26 August 2020
doi: 10.3389/fmats.2020.00255

Multifunctional Lightweight Mortars for Indoor Applications to Improve Comfort and Health of Occupants: Thermal Properties and Photocatalytic Efficiency

Chiara Giosuè[1], Mattia Pierpaoli[2], Alessandra Mobili[1], Maria Letizia Ruello[1] and Francesca Tittarelli[1,3]**

[1] Department of Materials, Environmental Sciences and Urban Planning (SIMAU), Università Politecnica delle Marche – INSTM Research Unit, Ancona, Italy, [2] Faculty of Electronics, Telecommunications and Informatics, Gdañsk University of Technology, Gdañsk, Poland, [3] Institute of Atmospheric Sciences and Climate, National Research Council (ISAC-CNR), Bologna, Italy

OPEN ACCESS

Edited by:
Emilia Morallon,
University of Alicante, Spain

Reviewed by:
Maria Angeles Lillo-Rodenas,
University of Alicante, Spain
Inês Flores-Colen,
Instituto Superior Técnico, Portugal
Mohammed Ouzzine,
Université Sultan Moulay Slimane, Morocco

***Correspondence:**
Chiara Giosuè
c.giosue@univpm.it
Francesca Tittarelli
f.tittarelli@univpm.it

Specialty section:
This article was submitted to Ceramics and Glass, a section of the journal Frontiers in Materials

Received: 11 May 2020
Accepted: 14 July 2020
Published: 26 August 2020

Citation:
Giosuè C, Pierpaoli M, Mobili A, Ruello ML and Tittarelli F (2020) Multifunctional Lightweight Mortars for Indoor Applications to Improve Comfort and Health of Occupants: Thermal Properties and Photocatalytic Efficiency. Front. Mater. 7:255. doi: 10.3389/fmats.2020.00255

A new generation of smart building materials, able to passively improve the indoor environment and the comfort of occupants owing to their interaction with the surrounding environment, can be addressed. This paper investigates the use of three highly porous aggregates to manufacture hydraulic lime-based multifunctional mortars to be used as indoor finishes. The same water/binder ratio was used for each mortar mix, and conventional calcareous sand was totally replaced by volume with zeolite, silica gel, and activated carbon. Nanosized titanium dioxide (TiO_2) was added to award a photocatalytic behavior under UV radiation to the mortars. Results show that, as expected, when highly porous aggregates are used, mortars absorb more water by capillary suction. However, even though the mortars manufactured with lightweight aggregates have a lower density, the mechanical behavior of zeolite and activated carbon mortars is comparable or even higher than that of sand mortars, thanks to an optimum interfacial transition zone (ITZ) between the binder paste and the aggregate. The photocatalytic activity, in terms of photocatalytic NO_x degradation efficiency and selectivity of unwanted produced NO_2, results to be optimal when silica gel-based mortar is tested. Additionally, the thermal-insulation properties are enhanced up to 40% by using all the unconventional aggregates.

Keywords: Indoor Air Quality, lightweight mortar, titanium dioxide photocatalytic oxidation, capillary water absorption, thermal conductivity

INTRODUCTION

A remarkable issue of modern time is the sustainability of the building sector since it contributes 40% on global carbon dioxide emissions (Wang et al., 2012). For this reason, nowadays European laws and directives are becoming stricter in terms of energy efficiency and, consequentially, more sealed buildings are assembled and not enough air changing can be guaranteed (Wolkoff, 2013). In this condition, the concentration of chemical, physical, and biological pollutants, such as volatile

organic compounds (VOCs), anhydrides, particulate matters, and molds, can be higher inside than outside, impairing the Indoor Air Quality (IAQ) of living environments. Currently, people are spending about 90% of their time indoor (Frey et al., 2015); thus, it is of utmost importance that the indoor living environment is wholesome to guarantee the health and comfort of occupants (Pierpaoli and Ruello, 2018).

Several strategies are used to improve the IAQ also in terms of thermal comfort; the conventional ones are source control, dilution by ventilation, and active engineered control systems (in heating, ventilation, and air-conditioning, HVAC) or stand-alone air purifiers (Matsumoto et al., 2009). Active control systems are generally more effective than passive systems for the control of IAQ, but they have a substantial energy loss that can be reduced by the addition of passive systems in the environment (Trník et al., 2016). Moreover, the combination of multiple techniques to improve IAQ, and in particular to remove pollutants, may result in a more efficient synergistic effect than the sum of the individual ones (Pierpaoli et al., 2017, 2019a). To remove pollutants, titanium dioxide (TiO_2) is the most studied photocatalytic agent, because of its chemical inertness, non-toxicity, and low cost. Therefore, there is an increasing interest in using such catalyst in cementitious materials (Ballari et al., 2011; Folli et al., 2012).

Smart materials are based on the innovative concept of designing the material composition by introducing functional components into the matrix (Han et al., 2016) able to give different functionalities to the same material such as good mechanical performances, lightness, and ability to improve IAQ in terms of low thermal conductivity, to act as an hygroscopic buffer (Senff et al., 2018), and/or to remove pollutants.

In this case, the addition of highly porous materials with adsorbent properties is the key aspect to providing the multifunctionality of mortars, as successfully demonstrated in previous works where they were added to commercial finishes (Giosuè et al., 2017a). Several studies have tested the NO_x photocatalytic degradation, where TiO_2, added at 1–4% by binder mass, gives a removal efficiency ranging from 30 to 80% (Senff et al., 2013, 2018), also under visible irradiation (Giosuè et al., 2018).

In the current study, the photocatalytic activity is associated with the adsorption of unconventional highly porous aggregates added to different mixes. The adsorption on a solid surface can be influenced by forces of electrostatic nature due to differences in polarity and differences in molecular weight and molecular geometry which induce selective deposition on the solid surface (Masel, 1996). The adsorption process is preferred on solids with a high specific surface since adsorption is a superficial process (Matsumoto et al., 2009). In mortars, the effectiveness of adsorbent aggregates to remove VOCs can reach 65%, as it has been previously tested (Tittarelli et al., 2015; Giosuè et al., 2019b). Adsorbent fillers/aggregates have been also tested to remove NO_x in cementitious systems with photocatalytic agents under UV-A radiation (Horgnies et al., 2012; Pierpaoli et al., 2019b).

The use of unconventional highly porous aggregates can also be employed to develop lightweight mortars with low sound transmission (Branco and Godinho, 2013) and minimal thermal transmittance (Benfratello et al., 2013; Branco and Godinho, 2013; Giosuè et al., 2019b) to the advantage of thermal efficiency and indoor sound comfort. It is well known that thermal conductivity can be reduced by the addition of aggregates with low bulk density and/or low thermal conductivity (Benfratello et al., 2013). Another positive effect is the reduction of the material density with a consequent lowering of dead loads on the structure. Nevertheless, in materials the reduction of density is often related to the reduction in compressive strength (Demirboga and Gül, 2003; Yu et al., 2015).

The current work is aimed to develop innovative multifunctional mortars for indoor finishes/renders able to passively improve IAQ, besides fulfilling the ordinary requirements (according to the standard EN 998). The main objective is not to find the mortar with the best

TABLE 1 | Properties of different aggregates.

Mix	Image	ID	Density kg/m^3	Water absorption %
Calcareous sand		S	2650	5
Zeolite		A1	1600	20
Silica gel		A2	1310	86
Activated carbon		A3	530	30

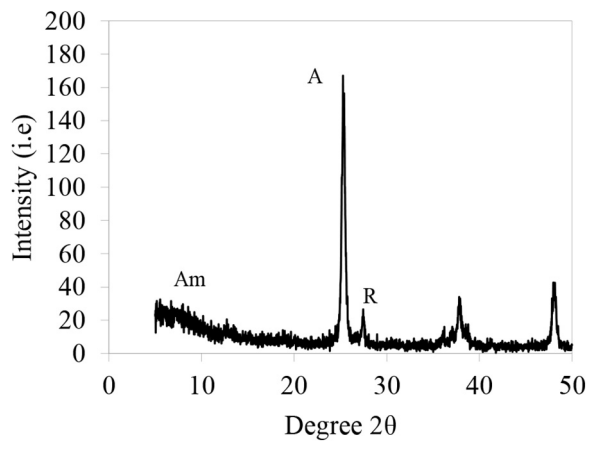

FIGURE 1 | X-ray diffraction (XRD) patterns of TiO_2, P-25 where anatase (A), rutile (R), and the amorphous phase (Am) are detected.

TABLE 2 | Mix proportions (g/L), density (kg/m^3), and accessible total porosity (%) of mortars.

Mix	Mix proportions							Density kg/m^3	Accessible porosity %
	Water	HL	S	A1	A2	A3	TiO_2		
M0-S	255	440	1535	–	–	–	–	1800	32
M0-S TiO_2	255	414	1535	–	–	–	26		
M1-A1	255	440	–	927	–	–	–	1390	41
M1-A1 TiO_2	255	414	–	927	–	–	26		
M2-A2	255	440	–	–	759	–	–	910	47
M2-A2 TiO_2	255	414	–	–	759	–	26		
M3-A3	255	440	–	–	–	683	–	1210	35
M3-A3 TiO_2	255	414	–	–	–	683	26		

mechanical properties, but to compare mortars that can act as multifunctional renders/finishes being able to improve also IAQ.

For this purpose, hydraulic lime is used as binder with and without the addition of TiO_2. Lime-based mortars are extensively used as renders/plasters in indoor applications. Moreover, hydraulic lime mortars are commonly used for rehabilitation of historical buildings where cement-based mortars are not allowed, and lime is a more sustainable binder than ordinary Portland cement (Barcelo et al., 2013; Lucas et al., 2013). It has been also demonstrated that hydraulic lime provides to mortars a higher depolluting activity than cement; this is due not only for the lower presence of mineralogical components that can hide the catalyst (Sugrañez et al., 2013; Kaja et al., 2019) but also for the higher porosity of its hardened microstructure (Karatasios et al., 2010; Giosuè et al., 2018).

The conventional sand is substituted by highly porous and adsorbent materials usually employed in filters for water–air cleaning processes as zeolite, silica gel, and activated carbon. As reference, a conventional sand-based mortar is used.

The mechanical strength and porosity of these mortars have been measured in a previous work (Giosuè et al., 2020). Here, the different compressive strength values are correlated with the corresponding microstructures observed by scanning electronic microscopy (SEM). Moreover, the behavior under capillary water absorption is investigated. In order to find the best mortar for improving the indoor comfort and health of indoor occupants, the corresponding thermal conductivity and photocatalytic activity are also tested. The previous work has demonstrated the optimum hygroscopic behavior of these mortars in terms of moisture buffering capacity and water vapor permeability but also a photocatalytic activity hidden by the adsorption process until saturation of specimens (Giosuè et al., 2020). Therefore, in this paper, to demonstrate the effectiveness of photocatalytic activity in batch, all mortars are tested in saturated conditions.

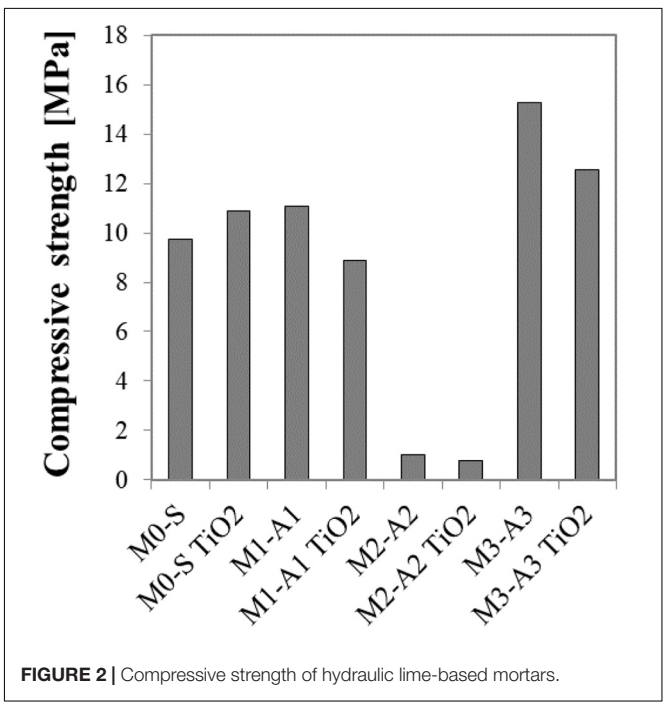

FIGURE 2 | Compressive strength of hydraulic lime-based mortars.

MATERIALS AND METHODS

Materials

The binder is a commercial hydraulic lime LIC 3.0, according to UNI EN 15368, with a density of 2650 kg/m^3. As aggregates, sand (S) is fully substituted by volume with selected unconventional aggregates, namely, natural clinoptilolite zeolite (A1), silica gel (A2), and activated carbon (A3). During the cast, all aggregates are added in saturate surface dry (SSD) condition, which means that all voids of aggregates are saturated by water but the surface is dry; hence, when the water necessary for the cast is added, no water exchange between the aggregate and the paste takes place. The density and water absorption of all aggregates to reach the SSD condition are evaluated and summarized in **Table 1**.

A commercially available titanium dioxide, TiO_2, P-25 Aeroxide by Evonik, is used as photocatalytic agent, added by replacing 5% of the binder weight. TiO_2, in powder form, was added to the dry cement mixture prior to the water addition, carefully mixed manually for 3 min and then with a mortar mixer.

As reported in the data sheet, its chemical composition is a mixture of anatase–rutile–amorphous phases, 78–14–8% in weight, respectively. Particles have nano-size dimension around 20–50 nm. The specific surface, measured by BET, is 35–65 m^2/g,

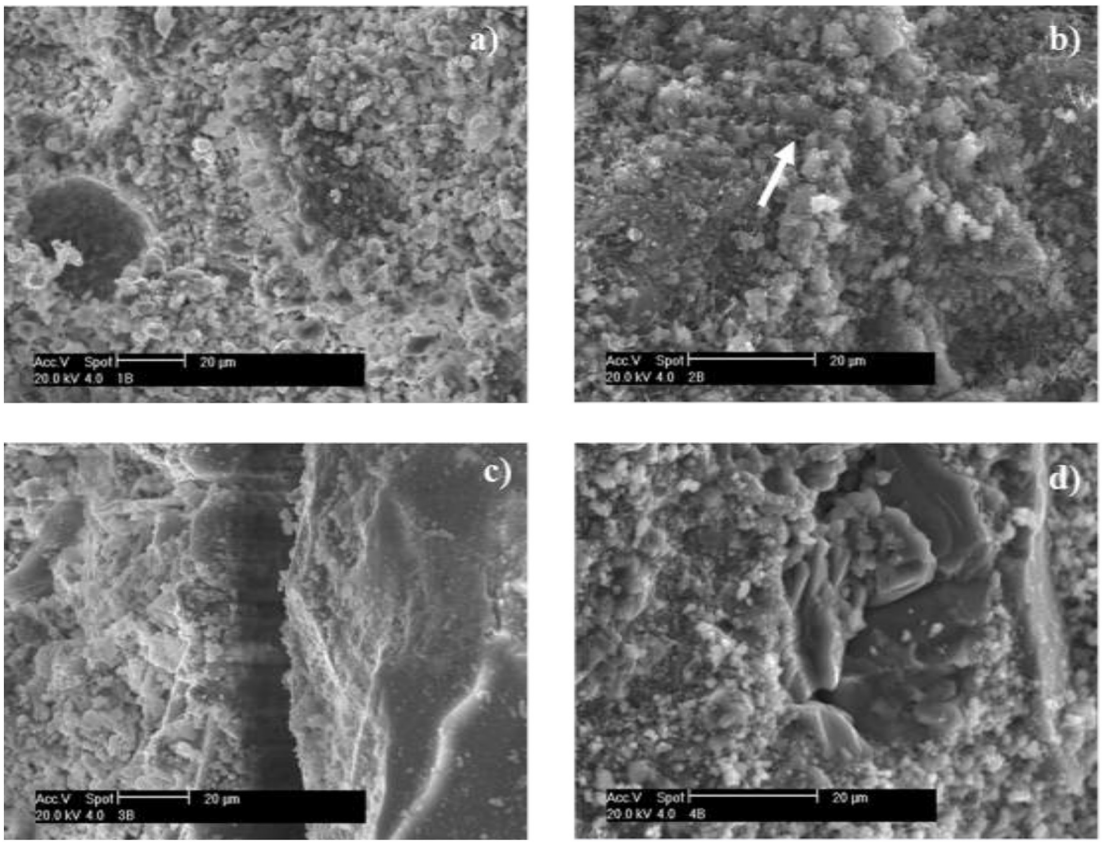

FIGURE 3 | SEM images of mortars manufactured with different aggregates and TiO_2. **(a)** HL-S TiO_2, **(b)** HL-A1 TiO_2, **(c)** HL-A2 TiO_2, **(d)** HL-A3 TiO_2.

and density is equal to 3100 kg/m^3. The pH value of 4% dispersion in water is 3.5–4.5. The X-ray diffraction (XRD) pattern is shown in **Figure 1** where the crystalline phases are detected.

The mixes are prepared by keeping constant the water to binder ratio at 0.6. Mix proportions, density, and accessible total porosity of cured mortars without TiO_2 (since these properties were not significantly affected by TiO_2 nanoparticles) are reported in **Table 2** (Giosuè et al., 2020).

Since the retail price in Euro/kg is about 0.10 for calcareous sand, 2.02 for zeolite, 0.59 for silica gel, 5.00 for activated carbon, 44 for TiO_2, and 0.14 for HL, the price in Euro/m^3 of the photocatalytic mortars with zeolite and activated carbon is about double that with conventional sand, whereas the price in Euro/m^3 of the silica gel photocatalytic mortar is about half that of conventional sand photocatalytic mortar.

Methods

Mortars are casted and then cured for 28 days according to the UNI EN 1015-11 procedure: at temperature (T) of 20°C and relative humidity (RH) of 95% for 7 days and then at 20°C T and 65% RH. After 28 days of curing, mortars are tested according to the current standards.

Properties such as mechanical performance, density, and porosity of these mortars have been already investigated in Giosuè et al. (2020) and are briefly summarized in the current paper. Compressive strength is measured by means of a hydraulic press (Galdabini) after 28 days of curing. Density is evaluated by the ratio between the weight of the specimen and its dimension, measured with a caliper. Each measurement is repeated three times, and the average values are reported. The dry weight is evaluated after placing the specimens in oven at $T = 105$°C until a constant weight is reached (when the change in the weight of the test specimen over 24 h period is less than 0.1%). Porosity is evaluated by means of MIP (Thermo Fisher, Pascal series 240) on samples after 28 days of curing on three fragments per mortar of 1 cm^3 volume, and the average results are reported.

In this study, the mechanical strengths are correlated with the microstructures observed by SEM. Moreover, the capillary water absorption, the photocatalytic behavior by NO_x degradation test, and thermal conductivity are further investigated.

The morphology is analyzed by means of the SEM ZEISS 1530 (Carl Zeiss, Oberkochen, Germany) equipped with a Schottky emitter, with two different secondary electrons detectors (the in-lens and the Everhart-Thornley) and operating at 10 keV (EDAX probe). Specimens are fragments of about 1 cm^3.

Capillary water absorption is investigated according to UNI EN 15801. Capillary water absorption is affected not only by the pores volume but also by the distribution and size of the pores, since the lower the pore diameter, the higher the level

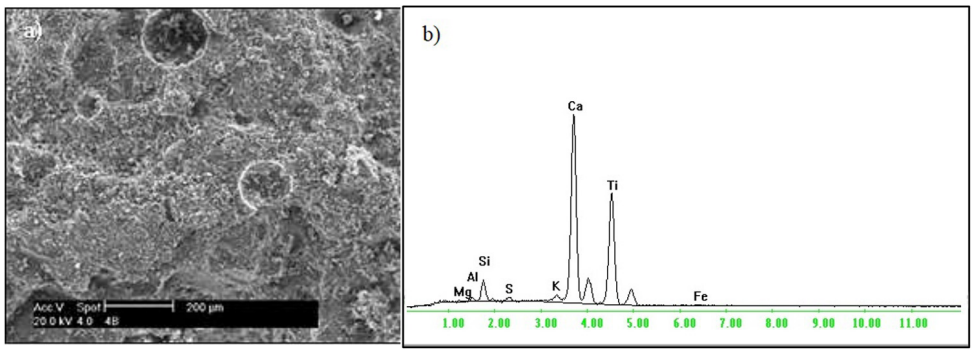

FIGURE 4 | SEM images **(a)** and EDAX **(b)** performed on HL-S TiO_2 mortar.

reached by the rising water, according to the Washburn's equation (Washburn, 1921). Test specimens are prisms 160 × 40 × 40 mm broken in two halves. Specimens are dried in an oven at 105°C until the constant mass is reached (difference in the weight values measured after 24 h should be lower than 0.1%). The specimens are placed on a water-saturated filter paper, and the capillary water absorbed by the tested surface (16 cm^2) is monitored over time by weighing the specimens periodically. The results are expressed as water absorbed per unit area Q_i (kg/m^2) at time t_i ($s^{0.5}$).

Concerning photocatalytic efficiency, after curing, the pH of mortars is measured in order to demonstrate the lowering of the basicity of the mixes. It is well known that CO_2 can penetrate within the matrix as easily as the porosity increases, interacting with the matrix through the carbonation process. This process causes the decrease of the pH and the densification of the matrix owing to the precipitation of calcite. In turn, calcite can cause the occlusion of the catalysts (Sugrañez et al., 2013). Also, the redox process that occurs at the TiO_2 surface is influenced by the pH, due to the Nernst relationship (MacPhee and Folli, 2016). 1 g of material is collected on a glass slide; then, a drop of water (about 1 ml) is added and the pH of the solution is measured.

The test adopted for assessing the photocatalytic property of the mortars follows the UNI 11247 procedure, which assesses the photocatalytic activity of inorganic photocatalytic materials by determining the degradation rate of nitrogen oxides (NO_x) in air. Therefore, the NOx photocatalytic activity is expressed by the ratio of removed NO_x over total NO_x flux under plug flow conditions. Briefly, a NO_x flux is directed inside the reactor by a NO_x tank, 499 ppb NO (SAPIO S.r.l., Monza, Italy), and it is kept constant with a dilution system (Calibrator 8188, Rancon Instruments S.p.A., Milan, Italy) by mixing with atmospheric air at $T = 25 \pm 2$°C and RH between 40 and 50%. NO and NO_2 concentrations are continuously monitored by a chemiluminescence NO_x analyzer (nitrogen oxide analyzer model 8841, Monitor Labs, Englewood, CO, United States) at the reactor outlet. The photoreactor consists of a 3-L borosilicate glass cylinder, in the center of which the specimens (8 cm diameter and 0.8 cm height) are placed. A UV metal halogen lamp, having a measured irradiance of 20 W/m^2, is placed outside the reactor over the specimen and placed at 25 cm from the specimen' surface. The irradiation of the sample is guaranteed until stable conditions are reached, usually 30 min.

The thermal conductivity (λ, in W/mK) of specimens is measured at room temperature ($T = 20$°C) and RH = 50%. Specimens are cylinders of 14 cm diameter and 3 cm height. The test is performed according to the UNI EN 12664 standard and λ calculated by the following equation (Eq. 1):

$$\lambda = \frac{Jd}{(T_1 - T_2)} \quad (1)$$

where J is the heat flux (W/m^2), d is the distance between thermocouples (m), and T_1 and T_2 are the temperatures at the two different sides of the sample (K). Before being tested, specimens have been conditioned at $T = 20$°C and RH = 50% until constant weight is reached (when the change in the weight of the test specimen over a 24 h period is less than 0.1%).

RESULTS AND DISCUSSION

Compressive Strength and Microstructural Observations

The compressive strength values already measured in Giosuè et al. (2020) and the morphological observations obtained by SEM are reported in **Figures 2**, **3**. For the sake of brevity, in **Figure 3**, only images of specimens manufactured with different aggregates and TiO_2 are shown.

Since the main aim of this paper is to compare the effects of different types of aggregates on the ability of mortars to improve IAQ in terms of thermal conductivity and photocatalytic activity, the mixes are prepared by keeping constant both the water amount and the same water-to-binder ratio. For this fact, it is worth underlining that while the resulting compressing strength values for A2 mortars are good for applications as finishes/renders, those for A1 and A3 mortars are too high and not suitable for this type of application.

However, the good mechanical behavior of the mortar manufactured with sand (S) can be explained by the high mechanical strength of natural sand, due to its low porosity and the good adhesion between sand and hydraulic lime paste

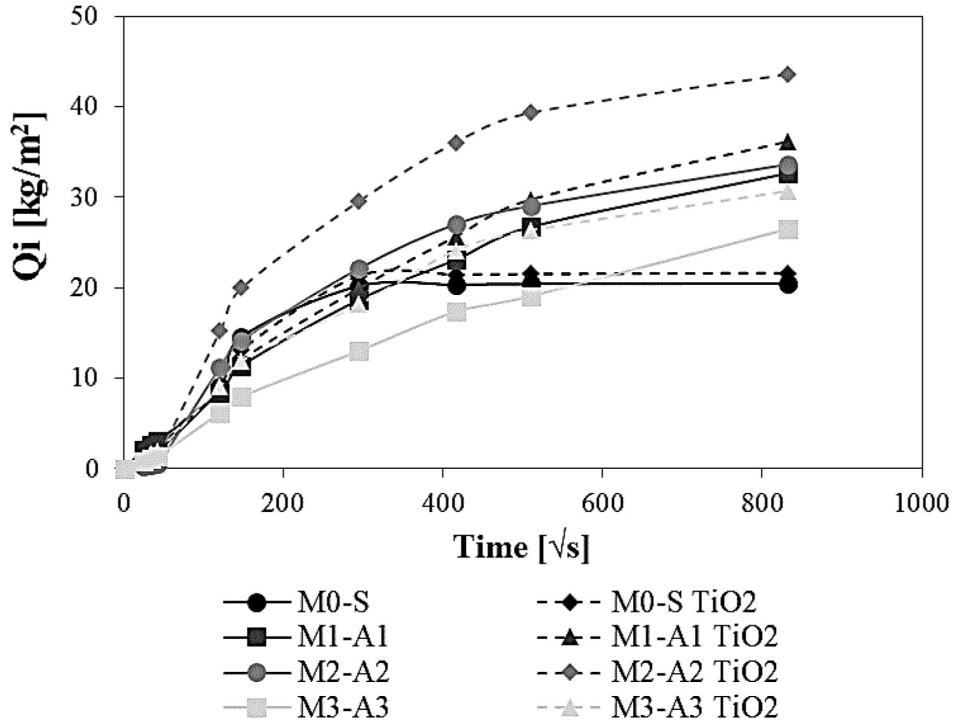

FIGURE 5 | Capillary water absorption in time of hydraulic lime-based mortars.

(**Figure 3a**). EDAX analysis (**Figure 4**) evidences Ca of the aggregate and of the binder with Si and S present in the hydraulic-lime paste. TiO_2 particles are not visible in SEM images, confirming their optimum dispersion in the mix; anyhow, their presence is evident by EDAX analysis performed on the paste (**Figure 4**) due to the appearance of the Ti peak.

When the mortar is manufactured with zeolite (A1), even though zeolite is more porous, lighter, and therefore less resistant than natural sand, the mechanical resistance of the mortar remains high thanks to the pozzolanic activity of zeolite that forms additional hydration products, well visible as indicated in **Figure 3b** (Caputo et al., 2008; Uzal et al., 2010). Moreover, thanks to the pozzolanic reaction, the interfacial transition zone (ITZ) between zeolite and the binder paste can be hardly recognized, highlighting the optimum adhesion between the two components.

On the other hand, in **Figure 3c**, the ITZ between silica gel and hydraulic lime is clearly visible due to an evident detachment between the two components. As a matter of fact, the adhesion between hydraulic-lime paste and this type of aggregate appears very poor, due to the smooth surface of silica gel particles. This issue explains the worst mechanical behavior of silica gel-based mortars.

The ITZ between hydraulic lime paste and activated carbon is better than that with silica gel. In this case, even though activated carbon is more porous, lighter, and therefore less mechanical resistant than sand, the mechanical strength of mortars is even greater than that of sand-based mortars, probably thanks to its surface roughness which improves the adhesion with the binder paste, guaranteeing an interlocking mechanism. This behavior was detected in other carbon-based materials with a porous surface that, acting as reservoirs, were able to provide a migration of water from their inside to the surrounding binder paste during the curing period, guaranteeing an optimum ITZ (Mrad and Chehab, 2019).

Capillary Water Absorption

The open porosity is one of the most influencing parameters for water absorption of mortars: the higher the open porosity, the higher the water quantity that can fill the pores. Therefore, the use of unconventional aggregates increases the water uptake of mortars because they increase the porosity of the mortars compared to conventional sand (Giosuè et al., 2017b). As already demonstrated for these mixes (Giosuè et al., 2020) and reported in **Table 2**, the mortars with the highest value of open porosity are those manufactured with silica gel, followed by zeolite-based mortars and finally activated carbon-based mortars. The reference mortar has obviously the lowest porosity value.

In the absence of TiO_2, as expected, the reference mortar, being the less porous, absorbs the lowest amount of water (**Figure 5**). Zeolite (A1)-based mortars adsorb an amount of water at 60%, higher than sand-based mortars. Silica gel (A2) mortars have the highest water absorption (80% higher than sand-based mortar) since they are the most porous.

Activated carbon-based mortars absorb lower (at the beginning of the test) and then higher (40%) amounts of water than sand-based mortars. This behavior is mainly related to the characteristics of the aggregate: activated carbon is hydrophobic

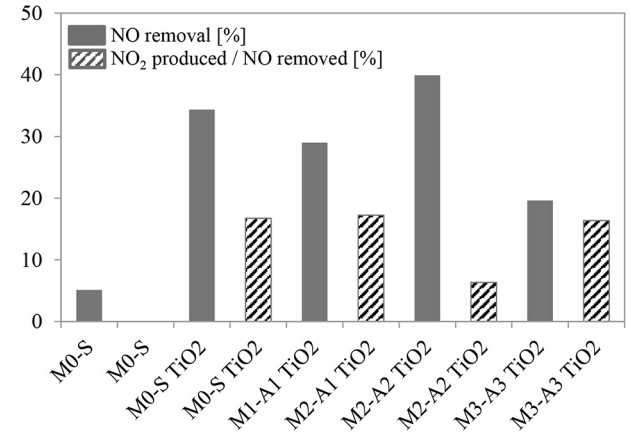

FIGURE 6 | Photocatalytic efficiency of mortars under UV-A radiation.

(Yang, 1987), with low affinity to water, at the early stage since it is a non-polar absorbent material, but it becomes hydrophilic for longer periods of contact with water and/or when some water has already been adsorbed (Giosuè et al., 2017b).

When the TiO_2 agent is added, generally the water absorption increases. This phenomenon, already shown in a previous study (Giosuè et al., 2017b), is due to the presence of TiO_2, since the activation of the photocatalyst gives hydrophilicity to mortars (Banerjee et al., 2015; Zhang et al., 2015).

Photocatalytic Oxidation

The behavior of mortars under photocatalytic radiation is reported in **Figure 6**. After the curing period, the pH of the specimens is evaluated as indicated in section "Methods." After the cast, the pH value of the cementitious product is around 13.5 (Tittarelli et al., 2018). The results show that the finishes lose their initial strong basicity since the detected pH values are equal to 8 for all mortars, apart from those of the M3 series (M3-A3 and M3-A3 TiO_2) with a pH of 8.5. For all TiO_2 specimens, a NO removal efficiency ranging from 20 to 40% is found. The lowest efficiency, equal to 20%, is registered in mortars manufactured with activated carbon; their dark color can reduce the reflectance of radiation and consequently influences the photocatalytic properties of the substrate (Chen and Poon, 2009; Daoud, 2013).

In the TiO_2-mediated NO photocatalytic oxidation, NO_2 is produced as an unwanted product of the reaction. For this reason, the photocatalytic mortar exhibiting a lower NO_2 production should be preferred. In this regard, the ratio between NO_2 and NO is considered: the higher the ratio, the higher the production of unwanted NO_2 during the reaction (Pierpaoli et al., 2018). Whereas the ratio between the produced NO_2 and the removed NO is constant and around 16% for reference, zeolite, and activated carbon specimens, it is significantly lower when silica gel is used. This synergistic effect was already found in previous studies (Pierpaoli et al., 2018, 2019b) and may be attributed to an enhanced reactivity with the Ti-OH via NO_2 disproportion (Eq. 9) caused by a more available adsorbed water in the vicinity of the photocatalyst (Dalton et al., 2002) and by the subsequent reaction of the nitrates with alkali or alkaline earth metals ions (Eq. 10).

TiO_2 photocatalysis

$$TiO_2 + h\nu \rightarrow TiO_2^* \left(h_{vb}^+ + e_{cb}^-\right) \quad (2)$$

$$TiO_2^* \left(h_{vb}^+\right) + H_2O_{ads} \rightarrow TiO_2 + OH_{ads}^\bullet + H^+ \quad (3)$$

$$TiO_2^* \left(e_{cb}^-\right) + O_{2ads} \rightarrow TiO_2 + O_{2\ ads}^- \quad (4)$$

Oxidation via $OH^\cdot$

$$NO_{ads} \overset{OH_{ads}^\bullet}{\rightarrow} HNO_{2ads} \overset{OH_{ads}^\bullet}{\rightarrow} NO_{2ads} + H_2O \quad (5)$$

$$HNO_{2ads} \rightleftarrows NO_{2\ ads}^- + H^+ \quad (6)$$

$$NO_{ads} \overset{OH_{ads}^\bullet}{\rightarrow} NO_{3\ ads}^- + H_{ads}^+ \quad (7)$$

Oxidation via O_2^-

$$NO_{ads} \overset{O_{2\ ads}^-}{\rightarrow} NO_3^- \quad (8)$$

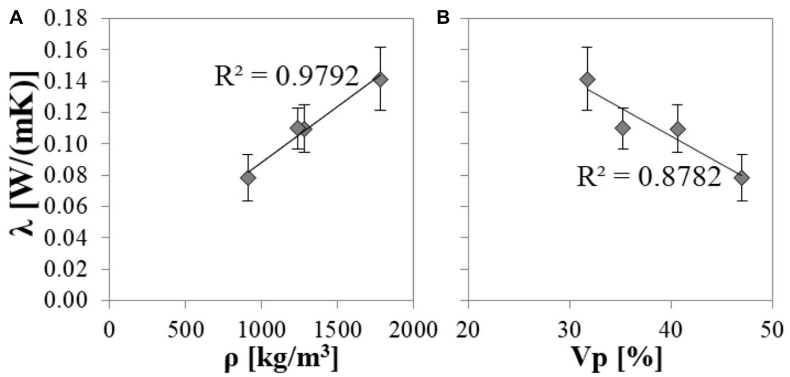

FIGURE 7 | Relation between **(A)** thermal conductivity and density and **(B)** thermal conductivity and total pore volume.

Disproportionation of NO_2

$$3NO_{2ads} + H_2O \rightarrow 2HNO_3 + NO \quad (9)$$

$$HNO_3 + H_2O \rightarrow H_3O^+_{aq} + NO^-_{3\,aq} \quad (10)$$

Thermal Conductivity

The enhancement of the indoor comfort of occupants is strictly related to the thermal insulation of the environment: if building materials with low thermal conductivity are used, the thermal comfort can be guaranteed with a lower energy consumption by active systems. According to the standard UNI EN 998-1, the threshold limits for λ to classify a mortar as a T1 or T2 thermal mortar are 0.100 W/mK and 0.200 W/mK, respectively.

In the current study, almost all mortars can be classified as T2 mortar since their λ is lower than 0.200 W/mK. In particular, the reference mortar has the highest value (λ = 0.142 W/mK), followed by activated carbon-based mortar and zeolite-based mortar with λ values of 0.110 and 0.110 W/mK, respectively. The lowest value of λ is detected in silica gel-based mortars (0.079 W/mK), which can be classified as a T1 mortar.

The λ of a mortar is related to both its density and porosity. The lower the density, the lower the thermal conductivity, and the higher the porosity, the lower the thermal conductivity (Demirboga and Gül, 2003). As expected, the use of highly porous aggregates permits to obtain lightweight mortars (Giosuè et al., 2018). Thanks to the total replacement of calcareous sand with silica gel (A2) and activated carbon (A3), lightweight finishes, highly appreciated for non-structural materials, can be obtained (Demirboga, 2003; Branco and Godinho, 2013).

Results of porosity and density of specimens are already shown in Giosuè et al. (2020), but in this paper the correlation between these properties and thermal conductivity is proposed and reported in **Figure 7**. Similar to the findings already published in other studies, a very good linear correlation between thermal conductivity and density (Coppola et al., 2018; Giosuè et al., 2019a) is obtained, as shown in **Figure 7A**. Usually, mortars with a high percentage of voids have strong insulating properties and can be used as plastering joints, building blocks, and panels able to guarantee the thermal comfort. Again, a linear correlation (but in this case with a lower coefficient) can be found between thermal conductivity and the total pore volume, as reported in **Figure 7B**.

CONCLUSION

In the present work, hydraulic lime-based mortars manufactured with unconventional highly porous aggregates are studied to be used as multifunctional indoor finishes. Calcareous sand (S) is replaced entirely by volume with three different lightweight aggregates, namely, zeolite, silica gel, and activated carbon. Mortars are prepared with and without the addition of TiO_2. The compressive strength values of these mortars are related to their microstructure observed by SEM. Then, the capillary water absorption, the photocatalytic oxidation of NO_x, and the thermal conductivity are also investigated.

From the current research, it is possible to stand that:

- The dispersion of TiO_2 nanoparticles in the different analyzed matrixes is good, as shown by SEM analysis;
- Even though the mortars manufactured with lightweight aggregates have a lower density, the mechanical behavior of zeolite and activated carbon mortars is comparable or even higher than that of sand mortars, thanks to an optimum ITZ between the binder paste and the aggregate. In the case of silica gel-based mortars, the worst mechanical strength is due to the bad adhesion observed between this aggregate and the paste;
- Zeolite, silica gel, and activated carbon-based mortar adsorb a total amount of water 60%, 80%, and 40% higher than that of the reference mortar, respectively, because of their higher total porosity;
- The mortar prepared with silica gel exhibits the highest photocatalytic activity and the lowest selectivity toward NO_2 because of the higher availability of adsorbed water, which reflects into an enhanced production of OH radicals due to an enhanced reactivity with Ti-OH via disproportion caused by a more available adsorbed water in the photocatalyst vicinity.
- An optimal linear correlation is confirmed between thermal conductivity and density, whereas a good linear correlation is found between porosity and density.

Further studies will be carried out in order to analyze the photocatalytic behavior of TiO_2 active under visible light.

Permission to Reuse and Copyright

Figures, tables, and images will be published under a Creative Commons CC-BY license, and permission must be obtained for use of copyrighted material from other sources (including republished/adapted/modified/partial figures and images from the internet). It is the responsibility of the authors to acquire the licenses, to follow any citation instructions requested by third-party rights holders, and to cover any supplementary charges.

DATA AVAILABILITY STATEMENT

The raw data supporting the conclusions of this article will be made available by the authors, without undue reservation.

AUTHOR CONTRIBUTIONS

CG: original research plan, methodology and investigation, material characterization, specimen preparation, original manuscript draft, and preliminary data curation. MP: collaboration in data curation of photocatalytic activities and manuscript editing. AM: collaboration in data curation of thermal conductivity, and manuscript review and editing. FT: coordination and supervision of the project, analysis of data, and manuscript draft and editing. MR: supervision of tests to evaluate the depolluting properties of mortars, interpretation of relative data, and manuscript editing. All authors contributed to the article and approved the submitted version.

REFERENCES

Ballari, M. M., Yu, Q. L., and Brouwers, H. J. H. (2011). Experimental study of the NO and NO2 degradation by photocatalytically active concrete. *Catal. Today* 161, 175–180. doi: 10.1016/j.cattod.2010.09.028

Banerjee, S., Dionysiou, D. D., and Pillai, S. C. (2015). Self-cleaning applications of TiO2 by photo-induced hydrophilicity and photocatalysis. *Appl. Catal. B Environ.* 17, 396–428. doi: 10.1016/j.apcatb.2015.03.058

Barcelo, L., Kline, J., Walenta, G., and Gartner, E. (2013). Cement and carbon emissions. *Mater. Struct.* 47, 1055–1065. doi: 10.1617/s11527-013-0114-5

Benfratello, S., Capitano, C., Peri, G., Rizzo, G., Scaccianoce, G., and Sorrentino, G. (2013). Thermal and structural properties of a hemp-lime biocomposite. *Constr. Build Mater.* 48, 745–754. doi: 10.1016/j.conbuildmat.2013.07.096

Branco, F. G., and Godinho, L. (2013). On the use of lightweight mortars for the minimization of impact sound transmission. *Constr. Build Mater.* 45, 184–191. doi: 10.1016/j.conbuildmat.2013.04.001

Caputo, D., Liguori, B., and Colella, C. (2008). Some advances in understanding the pozzolanic activity of zeolites: the effect of zeolite structure. *Cem. Concr. Compos.* 30, 455–462. doi: 10.1016/j.cemconcomp.2007.08.004

Chen, J., and Poon, C. S. (2009). Photocatalytic activity of titanium dioxide modified concrete materials – Influence of utilizing recycled glass cullets as aggregates. *J. Environ. Manage.* 90, 3436–3442. doi: 10.1016/j.jenvman.2009.05.029

Coppola, B., Courard, L., Michel, F., Incarnato, L., Scarfato, P., and Di, L. (2018). Hygro-thermal and durability properties of a lightweight mortar made with foamed plastic waste aggregates. *Constr. Build. Mater.* 170, 200–206. doi: 10.1016/j.conbuildmat.2018.03.083

Dalton, J. S., Janes, P. A., Jones, N. G., Nicholson, J. A., Hallam, K. R., and Allen, G. C. (2002). Photocatalytic oxidation of NOx gases using TiO2: a surface spectroscopic approach. *Environ. Pollut.* 120, 415–422. doi: 10.1016/s0269-7491(02)00107-0

Daoud, W. A. (2013). *Self-Cleaning Materials and Surfaces A Nanotechnology Approach*. Chichester: John Wiley & Sons.

Demirboga, R. (2003). Influence of mineral admixtures on thermal conductivity and compressive strength of mortar. *Energy Build.* 35, 189–192. doi: 10.1016/s0378-7788(02)00052-x

Demirboga, R., and Gül, R. (2003). Thermal conductivity and compressive strength of expanded perlite aggregate concrete with mineral admixtures. *Energy Build* 35, 1155–1159. doi: 10.1016/j.enbuild.2003.09.002

Folli, A., Pade, C., Hansen, T. B., De Marco, T., and Macphee, D. E. (2012). TiO2 photocatalysis in cementitious systems: insights into self-cleaning and depollution chemistry. *Cem. Concr. Res.* 42, 539–548. doi: 10.1016/j.cemconres.2011.12.001

Frey, S. E., Destaillats, H., Cohn, S., Ahrentzen, S., and Fraser, M. P. (2015). The effects of an energy efficiency retrofit on indoor air quality. *Indoor Air.* 25, 210–219. doi: 10.1111/ina.12134

Giosuè, C., Belli, A., Mobili, A., Citterio, B., Biavasco, F., Ruello, M. L., et al. (2017a). Improving the impact of commercial paint on indoor air quality by using highly porous fillers. *Buildings* 7:110. doi: 10.3390/buildings7040110

Giosuè, C., Mobili, A., Citterio, B., Biavasco, F., Ruello, M. L., and Tittarelli, F. (2020). Innovative hydraulic lime-based finishes with unconventional aggregates and TiO2 for the improvement of indoor air quality. *Manuf. Rev.* 7, 1–9.

Giosuè, C., Mobili, A., Di, C., and Tittarelli, F. (2019a). Performance of lightweight cement-based and alkali-activated mortars exposed to high-temperature. *Constr. Build Mater.* 220, 565–576. doi: 10.1016/j.conbuildmat.2019.05.193

Giosuè, C., Mobili, A., Yu, Q. L., Brouwers, H. J. H., Ruello, M. L., and Tittarelli, F. (2019b). Properties of multifunctional lightweight mortars containing zeolite and natural fibers. *J. Sustain. Cem. Mater.* 8, 214–217.

Giosuè, C., Pierpaoli, M., Mobili, A., Ruello, M. L., and Tittarelli, F. (2017b). Influence of binders and lightweight aggregates on the properties of cementitious mortars: from traditional requirements to indoor air quality improvement. *Materials* 10:978. doi: 10.3390/ma10080978

Giosuè, C., Yu, Q. L., Ruello, M. L., Tittarelli, F., and Brouwers, H. J. H. (2018). Effect of pore structure on the performance of photocatalytic lightweight lime-based finishing mortar. *Constr. Build Mater.* 171, 232–242. doi: 10.1016/j.conbuildmat.2018.03.106

Han, B., Wang, Y., Dong, S., and Zhang, L. (2016). Smart concretes and structures: a review. *J. Intell. Mater Syst. Struct.* 26, 1303–1345. doi: 10.1177/1045389x15586452

Horgnies, M., Dubois-Brugger, I., and Gartner, E. M. (2012). NOx de-pollution by hardened concrete and the influence of activated charcoal additions. *Cem. Concr. Res.* 42, 1348–1355. doi: 10.1016/j.cemconres.2012.06.007

Kaja, A. M., Brouwers, H. J. H., and Yu, Q. L. (2019). NOx degradation by photocatalytic mortars: the underlying role of the CH and C-S-H carbonation. *Cem Concr Res.* 125:105805. doi: 10.1016/j.cemconres.2019.105805

Karatasios, I., Katsiotis, M. S., Likodimos, V., Kontos, A. I., Papavassiliou, G., Falaras, P., et al. (2010). Photo-induced carbonation of lime-TiO2 mortars. *Appl. Catal. B Environ.* 95, 78–86. doi: 10.1016/j.apcatb.2009.12.011

Lucas, S. S., Ferreira, V. M., and Aguiar, J. L. B. (2013). Incorporation of titanium dioxide nanoparticles in mortars — Influence of microstructure in the hardened state properties and photocatalytic activity. *Cem. Concr. Res.* 43, 112–120. doi: 10.1016/j.cemconres.2012.09.007

MacPhee, D. E., and Folli, A. (2016). Photocatalytic concretes - The interface between photocatalysis and cement chemistry. *Cem Concr Res.* 85, 48–54. doi: 10.1016/j.cemconres.2016.03.007

Masel, R. I. (1996). *Principles of Adsorption and Reaction on Solid*. New York, NY: John Wiley & Sons, 818.

Matsumoto, H., Shimizu, M., and Sato, H. (2009). The contaminant removal efficiency of an air cleaner using the adsorption/desorption effect. *Build Environ.* 44, 1371–1377. doi: 10.1016/j.buildenv.2008.09.006

Mrad, R., and Chehab, G. (2019). Mechanical and microstructure properties of biochar-based mortar: an internal curing agent for PCC. *Sustainability* 11:2491. doi: 10.3390/su11092491

Pierpaoli, M., Fava, G., and Ruello, M. L. (2019a). Electroadsorptive removal of gaseous pollutants. *Appl. Sci.* 9:1162. doi: 10.3390/app9061162

Pierpaoli, M., Favoni, O., Fava, G., and Ruello, M. L. (2018). A novel method for the combined photocatalytic activity determination and bandgap estimation. *Methods Protoc.* 1, 1–12.

Pierpaoli, M., Giosuè, C., Ruello, M. L., and Fava, G. (2017). Appraisal of a hybrid air cleaning process. *Environ. Sci. Pollut. Res.* 24,12638–12645. doi: 10.1007/s11356-016-7880-x

Pierpaoli, M., and Ruello, M. L. (2018). Indoor air quality: a bibliometric study. *Sustainability* 10:3830. doi: 10.3390/su10113830

Pierpaoli, M., Zheng, X., Bondarenko, V., Fava, G., and Ruello, M. L. (2019b). Paving the path to a sustainable and efficient SiO 2 / TiO 2 photocatalytic composite. *Environments* 6:87. doi: 10.3390/environments6080087

Senff, L., Ascensão, G., Ferreira, V. M., Seabra, M. P., and Labrincha, J. A. (2018). Development of multifunctional plaster using nano-TiO 2 and distinct particle size cellulose fibers. *Energy Build.* 158, 721–735. doi: 10.1016/j.enbuild.2017.10.060

Senff, L., Tobaldi, D. M., Lucas, S., Hotza, D., Ferreira, V. M., and Labrincha, J. A. (2013). Formulation of mortars with nano-SiO2 and nano-TiO2 for degradation of pollutants in buildings. *Compos Part B.* 44, 40–47. doi: 10.1016/j.compositesb.2012.07.022

Sugrañez, R., Álvarez, J. I., Cruz-yusta, M., Mármol, I., Morales, J., Vila, J., et al. (2013). Enhanced photocatalytic degradation of NOx gases by regulating the microstructure of mortar cement modified with titanium dioxide. *Build. Environ.* 69, 55–63. doi: 10.1016/j.buildenv.2013.07.014

Tittarelli, F., Giosuè, C., Mobili, A., and Ruello, M. L. (2015). Influence of binders and aggregates on VOCs adsorption and moisture buffering activity of mortars for indoor applications. *Cem. Concr. Compos.* 57, 75–83. doi: 10.1016/j.cemconcomp.2014.11.013

Tittarelli, F., Mobili, A., Giosuè, C., Belli, A., and Bellezze, T. (2018). Corrosion behaviour of bare and galvanized steel in geopolymer and Ordinary Portland Cement based mortars with the same strength class exposed to chlorides. *Corros Sci.* 134, 64–77. doi: 10.1016/j.corsci.2018.02.014

Trník, A., Fo, J., Pavlíková, M., Pokorn, J., and Cern, R. (2016). Modified lime-cement plasters with enhanced thermal and hygric storage capacity for moderation of interior climate. *Energy Build.* 126, 113–127. doi: 10.1016/j.enbuild.2016.05.004

Uzal, B., Turanli, L., Yücel, H., Göncüoglu, M. C., and Çulfaz, A. (2010). Pozzolanic activity of clinoptilolite: a comparative study with silica fume, fly ash and a

non-zeolitic natural pozzolan. *Cem. Concr. Res.* 40, 398–404. doi: 10.1016/j.cemconres.2009.10.016

Wang, S., Yan, C., and Xiao, F. (2012). Quantitative energy performance assessment methods for existing buildings. *Energy Build.* 55, 873–888. doi: 10.1016/j.enbuild.2012.08.037

Washburn, E. W. (1921). Note on a method of determining the distribution of pore sizes in a porous material. *Proc. Natl. Acad. Sci. U. S. A.* 7, 115–116. doi: 10.1073/pnas.7.4.115

Wolkoff, P. (2013). Indoor air pollutants in office environments: assessment of comfort, health, and performance. *Int. J. Hyg. Environ. Health.* 216, 371–394. doi: 10.1016/j.ijheh.2012.08.001

Yang, R. (1987). *Gas Separation by Adsorption Processes*. Oxford: Butterworth Publisher.

Yu, Q. L., Spiesz, P., and Brouwers, H. J. H. (2015). Ultra-lightweight concrete: conceptual design and performance evaluation. *Cem. Concr. Compos.* 61, 18–28. doi: 10.1016/j.cemconcomp.2015.04.012

Zhang, R., Cheng, X., Hou, P., and Ye, Z. (2015). Influences of nano-TiO2 on the properties of cement-based materials: hydration and drying shrinkage. *Constr. Build Mater.* 81, 35–41. doi: 10.1016/j.conbuildmat.2015.02.003

Conflict of Interest: The authors declare that the research was conducted in the absence of any commercial or financial relationships that could be construed as a potential conflict of interest.

Colloidal Materials and Interfaces

Lourdes Basabe-Desmonts

Prof. Lourdes Basabe-Desmonts has been a Research Professor since 2012, the Director of the Microfluidics & BIOMICs Cluster UPV/EHU at the University of the Basque Country since 2019, and a Young Member of Jakiunde, the Academy of Science and Arts of the Basque Country, since 2016. Lourdes studied chemistry at the Universidad Autónoma de Madrid and completed a Ph.D. at the MESA+ Institute for Nanotechnology in the University of Twente, the Netherlands. In 2006, she joined the Biomedical Diagnostics Institute in Dublin, Ireland, and she moved to Spain in 2012. Her research interest is focused on the development lab-on-a-chip analytical microsystems.

Fernando Benito-Lopez

Prof. Fernando Benito-Lopez studied chemistry at the Universidad Autonoma de Madrid and completed his Master's studies in the Department of Inorganic Chemistry in 2002. He obtained his Ph.D. at the University of Twente, the Netherlands, in 2007. He carried out his postdoctoral research in the group of Prof. Dermot Diamond at Dublin City University, Dublin, where, in 2010, he became Team Leader in polymer microfluidics. In 2012, he moved to CIC microGUNE—a Research Centre working in Microtechnology in Spain. From 2015, he has been a Ramón y Cajal Fellow and leader of the Microfluidics Cluster UPV/EHU at the University of the Basque Country, Spain. In 2019, he became an Associate Research Professor and leader of the Microfluidics and Biomics Cluster UPV/EHU Group.

Monica Francesca Pucci

Dr. Monica Francesca Pucci, Ph.D. in mechanical engineering, is an assistant professor at IMT MINES Alès. She has background in mechanical engineering and has dedicated a significant part of her research to wetting and wetting dynamics. Those works have made her a renowned researcher in the field of impregnation of fibrous media driven by capillary forces for composite manufacturing. Her research activities are focused on the characterization of material microstructure and interface properties by means of Atomic Force Microscopy. In 2020, she was awarded the Daniel Valentin prize by the French association for composite materials (AMAC).

frontiers in Materials

REVIEW
published: 20 November 2020
doi: 10.3389/fmats.2020.582030

Advances in Microtechnology for Improved Cytotoxicity Assessment

Maite Garcia-Hernando[1,2], *Fernando Benito-Lopez*[2]* *and Lourdes Basabe-Desmonts*[1,3]*

[1]*BIOMICs Microfluidics Group, Microfluidics Cluster UPV/EHU, University of the Basque Country UPV/EHU, Vitoria-Gasteiz, Spain,* [2]*Analytical Microsystems & Materials for Lab-on-a-Chip (AMMa-LOAC) Group, Microfluidics Cluster UPV/EHU, Analytical Chemistry Department, University of the Basque Country UPV/EHU, Leioa, Spain,* [3]*IKERBASQUE, Basque Foundation of Science, Bilbao, Spain*

In vitro cytotoxicity testing is essential in the pharmaceutical and environmental industry to study the effects of potential harmful compounds for human health. Classical assays present several disadvantages: they are commonly based on live-death labelling, are highly time consuming and/or require skilled personnel to be performed. The current trend is to reduce the number of required cells and the time during the analysis, while increasing the screening capability and the accuracy and sensitivity of the assays, aiming single cell resolution. Microfabrication and surface engineering are enabling novel approaches for cytotoxicity assessment, offering high sensitivity and the possibility of automation in order to minimize user intervention. This review aims to overview the different microtechnology approaches available in this field, focusing on the novel developments for high-throughput, dynamic and real time screening of cytotoxic compounds.

Keywords: microtechnology, lab-on-a-chip, cytotoxicity, surface engineering, microfluidics, Sensors, Biosensors, single cell

OPEN ACCESS

Edited by:
Patricia Krawczak, IMT Lille Douai, France

Reviewed by:
M. Gabriella Santonicola, Sapienza University of Rome, Italy
Huaiyu Wang, Chinese Academy of Sciences (CAS), China

***Correspondence:**
Lourdes Basabe-Desmonts
lourdes.basabe@ehu.eus
Fernando Benito-Lopez
fernando.benito@ehu.eus

Specialty section:
This article was submitted to Colloidal Materials and Interfaces, a section of the journal Frontiers in Materials

Received: *14 July 2020*
Accepted: *26 October 2020*
Published: *20 November 2020*

Citation:
Garcia-Hernando M, Benito-Lopez F, Basabe-Desmonts L (2020) Advances in Microtechnology for Improved Cytotoxicity Assessment. Front. Mater. 7:582030. doi: 10.3389/fmats.2020.582030

INTRODUCTION

In the last decades, remarkable advancements have been made in the field of microtechnology to improve analytical processes in biology, through miniaturization, for biosensing DNA (Bulyk et al., 1999; Zhang et al., 2010) and protein arrays (He et al., 2008; Ramachandran et al., 2008; Lopez-Alonso et al., 2013; Gonzalez-Pujana et al., 2019), on-chip electrophoresis (Fritzsche et al., 2010; Ou, et al., 2019), microimmunoassays (Riahi et al., 2016; Hu et al., 2017), microfluidic cell sorting (Shields et al., 2015; Vaidyanathan et al., 2018) and for cellular membrane modelling (Hirano-Iwata et al., 2010; Strulson and Maurer, 2011; Galvez et al., 2020), among others (Beebe, et al., 2002; Sackmann, et al., 2014). In fact, microtechnology enables the precise control of the topography and the surface chemistry, leading to engineered platforms for the study of cellular processes or biosensing and, at the same time, bringing advantages such as time saving, reduced costs and working space, automation of the processes, increased sensitivity and reduced volumes of the required reagents (Wurm et al., 2010; Azuaje-Hualde et al., 2017).

Cytotoxicity assays are crucial in basic research, material science, environmental analysis, pharmaceutical industry and also, in the development of anticancer therapies, where the understanding of the resistance of cancer cells to new therapies is of major importance. Fluorescent and colorimetric assays are the most widely used methods for cytotoxicity assessment (Stoddart, 2011). There are many fluorescent dyes in the market for the measurement of cell viability, whose working principle varies from dye exclusion assays (penetrating the cellular membrane of death cells, staining them), DNA condensation-based assays (which emit fluorescence when they bind nucleic acid molecules) and assays monitoring

a metabolic function (Ramirez et al., 2010; Stoddart, 2011). Fluorescent dyes are popular because they are sensitive and provide an easy readout by fluorescence or optical microscopy. Besides, flow cytometry is a well stablished technique for the assessment of cellular toxicity, which combined with some of the previously mentioned alive/dead staining, enables the performance of highly sensitive analysis of cellular viability with single cell resolution (Adan et al., 2017). Since fluorescence gives a semi-quantitative analogic signal and many fluorescent dyes are compatible with single cell analysis, they are often combined with flow cytometry to obtain absolute and real quantification of alive and dead cells within a population. Besides the noteworthy resolution and efficacy of flow cytometry, it requires trained personnel to perform it, as well as staining procedures and manual handling, which take time and increase the possibility of human errors. Furthermore, flow cytometry does not permit real-time monitoring (Gelles and Chipuk, 2016). Therefore, miniaturized systems that reduce manual handling procedures and facilitate fast and easy measurements of cellular viability are promising alternatives to fight the current drawbacks in cytotoxicity assessment, such as the manual intervention, use of labels and the lack of real time information or monitoring.

Nowadays, the large variety of microfabrication techniques leads to the manufacturing of microsystems of many different natures. All the miniaturized platforms for cytotoxicity testing can be usually combined with traditional cellular viability assays, resulting on assays with the same working principle of the traditional staining protocols for the signalling of alive and dead cells, but with improved performance. This is due to the improvements that microtechnology brings in terms of real-time monitoring capability, increased sensitivity, reduced times for the cytotoxicity assessment, decreased volumes of the required reagents and thus, produces a lower cost per analysis. Also, thanks to their small dimensions, it opens the door to multiplexed and multisampling analysis, increasing the yield in the performed protocols (Wang et al., 2007; Sugiura et al., 2008). Furthermore, alternative working principles for the assessment of cytotoxicity are now available due to the sensitivity gained by working at the microscale.

This review aims to summarize the state of the art of the microtechnology used in cytotoxicity tests, and to discuss the novelty that microfabrication techniques and materials bring to this field of research. In this work, we aspire to build a bridge between microfabrication, material science and cytotoxicity, highlighting the advantages brought to the field. In order to do that, the most common microfabrication techniques, microsystems and materials for cytotoxicity will be first explained. Then, the different types of micro analytical platforms existing for cytotoxicity assessment will be comprehensively reviewed (**Figure 1**).

MICROFABRICATION TECHNIQUES USED IN CYTOTOXICITY

Microfabrication techniques were originally developed for the microelectronics industry, specifically for the manufacturing of microelectromechanical systems (MEMs), making possible the integration of sensors to develop fully functional microdevices. Due to the high precision and resolution of the features achieved by these techniques, they soon became useful for the control of tissues and cells at the microscale, becoming attractive for biosensing, leading to the development of BioMEMs (Eribol et al., 2016). The biocompatibility of the materials used in bio-applications is crucial, *e.g.,* the microdevices, in order to avoid any cellular toxic response. Therefore, micromachining for BioMEMs requires adaptations of the fabrication processes and/or the materials used for device fabrication in order to guarantee cellular viability (Fischer et al., 2011).

At the microscale, any small perturbation on the flow or a high density of adhered cells can cause huge stress to them, resulting on exhaustion of nutrients or even migration, which can be misunderstood as a cellular response to the toxic (Wang et al., 2007). These phenomena can be avoided through microfabrication; on one hand, inducing physical cell adhesion control by patterning small microwells on polymeric materials (Vajrala et al., 2019; Zhang et al., 2019) or on C- (Lee et al., 2006) and on U-shaped (Wang et al., 2007) microsieves in the culturing chambers. On the other hand, cell adhesion can be chemically controlled with micropatterns of proteins (Liu et al., 2013; Hamon et al., 2016) or hydrophilic-hydrophobic sites (Nath et al., 2004; Zhang et al., 2007), modulating cell adhesion by enhancing cell affinity for specific areas, keeping them comfortably located. These methods control cell adhesion density and homogeneity of the pattern. Moreover, in the case of C-shaped microsieves, the flow within the chamber is also slowed down, reducing shear stress in cells (Wang et al., 2007), making the device more appropriate for cell culture.

Sotf-Lithography

Photolithography, a lithographic process that uses optical methods for the printing of features, is the most used technique to make integrated circuits, traditionally on rigid surfaces (Levinson, 2005). In particular, the development of soft-lithography, which derives from photolithography and serves to replicate structures from rigid molds -like the ones made by photolithography- on elastomeric or flexible materials, made a huge breakthrough in the manufacturing of BioMEMs. It opened a range of possibilities to use microstructured elastomeric materials, more suitable to keep cellular comfort and to be closer to the mimicking of cellular environment, (Xia and Whitesides, 1998).

The most common material in soft-lithography is polydimethylsiloxane (PDMS), which allows for the fabrication of devices by fast molding techniques, featuring resolutions down to nanometer scale. Also, due to the deformability of this elastomeric material, it facilitates leak-proof fluidic connections as well as integration of valves and other fluidic components. It can be covalently bonded to another PDMS piece or glass surface by a simple plasma oxidation step, resulting on the generation of leaking free, well-sealed devices. Moreover, PDMS is biocompatible, transparent (Bélanger and Marois, 2001) and non fluorescent (Piruska et al., 2005) therefore, suitable for cell applications.

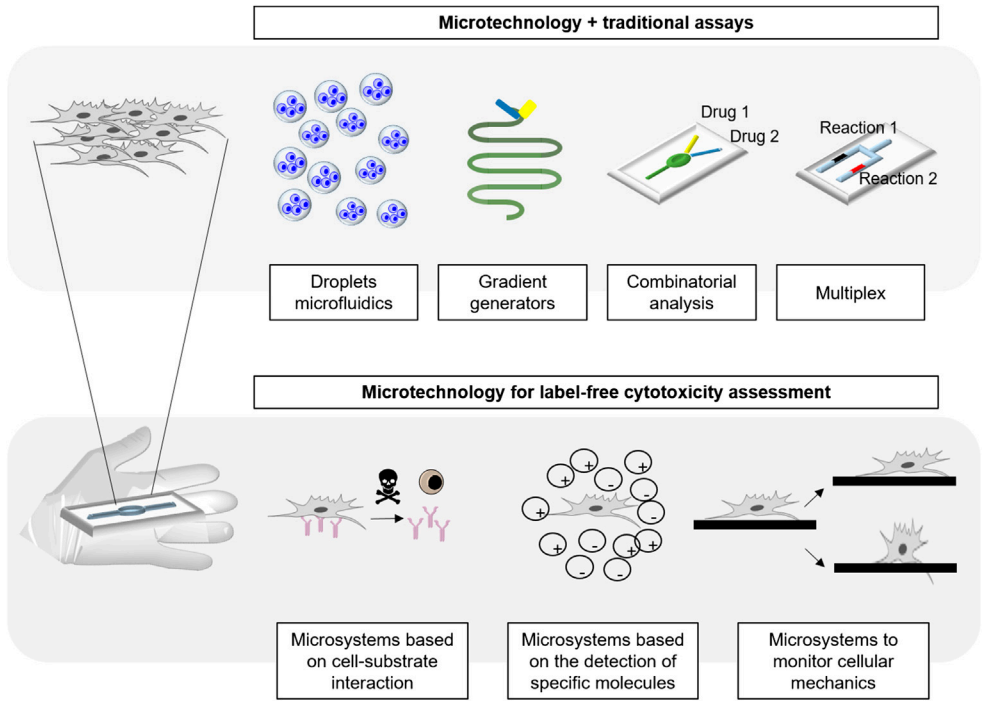

FIGURE 1 | Classification of microtechnology based cytotoxicity techniques in literature.

Due to the high resolution of photolithography, the location of cells can be accurately controlled, and the pattern can be precisely transferred to PDMS. The cell positioning capability of PDMS molds has been demonstrated and used for cytotoxicity assessment using U-shaped microsieves, with minimum separation of 8 μm, patterned within culturing chambers (**Figures 2A**). These features induced low flow regions and a good distribution of cells along the chamber to obtain cellular monolayers with adequate microenvironment (Wang et al., 2007). In the mentioned work, the percentage of cellular death in response to five toxins (digitonin, saponin, $CoCl_2$, $NiCl_2$ and acrolein) was obtained when using Live/Death staining thanks to an adequate cell positioning. Similar idea was used by Mo *et al.,* who combined a micropillar array for uniform cell positioning with a precisely controlled, low flow-rate gradient to reduce the shear stress to human induced pluripotent stem cells (HiPSC) derived neurospheres, and obtain reliable responses against riluzole drug (Mo et al., 2020).

Soft-lithography is the most popular technique to fabricate gradient generators in microdevices. They generate a gradient in the composition of a solution, like, in this case, the toxic compound to be tested. Thanks to this PDMS gradient generating devices, several works have demonstrated that High-Throughput (HTP) toxicity analysis of specific compounds can be simultaneously carried out, at different concentrations, on chip, for cytotoxicity assessment (Hosokawa et al., 2011; McCormick et al., 2017; Li et al., 2018)

PDMS has been the most commonly used material for the fabrication of prototypes during the last decade but it presents some drawbacks such as absorption of small molecules and high gas permeability, thus there is a demand to fabricate microfluidic devices made of other polymers. As an example, Nguyen *et al.* reported a hybrid polymeric microfluidic device for cytotoxicity testing, made of poly(methyl methacrylate) with integrated polyethylene terephthalate (Nguyen et al., 2019). The hybrid device was fabricated by milling machine, and was successfully used for cytotoxicity assessment, showing more reliable results than conventional PDMS devices, due to the poly(methyl methacrylate) natural impermeability to small molecules.

Electrode Patterning

Electrode patterning has been one of the most used microfabrication techniques for the monitoring of cytotoxicity responses from the emergence of microtechnology in this field, and it is usually based on additive (metal deposition, insulation), semi-additive (photolithography) and subtractive (etching) processes to fabricate the whole functional electric circuit. The integration or deposition of electrodes on PDMS is challenging (Lim et al., 2006; Guo et al., 2012), so rigid materials such as glass or silicon are commonly used as substrates for electrode patterning, which enables the adequate adhesion of the electrodes on the substrate.

For instance, there are a family of cytotoxicity tests based on gold microelectrode arrays named as xCELLigence Real Time Cell Analyzer (RTCA), which perform continuous monitoring of cytotoxicity by electrical impedance (Ke et al., 2011). This technology relies on the covering of 70–80% of the surface of a well in a 96 well plate with an array of microelectrodes, being this whole area able to measure impedance under a constant

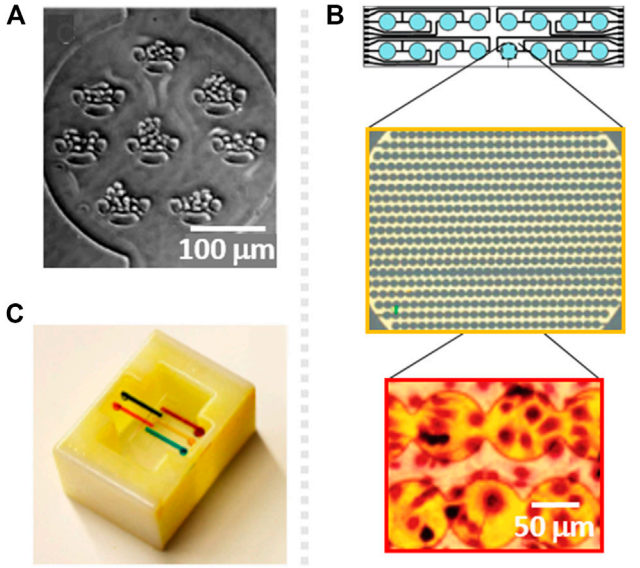

FIGURE 2 | (A) Schematic of a cytotoxicity testing microsystem with U-shaped sieves for cell adhesion control, fabricated by soft photolithography. Reproduced from (Wang et al., 2007) with permission from The Royal Society of Chemistry. **(B)** Design of an electrochemical impedance surface microelectrode array and zoomed picture of the electrodes (yellow) and the cells cultured on top (red), fabricated by electrode patterning. Reprinted with permission from (Xing et al., 2005). **(C)** 3D printed, reversibly pluggable microfluidic for toxicity screening. Reprinted with permission from (Ding et al., 2015) Copyright © 2015 American Chemical Society.

voltage (**Figures 2B**). A variation on the impedance measurements can be attributed to the natural proliferation of cells, to cell detachment and/or to changes in the cytoskeleton-surface interaction due to the response of the cells to external stimuli such as the presence of a toxic compound.

In another work, gold Interdigitated Electrode Structures were fabricated on glass by lithographic techniques, sealed with a PDMS upper part to create a cell culture chamber (Ceriotti et al., 2007). According to the results, the system based on Interdigitated Electrode Structures detected and quantified impedance changes caused by the modulation of cellular adhesion in response to sodium arsenite, like in previously mentioned microelectrode arrays.

Furthermore, due to the resolution of photolithography, surface gold microsensors can be patterned even for the positioning of single cells. For instance Asphahani et al. (2012), used single cell surface electrodes with a diameter of 30 µm to dynamically measure the adhesion of single cells to the electrode substrate in the presence of a hydrogen peroxide (H_2O_2), sodium arsenate ($NaAsO_2$) or disodium hydrogen arsenate (Na_2HAsO_4). This system requires the precise position of single cells on the electrodes, but the avoidance of cell adhesion out of the electrodes is crucial too, to help decreasing the noise that can affect the measurement of impedance of single cells. To address this challenge, the authors functionalized the gold electrodes with RGD peptide to induce ligand-mediated natural cell adhesion. As just mentioned, electrode patterning can be complemented with surface modification techniques to modify the gold electrode surface and provide specific capabilities to the sensors. For instance, Nery and co-workers integrated a microarray of gold sensors on glass through common Printed Circuit Board technology. Then, seven different selective membranes were deposited on the sensors, resulting on four ion selective electrodes for K^+, Na^+, H^+, and Ca^{2+}, and three partially selective membrane electrodes (amine-selective, cation-selective and anion- selective), as well as two unmodified gold electrodes for the sensing of red-ox reactions (Nery et al., 2014). The manufacturing and modification of these electrodes lead to the continuous monitoring of cellular death through potentiometric flow-through sensing, correlating changes in the media of the analytes with cellular cytotoxicity.

On the other hand, electrobiofabrication implies the use of electrode signals to specifically pattern electroactive polymers on the electrodes, which in comparison to traditional electrode functionalization strategies simplifies the fabrication of the devices, as demonstrated by Shang et al. (2018). Authors functionalized gold microelectrodes with a bio-based redox capacitor film, which enabled the *in situ* polymerization of chitosan, a redox-active polymer that amplifies the signal from an electron transfer. The system transduced molecular signals into electronic outputs, which allowed the quantification of cell viability of Caco-2 cells in presence of Triton X-100. Results were compared to the ones obtained by a live/dead fluorescent viability kit. The platform showed high sensitivity to measure molecular interactions by chronocoulometry and correlate them with cellular death. Carbon nanotubes are also promising materials for electrode manufacturing due to their high electrical conductivity, chemical stability and good mechanical properties. Aligned carbon nanotubes have been combined with surface electrode patterning techniques to fabricate sensitive floating surface electrodes. These novel electrodes became efficient tools for the electrophysiological monitoring of cells for cytotoxicity assessment (Ta et al., 2014; Ba et al., 2017). According to the authors, the system is in addition reusable, which avoids device-to-device repeatability issues.

3D Printing

3D printing technology was initially developed for rapid prototyping of devices, but soon, due to the improvements provided in precision, resolution, and repeatability, it became a promising technique for industrial production. Usually, traditional bio-MEM fabrication techniques, *e.g.*, electrode patterning and soft lithography (Ho et al., 2015; Capel et al., 2018), require different types of bulky equipment and imply multiple steps and long fabrication times, in order to get the final product. Techniques like soft-lithography are fine for laboratory scale, but when industrial scale is required, simpler fabrication processes such as 3D printing, are on demand. Furthermore, 3D printing offers a range of biocompatible materials that can be printed with good resolution and in a single step, facilitating large-scale production of devices (Hart et al., 2016; Capel et al., 2018). 3D printing technology is still in its infancy when it comes to cytotoxicity assessing microdevices, but some recently

developed platforms suggest that it is a promising tool that may facilitate the manufacturing of cytotoxicity testing microdevices in the near future.

For instance, ultra-high resolution Multijet 3D printing uses UV light to polymerize the photoresist, which is deposited in tiny droplets by the printer to obtain highly complex and well-defined features. Sweet *et al.* used this technique to fabricate a microdevice, which integrated a network of interconnected 3D enclosed microchannels of 750 μm diameter, for the screening of bacterial cells' resistance (Sweet et al., 2017). Due to the design and translucency of the material, UV spectroscopy based absorbance measurements were used to *in situ* determine bacterial cytotoxic response to antibiotics.

Some cytotoxicity platforms reported single 3D printed components such as a modular microfluidic cartridge to regulate reagent volumes during the analysis (Ding et al., 2015) (**Figures 2C**) or a 3D printed gradient generator to create multi-drug combinations (Chen et al., 2018). In both cases, 3D printing was combined with traditional fluorescent and absorbance cytotoxicity assays. Although just a piece of the system was fabricated by 3D printing, the versatility of the platform was increased, facilitating any modification in the design.

PLATFORMS FOR CYTOTOXICITY ASSESSMENT BY MICROTECHNOLOGY

Microfluidics Combined With Traditional Assays

Cytotoxicity assays are typically based on the colorimetric or fluorescent staining of cells for the determination of cell viability or for metabolite detection in order to identify specific events (Ramirez et al., 2010; Stoddart, 2011). These assays are known to be sensitive and effective but, when combined with microtechnology, multiplexing and reduced manual handling and analysis times, among others, become a reality.

Droplet Microfluidics

Droplet microfluidics provides HTP analysis in cell biology by the generation of microscale droplets through immiscible multiphase flows, resulting on picoliter-scale and monodisperse emulsion droplets. This technique leads to the miniaturization of the bioassays, avoiding capillary effects and evaporation, working as individual bio-microreactors. Moreover, the possibility of using this droplets with non-adherent cells is a reality (Mashaghi et al., 2016). The number of cells encapsulated in each droplet can be slightly modulated following Poisson distribution (Mazutis et al., 2013). Moreover, microdroplets are usually compatible with standard screening microscopies and readouts, enabling the combination with traditional colorimetric and fluorometric cytotoxicity assays. As an example of this combination, Du et al. (2013) measured two live/death fluorescent dyes within each droplet containing cells, when exposed to different concentrations of paclitaxel and 5-fluorouracil anticancer drugs. This was also demonstrated in a previous work, in which the process to make the droplets was consciously optimized to get a good Poisson distribution, allocating 25 cells per droplet with high probability (Yu et al., 2010). Cell viability was investigated in the presence of doxorubicin anticancer drug.

Boedicker *et al.* generated monodispersed aqueous droplets on chip, and tested the viability of bacterial cells in response to different antibiotics (Boedicker et al., 2008). Every droplet had an integrated fluorescent viability indicator. The encapsulation was carried out in a "stochastic confinement" in order to have higher cell density per droplet, looking for a reduced detection time. In this work, cellular viability was determined in response to different concentrations of seven antibiotics. Sarkar and coworkers have extensive expertize in generating droplets on chip, including droplet formation for cell viability assessment used for the development of anticancer therapies (Sarkar et al., 2015; Sarkar et al., 2020). They first reported a microfluidic droplet generator for the encapsulation of single cancer cells and for the monitoring of the individual cells in presence of doxorubicin anticancer drug with live/dead staining. They evaluated the sensitivity of cells to the drug, by monitoring their viability (Sarkar et al., 2015). More recently, they used the same droplet technology to compare immunotherapy with Natural Killer cells with different cell types, and determined that the treatment based on the combination of herceptin and $CD16^{+}$ Natural Killer cells was more effective for SKOV3 cells than for HER2 (Sarkar et al., 2020).

The HTP formation of droplets has also been reported on a PDMS nanowell array fabricated by soft lithography. Coupled with another PDMS holding layer for the containment of the oil, the droplets were formed when a cell suspension was added through a capillary, creating the droplets with the cells encapsulated (Du et al., 2013). Ethidium bromide and calcein staining were then used to assess cell viability in the presence of 5-fluorouracil, in the droplets, by fluorescence microscopy.

On the other hand, surface engineering techniques are tools that enable de patterning of droplets on surface, at specific locations. Geyer *et al.* used UV-initiated photografting of a hydrophilic polymer whose hydrophilicity was inverted by UV through a photomask to create superhydrophilic-superhydrophobic micropatterns on nanoporous polymer films, with drastic difference in wettability to spontaneously create an array of separated aqueous microdroplets (Geyer et al., 2011). These patterns were then used by Popova *et al.* for cytotoxicity testing (Popova et al., 2015). Each of these droplets worked as individual microreactors for cell culturing, and by a sandwiching technique, the doxorubicin anticancer drug was specifically added to the droplets. Using fluorescent viability staining, the alive and dead cells, in the presence of the doxorubicin, were observed in a HTP and pipetting-free way (**Figures 3A**).

Gradient Based Microsystems

The formation of gradients in microfluidic devices has applications in the field of cytotoxicity testing since gradient generators enable the screening of different concentrations of a

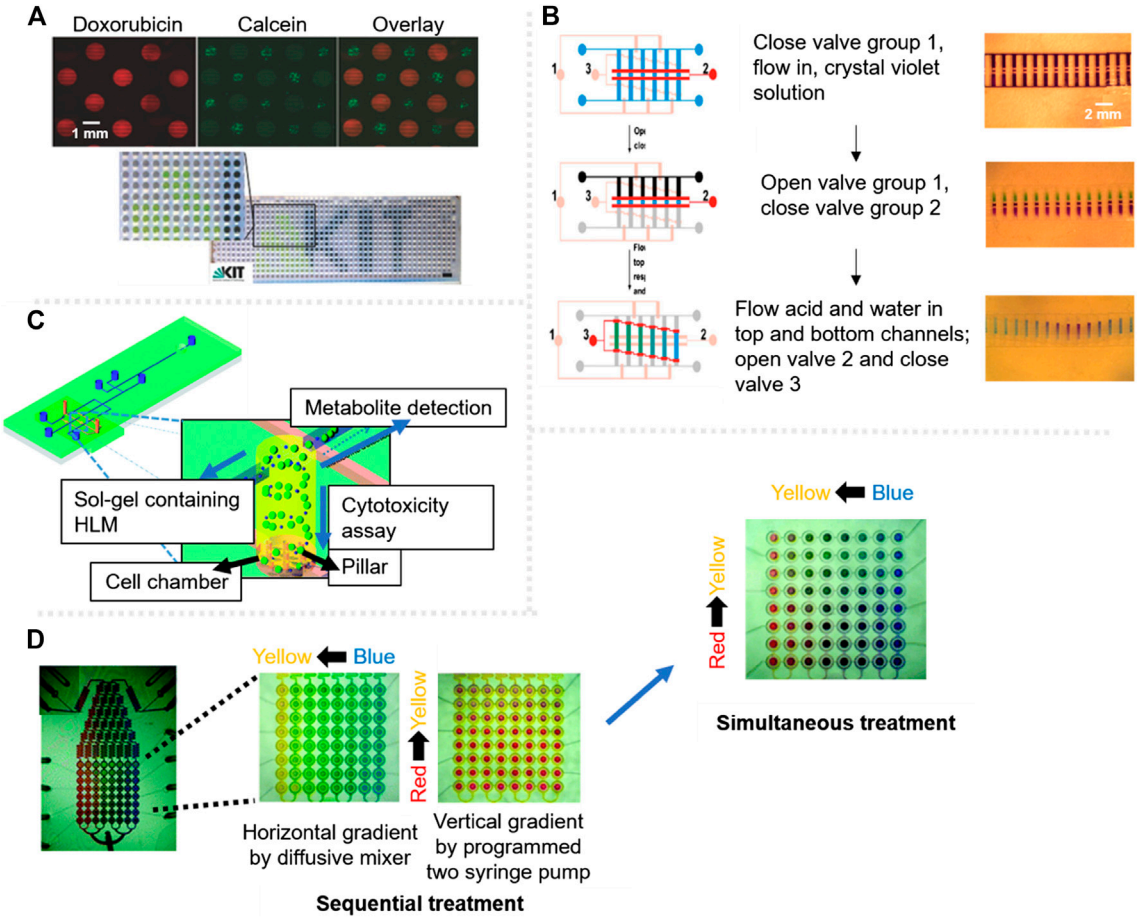

FIGURE 3 | Cytotoxicity assessment microsystems with fluorescent label based detection. **(A)** Droplet based platform showing cells after 18 h in the presence of doxorubicin drug (red) and calcein stained cells for viability test (green); the scale bar in bottom picture is 3 mm. Adapted from (Popova et al., 2015). **(B)** Schematic of the stepwise gradient operation on chip, signalling valves with colors, red for the open ones and pink for the closed ones. The fluidic channels are fabricated in a ladder shape, each colored channel represents a different solution. Adapted from (Dai et al., 2010). **(C)** Scheme of a three-layered microdevice for the simultaneous characterisation of drug metabolites and cytotoxicity assessment. Adapted from (Ma et al., 2009) with permission from The Royal Society of Chemistry. **(D)** Integrated microfluidic device for combinational cytotoxicity assessment by sequential treatment or simultaneous treatment. Adapted from (Kim et al., 2012) with permission from The Royal Society of Chemistry.

certain toxic compound at a single step (Dai et al., 2010) (**Figures 3B**). Ruan et al. (2009) reported a hybrid glass-PDMS microfluidic device with a multi-serpentine based gradient generator made by soft lithography. Cellular viability in response to different concentrations of AsO_3 and buthionine sulfoximine chemicals was investigated using acridine orange/ethidium bromide viability assay by fluorescence. When a multi-serpentine based gradient generator is combined with a high-density single-cell array, it results in a microsystem for simultaneous cytotoxicity assessment of numerous concentrations of KCN in this case, with single-cell resolution (Hosokawa et al., 2011). However, the flow-rates commonly used in serpentine gradient generators can be harmful for some cell types such as neurons, so in a recent work, an asymmetric microfluidic device was reported for the formation of drug gradients, which requires lower flows to generate gradients, as mentioned in the section above (Mo et al., 2020).

A multiple dilution method was used in a PDMS microfluidic device to improve the creation of a concentration gradient solution, avoiding distinct parts of the cell experiencing different drug concentrations during the test (Dai et al., 2010). Using Fluorescence Resonance Energy Transfer authors were able to measure cellular death by means of CFP-YFP fluorophores, performing simultaneous cytotoxicity testing of multiple concentrations of etoposide anticancer drug in parallel. The use of hydrogels is another approach to generate gradients in microfluidics. Hydrogels are able to form gradients due to their porous internal structure, which can be interestingly modulated to fulfill specific concentration requirements (Ahadian et al., 2014; Cosson and Lutolf, 2014). As an example, an agarose gel on a microelectrode patterned device allowed the cytotoxic electrochemical monitoring under different concentrations of cisplatin and paclitaxel chemotherapy drugs, which were created through the hydrogel (Tran et al., 2013).

3D printing technology opens the possibility of designing all kind of microfluidic circuitry, including the fabrication of advanced gradients (Sochol et al., 2016). Microsystems capable of generating a gradient of three (nitrofurantoin, tetracycline and trimethoprim) (Sweet et al., 2017) or four (doxorubicin, celecoxib, 5-fluorouracil, and cyclophosphamide) (Chen et al., 2018) toxic compounds allow the monitoring of the cytotoxic response against many combinations of compounds in a single run.

Multiplexing

Miniaturization offers multiplex analysis on chip and it has been reported for many bio-applications, increasing the number of analysis with single cell resolution and so cytotoxicity studies (Kersten et al., 2005; Zhao et al., 2015). Wang and co-workers developed a microfluidic device for multiplex cytotoxicity testing (Wang et al., 2007). The device had several independent cell culturing chambers with U-shaped micro sieves designed to allocate about ten cells per sieve, guaranteeing cell-cell contact, adequate stimulation and comfort. That design enabled the HTP cytotoxicity testing of three cell lines and two concentrations of five toxins (digitonin, saponin, $CoCl_2$, $NiCl_2$ and acrolein) simultaneously.

Droplet microfluidics provides with a different approach to perform simultaneous cell viability assessment, testing different concentrations of doxorubicin and daunorubicin drugs. Based on a hydrophilic/hydrophobic patterning, droplet arrays, working as independent bioreactors, can be individually loaded with the toxic compound of interest or concentrations of the toxic, which leads to HTP and even multiplexing analysis of cytotoxicity using fluorescent live/death assays (Popova et al., 2015; Popova et al., 2017).

Another multiplexing approach relies on the analysis of two different events in parallel, instead of measuring the cellular response to different toxic compounds or concentrations. A microsystem was reported for the characterisation of drug metabolites and for the analysis of their cytotoxic response (Ma et al., 2009). The microsystem had a PDMS bottom layer with three microwells with sol-gel containing encapsulated cells. On top, a quartz layer with a microfluidic network allowed the flow of metabolites (**Figures 3C**). Due to the multilayer design of the device, the sol-gel acted as a filter to separate drug metabolite detection and cytotoxicity testing, successfully fulfilling both analysis with no cross contamination.

Multifunctional materials deserve special attention for multiplexing. In particular, hydrogels are widely applied as nanocarriers for drug delivery purposes due to their stimuli-responsive behavior. Nanocarriers are easily captured by cells, so, their combination with a sensing functional material could lead to the simultaneous drug release and monitoring of the process (Wu et al., 2010). For instance, Wang and co-workers developed hybrid microspheres made of pH responsive acrylic acid and temperature responsive poly-*N*-isopropilacrylamide, combined with SiO_2 photonic crystal microspheres, which are dielectric structures with an energy band that favors the movement of photons (Wang et al., 2018). Temperature and pH responsiveness of these hybrid and inverse opal hydrogel photonic crystal microspheres, enabled the controllable drug loading/release, whereas due to the photonic crystal component, the cellular viability was dynamically monitored at every point during drug release. Actually, when cells were alive, the microenvironment surrounding them was acidic due to their secretion, green, but when the drug was released and apoptosis was triggered, the pH of the microenvironment was neutralized, changing the color of the spheres to red, which could be observed even by naked eye.

Combinatorial Drug Screening

As mentioned above, cytotoxicity tests are crucial in environmental and pharmacological industries, especially when the toxicity of a compound has to be assessed. Toxicology studies are not simple since the effect of a toxic compound can vary pretty much when in contact with other chemical compounds, sometimes causing an additive effect. However, the combination of more than one chemical or drug causes sometimes synergy (greater effect) or antagonism (lower effect), which may be considered in order to address their toxicity, or their effectiveness in case of therapeutic studies (Foucquier and Guedj, 2015). Therefore, combinatorial-drug-testing can decrease toxicity, reduce the development of drug resistance and even increase the effectiveness of therapies.

Combinatorial tests can be either based on the sequential or simultaneous addition of more than one toxic compound. Considering the first situation, a microsystem based on droplet arrays was reported for sequential toxic combinatorial testing in where the cells in the droplets were sequentially stimulated by two drugs, doxorubicin and daunorubicin (Popova et al., 2017). The microsystem enabled the visualization of cellular viability by fluorescence, combining live/death fluorescent staining. The results showed variations in cell viability when using a single drug or the sequential addition of the two drugs.

Sweet *et al.* developed a platform for simultaneous cytotoxicity analysis of more than one toxic, generating a gradient with the combination of three different compounds (Sweet et al., 2017). In addition, the platform enabled the identification of the relationship between the toxics. Binary combinations between the toxics correlated well with the results previously published in literature (Bollenbach, 2015). On the other hand, the combination of three toxics identified antagonistic (less effective), synergistic (more effective) and suppressive (least effective) regions during drug screening.

Curved microchannels for fluid mixing driven by Dean flow dynamics -the study of flow in curved channels- were integrated in cytotoxicity screening microsystems to generate gradients and mixing of three compounds, two anticancer drugs (doxorubicin and cisplatin) and the cell media, leading to highly efficient fluid mixing and single-step screening of twelve different combinations (Shen et al., 2020). The twelve combinations were simultaneously investigated for cell viability using a fluorescent live/death assay.

Moreover, a microdevice capable of performing combinatorial screening of two drugs (doxorubicin and mitoxantrone) was reported by Kim et al. (2012), either simultaneously or sequentially. The platform contains 64 individual cell-culture

chambers, avoiding the metabolites to be transferred from one chamber to another (**Figures 3D**). The design of the device allowed the sequential combination of compounds using an accurate gradual valve-opening process, first with one of the toxics, and 24 h after, with the second one. The system showed high screening capability and, with the integrated valve-system, the common drawbacks of existing microdevices on metabolite transference to different cell culturing chambers was sorted out.

Moreover, synergistic effect can be also obtained combining photo-therapy with chemotherapy, so Flont *et al.* evaluated the effect of doxorubicin drug and nano-encapsulated *meso*-tetraphenylporphyrin photosensitiser on chip (Flont et al., 2020). Using a microfluidic device mimicking the fluid flows, photodynamic therapy with a photosensitiser and chemotherapy with doxorubicin were sequentially applied to non-malignant and cancer ovarian cells simultaneously, demonstrating the synergistic effect of both therapies, leading to a higher rate of death cancer cells according to MTT viability assay.

Label-Free Microsystems

Common cytotoxicity assays based on enzymatic activity or membrane penetration processes require cell labelling for viability studies. Their widely spread use relies on their elevated effectiveness, reliability and sensitivity, which do not compromise cellular functions such as growth and proliferation. Many efforts are being done to enhance their signal and durability during continuous observation under excitation, *e.g.*, conjugating them with quantum dots to avoid photobleaching over long time exposure to light (Zhao et al., 2009; Zhao et al., 2013). Dye labelling, is time consuming, implies multiple steps and often only detects end points, not allowing continuous monitoring, without showing kinetic or dynamic data. Generally, dyes do not drastically affect essential cellular functions such as growth and proliferation, but there are evidences claiming that cell tracing dyes considerably increase living cell stiffness, deeply increasing the Young's modulus of the cellular membrane and therefore enhance cellular rigidity and adhesion (Lulevich et al., 2009). Hence, there is a current demand on label-free cytotoxicity monitoring systems for the dynamic analysis of cells upon toxic exposure. Microtechnology brings new approaches to assess cytotoxicity, correlating alternative parameters with cellular death, such as cell adhesion or mechanics, which can be hardly measured without microtechnology.

Microsystems Based on Cell-Substrate Interaction

Cell-substrate interactions are key in most of the vital cellular processes, such as proliferation, differentiation and migration. Regardless of the cell death mechanism, when cells are in the presence of a toxic, undergo morphological changes or disturbances in their membrane, compromising its integrity, which may affect cell adhesion to the substrate (Cho et al., 2008). In the past decades, electrochemical impedance spectroscopy has settled as one of the most popular techniques for the dynamic analysis of cell adhesion to a substrate (Ke et al., 2011), named as electric cell-substrate impedance sensing. The microsystems following this working principle, are based on an array of surface gold electrodes manufactured by lithographic techniques. Cells act as insulating particles, when they adhere to the electrodes, the area in contact with the electrolyte coming from the cell culturing medium is reduced, resulting on an increase on the electric resistance and a decrease in the capacitance values (Hug, 2003). Higher resistance and/or lower capacitance imply a higher density of cells covering the electrode. Based on this technology xCELLigence RTCA emerged for the dynamic monitoring of cellular adhesion on a microarray of gold sensors. In general, when cells are in the presence of a toxic compound, cell death is preceded by a number of morphological and biochemical pathways that at the end lead to death. Impedance based cell adhesion biosensors, enable continuous monitoring of cellular responses against a toxic, such as morphological changes, migration and death (Ke et al., 2011). Using this technology, several studies reported applications on cytotoxicity assessment and showed real-time and dynamic monitoring of cellular responses to different toxic compounds (Xing et al., 2005; Urcan et al., 2010; Irelan et al., 2011; Menotti et al., 2017). Even though electrochemical impedance continuously decreases in the presence of the drug, this value cannot be directly correlated with cellular detachment until signal reaches 0. Electrochemical impedance has been proven sensitive for the monitoring of cellular response to toxics. Nevertheless, until signal does not reach 0 (when there is no cell on the electrodes), due to that sensitivity, the platform may be probably detecting not only cellular detachment, but also changes in morphology caused by the presence of the toxic, and not just detachment or death (Atienza et al., 2005; Xing et al., 2005; Abassi et al., 2009; Susloparova et al., 2015). In order to confirm the correlation between change in impedance signal and quantification of cellular death, xCELLigence RTCA can be coupled with common fluorescent assays for a deeper understanding of the cytotoxic response.

Surface chemistry modification at the micro-scale enables the precise positioning of cells, which following specific adhesion patterns, can lead to new functionalities. In a recent work, microcontact-printing, which creates defined patterns of molecules on surfaces by stamping a micropatterned PDMS, was used to create single cell adhesion dots arrays to address cell viability by optical microscopy (Garcia-Hernando et al., 2020). Cell adhesion spots made by fibronectin protein were designed to allocate single cells, attributing an individual value to each cell. Due to this individuality, the technique enables the counting of adhered cells at every point, so, cellular detachment in the presence of K_2CrO_4 and DMSO chemical compounds was dynamically monitored for several hours, giving real time and quantitative information of cellular death (**Figures 4A**).

Piezoelectric quartz systems have also been proven useful for live cell biosensing, due to their excellent mass sensing capabilities, leading to the development of mass nanosensors called quartz crystal microbalances (Wang et al., 2011). A quartz crystal microbalances based benchtop platform, comprised of a microplate with a 2 × 2 mm resonant waveguide grating sensor per well was used to monitor cytotoxicity, based on the changes in the dynamic mass redistribution (Farkas et al., 2018). The employed microplate design allowed 384 simultaneous and high-resolution measurements every 3 s, per well. Using the

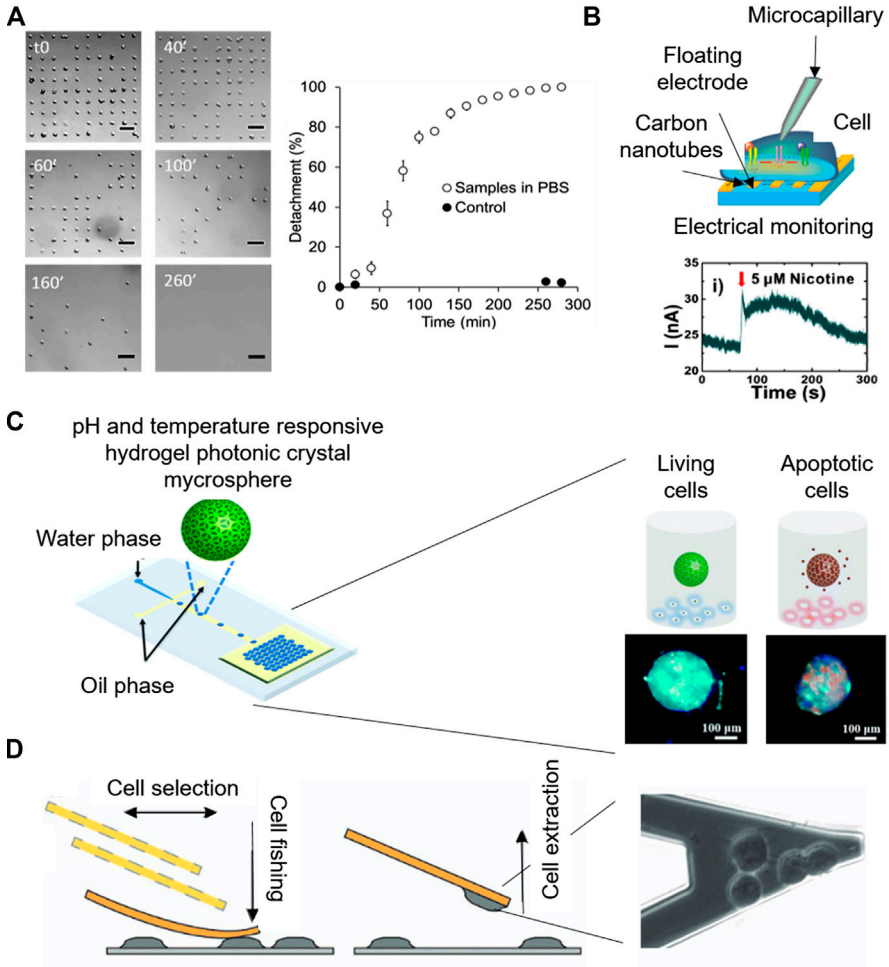

FIGURE 4 | Microsystems for label-free cytotoxicity testing. **(A)** Quantification of cell single-cell adhesion for cytotoxicity assessment by optical microscopy. Adapted from (Garcia-Hernando et al., 2020) Copyright © 2020 American Chemical Society. **(B)** Working principle of the electrophysiological monitoring of cells for cytotoxicity assessment on aligned carbon nanotubes based gold floating electrodes Adapted with permission from (Ta et al., 2014) Copyright © 2014 American Chemical Society. **(C)** Schematic of the Photonic crystal microspheres based cytotoxicity platform, showing the control variation under external stimuli for the detection of cell viability. Adapted from (Wang et al., 2018) with permission from The Royal Society of Chemistry. **(D)** Cytotoxicity monitoring system based on nanomotion sensing of cellular processes. Adapted with permission from (Ruggeri et al., 2017) Copyright © 2017, Springer Nature.

mentioned mass nanosensor, cell death was detected as a negative shift in the dynamic mass redistribution in the presence of toxic compounds. The cytotoxic response is represented in terms of cell size reduction, weakening the adhesion strength and promoting cellular detachment. Therefore, the platform was able to perform non-invasive and continuous measurements for real-time and dynamic monitoring of cytotoxic effects of Roundup Classic, polyethoxylated tallow amine and glyphosate herbicides.

Microsystems Based on the Detection of Specific Molecules

A potentiometric flow-through sensor was reported for label-free cytotoxicity testing. Instead of monitoring cell-substrate adhesion, gold sensors were specifically manufactured and modified to detect multiple parameters that were indirectly correlated with cellular death, such as ions and amines. The potentiometric selective sensing of cations, anions and amines, coupled with partial least squares multivariate statistical analysis, led to non-invasive measurements of cellular viability (Nery et al., 2014).

Quantitative electrophysiological determination of cytotoxic responses in the presence of chemical compounds such as histamine, anti-histamine drugs (chlorphenamine and cetirizine) and acetylcholine receptors (nicotine, daidzein, genistin, and tamoxifen) was carried out using carbon nanotube transistors (Ba et al., 2017; Ta et al., 2014) (**Figures 4B**). For instance, histamine is a neurotransmitter whose presence in the cellular microenvironment leads to the activation of numerous intracellular electrophysiological pathways, including the opening of the Ca^{2+} channel gates and the flow of these ions through the plasma membrane. Therefore, due to the quantitative electrochemical signals detected by the floating microsensors, the evaluation of the effect of anti-histamine drugs on non-excitable HeLa cells was carried out (Ba et al., 2017).

Beyond electrochemistry, pH sensing for the label-free and optical assessment of cytotoxicity has also been reported. Photonic crystals are periodic optical nanostructures with very interesting optical properties, due to their atomic energy gap that enables the movements of photons. Photonic crystal microspheres were reported for the colorimetric assessment of cellular viability even by naked eye (Wang et al., 2018). The microspheres were green when cells were alive, because their secretions made their surrounding microenvironment acidic. However, when cells were in presence of the toxic compound and their death was induced, the photonic crystals turned to red because of the neutralization of the cellular microenvironment (**Figures 4C**).

Mechanics to Monitor Cytotoxicity

The study of cellular mechanics offers a new approach to cytotoxicity assessment, based on a better readout at the cellular level. Cell mechanics results from the overall cellular events, so its study permits to observe the state of the general well-being, but also going to individual cellular events that in conventional assays would be hidden within intrinsic variability.

Due to its precision, atomic force microscopy is a powerful tool for nanomotion sensing in single-cell cytotoxicity tests (Zimmer et al., 2014; Ruggeri et al., 2017). Ruggeri et al. (2017) monitored nanometer-scale movements of cells with the nanomotion sensor, while complementary optical microscopy served to monitor cell attachment, cellular healthiness and micrometer scale movements (**Figures 4D**). Adding a fluorescent live/dead dye, loss of membrane integrity prior cell death was also detected by nanomotion sensing. Moreover, the cytotoxic responses to amyloids were detected and measured real time.

Single-cell compression method by means of atomic force microscopy can also accurately measure single-cell mechanics in nanotoxicity assessment. Zimmer et al. (2014) used single-cell compression following a protocol previously developed by their group (Lulevich et al., 2006), relying on compressing the cell between a spherical probe and a glass substrate. The cytotoxicity test carried out with this method enabled accurate single-cell mechanic profiles (shrinking, swelling and estimation of Young's modulus) leading to highly sensitive monitoring of nanotoxicity.

SINGLE CELL RESOLUTION

There is a wide range of options for cytotoxicity assessment of cell populations, including microsystems, bringing new insights in cytotoxicity assessment, such as the HTP capability, multiplexing, gradient formations and label-free dynamic monitoring of cellular viability. However, cell populations are highly heterogeneous, and single cell toxicity analysis could make a difference, identifying cell subpopulations that present higher or lower resistance to a certain dose of a toxic compound. There are two main techniques for the isolation of cells as single cells. On one hand, individual cells can be confined in cavities (Hosokawa et al., 2011), and on the other hand, they can be chemically guided to settle at specific locations by protein patterning techniques (Gonzalez-Pujana et al., 2019), enabling high density of single-cell arrays. Single-cell toxicity testing can provide with quantitative analysis. Fluorescent and colorimetric signals give qualitative data or relatively quantitative values in terms of intensity. However, the identification of single cells as dead or alive provides real numbers and percentages of cellular death, which is actually the basis of the well-stablished flow cytometry technique.

Optical microscopy and label-free monitoring of cytotoxicity is also possible for single-cells. In the recent work from Garcia-Hernando *et al.*, previously mentioned, an array of individual cell adhesion fibronectin islets was used to create single cell arrays for the monitoring of cytotoxicity by optical microscopy (Garcia-Hernando et al., 2020). This system offers two approaches for the assessment of cell viability, depending on the mechanism of action of the toxic compound. The results suggest that when fibronectin-integrin bonding keeps cells attached to the surface, under the effect of some compounds such as K_2CrO_4 and DMSO cells detach when they die. In this case, the system allows the quantification of cell detachment correlated with cellular death. Contrarily, other chemical compounds such as Hg_2SO_4 inhibit cell detachment when they die, keeping them dead and individually located on a surface. Adding a colorimetric viability staining, the viability of individual cells can be quantified by optical microscopy.

Agarose platforms, with microcavities for single-cell positioning by gravity, have been reported to measure cellular viability in the presence of nimustine DNA-crosslinker (Li et al., 2016). This microsystem enabled fluorescence microscopy based cellular viability assessment, after staining the cells with a fluorescent live/death assay, giving real percentages of death cells within a population. Hosokawa et al. (2011) also developed a microfluidic device with an array of microcavities to obtain high density single-cell arrays. Those cells were incubated in the presence of KCN and stained with a fluorescent live/death dye, identifying each cell as alive or dead, and giving real quantitative information of cellular viability, with the added value of a gradient generator, leading to a HTP screening of individual cells. In this way, cells were cultured as a population but analyzed as individual cells (**Figures 5A**). In another work, authors reported a single-cell array cytometry on chip for the analysis of tumor cell apoptosis induced by staurosporine anticancer drug. The microdevice was comprised of 440 mechanical traps of 18 μm width for the hydrodynamic positioning and mechanical trapping of single-cells (Wlodkowic et al., 2009). A fluorescent live/death staining was continuously flowed through the microfluidic device, in a low dose, in order to achieve a continuous labelling without deeply compromising cellular viability, due to the presence of the dye. The system was able to analyze the viability of 250 cells every 1 min, giving real percentages of cellular viability due to the single cell counting. In this particular case, authors obtained dynamic and real-time results of toxic induced cellular death thanks to the continuous loading of a low concentration of fluorescent viability tracker.

The study of individual cells is important due to the heterogeneity within populations. Electrochemical impedance demonstrates that the dynamic cytotoxic response of

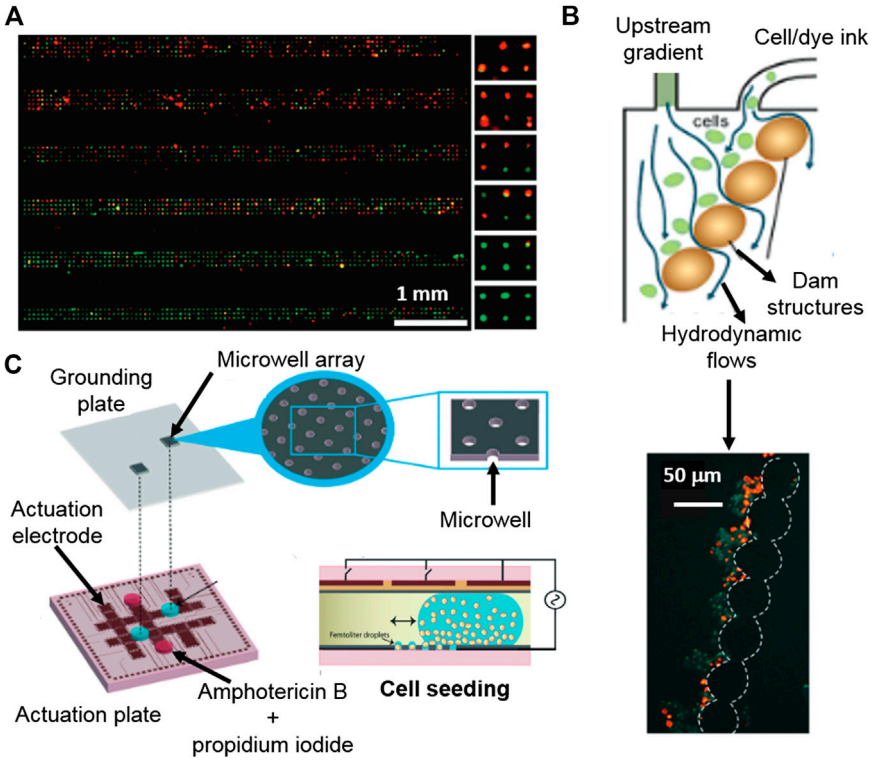

FIGURE 5 | Platforms for cytotoxicity assessment of single-cells and non-adherent cells. **(A)** Gradient generating microfluidic device based on high density single-cell arrays positioned in microcavities for HTP single-cell cytotoxicity testing. Reproduced with permission from (Hosokawa et al., 2011). Copyright © 2011 American Chemical Society. **(B)** Digital microfluidics device for single-cell toxicity testing based the entrapment of single non-adherent cells. Adapted from (Kumar et al., 2015) with permission from The Royal Society of Chemistry. **(C)** Microfluidic platform for the cytotoxicity assessment of single-cells isolated by hydrodynamic forces using integrated, dam cell-trapping structures. Adapted with permission from (Zhao et al., 2009) Copyright © 2009 American Chemical Society.

individual cells varies from one to others (Asphahani et al., 2012). In this work, the authors reported that not all the single cells gave the same impedance curve, meaning that the cytotoxic response was different from one cell to another, as a clear sign of heterogeneity within the population. Furthermore, the differences in the cytotoxic response were more evident at lower concentrations of the toxic compounds (H_2O_2, $NaAsO_2$ and Na_2HAsO_4), giving curves with higher variability. At higher concentrations of toxic compounds, cytotoxic impedance profiles were more similar between single cells, as a sign of high lethality.

Droplet microfluidics can be used for the encapsulation of isolated single-cells by, for instance, coupling droplet formation with an array of microcavities for the deposition of the encapsulated single-cells. An individual cell containing droplet array coupled with a viability fluorescent assay enabled the quantification of individual dead and alive cells, showing also variable cytotoxic responses to antifungal Amphotericin B, within the studied population (Kumar et al., 2015).

Cellular mechanics provide very specific information at the cellular level, offering an alternative readout of the molecular outputs of cellular events. Nanomotion is a promising technique to monitor the cellular well-being, which due to its sensitivity, can monitor cellular movements at the nano-scale in response to α-syn presynaptic protein and SiO_2 nanoparticles (Zimmer et al., 2014; Ruggeri et al., 2017).

NON-ADHERENT CELLS

Most of the current existing microsystems for cytotoxicity assessment are meant to be used for adherent cells, since working with them is less tedious and complex than manipulating non-adherent ones. Cytotoxicity assessment of non-adherent cells is mainly performed by flow cytometry, with accurate and reliable results, but again, involves handling of the sample and a temporary gap from the time the experiment is stopped until the time when analysis takes place (Jahan-Tigh et al., 2012). Advances in non-adherent cell viability systems are on demand, since cytotoxicity testing of, for instance, blood cells and circulating tumor cells are crucial in the biomedical industry.

There are not many options available for the entrapment and subsequent analysis of non-adherent cells, being hydrodynamic forces one of them. A microdevice with integrated dam structures for cell-trapping was used to trap cells by hydrodynamic forces, which were applied by an appendant microfluidic channel (Zhao et al., 2009). Once the non-adherent cells were positioned and

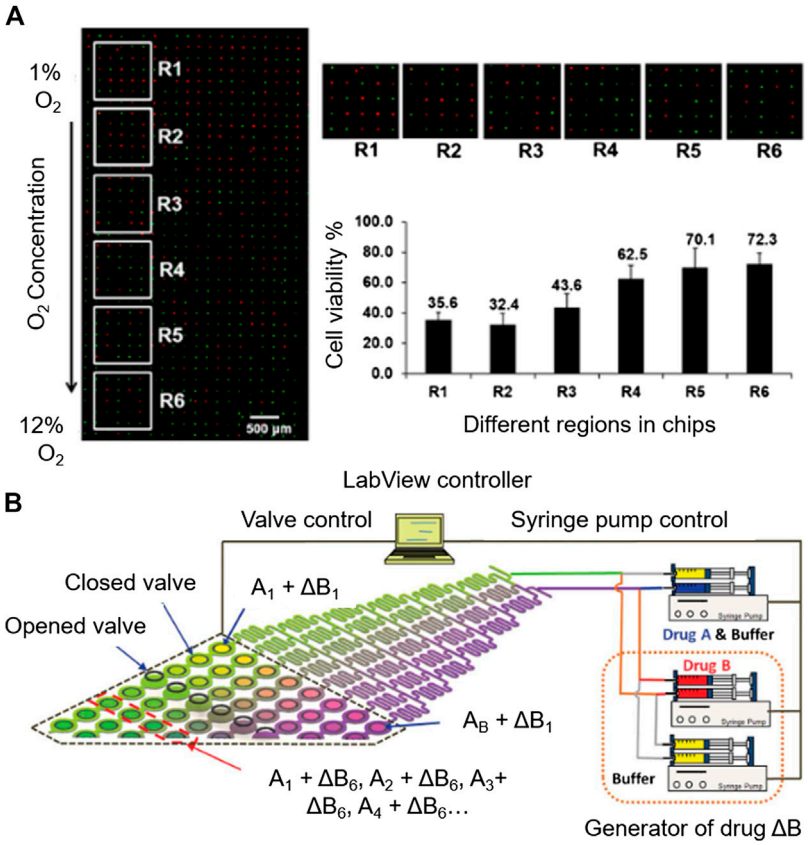

FIGURE 6 | Automation potential of microsystems for cytotoxicity assessment. **(A)** Automated imaging by fluorescence microscopy. Reproduced with permission from (Li et al., 2018). Copyright © 2018 American Chemical Society. **(B)** Automatable microfluidic system for combinatorial cytotoxicity screening. Reproduced from (Kim et al., 2012) with permission from The Royal Society of Chemistry.

localized, a live/death fluorescent tracker was used and their intensities were obtained and correlated with the cytotoxic response to the presence of cycloheximide, etoposide and camptothecin antileukemic drugs (**Figures 5B**).

Droplet microfluidics can be used as tools for the encapsulation and confinement of non-adherent cells. Popova and co-workers demonstrated that an array of droplets made on hydrophilic spots enables the encapsulation and cytotoxicity assessment of T-lymphocytes (Popova et al., 2017). Besides, digital microfluidics permits the confinement of non-adherent individual cells in droplets using an electrowetting-on-dielectric platform. The individually encapsulated cells were positioned as an array of single cells. Then, a stain with cell live/death trackers was used for viability individual cells studies by fluorescence microscopy (Kumar et al., 2015) (**Figures 5C**).

Floating gold electrode sensors, based on aligned semi-conducing single walled carbon nanotubes, were used for dynamic cytotoxicity monitoring of non-adherent small lung cancer cells in the presence of nicotine and inhibitors of nicotinic acetylcholine receptors, measuring cell's electrophysiological responses (Ta et al., 2014). When these cells are in a nicotine containing environment, the opening of the Ca^{2+} channels of the plasma membrane is triggered, causing Ca^{2+} to flow inside of the cell. This results in a depolarization of the cell, resulting on an increased negative current detected by the electrodes. The sensitivity of the technique enabled the cytotoxicity testing of single-cells.

AUTOMATION

Microfabrication enables the integration of several components within the same microsystem, leading to the development of fully integrated devices. They can perform automated processes avoiding handling operations, reducing sample loss and contamination risk, increasing throughput, improving the ease of use and repeatability for, at the end, reduce human errors. Moreover, thanks to automation, remote operation of the microsystems (fluid control and analysis) is possible in case it is required for a particular application (Melin and Quake, 2007).

Many efforts have been made in the automation of microsystems for cytotoxicity testing. Due to the wide use of fluorescent live/dead trackers, automated image processing has been reported in cytotoxicity platforms (Hosokawa et al., 2011; Popova et al., 2017; Li et al., 2018) (**Figures 6A**). This simplifies data collection, since the platforms can be programmed to take microscopy pictures periodically, for their subsequent analysis, without the need of human supervision.

Protocols based on electrochemical monitoring are also compatible with programming during data acquisition, in a dynamic way, far from end-point measurements. xCELLigence RTCA technology is a good example of that, since the manual sample handling is limited to loading the cells into the platform. From this point on, the system continuously measured impedance over time, collecting automatically dynamic data of cells during cytotoxic response (Gurkan et al., 2011; Ke et al., 2011).

Data interpretation can be automated, for instance, when combinatorial toxic screening is performed. The effect of the combined toxics and their concentrations can be automatically uploaded to a combinational library of chemical compounds, facilitating searching for toxic combinations, speeding up the discovery process of unexpectedly harmful toxics or in contrary, finding the most efficient drug combinations for therapy (Ding et al., 2015). On the other hand, Sarkar *et al.,* used algorithms to assess cytotoxicity mediated by Natural Killer cells. A droplet microfluidics generator was used to trap a target cancer cell with a natural killer cell (1:1 ratio), and the interaction between them was accurately studied by time-lapse images, focusing on interaction duration, frequency and cell viability. With the obtained information, algorithms were developed for automatically interpreting the dynamics of natural killer cells as anticancer therapy (Sarkar et al., 2020).

As an example of automated performance is the microfluidic system for sequential combinatorial therapy testing developed by Flont et al. (2020).Going to more complex automation systems, Kim *et al.,* developed a fully programmable microsystem for drug screening (Kim et al., 2012). The platform is comprised of an upstream concentration generation module coupled to an array of 64 individual chambers for cell culturing. The access to each of the cell culture chambers is individually modulated with a valve-array through a pneumatic channel designed to deliver the desired toxic combination to the chambers, controlled by Labview software (**Figures 6B**). The synchronized valve-system opens the door for a complete automation of the system. This platform simplifies the screening of toxic compound combinations in the investigation of novel effective therapies against cancer.

NANOTOXICOLOGY

Nanotoxicology is a subfield of toxicology that focuses on the toxic effects of nano-sized particles, often not caused by the material itself, but by the nano-scale related properties of these particles (Auffan et al., 2009; Catalán et al., 2016; Fadeel, 2019). For instance, the high surface-to-volume ratio of nanoparticles makes them highly reactive when compared to bulk materials (Recordati et al., 2015). Nanoparticles can penetrate cellular membranes, biological barriers and tissues, so they interact with biological systems at the molecular, cellular, organismal and ecosystem levels (Pietroiusti et al., 2018), The increasing interest of using nanoparticles in medicine, opens new possibilities for microtechnology, for instance to mimic whole organs (Organ-on-A-Chip technology), generating devices able to precisely study the effect of nanomaterials in a similar environment to *in vivo* (Ashammakhi et al., 2020).

Due to the capability of engineered nanomaterials to interact with the cellular membrane—by adsorption, penetration or endocytosis—the study of the interaction between nanomaterials and the cell membrane is important and challenging (Zhang et al., 2012; Churchman et al., 2013). Membrane-on-chip microplatforms emerge for high throughput membrane sensing, giving information of the events happening on a supported cellular membrane. The most used membrane biosensing microtechnology comprises electrochemical sensors fabricated with self-assembled monolayers supported on mercury electrodes that provide information of the interactions or damage on the membrane (Owen et al., 2020; Rashid et al., 2017). Recently, Owen *et al.* reported an automated, rapid and HTP sensing microfluidic platform for the screening of nanomaterial-biomembrane interactions (Owen et al., 2020). The integrated microfluidic device provided electrochemical information of the interactions of chlorpromazine and citrate coated gold nanomaterial with 1,2-dioleoyl-sn-*glycero*- 3- phosphocoline membranes, supposing an easy-to-use interface to assess cytotoxicity based on membrane damage (less than 6 min per assay).

Due to the high toxicity and barrier penetration capability of nanoparticles, the studies of their effects on three-dimensional environments, mimicking natural biosystems, enable more reliable approaches to evaluate the physiological effects of nanomaterials (Ashammakhi et al., 2020). For instance, Arends *et al.* reported a microfluidic device to study the diffusion of nanoparticles through the basal layer, which is key to control the movement of nanoparticles between blood vessels and the surrounding extravascular space, observing a charge dependant accumulation of the species, similar to the one observed *in vivo* (Arends et al., 2015).

CONCLUSION

Cytotoxicity assessment is vital in the pharmaceutical and environmental industry for the identification of potentially harmful compounds, as well as for the development of new therapies in medicine. Currently, the most popular techniques are based on labelling cells with fluorescent or colorimetric stains, targeting disrupted membranes of dead cells or specific metabolites. These are very sensitive and effective, but the application of microtechnology in cytotoxicity testing opens the door to more efficient methods that can also be complemented with traditional assays.

Within microtechnology, many techniques have been proven efficient for reliable and sensitive cytotoxicity assessment. It must be highlighted that working at the microscale, HTP approach is possible. Moreover, multiplexed and gradient cytotoxicity assessment systems, capable of collecting higher amounts of data for the correct interpretation of toxicity, become available for general use. Many microdevices for combinatorial toxic screening have been reported, which facilitate research on the

identification of potentially toxic compounds, enabling the development of more effective therapies in medicine.

Furthermore, the use of microtechnology for cytotoxicity testing permits the measurement of cellular events such as cell-substrate adhesion, electrophysiology and mechanics of cytotoxicity in a label free manner, avoiding the addition of external labels that even at a low level, could affect cellular functions. Additionally, label-free sensing allows dynamic and continuous monitoring of cells during testing, providing to the user with additional data, *e.g.*, continuous monitoring of cellular well-being, even before death, as well as kinetic responses against toxic compounds.

Besides, cytotoxicity assessment at single-cell level is possible using microtechnology. This enables the study of cytotoxic responses of cell subpopulations within heterogeneous populations, which helps investigating cellular resistance, as well as vulnerabilities of cells to chemical compounds. Single-cell resolution also enables real quantification of cellular viability, which would bring cytotoxicity assessment platforms close to the concept of flow cytometry on a surface. Moreover, the assessment could be automated using programmable microdevices, which facilitates their use, leading to more efficient analyses, reducing human handling and thus, errors.

Nanotoxicology is a recent field within cytotoxicity assessment which is growing fast, because of the emerging interest in nanoparticles for therapy. Reliable information on the effects of engineered nanoparticles on biosystems is crucial, and microtechnology is emerging as a powerful tool for screening nanoparticle—biological system interactions.

Despite the previous advances, microtechnology is still far for being implemented in daily cytotoxicity assessment. Although the presented micro-systems have been successfully implemented for cytotoxicity assessment, their fabrication is still laborious and long, and it sometimes require specific micromachining equipment, complicating the mass production of devices. The use of microplatforms for cytotoxicity testing is very useful for now when it comes to specific cytotoxic measurements or information that cannot be obtained with traditional assays, such as cytotoxicity dynamics, real-time monitoring, gradient formation and multiplexing; or information that can be obtained easily and faster than with traditional tools, such as single cell testing or combinatorial testing. However, microtechnology seems to have already a place in cytotoxicity assessment, and it is lately gaining importance and popularity, considering the increasing number of publications appearing every year with novel approaches. It can be expected that new trends in this field will focus on the improvement of the fabrication of the devices, simplifying processes for potential mass production and looking for suitable materials with properties that permit a good performance of the analyses. Therefore, evidence points out that the future of cytotoxicity assays will be highly conditioned by the developments made in microtechnology.

AUTHOR CONTRIBUTIONS

MGH: Conceptualization, Ideas, Investigation, Writing - Original Draft, Writing - Review and Editing. FBL and LBD: Conceptualization, Ideas, Resources, Management, Writing - Review and Editing, Supervision, Project administration, Funding acquisition.

ACKNOWLEDGMENTS

Authors would like to acknowledge the funding support from: University of the Basque Country (PIF16/204), the funding support from Gobierno de España, Ministerio de Economía y Competitividad, with Grant No. BIO2016-80417-P (AEI/FEDER, UE) and Gobierno Vasco under grand IT1271-19.

REFERENCES

Abassi, Y. A., Xi, B., Zhang, W., Ye, P., Kirstein, S. L., Gaylord, M. R., et al. (2009). Kinetic cell-based morphological screening: prediction of mechanism of compound action and off-target effects. *Chem. Biol.* 16, 712–723. doi:10.1016/j.chembiol.2009.05.011

Adan, A., Alizada, G., Kiraz, Y., Baran, Y., and Nalbant, A. (2017). Flow cytometry: basic principles and applications. *Crit. Rev. Biotechnol.* 37, 163–176. doi:10.3109/07388551.2015.1128876

Ahadian, S., Ramón-Azcón, J., Estili, M., Obregón, R., Shiku, H., and Matsue, T. (2014). Facile and rapid generation of 3D chemical gradients within hydrogels for high-throughput drug screening applications. *Biosens. Bioelectron.* 59, 166–173. doi:10.1016/j.bios.2014.03.031

Arends, F., Sellner, S., Seifert, P., Gerland, U., Rehberg, M., and Lieleg, O. (2015). A microfluidics approach to study the accumulation of molecules at basal lamina interfaces. *Lab Chip.* 15, 3326–3334. doi:10.1039/c5lc00561b

Ashammakhi, N., Darabi, M. A., Çelebi-Saltik, B., Tutar, R., Hartel, M. C., Lee, J., et al. (2020). Microphysiological systems: next generation systems for assessing toxicity and therapeutic effects of nanomaterials. *Small Methods.* 4, 1900589. doi:10.1002/smtd.201900589

Asphahani, F., Thein, M., Wang, K., Wood, D., Wong, S. S., Xu, J., et al. (2012). Real-time characterization of cytotoxicity using single-cell impedance monitoring. *Analyst.* 137, 3011–3019. doi:10.1039/c2an16079j

Atienza, J. M., Zhu, J., Wang, X., Xu, X., and Abassi, Y. (2005). Dynamic monitoring of cell adhesion and spreading on microelectronic sensor arrays. *J. Biomol. Screen.* 10 (8), 795–805. doi:10.1177/1087057105279635

Auffan, M., Rose, J., Bottero, J., Lowry, G. V., Jolivet, J., and Wiesner, M. R. (2009). Towards a definition of inorganic nanoparticles from an environmental, health and safety perspective. *Nat. Nanotechnol.* 4, 634–641. doi:10.1038/nnano.2009.242

Azuaje-Hualde, E., García-Hernando, M., Etxebarria-Elezgarai, J., De Pancorbo, M. M., Benito-Lopez, F., and Basabe-Desmonts, L. (2017). Microtechnologies for cell microenvironment control and monitoring. *Micromachines.* 8, 166. doi:10.3390/mi8060166

Ba, V. A. P., Cho, D., Kim, D., Yoo, H., Ta, V., and Hong, S. (2017). Quantitative electrophysiological monitoring of anti–histamine drug effects on live cells via reusable sensor platforms. *Biosens. Bioelectron.* 94, 707–713. doi:10.1016/j.bios.2017.03.063

Beebe, D. J., Mensing, G. A., and Walker, G. M. (2002). Physics and applications of microfluidics in biology. *Annu. Rev. Biomed. Engineer.,Engineer.* 4 (1), 261–286. doi:10.1146/annurev.bioeng.4.112601.125916

Bélanger, M., and Marois, Y. (2001). Hemocompatibility, biocompatibility, inflammatory and *in vivo* studies of primary reference materials low-density polyethylene and polydimethylsiloxane: a review. *J. Biomed. Mat. Res.* 58, 467–477. doi:10.1002/jbm.1043

Boedicker, J. Q., Li, L., Kline, T. R., and Ismagilov, R. F. (2008). Detecting bacteria and determining their susceptibility to antibiotics by stochastic confinement in

nanoliter droplets using plug-based microfluidics. *Lab Chip.* 8, 1265–1272. doi:10.1039/b804911d

Bollenbach, T. (2015). Antimicrobial interactions: mechanisms and implications for drug discovery and resistance evolution. *Curr. Opin. Microbiol.* 27, 1–9. doi:10.1016/j.mib.2015.05.008

Bulyk, M. L., Gentalen, E., Lockhart, D. J., and Church, G. M. (1999). Quantifying DNA–protein interactions by double-stranded DNA arrays. *Nat. Biotechnol.* 17, 573–577. doi:10.1038/9878

Capel, A. J., Rimington, R. P., Lewis, M. P., and Christie, S. D. (2018). 3D printing for chemical, pharmaceutical and biological applications. *Nat. Rev. Chem.* 2, 422–436. doi:10.1038/s41570-018-0058-y

Catalán, J., Siivola, K. M., Nymark, P., Lindberg, H., Suhonen, S., Järventaus, H., et al. (2016). *In vitro* and *in vivo* genotoxic effects of straight versus tangled multi-walled carbon nanotubes. *Nanotoxicology.* 10, 794–806. doi:10.3109/17435390.2015.1132345

Ceriotti, L., Ponti, J., Colpo, P., Sabbioni, E., and Rossi, F. (2007). Assessment of cytotoxicity by impedance spectroscopy. *Biosens. Bioelectron.* 22, 3057–3063. doi:10.1016/j.bios.2007.01.004

Chen, X., Chen, H., Wu, D., Chen, Q., Zhou, Z., Zhang, R., et al. (2018). 3D printed microfluidic chip for multiple anticancer drug combinations. *Sens. Actuat. B-Chem.* 276, 507–516. doi:10.1016/j.snb.2018.08.121

Cho, M., Niles, A., Huang, R., Inglese, J., Austin, C. P., Riss, T., et al. (2008). A bioluminescent cytotoxicity assay for assessment of membrane integrity using a proteolytic biomarker. *Toxicol. In Vitro.* 22, 1099–1106. doi:10.1016/j.tiv.2008.02.013

Churchman, A. H., Wallace, R., Milne, S. J., Brown, A. P., Brydson, R., and Beales, P. A. (2013). Serum albumin enhances the membrane activity of ZnO nanoparticles. *Chem. Commun.* 49, 4172–4174. doi:10.1039/c3cc37871c

Cosson, S., and Lutolf, M. (2014). Hydrogel microfluidics for the patterning of pluripotent stem cells. *Sci. Rep.* 4, 4462. doi:10.1038/srep04462

Dai, W., Zheng, Y., Luo, K. Q., and Wu, H. (2010). A prototypic microfluidic platform generating stepwise concentration gradients for real-time study of cell apoptosis. *Biomicrofluidics.* 4, 024101. doi:10.1063/1.3398319

Ding, Y., Li, J., Xiao, W., Xiao, K., Lee, J., Bhardwaj, U., et al. (2015). Microfluidic-enabled print-to-screen platform for high-throughput screening of combinatorial chemotherapy. *Anal. Chem.* 87, 10166–10171. doi:10.1021/acs.analchem.5b00826

Du, G., Pan, J., Zhao, S., Zhu, Y., den Toonder, J. M., and Fang, Q. (2013). Cell-based drug combination screening with a microfluidic droplet array system. *Anal. Chem.* 85, 6740–6747. doi:10.1021/ac400688f

Eribol, P., Uguz, A., and Ulgen, K. (2016). Screening applications in drug discovery based on microfluidic technology. *Biomicrofluidics.* 10, 011502. doi:10.1063/1.4940886

Fadeel, B. (2019). The right stuff: on the future of nanotoxicology. *Front. Toxicol.* 1, 1. doi:10.3389/ftox.2019.00001

Farkas, E., Szekacs, A., Kovacs, B., Olah, M., Horvath, R., and Szekacs, I. (2018). Label-free optical biosensor for real-time monitoring the cytotoxicity of xenobiotics: a proof of principle study on glyphosate. *J. Hazard. Mater.* 351, 80–89. doi:10.1016/j.jhazmat.2018.02.045

Fischer, R., Steinert, S., Fröber, U., Voges, D., Stubenrauch, M., Hofmann, G., et al. (2011). Cell cultures in microsystems: biocompatibility aspects. *Biotechnol. Bioeng.* 108, 687–693. doi:10.1002/bit.22951

Flont, M., Jastrzębska, E., and Brzózka, Z. (2020). Synergistic effect of the combination therapy on ovarian cancer cells under microfluidic conditions. *Anal. Chim. Acta.* 1100, 138–148. doi:10.1016/j.aca.2019.11.047

Foucquier, J., and Guedj, M. (2015). Analysis of drug combinations: current methodological landscape. *Pharmaco. Res. Perspect.* 3, e00149. doi:10.1002/prp2.149

Fritzsche, S., Hoffmann, P., and Belder, D. (2010). Chip electrophoresis with mass spectrometric detection in record speed. *Lab Chip.* 10, 1227–1230. doi:10.1039/c000349b

Galvez, J. M. M., Garcia-Hernando, M., Benito-Lopez, F., Basabe-Desmonts, L., and Shnyrova, A. V. (2020). Microfluidic chip with pillar arrays for controlled production and observation of lipid membrane nanotubes. *Lab Chip.* 20 (15), 2748–2755. doi:10.1039/d0lc00451k

Garcia-Hernando, M., Calatayud-Sanchez, A., Etxebarria-Elezgarai, J., de Pancorbo, M. M., Benito-Lopez, F., and Basabe-Desmonts, L. (2020). Optical single cell resolution cytotoxicity biosensor based on single cell adhesion dot arrays. *Anal. Chem.* 92 (14), 9658–9665. doi:10.1021/acs.analchem.0c00940

Gelles, J. D., and Chipuk, J. E. (2016). Robust high-throughput kinetic analysis of apoptosis with real-time high-content live-cell imaging. *Cell Death & Dis.* 7, e2493. doi:10.1038/cddis.2016.332

Geyer, F. L., Ueda, E., Liebel, U., Grau, N., and Levkin, P. A. (2011). Superhydrophobic–superhydrophilic micropatterning: towards genome-on-a-chip cell microarrays. *Angew. Chem. Int. Ed.* 50, 8424–8427. doi:10.1002/anie.201102545

Gonzalez-Pujana, A., Santos-Vizcaino, E., García-Hernando, M., Hernaez-Estrada, B., de Pancorbo, M. M., Benito-Lopez, F., et al. (2019). Extracellular matrix protein microarray-based biosensor with single cell resolution: integrin profiling and characterization of cell-biomaterial interactions. *Sens. Actuat. B- Chem.* 299, 126954. doi:10.1016/j.snb.2019.126954

Guo, L., Guvanasen, G. S., Liu, X., Tuthill, C., Nichols, T. R., and DeWeerth, S. P. (2012). A PDMS-based integrated stretchable microelectrode array (isMEA) for neural and muscular surface interfacing. *IEEE Trans. Biomed.* 7, 1–10. doi:10.1109/TBCAS.2012.2192932

Gurkan, U. A., Anand, T., Tas, H., Elkan, D., Akay, A., Keles, H. O., et al. (2011). Controlled viable release of selectively captured label-free cells in microchannels. *Lab Chip.* 11, 3979–3989. doi:10.1039/c1lc20487d

Hamon, C., Henriksen-Lacey, M., La Porta, A., Rosique, M., Langer, J., Scarabelli, L., et al. (2016). Tunable nanoparticle and cell assembly using combined self-powered microfluidics and microcontact printing. *Adv. Funct. Mat.* 26, 8053–8061. doi:10.1002/adfm.201602225

Hart, L. R., Li, S., Sturgess, C., Wildman, R., Jones, J. R., and Hayes, W. (2016). 3D printing of biocompatible supramolecular polymers and their composites. *ACS Appl. Mat. Interfaces.* 8, 3115–3122. doi:10.1021/acsami.5b10471

He, M., Stoevesandt, O., Palmer, E. A., Khan, F., Ericsson, O., and Taussig, M. J. (2008). Printing protein arrays from DNA arrays. *Nat. Methods.* 5, 175–177. doi:10.1038/nmeth.1178

Hirano-Iwata, A., Oshima, A., Nasu, T., Taira, T., Kimura, Y., and Niwano, M. (2010). Stable lipid bilayers based on micro-and nano-fabrication. *Supramol. Chem.* 22, 406–412. doi:10.1080/10610278.2010.487564

Ho, C. M. B., Ng, S. H., Li, K. H. H., and Yoon, Y. (2015). 3D printed microfluidics for biological applications. *Lab Chip.* 15, 3627–3637. doi:10.1039/c5lc00685f

Hosokawa, M., Hayashi, T., Mori, T., Yoshino, T., Nakasono, S., and Matsunaga, T. (2011). Microfluidic device with chemical gradient for single-cell cytotoxicity assays. *Anal. Chem.* 83, 3648–3654. doi:10.1021/ac2000225

Hu, B., Li, J., Mou, L., Liu, Y., Deng, J., Qian, W., et al. (2017). An automated and portable microfluidic chemiluminescence immunoassay for quantitative detection of biomarkers. *Lab Chip.* 17, 2225–2234. doi:10.1039/c7lc00249a

Hug, T. S. (2003). Biophysical methods for monitoring cell-substrate interactions in drug discovery. *Assay Drug Dev. Techn.* 1, 479–488. doi:10.1089/154065803322163795

Irelan, J. T., Wu, M., Morgan, J., Ke, N., Xi, B., Wang, X., et al. (2011). Rapid and quantitative assessment of cell quality, identity, and functionality for cell-based assays using real-time cellular analysis. *J. Biomol. Screen.* 16, 313–322. doi:10.1177/1087057110397359

Jahan-Tigh, R. R., Ryan, C., Obermoser, G., and Schwarzenberger, K. (2012). Flow cytometry. *J. Invest. Dermatol.* 132, 1–6. doi:10.1038/jid.2012.282

Ke, N., Wang, X., Xu, X., and Abassi, Y. A. (2011). The xCELLigence system for real-time and label-free monitoring of cell viability. *Methods Mol. Biol.* 740, 33–43. doi:10.1007/978-1-61779-108-6_6

Kersten, B., Wanker, E. E., Hoheisel, J. D., and Angenendt, P. (2005). Multiplex approaches in protein microarray technology. *Expert. Rev. Proteomic.* 2, 499–510. doi:10.1586/14789450.2.4.499

Khalid, N., Kobayashi, I., and Nakajima, M. (2017). Recent lab-on-chip developments for novel drug discovery. *Wires Syst. Biol. Med.* 9, e1381. doi:10.1002/wsbm.1381

Kim, J., Taylor, D., Agrawal, N., Wang, H., Kim, H., Han, A., et al. (2012). A programmable microfluidic cell array for combinatorial drug screening. *Lab Chip.* 12, 1813–1822. doi:10.1039/c2lc21202a

Kumar, P., Vriens, K., Cornaglia, M., Gijs, M., Kokalj, T., Thevissen, K., et al. (2015). Digital microfluidics for time-resolved cytotoxicity studies on single non-adherent yeast cells. *Lab Chip.* 15, 1852–1860. doi:10.1039/c4lc01469c

Lee, P. J., Hung, P. J., Rao, V. M., and Lee, L. P. (2006). Nanoliter scale microbioreactor array for quantitative cell biology. *Biotechnol. Bioeng.* 94, 5–14. doi:10.1002/bit.20745

Levinson, H. J. (2005). *Principles of lithography*. Bellingham, WA: SPIE press, Vol. 146

Li, L., Li, Y., Shao, Z., Luo, G., Ding, M., and Liang, Q. (2018). Simultaneous assay of oxygen-dependent cytotoxicity and genotoxicity of anticancer drugs on an integrated microchip. *Anal. Chem.* 90, 11899–11907. doi:10.1021/acs.analchem.8b02070

Li, L., Wang, W., Ding, M., Luo, G., and Liang, Q. (2016). Single-cell-arrayed agarose chip for *in situ* analysis of cytotoxicity and genotoxicity of DNA cross-linking agents. *Anal. Chem.* 88, 6734–6742. doi:10.1021/acs.analchem.6b01008

Lim, K. S., Chang, W., Koo, Y., and Bashir, R. (2006). Reliable fabrication method of transferable micron scale metal pattern for poly (dimethylsiloxane) metallization. *Lab Chip.* 6, 578–580. doi:10.1039/b514755g

Liu, W., Li, Y., Wang, T., Li, D., Fang, L., Zhu, S., et al. (2013). Elliptical polymer brush ring array mediated protein patterning and cell adhesion on patterned protein surfaces. *ACS Appl. Mat. Interfaces.* 5, 12587–12593. doi:10.1021/am403808s

Lopez-Alonso, A., Jose, B., Somers, M., Egan, K., Foley, D. P., Ricco, A. J., et al. (2013). Individual platelet adhesion assay: measuring platelet function and antiplatelet therapies in whole blood via digital quantification of cell adhesion. *Anal. Chem.* 85, 6497–6504. doi:10.1021/ac401076s

Lulevich, V., Shih, Y., Lo, S. H., and Liu, G. (2009). Cell tracing dyes significantly change single cell mechanics. *J. Phys. Chem. B.* 113, 6511–6519. doi:10.1021/jp8103358

Lulevich, V., Zink, T., Chen, H., Liu, F., and Liu, G. (2006). Cell mechanics using atomic force microscopy-based single-cell compression. *Langmuir.* 22, 8151–8155. doi:10.1021/la060561p

Ma, B., Zhang, G., Qin, J., and Lin, B. (2009). Characterization of drug metabolites and cytotoxicity assay simultaneously using an integrated microfluidic device. *Lab Chip.* 9, 232–238. doi:10.1039/b809117j

Mashaghi, S., Abbaspourrad, A., Weitz, D. A., and van Oijen, A. M. (2016). Droplet microfluidics: a tool for biology, chemistry and nanotechnology. *Trac-Trend. Anal. Chem.* 82, 118–125. doi:10.1016/j.trac.2016.05.019

Mazutis, L., Gilbert, J., Ung, W. L., Weitz, D. A., Griffiths, A. D., and Heyman, J. A. (2013). Single-cell analysis and sorting using droplet-based microfluidics. *Nat. Protoc.* 8, 870. doi:10.1038/nprot.2013.046

McCormick, S. C., Kriel, F. H., Ivask, A., Tong, Z., Lombi, E., Voelcker, N. H., et al. (2017). The use of microfluidics in cytotoxicity and nanotoxicity experiments. *Micromachines.* 8, 124. doi:10.3390/mi8040124

Melin, J., and Quake, S. R. (2007). Microfluidic large-scale integration: the evolution of design rules for biological automation. *Annu. Rev. Biophys. Biomol. Struct.* 36, 213–231. doi:10.1146/annurev.biophys.36.040306.132646

Menotti, J., Alanio, A., Sturny-Leclère, A., Vitry, S., Sauvage, F., Barratt, G., et al. (2017). A cell impedance-based real-time *in vitro* assay to assess the toxicity of amphotericin B formulations. *Toxicol. Appl. Pharm.* 334, 18–23. doi:10.1016/j.taap.2017.08.017

Mo, S. J., Lee, J., Kye, H. G., Lee, J. M., Kim, E., Geum, D., et al. (2020). A microfluidic gradient device for drug screening with human iPSC-derived motoneurons. *Analyst.* 145, 3081–3089. doi:10.1039/c9an02384d

Nath, N., Hyun, J., Ma, H., and Chilkoti, A. (2004). Surface engineering strategies for control of protein and cell interactions. *Surf. Sci.* 570, 98–110. doi:10.1016/j.susc.2004.06.182

Nery, E. W., Jastrzębska, E., Żukowski, K., Wróblewski, W., Chudy, M., and Ciosek, P. (2014). Flow-through sensor array applied to cytotoxicity assessment in cell cultures for drug-testing purposes. *Biosens. Bioelectron.* 51, 55–61. doi:10.1016/j.bios.2013.07.023

Nguyen, T., Jung, S. H., Lee, M. S., Park, T., Ahn, S., and Kang, J. H. (2019). Robust chemical bonding of PMMA microfluidic devices to porous PETE membranes for reliable cytotoxicity testing of drugs. *Lab Chip.* 19, 3706–3713. doi:10.1039/c9lc00338j

Ou, X., Chen, P., Huang, X., Li, S., and Liu, B. (2019). Microfluidic chip electrophoresis for biochemical analysis. *J. Sep. Sci.* 43, 258–270. doi:10.1002/jssc.201900758

Owen, J., Kuznecovs, M., Bhamji, R., William, N., Domenech-Garcia, N., Hesler, M., et al. (2020). High-throughput electrochemical sensing platform for screening nanomaterial–biomembrane interactions. *Rev. Sci. Instrum.* 91, 025002. doi:10.1063/1.5131562

Pietroiusti, A., Stockmann-Juvala, H., Lucaroni, F., and Savolainen, K. (2018). Nanomaterial exposure, toxicity, and impact on human health. *Wiley Interdiscip. Rev. Nanomed.* 10, e1513. doi:10.1002/wnan.1513

Piruska, A., Nikcevic, I., Lee, S. H., Ahn, C., Heineman, W. R., Limbach, P. A., et al. (2005). The autofluorescence of plastic materials and chips measured under laser irradiation. *Lab Chip.* 5, 1348–1354. doi:10.1039/b508288a

Popova, A. A., Depew, C., Permana, K. M., Trubitsyn, A., Peravali, R., Ordiano, J. A. G., et al. (2017). Evaluation of the droplet-microarray platform for high-throughput screening of suspension cells. *SLAS Technol.* 22, 163–175. doi:10.1177/2211068216677204

Popova, A. A., Schillo, S. M., Demir, K., Ueda, E., Nesterov-Mueller, A., and Levkin, P. A. (2015). Droplet-Array (DA) sandwich chip: a versatile platform for High-Throughput cell screening based on Superhydrophobic–Superhydrophilic micropatterning. *Adv. Mat.* 27, 5217–5222. doi:10.1002/adma.201502115

Ramachandran, N., Raphael, J. V., Hainsworth, E., Demirkan, G., Fuentes, M. G., Rolfs, A., et al. (2008). Next-generation high-density self-assembling functional protein arrays. *Nat. Methods.* 5, 535–538. doi:10.1038/nmeth.1210

Ramirez, C. N., Antczak, C., and Djaballah, H. (2010). Cell viability assessment: toward content-rich platforms. *Expert. Opin. Drug. Dis.* 5, 223–233. doi:10.1517/17460441003596685

Rashid, A., Vakurov, A., Mohamadi, S., Sanver, D., and Nelson, A. (2017). Substituents modulate biphenyl penetration into lipid membranes. *Biochim. Biophys. Acta Biomembr.* 1859, 712–721. doi:10.1016/j.bbamem.2017.01.023

Recordati, C., De Maglie, M., Bianchessi, S., Argentiere, S., Cella, C., Mattiello, S., et al. (2015). Tissue distribution and acute toxicity of silver after single intravenous administration in mice: nano-specific and size-dependent effects. *Part Fibre Toxicol.* 13, 12. doi:10.1186/s12989-016-0124-x

Riahi, R., Shaegh, S. A. M., Ghaderi, M., Zhang, Y. S., Shin, S. R., Aleman, J., et al. (2016). Automated microfluidic platform of bead-based electrochemical immunosensor integrated with bioreactor for continual monitoring of cell secreted biomarkers. *Sci. Rep.* 6, 1–14. doi:10.1038/srep24598

Ruan, J., Wang, L., Xu, M., Cui, D., Zhou, X., and Liu, D. (2009). Fabrication of a microfluidic chip containing dam, weirs and gradient generator for studying cellular response to chemical modulation. *Mat. Sci. Eng. C.* 29, 674–679. doi:10.1016/j.msec.2008.12.009

Ruggeri, F. S., Mahul-Mellier, A., Kasas, S., Lashuel, H. A., Longo, G., and Dietler, G. (2017). Amyloid single-cell cytotoxicity assays by nanomotion detection. *Cell Death Dis.* 3, 1–8. doi:10.1038/cddiscovery.2017.53

Sackmann, E. K., Fulton, A. L., and Beebe, D. J. (2014). The present and future role of microfluidics in biomedical research. *Nature.* 507, 181–189. doi:10.1038/nature13118

Sarkar, S., Cohen, N., Sabhachandani, P., and Konry, T. (2015). Phenotypic drug profiling in droplet microfluidics for better targeting of drug-resistant tumors. *Lab Chip.* 15, 4441–4450. doi:10.1039/c5lc00923e

Sarkar, S., Kang, W., Jiang, S., Li, K., Ray, S., Luther, E., et al. (2020). Machine learning-aided quantification of antibody-based cancer immunotherapy by natural killer cells in microfluidic droplets. *Lab Chip.* 20 (13), 2317–2327. doi:10.1039/D0LC00158A

Shang, W., Liu, Y., Kim, E., Tsao, C., Payne, G. F., and Bentley, W. E. (2018). Selective assembly and functionalization of miniaturized redox capacitor inside microdevices for microbial toxin and mammalian cell cytotoxicity analyses. *Lab Chip.* 18, 3578–3587. doi:10.1039/c8lc00583d

Shen, S., Zhang, X., Zhang, F., Wang, D., Long, D., and Niu, Y. (2020). Three-gradient constructions in a flow-rate insensitive microfluidic system for drug screening towards personalized treatment. *Talanta.* 208, 120477. doi:10.1016/j.talanta.2019.120477

Shields, C. W., IV, Reyes, C. D., and López, G. P. (2015). Microfluidic cell sorting: a review of the advances in the separation of cells from debulking to rare cell isolation. *Lab Chip.* 15, 1230–1249. doi:10.1039/c4lc01246a

Sochol, R., Sweet, E., Glick, C., Venkatesh, S., Avetisyan, A., Ekman, K., et al. (2016). 3D printed microfluidic circuitry via multijet-based additive manufacturing. *Lab Chip.* 16, 668–678. doi:10.1039/c5lc01389e

Stoddart, M. J. (2011). Cell viability assays: introduction. *Methods. Mol. Biol.* 740, 1–6. doi:10.1007/978-1-61779-108-6_1

Strulson, M. K., and Maurer, J. A. (2011). Microcontact printing for creation of patterned lipid bilayers on tetraethylene glycol self-assembled monolayers. *Langmuir.* 27, 12052–12057. doi:10.1021/la201839w

Sugiura, S., Edahiro, J., Kikuchi, K., Sumaru, K., and Kanamori, T. (2008). Pressure-driven perfusion culture microchamber array for a parallel drug cytotoxicity assay. *Biotechnol. Bioeng.* 100, 1156–1165. doi:10.1002/bit.21836

Susloparova, A. A., Koppenhöfer, D., Law, J. K. Y., Vu, X. T., and Ingebrandt, S. (2015). Electrical cell-substrate impedance sensing with field-effect transistors is able to unravel cellular adhesion and detachment processes on a single cell level. *Lab Chip.* 15, 668–679. doi:10.1039/c4lc00593g

Sweet, E. C., Chen, J. C., Karakurt, I., Long, A. T., and Lin, L. (2017). 3D printed three-flow microfluidic concentration gradient generator for clinical E. coli-antibiotic drug screening. IEEE 30th international conference on micro electro mechanical systems (MEMS), Las Vegas, NV, January 22–26, 2017, (IEEE) 205–208

Ta, V., Park, J., Park, E. J., and Hong, S. (2014). Reusable floating-electrode sensor for the quantitative electrophysiological monitoring of a nonadherent cell. *ACS Nano.* 8, 2206–2213. doi:10.1021/nn4053155

Tran, T. B., Cho, S., and Min, J. (2013). Hydrogel-based diffusion chip with electric cell-substrate impedance sensing (ECIS) integration for cell viability assay and drug toxicity screening. *Biosens. Bioelectron.* 50, 453–459. doi:10.1016/j.bios.2013.07.019

Urcan, E., Haertel, U., Styllou, M., Hickel, R., Scherthan, H., and Reichl, F. X. (2010). Real-time xCELLigence impedance analysis of the cytotoxicity of dental composite components on human gingival fibroblasts. *Dent. Mater. J.* 26, 51–58. doi:10.1016/j.dental.2009.08.007

Vaidyanathan, R., Yeo, T., and Lim, C. T. (2018). Microfluidics for cell sorting and single cell analysis from whole blood. *Methods Cell Biol.* 147, 151–173. doi:10.1016/bs.mcb.2018.06.011

Vajrala, V. S., Belaïdi, F. S., Lemercier, G., Zigah, D., Rigoulet, M., Devin, A., et al. (2019). Microwell array integrating nanoelectrodes for coupled opto-electrochemical monitorings of single mitochondria. *Biosens. Bioelectron.* 126, 672–678. doi:10.1016/j.bios.2018.11.036

Wang, G., Dewilde, A. H., Zhang, J., Pal, A., Vashist, M., Bello, D., and Therrien, J. M. (2011). A living cell quartz crystal microbalance biosensor for continuous monitoring of cytotoxic responses of macrophages to single-walled carbon nanotubes. *Part Fibre Toxicol.* 8, 4. doi:10.1186/1743-8977-8-4

Wang, T., Liu, J., and Nie, F. (2018). Non-dye cell viability monitoring by using pH-responsive inverse opal hydrogels. *J. Mater. Chem. B.* 6, 1055–1065. doi:10.1039/c7tb02631e

Wang, Z., Kim, M., Marquez, M., and Thorsen, T. (2007). High-density microfluidic arrays for cell cytotoxicity analysis. *Lab Chip.* 7, 740–745. doi:10.1039/b618734j

Wlodkowic, D., Faley, S., Zagnoni, M., Wikswo, J. P., and Cooper, J. M. (2009). Microfluidic single-cell array cytometry for the analysis of tumor apoptosis. *Anal. Chem.* 81, 5517–5523. doi:10.1021/ac9008463

Wu, W., Shen, J., Banerjee, P., and Zhou, S. (2010). Coreâ€"shell hybrid nanogels for integration of optical temperature-sensing, targeted tumor cell imaging, and combined chemo-photothermal treatment. *Biomaterials.* 31, 7555–7566. doi:10.1016/j.biomaterials.2010.06.030

Wurm, M., Schöpke, B., Lutz, D., Müller, J., and Zeng, A. (2010). Microtechnology meets systems biology: the small molecules of metabolome as next big targets. *J. Biotechnol.* 149, 33–51. doi:10.1016/j.jbiotec.2010.05.002

Xia, Y., and Whitesides, G. M. (1998). Soft lithography. *Annu. Rev. Mater. Sci.* 28, 153–184. doi:10.1146/annurev.matsci.28.1.153

Xing, J. Z., Zhu, L., Jackson, J. A., Gabos, S., Sun, X., Wang, X., et al. (2005). Dynamic monitoring of cytotoxicity on microelectronic sensors. *Chem. Res. Toxicol.* 18, 154–161. doi:10.1021/tx049721s

Yu, L., Chen, M. C., and Cheung, K. C. (2010). Droplet-based microfluidic system for multicellular tumor spheroid formation and anticancer drug testing. *Lab Chip.* 10, 2424–2432. doi:10.1039/c004590j

Zhang, D., Peng, Y., Qi, H., Gao, Q., and Zhang, C. (2010). Label-free electrochemical DNA biosensor array for simultaneous detection of the HIV-1 and HIV-2 oligonucleotides incorporating different hairpin-DNA probes and redox indicator. *Biosens. Bioelectron.* 25, 1088–1094. doi:10.1016/j.bios.2009.09.032

Zhang, H., Lee, Y. Y., Leck, K. J., Kim, N. Y., and Ying, J. Y. (2007). Recyclable hydrophilic– hydrophobic micropatterns on glass for microarray applications. *Langmuir.* 23, 4728–4731. doi:10.1021/la063759i

Zhang, L., Chen, P., Zhou, Z., Hu, Y., Sha, Q., Zhang, H., et al. (2019). Agarose-based microwell array chip for high-throughput screening of functional microorganisms. *Talanta.* 191, 342–349. doi:10.1016/j.talanta.2018.08.090

Zhang, S., Nelson, A., and Beales, P. A. (2012). Freezing or wrapping: the role of particle size in the mechanism of nanoparticle–biomembrane interaction. *Langmuir.* 28, 12831–12837. doi:10.1021/la301771b

Zhao, L., Cao, J., Wu, Z., Li, J., and Zhu, J. (2013). Lab-on-a-chip for anticancer drug screening using quantum dots probe based apoptosis assay. *J. Biomed. Nanotechnol.* 9, 348–356. doi:10.1166/jbn.2013.1546

Zhao, L., Cheng, P., Li, J., Zhang, Y., Gu, M., Liu, J., et al. (2009). Analysis of nonadherent apoptotic cells by a quantum dots probe in a microfluidic device for drug screening. *Anal. Chem.* 81, 7075–7080. doi:10.1021/ac901121f

Zhao, Y., Cheng, Y., Shang, L., Wang, J., Xie, Z., and Gu, Z. (2015). Microfluidic synthesis of barcode particles for multiplex assays. *Small.* 11 (2), 151–174. doi:10.1002/smll.201401600

Zimmer, C. C., Liu, Y. X., Morgan, J. T., Yang, G., Wang, K., Kennedy, I. M., et al. (2014). New approach to investigate the cytotoxicity of nanomaterials using single cell mechanics. *J. Phys.l Chem. B.* 118, 1246–1255. doi:10.1021/jp410764f

Conflict of Interest: The authors declare that the research was conducted in the absence of any commercial or financial relationships that could be construed as a potential conflict of interest.

frontiers in Materials

ORIGINAL RESEARCH
published: 19 May 2020
doi: 10.3389/fmats.2020.00143

Dynamic Wetting of Molten Polymers on Cellulosic Substrates: Model Prediction for Total and Partial Wetting

Monica Francesca Pucci[1*†], *Benoît Duchemin*[2], *Moussa Gomina*[1] *and Joël Bréard*[2]

[1] CRISMAT, UMR 6508 CNRS, ENSICAEN, Caen, France, [2] LOMC, UMR 6294 CNRS, Normandie Univ ULH, Le Havre, France

This work consists in an experimental investigation of forced dynamic wetting of molten polymers on cellulosic substrates and an estimation of models describing this dynamic. A previous work of Pucci et al. (2018) showed that for totally wetting liquids (as paraffin oils), temperature-induced variations in dynamic wetting are included into the capillary number (*Ca*) and then a master curve of dynamic contact angle (θ_d) as a function of *Ca* can be obtained. The hydrodynamic theory (HDT) correctly describes the dynamic wetting for $Ca > 2 \cdot 10^{-3}$. For lower *Ca*, a change in the dynamic wetting behavior was observed. Here, partially wetting liquids (polyethylene glycols, *a.k.a.* PEGs) at different molecular weight (*Mn*) were used at temperatures above their melting point to investigate the dynamic wetting behavior on cellulosic substrates for a large range of *Ca*. It was found that the dynamic curves of θ_d vs. *Ca* depend on *Mn*. Moreover, the HDT correctly describes the experimental measurements for $Ca > 2 \cdot 10^{-3}$. Below this threshold the dynamic contact angle decreases toward the static one. A linear correlation between parameters obtained fitting the HDT and the molecular weight of polymer was found. The prediction of dynamic wetting for low *Ca* ($Ca < 2 \cdot 10^{-3}$) with the molecular kinetic theory (MKT) was also evaluated and discussed.

Keywords: dynamic wetting, capillary effects, molten polymer, molecular weight, cellulosic films

OPEN ACCESS

Edited by:
Patricia Krawczak, IMT Lille Douai, France

Reviewed by:
Veronique Michaud, Federal Institute of Technology in Lausanne, Switzerland
Christophe Binetruy, Ecole Centrale de Nantes, France

***Correspondence:**
Monica Francesca Pucci
monica.pucci@mines-ales.fr

***Present address:**
Monica Francesca Pucci, LMGC, IMT Mines Alés, UMR 5508 CNRS, Univ Montpellier, Alés, France

Specialty section:
This article was submitted to Colloidal Materials and Interfaces, a section of the journal Frontiers in Materials

Received: *17 March 2020*
Accepted: *24 April 2020*
Published: *19 May 2020*

Citation:
Pucci MF, Duchemin B, Gomina M and Bréard J (2020) Dynamic Wetting of Molten Polymers on Cellulosic Substrates: Model Prediction for Total and Partial Wetting. Front. Mater. 7:143. doi: 10.3389/fmats.2020.00143

1. INTRODUCTION

Dynamic wetting occurs in many everyday situations, when water flows on a floor tile or pearl on a plant leaf for example. It concerns different industrial domains and among them, composite manufacturing (Bréard et al., 2003; Verrey et al., 2006; Park et al., 2011; Pucci et al., 2015, 2017b; Caglar et al., 2019). In this case, the flow of a molten polymer in a fibrous preform is governed by a competition of capillary and viscous effects that are included in the dimensionless capillary number *Ca* (Ruiz et al., 2006):

$$Ca = \frac{\eta v}{\gamma_{LV}} \quad (1)$$

where v is the liquid velocity, η and γ_{LV} are the dynamic viscosity and the liquid surface tension, respectively. Dynamic wetting phenomena are described by a dynamic contact angle θ_d depending on the *Ca*. Forced dynamic wetting occurs when the liquid velocity v is set via an external force, in

contrast to the spontaneous wetting where only capillary effects drive the flow (Sauer and Kampert, 1998; Mohammad Karim et al., 2016). In all cases, θ_d is defined as an advancing contact angle (θ_a), when the triple contact line advances on the dry solid surface with a positive convention of v and Ca, or a receding contact angle (θ_r) when it recedes from the wetted surface with a negative convention of v and Ca (De Gennes et al., 2013). For $v \approx 0$ m/s (at static conditions) the angle formed between the liquid and the solid is defined by an equilibrium contact angle (θ_e), according to the Young's law, for ideal substrates (Pucci et al., 2017a). In fact, substrates have morphological defects and chemical heterogeneities generating an angle hysteresis and at $v \approx 0$ m/s the equilibrium contact angle will be between a static advancing contact angle $\theta_{a,s}$ and a static receding one $\theta_{r,s}$ (Petrov et al., 2003; Bonn et al., 2009; Pucci et al., 2017a). Depending on the equilibrium or static contact angle, liquids can be classified as totally wetting (e.g., paraffin and silicon oils), for which the θ_e is $\approx 0^\circ$ and as partially wetting (e.g., polyethylene glycols), when the θ_e is different from 0°.

In literature, to the best of our knowledge, the majority of experimental works investigated the dynamic wetting using totally wetting liquids and via a visual method, observing the spontaneous spreading of a drop (the speed of the liquid front is not constant), especially at room temperature (Tanner, 1979; Schneemilch et al., 1998; Prevost et al., 1999; Le Grand et al., 2005; Kumar and Deshpande, 2006; Seveno et al., 2009; Duursma et al., 2010; Duvivier et al., 2011). Some works using microfluidic techniques proved that, with partially wetting liquids, established models in literature are no longer valid (Wielhorski et al., 2012; Abdelwahed et al., 2014). A recent work studied molten polymers but in a spontaneous regime of drop spreading (Zhang et al., 2017). This procedure has been applied to rods or fibers with a large diameter (Zhang et al., 2019) but it turns out to be more difficult for thinner fibers (Hansen et al., 2017). Moreover, this method is not suitable to study the forced wetting at a specific range of Ca, since the liquid velocity v is not imposed but it depends on the liquid and on the spontaneous solid/liquid interactions.

In this work, a procedure easily applicable to different types of substrates and fibers and at different conditions of temperature and liquid viscosity was carried out at a large range of Ca, using the weight tensiometric method. This method, based on the Wilhelmy principle, becomes more interesting for studying forced wetting under different conditions for total and partial wetting, imposing the liquid velocity and in both advancing and receding modes (Pucci et al., 2018). Polyethylene glycols, *a.k.a.* PEGs, at different molecular weight (Mn) were characterized in terms of surface tension and viscosity as a function of temperature and used for tensiometric tests of forced wetting on cellulosic substrates having a very low roughness ($<<$ 100 nm) and with an homogeneous chemical composition of surface (Pucci et al., 2018), in order to validate this protocol. Results are then relevant for a better understanding of dynamic wetting behavior of molten polymers and to estimate the prediction of this behavior by existing models in literature. A discussion about models validity, the obtained physical parameters and their sensitivity deriving from experimental results is then presented. Moreover, the experimental protocol could be directly applied to study the dynamic wetting of these molten polymers on fibers.

2. MODELS OF FORCED WETTING: HDT VS. MKT

Two approaches are mostly used in literature to describe the dynamic wetting. The hydrodynamic theory (HDT) takes into account the viscous dissipation at the core of the liquid, far from the triple contact line. This approach describes forced dynamic wetting for high Ca ($Ca > 10^{-3}$) at a macro-mesoscopic scale (in the order of mm-μm) where the unbalanced driving capillary force is equilibrated by the friction one (De Gennes, 1985). From this viscocapillary balance, the Tanner-De Gennes law was derived and then generalized by Cox and Voinov (C-V), obtaining the following equation (Cox, 1962; Voinov, 1976):

$$\theta_d^3 - \theta_e^3 = 9ln\left(\frac{x_{max}}{x_{min}}\right)\frac{\eta v}{\gamma_{LV}} = 9\Gamma Ca \tag{2}$$

where x_{max} and x_{min} are two cutoff lengths employed to integer the energy dissipation. x_{max} was estimated by De Gennes (De Gennes et al., 2013) in the order of the capillary length k^{-1} ($\approx 10^{-3}$ m), beyond which capillary effects are not meaningful, x_{min} is around a characteristic molecular size ($\approx 10^{-9}$ m). The capillary length is defined as follows:

$$k^{-1} = \sqrt{\frac{\gamma_{LV}}{\rho g}} \tag{3}$$

where ρ is the liquid density and g the acceleration of gravity. The Γ value is indeed defined as :

$$\Gamma = ln\left(\frac{x_{max}}{x_{min}}\right) \tag{4}$$

Two free parameters have to be identified in this approach (Equation 2): Γ and θ_e. Γ seems to be exclusively a characteristic of liquid properties according to the hydrodynamic approach, and experimental studies found a range of Γ approximately between 10 and 20 for total wetting liquids (De Gennes, 1985; Marsh et al., 1993; Bonn et al., 2009). However, the physical significance of Γ and particularly of the x_{min} was questioned, because this value was sometimes found to be less than atomic or molecular dimensions (Schneemilch et al., 1998; Petrov et al., 2003). For total wetting, the equilibrium contact angle can be set to 0 and then Γ is the only free parameter in the HDT. It was proven in a previous work (Pucci et al., 2018) with totally wetting liquids that this theory describes well dynamic wetting for $Ca > 2 \cdot 10^{-3}$ at different temperatures. In fact the effect of temperature is included in the Ca and physical parameters of Γ were found. Open issues remain about the dynamic behavior of totally wetting liquids at low Ca; the prediction with the MKT will be discussed in this work. For partial wetting, the static contact angles were measured and inserted in models predicting forced dynamic wetting, in order to have also in this case only one free parameter (Γ). The prediction with HDT and MKT will also be discussed.

The molecular kinetic theory (MKT) investigates dynamic wetting for low *Ca* at a microscopic scale (in the order of *nm*). The unbalanced driven capillary force is here equilibrated by a microscopic dissipation in the vicinity of the contact line (Snoeijer and Andreotti, 2013). Contact line motion is a thermally activated process, described by molecular displacements characterized by a jump length λ (of the order of *nm*) and a quasi-equilibrium displacement frequency k^0 (of the order of 10^6 *Hz*) between adsorption sites of the solid surface (Blake and Haynes, 1969). Liquid velocity v is defined as follows:

$$v = 2k^0\lambda sinh\left[\frac{\gamma_{LV}\lambda^2(cos\theta_e - cos\theta_d)}{2k_BT}\right] \quad (5)$$

where T is the absolute temperature [K] and k_B is the Boltzmann constant, equal to $1.3806 \cdot 10^{-23}$ J K^{-1}. From a linear approximation for which $sinh(x) \approx x$ this equation becomes:

$$v = \frac{k^0\lambda^3}{k_BT}\gamma_{LV}(cos\theta_e - cos\theta_d) \quad (6)$$

In this approach the free parameters are: θ_e, λ, and k^0 (Ranabothu et al., 2005). Another simplified form of this equation can be written considering very small angles, for which $\cos\theta \approx 1 - \frac{\theta^2}{2}$ and, as a consequence, a polynomial function is obtained:

$$v = \frac{k^0\lambda^3}{k_BT}\gamma_{LV}\left(\frac{\theta_d^2 - \theta_e^2}{2}\right) \quad (7)$$

The term $\frac{k_BT}{k^0\lambda^3}$ in the Equations (6) and (7) was defined by Blake and De Coninck (Blake and De Coninck, 2002) as a contact line friction ξ and was related to the work of adhesion, as follows:

$$\xi = \frac{k_BT}{k^0\lambda^3} = \eta\left(\frac{v_L}{\lambda^3}\right)exp\left(\frac{\lambda^2 W_a}{k_BT}\right) \quad (8)$$

where v_L is the molecular flow volume and W_a is the work of adhesion:

$$W_a = \gamma_{LV}(1 + \cos\theta_e) \quad (9)$$

Then, if we replace the contact line friction in the linear (Equation 6) and in the simplified (Equation 7) equations, and we want to define the contact angles as a function of the capillary number, the equations become the followings:

$$(cos\theta_e - cos\theta_d) = \frac{\xi}{\eta}Ca \quad (10)$$

$$\theta_d^2 - \theta_e^2 = 2\frac{\xi}{\eta}Ca \quad (11)$$

It is interesting to note that, contrarily to the previous expressions (Equations 5–7) where free parameters were three (θ_e, k^0, and λ) now, if θ_e is known, there will be only one free parameter (ξ), as in the HDT. Moreover, if v_L can be determined, λ could be determined and then k_0 (Equation 8). Another important observation has to be made about the polynomial form of MKT for very small angles (Equation 11): this equation is very similar to the HDT law proposed by Cox-Voinov (Equation 2), but with exponent 2 vs. 3 for the HDT.

The predictions of these models for totally and partially wetting liquids at different temperature and viscosity conditions were here evaluated.

3. MATERIALS AND METHODS

3.1. Materials

3.1.1. Cellulosic Films

Cellulosic films, referenced as NatureFlex™ 23 NP and provided by Innovia films®, were used in this study. They were chosen as model substrates to analyse the wetting of plant fibers. Surface characterization of these films has been carried out in a previous work (Pucci et al., 2018). Before wetting tests, cellulosic films were immersed for 1 h in ethanol, to remove the glycerol on surface that had the function of plasticizer, and then they were ambient air-dried (23°C, 50% RH). To be able to carry out dynamic wetting tests (controlled liquid immersion and removal) on these films of thickness 23 μm while avoiding buckling when the sample touches the liquid, films of length 20 mm (along the immersion axis) and width 10 mm were used (Pucci et al., 2018).

3.1.2. Polymers

Polymers used to perform partial wetting tests in dynamic mode were three polyethylene glycols (PEGs). PEGs were chosen due to their large availability at different molecular weight and their quite low melting point. The first one with a molecular weight of 1450 g/mol (PEG1450) was provided by ACROS ORGANICS (ref. 418040010), its melting point was at 44 − 48°C. The second one with a molecular weight of 3,350 g/mol (PEG3350) was from DOW (ref. 19760), its melting point was at 53 − 57°C. The third one with a molecular weight of 10,000 g/mol (PEG10000) was from ALFA AESAR (ref. 10200251), its melting point was at 58−63°C. Their surface tension and viscosity beyond the melting point were measured as a function of temperature (sections 3.2.1, 3.2.2). Paraffin oil used to study the total wetting was provided by ACROS ORGANICS (ref. 171400010). Its melting point was at −24°C. Major details are reported in the previous work (Pucci et al., 2018).

3.2. Methods

3.2.1. Rheological Tests

A Physica MCR 501 rheometer from Anton Paar was used to measure viscosity of PEGs as a function of temperature. The used geometry was a standard cone/plate system with a 50 *mm* diameter, a 1° cone angle and a cone truncation of 50 μm. Preliminary tests were conducted varying the shear rate, assuring that liquids can be considered as Newtonian fluids at the tested conditions of dynamic wetting (Lu et al., 2016). Then, the shear rate was fixed at 100 s^{-1} and the temperature rate was set at 0.01 °C/s. Two rheological measurements for each liquid were performed in order to verify the repeatability.

3.2.2. Pendant and Sessile Drop Tests

A Krüss DSA100 tensiometer equipped with a thermalized syringe (DO3241) and a high temperature chamber (TC21) was used to measure surface tension of PEGs via the pendant drop method. This visual method permits measuring surface tension of liquids at very high temperatures (up to 400°C) (Berry et al., 2015), that is relevant for molten polymers. Knowing the needle diameter (it was of 1.65 mm in this study) and the liquid density, surface tension is determined from the fit of the pendant drop profile (**Figure 1A**) with the Laplace equation integrated in the Drop Shape Analysis 1.92.1.1 software (Song and Springer, 1996a,b). To determine liquid density at each test temperature, images of sessile drop on a microscope glass slide were acquired (**Figure 1B**) to obtain the volume of drop (this is also implemented in the software of DSA100) and each drop mass was measured. Test temperatures were 65, 75, 85, 95, and 105 °C. Three sessile drop tests were carried out to measure density and ten pendant drop tests to determine surface tension for each of these temperatures, in order to have reliable trend of surface tension vs. temperature. Supplementary details of this procedure are reported in Pucci et al. (2018).

3.2.3. The Wilhelmy Method: Spontaneous and Forced Wetting

A Krüss K100SF tensiometer with a temperature generator and control unit was used to perform dynamic wetting tests with cellulosic films and PEGs. Polymers were heated in the tensiometer up to the highest temperature that can be achieved with this set-up: T = 75°C, i.e., above the melting point.

In order to measure a static contact angle, that is ideally the apparent equilibrium contact angle (θ_e), tensiometric tests of spontaneous wetting were performed. The vessel containing the molten polymer raises at a constant velocity until the detection of the film surface. At this moment, a meniscus is spontaneously formed on the perimeter of the film (the wetted length p), resulting in an increase of the liquid mass m that is recorded by the tensiometer. This increase occurs up to a constant value that defines the static condition of meniscus (equilibrium condition). Therefore, this mass can be used in the Wilhelmy equation to determine a static contact angle:

$$F = mg = p\gamma_{LV}\cos\theta \tag{12}$$

where F is the capillary force.

Figure 2 shows curves recorded by the tensiometer of spontaneous wetting on cellulosic substrates for PEG1450, 3350, and 10000. It is possible to observe that the time to reach the static condition (achieving a constant value of meniscus mass) increases with Mn. However, after 120 s static conditions were achieved for all PEGs.

To determine dynamic contact angles θ_d, forced wetting was also performed at the K100SF tensiometer. Different velocities were imposed for immersion and withdrawal of cellulosic film in liquid, from 0.1 to 500 mm/min, in order to obtain experimental measurements in a large range of capillary numbers. Cellulosic film was first immersed in the liquid vessel by the upward motion of the latter (advancing mode), then it was maintained at this position for 120 s (static advancing mode), and finally it was withdrawn from the bath up to the initial position (receding

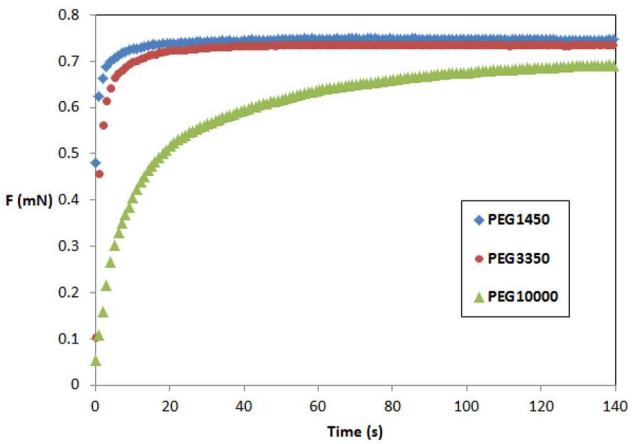

FIGURE 2 | Spontaneous dynamic wetting curves obtained at the tensiometer.

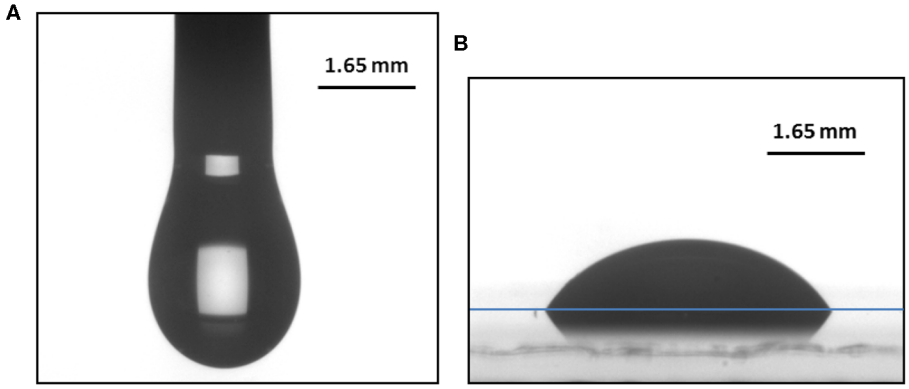

FIGURE 1 | (A) Pendant drop of PEG10000 at T = 95°C. **(B)** Sessile drop of PEG10000 at 95°C on a microscope glass slide.

motion). Further details of test are described in Pucci et al. (2018). Buoyancy correction was neglected here (Pucci et al., 2017a). At very low velocities it can occur that the force referring to the static contact angle does not differ from the advancing and receding ones (as in **Figure 3**). **Figure 3** shows a forced wetting test for PEG1450 on the cellulosic film at $v = 0.5$ mm/min. This static condition was then used to determine a static contact angle from forced wetting tests. Moreover, since the hysteresis is ≈ 0, this confirms that substrates can be approximated as ideal, that means physico-chemically homogeneous (Schneemilch et al., 1998).

Mean values of capillary forces obtained at the tensiometer in the advancing, static and receding modes were used to find the advancing and receding contact angles by means of the Wilhelmy equation (Equation 12). Static contact angles obtained by the spontaneous wetting and the forced one at the lowest velocity were compared. These values can be inserted into models predicting dynamic wetting, in order to reduce the number of free parameters to fit.

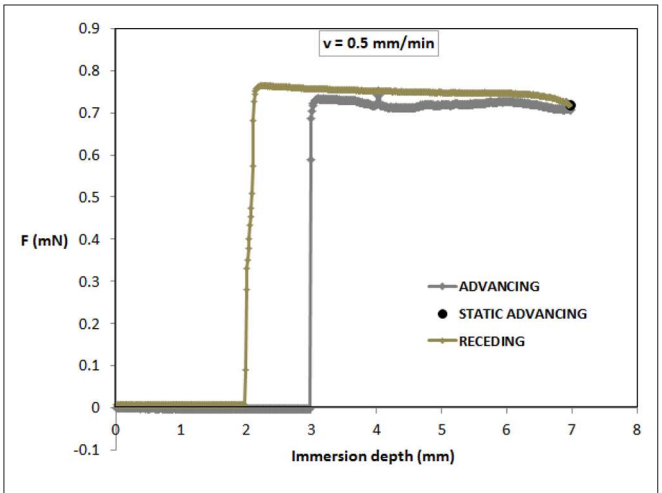

FIGURE 3 | Forced dynamic wetting curve for PEG1450 on cellulosic film at $v = 0.5$ mm/min.

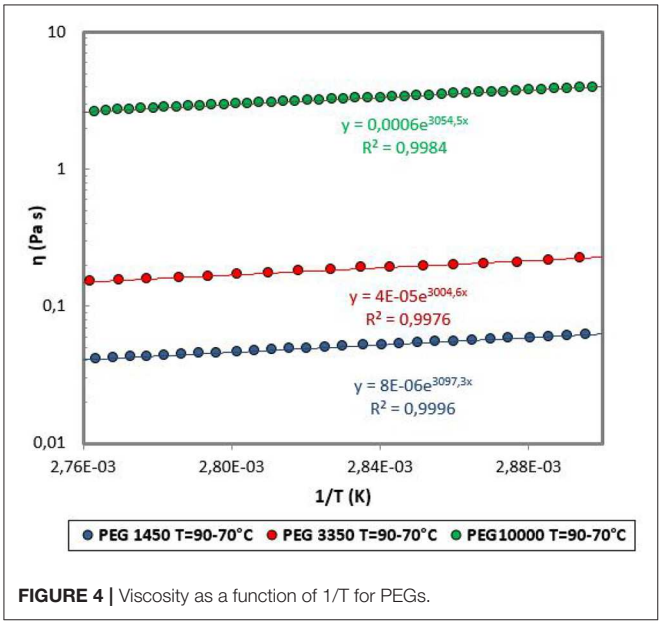

FIGURE 4 | Viscosity as a function of 1/T for PEGs.

4. RESULTS AND DISCUSSION

4.1. Liquid Viscosity and Surface Tension

Viscosity was measured as a function of temperature from T = 70°C (above the melting point) to 90°C. **Figure 4** shows results of experimental semi-logarithmic curves obtained by using the rheometer for the three PEGs as a function of 1/T. As expected, the higher molecular mass PEG has the highest viscosity. The dependence of viscosity on temperature is exponential and well described by the Arrhenius law.

About surface tension determination, images of pendant and sessile drops were acquired at different temperatures and **Figure 5** shows surface tension as a function of temperature. The surface tension decreases linearly as a function of temperature, according to the law of

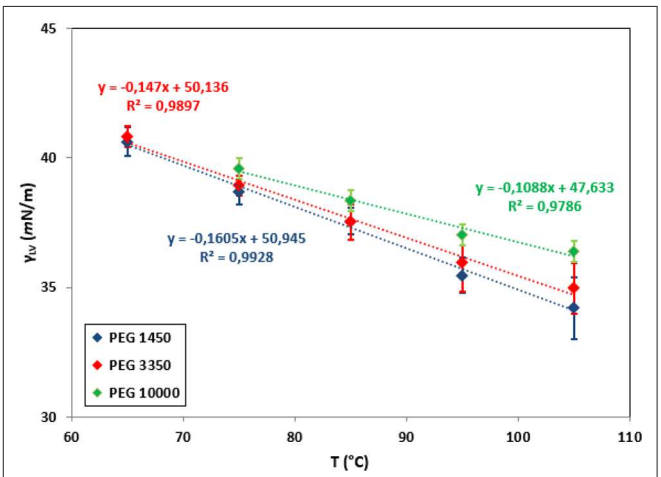

FIGURE 5 | Surface tension as a function of temperature for PEGs.

TABLE 1 | Viscosity, density, and surface tension of polymers at $T = 75°C$.

$T = 75°C$	η (Pa s)	ρ (g/cm^3)	γ_{LV} (mN/m)
PEG1450	0.056 ± 0.001	1.090 ± 0.030	38.9 ± 0.5
PEG3350	0.207 ± 0.002	1.091 ± 0.030	39.1 ± 0.4
PEG10000	3.519 ± 0.030	1.092 ± 0.030	39.5 ± 0.4
Paraffin oil (Pucci et al., 2018)	0.016 ± 0.006	0.830 ± 0.030	21.9 ± 0.7

TABLE 2 | Comparison of static contact angles obtained in spontaneous and forced wetting modes with PEGs at $T = 75°C$.

$T = 75°C$	$\theta_{s,spont}$ (rad)	$\theta_{s,forc}$ (rad)
PEG1450	0.31 ± 0.04	0.33 ± 0.06
PEG3350	0.36 ± 0.05	0.38 ± 0.09
PEG10000	0.45 ± 0.03	0.49 ± 0.06

Eötvös (Sauer and Dipaolo, 1991; Grundke et al., 1996). Moreover, surface tension is higher for PEG with highest molecular weight. Another important observation is that the difference in surface tension due to *Mn* is more significant as temperature increases (Moreira and Demarquette, 2001).

Viscosities, densities and surface tensions values obtained for the PEGs at T = 75°C are given in **Table 1**. Comparing with paraffin oil used in a previous work at T = 75°C (Pucci et al., 2018), it is possible to observe that the range of viscosity is significantly different for PEGs, due to the molecular weight. The surface tension of PEGs is also higher than for paraffin oil, due to the fact that they are partially wetting liquids.

4.2. Static Contact Angle

In order to determine a static contact angle from spontaneous wetting curves, the constant force value achieved at static conditions (beyond a hold for 120 s) was inserted into the Wilhelmy equation (Equation 12). In parallel, tensiometric curves of forced wetting with the lowest velocity were used to obtain the mass of meniscus in the static condition, 120 s after the advancing and just before the receding (as shown in **Figure 3**). The Wilhelmy equation was also used in this case. **Table 2** shows static contact angle values obtained with both methods, from the spontaneous and the forced wetting. Values correspond to an average with a standard deviation over three measurements.

The two sets of values obtained with the two methods are in agreement. The angles obtained for the forced wetting are slightly higher due to the dependence on velocity, that makes them quasi-static contact angles or static advancing contact angles (Pucci et al., 2017b). Values obtained in the spontaneous configuration were then used as θ_e in models predicting dynamic wetting.

4.3. Advancing and Receding Contact Angles

The advancing and receding contact angles were determined according to the Wilhelmy principle as a function of the immersion and withdrawal velocity. **Figure 6** shows the results obtained for PEGs at $T = 75°C$ on cellulosic films at different velocities.

The advancing contact angle increases when the velocity of immersion is increased (Petrov et al., 2003). Moreover, for a given velocity, the larger the *Mn* of PEG, the higher the advancing contact angle. These results also correlate with higher viscosity and higher surface tension for large *Mn*, which implies a higher *Ca* (Equation 1). Therefore, it is relevant to further discuss the results as a function of the *Ca* (sections 4.4, 4.5).

On the other hand, the receding contact angle decreases when the withdrawal velocity increases, and at a given velocity, this parameter also decreases when *Mn* is increased. Moreover, for each polymer, there is a transition from partial to total wetting. This transition was reported in literature (Brochard-Wyart and De Gennes, 1992; Maleki et al., 2007, 2011). In this study, it appears that the transition occurs at lower velocity when *Mn* is higher. Modeling of dewetting was not carried out, but this issue could be addressed in future works. The prediction of advancing contact angle with the HDT and the MKT was then undertaken for PEGs and compared with the behavior of totally wetting liquids at different temperatures (i.e., paraffin oil Pucci et al., 2018).

4.4. HDT Prediction

To fit with models the experimental data of advancing contact angle as a function of *Ca*, parameters such as the capillary length k^{-1} and the ratio of viscosity on surface tension (η/γ_{LV}) were determined for each polymer. These parameters are compared with those of paraffin oil (Pucci et al., 2018) in **Table 3**.

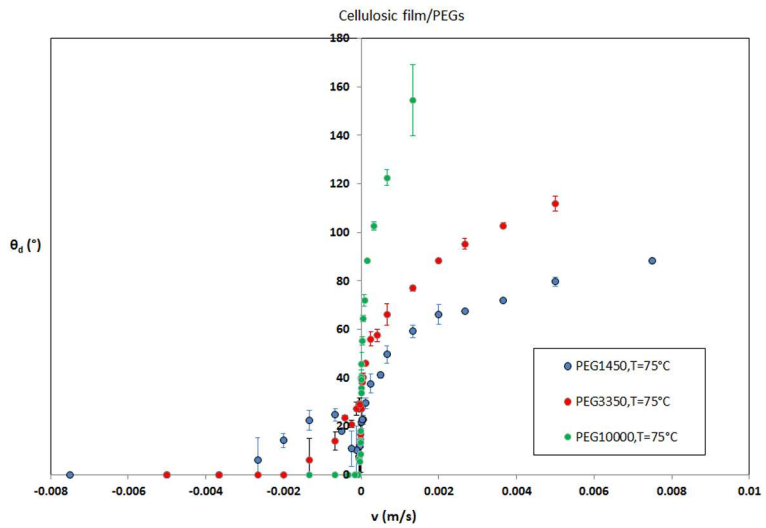

FIGURE 6 | Dynamic contact angles as a function of the immersion and withdrawal velocity.

For paraffin oils it has been proven in Pucci et al. (2018) that the HDT fits well the experimentally measured values of contact angles for $Ca > 2 \cdot 10^{-3}$. In the same way, fits of experimental data for PEGs with Cox-Voinov law were carried out, imposing the measured static contact angle, in order to estimate the free parameter Γ. In addition, an analysis was undertaken to assess the sensitivity of Γ to the parameters determined experimentally. It was carried out in terms of the number of measurements of contact angles (N points in **Figure 7**, referring to the average values over three measurements) and *Ca* for each PEG, starting from the lowest *Ca* value and expanding to the higher values, then in the opposite direction. Histograms in **Figure 7** show results of sensitivity analysis: the bars indicate the Γ values and the gray triangles represent the coefficients of determination (COD) R^2. For all PEGs, we note that when *Ca* increases (graphs on the left side in **Figure 7**), Γ decreases continuously while COD increases from a low value (around 0.6 for $Ca = 7 \cdot 10^{-5}$ in the case of PEG1450) to reach a plateau of around 0.99 beyond

TABLE 3 | Capillary length and viscosity to surface tension ratio for polymers.

	k^{-1} (*mm*)	(η/γ_{LV}) (s/*m*)
PEG1450, 75°*C*	1.90 ± 0.09	1.44 ± 0.01
PEG3350, 75°*C*	1.91 ± 0.07	5.29 ± 0.01
PEG10000, 75°*C*	1.92 ± 0.07	89.15 ± 0.25
Paraffin oil (Pucci et al., 2018), 25°*C*	1.80 ± 0.17	5.38 ± 0.11
Paraffin oil (Pucci et al., 2018), 50°*C*	1.71 ± 0.34	1.73 ± 0.20
Paraffin oil (Pucci et al., 2018), 75°*C*	1.63 ± 0.23	0.77 ± 0.20

FIGURE 7 | Sensitivity of Γ for PEG1450 (blue), PEG3350 (red), and PEG10000 (green): from the lowest *Ca* to the highest one **(left)**; from the highest *Ca* to the lowest one **(right)**.

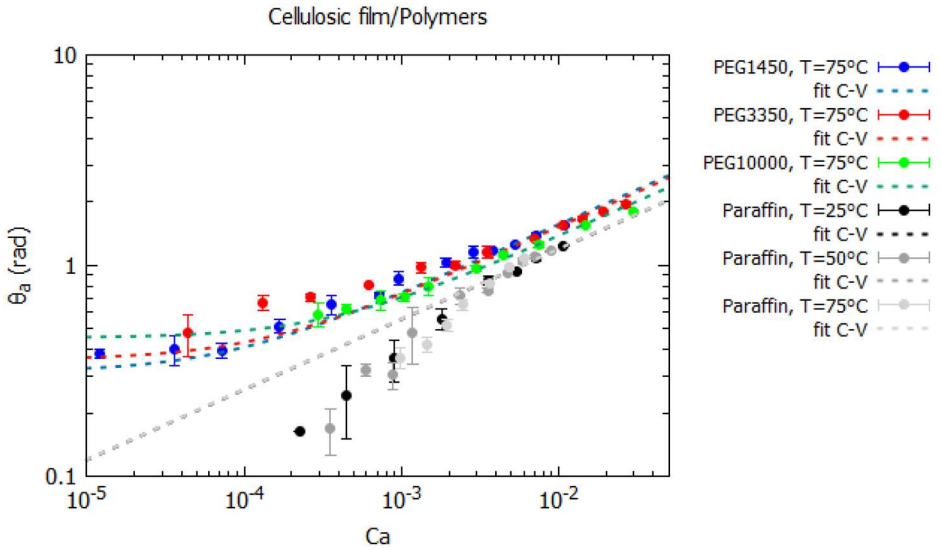

FIGURE 8 | θ_a as a function of *Ca* for polymers at different temperatures on cellulosic films and prediction of Cox-Voinov law.

$Ca = 2 \cdot 10^{-3}$ (case of PEG1450). Here we find the transition threshold mentioned above for paraffins. This threshold is more difficult to determine for PEG3350 and PEG10000, but the $Ca = 2 \cdot 10^{-3}$ is well at the limit of the zones of strong variation of R^2. When *Ca* is varied from high values to low values (**Figure 7**—right side), the variation of Γ is much less pronounced than in the previous mode. For PEG1450 high and stable values of R^2 are observed for $Ca > 2 \cdot 10^{-3}$. The threshold is difficult to detect on the graphs of PEG3350 and PEG10000. However, the Γ value is stable and lower in the same range for all *Mn* values. Therefore, results confirm that this threshold is valid for totally and partially wetting polymers and at different temperatures. The HDT, and particularly Cox-Voinov (C-V) law, fits well forced wetting behavior for $Ca > 2 \cdot 10^{-3}$, in agreement with results found in literature (Petrov et al., 2003).

Figure 8 shows experimental results of θ_d vs. *Ca* and HDT prediction for $Ca > 2 \cdot 10^{-3}$. This graph shows well the difference between total and partial wetting (paraffin oil vs. PEGs). Paraffin oil at different temperatures is well-predicted by Cox-Voinov law for $Ca > 2 \cdot 10^{-3}$ and a master curve was found (Pucci et al., 2018). Below the threshold, at low *Ca*, a change in slope occurs. For PEGs, fit curves are different as a function of *Mn* and well predict wetting behavior for $Ca > 2 \cdot 10^{-3}$. At low *Ca* the θ_a tends to the static contact angle. Anyway, for all polymers a change of behavior was observed at the threshold of $Ca = 2 \cdot 10^{-3}$.

Γ and R^2 values derived from the fits with imposed static contact angles for the PEGs are compared to previous results measured for paraffins (Pucci et al., 2018) at different temperatures in **Table 4**. Γ for paraffin oil was found to be consistent with estimated values from the molecular sizes (Pucci et al., 2018) and not dependent on temperature. For PEGs, the sizes of macromolecules depend on *Mn* and estimating x_{min} (in Equation 4) is a difficult question. However, Γ decreases with the increase of *Mn*, suggesting an increase of x_{min}.

TABLE 4 | Obtained parameters from HDT fit at high *Ca* for partially and totally wetting polymers.

	$\theta_{s,imposed}$ (rad)	Γ from fit for $Ca > 2 \cdot 10^{-3}$	R^2
PEG1450, 75°*C*	0.31	42.5 ± 3.0	0.975
PEG3350, 75°*C*	0.36	39.1 ± 2.1	0.997
PEG10000, 75°*C*	0.45	28.7 ± 1.3	0.994
Paraffin (Pucci et al., 2018), 25°*C*	0	19.0 ± 0.7	0.984
Paraffin (Pucci et al., 2018), 50°*C*	0	19.2 ± 1.1	0.965
Paraffin (Pucci et al., 2018), 75°*C*	0	19.2 ± 2.4	0.997

Figure 9 shows the diminution of Γ as a function of *Mn*, which seems to be well described by a linear law. Further works would focus on the application of HDT in the case of partially wetting polymers as well as the linear dependence of Γ to *Mn* and how to include these results in the models to predict dynamic wetting behavior.

4.5. MKT Prediction

At low *Ca* ($Ca < 2 \cdot 10^{-3}$) the MKT was evaluated for total and partial wetting of polymers on cellulosic substrates. This theory may predict dynamic of wetting at a microscopic (or local) scale, considering microscopic contact angles (Petrov et al., 2003; Bonn et al., 2009).

In order to consider this theory for total wetting and particularly for paraffin, the static contact angle was assumed equal to 0 as in the case of the HDT. Regarding the dynamic contact angles, since the advancing contact angles at low velocity were found to be very small, the polynomial form of MKT (Equation 11) was applied to experimental data for $Ca < 2 \cdot 10^{-3}$. **Figure 10** shows the results, indicating that for paraffin oil this

law fits quite well the experimental data at different temperatures and at $Ca < 2 \cdot 10^{-3}$, allowing to obtain the coefficient of contact line friction ξ (Blake and De Coninck, 2002), shown in **Table 5**. The coefficient of contact line friction decreases as the temperature is increased, and then it is higher when the viscosity is higher, according to the literature (Zhang et al., 2017).

Regarding the partial wetting with PEGs at low *Ca*, the assumption of very small contact angles does not hold, but the linear approximation of MKT (Equation 10) was used. **Figure 8** shows the results of fit, indicating that the model do not predict well the wetting behavior of PEGs at low *Ca*, with aberrant results (ξ and R^2 of fit are shown in **Table 5**). The reason could be related to the measurements of static contact angles that do not fulfill the MKT assumption of a microscopic contact angle. Measured values of apparent contact angles are better described by the HDT (**Figure 8**). However, further works should be carried out on the MKT and the meaning of microscopic contact angles, mainly with partially wetting liquids like molten polymers used for composites processing.

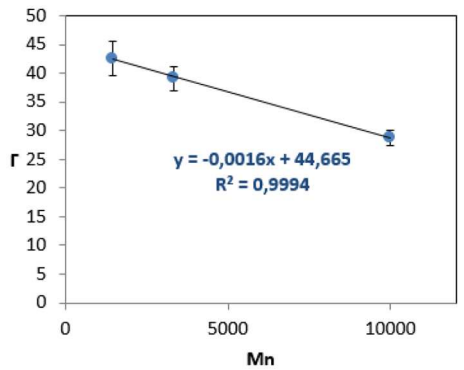

FIGURE 9 | Γ obtained from the HDT fit for $Ca > 2 \cdot 10^{-3}$ vs. *Mn*.

5. CONCLUSION

An experimental study of the forced dynamic wetting of molten polymers on cellulosic films was carried out, with comparisons to hydrodynamic and molecular kinetic models. The interest here was to test some conditions of wetting (low and high *Ca* at different *T* and *Mn*) and to find relevant parameters affecting the manufacturing of composites with a liquid resin, thermoset or thermoplastic. To the best of our knowledge, wetting with molten polymers is poorly known and little documented in literature. An experimental procedure was carried out to measure liquid properties and static and dynamic contact angles at different conditions. The results proved that HDT models can be applied to totally and partially wetting polymers for high *Ca*, but parameters found from models are surprising in the case of PEGs depending on the *Mn*. At low *Ca*, the total wetting can be described by the MKT because the contact angles are small, but this theory do not predict the dynamic behavior of partially wetting polymers. At low *Ca* for PEGs, the advancing contact angle decreases toward the static one and

TABLE 5 | Obtained parameters from MKT fit at low *Ca* for partially and totally wetting polymers.

	$\theta_{s,imposed}$ (rad)	ξ from fit for $Ca < 2 \cdot 10^{-3}$ (Pa s)	R^2
Paraffin (Pucci et al., 2018), 25°C	0	11.1 ± 1.9	0.982
Paraffin (Pucci et al., 2018), 50°C	0	3.9 ± 0.6	0.956
Paraffin (Pucci et al., 2018), 75°C	0	1.0 ± 0.3	0.906
PEG1450, 75°C	0.31	15.3 ±1.4	0.916
PEG3350, 75°C	0.36	73.4 ±15.2	0.586
PEG10000, 75°C	0.45	522.1 ± 42.1	0.842

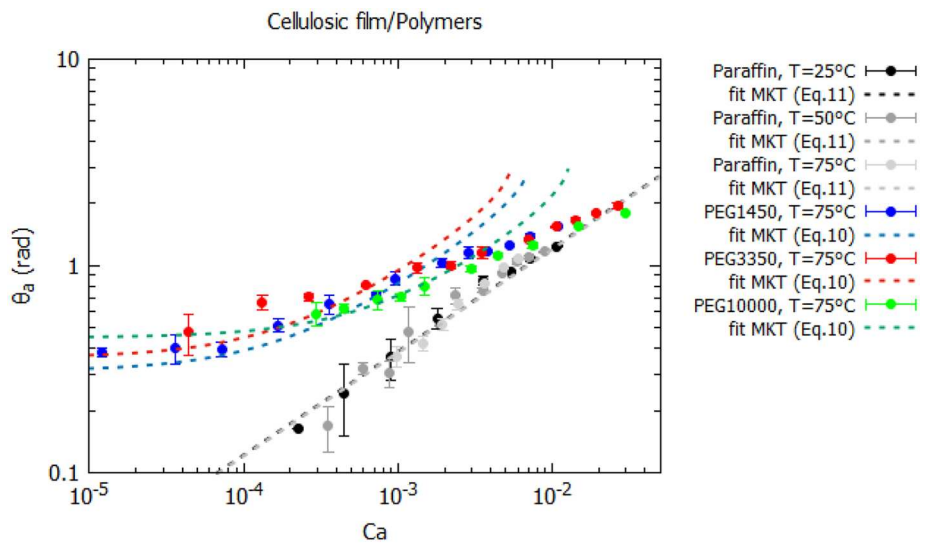

FIGURE 10 | θ_a as a function of *Ca* for polymers at different temperatures on cellulosic films and prediction of MKT.

further analyses have to be developed, in order to establish new models describing this behavior. Reliable parameters of dynamic wetting could be then inserted into numerical models predicting flow processes.

DATA AVAILABILITY STATEMENT

All datasets generated for this study are included in the article/supplementary material.

AUTHOR CONTRIBUTIONS

All authors listed have made a substantial, direct and intellectual contribution to the work, and approved it for publication.

FUNDING

Authors would thank Bpifrance for the financial support in this study and the Depestele Group for providing materials.

REFERENCES

Abdelwahed, M. A. B., Wielhorski, Y., Bizet, L., and Bréard, J. (2014). Bubble formation and transport in t-junction for application to liquid composite molding: wetting effect. *J. Compos. Mater*. 48, 37–48. doi: 10.1177/0021998312467553

Berry, J. D., Neeson, M. J., Dagastine, R. R., Chan, D. Y., and Tabor, R. F. (2015). Measurement of surface and interfacial tension using pendant drop tensiometry. *J. Colloid Interface Sci*. 454, 226–237. doi: 10.1016/j.jcis.2015.05.012

Blake, T., and De Coninck, J. (2002). The influence of solid-liquid interactions on dynamic wetting. *Adv. Colloid Interface Sci*. 96, 21–36. doi: 10.1016/S0001-8686(01)00073-2

Blake, T., and Haynes, J. (1969). Kinetics of liquidliquid displacement. *J. Colloid Interface Sci*. 30, 421–423. doi: 10.1016/0021-9797(69)90411-1

Bonn, D., Eggers, J., Indekeu, J., Meunier, J., and Rolley, E. (2009). Wetting and spreading. *Rev. Modern Phys*. 81:739. doi: 10.1103/RevModPhys.81.739

Bréard, J., Henzel, Y., Trochu, F., and Gauvin, R. (2003). Analysis of dynamic flows through porous media. Part I: comparison between saturated and unsaturated flows in fibrous reinforcements. *Polym. Compos*. 24, 391–408. doi: 10.1002/pc.10038

Brochard-Wyart, F., and De Gennes, P. (1992). Dynamics of partial wetting. *Adv. Colloid Interface Sci*. 39, 1–11. doi: 10.1016/0001-8686(92)80052-Y

Caglar, B., Tekin, C., Karasu, F., and Michaud, V. (2019). Assessment of capillary phenomena in liquid composite molding. *Compos. Part A Appl. Sci. Manufact*. 120, 73–83. doi: 10.1016/j.compositesa.2019.02.018

Cox, B. (1962). On driving a viscous fluid out of a tube. *J. Fluid Mech*. 14, 81–96. doi: 10.1017/S0022112062001081

De Gennes, P.-G. (1985). Wetting: statics and dynamics. *Rev. Modern Phys*. 57:827. doi: 10.1103/RevModPhys.57.827

De Gennes, P.-G., Brochard-Wyart, F., and Quéré, D. (2013). *Capillarity and Wetting Phenomena: Drops, Bubbles, Pearls, Waves*. Springer Science & Business Media.

Duursma, G., Sefiane, K., and David, S. (2010). Advancing and receding contact lines on patterned structured surfaces. *Chem. Eng. Res. Design* 88, 737–743. doi: 10.1016/j.cherd.2009.10.004

Duvivier, D., Seveno, D., Rioboo, R., Blake, T., and De Coninck, J. (2011). Experimental evidence of the role of viscosity in the molecular kinetic theory of dynamic wetting. *Langmuir* 27, 13015–13021. doi: 10.1021/la202836q

Grundke, K., Uhlmann, P., Gietzelt, T., Redlich, B., and Jacobasch, H.-J. (1996). Studies on the wetting behaviour of polymer melts on solid surfaces using the wilhelmy balance method. *Colloids Surf. A* 116, 93–104. doi: 10.1016/0927-7757(96)03624-2

Hansen, D., Bomholt, N., Jeppesen, J. C., and Simonsen, A. C. (2017). Contact angle goniometry on single micron-scale fibers for composites. *Appl. Surf. Sci*. 392, 181–188. doi: 10.1016/j.apsusc.2016.09.018

Kumar, S. M., and Deshpande, A. P. (2006). Dynamics of drop spreading on fibrous porous media. *Colloids Surf. A* 277, 157–163. doi: 10.1016/j.colsurfa.2005.11.056

Le Grand, N., Daerr, A., and Limat, L. (2005). Shape and motion of drops sliding down an inclined plane. *J. Fluid Mech*. 541, 293–315. doi: 10.1017/S0022112005006105

Lu, G., Wang, X.-D., and Duan, Y.-Y. (2016). A critical review of dynamic wetting by complex fluids: from newtonian fluids to non-newtonian fluids and nanofluids. *Adv. Colloid Interface Sci*. 236, 43–62. doi: 10.1016/j.cis.2016.07.004

Maleki, M., Reyssat, E., Quéré, D., and Golestanian, R. (2007). On the landau-levich transition. *Langmuir* 23, 10116–10122. doi: 10.1021/la700822y

Maleki, M., Reyssat, M., Restagno, F., Quéré, D., and Clanet, C. (2011). Landau-levich menisci. *J. Colloid Interface Sci*. 354, 359–363. doi: 10.1016/j.jcis.2010.07.069

Marsh, J. A., Garoff, S., and Dussan, E. B. (1993). Dynamic contact angles and hydrodynamics near a moving contact line. *Phys. Rev. Lett*. 70:2778. doi: 10.1103/PhysRevLett.70.2778

Mohammad Karim, A., Davis, S., and Kavehpour, H. (2016). Forced versus spontaneous spreading of liquids. *Langmuir* 32, 10153–10158. doi: 10.1021/acs.langmuir.6b00747

Moreira, J. C., and Demarquette, N. R. (2001). Influence of temperature, molecular weight, and molecular weight dispersity on the surface tension of PS, PP, and PE. I. experimental. *J. Appl. Polym. Sci*. 82, 1907–1920. doi: 10.1002/app.2036

Park, C. H., Lebel, A., Saouab, A., Bréard, J., and Lee, W. I. (2011). Modeling and simulation of voids and saturation in liquid composite molding processes. *Compos. Part A* 42, 658–668. doi: 10.1016/j.compositesa.2011.02.005

Petrov, J. G., Ralston, J., Schneemilch, M., and Hayes, R. A. (2003). Dynamics of partial wetting and dewetting in well-defined systems. *J. Phys. Chem. B* 107, 1634–1645. doi: 10.1021/jp026723h

Prevost, A., Rolley, E., and Guthmann, C. (1999). Thermally activated motion of the contact line of a liquid 4 he meniscus on a cesium substrate. *Phys. Rev. Lett*. 83:348. doi: 10.1103/PhysRevLett.83.348

Pucci, M. F., Duchemin, B., Gomina, M., and Bréard, J. (2018). Temperature effect on dynamic wetting of cellulosic substrates by molten polymers for composite processing. *Compos. Part A* 114, 307–315. doi: 10.1016/j.compositesa.2018.08.031

Pucci, M. F., Liotier, P.-J., and Drapier, S. (2015). Capillary effects on flax fibers-modification and characterization of the wetting dynamics. *Compos. Part A* 77, 257–265. doi: 10.1016/j.compositesa.2015.03.010

Pucci, M. F., Liotier, P.-J., and Drapier, S. (2017a). Tensiometric method to reliably assess wetting properties of single fibers with resins: validation on cellulosic reinforcements for composites. *Colloids Surf. A* 512, 26–33. doi: 10.1016/j.colsurfa.2016.09.047

Pucci, M. F., Liotier, P.-J., Seveno, D., Fuentes, C., Van Vuure, A., and Drapier, S. (2017b). Wetting and swelling property modifications of elementary flax fibres and their effects on the liquid composite molding process. *Compos. Part A* 97, 31–40. doi: 10.1016/j.compositesa.2017.02.028

Ranabothu, S. R., Karnezis, C., and Dai, L. L. (2005). Dynamic wetting: hydrodynamic or molecular-kinetic? *J. Colloid Interface Sci*. 288, 213–221. doi: 10.1016/j.jcis.2005.02.074

Ruiz, E., Achim, V., Soukane, S., Trochu, F., and Bréard, J. (2006). Optimization of injection flow rate to minimize micro/macro-voids formation in resin transfer molded composites. *Compos. Sci. Technol*. 66, 475–486. doi: 10.1016/j.compscitech.2005.06.013

Sauer, B. B., and Dipaolo, N. V. (1991). Surface tension and dynamic wetting on polymers using the wihelmy method: applications to high molecular weights and elevated temperatures. *J. Colloid Interface Sci*. 144, 527–537. doi: 10.1016/0021-9797(91)90418-8

Sauer, B. B., and Kampert, W. G. (1998). Influence of viscosity on forced and spontaneous spreading: Wilhelmy fiber studies including practical

methods for rapid viscosity measurement. *J. Colloid Interface Sci.* 199, 28–37. doi: 10.1006/jcis.1997.5319

Schneemilch, M., Hayes, R. A., Petrov, J. G., and Ralston, J. (1998). Dynamic wetting and dewetting of a low-energy surface by pure liquids. *Langmuir* 14, 7047–7051. doi: 10.1021/la980476k

Seveno, D., Vaillant, A., Rioboo, R., Adao, H., Conti, J., and De Coninck, J. (2009). Dynamics of wetting revisited. *Langmuir* 25, 13034–13044. doi: 10.1021/la901125a

Snoeijer, J. H., and Andreotti, B. (2013). Moving contact lines: scales, regimes, and dynamical transitions. Annu. Rev. Fluid Mech. 45, 269–292. doi: 10.1146/annurev-fluid-011212-140734

Song, B., and Springer, J. (1996a). Determination of interfacial tension from the profile of a pendant drop using computer-aided image processing: 1. theoretical. *J. Colloid Interface Sci.* 184, 64–76. doi: 10.1006/jcis.1996.0597

Song, B., and Springer, J. (1996b). Determination of interfacial tension from the profile of a pendant drop using computer-aided image processing: 2. experimental. *J. Colloid Interface Sci.* 184, 77–91. doi: 10.1016/S0021-9797(96)90598-6

Tanner, L. (1979). The spreading of silicone oil drops on horizontal surfaces. *J. Phys. D* 12:1473. doi: 10.1088/0022-3727/12/9/009

Verrey, J., Michaud, V., and Månson, J.-A. (2006). Dynamic capillary effects in liquid composite moulding with non-crimp fabrics. *Compos. Part A* 37, 92–102. doi: 10.1016/j.compositesa.2005.04.011

Voinov, O. (1976). Hydrodynamics of wetting. *Fluid Dyn.* 11, 714–721. doi: 10.1007/BF01012963

Wielhorski, Y., Abdelwahed, M. A. B., Bizet, L., and Bréard, J. (2012). Wetting effect on bubble shapes formed in a cylindrical t-junction. *Chem. Eng. Sci.* 84, 100–106. doi: 10.1016/j.ces.2012.08.008

Zhang, Y., Fuentes, C. A., Koekoekx, R., Clasen, C., Van Vuure, A. W., De Coninck, J., et al. (2017). Spreading dynamics of molten polymer drops on glass substrates. *Langmuir* 33, 8447–8454. doi: 10.1021/acs.langmuir.7b01500

Zhang, Y., Moins, S., Coulembier, O., Seveno, D., and De Coninck, J. (2019). Capillary rise of polydimethylsiloxane around a poly (ethylene terephthalate) fiber versus viscosity: existence of a sharp transition in the dynamic wetting behavior. *J. Colloid Interface Sci.* 536, 499–506. doi: 10.1016/j.jcis.2018.10.082

Conflict of Interest: The authors declare that this study received funding from Bpifrance. The funder was not involved in the study design, collection, analysis, interpretation of data, the writing of this article or the decision to submit it for publication.

Energy Materials

Vanessa Fierro

Prof. Vanessa Fierro is a CNRS Research Professor at Institut Jean Lamour, France, a joint laboratory of the University of Lorraine and the CNRS, where she heads the Bio-sourced Materials Research Team. Vanessa has over 300 scientific publications, an h-index of 57 (Google Scholar, accessed February 2021), and an extensive background in porous materials for energy and environmental applications. She received the Charles E. Pettinos Award from the American Carbon Society in 2019 and the CNRS Silver Medal in 2020.

Maria Victoria Martínez-Huerta

Dr. Mª Victoria Martínez Huerta is a Senior Scientist from CSIC at the Institute of Catalysis and Petrochemistry (ICP) and has been the Head of the Group Electrocatalysis for Energy and Environment since 2018. Its lines of research are linked to the development of sustainable electrocatalysts for energy conversion and storage and environmental applications that involve a reduction in the environmental impact derived from the use of fossil fuels, mainly in those applications that use hydrogen as an energy carrier, such as fuel cells, electrolyzers, and unitized regenerative fuel cells.

Maria Jesus Lazaro

Dr. Mª Jesús Lázaro (Ph.D. in Chemistry) is a Research Professor at the CSIC at the Instituto de Carboquímica (ICB_CSIC). She has more than 250 publications in indexed scientific journals (H Scopus = 49, H WOS = 46). She has carried out more than 90 projects and contracts related to the conversion and storage of clean energy, developing catalysts and materials for fuel cells, electrolyzers, and batteries. She is the Institutional Delegate of CSIC in Aragon. In addition, she is the president of the Spanish Coal Group of the European Carbon and the AMIT-Aragón.

frontiers in Materials

REVIEW
published: 22 July 2020
doi: 10.3389/fmats.2020.00217

Energy Storage in Supercapacitors: Focus on Tannin-Derived Carbon Electrodes

*Jimena Castro-Gutiérrez, Alain Celzard and Vanessa Fierro**

Université de Lorraine, CNRS, IJL, Epinal, France

Supercapacitors (SCs) are energy storage devices that bridge the gap between batteries and conventional capacitors. They can store more energy than capacitors and supply it at higher power outputs than batteries. These features, combined with high cyclability and long-term stability, make SCs attractive devices for energy storage. SCs are already present in many applications, either in combination with other energy storage devices (mainly batteries), or as autonomous energy sources. Porous carbons are presently used in the electrodes of commercial SCs due to their high surface area and their good conductivity. However, new porous materials are continuously being developed. Herein, an outline of the principles of the energy storage mechanism in SCs is presented as a guide to illustrate the research on porous carbons materials for SC applications. Indeed, an overview of these carbons and their synthesis methods is also presented. In the context of an urgent need to progress toward the development of environmentally friendly technologies and methods, the final part of this review focuses on the studies carried out using biosourced carbon precursors, such as tannins, which are natural polyphenolic molecules. In particular, mimosa tannin-derived carbon materials with controlled micro- and mesoporosity can be produced by methods with lower environmental impact and lower health and safety risks because crosslinkers are not needed to produce resins.

Keywords: supercapacitors, energy storage, porous carbons, OMCs, tannins

OPEN ACCESS

Edited by:
Emilia Morallon,
University of Alicante, Spain

Reviewed by:
Ramiro Ruiz Rosas,
University of Malaga, Spain
Juan Manuel Sieben,
Universidad Nacional del Sur, Argentina

****Correspondence:***
Vanessa Fierro
vanessa.fierro@univ-lorraine.fr

Specialty section:
This article was submitted to Energy Materials, a section of the journal Frontiers in Materials

Received: *08 May 2020*
Accepted: *12 June 2020*
Published: *22 July 2020*

Citation:
Castro-Gutiérrez J, Celzard A and Fierro V (2020) Energy Storage in Supercapacitors: Focus on Tannin-Derived Carbon Electrodes. Front. Mater. 7:217. doi: 10.3389/fmats.2020.00217

INTRODUCTION

World's electricity consumption has increased significantly in recent decades, from ∼11,000 TWh in 1990 to ∼23,000 TWh in 2016, according to the International Energy Agency (IEA), and there is still a strong dependence on fossil fuels such as coal, oil and gas as energy sources (IEA, 2019). Furthermore, it is generally agreed that the increasing concentration of greenhouse gases in the atmosphere from the 1950s is partly attributable to the burning of fossil fuels, which is causing global climate change (Pachauri et al., 2015). The limits of fossil fuels reserves and the increasing global warming have amplified awareness on the need to phase out the fossil fuel industry. The transition to energy production from renewable sources and environmentally friendly technologies is a public demand. This poses a challenge for the production of electricity based on fluctuating energy sources such as solar or wind, among others. Thus, research aiming to improve the performance of energy storage devices is of great relevance nowadays.

The role of energy storage devices in the electrical system is to collect excess of energy during high production peaks and act as a reservoir, releasing energy when required. **Figure 1A** lists some of the different storage technologies used at different steps of the electrical system (IEA, 2014; Aneke and Wang, 2016). Pumped-storage hydropower and compressed air energy storage are widely used in electric power plants for large-scale production. On the other hand, batteries are suitable for a wider range of mid- and short-term storage applications such as distribution to remote sites, electric vehicles, small-scale production and off-grid storage for houses or buildings, and portable electronic devices also rely on battery use. On the contrary, supercapacitors (SCs) are high-power devices, meaning that they can supply stored energy at fast rates, and they are mostly used in short-term applications where bursts of electricity are needed.

SCs are presently used in a variety of applications, which could be further developed as stand-alone energy suppliers if their energy densities were increased (Sharma and Bhatti, 2010; Aneke and Wang, 2016; González et al., 2016; Wang et al., 2016). Accordingly, the international community has established the pursuit of improving the SCs performances as one of the short-term actions in the context of research and development on energy storage (IEA, 2014). This review is not intended to be exhaustive but to present a global vision of the principles underlying the energy storage mechanism in SCs, and to explain how these principles have guided the research of materials in this field, in particular for the production of carbon electrodes. Given the environmental issues mentioned above, the last part of this review incorporates studies using non-toxic and environmentally friendly carbon precursors, such as tannin extracts, to produce carbon electrodes for SCs.

SUPERCAPACITORS

Basic Principles

A SC consists of two parallel electrodes separated by a non-conductive material impregnated with an electrolyte, as illustrated in **Figure 1B**. By applying a potential between the electrodes, the ions in the electrolyte are attracted to the electrode of opposite charge. Derived from charge accumulation and the interaction with the electrode surface, an electrostatic double-layer (EDL) is created on each electrode (González et al., 2016). Hence, there are two contributions to the total capacitance of the device, represented by the two capacitors in series shown in the simplified electric circuit of **Figure 1B**. An equivalent series resistance (ESR) is added to the circuit to account for the resistance of all the components of the device (Xie et al., 2018). The EDL generation process is ideally reversible, resulting in fast responses for charge and discharge, which result in high power in SCs. In addition, high cyclability, i.e., retention of capacitance after repetitive cycles of charge and discharge, and long lifetimes are achieved due to the low degradation of components derived from the reversibility of the EDL formation process.

From a macroscopic point of view, the capacitance C of a SC can be calculated as in a regular capacitor of parallel plates:

$$C = \frac{\varepsilon_0 \varepsilon A}{d} \tag{1}$$

where ε_0 is the permittivity of vacuum, ε is the permittivity of the electrolyte, A is the area of the electrode, and d is the effective thickness of the EDL. The energy, E, of a capacitor is calculated as follows:

$$E = \int CV dV \tag{2}$$

where V is the applied voltage to the device, also called potential window. For an ideal EDL SC, C is not a function of V and Equation (2) becomes:

$$E = \frac{1}{2} CV^2 \tag{3}$$

The power, P, is then calculated through:

$$P = \frac{E}{t_{dis}} \tag{4}$$

where t_{dis} is the discharge time. **Figure 2** shows a Ragone plot of typical values of energy and power of SCs compared to those of other energy storage devices such as batteries, fuel cells and capacitors.

Applications

The characteristic E and P-values of SCs bridge the gap between conventional capacitors and batteries, as shown in **Figure 2**. Hence, SCs find their applications either as autonomous energy sources or in combination with other devices, as detailed below (Kötz and Carlen, 2000; Miller and Burke, 2008; Conte, 2010; Sharma and Bhatti, 2010; Gu and Yushin, 2014; Aneke and Wang, 2016; González et al., 2016; Gautham Prasad et al., 2019; IOXUS Inc, 2020; Maxwell Technologies Inc., 2020):

- *Memory back-ups.* Fast-response SCs are a short-term solution to a brief interruption of power supply to the memory.
- *Portable tools.* SCs are used as an energy source in camera flashes or portable screwdrivers, since only bursts of energy are required along with rapid and constant recharging.
- *Distribution and storage of electrical energy.* SCs are able to compensate short-duration voltage fluctuations in the distribution line and to match the variations between production and consumption. In addition, SCs are used to restart collapsed power systems or to supply energy until the primary source is restored. SCs are also used as storage devices in renewable energy production plants, especially in wind power applications, as they require little maintenance.
- *Decoupling of power and energy needs.* SCs are used to meet the power needs while the principal source of energy is provided by a different system. This type of decoupling is found in hybrid and electric vehicles.

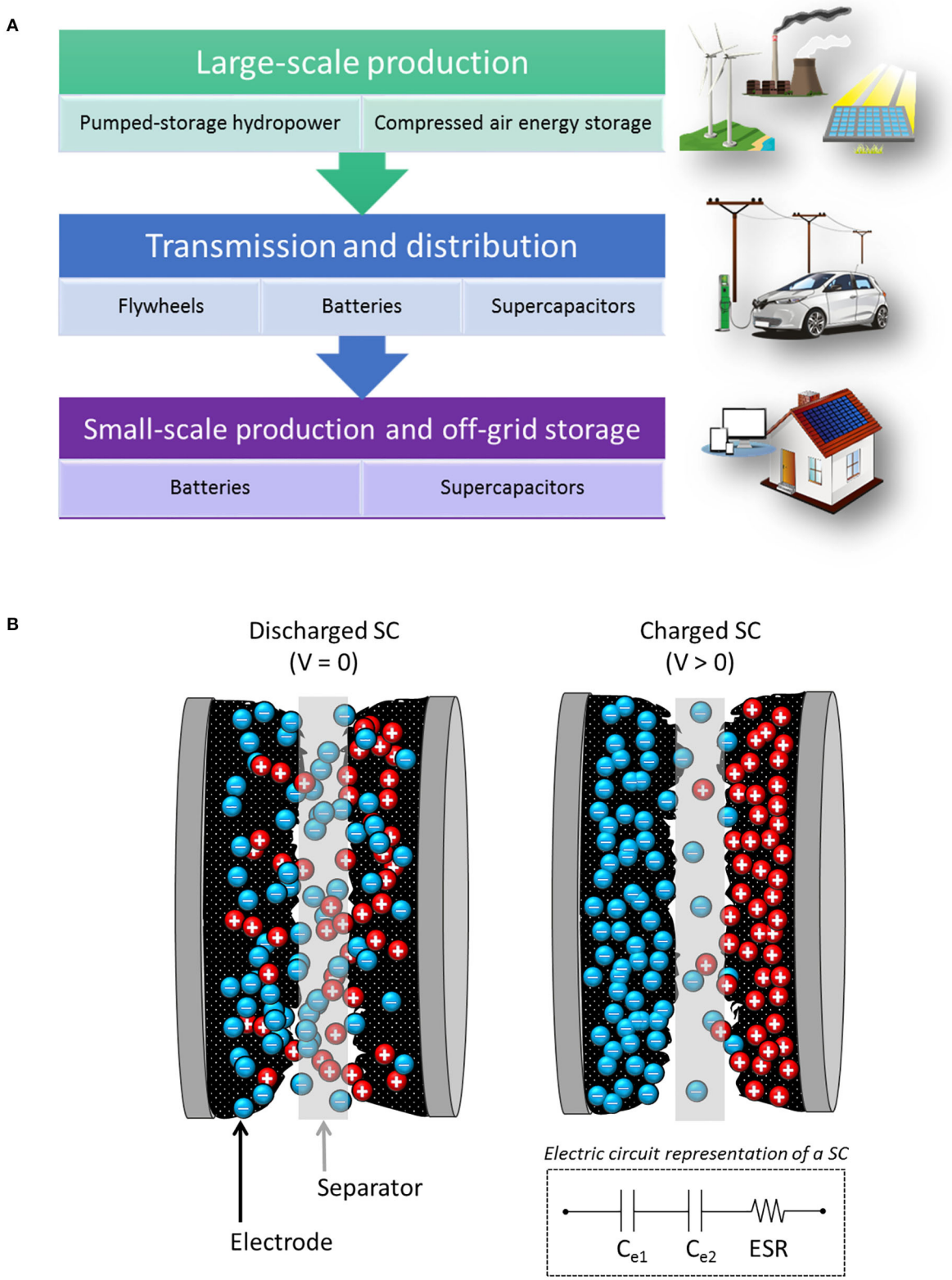

FIGURE 1 | (A) Energy storage technologies used at different scales in the power system (IEA, 2014; Aneke and Wang, 2016). **(B)** Mechanism of formation of the electrostatic double-layer (EDL) in a SC. In the associated electric circuit, capacitors C_{e1} and C_{e2} represent the contribution to the total capacitance of the EDL formed at the surface of each electrode. The equivalent series resistance (ESR) is also shown.

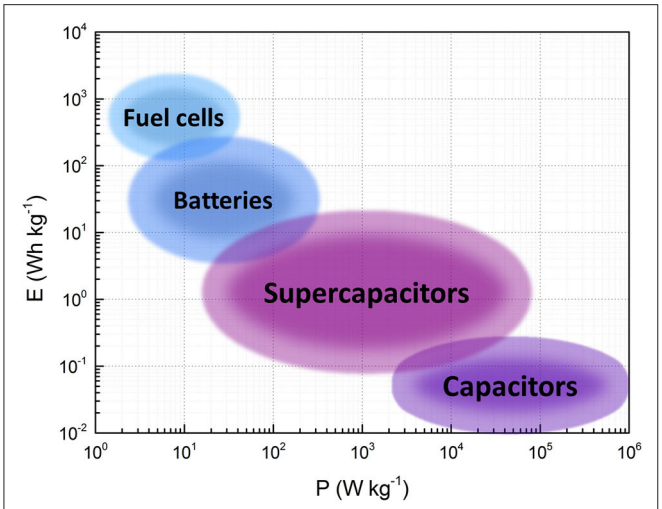

FIGURE 2 | Ragone plot showing the typical values of energy and power of different energy storage devices (Inamuddin et al., 2018).

- *Regeneration devices*. The energy released by machines with repetitive and constant movements can be recovered by SCs. Thus, SCs are found, for example, in cranes and elevators or in the braking systems of hybrid or electric vehicles like buses, delivery or garbage trucks and trains.

One of the main disadvantages of SCs compared to batteries is that they store less energy, which limits their use as autonomous devices. It is clear from Equation (3) that there are two ways to overcome this drawback: widening the potential window or increasing the capacitance. The former is strongly associated with the choice of electrolyte and the latter with the properties of the electrode. Nevertheless, they are intimately related to each other, because there must be a synergy between all the components of the SC. A clear example of this synergy is the pseudocapacitive behavior that some materials present when used as electrodes, where rapid Faradaic (redox) reactions occur on or near the surface of the electrode. The presence of redox reactions depends on the properties of the electrode material and on the affinity of the electrolyte toward it. SC devices with electrodes made of materials in which both EDL and pseudocapacitance storage mechanisms are present are also referred to as pseudocapacitors (PSCs) and could reach even higher values of capacitance. However, the increased capacitance in PSCs may be accompanied by a loss of power and long-term stability compared to that of SCs (González et al., 2016).

New materials are constantly being developed and their performance as electrodes for SCs must be evaluated. In the following section, the electrochemical testing techniques commonly used on a laboratory scale are briefly described in order to illustrate the expected behavior of a SC. Next, the types and general characteristics of commonly used electrolytes and the advances in the research for porous materials as electrodes for SCs are discussed.

Electrochemical Testing Techniques

Cell Configuration

Figure 3 shows schemes of cell configurations normally used for SC testing. The three-electrode cells (**Figure 3A**) are useful for estimating the contributions of pseudocapacitance or for better understanding the more fundamental behavior of materials, while the two-electrode cells (**Figure 3B**) are used to evaluate the performance of materials in operating conditions closer to those of real SC devices (Xie et al., 2018). T-type cells are a combination of two- and three-electrode cell configurations (**Figure 3C**), which allow studying the performance of each electrode in a SC along with the performance of the whole system operating at the equilibrium potential of both electrodes (Sevilla et al., 2019). Thus, a three-electrode configuration measures the performance of a single electrode (the working electrode in **Figure 3A**), whereas a two-electrode configuration evaluates the performance of two electrodes as a system (the cell). As shown in **Figure 1B**, in a symmetric SC, the two electrodes are made of the same material and, based on the associated simplified circuit, its capacitance, C, can be calculated assuming that the contribution of each electrode is identical, i.e., $C_{e1} = C_{e2} = C_e$. Therefore:

$$\frac{1}{C} = \frac{1}{C_e} + \frac{1}{C_e} \tag{5}$$

$$C = \frac{C_e}{2} \tag{6}$$

Reporting normalized values of capacitance allows for the comparison of results from different studies. Thus, from Equation (6) and considering that the normalization factor of the cell is twice the normalization factor of an electrode, i.e., $N = 2N_e$ (Zuliani et al., 2015):

$$C_N = \frac{C}{N} = \frac{C_e}{2N} = \frac{C_e}{4N_e} = \frac{C_{e,N_e}}{4} \tag{7}$$

N is generally chosen to be either the mass or the volume of the electrodes. For simplicity, from now on, C and C_e will refer to the capacitances normalized by the mass of the electrode(s), called specific cell capacitance and specific electrode capacitance, respectively.

Many of the materials that can be used as electrodes for SCs are in powder form, so it is necessary to use a binder to agglomerate the powder particles and create a paste, or slurry, from which the electrodes are obtained. Some additives can also be mixed with the active material to improve their electrical conductivity. A correct assessment of the materials performance requires giving the calculations of normalized capacitance as a function of the total mass or the total volume of the electrode, i.e., including binder and/or the additives.

Cyclic Voltammetry (CV)

During cyclic voltammetry (CV) tests, a potential (V) is applied and increased at constant rate over time (scan rate) while the current response, I, is measured. An ideal SC would exhibit a rectangular curve when I is plotted as a function of V, see

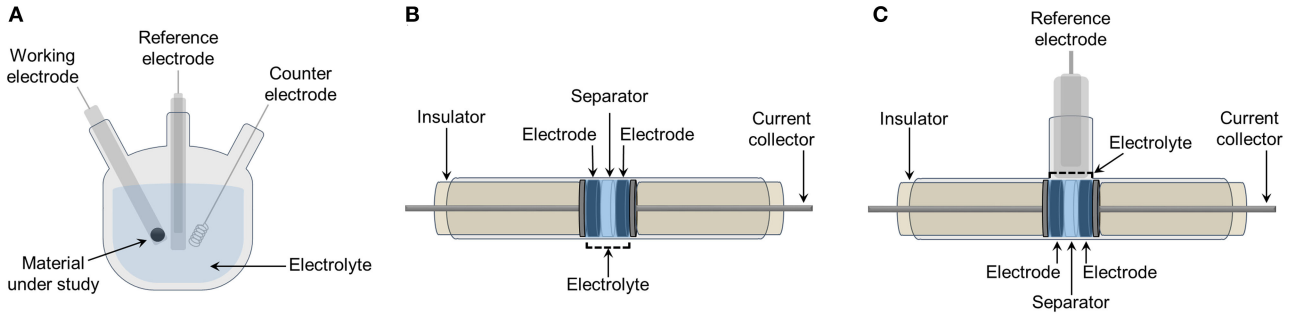

FIGURE 3 | Different configurations for the electrochemical characterization of SCs: **(A)** three-electrode cell, **(B)** two-electrode cell, and **(C)** T-type cell.

Figure 4A. During charging, the sharp increase in I at the beginning of the cycle is due to the rapid formation of the EDL and it remains constant when V increases because no Faradaic reaction occurs. Given the reversible nature of the EDL formation mechanism, the CV curve during discharge obtained when V decreases is the exact inverse of the charging curve. Evidently, the CV curves of the real SCs deviate from the ideal one, and those of PSCs also display I peaks due to the generation of charge by redox reactions, as shown in **Figure 4A**. In addition, widening the potential window in CV measurements allows identifying the point at which decomposition of the electrolyte occurs, manifesting by an I peak at each edge of the CV curve. Then, this information can be used to set the operating voltage of a SC cell. From CV data, C is calculated by:

$$C = \frac{\oint IdV}{2sVm} \tag{8}$$

where the numerator is the area delimited by the CV curve, s is the scan rate, V is the potential window and m is the sum of the masses of the two electrodes in the cell. If a three-electrode configuration is used, C_e can be calculated by substituting m in Equation (8) for the mass of the working electrode, m_e.

Galvanostatic Charge-Discharge (GCD)

In the galvanostatic charge-discharge (GCD) technique, a constant I is applied to the system while the response V is recorded as a function of time. The method is normally carried out with a two-electrode configuration. In an ideal SC, charge and discharge have a linear mirror behavior, resulting in triangular curves. In real SCs and PSCs, the curves deviate from the linear behavior, see **Figure 4B**. Any device will exhibit a sudden drop in potential during the transition from charge to discharge. This is called IR drop and it is directly associated with the ESR of the device. From GCD data, C is calculated by:

$$C = \frac{I}{(\Delta V/\Delta t)\, m} \tag{9}$$

where I is the constant current applied, $\Delta V/\Delta t$ is the slope of the discharge curve and m is the sum of the masses of the two electrodes in the SC. C_e can then be approximated using Equation (7). Using this value of C, those of E and P of the SC can be calculated directly from Equations (3) and (4), respectively, keeping in mind that V in Equation (3) is the actual operating potential, therefore the IR drop must be subtracted from the maximum potential reached by the cell, i.e., $V = V_{\max} - IR_{drop}$.

GCD tests performed at increasing values of I provide insight into the kinetic behavior of the materials at faster charging rates. Although this can also be evaluated by increasing the scan rate in CV tests, GCD tests are preferred for kinetic analysis because the operating conditions are closer to those of real devices (Beguin and Frackowiak, 2013; Xie et al., 2018).

Electrochemical Impedance Spectroscopy (EIS)

Electrochemical impedance spectroscopy (EIS) is used to analyze the response of a material to a low-amplitude oscillating potential signal. A Nyquist plot represents the real and imaginary parts of the complex impedance, Z_r and Z_i, respectively. Examples of curves obtained for an ideal SC, a real SC and a PSC are shown in **Figure 4C**. Analysis of Nyquist plots allows associating an equivalent circuit for each type of device, see **Figures 4E–G**, which provides information on the electrochemical system (Bard and Faulkner, 2001; Beguin and Frackowiak, 2013; Xie et al., 2018). For instance, a straight vertical line appears for a material with an ideal SC behavior. Its point of intersection with the Z_r axis represents the value of the ESR of the device, R_s. The pseudocapacitive behavior adds a second charge transfer resistance to the system, R_{ct}, and a semicircle is observed in the Nyquist plot at high frequencies (HF, $> \sim 10^3$ Hz). In porous materials, the limited ion diffusion within the pores is modeled in the equivalent circuit as a constant phase element, Z_{CPE}, and it manifests itself in the Nyquist plot as a straight line in the HF for a SC and after the semicircle for the PSC (Beguin and Frackowiak, 2013). The longer the line, the more difficult it is for the electrolyte to access the whole surface of the material. Once the surface is completely impregnated, the capacitance no longer depends on the frequency, hence the vertical line appearing at low frequencies (LF, $\sim 10^{-3}$ Hz). In all cases, the intersection with the Z_r axis of the vertical line at LF is defined as the equivalent distributed resistance (EDR) that takes into account the ESR and the charge transfer and ion diffusion resistance of the material.

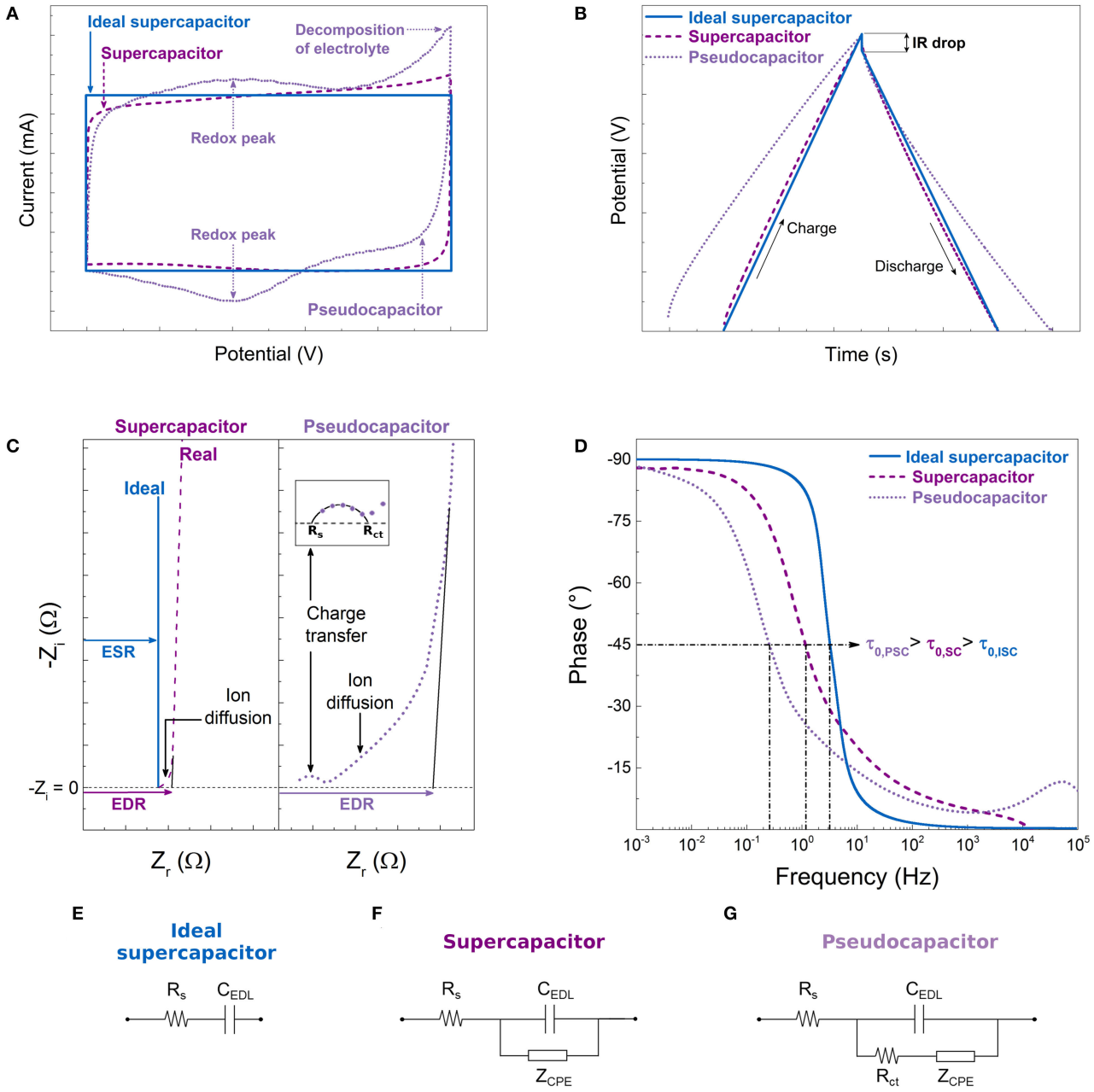

FIGURE 4 | Expected behavior of a supercapacitor (SC) and a pseudocapacitor (PSC) compared to that of an ideal SC during different electrochemical tests: **(A)** cyclic voltammetry, **(B)** galvanostatic charge-discharge, and **(C,D)** electrochemical impedance spectroscopy. Simplified equivalent circuits for: **(E)** ideal SC, **(F)** SC, and **(G)** PSC.

Data obtained from EIS measurements can also be represented in a Bode diagram, see **Figure 4D**, where the phase and/or modulus of the complex impedance are/is plotted as a function of frequency. Bode diagrams are useful tools for easily identifying the relaxation time constant, τ_0, of the device, which is the inverse of the frequency at which the phase angle is 45°. This parameter is related to the power output of the SC. A low τ_0 leads to a rapid charge-discharge resulting in a high power capability (Orazem and Tribollet, 2008; Inamuddin et al., 2018).

ELECTROLYTES USED IN SCs

The energy stored in a SC can be considerably increased by widening the potential window, see again Equation (3), which is essentially limited by the stability of the electrolyte. Increasing the potential beyond this limit causes the decomposition of the electrolyte, resulting in unwanted reactions that sharply increase the current, reduce the performance and can degrade the materials in the SC (Zhong et al., 2015). Even though the

selection of the electrolyte is mainly defined by its stability, other properties such as conductivity, ion size and mobility, ion-electrode interaction or thermal stability must also be considered. Currently, aqueous and organic liquid electrolytes are the most widely used. **Table 1** shows their general properties.

Aqueous electrolytes are perhaps the most used in academic research because they have a low cost, they are easy to handle, and they present high ionic conductivity and mobility leading to a low ESR (González et al., 2016). Among them, acidic, alkaline, or neutral solutions can be used (Zhong et al., 2015; Wang et al., 2016). Acidic and alkaline electrolytes are likely to provide pseudocapacitance contributions by reacting with oxygen or nitrogen surface functional groups present in carbon electrodes (Zhai et al., 2011; Salinas-Torres et al., 2019). The potential window of aqueous electrolytes is limited to ∼1.2 V, beyond which water begins to decompose. Besides, they are not suitable for applications where the temperature is much lower than 0°C or much higher than 100°C (Zhong et al., 2015). Organic electrolytes predominate on the market because they offer the possibility of using larger potential windows. They consist of salts dissolved in organic solvents that can reach potential windows up to 3.5 V and operate at temperatures as low as −40°C (Zhong et al., 2015). However, the larger ion size of typical organic electrolytes limits their mobility, so they have lower conductivities than those of aqueous electrolytes (Wang et al., 2016). In addition, organic electrolytes still face the problems related to their high toxicity, flammability and high costs due to the necessary purification processes and the controlled environment for the assembly of the SCs (Zhong et al., 2015).

CARBON MATERIALS AS ELECTRODES FOR SUPERCAPACITORS

The use of porous carbon materials as electrodes for SCs has increased over the years. Such materials indeed have high chemical and thermal stability, good conductivity, possibility of adjusting their textural properties, and industrial processes for electrode synthesis and production already established. In addition, carbon cloths or monoliths can be produced and used directly as electrodes, eliminating the need of binders to maintain their shape (Kötz and Carlen, 2000; Sevilla and Mokaya, 2014; Wang et al., 2016). From Equation (1), it can be seen that a material with a high surface area should result in a high-capacitance SC as long as this surface is accessible to electrolyte ions. The latter highlighted the importance of matching the size of the pores to the size of the electrolyte ions. Some studies had also reported that a hierarchical porous structure connecting micro-, meso- and macropores (pore width $w < 2$ nm, $2 < w < 50$ nm, and $w > 50$ nm, respectively) helps improve SC performances by providing interconnected channels that facilitate ion diffusion in the material (Frackowiak, 2007; Inagaki et al., 2010). Porous carbon materials are also of particular interest because the addition of specific functional groups to their surface results in higher capacitances due to improved conductivity and/or higher pseudocapacitance contributions (Paraknowitsch and Thomas, 2013).

Efforts to increase the energy density in carbon-based SCs focus on these three aspects: development of porous materials with high surface area, tailoring of pore size, and modification of surface chemistry. The following subsections deal with the description of the synthesis processes and the resultant properties of different porous carbon materials for their application as electrodes for SCs.

Activated Carbons

Most electrodes in SCs are based on powders of activated carbon (AC). There is a predominant use of biomass as raw material for commercial and laboratory production of ACs, given that agricultural, forestry, municipal and animal byproducts are abundant and inexpensive. Coal or coke can also be used to produce ACs (Zhao et al., 2012; Tellez-Juárez et al., 2014; González-García, 2018). **Figure 5** shows schematically the production process by physical or chemical activation methods.

Physical activation is based on the partial and controlled gasification of a carbonaceous material in an atmosphere containing an oxidizing gas, such as steam, CO_2, air or their mixes, at temperatures ranging from 350 to 1,000°C. Before physical activation, pyrolysis at temperatures between 400 and 900°C or hydrothermal carbonization (HTC) at lower temperatures (130 to 250°C) is generally required (Cha et al., 2016; Selmi et al., 2018; Mbarki et al., 2019). The final textural and chemical properties of the ACs depend largely on the activation time and temperature. When the same activating agent is used, a higher degree of activation leads to a higher development of porosity and a broadening of the pore size distribution (PSD). Physical activation normally produces materials with surface areas up to ∼1,800 $m^2\ g^{-1}$ and maximum pore volumes of ∼0.9 $cm^3\ g^{-1}$ (Sevilla and Mokaya, 2014; González-García, 2018).

Chemical activation is carried out using compounds such as KOH, NaOH, H_3PO_4, or $ZnCl_2$, among others. The precursor is mixed with the activating agent and then subjected to pyrolysis at temperatures between 400 and 900°C. Finally, the AC needs to be washed to remove the residues generated during the activation process. Direct chemical activation of biomass is preferred when using $ZnCl_2$ or H_3PO_4 because they dehydrate biomass, which reduces the quantity of volatile matter released during pyrolysis, thus increasing the carbon yield (Fierro et al., 2005, 2010). KOH or NaOH can be used to activate either untreated biomass or char (Fierro et al., 2007; Basta et al., 2009; Acosta et al., 2018). Higher amounts of activating agent result in more developed porosity. H_3PO_4 and $ZnCl_2$ generate micropores and small mesopores and lead to ACs with surface areas lower than 2,000 $m^2\ g^{-1}$. On the other hand, KOH can produce higher surface areas, wider PSD and pore volumes of 2.7 $cm^3\ g^{-1}$ or more. Such further development of porosity is probably due to the generation of CO_2 as a by-product of the reaction between the carbon and KOH (Sevilla and Mokaya, 2014). The use of less corrosive or harmless salts for the activation of biomass and biomass-derived precursors, such as potassium carbonate, potassium bicarbonate, potassium oxalate, or sodium thiosulfate, has been explored (Fuertes et al., 2018; Díez et al., 2019). Materials with high surface

TABLE 1 | Properties of aqueous and organic electrolytes often used in SCs (Lide, 2004; Conte, 2010; Zhong et al., 2015; Lu et al., 2018).

Type	Electrolyte	Potential window [V]	Solvated ion size [nm]		Conductivity [S cm^{-1}] (concentration)	Freezing and boiling point [°C]
			Cation	Anion		
Aqueous	H_2SO_4	0.7–1.0	0.28	0.38	0.8 (1 M)	
	KOH	0.9–1.0	0.33	0.30	0.6 (6 M)	
	Na_2SO_4	1–1.8	0.36	0.38	0.01 (0.1 M)	
Organic	$TEABF_4$/ACN	2.5–2.8	1.3	1.16	0.05 (0.65 M)	−49 to +82°C
	$TEABF_4$/PC	2.5–3.5	1.35	1.4	0.01 (0.65 M)	−49 to +242°C

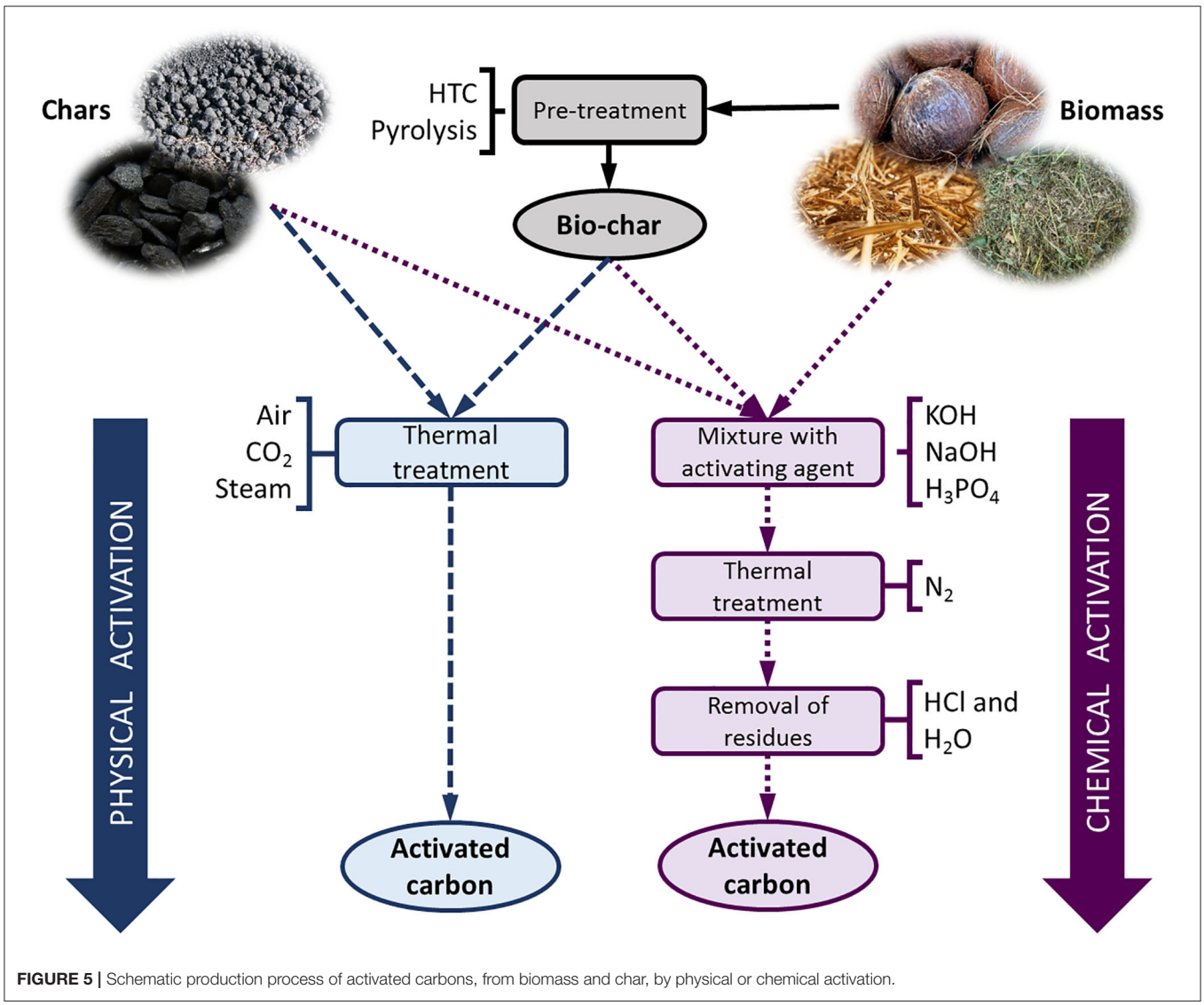

FIGURE 5 | Schematic production process of activated carbons, from biomass and char, by physical or chemical activation.

areas and pore volumes, up to 2,750 m^2 g^{-1} and 2.4 cm^3 g^{-1}, respectively, have been reported.

The advanced materials described in the following sections can also be activated to improve their textural properties. However, here they differ from ACs materials since their physicochemical properties are mainly related to synthesis rather than the activation process.

Carbide-Derived Carbons and Zeolite-Templated Carbons

In order to have a higher control of the microporosity, different methods for the synthesis of carbon materials from carbides or zeolites have been developed (Lee et al., 2006; Inagaki et al., 2010). High-temperature chlorination (400–1,200°C) of silicon or titanium carbide is used to remove metal atoms and obtain

microporous materials. Such carbide-derived carbons (CDCs) exhibit surface areas between 1,000 and 2,000 $m^2\ g^{-1}$ and a uniform and disordered pore structure. The pore size can be adjusted from 0.6 to 1.1 nm by changing the carbide precursor, the chlorination or the heat-treatment temperature (Zhai et al., 2011). On the other hand, zeolite-templated carbons (ZTCs) are produced by incorporating a carbon precursor, e.g., phenol, inside the zeolite structure and carbonizing it. After template removal, a structure with the same periodicity as the original zeolite is obtained. ZTCs reach surface areas higher than 2,000 $m^2\ g^{-1}$ and present pore volumes of 1 $cm^3\ g^{-1}$ or more (Lee et al., 2006; Mostazo-López et al., 2018). For both CDCs and ZTCs, the pore structure consists only of micropores with a minor presence of mesopores. Activation of these materials introduces mesoporosity and broadens the micropores, which can improve ion diffusion in the porous materials when used as electrodes for SCs (Mostazo-López et al., 2018).

Carbon Gels

Pyrolysis of organic gels prepared from resorcinol-formaldehyde resins has been used to produce carbon gels (CGs) with surface areas between ∼500 and ∼1,000 $m^2\ g^{-1}$ and presenting a high fraction of mesopores. In general, the production of CGs involves five steps: polymerization of the precursor to form an organic gel, aging, solvent exchange, drying, and carbonization (Grishechko et al., 2016; Ciszewski et al., 2019). CGs are classified, according to the drying technique, as aerogels, xerogels, or cryogels whether supercritical, subcritical or freeze drying, respectively, has been used (Braghiroli et al., 2019). Each step of the synthesis process has an impact on the porous texture of the resultant CGs. On the one hand, the precursor to catalyst ratio and the pH of the solution modify the polymerization process and lead to materials of different textures (Szczurek et al., 2011a,b). On the other hand, controlling the drying process is of paramount importance to avoid the formation of cracks or the shrinkage of the material (Feinle et al., 2016). For SC applications, it has been found that the mainly mesoporous structure of CGs limits the effectiveness of the EDL mechanism and that activation generally allows developing a narrow porosity not accessible to ions, leading to a moderate improvement in electrochemical performance compared to the increase in surface area (Pandolfo and Hollenkamp, 2006; Zhang and Zhao, 2009).

Nanostructured Carbons

Carbon nanotubes, nanofibers and nanospheres (CNTs, CNFs, and CNSs, respectively) have also been used as electrodes of SCs. Although the surface area of CNFs and CNTs is moderate, ∼400 $m^2\ g^{-1}$, they have been considered for SCs electrodes given that their entanglement results in multiple charge storage sites (Gu and Yushin, 2014), as seen in **Figures 6A,B**. CNFs and CNTs obtained by electrospinning techniques or by direct growth on conductive substrates allow flexible mats to be produced, which can be directly used as electrodes in SCs (Ra et al., 2009; Kim et al., 2012; Gu and Yushin, 2014). Likewise, aligned CNFs and CNTs can be grown directly on current collectors (Kim et al., 2003; Gao et al., 2008; Zheng et al., 2017). SCs with electrodes based on aligned CNFs or CNTs could exhibit improved performance at high charging rates due to a shortening of the conductive path for the charges (Inagaki et al., 2010). However, the performance of CNTs as electrodes in SCs is strongly affected by the presence of impurities (Frackowiak and Beguin, 2001). In addition, activation is generally needed to create micropores on the surface of CNFs and increase the number of charge storage sites (Inagaki et al., 2010; Gu and Yushin, 2014). On the other hand, it is nowadays possible to synthesize a wide variety of CNSs, whether solid, hollow, or onion-like, among others, and with micro-, meso-, and/or macropores, see examples in **Figures 6C,D**. The surface areas vary from low, $< 100\ m^2\ g^{-1}$, to high, ∼2,000 $m^2\ g^{-1}$, and the sphere sizes range from tens of nm to hundreds of μm (Liu et al., 2015). The strategies for synthesizing CNSs include different types of hard- and soft-template techniques, emulsion polymerization, self-assembly or the Stöber method (Liu et al., 2015; Li et al., 2016). Typically, petrochemical precursors are used to produce CNSs, but HTC processes have successfully used glucose, sucrose, cellulose or tannin to obtain CNSs (Braghiroli et al., 2015b; Liu et al., 2015; Li et al., 2016). Uniform CNSs can be packed in high-density electrodes, maintaining the electrolyte accessibility thanks to voids between the particles. Therefore, this type of electrode allows a large amount of energy to be stored in small-volume devices (Ferrero et al., 2015). Despite the advantages of CNSs, the multi-step synthesis process, the use of hazardous substances to etch the hard templates and the low yields associated with soft-template methods limit their extensive use for widespread production (Liu et al., 2015; Li et al., 2016).

Ordered Mesoporous Carbons

In order to develop materials with a hierarchical pore structure, many studies have been devoted to the design and engineering of ordered mesoporous carbons (OMCs) with tuned morphology and porosity. If necessary, an activation process is carried out to increase their surface area. In this way, OMCs have the advantage of having a hierarchical pore structure to provide interconnected channels for the diffusion of electroactive species, thus making them suitable for application in SCs (González et al., 2016; Lim et al., 2016; Wang et al., 2016). OMCs can be synthesized by hard- or soft-template methods. Both are shown in **Figure 7A**, and further details are given below.

The hard-template method uses an inorganic material that is filled with the carbon precursor. After polymerization, the composite is subjected to carbonization, and the template is then removed. As a result, the OMC obtained is an inverse replica of the template (Lee et al., 2006). Mesoporous silicas are the most used in this kind of techniques, but having to synthesize such templates before sacrificing them makes the procedure expensive, polluting and time-consuming. Thus, efforts to synthesize OMCs from biosourced templates have been made to take advantage of naturally ordered and hierarchical structures found in diatomaceous earth, pollen grains or leaves, among others (Liu et al., 2012; Xia et al., 2012; Gao et al., 2017). However, the procedure still involves the use of hazardous substances to crosslink the precursor and/or to etch the template.

In the soft-template method, an amphiphilic surfactant is used in solution to form micelles. The hydrophilic part of the micelle interacts with the carbon precursor that

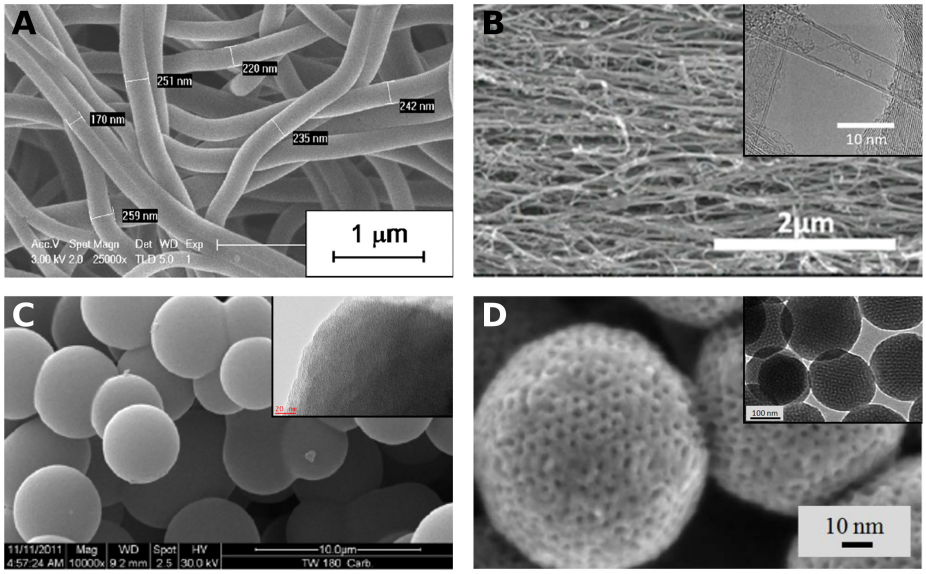

FIGURE 6 | (A) Electrospun CNFs from Kraft lignin (Adapted from Vivo-Vilches et al., 2019). SEM (and TEM in the insets) images of: **(B)** commercial CNTs-Poly(dicyclopentadiene) composite yarn (Adapted from Xin et al., 2020); **(C)** solid CNSs derived from tannin (Adapted with permission of Elsevier, from Braghiroli et al., 2012; permission conveyed through Copyright Clearance Center, Inc.); **(D)** ordered mesoporous CNSs from phenol (Adapted from Chang et al., 2015).

polymerizes around the surfactant. Then, the carbonization process eliminates the surfactant, revealing the mesoporosity at the same time (Libbrecht et al., 2017). Different combinations of commercially available block copolymers such as Pluronic® or Vorasurf® as surfactants and phenol, phloroglucinol, resorcinol, or tannin as carbon precursors have been used to successfully synthesize OMCs by soft-template methods (Meng et al., 2006; Wickramaratne and Jaroniec, 2013; Braghiroli et al., 2016; Libbrecht et al., 2017).

In both hard- and soft-templating, the mesopore order is determined by the characteristics of the template. Given the diversity of templates and precursors available, OMCs have surface areas from ∼500 to more than 2,000 m^2 g^{-1}, and various PSDs in the micro—mesopore range. Thus, the versatility of OMCs turns them into an interesting choice of materials to be used as SC electrodes. **Figures 7B–E** shows examples of OMCs with different pore structures.

Doped Materials

A potential route to increase the energy stored in SCs is heteroatom doping of carbon materials, which promotes fast Faradaic reactions and enhances their performances *via* pseudocapacitance contributions. All the materials described in the previous sections (Sections Activated Carbons to Ordered Mesoporous Carbons) are subject to surface modification. Although doping with boron, sulfur or phosphorus has been investigated (Paraknowitsch and Thomas, 2013; Bairi et al., 2015; Chen et al., 2015; Elmouwahidi et al., 2018), the introduction of heteroatoms such as oxygen (O) or nitrogen (N) is recurrent because it is relatively easy to perform. In consequence, O- and N-doping have been studied in depth. **Figure 8A** displays the most common O- and N- surface functional groups associated with improving the performance of carbon-based SCs.

Oxygen functionalities are normally found in porous carbon materials. To further dope the materials with oxygen, activation and/or oxidation treatments in HNO_3, H_2SO_4, or using O_2 can be carried out; electro-oxidation using different basic, neutral or acidic electrolytes has also been explored (Inagaki et al., 2010; Berenguer et al., 2013; Sevilla and Mokaya, 2014). The final amount and the type of functionality on the carbon surface depend on the precursor and the synthesis method. Some of the proposed redox reactions involving oxygen surface groups are shown in **Figures 8B–F** (Chen et al., 2012; Sánchez-Sánchez et al., 2016). In acidic electrolytes, it has been reported that quinone functionalities have the largest contribution to capacitance, **Figure 8B** (Hulicova-Jurcakova et al., 2009). Even though the carboxylic groups could increase the capacitance through the generation of charges, see **Figure 8E**, their high polarity could also produce resistance to ion diffusion, reducing the performance (Sevilla and Mokaya, 2014). Nevertheless, carboxylic and phenolic groups are also likely to react in alkaline solutions, see **Figures 8D,F**, with a positive impact on the SC performance (Zuliani et al., 2018).

N-doping by post-treatment is carried out by HTC and/or annealing of a mixture of the carbon material with a nitrogen precursor, e.g., ammonia or urea (Inagaki et al., 2018). N-doping can also be performed *in situ* by direct pyrolysis of a nitrogen-rich carbon precursor (Raymundo-Piñero et al., 2009) or by multi-step methods to produce CNSs (Braghiroli et al., 2015b; Ferrero et al., 2015; Wang et al., 2018), CNTs (Ayala et al., 2010), or OMCs (Sánchez-Sánchez et al., 2016; Moussa

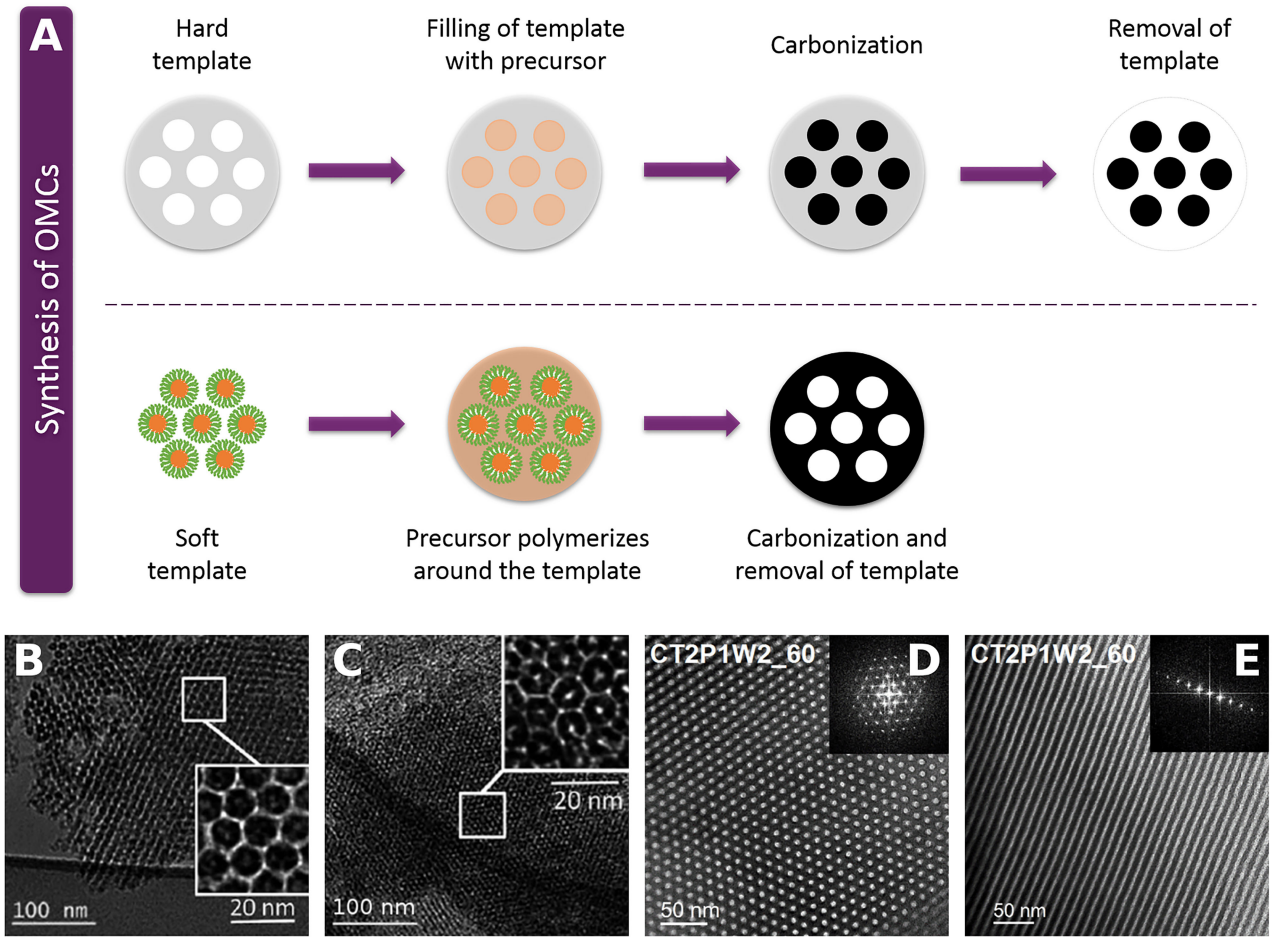

FIGURE 7 | (A) Schematic synthesis of OMCs by hard and soft template methods. **(B,C)** Hard-templated OMCs using SBA-15 as template and aminobenzoic acid as precursor (Adapted from Sánchez-Sánchez et al., 2016 by permission of The Royal Society of Chemistry). **(D,E)** Soft-templated OMCs using Pluronic® F127 as template and mimosa tannin as precursor (Adapted from Castro-Gutiérrez et al., 2018 by permission of The Royal Society of Chemistry).

et al., 2018). Isolating the contribution of N-functionalities to the SCs performance is a difficult task since nitrogen is always present with oxygen and can lead to modifications of textural properties. However, a correlation between the SCs performance and the amount and type of nitrogen functionalities has been reported (Frackowiak et al., 2006; Hulicova-Jurcakova et al., 2009; Braghiroli et al., 2015c). N-doped materials can reach high values of capacitance even if their surface areas are relatively low. This have been attributed to pseudocapacitance contributions but also to improved wettability and conductivity of the materials (Inagaki et al., 2010). Most studies agree that the major contribution to pseudocapacitance comes from the pyridinic, pyrrolic, and pyridine groups, see **Figures 8G–K** (Deng et al., 2016). However, some studies have suggested that quaternary groups interact with protons or anions in H_2SO_4 or KOH electrolytes, respectively, and could promote electron transfer through the carbon structure (Deng et al., 2016).

TRANSITION TO BIOSOURCED PRECURSORS OF POROUS CARBON MATERIALS

Apart from ACs, which are often produced on an industrial scale from biomass materials, most of the synthesis methods described in section Carbon Materials as Electrodes for Supercapacitors use precursors of petrochemical origin. For example, resorcinol or phenol crosslinked with formaldehyde are widely used to synthesize different types of OMCs (Zhu et al., 2016; Lu et al., 2018; Li et al., 2019). In an effort to research more environmentally friendly technologies and methods, biosourced substitutes for ordinary carbon precursors have been explored. A salt template-assisted, chemical activation process was applied by subjecting gelatin, sucrose, glucose or tannic acid (TA) mixed with KCl and $Na_2S_2O_3$ to carbonization (Fuertes et al., 2018; Sevilla et al., 2019). The resultant micro-mesoporous carbon materials had high surface areas in the range of 1,900–2,720

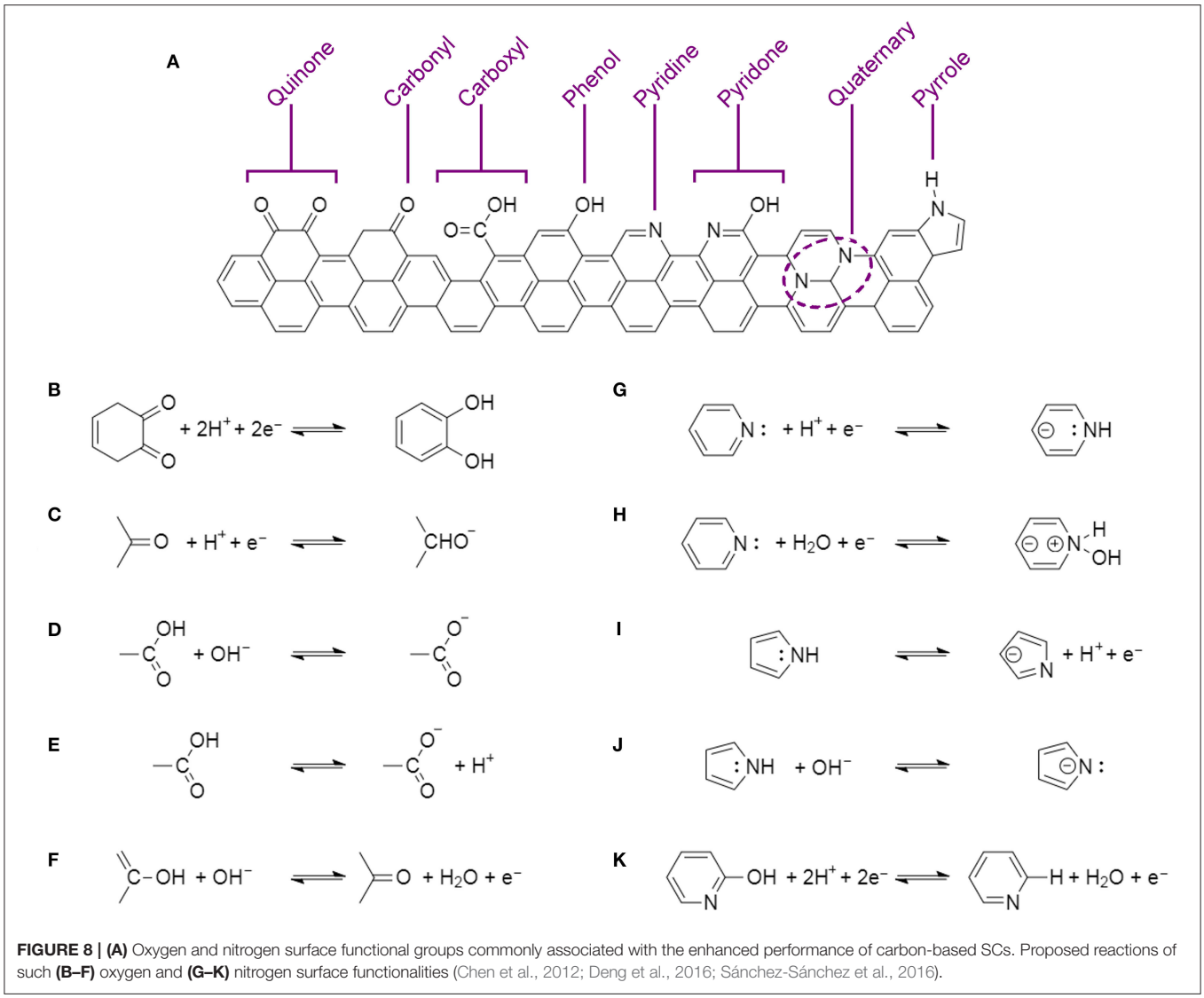

FIGURE 8 | (A) Oxygen and nitrogen surface functional groups commonly associated with the enhanced performance of carbon-based SCs. Proposed reactions of such **(B–F)** oxygen and **(G–K)** nitrogen surface functionalities (Chen et al., 2012; Deng et al., 2016; Sánchez-Sánchez et al., 2016).

m^2 g^{-1}. TA has also been used to produce micro-mesoporous CNSs by direct heat-treatment of the precursor mixed with urea and an eutectic salt ($NaCl/ZnCl_2$) (Tiruye et al., 2017) and to synthesize CNFs by carbonization of a glass fabric previously impregnated with TA (Hu et al., 2020). Hard-templating of sucrose with cubic and 2D hexagonal silica templates produced highly porous materials with surface areas as high as 2,000 m^2 g^{-1} (Vix-Guterl et al., 2005). Also based on the use of silica templates, OMCs with surface areas higher than 900 m^2 g^{-1} were synthesized from different types of biomass-derived phenols such as phloroglucinol, gallic acid, catechin, and mimosa tannin (Sanchez-Sanchez et al., 2017a). By soft-template routes, it has been reported that 2D hexagonal OMCs with surface areas ~700 m^2 g^{-1} were obtained by hydrothermal treatment of β-cyclodextrin, extracted from starch, mixed with Pluronic® F127 and P123 (Feng et al., 2014) or by evaporation-induced self-assembly (EISA) using a mixture of lignin, phloroglucinol, glyoxal, and Pluronic® F127 (Herou et al., 2019). Besides, a phase-separation method was able to produce N-doped 2D hexagonal OMC with a moderate area of 523 m^2 g^{-1} from phloroglucinol, glyoxylic acid, and guanine (Moussa et al., 2018).

TANNINS AS CARBON PRECURSOR

Tannins are polyphenolic substances present in many plants and trees. They have been used in the leather manufacturing process since the Middle Ages (SilvaTeam, 2018; CAPPEQ, 2019b). Their industrial production increased in the 1970s thanks to the development of tannin adhesives for wood (Fierro et al., 2018). Nowadays, tannins are used not only for tanning leather (hence their name), but also as wine additives, food supplements and cosmetic ingredients (CAPPEQ, 2019c). Although there are several methods for extracting tannins, the solid-liquid method is the one traditionally used on an industrial scale due to its simplicity, efficiency and low cost (de Hoyos-Martínez et al., 2019). The solid-liquid extraction method involves the

dissolution of tannins in water at moderate temperature (60–70°C), after which the solution is concentrated and spray-dried to obtain a red-brown powder (CAPPEQ, 2019a; de Hoyos-Martínez et al., 2019). The chemical composition of the final powder strongly depends on the plant species and the part of the plant from which the tannin has been extracted. However, the similarities in their compositions allow them to be classified into two broad categories, namely hydrolysable or condensed (Tondi and Petutschnigg, 2015; de Hoyos-Martínez et al., 2019). In particular, condensed tannins are of primary interest in the synthesis of carbon materials as they contain more than 70–80% of polyflavonoids. Their aromatic rings with hydroxyl groups give polyflavonoids a reactivity similar to that of phenolic molecules of petrochemical origin such as phenol or resorcinol (Pizzi, 1982; Fierro et al., 2018), as well as a high carbon yield upon pyrolysis, ∼50%. More details on the properties of condensed tannins are given in the next subsection.

Condensed Tannins

The polyflavonoids of condensed tannins are composed of flavan-3-ol moieties made up of two phenolic rings (A and B) linked by a heterocyclic ring. **Figure 9** shows the main four types of flavonoid molecules of condensed tannins as well as with the type of trees in which they are found. Thus, mimosa (*Acacia mearnsii*), quebracho (*Schinopsis balansae* and *Schinopsis lorentzii*), and maritime pine (*Pinus pinaster*) are the most used species for the extraction of condensed tannins, representing 90% of the world's production (Fierro et al., 2018; Shirmohammadli et al., 2018). The reactivity of the flavonoid units depends on the position of the -OH groups and the available reaction sites. In this sense, it has been shown that the A-ring is more reactive than the B-ring (Pizzi, 1982). Indeed, tannins can naturally autocondense by linking the units at positions 4,6 for profisetinidin and prorobinetinidin or 4,8 for procyanidin and prodelphinidin (see again **Figure 9**), producing oligomers of up to 10 or 11 units (Haslam, 2007). The ability of condensed tannins to autocondense and react with aldehydes to form phenolic resins makes them an attractive alternative to produce high added-value materials.

In addition to their good chemical reactivity, tannins have the advantage of being non-toxic in the event of exposure to low amounts, and high doses can only cause irritation or have anti-nutritional effects (Schlienger et al., 2012). Compared to the toxicity and hazards of substances like resorcinol, phenol or formaldehyde, as shown in **Table 2**, tannins should be considered as excellent ecological and non-toxic alternative precursor to produce porous carbons.

Synthesis of Porous Carbons

Condensed tannins have been used to produce a wide variety of high added-value materials. The tannin-derived products can be converted into carbon by high-temperature treatment. The resulting materials are glass-like due to the non-graphitizing nature of the precursor, and present isotropic properties and good electrical conductivity. As for petrochemical precursors, the synthesis of porous materials from tannin usually requires the preparation of a resin by crosslinking with formaldehyde, hexamine, or glutaraldehyde, among other possible aldehydes. Thus, different materials have been synthesized such as foams (Tondi et al., 2009; Lacoste et al., 2013; Jana et al., 2014; Szczurek et al., 2014; Delgado-Sánchez et al., 2018), gels (Szczurek et al., 2011a,b; Amaral-Labat et al., 2013; Braghiroli et al., 2019), microspheres (Grishechko et al., 2016), or polyHIPEs (Szczurek et al., 2013). Furthermore, tannin autocondensation reactions enable its polymerization without having to use crosslinkers, opening the way for the production of OMCs by self-assembly techniques (Schlienger et al., 2012; Braghiroli et al., 2016). The following section describes some of the methods used to obtain micro-mesoporous carbon materials from tannin, as well as their performance when used as electrodes for SCs, they are summarized in **Table 3**.

Sol-Gel

CGs were produced from mimosa tannin and formaldehyde (TF) organic cryogels (Amaral-Labat et al., 2012). The pH of mimosa tannin solutions was adjusted with either acetic acid or NaOH diluted in water to obtain a pH ranging from 3.3 to 7.3. Such solutions were placed in an oven at 85°C for 5 days, in which gelation and aging took place. After exchanging water for *tert*-butanol, the gels were freeze-dried to obtain TF cryogels. Finally, CGs were produced by carbonization of TF cryogels at 900°C. Surface areas from 399 to 1,420 $m^2\ g^{-1}$ were obtained, with minimum values found for pH 4.3 and 5.3 and attributed to pore collapse during carbonization. The highest surface areas were found for pH > 6. This unusual development of surface area was ascribed to the presence of NaOH, which could act as an activating agent during the carbonization process. The textural characterization revealed that the CGs were mainly micro- and macroporous materials, with an unusually low amount of mesopores.

In order to test their electrochemical performance, the CGs were ground to prepare pellets by mixing the corresponding sample, carbon black and PVDF (75:5:20 wt. %), and then symmetrical SCs were assembled and tested in a T-type cell. CV tests were carried out from 2 to 50 mV s^{-1} using 4 M H_2SO_4 as electrolyte in a potential window of 1 V. The values of C_e of the CGs at 2 mV s^{-1} ranged from 30 to 109 F g^{-1}, similar to the values found for more expensive carbon aerogels. As expected, the best performance was observed for the materials with the highest surface area. However, as the scan rate increased, the CV curves became narrower and lost their quasi-rectangular shapes, indicating a loss of SC behavior and resulting in a decrease of C_e. It was concluded that, although these CGs were highly porous, the values of capacitance were generally lower than expected due to the large amount of macropores that do not account for the capacitance. Besides, the sharp drop in C_e with the increase in scan rate was related to the absence of mesopores to facilitate the diffusion of electrolyte ions in the micropores.

Hydrothermal Carbonization

Hydrothermal treatments of aqueous solutions of tannins take advantage of their autocondensation at very acidic or basic pH. By varying pH, tannin concentration and temperature, it is possible to obtain gels or spheres. Besides, it is possible to perform

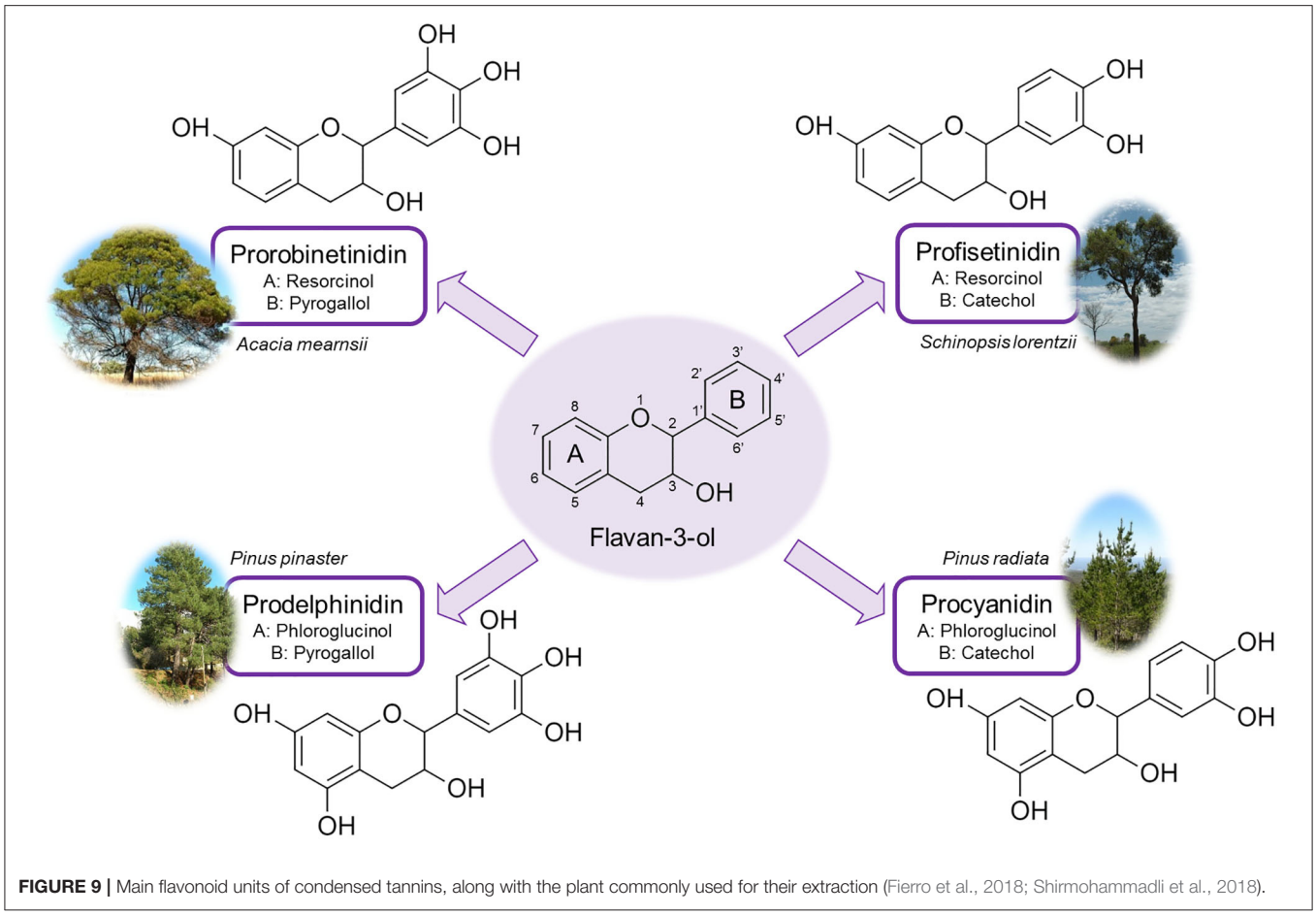

FIGURE 9 | Main flavonoid units of condensed tannins, along with the plant commonly used for their extraction (Fierro et al., 2018; Shirmohammadli et al., 2018).

N-doping *in situ* by using ammonia solutions instead of water during the HTC process. Several examples of the electrochemical performances of carbonized, tannin-derived, HTC materials are described below.

N-doped materials were produced by HTC of mimosa tannin (Braghiroli et al., 2015a,b). Two functionalization routes were followed: (i) dissolution of tannin in an aqueous ammonia solution, evaporation at room temperature, then dissolution of the solid residue in water solution followed by HTC; and (ii) dissolution of tannin in an aqueous ammonia solution followed by HTC. The former resultant material was called EAT (for "evaporated aminated tannin"), and the latter was called AT (for "aminated tannin"). A reference material, prepared by direct HTC of tannin in water, called T, was also synthesized. HTC was carried out at temperatures ranging from 180 to 220°C for 24 h, and the recovered materials were carbonized at 900°C. The morphology radically changed from CNSs for the reference materials to CG structure for the EAT-materials, while the carbon obtained by the AT-route presented a mixed morphology, see **Figures 10A–C**. The carbon materials exhibited surface areas between 113 and 684 $m^2\ g^{-1}$. AT- and T-materials had a high proportion of ultramicropores (pores of width < 0.7 nm), higher than 79%, while EAT-materials presented a majority of mesopores. The micropore volume remained around ∼0.21 $cm^3\ g^{-1}$ in almost all cases. Regarding the presence of heteroatoms, the AT-route introduced the highest amount of nitrogen into the material with a maximum of 8.1 wt. % for HTC carried out at 220°C. The oxygen content decreased with the temperature, regardless of the functionalization route, remaining between 5.6 and 15.9 wt. %.

The electrochemical performances of carbon materials derived from HTC at 180 and 210°C were evaluated (Braghiroli et al., 2015b). Electrodes for symmetrical SCs were prepared by mixing the powdered carbon material with carbon black and PVDF (75:5:20 wt. %), and assembled in a T-type cell, using 4 M H_2SO_4 as electrolyte. CV tests were carried out using a potential window of 1 V. The obtained curves were asymmetric, indicating the existence of considerable resistance; examples are shown in **Figure 10D**. CV curves also showed humps characteristic of redox reactions occurring due to the high content of heteroatoms (N and O). Thanks to the pseudocapacitance contributions of these reactions, C_e reached values as high as 322 F g^{-1} at 2 mV s^{-1}. However, as the scan rate increased, C_e dropped considerably. This behavior was attributed to the large size of the mesopores, 27–34 nm, which do not significantly account for the capacitance and do not successfully shorten the ion diffusion pathways as the narrower mesopores would. In order to study the effect of doping, the interfacial capacitance was calculated by

TABLE 2 | Hazard statements for phenol, resorcinol, formaldehyde, and tannin with data from the Kim et al. (2018) and the National Institute for Occupational Safety Health (2018).

	Phenol	Resorcinol	Formaldehyde	Tannin
PEL	TWA 5 ppm (skin)	Not reported	TWA 0.75 ppm STEL 2 ppm	No adverse human health effects* Does not have skin or eye irritation effects*
REL	TWA 5 ppm (skin) STEL 15.6 ppm (skin)	TWA 10 ppm STEL 20 ppm	TWA 0.016 ppm STEL 0.1 ppm	
GHS and NFPA hazards		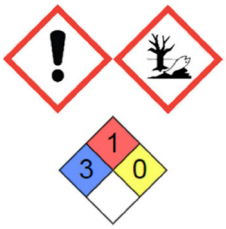		Not reported for profisetinidin, prorobinetinidin, prodelphinidin and procyanidin

*PEL, permissible exposure limit; REL, recommended exposure limit; TWA, time-weighted average over 8 h; STEL, short-term exposure limits over 15 min; GHS, globally harmonized system; NFPA, National fire protection association. *According to SilvaChimica (St Michelle Mondovi, Italy), provider of mimosa, quebracho, and tara tannins.*

TABLE 3 | Summary of methods, properties and electrochemical performance of tannin-derived carbon materials.

Tannin precursor/ Synthesis method	Carbon material	Activation/ Doping	BET area (m^2 g^{-1})	Cell type	Electrolyte	Potential window (V)	C_e (F g^{-1})	References
Mimosa/Sol-gel	Cryo-CGs	–/–	399–1 420	T	4 M H_2SO_4	1.0	30–109, at 2 mV s^{-1}	Amaral-Labat et al., 2012
Mimosa/HTC	CMSs and CG-like	–/N, O	442–684	T	4 M H_2SO_4	1.0	181–322, at 2 mV s^{-1}	Braghiroli et al., 2015b
Mimosa/HTC	Aero-, cryo- and xero-CGs	–/N, O	496–864	T	4 M H_2SO_4	1.0	231–388, at 2 mV s^{-1}	Braghiroli et al., 2015c
Pine/HTC	CMSs and CG-like	–/N, O	80–652	3-e 2-e	1 M H_2SO_4	0.9	114–321, at 0.5 mV s^{-1} 112–258, at 0.1 A g^{-1}	Sanchez-Sanchez et al., 2017b
Quebracho/ Microwave-assisted	MCs	–/P, N	113–855	3-e	1 M H_2SO_4 6 M KOH	0.8	172–272, at 5 mVs^{-1} 176–236, at 5 mVs^{-1}	Nasini et al., 2014
Mimosa/Hard-templating	OMCs	–/–	1006	3-e 2-e	1 M H_2SO_4	0.8	~250, at 0.5 mVs^{-1} ~196, at 0.1 A g^{-1}	Sanchez-Sanchez et al., 2017a
Mimosa/ Phase separation	OMCs	CO_2/–	563–1137	3-e 2-e	2 M H_2SO_4	0.8	158–286, at 0.5 mV s^{-1} Up to 244, at 0.1 A g^{-1}	Sanchez-Sanchez et al., 2018
Mimosa/ Mechanosynthesis	OMCs	CO_2/–	567–2061	2-e	1 M H_2SO_4 1 M Na_2SO_4 1 M $TEABF_4$/ACN	1.0 1.6 2.7	138–147, at 0.2 A g^{-1} 94–100, at 0.2 A g^{-1} 103–109, at 0.2 A g^{-1}	Castro-Gutiérrez et al., 2019

C_e, specific electrode capacitance; HTC, hydrothermal carbonization; CGs, carbon gels; CMSs, carbon microspheres; MCs, mesoporous carbons; OMCs, ordered mesoporous carbons; T, T-type cell; 3-e, three-electrode cell; 2-e, two-electrode cell.

normalizing C_e by the surface area and was plotted against the O and N contents (wt. %), see **Figures 10E,F**. It was found that the interfacial capacitance increased with the O content, but showed a maximum value for an N content between 3 and 6 wt. %. A large amount of heteroatoms is believed to block the pores, resulting in reduced electrochemical performance.

A follow-up study evaluated the electrochemical performances of N-doped CGs produced by HTC of EAT (Braghiroli et al., 2015c). In this case, aqueous solutions of different concentrations of EAT were submitted to HTC at 180°C for 24 h. The recovered products were then dried to produce organic aerogels, cryogels, or xerogels, and the latter materials were further carbonized at 900°C to obtain N-doped CGs. The materials exhibited both micro- and mesoporosity in a proportion of ~40/60, and the highest surface areas were obtained for the highest concentration of EAT, reaching a maximum of 864 m^2 g^{-1}. For all the CGs, the N content remained around 2.5 wt. %, and an O content higher than 13.9 wt. % was observed. Electrodes for symmetrical SCs were prepared and assembled as described above for AT- and EAT-materials. Again, the CV curves were asymmetrical with the characteristic humps due to redox reactions, similar to those displayed in **Figure 10D**. At a scan rate of 2 mV s^{-1}, the ultramicropore volume was found to have more impact on the C_e values than the surface area. The capacitance increased significantly up to an ultramicropore volume of 0.2 cm^3 g^{-1},

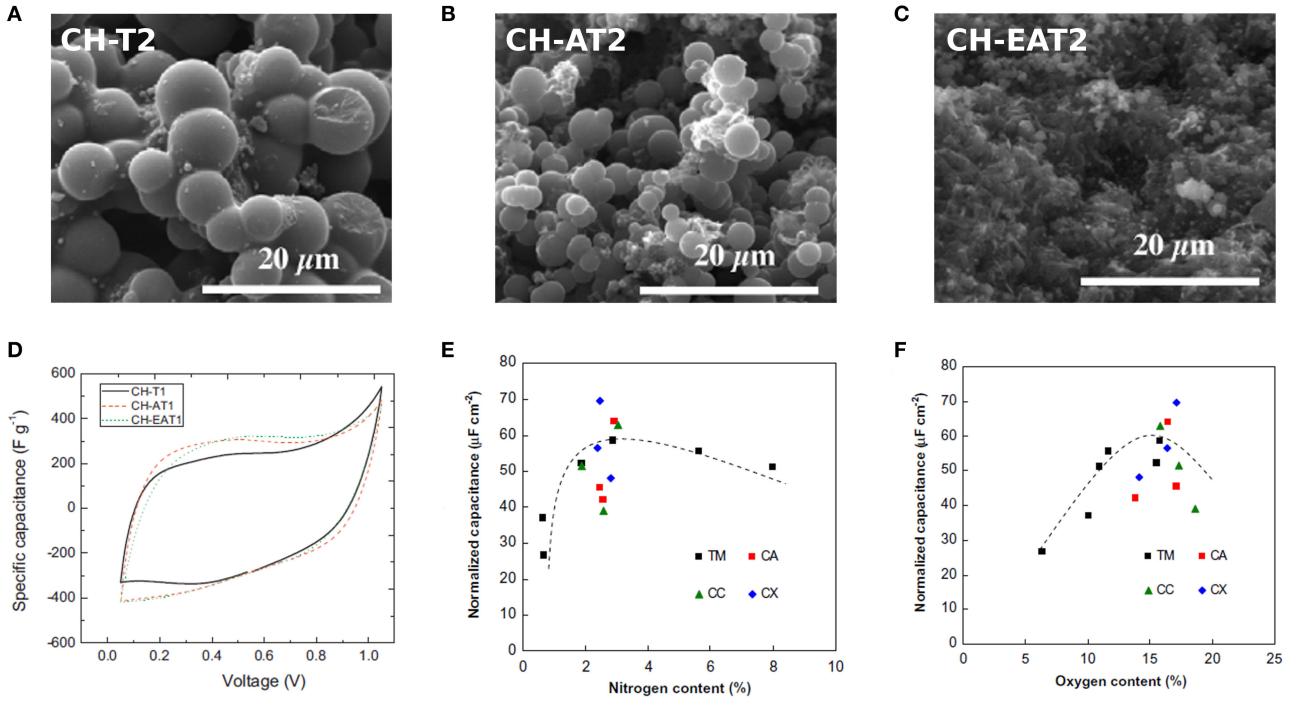

FIGURE 10 | SEM images of materials obtained after HTC at 210°C and subsequent pyrolysis at 900°C of tannin in: **(A)** water, or **(B)** ammonia solution, and **(C)** evaporated aminated tannin in water. **(D)** Examples of cyclic voltammetry curves obtained at 2 mV s^{-1} from carbonized (900°C) HTC materials produced at 180°C (Adapted with permission of Elsevier, from Braghiroli et al., 2015b; permission conveyed through Copyright Clearance Center, Inc.). Normalized capacitance as a function of **(E)** nitrogen and **(F)** oxygen content of: carbonized HTC materials produced at 180 and 210°C, referred to as TM, and of EAT-derived CGs, referred to as CA, CC, and CX for carbon aerogels, cryogels and xerogels, respectively (Adapted with permission of Elsevier, from Braghiroli et al., 2015c; permission conveyed through Copyright Clearance Center, Inc.). The sample labels correspond to those used in their respective source references.

for which it reached a maximum value of ~400 F g^{-1}. A further increase in the volume did not affect the capacitance values. Contrary to what was expected, the values were more scattered than in the trends previously observed when comparing the effect of O and N doping on the interfacial capacitance with the results of Braghiroli et al. (2015b) (see again **Figures 10E,F**). Recalling that all CGs have a similar N content, this scattering might be due to their larger differences of pore texture. The enhancement in the capacitance due to N-doping could be positively or negatively influenced by, for example, a larger or lower surface area, explaining the scattering of the values in **Figure 10E**. An analogous reasoning would also explain the behavior observed for the effect of the O content in **Figure 10F**.

Another study proved that N-doped carbon materials can also be obtained by HTC treatment of aminated pine tannin (Sanchez-Sanchez et al., 2017b). The synthesis reported by Braghiroli et al. (2015b) was used by replacing mimosa tannin with pine tannin and carrying out the HTC process at 190°C. The tannin extraction from *Pinus pinaster* was carried out by two methods. In method (i), a mix of pine bark and water in weight ratio of 1:6 was heated up to 90°C for 90 min. In method (ii), the same mix used in (i) but in a 1:5 weight ratio was heated up to 75°C; then, an aqueous solution containing 2 and 0.5% of Na_2SO_3 and Na_2CO_3, respectively, was added to the mixture while maintaining the temperature for an additional 60 min. The suspensions from methods (i) and (ii) were filtered, washed with water and spray-dried, leading to tannin powders referred as TW or TNa, respectively. The morphology of the carbon materials was similar to that obtained from the same treatment of mimosa tannin, i.e., showing a transition from spherical particles to a gel-like structure. Most of the materials presented a high microporosity that led to surface areas between ~300 and ~700 m^2 g^{-1}. However, samples obtained from the direct HTC of TNa and from the EAT-route did not develop any porous texture, which is the reason why they were excluded from the electrochemical tests.

A three-electrode configuration was used to evaluate the electrochemical performance of the pine tannin-derived materials in a potential window of 0.9 V in 1 M H_2SO_4. Electrodes were prepared by mixing the porous carbon, carbon black and PTFE (85:5:10 wt. %). Faradaic peaks were observed on the CV curves at low scan rates (0.5 mV s^{-1}). Remarkably, the TW-materials retained a quasi-rectangular CV curve for a high scan rate of 1 V s^{-1}, but the deviations from the ideal rectangular shape suggest that the diffusion of ions in the narrow micropores was hindered. At low scan rate, C_e of TW-materials was above 200 F g^{-1} due pseudocapacitance contributions. However, for a scan rate of 20 mV s^{-1}, C_e has already decreased to ~40%

of its original values because redox reactions do not occur at faster scan rates. Capacitance then continued to decrease but at a considerably slower rate, almost reaching a plateau at 1 V s^{-1}. In addition, a linear increase in interfacial capacitance with the surface concentration of heteroatoms (N and O) was observed for the TW-materials. As the scan rate increased, the slope of the fitted line decreased, becoming almost a horizontal line at 1 V s^{-1}. This implies that, for fast scan rates, the heteroatom content does not contribute to the capacitance, in agreement with the previous statements. TNa-A sample, obtained from aminated TNa, exhibited the lowest performance, whatever the scan rate and despite a surface area and density of surface functionalities similar to those of other materials from the TW-series. Furthermore, TNa-A exhibited the lowest value of interfacial capacitance, indicating that a large part of the surface of the material was not accessible to the electrolyte ions. The high amount of surface functionalities was not able to compensate the lack of charge storage sites resulting in the poor performance observed. In addition, GCD and EIS measurements were carried out using a two-electrode cell. The calculation of C_e from the GCD curves gave values similar to those obtained from the CV curves, and a drastic drop in capacitance was observed as the applied current increased. Again, TNa-A had the lowest performance. In general, the doped materials from the TW-series had the highest values of capacitance, confirming the beneficial role of surface modification. However, there are still some drawbacks to the doping procedure followed, as the EIS and GCD tests also revealed that the doped materials had larger EDR values and lower stability after continuous cycling than their non-doped counterparts.

Microwave-Assisted Synthesis

P- and N-doped carbons (PNDCs) have been successfully produced by a microwave technique using quebracho tannin as carbon precursor (Gopal Bairi et al., 2013). Melamine and hexamine were used as N source and polyphosphoric acid as P source. The synthesis was carried out by dissolving melamine and tannin in water, then a solution of hexamine was added and the whole mixture was heated to its boiling point. Finally, the resultant material was mixed with polyphosphoric acid and subjected to microwaves for 30 min. The temperature reached was estimated to be between 1,200 and 1,400°C during the process carried out in a 1.25 kW−2.4 GHz microwave oven. The physicochemical properties and performances of the PNDCs obtained from three different tannin:melamine:hexamine molar ratios as electrodes for SCs were further studied by the same research group (Nasini et al., 2014). The samples were referred to as PNDC-x, where $x = 1$, 2, or 3: the higher the value of x, the lower the amount of melamine and hexamine used for synthesis.

A large amount of heteroatoms was successfully introduced on the surface of the carbon. However, this was achieved by sacrificing considerably the available surface. The sample PNDC-1, having the highest content of surface functionalities (N 9.7 at. %, P 9.0 at. %, and O 14.9 at. %), thus had the lowest BET area, 113 m^2 g^{-1} due to an accumulation of heteroatoms that could hinder access to the pores. Moreover, the higher contents of N and P are the consequence of the use of large quantities of hexamine and polyphosphoric acid, both substances reducing the amount of gases released during pyrolysis, increasing the carbon yield, but also reducing the development of the porous texture. Decreasing the level of doping increased the surface area and increased the volumes of micro- and mesopores. The sample PNDC-3 thus had the lowest content of heteroatoms and exhibited a surface area of 855 m^2 g^{-1} with a total pore volume of 0.65 cm^3 g^{-1}. Intermediate values of heteroatom content and textural properties were found for PNDC-2. PNDCs are mesoporous materials, and most of their pore volume is due to narrow mesopores (of width ∼3–4 nm) at the levels of 99, 78, and 89% for PNDC-1, PNDC-2, and PNDC-3, respectively.

The electrochemical performance of electrodes composed of PNDC, carbon black and PTFE (90:5:5 wt. %) was evaluated in a three-electrode cell using either 1 M H_2SO_4 or 6 M KOH as electrolytes. The CV curves of all materials in acidic medium revealed the typical peaks associated with redox reactions. At 5 mV s^{-1}, the calculated C_e for PNDC-2 and PNDC-3 was 272 and 246 F g^{-1} and, despite its low surface area, PNDC-1 exhibited a capacitance of 172 F g^{-1} mainly due to pseudocapacitance contributions. As expected, C_e decreased for higher scan rates. A faster drop in capacitance was observed for PNDC-2 than for PNDC-3. At 100 mV s^{-1}, PNDC-2 lost 30% of its capacitance, while PNDC-3 lost only 12%. The higher content of heteroatoms of PNDC-2, compared to PNDC-3, implies that at low scan rate, the contributions of pseudocapacitance are larger. However, at faster rates, redox reactions no longer occur, which reduces the performance of the material. On the other hand, the more stable performance of PNDC-3 is explained by the strong presence of mesopores and a low content of heteroatoms. Thus, for this material, the charge is mainly stored by an EDL mechanism that is not affected by an increase in the scan rate because the mesopores facilitate the diffusion of ions. In alkaline medium, PNDC-3 exhibited a behavior similar to that in acidic medium. However, lower values of C_e were reached; this decrease in capacitance might be caused by the larger size and lower mobility of ions in KOH, compared to those in H_2SO_4 (see **Table 1**). PNDC-2 exhibited the best performance of the series across the range of scan rates, attributed to a combination of sufficiently high surface area, pore volume and pseudocapacitance contribution of the surface functionalities that are reactive in alkaline media. Subsequent studies have extended this synthesis method to produce PNDCs from aminated quebracho tannin (Bairi et al., 2015) and Si- and P-doped carbons from quebracho tannin (Ramasahayam et al., 2015). In both studies, behaviors and values of capacitance similar to those detailed above were found.

Hard-Templating

OMCs have been produced by hard-templating using mimosa tannin and other tannin-related molecules such as phloroglucinol, gallic acid, and catechin (Sanchez-Sanchez et al., 2017a). SBA-15 silica template was synthesized using a mixture of tetraethyl orthosilicate (TEOS), Pluronic® P123, HCl, and water (molar ratio 1:0.017:6.04:145.8) that was stirred at 40°C for 4 h and aged at 125°C for 72 h. The product, recovered by filtration, was heat-treated in air at 550°C for 6 h. An ethanol solution of

the corresponding precursor (0.01 mol/40 mL) was added to the SBA-15, previously degassed under vacuum (150°C, 2 h). Ethanol was evaporated under vacuum and, if necessary, the obtained solid was washed with deionized water to eliminate the excess of precursor deposited on the silica particles. These composites were carbonized under nitrogen flow according to a two-step temperature program: heating from room temperature to 100°C (1°C min^{-1}) and holding the temperature for 2 h in order to remove moisture and polymerize the precursors, then heating up to 900°C (2°C min^{-1}) and holding the temperature for 1 h. The template was removed from the carbonized composites with HF, washed with deionized water and finally dried at 80°C for 12 h. The OMCs were labeled according to their precursors as TanC, PhC, GaC, and CatC for tannin, phloroglucinol, gallic acid, and catechin, respectively.

Figure 11A shows the schematic synthesis process and TEM images of the produced OMCs. TEM images revealed some discontinuities in the structure for CatC and TanC, indicating that catechin and mimosa tannin permeated the template heterogeneously. The large size of these molecules could block some of the pores, preventing the complete filling of the template and resulting in the gaps observed. XRD measurements revealed that all materials exhibited a structure in the *p6mm* space group (2D hexagonal), and that the long-range order decreased as the size of the precursor molecule increased, in agreement with TEM results. Nevertheless, TanC had the advantage of achieving the highest carbon yield (80%) among the carbon precursors used for this study. The textural characterization showed that all the OMCs exhibited BET surface areas of ∼1,000 m^2 g^{-1} and total pore volumes higher than 0.87 cm^3 g^{-1}, of which 75–87% came from mesopores. Chemical characterization by elemental analysis and XPS revealed oxygen as the main heteroatom in the material, which was expected given its abundance in the precursor molecules.

The electrochemical performance was evaluated in 1 M H_2SO_4. CV tests were carried out in a three-electrode cell while GCD and EIS measurements were done in a two-electrode cell. The electrodes, prepared by mixing the OMC, carbon black and PTFE (85:5:10 wt. %), were spread onto graphite foil and pressed at 5 MPa. Rectangular CV curves were observed up to a scan rate of 100 mV s^{-1}. At 0.5 mV s^{-1}, C_e reached values higher than 200 F g^{-1}, which are in the same range of other carbons with similar textural properties but that required additional oxidation post-treatments (Jurewicz et al., 2004; Tanaka et al., 2015). GCD tests led to quasi-triangular curves whose slight curvature suggests the occurrence of redox reactions due to the presence of oxygen on the surface. For both CV and GCD tests, as the charging rate increased (scan rate or applied current), C_e decreased. In particular, TanC presented a capacitance retention of 42 % at 100 mV s^{-1} and 51 % at 12 A g^{-1}, higher than the ∼30% retention reported for the pine tannin-derived HTC carbons described above and tested under similar conditions (Sanchez-Sanchez et al., 2017b). The enhanced performance of OMCs as electrodes for SCs confirms the beneficial role of a hierarchical porous structure as a means of improving ion diffusion in the carbon material.

Soft-Templating

Phase Separation

Mimosa tannin was successfully used as precursor to produce OMCs by an easy and simple phase-separation method (Braghiroli et al., 2016). The synthesis only required the mixing, at room temperature, of two solutions: one of mimosa tannin, the other of Pluronic® F127. Immediately after mixing, a phase-separation occurred and after 2 days, complete sedimentation of the resultant mesophase was observed. The recovered mesophase was dried at 80°C and carbonized at temperatures ranging from 400 to 900°C. The pH of the tannin solution was varied from 0 to 4.2 but no significant change in the carbon yield or the porosity were observed by modifying this parameter. The synthesis process is shown in **Figure 11B**, and TEM images of OMCs obtained for different pH values are presented. Thermogravimetric analysis showed that the Pluronic® F127 degrades at 400°C, so carbonization at higher temperatures is required to remove it completely from the material. Higher temperature treatments resulted in more developed microporosity and consequently higher surface areas: a maximum of ∼700 m^2 g^{-1} BET area was reached. These values of surface area are ∼200 m^2 g^{-1} higher than those obtained from an EISA method also using mimosa tannin as precursor and carbonizing the mesophase at a maximum temperature of 850°C (Schlienger et al., 2012).

Some modifications to the phase-separation method were made in a following study that also investigated the effect of the assembly temperature (Sanchez-Sanchez et al., 2018). The pH was varied from 1 to 4.5 and the assembly temperature ranged from 10 to 30°C. The mixed tannin/F127 solutions were keep at a constant assembly temperature for 72 h, and then they remained at room temperature for 5 days until complete phase-separation. The retrieved resins were dried at 60°C and carbonized in two consecutive steps: increasing the temperature up to 400°C, holding it for 4 h, and then heating until 900°C and holding for 1 h. In agreement with the previous work of Braghiroli et al. (2016), it was found that for a fixed temperature, the pH did not change considerably the porous texture. On the contrary, for a given pH, an effect of the assembly temperature was observed, where the greatest change occurred at pH 3 after increasing the temperature from 20 to 30°C. The solution of pH 3 assembled at 30°C gave the carbon material, called F3/30, having the highest values of surface area and micro- and mesopore volumes, 750 m^2 g^{-1}, 0.24 and 0.49 cm^3 g^{-1}, respectively. Therefore, F3/30 was selected for CO_2 activation to improve its porous texture further.

As expected, for the resultant activated carbon, labeled C3/30, an increased surface area (∼1,100 m^2 g^{-1}) and a widening of pores were observed. Three- and two-electrode cells were used for its electrochemical characterization, using 2 M H_2SO_4 as electrolyte and electrodes composed of a mixture of the studied carbon, carbon black and PTFE (85:5:10 wt. %). It was found that the main mechanism of storage of energy was the EDL, since the contribution of pseudocapacitance from heteroatoms was negligible. In addition, CV and GCD tests showed that the activation process increased the capacitance of the material by 1.5 times, probably due to the widening and

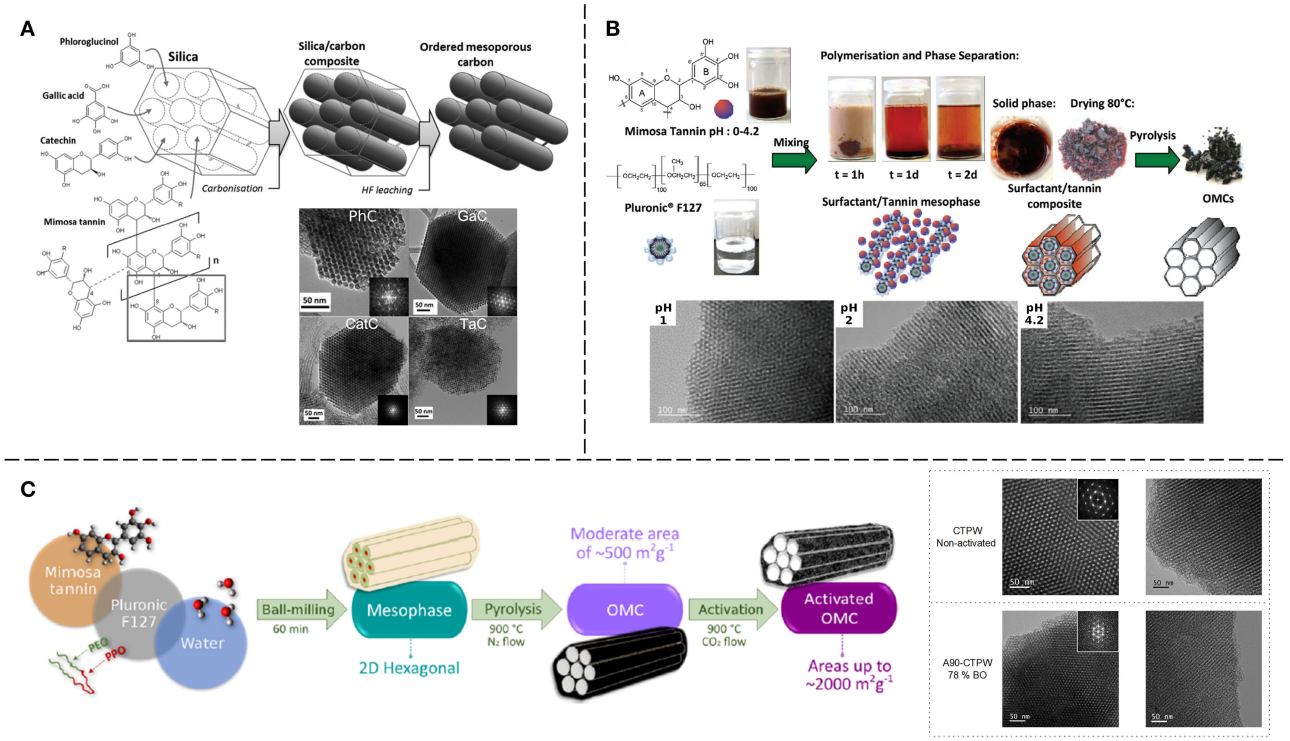

FIGURE 11 | Synthesis of OMCs from mimosa tannin by: **(A)** hard-templating, also carried out using other biomass-derived phenolic molecules (Adapted with permission of Elsevier, from Sanchez-Sanchez et al., 2017a; permission conveyed through Copyright Clearance Center); and soft-templating through **(B)** phase separation (Adapted from Braghiroli et al., 2016 by permission of The Royal Society of Chemistry) and **(C)** mechanosynthesis (Adapted with permission from Castro-Gutiérrez et al., 2019. Copyright 2019 American Chemical Society).

opening of previously blocked pores, which resulted in improved connectivity of the pore network and surface accessibility to electrolyte ions. Even more, the electrochemical tests showed that the rate capabilities of C3/30 were comparable to those measured for the hard-templated TanC obtained from the same precursor, mimosa tannin, but through a less eco-friendly synthesis method (Sanchez-Sanchez et al., 2017a), thus showing the advantage of the soft-template method.

Mechanosynthesis

Mechanosynthesis methods, for which mechanical energy is supplied to the materials by shearing, stretching, or grinding (James et al., 2012), are commonly used to produce ceramics, metal alloys, and organic materials (Kaupp, 2009, 2011; Wang, 2013). This type of solid-state synthesis has attracted interest for producing OMCs since they require little or no solvent, short synthesis times compared to other methods and fewer synthesis steps, which results in cheaper and more eco-friendly products (James et al., 2012; Wang, 2013; Zhu et al., 2016). Ball-milling has been found to be an appropriate method for synthesizing OMCs, as it can provide higher energy and repeatability than manual grinding, thereby increasing its potential for use on an industrial scale (Wang, 2013). OMCs were indeed obtained by ball-milling mimosa tannin, Pluronic® F127 and metal acetates used as crosslinkers. After washing, drying and carbonization, 2D hexagonal geometries were observed (Zhang et al., 2017).

More recently, another study reported an easy, one-pot mechanosynthesis method for preparing OMCs with a 2D hexagonal structure by ball-milling, where only mimosa tannin (T), Pluronic® F127 (P) and small amounts of water (W) were needed (Castro-Gutiérrez et al., 2018). This surfactant-water-assisted mechanochemical mesostructuration (SWAMM) method does not involve curing or drying steps before carbonization or the use of hazardous substances as crosslinkers. The influence of synthesis parameters such as milling time, pH, P:W weight ratio and carbonization temperature on the textural properties of the obtained carbon materials was analyzed. Optimal values of milling time (60 min) and pH (unchanged) to produce uniform PSDs were found and it was shown that by changing the P:W weight ratio, it was possible to produce either ordered or disordered mesoporous materials. Increasing the carbonization temperature from 900 to 1,100°C resulted in the development of micro- and mesoporosity, but higher temperatures, up to 1,500°C, did not seem to have a significant impact on the textural properties of the OMCs. Nonetheless, Raman spectra revealed that despite being in the non-graphitizable regime, higher carbonization temperatures yielded materials with improved long-range order at the nanoscale. Several applications were explored with promising results, such as the adsorption of hydrocarbons from water, the adsorption of CO_2 and, after activation, the storage of energy in SCs.

Energy storage in SCs was further investigated in a follow-up study, where the electrochemical performances of activated OMCs (AOMCs) produced by the SWAMM method were evaluated (Castro-Gutiérrez et al., 2019). The OMC was placed inside a tubular furnace and heated up to 900°C (5°C min^{-1}) under N_2 flow, then N_2 was switched to CO_2 to physically activate the samples for durations ranging from 15 to 120 min. The samples were labeled A*t*-CTPW with *t* standing for the time in minutes. TEM images of as-synthesized and A90-CTPW materials are shown in **Figure 11C** with a scheme of the synthesis method. It was observed that the ordered mesoporous structure was maintained up to a burn-off of 78% (A90-CTPW). The surface area of the AOMCs increased with burn-off, reaching a maximum of ∼2,000 m^2 g^{-1} for a burn-off of ∼80%. Higher activation times resulted in a sudden decrease of surface area due to pore widening and merging, evidenced by the PSDs and the derived calculations of ultramicro-, supermicro- (0.7 < pore width < 2 nm) and mesopore volumes. Electrodes were prepared with samples A30- to A-90-CTPW that were mixed with carbon black and PTFE (85:5:10 wt. %) to form a paste from which electrodes with carbon loads of ∼10 mg cm^{-2} were cut and assembled in a two-electrode cell.

CV tests performed in 1 M H_2SO_4 revealed rectangular curves at 5 mV s^{-1}, with C_e values between 136 and 160 F g^{-1}, the maximum being reached by A75-CTPW. Only A60- and A75-CTPW retained more than 60% of their initial capacitance at 500 mV s^{-1}, which was attributed to a combination of high surface area originating from a high micropore volume (<0.50 cm^3 g^{-1}), providing multiple charge storage sites, and a suitable PSD, favoring ion diffusion at high charging rates. A further characterization was then carried out on these samples, using also 1 M $TEABF_4$/ACN as electrolyte. Examples of CV curves in aqueous and organic electrolytes are shown in **Figures 12A,D**. During GCD tests, A60- and A75-CTPW exhibited triangular curves in the aqueous electrolyte. However, A75-CTPW performed better once the applied current increased, showing a capacitance retention, C_{ret}, of 70%, whereas that observed for A60-CTPW was only 51%, both at a high current of 80 A g^{-1}, see **Figure 12B**. In the organic electrolyte, A60- and A75-CTPW behaved in a similar way and a more rapid drop of C_{ret} was observed compared to that in the aqueous electrolyte (**Figure 12E**). This was ascribed to the larger size and lower mobility of the ions in the organic electrolyte that increased the resistance of the SC cell, thereby decreasing its performance. In all cases, the tannin-derived AOMCs presented superior or comparable rate capabilities than those previously reported for similar materials (also displayed in **Figures 12B,E**) with the advantage of being produced by an easy and eco-friendly method. Even more, A60- and A75-CTPW exhibited great long-term stability over time and after continuous cycling at 5 A g^{-1}. More precisely, in the aqueous electrolyte, C_{ret} remained at ∼98% after 10,000 cycles and ∼94% after 50 h of potentiostatic hold at 1 V, while in the organic electrolyte C_{ret} was above 90% after 8,000 cycles and reached 86 % after 72 h of potentiostatic hold at 2.7 V.

As expected, the values of *E* and *P* in organic electrolyte are considerably higher than in aqueous electrolyte, see **Figures 12C,F**. Indeed, a maximum *E* of 28 Wh kg^{-1} (at a *P* output of 138 W kg^{-1}) was attained in the organic electrolyte, more than 5 times the maximum *E* of 5 Wh kg^{-1} (at a *P* output of 44 W kg^{-1}) reached in the aqueous electrolyte. For the organic electrolyte, it is important to note that, despite the drastic drop in *E* observed, the selected AOMCs were still able to store ∼13 Wh kg^{-1} at a high *P* of 12 kW kg^{-1}. Finally, the electrochemical performances of the selected AOMCs were also evaluated in 1 M Na_2SO_4, a neutral aqueous electrolyte. The results are shown in **Figures 12G–I**. In general, lower values of C_e and C_{ret} were found compared to those obtained in acidic medium (H_2SO_4). The lower performance of the SCs in Na_2SO_4 can be related to a larger size and lower mobility of the Na^+ ion. The larger size results in fewer charge storage sites, leading to a lower capacitance while the lower mobility hinders diffusion at high charging rates. Nevertheless, the advantage of the neutral electrolyte lies in the possibility of extending the operating potential window. Consequently, an increase of ∼60% of the maximum *E* was observed with respect to that reached in acidic medium.

SUMMARY AND PERSPECTIVES

SCs are devices with high power outputs, rate capability, cyclability, and long lifetimes. However, the amount of stored energy in SCs is lower than that found in batteries. In this sense, research in recent decades has focused on the development of new materials that can improve SC performance, not only by increasing the storage capacity but also by increasing the rate capability and the long-term stability. Porous carbons have proven to be adequate materials for SC electrodes and, indeed, ACs are already widely used in commercial devices. Multiple synthesis methods have been developed to control the textural and chemical properties of porous carbons; in particular, templated carbons, such as OMCs, are promising electrode materials because they can be produced with different morphologies, high surface area and adjusted hierarchical porosity. The possibility of tuning the pore size is of significant importance as it allows full accessibility of the electrolyte into the material, while the hierarchical structure provides channels facilitating the diffusion of ions toward the smallest accessible pores. The modification of the surface chemistry of porous carbons presents another route to increase SC performance, and doping with oxygen, nitrogen or other heteroatoms can induce redox reactions that increase the energy stored in the device. Even if all the surface functionalities do not always induce redox reactions, doping can also improve other characteristics of the material such as electrical conductivity, wettability, or stability.

Besides, the quest for environmentally friendly technologies has pushed research to find substitutes for synthetic and hazardous molecules commonly used as carbon precursors or crosslinkers. Among the various biosourced precursors, tannins are excellent alternatives to petrochemical carbon sources because of their phenolic nature. In addition, condensed tannins have a reactivity similar to that of phenol or resorcinol, so tannins can replace them in already established synthesis methods. The autocondensation property of condensed tannins also offers the opportunity of avoiding the use of crosslinkers, which

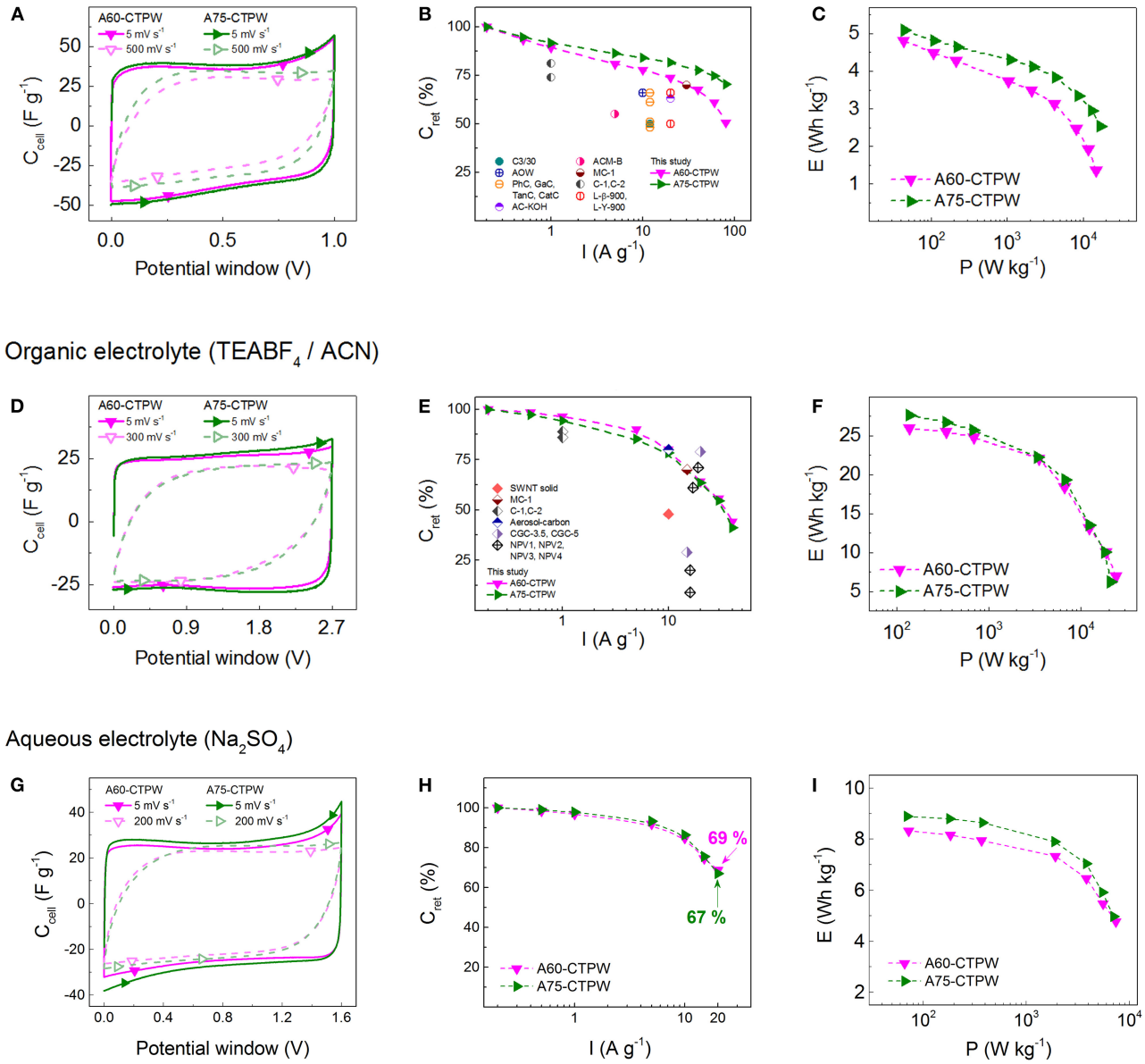

FIGURE 12 | Electrochemical performances of activated OMCs derived from mimosa tannin: **(A,D,G)** CV curves; **(B,E,H)** capacitance retention as a function of applied current; and **(C,F,I)** specific energy as a function of specific power (Ragone-like graphs) calculated from the GCD curves. The tests were carried out in **(A–C)** 1 M H_2SO_4 aqueous electrolyte (acidic medium), **(D–F)** 1 M $TEABF_4$/ACN organic electrolyte and (G-I) 1 M Na_2SO_4 aqueous electrolyte (neutral medium). (Adapted with permission from Castro-Gutiérrez et al., 2019. Copyright 2019 American Chemical Society).

makes them suitable precursors for self-assembly methods. As described in the last section of this review, several studies have demonstrated the versatility of tannins to produce porous carbon materials through "green" processes reducing or even eliminating the use of toxic or hazardous substances and thus decreasing their negative environmental impact. In addition, tannins are extracted industrially and marketed on a large scale, because they are essential for the leather, wine and food industry. Therefore, they are readily available at low cost. Thus, the production of porous carbons from tannin will provide and add value to this precursor derived from biomass.

In general, the main disadvantages of producing advanced porous carbon materials are their complex multi-step procedures and their tedious synthesis. Therefore, future materials research efforts for SCs should continue to focus on the development and optimization of easy and environmentally friendly procedures such as one-pot synthesis methods that allow for *in situ* doping and/or activation of biomass or biosourced precursors.

Simplifying and reducing the number of steps would reduce costs and increase scalability, resulting in a use of biosourced carbons that is more widespread in commercial SC devices.

AUTHOR CONTRIBUTIONS

JC-G performed writing original draft and conceptualization. AC performed writing—review and editing. VF performed conceptualization, supervision, funding acquisition, and writing—review and editing. All authors contributed to the article and approved the submitted version.

FUNDING

This study was partly funded by the French PIA project Lorraine Université d'Excellence, reference ANR-15-IDEX-04-LUE and the TALiSMAN project, funded by FEDER (2019-000214).

ACKNOWLEDGMENTS

JC-G gratefully acknowledges CONACYT-SENER (601021/438978) for the scholarship awarded to support her Ph.D. studies, resulting in the work presented herein.

REFERENCES

Acosta, R., Nabarlatz, D., Sánchez-Sánchez, A., Jagiello, J., Gadonneix, P., Celzard, A., et al. (2018). Adsorption of bisphenol A on KOH-activated tyre pyrolysis char. *J. Environ. Chem. Eng.* 6, 823–833. doi: 10.1016/j.jece.2018.01.002

Amaral-Labat, G., Grishechko, L. I., Fierro, V., Kuznetsov, B. N., Pizzi, A., and Celzard, A. (2013). Tannin-based xerogels with distinctive porous structures. *Biomass Bioenergy* 56, 437–445. doi: 10.1016/j.biombioe.2013.06.001

Amaral-Labat, G., Szczurek, A., Fierro, V., Stein, N., Boulanger, C., Pizzi, A., et al. (2012). Pore structure and electrochemical performances of tannin-based carbon cryogels. *Biomass Bioenergy* 39, 274–282. doi: 10.1016/j.biombioe.2012.01.019

Aneke, M., and Wang, M. (2016). Energy storage technologies and real life applications – a state of the art review. *Appl. Energy* 179, 350–377. doi: 10.1016/j.apenergy.2016.06.097

Ayala, P., Arenal, R., Rümmeli, M., Rubio, A., and Pichler, T. (2010). The doping of carbon nanotubes with nitrogen and their potential applications. *Carbon* 48, 575–586. doi: 10.1016/j.carbon.2009.10.009

Bairi, V. G., Nasini, U. B., Kumar Ramasahayam, S., Bourdo, S. E., and Viswanathan, T. (2015). Electrocatalytic and supercapacitor performance of phosphorous and nitrogen co-doped porous carbons synthesized from aminated tannins. *Electrochim. Acta* 182, 987–994. doi: 10.1016/j.electacta.2015.10.011

Bard, A. J., and Faulkner, L. R. (2001). *Electrochemical Methods: Fundamentals and Applications*, 2 Edn. Hoboken, NJ: Wiley.

Basta, A. H., Fierro, V., El-Saied, H., and Celzard, A. (2009). 2-Steps KOH activation of rice straw: an efficient method for preparing high-performance activated carbons. *Bioresour. Technol.* 100, 3941–3947. doi: 10.1016/j.biortech.2009.02.028

Beguin, F., and Frackowiak, E (Eds.). (2013). *Supercapacitors: Materials, Systems, and Applications*. Weinheim: John Wiley & Sons, Ltd.

Berenguer, R., Nishihara, H., Itoi, H., Ishii, T., Morallón, E., Cazorla-Amorós, D., et al. (2013). Electrochemical generation of oxygen-containing groups in an ordered microporous zeolite-templated carbon. *Carbon* 54, 94–104. doi: 10.1016/j.carbon.2012.11.007

Braghiroli, F. L., Amaral-Labat, G., Boss, A., Lacoste, C., and Pizzi, A. (2019). Tannin gels and their carbon derivatives: a review. *Biomolecules* 9:587. doi: 10.3390/biom9100587

Braghiroli, F. L., Fierro, V., Izquierdo, M. T., Parmentier, J., Pizzi, A., and Celzard, A. (2012). Nitrogen-doped carbon materials produced from hydrothermally treated tannin. *Carbon* 50, 5411–5420. doi: 10.1016/j.carbon.2012.07.027

Braghiroli, F. L., Fierro, V., Izquierdo, M. T., Parmentier, J., Pizzi, A., Delmotte, L., et al. (2015a). High surface – highly N-doped carbons from hydrothermally treated tannin. *Ind. Crops Prod.* 66, 282–290. doi: 10.1016/j.indcrop.2014.11.022

Braghiroli, F. L., Fierro, V., Parmentier, J., Pasc, A., and Celzard, A. (2016). Easy and eco-friendly synthesis of ordered mesoporous carbons by self-assembly of tannin with a block copolymer. *Green Chem.* 18, 3265–3271. doi: 10.1039/C5GC02788H

Braghiroli, F. L., Fierro, V., Szczurek, A., Stein, N., Parmentier, J., and Celzard, A. (2015b). Electrochemical performances of hydrothermal tannin-based carbons doped with nitrogen. *Ind. Crops Prod.* 70, 332–340. doi: 10.1016/j.indcrop.2015.03.046

Braghiroli, F. L., Fierro, V., Szczurek, A., Stein, N., Parmentier, J., and Celzard, A. (2015c). Hydrothermally treated aminated tannin as precursor of N-doped carbon gels for supercapacitors. *Carbon* 90, 63–74. doi: 10.1016/j.carbon.2015.03.038

CAPPEQ (2019a). *How to Extract Tannin? Tannins.* Available online at: https://www.tannins.org/how-to-extract-tannin/ (accessed February 3, 2020).

CAPPEQ (2019b). *Tannin, A History Close to Your Own. Tannins.* Available online at: https://www.tannins.org/history-of-tannin/ (accessed February 3, 2020).

CAPPEQ (2019c). *Tannin: One Substance, Different Applications. Tannins.* Available online at: https://www.tannins.org/applications/ (accessed February 3, 2020).

Castro-Gutiérrez, J., Díez, N., Sevilla, M., Izquierdo, M. T., Ghanbaja, J., Celzard, A., et al. (2019). High-rate capability of supercapacitors based on tannin-derived ordered mesoporous carbons. *ACS Sust. Chem. Eng.* 7, 17627–17635. doi: 10.1021/acssuschemeng.9b03407

Castro-Gutiérrez, J., Sanchez-Sanchez, A., Ghanbaja, J., Díez, N., Sevilla, M., Celzard, A., et al. (2018). Synthesis of perfectly ordered mesoporous carbons by water-assisted mechanochemical self-assembly of tannin. *Green Chem.* 20, 5123–5132. doi: 10.1039/C8GC02295J

Cha, J. S., Park, S. H., Jung, S.-C., Ryu, C., Jeon, J.-K., Shin, M.-C., et al. (2016). Production and utilization of biochar: a review. *J. Industr. Eng. Chem.* 40, 1–15. doi: 10.1016/j.jiec.2016.06.002

Chang, P.-Y., Bindumadhavan, K., and Doong, R.-A. (2015). Size effect of ordered mesoporous carbon nanospheres for anodes in li-ion battery. *Nanomaterials* 5, 2348–2358. doi: 10.3390/nano5042348

Chen, C.-M., Zhang, Q., Zhao, X.-C., Zhang, B., Kong, Q.-Q., Yang, M.-G., et al. (2012). Hierarchically aminated graphene honeycombs for electrochemical capacitive energy storage. *J. Mater. Chem.* 22:14076. doi: 10.1039/c2jm31426f

Chen, H., Liu, D., Shen, Z., Bao, B., Zhao, S., and Wu, L. (2015). Functional biomass carbons with hierarchical porous structure for supercapacitor electrode materials. *Electrochim. Acta* 180, 241–251. doi: 10.1016/j.electacta.2015.08.133

Ciszewski, M., Koszorek, A., Radko, T., Szatkowski, P., and Janas, D. (2019). Review of the selected carbon-based materials for symmetric supercapacitor application. *J. Elec. Mater.* 48, 717–744. doi: 10.1007/s11664-018-6811-7

Conte, M. (2010). Supercapacitors technical requirements for new applications. *Fuel Cells* 10, 806–818. doi: 10.1002/fuce.201000087

de Hoyos-Martínez, P. L., Merle, J., Labidi, J., and Charrier – El Bouhtoury, F. (2019). Tannins extraction: a key point for their valorization and cleaner production. *J. Clean. Prod.* 206, 1138–1155. doi: 10.1016/j.jclepro.2018.09.243

Delgado-Sánchez, C., Santiago-Medina, F., Fierro, V., Pizzi, A., and Celzard, A. (2018). Optimisation of "green" tannin-furanic foams for thermal insulation by experimental design. *Mater. Des.* 139, 7–15. doi: 10.1016/j.matdes.2017.10.064

Deng, Y., Xie, Y., Zou, K., and Ji, X. (2016). Review on recent advances in nitrogen-doped carbons: preparations and applications in supercapacitors. *J. Mater. Chem. A* 4, 1144–1173. doi: 10.1039/C5TA08620E

Díez, N., Ferrero, G. A., Sevilla, M., and Fuertes, A. B. (2019). A sustainable approach to hierarchically porous carbons from tannic acid and their utilization in supercapacitive energy storage systems. *J. Mater. Chem. A* 7, 14280–14290. doi: 10.1039/C9TA01712G

Elmouwahidi, A., Castelo-Quibén, J., Vivo-Vilches, J. F., Pérez-Cadenas, A. F., Maldonado-Hódar, F. J., and Carrasco-Marín, F. (2018). Activated carbons from agricultural waste solvothermally doped with sulphur as electrodes for supercapacitors. *Chem. Eng. J.* 334, 1835–1841. doi: 10.1016/j.cej.2017.11.141

Feinle, A., Elsaesser, M. S., and Hüsing, N. (2016). Sol–gel synthesis of monolithic materials with hierarchical porosity. *Chem. Soc. Rev.* 45, 3377–3399. doi: 10.1039/C5CS00710K

Feng, S., Li, W., Wang, J., Song, Y., Elzatahry, A. A., Xia, Y., et al. (2014). Hydrothermal synthesis of ordered mesoporous carbons from a biomass-derived precursor for electrochemical capacitors. *Nanoscale* 6, 14657–14661. doi: 10.1039/C4NR05629A

Ferrero, G. A., Fuertes, A. B., and Sevilla, M. (2015). N-doped microporous carbon microspheres for high volumetric performance supercapacitors. *Electrochim. Acta* 168, 320–329. doi: 10.1016/j.electacta.2015.04.052

Fierro, V., Muñiz, G., Basta, A. H., El-Saied, H., and Celzard, A. (2010). Rice straw as precursor of activated carbons: activation with ortho-phosphoric acid. *J. Hazard. Mater.* 181, 27–34. doi: 10.1016/j.jhazmat.2010.04.062

Fierro, V., Sánchez-Sánchez, A., and Celzard, A. (2018). "Tannins as precursors of supercapacitor electrodes," in *Sustainable Energy Technologies*, eds E. Rincón-Mejía and A. de las Heras (Boca Raton, FL: CRC Press), 201–228.

Fierro, V., Torné-Fernández, V., and Celzard, A. (2007). Methodical study of the chemical activation of Kraft lignin with KOH and NaOH. *Microp. Mesopor. Mater.* 101, 419–431. doi: 10.1016/j.micromeso.2006.12.004

Fierro, V., Torné-Fernández, V., Montané, D., and Celzard, A. (2005). Study of the decomposition of kraft lignin impregnated with orthophosphoric acid. *Thermochim. Acta* 433, 142–148. doi: 10.1016/j.tca.2005.02.026

Frackowiak, E. (2007). Carbon materials for supercapacitor application. *Phys. Chem. Chem. Phys.* 9:1774. doi: 10.1039/b618139m

Frackowiak, E., and Beguin, F. (2001). Carbon materials for the electrochemical storage of energy in capacitors. *Carbon* 39, 937–950. doi: 10.1016/S0008-6223(00)00183-4

Frackowiak, E., Lota, G., Machnikowski, J., Vix-Guterl, C., and Béguin, F. (2006). Optimisation of supercapacitors using carbons with controlled nanotexture and nitrogen content. *Electrochim. Acta* 51, 2209–2214. doi: 10.1016/j.electacta.2005.04.080

Fuertes, A. B., Ferrero, G. A., Diez, N., and Sevilla, M. (2018). A green route to high-surface area carbons by chemical activation of biomass-based products with sodium thiosulfate. *ACS Sust. Chem. Eng.* 6, 16323–16331. doi: 10.1021/acssuschemeng.8b03264

Gao, L., Peng, A., Wang, Z. Y., Zhang, H., Shi, Z., Gu, Z., et al. (2008). Growth of aligned carbon nanotube arrays on metallic substrate and its application to supercapacitors. *Solid State Commun.* 146, 380–383. doi: 10.1016/j.ssc.2008.03.034

Gao, Z., Zhang, Y., Song, N., and Li, X. (2017). Biomass-derived renewable carbon materials for electrochemical energy storage. *Mater. Res. Lett.* 5, 69–88. doi: 10.1080/21663831.2016.1250834

Gautham Prasad, G., Shetty, N., Thakur, S., Rakshitha, and Bommegowda, K. B. (2019). Supercapacitor technology and its applications: a review. *IOP Conf. Ser. Mater. Sci. Eng.* 561:012105. doi: 10.1088/1757-899X/561/1/012105

González, A., Goikolea, E., Barrena, J. A., and Mysyk, R. (2016). Review on supercapacitors: technologies and materials. *Renew. Sust. Energ. Rev.* 58, 1189–1206. doi: 10.1016/j.rser.2015.12.249

González-García, P. (2018). Activated carbon from lignocellulosics precursors: A review of the synthesis methods, characterization techniques and applications. *Renew. Sust. Energy Rev.* 82, 1393–1414. doi: 10.1016/j.rser.2017.04.117

Gopal Bairi, V., Bourdo, S. E., Nasini, U. B., Ramasahayam, S. K., Watanabe, F., Berry, B. C., et al. (2013). Microwave-assisted synthesis of nitrogen and phosphorus co-doped mesoporous carbon and their potential application in alkaline fuel cells. *Sci. Adv. Mat.* 5, 1275–1281. doi: 10.1166/sam.2013.1583

Grishechko, L. I., Amaral-Labat, G., Fierro, V., Szczurek, A., Kuznetsov, B. N., and Celzard, A. (2016). Biosourced, highly porous, carbon xerogel microspheres. *RSC Adv.* 6, 65698–65708. doi: 10.1039/C6RA09462G

Gu, W., and Yushin, G. (2014). Review of nanostructured carbon materials for electrochemical capacitor applications: advantages and limitations of activated carbon, carbide-derived carbon, zeolite-templated carbon, carbon aerogels, carbon nanotubes, onion-like carbon, and graphene: nanostructured carbon materials for electrochemical capacitor applications. *Wiley Interdiscip. Rev. Energ. Environ.* 3, 424–473. doi: 10.1002/wene.102

Haslam, E. (2007). Vegetable tannins – lessons of a phytochemical lifetime. *Phytochemistry* 68, 2713–2721. doi: 10.1016/j.phytochem.2007.09.009

Herou, S., Ribadeneyra, M. C., Madhu, R., Araullo-Peters, V., Jensen, A., Schlee, P., et al. (2019). Ordered mesoporous carbons from lignin: a new class of biobased electrodes for supercapacitors. *Green Chem.* 21, 550–559. doi: 10.1039/C8GC03497D

Hu, L., Zang, L., Yang, J., Liu, Q., Qiao, X., Qiu, J., et al. (2020). A scalable strategy for carbon derived from complex six-membered ring-like tannin on glass fiber for 1D/2D flexible all solid state supercapacitors. *J. Electroanal. Chem.* 856:113693. doi: 10.1016/j.jelechem.2019.113693

Hulicova-Jurcakova, D., Seredych, M., Lu, G. Q., and Bandosz, T. J. (2009). Combined effect of nitrogen- and oxygen-containing functional groups of microporous activated carbon on its electrochemical performance in supercapacitors. *Adv. Funct. Mater.* 19, 438–447. doi: 10.1002/adfm.200801236

IEA (2014). *Technology Roadmap Energy Storage*.

IEA (2019). *Data and Statistics*. IEA. Available online at: https://www.iea.org/data-and-statistics (accessed December 12, 2019).

Inagaki, M., Konno, H., and Tanaike, O. (2010). Carbon materials for electrochemical capacitors. *J. Power Sourc.* 195, 7880–7903. doi: 10.1016/j.jpowsour.2010.06.036

Inagaki, M., Toyoda, M., Soneda, Y., and Morishita, T. (2018). Nitrogen-doped carbon materials. *Carbon* 132, 104–140. doi: 10.1016/j.carbon.2018.02.024

Inamuddin, Ahmer, M. F., Asiri, A. M., and Zaidi, S. (2018). *Electrochemical Capacitors: Theory, Materials and Applications*. Millersville, PA: Materials Research Forum LLC.

IOXUS Inc. (2020). *Applications. IOXUS.* Available online at: https://ioxus.com/english/applications/ (accessed April 14, 2020).

James, S. L., Adams, C. J., Bolm, C., Braga, D., Collier, P., Friščić, T., et al. (2012). Mechanochemistry: opportunities for new and cleaner synthesis. *Chem. Soc. Rev.* 41, 413–447. doi: 10.1039/C1CS15171A

Jana, P., Fierro, V., Pizzi, A., and Celzard, A. (2014). Biomass-derived, thermally conducting, carbon foams for seasonal thermal storage. *Biomass Bioenergy* 67, 312–318. doi: 10.1016/j.biombioe.2014.04.031

Jurewicz, K., Vix-Guterl, C., Frackowiak, E., Saadallah, S., Reda, M., Parmentier, J., et al. (2004). Capacitance properties of ordered porous carbon materials prepared by a templating procedure. *J. Phys. Chem. Solids* 65, 287–293. doi: 10.1016/j.jpcs.2003.10.024

Kaupp, G. (2009). Mechanochemistry: the varied applications of mechanical bond-breaking. *CrystEngComm* 11, 388–403. doi: 10.1039/B810822F

Kaupp, G. (2011). Reactive milling with metals for environmentally benign sustainable production. *CrystEngComm* 13:3108. doi: 10.1039/c1ce05085k

Kim, S., Chen, J., Cheng, T., Gindulyte, A., He, J., He, S., et al. (2018). PubChem 2019 update: improved access to chemical data. *Nucleic Acids Research* 47, D1102–D1109. doi: 10.1093/nar/gky1033

Kim, T.-Y., Lee, K.-R., Eun, K. Y., and Oh, K.-H. (2003). Carbon nanotube growth enhanced by nitrogen incorporation. *Chem. Phys. Lett.* 372, 603–607. doi: 10.1016/S0009-2614(03)00465-2

Kim, Y.-S., Kumar, K., Fisher, F. T., and Yang, E.-H. (2012). Out-of-plane growth of CNTs on graphene for supercapacitor applications. *Nanotechnology* 23:015301. doi: 10.1088/0957-4484/23/1/015301

Kötz, R., and Carlen, M. (2000). Principles and applications of electrochemical capacitors. *Electrochim. Acta* 45, 2483–2498. doi: 10.1016/S0013-4686(00)00354-6

Lacoste, C., Basso, M. C., Pizzi, A., Laborie, M.-P., Garcia, D., and Celzard, A. (2013). Bioresourced pine tannin/furanic foams with glyoxal and glutaraldehyde. *Ind. Crops Prod.* 45, 401–405. doi: 10.1016/j.indcrop.2012.12.032

Lee, J., Kim, J., and Hyeon, T. (2006). Recent progress in the synthesis of porous carbon materials. *Adv. Mater.* 18, 2073–2094. doi: 10.1002/adma.200501576

Li, J.-G., Ho, Y.-F., Ahmed, M. M. M., Liang, H.-C., and Kuo, S.-W. (2019). Mesoporous carbons templated by PEO-PCL block copolymers as electrode materials for supercapacitors.pdf. *Chem. Eur. J.* 25, 10456–10463. doi: 10.1002/chem.201901724

Li, S., Pasc, A., Fierro, V., and Celzard, A. (2016). Hollow carbon spheres, synthesis and applications – a review. *J. Mater. Chem. A* 4, 12686–12713. doi: 10.1039/C6TA03802F

Libbrecht, W., Verberckmoes, A., Thybaut, J. W., Van Der Voort, P., and De Clercq, J. (2017). Soft templated mesoporous carbons: tuning the porosity for the adsorption of large organic pollutants. *Carbon* 116, 528–546. doi: 10.1016/j.carbon.2017.02.016

Lide, D. R. ed. (2004). *CRC Handbook of Chemistry and Physics, 85th edn*. Boca Raton, FL: CRC Press.

Lim, E., Jo, C., and Lee, J. (2016). A mini review of designed mesoporous materials for energy-storage applications: from electric double-layer capacitors to hybrid supercapacitors. *Nanoscale* 8, 7827–7833. doi: 10.1039/C6NR00796A

Liu, D., Yuan, P., Tan, D., Liu, H., Wang, T., Fan, M., et al. (2012). Facile preparation of hierarchically porous carbon using diatomite as both template and catalyst and methylene blue adsorption of carbon products. *J. Colloid Interface Sci.* 388, 176–184. doi: 10.1016/j.jcis.2012.08.023

Liu, J., Wickramaratne, N. P., Qiao, S. Z., and Jaroniec, M. (2015). Molecular-based design and emerging applications of nanoporous carbon spheres. *Nat. Mater.* 14, 763–774. doi: 10.1038/nmat4317

Lu, S., Song, Y., Guo, K., Chen, X., Xu, J., and Zhao, L. (2018). Effect of aqueous electrolytes on the electrochemical behaviors of ordered mesoporous carbon composites after KOH activation as supercapacitors electrodes. *J. Electroanal. Chem.* 818, 58–67. doi: 10.1016/j.jelechem.2018.04.025

Maxwell Technologies Inc. (2020). *Cells - Overview. Maxwell Technologies.* Available online at: https://www.maxwell.com/products/ultracapacitors/cells/ (accessed April 14, 2020).

Mbarki, F., Selmi, T., Kesraoui, A., Seffen, M., Gadonneix, P., Celzard, A., et al. (2019). Hydrothermal pre-treatment, an efficient tool to improve activated carbon performances. *Ind. Crops Prod.* 140:111717. doi: 10.1016/j.indcrop.2019.111717

Meng, Y., Gu, D., Zhang, F., Shi, Y., Cheng, L., Feng, D., et al. (2006). A family of highly ordered *Mesoporous polymer* resin and carbon structures from organic–organic self-assembly. *Chem. Mater.* 18, 4447–4464. doi: 10.1021/cm060921u

Miller, J. R., and Burke, A. F. (2008). Electrochemical capacitors: challenges and opportunities for real-world applications. *Electrochem. Soc. Interface* 17, 53–57. doi: 10.1201/9781420069709.ch8

Mostazo-López, M. J., Ruiz-Rosas, R., Castro-Muñiz, A., Nishihara, H., Kyotani, T., Morallón, E., et al. (2018). Ultraporous nitrogen-doped zeolite-templated carbon for high power density aqueous-based supercapacitors. *Carbon* 129, 510–519. doi: 10.1016/j.carbon.2017.12.050

Moussa, G., Hajjar-Garreau, S., Taberna, P.-L., Simon, P., and Matei Ghimbeu, C. (2018). Eco-friendly synthesis of nitrogen-doped mesoporous carbon for supercapacitor application. *C* 4:20. doi: 10.3390/c4020020

Nasini, U. B., Bairi, V. G., Ramasahayam, S. K., Bourdo, S. E., Viswanathan, T., and Shaikh, A. U. (2014). Phosphorous and nitrogen dual heteroatom doped mesoporous carbon synthesized via microwave method for supercapacitor application. *J. Power Sourc.* 250, 257–265. doi: 10.1016/j.jpowsour.2013.11.014

National Institute for Occupational Safety and Health (2018). *NIOSH Pocket Guide to Chemical Hazards.* Available online at: https://www.cdc.gov/niosh/npg/npgsyn-a.html# (accessed April 24, 2020).

Orazem, M. E., and Tribollet, B. (2008). *Electrochemical Impedance Spectroscopy*. Hoboken, N.J: Wiley.

Pachauri, R. K., Mayer, L., and Intergovernmental Panel on Climate Change (Eds.). (2015). *Climate Change 2014: Synthesis Report*. Geneva: Intergovernmental Panel on Climate Change.

Pandolfo, A. G., and Hollenkamp, A. F. (2006). Carbon properties and their role in supercapacitors. *J. Power Sourc.* 157, 11–27. doi: 10.1016/j.jpowsour.2006.02.065

Paraknowitsch, J. P., and Thomas, A. (2013). Doping carbons beyond nitrogen: an overview of advanced heteroatom doped carbons with boron, sulphur and phosphorus for energy applications. *Energy Environ. Sci.* 6:2839. doi: 10.1039/c3ee41444b

Pizzi, A. (1982). Condensed tannins for adhesives. *Ind. Eng. Chem. Prod. Res. Dev.* 21, 359–369. doi: 10.1021/i300007a005

Ra, E. J., Raymundo-Piñero, E., Lee, Y. H., and Béguin, F. (2009). High power supercapacitors using polyacrylonitrile-based carbon nanofiber paper. *Carbon* 47, 2984–2992. doi: 10.1016/j.carbon.2009.06.051

Ramasahayam, S. K., Nasini, U. B., Shaikh, A. U., and Viswanathan, T. (2015). Novel tannin-based Si, P co-doped carbon for supercapacitor applications. *J. Power Sources* 275, 835–844. doi: 10.1016/j.jpowsour.2014.11.020

Raymundo-Piñero, E., Cadek, M., and Béguin, F. (2009). Tuning carbon materials for supercapacitors by direct pyrolysis of seaweeds. *Adv. Funct. Mater.* 19, 1032–1039. doi: 10.1002/adfm.200801057

Salinas-Torres, D., Ruiz-Rosas, R., Morallón, E., and Cazorla-Amorós, D. (2019). Strategies to enhance the performance of electrochemical capacitors based on carbon materials. *Front. Mater.* 6:115. doi: 10.3389/fmats.2019.00115

Sánchez-Sánchez, A., Fierro, V., Izquierdo, M. T., and Celzard, A. (2016). Functionalized, hierarchical and ordered mesoporous carbons for high-performance supercapacitors. *J. Mater. Chem. A* 4, 6140–6148. doi: 10.1039/C6TA00738D

Sanchez-Sanchez, A., Izquierdo, M. T., Ghanbaja, J., Medjahdi, G., Mathieu, S., Celzard, A., et al. (2017a). Excellent electrochemical performances of nanocast ordered mesoporous carbons based on tannin-related polyphenols as supercapacitor electrodes. *J. Power Sources* 344, 15–24. doi: 10.1016/j.jpowsour.2017.01.099

Sanchez-Sanchez, A., Izquierdo, M. T., Mathieu, S., González-Álvarez, J., Celzard, A., and Fierro, V. (2017b). Outstanding electrochemical performance of highly N- and O-doped carbons derived from pine tannin. *Green Chem.* 19, 2653–2665. doi: 10.1039/C7GC00491E

Sanchez-Sanchez, A., Izquierdo, M. T., Medjahdi, G., Ghanbaja, J., Celzard, A., and Fierro, V. (2018). Ordered mesoporous carbons obtained by soft-templating of tannin in mild conditions. *Microp. Mesop. Mater.* 270, 127–139. doi: 10.1016/j.micromeso.2018.05.017

Schlienger, S., Graff, A.-L., Celzard, A., and Parmentier, J. (2012). Direct synthesis of ordered mesoporous polymer and carbon materials by a biosourced precursor. *Green Chem.* 14, 313–316. doi: 10.1039/C2GC16160E

Selmi, T., Sanchez-Sanchez, A., Gadonneix, P., Jagiello, J., Seffen, M., Sammouda, H., et al. (2018). Tetracycline removal with activated carbons produced by hydrothermal carbonisation of agave Americana fibres and mimosa tannin. *Ind. Crops Prod.* 115, 146–157. doi: 10.1016/j.indcrop.2018.02.005

Sevilla, M., Diez, N., Ferrero, G. A., and Fuertes, A. B. (2019). Sustainable supercapacitor electrodes produced by the activation of biomass with sodium thiosulfate. *Energy Storage Mater.* 18, 356–365. doi: 10.1016/j.ensm.2019.01.023

Sevilla, M., and Mokaya, R. (2014). Energy storage applications of activated carbons: supercapacitors and hydrogen storage. *Energy Environ. Sci.* 7, 1250–1280. doi: 10.1039/C3EE43525C

Sharma, P., and Bhatti, T. S. (2010). A review on electrochemical double-layer capacitors. *Energ. Conv. Manage.* 51, 2901–2912. doi: 10.1016/j.enconman.2010.06.031

Shirmohammadli, Y., Efhamisisi, D., and Pizzi, A. (2018). Tannins as a sustainable raw material for green chemistry: a review. *Ind. Crops Prod.* 126, 316–332. doi: 10.1016/j.indcrop.2018.10.034

SilvaTeam (2018). *All About Tannins.* Available online at: https://www.silvateam.com/en/who-we-are/extracts-nature/all-about-tannins.html (accessed April 1, 2019).

Szczurek, A., Amaral-Labat, G., Fierro, V., Pizzi, A., and Celzard, A. (2011a). The use of tannin to prepare carbon gels. Part *II. carbon cryogels. Carbon* 49, 2785–2794. doi: 10.1016/j.carbon.2011.03.005

Szczurek, A., Amaral-Labat, G., Fierro, V., Pizzi, A., Masson, E., and Celzard, A. (2011b). The use of tannin to prepare carbon gels. Part I: carbon aerogels. *Carbon* 49, 2773–2784. doi: 10.1016/j.carbon.2011.03.007

Szczurek, A., Fierro, V., Pizzi, A., and Celzard, A. (2013). Mayonnaise, whipped cream and meringue, a new carbon cuisine. *Carbon* 58, 245–248. doi: 10.1016/j.carbon.2013.02.056

Szczurek, A., Fierro, V., Pizzi, A., and Celzard, A. (2014). Emulsion-templated porous carbon monoliths derived from tannins. *Carbon* 74, 352–362. doi: 10.1016/j.carbon.2014.03.047

Tanaka, S., Fujimoto, H., Denayer, J. F. M., Miyamoto, M., Oumi, Y., and Miyake, Y. (2015). Surface modification of soft-templated ordered mesoporous carbon for electrochemical supercapacitors. *Micropor Mesopor Mater.* 217, 141–149. doi: 10.1016/j.micromeso.2015.06.017

Tellez-Juárez, M. C., Fierro, V., Zhao, W., Fernández-Huerta, N., Izquierdo, M. T., Reguera, E., et al. (2014). Hydrogen storage in activated carbons produced from coals of different ranks: Effect of oxygen content. *Int. J. Hydrogen Energy* 39, 4996–5002. doi: 10.1016/j.ijhydene.2014.01.071

Tiruye, G. A., Muñoz-Torrero, D., Berthold, T., Palma, J., Antonietti, M., Fechler, N., et al. (2017). Functional porous carbon nanospheres from sustainable

precursors for high performance supercapacitors. *J. Mater. Chem. A* 5, 16263–16272. doi: 10.1039/C7TA01951C

Tondi, G., Fierro, V., Pizzi, A., and Celzard, A. (2009). Tannin-based carbon foams. *Carbon* 47, 1480–1492. doi: 10.1016/j.carbon.2009.01.041

Tondi, G., and Petutschnigg, A. (2015). Middle infrared (ATR FT-MIR) characterization of industrial tannin extracts. *Ind. Crops Prod.* 65, 422–428. doi: 10.1016/j.indcrop.2014.11.005

Vivo-Vilches, J., Celzard, A., Fierro, V., Devin-Ziegler, I., Brosse, N., Dufour, A., et al. (2019). Lignin-based carbon nanofibers as electrodes for vanadium redox couple electrochemistry. *Nanomaterials* 9:106. doi: 10.3390/nano9010106

Vix-Guterl, C., Frackowiak, E., Jurewicz, K., Friebe, M., Parmentier, J., and Béguin, F. (2005). Electrochemical energy storage in ordered porous carbon materials. *Carbon* 43, 1293–1302. doi: 10.1016/j.carbon.2004.12.028

Wang, G.-W. (2013). Mechanochemical organic synthesis. *Chem. Soc. Rev.* 42, 7668–7700. doi: 10.1039/c3cs35526h

Wang, J.-G., Liu, H., Sun, H., Hua, W., Wang, H., Liu, X., et al. (2018). One-pot synthesis of nitrogen-doped ordered mesoporous carbon spheres for high-rate and long-cycle life supercapacitors. *Carbon* 127, 85–92. doi: 10.1016/j.carbon.2017.10.084

Wang, Y., Song, Y., and Xia, Y. (2016). Electrochemical capacitors: mechanism, materials, systems, characterization and applications. *Chem. Soc. Rev.* 45, 5925–5950. doi: 10.1039/C5CS00580A

Wickramaratne, N. P., and Jaroniec, M. (2013). Phenolic resin-based carbons with ultra-large mesopores prepared in the presence of poly(ethylene oxide)–poly(butylene oxide)–poly(ethylene oxide) triblock copolymer and trimethyl benzene. *Carbon* 51, 45–51. doi: 10.1016/j.carbon.2012.08.007

Xia, Y., Zhang, W., Xiao, Z., Huang, H., Zeng, H., Chen, X., et al. (2012). Biotemplated fabrication of hierarchically porous NiO/C composite from lotus pollen grains for lithium-ion batteries. *J. Mater. Chem.* 22, 9209–9215. doi: 10.1039/c2jm16935e

Xie, J., Yang, P., Wang, Y., Qi, T., Lei, Y., and Li, C. M. (2018). Puzzles and confusions in supercapacitor and battery: theory and solutions. *J. Power Sources* 401, 213–223. doi: 10.1016/j.jpowsour.2018.08.090

Xin, W., Severino, J., Venkert, A., Yu, H., Knorr, D., Yang, J.-M., et al. (2020). Fabrication and characterization of solid composite yarns from carbon nanotubes and poly(dicyclopentadiene). *Nanomaterials* 10:717. doi: 10.3390/nano10040717

Zhai, Y., Dou, Y., Zhao, D., Fulvio, P. F., Mayes, R. T., and Dai, S. (2011). Carbon materials for chemical capacitive energy storage. *Adv. Mater.* 23, 4828–4850. doi: 10.1002/adma.201100984

Zhang, L. L., and Zhao, X. S. (2009). Carbon-based materials as supercapacitor electrodes. *Chem. Soc. Rev.* 38:2520. doi: 10.1039/b813846j

Zhang, P., Wang, L., Yang, S., Schott, J. A., Liu, X., Mahurin, S. M., et al. (2017). Solid-state synthesis of ordered mesoporous carbon catalysts via a mechanochemical assembly through coordination cross-linking. *Nat. Commun.* 8:15020. doi: 10.1038/ncomms15020

Zhao, W., Fierro, V., Fernández-Huerta, N., Izquierdo, M. T., and Celzard, A. (2012). Impact of synthesis conditions of KOH activated carbons on their hydrogen storage capacities. *Int. J. Hydrogen Energy* 37, 14278–14284. doi: 10.1016/j.ijhydene.2012.06.110

Zheng, W., Lv, R., Na, B., Liu, H., Jin, T., and Yuan, D. (2017). Nanocellulose-mediated hybrid polyaniline electrodes for high performance flexible supercapacitors. *J. Mater. Chem. A* 5, 12969–12976. doi: 10.1039/C7TA01990D

Zhong, C., Deng, Y., Hu, W., Qiao, J., Zhang, L., and Zhang, J. (2015). A review of electrolyte materials and compositions for electrochemical supercapacitors. *Chem. Soc. Rev.* 44, 7484–7539. doi: 10.1039/C5CS00303B

Zhu, J., Yang, J., Miao, R., Yao, Z., Zhuang, X., and Feng, X. (2016). Nitrogen-enriched, ordered mesoporous carbons for potential electrochemical energy storage. *J. Mater. Chem. A* 4, 2286–2292. doi: 10.1039/C5TA09073C

Zuliani, J. E., Caguiat, J. N., Kirk, D. W., and Jia, C. Q. (2015). Considerations for consistent characterization of electrochemical double-layer capacitor performance. *J. Power Sources* 290, 136–143. doi: 10.1016/j.jpowsour.2015.04.019

Zuliani, J. E., Tong, S., Jia, C. Q., and Kirk, D. W. (2018). Contribution of surface oxygen groups to the measured capacitance of porous carbon supercapacitors. *J. Power Sources* 395, 271–279. doi: 10.1016/j.jpowsour.2018.05.046

Conflict of Interest: The authors declare that the research was conducted in the absence of any commercial or financial relationships that could be construed as a potential conflict of interest.

frontiers in Materials

ORIGINAL RESEARCH
published: 26 November 2020
doi: 10.3389/fmats.2020.578518

Non-precious Melamine/Chitosan Composites for the Oxygen Reduction Reaction: Effect of the Transition Metal

B. Aghabarari[1], *M. V. Martínez-Huerta*[2]*, *M. C. Capel-Sánchez*[2] *and M. J. Lázaro*[3]*

[1] Department of Nanotechnology and Advanced Material, Materials and Energy Research Center (MERC), Tehran, Iran, [2] Instituto de Catálisis y Petroleoquímica, CSIC, Madrid, Spain, [3] Instituto de Carboquímica, CSIC, Zaragoza, Spain

The development of active and low-cost electrocatalysts for the oxygen reduction reaction (ORR) is crucial for the sustainable commercialization of fuel cell technologies. In this study, we have synthetized Me/Mo_2C (Me = Fe, Co, Cu)-based composites embedded in N- and P-dual doped carbon by means of inexpensive industrial materials, such as melamine and chitosan, as C and N sources, and the heteropolyacid $H_3PMo_{12}O_{40}$ as P and Mo precursor. The effect of the transition metal (Fe, Co, and Cu) on the ORR in alkaline medium has been investigated. The physicochemical properties of the electrocatalysts were performed by X-ray diffraction (XRD), X-ray photoelectron spectroscopy (XPS), Raman spectroscopy, and transmission electron microscopy (TEM). Activity towards ORR was carried out in a three-electrode cell using a ring-disk electrode in 0.1M NaOH. The results obtained clearly show the important role played by each transition metal (Fe, Co, and Cu) in the electrochemical activity. Among them, Fe gives rise to the best performing composite in carrying out the oxygen reduction reaction. The formation Fe_3C/Mo_2C species embedded in N- and P-dual doped carbon seems to be the determining role in the increase of the ORR performance.

Keywords: oxygen reduction, composites, chitosan, melamine, electrocatalyst, heteropolyacid

OPEN ACCESS

Edited by:
Emilia Morallon,
University of Alicante, Spain

Reviewed by:
Jialiang Wang,
University of Wisconsin-Madison, United States
Dongsheng Geng,
University of Science and Technology Beijing, China

***Correspondence:**
M. V. Martínez-Huerta
mmartinez@icp.csic.es
M. J. Lázaro
mlazaro@icb.csic.es

Specialty section:
This article was submitted to Energy Materials, a section of the journal Frontiers in Materials

Received: *30 June 2020*
Accepted: *05 October 2020*
Published: *26 November 2020*

Citation:
Aghabarari B, Martínez-Huerta MV, Capel-Sánchez MC and Lázaro MJ (2020) Non-precious Melamine/Chitosan Composites for the Oxygen Reduction Reaction: Effect of the Transition Metal. Front. Mater. 7:578518. doi: 10.3389/fmats.2020.578518

INTRODUCTION

The oxygen reduction reaction (ORR) is the main electrochemical reaction occurring at the cathode of polymer electrolyte fuel cells. Due to the inherently slow reaction kinetics of the ORR, platinum precious metal is required as an electrocatalyst because of its high activity and durability (Stephens et al., 2012; Shao et al., 2016; Martínez-Huerta and Lázaro, 2017). However, Pt must be substituted or dramatically reduced in the ORR cathode in order to reduce the cost and to ensure sustainable development for commercial applications. The development of active and precious-metal-free catalysts thereby becomes an imperative issue in the field of electrocatalysis (Jaouen et al., 2011; Wang et al., 2019).

One of the most significant ways to reduce the cost and improve the kinetics of the ORR is the utilization of an alkaline environment. In this condition, oxygen is reduced to water at the cathode via two possible reaction pathways: the direct four-electron ($4e^-$) pathway and the energetically undesirable two-stage ($2e^-$) pathway with a peroxide intermediate (Martínez-Huerta and Lázaro, 2017). The elementary reaction routes in alkaline media are (**Eqs 1**, **2**, and **3**):

Direct four-electron pathway: $O_2 + 2H_2O + 4e^- \rightarrow 4OH^-$ (1)

Two-stage pathway: $O_2 + 2H_2O + 2e^- \rightarrow HO_{2^-} + OH^-$ (2)

$HO_{2^-} + OH^- + 2e^- \rightarrow 3OH^-$ (3)

Among non-precious metal catalysts, N-doped carbon with transition metals (for example, Fe or Co) have proven to have remarkably enhanced electrocatalytic activity for ORR in an alkaline environment (Wu et al., 2011; Palaniselvam et al., 2016; Shao et al., 2016; Wang et al., 2019; Yasuda et al., 2016; Wang et al., 2019). Conventionally, these catalysts are synthetized by pyrolysis of mixtures containing a carbon material, a metal salt, and a nitrogen-rich organic compound in the presence of an inert gas. Additionally, N species can be incorporated into the carbon nanostructures by pyrolysis of abundant eco-friendly raw material sources, which has benefits such as low cost or easy synthetic conditions (Chung et al., 2013; Li et al., 2014a; Das and Yurtcan, 2016; Pan et al., 2016; Qiao et al., 2016).

In this study, N-doped carbon matrix is obtained from two low-cost industrial materials, chitosan and melamine. Chitosan is a plentiful, harmless and low cost biopolymer, which is a waste product derivative of the crabbing and shrimp canning industry (Marguerite, 2006). Chitosan has been chosen as both carbon and N sources due to its abundant N-bearing groups (Wu et al., 2015; Xie et al., 2015; Aghabarari et al., 2017; Aghabarari et al. 2013). Qiao et al. prepared graphene/nitrogen-doped porous carbon sandwiches for the metal-free oxygen reduction reaction using chitosan as a nitrogen source (Qiao et al., 2016). Nitrogen doping increased the electrical conductivity and the number and the nature of the active sites for the ORR. Melamine is also a nitrogen-rich organic molecule and low-cost raw material in the chemical industry. Melamine possesses a three-dimensional monoclinic structure which is similar to C_3N_4. Its decomposition favors the incorporation of nitrogen in carbonaceous materials obtained by pyrolysis (Sheng et al., 2011; Liu et al., 2013; Li et al., 2014b; Peng et al., 2014). Rybarczyk et al. also studied the formation of nitrogen-doped porous carbonaceous materials by thermal decomposition of a mixture of chitosan and melamine in an inert atmosphere (Rybarczyk et al., 2015; Khan et al., 2020). They found that, in addition to the entire nitrogen content and the kind of nitrogen group (pyridinic N or quaternary N), the content of carbon "kinks" and/or surface roughness also deeply influenced the ORR activity.

Transition metal carbides are highly attractive since they exhibit electronic and catalytic properties similar to Pt (Guil-López et al., 2010; Roca-Ayats et al., 2014; Zhong et al., 2015). Recently, a number of research groups have demonstrated that molybdenum carbides can be active electrocatalysts for the oxygen reduction reaction (Liao et al., 2014; Fan et al., 2017; Zhang et al., 2017; Li et al., 2019). The physicochemical properties of molybdenum carbides, such as mechanical hardness, thermal stability, singular metal–carbon chemical bonds, and noble-metal-like d-state density around the Fermi level, make them very promising materials for obtaining advanced ORR composites.

Herein, we have synthetized Me/Mo_2C (Me = Fe, Co, Cu)-based composites embedded in N- and P-dual doped carbon using a facile synthesis strategy developed by our research group (Aghabarari et al., 2019). For this preparation, the corresponding metallic precursor and molybdophosphoric acid (HMoP) are pyrolyzed together with the mixture chitosan/melamine as carbon and nitrogen sources. HMoP was used as a source of P and Mo. The effect of the transition metal (Fe, Co, and Cu) on the structure and ORR activity has been investigated. The physicochemical properties of the electrocatalysts were performed by Raman spectroscopy, X-ray diffraction (XRD), X-ray photoelectron spectroscopy (XPS), and transmission electron microscopy (TEM). Activity towards ORR was carried out in a three-electrode electrochemical cell using a ring-disk electrode in 0.1M NaOH.

EXPERIMENTAL

Composites Synthesis

The preparation of the composites follows the synthetic strategy developed by our research group (Aghabarari et al., 2019) and is schematically illustrated in **Figure 1**. For the synthesis of composites, an appropriate amount of the chloride salt precursor (Sigma-Alderich Company) of Co, Fe, or Cu (20 wt % with respect to the composite melamine/chitosan) was dissolved in water and then was added to a solution of chitosan in acetic acid solution. After that, a solution of melamine was added drop by drop to the mixture and stirred vigorously (weight ratio melamine/chitosan = 1/1). In the next step, the appropriate amount of the $H_3PMo_{12}O_{40}$ solution (10 wt % with respect to the composite melamine/chitosan) was added to the mixture and, after 2 h stirring, the solution was dried at 70°C in a vacuum oven. The sample was pyrolized in a tubular quartz furnace at 800°C over 3h. The product was washed with 10 wt% HCl solution. The acid-treated solid sample was filtered and washed with water until free of chlorine ions. Finally, the sample was dried at 70°C in a vacuum oven to obtain the final catalysts. The three catalysts were labeled as Fe/Mo_2C/NPC, Co/Mo_2C/NPC, and Cu/Mo_2C/NPC. For comparison, melamine/chitosan (NPC) composite was also prepared using a similar route but without adding any metal and heteropolyacid into the composite.

Characterization of the Electrocatalytic Materials

X-ray diffraction analyses of the composites were carried out on a PANalytical X'Pert Pro X-ray diffractometer with a Cu Kα source. X-ray Photoelectron Spectroscopy (XPS) data was analyzed with a PHOIBOS 150 9MCD spectrometer with Multi-Channeltron detector fitted with a Mg Kα radiation ($h\nu$ = 1,253.6 eV) and an XRC-1000 X-ray gun. TEM images were obtained using a high resolution of transmission electron microscopy (HRTEM) JEOL 2100F operating at an accelerating voltage of 200 kV. Raman spectroscopy was carried out with a Renishaw in Via Raman

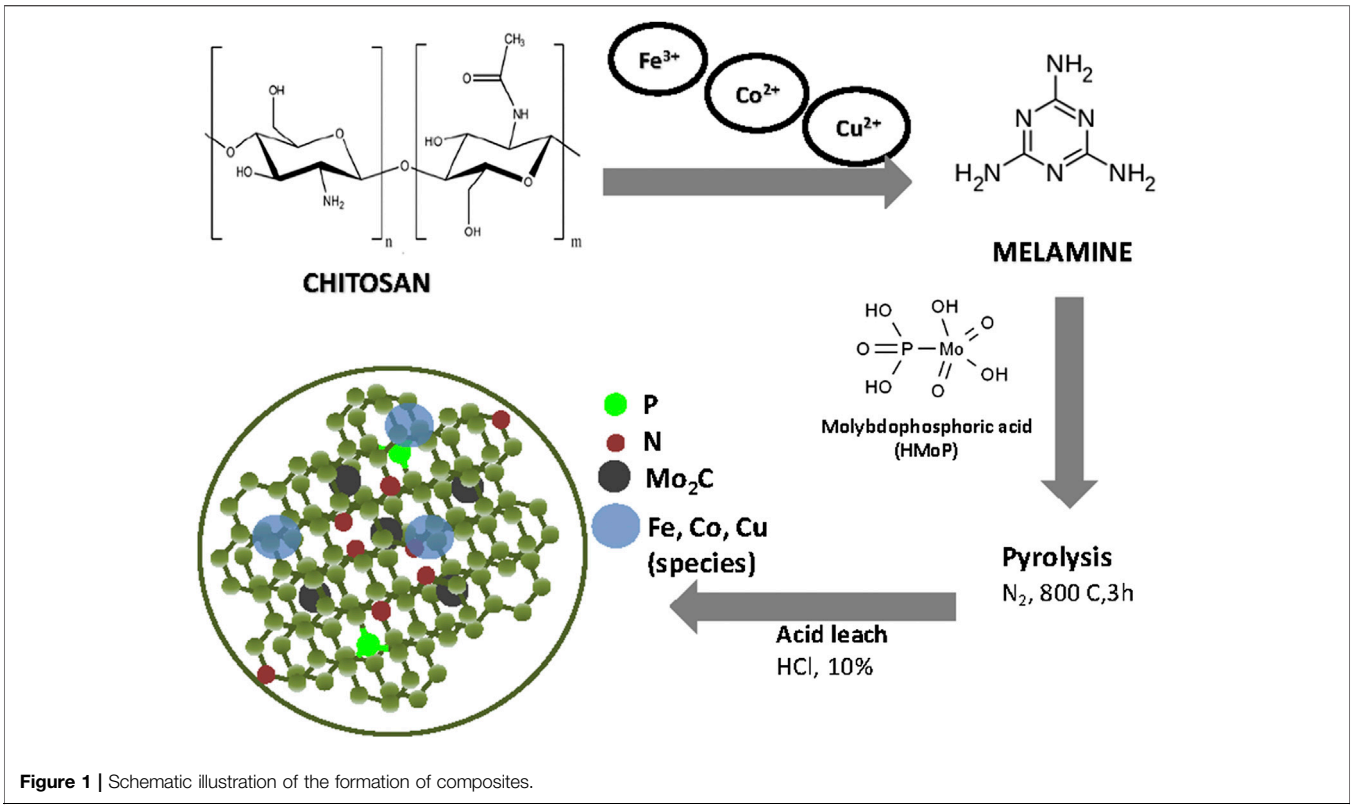

Figure 1 | Schematic illustration of the formation of composites.

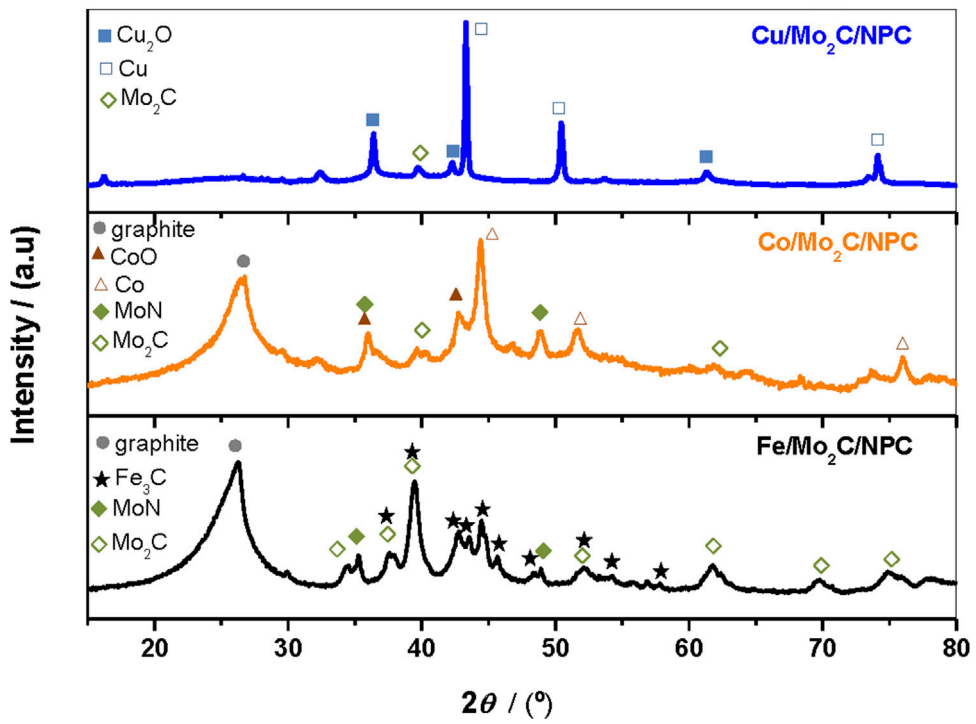

Figure 2 | X-ray diffraction (XRD) patterns of composites.

TABLE 1 | Surface elemental contents examined by XPS (wt.%)

Catalyst	C 1s	N 1s	Fe 2p	Co 2p	Cu 2p	P 2p	Mo 3d
Fe/Mo_2C/NPC	65	2.7	8.8	—	—	0.6	3.6
Co/Mo_2C/NPC	70	6.7	—	5.0	—	0.3	6.7
Cu/Mo_2C/NPC	47	5.0	—	—	25	0.9	7.9

Microscope spectrometer equipped with a laser beam emitting at 532 nm and 5 mW output power.

The electrochemical characterization of the composites was performed in a three-electrode cell system at room temperature controlled by an Autolab PGSTAT302N potentiostat-galvanostat. A glassy carbon rod and a reversible hydrogen electrode (RHE) were used as the counter electrode and the reference electrode, respectively. For the working electrode, a rotating ring-disk electrode (RRDE, PINE) with a glassy carbon disk with 0.196 cm^2 of area and a Pt ring was employed. The supporting electrolyte was 0.1M NaOH aqueous solution. The working electrode was prepared by adding 30 μL of catalytic ink. For the catalytic ink, 4 mg of composite was dispersed in 385 μL of Isopropyl alcohol (IPA) and water, IPA:H2O (1;1) solution and 15 μL of Nafion® (5 wt.%, Sigma-Aldrich) as a binder. For all measurements, N_2 (99.99%, Air Liquid) was employed to make an inert environment, and O_2 (99.99%, Air Liquid) was used for ORR measurements. In order to analyze the H_2O_2 yield, the ORR activity was performed while keeping the Pt ring at 1.2 V.

RESULTS AND DISCUSSION

X-ray diffractograms of electrocatalysts are shown in **Figure 2**. All composites show diffraction peaks corresponding to Mo_2C (JPCDS 00-035-0787), while MoN (JPCDS 01-077-1999) is observed in Co and Fe composites. The diffraction peak at 26.6° confirms the correct graphitization of carbon in the Fe and Co composites. However, the highest crystallinity of Cu_2O (JPCDS 01-077-0199) and Cu (JPCDS 00-001-1242) contrasts with the low crystallinity of the carbon in the Cu/Mo_2C/NPC composite. It seems that copper promotes a lower graphitization degree of the carbon during the pyrolysis process. Co/Mo_2C/NPC shows diffraction peaks assigned to Co (JPCDS 00-001-1255) and CoO (JPCDS 01-072-1474). A diffraction pattern of Fe_3C (JPCDS 00-034-0001) was also observed in the Fe/Mo_2C/NPC composite.

During the pyrolysis process, chitosan and melamine gradually decompose to several carbon-nitrogen intermediates. Functionalization chitosan biopolymer with melamine becomes effective due to the strong interaction between the pyranose units and the amine groups, which results in the crosslinked networks (Rybarczyk et al., 2015). It is also reported that the pyrolysis of melamine generates a series of intermediate condensed phases, such as so-called melem ($C_6N_7(NH_2)_3$) or graphitic carbon nitride materials (g-C_3N_4), and then further releases some chemically reactive hydrogen-, carbon-, and nitrogen-containing atomic species, such as $C_3N_3^+$,$C_2N_2^+$ and CN_2H^+, at higher temperatures (Huang et al., 2015). These reactive intermediates can behave as powerful reducing agents to reduce different metal oxides to metal carbide, nitride, or metallic particles during the pyrolysis treatment. Furthermore, the simultaneous formation of C=C species from intermediates is considered as the carbon source of graphite (Li et al., 2014b; Yang et al., 2015).

The surface elemental compositions and electronic configurations of the atoms in the composites were investigated by employing XPS. **Table 1** summarizes the chemical surface composition in weight % of the catalysts. It is important to note that the copper content on the surface far exceeds the Fe and Co surface content of the other two composites and is also more than twice the nominal value, which would indicate a poor dispersion or higher segregation of copper on the carbon matrix. The transition metal used (Fe, Co, or Cu) affects the amount of N, P, and Mo incorporated into the composite. Cobalt composite shows the higher surface N content (6,7 wt.%), and copper composite the higher amount of P (0.9 wt.%) and Mo (7.9 wt.%). All samples display low P content, being lower than 1 wt.%.

The high-resolution N1s and P2p XPS spectra of the composites were shown in **Figures 3A** and **B**, respectively. The N1s peak deconvolution of the three catalysts proposes three nitrogen components with the binding energies centered at about 398, 400, and 401 eV, corresponding to pyridinic N, pyrrolic N, and quaternary N, respectively. Additionally, in **Figure 3A**, the peak at the lower binding energy at 397 eV is assigned to Mo3p in all catalysts (Li et al., 2016). However, this peak could also be assigned to nitride species, such as MoN in cobalt and iron composites, according to XRD analysis. The P2p XPS spectra display a broad and low intensity peak centered at 133-133.5 eV, assigned to P-C (Razmjooei et al., 2014; Razmjooei et al., 2015). These XPS results indicate that N and P are incorporated into the carbon matrix in the three catalysts.

The spectra for Fe 2p, Co2p, and Cu2p core level are shown in **Figure 4**. The Fe2p spectra in **Figure 4A** shows peaks at 711.1 and 724.9 eV, which are assigned to Fe2p3/2 and Fe2p1/2 respectively Fe_3O_4 (Wagner et al., 1979). The surface oxidation of the iron samples does not allow the analysis of the inner layer, and therefore the detection of the iron carbide observed by XRD. Co2p shows binding energies of Co2p3/2 and Co2p1/2 at 782.3 and 798.1 eV, respectively, and the respective "satellite" peaks, which can be attributed to Co^{2+}–like species (Wagner et al., 1979; Luque-Centeno et al., 2020). The Cu2p core level spectra is displayed in **Figure 4C**. The main Cu2p3/2 signal is composed of two contributions at 932.7 and a shoulder at 934.4 eV, where the former is assigned to surface Cu^0 and the latter to Cu^{2+} with the respective satellite peaks (Wagner et al., 1979; Ania et al., 2015). In a similar way, the Mo3d core level spectra shows the thin oxidized layer on the molybdenum carbide surface and MoO_3 is only detected by XPS (not shown).

The TEM images of the NPC samples are displayed in **Figure 5**. All composites show metal particles embedded in an amorphous graphite structure. In Fe/Mo_2C/NPC, the nanoparticles are uniformly dispersed in the carbon matrix. This dispersion decreases in Co/Mo_2C/NPC and gets much worse in Cu/Mo_2C/NPC. Iron and cobalt composites show the presence of particles with average particle sizes between 10 and

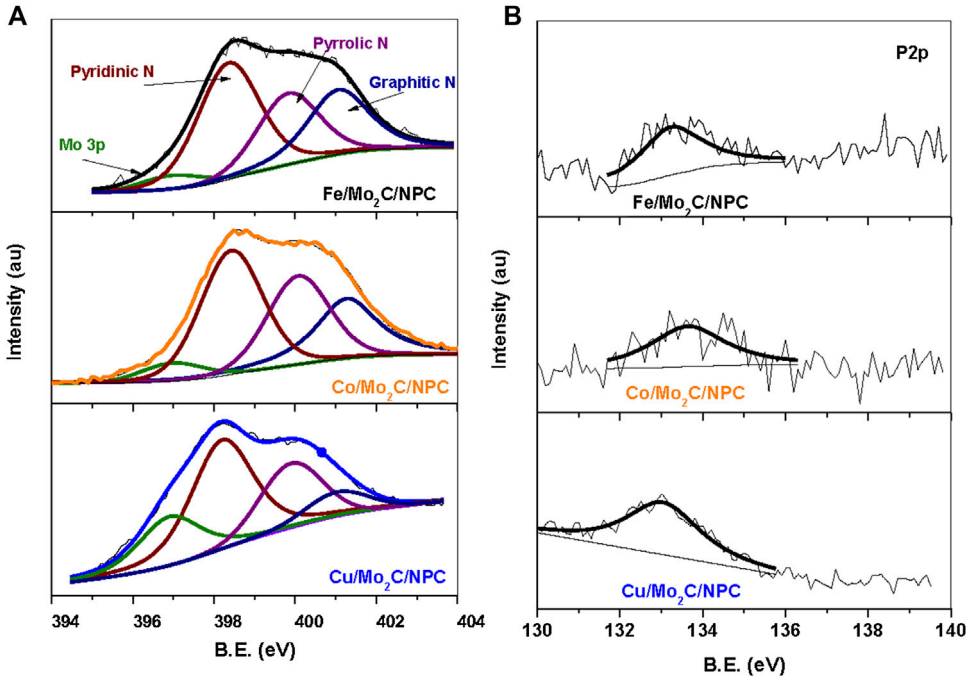

Figure 3 | High-resolution N1s XPS spectra **(A)** and P2p **(B)** of composites.

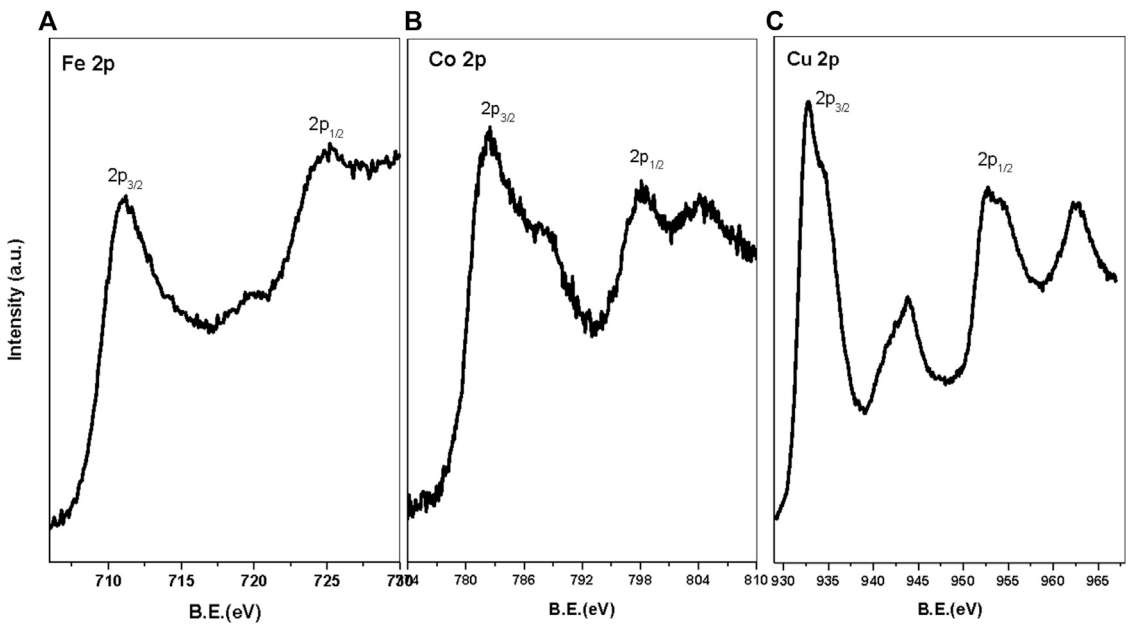

Figure 4 | High-resolution Fe 2p (**A**), Co 2p (**B**), and Cu 2p (**C**) XPS spectra.

30 nm cover of a thickness of the external carbon sheet. However, Cu/Mo_2C/NPC shows the presence of copper aggregates in the carbon matrix with an irregular morphology, and some metal nanoparticles outside of the carbon matrix (**Figure 5C**).

The Raman spectra of the composites show the characteristic peak corresponding to the D and G bands at 1350 cm^{-1} and 1580 cm^{-1}, respectively (**Figure 6**). The D band is assigned to the A1g breathing mode of disordered graphite structure and is due to the defect sites in

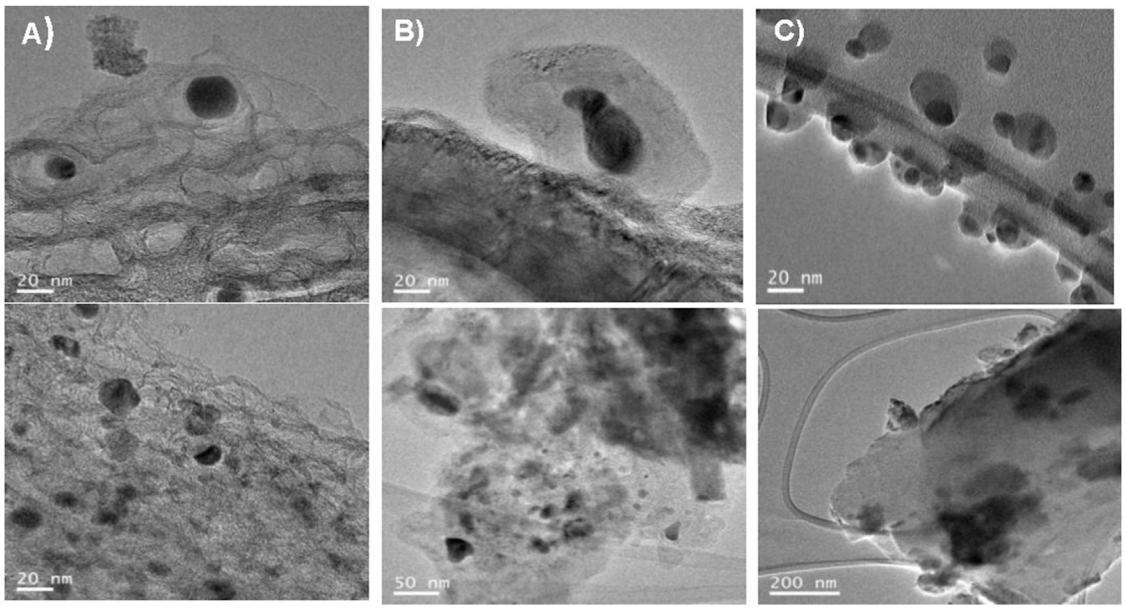

Figure 5 | TEM images of Fe/Mo2C/NPC **(A)**, Co/Mo2C/NPC **(B)**, and Cu/Mo2C/NPC **(C)**.

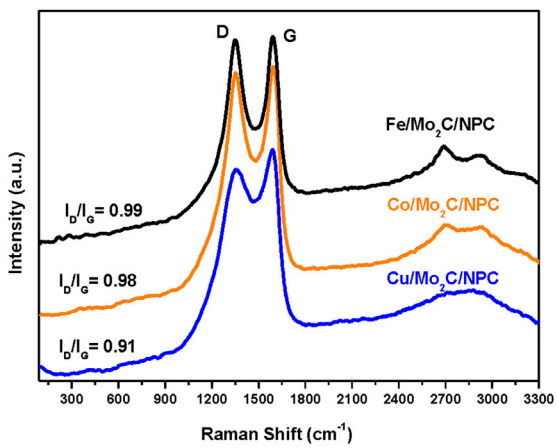

Figure 6 | Raman spectra of the composites. The calculated I_D/I_G values are also presented.

the hexagonal framework of graphite materials. The G band corresponds to the E2g stretching mode of graphite structure and denotes the sp^2 hybridized carbon atom structure (Yang et al., 2018). Both Raman bands have their corresponding overtones between 2500 and 3000 cm^{-1}, respectively. The height of the D peak usually increases upon chemical alteration of carbon structure. The ratio of D and G bands (I_D/I_G) is a good indicator of the disorder degree, graphitization, and crystallinity of the composites (values are indicated in **Figure 6**). It is observed that the I_D/I_G ratio is lower for the Cu (0.91) composite with respect to Co and Fe composites (ca. 0.99), which indicate a higher disorder degree and defects of the graphite formed in the latter catalysts. Certainly, several studies have established the relevance of defects, which seem to be one of the most challenging targets, in ORR electrocatalysis (Quílez-Bermejo et al., 2020). It is also observed that the intensity of the two-dimensional (2D) peak (~2690 cm^{-1}) increase in the Co composite and, particularly, in the Fe composite, revealing better graphitization of the carbon framework (Cheng et al., 2017). This suggests that the doping and graphitic structure of carbon matrix is not too dependent on the Co and Fe metal transition, but it changes with the copper metal.

The electrocatalytic activity of the composites was studied in alkaline media using a rotating ring-disk electrode (RRDE) technique with a rotation rate of 1,600 rpm. The key values for evaluating the ORR catalytic activity are the onset potential (obtained at -0.1 mA cm^{-2}), half-wave potential ($E_{1/2}$) and the diffusion-limiting current. The ORR activity and H_2O_2 yields of the electrocatalysts are displayed in **Figures 7A** and **B**, respectively. NPC was added for comparison. As evidenced in **Figure 7A** and **Table 2**, Fe/Mo_2C/NPC exhibits the best performance with an onset potential of 0.922 V (vs RHE) at -0.1 mA cm^{-2}, and limiting current density of -4.39 mA cm^{-2} at 0.2 V. In all other composites, the onset potential and limiting current gradually decreases from Co/Mo_2C/NPC (0.850 V, -3.57 mA cm^{-2}), NPC (0.714 V, -1.86 mA cm^{-2}), to Cu/Mo_2C/NPC (0.683 V, -1.64 mA cm^{-2}). It is observed that the plateau is inclined in all composites, which could indicate some diffusion limitations or inhomogeneous distribution of active sites on the electrode. The $E_{1/2}$ values can embody the capacity that a fuel cell cathode needs, holding a high working potential to provide high energy conversion efficiency. From **Table 2**, it can be seen that the Fe composite shows the highest $E_{1/2}$ value (0.811 V), further indicating the highly active nature of the Fe/Mo_2C/NPC towards ORR. These results demonstrate that the transition metal considerably affects the ORR activity in the Mo_2C/NPC

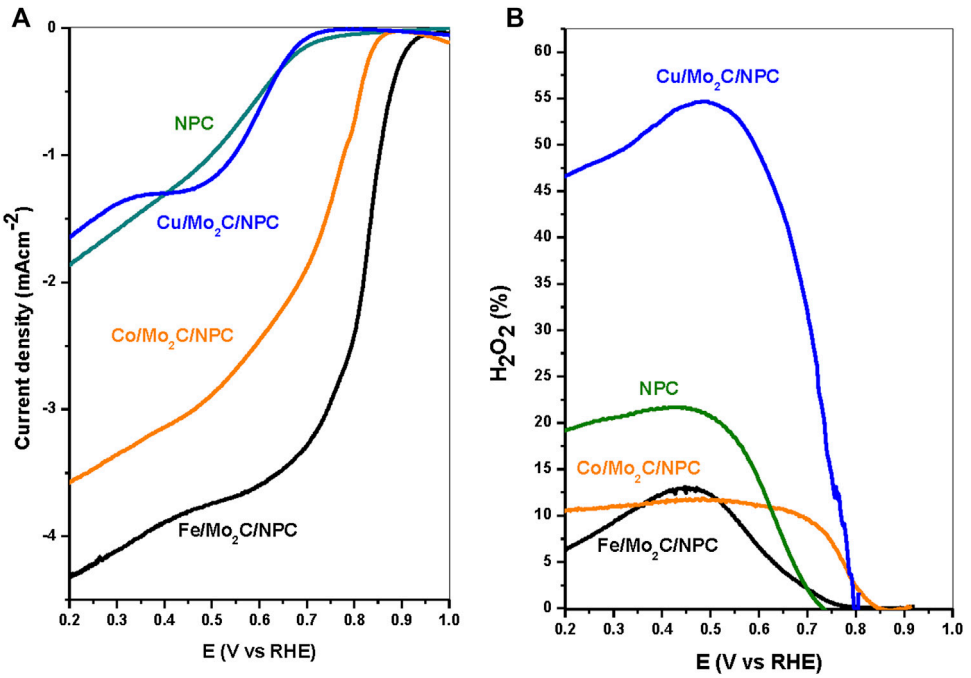

Figure 7 | ORR **(A)** and H2O2 yield **(B)** polarization curves for all catalysts at 1,600 rpm in 0.1 M NaOH, 10 mV s-1. The applied potential at the ring electrode was 1.2 V for the ORR.

TABLE 2 | Electrochemical parameters for ORR of the composites

Catalyst	E_{onset} (V) at -0.1 mA cm^{-2}	$E_{1/2}$(V)	J_L(mA cm^{-1}) at 0.2 V
Fe/Mo_2C/NPC	0.922	0.811	4.39
Co/Mo_2C/NPC	0.850	0.710	3.57
Cu/Mo_2C/NPC	0.683	0.576	1.64
NPC	0.714	0.502	1.86

composites. The polarization curves indicate that the Fe/Mo_2C/NPC catalyst has very high ORR activities and is comparable with conventional Pt/C catalysts, in which the onset potential is usually identified ca. 0.990 V (Jiang et al., 2015). Therefore, the gap between the onset potential of Fe/Mo_2C/NPC and the standard Pt/C is only 32 mV.

Based on the ring current generated from the oxidation of H_2O_2, we can observe that the Cu/Mo_2C/NPC catalyst produces a higher level of H_2O_2 (ca. 50%) than iron and cobalt composites do. The peroxide formations of the latter two are lower than 13% in all potential ranges studied. These results reveal that the Cu composite follows a combined 2-3 e^- electron-transfer number. In addition, the RRDE measurements reveal that the production of the corrosive H_2O_2 is highly suppressed on Fe/Mo_2C/NPC and Co/Mo_2C/NPC, promoting a $4e^-$ pathway. It is also observed that NPC produced a higher level of H_2O_2 compared to Fe- and Co-based composites. This may be due to how in free-metals-doped carbons, the carbon atoms next to heteroatoms exhibit excellent bonding ability to adsorb OOH, thus assisting the easy formation of the peroxide intermediate (Brouzgou et al., 2016; Sun et al., 2018).

Therefore, Fe/Mo_2C/NPC exhibits a higher onset potential and limiting current density, and has a selectivity of about four electrons in alkaline media, while Cu/Mo_2C/NPC has the lowest electron transfer number and worst ORR performance. These results indicate that Fe/Mo_2C/NPC composite is a promising electrocatalyst for H_2O production.

It is known that nitrogen and phosphorous dual-doped carbons improve the catalytic activity for ORR due to the synergetic effects (Choi et al., 2012; Li et al., 2015; Qiao et al., 2015). DFT simulations have demonstrated that quaternary nitrogen, along with phosphorus groups, are responsible for the improvement in the electrocatalytic activity in alkaline solution (Li et al., 2017). Also, the higher disorder degree and defects promoted by doped-carbons have revealed its significance in ORR activity (Quílez-Bermejo et al., 2020). According to our results, N and P are incorporated into the carbon matrix in the three composites. However, it has been shown that the transition metal is essential to obtain optimal carbon framework for ORR, with the copper being the one that promotes the formation of a less graphitized and defective carbon matrix during the synthetic process.

Furthermore, previous studies by our group show that the presence of the heteropolyacid HPMo can improve the ORR activity of graphene/chitosan composites compared to HPMo-free catalysts (Aghabarari et al., 2017). However, it should be pointed out that the order of surface N, P, and Mo amounts are not consistent with the catalyst's ORR performance. The Cu-composite has the highest Mo and P amounts and the second highest N amount, but it

has the lowest ORR performance. Clearly, the results obtained provide evidence of the important role played by each transition metal in the formation of active sites for ORR.

The Fe_3C encapsulated in dual-doped carbon materials seems to be an important active site (Yang et al., 2015; Ren et al., 2016). The outer protective graphitic layers stabilize the carbide nanoparticles, while the Fe_3C/Mo_2C nanoparticles should play a synergetic role in activating the outer surface of the graphitic layers towards the ORR. Such an enhanced catalytic activity has been explained from the large amounts of oxygen vacancies created by Mo_2C and Fe_3C as electron donors. On the other site, the outstanding ORR performance of Fe_3C-based ORR catalysts can be also attributable to the factors of the N dopants and Fe–N_x coordination species (Jiang et al., 2015). Furthermore, in this complex system we cannot rule out the presence of electrochemically active Fe-P interactions either. Recently, Razmjooei et al. found that the introduction of Fe on P-functionalized graphene caused remarkable synergistic effects, which were beneficial for ORR (Razmjooei et al., 2015). Therefore, these results highlighted the advantage of the facile synthetic approach to obtain a complex formed by Fe_3C along Mo_2C embedded in N- and P-dual doped carbon, which leads to significant ORR activity. However, the active sites of the Fe-related species need to be further elaborated, which is under progress.

CONCLUSIONS

In summary, a facile and cost-effective strategy for the production of Me/Mo_2C (Me = Fe, Co, Cu)-based composites embedded in N- and P-dual doped carbon matrices has been developed. For this end, inexpensive industrial materials, such as melamine and chitosan, as C and N sources and the heteropolyacid $H_3PMo_{12}O_{40}$ as P and Mo precursor were successfully used. Among transition metals considered, Fe gives rise to the best performing composite in carrying out the oxygen reduction reaction. It has been proposed that this enhanced ORR activity is due to the different synergistic effects obtained in the Fe_3C/Mo_2C species coordinated with N- and P-dual doped carbon. Therefore, this work is expected to improve the production of non-noble carbide-based heterostructure composites for practical applications in fuel cells and other applications, such as metal-air batteries.

DATA AVAILABILITY STATEMENT

The raw data supporting the conclusions of this article will be made available by the authors, without undue reservation.

AUTHOR CONTRIBUTIONS

B.A. conceptualization, methodology, investigation, materials. M.-C.S. analysis, interpretation. M.L. review, funding acquisition, suggestions. M.M.-H. supervision, logical interpretation, writing—review and editing.

ACKNOWLEDGMENTS

The authors acknowledge the Ministerio de Ciencia, Innovación y Universidades (MCIU), and FEDER for the funding received for the project, with references ENE2017-83976-C2-1-R, Spanish National Research Council COOPB20202, and MERC project 721399002.

REFERENCES

Aghabarari, B., Luque-Centeno, J. M., Capel-Sánchez, M., Lázaro Elorri, M. J., and Martínez-Huerta, M. V. (2019). Ni-based composites from chitosan biopolymer a one-step synthesis for oxygen evolution reaction. *Catalysts* 9, 471–481. doi:10.3390/catal9050471

Aghabarari, B., Martínez-Huerta, M. V., Ghiaci, M., Fierro, J. L. G., and Peña, M. A. (2013). Hybrid chitosan derviative-carbon support for oxygen reduction reactions. *RSC Adv.* 3, 5378–5381. doi:10.1016/j.ijhydene.2017.06.159

Aghabarari, B., Nezafati, N., Roca-Ayats, M., Capel-Sánchez, M. C., Lázaro, M. J., and Martínez-Huerta, M. V. (2017). Effect of molybdophosphoric acid in iron and cobalt graphene/chitosan composites for oxygen reduction reaction. *Int. J. Hydrogen Energy* 42, 28093-28101. doi:10.1016/j.ijhydene.2017.06.159

Ania, C. O., Seredych, M., Rodriguez-Castellon, E., and Bandosz, T. J. (2015). New copper/GO based material as an efficient oxygen reduction catalyst in an alkaline medium: the role of unique Cu/rGO architecture. *Appl. Catal. B Environ.* 163, 424–435. doi:10.1016/j.apcatb.2014.08.022

Brouzgou, A., Song, S., Liang, Z.-X., and Tsiakaras, P. (2016). Non-precious electrocatalysts for oxygen reduction reaction in alkaline media: latest achievements on novel carbon materials. *Catalysts* 6, 159.

Cheng, Y. H., Zhou, S. B., Hu, P., Zhao, G. D., Li, Y. X., Zhang, X. H., et al. (2017). Enhanced mechanical, thermal, and electric properties of graphene aerogels via supercritical ethanol drying and high-temperature thermal reduction. *Sci. Rep.* 7, 11. doi:10.1038/s41598-017-01601-x

Choi, C. H., Park, S. H., and Woo, S. I. (2012). Phosphorus-nitrogen dual doped carbon as an effective catalyst for oxygen reduction reaction in acidic media: effects of the amount of P-doping on the physical and electrochemical properties of carbon. *J. Mater. Chem.* 22, 12107–12115.

Chung, H. T., Won, J. H., and Zelenay, P. (2013). Active and stable carbon nanotube/nanoparticle composite electrocatalyst for oxygen reduction. *Nat. Commun.* 4, 1922. doi:10.1038/ncomms2944

Das, E., and Yurtcan, A. B. (2016). Effect of carbon ratio in the polypyrrole/carbon composite catalyst support on PEM fuel cell performance. *Int. J. Hydrogen Energy* 41, 13171–13179. doi:10.1016/j.ijhydene.2016.05.167

Fan, X., Liu, Y., Peng, Z., Zhang, Z., Zhou, H., Zhang, X., et al. (2017). Atomic H-induced Mo2C hybrid as an active and stable bifunctional electrocatalyst. *ACS Nano* 11, 384–394. doi:10.1021/acsnano.6b06089

Guil-López, R., Martínez-Huerta, M. V., Guillén-Villafuerte, O., Peña, M. A., Fierro, J. L. G., and Pastor, E. (2010). Highly dispersed molybdenum carbide as non-noble electrocatalyst for PEM fuel cells: performance for CO electrooxidation. *Int. J. Hydrogen Energy* 35. doi:10.1016/j.ijhydene.2010.05.044

Huang, K., Bi, K., Liang, C., Lin, S., Wang, W. J., Yang, T. Z., et al. (2015). Graphite carbon-supported Mo2C nanocomposites by a single-step solid state reaction for electrochemical oxygen reduction. *PLoS One* 10. doi:10.1371/journal.pone.0138330

Jaouen, F., Proietti, E., Lefevre, M., Chenitz, R., Dodelet, J.-P., Wu, G., et al. (2011). Recent advances in non-precious metal catalysis for oxygen-reduction reaction in polymer electrolyte fuel cells. *Energy Environ. Sci.* 4, 114–130. doi:10.1039/C0EE00011F

Jiang, H., Yao, Y., Zhu, Y., Liu, Y., Su, Y., Yang, X., et al. (2015). Iron carbide nanoparticles encapsulated in mesoporous Fe-N-doped graphene-like carbon

hybrids as efficient bifunctional oxygen electrocatalysts. *ACS Appl. Mater. Interfaces* 7, 21511–21520. doi:10.1021/acsami.5b06708

Khan, A., Goepel, M., Colmenares, J. C., and Gläser, R. (2020). Chitosan-based N-doped carbon materials for electrocatalytic and photocatalytic applications. *ACS Sustain. Chem. Eng.* 8, 4708–4727. doi:10.1021/acssuschemeng.9b07522

Li, J.-S., Wang, Y., Liu, C.-H., Li, S.-L., Wang, Y.-G., Dong, L.-Z., et al. (2016). Coupled molybdenum carbide and reduced graphene oxide electrocatalysts for efficient hydrogen evolution. *Nat. Commun.* 7, 11204. doi:10.1038/ncomms11204

Li, P., Qiu, Y., Liu, S., Li, H., Zhao, S., Diao, J., et al. (2019). Heterogeneous Mo 2 C/Fe 5 C 2 nanoparticles embedded in nitrogen-doped carbon as efficient electrocatalysts for the oxygen reduction reaction. *Eur. J. Inorg. Chem.* 2019, 3235–3241. doi:10.1002/ejic.201900390

Li, Q., Cao, R., Cho, J., and Wu, G. (2014a). Nanocarbon electrocatalysts for oxygen reduction in alkaline media for advanced energy conversion and storage. *Adv. Energy Mater.* 4, 1301415. doi:10.1002/aenm.201301415

Li, R., Cao, A., Zhang, Y., Li, G., Jiang, F., Li, S., et al. (2014b). Formation of nitrogen-doped mesoporous graphitic carbon with the help of melamine. *ACS Appl. Mater. Interfaces* 6, 20574–20578. doi:10.1021/am5061323

Li, R., Wei, Z., and Gou, X. (2015). Nitrogen and phosphorus dual-doped graphene/carbon nanosheets as bifunctional electrocatalysts for oxygen reduction and evolution. *ACS Catal.* 5, 4133–4142. doi:10.1021/acscatal.5b00601

Li, Z., Zhao, W., Yin, C., Wei, L., Wu, W., Hu, Z., et al. (2017). Synergistic effects between doped nitrogen and phosphorus in metal-free cathode for zinc-air battery from covalent organic frameworks coated CNT. *ACS Appl. Mater. Interfaces* 9, 44519–44528. doi:10.1021/acsami.7b14815

Liao, L., Bian, X., Xiao, J., Liu, B., Scanlon, M. D., and Girault, H. H. (2014). Nanoporous molybdenum carbide wires as an active electrocatalyst towards the oxygen reduction reaction. *Phys. Chem. Chem. Phys.* 16, 10088–10094. doi:10.1039/c3cp54754j

Liu, Z., Zhang, G., Lu, Z., Jin, X., Chang, Z., and Sun, X. (2013). One-step scalable preparation of N-doped nanoporous carbon as a high-performance electrocatalyst for the oxygen reduction reaction. *Nano Res.* 6, 293–301. doi:10.1007/s12274-013-0307-9

Luque-Centeno, J. M., Martínez-Huerta, M. V., Sebastián, D., Pardo, J. I., and Lázaro, M. J. (2020). CoTiO3/NrGO nanocomposites for oxygen evolution and oxygen reduction reactions: synthesis and electrocatalytic performance. *Electrochim. Acta* 331, 135396–135407. doi:10.1016/j.electacta.2019.135396

Marguerite, R. (2006). Chitin and chitosan: properties and applications. *Prog. Polym. Sci.* 31, 603–632.

Martínez-Huerta, M. V., and Lázaro, M. J. (2017). Electrocatalysts for low temperature fuel cells. *Catal. Today* 285, 3–12. doi:10.1016/j.cattod.2017.02.015

Palaniselvam, T., Kashyap, V., Bhange, S. N., Baek, J.-B., and Kurungot, S. (2016). Nanoporous graphene enriched with Fe/Co-N active sites as a promising oxygen reduction electrocatalyst for anion exchange membrane fuel cells. *Adv. Funct. Mater.* 26, 2150–2162. doi:10.1002/adfm.201504765

Pan, T., Liu, H., Ren, G., Li, Y., Lu, X., and Zhu, Y. (2016). Metal-free porous nitrogen-doped carbon nanotubes for enhanced oxygen reduction and evolution reactions. *Sci. Bull.* 61, 889–896. doi:10.1007/s11434-016-1073-3

Peng, H., Liu, F., Liu, X., Liao, S., You, C., Tian, X., et al. (2014). Effect of transition metals on the structure and performance of the doped carbon catalysts derived from polyaniline and melamine for ORR application. *ACS Catal.* 4, 3797–3805. doi:10.1021/cs500744x

Qiao, M., Tang, C., He, G., Qiu, K., Binions, R., Parkin, I. P., et al. (2016). Graphene/nitrogen-doped porous carbon sandwiches for the metal-free oxygen reduction reaction: conductivity versus active sites. *J. Mater. Chem. A* 4, 12658–12666. doi:10.1039/c6ta04578b

Qiao, X., Liao, S., You, C., and Chen, R. (2015). Phosphorus and nitrogen dual doped and simultaneously reduced graphene oxide with high surface area as efficient metal-free electrocatalyst for oxygen reduction. *Catalysts* 5, 981–991. doi:10.3390/catal5020981

Quílez-Bermejo, J., Morallón, E., and Cazorla-Amorós, D. (2020). Metal-free heteroatom-doped carbon-based catalysts for ORR. A critical assessment about the role of heteroatoms. *Carbon N. Y.* 165, 434–454. doi:10.1016/j.carbon.2020.04.068

Razmjooei, F., Singh, K. P., Bae, E. J., and Yu, J. S. (2015). A new class of electroactive Fe- and P-functionalized graphene for oxygen reduction. *J. Mater. Chem. A* 3, 11031–11039. doi:10.1039/c5ta00970g

Razmjooei, F., Singh, K. P., Song, M. Y., and Yu, J.-S. (2014). Enhanced electrocatalytic activity due to additional phosphorous doping in nitrogen and sulfur-doped graphene: a comprehensive study. *Carbon N. Y.* 78, 257–267. doi:10.1016/j.carbon.2014.07.002

Ren, G., Lu, X., Li, Y., Zhu, Y., Dai, L., and Jiang, L. (2016). Porous core-shell Fe3C embedded N-doped carbon nanofibers as an effective electrocatalysts for oxygen reduction reaction. *ACS Appl. Mater. Interfaces* 8, 4118–4125. doi:10.1021/acsami.5b11786

Roca-Ayats, M., García, G., Peña, M. A., and Martínez-Huerta, M. V. (2014). Titanium carbide and carbonitride electrocatalyst supports: modifying Pt-Ti interface properties by electrochemical potential cycling. *J. Mater. Chem. A* 2. doi:10.1039/c4ta03782k

Rybarczyk, M. K., Lieder, M., and Jablonska, M. (2015). N-doped mesoporous carbon nanosheets obtained by pyrolysis of a chitosan-melamine mixture for the oxygen reduction reaction in alkaline media. *RSC Adv.* 5, 44969–44977. doi:10.1039/c5ra05725f

Shao, M., Chang, Q., Dodelet, J.-P., and Chenitz, R. (2016). Recent advances in electrocatalysts for oxygen reduction reaction. *Chem. Rev.* 116, 3594–3657. doi:10.1021/acs.chemrev.5b00462

Sheng, Z.-H., Shao, L., Chen, J.-J., Bao, W.-J., Wang, F.-B., and Xia, X.-H. (2011). Catalyst-free synthesis of nitrogen-doped graphene via thermal annealing graphite oxide with melamine and its excellent electrocatalysis. *ACS Nano* 5, 4350–4358. doi:10.1021/nn103584t

Stephens, I. E. L., Bondarenko, A. S., Gr+©nbjerg, U., Rossmeisl, J., and Chorkendorff, I. (2012). Understanding the electrocatalysis of oxygen reduction on platinum and its alloys. *Energy Environ.Sci.* 5, 6744–6762. doi:10.1039/C2EE03590A

Sun, Y., Sinev, I., Ju, W., Bergmann, A., Dresp, S., Kühl, S., et al. (2018). Efficient electrochemical hydrogen peroxide production from molecular oxygen on nitrogen-doped mesoporous carbon catalysts. *ACS Catal.* 8, 2844–2856. doi:10.1021/acscatal.7b03464

Wagner, C. D., Riggs, W. M., Davis, L. E., and Moulder, J. F. (1979). *Handbook of X-ray photoelectron spectroscopy*. , ed. G. E. Muilenberg Minnesota: Perkin-Elmer Corporation.

Wang, X. X., Swihart, M. T., and Wu, G. (2019). Achievements, challenges and perspectives on cathode catalysts in proton exchange membrane fuel cells for transportation. *Nat. Catal.* 2, 578–589. doi:10.1038/s41929-019-0304-9

Wu, G., More, K. L., Johnston, C. M., and Zelenay, P. (2011). High-performance electrocatalysts for oxygen reduction derived from polyaniline, iron, and cobalt. *Science* 332, 443–447.

Wu, T. X., Wang, G. Z., Zhang, X., Chen, C., Zhanga, Y. X., and Zhao, H. J. (2015). Transforming chitosan into N-doped graphitic carbon electrocatalysts. *Chem. Commun.* 51, 1334–1337. doi:10.1039/c4cc09355k

Xie, S. L., Huang, S. C., Wei, W. J., Yang, X. Z., Liu, Y., Lu, X. H., et al. (2015). Chitosan waste-derived Co and N Co-doped carbon electrocatalyst for efficient oxygen reduction reaction. *ChemElectroChem* 2, 1806–1812. doi:10.1002/celc.201500199

Yang, W., Liu, X., Yue, X., Jia, J., and Guo, S. (2015). Bamboo-like carbon nanotube/Fe3C nanoparticle hybrids and their highly efficient catalysis for oxygen reduction. *J. Am. Chem. Soc.* 137, 1436–1439. doi:10.1021/ja5129132

Yang, X., Xu, Y., Xue, B., Jiang, Y., and Li, F. (2018). Cordierite reinforced graphite nanocomposite with superior adsorption capacity synthesized by in-situ carbon-bed pyrolysis method. *Microporous Mesoporous Mater.* 265, 219–226. doi:10.1016/j.micromeso.2018.02.019

Yasuda, S., Furuya, A., Uchibori, Y., Kim, J., and Murakoshi, K. (2016). Iron-nitrogen-doped vertically aligned carbon nanotube electrocatalyst for the oxygen reduction reaction. *Adv. Funct. Mater.* 26, 738–744. doi:10.1002/adfm.201503613

Zhang, Y., Li, C., Chen, Z., Ni, Y., Kong, F., Kong, A., et al. (2017). Ionic liquid-derived MoC nanocomposites with ordered mesoporosity as efficient Pt-free electrocatalyst for hydrogen evolution and oxygen reduction. *Catal. Letters* 147, 253–260. doi:10.1007/s10562-016-1914-3

Zhong, Y., Xia, X. H., Shi, F., Zhan, J. Y., Tu, J. P., and Fan, H. J. (2015). Transition metal carbides and nitrides in energy storage and conversion. *Adv. Sci.* 3, 1500286. doi:10.1002/advs.201500286

Conflict of Interest: The authors declare that the research was conducted in the absence of any commercial or financial relationships that could be construed as a potential conflict of interest.

Environmental Material

Elisa Franzoni

Prof. Elisa Franzoni has a Ph.D. in Materials Engineering and is an Associate Professor in Materials Science and Technology at the University of Bologna, where she leads the research group Materials and Technologies for Cultural Heritage. In 2020, she coordinated the project HAP4MARBLE and participated in both ROCK and SHELTER. She was in charge of research projects funded by the industry and has collaborated on research with national and international universities, private companies, and public authorities in the field of materials for cultural heritage. She is a member of RILEM and an Associate Editor of Materials and Structures (IF 2.90). She is the author of more than 150 scientific publications (90 in Scopus, H-index 27) and the creator of one patent.

frontiers in Materials

ORIGINAL RESEARCH
published: 18 February 2021
doi: 10.3389/fmats.2021.583112

Experimental Study on an Innovative Biopolymeric Treatment Against Salt Deterioration of Materials in Cultural Heritage

Mattia Bassi[1], *Enrico Sassoni*[1,2] *and Elisa Franzoni*[1,2]*

[1]Interdepartmental Centre for Industrial Research in Building and Construction (CIRI Building and Construction), University of Bologna, Bologna, Italy, [2]Department of Civil, Chemical, Environmental and Materials Engineering (DICAM), University of Bologna, Bologna, Italy

Salt crystallization is one of the harshest deterioration mechanisms affecting heritage materials, causing impressive decay patterns and the loss of a high thickness of original materials. Although salt damage has been widely investigated in the literature from the theoretical and experimental points of view, the solutions to mitigate this problem are still extremely limited. In the present paper, a new biopolymeric treatment based on chitosan was tested on two kinds of porous limestones widely used in historic architecture, aiming at inhibiting the crystallization of sodium sulphate inside the stone and promoting the formation of salt efflorescence over the surface, rather than harmful subflorescence inside the pore network. The treatment was applied to the bare stone and also after an inorganic pre-treatment based on the formation of hydroxyapatite in the stone. Hydroxyapatite was recently proposed for the consolidation and protection of carbonate stones and here it is expected to provide an effective anchoring layer for the chitosan coating on the pores surface, and also to prevent the calcite washout from the stone and hence the removal of chitosan. The effect of hydroxyapatite alone was also tested, for comparison's sake. Treated and untreated stone specimens were subjected to two different accelerated salt crystallization tests, one based on crystallization cycles (wetting-drying cycles) and the other one based on continuous capillary absorption of a saline solution ("wick effect"), evaluating the results in terms of weight loss, efflorescence formation, and changes in porosity and mechanical properties. The results showed that all the treatments are compatible with the stones, and the combined treatment (hydroxyapatite + chitosan) is extremely promising for the prevention of salt damage.

Keywords: chitosan, hydroxyapatite, salt inhibitor, sodium sulphate (mirabilite and thenardite), biopolymer, efflorescence, limestone, salt crystallization tests

OPEN ACCESS

Edited by:
Guang-Ling Song,
Xiamen University, China

Reviewed by:
Dusan Losic,
University of Adelaide, Australia
Peng Wang,
Harbin Medical University, China
Pagona-Noni Maravelaki,
Technical University of Crete, Greece

***Correspondence:**
Elisa Franzoni
elisa.franzoni@unibo.it

Specialty section:
This article was submitted to Environmental Materials, a section of the journal Frontiers in Materials

Received: *15 July 2020*
Accepted: *08 January 2021*
Published: *18 February 2021*

Citation:
Bassi M, Sassoni E and Franzoni E (2021) Experimental Study on an Innovative Biopolymeric Treatment Against Salt Deterioration of Materials in Cultural Heritage. Front. Mater. 8:583112. doi: 10.3389/fmats.2021.583112

INTRODUCTION

One of the major causes of deterioration and damage of cultural heritage is the presence of salts within historic building materials such as stone, brick, mortars and plasters, and also in more recent materials such as concrete (Charola, 2000; Sandrolini and Franzoni, 2007; Doehne and Price, 2010; Espinosa-Marzal and Scherer, 2010; Franzoni, 2014; Charola and Bläuer, 2015; Charola and Wendler, 2015; Lubelli et al., 2018; Andreotti et al., 2019). Damage is caused by crystallization

of salts, due to evaporation and/or cooling of saline solutions, and in particular by the solubilization/crystallization cycles, due to the strong sensitivity of salts to the thermo-hygrometric conditions. This leads to formation of internal mechanical stress in the material, protracted over time. In most cases, this stress can easily overcome the tensile strength of building materials, usually quite low, causing formation and propagation of cracks, which affect structural and decorative elements of buildings (Flatt, 2002; Scherer, 2004).

Salts can enter building materials in different ways, the main one being certainly the capillary absorption of moisture from the soil (Charola, 2000; Doehne and Price, 2010; Franzoni, 2014; Charola and Bläuer, 2015; Charola and Wendler, 2015). In this case, water coming from rain, underground water sources or broken pipes, filters through the ground dissolving the salts contained in it. The saline solution is absorbed by the wall by capillarity, up to a height that depends on the evaporation rate, related to thermo-hygrometric conditions (temperature, T, and relative humidity, RH) and materials porosity (Sandrolini and Franzoni, 2007; Charola and Bläuer, 2015; Charola and Wendler, 2015). As long as the water supply is greater than the evaporation rate, the wall will appear wet on the surface and salts will crystallize over the surface as efflorescence, involving mainly aesthetical damage. When the evaporation rate increases, the evaporation front will move inwards, where the salt solution will reach the supersaturation necessary for the crystallization of salts within the porous network of the materials, causing formation of potentially harmful subflorescence (Franzoni, 2014; Andreotti et al., 2019). In addition to capillary rise, salts can be autochthonous in the materials (for example, in Portland cement or in bricks) or can come from external sources such as deicing salts used in roads, from chemical products used in agriculture, from marine spray in the case of buildings near the coast or from the chemical reactions between building materials and air pollutants (Charola and Bläuer, 2015; Charola and Wendler, 2015).

Over the last decades, the phenomenon of damage caused by salt crystallization has been widely studied and many theories have been formulated. It is now clear that, following evaporation or cooling of a salt solution, supersaturation conditions are reached, i.e., conditions where the concentration of salt dissolved in solution is greater than the saturation one, at the same temperature: in this case, salt crystals precipitate in the pores of the material (Scherer, 2004; Doehne and Price, 2010). As a crystal grows and approaches the inner pore wall, repulsive forces arise to prevent the direct contact between the two surfaces: this "disjoining pressure" is attributed to repulsive Van der Waals forces in the case of ice or to electrostatic forces in the case of salt crystals (Scherer, 1999; Houck and Scherer, 2006; Andreotti et al., 2019). Therefore, the two surfaces organize the orientation of the water molecules and ions in different ways, to minimize their surface energy, and this prevents the direct contact between the crystal and the pore wall, allowing the persistence of a thin liquid film (a few nanometers thick) (Scherer, 1999). Internal tensile forces are generated in this liquid film and, if this layer did not exist, the crystal would not damage the material. However, the energy necessary to overcome repulsive forces (energy that would allow direct contact between the surfaces) is usually greater than the tensile strength of the material and this causes the formation of cracks and the subsequent failure of the material itself (Houck and Scherer, 2006; Espinosa-Marzal and Scherer, 2010). The amount of damage will depend on various factors, first of all the degree of supersaturation reached, which in turn is influenced by the type of salt, material porosity, pore size distribution, etc. (Scherer, 2004; Angeli et al., 2007).

Increasing the tensile strength of decayed building materials by application of consolidating materials can indirectly reduce their deterioration due to physical-mechanical processes, such as ice and salt damage. However, the goal of consolidation is restoring the cohesion of decayed materials and not preserving them from future deterioration processes, hence alternative strategies have been explored to mitigate salt damage. Of course, controlling the environmental conditions (T and RH) and eliminating water sources (first of all, capillary rise) can help reduce damaging of walls. However, it is impossible to control temperature and relative humidity in outdoors environment and also the elimination of rising damp is definitely challenging (Flatt, 2002; Franzoni, 2014; Franzoni, 2018; Andreotti et al., 2019). In fact, although there are different methods to prevent rising damp, many of these methods are not fully effective and compatible, or simply are difficult to apply in historic structures (Franzoni, 2014). Some interventions, such as the use of hydrophobic treatments or the application of scarcely porous layers on the masonry surfaces, are even counterproductive, leading to a higher rise of damp and, often, to more severe damage caused by moisture and salts (Franzoni, 2014).

Several studies have focused on the use of modifiers of salt crystallization, which can act during both steps of the crystallization process (nucleation and growth of crystals) and can be distinguished in two different groups: inhibitors and promoters (Rodriguez-Navarro et al., 2002; Granneman et al., 2019; Bracciale et al., 2020). Crystal nucleation inhibitors are modifiers that increase the degree of supersaturation necessary to allow for the nucleation of crystals, thus increasing the time between the formation of supersaturation condition and the crystallization of salt. This results in the transport of the supersaturated salt solution over longer distances, thus favoring the formation of efflorescence rather than more harmful subflorescence. On the other hand, at higher level of supersaturation, if conditions for crystallization of the supersaturated solution occur, more severe damage will be experienced (Granneman et al., 2019; Bracciale et al., 2020). Crystal growth inhibitors are modifiers that retard crystal growth, covering the whole crystal surface and preventing the addition or the detachment of salt units (Granneman et al., 2019). Nucleation promoters work in the opposite way, increasing the salt nucleation rate that occurs at lower supersaturation (near or at the saturation condition), thus causing less damage to the substrate (Granneman et al., 2019). Different substances were tested in the last years as crystallization modifiers, like ferrocyanides (Rodriguez-Navarro et al., 2002; Selwitz and Doehne, 2002; Lubelli and van Hees, 2007; Rivas et al., 2010; Gupta et al., 2012) as inhibitors for sodium chloride, phosphonates (Lubelli and van Hees, 2007; Ruiz-Agudo et al.,

2012) as inhibitors for sodium sulphate and borax (Smith et al., 2010; Granneman et al., 2017) as promoter for sodium sulphate, just to name the most promising ones. A different strategy, adopted for example in (Houck and Scherer, 2006), is based on eliminating the crystallization pressure between the growing salt crystal and the inner pore wall by deposition of a thin polymeric layer. If the material surface could be modified so that the salt crystal does not repel it, the crystal itself would be able to grow in direct contact with the pore wall: in this case, the liquid film will not be maintained and, therefore, no pressure or damage will be generated in the material (Houck and Scherer, 2006). All of these products have different effectiveness and give different results depending on the type of salt, the porous substrate on which they are applied, the concentration used, etc., so that an improvement in the resistance to salt crystallization is usually found, but sometimes an increase in damage is experienced. The development of these crystallization modifiers is still mostly in the experimental phase, with many laboratory tests and few onsite applications, so more studies seem necessary (Granneman et al., 2019; Bracciale et al., 2020). In recent years, biomass-derived inhibitors were developed for the prevention of salt crystallization damage caused by different types of salt, focusing mainly on sodium sulphate and sodium chloride due to their destructive potential. It is the case, for example, of phosphocitrate, that was already tested with good results on different materials in laboratory and in the field (Cassar et al., 2008; Franceschini et al., 2015; Bracciale et al., 2020). These products, besides being derived from renewable sources, are non-toxic and usually soluble in water and/or alcohol, thus avoiding the use of harmful solvents (Bracciale et al., 2020), giving benefits to environment and human health. It is in this perspective that, in the present paper, a new bio-based protective material against salt crystallization (chitosan) was employed to improve the resistance of two porous carbonate stones to salt damage, alone and combined with a recently developed consolidant (hydroxyapatite). The present paper follows a previous preliminary study, in which this combined treatment was proposed for the first time, with encouraging results (Andreotti et al., 2019). An overview of the main properties of hydroxyapatite and chitosan is provided in the following.

Since more than a century, various organic and inorganic consolidating materials have been proposed for stone and other porous materials, with different results. Among these, the use of hydroxyapatite (HAP) and other calcium phosphate phases (CaP) has been studied since 2011 for consolidation and protection of carbonate stones (Sassoni et al., 2011). The CaP-based treatment has high potential because it provides significant mechanical consolidation in a short time, without altering porosity or transport properties of the substrate (Naidu et al., 2011; Sassoni et al., 2011; Sassoni et al., 2016a; Sassoni et al., 2016b; Sassoni, 2018). Hydroxyapatite, which is the main inorganic constituent of human teeth and bones, is a good consolidant for carbonate substrates as it is much less soluble than calcite and, at the same time, has a similar crystalline structure (Sassoni et al., 2011). As reported in the literature, the formation of HAP *in situ* is expected to occur by reaction between a carbonate-rich substrate, which provides calcium ions through dissolution, and an aqueous solution of a phosphate salt, usually diammonium hydrogen phosphate ($(NH_4)_2HPO_4$, indicated as DAP), which provides PO_4^{3-} ions (Naidu et al., 2011; Sassoni et al., 2011; Sassoni, 2018), according to the following reaction:

$$10CaCO_3 + 5(NH_4)_2HPO_4 \rightarrow Ca_{10}(PO_4,CO_3)_6(OH,CO_3)_2 + 5(NH_4)_2CO_3 + 3CO_2 + 2H_2O$$

One of the advantages of the use of the DAP-treatment is that all the by-products of the reaction, i.e., ammonium carbonate, carbon dioxide and water, are innocuous and volatile and, therefore, unwanted residues are not expected to remain in the stone.

In very recent years, the use of natural and biodegradable substances, mainly biopolymers, has been proposed in the field of conservation of building materials, as well as in other sectors. The idea backgrounding this new class of conservation materials is that they can potentially provide some interesting properties for a certain number of years, then naturally disappearing without leaving unwanted residues (Ocak et al., 2009; Ocak et al., 2015; Pedna et al., 2016; Andreotti et al., 2018). This requires that the treatment is applied again after some years, during maintenance works, but it also involves some advantages in comparison with traditional polymers used in conservation for many decades. In fact, traditional polymers are subject to unavoidable aging processes and performance loss in a limited number of years, but they are also hard to remove once they transformed during aging (by cross-linking, chain scission, crystallization, oxidation, etc.), thus influencing, and sometimes jeopardizing, the possibility to re-treat the materials with new consolidating and/or protective substances. In fact, the application of different polymeric treatments to heritage materials caused severe problems during last decades. In this context, some biopolymer-based water-repellents have been proposed (Ocak et al., 2009; Ocak et al., 2015; Pedna et al., 2016; Andreotti et al., 2018) for the protection of heritage materials against rain absorption, and chitosan was proposed as a treatment to fight salt damage (Andreotti et al., 2019).

Chitosan is already widely used in agriculture, in food sector, in environmental protection and in various biomedical applications, where its antibacterial and antioxidant properties are exploited (Muxika et al., 2017). Chitosan is produced from chitin, a marine origin polysaccharide that is widely available, being the second most abundant natural polymer after cellulose (Muxika et al., 2017; Philibert et al., 2017). Chitin is the main structural component in the exoskeleton of marine invertebrates and insects, as well as molluscs and crustaceans. When combined with calcium carbonate, like in shells of crustaceans and insects, chitin produces a strong composite, exhibiting improved hardness and stiffness compared to pure chitin and also a greater tenacity and ductility than pure $CaCO_3$ (Muxika et al., 2017; Andreotti et al., 2019). Chitin is a linear polysaccharide, consisting in N-acetyl-D-glucosamine units, connected by β—1.4 bonds (Muxika et al., 2017; Philibert et al., 2017; Andreotti et al., 2019), which is mostly obtained from industrial waste in the processing of marine shells, shrimps and similar, hence it is abundantly available. Despite its outstanding characteristics such

as biocompatibility, biodegradability and high mechanical strength, its exploitability is limited by its very low solubility (Muxika et al., 2017; Philibert et al., 2017; Andreotti et al., 2019). This turns the attention to chitosan, the main derivative of chitin. Chitosan is a copolymer obtained from the alkaline deacetylation of chitin, a process involving the treatment of chitin with hydroxides at high temperature. It consists in D-glucosamine and N-acetyl-D-glucosamine units, connected by β—1.4 glycosidic bonds (Muxika et al., 2017; Philibert et al., 2017; Andreotti et al., 2019). The ratio between the two units is called degree of deacetylation: for values ≥50%, chitosan becomes soluble in acidic media and, in this case, the aminic groups and the polymer become cationic, allowing them to interact with different molecules. This positive charge is believed to be responsible for its antimicrobial activity, allowing it to interact with negatively charged cellular membranes of microorganisms (Muxika et al., 2017).

The research in (Andreotti et al., 2019) was the first example of study on the behavior and the effects of chitosan applied to porous building materials. The study addressed prevention of salt crystallization damage by covering the pore surface with a chitosan coating, which can inhibit salt crystallization inside the pore network of the material. Chitosan was selected for some interesting properties: presence of functional groups in the molecular structure, acting as anchoring groups towards the mineral surfaces; film-forming capacity, to generate a continuous coating on the pore walls; highly flexible chains that allow for the interaction with any type of salt. Moreover, this polymer is not hydrophobic and does not alter the water transport properties of the treated substrate, which is beneficial for salt damage resistance and for preventing other deterioration processes (Houck and Scherer, 2006). In addition, it is bio-based and biodegradable, thus providing a minimum toxicity and complying with the new concept of "reversibility of treatment" explained above. Three different experimental setups were used in (Andreotti et al., 2019) and the results are briefly reported in the following. A first crystallization test was carried out by cooling a saturated aqueous solution of sodium sulphate and chitosan, showing that the polymer has a strong inhibiting effect on the salt crystallization, basically blocking it up to 2 °C, while in absence of chitosan salt crystallization occurred at 13.1 °C. The fact that chitosan inhibits sodium sulphate crystallization in the solution is thought to be due to its polyelectrolytic nature, providing a high number of positively charged sites that sequester sulphate ions. However, it was also reported that some polymers that inhibit salt crystallization when in solution might favor it when they are adsorbed on a solid surface, due to some polymer chain orientation (Ruiz-Agudo et al., 2006), so this aspect was specifically taken into account. A second test was carried out on different powdered substrates treated with chitosan. The powders, thanks to their large specific surface, allowed to demonstrate the remarkable film-forming ability of chitosan, which was adsorbed on the solid surface, creating a coating. Notably, the DAP-based consolidating treatment, applied before the polymer, caused an increase in the amount of chitosan adsorbed, probably thanks to the roughness of CaP phases that act as anchoring surfaces. When subjected to water flow, the treated powders (both with and without the DAP pre-treatment) exhibited initial solubilization of the thick chitosan layer, after which the adsorbed polymer was not further leached in water. In the final test, limestone samples were treated to investigate whether the inhibiting effect of chitosan observed in solution actually delay salt crystallization inside the stone, thus promoting formation of efflorescence over the surface, rather than development of mechanical stress inside the stone. While the polymeric treatment alone caused greater damage in the samples compared to the untreated references, as the retarding action of chitosan caused a higher supersaturation degree and a greater crystallization pressure in the zones of the pore walls not covered by the chitosan film, in the samples treated with DAP and then chitosan there was a remarkable benefit, with promotion of efflorescence and increase in the resistance to degradation.

While a preliminary evaluation of the adhesion and thickness of the investigated coatings on controlled, flat and non-porous surfaces of calcite and silica, and on powders of the two minerals, was carried out in the previous study with encouraging results (Andreotti et al., 2019), this paper focuses on the performance of the treatments in real stones, selecting two different salt crystallization tests aimed at producing a less drastic and hence more easy-to-interpret deterioration in the stone, with respect to the previous study. The two tests were carried out in order to consider two different mechanisms presently adopted to reproduce the damage by salts in laboratory, namely salt crystallization cycles and "wick effect". In this frame, it was decided to use the same shape of the samples adopted in the relevant standards and literature papers, i.e., cylinders for salt crystallization cycles (EN 12370, 1999) and prisms for the "wick test" (Goudie, 1986).

Starting from the preliminary findings briefly summarized above, the present study aims at further investigating the behavior of chitosan, by applying it to different substrates. In addition to the polymeric treatment alone, pre-treatment by DAP (followed by chitosan application) and treatment by DAP alone were also tested. The CaP phases that form in the material after the DAP treatment have been shown to provide good consolidating effectiveness, thus providing some benefits also in terms of resistance to salt crystallization pressure. Moreover, in the double treatment (DAP solution followed by chitosan), the CaP layer is expected to provide a good anchorage for the formation of a more homogeneous and defect-free polymeric layer, and also to protect calcite from dissolution in both neutral and slightly acidic water (Sassoni, 2018), thus preventing possible washout of the coating, which could cause a loss of effectiveness (Andreotti et al., 2019).

MATERIALS

Stones

The lithotypes chosen for this research are two types of bioclastic limestone, widely used in historic architecture of specific geographical areas, but also representative of porous carbonate stones used in many countries.

The first one is Globigerina limestone (labeled as "G"), which had been used also in the cited preliminary study (Andreotti et al., 2019). This stone is the major lithotype of the island of Malta, widely used in historic architecture and subject to severe deterioration by atmospheric agents and salts, leading to alveolization, flaking and pulverization (Sassoni et al., 2016a). It is an organogenic limestone composed mainly of calcite (about 95%), with traces of quartz and other impurities, and having a yellow-cream color.

The second lithotype was Lecce stone (labeled as "L"), a limestone used in southern Italy and, in particular, in Salento, which was chosen because it is similar to Globigerina limestone, but different enough to verify the repeatability of the results on a different substrate. Lecce stone is an organogenic limestone too, yellow-greyish in color, with a quite homogeneous composition based on calcite (about 95%), including a strong presence of marine fossils of different sizes, and a minor presence of phosphatic minerals (fluorapatite). The nature of this stone, as well as that of Globigerina limestone, makes it very vulnerable to deteriorating agents and salts in particular (Calia et al., 2013).

The slabs of Lecce stone from Cursi-Zollino-Melpignano quarry, Lecce (supplied by Décor S. r.l.) and the slabs of Globigerina limestone from the Qrendi area, Malta (Franka type, supplied by Xelini Skip Hire and High-up Service), were cut into eight prisms ($3 \times 3 \times 25$ cm^3, the longest side cut parallel to the stone bedding planes) and 21 cylinders (5 cm in diameter, 5 cm in height, core-drilled perpendicular to the bedding planes). The samples were gently washed with deionized water and placed in an oven at 60 °C until constant weight, then cooled to room temperature. Cylinders and prisms are indicated with the letters "C" and "P", respectively, following the letter indicating the type of stone (L_C, L_P, G_C, G_P).

Treatments

In the light of previous literature studies, where the application of DAP-based solutions was tested on different substrates, adopting different DAP concentrations and different additional compounds (Naidu et al., 2011; Sassoni et al., 2011; Franzoni et al., 2015; Sassoni et al., 2016a; Sassoni et al., 2016b; Sassoni, 2018), a solution containing 0.1 M DAP + 0.1 mM $CaCl_2$ in 10 vol % ethanol was used in the present study. DAP, $CaCl_2$?$2H_2O$ and ethanol were purchased from Sigma-Aldrich (reagent grade). A low concentration of DAP is preferable to avoid formation of a too thick film over the pore surface, which would more prone to cracking during drying, as well as to prevent formation of metastable CaP phases and the possible persistence of unreacted DAP in the treated stone. Because the lower the DAP concentration, the lower the amount of PO_4^{3-} ions necessary to form HAP, ethanol and $CaCl_2$ were added to the DAP solution. Ethanol exerts a weakening action on the hydration sphere of phosphate ions in solution and hence promotes formation of CaP (Graziani et al., 2016; Sassoni et al., 2018), while $CaCl_2$ guarantees a better surface coverage by providing additional calcium ions, also preventing excessive dissolution of the substrate (Naidu and Scherer, 2014).

For the polymeric treatment, based on the results obtained in (Andreotti et al., 2019), a 0.05 wt% chitosan solution was prepared. As mentioned in the Introduction, chitosan can be solubilized only in acidic media. For this reason, the pH of the solution was brought to ~3 with the addition of acetic acid, which was chosen because it does not leave any unwanted components in the solution. Once the chitosan was completely dissolved, the solution was brought back to neutrality (pH between six and 7), not to damage the stone substrate. pH adjustment was obtained by adding 15 ml of a 0.03% NaOH solution to 1 L of chitosan solution.

The labels and number of specimens per type of treatment are summarized in the following:

- two cylinders for each lithotype were not treated, remaining as reference material (labeled as "UT");
- two prisms and three cylinders for each lithotype were not treated and were subjected to the crystallization tests (labeled as "UT_SALT");
- two prisms and five cylinders for each lithotype were treated only with the chitosan solution (labeled as "CHIT"). Except for two cylinders, which were left non-degraded, all these samples were subjected to the crystallization tests ("CHIT_SALT");
- two prisms and five cylinders for each lithotype were treated only with the consolidating solution (labeled as "HAP"). Except for two cylinders, which were left non-degraded, all these samples were subjected to the crystallization tests ("HAP_SALT");
- two prisms and six cylinders for each lithotype were treated first with the consolidating solution and then with the chitosan one (labeled as "HAP + CHIT"). Except for two cylinders, which were left non-degraded, all these samples were subjected to the crystallization tests ("HAP + CHIT_SALT").

METHODS

Characterization

The main characteristics of the stones used in the research were first investigated. The values of bulk density, open porosity and dynamic elastic modulus were measured not only in the untreated stone specimens, but also in subsequent phases, to check the effectiveness of the treatments and the extent of degradation induced by the salt crystallization tests.

The bulk density, ρ_g [g/cm^3], of the stone samples was determined as the ratio of dry mass over volume, as average for all the specimens. The size of the specimens was measured with a caliper and the dry mass was measured after oven drying at 50 °C until constant mass and cooling to room temperature.

Water absorption test was carried out according to (EN 15801, 2009) on three cylinders (UT) of each lithotype and on all the prisms. The samples were placed vertically on a filter paper pack partially immersed in deionized water, checking that the water level did not exceed the height of the filter paper, so that the samples absorbed water by capillarity only from the base surface. The samples were weighed at increasing time intervals for a total of 24 h. The capillary water absorption coefficient, AC [kg/m$^2\sqrt{s}$], is represented by the slope of the first linear part of

the curve, and the total water absorption after 24 h, WA_{24hrs} [wt %], is calculated as follows: $WA_{24hrs} = (W_{24hrs}–W_{dry})/W_{dry}$. This test was carried out on two cylindrical replicates for each treatment too (CHIT, HAP, HAP + CHIT), to evaluate if and how much the treatments altered the transport properties of the materials. In fact, porosity and transport properties are fundamental aspects to consider when investigating the crystallization of any saline solution. Moreover, any treatment in the conservation of heritage materials is required to cause very limited porosity alterations, to avoid damages and defects both in short and long time.

Tensile splitting test was carried out on cylinders after the salt crystallization cycles (2 replicates for each condition) and on UT samples, to determine the tensile strength σ_t [MPa] of the stone before and after degradation. In fact, salt degradation leads to a loss of cohesion between the stone particles, the detachment of an outer layer and the formation of internal micro-fractures: this leads to decrease in the tensile strength of the material. Consolidating substances, such as hydroxyapatite, are applied to restore the cohesion between the particles and bring back the tensile strength of the stone to its original value, thus increasing its resistance to degradation. For this reason, the splitting test on degraded samples is an indication of the effectiveness of the treatments applied. The test was carried out using an Amsler-Wolpert loading machine (maximum load 20 kN) at a constant displacement rate of 4 mm/min and cardboard couplers (1 mm thick) to allow for uniform compression along the sample. Before carrying out this test, the lateral surface of the samples was gently scratched with fine sandpaper to remove any possible protuberances.

Open porosity and pore size distribution of the two stones were determined by mercury intrusion porosimetry (MIP), using a Thermo Scientific Pascal 140 (macropores unit) and a Pascal 240 (micropores unit). In particular, two fragments of each lithotype were analysed, about 1 g in weight. This analysis was performed also on the treated and the salt deteriorated samples, collecting one fragment for each condition from cylindrical samples, to analyse the changes in porosity. The fragments of the salt deteriorated samples (described in § 4.2.1) were taken close to the top surface of the cylinders (at the center of such surface), excluding the external salt crust. Before the analyses, these fragments were desalinated with a poultice of cellulose pulp and deionized water (weight ratio 1 : 4), which was wrapped in a PE film and left to act for 24 h. Afterwards, the film was removed and the poultice was allowed to completely dry. Desalination was carried out to remove the salt crystals deposited in the pores, thus allowing to investigate the variation of the stone porosity due to deterioration of only.

The external surface of untreated and treated samples was observed using a Philips XL20 SEM scanning electron microscope (SEM), equipped with energy dispersive spectrometry (EDS, EDAX probe). The sample surface was made conductive by sputtering with aluminum before SEM observation.

The dynamic elastic modulus E_d [GPa] was measured on the cylinders before and after treatments, and on the prisms at each stage of the research. Ultrasonic tests for the determination of dynamic elastic modulus were carried out with a Matest instrument, with 55 kHz transducers and rubber couplers to improve the contact between surfaces. For cylinders, the measurement was performed across the height of each sample, while for prisms 10 elastic modulus values were measured for each sample, i.e., at 4 cm intervals along the height of the prism and in two orthogonal directions. In fact, as the prisms are 25 cm high, they could exhibit internal inclusions (for example, fossils in Lecce stone), causing a certain degree of heterogeneity and variability of the values. The dynamic elastic modulus for the prisms was obtained averaging all the 10 values obtained for each sample and the two samples of each condition. For the prisms, E_d was measured in the original stone specimens, in the samples treated with consolidant and/or polymer, in the samples deteriorated by the salt crystallization test and in these latter samples after desalination. In fact, after the salt crystallization cycles, the prisms where subjected to three desalination procedures, by using the same poulticing method described above. Before any E_d measurement, the samples were dried in oven at 50 °C for 24 h.

Treatment Procedure

Both consolidating and biopolymeric solutions were applied to stone samples by capillarity. In the case of the consolidant, four prisms and 11 cylinders of each lithotype were placed in vessels under a 5 mm solution head, the prisms lying on a lateral face to allow for a better absorption. For the first 2 h, necessary refills were carried out and then, when the samples appeared completely wet, the vessels were covered, and the samples were left to absorb the solution up to a total of 24 h. Afterwards, a quick washing under deionized water was carried out, to eliminate unreacted DAP and any possible surface patina, and the samples were dried in room conditions until constant weight. The biopolymeric treatment was applied according to the same procedure. In particular, the chitosan solution was applied to two prisms and five cylinders of untreated stone and two prisms and six cylinders of stone that had been previously treated with the DAP-based consolidating solution and left to dry.

After each treatment application and subsequent drying, the samples were weighed to determine their weight increase, an indication of the amount of hydroxyapatite and/or polymer deposited in the stone. The dynamic elastic modulus was measured again on treated samples, after drying. The weights and the dynamic elastic modulus values were averaged for the five replicates of UT, CHIT and HAP cylinders, the six replicates of the HAP + CHIT cylinders and the two prismatic replicates of each type.

Crystallization Tests

Sodium sulphate is normally used for accelerated weathering tests in laboratory because it is one of the most harmful salts in nature (Rodriguez-Navarro et al., 2000; Tsui et al., 2003; Steiger and Asmussen, 2008; Espinosa-Marzal and Scherer, 2009; Flatt et al., 2014). The peculiarity of this salt is its capacity to crystallize in eight different forms and, above all, to have two phases that can crystallize at normal environmental temperature and humidity: thenardite (anhydrous phase) and mirabilite (decahydrate phase) (Steiger and Asmussen, 2008; Flatt et al., 2014). The greatest

damage occurs when thenardite is dissolved and mirabilite precipitates: in this case, during the dissolution of thenardite, a solution highly supersaturated with respect to mirabilite is formed, which causes a strong crystallization pressure inside the material when mirabilite precipitates, which occurs with a large volumetric expansion (about 314%) (Flatt, 2002; Espinosa-Marzal and Scherer, 2009).

An accelerated salt deterioration test procedure is proposed in the European standard (EN 12370, 1999). This procedure involves cycles of total immersion in a saturated (14 wt%) sodium sulphate decahydrate solution for 2 h, followed by oven drying at 105 °C for at least 16 h and finally cooling to room temperature. For each new cycle, new saline solution with the same concentration is used, which leads to the accumulation of a very high amount of salt inside the samples. This procedure results extremely aggressive towards materials and it is not considered very representative of real salt damage mechanisms occurring in historic buildings (Lubelli et al., 2018), both due to the impressive amount of salt accumulated and high drying temperature. For this reason, a 14 wt% sodium sulphate decahydrate solution was used for the present crystallization tests, as in the EN standard, but it was decided to slightly modify the testing procedure.

In a first type of crystallization test, the cylindrical samples of both lithotype (3 replicates for UT, CHIT and HAP and four replicates for HAP + CHIT) were subjected to cycles of impregnation, followed by drying. During the first cycle, the samples were impregnated by partial immersion in the saline solution. The samples, divided according to the lithotype and type of treatment, were placed in separate vessels with 400 ml of saline solution and the solution level (about 5 mm) was kept constant by refilling with deionized water. The impregnation phase lasted 4 h, followed by drying for 44 h in laboratory conditions (T = 20–25 °C, RH = 45–80%). In all the subsequent cycles, the wetting phase (4 h) was carried out using deionized water only, in order to keep the total salt amount in the samples constant and to induce salt accumulation at the upper surface. After each drying phase (44 h), the samples were gently brushed to remove both efflorescence and debris or powder detached from the substrate. For each cycle, the samples were weighed at the end of the immersion phase (W_{wet}) and twice at the end of the drying phase, before and after brushing (W_{dry} and $W_{dry,\ brushed}$). All these values were averaged for the samples of the same group. A total of 12 cycles was carried out following this procedure. After 12 cycles, the samples were still in good conditions, probably due to a too limited aggressiveness of the procedure adopted. In fact, the brushing of the efflorescence after each drying phase likely reduced the amount of salt present inside the samples and, moreover, the high air RH present in some drying phases may have prevented the complete drying and the transformation of mirabilite into thenardite, limiting the damage in the subsequent rewetting. Thus, it was decided to carry out further eight cycles, each lasting 24 h and consisting of 4 h of capillary absorption of deionized water, 18 h of oven drying at 50 °C (temperature chosen not to damage the polymeric coating) and 2 h of cooling in room conditions. In this way, the oven drying, with RH varying between 8 and 12%, certainly caused formation of thenardite at each cycle and the subsequent formation of mirabilite in the wetting phase, leading to the ideal conditions for the occurrence of a more severe damage. The brushing phase and the weight measurements at each cycle remained the same.

In a second type of crystallization test, two prismatic samples for each condition were subjected to continuous capillary absorption of the saline solution with concomitant evaporation, a condition called "wick effect" (Goudie, 1986; Andreotti et al., 2019), which reproduces the typical salt supply that occurs during capillary rise from the soil in a real building. Each sample was placed vertically in a beaker filled with 200 ml of 14 wt% sodium sulphate decahydrate solution (height of immersion: 5 cm). To prevent evaporation from the free surface of the saline solution, a layer of melted paraffin was poured over the solution: after solidification, the paraffin adhered to the sample and the beaker, preventing evaporation. The samples were placed in a climatic chamber at T = 22 ± 0.5 °C and RH = 80 ± 2%. The test ended when the solution was completely absorbed by the samples and evaporated from their surface, which happened after 5 days for G and 7 days for L. The slightly different drying times for the different samples and treatments were probably due also to the morphology and thickness of the layers of efflorescence on the samples surface. After drying, the samples were gently brushed to remove efflorescence and debris and placed in an oven at 60 °C until complete drying, and finally weighed ($W_{dry,\ brushed}$). Considering that all the prisms were still in good conditions, it was decided to repeat this same test again, on one sample for each type.

The debris obtained after the first continuous absorption test were collected separately for each type of samples, then they were firstly dried in oven at 60 °C for 24 h and then cooled to room temperature in a desiccator. Once dry, they were put in boiling deionized water for 10 min and subsequently filtered, in order to extract the salt ions from the solid part (debris of stone). The saline solutions obtained were then analysed by ion chromatography (Dionex ICS 1000) to obtain the amount of sulphate anions and, by calculation, the percentage weight of solid fraction (ΔW_{solid}) and sodium sulphate (Na_2SO_4) fraction (ΔW_{salt}) referred to the initial weight of the samples.

RESULTS AND DISCUSSION

Characteristics of the Stones and Effects of the Treatments

The characteristics of stone cylinders before and after treatments are reported in **Table 1**, in terms of weight and elastic modulus variation, while the characteristics of stone prisms before and after treatments are reported in **Table 2**. The weight increases of the samples are almost negligible for all the treatments, due to the low concentration of the solutions applied, which is positive as it suggests that only a thin coating of the two substances formed over the pore surface, avoiding any pore clogging effect. For HAP + CHIT samples, due to the double treatment, the weight variation was slightly greater but, in any case, extremely limited. Interestingly, the weight increases due to chitosan application in the double treatment (HAP + CHIT) was lower with respect to

TABLE 1 | Characteristics of cylindrical samples: mass variation after treatment in dry condition (ΔW), dynamic elastic modulus before and after treatment (E_d), variation of dynamic elastic modulus (ΔE_d).

Substrate	Treatment	ΔW [g]		E_d [GPa]		ΔE_d [GPa]
		After DAP	After chitosan	Before	After	
L_C	CHIT		+0.22 ± 0.043	16.25 ± 3.278	17.01 ± 3.402	+0.76
	HAP	+0.23 ± 0.022		16.10 ± 2.932	16.56 ± 3.162	+0.45
	HAP + CHIT	+0.28 ± 0.059	+0.05 ± 0.027	18.27 ± 2.177	18.99 ± 2.210	+0.72
G_C	CHIT		+0.22 ± 0.055	13.76 ± 0.449	13.94 ± 0.457	+0.17
	HAP	+0.27 ± 0.019		13.67 ± 0.244	13.93 ± 0.083	+0.27
	HAP + CHIT	+0.33 ± 0.102	+0.02 ± 0.015	13.90 ± 0.268	14.04 ± 0.158	+0.13

TABLE 2 | Characteristics of prismatic samples: mass variation after treatment in dry condition (ΔW), dynamic elastic modulus before and after treatment (E_d), variation of dynamic elastic modulus (ΔE_d).

Substrate	Treatment	ΔW [g]		E_d [GPa]		ΔE_d [GPa]
		After DAP	After chitosan	Before	After	
L_P	CHIT		+0.63 ± 0.007	15.54 ± 0.109	15.86 ± 0.034	+0.33
	HAP	+0.55 ± 0.014		15.73 ± 0.288	16.79 ± 0.160	+1.06
	HAP + CHIT	+0.45 ± 0.127	+0.15 ± 0.057	15.70 ± 0.235	16.71 ± 0.164	+1.01
G_P	CHIT		+0.64 ± 0.014	13.08 ± 0.035	13.25 ± 0.118	+0.17
	HAP	+0.66 ± 0.007		13.06 ± 0.056	13.66 ± 0.052	+0.60
	HAP + CHIT	+0.72 ± 0.000	+0.12 ± 0.014	13.41 ± 0.084	13.89 ± 0.246	+0.48

the CHIT treatment alone, which was found also in a previous study (Andreotti et al., 2019). This aspect is probably related to the mechanism of adsorption of chitosan over different solid substrates (in this case, the layer of CaP phases), which may depend on several factors, including the chemical nature of the substrate, the pH of the solution, etc. (Andreotti et al., 2019), and which was not specifically investigated in the present study. It is also possible that the capillary absorption of the chitosan solution was somehow slowed down in the HAP-treated stone (see **Figure 1** below).

All the treatments also caused a systematic increase in the dynamic elastic modulus, although quite limited and difficult to distinguish from the intrinsic variability for this parameter in the two stones analysed. In fact, the elastic modulus of untreated Lecce stone and Globigerina limestone, averaged between all samples used, is 16.47 ± 2.756 GPa and 13.75 ± 0.345 GPa, respectively. The E_d increase reached a maximum of 0.72 GPa for Lecce stone and 0.27 GPa for Globigerina limestone (**Table 1**), hence within the respective standard deviations of the untreated value. The standard deviation of the dynamic elastic modulus for Lecce stone is quite high due to the presence of marine fossils within this stone and hence its heterogeneous microstructure. Both the weight increase and the E_d increase after treatments are generally slightly higher for prisms than for cylinders, owing to the smaller thickness of the first ones, which allowed a greater absorption of the solutions and deposition of HAP and/or chitosan in the stone.

The results of the water absorption test on the cylinders are shown in **Figure 1**, while the average values of capillary water absorption coefficients (AC) and the total water absorption at 24 h (WA%) are reported in.

Supplementary Table S1. The MIP curves of the samples with and without the treatments are reported in **Figure 2**.

After 24 h of capillary absorption, the samples were not completely saturated yet, as the slope of the last part of the curves in **Figure 1** is still slightly increasing. This is due to the presence of pores of different sizes within the material, as shown by the MIP analyses in **Figure 2**. The bigger pores are the first to absorb water and be saturated, later acting as reservoir for the thinner pores that could take a much longer time to be saturated. Nonetheless, in the untreated condition the capillary absorption was almost complete after 24 h. The total water absorption at 24 h and the total porosity are similar for the two stones, with slightly higher porosity for Globigerina limestone and slightly higher variability of results for Lecce stone, the latter due to the more heterogeneous microstructure of this lithotype. The AC coefficient of Globigerina limestone is higher than that of Lecce stone, consistently with its slightly higher porosity and larger pore mean radius found by MIP.

After treatments, all the samples exhibited similar total porosity and pore size distribution (**Figure 2** and **Supplementary Table S1**), and the differences are attributable to the intrinsic variability of the stones. Despite this, the treatments modified the capillary water absorption rate of the stones. In Lecce stone, all the treatments slowed down the water capillary absorption compared to UT samples, especially in the case of HAP and HAP + CHIT. In Globigerina limestone, slight variations in AC were registered after the CHIT and the HAP treatments, while the combined treatment HAP + CHIT caused a marked reduction in AC. The modification of the capillary absorption rate could suggest a pore clogging effect, but the variation in the pore size distribution is negligible, as shown

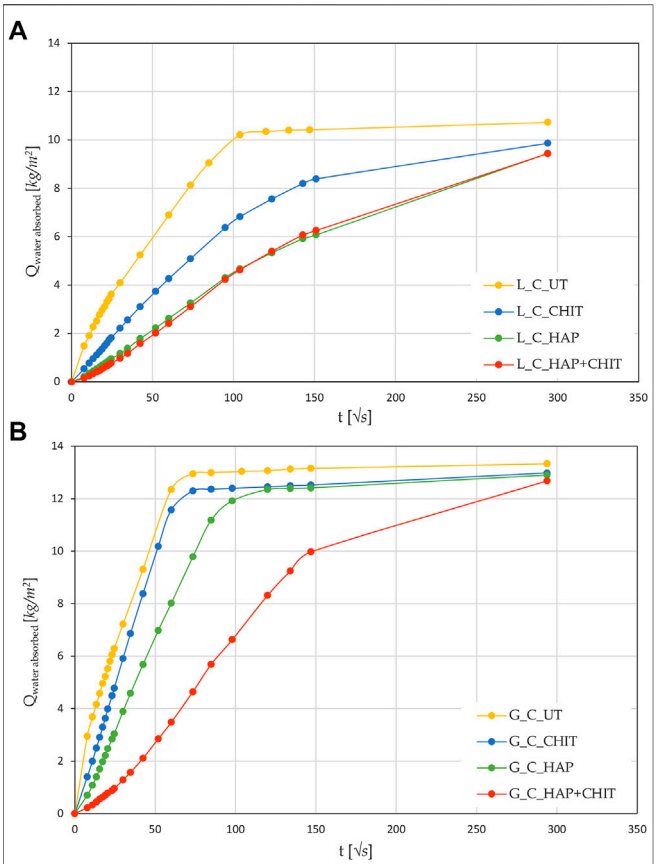

FIGURE 1 | Capillary water absorption curves for the untreated (UT) and treated cylindrical samples for **(A)** Lecce stone and **(B)** Globigerina limestone. Values are averages for at least two samples.

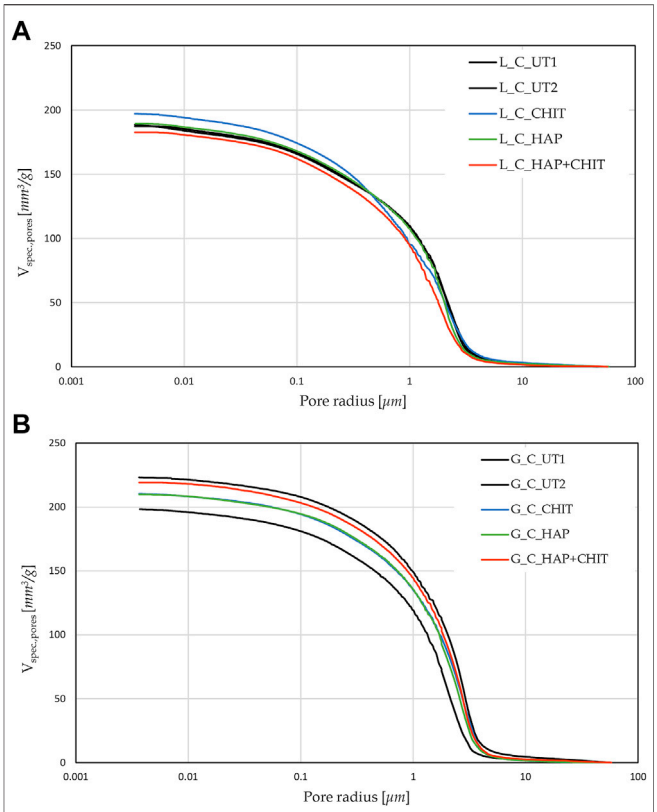

FIGURE 2 | Pore size distribution of various type of stone samples, obtained with MIP test, compared to the relative UT samples, for **(A)** Lecce stone and **(B)** Globigerina limestone.

in the results of MIP test (**Figure 2**), hence no significant pore occlusion occurred. The reduction of AC could be due to changes in the roughness of the pores surface after treatments and/or modifications in the contact angle with water. In the case of HAP-treated stone, changes in sorptivity comparable to those found in the present paper have been found in previous studies (Sassoni et al., 2011; Sassoni et al., 2016a), as a result of the moderate alterations in the static contact angle (Sassoni et al., 2016a; Sassoni et al., 2020) and in pore size distribution (Sassoni et al., 2011; Sassoni et al., 2016a).

Based on SEM images taken on the external surface of untreated and treated samples of Globigerina (**Supplementary Figure S1**), it is possible to observe that neither the single treatments (HAP or CHIT) nor the combined treatment (HAP + CHIT) led to formation of a clearly distinguishable coating over the stone surface. Accordingly, EDS analysis did not reveal any element that could be attributed to newly formed coatings (such as P in the HAP and HAP + CHIT coatings). Given the high porosity of the stone, the DAP and chitosan solutions were quickly absorbed into the pore network (thus leading to the changes in pore size distribution and water sorptivity discussed above), while no accumulation on the treated surface took place. The lack of coating accumulation on the surface was likely helped by rinsing with water at the end of the treatment application. The samples were rinsed with water to remove the excess of unreacted DAP (with chitosan possibly deposited on top) that accumulated on the sample surface, so as to prevent formation of a surface crust and pore clogging, with consequent alterations in the stone transport properties. Similar results were obtained also in the case of Lecce stone (SEM images are omitted for brevity's sake).

In any case, the present results suggest that:

- the AC modifications due to the three kinds of treatments are different in the two stones. In particular, the impact of the treatments is smaller in L than in G, probably due to the much quicker capillary absorption of the latter, which overcomes the possible microstructure modifications caused by the treatments;
- the same chitosan solution tested here, when applied as a coating over a glass slide, exhibited a static contact angle of about 65 °, i.e. much higher than stone, although still in the hydrophilic field (<90 °). This may explain the slower capillary absorption of L_CHIT and L_HAP + CHIT compared with the untreated Lecce stone. In the case of Globigerina limestone, having a much faster capillary absorption, the AC coefficient of the stone was almost unaltered by CHIT treatment, while it

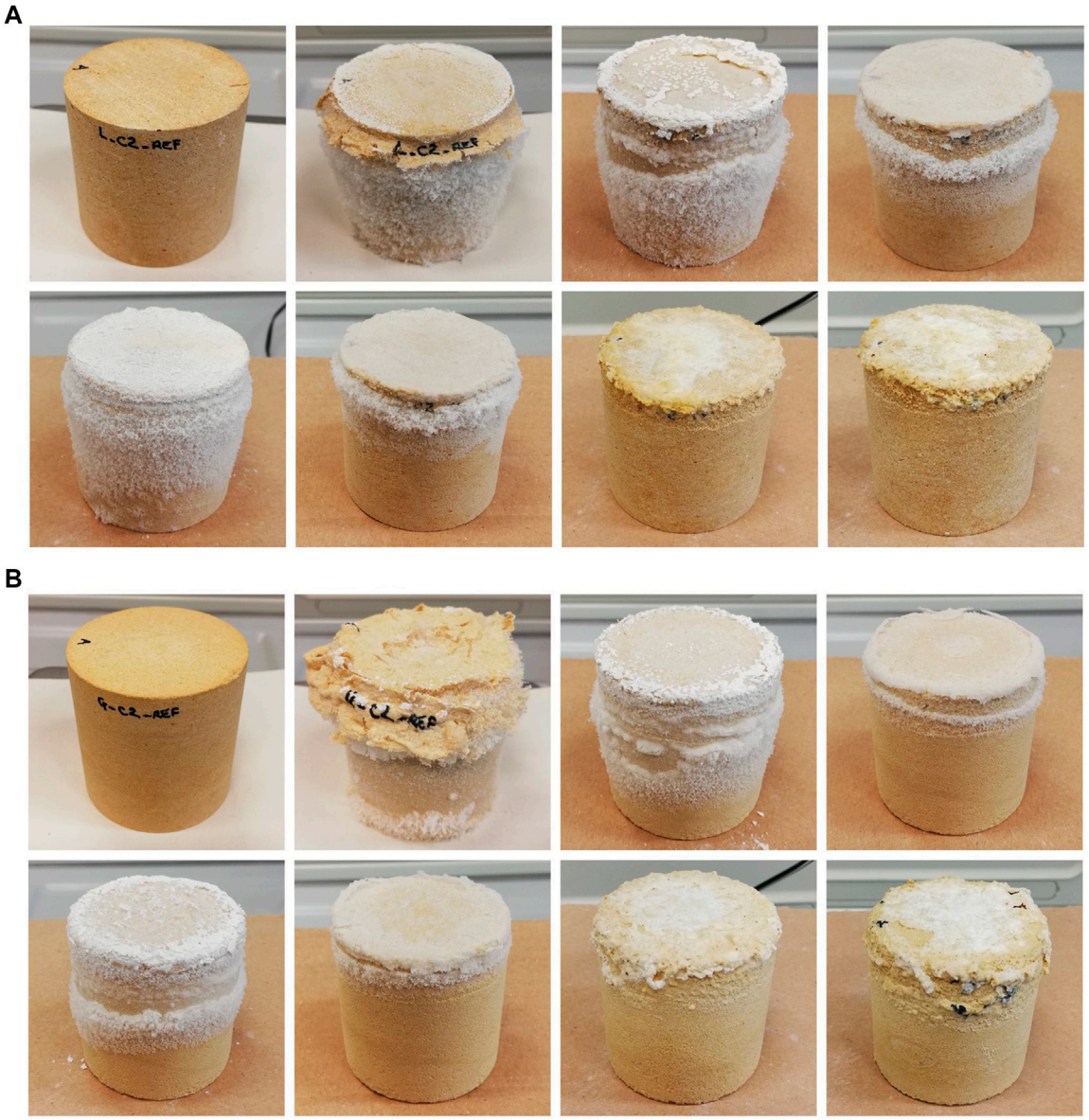

FIGURE 3 | Significant UT cylinders at the 1st, 2nd, 4th, 6th, 10th, 12th, 16th and 20th cycles of the salt crystallization test for: **(A)** Lecce stone and **(B)** Globigerina limestone. The photos were taken after the drying phase, before brushing.

decreased for the double treatment (G_HAP + CHIT), although less than in Lecce stone.

It is also possible that the slowing down of the capillary absorption rate found in the test is transitory, maybe related to some washout of the chitosan layer and/or of some unreacted DAP. In fact, in the previous study, the chitosan coating applied over calcite was found to be washed out by water until reaching the adsorbed layer, which in turn was not sensitive to water flow (Andreotti et al., 2019). Unfortunately, it was not possible to repeat the test on the same cylindrical samples, as they were broken and used for other analyses, hence this aspect will be investigated in future studies.

Effects of the Salt Crystallization Tests

Tests on Cylinders

The appearance of the untreated cylindrical samples during the 20 crystallization cycles (the first 12 carried out with drying at room temperature and the other 8 with oven drying at 50 °C) is reported in **Figure 3**, for some selected cycles and for one representative sample. At the end of the first cycle, no deterioration was found, as expected, because no thenardite to mirabilite transformation had taken place yet. It can be clearly observed that oven drying increased the aggressiveness of the crystallization cycles (see the photos of the 16th and 20th cycles in **Figure 3**), as expected. However, the untreated cylindrical samples were still in relatively good conditions even at the end of

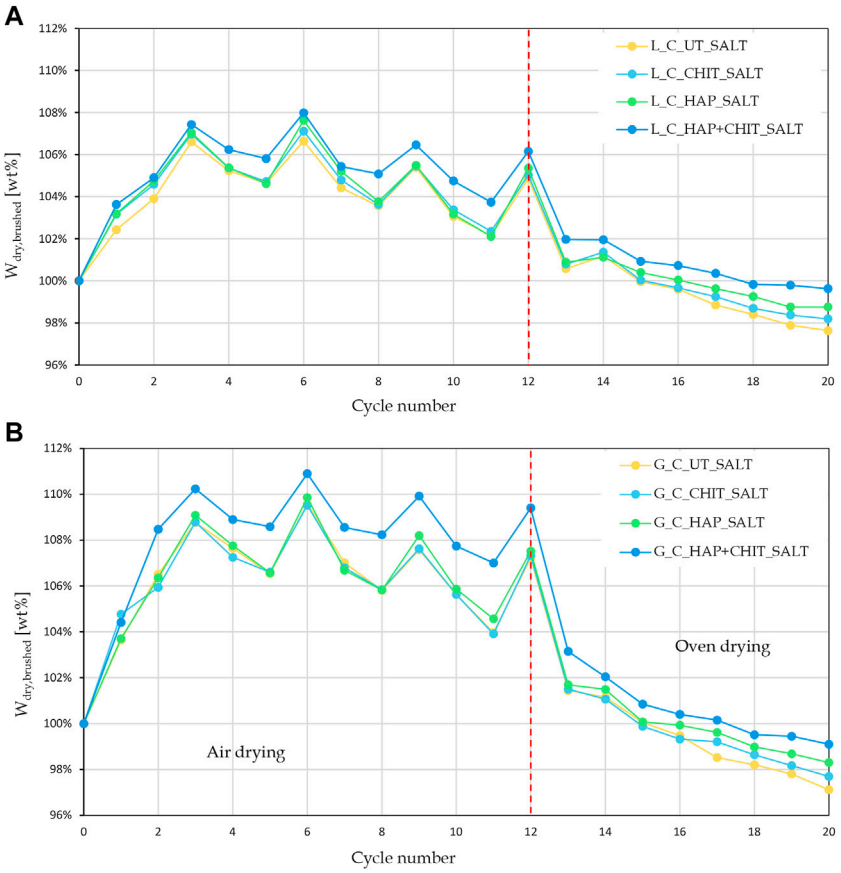

FIGURE 4 | Weight variation of the cylindrical samples after drying and brushing, at each cycle of the salt crystallization test for: **(A)** Lecce stone (UT and with different treatments) and **(B)** Globigerina limestone (UT and with different treatments).

the 20th crystallization cycle. The limited severity of the adopted testing conditions seems to be due to two main reasons:

- the saline solution was used in the first wetting cycle only, while deionized water was used in the following cycles. This means that a major amount of the salt that was introduced in the first absorption cycle was removed when efflorescence and debris were brushed away at the end of the first cycle and this amount was not re-introduced in the samples in the subsequent cycles. This is confirmed by the definitely more

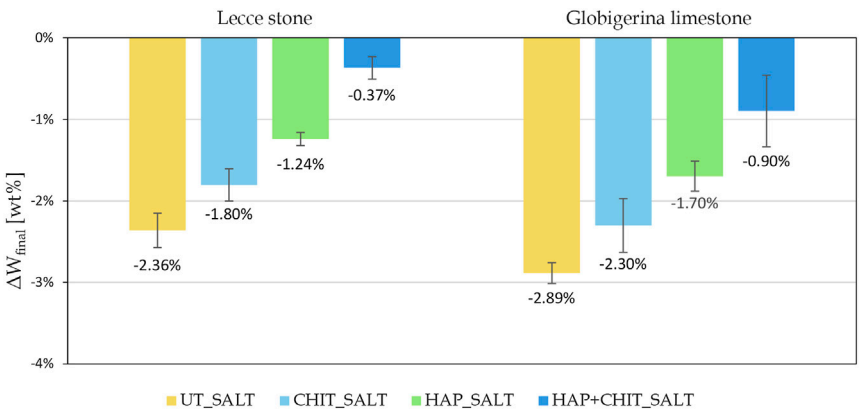

FIGURE 5 | Change in the final dry weight, after brushing, compared to the initial weight of the cylindrical samples.

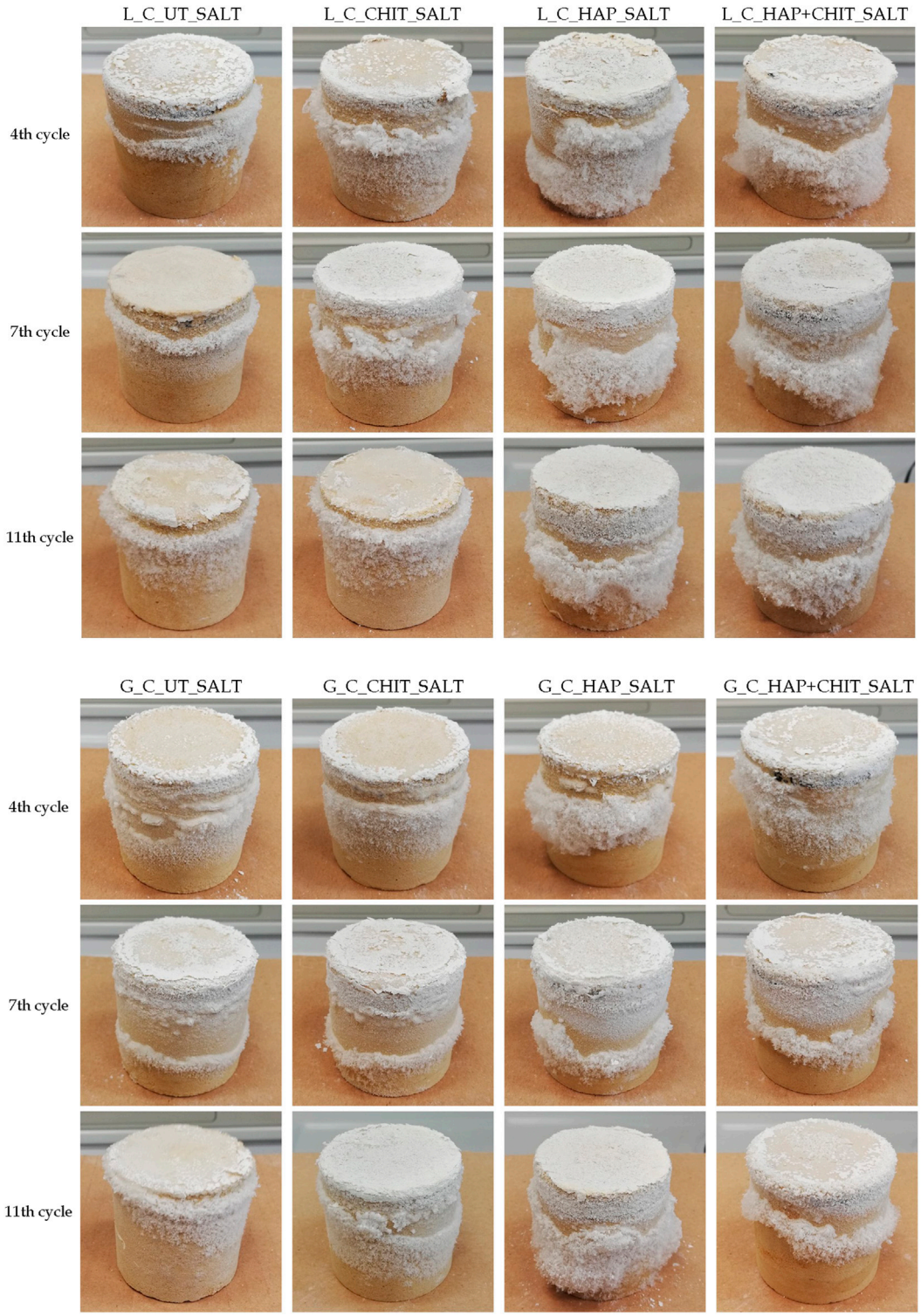

FIGURE 6 | Lecce stone samples and Globigerina limestone samples during the cycles (dried condition, before brushing), where the difference in the amount of efflorescence formed in the different type of samples can be seen. The pictures of the cycles with oven drying are not reported, because the "cementification" of debris during drying made impossible to distinguish the layer of efflorescence.

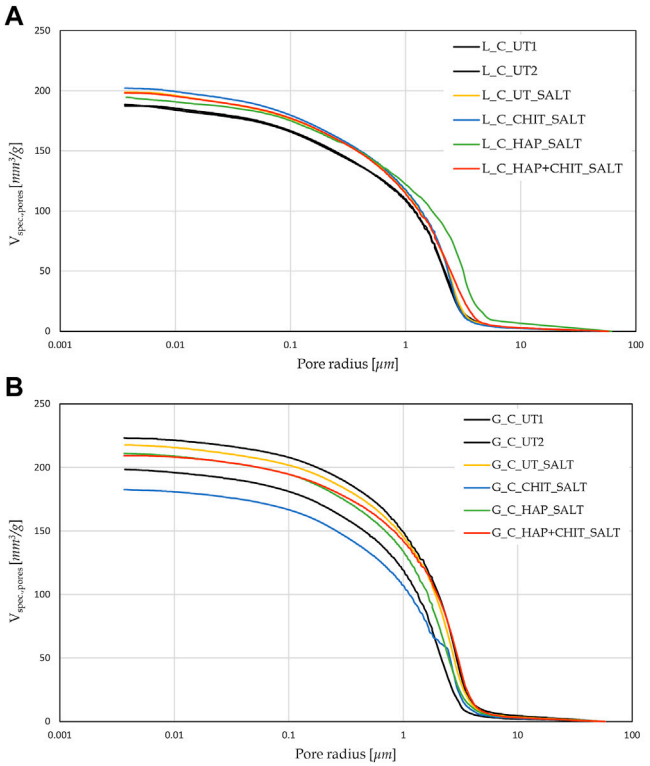

FIGURE 7 | Pore size distribution of stone samples, obtained with MIP test, after the salt crystallization test (and desalination by poulticing) for: **(A)** Lecce stone and **(B)** Globigerina limestone.

abundant salt crystals formation observed at the end of the second cycle (**Figure 3**), which was not found in the following ones;—the stone fragments that tended to detach during the wetting phase were apparently "cemented" by salt during the subsequent drying phase and this greatly limited the weight loss of the samples, making it difficult to quantify the actual degree of deterioration.

The weight variations of the samples after each drying + brushing phase ($W_{dry,\ brushed}$) are reported in **Figure 4**, while the variation of the final dry weight compared to the initial one (ΔW_{final}) is reported in **Figure 5**.

The graphs in **Figure 4** clearly indicate that the first part of the test, with drying at room temperature, led to a strong weight increase, with no apparent damage in the stones. This can be ascribed to the fact that the samples did not completely dry in laboratory conditions prior to the next wetting cycle, thus also preventing the transformation from mirabilite to thenardite and limiting the damage. Moreover, the peaks in the first part of the test suggest that the variations in the air RH at each drying cycle caused a variable degree of drying before the next wetting phase. Only in the second part, when oven drying was used, there was a continuous weight loss, below the initial weight of the samples. Concerning the effect of the treatments, it can be noted that the curves of the UT_SALT samples are the lowest in **Figure 4**, with a maximum weight loss (ΔW_{final}) equal to $-2.36 \pm 0.21\%$ for L and $-2.89 \pm 0.13\%$ for G (**Figure 5**). All the treatments improved the performance of the stones, the benefit increasing in the following order: UT ≈ CHIT < HAP < HAP + CHIT. The fact that the HAP treatment alone has a positive effect on the salt resistance of the stone can be ascribed to several factors, which act simultaneously: 1) an increase in the stone tensile strength (as suggested by the increase in the elastic modulus and as seen in the literature (Naidu et al., 2011; Sassoni et al., 2011; Sassoni et al., 2016a; Sassoni et al., 2016b; Sassoni, 2018)), with a consequent improvement in the salt resistance (Sassoni et al., 2016b); 2) the fact that a greater roughness of the pore surfaces allows for a better capillary flow towards the outside once this roughness is wet, promoting efflorescence (Scherer and Wheeler, 2008; Andreotti et al., 2019); 3) the preventive action towards calcite dissolution (Graziani et al., 2015; Sassoni et al., 2016a; Sassoni et al., 2016b; Andreotti et al., 2019). All these positive effects seem to add to those of chitosan in the samples with the double treatment, where the presence of the polymer helps reduce the stone degradation, by increasing the formation of external efflorescence compared to the UT samples (**Figure 6**). In fact, the HAP + CHIT_SALT samples exhibited a systematically lower weight loss at every cycle than all the other samples, which

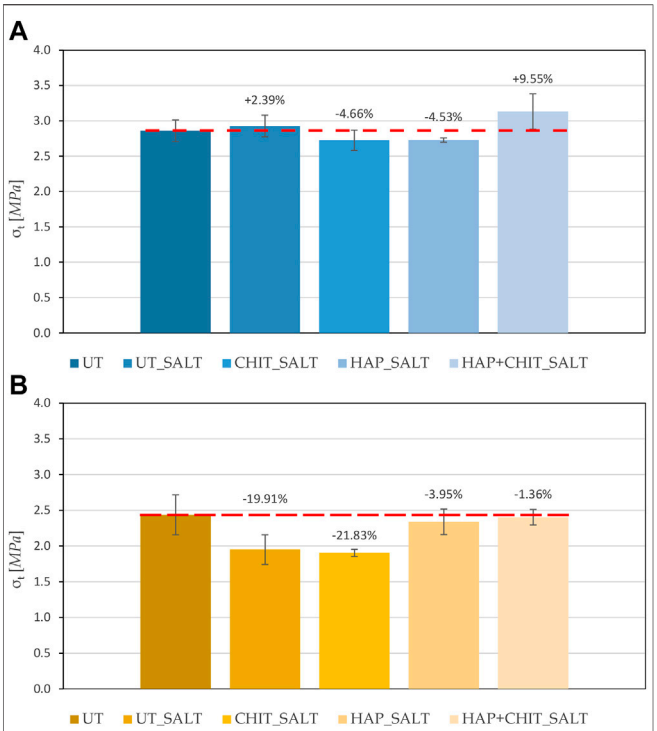

FIGURE 8 | Tensile strength of the cylindrical samples, obtained with splitting test, after the crystallization test and compared with the UT sample, for: **(A)** Lecce stone and **(B)** Globigerina limestone. The dotted line indicates the initial value of the UT reference (2.86 MPa for L and 2.44 MPa for G).

indicates better resistance to salt damage: at the end of the cycles, the HAP + CHIT treatment made the weight loss decrease by 84% in Lecce stone and by 69% in Globigerina limestone, with respect to the untreated samples. The polymeric treatment alone induced a behavior quite similar to the untreated samples, hence it seems that the inhibiting action of chitosan alone is not sufficient, or, most likely, the polymer is not well distributed and anchored to the pore surface. As a matter of fact, chitosan seems to promote the formation of efflorescence rather than subflorescence, as confirmed by the fact that the final weight loss of the samples is lower than that of the untreated samples. However, it is also possible that the inhibiting effect of chitosan causes a greater supersaturation of the saline solution inside the pores, which causes local stress concentrations in those areas of the pores surface that are not covered by the chitosan coating. In the case of HAP + CHIT, this problem was not found, as the CaP layer improved the coverage and the adhesion of chitosan.

The MIP analysis was carried out on the samples subjected to the saline crystallization test, after desalination of the fragments by poulticing, and the results are reported in **Figure 7** and **Supplementary Table S2**, in comparison with UT samples (not subjected to any salt crystallization). The differences in the curves for the various treatments and with respect to UT samples are very limited and seem ascribable to the intrinsic variability of the material, which is lower for G and higher for L. In fact, it is noteworthy that, being MIP a destructive test, it was not possible to perform it on exactly the same cylinders before and after the crystallization test. The limited porosity variation is probably related also to the low aggressiveness of the crystallization cycle procedure, which led to a limited deterioration in all the samples.

The results of the tensile splitting test carried out on the stone cylinders after the salt crystallization cycles, drying and brushing, are reported in **Figure 8**. In the case of Globigerina limestone, it can be clearly observed that, for the untreated condition, salt crystallization cycles caused a marked reduction in tensile strength. In the case of the treated specimens, a lower reduction in tensile strength was experienced, the benefit increasing in the order UT ≈ CHIT < HAP < HAP + CHIT. This trend confirms what already found in terms of weight loss (**Figure 5**). In the case of Lecce stone, the results of the tensile splitting test exhibit a less evident trend (**Figure 8A**), but again the HAP + CHIT treatment was able to provide the greatest benefit. In particular, it should be considered that the consolidating treatment of hydroxyapatite increases the strength of the material, which is subsequently decreased by degradation due to salt crystallization test. Therefore, the tensile strength of the L_HAP + CHIT sample, which is higher than the L_UT sample by 9.55%, represents the residual strength after consolidation and subsequent salt degradation. The fact that, for this treatment condition, the residual strength is the highest is in agreement with the lowest weight loss measured at the end of the salt crystallization test for this condition. In fact, the reduced material loss is expected to have helped maintain the high tensile strength even after salt degradation. However, when evaluating the results of the tensile splitting test, it should be kept in mind that only two replicates for each condition were available for each condition, because all the samples were obtained from the same quarry slab (for greater representativeness and homogeneity of the material) and some replicates had been used for other analyses. Additional tests on a higher number of samples will be necessary to confirm the observed trends.

Tests on Prisms

As reported above, the prismatic samples, at the end of the first absorption test, exhibited a considerable amount of efflorescence on the surface, as shown in **Figure 9**, but after brushing no really significant deterioration of the stone substrates was observed. The repetition of the test (on a single sample per type) caused significant degradation, with formation of efflorescence and detachment of a layer from the sample surface, as reported in **Figure 10**. The weight variation of the prisms after the first and the second continuous absorption tests, after drying and brushing ($W_{dry,\ brushed}$), is reported in **Supplementary Figure S2**, while the corresponding changes of final dry weight compared to the initial one (ΔW_{final}), are reported in **Figure 11**. These values refer to the single prismatic sample of each condition that was used for both tests. **Supplementary Table S3** also report a summary of the weight loss reduction caused by the treatments in the two stones in comparison with untreated references, in the two salt crystallization tests. The values in **Figures 9–11** and **Supplementary Table S3** allow to derive some remarks:

FIGURE 9 | Prismatic samples at the end of the first continuous absorption test, before brushing.

- The first absorption test led to an increase in the weight of all samples, due to the accumulation of salt in the stone, but the damage was very limited. The deposition of salts inside both stones was higher for UT samples, indicating that all the treatments favored the formation of efflorescence rather than subflorescence.

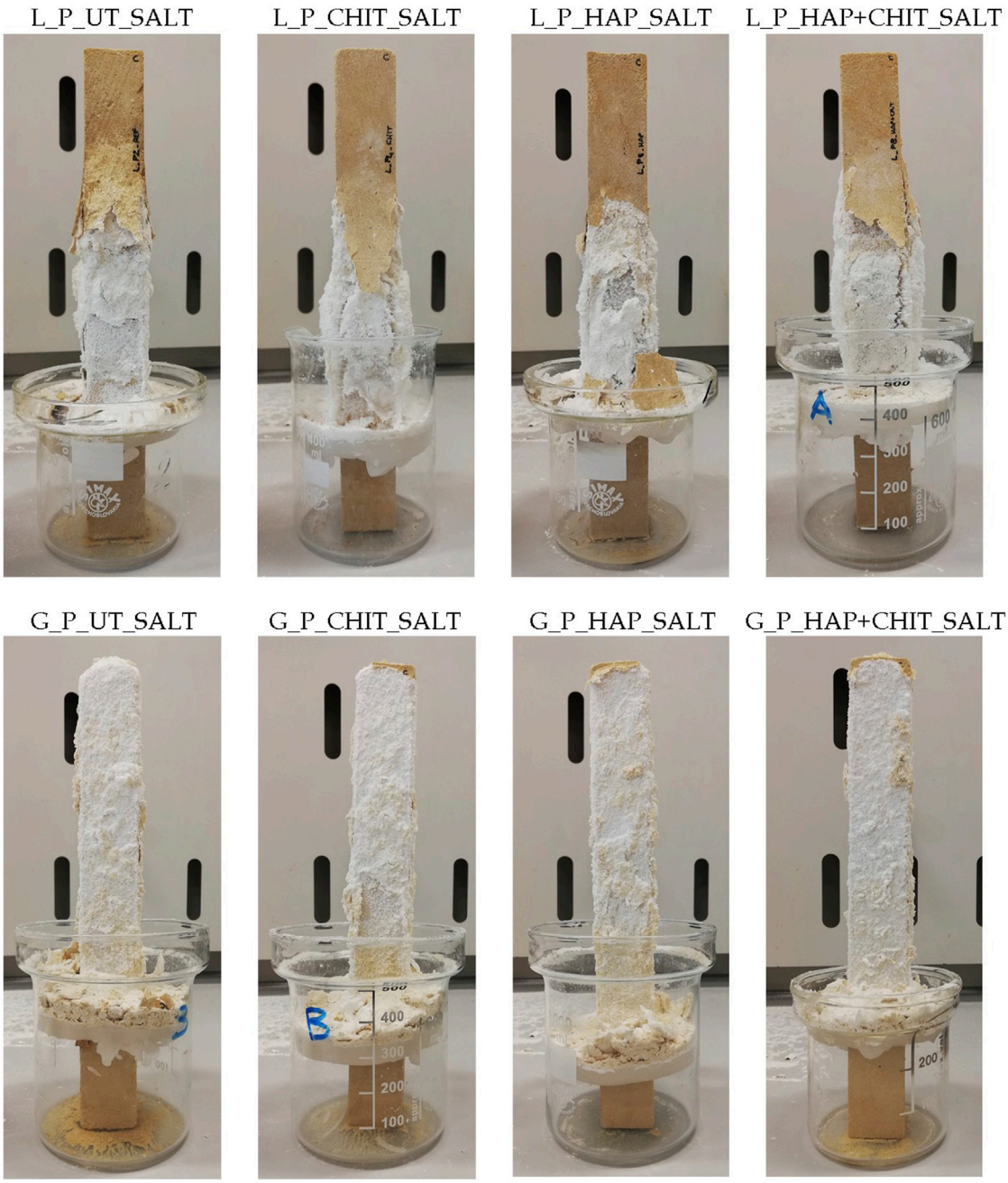

FIGURE 10 | Prismatic samples at the end of the second continuous absorption test, before brushing.

- After the first test, the samples were oven-dried (expectedly causing the formation of thenardite) and the second test started, hence the salt already present in the pores transformed into mirabilite, causing severe deterioration. The final weight loss at the end of the second test was quite limited in L and evident in G. It is interesting to note that the "wick test" carried out on prisms produced a very different damage in the two stones, while their deterioration was similar after the salt crystallization cycles on cylinders (**Figure 5**), although again slightly higher in G than in L. This can be ascribed to the different mechanism of salt damage in the two tests, but also to the smaller thickness of prisms compared to cylinders, making the impact of weight loss larger in the former ones.
- After the second test, all the treatments caused a lower deterioration (smaller weight loss) in the stone samples, the improvement increasing in the following order: CHIT < HAP < HAP + CHIT, again confirming the trend already

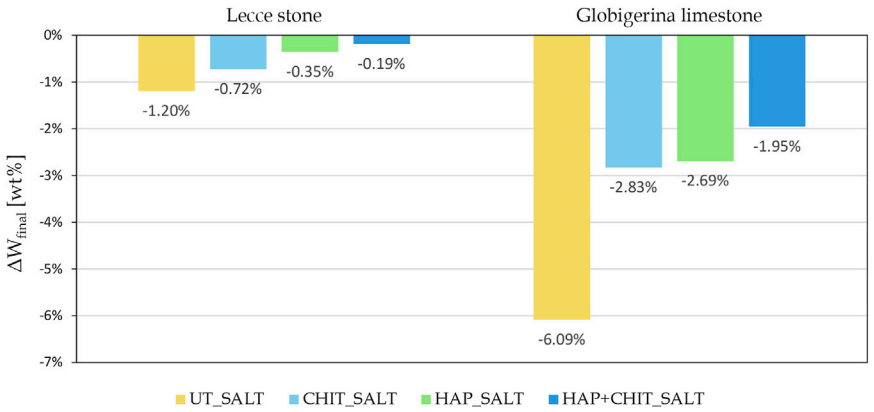

FIGURE 11 | Change in the final dry weight of the prisms after the second absorption test, after brushing, compared to the initial weight for the samples.

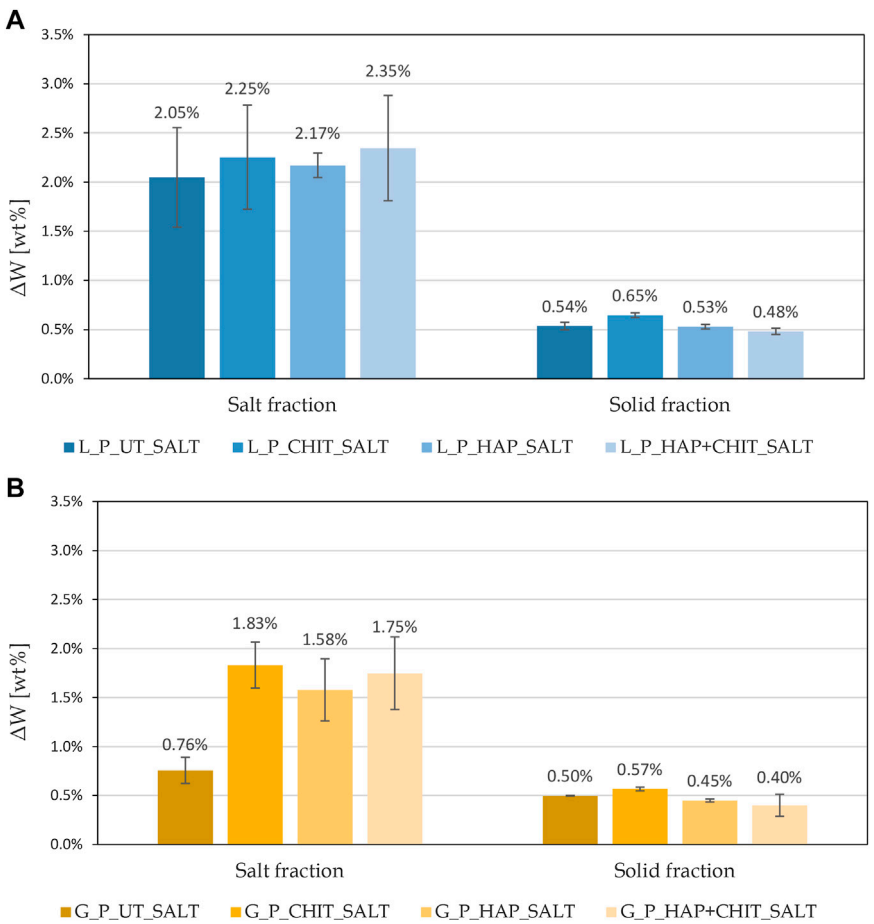

FIGURE 12 | Weight percentages of salt fraction and solid fraction in debris, referred to the initial weight of the prismatic samples, obtained after brushing at the end of the first absorption test, for: **(A)** Lecce stone and **(B)** Globigerina limestone.

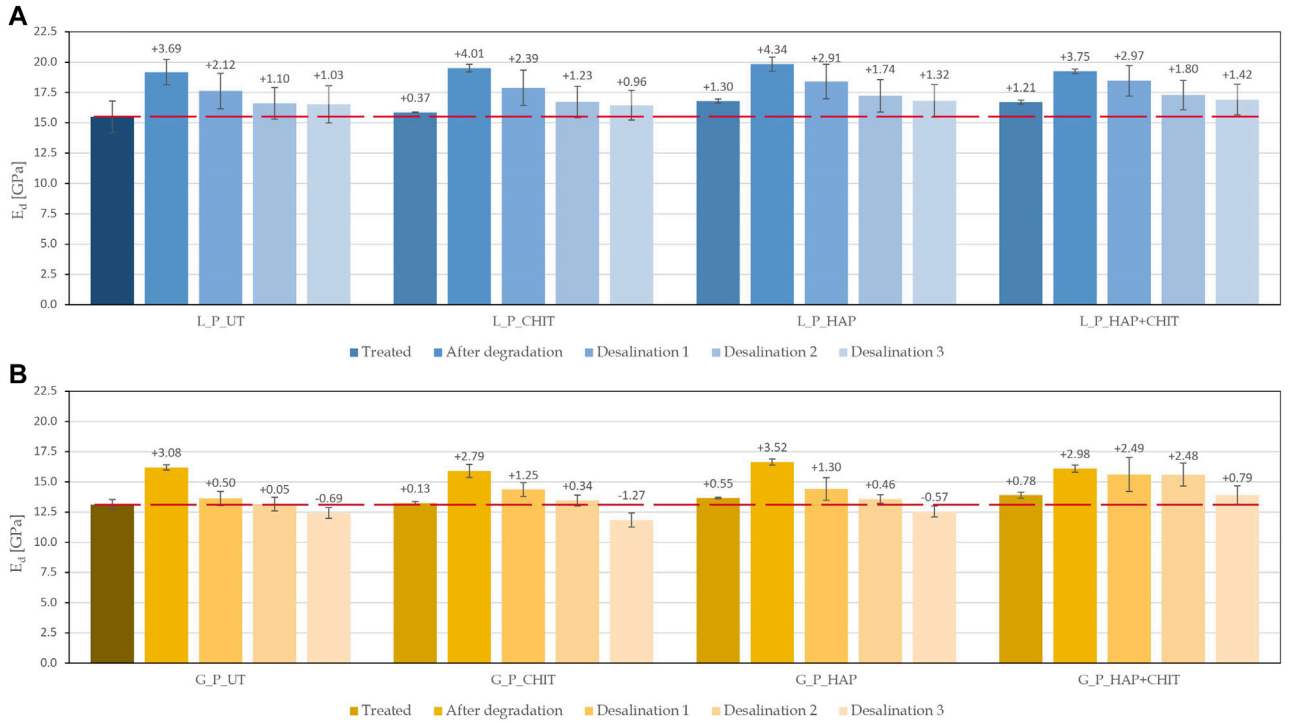

FIGURE 13 | Dynamic elastic modulus of the prismatic samples at each stage of the research (the dotted line indicates the initial value of the UT reference), for: **(A)** Lecce stone and **(B)** Globigerina limestone. The dotted line indicates the initial value of the UT reference (15.49 GPa for L and 13.11 GPa for G).

observed. The combined HAP + CHIT treatment led to a remarkable improvement with respect to the untreated conditions, as the weight loss decreased by 84% in Lecce stone and by 68% in Globigerina limestone, which were actually the same percentages of reduction found in the cylinders. Unlike the crystallization cycles on cylinders, in this case also the chitosan treatment alone led to a significant improvement (**Supplementary Table S3**). This was ascribed to the fact that the chitosan alone was not as well anchored to the pore surface as in the case of the HAP pre-treatment, so it was probably partially removed (alongside calcite) during the multiple wetting cycles carried out in the cylinders, while it was not so altered during the two cycles of continuous absorption carried out in the prisms.

The debris brushed at the end of the first absorption test were analysed and the results are reported in **Figure 12**, as weight percentages of solid fraction (ΔW_{solid}) and sodium sulphate (Na_2SO_4) fraction (ΔW_{salt}) with respect to the initial weight of the samples. The results in terms of stone loss confirm the limited deterioration achieved after the first complete absorption of the saline solution. The presence of chitosan in this type of test, both alone and in combination with hydroxyapatite, caused an increase in the saline fraction, therefore in the amount of efflorescence formed, as can be seen also in **Figure 9**. Moreover, in HAP + CHIT samples, there was also a lower quantity of solid fraction, indicating that the combined treatment has a beneficial effect, promoting efflorescence and limiting damage in the stone. This confirms what was also found in the crystallization test on the cylinders. The CHIT samples, on the other hand, despite a greater quantity of efflorescence than the untreated ones, did not cause any reduction in the solid fraction lost (or even a slight increase), indicating that the polymer alone was not so effective.

Although the weight variation of the samples during the salt crystallization tests can generally provide a useful indication about the deterioration state of the sample, it must be noted that this variation is the sum of a positive term (the salts deposited in the stone pores) and a negative term (the stone debris lost due to deterioration). For this reason, to better evaluate the deterioration of the stone, the dynamic elastic modulus was measured before treatment, after treatment, after the salt crystallization test (after brushing) and also after progressive desalination by poulticing. The values obtained at each phase are reported in **Figure 13**. An increase in the dynamic elastic modulus may indicate an effective consolidation treatment and/or some salt accumulation in the pores, while a reduction indicates internal damage in the material due to salt crystallization (cracking). It is noteworthy that the sensitivity of ultrasonic velocity measurement to micro-cracks development in the stone is very high, as these micro-cracks strongly affect the path followed by ultrasonic wave.

As desirable, after treatments, all the samples showed an increase in the elastic modulus, obviously greater for the

consolidated ones (HAP and HAP + CHIT). After the salt crystallization test, the maximum E_d value was found, as the salt crystals inside the stone samples partially filled the pores and provided a faster ultrasonic transmission. In each of the three desalination phases, the salt ions were transported into the poultice and removed from the samples. Consistently, the elastic modulus progressively decreased after each poultice application, as the pores (previously filled by salts) were progressively emptied. In the case of Globigerina limestone, after desalination for the third time, the UT, CHIT and HAP samples exhibited a lower E_d value than the initial condition, which suggests crack formation during the salt crystallization test. On the contrary, in the case of the HAP + CHIT treatment, the final E_d was still higher than the initial condition (the value being actually very close to that right after treatment), which suggests limited damaging during the salt crystallization test. In the case of Lecce stone, after desalination for 3 times all the specimens exhibited an E_d value still higher than the initial one, again the value of the HAP + CHIT sample being the highest. Although the permanence of some residual salts inside the samples even after the third desalination cannot be completed excluded, still the observed trend confirms the potential of the HAP + CHIT treatment to prevent salt damage.

CONCLUSION

In the present paper, three treatments were tested, aiming at preventing salt crystallization damage in porous limestone: an hydroxyapatite-based consolidant (expected to strengthen the stone), a chitosan solution (expected to inhibit salt crystallization and favor the formation of efflorescence rather than harmful subflorescence) and a combination of these two treatments (where hydroxyapatite is expected to also improve the anchoring of chitosan). Lecce stone and Globigerina limestone were used, being representative of highly porous lithotypes widely used in heritage buildings and severely affected by salt damage onsite.

All the treatments were characterized by low concentration and hence they caused only a slight increase in the weight of the samples, indicating a small amount of products deposited. As a consequence, the treatments basically did not alter the porosity of the stone, demonstrating an excellent compatibility, although they somehow altered the capillary water absorption rate (especially for the combined treatment), although this latter aspect is still under investigation. The possibility that the alteration of the absorption rate given by the treatments is transitory is supported by the results of the crystallization tests. In fact, the prisms, despite absorbing saline solution at slightly different rates, all dried out in similar times (6–7 days); moreover, the weights of the cylinders at the end of the wetting phase of each cycle did not show substantial differences. Therefore, it seems that this slowdown was only transitory and did not have an important impact on the results. This aspect, however, still requires full elucidation and, in order to better understand the transitory or permanent nature of the phenomenon, further tests are necessary. All the treatments also caused a slight increase in the dynamic elastic modulus of the stones, suggesting a positive effect in terms of mechanical properties.

Two accelerated laboratory tests were carried out to investigate the effectiveness of the treatments. The first one was carried out on stone cylinders and involved salt crystallization cycles in a sodium sulphate solution (wetting and drying cycles). These cycles were designed by modifying the procedure of the EN 12370 standard, in order to make the entire test less aggressive than that in the standard. This first kind of salt crystallization test allowed to make the following remarks:

- drying in room conditions (adopted in the first 12 cycles) likely prevented the full transformation thenardite ↔ mirabilite during the cycles, hence it was too mild and made it necessary to adopt oven drying at 50 °C for the following eight cycles. Although a clear weight loss was induced in the samples by this second drying method, an improvement of the procedure used for the cycles still seems necessary, to find a compromise between the too aggressive method suggested by the EN standard and the too mild one adopted in this research;
- all the treatments promoted the formation of efflorescence compared to the untreated stone samples. In the presence of chitosan, this was ascribed to the inhibiting effect of the polymer, while in the case of the HAP treatment alone this seems due to the extremely rough surface of the calcium phosphate phases formed over the pores surface, promoting the water flow towards the stone surface (Scherer and Wheeler, 2008);
- all the treatments led to an improvement in the stone resistance to salt crystallization, measured in terms of sample weight loss. The improvement increased according to the order CHIT < HAP < HAP + CHIT, the combined treatment providing an outstanding improvement (weight loss decrease by 84% in Lecce stone and by 69% in Globigerina limestone, with respect to the untreated samples);
- the combined HAP + CHIT treatment also gave the best results in terms of tensile strength of the stone after the salt crystallization cycles, basically leading to a residual strength after the cycles equal to (or even slightly higher than) the unweathered original stones.

The second test used to investigate the salt crystallization resistance was based on the continuous capillary absorption of a fixed amount of sodium sulphate solution by prismatic stone samples, up to their complete drying ("wick test"). Two complete cycles of absorption were carried out, allowing to derive the following conclusions:

- like in the previous test, all the treatments promoted the formation of efflorescence compared to the untreated stones. This was assessed not only by visual observation, but also by weighing the amount of salts detached/brushed from the samples at the end of the test;
- all the treatments led to an improvement in the stone resistance to salt crystallization. The weight loss decreased according to the same order as in the previous test, the combined treatment providing basically the same outstanding improvement as in the test on cylinders;
- after the test and the desalination of the prismatic samples by poulticing, the dynamic elastic modulus was measured in the

samples. The combined HAP + CHIT treatment confirmed its very good performance, leading to the highest values (even higher than the original unweathered stone samples in the case of Globigerina limestone).

The comparison between the combined HAP + CHIT treatment and other modifiers tested over last years and mentioned in the Introduction is not an easy task, as differences in the materials used or in the test carried out lead to results that are difficult to compare. In (Cassar et al., 2008), prismatic samples of different quality types of Globigerina limestone, untreated and treated with a phosphorylated inhibitor, were subjected to weathering by a sodium sulphate solution, in a test similar to the "wick test" used in this research. The inhibitor led to an improvement in the saline solution capillary flow through the porous materials, helping crystallization occur on the surface of the stone and not within the pores. Moreover, the treatment led to a reduction in debris loss during the salt crystallization test by about 47% with respect to the untreated samples while, in similar conditions, HAP + CHIT reduced the weight loss by 69%. In (Sammut et al., 2014), cubic stone samples of Globigerina limestone, treated with citrate and phosphocitrate with different treatment methods (capillary rise, brushing and poultice), were subjected to salt crystallization cycles. Although the treatment gave positive effects on the rate of transport of the saline solution, data on the stone loss during crystallization cycles are not reported, as the differences obtained in various conditions were too small to draw conclusions. Other examples, were different substrates or types of tests were used, are reported in (Rodriguez-Navarro et al., 2002; Selwitz and Doehne, 2002; Lubelli and van Hees, 2007; Rivas et al., 2010; Ruiz-Agudo et al., 2010; Smith et al., 2010; Gupta et al., 2012; Ruiz-Agudo et al., 2012; Granneman et al., 2019; Bracciale et al., 2020). Concerning the cost of the investigated treatment, the experimental campaign is at an early stage, hence this aspect has not been specifically evaluated yet. However, considering that the most expensive chemical used is chitosan and that its concentration in solution is very low (0.05 wt%), the cost/liter of the chitosan treatment is expected to be comparable with other commonly used conservation treatments. Moreover, chitosan is presently exploited in a wide variety of applications and its use is expected to strongly increase in the future, suggesting that its cost might decrease thanks to the set-up of improved technologies for its production.

The combined treatment, composed by a first application of phosphate consolidant and a second application of a chitosan solution, gave extremely promising results in terms of reduction of salt deterioration in both the porous limestones investigated in this study, with an improvement in the reduction of salt deterioration in line or even greater than other crystallization modifiers. The calcium phosphate phases formed in the first step of the treatment have been shown to improve the tensile strength of stone and to favor the formation of efflorescence rather than subflorescence, but they are also thought to improve the anchoring of the chitosan layer and to prevent the leaching of the calcite substrate, which might lead to the leaching of the chitosan layer too.

The water-based hydroxyapatite consolidant is known to be compatible with stone and friendly for the environment and the conservators, and chitosan is a non-toxic and environmentally friendly biopolymer, hence the combined treatment can be seen as a fully "green" solution for conservation.

The performance of the tested treatments was investigated in this paper through short-term laboratory tests on stone specimens, with encouraging results, but further tests will be necessary to assess the long-term effectiveness and the actual duration of the new treatments. In particular, the fact that chitosan is expected to biodegrade with time is considered a positive feature, which avoids that aged and useless polymeric residues remain in the stone and which can be coped with by periodically re-applying the treatment. However, the duration of this polymer in onsite conditions needs to be investigated, in order to assess whether it is compatible with applications in the conservation field. The effectiveness of the new treatments in different heritage substrates is a further aspect needing investigation and requiring further studies.

DATA AVAILABILITY STATEMENT

The original contributions presented in the study are included in the article/**Supplementary Material**, further inquiries can be directed to the corresponding author.

AUTHOR CONTRIBUTIONS

All authors have read and agree to the published version of the manuscript. Author Contributions: Conceptualization, EF; methodology, EF, ES and MB; experimental investigation: MB and ES; data analysis and interpretation, EF, MB and ES; writing—original draft preparation, MB and EF; writing—review and editing, EF, ES and MB; supervision, EF.

ACKNOWLEDGMENTS

All the members of the RILEM Technical Committee "271-ASC: Accelerated laboratory test for the assessment of the durability of materials with respect to salt crystallization" (Chair: Barbara Lubelli, Deputy Chair: Inge Rörig-Dalgaard) are gratefully acknowledged for the interesting and fruitful discussion about the aggressiveness of standard salt crystallization tests.

SUPPLEMENTARY MATERIAL

The Supplementary Material for this article can be found online at: https://www.frontiersin.org/articles/10.3389/fmats.2021.583112/full#supplementary-material.

REFERENCES

Andreotti, S., Franzoni, E., Degli Esposti, M., and Fabbri, P. (2018). Erratum: Andreotti, S.; Franzoni, E.; fabbri, P. Poly(hydroxyalkanoate)s-Based hydrophobic coatings for the protection of stone in cultural heritage. Materials 2018, 11, 165. *Materials* 11 (3), 389. doi:10.3390/ma11030389

Andreotti, S., Franzoni, E., Ruiz-Agudo, E., Scherer, G. W., Fabbri, P., Sassoni, E., et al. (2019). New polymer-based treatments for the prevention of damage by salt crystallization in stone. *Mater. Struct.* 52 (17), 1–28. doi:10.1617/s11527-018-1309-6

Angeli, M., Jean-Philippe, B., Benavente, D., Menéndez, B., Hébert, R., and David, C. (2007). Salt crystallization in pores: quantification and estimation of damage. *Environ. Geol.* 52 (2), 187–195. doi:10.1007/s00254-006-0474-z

Bracciale, M. P., Sammut, S., Cassar, J., Santarelli, M. L., and Marrocchi, A. (2020). Molecular crystallization inhibitors for salt damage control in porous materials: an overview. *Molecules* 25 (8), 1873. doi:10.3390/molecules25081873

Calia, A., Laurenzi Tabasso, M., Maria Mecchi, A., and Quarta, G. (2013). The study of stone for conservation purposes: Lecce stone (Southern Italy). *Geol. Soci., London, Special Publications* 391 (1), 139–156. doi:10.1144/sp391.8

Cassar, J., Marrocchi, A., Santarelli, M. L., and Muscat, M. (2008). Control de los daños por cristalizaciòn en la caliza de Malta mediante inhibidores de sales. *Materiales de Costrucciòn* 58, 289–290. doi:10.3989/mc.2008.v58.i289-290.83

Charola, A. E., and Bläuer, C. (2015). Salts in masonry: an overview of the problem. *RBM.* 21 (4-6), 119–135. doi:10.1515/rbm-2015-1005

Charola, A. E. (2000). Salts in the deterioration of porous materials: an overview. *J. Am. Inst. Conserv.* 39 (3), 327–343. doi:10.1179/019713600806113176

Charola, A. E., and Wendler, E. (2015). An overview of the water-porous building materials interactions. *RBM.* 21 (2-3), 55–65. doi:10.1515/rbm-2015-2006

Doehne, E., and Price, C. A. (2010). *Stone conservation: an overview of current research*. 2nd Edn, Los Angeles, CA, United States: Getty Publications

EN 12370 (1999). *Natural stone test methods – determination of resistance to salt crystallization*, United Kingdom: BSI

EN 15801 (2009). *Conservation of cultural property – test methods – determination of water absorption by capillarity*, Santry Dublin, Ireland: NSAI

Espinosa-Marzal, R. M., and Scherer, G. W. (2010). Advances in understanding damage by salt crystallization. *Acc. Chem. Res.* 43 (6), 897–905. doi:10.1021/ar9002224

Espinosa-Marzal, R. M., and Scherer, G. W. (2009). Crystallization of sodium sulfate salts in limestone. *Environ. Earth Sci.* 56, 605–621. doi:10.1007/s00254-008-1441-7

Flatt, R. J., Caruso, F., Sanchez, A. M., and Scherer, G. W. (2014). Chemo-mechanics of salt damage in stone. *Nat. Commun.* 5, 4823. doi:10.1038/ncomms5823

Flatt, R. J. (2002). Salt damage in porous materials: how high supersaturations are generated. *J. Cryst. Growth* 242 (3-4), 435–454. doi:10.1016/s0022-0248(02)01429-x

Franceschini, M., Broggi, A., Bracciale, M. P., Sommei, L., Santarelli, M. L., and Marrocchi, A. (2015). Effectiveness of phosphocitrate as salt crystallization inhibitor in porous materials: case study of the roman mosaic ofOrpheus and the beasts(Perugia, Italy). *Int. J. Architect. Herit.* 9 (3), 195–200. doi:10.1080/15583058.2012.760121

Franzoni, E. (2014). Rising damp removal from historical masonries: a still open challenge. *Construct. Build. Mater.* 54, 123–136. doi:10.1016/j.conbuildmat.2013.12.054

Franzoni, E., Sassoni, E., and Graziani, G. (2015). Brushing, poultice or immersion? The role of the application technique on the performance of a novel hydroxyapatite-based consolidating treatment for limestone. *J. Cult. Herit.* 16 (2), 173–184. doi:10.1016/j.culher.2014.05.009

Franzoni, E. (2018). State-of-the-art on methods for reducing rising damp in masonry. *J. Cult. Herit.* 31, S3–S9. doi:10.1016/j.culher.2018.04.001

Goudie, A. S. (1986). Laboratory simulation of "the wick effect" in salt weathering of rock. *Earth Surf. Process. Landforms* 11 (3), 275–285. doi:10.1002/esp.3290110305

Granneman, S. J. C., Lubelli, B., and van Hees, R. P. J. (2019). Mitigating salt damage in building materials by the use of crystallization modifiers—a review and outlook. *J. Cult. Herit.* 40, 183–194. doi:10.1016/j.culher.2019.05.004

Granneman, S. J. C., Shahidzadeh, N., Lubelli, B., and van Hees, R. P. J. (2017). Effect of borax on the wetting properties and crystallization behavior of sodium sulfate. *CrystEngComm* 19 (7), 1106–1114. doi:10.1039/c6ce02163h

Graziani, G., Sassoni, E., and Franzoni, E. (2015). Consolidation of porous carbonate stones by an innovative phosphate treatment: mechanical strengthening and physical-microstructure compatibility in comparison with TEOS-based treatments. *Heritage Science* 3 (1), 1–6. doi:10.1186/s40494-014-0031-0

Graziani, G., Sassoni, E., Franzoni, E., and Scherer, G. W. (2016). Hydroxyapatite coatings for marble protection: optimization of calcite covering and acid resistance. *Appl. Surf. Sci.* 368, 241–257. doi:10.1016/j.apsusc.2016.01.202

Gupta, S., Terheiden, K., Pel, L., and Sawdy, A. (2012). Influence of ferrocyanide inhibitors on the transport and crystallization processes of sodium chloride in porous building materials. *Cryst. Growth Des.* 12 (8), 3888–3898. doi:10.1021/cg3002288

Houck, J., and Scherer, G. W. (2006). Controlling stress from salt crystallization. *Fracture and failure of natural building stones*. Dordrecht, The Nederlands: Springer, 299–312. Chap 5

Lubelli, B., Cnudde, V., Diaz-Goncalves, T., Franzoni, E., van Hees, R. P. J., Ioannou, I., et al. (2018). Towards a more effective and reliable salt crystallization test for porous building materials: state of the art. *Mater. Struct.* 51 (2), 1–21. doi:10.1617/s11527-018-1180-5

Lubelli, B., and van Hees, R. P. J. (2007). Effectiveness of crystallization inhibitors in preventing salt damage in building materials. *J. Cult. Herit.* 8 (3), 223–234. doi:10.1016/j.culher.2007.06.001

Muxika, A., Etxabide, A., Uranga, J., Guerrero, P., and de la Caba, K. (2017). Chitosan as a bioactive polymer: processing, properties and applications. *Int. J. Biol. Macromol.* 105 (2), 1358–1368. doi:10.1016/j.ijbiomac.2017.07.087

Naidu, S., and Scherer, G. W. (2014). Nucleation, growth and evolution of calcium phosphate films on calcite. *J. Colloid Interface Sci.* 435, 128–137. doi:10.1016/j.jcis.2014.08.018

Naidu, S., Sassoni, E., and Scherer, G. W. (2011). New treatment for corrosion-resistant coatings for marble and consolidation of limestone. in Jardins de Pierres – Conservation of stone in Parks, Gardens and Cemeteries, Paris, France, June 2011, 289–294

Ocak, Y., Sofuoglu, A., Tihminlioglu, F., and Böke, H. (2009). Protection of marble surfaces by using biodegradable polymers as coating agent. *Prog. Org. Coating* 66 (3), 213–220. doi:10.1016/j.porgcoat.2009.07.007

Ocak, Y., Sofuoglu, A., Tihminlioglu, F., and Böke, H. (2015). Sustainable bio-nano composite coatings for the protection of marble surfaces. *J. Cult. Herit.* 16 (3), 299–306. doi:10.1016/j.culher.2014.07.004

Pedna, A., Pinho, L., Frediani, P., and Mosquera, M. J. (2016). Obtaining SiO 2 -fluorinated PLA bionanocomposites with application as reversible and highly-hydrophobic coatings of buildings. *Prog. Org. Coating* 90, 91–100. doi:10.1016/j.porgcoat.2015.09.024

Philibert, T., Lee, B. H., and Fabien, N. (2017). Current status and new perspectives on chitin and chitosan as functional biopolymers. *Appl. Biochem. Biotechnol.* 181 (4), 1314–1337. doi:10.1007/s12010-016-2286-2

Rivas, T., Alvarez, E., Mosquera, M. J., Alejano, L., and Taboada, J. (2010). Crystallization modifiers applied in granite desalination: the role of the stone pore structure. *Construct. Build. Mater.* 24 (5), 766–776. doi:10.1016/j.conbuildmat.2009.10.031

Rodriguez-Navarro, C., Doehne, E., and Sebastian, E. (2000). How does sodium sulfate crystallize? Implications for the decay and testing of building materials. *Cement Concr. Res.* 30 (10), 1527–1534. doi:10.1016/s0008-8846(00)00381-1

Rodriguez-Navarro, C., Linares-Fernandez, L., Doehne, E., and Sebastian, E. (2002). Effects of ferrocyanide ions on NaCl crystallization in porous stone. *J. Cryst. Growth* 243 (3-4), 503–516. doi:10.1016/s0022-0248(02)01499-9

Ruiz-Agudo, E., Lubelli, B., Sawdy, A., van Hees, R., Price, C., and Rodriguez-Navarro, C. (2010). An integrated methodology for salt damage assessment and remediation: the case of San Jerónimo Monastery (Granada, Spain). *Environ Earth Sci* 63 (7), 1475–1486. doi:10.1007/s12665-010-0661-9

Ruiz-Agudo, E., Putnis, C. V., Pel, L., and Rodriguez-Navarro, C. (2012). Template-assisted crystallization of sulfates onto calcite: implications for the prevention of salt damage. *Cryst. Growth Des.* 13 (1), 40–51. doi:10.1021/cg300744x

Ruiz-Agudo, E., Rodriguez-Navarro, C., and Sebastián-Pardo, E. (2006). Sodium sulfate crystallization in the presence of phosphonates: implications in ornamental stone conservation. *Cryst. Growth Des.* 6 (7), 1575–1583. doi:10.1021/cg050503m

Sammut, S., Cassar, J., Marrocchi, A., Santarelli, M. L., Russo, C., and Sommei, L. (2014). Investigating a method to limit damage in Globigerina limestone, a soft porous stone widely used in historic buildings. Proceedings of SWBSS 2014 3rd international conference on salt weathering of buildings and stone sculptures, Brussels, Belgium, 14-16 October 2014. Royal Institute for Cultural Heritage Brussels, 101–115

Sandrolini, F., and Franzoni, E. (2007). Repair Systems for the Restoration of Ancient Buildings—dampness Rise Problem/Instandsetzungssysteme für das Restaurieren historischer Gebäude—aufsteigende feuchtigkeit. *RBM.* 13 (3), 161–172. doi:10.1515/rbm-2007-6129

Sassoni, E., Franzoni, E., Stefanova, M., Kamenarov, Z., Scopece, P., and Verga Falzacappa, E. (2020). Comparative study between ammonium phosphate and ethyl silicate towards conservation of prehistoric paintings in the magura cave (Bulgaria). *Coatings* 10 (3), 250. doi:10.3390/coatings10030250

Sassoni, E., Graziani, G., and Franzoni, E. (2016a). An innovative phosphate-based consolidant for limestone. Part 1: effectiveness and compatibility in comparison with ethyl silicate. *Construct. Build. Mater.* 102 (1), 918–930. doi:10.1016/j.conbuildmat.2015.04.026

Sassoni, E., Graziani, G., and Franzoni, E. (2016b). An innovative phosphate-based consolidant for limestone. Part 2: durability in comparison with ethyl silicate. *Construct. Build. Mater.* 102 (1), 931–942. doi:10.1016/j.conbuildmat.2015.10.202

Sassoni, E., Graziani, G., Franzoni, E., and Scherer, G. W. (2018). Calcium phosphate coatings for marble conservation: influence of ethanol and isopropanol addition to the precipitation medium on the coating microstructure and performance. *Corrosion Sci.* 136, 255–267. doi:10.1016/j.corsci.2018.03.019

Sassoni, E. (2018). Hydroxyapatite and other calcium phosphates for the conservation of cultural heritage: a review. *Materials* 11 (4), 1–48. doi:10.3390/ma11040557

Sassoni, E., Naidu, S., and Scherer, G. W. (2011). The use of hydroxyapatite as a new inorganic consolidant for damaged carbonate stones. *J. Cult. Herit.* 12 (4), 346–355. doi:10.1016/j.culher.2011.02.005

Scherer, G. W. (1999). Crystallization in pores. *Cement Concr. Res.* 29 (8), 1347–1358. doi:10.1016/s0008-8846(99)00002-2

Scherer, G. W. (2004). Stress from crystallization of salt. *Cement Concr. Res.* 34 (9), 1613–1624. doi:10.1016/j.cemconres.2003.12.034

Scherer, G. W., and Wheeler, G. S. (2008). Silicate consolidants for stone. *Kemi* 391, 1–25. doi:10.4028/www.scientific.net/kem.391.1

Selwitz, C., and Doehne, E. (2002). The evaluation of crystallization modifiers for controlling salt damage to limestone. *J. Cult. Herit.* 3 (3), 205–216. doi:10.1016/s1296-2074(02)01182-2

Smith, B. J., Gomez-Heras, M., Viles, A., and Cassar, J. (2010). *Limestone in the built environment: present-day challenges for the preservation of the past*. London, United Kingdom: Geological Society of London, 331

Steiger, M., and Asmussen, S. (2008). Crystallization of sodium sulfate phases in porous materials: the phase diagram Na2SO4-H2O and the generation of stress. *Geochem. Cosmochim. Acta* 72 (17), 4291–4306. doi:10.1016/j.gca.2008.05.053

Tsui, N., Flatt, R. J., and Scherer, G. W. (2003). Crystallization damage by sodium sulfate. *J. Cult. Herit.* 4 (2), 109–115. doi:10.1016/s1296-2074(03)00022-0

Conflict of Interest: The authors declare that the research was conducted in the absence of any commercial or financial relationships that could be construed as a potential conflict of interest.

Mechanics of Materials

Laure Bouquerel

Dr. Laure Bouquerel graduated in 2016 from the Engineering school of Ecole Centrale de Nantes, France, with a double diploma from Cranfield University, United Kingdom, in Advanced Materials. In 2019, she defended her Ph.D. at Mines Saint-Etienne, France, funded by Hexcel Reinforcements and in collaboration with INSA-Lyon, France. During her Ph.D., she focused on modeling the mechanical behavior of dry carbon-fiber reinforcements during forming for primary aircraft structure applications. Since 2019, she has been working at Hexcel Reinforcements as an R&T Engineer and has been involved in dry carbon-fiber reinforcement characterization as well as material development.

Declaration by Dr. Larissa Gorbatikh: "The corresponding author, Dr. Larissa Gorbatikh, would like to instead highlight the contribution of the manuscript's first author, Dr. Man Zhu."

Man Zhu

Dr. Man Zhu was born in China and is currently a PostDoc student at Nanjing University of Aeronautics and Astronautics, China. She received her Master's degree in Solid Mechanics in 2015 from Beihang University, China, and her Ph.D. in Materials Engineering in 2019 from KU Leuven, Belgium. Her research interest is in fatigue and fracture analysis of composite materials.

Stephanie TerMaath

Dr. Stephanie C. TerMaath is an Associate Professor and a Zeanah Faculty Fellow at the University of Tennessee, Knoxville, in the Mechanical, Aerospace, and Biomedical Engineering Department. Her research group develops numerical models to solve multi-physics problems. Before joining the faculty, she managed a physics-based computing group at Applied Research Associates (ARA) and held positions at Boeing Phantom Works and Lockheed Martin Aeronautics, where she worked on numerous programs, including the High Speed Civil Transport, 737, 777, C-17, Delta IV, and Joint Strike Fighter. She currently leads an afterschool program to teach STEM to girls at socioeconomically disadvantaged elementary schools.

Evelyn KF Yim

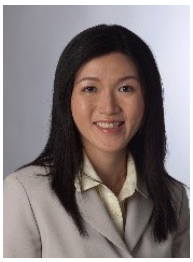

Dr. Evelyn Yim received her Ph.D. in Biomedical Engineering at the Johns Hopkins University before her post-doctoral training at Duke University. Between 2007 and 2015, Evelyn was a faculty member with joint appointments in the Departments of Biomedical Engineering and Surgery at the National University of Singapore and as a principal investigator in the Mechanobiology Institute Singapore. Evelyn joined the Department of Chemical Engineering at the University of Waterloo in 2016. Experienced with nanofabrication technologies and stem cell culture, Evelyn and her group are interested in applying their knowledge of biomaterial-stem cell interaction to direct stem cell differentiation and tissue engineering applications.

frontiers in Materials

ORIGINAL RESEARCH
published: 27 January 2021
doi: 10.3389/fmats.2020.571779

A Contribution to the Study of the Forming of Dry Unidirectional HiTape® Reinforcements for Primary Aircraft Structures

Laure Bouquerel[1]*, *Nicolas Moulin*[2] *and Sylvain Drapier*[2]

[1]R&T Reinforcements, Hexcel Reinforcements SASU, Route des Nappes, Les Avenières, France, [2]Mines Saint-Etienne, University of Lyon, CNRS, UMR 5307 LGF, Centre SMS, Saint-Etienne, France

In the context of developing competitive liquid composites molding processes for primary aircraft structures, modeling the forming stage of automatically-placed initially flat stacks of dry reinforcements is of great interest. In the case of HiTape®, a dry unidirectional carbon fiber reinforcement designed to achieve performances comparable to state-of-the-art pre-impregnated materials, the presence of a thermoplastic veil on each side of the material for both processing and mechanical purposes should also be considered when modeling forming in hot conditions. As a dry unidirectional reinforcement, HiTape® is expected to exhibit a transversely isotropic behavior. Computation cost and strong characterization challenges led us to model its behavior at the forming process temperature (above the thermoplastic veil melting temperature) through a homogeneous equivalent continuous medium exhibiting four 'classical' deformation modes and a specific structural mode, namely out-of-plane bending. The response of both single plies and stacks of HiTape® to this latter structural mode was characterized at the forming process temperature using a modified *Peirce flexometer*. Results on single plies showed a non-linear softening moment-curvature behavior and a corresponding flexural stiffness much lower than what can be inferred from continuum mechanics. Moreover, testing stacks revealed that the veil acts as a thin load transfer layer between the plies undergoing relative in-plane displacement, *i.e.* inter-ply sliding. This inter-ply response was then characterized separately at the forming process temperature thanks to a specific method relying on a *pull-through* test. Experiments performed at pressures and speeds representative of the forming stage revealed that a hydrodynamic lubricated friction regime predominates, *i.e.* a linearly increasing relationship between the friction coefficient and the modified Hersey number. From an industrial point of view, high forming pressures and low speeds are therefore recommended to promote inter-ply slip to limit the occurrence of defects such as wrinkles.

Keywords: bending, carbon fiber, dry, forming, friction, reinforcement, thermoplastic, unidirectional

OPEN ACCESS

Edited by:
Patricia Krawczak,
IMT Lille Douai, France

Reviewed by:
Damien Soulat,
ENSAIT, France
Frédéric Charles Lebon,
Aix-Marseille Université, France

***Correspondence:**
Laure Bouquerel
laure.bouquerel@hexcel.com

Specialty section:
This article was submitted to Mechanics of Materials, a section of the journal Frontiers in Materials

Received: *11 June 2020*
Accepted: *04 November 2020*
Published: *27 January 2021*

Citation:
Bouquerel L, Moulin N and Drapier S (2021) A Contribution to the Study of the Forming of Dry Unidirectional HiTape® Reinforcements for Primary Aircraft Structures. Front. Mater. 7:571779. doi: 10.3389/fmats.2020.571779

INTRODUCTION

For decades, composite materials have been recognized as optimal solutions for lightweight structures in the industry of transportation. They have widely participated to the development of innovative aircraft structures, including heavily loaded primary structures. Carbon fiber based composites are now used extensively and represent up to more than half of the weight of modern aircraft structures. Classically, the best performances are reached with long fiber semi-products pre-impregnated with non-consolidated organic resin, and processed in autoclave environments. However, such semi-products, made up of the controlled arrangement of tows containing thousands of carbon fibers require heavy storage and processing environments. In the context of continuous cost reduction and production rate increase, liquid composites molding (LCM) processes (Hexcel, 2015a) appear now as ideal routes for manufacturing primary aircraft structures. These Out-of-Autoclave (OOA) processes consist in draping and shaping dry composite semi-products, and then inject (for Resin Transfer Molding for instance) or infuse (in infusion-based processes) liquid resins in this potentially complex fibrous architecture.

In this context, Hexcel Reinforcements is continuously developing specific reinforcements solutions for primary aircraft structures manufactured with LCM processes. HiTape® (Hexcel, 2015b) is a dry unidirectional (UD) tape made up of parallel spread tows of thousands of carbon fibers with a thermoplastic (TP) veil on either side (**Figure 1A**). The veil is a key feature of this innovative reinforcement; not only it enables automated dry fiber placement (DFP) but it also contributes to yield mechanical properties equivalent to pre-impregnated based composites (Hexcel, 2015b), with high fiber volume fractions of 58–60% reached with OOA processes.

Going a step further in increasing production rates, dry semi-products such as HiTape® can be first deposited with automated placement in 2D stacks of several plies, and then formed in an automated way under mechanical loading to reach a given geometry and fiber arrangement. In this paper, the considered forming process solution is double-membrane hot vacuum forming as illustrated in **Figure 1B**. It consists firstly in compacting the dry stack between soft membranes by pulling vacuum (①), and secondly in forcing this membranes/stack set to deform (Pickett, 2018) by pulling vacuum between the mold and the membranes/stack set yielding an about 1 bar forming pressure (②). This forming step is performed above the melting temperature of the veil, notably for the veil to maintain the shape of the resulting preform. Preventing defects and imperfections (e.g., wrinkles) occurrence during this crucial forming stage is of prime importance and requires to understand the ply response to thermo-mechanical loading, and how plies move with respect to each other.

The aim of this paper is to characterize the behavior of HiTape® reinforcements in order to feed models of the forming process of stacks. To the knowledge of the authors, literature on the characterization of such dry UD materials is quite sparse. In ***Section 2***, we hence propose a literature review on the behavior of related materials such as dry multi-axial reinforcements and pre-impregnated UDs, in order to define the major deformation modes to be identified for forming modeling, along with the corresponding appropriate experimental methods. Such review allows us to identify the most relevant deformation modes of HiTape® to be characterized: bending and inter-ply sliding. In ***Section 3***, the implementation of corresponding dedicated experimental methods is described. Finally, results of HiTape® characterization in bending and inter-ply sliding are presented and discussed in ***Section 4***.

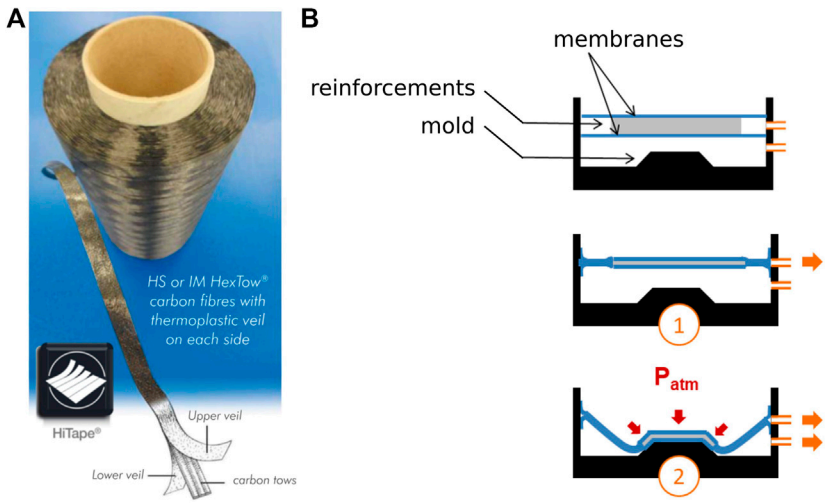

FIGURE 1 | Industrial context: **(A)** HiTape® reinforcements for LCM processes (Hexcel, 2015b) and **(B)** schematics of double-membrane hot vacuum forming process, which consists in a compaction stage followed by a forming stage.

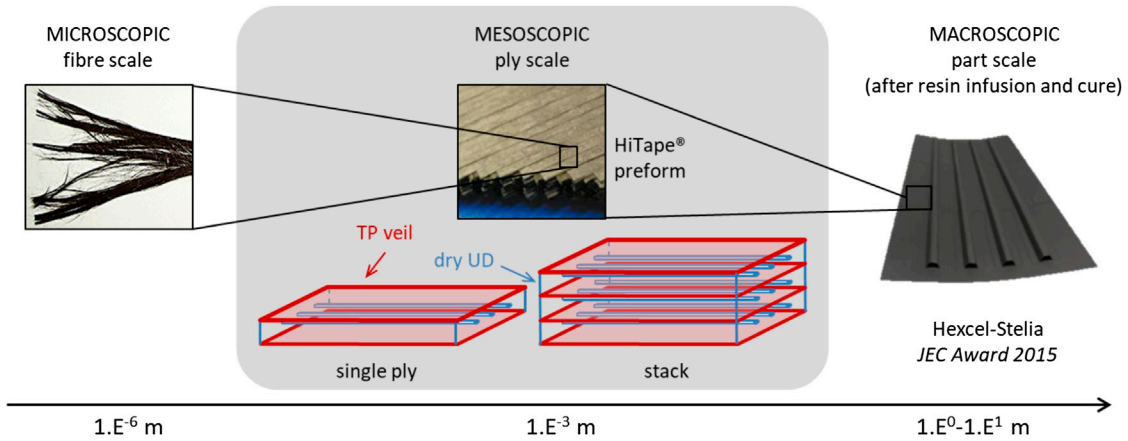

FIGURE 2 | The three main scales of observation of composites materials; an intermediate (mesoscopic) ply scale is selected for forming modeling and HiTape® characterization.

FROM STATE OF THE ART TO CONSIDERATIONS ON HITAPE® REINFORCEMENTS MECHANICAL BEHAVIOR

Extensive work has been performed on the characterization of the forming behavior of composite semi-products with heavy multi-axial complex architectures, either for pre-impregnated (e.g., Ten Thije et al. (2011), Lightfoot et al. (2013)) or dry reinforcements (e.g., Boisse (2004), Cao et al. (2008), Senner et al. (2014)). However, the particular structure of HiTape® is expected to yield a specific intermediate type of behavior. On one hand, an individual ply (intra-ply) is likely to respond like pre-impregnated UD materials (Leutz, 2015), i.e., with a theoretically transversely isotropic behavior, but with even less cohesion and very low stiffness in the isotropy plane orthogonal to the fiber direction. On the other hand when considering several plies forming in industrial conditions (hence at the veil melting temperature), the presence of the melted veil at the interface between plies (inter-ply) may modify HiTape® stacks response compared to multi-axial dry semi-products (Creech and Pickett, 2006). The aim of this section is to perform a selective literature review in order to identify which characterization work should be carried out on HiTape® in order to describe its mechanical behavior to be used as input for forming simulations.

Intermediate Scale of Observation

Reinforcements are intrinsically multi-scale materials as they are classically composed of thousands of fibers gathered in tows (possibly spread) which are assembled in tapes or plies, then laid up as a stack (**Figure 2**). The scale of observation for this study must allow for the identification of the main mechanisms which control both intra-ply and inter-ply responses during forming, but should also enable modeling the process with tractable computational efforts.

Modeling the forming at fiber scale would help understanding interactions between fibers, but it is not suited for representing the forming of stacks which contain millions of fibers with specific architectures, nor accounting for the contact between top and bottom plies with the surrounding tooling. On the opposite, the part (or stack) scale is too coarse as heterogeneous layer-wize constitutive responses are expected. The material response model should indeed be able to capture local effects (inter-ply shear, frame rotations . . .) which control the relative motion between plies as well as the intra-ply response itself. It should also represent the large deformations undergone by the whole stack, which translate into finite strains and rotations that a continuous approach can certainly not handle even with refined kinematics (Dufort et al., 2001). Eventually, an intermediate scale, so-called mesoscopic, is considered for modeling HiTape® forming as well as to characterize the ply and stack responses. Indeed, as illustrated in **Figure 2**, modeling each ply through an equivalent homogeneous medium (potentially non-linear and orthotropic) ensures acceptable computational efforts (Fagiano, 2010; Dörr et al., 2017) while allowing for a reasonably fine description of the mechanisms acting in the ply and between plies (Bouquerel et al., 2017).

Deformation Modes at ply Scale During Forming and Corresponding Characterization Methods

As illustrated in **Figures 3A,B**, reinforcements exhibit both in-plane and out-of-plane (*i.e.* along thickness direction) intra-ply deformation mechanisms: traction, compression as well as shear. Moreover, like any fibrous medium, HiTape® may also display structural modes like out-of-plane bending due to the reinforcement intrinsic thickness. Finally, these intra-ply modes must be complemented by specific ones associated with the presence of the TP veil on either side of the layers, which come into play when considering HiTape® stacks. These inter-ply

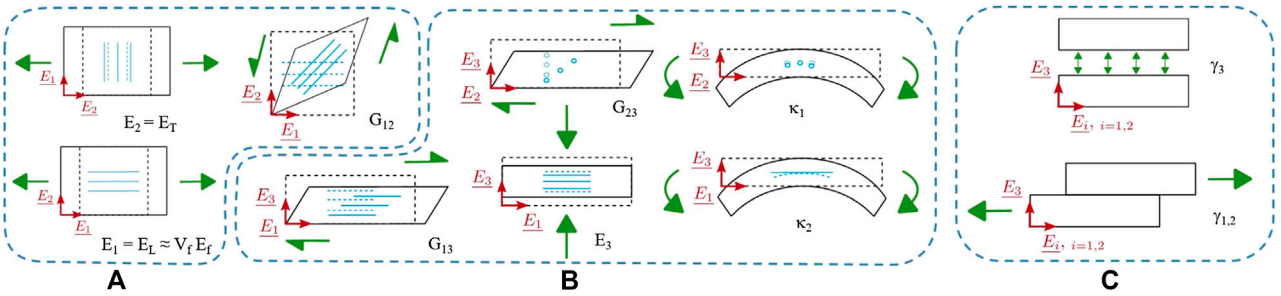

FIGURE 3 | Deformation mechanisms of reinforcements at ply scale during forming, illustrated in the case of a UD with fibers oriented along $\underline{E_1}$ direction: **(A)** in-plane modes, **(B)** out-of-plane modes with specific bending about axis $\underline{E_2}$: $\mathcal{M} = B\kappa_2$, and **(C)** inter-ply loading with specific inter-ply sliding in plane $(O, \underline{E_1}, \underline{E_2})$, with friction coefficients $\gamma_{1,2}$.

modes correspond to sliding or opening/closing as presented in **Figure 3C**.

In this section let us consider these intra- and inter-ply deformation modes and how the corresponding responses can be identified. We shall not describe all these modes in detail, but focus on the predominant ones during forming.

Tensions and Compressions

The longitudinal response along fiber direction $\underline{E_1}$ (**Figure 3A**) is dominated by fibers quasi-inextensibility. Tension behavior can hence be approximated by a simple rule of mixture $E_L \approx V_f E_f$ where E_L is the reinforcement longitudinal modulus, V_f the fiber volume fraction and E_f the fiber longitudinal modulus in tension known to be constant for carbon fibers and available in the fiber data sheet. As for compression in this same longitudinal direction, it is assumed that the external compaction that occurs in double-membrane forming constrains the transverse displacement on either side of the plies, and therefore largely limits the occurrence of potential out-of-plane fiber micro-buckling that may appear if layers are free (Drapier et al., 1996; Drapier and Wisnom, 1999). Moreover, due to the high volume fraction ($V_f \approx 60\%$ under 1 bar compaction as measured by Blais (2016)) and in-plane confinement of plies, in-plane fiber micro-buckling could only appear at extremely high loads (Rosen, 1964; Drapier et al., 1996) which cannot be reached in standard forming conditions. In conclusion, the prescribed transverse compaction during forming limits the potential difference in tension-compression response, and the longitudinal compressive modulus can hence be taken equal to the constant elongation modulus E_L.

In transverse directions $\underline{E_2}$ and $\underline{E_3}$, the characterization of tension behavior of UDs is quite a challenge due to the lack of cohesion. Pre-impregnated UDs were tested in transverse direction by Leutz (2015) and Margossian et al. (2016), but results were scattered with low repeatability. In the case of HiTape®, the internal structure with no resin support inside plies exhibits little cohesion only brought by a slight entanglement of the UD dry fibers network, whereas TP veil on either side of the tape brings a superficial cohesion just sufficient for handling and processing. This structure makes both elongational responses in transverse directions almost impossible to characterize. Therefore, for modeling purpose, it can be assumed that transverse stiffnesses correspond to a little fraction of the longitudinal modulus, *i.e.* $E_T = \alpha E_L$ with $\alpha \ll 1$.

In transverse compression, the response of the fibrous material is driven by the fiber network rearrangement as well as fiber-to-fiber contacts (Xiong et al., 2019). Recalling that we consider double-membrane forming processes where the individual layers of the stack are compacted along thickness direction ($\underline{E_3}$) before forming, compression behavior understanding appears to be of prime importance. Such non-linear behavior is already known as it was determined using a standard testing machine to compact HiTape® stacks between circular platens in previous works (Celle et al., 2008; Blais, 2016; Blais et al., 2017).

Shears

Considering the small thickness of HiTape® (approximately 0.2 mm), we can assume that transverse shear–*i.e.* in planes $\left(O, \underline{E_2}, \underline{E_3}\right)$ and $\left(O, \underline{E_1}, \underline{E_3}\right)$ as depicted in **Figure 3B**–is negligible. Conversely, in-plane shear (**Figure 3A**) may develop during forming. This deformation mechanism indeed dominates the formability of composites semi-products such as woven ones (Cao et al., 2008) due to the relative mobility of the fiber tows (Boisse, 2004). Two types of specific characterization methods were hence developed to evaluate the formability of both dry and pre-impregnated semi-products: the bias-extension (Orawattanasrikul, 2006; Charmetant, 2011) and the picture-frame (Kawabata, 1980) tests.

To the knowledge of the authors, literature on the characterization of the in-plane shear behavior of dry UD reinforcements under forming conditions is quite sparse. Related studies may be found for UD-NCF (Trejo et al., 2020) as well as for pre-impregnated UD tapes with various strategies proposed to maintain the specimen integrity during testing: Leutz (2015) tested 4-ply stacks (**Figure 4**), McGuinness and Bradaigh (1998) used membranes to maintain a single ply but struggled to isolate the ply response from the membrane one, and Larberg et al. (2012) considered cross-plied. However, all these tests demonstrated a rapid decohesion following the occurrence of

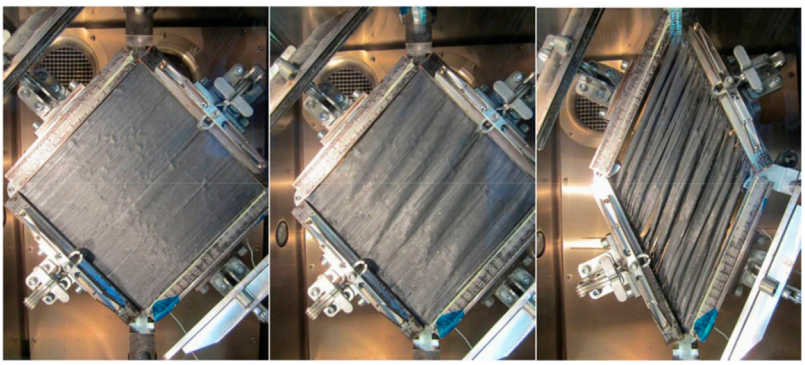

FIGURE 4 | An example of in-plane shear characterization of pre-impregnated UD carbon/epoxy: picture-frame test on a 4-ply stack of UD of same orientation (left to right: initial configuration, intermediate shear angle of 2°, final shear angle of 40°) (Leutz, 2015).

out-of-plane instabilities, either fiber micro-buckling or ply buckling. Due to the only superficial cohesion of HiTape®, in-plane shear characterization seems out of reach from a technological point of view. More importantly, due to the compaction which limits the fiber transverse displacements during forming, the formability of a stack of HiTape® plies is expected to be driven more by the relative motion of thin HiTape® individual plies than by intra-ply in-plane shear as it is highlighted in the following.

Out-of-Plane Bending

Many recent studies showed that accounting for ply scale out-of-plane bending behavior of either dry or pre-impregnated semi-products (Cao et al., 2008; Haanappel et al., 2014) in forming simulations allows the prediction of wrinkles occurrence in thick architectures (Boisse et al., 2011), and more generally is a step forward to reliable simulations (Madeo et al., 2015). Moreover, even for thin plies, the bending behavior controls the overall formability to a great extent (Liang et al., 2014). Although the hypothesis of continuity is often made for fibrous media–especially those with high fiber volume fraction–, bending behavior cannot be directly deduced from the elongation stiffness for these media, mainly because of internal relative motion between fibers during deformation (Kang and Yu, 1995). For this reason, reinforcements bending behavior should be characterized.

Due to the low bending stiffness of composite semi-products, classical characterization methods such as three- or four-point bending tests have classically been discarded by the textile industry. Peirce (Peirce, 1930) early proposed a ply scale linear elastic bending model for cloth, extending Euler-Bernoulli's beam theory to large deflections but small deformations using a correction term. This model led to a simple, cost-effective and rapid bending characterization method called fixed angle flexometer, and involving a strip of fabric bending under its own weight. Using this method Leutz (2015) measured the bending stiffnesses B_i about direction $\underline{E_i}$ $(i = 1, 2)$ of pre-impregnated UDs in thermally controled environments and showed that the ratio of bending stiffnesses B_2/B_1 is about 10^3. Indeed, bending about $\underline{E_2}$ is dominated by the fiber longitudinal stiffness whereas bending about $\underline{E_1}$ is almost solely controled by the molten resin as illustrated in **Figure 3B**. In the case of HiTape® this bending ratio is expected to be even higher due to the absence of molten resin. We can therefore infer that B_2 (B thereafter) dominates in forming modeling, *i.e.* the influence of B_1 on forming simulation may be negligible. Still, the question of how to measure bending stiffness B_1 remains open for future works.

Going a step forward, fibrous semi-products were shown to exhibit a non-linear bending response (Liang et al., 2014). Their tangent behavior can be more generally defined by the differential form $B(\kappa) = \mathrm{d}\mathcal{M}(\kappa)/\mathrm{d}\kappa$ in the corresponding plane, where $\mathcal{M}$ is the bending moment per unit width, B the bending stiffness per unit width, and κ the curvature (Clapp et al., 1990). Following Peirce (1930), various models were introduced to account for the non-linearity of the moment-curvature relationship: bi-linear (Huang, 1979), non-linear for small curvatures and linear for larger curvatures (Abbott et al., 1971; Clapp et al., 1990), with a threshold (Grosberg, 1966), etc.

In order to characterize this particular behavior, a specific apparatus called Kawabata Evaluation System KES-FB2 (Kawabata, 1980) was designed and successfully used on fabrics (Ngo Ngoc et al., 2002) and non-crimp fabric (NCF) multi-plies (Lomov et al., 2003) for example; however this type of apparatus is rather cumbersome and limited to room temperature. Other characterization methods were further derived from the fixed angle flexometer test to characterize non-linear behaviors: de Bilbao et al. (2008) increased step by step the free length of the strip for NCFs and interlocks, while other approaches were based on recording the deformed shape of the sample and using image processing to relate the bending moment to the sample curvature. In order to characterize a wide range of curvatures, Liang et al. (2014) also added a lumped mass at the end of the strip.

Besides, some methods were developed to take into account the temperature-dependency of the bending behavior of pre-impregnated reinforcements, for UD carbon/PEEK[1] and UD

[1]PEEK: PolyEtherEtherKetone

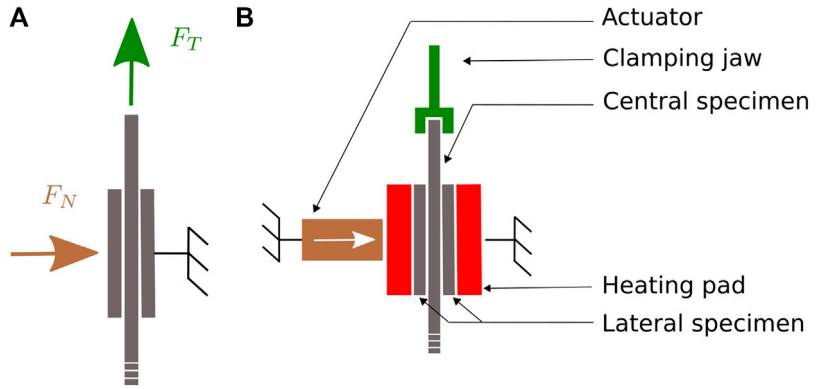

FIGURE 5 | (A) Principle of the pull-through test and **(B)** schematic of the inter-ply friction characterization setup.

carbon/PPS[2] for example (Liang, 2016). In those studies, managing the increase of temperature in the sample before testing was reported to be challenging. A specific apparatus called hot vertical cantilever (Soteropoulos et al., 2011; Alshahrani and Hojjati, 2017) was hence proposed in order to load the sample only when the desired temperature was reached. However, a deformation of the sample was already observed before applying the load due to the temperature rise (Angel and Graef, 2016). In addition, the homogeneity and control of the environment are critical and can significantly influence the results (Angel and Graef, 2016). To overcome this, other tests were proposed on smaller volumes: for instance in a 3-point bending DMA machine (Margossian et al., 2015) or with a rheometer (Sachs et al., 2014).

Inter-ply Response

The two inter-ply deformation modes are depicted on **Figure 3C**, namely inter-ply opening (decohesion) and sliding. In the case of double-membrane forming processes, it seems wise to assume that decohesion along direction $\underline{E_3}$ is not likely to occur due to external loading. Conversely, sliding between plies is expected to be a key factor controlling the formability of a stack (Guzman-Maldonado et al., 2019); inter-ply sliding needs therefore to be characterized, and is dominated by the presence of the TP veil.

Characterization Methods of Inter-Ply Sliding

Standard methods were developed for the characterization of the frictional behavior of sheets of materials–standards related to inter-fiber or inter-tow friction are not discussed here. They involve a fixed plane, either horizontal or inclined, onto which a first sample of tested material is attached, and over which a mobile block holding a second sample is translated. The static (*i.e.* when relative motion is initiated) and dynamic (*i.e.* during relative motion) friction coefficients are calculated using Coulomb's law, which assumes that friction coefficients are independent of both relative sliding velocity and normal pressure:

$$\mathrm{CoF} = \frac{F_T}{F_N} \tag{1}$$

where CoF is the friction coefficient, and F_T and F_N are the applied tangent and normal forces, respectively.

However, these methods have been developed to represent friction conditions that sheet materials may encounter during handling or automated processing, but they are not representative of composite forming conditions. Indeed, not only are they limited to room temperature, but the required force corresponding to forming (*i.e.* of the order of magnitude of a few hN for standard tests) cannot be applied with such methods. Those are the reasons why other tests were developed for composite semi-products friction characterization. A horizontal plane with a specific system for applying normal pressure was proposed by Hivet et al. (2012), Montero et al. (2017), but the pressure still seems too low for our forming conditions. To achieve normal pressures of about 1 bar, the *pull-out* and the *pull-through* tests (illustrated on **Figure 5A**) are the most common ones; they are described in the benchmark of Sachs et al. (2012). In these tests, a reinforcement sample (referred to as central specimen) is placed between two plates covered with reinforcement samples (referred to as lateral specimens) and a normal force is applied. The central sample is then loaded in tension and forced to slide, while the corresponding force is recorded. The difference between the two apparatuses lies in the contact area, which is constant during the test for the pull-through while it decreases for the pull-out.

Inter-ply Friction Behavior of Reinforcements

In the literature, Coulomb's law (**Eq. 1**) for dry friction is generally used to model the friction behavior during inter-ply sliding of solid-state reinforcements, *i.e.* either dry (Hivet et al., 2012) or containing thermoplastic below its melting temperature (Sachs et al., 2012) as illustrated in **Figure 6B** (top). Indeed, after a transient phase, the coefficient of friction reaches a plateau value often interpreted as the dynamic coefficient of friction. However,

[2]PPS: PolyPhenylene Sulfide

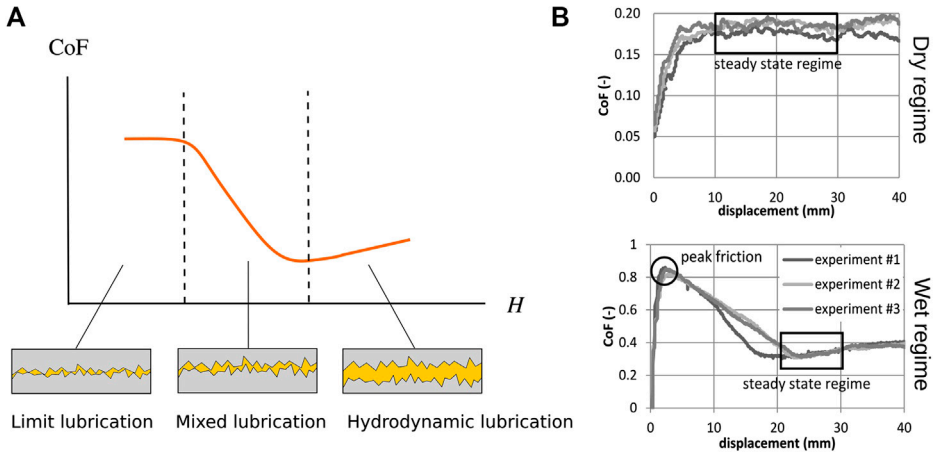

FIGURE 6 | (A) Stribeck curve and schematic illustration of the different lubrication regimes and **(B)** examples of dry **(top)** and wet **(bottom)** friction for Twintex® PP from Sachs et al. (2012).

the hypothesis of a single constant friction coefficient for solid-state reinforcements is too coarse; normal pressure in particular has a strong influence on the friction coefficient Hivet et al. (2012). Thus more complex models were proposed; for example Howell's model (Howell and Mazur, 1953) describes a power law between tangent and normal forces such that $F_T = k F_N^m$ where k and m are parameters to be determined experimentally (Das et al., 2005; Cornelissen et al., 2014; Najjar et al., 2014), which leads to a dynamic friction coefficient which depends on the normal force. A review of these models is proposed by Yuksekkay (2009). In the case of dry reinforcements, an inter-ply friction coefficient of 0.3 is frequently assumed (Fetfatsidis et al., 2013) in the absence of experimental data. This is consistent, for example, with the results obtained by Hivet et al. (2012) who identified a friction coefficient between 0.15 and 0.4 for a dry woven reinforcement.

As soon as the reinforcement contains resin in a molten state, this resin may play the role of a lubricant and strongly influences the friction response; this is called lubricated contact. In that case, the friction coefficient depends on resin viscosity η, sliding speed ν and normal force applied F_N; three parameters assembled in the Hersey number H defined by:

$$H = \frac{\eta \nu}{F_N}. \tag{2}$$

Based on a phenomenological approach, Stribeck's theory (Stribeck, 1903) expresses the existence of a minimum on the curve of friction coefficient *vs.* Hersey number. Three different lubrication regimes illustrated on **Figure 6A** can then be highlighted. In the limit regime, the lubricating film is very thin, *i.e.* its thickness is of the same order of magnitude as the roughness of the two surfaces; in this case the friction behavior depends both on the lubricant and the physico-chemical properties of the surfaces. In the mixed regime, there co-exist some areas where the two surfaces are in direct contact and some areas where they are separated by a lubricating film (Frêne and Zaïdi, 2011). In the hydrodynamic regime, the two surfaces are completely separated by a lubricating film; the roughness of the surfaces is then negligible. In this case, the relationship between the friction coefficient and the Hersey number is increasing linearly (Hersey, 1914). Stribeck's theory was frequently used for either thermoplastic (Gorczyca et al., 2007; Ten Thije et al., 2011; Vanclooster et al., 2010; Fetfatsidis et al., 2013; Zhu et al., 2011; Wang et al., 2013) or thermoset (Rashidi et al., 2020) pre-impregnated reinforcements friction characterization for forming modeling. In this case of reinforcements containing a resin in the fluid state, the same type of curve with stabilization of the friction coefficient is obtained as illustrated in **Figure 6B** (bottom), and a hydrodynamic regime is generally observed. Affine (Najjar et al., 2014) or power laws (Haanappel et al., 2014) for example can be used to relate the friction coefficient to the Hersey number; in other cases, the hydrodynamic regime is directly assumed (Bel et al., 2012). If the normal pressure is high, the resin at the interface may migrate and limit lubrication may occur: a mixed lubrication model is then more suitable (Larberg and Akermo, 2011; Leutz, 2015). For reinforcements containing molten thermoplastic, the friction coefficient varies over a wider range, for example values between 0.1 and 1.8 were measured by Sachs et al. (2012).

In both cases (presence or not of a resin in a fluid state), during the transient regime prior to stabilization of the tangential force, the latter can reach a maximum value (**Figure 6B**) which becomes more evident as the velocity increases (Ten Thije et al., 2011). If Fetfatsidis et al. (2013) used this maximum force value to deduce a static coefficient of friction, this interpretation is however not unanimous. Indeed, in the case of the work of Ten Thije et al. (2011), the tangent force peak did not correspond to the initiation of relative motion but to a displacement value already higher than the one matching the maximum elongation of the sample before rupture. This means that the sample had already started to slide, and this maximum coefficient of friction did not correspond to a static coefficient of friction. Instead, the transition from peak to plateau was interpreted as a rearrangement of the reinforcement.

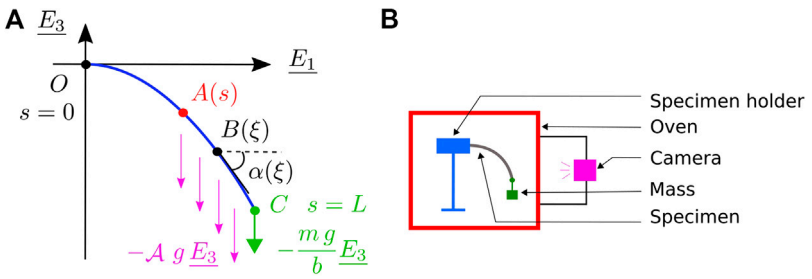

FIGURE 7 | (A) Principle and notations for the bending moment calculation with **Eq. 7** and **(B)** schematic of the bending test.

Finally, a dependence of the friction coefficient upon fiber orientation was observed. Testing a carbon/epoxy UD, Leutz (2015) for example obtained a friction coefficient varying from 0.88 for orientations of 0°/90°[3] to 1.37 for 0°/0°, with an intermediate value for 90°/90°. Larberg and Akermo (2011), who identified a mixed lubrication model, obtained on the same type of material a maximum coefficient of friction for 0°/45° and 0°/30°, about 25% higher than that obtained with orientations of 0°/90°and 0°/0°.

Conclusions on HiTape® Characterization Strategy

The literature review conducted so far highlights the two deformation mechanisms that primary require characterization in order to feed forming simulations of HiTape®: bending and inter-ply friction. In particular for inter-ply friction, the presence of the TP veil (which differs from a continuous film) raises the question of which of the mixed or hydrodynamic lubrication regime predominates. Such characterization works need to be conducted under conditions as close as possible from double-membrane vacuum hot forming process, hence at the forming process temperature (which is above the melting temperature of the TP veil) and for external pressures between 0.5 and 1.5 bar. In the following, the selected methods for both non-linear bending behavior and interply friction behavior characterizations are introduced.

MATERIALS AND METHODS

Materials

The characterized HiTape®[4] reinforcement was composed of Hexcel HexTow® fibers with a thermoplastic veil on each side of the tape. This tape was 12.7 mm wide and had an areal weight of 210 g/m^2.

Out-of-Plane Bending Characterization Method

In order to characterize the non-linear bending behavior of HiTape® at ply scale and at the forming process temperature (T_{proc}) which is above the melting temperature of the TP veil (T_{melt}), a modified flexometer based on the same principle than previous studies (de Bilbao et al., 2010; Liang et al., 2014) was designed. The selected method to identify the non-linear bending response consisted in recording the deformed shape, calculating the bending moment over the sample length, and deriving a bending moment-curvature relationship. Such procedure was extended from previous studies (Clapp et al., 1990; de Bilbao et al., 2008; 2010; Liang et al., 2014) carried out on both pre-impregnated and dry materials.

Test Setup

The bending test apparatus, represented in **Figure 7B**, was composed of a frame with a specimen holder developed to limit edge effect due to the clamp. Thermocouples were used for temperature monitoring. This apparatus was placed in a thermoregulated oven equipped with a glass window. A CCD camera was positioned outside the oven and a LabVIEW program[5] recorded in real time both photographs of the sample and temperature of the thermocouples, with a chosen acquisition frequency and duration. A set of masses to be positioned at the free end of the sample was available to increase sample curvature. The grip system to attach the selected mass to the sample tip justified to model it as a point force oriented with gravity.

Test Procedure

The sample (either unit plies or stacks obtained with DFP) was first pre-consolidated under vacuum at T_{proc} in order to be as close as possible to double-membrane vacuum hot forming process conditions. The sample was then placed in the oven at T_{proc}. When it no longer deformed, a photograph of the sample was recorded and post-processed.

Data Post-processing

Using the output photograph of the deformed sample, the cartesian coordinates (x, z) of the mean-line of the deformed sample in the orthonormal basis $\left(\underline{E_1}, \underline{E_3}\right)$ were obtained by digital image processing. Then, a program ran the following steps (corresponding notations are illustrated in **Figure 7A**):

1. Derive the relationship $\widehat{z} = f(x)$ using a Levenberg-Marquardt algorithm (Marquardt, 1963) to find the optimal couple (k_1, k_2)

[3]Orientation of samples in contact, in degrees with respect to loading direction.
[4]Permission from the product owner was obtained for this study.
[5]www.ni.com/fr-fr/shop/labview.html

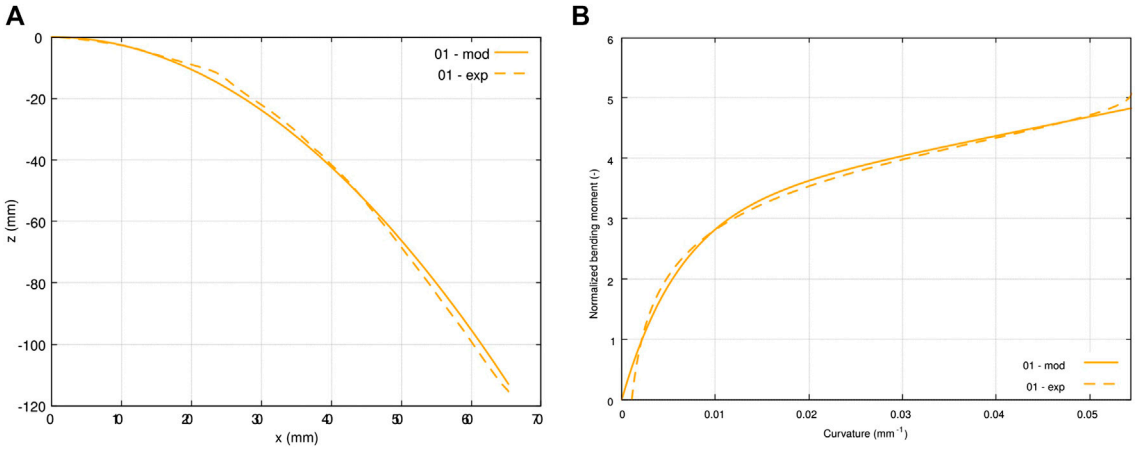

FIGURE 8 | Comparison between experimental data (dashed lines) and model (solid lines) for a single ply tested at room temperature: **(A)** deformed sample mean line with $\mathrm{err}_{\%}^{(z)}$ = 1.3% and **(B)** normalized bending moment–curvature relationship with $\mathrm{err}_{\%}^{(\mathcal{M})}$ = 3.8%.

minimizing the distance between the experimental data (x, z) and the following function:

$$\hat{z} = f(x) = -k_1 \ln\left(1 + (k_2 x)^2\right) \tag{3}$$

which is referred to as deformed shape function thereafter. This particular form illustrated for instance in **Figure 8A** is justified in ***Section 4.1.2.1***.

2. Compute curvature $\kappa(x)$ from the established relationship $\hat{z} = f(x)$:

$$\kappa(x) = \frac{f''(x)}{\left(1 + f'(x)^2\right)^{3/2}}. \tag{4}$$

3. Compute curvilinear abscissa $s(x)$ as follows:

$$s(x) = \int_{t=0}^{x} \sqrt{1 + f'(t)^2}\,\mathrm{d}t. \tag{5}$$

4. Compute bending moment per unit width $\mathcal{M}(s)$ for each point $A(s)$ of the deformed sample. To this end, a first analytical expression could be derived for a sample of width b loaded under its own areal weight $\mathcal{A}$ (ply areal weight multiplied by number of plies) under gravity g (see also **Figure 7A**):

$$\mathcal{M}(s) = -\int_{\xi=s}^{L} \underline{AB(\xi)} \wedge \mathcal{A}g\underline{E_3}\,\mathrm{d}\xi \approx \int_{\xi=s}^{L} \mathcal{A}g(\xi - s)\cos(\alpha(\xi))\mathrm{d}\xi \tag{6}$$

where s is the curvilinear abscissa at point A such that $s = 0$ at clamping O and $s = L$ at free end C, and the curvilinear abscissa ξ and angle α are the coordinates of the current $B(\xi)$ point from $A(s)$ to C in the associated Frénet's basis. The additional mass m placed at the free end of the sample also contributed to the bending moment which then reads:

$$\mathcal{M}(s) \approx \int_{\xi=s}^{L} \mathcal{A}g(\xi - s)\cos(\alpha(\xi))\mathrm{d}\xi + \frac{mg}{b}\underline{A(s)C} \cdot \underline{E_1}. \tag{7}$$

5. Derive a relationship between bending moment and curvature $\widehat{\mathcal{M}} = g(\kappa)$ using a Levenberg-Marquardt algorithm (Marquardt, 1963) to optimize the triplet $(R_0, R_{\mathrm{inf}}, \kappa_{\mathrm{lim}})$ by minimizing the distance between the moment $\mathcal{M}$ computed from expression seven and Voce's model (Voce, 1955) which reads:

$$\hat{\mathcal{M}} = g(\kappa) = \mathcal{M}_0 + R_0\kappa + R_{\mathrm{inf}}\left(1 - e^{-\kappa/\kappa_{\mathrm{lim}}}\right) \text{ with } \mathcal{M}_0 = 0. \tag{8}$$

Voce's model (Pannier, 2006) is illustrated in **Figure 8B** and its justification is given in ***Section 4.1.2.1***.

The outputs of the corresponding program were the following: the range of curvatures of the deformed sample, the optimized couple (k_1, k_2) in **Eq. 3** describing the shape of the deformed sample, the optimized triplet $(R_0, R_{\mathrm{inf}}, \kappa_{\mathrm{lim}})$ in **Eq. 8** giving the bending moment vs. curvature relationship, and finally, in any point of the deformed sample: the curvilinear abscissa, the curvature and the bending moment.

The two successive regressions–firstly on coordinates (x, z) in step 3.2.3 and secondly on points $(\kappa, \mathcal{M})$ in step 3.2.3 – induced an uncertainty which could be quantified by the two following errors that describe the mean scatter between experimental data $(z_i, \mathcal{M}_i)$ and their homologous from the corresponding model $(\hat{z}_i(x_i), \hat{\mathcal{M}}_i(\kappa_i))$ at the ith point of the deformed sample:

$$\mathrm{err}_{\%}^{(z)} = \frac{\sqrt{\frac{\sum_{i=1}^{N}(\hat{z}_i(x_i) - z_i)^2}{N}}}{|z|_{\max} - |z|_{\min}}; \mathrm{err}_{\%}^{(\mathcal{M})} = \frac{\sqrt{\frac{\sum_{i=1}^{N}(\hat{\mathcal{M}}_i(\kappa_i) - \mathcal{M}_i)^2}{N}}}{|\mathcal{M}|_{\max} - |\mathcal{M}|_{\min}}. \tag{9}$$

For commodity reasons, these errors were normalized by the range of values obtained experimentally. We could then define the two following validity criteria for any tested sample: $\mathrm{err}_{\%}^{(z)} < 5\%$ and $\mathrm{err}_{\%}^{(\mathcal{M})} < 5\%$. In some cases an angle locally formed on the samples (due to the clamping condition for

example); such phenomenon was related to the tendency of the quasi-inextensible fibers to out-of-plane buckle in the inner radius of the curvature, especially for thick stacks. In this case, the samples exhibited an angular mean-line with a poor quality of regression that the validity critera allowed to reject. However it was not always sufficient and a complementary visual check of the quality of the regression was realized. Eventually, the coefficient of variation $\sigma_{\%}^{(a)}$ was of interest to measure the mean scatter of a set of N data a_i around its mean $\overline{a}$:

$$\sigma_{\%}^{(a)} = \frac{\sqrt{\sum_{i=1}^{N}(a_i - \overline{a})^2}}{\overline{a}}. \tag{10}$$

Inter-ply Friction Characterization

Based on previous studies (Gorczyca et al., 2007; Vanclooster et al., 2010; Ten Thije et al., 2011; Zhu et al., 2011; Fetfatsidis et al., 2013; Wang et al., 2013), the pull-through test principle was selected to characterize HiTape® inter-ply lubricated friction at ply scale. Let us recall the principle of this test illustrated on **Figure 5A**: a central sample is placed in-between two fixed lateral samples and a controled normal pressure is applied across the thickness of the reinforcements, the central sample is then pulled through the setup. The tensile traction force F_T is recorded as a function of the central sample displacement. This test principle is selected because it enables to apply a normal pressure that is both homogeneous on the surface and constant during the test.

The test setup was designed such that conditions representative of double-membrane vacuum hot forming were covered. As forming pressure is about 1 bar–but may vary locally –, normal stresses in the range 0.5–1.5 bar were considered. The relative speed between two adjacent plies was tricky to estimate; in the case of vacuum forming, which is a slow forming process, a relative speed of the order of magnitude of a few millimeters in some seconds was considered, i.e., 1–10 mm min^{-1}. Finally, the forming process temperature T_{proc} such that $T_{\text{proc}} > T_{\text{melt}}$ was prescribed. In this study, temperature was kept constant as it is considered that the stack is heated up to T_{proc} before starting forming; in future works the influence of a variation of temperature around T_{proc} may be studied.

Test Setup

A fixture was designed both to hold the lateral specimens in place and to apply the desired normal pressure and temperature conditions. **Figure 5B** provides a schematic of the final bench. The closing pressure was prescribed by an actuator. The lateral samples were placed in contact with heating pads and were fixed by means of a specific system. This apparatus was designed to be mounted on a standard traction machine, and the central sample attachement was fixed to the crosshead of the machine. The test was controled using the traction machine software, and an acquisition station enabled the force, displacement, and time data of the traction machine to be recorded in real time, as well as the temperature of the heating pads.

Temperature homogeneity inside the samples was checked by placing thermocouples in the central sample just upstream of the test area and carrying out the test: it was then verified that when the thermocouple came into the test area, *i.e.* in contact with the heating pads, the setpoint temperature T_{proc} was reached almost immediately. Indeed, the isothermal temperature regime was quasi-instantaneously reached since carbon is a good heat conductor, but also because the pressure applied compacted the sample hence increased fiber-to-fiber contacts, the reinforcement was thin, and the low speed resulted in little contact changes over time.

Test Procedure

The test procedure consisted first in fixing both lateral specimens to the heating pads and clamping the central specimen in the upper attachement of the traction machine crosshead. The actuator was then activated to apply the closing pressure, and the temperature of the pads increased up to the setpoint temperature T_{proc}. When T_{proc} was reached homogeneously both on the pads and in the central sample, the test started. It began with a preload of 10 N at a crosshead displacement rate of 10 mm min^{-1}, after which the crosshead kept pulling the central specimen at the preselected displacement rate. The input parameters of the test were: the displacement rate of the crosshead representing the relative speed between tow adjacent plies, and the normal stress applied. The outputs were: displacement, tensile force, normal force, and temperature as a function of time.

Data Post-processing

The friction coefficient CoF and modified Hersey number H^* were calculated as follows:

$$\text{CoF} = \frac{F_{\text{T}}}{2\,F_N} \;;\; H^* = \frac{H}{\eta} = \frac{\nu}{F_N} \tag{11}$$

where F_T and F_N are, respectively, the tangential force and the normal force, η is the TP veil viscosity and ν the sliding velocity. Let us notice that the factor 2 in the expression of the friction coefficient appears (compared to **Eq. 1**) since it was assumed that the problem is perfectly symmetrical and consequently the contact area is twice the tested surface. We decided to consider H^*, i.e., the Hersey number without the influence of viscosity, since in this study isothermal conditions were fulfilled and hence viscosity was assumed to be constant in the considered normal pressure range.

RESULTS AND DISCUSSION

Out-of-Plane Bending

The out-of-plane bending characterization was achieved in three steps: first some tests on single plies were performed in order to validate the proposed methodology, then single plies were characterized, and finally the method was extended to UD stacks to get closer to industrial needs. For confidentiality reasons, all the moment values presented are normalized.

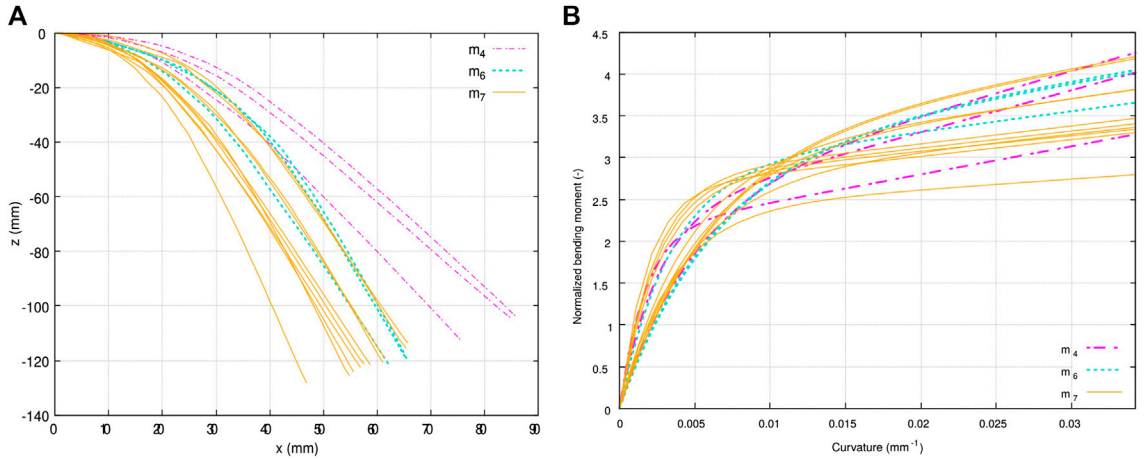

FIGURE 9 | Results of bending tests on single plies at room temperature using three different lumped masses m_4, m_6 and m_7 such that $m_7 > m_6 > m_4$: **(A)** experimental data of the deformed sample mean line and **(B)** normalized bending moment–curvature relationship using Voce's model. Each curve corresponds to one single test.

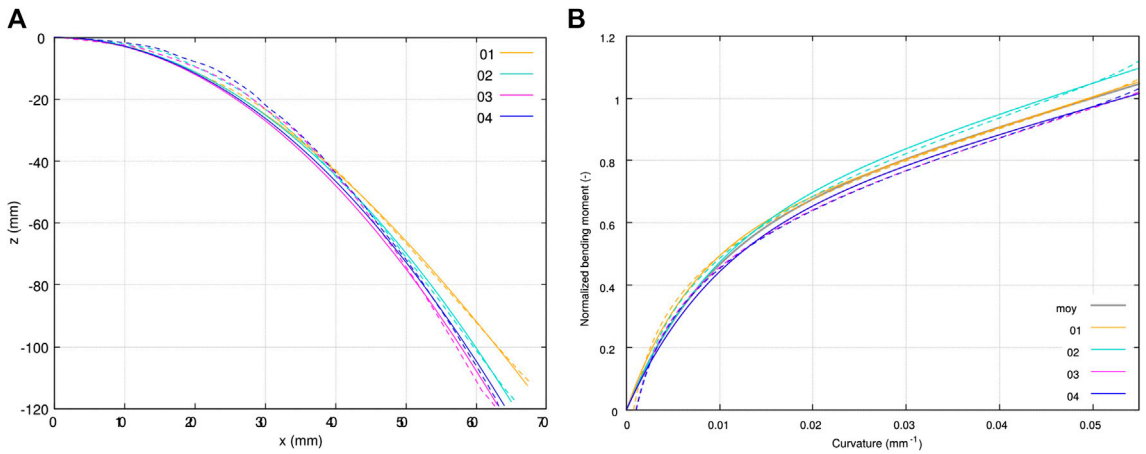

FIGURE 10 | Results of bending tests on single plies at T_{proc} (experimental data in dashed line, optimized model in solid line): **(A)** deformed sample mean line with $err_{\%}^{(z)} < 2.5\%$, and **(B)** normalized bending moment–curvature relationship using Voce's model with $err_{\%}^{(\mathcal{M})} < 3\%$. Curves 01 to 04 correspond to single tests; curve moy is the average model.

Results

Preliminary Tests on Single Plies at Room Temperature

Preliminary tests were first conducted in order to validate the proposed methodology; these tests were carried out at room temperature to validate the approach in lighter conditions. In order to assess the test repeatability, 10 samples were first tested at room temperature with the same lumped mass m_7 and same operator. The deformed shapes are plotted in **Figure 9A** (orange solid lines) and Voce's models corresponding to moment-curvature relationships are plotted in **Figure 9B** (orange solid lines). The scattering in deformed shape led to 8% relative standard deviation on maximum bending moments, computed using **Eq. 7** at clamping for each sample. Note that these values are not visible on **Figure 9B** and correspond to different curvature values depending on the sample. This scatter was mainly due to variability on the positioning of the lumped mass at the tip of the sample. However, although rather low at room temperature, it was verified that this scatter was even reduced in temperature conditions.

This test was repeated with two other lumped masses m_4 and m_6 such that $m_7 > m_6 > m_4$ with a difference of 50% between m_4 and m_7, in order to modify the maximum loading (for confidentiality reasons, values of lumped masses are not given). The deformed shapes obtained for the three samples of the test are plotted in **Figure 9A** (purple and green dashed lines); as the mass increases, the maximum curvature of the sample (*i.e.* close to clamping) increased. Voce's models corresponding to moment-curvature relationships are plotted in **Figure 9B** (purple

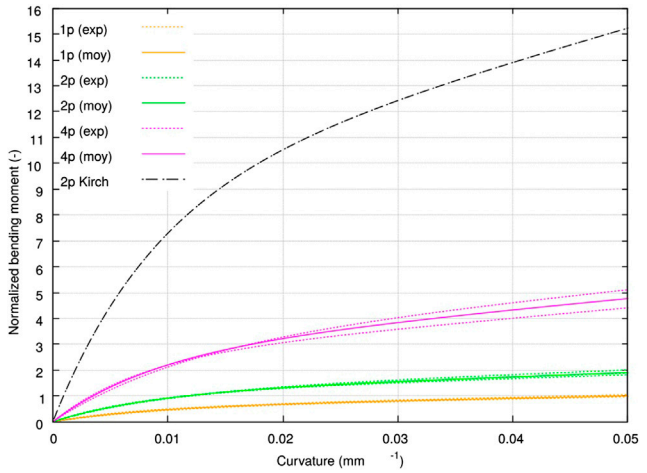

FIGURE 11 | Normalized bending response at T_{proc} for a single ply (1p) and for 2- (2p) and 4-ply (4p) UD stacks, and theoretical response for a ply of double thickness (2p Kirch). Each experimental (exp) curve corresponds to one single test; solid lines (moy) show corresponding average optimized models.

and green dashed lines); one can observe that the moment-curvature relationships obtained are within the envelope defined by the results with m_7. Therefore, for different loads, different ranges of curvatures could be described but the characterized bending response remained the same. It was thus the intrinsic response of the material that was characterized by this test. In a previous work, de Bilbao et al. (2010) illustrated the same test characteristic by changing the length of the sample.

Results for Single Plies at T_{proc}

In order to identify the out-of-plane bending behavior of single plies under forming conditions, tests were conducted at T_{proc} for four samples. **Figure 10A** presents the experimental deformed shapes of the four samples along with the corresponding optimized model obtained in step 3.2.3 with **Eq. 3**. The error $\mathrm{err}_{\%}^{(z)}$ was lower than 2.5% for all four samples which justified the choice of the deformed shape function (**Eq. 3**) to describe the non-linear deformed shape of the samples at T_{proc} (**Figure 10A**).

In **Figure 10B**, curvatures and normalized bending moments computed using **Eqs 4** and **7**, respectively, are plotted for the four samples, as well as the corresponding optimized Voce's models (**Eq. 8**). The average model is also plotted, its parameters R_0, R_{inf} et κ_{lim} were taken as the average of the parameters of the four samples. This **Figure 10B** illustrates that the selected Voce's model described in a satisfactory manner the moment-curvature relationship at T_{proc}, with an error $\mathrm{err}_{\%}^{(\mathcal{M})}$ lower than 3% for every sample.

Results on Stacks at T_{proc}

The bending test was extended to UD stacks of two, four, six and eight plies, with at least three samples for each. Tests on six- and 8-ply stacks could not be processed since the validity criteria were not satisfied. **Figure 11A** presents the averaged bending moment *vs.* curvature for various numbers of plies including a single ply, obtained by averaging Voce's model triplets of parameters. One can notice, again, that the Voce's model enabled to describe properly the moment-curvature evolution for either single plies, two- or 4-ply stacks.

Discussion

Comments on the Choice of the Models

Let us first observe in **Figure 8** the deformed shape and the moment-curvature relationship obtained for one sample tested at room temperature, meeting the validity criterion. The results presented in this figure exhibit a very low error between the deformed function and the mean-line obtained using image processing. This was also demonstrated with further results plotted in **Figure 10A** where $\mathrm{err}_{\%}^{(z)} < 2.5\%$ for the four samples. This justified the choice of the deformed function selected (**Eq. 3**). Indeed, such function exhibited the following characteristics: the origin of the graph was positioned at the clamping ($z(0) = 0$), the slope vanished at this same point ($z'(0) = 0$), and the function tended to a linear behavior at the free end of the sample–three features observed on experimental data.

Besides, **Figure 8B** shows that the selected Voce's model (**Eq. 8**) satisfactorily described the moment-curvature relationship obtained experimentally, with little error. Again, this tendency was more general as illustrated in **Figure 10B** with a very low error on the moment ($\mathrm{err}_{\%}^{(\mathcal{M})} < 3\%$ for every sample). Voce's model provided a good description of the observed behavior by the mean of a single class function $\mathcal{C}^2$ which is non-linear for small curvatures and quasi-linear beyond a certain curvature threshold κ_{lim}. In **Eq. 8**, R_0 corresponds to the slope of the quasi-linear part for curvature higher than this threshold κ_{lim} and is referred to as asymptotic tangent bending stiffness (per unit of width) thereafter; it is the minimum value of the bending stiffness. Furthermore, $R_0 + R_{inf}/\kappa_{lim}$ corresponds to the initial slope (*i.e.* for curvatures close to 0) and is referred to as initial tangent bending stiffness (per unit of width); it is the maximum value of the bending stiffness.

Overall, the proposed models yielded a good fit of the experimental data. In **Figures 8B**,**10B**, it can be observed that the major differences between the raw results and the Voce's model (Voce, 1955) are located either at the foot of the curve (low moments and low curvatures) corresponding to the free end of the sample where the moment vanishes, or at the end of the curve (high moment and high curvatures) corresponding to the clamp where the moment is maximum. Firstly, with regard to the foot of the curve, it should be noted that while the computed bending moment *exactly* equals zero at the free end of the sample, the curvature tends toward zero but only *approximately* because of the deformed shape function used (**Eq. 3**). This is not physical as it would describe a deformation in a stress-free state. Therefore we chose to impose $\mathcal{M}_0 = 0$ in Voce's model; this was not the case in other works (de Bilbao et al., 2010; Liang et al., 2014). Secondly, the large curvatures-large moments extremity of the experimental response seems to reveal a sort of vertical tangent which would correspond to a capping of the curvature. This was actually due to the clamping which prescribed a zero slope to the sample,

whereas Voce's model intrinsically does not account for this effect on the curvature. However, this effect was concentrated and did not affect the overall response identified; at the most it could increase artificially the error $\mathrm{err}_{\%}^{(\mathcal{M})}$ calculated (**Eq. 9**).

Using intermediate models to build the moment-curvature relationship required to estimate the error introduced by the two successive regressions. The uncertainty on bending stiffness B due to the uncertainty on curvature κ is given by:

$$\Delta B = \frac{R_{\mathrm{inf}}}{\kappa_{\mathrm{lim}}^2} e^{-\kappa/\kappa_{\mathrm{lim}}} \Delta\kappa. \tag{12}$$

This shows that the initial tangent stiffness (*i.e.* for $\kappa = 0$) is influenced by k_1 and k_2 through the curvature fitting. Conversely, the asymptotic tangent stiffness (for larger curvatures) is not affected, since $\Delta B \to 0$ when $\kappa \to +\infty$.

Comments on the Curvature Range Covered

In these tests, the curvatures described by the deformed functions were between 0.0576 and 0.0010 mm^{-1}, which correspond to curvature radii from 17 to 1,000 mm approximately. Our aim was to describe curvatures representative of industrial geometries, for which curvature radii can reach 5 mm (corresponding to a curvature of 0.2 mm^{-1}). Such high curvature could not be reached experimentally with this method without the occurrence ofùtextitbreaks in the deformed shape, as explained earlier. However, since Voce's model is linear beyond the threshold curvature which is much lower than 0.2 mm^{-1} (κ_{lim} = 0.0088 mm^{-1} here), the moment-curvature relationship could then be extrapolated to larger curvatures. Hence, the model obtained here can be extended to curvature range of industrial geometries.

Comments on the Identified Responses

First, a comparison between **Figures 9B**,**10B** highlights that with increasing temperature the bending moment is reduced for a given range of curvature. The softening effect of temperature is observed with a stiffnesses ratio between the two temperatures of the order of 10^0 for the asymptotic bending stiffness and 10^1 for the initial bending stiffness.

The results obtained at T_{proc} with the proposed procedure were cross-checked with preliminary tests using a fixed angle flexometer (Peirce, 1930) as introduced earlier. It was verified that the bending stiffness value given by Peirce model (Peirce, 1930) was within the range of bending stiffnesses (*i.e.* bounded by the asymptotic and initial tangent stiffnesses) obtained by the proposed method. More precisely, it was observed that Peirce stiffness is closer to the initial tangent bending stiffness, which is consistent since the fixed angle flexometer generates only small curvatures as the sample only bends under its own weight.

One limitation of this bending test was the thickness of the specimens, as it limited the number of plies of the tested stacks. Indeed, a too large thickness (or number of plies) led to the local buckling phenomenon explained earlier: an opening (fish-eye) induced by the through-thickness decohesion of the sample appeared. This phenomenon was due both to the inextensibility of individual fibers and to local singularities. In that case, the hypothesis of continuity of the material, and consequently the interpretation of the results according to the above method, were no longer valid. It was therefore decided to minimize these effects, which consisted in reducing the sample curvature by decreasing the additional mass. However, lower curvatures were obtained and therefore the quasi-linear response could not be appropriately described as the value of the regression parameter R_0 and consequently the asymptotic tangent bending stiffness could be overestimated. The choice of the mass was thus a compromise between maintaining the cohesion of the sample, and testing over a wide range of curvatures.

With this method we characterized the bending responses of single plies as well as two- and 4-ply stacks at T_{proc}, and an average model was derived for each configuration; they are recalled in **Figure 11**. This figure clearly illustrates the need for identification of plies and stacks bending response for two reasons. Firstly, predicting individual ply non-linear response is a real challenge since a simple calculation of the theoretical linear bending stiffness of a continuous (Kirchhoff) beam with longitudinal stiffness and dimensions corresponding to a HiTape® ply shows two orders of magnitude difference with the identified experimental response. Secondly, a supplementary curve may be observed on this figure: it corresponds to the theoretical bending response of a homogeneous continuous medium according to Kirchhoff theory, with the same experimental behavior than one single ply at T_{proc} but of double-thickness. As it can be verified, this latter theoretical behavior of a double-thickness single ply appears to be four times stiffer than the experimental behavior identified for a 2-ply stack.

Theses differences can certainly be partly attributed to the invalidity of the continuous medium theory in this context, as there may have been some fibrous rearrangements during testing, but we also assume that they are accentuated by the presence of the thermoplastic veil at the inter-ply. Indeed, during the bending of a stack, the fiber inextensibility induces transverse shear which can only concentrate in the soft TP veil, otherwise out-of-plane buckling of plies in the inner curvature would occur (Drapier et al., 1996, 2001). In other words, this means that the overall forming capability of the stack originates from inter-ply sliding. In conclusion, either for single plies or stacks, the continuous media (Cauchy) theory can clearly not describe the response of single HiTape® plies, and the major role of the TP veil is demonstrated in the bending of a stack.

Inter-Ply Sliding

Results

Let us recall the pressure and speed ranges representative of hot vacuum forming conditions that we introduced in ***Section 3.3***: pressures around 1 bar and relative speeds of two adjacent plies of the order of magnitude of a few millimeters in some seconds, *i.e.* 1–10 mm min^{-1}. In order to assess the relative influence of velocity and normal pressure in thoses ranges, five configurations were tested with four to five samples each. Keeping speed at 2.0 mm min^{-1}, tests were carried out at 1.35, 1.00 and 0.50 bar, respectively. Tests at bounding pressures of 1.35 and 0.50 bar were also performed at 0.5 mm min^{-1}. As this work was the first

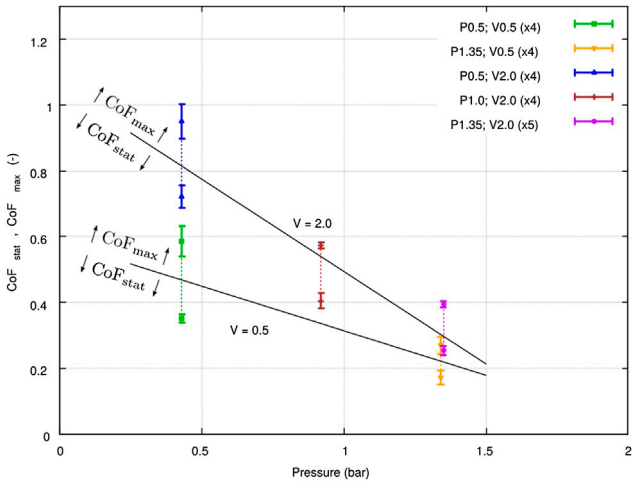

FIGURE 12 | Results of inter-ply sliding test: maximum and static friction coefficients vs. pressure.

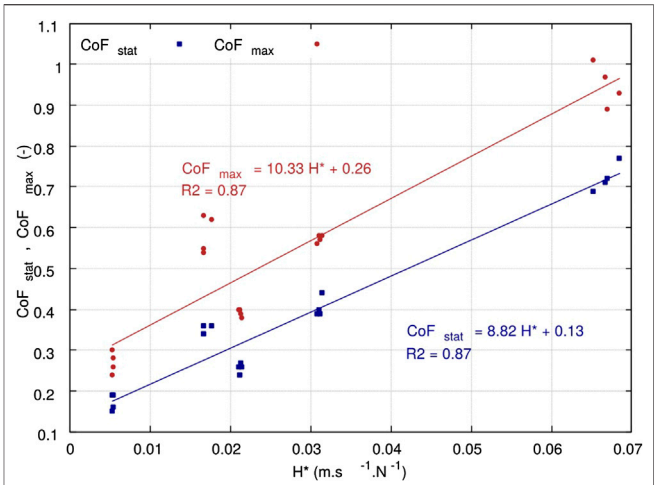

FIGURE 14 | Stribeck curve for HiTape® over the pressure and speed ranges representative of double-membrane hot vacuum forming conditions.

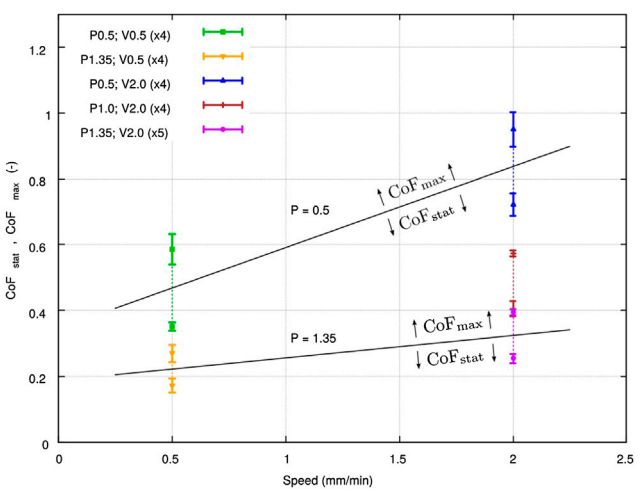

FIGURE 13 | Results of inter-ply sliding test: maximum and static friction coefficients vs. adjacent plies relative speed.

inter-ply sliding characterization of HiTape®, we decided to focus on 0°/0° sliding, *i.e.* both lateral and central specimen were aligned with loading direction.

The resulting tangent force *vs.* displacement curves (not presented for confidentiality reasons) exhibited the same shape than wet friction results of friction coefficient *vs.* displacement from literature, for example from Sachs et al. (2012) (**Figure 6B** bottom). Such comparison makes sense as friction coefficient is related to tangent force only by normal force which is kept constant during the test. After tensionning of the sample, displacement initiated (at a tangent force value F_{stat}). Then, as the prescribed displacement increased, the tangent force also increased to a maximum value F_{max} and then decreased. F_{stat} was used to compute the static friction coefficient CoF_{stat} using **Eq. 11** with $F_T = F_{stat}$. Similarly F_{max} was also used to compute a so-called maximum friction coefficient CoF_{max} using **Eq. 11** with $F_T = F_{max}$. Let us highlight that as the normal force F_N was kept constant during the test, the friction coefficient *vs.* displacement curve also exhibited the same shape than **Figure 6B** (bottom).

The results of static and maximum coefficients of friction are presented with their standard deviations as a function of pressure in **Figure 12** and as a function of the relative speed in **Figure 13**. A strong influence of pressure and velocity was observed in the ranges of pressure and velocity studied. Note that the standard deviations on every configuration were small (less than 10%) compared to the differences observed from one configuration to another.

Discussion

The shape of the tangent force-displacement response obtained was consistent with literature results presented for composites pre-impregnated with a TP resin tested in a molten state, as illustrated in **Figure 6B** taken from Sachs et al. (2012). However, unlike in Ten Thije et al. (2011) and Fetfatsidis et al. (2013), the tangent force measured in our experiment did not clearly stabilize. Consequently, we could not extract from the presented tests a dynamic fiction coefficient. This phenomenon is attributed to a fibrous rearrangement during the test and to possible penetration of the veil inside the UD fiber bed.

When forming a stack, the expected relative displacement between two adjacent plies is of the range of a few millimeters. Moreover, purely geometrical considerations show that forming two 0.2 mm thick inextensible layers on a quadrant implies a relative displacement between of 0.3 mm the two layers. This highlights that only the very first millimeters of sliding of the test are of interest for us. Using bounding values of F_{stat} and F_{max} for the tangent force is therefore justified, and we can state that friction coefficient during forming is bounded by CoF_{stat} and CoF_{max}.

In order to conclude on the type of lubricated regime that characterizes the inter-ply response during hot forming, both coefficients of friction obtained $Co F_{stat}$ and $Co F_{max}$ are plotted as functions of the modified Hersey number (**Eq. 11**) in **Figure 14**. In both cases, an increasing linear relationship between the friction coefficients and the modified Hersey number H^* may be observed. Recalling the Stribeck curve (**Figure 6**), we can therefore conclude that a hydrodynamic lubricated regime prevailed, which corresponds to the presence of a lubricating film of thickness larger than the roughness of the reinforcement. In terms of industrial forming, this means that inter-ply mobility is promoted at low Hersey numbers, *i.e.* at high forming pressures and low velocities, and may not depend of the relative orientations of the plies.

CONCLUSION

In this work, the deformation mechanisms of HiTape® reinforcements were inventoried: intra-ply mechanisms control the response of a single ply, and inter-ply mechanisms (especially inter-ply sliding) are involved when considering the forming of stacks. More precisely, HiTape® mainly deforms in bending (and forms wrinkles) which is controled by the fiber response as well as the presence of the TP veil that acts between plies as a lubricating layer providing shear compliance especially at the forming process temperature (which is above the veil melting temperature). This study was therefore dedicated to the characterization of two deformation modes encountered by HiTape® reinforcements during double-membrane hot vacuum forming process and for which the behavior was unknown, namely out-of-plane bending and inter-ply friction. Dedicated apparatuses were designed on purpose, in order to meet the requirements of handling, heating, and finely controling the characterization of non-linear bending response and inter-ply sliding in conditions representative of the industrial double-membrane hot vacuum forming processes.

For bending, a modified Peirce's flexometer was designed and validated. It enabled to assess the complete isothermal moment-curvature non-linear relationship in a single test, taking advantage of the curvature range covered by the deformation of single plies and stacks under a terminal loading that could be adjusted to reach the curvatures in scope. The bending responses identified correspond to fibrous media bending for which the internal mobility of the fibers leads to a range of stiffnesses much lower that what can be expected in continuous Cauchy's media with the same elongational modulus. Also, the bending stiffnesses identified for stacks clearly showed that the thermoplastic veil between plies has a strong influence and controls to a high extent the stack bending overall response.

Such results justified the development of a second apparatus designed for the characterization of inter-ply friction: a pull-through test with controled temperature and pressure. A hydrodynamic lubricated friction regime was observed through a linearly increasing relationship between the friction coefficients–both static and maximum–and the modified Hersey number (divided by the assumed constant viscosity of the thermoplastic veil). From an industrial point of view, this result showed that in order to limit the occurrence of wrinkle-type defects during forming, inter-ply sliding should be promoted with forming conditions inducing high pressure and low velocity. This guideline should be verified in further work with dedicated forming experiments.

DATA AVAILABILITY STATEMENT

The datasets presented in this article are not readily available because they are confidential. Requests to access the datasets should be directed to laure.bouquerel@hexcel.com.

AUTHOR CONTRIBUTIONS

LB: main co-author, the material presented herein comes out from her PhD work. NM: LB's co-supervisor and co-contributor to this article. SD: LB's main supervisor and co-contributor to this article.

FUNDING

This work produced in LB's PhD was supported both by ANRT, the French National Agency for Research and Technology, under the grant 2016/0094, and by the company Hexcel Reinforcements SASU.

REFERENCES

Abbott, G. M., Grosberg, P., and Leaf, G. A. V. (1971). The mechanical properties of woven fabrics Part VII : the hysteresis during bending of woven fabrics. *Textil. Res. J.* 41, 345–358. doi:10.1177/004051757104100411

Alshahrani, H., and Hojjati, M. (2017). A new test method for the characterization of the bending behavior of textile prepregs. *Composites Part A : Applied Science and Manufacturing.* 97, 128–140. doi:10.1016/j.compositesa.2017.02.027

Angel, B., and Graef, J. (2016). Study of the bending stiffness of fibre-reinforced thermoplastics at forming temperature. *JEC Composites Magazine.*, 103, 76–79.

Bel, S., Hamila, N., Boisse, P., and Dumont, F. (2012). Finite element model for NCF composite reinforcement preforming: composites Part A: applied Science and manufacturing: importance of inter-ply sliding. *Compos. Part A: Appl. Sci. Manuf.* 43 (12), 2269–2277. doi:10.1016/j.compositesa.2012.08.005

Blais, M. (2016). Modélisation et suivi du procédé par infusion de résine sur une nouvelle génération de renforts structuraux pour l'aéronautique. PhD. thesis, Saint-Étienne (France): Ecole Nationale Supérieure des Mines de Saint-Etienne.

Blais, M., Moulin, N., Liotier, P. J., and Drapier, S. (2017). Resin infusion-based processes simulation : coupled Stokes-Darcy flows in orthotropic preforms undergoing finite strain. *Int. J. Material Form.* 10 (1), 43–54. doi:10.1007/s12289-015-1259-2

Boisse, P., Hamila, N., Vidal-Sallé, E., and Dumont, F. (2011). Simulation of wrinkling during textile composite reinforcement forming. Influence of tensile, in-plane shear and bending stiffnesses. *Compos. Sci. Technol.* 71, 683–692. doi:10.1016/j.compscitech.2011.01.011

Boisse, P. (2004). *Mise en forme des renforts fibreux de composites.* Techniques de l'ingénieur Plasturgie: procédés spécifiques aux composites Ref: TIB474DUO. Article ref: am3734

Bouquerel, L., Moulin, N., Drapier, S., Boisse, P., and Beraud, J.-M. (2017). Modelling and simulating the forming of new dry automated lay-up reinforcements for primary structures. *AIP conference proceedings.* 1896 (1), 030008. doi:10.1063/1.5007995

Cao, J., Akkerman, R., Boisse, P., Chen, J., Cheng, H. S., de Graaf, E. F., et al. (2008). Characterization of mechanical behavior of woven fabrics: experimental methods and benchmark results. *Compos. Appl. Sci. Manuf.* 39, 1037–1053. doi:10.1016/j.compositesa.2008.02.016

Celle, P., Drapier, S., and Bergheau, J. M. (2008). Numerical aspects of fluid infusion inside a compressible porous medium undergoing large strains. *European Journal of Computational Mechanics.* 18, 819–827. doi:10.3166/remn.17.819-827

Charmetant, A. (2011). Approches hyperélastiques pour la modélisation du comportement mécanique de préformes tissées de composites. PhD. thesis, Villeurbanne (France): Institut National des Sciences Appliquées de Lyon

Clapp, T. G., Peng, H., Ghosh, T. K., and Eischen, J. W. (1990). Indirect measurement of the moment-curvature relationship for fabrics. *Textil. Res. J.* 60, 525–533. doi:10.1177/004051759006000906

Cornelissen, B., Sachs, U., Rietman, B., and Akkerman, R. (2014). Dry friction characterisation of carbon fibre tow and satin weave fabric for composite applications. *Composites Part A : Applied Science and Manufacturing.* 56, 127–135. doi:10.1016/j.compositesa.2013.10.006

Creech, G., and Pickett, A. K. (2006). Meso-modelling of non-crimp fabric composites for coupled drape and failure analysis. *J. Mater. Sci.* 41 (20), 6725–6736. doi:10.1007/s10853-006-0213-6

Das, A., Kothari, V. K., and Vandana, N. (2005). A study on frictional characteristics of woven fabrics. *Autex Res. J.* 5 (3)., 133–140

de Bilbao, E., Soulat, D., Hivet, G., and Gasser, A. (2010). Experimental study of bending behaviour of reinforcements. *Exp. Mech.* 50, 333–351. doi:10.1007/s11340-009-9234-9

de Bilbao, E., Soulat, D., Hivet, G., Launay, J., and Gasser, A. (2008). Bending test of composite reinforcements. *Int. J. Material Form.* 1, 835–838. doi:10.1007/s12289-008-0265-z

Dörr, D., Brymerski, W., Ropers, S., Leutz, D. M., Joppich, T., Kärger, L., et al. (2017). A benchmark study of finite element codes for forming simulation of thermoplastic UD-Tapes *Procedia CIRP.* 66. 101–106. doi:10.1016/j.procir.2017.03.223

Drapier, S., Grandidier, J.-C., Gardin, C., and Potier-Ferry, M. (1996). Structure effect and microbuckling. *Composites Scicence and Technology.* 56 (7), 861–867. doi:10.1016/0266-3538(96)00033-4

Drapier, S., Grandidier, J. C., and Potier-Ferry, M. (2001). A structural approach of plastic microbuckling in long fibre composites: comparison with theoretical and experimental results. *Int. J. Solid Struct.* 38, 3877–3904. doi:10.1016/S0020-7683(00)00247-X

Drapier, S., and Wisnom, M. R. (1999). Finite-element investigation of the compressive strength of non-crimp-fabric-based composites. *Compos. Sci. Technol.* 59, 1287–1297. doi:10.1016/S0266-3538(98)00165-1

Dufort, L., Drapier, S., and Grédiac, M. (2001). The cross section warping in short beams under three point bending : an analytical study. *Compos. Struct.* 52, 1233–1246.

Fagiano, C. (2010). Computational modeling of tow-placed composite laminates with fabrication features. PhD thesis. Delft (Netherlands): Technische Universiteit Delf.

Fetfatsidis, K. A., Jauffrès, D., Sherwood, J. A., and Chen, J. (2013). Characterization of the tool/fabric and fabric/fabric friction for woven-fabric composites during the thermostamping process. *Int. J. Material Form.* 6, 209–221. doi:10.1007/s12289-011-1072-5

Frêne, J., and Zaïdi, H. (2011). *Introduction à la tribologie.* Techniques de l'ingénieur : frottement et usure Ref: TIB464DUO. Article ref:TRI 100-1

Gorczyca, J. L., Sherwood, J. A., and Chen, J. (2007). A friction model for thermostamping commingled glass-polypropylene woven fabrics. *Composites Part A : Applied Science and Manufacturing.* 38 (2), 393–406. doi:10.1016/j.compositesa.2006.03.006

Grosberg, P. (1966). The mechanical properties of woven fabrics Part II: the bending of woven fabric. *Textil. Res. J.* 36, 205–211. doi:10.1177/004051756603600301

Guzman-Maldonado, E., Wang, P., Hamila, N., and Boisse, P. (2019). Experimental and numerical analysis of wrinkling during forming of multi-layered textile composites. *Compos. Struct.* 208, 213–223. doi:10.1016/j.compstruct.2018.10.018

Haanappel, S. P., ten Thije, R. H. W., Sachs, U., Rietman, B., and Akkerman, R. (2014). Formability analyses of uni-directional and textile reinforced thermoplastics. *Composites Part A : Applied Science and Manufacturing.* 56, 80–92. doi:10.1016/j.compositesa.2013.09.009

Hersey, M. D. (1914). The laws of lubrication of horizontal journal bearings. *J. Wash. Acad. Sci.* 4, 542–552. doi:10.2307/24520857

Hexcel (2015a). Direct processes technology manual. *Tech. rep.* Available at: https://www.hexcel.com/Resources/Technology-Manuals.

Hexcel (2015b). HiTape® A new efficient composite technology for primary aircraft structures. *SAMPE J.* 51, 7–15.

Hivet, G., Allaoui, S., Cam, B. T., Ouagne, P., and Soulat, D. (2012). Design and potentiality of an apparatus for measuring yarn/yarn and fabric/fabric friction. *Exp. Mech.* 52, 1123–1136. doi:10.1007/s11340-011-9566-0

Howell, H. G., and Mazur, J. (1953). Amontons' law and fibre friction. *Journal of the Textile Institute Transactions.* 44, T59–T69. doi:10.1080/19447025308659728

Huang, N. C. (1979). Finite biaxial extension of completely set plain woven fabrics. *J. Appl. Mech.* 46, 651. doi:10.1115/1.3424621

Kang, T. J., and Yu, W. R. (1995). Drape simulation of woven fabric by using the Finite-element method. *J. Textil. Inst.* 86, 635–648. doi:10.1080/00405009508659040

Kawabata, S. (1980). *The standardization and analysis of hand evaluation.* 2nd edn. (Osaka, Japan: Hand Evaluation Standardization Committee).

Larberg, Y. R., Akermo, M., and Norrby, M. (2012). On the in-plane deformability of cross-plied unidirectional prepreg. *J. Compos. Mater.* 46, 929–939. doi:10.1177/0021998311412988

Larberg, Y. R., and Akermo, M. (2011). On the interply friction of different generations of carbon/epoxy prepreg systems. *Composites Part A : Applied Science and Manufacturing.* 42, 1067–1074. doi:10.1016/j.compositesa.2011.04.010

Leutz, D. M. (2015). *Forming simulation of AFP material layups : material characterization, simulation and validation.* Munich, Germany: Technische Universität München.

Liang, B. (2016). Experimental and numerical study of the bending behaviour of textile reinforcements and thermoplastic prepregs. PhD thesis, Villeurbanne, France: Institut National des Sciences Appliquées de Lyon.

Liang, B., Hamila, N., Peillon, M., and Boisse, P. (2014). Analysis of thermoplastic prepreg bending stiffness during manufacturing and of its influence on wrinkling simulations. *Compos. Part A Appl. Sci. Manuf.* 67, 111–122. doi:10.1016/j.compositesa.2014.08.020

Lightfoot, J. S., Wisnom, M. R., and Potter, K. (2013). A new mechanism for the formation of ply wrinkles due to shear between plies. *Compos. Part A Appl. Sci. Manuf.* 49, 139–147. doi:10.1016/j.compositesa.2013.03.002

Lomov, S. V., Verpoest, I., Barburski, M., and Laperre, J. (2003). Carbon composites based on multiaxial multiply stitched preforms. Part 2. KES-F characterisation of the deformability of the preforms at low loads. *Compos. Part A Appl. Sci. Manuf.* 34, 359–370. doi:10.1016/S1359-835X(03)00025-3

Madeo, A., Ferretti, M., Dell'Isola, F., and Boisse, P. (2015). Thick fibrous composite reinforcements behave as special second-gradient materials: three-point bending of 3D interlocks. *Z. Angew. Math. Phys.* 66, 2041–2060. doi:10.1007/s00033-015-0496-z

Margossian, A., Bel, S., and Hinterhoelzl, R. (2015). Bending characterisation of a molten unidirectional carbon fibre reinforced thermoplastic composite using a Dynamic Mechanical Analysis system. *Compos. Part A Appl. Sci. Manuf.* 77, 154–163. doi:10.1016/j.compositesa.2015.06.015

Margossian, A., Bel, S., and Hinterhoelzl, R. (2016). On the characterisation of transverse tensile properties of molten unidirectional thermoplastic composite tapes for thermoforming simulations. *Compos. Part A Appl. Sci. Manuf.* 88, 48–58. doi:10.1016/j.compositesa.2016.05.019

Marquardt, D. W. (1963). An algorithm for least-squares estimation of nonlinear parameters. *J. Soc. Ind. Appl. Math.* 11, 431–441. doi:10.1137/0111030

McGuinness, G. B., and Bradaigh, C. O. (1998). Characterisation of thermoplastic composite melts in rhombus-shear : the picture-frame experiment. *Compos. Part A Appl. Sci. Manuf.* 29, 115–132. doi:10.1016/S1359-835X(97)00061-4

Montero, L., Allaoui, S., and Hivet, G. (2017). Characterisation of the mesoscopic and macroscopic friction behaviours of glass plain weave reinforcement. *Compos. Appl. Sci. Manuf.* 95, 257–266. doi:10.1016/j.compositesa.2017.01.022

Najjar, W., Pupin, C., Legrand, X., Boude, S., Soulat, D., and Dal Santo, P. (2014). Analysis of frictional behaviour of carbon dry woven reinforcement. *J. Reinforc. Plast. Compos.* 33, 1037–1047. doi:10.1177/0731684414521670

Ngo Ngoc, C., Bruniaux, P., and Castelain, J. M. (2002). "Modeling friction for yarn/fabric simulation Application to bending hysteresis," in *14th European Simulation Symposium*. Editor V. Krug (Dresden, Germany: SCS Europe BVBA).

Orawattanasrikul, S. (2006). .Experimentelle Analyse des Scherdeformation biaxial verstärkter Mehlagengesticke. PhD thesis. Dresden, Germany: Technische Universität Dresden.

Pannier, Y. (2006). Identification de paramètres élastoplastiques par des essais statiquement indéterminés : mise en oeuvre expérimentale et validation de la méthode des champs virtuels. PhD thesis, Paris (France): Arts et Métiers ParisTech.

Peirce, F. T. (1930). The "handle" of cloth as a measurable quantity. *Journal of the Textile Institute Transactions.* 21, T377–T416. doi:10.1080/19447023008661529

Pickett, A. K. (2018). *Process and mechanical modelling of engineering composites.* Stuttgart, Germany: IFB University of Stuttgart.

Rashidi, A., Montazerian, H., Yesilcimen, K., and Milani, A. (2020). Experimental characterization of the inter-ply shear behavior of dry and prepreg woven fabrics: significance of mixed lubrication mode during thermoset composites processing. *Compos. Appl. Sci. Manuf.* 129, 105725. doi:10.1016/j.compositesa.2019.105725

Rosen, B. (1964). Mechanics of composite strengthening. in *Seminar of the American society for metals.* Cleveland, OH: Metal Parks, 37–75.

Sachs, U., Akkerman, R., and Haanappel, S. P. (2014). Bending characterization of UD composites. *Key Eng. Mater.* 611-612, 399–406. doi:10.4028/www.scientific.net/KEM.611-612.399

Sachs, U., Fetfatsidis, K. A., Schumacher, J., Ziegmann, G., Allaoui, S., Hivet, G., et al. (2012). A friction-test benchmark with Twintex PP. *Key Eng. Mater.* 504-506, 307–312. doi:10.4028/www.scientific.net/KEM.504-506.307

Senner, T., Kreissl, S., Merklein, M., Meinhardt, M., and Lipp, A. (2014). Bending of unidirectional non-crimp-fabrics: experimental characterization, constitutive modeling and application in finite element simulation. *J. Inst. Eng. Prod.* 9, 1–10. doi:10.1007/s11740-014-0568-5

Soteropoulos, D., Fetfatsidis, K. A., Sherwood, J. A., and Langworthy, J. (2011). Digital method of analyzing the bending stiffness of non-crimp fabrics. AIP Conference Proceedings, 1353, 913–917. doi:10.1063/1.3589632

Stribeck, R. (1903). *Die wesentlichen Eigenschaften der Gleit- und Rollenlager.* Berlin, Germany: Springer.

Ten Thije, R. H. W., Akkerman, R., Ubbink, M., and Van Der Meer, L. (2011). A lubrication approach to friction in thermoplastic composites forming processes. *Composites Part A : Applied Science and Manufacturing.* 42, 950–960. doi:10.1016/j.compositesa.2011.03.023

Trejo, E. A., Ghazimoradi, M., Butcher, C., and Montesano, J. (2020). Assessing strain fields in unbalanced unidirectional non-crimp fabrics. *Compos. Appl. Sci. Manuf.* 130, 105758. doi:10.1016/j.compositesa.2019.105758

Vanclooster, K., Lomov, S. V., and Verpoest, I. (2010). Simulation of multi-layered composites forming. *Int. J. Material Form.* 3, 695–698. doi:10.1007/s12289-010-0865-2

Voce, E. (1955). A practical strain-hardening function. *Metallurgica.* 51, 219–226.

Wang, P., Hamila, N., and Boisse, P. (2013). Thermoforming simulation of multilayer composites with continuous fibres and thermoplastic matrix. *Compos. B Eng.* 52, 127–136. doi:10.1016/j.compositesb.2013.03.045

Xiong, H., Hamila, N., and Boisse, P. (2019). Consolidation modeling during thermoforming of thermoplastic composite prepregs. *Materials.* 12, 2853. doi:10.3390/ma12182853

Yuksekkay, M. E. (2009). More about fibre friction and its measurements. *Textil. Prog.* 41 (3), 141–193. doi:10.1080/00405160903178591

Zhu, B., Yu, T. X., Zhang, H., and Tao, X. M. (2011). Experimental investigation of formability of commingled woven composite preform in stamping operation. *Compos. B Eng.* 42, 289–295. doi:10.1016/j.compositesb.2010.05.006

Conflict of Interest: LB was employed by the company Hexcel Reinforcements SASU.

The remaining authors declare that the research was conducted in the absence of any commercial or financial relationships that could be construed as a potential conflict of interest.

frontiers in Materials

ORIGINAL RESEARCH
published: 12 November 2020
doi: 10.3389/fmats.2020.572995

An Incremental Cohesive Law for Delamination Under a Mixed Mode Loading

Man Zhu[1,2], *Larissa Gorbatikh*[2]* *and Stepan V. Lomov*[2,3]

[1]State Key Laboratory of Mechanics and Control of Mechanical Structures, Nanjing University of Aeronautics and Astronautics, Nanjing, China, [2]Department of Materials Engineering, KU Leuven, Leuven, Belgium, [3]Center for Design, Manufacturing and Materials, Skolkovo Institute of Science and Technology, Moscow, Russia

Cohesive zone models rely on the formulation of a cohesive constitutive law. The latter describes the relation between displacement and traction in a cohesive element at an integration point. Cohesive constitutive laws in the presence of opening and shearing modes are less studied in comparison with those formulated for a single mode, particularly when the mode mixity changes. The mode mixity at an integration point is determined by the load history at the point. In this study, a formulation of the cohesive constitutive law is proposed for a mixed mode loading condition with the ability to deal with the variation in mode mixity. The proposed law is constructed incrementally and takes into account the load history. The validation is performed by simulating delamination in carbon fiber/epoxy composites in the mixed-mode bending test that is commonly used to characterize the inter-laminar fracture toughness. Although the mode mixity is fixed in this test at the specimen level, it varies locally at the element level. Cohesive constitutive laws proposed in the literature predict macroscopic delamination behavior that is dependent on the strength of the interface, while, according to the analysis of linear elastic fracture mechanics, the dependence is expected to be only on the fracture toughness. Predictions with the current formulation, where the cohesive law is updated incrementally, show low sensitivity to the interface strength. The structural response simulated with it had a good agreement with the analytical solution of linear elastic fracture mechanics.

Keywords: cohesive law, delamination, mixed mode, composite, finite element method

OPEN ACCESS

Edited by:
Patricia Krawczak,
IMT Lille Douai, France

Reviewed by:
Frédéric Lachuad,
Institut Supérieur de l'Aéronautique et de l'Espace (ISAE-SUPAERO), France
Paolo S. Valvo,
University of Pisa, Italy

***Correspondence:**
Larissa Gorbatikh
larissa.gorbatikh@kuleuven.be

Specialty section:
This article was submitted to Mechanics of Materials, a section of the journal Frontiers in Materials

Received: *15 June 2020*
Accepted: *02 October 2020*
Published: *12 November 2020*

Citation:
Zhu M, Gorbatikh L and Lomov SV (2020) An Incremental Cohesive Law for Delamination Under a Mixed Mode Loading. Front. Mater. 7:572995. doi: 10.3389/fmats.2020.572995

INTRODUCTION

Laminated materials can experience de-cohesion or delamination under different loading conditions, from simple single mode to more complex mixed mode conditions. The mixed mode conditions, where both normal and shear tractions act on the inter-laminar interface, are, for example, present in structures that are curved, like flanges of the ribs in aircraft wings (Gözlüklü and Coker, 2012; Gozluklu et al., 2015). The mixed mode can also develop in plane structures subjected to simple loading conditions after the onset of delamination, like in the case of laminated plates subjected to compression after impact (González et al., 2012). Modeling tools facilitate design of reliable structures.

Cohesive zone models (CZMs) have successfully proven their efficiency in modeling interface behavior in laminated materials including fibre-reinforced composites (Alfano and Crisfield, 2001; Borg et al., 2002; Turon et al., 2006; Joki et al., 2016; Jensen et al., 2019; Liu et al., 2019). The concept

of CZMs was originally proposed by Barenblatt (Barenblatt, 1959; Barenblatt, 1962) and Dugdale (Dugdale, 1960) as an approach to depicting crack formation and development. In CZMs, cohesive elements are placed in the potential crack path, and the propagation of a crack is described by the behavior of the integration points in cohesive elements. In CZMs, the damage status of the integration points develops in a progressive way controlled by a cohesive constitutive law. This cohesive constitutive law is formulated as a relationship between the traction and the displacement jump caused by normal and shear tractions acting at the interface. An accurate cohesive constitutive law is essential for simulating delamination behavior correctly. Cohesive laws for single modes (i.e., pure mode I and pure mode II) have been studied extensively with many formulations available. Modeling of delamination under a mixed-mode condition is still an active research subject. In some studies it is proposed to treat the mixed mode as a special case of single modes and to formulate their cohesive laws in the way it is done for single modes. An additional precondition is often assumed that the mode mixity should be fixed during the whole loading history. However the fixed mode mixity is hardly ensured in practical situations. Even if the mode mixity is considered to be fixed at the macro-scale, it may vary locally, like in the mixed-mode bending (MMB) test which is designed to characterize inter-laminar fracture toughness of the composite at a fixed mode mixity at macro-scale (ASTM D6671, 2013). Moreover, whether the constant mode mixity at the macro-scale can be ensured in MMB test has been questioned in the literature (Bennati et al., 2013a; Bennati et al., 2013b). Detailed simulations of the MMB test have also shown that the mode mixity varies at different integration points of cohesive elements and that even at the same integration point the mode mixity changes as the test progresses (Turon et al., 2010; Harper et al., 2012; De Moura et al., 2016). Therefore, the question rises "How to include variations in mode mixity into the cohesive constitutive law?".

In the state-of-the-art simulations (Turon et al., 2006; Turon et al., 2010; Turon et al., 2018; Jensen et al., 2019), a popular way to consider the variable mode mixity is based on a set of pre-defined values of mode mixities. Firstly, different cohesive constitutive laws are defined for these fixed mode mixities. Then, during the loading history each integration point is checked for its mode mixity and once the latter is changed the cohesive law acting there is revised to account for the new mode mixity. By using this methodology, a strong assumption is made, namely that the damage evolution at the integration point under variable mode mixity is the same as the one with a fixed mode mixity. This means the effect of the loading history is not considered.

Another issue with the mixed-mode simulation by using existing cohesive constitutive laws is that the force-displacement relation in the MMB test at macro-scale depends on the inter-laminar strength of cohesive elements. This conflicts with the linear elastic fracture mechanics (LEFM) analysis according to which delamination is only controlled by the fracture toughness of the interface. Indeed, let us take a look at an analytical expression of the force-displacement relation in the MMB test (as shown in **Figure 1**) (ASTM D6671, 2013):

$$U_{\text{lever}} = \frac{P_{\text{lever}}}{8bE_{11}h^3L^2}\left[4(3c-L)^2(a+h\chi)^3 + (c+L)^2\left(2L^3 + 3(a+0.42h\chi)^3\right)\right] \quad (1)$$

$$P_{\text{lever}} = \sqrt{\frac{16G_c b^2 E_{11} h^3 L^2}{12(3c-L)^2(a+h\chi)^2 + 9(c+L)^2(a+0.42h\chi)^2}} \quad (2)$$

$$\chi = \sqrt{\frac{E_{11}}{11G_{13}}\left\{3 - 2\left(\frac{\Gamma}{1+\Gamma}\right)^2\right\}},\ \Gamma = 1.18\frac{\sqrt{E_{11}E_{22}}}{G_{13}} \quad (3)$$

where U_{lever} and P_{lever} are the applied displacement on MMB specimen and corresponding reaction force; c and L are the geometry parameters of the test set-up; b and h are the width and thickness of the specimen; a is the crack length; E_{11}, E_{22}, and G_{13} are the longitudinal Young's modulus, transverse Young's modulus and shearing modulus of the composite laminates, respectively; G_c is the fracture toughness of the inter-laminar interface. From **Eqs 1–3**, it can be seen that once the test set-up and specimen geometry are fixed, the structural response of the specimen is only determined by the inter-laminar fracture toughness and has no dependency on the inter-laminar strength. However, this is not the case when the MMB test was simulated with the existing mixed-mode cohesive constitutive law (Turon et al., 2010; Harper et al., 2012). More specifically, different load-displacement relations were obtained

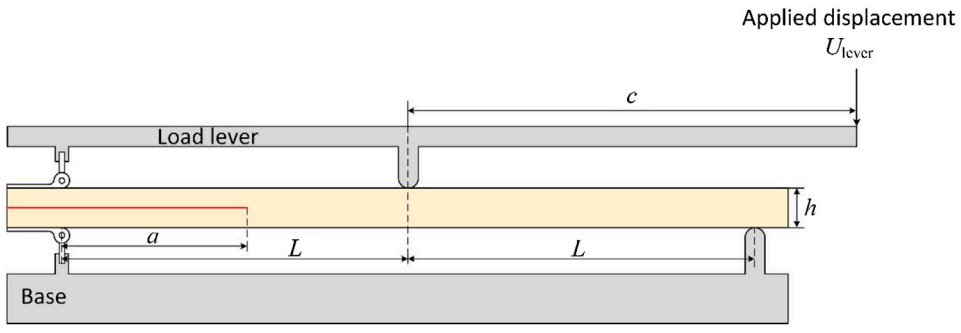

FIGURE 1 | Apparatus of the MMB test.

for different values of the inter-laminar strength in cohesive elements. The application of this model relies on the selection of a specific value of the inter-laminar strength.

To get rid of this inter-laminar strength dependency, Turon et al. revised their original cohesive constitutive law twice (Turon et al., 2010; Turon et al., 2018), which is one of the mostly used CZMs for simulating delamination in composite structures. In their first update (Turon et al., 2010), a relationship between the pure mode I and mode II inter-laminar strength was given:

$$\frac{\sigma_{20}}{\sigma_{10}} = \sqrt{\frac{G_{c\_II}}{G_{c\_I}}} \tag{4}$$

where σ_{10} and σ_{20} are pure mode I and II inter-laminar strength, respectively; G_{c_I} and G_{c_II} are inter-laminar fracture toughness under pure mode I and II loading conditions, respectively. Only when this relationship is satisfied, the dependence of MMB test's structural response on the inter-laminar strength can be eliminated. However, the mandatory requirement of the relationship between pure mode I and II inter-laminar fracture toughness and strength values makes no sense from a physical point of view. This relationship was then abandoned in the second update by Turon et al. (2018). Instead, a mode-dependent stiffness was adopted as a function of mode mixity, namely

$$K_m = (1 - B)K_{\mathrm{I}} + BK_{\mathrm{II}} \tag{5}$$

where K_{I}, K_{II} and K_m are the stiffness used in the cohesive law for pure mode I, mode II and mixed-mode with a mode mixity of B, respectively (see details of the cohesive law definition in the next section). With this modified formulation of the cohesive constitutive law, the dependence of the macro-scale response on the inter-laminar strength can be eliminated but only during the delamination propagation after the peak load. The peak load is still affected by the inter-laminar strength, which is against the conclusion of the study of Lu et al. (2019). Lu et al. systematically analyzed the effect of inter-laminar strength on the delamination behavior, and it was found that in the presence of a stress concentration, such as a pre-delamination, the structural response is strength independent including both peak load and the response in the propagation part.

In this paper, a new formulation of a cohesive constitutive law is proposed for simulating delamination with variable mode mixity. The constitutive law is constructed incrementally based on the deformation, traction and mode mixity at the integration point obtained from the previous simulation step. In this way the effect of loading history is included in the cohesive law. For simplicity, the formulation of the proposed cohesive constitutive law is firstly explained for a pure mode condition in *Bi-Linear Cohesive Constitutive Law in the Case of a Single Mode*, and then extended to the variable mode mixity cases in *Cohesive Constitutive Law for Variable Mode Mixity*. The developed cohesive constitutive law is validated by simulating MMB test, and the results are shown in *Results of FEM Validation and Discussion*. Discussions about the mixed-mode constitutive law is also presented in the same section. Finally, *Conclusions and Outlook* summarizes conclusions and highlights of this study.

BI-LINEAR COHESIVE CONSTITUTIVE LAW IN THE CASE OF A SINGLE MODE

A classical bilinear cohesive law is adopted in this study. It has been utilized many times in the literature both for the simulation of static and fatigue delamination due to its simplicity in implementation (Alfano and Crisfield, 2001; Turon et al., 2006; Kawashita and Hallett, 2012; Nojavan et al., 2016). The bilinear cohesive law developed by Turon (Turon et al., 2006) is widely used for modeling delamination in composite structures, and serves as basis in this study.

In the three-dimensional formulation, the displacement jump δ_i and traction σ_i of the integration point in cohesive element have three components, one indicating opening deformation and the other two describing shearing deformation. However, in the simulation of a pure mode, only one component of the displacement jump is non-zero and the cohesive law can be simplified to the relation between two scalars: displacement jump and traction for the relevant mode. The bilinear cohesive relation between the jump and the traction consists of two sections: an initial linearly elastic response, which is followed by linear softening. **Figure 2A** gives a sketch of the bilinear cohesive law. The integration point behaves linearly-elastically with the initial stiffness, K_0, until the initial displacement δ_0 is

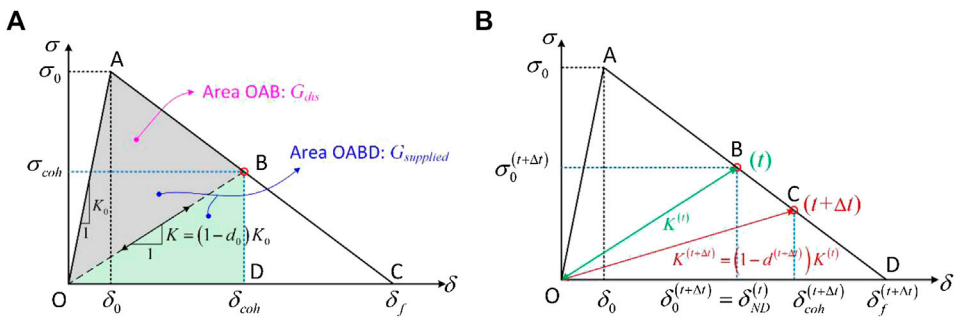

FIGURE 2 | Sketch of the bilinear cohesive law: **(A)** damage variable d_0; **(B)** incremental type damage variable $d^{(t+\Delta t)}$.

reached, after which the interface traction σ decreases as the displacement jump increases. The initial displacement, δ_0, is the displacement jump corresponding to the inter-laminar strength of the integration points in cohesive element σ_0: $\delta_0 = \sigma_0/K_0$. A damage variable, d_0, is defined as the degradation of the initial stiffness, $K = (1 - d_0)\, K_0$. The integration point becomes traction free, when displacement jump reaches the critical value δ_f.

The traction at the integration point σ_{coh} can be determined as a function of the displacement jump, δ_{coh}, and damage variable, d_0:

$$\sigma_{\text{coh}} = (1 - d_0) K_0 \delta_{\text{coh}} \tag{6}$$

The damage variable, d_0, is equal to zero in the elastic region OA, and increases from zero at point A to unity at point C in the softening region AC:

$$d_0 = \begin{cases} 0, & 0 \le \delta_{\text{coh}} < \delta_0, \\ \dfrac{\delta_f (\delta_{\text{coh}} - \delta_0)}{\delta_{\text{coh}} \left(\delta_f - \delta_0\right)}, & \delta_0 \le \delta_{\text{coh}} < \delta_f, \\ 1, & \delta_f \le \delta_{\text{coh}}. \end{cases} \tag{7}$$

The area under the traction-displacement jump curve (i.e., area OAC in **Figure 2A**) equals G_c, which is the critical energy release rate of the integration point. G_c is also interpreted as the inter-laminar fracture toughness. The displacement at which the element becomes traction free (sometimes referred as failure displacement) can be calculated as follows:

$$\delta_f = \frac{2G_c}{K_0 \delta_0} \tag{8}$$

The strain energy release rate (SERR), which has been supplied to the cohesive element up to the moment when the displacement jump reaches the value of δ_{coh}, noted here as G_{sup}, is equal to the area under the cohesive law, as shown by area OABD in **Figure 2A**:

$$G_{\text{sup}} = \int_0^{\delta_{\text{coh}}} \sigma(\delta) \mathrm{d}\delta \tag{9}$$

The energy dissipated due to accumulated damage, G_{dis}, is represented by area OAB in **Figure 2A**. It is the amount of energy that cannot be recovered after unloading: $G_{\text{dis}} = G_{\text{sup}} - (1/2) K \delta_{\text{coh}}^2$, and a new traction free surface (in other words, a crack) will be created once it is equal to the fracture toughness, G_c.

Based on the traditional bilinear constitutive law, we propose an incremental type of damage variable $d^{(t+\Delta t)}$, which describes reduction of stiffness $K^{(t)}$ to $K^{(t+\Delta t)}$ (**Figure 2B**). In the following analysis, the superscripts (t) and $(t+\Delta t)$ indicate the variables that are obtained at time t and $t+\Delta t$, respectively. The definition of the incremental type of damage variable allows the cohesive constitutive law to be updated in an incremental way which will be beneficial to the simulation of the case with a variable mode mixity. At simulation time t, the residual stiffness of the cohesive element is $K^{(t)}$, as simulation time (deformation) progresses the integration point behaves following the constitutive curve O-B-D, as shown in **Figure 2B**. No reduction of $K^{(t)}$ happens until the displacement reaches $\delta_0^{(t+\Delta t)}$ at time $t+\Delta t$, followed by which the incremental damage variable, $d^{(t+\Delta t)}$, increases from zero to one at $\delta_f^{(t+\Delta t)}$. The area under the constitutive curve O-B-D, is the residual SERR to be dissipated after time t, and its value is the difference between the fracture toughness and dissipated SERR: $G_{\text{res}}^{(t+\Delta t)} = G_c - G_{\text{dis}}^{(t)}$. It is the total energy to be dissipated from time t till the integration point becomes traction free.

Here we define a parameter, "no-damage displacement" at time t, $\delta_{ND}^{(t)}$, and its value is obtained at the last simulation step from time $t - \Delta t$ to t:

$$\delta_{ND}^{(t)} = \begin{cases} \delta_{\text{coh}}^{(t)}, & d^{(t)} > 0, \\ \delta_0^{(t)}, & d^{(t)} = 0, \end{cases} \tag{10}$$

where $d^{(t)}$ is the damage accumulated between time $t - \Delta t$ and t; $\delta_{\text{coh}}^{(t)}$ and $\delta_0^{(t)}$ are the displacement jump of the cohesive element and initial displacement at time t, respectively. The "no-damage displacement," $\delta_{ND}^{(t)}$, means that if the element is unloaded and reloaded from time t, no further reduction of residual stiffness will happen before the displacement jump reaches this value. It is used for determining the initial displacement for the next simulation step, i.e., from time t to $t + \Delta t$: $\delta_0^{(t+\Delta t)} = \delta_{ND}^{(t)}$. The traction level corresponding to this displacement jump is then defined as "no-damage traction":

$$\sigma_{ND}^{(t)} = K^{(t)} \delta_{ND}^{(t)} \tag{11}$$

The initial value of initial displacement at $t = 0$, $\delta_0^{(t=0)}$ is equal to δ_0 that is corresponding to the inter-laminar strength σ_0. Based on the constitutive law at time $t + \Delta t$, i.e., curve OBD in **Figure 2B**, the displacement at which the traction becomes zero, $\delta_f^{(t+\Delta t)}$, can be determined by the residual SERR $G_{\text{res}}^{(t+\Delta t)}$, stiffness $K^{(t)}$, and initial displacement $\delta_0^{(t+\Delta t)}$:

$$\delta_f^{(t+\Delta t)} = \frac{2G_{\text{res}}^{(t+\Delta t)}}{K^{(t)} \delta_0^{(t+\Delta t)}} \tag{12}$$

The incremental damage variable, d, stiffness, K, and traction, σ, at time $t + \Delta t$ can finally be updated as:

$$d^{(t+\Delta t)} = \begin{cases} 0, & 0 \le \delta_{\text{coh}}^{(t+\Delta t)} < \delta_0^{(t+\Delta t)}, \\ \dfrac{\delta_f^{(t+\Delta t)} \left[\delta_{\text{coh}}^{(t+\Delta t)} - \delta_0^{(t+\Delta t)}\right]}{\delta_{\text{coh}}^{(t+\Delta t)} \left[\delta_f^{(t+\Delta t)} - \delta_0^{(t+\Delta t)}\right]}, & \delta_0^{(t+\Delta t)} \le \delta_{\text{coh}}^{(t+\Delta t)} < \delta_f^{(t+\Delta t)}, \\ 1, & \delta_f^{(t+\Delta t)} \le \delta_{\text{coh}}^{(t+\Delta t)}. \end{cases} \tag{13a}$$

$$K^{(t+\Delta t)} = \left(1 - d^{(t+\Delta t)}\right) K^{(t)} \tag{13b}$$

$$\sigma_{\text{coh}}^{(t+\Delta t)} = K^{(t+\Delta t)} \delta_{\text{coh}}^{(t+\Delta t)} \tag{13c}$$

With the definition of the incremental type damage variable, the update of constitutive curve is conducted in an incremental

way: it is only determined by the constitutive curve at the last simulation step, and the effect of history loading is included.

COHESIVE CONSTITUTIVE LAW FOR VARIABLE MODE MIXITY

In the simulation of mixed-mode delamination, the displacement jump and traction cannot be treated as scalars, and therefore the displacement jump and traction in the cohesive constitutive equation are considered as vectors with three components. With the definition of incremental damage variable, the constitutive equation for a three-dimensional cohesive element can be expressed as follows:

$$\sigma_i^{(t+\Delta t)} = K_{ij}^{(t+\Delta t)}\delta_j^{(t+\Delta t)}, \quad i = 1,2,3; \quad j = 1,2,3 \tag{14a}$$

$$K_{ij}^{(t+\Delta t)} = \left[1 - d^{(t+\Delta t)}\left(1 + \overline{\delta}_{1j}\frac{\langle -\delta_j^{(t+\Delta t)}\rangle}{\delta_j^{(t+\Delta t)}}\right)\right]\overline{\delta}_{ij}K^{(t)} \quad i = 1,2,3; \quad j = 1,2,3 \tag{14b}$$

Where subscript i and j denote the mode of deformation: $i, j = 1$-opening mode (Mode I), $i, j = 2$-shearing mode (Mode II) and $i, j = 3$-shearing mode (Mode III); δ_j ($j = 1, 2, 3$) is the displacement jump for the corresponding modes; σ_i ($i = 1, 2, 3$) is the corresponding traction in each single mode; $K_{ij}^{(t+\Delta t)}$ is the stiffness tensor describing the relation between displacement jump vector and traction vector; $\overline{\delta}_{ij}$ is the Kronecker delta; $\langle \cdot \rangle$ is the Macaulay bracket defined as $\langle x \rangle = 1/2(|x| + x)$ to consider no damage under compression. The traction vector, $\sigma_i^{(t+\Delta t)}$, is determined by the displacement jump vector, $\delta_j^{(t+\Delta t)}$, the value of residual stiffness at time t, $K^{(t)}$, and incremental damage variable $d^{(t+\Delta t)}$ which is determined by **Eq. 13a**.

With the three-dimensional constitutive law, the mixed-mode deformation can be considered, as a mixture of deformations under different (pure) modes. The isotropic properties are assumed for shear modes (i.e., the plane of Mode II and III), and a displacement jump in general shear mode is defined as the resultant of the two shearing displacement jump:

$$\delta_s = \sqrt{\delta_2^2 + \delta_3^2} \tag{15}$$

The corresponding resultant shear traction is calculated as:

$$\sigma_s = \sqrt{\sigma_2^2 + \sigma_3^2} \tag{16}$$

An equivalent mixed-mode displacement jump is then defined as the resultant of opening and shearing displacement jump:

$$\delta_m = \sqrt{\langle \delta_1 \rangle^2 + \delta_s^2} \tag{17}$$

The mode mixity B is defined as the ratio of supplied SERR in shear mode to the total supplied SERR:

$$B = \frac{G_{s\_\mathrm{sup}}}{G_{\mathrm{sup}}}, \tag{18}$$

where G_{sup} is the total supplied SERR under mixed-mode loading, equal to the sum of supplied SERR in mode I, G_{1_sup}, and shear mode G_{s_sup}.

Different from the one-dimensional constitutive law for pure mode simulation, under the mixed-mode load condition, the constitutive law is three-dimensional as shown in **Figure 3A** by the black curve. It can be decomposed into two independent constitutive curves, representing the cohesive behavior under mode I and the resultant behavior under shear modes, respectively, as shown in **Figure 3** by the red and green curves. The subscripts 1, s, and m in **Figure 3** represent mode I, general shear mode and mixed-mode, respectively.

The development of the cohesive law in the mixed-mode space relies on the cohesive behavior in mode I and the resultant shear mode behavior. **Figures 3B,C** depicts the decomposed constitutive laws. The areas of the red regions in **Figures 3B,C** are the dissipated SERR at time t in mode I, $G_{1\_\mathrm{dis}}^{(t)}$, and shear mode, $G_{s\_\mathrm{dis}}^{(t)}$, which are the SERR dissipated in each mode caused by the historical loading. The supplied SERR at time t, $G_{\mathrm{sup}}^{(t)}$, is the sum of the dissipated SERR and recoverable SERR:

$$G_{i\_\mathrm{sup}}^{(t)} = G_{i\_\mathrm{dis}}^{(t)} + \frac{1}{2}K^{(t)}\left[\delta_i^{(t)}\right]^2, \qquad i = 1, s \tag{19}$$

At simulation time $t + \Delta t$ the displacement jump and traction are updated based on the cohesive law, and the new dissipated SERR is calculated as the green area in **Figures 3B,C**, and therefore the dissipated SERR at $t + \Delta t$ is updated as:

$$G_{i\_\mathrm{dis}}^{(t+\Delta t)} = \begin{cases} G_{i\_\mathrm{dis}}^{(t)} + \frac{1}{2}\left[K^{(t)} - K^{(t+\Delta t)}\right]\delta_{i0}^{(t+\Delta t)}\delta_i^{(t+\Delta t)}, & d^{(t+\Delta t)} > 0 \\ G_{i\_\mathrm{dis}}^{(t)}, & d^{(t+\Delta t)} = 0 \end{cases}, \quad i = 1, s \tag{20}$$

The supplied SERR at time $t + \Delta t$ is equal to the dissipated SERR at time $t + \Delta t$ plus the area of blue region in **Figures 3B,C**:

$$G_{i\_\mathrm{sup}}^{(t+\Delta t)} = G_{i\_\mathrm{dis}}^{(t+\Delta t)} + \frac{1}{2}K^{(t+\Delta t)}\left[\delta_i^{(t+\Delta t)}\right]^2, \qquad i = 1, s \tag{21}$$

The mode mixity at time $t + \Delta t$ is then determined by **Eq. 18**. For the mixed-mode cases with only mode I and mode II deformation, the critical SERR or fracture toughness under such a mode mixity can be obtained by applying B-K criterion (Benzeggagh and Kenane, 1996):

$$G_{c\_m}^{(t+\Delta t)} = G_{c\_\mathrm{I}} + \left(G_{c\_\mathrm{I}} - G_{c\_\mathrm{II}}\right)\left[B^{(t+\Delta t)}\right]^{\eta} \tag{22}$$

where G_{c_I} and G_{c_II} are the fracture toughness for pure mode I and mode II, and η is a fitting parameter fitted from the experimental results. The validation case in this study is a MMB test, where only the mixture of mode I and II is considered, and therefore the use of B-K criterion is feasible. For those interested to use the proposed mixed-mode cohesive constitutive law to the mixture of all three modes, a different criterion for calculating the fracture toughness may be needed or validation of the B-K criterion first.

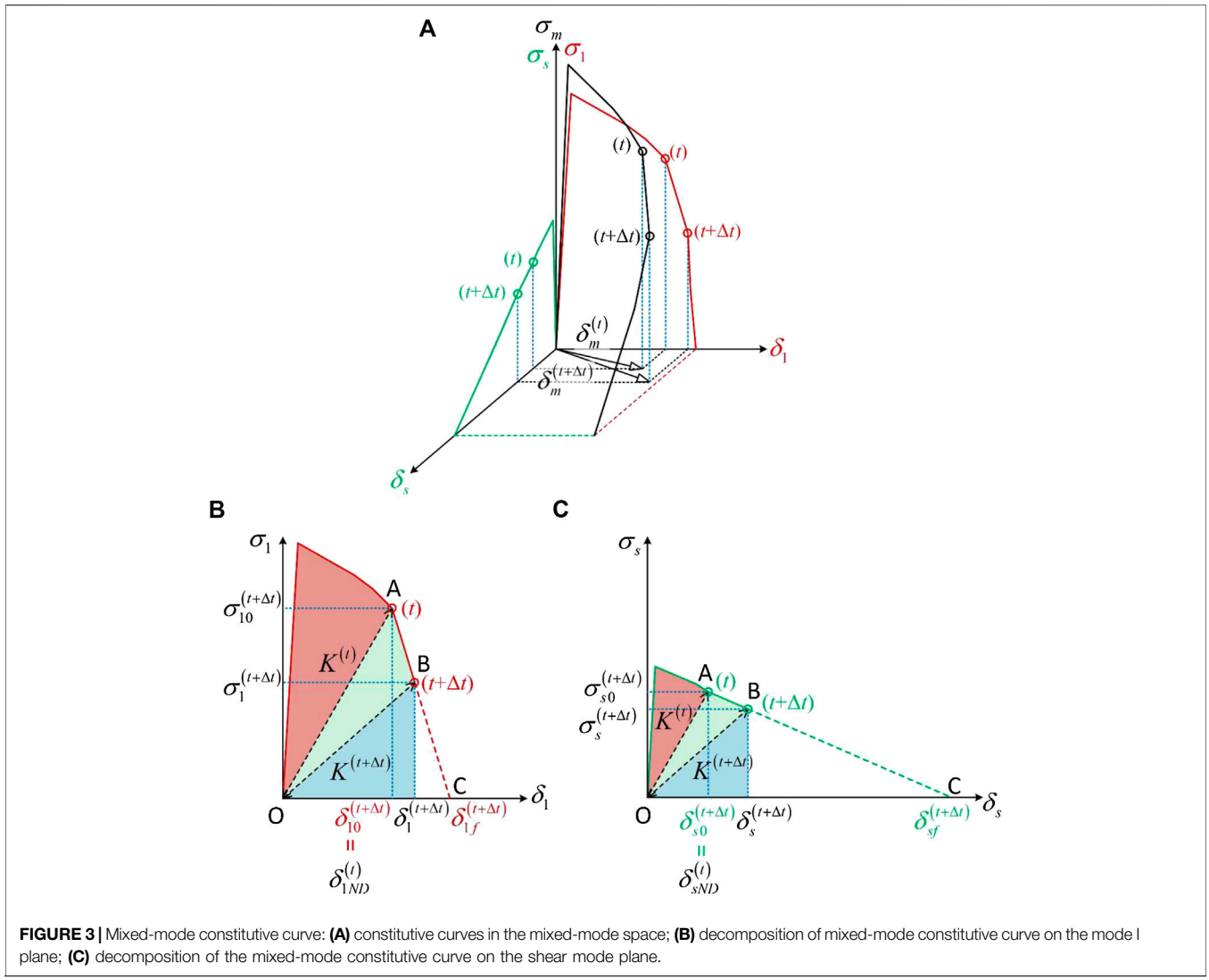

FIGURE 3 | Mixed-mode constitutive curve: **(A)** constitutive curves in the mixed-mode space; **(B)** decomposition of mixed-mode constitutive curve on the mode I plane; **(C)** decomposition of the mixed-mode constitutive curve on the shear mode plane.

The cohesive constitutive law for each single mode should be updated based on the latest mode mixity, i.e., $B^{(t+\Delta t)}$. However, the determination of $B^{(t+\Delta t)}$ depends on the updated cohesive law, as described by **Eqs 18–21**. To avoid the complicated iteration, the mode mixity at time t, $B^{(t)}$, is used as the value of $B^{(t+\Delta t)}$ for updating the constitutive law at time $t + \Delta t$, with an assumption that the mode mixity B doesn't change significantly if the time increment Δt is small. The updated value of $B^{(t+\Delta t)}$ is then used to obtain the cohesive law for the next simulation step from time $t + \Delta t$ to time $t + \Delta t + \Delta t'$. The feasibility of this assumption will be discussed in the next section.

The cohesive law at time $t + \Delta t$ depends on three variables: the initial stiffness, $K^{(t)}$, initial displacement, $\delta_{i0}^{(t+\Delta t)}$ $(i = 1, s)$, and displacement at which traction becomes zero, $\delta_{if}^{(t+\Delta t)}$ $(i = 1, s)$. The initial stiffness, $K^{(t)}$, is obtained during the previous simulation step. Similar to the one-dimensional cohesive law, the initial displacement is equal to the no-damage displacement in each mode: $\delta_{i0}^{(t+\Delta t)} = \delta_{iND}^{(t)}$ $(i = 1, s)$. Their initial values at $t = 0$ are correspond to the interfacial strengths, σ_{i0} $(i = 1, s)$:

$$\delta_{i0}^{(t=0)} = \delta_{iND}^{(t=0)} = \frac{\sigma_{i0}}{K_0} \tag{23}$$

The displacement for the traction free condition is determined by the residual SERR $G_{\text{res}}^{(t+\Delta t)}$. At the time of $t+\Delta t$, with mode mixity $B^{(t+\Delta t)}$, if the integration point is loaded till traction is zero, the total SERR dissipated is equal to the fracture toughness $G_{c\_m}^{(t+\Delta t)}$ obtained from **Eq. 22**. On the other hand, the fracture toughness, $G_{c\_m}^{(t+\Delta t)}$, is the sum of critical SERR on mode I and shear mode under mode mixity of $B^{(t+\Delta t)}$:

$$\begin{aligned} G_{m\_c}^{(t+\Delta t)} &= G_{1\_c}^{(t+\Delta t)} + G_{s\_c}^{(t+\Delta t)}, \\ G_{1\_c}^{(t+\Delta t)} &= G_{1\_\text{dis}}^{(t)} + \frac{1}{2}K^{(t)}\delta_{10}^{(t+\Delta t)}\delta_{1f}^{(t+\Delta t)}, \\ G_{s\_c}^{(t+\Delta t)} &= G_{s\_\text{dis}}^{(t)} + \frac{1}{2}K^{(t)}\delta_{s0}^{(t+\Delta t)}\delta_{sf}^{(t+\Delta t)}, \end{aligned} \tag{24}$$

The ratio of the critical SERR for the shear modes to the (mixed-mode) fracture toughness also satisfies the definition of

mode mixity, which should be identical to the value calculated in **Eq. 18**:

$$B^{(t+\Delta t)} = \frac{G_{s\_c}^{(t+\Delta t)}}{G_{m\_c}^{(t+\Delta t)}} \tag{25}$$

Substituting **Eq. 25** into **Eq. 24**, the displacements at zero tractions for the opening and shear modes can be obtained as follows:

$$\begin{aligned}\delta_{1f}^{(t+\Delta t)} &= \frac{2\left[B^{(t+\Delta t)}G_{m\_c}^{(t+\Delta t)} - G_{1\_\mathrm{dis}}^{(t)}\right]}{K\delta_{10}^{(t+\Delta t)}},\\ \delta_{sf}^{(t+\Delta t)} &= \frac{2\left[\left(1-B^{(t+\Delta t)}\right)G_{m\_c}^{(t+\Delta t)} - G_{s\_\mathrm{dis}}^{(t)}\right]}{K\delta_{s0}^{(t+\Delta t)}}.\end{aligned} \tag{26}$$

Once the cohesive law on a single plane is determined, the cohesive law in the mixed-mode space (as shown in **Figure 3A**) can be updated. The mixed-mode initial displacement and failure displacement are calculated as the resultant of the ones under a single mode, namely $\delta_{m0}^{(t+\Delta t)} = \sqrt{\left(\delta_{10}^{(t+\Delta t)}\right)^2 + \left(\delta_{s0}^{(t+\Delta t)}\right)^2}$ and $\delta_{mf}^{(t+\Delta t)} = \sqrt{\left(\delta_{1f}^{(t+\Delta t)}\right)^2 + \left(\delta_{sf}^{(t+\Delta t)}\right)^2}$. Substituting these into **Eqs 13a** and **13b**, the incremental damage variable d and stiffness K at time $t + \Delta t$ can be obtained as in the one-dimensional cohesive law. The three-dimensional cohesive law is finally determined by **Eqs. 14a** and **14b**.

Besides the stiffness tensor, K_{ij}, defined by cohesive constitutive law in Eq. 14, a tangent tensor, $\dot{K}_{ij}$, describing the relation between the displacement increment and traction increment is needed in finite element simulation for predicting the next displacement increment. It is obtained by differentiating the cohesive constitutive law in Eq. (14):

$$\begin{aligned}\dot{\sigma}_i^{(t+\Delta t)} = &\left[1-d^{(t+\Delta t)}\right]\overline{\delta}_{ij}K^{(t)}\dot{\delta}_j^{(t+\Delta t)} - \left[\delta_j^{(t+\Delta t)} + \overline{\delta}_{1j}\langle -\delta_1^{(t+\Delta t)}\rangle\right]\\ &\overline{\delta}_{ij}K^{(t)}\dot{d}^{(t+\Delta t)},\\ &i,j = 1,2,3\end{aligned} \tag{27}$$

where $\dot{\delta}_j^{(t+\Delta t)}$, $\dot{\sigma}_i^{(t+\Delta t)}$ and $\dot{d}^{(t+\Delta t)}$ are derivatives of the displacement jump vector, traction vector and damage variable. The damage variable is a function of the displacement jump as shown by **Eq. 13a**, and therefore its derivative should be expressed as:

$$\dot{d}^{(t+\Delta t)} = \begin{cases} \dfrac{\delta_{mf}^{(t+\Delta t)}\delta_{m0}^{(t+\Delta t)}\left[\delta_i^{(t+\Delta t)} + \overline{\delta}_{1i}\langle -\delta_1^{(t+\Delta t)}\rangle\right]}{\left[\delta_{mf}^{(t+\Delta t)} - \delta_{m0}^{(t+\Delta t)}\right]\left(\delta_m^{(t+\Delta t)}\right)^3}\dot{\delta}_i^{(t+\Delta t)}, & \\ \qquad\qquad \delta_{m0}^{(t+\Delta t)} < \delta_m^{(t+\Delta t)} < \delta_{mf}^{(t+\Delta t)} & \\ 0, \qquad\qquad \delta_m^{(t+\Delta t)} < \delta_{m0}^{(t+\Delta t)} \quad or \quad \delta_m^{(t+\Delta t)} > \delta_{mf}^{(t+\Delta t)} & \end{cases} \tag{28}$$

Substituting **Eq. 28** into **Eq. 27**, the tangent tensor is calculated as:

$$\dot{K}_{ij} = \begin{cases} \left[1-d^{(t+\Delta t)}\right]\overline{\delta}_{ij}K^{(t)} - \overline{\delta}_{ij}K^{(t)}D_{ij}^{(t+\Delta t)}, & \delta_{m0}^{(t+\Delta t)} < \delta_m^{(t+\Delta t)} < \delta_{mf}^{(t+\Delta t)} \\ \left[1-d^{(t+\Delta t)}\right]\overline{\delta}_{ij}K^{(t)}, & \delta_m^{(t+\Delta t)} < \delta_{m0}^{(t+\Delta t)} \ or \ \delta_m^{(t+\Delta t)} > \delta_{mf}^{(t+\Delta t)} \end{cases},$$

$$D_{ij}^{(t+\Delta t)} = \frac{\left[\delta_j^{(t+\Delta t)} + \overline{\delta}_{1j}\langle -\delta_1^{(t+\Delta t)}\rangle\right]\left[\delta_i^{(t+\Delta t)} + \overline{\delta}_{1i}\langle -\delta_1^{(t+\Delta t)}\rangle\right]\delta_{mf}^{(t+\Delta t)}\delta_{m0}^{(t+\Delta t)}}{\left[\delta_{mf}^{(t+\Delta t)} - \delta_{m0}^{(t+\Delta t)}\right]\left(\delta_m^{(t+\Delta t)}\right)^3}. \tag{29}$$

RESULTS OF FEM VALIDATION AND DISCUSSION

The developed formulation of the mixed-mode cohesive constitutive law is tested by simulating mixed-mode delamination in fibre-reinforced composites. The incremental mixed-mode cohesive law was implemented into the cohesive element as a user-defined material (UMAT) subroutine in FE software Abaqus Implicit. In the simulation, 8-node solid element C3D8I was chosen for modeling composite plies and 8-node cohesive element COH3D8 was applied to the inter-laminar interface. The cohesive elements have a zero thickness.

FEM Model Description

The MMB test defined in ASTM D6671 (ASTM D6671, 2013) is frequently used to characterize the mixed-mode delamination behavior, as shown in **Figure 1**. The MMB test set-up is designed such as to combine Mode I and II loadings. The supplied SERR at the crack tip can be calculated as (Reeder and REWS, 1990):

$$\begin{aligned}G_I &= \frac{3P_{\mathrm{lever}}^2(3c-L)^2}{4b^2h^3L^2E_{1f}}(a+\chi h)^2,\\ G_{II} &= \frac{9P_{\mathrm{lever}}^2(c+L)^2}{16b^2h^3L^2E_{1f}}(a+0.42\chi h)^2,\\ G_m &= G_{\mathrm{I}} + G_{\mathrm{II}},\end{aligned} \tag{30}$$

where G_{I} and G_{II} are the Mode I and II components of SERR; G_m is the total mixed-mode SERR; P_{lever} is the applied load at the end of the load lever; a is the crack length; b and h are the specimen width and half thickness, L is the half span length, and c is the lever length, χ is the crack length correction parameter calculated by **Eq. 3**, and E_{1f} is the bending modulus of the composite:

$$E_{1f} = \frac{8(a+\chi h)^3 + \left[6(a+0.42\chi h)^3 + 4L^3\right](c+L)^2}{16L^2bh^3C} \tag{31a}$$

where C is the compliance obtained from the load displacement curve. The mode mixity B at the specimen level is then calculated as $B = G_{\mathrm{II}}/G_m$.

The displacement applied at the end of the specimen U_{end}, in the middle point U_{mid} and at the end of the load lever U_{lever} satisfy the following relation (Camanho et al., 2003):

$$U_{\mathrm{lever}} = \left(\frac{3c-L}{4L}\right)U_{\mathrm{end}} + \left(\frac{c+L}{L}\right)\left(U_{\mathrm{mid}} + \frac{1}{4}U_{\mathrm{end}}\right) \tag{32}$$

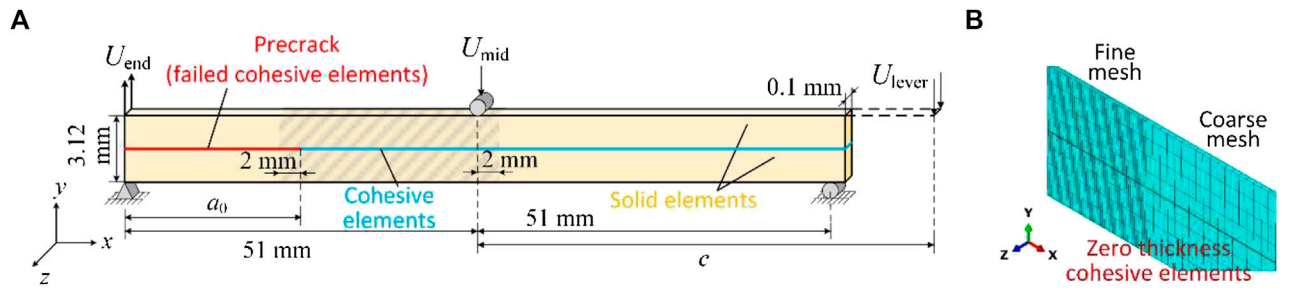

FIGURE 4 | Modeling MMB specimen in FEM: **(A)** geometry of the model and boundary conditions; **(B)** zoom-in view of the mesh.

TABLE 1 | Material properties of AS4/PEEK UD laminates (Turon et al., 2010).

Elastic properties	E_{11} (GPa)	$E_{22} = E_{33}$ (GPa)	$\nu_{12} = \nu_{13}$ (—)	ν_{23} (—)	$G_{12} = G_{13}$ (GPa)	G_{23} (GPa)
	122.7	10.1	0.25	0.45	5.5	3.7
Interlaminar properties	G_{c_I} (N/mm)	G_{c_II} (N/mm)	η		σ_{10} (MPa)	σ_{20} (MPa)
	0.969	1.719	2.0		80	100

TABLE 2 | Geometry parameters of MMB tests.

Mode mixity at specimen level $B = G_{II}/(G_I + G_{II})$	**20%**	**50%**	**80%**
Pre-crack a_0 (mm)	33.70	34.10	31.40
Lever length c (mm)	109.89	44.60	28.47

TABLE 3 | Four sets of values for the interlaminar strength used in the simulation.

Set no	**Set1**	**Set2**	**Set3**	**Set4**
σ_{10}^{static} (MPa)	80	80	80	30
σ_{s0}^{static} (MPa)	100	106.55	120	100

The model to simulate the MMB test is shown in **Figure 4**. To simplify the simulation, the displacement is applied at three positions respectively, instead of simulating the load lever explicitly. A constraint equation is defined to meet the boundary condition defined by **Eq. 32**, which can be viewed as the application of a virtual load lever.

The same geometry of MMB specimen simulated by Turon et al. (2018) is used in this study. It is 102.0 mm long and 3.12 mm thick with a precrack placed at the middle plane. The material properties of the laminate are listed in **Table 1**.

The details of the geometry model and applied boundary conditions are illustrated in **Figure 4**. A layer of cohesive elements with damage variable $d = 1$ are placed at the position of the pre-crack to simulate the traction free surface, which cannot hold tension or shear but compression to prevent the penetration between the upper and lower arms. The potential path for the delamination propagation is simulated as one layer of cohesive elements with the incremental cohesive constitutive law proposed in *Cohesive Constitutive Law for Variable Mode Mixity* and the input parameters of the law are reported in **Table 1**. The upper and lower arms of MMB specimen were simulated by solid elements. To accelerate the simulation, only one element is placed along the width direction of the specimen, i.e., z direction in **Figure 4**, and the width of the model was equal to the element width 0.1 mm. A state of generalized plane strain was assumed in the width direction: the front and back edges of the model were kept parallel during the deformation. This assumption means that the displacement δ_z is constant throughout the x-y plane of the model. A fine mesh along the x direction, was set at the end of the pre-crack and beginning of the potential delamination path, depicted as gray zone in **Figure 4**. The preliminary mesh sensitivity study shows that the simulation result is not sensitive to the mesh size when it is smaller than 0.05 mm. Therefore, a value of 0.05 was chosen as the refined mesh size. Coarse mesh was used in the other parts, where the element length was 0.2 mm. Four layers of solid elements were placed along the thickness direction, i.e., y direction, on the upper and lower arms respectively.

The MMB test with a mode mixity B at the specimen level equal to 20%, 50% and 80% are simulated. According to **30** and **31a**, the corresponding pre-crack length a_0 and lever length c are listed in **Table 2**. The displacement is applied at the end of the load lever U_{lever}, and the reaction force obtained at the same position is recorded.

Effect of the Inter-Laminar Strength

The analytical solution of the reaction force and displacement can be obtained by **Eqs 1–3** based on LEFM (ASTM D6671, 2013). Four sets of values for the inter-laminar strength were chosen in this study for testing its effect on the delamination growth at a specimen level (**Table 3**).

The inter-laminar strength in Set1 is used by Turon. et al. (2006) for carbon fiber/PEEK composite AS4/PEEK; the strengths in Set2 is determined to satisfy the condition defined by **Eq. 4** to eliminate the strength dependency in Turon's model (Turon et al., 2010); the values in Set3 and Set4 are chosen arbitrarily. The resulting

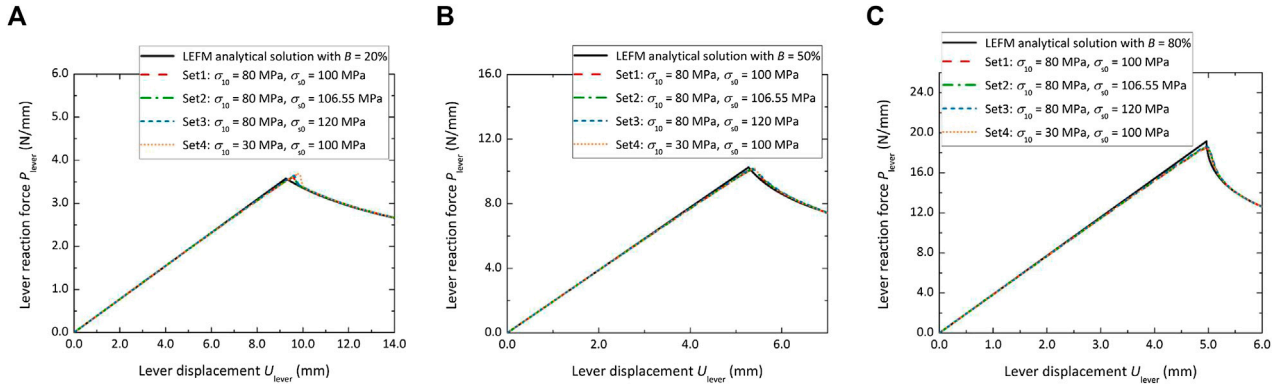

FIGURE 5 | The dependence of the load-displacement curve on the inter-laminar normal and shear strength with: **(A)** mode mixity of 20%; **(B)** mode mixity of 50%; **(C)** mode mixity of 80%.

reaction force-displacement curves with these different sets of the inter-laminar strength are plotted in **Figure 5**, where the reaction force at the lever end is expressed as the linear force along the width direction (i.e., z direction). No matter which set of inter-laminar strength is used, the simulation results meet with each other and all have a good agreement with the analytical solution under all the mode mixity load conditions. In the simulations of mode mixity B equal to 50% and 80%, there is no dependence of structural response on the selected inter-laminar strength. In the case of B = 20%, the selection of inter-laminar strength only has a minor effect on the maximum force, and the largest difference on the maximum force is 2.22%. The propagation behavior i.e., structural response after the maximum load, has no dependence on the strength value in this case. With the developed cohesive constitutive law, there is no need to select a special strength value for a correct mixed-mode delamination behavior.

In this study, the mode mixity is calculated using the supplied SERR, which is as the ratio between the supplied SERR for shearing to the total supplied SERR expressed by **Eq. 18**. This is identical to the definition of the mode mixity described in the MMB test standard (ASTM D6671, 2013). The definition of the mode mixity used by Turon et al. (2006) is based on the displacement jump: $B = \delta_s^2/\delta_m^2$, which gives very different predictions of the mode mixity from the supplied SERR based on **Eq. 18**. The difference becomes even more significant when the mode mixity at the integration point undergoes significant changes during the loading history. Only when the cohesive law for each single mode mixity has a similar shape, the two definitions of the mode mixity produce the same results. The difference in definition of mode mixity explains why Turon's model can only predict the correct structural response of MMB test when a specific relation between the mode I and shear mode inter-laminar strength is satisfied.

Variable Mode Mixity at the Integration Point

MMB test is designed for characterizing the mixed-mode delamination behavior under fixed mode mixity at specimen level. The mode mixity is determined by specimen geometry, the lever length c and material elastic properties, as depicted by **Eq. 30**. In the current simulations, all these parameters are fixed to obtain a mode mixity of 20%, 50% and 80% at specimen level. However, the mode mixity at the integration point does not stay constant during the loading process. This phenomenon has also been observed by Turon et al. (2010).

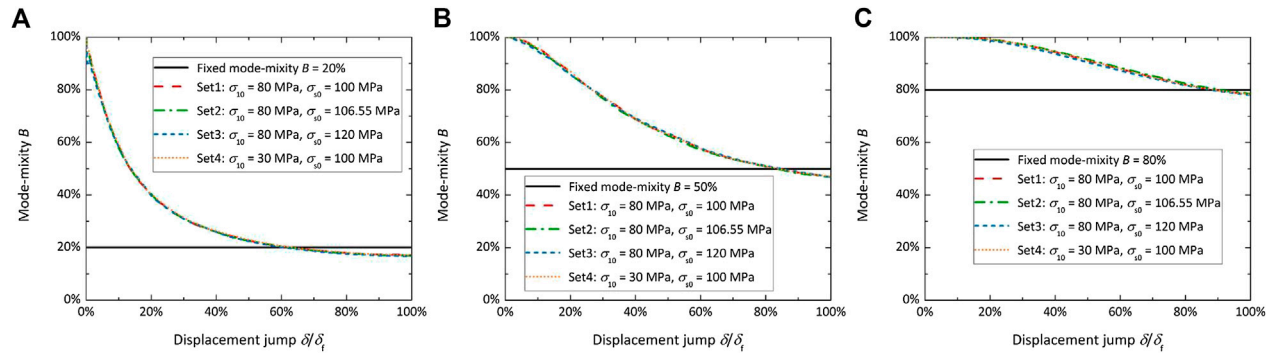

FIGURE 6 | Change of the mode mixity at the integration point which is 5 mm away from the pre-crack tip with: **(A)** mode mixity of 20%; **(B)** mode mixity of 50%; **(C)** mode mixity of 80%.

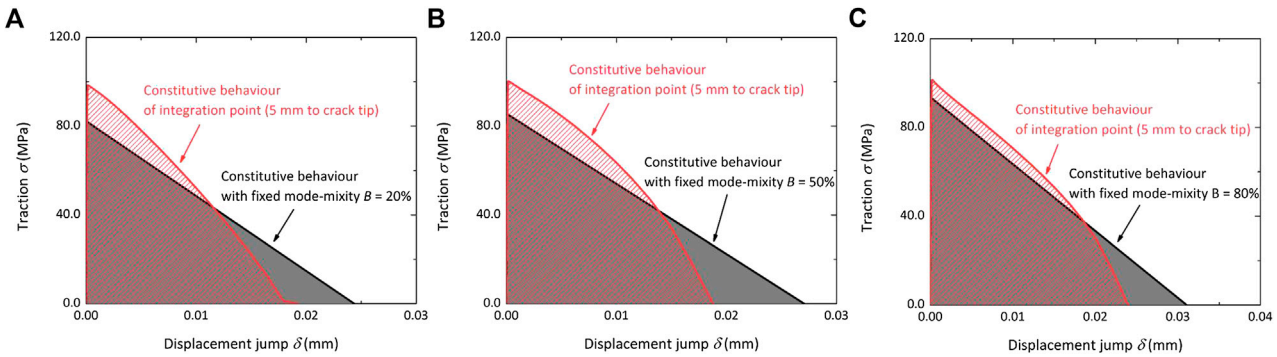

FIGURE 7 | Comparison of the constitutive law output from the integration point 5 mm away from the pre-crack tip to the one for the fixed mode mixity with: **(A)** mode mixity of 20%; **(B)** mode mixity of 50%; **(C)** mode mixity of 80%.

To illustrate how the mode mixity changes, it was evaluated at the integration point 5 mm away from a pre-crack tip during the whole loading history. It is shown in **Figure 6**, where the x axis is the normalized displacement jump (that includes both normal and shear displacements) at the integration point. The displacement jump is normalized by the value of the displacement jump when the traction at the integration point is zero. As shown in **Figure 6**, similarly to the observation of Turon et al. (2010), the mode mixity is not fixed as the beam theory at specimen level predicts. Instead it decreases monotonically approaching the level close to the one defined at the specimen level when the integration point becomes traction free, i.e., 20%, 50% and 80% for **Figures 6A–C**, respectively. Because the predicted structural behavior from the proposed cohesive law has little sensitivity to the inter-laminar strength, the discrepancy of mode mixity at the specimen level and at the integration point level cannot be attributed to the dependence of delamination behavior on the inter-laminar strength, which was used to explain the dependence of predicted load-displacement on the selection of the inter-laminar strength in Turon's study (Turon et al., 2010).

Mixed-Mode Constitutive Law at Integration Point

Due to the variable mode mixity at the integration point, the constitutive behavior obtained at the integration point also differs from the one for a fixed mode mixity. **Figure 7** shows the mixed mode constitutive law at the integration point which is 5 mm to a pre-crack tip. The mixed mode constitutive law at the integration point deviates from the typical triangle shape for the case of a fixed mode mixity. The total SERR dissipated when the integration point becomes traction free is output, which can be considered as the fracture toughness of the interface under such a load condition. The values of fracture toughness used in LEFM analysis for the fixed mode mixity defined at specimen level are also listed. It can be found that these two values agrees with each other for all the mode mixities and sets of inter-laminar strengths, as listed in **Table 4**. The similar values of fracture toughness output from FEM and used in LEFM analysis for fixed mode mixity at specimen level explains why the predicted reaction force-displacement curve at specimen level has a good agreement with the LEFM analysis even if the mode mixity at integration point deviates from the one defined at specimen level for all the mode mixities and selections of inter-laminar strengths.

TABLE 4 | Fracture toughness of interface output from different simulation cases.

Mode-mixity at specimen level	LEFM (N/mm)	Set1 (N/mm)	Set2 (N/mm)	Set3 (N/mm)	Set4 (N/mm)
20%	1.00	0.99	0.99	0.99	0.99
50%	1.16	1.15	1.15	1.15	1.15
80%	1.45	1.44	1.43	1.45	1.44

Feasibility of the Assumption of Small Mode Mixity Change

In *Cohesive Constitutive Law for Variable Mode Mixity*, an assumption was made for simplifying the development of three-dimensional cohesive constitutive law: the change of mode mixity is small, and therefore the mode mixity obtained from previous simulation step is directly used as the mode mixity for the current simulation increment. The error between the actual mode mixity in the simulation increment and the value used for developing the cohesive law for this simulation increment is calculated, as shown in **Figure 8**. The results are from the simulation with the inter-laminar strengths from Set1. It can be found that the error of the mode mixity is always below 7% for all the mode mixities.

CONCLUSION AND OUTLOOK

A new formulation of a cohesive constitutive law was developed in this study, which is capable of simulating delamination with variable mode mixity and has little sensitivity to the inter-laminar strength. An incremental type of damage variable is proposed, a factor accounting for the reduction of the residual stiffness in

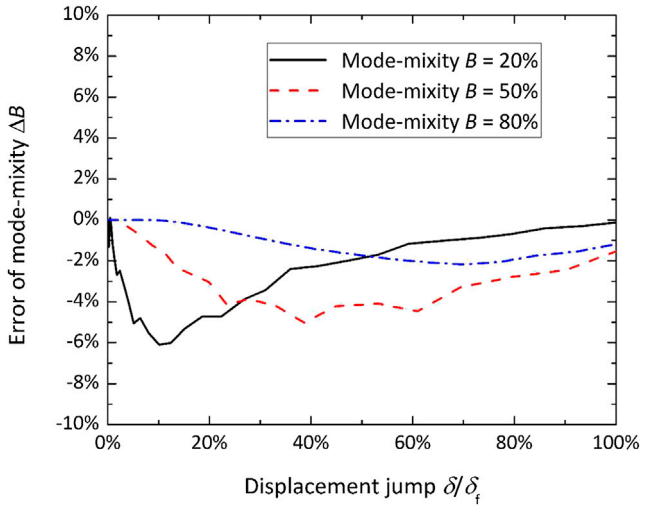

FIGURE 8 | Error of mode mixity from the assumption of small change of mode mixity.

the traction-displacement cohesive law. It allows updating the constitutive law step by step (incrementally) and includes the effect of loading history. The mode mixity at the integration point is updated during the loading, and calculated in the formulation of the supplied SERR.

The model was validated by simulating MMB test with three different mode mixities. Simulations were run for four different values of the inter-laminar strength, and for these simulation cases, the reaction force-displacement for the loaded MMB specimen has a good agreement with the analytical solution from LEFM analysis. There is only a minor dependence on the inter-laminar strength. In the case of B = 20% the largest difference in the maximum load is 2.22%, and this dependence disappears in the propagation part after the maximum load. The dependence on the strength is eliminated in the simulations with mode mixity of 50% and 80%. The mode mixity at the integration point is found to be different from the constant mode mixity applied macroscopically at the specimen level. However, the total SERR dissipated (up to the displacement when the integration point becomes traction free) is almost equal to the fracture toughness input to LFEM analysis for the fixed mode mixity at specimen level and is independent of the inter-laminar strength. The agreement of the output fracture toughness with the fracture toughness used in LEFM analysis for fixed mode mixity at specimen level explains the correctly predicted reaction force-displacement curve for all the studied cases.

For those who are interested to perform characterization under true constant mode-mixity conditions Sørensen et al. (2006) proposed a test method where a double cantilever beam specimen is loaded with uneven bending moments (DCB-UBM). An FEM study of the DCB-UBM test with the proposed incremental cohesive law would be interesting to confirm that the mode mixities are indeed the same at the macro- and micro-scale in this test.

The validation case in this study is an MMB test, for which experimental data are available. A case study with all three modes of delamination supported by experimental data is needed to complete the validation of the proposed mixed-mode cohesive law.

DATA AVAILABILITY STATEMENT

The raw data supporting the conclusions of this article can be made available upon request by the authors, without undue reservation.

AUTHOR CONTRIBUTIONS

MZ: model development, simulation, analysis, article writing; LG: data interpretation, supervision, article editing; SL: data interpretation, supervision, article editing.

FUNDING

The work has been funded by the SBO project "M3Strength," which fits in the MacroModelMat (M3) research program, coordinated by Siemens (Siemens Digital Industries Software, Belgium) and funded by SIM (Strategic Initiative Materials in Flanders) and VLAIO (Flanders Innovation & Entrepreneurship). S.V. Lomov holds Toray Chair for Composite Materials at KU Leuven, support from which is gratefully acknowledged.

REFERENCES

Alfano, G., and Crisfield, M. A. (2001). Finite element interface models for the delamination analysis of laminated composites: mechanical and computational issues. *Int. J. Numer. Methods Eng.* 50, 1701–1736. doi:10.1002/nme.93

ASTM D6671/D6671M-13 (2013). *Standard test method for mixed mode I-mode II interlaminar fracture toughness of unidirectional fiber reinforced polymer matrix composites*. West Conshohocken, PA: ASTM International.

Barenblatt, G. I. (1959). The formation of equilibrium cracks during brittle fracture. General ideas and hypotheses. Axially-symmetric cracks. *J. Appl. Math. Mech.* 23, 622–636. doi:10.1016/0021-8928(59)90157-1

Barenblatt, G. I. (1962). The mathematical theory of equilibrium cracks in brittle fracture. *Adv. Appl. Mech.* 7, 55–129. doi:10.1016/s0065-2156(08)70121-2

Bennati, S., Fisicaro, P., and Valvo, P. S. (2013a). An enhanced beam-theory model of the mixed-mode bending (MMB) test-part I: literature review and mechanical model. *Meccanica* 48, 443–462. doi:10.1007/s11012-012-9686-3

Bennati, S., Fisicaro, P., and Valvo, P. S. (2013b). An enhanced beam-theory model of the mixed-mode bending (MMB) test-part II: applications and results. *Meccanica* 48, 465–484. doi:10.1007/s11012-012-9682-7

Benzeggagh, M. L., and Kenane, M. (1996). Measurement of mixed-mode delamination fracture toughness of unidirectional glass/epoxy composites with mixed-mode bending apparatus. *Compos. Sci. Technol.* 56, 439–449. doi:10.1016/0266-3538(96)00005-x

Borg, R., Nilsson, L., and Simonsson, K. (2002). Modeling of delamination using a discretized cohesive zone and damage formulation. *Compos. Sci. Technol.* 62, 1299–1314. doi:10.1016/s0266-3538(02)00070-2

Camanho, P. P., Davila, C. G., and De Moura, M. F. (2003). Numerical simulation of mixed-mode progressive delamination in composite materials. *J. Compos. Mater.* 37, 1415–1438.

De Moura, M. F. S. F., Gonçalves, J. P. M., and Silva, F. G. A. (2016). A new energy based mixed-mode cohesive zone model. *Int. J. Solid Struct.* 102-103, 112–119. doi:10.1016/j.ijsolstr.2016.10.012

Dugdale, D. S. (1960). Yielding of steel sheets containing slits. *J. Mech. Phys. Solid.* 8, 100–104. doi:10.1016/0022-5096(60)90013-2

González, E. V., Maimí, P., Camanho, P. P., Turon, A., and Mayugo, J. A. (2012). Simulation of drop-weight impact and compression after impact tests on composite laminates. *Compos. Struct.* 94, 3364–3378. doi:10.1016/j.compstruct.2012.05.015

Gözlüklü, B., and Coker, D. (2012). Modeling of the dynamic delamination of L-shaped unidirectional laminated composites. *Compos. Struct.* 94, 1430–1442. doi:10.1016/j.compstruct.2011.11.015

Gozluklu, B., Uyar, I., and Coker, D. (2015). Intersonic delamination in curved thick composite laminates under quasi-static loading. *Mech. Mater.* 80, 163–182. doi:10.1016/j.mechmat.2014.07.013

Harper, P. W., Sun, L., and Hallett, S. R. (2012). A study on the influence of cohesive zone interface element strength parameters on mixed mode behaviour. *Compos. Appl. Sci. Manuf.* 43, 722–734. doi:10.1016/j.compositesa.2011.12.016

Jensen, S. M., Martos, M. J., Bak, B. L. V., and Lindgaard, E. (2019). Formulation of a mixed-mode multilinear cohesive zone law in an interface finite element for modelling delamination with R-curve effects. *Compos. Struct.* 216, 477–486. doi:10.1016/j.compstruct.2019.02.029

Joki, R. K., Grytten, F., Hayman, B., and Sørensen, B. F. (2016). Determination of a cohesive law for delamination modelling-accounting for variation in crack opening and stress state across the test specimen width. *Compos. Sci. Technol.* 128, 49–57. doi:10.1016/j.compscitech.2016.01.026

Kawashita, L. F., and Hallett, S. R. (2012). A crack tip tracking algorithm for cohesive interface element analysis of fatigue delamination propagation in composite materials. *Int. J. Solid Struct.* 49, 2898–2913. doi:10.1016/j.ijsolstr.2012.03.034

Liu, Q., Gorbatikh, L., and Lomov, S. V. (2019). A combined use of embedded and cohesive elements to model damage development in fibrous composites. *Compos. Struct.* 223, 110921. doi:10.1016/j.compstruct.2019.110921

Lu, X., Ridha, M., Chen, B. Y., Tan, V. B. C., and Tay, T. E. (2019). On cohesive element parameters and delamination modelling. *Eng. Fract. Mech.* 206, 278–296. doi:10.1016/j.engfracmech.2018.12.009

Nojavan, S., Schesser, D., and Yang, Q. D. (2016). A two-dimensional *in situ* fatigue cohesive zone model for crack propagation in composites under cyclic loading. *Int. J. Fatig.* 82, 449–461. doi:10.1016/j.ijfatigue.2015.08.029

Reeder, J. R., and Crews, J. H. (1990). Mixed-mode bending method for delamination testing. *AIAA J.* 28, 1270–1276. doi:10.2514/3.25204

Sørensen, B. F., Jørgensen, K., Jacobsen, T. K., and Østergaard, R. C. (2006). DCB-specimen loaded with uneven bending moments. *Int. J. Fract.* 141, 163–176. doi:10.1007/s10704-006-0071-x

Turon, A., Camanho, P. P., Costa, J., and Dávila, C. G. (2006). A damage model for the simulation of delamination in advanced composites under variable-mode loading. *Mech. Mater.* 38, 1072–1089. doi:10.1016/j.mechmat.2005.10.003

Turon, A., Camanho, P. P., Costa, J., and Renart, J. (2010). Accurate simulation of delamination growth under mixed-mode loading using cohesive elements: definition of interlaminar strengths and elastic stiffness. *Compos. Struct.* 92, 1857–1864. doi:10.1016/j.compstruct.2010.01.012

Turon, A., González, E. V., Sarrado, C., Guillamet, G., and Maimí, P. (2018). Accurate simulation of delamination under mixed-mode loading using a cohesive model with a mode-dependent penalty stiffness. *Compos. Struct.* 184, 506–511. doi:10.1016/j.compstruct.2017.10.017

Conflict of Interest: The authors declare that the research was conducted in the absence of any commercial or financial relationships that could be construed as a potential conflict of interest.

frontiers in Materials

ORIGINAL RESEARCH
published: 11 February 2021
doi: 10.3389/fmats.2020.590747

Characterization of Surface Fatigue Crack Nucleation and Microstructurally Small Crack Growth in High Strength Aluminum Alloys

Robert Fleishel[1], *Cole Cauthen*[2], *Steven Daniewicz*[3], *Andrew Baker*[4], *J. Brian Jordon*[2] *and Stephanie TerMaath*[1]*

[1]Department of Mechanical, Aerospace, and Biomedical Engineering, The University of Tennessee, Knoxville, TN, United States, [2]Department of Mechanical Engineering, The University of Alabama, Tuscaloosa, AL, United States, [3]Department of Metallurgical and Materials Engineering, The University of Alabama, Tuscaloosa, AL, United States, [4]Boeing Research and Technology, The Boeing Company, Berkeley, MO, United States

It is well established that fatigue crack nucleation and small crack growth in high strength aluminum alloys are highly influenced by the surrounding microstructure including grain boundaries, texture, inclusion barriers, among other factors. As such, specific and targeted experimental and computational methods are necessary to accurately capture and predict the discrete behavior of microstructurally small fatigue cracks. In this study, surface fatigue crack nucleation and microstructurally small crack growth in high strength aluminum alloys, commonly used in aerospace applications, are evaluated through a holistic approach encompassing fatigue testing, crack measurement, and computational prediction of crack growth rates. During fatigue testing, crack shapes and growth are quantified using a novel surface replication technique that is applied to investigate crack nucleation, as well as to collect validation data that includes an accurate description of crack shape during crack propagation, a challenging and essential component in predicting crack growth. Computational simulation of fatigue crack growth in non-straight, complex surface crack arrays typically requires high fidelity analysis using computationally expensive methods to account for the mathematical and geometrical complexities inherent in the solution. A dislocation distribution based technique has been previously demonstrated to rapidly and accurately predict the stress intensity factors for through cracks of complex shape. This method was expanded and investigated as an approach for rapidly predicting the crack growth rate of kinked and tortuous surface crack arrays, using the crack configuration and bulk material properties as inputs. To investigate the accuracy and effectiveness of this characterization approach, surface crack growth in AA7075-T7351 was experimentally analyzed and modeled under high cycle and low cycle fatigue conditions. This comprehensive approach was determined to be an expedient and applicable method for characterizing and evaluating the nucleation and crack growth rate of non-planar microstructurally small and short crack configurations.

Keywords: crack growth rate analysis, fatigue–cracks, aluminum alloy, computational modeling, surface crack behavior

OPEN ACCESS

Edited by:
Patricia Krawczak,
IMT Lille Douai, France

Reviewed by:
Frédéric Charles Lebon,
Aix-Marseille Université, France
Andrea Spagnoli,
University of Parma, Italy

****Correspondence:***
Stephanie TerMaath
stermaat@utk.edu

Specialty section:
This article was submitted to Mechanics of Materials, a section of the journal Frontiers in Materials

Received: *02 August 2020*
Accepted: *10 December 2020*
Published: *11 February 2021*

Citation:
Fleishel R, Cauthen C, Daniewicz S, Baker A, Jordon J B and TerMaath S (2021) Characterization of Surface Fatigue Crack Nucleation and Microstructurally Small Crack Growth in High Strength Aluminum Alloys. Front. Mater. 7:590747. doi: 10.3389/fmats.2020.590747

INTRODUCTION

Predicting the crack growth rate and direction in the early stages of crack growth is challenging due to several phenomena. The rate and direction of crack growth immediately following initiation is heavily dependent on microstructure (Hussain 1997; Stephens et al., 2001), and both can change rapidly as a crack grows across grain boundaries, through imperfections, and around inclusions. This behavior can cause microstructurally small cracks to kink or for several smaller cracks to form, later coalescing into a single dominant crack, in the early stages of crack growth. To characterize crack nucleation and to predict the growth of small cracks requires accurate correlation of crack shape with crack growth rate and a computational approach that accounts for complex crack shapes due to direction changes and crack branching. The objective of this research is to evaluate the accuracy and efficiency of a comprehensive approach to characterizing crack nucleation and predicting the crack growth rate of small cracks using a novel surface replication technique to obtain high resolution crack shapes and a computational predictive capability for the propagation of such non-straight cracks. The research was performed through experimental and computational components.

Recent analytical modeling of microstructurally small surface cracks has been successfully performed (Cauthen et al., 2017), in which a strip yield model (Daniewicz and Aveline, 2000) and CTOD (crack tip opening displacement) method were applied for a straight surface fatigue crack. An analytical multistage fatigue model, also assuming a straight crack, has been used to predict microstructurally small crack growth of aluminum alloys (McDowell et al., 2003; Xue et al., 2007; Bernard et al., 2013; McCullough et al., 2019). Research has also been performed to explore the non-straight nature of microcracks, including the effects of grain and crystal orientations (Herbig et al., 2011; Castelluccio and McDowell, 2012; Castelluccio and McDowell, 2016; Wilson et al., 2018). While many methods are available for predicting crack growth that account for both microstructure and crack shape using high fidelity modeling, including finite element methods (Wilson and Dunne, 2019), boundary element methods (Sun and Ma, 1997), and peridynamics (Silling and Abe, 2014), these methods require explicit modeling of the microstructure and significant computational time for a single analysis. The need to know the exact microstructure present around the crack tip makes applying such methods to existing crack configurations, especially in time critical situations such as during an inspection to determine remaining life, difficult.

Experimental approaches for quantification of nucleation and fatigue crack growth mechanisms in metals are well documented. Some methods employ micronotches where the initiation event can be readily located and observed. However this method does limit the observation of naturally occurring cracks where the initiation mechanisms which come from microstructural features or defects, such as intermetallic particles and persistent slip bands (PSBs) can be quantified (Gall et al., 1999; Xue et al., 2007; Ma et al., 2019; Zerbst et al., 2019; Dai et al., 2020). As such, without knowing the location of where the fatigue crack initiated, taking *in-situ* measurements without the use of a micronotch is improbable. An alternate approach that allows for naturally occurring fatigue cracks to initiate from microstructural features and/or defects is the surface replica approach. The main idea of the surface replica technique is to take intermittent surface replicas of the fatigue specimen over the lifetime of the test. Once the test is complete, analysis of the surface replicas can be examined in reverse order since the fatigue crack(s) that lead to ultimate fracture are the largest and easy to identify under low magnification and tracking them is straightforward. A relatively new technique for taking surface replicas uses a fast drying two-part silicon rubber compound that does not experience shrinkage compared to the more traditional acetate tape method (Newman et al., 1994). The procedure to make the surface replicas using the fast drying two-part silicon rubber compound, commercially known as Repliset, was first demonstrated by Newman et al. (2009). To demonstrate the use of fast drying two-part silicon rubber compound on quantifying fatigue mechanisms, previous work (Jordon et al., 2012) showed that the method could be used to quantify the fatigue crack nucleation stage and small crack growth rates in a high strength aluminum alloy. While the fast drying two-part silicon rubber replica method is not ideal for directly measuring subsurface crack growth, it has been used to further understand the mechanisms of surface dominated crack nucleation and growth from naturally occurring cracks. Recently, other metals have been examined using the fast drying two-part silicon rubber replica method including titanium (Hu et al., 2019; Zhu et al., 2019), magnesium alloys (Bernard et al., 2013; Cauthen et al., 2017), stainless steel (Deng et al., 2016), and nickel based super alloys (Deng et al., 2015; Qin et al., 2015; Deng et al., 2016; Zhu et al., 2016; Ye et al., 2017; Zhu et al., 2018), where these studies explored the effects of variation in grain size, maximum stress, and stress ratios (R values) on fatigue crack growth behavior. In addition, the fast drying two-part silicon rubber replica method has also been employed on a range of specimen geometries from standard notched specimen types (Bernard et al., 2013; Cauthen et al., 2017; Zhu et al., 2018), to laser created micro notches (Qin et al., 2015; Zhu et al., 2019), and aerospace components (Newman et al., 2009; Altıntaş and Güngör, 2013). The present study focuses on using the novel fast drying two-part silicon rubber replica method to quantify the fatigue crack nucleation and microstructurally small crack growth mechanisms of AA7075-T7351. In particular, the use of the surface replica approach provides direct and high resolution observation of both the surface crack initiation event and the subsequent propagation of small cracks where the crack kinking can be directly quantified. One of the advantages of this experimental method is the opportunity to directly correlate crack growth to sources of crack initiation that are also confirmed under high resolution scanning electron microcopy. As such, to the best of the authors' knowledge, this is the first investigation to quantify surface crack nucleation that is directly linked to microstructurally small fatigue crack growth in AA7075-T7351 using the two-part silicon rubber replica method.

Using these measurements, the fatigue crack growth rates (FCGR) are numerically determined and compared to the experimental results to validate a fatigue crack growth model

using a dislocation distribution based technique (DDT). DDT has been previously demonstrated to rapidly and accurately predict the stress intensity factors for a variety of problems (Lardner 1974; Barber 1992; Hills et al., 1996), including long, through crack arrays of complex shape (TerMaath et al., 2006; Yavuz et al., 2006). Dislocation distributions have also been used to model fatigue crack growth behavior (Yavuz et al., 2020). This method was expanded to predict the fatigue crack growth rate (FCGR) of short, surface cracks. To develop a rapid prediction capability for predicting the fatigue crack growth rate (FCGR) in kinked and tortuous surface crack arrays, a DDT was expanded to include short, surface crack analysis using the crack configuration and bulk material properties as inputs. While a goal of this research was to evaluate the DDT using experimental data that was correlated to the replica data, this method was chosen because it has been demonstrated for large arrays of cracks of complex shape and is robust as cracks grow near each other and coalesce, an important feature for future development and applicability to real world structures. FCGR prediction is achieved by combining a method for calculating the stress intensity factor (SIF, designated as K for linear elastic behavior) of complex shaped cracks (TerMaath, 2001) with empirical SIF based crack growth models (Paris, 1961) and geometric factors to account for surface crack depth (Raju and Newman, 1979). The use of a geometric factor vs. a strip-yield model to account for surface cracking reduces the complexity of the analysis and is less computationally expensive, an important consideration for future development for large arrays of surface cracks. The use of bulk material crack growth data enables this model to be applicable without specialized data collection or knowledge of the exact microstructure surrounding the crack due to the fact that K-based experimental crack growth data is more commonly available than CTOD experimental data. This model is explored for its applicability to determine the FCGR of small cracks in non-straight configurations, with the change in crack driving force, the stress intensity factor, accounting for the non-straight nature of the crack.

MATERIALS AND METHODS

To investigate the applicability of the integrated experimental and computational approach for characterizing the fatigue crack growth behavior of kinked surface cracks, microstructurally small crack growth in AA7075-T7351 was experimentally analyzed and computationally modeled under high cycle and low cycle fatigue conditions. This legacy material was chosen to demonstrate the characterization approach due to its widespread use and well-established microstructural variability. The crack growth was measured on the surface of a shallow notched flat fatigue specimen using a novel, fast drying two-part silicon rubber surface replication technique. Fractography and Electron Backscatter Diffraction (EBSD) mapping of specimens were performed post-fracture to determine the source of crack initiation and distribution of intermetallic particles within the material, as well as to characterize the microstructure at the location of crack initiation. The crack configurations captured via surface replication were then input into the computational model to calculate the crack growth rate at varying stages of crack propagation and the computational results were compared to the experimental data.

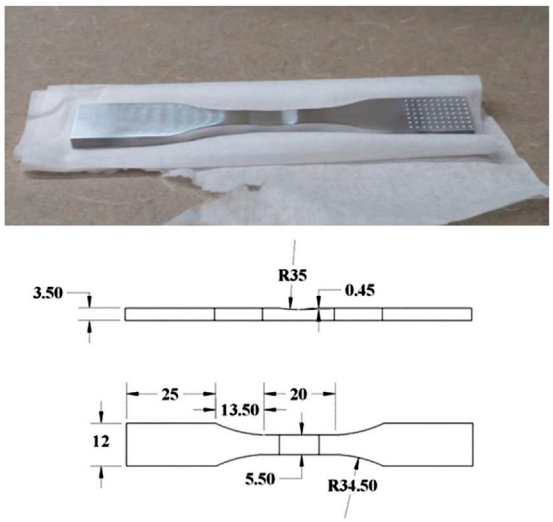

FIGURE 1 | (A) Flat tensile specimen with shallow notch used for fatigue testing. **(B)** Specimen dimensions (mm).

Experimental Testing

The material used for testing in this study was a 63.5 mm thick rolled plate of AA7075-T7351. In this study, the fatigue specimens were cut out of the plate in the longitudinal orientation at the quarter thickness (t/4) and half thickness (t/2) in order to assess the effect of location dependent mechanisms in the rolled plate. This specimen design used in this study was a flat specimen with a reduced gauge, where this reduced gauge contains a shallow notch to facilitate fatigue crack initiation (**Figure 1**). While most of the specimen geometry was machined using wire electrical discharge machining (EDM), the shallow notch was prepared using a traditional milling tool. In addition, the shallow notch was machined into one side of the specimen geometry to facilitate natural crack initiation within a general location. Following machining, all surfaces were lightly polished using progressively finer polishing paper until a smooth surface was achieved. This specimen geometry was first used by (Tokaji et al., 2004) and has been successfully implemented to measure microstructurally small surface fatigue crack growth for magnesium alloys (Bernard et al., 2013; Cauthen et al., 2017; Cauthen et al., 2020).

Fatigue crack growth was evaluated for the test specimens in both the low cycle fatigue (LCF) and high cycle fatigue (HCF) regime at a load ratio of $R = 0.1$ and a test frequency below 10 Hz. Load levels for these regimes were chosen such that cycles to failure for LCF testing was approximately 10^4 cycles, and cycles to failure for HCF testing was approximately 10^5 cycles. Preliminary testing was conducted to find these desired load levels, and a stress range of 420 and 260 MPa was chosen for LCF and HCF

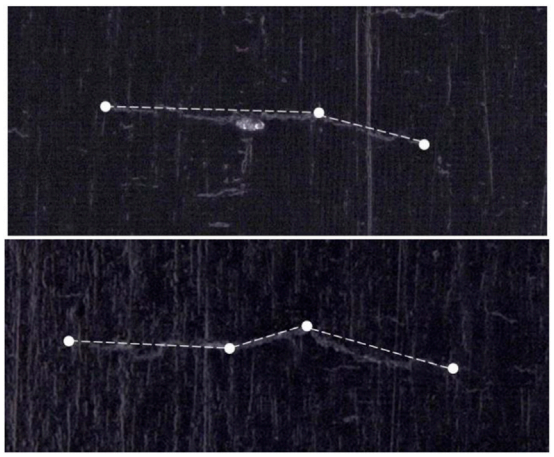

FIGURE 2 | Examples of idealized kinked crack configurations overlaid on surface replication images. **(A)** a crack with two segments and a single kink, **(B)** a crack with three segments and two kinks.

testing, respectively. Eight samples, four in the HCF and four in the LCF regimes, were tested. The fatigue crack growth tests were conducted in ambient laboratory air and relative humidity and were terminated when full separation of the specimen was achieved. The application of the replica method for quantifying fatigue crack growth required the regular interruption of the fatigue tests at a mean cyclic load. Once stopped, the fatigue sample was dusted with particle free compressed air to remove any surface contaminates. Following the procedure detailed by Jordon et al. (2012), the Repliset® material, which is a two-part silicon rubber replica, was dispensed on to the shallow notch of the fatigue specimen using a mixing nozzle and dispensing gun. Tape was placed over the Repliset® material to hold it in place during the curing phase, where the curing time for the Repliset® material was approximately 5–10 min. Once cured, the tape was carefully pulled away from the specimen revealing an inverted replication of the surface of the shallow notch. This procedure was repeated such that 20–40 replicas were made over the life of each fatigue specimen. In the post-test crack evaluation procedure described by Jordon et al. (2012) each replica was coated with gold-palladium to improve the conductivity of the surface for scanning electron microscopy (SEM). However, they noted that the downside to using SEM to measure cracks was the tendency to melt the micron-sized features of the replicas under high magnification. As an alternate approach to using an SEM to measure the cracks, Bernard et al. (2013) demonstrated the efficacy of using an optical microscopy z-axis stitching method to measure cracks instead of the SEM approach. Similar, to Bernard et al. (2013), the surface replications in this present study were viewed and measured using a Keyence vhx-1000 optical microscope equipped with a Z axis imaging stacking feature that allowed for the entire surface of the replica to remain in focus. Crack measurements were made for one LCF and one HCF specimen at both considered thicknesses, for a total of four samples. Note that due to the nature of preparing each replica by hand, some of the replicas were applied with insufficient pressure during the curing process resulting in poor impressions, thus rendering some images of the crack not usable. For surface replications with low quality images, the data points were removed from the analysis. Between 15–30 data points were available for each of these four specimens. The replica images were used to create simplified crack geometries for input into the SIF prediction code. Depending on the crack shape, the surface cracks were dimensioned and modeled as a single, straight crack consisting of two crack segments, a two segment crack with a single kink, or a three segment crack with two kinks. Examples of the idealized kinked crack geometries overlaid on surface replication images are shown in **Figure 2**. A high and low value were measured for each crack segment length to capture uncertainty due to image quality and measurement error. The total crack length was the sum of the lengths of all crack segments.

Experimentally observed crack growth rates were calculated using the crack length measurements obtained from each surface replication. A two-point secant method was used to calculate the fatigue crack growth rate (**Eq. 1**).

$$\left(\frac{dc}{dN}\right)_n = \frac{c_{n+1} - c_{n-1}}{N_{n+1} - N_{n-1}} \quad [1]$$

where c is the total crack length, N is the cycle count, and n is the surface replication number. Note that because c is the total crack length, the computed growth rate is that of the entire crack, not an individual crack tip.

To characterize the microstructure and crack initiation, the fracture surface of each specimen was imaged using a scanning electron microscope (SEM). The crack initiation area of each specimen was examined, and the source of crack initiation was determined. Lastly, focus ion milling (FIB) was performed on the surface of the two LCF fractured specimens near the crack initiation site. Misorientation of grains was quantified at this location using EBSD. The observed fatigue crack's position, crack length, and crack depth, d, were measured.

Fatigue Crack Growth Rate Prediction Methodology

The computational approach developed and evaluated in this study consists of several steps to predict FCGR as described in this section. The DDT approach to calculate SIFs at the crack tips assumes a 2D infinite plate with a through crack and linear elastic behavior under remote stress. Therefore, the surface crack location in the bar and finite bar geometry must be measured and accounted for in another step in the analysis. Once ΔK_{I} and ΔK_{II} (representing mode I and II crack behavior respectively) are determined for each crack tip, a single equivalent stress intensity factor range (ΔK_{eq}) is calculated according to Tanaka (Tanaka, 1974). A geometry factor is then applied to account for the surface crack depth. Using this corrected ΔK_{eq}, the crack growth rate for the total crack growth is calculated via Paris law (Paris, 1961).

Kinked Crack SIF Prediction

The computational model used to predict SIFs for microstructurally small crack growth is based on dislocation distribution theory that was originally developed for static loading (TerMaath et al., 2006; Yavuz et al., 2006) and adapted to fatigue loading (Yavuz et al., 2020). This model was chosen because it can solve for SIFs at the crack tips of kinked and branched cracks as well as combinations of the two. It also calculates the SIF at kinks by including the effects of wedge singularities so that crack growth at these locations can be evaluated. Importantly, it has been proven to be robust for cracks growing close to each other (TerMaath et al., 2006) and for large arrays of cracks of complex shapes (Yavuz et al., 2006), such that future development can capture this important scenario. Integrals are solved analytically (without numerical integration) eliminating this source of error. While not needed for this study, a significant benefit of this method is the capability to solve the stress and displacement field in a plate containing a large array of cracks of complex shapes, which can be highly interacting. This method is based on the isotropic bulk materials of the plate and assumes linear elastic behavior in an infinite body containing through cracks. A summary of this SIF prediction method is included in this section and full mathematical derivations are provided in (TerMaath, 2001).

The method is built on the superposition of two elastic problems, the trivial solution of the uncracked plate and the auxiliary problem that contains the cracks with prescribed tractions applied to the boundaries such the crack faces are traction free when the two problems are added (**Eq. 2**). Cracks are modeled as a series of crack segments of sufficient resolution to capture the crack configuration (as demonstrated in **Figure 2**). Thus, the foundation of the analysis is to solve for the crack opening displacement profiles for each crack segment that satisfy the global traction free condition. Once the opening displacement profile of each crack segment is determined, SIFs at crack tips and kinks, as well as the full stress and displacement fields in the plate, can be determined.

$$\sigma_{xy}^{\infty} n_y + \sigma_{xx}^{\infty} n_x = -n_y \sum_{i=1}^{ncs} s_{xy}(Z_{1i}, Z_{2i}) - n_x \sum_{i=1}^{ncs} s_{xx}(Z_{1i}, Z_{2i}) \quad [2a]$$

$$\sigma_{yy}^{\infty} n_y + \sigma_{xy}^{\infty} n_x = -n_y \sum_{i=1}^{ncs} s_{yy}(Z_{1i}, Z_{2i}) - n_x \sum_{i=1}^{ncs} s_{xy}(Z_{1i}, Z_{2i}) \quad [2b]$$

The variable σ^{∞} represents the far field loading conditions, n_y and n_x are the normals of the crack segment, *ncs* is the total number of crack segments in the analysis, and *s* denotes the tractions induced in a specific crack segment from the dislocation distributions. *Z* is the Cauchy singular integral used to solve for local stresses (**Eq. 3**), and one and two denote the tangential and normal direction of the crack segment, respectively.

$$Z_{1i} = \int_0^{a_i} \frac{\mu_i(t)dt}{z-t} \quad [3a]$$

$$Z_{2i} = \int_0^{a_i} \frac{\mu_i(t)dt}{(z-t)^2} \quad [3b]$$

The variable μ denotes the dislocation distribution at a point due to an opening displacement profile, *i* represents a specific crack segment, *z* is the location of the traction free point in complex notation, and *t* is the distance along the crack from the kink.

The traction free conditions are enforced at a user specified number of points along the crack segments and the point allocation is biased resulting in a higher density of points near the crack tips and kinks (TerMaath, 2001). The dislocation distributions are derived from opening displacement profiles that are constructed by summing terms from three types of critical crack behaviors (**Eq. 4**) to provide an overall crack shape with sufficient flexibility to capture the actual crack shape that meets the traction free boundary condition within a specified error. **Eqs 4A–C** are referred to as the Wedge, Polynomial, and Tip series, respectively, and each term in a series represents a degree of freedom. The total number of terms used for each series is designated as *nw*, *np*, and *nt*. Each series is used independently in the tangential and normal modes of deformation. Wedge series account for the stress singularity at a kink, polynomial series provide the opening and sliding crack displacements, and tip terms capture the singularity at a crack tip.

$$W(t) = \sum_{j=0}^{nw-2} A_{\rho j}\left(\left(\frac{t}{a}\right)^{\rho+j} - (nw-j)\left(\frac{t}{a}\right)^{\rho+nw-1} + (nw-j-1)\left(\frac{t}{a}\right)^{\rho+nw}\right) \quad [4a]$$

$$P(t) = \sum_{j=0}^{np-2} A_{0j}\left[\left(\frac{t}{a}\right)^{j} - (np-j)\left(\frac{t}{a}\right)^{np-1} + (np-j-1)\left(\frac{t}{a}\right)^{np}\right] \quad [4b]$$

$$T(t) = \sum_{j=0}^{nt-2} A_{\frac{1}{2}j}\left[\left(\frac{a-t}{a}\right)^{\frac{2j+1}{2}} - (nt-j)\left(\frac{a-t}{a}\right)^{\frac{2(nt-1)+1}{2}} + (nt-j-1)\left(\frac{a-t}{a}\right)^{\frac{2nt+1}{2}}\right] \quad [4c]$$

The variable *A* is the weighting coefficient of each term in the profile, and ρ is a measure of the wedge distortion per kink. After the opening profiles are constructed, they are converted to dislocation distributions and are then integrated according to **Eq. 3**. The opening displacements are turned on and off at crack segment ends via the use of Dirac delta and Heaviside step functions. Non-trivial physical constraints are applied at adjoining crack segments to ensure material continuity.

The weighting coefficients from the opening displacement profiles are solved using a least squares fit to determine the contribution of each dislocation distribution to the overall problem solution. The weighting coefficients of the $j = 0$ tip series directly represent the singularity of the crack tip, and thus the mode I and II stress intensity factor are solved according to **Eq. 5**, where *G* is the shear modulus of the material and κ is

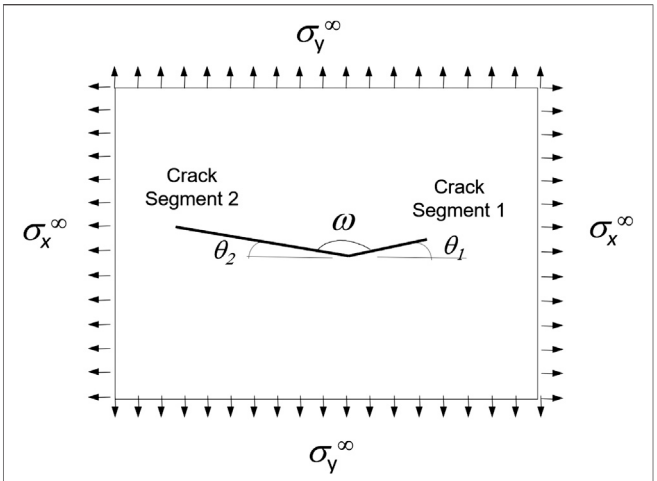

FIGURE 3 | Crack configuration for two crack segments and a single kink.

Kosolov's constant which allows for plane strain or plane stress solutions.

$$\begin{bmatrix} K_I \\ K_{II} \end{bmatrix} = \frac{2G}{1+\kappa} \begin{bmatrix} A_{\frac{1}{2}0}^{[1]} \\ A_{\frac{1}{2}0}^{[2]} \end{bmatrix} \quad [5]$$

Convergence and Uncertainty Quantification to Inform Kinked Crack Modeling

It is essential for the analytical model to provide converged and accurate results with minimized computation time. Therefore, a convergence study on the model form parameters and uncertainty quantification (UQ) on the parameters representing measurement error were performed using the SIF prediction method to inform code optimization. The crack configuration investigated is shown in **Figure 3** for the case of a V shaped crack with a single kink. This configuration was chosen as it is representative of the crack growth patterns observed from the replications of the experimental specimens, and literature values for this crack configuration are available for validation. For this case, the crack is loaded in normal unit tension only. The baseline length of crack segment one is 0.6 with an angle θ_1 equal to 60° and the length of crack segment two is 1 with an angle θ_2 of 0. It should be noted that all parameters investigated in the current effort are considered as independent parameters.

A convergence study on the four model form parameters that are user-specified and defined as integer values consisted of the number of points assigned to each crack segment (the traction free condition is enforced at these points) and the number of wedge, tip and polynomial terms in approximating the opening displacement profile of each crack segment. Based on the results, the model form parameters were held at the following converged values for all analyses: 50 points were allocated along all crack segments and six terms were designated for all opening displacement profiles.

Measurement error is introduced when obtaining crack lengths and angles from images and is dependent on both image quality and human error. This experimental error was defined by 4 parameters: the measured length and angle of each crack segment. Measurement parameters were defined as normal distributions using the mean and standard deviations provided in **Table 1** and were sampled using a Latin hypercube sampling function. Latin hypercube sampling stratifies the individual variables of the input vector, sampling from these strata, and randomly pairing them to build samples of the full input vector (Helton and Davis, 2003). A 10% standard deviation was chosen for the measurement error of the lengths and the 1.75° for the angles based on the resolution of the images obtained from the specimen replications.

For automated sampling and generation of input files, we utilized Distribution-based Input for Computational Evaluations (DICE). DICE is a general-purpose tool used for the design of experimental parametric studies (Nahshon and Reynolds 2016). DICE receives a parameter file and replaces the parameter values in text files based on user-defined parameters for the study being performed. DICE outputs a series of ready-to-execute analysis input files. The four input parameters were defined in a parameter definition file and sampled as probabilistic parameters as previously described.

UQ results are provided in **Table 1**. According to the standard deviation values, some parameters contributed higher uncertainty than others to the results. However, all standard deviations are on the order of two decimal places in the accuracy of the SIFs. This error is well within current capability to measure the SIF of a material and it was deemed that the uncertainty due to measurement error was acceptable for this study.

Straight Crack SIF Predictions

To generate straight crack results, the mode I and II SIFs were calculated according to **Eq. 6** using the direct distance and incline between the crack tips and then converted to the effective SIF for use in the computational model.

$$K_I = \sigma_y^\infty \sqrt{\pi a}\left(cos^2\theta + \alpha cos^2\theta\right) \quad [6a]$$

$$K_{II} = \sigma_y^\infty \sqrt{\pi a}\,(1-\alpha)\,(\cos\theta)\,(\sin\theta) \quad [6b]$$

where θ is the angle to the x-axis and $\sigma_x^\infty = \alpha\sigma_y^\infty$.

Validation of SIF Predictions

While the computational code was rigorously validated in previous publications on this method (TerMaath, 2001), a few additional cases representing the microcracks under investigation were analyzed using the SIF prediction method and compared with known values. A single straight crack at an incline in an infinite plate crack was divided into two equal crack segments for varying crack lengths such that $c = 2a$. The crack was loaded in unit biaxial tension and compared to the theoretical solution given in **Eq. 6** (Sih et al., 1962). For unit biaxial tension loading, $\sigma_y^\infty = 1$ and the loading variable α is equal to one so that the tension loading in both directions is equal to the unit value. The results of this comparison are provided in **Table 2** and it is demonstrated the SIF predictions agree with the calculated values in all cases.

TABLE 1 | UQ results for each input parameter relative to the output parameters.

Varied input	Output variation							
	$K_{I,1}$		$K_{II,1}$		$K_{I,2}$		$K_{II,2}$	
	Mean	Std	Mean	Std	Mean	Std	Mean	Std
cs 1 length mean: 0.6 std: 0.06	0.8440	0.0079	0.9387	0.0115	1.4796	0.0143	0.0200	0.0079
cs 1 angle mean: 135° std: 1.75°	0.8442	0.0459	0.9379	0.0126	1.4796	0.0076	0.0200	0.0459
cs 2 length mean: 1.0 std: 0.1	0.8440	0.0302	0.9378	0.0303	1.4789	0.0527	0.0199	0.0302
cs 2 angle mean: 0.0° std: 1.75°	0.8436	0.0040	0.9390	0.0013	1.4783	0.0022	0.0199	0.0040

TABLE 2 | Validation of SIF predicted values for an inclined straight crack SIF and a single kinked crack (specifically the crack tip of segment 1) with known values.

Crack Configuration	K_I		K_{II}	
Inclined straight crack (Sih et al., 1962)	**Predicted**	**Known**	**Predicted**	**Known**
c = 2.010, θ = 0.49°	1.7769	1.7769	0	0
c = 2.107, θ = 4.79°	1.8194	1.8194	0	0
c = 2.227, θ = 8.95°	1.8704	1.8704	0	0
cs 1 length variation of a single kinked crack (Ishida and Nishino, 1982)				
a = 0.02	1.1678	1.1747	0.6478	0.6537
a = 0.2	1.2857	1.2850	0.6459	0.6464
a = 0.4	1.4028	1.4034	0.6358	0.6324

TABLE 3 | Comparison of literature values, DDT results, and FE outputs for serval crack configurations.

case	DDT error (%)	DDT run time (seconds)	FE error (%)	FE run time (seconds)
Straight crack	0.02	0.18	2.51	7.50
Symmetric crack with one kink	0.02	0.46	2.09	4.00
Symmetric crack with two kinks	0.05	0.81	3.49	4.10

A second case for unit biaxial loading was performed using the crack configuration in **Figure 3** for varying lengths of crack segment one which is held at a constant angle, $\theta_1 = 60^\circ$ and for constant values of crack segment two of $a_2 = 2$ and $\theta_2 = 0^\circ$. The comparison of the predicted SIFs with a known solution are provided in **Table 2** (Ishida and Nishino, 1982). Again, the values are a close match.

To compare the prediction code with another computational method, two dimensional finite element (FE) models of through cracks were created in Abaqus (2014) for several different crack configurations. These were used to validate the SIF prediction method for cases where literature values are not available and to provide a comparison in computational cost differences relative to FE. The FE models evaluated mode I and II SIFs via the contour integral method, with quarter tip quadratic elements surrounding the crack tips. To obtain relevant comparisons to the SIF predictive code, which assumes a crack in an infinite plate, cracks were created in the center of a square with large dimensions relative to the crack, with the edge length being at least 10x larger than the total crack length for all cases studied. The converged number of elements required for the FE models ranged from 50,058 to 95,728. **Table 3** shows the results for serval test cases, comparing SIF outputs and run times. In all cases studied, the predictive code was more accurate and required less computation time. For the problems studied in this paper, the time reduction is not of significant importance, but for cases with hundreds or thousands of crack segments, the reduction in computation time will be considerable. When considering meshing a large crack array in FE or another high resolution method, the modeling and computational times can become prohibitive and a lower fidelity method is essential.

Mixed Mode Calculation to Determine the Effective SIF

The mode I and mode II SIF values at each crack tip were combined into a single effective SIF, K_{eq}, to be input into a fatigue crack growth rate model. A wide range of methods to calculate K_{eq} are available in literature. The method by Tanaka (1974), **Eq. 7**, was used due to its simplicity and applicability to the Paris model for crack growth (Qian and Fatemi 1996).

$$K_{eq} = \sqrt[4]{K_I^4 + 8K_{II}^4} \quad [7]$$

Edge and Surface Effects

The SIF predictive method used to compute K assumes through cracks in an infinite plate, whereas the experimental testing produced surface cracks in specimens with a finite bar configuration. Therefore, both surface and edge effects were

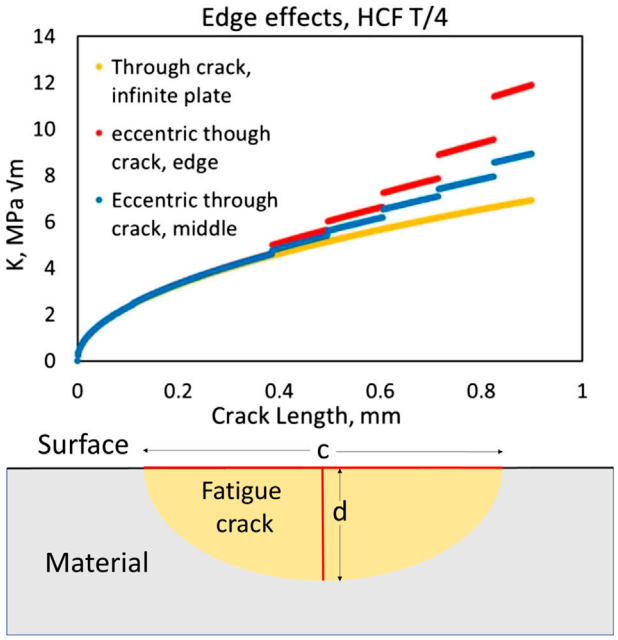

FIGURE 4 | (A) Comparison of SIF results for varying crack location and plate size. Note that the solutions for the eccentric crack are piecewise due to the tabular look up format for some of the data. **(B)** Diagram of surface fatigue crack.

evaluated to determine the effects of these two assumptions on the model and to account for each.

To determine the range of validity of the infinite plate assumption and to account for edge effects, literature values for straight, off-center cracks in a finite bar were compared to solutions for a crack of the same dimensions in an infinite plate. For short cracks located away from the edge, edge effects are minimal and the results for the infinite plate solution are in reasonable agreement with those for a finite bar. As the crack grows closer to the edge and the crack length is on the order of the dimensions of the bar, the differences become significant and the limit of validity of the SIF predictions must be determined. To determine this limit, the center of each observed crack was measured relative to the specimen edge on the fracture surface and input into the solution from a SIF handbook (Murakami, 1987). An error in the range of 5–10% between finite bar and infinite plate results was considered acceptable. Once the crack grew to a length that caused an error over the specified limit, the SIF results were considered invalid. A representative example of this calculation using specimen HCF T/4 is shown **Figure 4**.

SIF solutions for straight surface cracks are available in a variety of handbooks and publications (Murakami, 1987; Dowling, 2012). A simple solution to a surface crack problem is to apply a geometry factor, F, which is a function of the aspect ratio to the through crack solution to obtain the SIF at either the surface of the crack or the deepest point (**Eq. 8**). ΔK_{eff} will be used to an effective stress intensity factor range after this surface crack correction factor has been applied. For example, a crack with an aspect ratio of 1 (the ratio of crack depth, d, to the surface crack length, c) has a geometry factor of $F = 0.73$ that is applied to find the SIF at deepest point of the crack (Dowling 2012).

$$K_{eff} = F * K_{eq} \quad [8]$$

To determine the aspect ratio of the experimentally observed surface cracks, both literature estimates and aspect ratios on the final fracture surfaces were collected. Prior research suggests that crack aspect ratio remains consistent regardless of the initiating flaw geometry (Toribio et al., 2016) and is governed by the Paris law crack growth exponent, m, and loading configuration. The aspect ratios of the fatigue cracks on the final fracture surfaces were also measured, which ranged from 1.08 to 0.645 for the specimens tested. An average aspect ratio of $2d/c = 0.9$ was applied to all experimentally investigated crack configurations. This value was chosen as representative to the majority of aspect ratios seen on the fracture surface, as well as its agreement to values seen in literature. A table with surface crack geometry factors for different crack aspect ratios is shown in **Table 4**. Using this average crack aspect ratio, a surface crack geometry factor of $F = 0.705$ was computed using the results presented in (Murakami, 1987), which accounts for crack depth and aspect ratio in a finite bar. The effects of using this average aspect ratio vs. the actual aspect ratio measured from the replications will be presented and reviewed in the discussion section.

Paris Law FCGR Calculations

Once an effective SIF range was calculated, the values were input into a Paris Law predictive model (Paris, 1961) to calculate FCGR. The general form of this model relates ΔK_{eff} to crack growth via an exponential relationship (**Eq. 9**). This model was chosen because material data to calculate the constants is commonly available for AA7075-T7351 as well as many other material types.

$$\frac{dc}{dN} = C\left(\Delta K_{eff}\right)^m \quad [9]$$

Where dc/dN is the crack growth per loading cycle, ΔK is the stress intensity factor range, and C, m are constants fitted to experimental crack growth data. The C and m constants for the Paris law crack growth model were calculated using datasets from (Newman et al., 2005) and the Metallic Materials Properties Development and Standardization, MMPDS, (FAA, 2015) for 7075-T7351 tested at a load ratio of $R = 0.1$. A combination of data sets was used to capture the wide range of SIFs produced in

TABLE 4 | Surface crack correction factors for various surface crack aspect ratios.

2d/c	Correction factor
0.2	0.2623
0.4	0.422
0.5	0.483
0.6	0.550
0.7	0.609
0.8	0.660
0.9	0.705
1	0.745
2	0.959

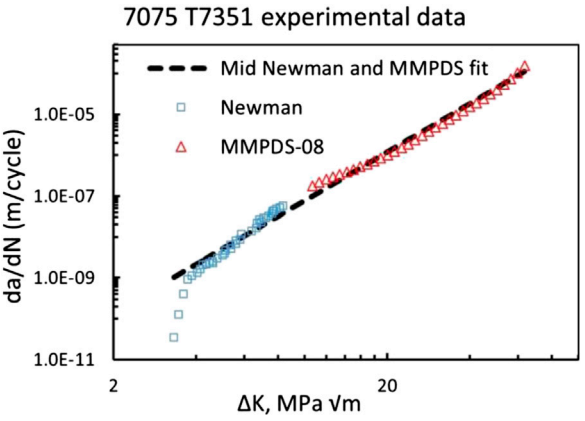

FIGURE 5 | Fatigue crack growth rate data and linear fit used for Al 7075-T7531 tested at a load ratio of $R = 0.1$.

this research. The entirety of the MMPDS data was used, as well as the upper portion (region II in the crack growth curve) of the Newman data. The data and fitted curve used in the computational study is shown in **Figure 5**. The fitted curve covered a range of stress intensity factors from 3.86 to 63.46 MPa $\sqrt{m}$, and yielded an m exponent of 3.93 and C equal to 9.04e-12 (m/cycle)/(MPa $\sqrt{m})^m$.

RESULTS

Experimental Fatigue Crack Growth Behavior

Table 5 displays the fatigue test results for the AA7075 specimens cut from both middle thickness (t/2) and quarter thickness (t/4) of the rolled plate. In general, the material displayed a consistent number of cycles to failure regardless of the thickness at which the specimen was cut. However, 1 t/4 LCF specimen failed at 100 cycles. The likely reason for this significant deviation in fatigue life is related to the source of crack initiation and will be discussed in more detail in the discussion section. Based on this fatigue life data, it appears there is no preferred sampling thickness for this batch of AA7075-T7351.

The two HCF specimens exhibited almost identical crack length vs. cycle trends except with regards to crack initiation. The two LCF specimens also closely compare, where the dominant crack spent the majority of the fatigue life under a crack length of 250 μm. The t/2 and t/4 thickness of the plate displayed very minimal differences in both the crack growth rate and number of cycles to failure.

The crack growth rate trends for the LCF specimens are different than the trends for the HCF specimens. From the beginning of the crack growth for both LCF specimens, the crack growth rate was observed to fluctuate and is non-linear. This trend continued to the end of fatigue life.

Fracture Surface Analysis

Through SEM, the source of crack initiation was determined to be a cracked intermetallic particle for each specimen observed in this study. In the vast majority of cases, a fatigue crack was found to nucleate from one or more particles at a single location and then propagate radially outward. In fact, we observed that a single specimen contained numerous large intermetallic particles (≈60 μm) throughout the fracture surface, but no noticeable fatigue crack was observed to initiate or propagate from these large particles. Of all the intermetallic particles that initiated fatigue cracks, the size ranged from approximately 10–30 μm. Upon scanning the intermetallic with EDS, all particles were determined to be iron-rich intermetallics. SEM images in back-scatter electron (BSE) mode of representative fracture surfaces illustrating the initiation site for LCF and HCF regimens are shown in **Figures 6A–D**, respectively. A summary of these crack initiating particles based on SEM analysis is presented in **Table 5**.

TABLE 5 | Fatigue test results and particle size of crack initiating defects.

Specimen	Stress range	Cycles to failure	Particle size (μm)
LCF t/2	420	7,013	30.3
HCF t/2	260	55,365	18.4
LCF t/4	420	6,982	19.9
HCF t/4	260	58,308	14.7

EBSD was conducted on the surface of two specimens (one LCF t/2 and one LCF t/4) where the crack initiated and grain misorientation was measured. **Figure 7** displays the grain orientation map and misorientation map for the LCF t/2 (7(a)) and LCF t/4 (7(b)) samples. Large, equiaxed grains were observed based on EBSD scan results for the LCF t/2 specimen at the initiation site (**Figure 7A**). The scan on the t/4 specimen (**Figure 7B**) revealed an equiaxed grain structure with combination of large grains and small grains. High angle misorientation was observed between most of the identifiable grains for both the t/2 and t/4 LCF specimens. The dominant cracks observed in this study were observed to have initiated in a region with large grains and high grain misorientation.

The fatigue crack dimensions were measured on the fracture surface and used to determine the final crack aspect ratio and to compute the maximum crack length at the validity limit due to edge effects as indicated by the vertical lines in **Figure 8**.

Fatigue Crack Growth Prediction

The results of the kinked model predictions compared to the experimental results are shown in **Figure 8** next to the geometries of the final crack configurations. The variation in the experimental crack growth rates is comparible to those determined in the FCGR charicterization of this alloy (Jordon et al., 2012), where the variations in crack growth rate change at a analogous amplitude over a similar distance of crack growth as the crack grows though changing microstructure.

DISCUSSION

Microstructural Effects

The t/2 and t/4 thicknesses of the plate displayed very minimal differences in both crack growth rate and number of cycles to

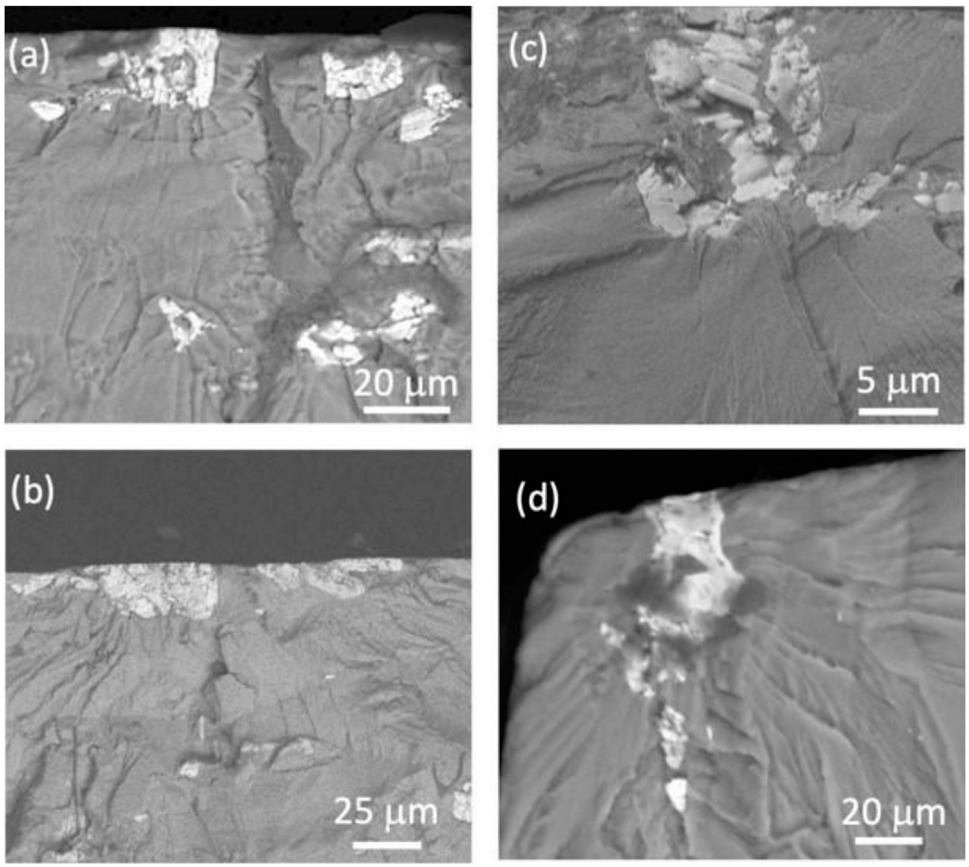

FIGURE 6 | Representative back-scatter electron (BSE) images of iron-rich intermetallic particles that initiated fatigue cracks in the **(A)**, **(B)** low cycle fatigue (LCF) and the **(C)**, **(D)** high cycle fatigue (HCF) regimes. Note that the iron-rich intermetallic particles are brighter compared to the darker aluminum matrix.

failure, though the t/4 specimens consistently demonstrated a longer fatigue life to crack initiation, when compared to the t/2 specimens. Both EBSD scans conducted displayed a similar grain structure when comparing the t/2 and t/4 LCF specimens. The scans revealed an equiaxed grain structure with primarily large grains, and high grain misorientation was observed between most of the identifiable grains. Based on the data captured in this study, it appears there is no preferred plate thickness for fatigue loading. This is an important observation because similar observations on crack initiation mechanisms revealed that cracks can initiate from casting pores in thick rolled plates (Cauthen et al., 2020). From the results presented in Table 8, it is clear that neither thickness possessed preferred crack growth resistance and therefore differences in fatigue life are dictated by crack initiation and microstructure.

An abundance of iron-rich intermetallic particles was found on the fracture surfaces, where intermetallic particles were found to initiate the dominant crack. EBSD results revealed an equiaxed grain structure with primarily large grains and high grain misorientation at the location of surface crack initiation. Furthermore, no evidence of surface crack initiation from persistence slip bands (PSB) was observed in contrast to observations made in other high strength aluminum alloys with high grain misorientations (Cauthen et al., 2020). However, due to the relatively high dispersion of the iron-rich intermetallic particles present in the legacy AA7075, it is not surprising that we observed cracks primarily initiating from these particles. These particles not only initiate cracks in AA7075 but can also influence the growth rates. The perturbation observed in small crack growth rates shown in Figure 13 has been shown to be influenced by discontinuities such as iron-rich intermetallic particles. In fact, crack growth rates have been observed to decrease significantly when cracks approached obstacles such as particles stringers in legacy AA7075. Once the driving forces exceeds the resistance provided by the iron-rich particle, the crack growth rate increases dramatically (Jordon et al., 2012).

Model Performance

After accounting for the actual crack depth in the LCF t/2 specimen, as discussed below, crack growth modeling predicted the FCGR obtained from experimental results within the measurement error bounds and range of validity (**Figure 8**) for all four specimens. The model reasonably predicted the crack growth rate early in the crack life, even in areas known to have large microstructural effects that cause fluctuations in the growth rate and limit the validity of a linear elastic, SIF based approach.

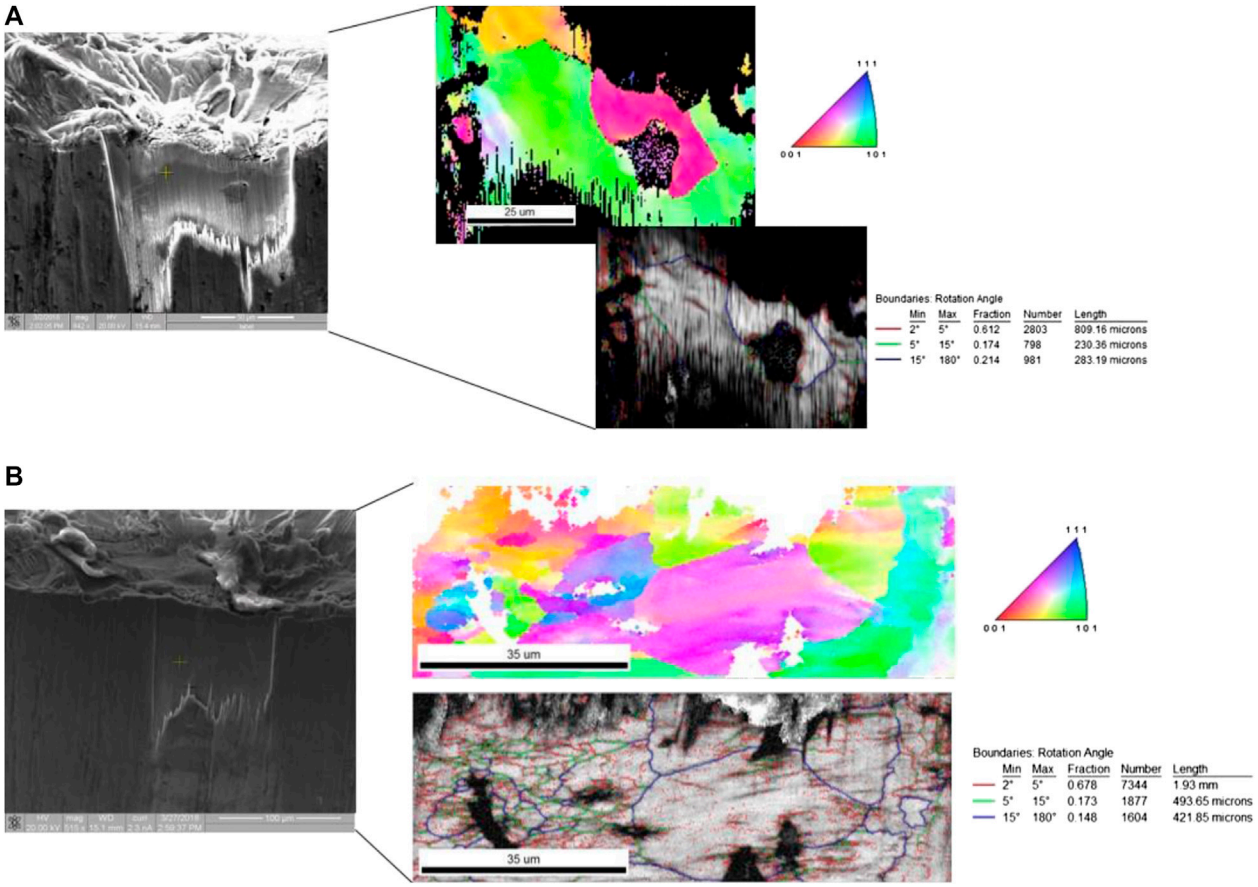

FIGURE 7 | EBSD scans at the initiation site of the **(A)** LCF t/2 and **(B)** LCF t/4 specimens. Both sites were FIBed such that a smooth 50-100 μm wide surface remained for EBSD analysis.

For all specimens tested, the model begins to severely over predict the growth rate at longer crack lengths. Note that this length scale is beyond the validity limit (shown as the vertical line in **Figure 8**) for which edge effects were estimated to be significant (greater than a 10%). This over prediction may be caused by plasticity induced crack closure effects, where crack closure occurs due to the combination of plastically deformed material left in the wake of the advancing crack and ahead of the crack tip (Walker et al., 2016).

The assumed crack depth also had a large effect on the predicted FCGR. The models were built on several assumptions, one of which was that the surface crack aspect ratio could be held constant at an average value with minimal error on the predicted FCGR. As seen in **Table 4**, as the crack becomes deeper, the surface geometry factor approaches one and converges to the SIF predicted by a through crack. For shallow cracks, the geometry factor is reduced. The geometry factor is applied to the effective SIF at each crack tip which is then input into the Paris law growth model, **Eq. 9**, where the crack growth is related to the SIF range raised to the m exponent. Therefore, the effect of the geometry factor error is raised by the power m. Thus, the effect of the error in the aspect ratio is higher for cracks with high SIFs than cracks with low SIFs, which helps explain the increased error caused by the geometry factor in the LCF T/2 FCGR predictions.

For the LCF T/2 specimen, the crack was shallower than the assumed aspect ratio, causing the actual crack growth to be lower than the original prediction. The FCGR was recalculated using the final aspect ratio observed on the fracture surface of 0.6 for this specimen and the results are compared in **Figure 9**. The results using the actual aspect ratio show a much better fit when compared to the experimental results. To further explore the error caused by an incorrect aspect ratio, we investigated the results for the HCF T/4 specimen (actual aspect ratio of 1.08) for varying aspect ratios. FCGRs were calculated using the bounding aspects ratios of 2 (approaching a through crack) and of 0.5 (representing a shallow crack) as presented in **Figure 9**. The assumed crack depth is shown to have a large effect on the predicted growth rate, although the assumed value of 0.9 predicted the FGCR within the bounds of the experimental results. Therefore, it is concluded that it is necessary to use a realistic crack depth to determine the aspect ratio and subsequent geometry factor. If measurement error prohibits determination of a highly accurate crack aspect ratio, the problem can be bounded by a high and low estimation.

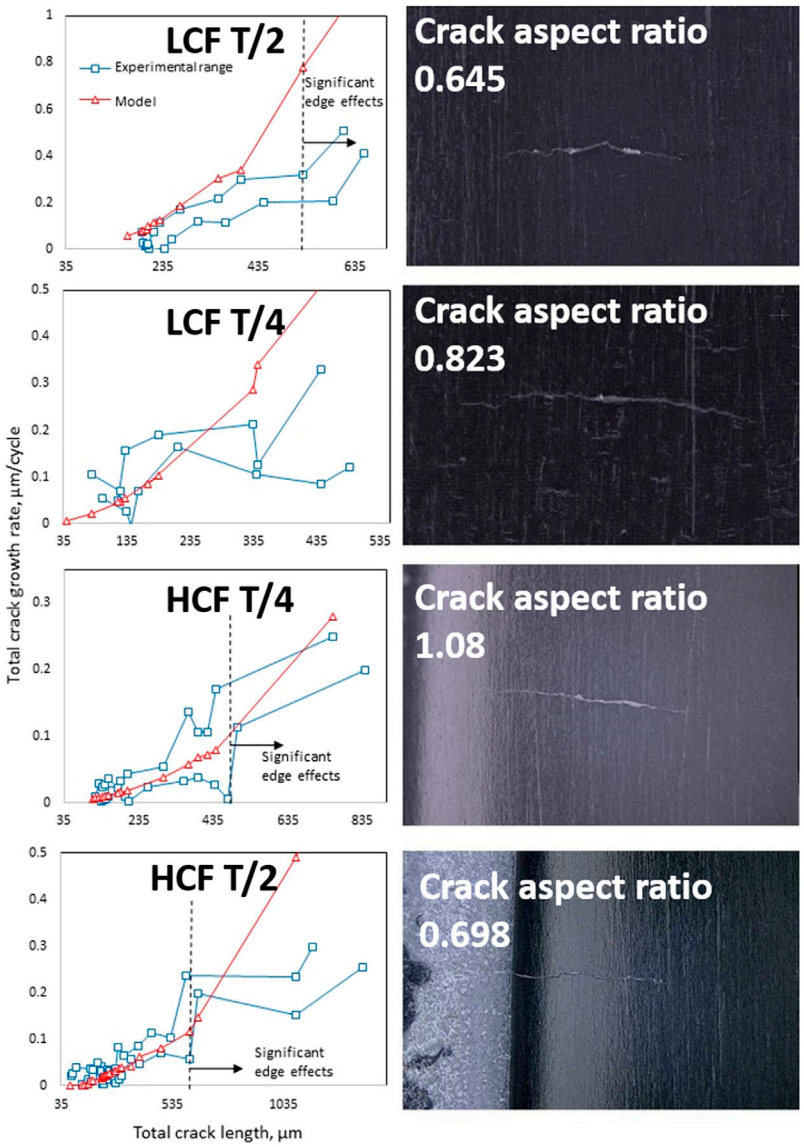

FIGURE 8 | Model predictions vs. experimental crack growth for the **(A)** LCF t/2, **(B)** LCF t/4, **(C)** HCF t/4, and **(D)** HCF t/2. The red line shows the predicted value of crack growth at each crack length, and the green lines show the high and low estimates of experimental crack growth. The vertical blue line shows the rack length where significant edge effects begin.

Effects of Crack Shape

One pupose of this study was to investigate the usefulness of using DDT to model kinked surface fatigue crack growth. To do this, the SIFs predicted by the kinked crack model for the four specimens are compared to the SIFs predicted by modeling the cracks as straight. As shown in **Figure 10** for specimen LCF T/2 results, the higher fidelity gained by including the kinks in the crack shape had a relatively small, but noticeable effect on the predicted crack growth for the fatigue specimens investigated in this study.

A more substantial difference occurs in the mode II SIF between the straight and kinked models. The comparison for specimen LCF T/2 exhibited the largest divergence beween kinked and straight crack solutions, with more divergence between the solutions as the crack grows longer. This specimen configuration had a pronounced kink in the middle and displayed the fastest crack growth of the four specimens. As observed from a close inspection of the final crack configurations shown in **Figure 8**, the crack configurations were relatively flat or exhibited large kink opening angles, scenarios that are very close to a straight crack approximation and were loaded under tension applied perpendicular to the crack causing the importance of including kinks to be diminished.

To calculate the significance of including the kinks in the model prediction, a comparison between the experimental,

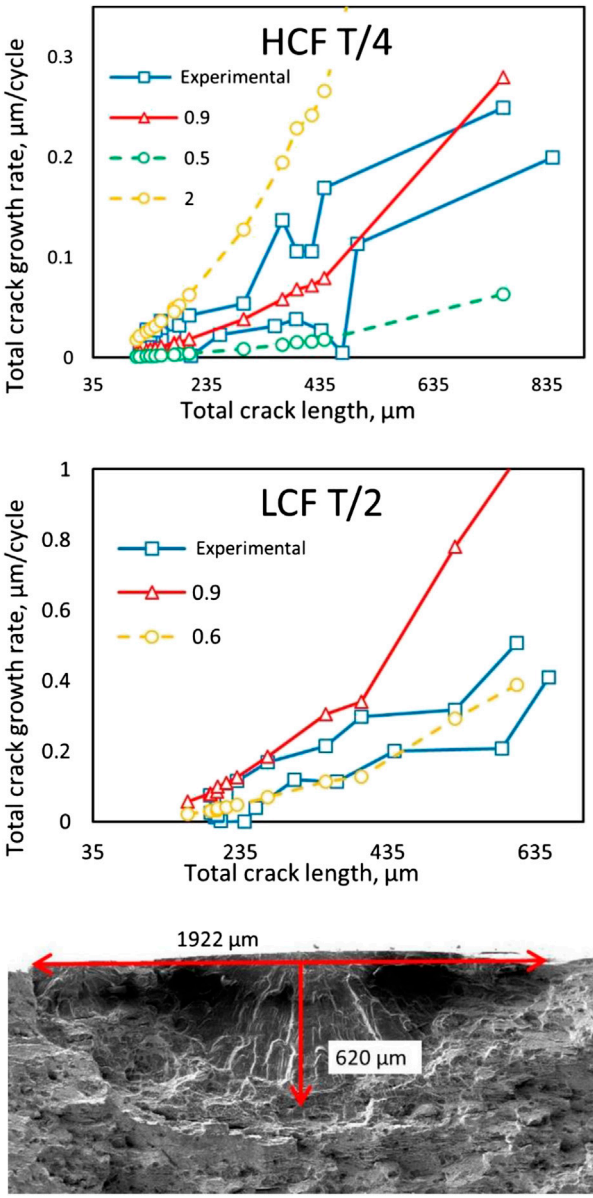

FIGURE 9 | (A) Effect of crack depth on the FGCR of specimen HCF T/4 for crack aspect ratios of 0.5, 0.9, and 2.0 **(B)** Experimental vs. model results for sample LCF T/2, showing model results assuming an aspect ratio of 0.9 vs. the actual aspect ratio of 0.6 **(C)** The fracture surface and final aspect ratio of the crack seen observed on sample LCF T/2.

straight, and kinked model values was made via a comparison of the percent error, using **Eqs 10** and **11**.

$$\text{Percent Error} = 100 * \frac{dc/dN_{\text{experimental}} - dc/dN_{\text{model}}}{dc/dN_{\text{experimental}}}$$

$$\text{Percent improvment} = \%\,\text{Error}_{\text{stright}} - \%\,\text{Error}_{\text{kink}}$$

The percent improvement between the straight and kinked crack models was related to the amount of deviation from straight of the actual crack shape unsurprisingly. The straighter cracks observed, in samples HCF T/4 and LCF T/4, showed smaller improvements between the models than the more kinked cracks, HCF T/2 and LCF T/2.

Within each sample though, differences between the performance of straight and kinked crack models appear to be primarily a function of difference between the angles, or directions, of the crack tips in each model. An example of this correlation is seen in the comparison of stress intensity factors between the straight and kinked models of sample LCF T/2 in **Figure 10B**. During the beginning of crack growth, when the observed crack was a sharp "*V*" shape, crack kinking of the crack tip angles of the real crack were captured better by the kinked model. Data points in this range had a higher percent improvement between the straight and kinked models, in the range of 30–52%, than the LCF T/2 crack as a whole. As the crack grew longer and became straighter as the crack tips turned toward a direction of maximum normal stress, the differences between the straight and kinked models decreased, even though the crack was modeled in more detail with multiple kinks. A similar observation can be seen in sample HCF T/2, when higher differences between the

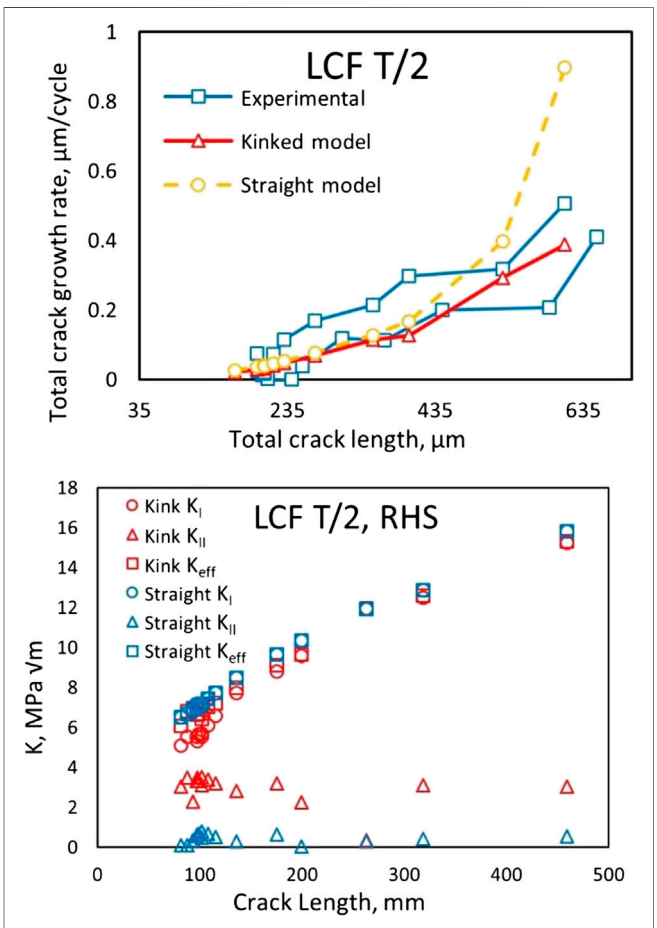

FIGURE 10 | (A) Comparison of predicted FCGR for two LCF T/2 model configurations: a crack with a single kink and straight crack **(B)** Comparison of predicted FCGR (modes I, II, and effective) for the same two configurations.

straight and kinked model are observed near the crack kinks, but then decreases as the crack grows outward in the direction of higher normal stresses away from the kink. These examples show that differences between a straight crack model and a kinked crack model are more severe when the kinking is closer to the crack tip, with the difference diminishing as the crack grows and straightens away from kinks.

CONCLUSIONS

In this study, the nucleation and microstructurally small crack growth under fatigue loading for AA7075-T7351 was experimentally obtained, measured, and then modeled using a computational method based on DDT. In this work, microstructurally small fatigue crack growth was quantified using a novel surface replication process through interrupted fatigue testing. The replication process employed in this study used a fast-curing two-part epoxy that provided a submicron resolution of crack nucleation and propagation. This high-resolution surface replication process uniquely captured the microstructurally influenced fatigue crack growth behavior of the AA7075- T735 for the first time. In addition, using the spatial information taken from the replicas, the exact location for the fatigue initiation events on the fracture surface was known and subsequently imaged through scanning electron microscopy. As such, iron-rich intermetallic particles and clusters of particles were found to initiate fatigue cracks in this alloy. While iron-rich particles initiating fatigue cracks in AA7xxx alloys is not new information, the use the replica process coupled with post-mortem fracture surface analysis removed any ambiguity from the process of identifying sources of fatigue crack initiation.

Regarding the use of the surface replication process for model calibration, The high resolution replication technique provides critical input data for the prediction of the FCGR by providing a quantified crack shape. For the specimens investigated, crack growth modeling was found to predict experimental crack growth rates with an acceptable degree of accuracy. An important finding is that the geometry correction factor must be highly accurate, further emphasizing the importance of the high resolution technique to obtain crack shapes. Furthermore, the importance of explicitly modeling the kinks is exhibited when the angle or direction of the crack tips deviates from the shape of a straight crack, especially when the distance from the kink to the crack tip is small.

These results lead to the question of: what are the requirements in terms of crack configuration resolution for crack modeling to obtain converged and accurate results? Future work should address what amount of crack kinking/angle change is necessary and how many kinks/crack segments are required to obtain a given level of accuracy. Additionally, complex loading conditions may also necessitate higher fidelity modeling of the cracks. As a preliminary example, comparison of the results in **Table 2** for biaxial loading demonstrate significant differences in the SIFs between a kinked crack and a straight crack model. (The straight cracks in **Table 2** were created by generating a straight line between the two crack tips of the corresponding kinked cracks).

Another important consideration is investigating the limits of prediction accuracy with regards to the geometry factor. This factor was successfully applied for this focused study on one specimen type using a factor derived for straight cracks. A comprehensive study is needed to determine the applicability of this assumption for cracks with more significant kinking and branching and to explore the need to vary the geometry factor per crack segment. An extensive sensitivity analysis should be performed to explore the effects of varying crack segment shape, crack segment length, crack depth relative to plate thickness, loading conditions, and number of cracks relative to the geometry factor on the FCGR prediction accuracy.

Future Research and Development

The computational method was able to predict the FCGR for the cracks studied in this research. While the modeling resolution to include the effects of kink was not significant in this investigation, the computational foundation to predict the FCGR of kinked cracks was demonstrated. The method has been shown to be computationally efficient on a generic laptop computer and converges rapidly for a minimal number of DOF (measured by the number of opening terms included in an analysis). By integrating to obtain the solution, the method avoids many numerical approximations that increase the error in the results. Future applications of this method will benefit from the capability to obtain stress fields at discontinuities, including kinks and crack branching locations. Computational results also include full stress and displacement fields which will enable the prediction of crack path in future enhancements. Additionally, the method has been proven to converge for multiple crack arrays, even when the ligaments are very small between cracks (TerMaath et al., 2006). In summary, the method provides a fast yet accurate approach to evaluate existing crack patterns and conditions under general loading conditions and is applicable to small cracks through the use of the geometry factor. While the method is limited to modeling a crack array in a plate, this approximation does represent many real world scenarios. For example, this method has many potential applications for existing crack patterns that can be measured including:

- Informing inspection intervals
- Monitoring structural health
- Determining residual strength degradation
- Evaluating load-carrying capacity
- Informing repair and retirement strategies
- Locating areas where potential for new damage initiation is high (i.e., if corrosion, material defects, or overlooked cracks are present in a highly stressed area)
- Performing statistical studies using Monte Carlo simulation

DATA AVAILABILITY STATEMENT

The datasets presented in this article are not readily available because Data was generated under projects with proprietary restrictions by the sponsors. Requests to access the datasets should be directed to stermaat@utk.edu.

AUTHOR CONTRIBUTIONS

RF – analytical framework development, calculations and results post-processing, sensitivity analysis and uncertainty quantification, paper writing. CC – experimental testing and results post-processing, analytical framework development, paper writing. SD – project coordination. JJ – project coordination, results post-processing, paper writing. AB - project administration. ST –analytical framework development and coding, calculations and results post-processing, paper writing, and project coordination.

FUNDING

The authors would like to thank Boeing for the partial funding of this project. Partial financial support was also provided by the Office of Naval Research (ONR) Structural Reliability Program through a Young Investigator Program grant (N00014-14-1-0516/N00014-16-1-2370) under the direction of Dr. Paul Hess.

ACKNOWLEDGMENTS

Testing facilities used in this study were provided by the University of Alabama and the Central Analytical Facility. The authors thank the staff at the Central Analytical Facility for assistance with microscopy. The authors also thank University of Tennessee PhD students Cody Crusenberry and Corey Arndt for their help with the UQ. The DICE software was provided and developed at the Naval Surface Warfare Center Carderock Division and the authors appreciate the technical support from NAVSEA engineers Ken Nahshon and Nick Reynolds.

REFERENCES

Abaqus (2014). Abaqus analysis user's guide version 6.14. Available at: https://blogs.3ds.com/korea/wp-content/uploads/sites/6/2015/11/Co-Simulation-Using-Abaqus-and-FTire.pdf.

Altıntaş, E., and Güngör, E. (2013). Alternative surface roughness measurement technique for inaccessible surfaces of jet engine parts using the rubber silicon replica method. *Metallogr. Microstruct. Anal.* 2, 337–342. doi:10.1007/s13632-013-0092-6

Barber, J. (1992). *Elasticity*. Boston, MA: Kluwer academic publishers.

Bernard, J. D., Jordon, J. B., Lugo, M., Hughes, J. M., Rayborn, D. C., and Horstemeyer, M. F. (2013). Observations and modeling of the small fatigue crack behavior of an extruded AZ61 magnesium alloy. *Int. J. Fatig.* 52, 20–29. doi:10.1016/j.ijfatigue.2013.02.015

Castelluccio, G. M., and McDowell, D. L. (2012). Assessment of small fatigue crack growth driving forces in single crystals with and without slip bands. *Int. J. Fract.* 176 (1), 49–64. doi:10.1007/s10704-012-9726-y

Castelluccio, G. M., and McDowell, David. L. (2016). Microstructure-sensitive small fatigue crack growth assessment: effect of strain ratio, multiaxial strain state, and geometric discontinuities. *Int. J. Fatig.* 82, 521–529. doi:10.1016/j.ijfatigue.2015.09.007

Cauthen, C., Anderson, K. V., Avery, D. Z., Baker, A., Williamson, C. J., Daniewicz, S. R., et al. (2020). Fatigue crack nucleation and microstructurally small crack growth mechanisms in high strength aluminum alloys. *Int. J. Fatig.* 140, 105790. doi:10.1016/j.ijfatigue.2020.105790

Cauthen, C., Daniewicz, S. R., and Shamsaei, N. (2017). Modeling fatigue crack growth behavior in rolled AZ31 magnesium alloy using CTOD based strip yield modeling. *Int. J. Fatig.* 96, 196–207. doi:10.1016/j.ijfatigue.2016.11.031

Dai, P., Luo, X., Yang, Y., Kou, Z., Huang, B., Zang, J., et al. (2020). The fracture behavior of 7085-T74 Al alloy ultra-thick plate during high cycle fatigue. *Metall. Mater. Trans.* 51, 3248–3255. doi:10.1007/s11661-020-05759-4

Daniewicz, S. R., and Aveline, C. R. (2000). Strip-yield and finite element analysis of part-through surface flaws. *Eng. Fract. Mech.* 67 (1), 21–39. doi:10.1016/S0013-7944(00)00032-1

Deng, G. J., Tu, S. T., Zhang, X. C., Wang, J., Zhang, C. C., Qian, X. Y., et al. (2016). Small fatigue crack initiation and growth mechanisms of nickel-based superalloy GH4169 at 650 °C in air. *Eng. Fract. Mech.* 153, 35–49. doi:10.1016/j.engfracmech.2015.12.014

Deng, G. J., Tu, S. T., Zhang, X. C., Wang, Q. Q., and Qin, C. H. (2015). Grain size effect on the small fatigue crack initiation and growth mechanisms of nickel-based superalloy GH4169. *Eng. Fract. Mech.* 134, 433–450. doi:10.1016/j.engfracmech.2015.01.002

Dowling, N. E. (2012). *Mechanical behavior of materials: engineering methods for deformation, fracture, and fatigue*. London, United Kingdom: Pearson.

FAA (2015). *Metallic materials properties development and standardization*. Washington, D.C., United States: Federal Aviation Administration.

Gall, K., Yang, N., and Horstemeyer, M. (1999). The debonding and fracture of Si particles during the fatigue of a cast Al-Si alloy. *Mater. Trans.* 30, 3079–3088. doi:10.1007/s11661-999-0218-2

Helton, J. C., and Davis, F. J. (2003). Latin hypercube sampling and the propagation of uncertainty in analyses of complex systems. *Reliab. Eng. Syst. Saf.* 81 (1), 23–69. doi:10.1016/S0951-8320(03)00058-9

Herbig, M., King, A., Peter, R., Henry, P., Erik, M., Marrow, J., et al. (2011). 3-D growth of a short fatigue crack within a polycrystalline microstructure studied using combined diffraction and phase-contrast X-ray tomography. *Acta Mater.* 59 (2), 590–601. doi:10.1016/j.actamat.2010.09.063

Hills, D., Kelly, P., Dai, D., and Korsunsky, A. (1996). *Solution of crack problems: the distributed dislocation technique*. Alphen aan den Rijn, Netherlands: Kluwer Academic Publishers.

Hu, X., Zhu, L., Jiang, R., Song, Y., and Qu, S. (2019). Small fatigue crack growth behavior of titanium alloy TC4 at different stress ratios. *Fatig. Fract. Eng. Mater. Struct.* 42, 339–351. doi:10.1111/ffe.12911

Hussain, K. (1997). Short fatigue crack behaviour and analytical models: a review. *Eng. Fract. Mech.* 58 (4), 327–354. doi:10.1016/S0013-7944(97)00102-1

Ishida, M., and Nishino, T. (1982). Formulae of stress intensity factor of bent cracks in plane problems. *Trans. Japan Soc. Mech. Eng.* 48, 430.

Jordon, J. B., Bernard, J. D., and Newman, J. C., Jr (2012). Quantifying microstructurally small fatigue crack growth in an aluminum alloy using a silicon-rubber replica method. *Int. J. Fatig.* 36 (1), 206–210. doi:10.1016/j.ijfatigue.2011.07.016

Lardner, R. (1974). *Mathematical theory of dislocations and fracture*. Tonawanda, NY: University of Toronto press.

Ma, M., Zhang, J., Yi, D., and Wang, B. (2019). Investigation of high-cycle fatigue and fatigue crack propagation characteristic in 5083-O aluminum alloy. *Int. J. Fatig.* 126, 357–368. doi:10.1016/j.ijfatigue.2019.05.020

McCullough, R. R., Jordon, J. B., Allison, P. G., Rushing, T., and Garcia, L. (2019). Fatigue crack nucleation and small crack growth in an extruded 6061 aluminum alloy. *Int. J. Fatig.* 119, 52–61. doi:10.1016/j.ijfatigue.2018.09.023

McDowell, D. L., Gall, Ken., Horstemeyer, M. F., and Fan, J. (2003). Microstructure-based fatigue modeling of cast A356-T6 alloy. *Eng. Fract. Mech.* 70 (1), 49–80. doi:10.1016/S0013-7944(02)00021-8

Murakami, Y. (1987). *Stress intensity factors*. Oxford, United Kingdom: Pergamon Press.

Nahshon, K., and Reynolds, N. (2016). *DICE: distribution-based input for computational evaluations*. West Bethesda, MD: Naval Surface Warfare Center.

Newman, J. A., Willard, S. A., Smith, S. W., and Piascik, R. S. (2009). Replica-based crack inspection. *Eng. Fract. Mech.* 76, 898–910. doi:10.1016/j.engfracmech.2008.12.012

Newman, J., Jr, Schneider, J., Daniel, A., and McKnight, D. (2005). Compression pre-cracking to generate near threshold fatigue-crack-growth rates in two aluminum alloys. *Int. J. Fatig.* 27 (10-12), 1432–1440. doi:10.1016/j.ijfatigue.2005.07.006

Newman, J. C., Jr, Wu, X. R., Venneri, S. L., and Li, C. G. (1994). *Small-crack effects in high-strength aluminum alloys*. Hampton, VA: NASA, Langley Research Center.

Qian, J., and Fatemi, A. (1996). Mixed mode fatigue crack growth: a literature survey. *Eng. Fract. Mech.* 55 (6), 969–990. doi:10.1016/S0013-7944(96)00071-9

Qin, C. H., Zhang, X. C., Ye, S., and Tu, S. T. (2015). Grain size effect on multi-scale fatigue crack growth mechanism of Nickel-based alloy GH4169. *Eng. Fract. Mech.* 142, 140–153. doi:10.1016/j.engfracmech.2015.06.003

Raju, I. S., and Newman, J. C., Jr (1979). Stress-intensity factors for a wide range of semi-elliptical surface cracks in finite-thickness plates. *Eng. Fract. Mech.* 11 (4), 817–829. doi:10.1016/0013-7944(79)90139-5

Sih, G. C., Paris, P. C., and Erdogan, F. (1962). Crack-tip, stress-intensity factors for plane extension and plate bending problems. *J. Appl. Mech.* 29, 306–312. doi:10.1115/1.3640546

Silling, S. A., and Abe, A. (2014). Peridynamic model for fatigue cracking. Albuquerque, NM: Sandia National Laboratories. SAND2014-18590.

Stephens, R. I., Ali, F., Stephens, R. R., and Fuchs, H. O. (2001). *Metal fatigue in engineering*. New York, NY: John Wiley and Sons.

Sun, D., and Ma, X. (1997). An application of the boundary element method to the fatigue crack propagation in a cracked heterogeneous body. *Eng. Fract. Mech.* 56 (6), 839–840. doi:10.1016/S0013-7944(96)00059-8

Tanaka, K. (1974). Fatigue crack propagation from a crack inclined to the cyclic tensile axis. *Eng. Fract. Mech.* 6 (3), 493–507. doi:10.1016/0013-7944(74)90007-1

TerMaath, S. C. (2001). A two-dimensional analytical technique for studying fracture in brittle materials containing interacting kinked and branched cracks. PhD dissertation. Ithaca (NY): Cornell University.

TerMaath, S. C., Phoenix, S. L., and Hui, C-Y. (2006). A technique for studying interacting cracks of complex geometry in 2D. *Eng. Fract. Mech.* 73 (8), 1086–1114. doi:10.1016/j.engfracmech.2004.09.009

Tokaji, K., Kamakura, M., Ishiizumi, Y., and Hasegawa, N. (2004). Fatigue behaviour and fracture mechanism of a rolled AZ31 magnesium alloy. *Int. J. Fatig.* 26 (11), 1217–1224. doi:10.1016/j.ijfatigue.2004.03.015

Toribio, J., Matos, J. C., and González, B. (2016). Aspect ratio evolution associated with surface cracks in sheets subjected to fatigue. *Int. J. Fatig.* 92, 588–595. doi:10.1016/j.ijfatigue.2016.03.028

Walker, K. F., Wang, C. H., and Newman, J. C., Jr (2016). Closure measurement and analysis for small cracks from natural discontinuities in an aluminium alloy. *Int. J. Fatig.* 82, 256–262. doi:10.1016/j.ijfatigue.2015.03.016

Wilson, D., and Dunne, F. P. E. (2019). A mechanistic modelling methodology for microstructure-sensitive fatigue crack growth. *J. Mech. Phys. Solid.* 124, 827–848. doi:10.1016/j.jmps.2018.11.023

Wilson, D., Zheng, Z., and Dunne, F. P. E. (2018). A microstructure-sensitive driving force for crack growth. *J. Mech. Phys. Solid.* 121, 147–174. doi:10.1016/j.jmps.2018.07.005

Xue, Y., Dl McDowell, M. F. H., Dale, M. H., and Jordon, J. B. (2007). Microstructure-based multistage fatigue modeling of aluminum alloy 7075-T651. *Eng. Fract. Mech.* 74 (17), 2810–2823. doi:10.1016/j.engfracmech.2006.12.031

Yavuz, A. K., Phoenix, S. L., and TerMaath, S. C. (2006). An accurate and fast analysis for strongly interacting multiple crack configurations including kinked (V) and branched (Y) cracks. *Int. J. Solid Struct.* 43 (22-23), 6727–6750. doi:10.1016/j.ijsolstr.2006.02.005

Yavuz, A. K., Ahmed, T., and Halit, S. T. (2020). "Computer simulation of fatigue crack growth under different loading conditions using boundary cracklet method (BCM)," in Advances in science and engineering technology international conferences (ASET), Dubai, United Arab Emirates, February 4–April 9, 2020 (New York, NY: IEEE), 9118170.

Ye, S., Gong, J. G., Zhang, X. C., Tu, S. T., and Zhang, C. C. (2017). Effect of stress ratio on the fatigue crack propagation behavior of the nickel-based GH4169 alloy. *Acta Metall. Sin.* 30, 809–821. doi:10.1007/s40195-017-0567-6

Zerbst, U., Madia, M., Klinger, C., Bettge, D., and Murakami, Y. (2019). Defects as a root cause of fatigue failure of metallic components. I: basic aspects. *Eng. Fail. Anal.* 97, 777–792. doi:10.1016/j.engfailanal.2019.01.055

Zhu, L., Hu, X., Jiang, R., Song, Y., and Qu, S. (2019). Experimental investigation of small fatigue crack growth due to foreign object damage in titanium alloy TC4. *Mater. Sci. Eng.* 739, 214–224. doi:10.1016/j.msea.2018.10.031

Zhu, L., Wu, Z., Hu, X., and Song, Y. (2018). Comparative study of small crack growth behavior between specimens with and without machining-induced residual stress of alloy GH4169. *J. Mech. Sci. Technol.* 32, 5251–5261. doi:10.1007/s12206-018-1023-x

Zhu, L., Wu, Z. R., Hu, X. T., and Song, Y. D. (2016). Investigation of small fatigue crack initiation and growth behaviour of nickel base superalloy GH4169. *Fatig. Fract. Eng. Mater. Struct.* 39, 1150–1160. doi:10.1111/ffe.12430

Conflict of Interest: Author AB was employed by The Boeing Company.

The remaining authors declare that the research was conducted in the absence of any commercial or financial relationships that could be construed as a potential conflict of interest.

frontiers in Materials

ORIGINAL RESEARCH
published: 14 January 2021
doi: 10.3389/fmats.2020.595295

Changing Compliance of Poly(Vinyl Alcohol) Tubular Scaffold for Vascular Graft Applications Through Modifying Interlayer Adhesion and Crosslinking Density

YeJin Jeong[1], *Yuan Yao*[1], *Tizazu H. Mekonnen*[2] *and Evelyn K. F. Yim*[1,3,4]*

[1]*Department of Chemical Engineering, University of Waterloo, Waterloo, ON, Canada,* [2]*Institute of Polymer Research, Department of Chemical Engineering, University of Waterloo, ON, Canada,* [3]*Waterloo Institute for Nanotechnology, University of Waterloo, Waterloo, ON, Canada,* [4]*Center for Biotechnology and Bioengineering, University of Waterloo, Waterloo, ON, Canada*

Poly(vinyl alcohol) (PVA) is a water-soluble polymer and forms a hydrogel that has been studied as a potential small-diameter (<6 mm) vascular graft implant. The PVA hydrogel crosslinked using sodium trimetaphosphate (STMP) has been shown to have many beneficial properties such as bioinert, low-thrombogenicity, and easy surface modification. Compared to conventional synthetic vascular graft materials, PVA has also shown to possess better mechanical properties; however, the compliance and other mechanical properties of PVA grafts are yet to be optimized to be comparable with native blood vessels. Mechanical compliance has been an important parameter to be studied for small-diameter vascular grafts, as compliance has been proposed to play an important role in intimal hyperplasia formation. PVA grafts are made using dip-casting a cylindrical mold into crosslinking solution. The number of dipping can be used to control the wall thickness of the resulting PVA grafts. In this study, we hypothesized that the number of dip layers, chemical and physical crosslinking, and interlayer adhesion strength could be important parameters in the fabrication process that would affect compliance. This work provides the relationship between the wall thickness, burst pressure, and compliance of PVA. Furthermore, our data showed that interlayer adhesion as well as chemical and physical crosslinking density can increase the compliance of PVA grafts.

Keywords: vascular graft, compliance, interlayer adhesion, crosslinking density, poly(vinyl alcohol), dip-casting

OPEN ACCESS

Edited by:
Patricia Krawczak,
IMT Lille Douai, France

Reviewed by:
Guoping Guan,
Donghua University, China
Geoffrey Robert Mitchell,
Polytechnic Institute of Leiria, Portugal

***Correspondence:**
Evelyn K. F. Yim
eyim@uwaterloo.ca

Specialty section:
This article was submitted to Mechanics of Materials, a section of the journal Frontiers in Materials

Received: *15 August 2020*
Accepted: *01 December 2020*
Published: *14 January 2021*

Citation:
Jeong Y, Yao Y, Mekonnen TH and Yim EKF (2021) Changing Compliance of Poly(Vinyl Alcohol) Tubular Scaffold for Vascular Graft Applications Through Modifying Interlayer Adhesion and Crosslinking Density. Front. Mater. 7:595295. doi: 10.3389/fmats.2020.595295

INTRODUCTION

Small diameter synthetic vascular grafts, which are grafts with diameter < 6 mm, are not commercially available due to having low patency. The low patency has been attributed to many mechanical and biological factors (Abbott et al., 1987). Among the different factors, mechanical compliance has been shown as one of the potential parameters that can influence the performance of small diameter vascular grafts (Jeong et al., 2020; Szafron, 2019). Compliance is defined in vascular graft engineering as the elasticity of the conduit when exposed to internal pressure (Szafron, 2019). The commercially available synthetic grafts, such as expanded polytetrafluoroethylene (ePTFE) and Dacron, have significantly lower compliance than native blood vessels (Tai et al., 2000). However, the

exact role compliance plays in the failure of small diameter vascular graft still remains elusive (Jeong et al., 2020). This is partially due to the difficulty in fabricating grafts using one material with variable, controllable, and predictable compliance.

One of the materials that is being studied as a potential off-the-shelf small-diameter vascular graft is poly(vinyl alcohol) (PVA) (Pohan et al., 2019; Cutiongco et al., 2015; Yao, 2020; Elshazly, 2004; Cutiongco et al., 2016b). PVA is a bioinert and low thrombogenic polymer that allows for easy chemical and topographical surface modification (Yao, 2020). In addition to having beneficial biomaterial properties, PVA has tunable mechanical properties (Cutiongco et al., 2016b). As a result, PVA is used in various applications. PVA vascular grafts are fabricated via dip-casting using cylindrical molds. PVA grafts have been shown to have dimensions and suture retention strength close to the native artery while withstanding burst pressure higher than that of the maximum systolic blood pressure (Chaouat, 2008). Although PVA grafts have higher compliance than ePTFE grafts, PVA grafts are still not as compliant as the native blood vessels (Pohan et al., 2020). Therefore, there is a need to investigate the different fabrication conditions of PVA grafts to further increase the compliance of PVA grafts. One limiting parameter to increasing compliance is the mechanical integrity of the grafts. As the grafts need to withstand the physiological pressure, increase in compliance cannot sacrifice the mechanical integrity of the grafts to ensure the safety of the patients. One of the parameters used to test the mechanical integrity of the vascular grafts is burst pressure. Burst pressure is the internal pressure at which the graft bursts, and is known to be closely correlated to the wall thickness of a tube (Menon, 2011). The motivation of this study is to make grafts with varying compliance using PVA, and identifying the burst pressure at respective compliance.

To further identify the parameters that can contribute to the mechanical properties of the PVA grafts, the interlayer adhesion and crosslinking density were explored. Interlayer adhesion and crosslinking density have been shown to contributed to dip-casting polymer and hydrogel mechanical properties. An increase in interlayer adhesion is known to increase the mechanical integrity of hydrogels (Kim et al., 2020). Interlayer adhesion is a critical factor since PVA grafts are fabricated through dip-casting multiple layers to reach the desired wall thickness. Additionally, the crosslinking density of the hydrogels can affect the mechanical properties of the polymer (Kim et al., 2020; Leone, 2010; Peppas et al., 2006). Increasing crosslinking density can result in stiffer hydrogels. PVA is a material with multiple mechanisms of chemical crosslinking with different chemical crosslinkers (Puy et al., 2019) and physical crosslinking with physical entanglement or via hydrogen-bonding (XIONG, 2008; Chen et al., 2016). In an effort to increase compliance while maintaining high burst pressure, interlayer adhesion and crosslinking densities were altered by altering fabrication process. We hypothesize that the increase in interfacial energy will allow for higher compliance and higher burst pressure when the grafts have the same wall thickness. Also, we hypothesize that a decrease in crosslinking density will result in higher compliance and lower burst pressure when the grafts have the same wall thickness. Lastly, we hypothesize that post-fabrication processing can cause physical crosslinking, and impact the compliance and burst pressure.

MATERIALS AND METHODS

Poly(vinyl alcohol) Vascular Graft Fabrication Process

Standard PVA crosslinking method was used for graft fabrication as described previously (Cutiongco et al., 2015). Briefly, cylindrical molds are dip-cast in the crosslinking solution, then dried in controlled environment as shown in **Figure 1A**. The complete list of the parameters that were varied during the fabrication of the grafts is shown in **Supplementary Table S1**. All of the grafts made using different fabrication parameters had 9 layers. The images of the grafts that were successfully fabricated using different fabrication parameters are shown in **Figure 1B**. The abbreviations and the fabrication conditions that was altered from the standard fabrication conditions is explained in **Figure 1C**.

PVA Crosslinking Solution Preparation

For standard crosslinking density grafts, a 10% aqueous solution of PVA (Sigma-Aldrich, 85–124 kDa, 87–89% hydrolyzed) was mixed with 15% w/v sodium trimetaphosphate (STMP, Sigma-Aldrich) and 30% w/v NaOH at the volumetric ratio of 12:1:0.4, respectively, to create crosslinking solution. PVA grafts were fabricated using base-catalyzed STMP crosslinking. The PVA crosslinking solution was immediately dip-cast on a cylinder mold to form tubular PVA grafts.

To fabricate PVA grafts with different crosslinking density, 10% w/v PVA solutions of different molecular weights were used. Instead of the standard molecular weight of PVA (Sigma-Aldrich, 85–124 kDa, 87–89% hydrolyzed) low molecular weight PVA (Sigma-Aldrich, 13–23 kDa, 87–89% hydrolyzed) (LMW), or medium molecular weight PVA (Sigma-Aldrich, 31–50 kDa, 87–89% hydrolyzed) (MMW) were used while all other parameters were kept the same as the standard method. A low STMP (LS) concentration of 7.5% w/v was used to crosslink PVA with the standard PVA concentration and NaOH concentration. Lastly, low NaOH (LN) concentration of 15% w/v was used to fabricate grafts with decreased crosslinking density.

Dip-Casting PVA Vascular Graft

PVA vascular grafts were cast as previously described (**Figure 1A**) (Pohan et al., 2019). In short, the molds for the tubular grafts were plasma cleaned, then dipped in PVA crosslinking solution. The coated molds were dried at 20–21°C and 30% humidity for varying waiting time, before dipping in the crosslinking solution again for the next layer. For the first four dips, the drying time between dips was 15 min, the drying time between dips in the fifth to seventh dip was 25 min, and drying time between dips for the eighth dip and higher was 30 min. The molds were inverted every-other dips to ensure even crosslinking throughout the mold. After the dipping completed, the PVA grafts were dried at 18°C and 70–80% humidity for 3 days.

Upon completion of the final drying step, the PVA grafts were rehydrated in 10x phosphate buffered saline (PBS) for 2 h, 1x phosphate buffered saline (PBS) for 2 h, then in deionized (DI) water for 2 h. For the samples used in phosphate quantification assay, samples were rehydrated in 9% w/v sodium chloride (NaCl) for 2 h, 0.9% w/v NaCl for

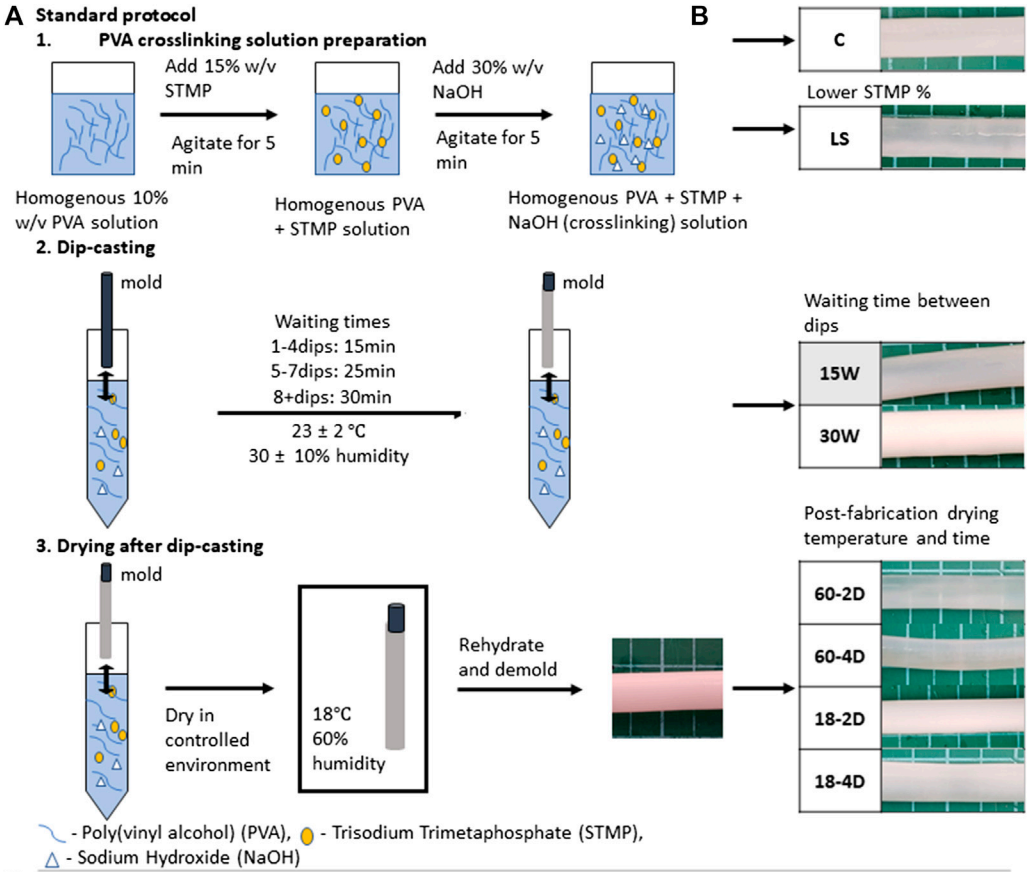

C

Abbreviations	Description
C	Control. Made following standard protocol (shown above). Samples had 9 layers.
LS	Low STMP. Made using 7.5% STMP instead of the standard concentration. Samples had 9 layers.
15W	15-minute waiting between dips. Made using 15-minute dry times between dips instead of the standard drying times. Samples had 9 layers.
30W	30-minute waiting between dips. Made using 30-minute dry times between dips instead of the standard drying times. Samples had 9 layers.
60-2D	Dried in 60°C post fabrication for 2 weeks. Made using the standard protocol, then dried at 60°C post fabrication for 2 weeks. Samples had 9 layers.
60-4D	Dried in 60°C post fabrication for 4 weeks. Made using the standard protocol, then dried at 60°C post fabrication for 4 weeks. Samples had 9 layers.
18-2D	Dried in 18°C post fabrication for 2 weeks. Made using the standard protocol, then dried at 18°C post fabrication for 2 weeks. Samples had 9 layers.
18-4D	Dried in 18°C post fabrication for 4 weeks. Made using the standard protocol, then dried at 18°C post fabrication for 4 weeks. Samples had 9 layers.

FIGURE 1 | Standard graft fabrication protocol and description of the varied parameter for each experimental groups. **(A)** Standard protocol, **(B)** representative images of the fabricated grafts for each experimental group, and **(C)** abbreviations and descriptions of the varied parameter for each experimental group. Samples for all groups were fabricated following the standard protocol except for the described parameter.

another 2 h, and then in DI water for 2 more hours. The grafts were removed from the molds once they were fully rehydrated. The completed grafts were then kept in DI water until experiments. This procedure was kept the same as the standard method for the different groups unless otherwise specified. Grafts with different drying times were also fabricated as a method to test how the dry time could vary the interfacial energy. The drying times were either consistent 15 min (15 W) or 30 min (30 W) between dips for these samples. In sample group to test the role of drying rate on interfacial energy, PVA grafts were fabricated at higher humidity (HH) of 60 ± 5% during fabrication.

Post-Fabrication Treatment of Extra-Dried PVA Vascular Grafts

After the rehydration step, some vascular grafts fabricated using the standard protocol were dried again to facilitate further crosslinking. Upon removal from the mold, the grafts were washed by submerging the grafts in DI water for 5 days. The grafts were dried again afterward at different conditions. The

post-fabrication drying conditions were: 2 weeks at 60°C (60-2D), 4 weeks at 60°C (60-4D), 2 weeks at 18°C (18-2D), and 4 weeks at 18°C (18-4D). Before testing, the grafts were rehydrated in DI water.

Storage of the Fabricated Grafts

The samples were kept at room temperature at all times. All samples were stored in DI water in a 50 mL conical tube upon completion of the fabrication. DI water was poured out and replenished with fresh DI water every 7 days during storage.

PVA Film Preparation

4 g ± 0.2 g of 10% w/v PVA solution was poured into petri dishes with diameter of 35 mm. The petri dish was covered and stored at 18°C chamber with a relative humidity of 70–80% for 3 days. The petri dish was then uncovered and stored at 18 C and 70–80% humidity for another 4 days. The dried PVA film (Film) was removed from the petri dish. Films were stored in petri dish until use.

Inner-Diameter and Wall Thickness

2 mm segment rings were cut from the tubular PVA grafts at the ends and at the center of the samples. Images of the 2 mm segments were taken, and the inner diameter and wall thickness of the segments were measured for each segment from the images using MatLab. For each individual sample, the measurements of the inner diameter and the wall thickness from segments at different regions were averaged to yield the average inner diameter and the wall thickness of the sample.

Compliance

3 cm segments of PVA grafts were exposed to 120 and 80 mmHg of hydrostatic pressure. Images of the grafts were taken at the defined pressures. The outer diameters of the grafts were measured, then the compliances of the grafts were calculated using the following equation (Chaouat, 2008):

$$\frac{\text{diameter at 120 mmHg} - \text{diameter at 80 mmHg}}{\text{diameter at 120 mmHg}} \times 100 = \%\ \text{compliance per 40 mmHg} \quad (1)$$

ePTFE vascular graft (Gore-Tex®, catalog number V04070L) with the inner diameter of 4 mm was used to measure the compliance of the ePTFE graft with comparable size using the stated setup.

Burst Pressure

4 cm segments of PVA grafts were exposed to internal pressure induced by nitrogen gas at room temperature. The pressure was increased gradually until the graft burst. The burst pressure was recorded at the pressure at which the graft burst. A normalized burst pressure was calculated as burst pressure normalized per unit thickness by dividing the burst pressure of the samples by their wall thickness.

Lap Shear Test

Lap shear test was performed following protocols described in published literature with modifications (Court et al., 2001). 1 cm segments were cut from tubular PVA grafts. The segments were cut open longitudinally, then they were held in a flat position and dried at 60°C for 7 days. Segments prepared as such were partially rehydrated for 15 min and trimmed into 5 mm × 10 mm rectangular specimens. The surface of the specimens was patted dry using a paper towel. Then, the segment was glued onto two polylactic acid (PLA) holders so that the trimmed PVA segment was sandwiched between the two PLA holders. The PVA hydrogel segment was further rehydrated in DI water for 30 min. After rehydration, any residual water on the surface was removed. The non-overlapping parts of the holders were loaded onto a tensile testing equipment (AGSX Shimadzu, Japan), which was equipped with 1 kN load cell, and stretched at a rate of 25 mm/min until failure. Images of the samples after the test were taken using the laser confocal microscope (Olympus LEXT OLS5000-SAF, Japan) to measure the thickness variation within the destroyed samples. The heights of the samples were measured using Olympus data analysis software.

Phosphate Quantification Assay

Phosphate quantification was performed according to the manufacturer protocol outlined in the phosphate quantification assay (Phosphate Assay Kit, Colorimetric, ab65622, Abcam). In brief, the rehydrated PVA grafts were dried at 60°C for 7 days. The dried grafts were then degraded in 10% nitric acid, then diluted to varying concentrations. The degraded polymer solutions were added into micro-plate and allowed to react with the assay reagent. The absorbances of the solutions were then measured. Using the absorbance, the amount of phosphate in the PVA graft was calculated.

Fourier-Transform Infrared Spectroscopy

Fourier-transform infrared (FTIR) spectroscopy was performed following a published protocol (Pohan et al., 2020). PVA grafts were cut to 1 cm segments, and the segments were then cut open longitudinally. The grafts were dried flat. Fourier-transform infrared (FTIR) spectroscopy was performed using Thermo Fisher Scientific FTIR (Nicolett 6700) fitted with germanium and a high sensitivity pyroelectric detector. Percent transmittance of the samples were collected between 400 and 4,000 cm^{-1}. Sixty-four scans were acquired at a spectral resolution of 4 cm^{-1}. Data were normalized by modifying previously published protocol (Ahmed et al., 2019). The data was normalized to the highest % transmittance and the PVA film spectrum was subtracted from the % transmittance spectra.

Differential Scanning Calorimetry

Differential scanning calorimetry (DSC; TA Instruments DSC Q2000) was performed following the published protocol (Pohan et al., 2020). In brief, the samples were dried at 60°C for at least 1 week 10 g ± 0.1 g of samples were measured and added into the Tzero Aluminum Hermetic pan. The heating cycle was set from 30°C to 260°C at the ramp rate of 10°C/min. Data were analyzed using the TA Universal Analysis software. Fractional crystallinity was calculated using heat of melting of 100% crystalline PVA of 138.60 J/g (Peppas and Merrill, 1976).

Swelling Ratio

PVA grafts were submerged in DI water for at least a week to ensure thorough removal of charged ions from the grafts. Small sections of the tubular grafts were cut from the PVA grafts. Any residual DI water lingering on the PVA sections were removed prior to measuring the weights of the sections. The sections were then dried at 60°C for 5 days. The weights of the sections were measured every day for the subsequent days until the weight of the sections did not change further. Swelling ratio was calculated using the following equation (Lack, 2004):

$$\text{Swelling ratio} = \frac{\text{weight of hydrated polymer sample}}{\text{weight of dried polymer sample}} \quad (2)$$

Elastic Modulus

For longitudinal elastic modulus and ultimate strength measurement, the grafts were cut into 8 cm segments. The prepared samples were loaded onto the tensile machine (AGSX Shimadzu, Japan) with the gauge lengths of 2 cm. The samples were then stretched at a rate of 25mm/min until the tensile failure of the sample. For circumferential elastic modulus and ultimate strength measurement, the grafts were cut into 2 mm width rings. Curved holders were loaded onto the tensile testing machine grips. The PVA rings were loaded onto the holders so that the rings were held by the holders. The holders were then separated to achieve a gauge length of 5 mm. The samples were then stretched at a rate of 10 mm/min until the sample failed.

Suture Retention Strength

Suture retention strength of the PVA grafts were measured using published protocol with modifications (Chaouat, 2008; Pohan et al., 2020). PVA grafts were cut into 4 cm segments. Using 7–0 suture, a single suture was made 5 mm from the edge of the segment for each sample. The remaining suture end was taped securely onto an immovable surface so that the sample was hanging by the suture. Load was applied at 10 g/min onto the sample until the sample broke. The weight at which the sample broke was measured.

Statistical Analysis

Statistical significance was determined using a two-way ANOVA followed by Tukey's multiple comparison analysis with 95% confidence interval using MatLab. The data are presented as mean ± standard deviation. For all the presented data, $p < 0.05$ is denoted by * unless otherwise specified in the figure caption. The correlations between components were compared using principle component analysis (PCA). PCA plots were generated using JMP statistical software.

RESULTS

Compliance and Burst Pressure of the Grafts With Varying Wall Thickness

The relationships between the burst pressure vs wall thickness and compliance vs wall thickness are shown in **Figure 2**. The cross-sectional images of the PVA grafts with different layers are shown in **Figure 2A**. The red arrow highlights the region in the graft that has different transparency. The wall thickness of the grafts increased linearly with the increased number of layers (**Figure 2B**). As shown in **Figure 2C**, a linear increase in burst pressure with increasing wall thickness was also observed. The compliance of the grafts displayed an inverse relationship with the wall thickness (**Figure 2D**).

Properties of the Grafts Fabricated Using Different Fabrication Conditions

All of the grafts that were made using different fabrication parameters had 9 layers. The complete list of conditions used for fabrications and their fabrication outcomes are shown in **Supplementary Table S1**. The images of the grafts that fabricated successfully are shown in **Figure 1B**. The cross-sectional images of the successfully fabricated grafts are shown in **Figure 3A**. The wall thickness of the grafts was quantified (**Figure 3B**). LS, 15 W, 60-2D, and 60-4D had significantly thinner walls than the control group, while 30 W, 18-2D, and 18-4D showed no statistical difference from the control group. The wall thickness of 15 W was significantly thinner than 30 W. 60-2D and 60-4D did not show any statistical difference in wall thickness. Also, 18-2D and 18-4D did not show any statistical difference in wall thickness.

Despite having thinner walls than the control, grafts from LS, 60-2D, and 60-4D conditions had significantly lower compliance than the control group ($p < 0.05$, **Figure 4A**). Regardless of the post-fabrication drying temperature, the samples that were subjected to extra dehydration process post-fabrication had significantly lower compliance than the control group (**Figure 4A**). 30 W had lower compliance than the control group as well, despite having comparable wall thickness. Lastly, 15 W did not have statistically significant differences in compliance compared to the control group despite having thinner wall thickness. Within each group with the same fabrication or post-fabrication variations, all groups displayed an inverse relationship between wall thickness and compliance (**Figure 4B**). The burst pressure of 15 W was significantly lower than control, which was as expected due to the lower wall thickness of the group (**Figure 4C**). However, 60-2D and 60-4D had higher burst pressure than the controls despite having thinner walls. LS, 30 W, 18-2D, and 18-4D did not have significantly different burst pressure with respect to the control group. Within each group with the same fabrication or post-fabrication variations, all of the groups showed positive linear relationship between the wall thickness and the burst pressure (**Figure 4D**). Swelling ratio was used to estimate the crosslinking density. LS, 60-2D, and 60-4D had less swelling than the control group (**Figure 4E**). 15 W had higher swelling ratio than the control group. No correlation between the swelling ratio and the wall thickness was observed (**Figure 4F**). Further assessment of the burst pressure was performed by normalizing the burst pressure per unit thickness (**Supplementary Figure S1**). When the data was normalized to wall thickness, LS, 60-2D, and 60-4D had significantly higher normalized burst pressure than the control group.

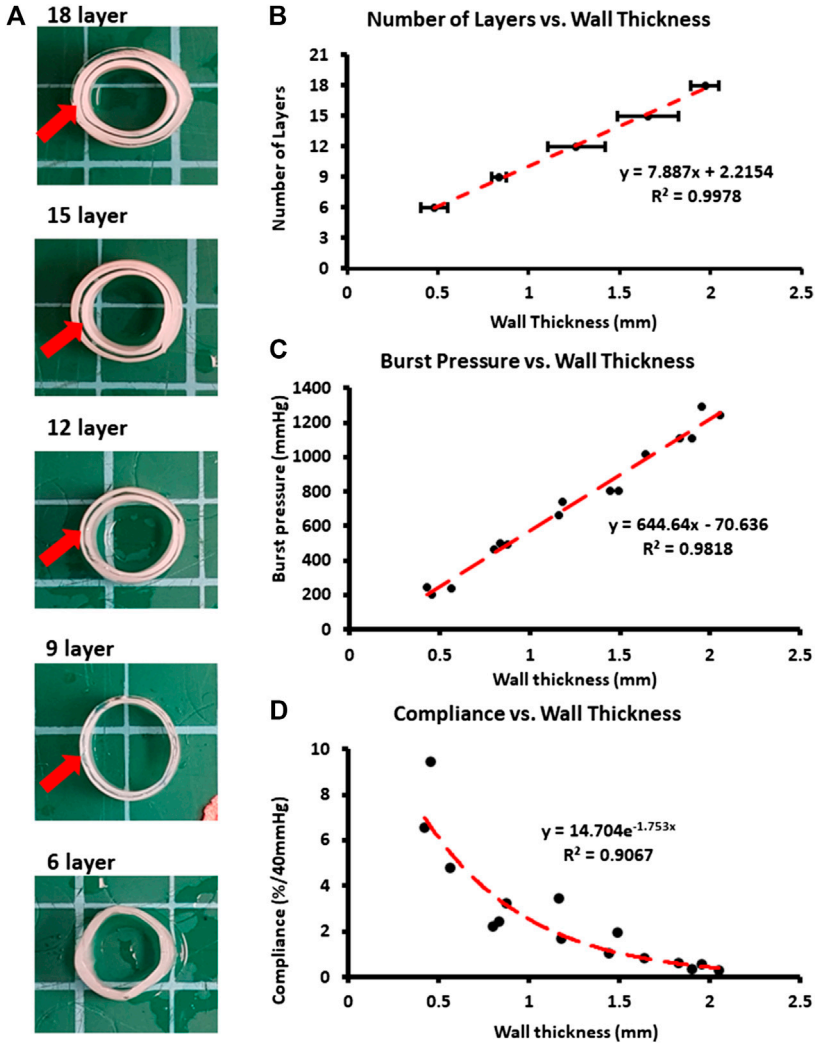

FIGURE 2 | Physical and mechanical characterization of grafts with differential number of layers. **(A)** Cross-sectional images. Red arrows used to identify difference level of transparency between layers. **(B)** Wall thickness of the samples for differential number of layers. **(C)** Burst pressure plotted against the wall thickness. **(D)** Compliance plotted against the wall thickness. *p < 0.05 between indicated groups. n = 9 for all groups. Error bar represents standard deviation.

Additionally, 60-2D and 60-4D had higher normalized burst pressure than 18-2D and 18-4D.

Phosphate content was quantified for the samples to verify the crosslinking density of the covalent crosslinking with STMP. There was no significant difference in phosphate content among the control, LS, 15W, 30W, 60-2D, and 18-2D (**Figure 5A**). On the other hand, both LS and 15 W had significantly higher phosphate content than the 18-2D and Film. FTIR was performed to identify if there were any changes in crosslinking between the groups or if there were any changes in functional groups introduced due to change in the fabrication process. **Figure 5B** shows FTIR data using normalized percent transmittance of the control group (C), LS, 60-2D, and 18-2D rehydrated in NaCl. All of the groups displayed peaks at similar wavenumbers, indicating there were no noticeable differences between samples in terms of functional groups. DSC was performed to further assess the degree of crosslinking. **Figure 6** shows the DSC thermogram for control, 60-2D, and 18-2D. 18-2D had higher degree of crystallinity and crystallization temperature than the control group. Additional DSC data is shown in **Supplementary Figure S2**.

The interlayer adhesion was assessed in **Figure 7**. The shear strength of all of the groups were not significantly different from the control group. However, 15 W had the average shear strength of 3.75 MPa, which was more than twice higher than that of the control group (1.69 MPa). Statistical analysis between 15 W and control revealed $p = 0.057$. The interlayer adhesion of 15 W was also significantly higher than 30 W ($p < 0.05$). The 3D images of the polymers after the adhesive shear tests are shown in **Figure 5B**, then were used to acquire the height profile used to plot graphs in **Figures 7C–J**. These height profiles were then used to identify whether the polymers had high interlayer adhesion. 15 W had the highest slope, and therefore high interlayer adhesion, while other groups showed flat lines.

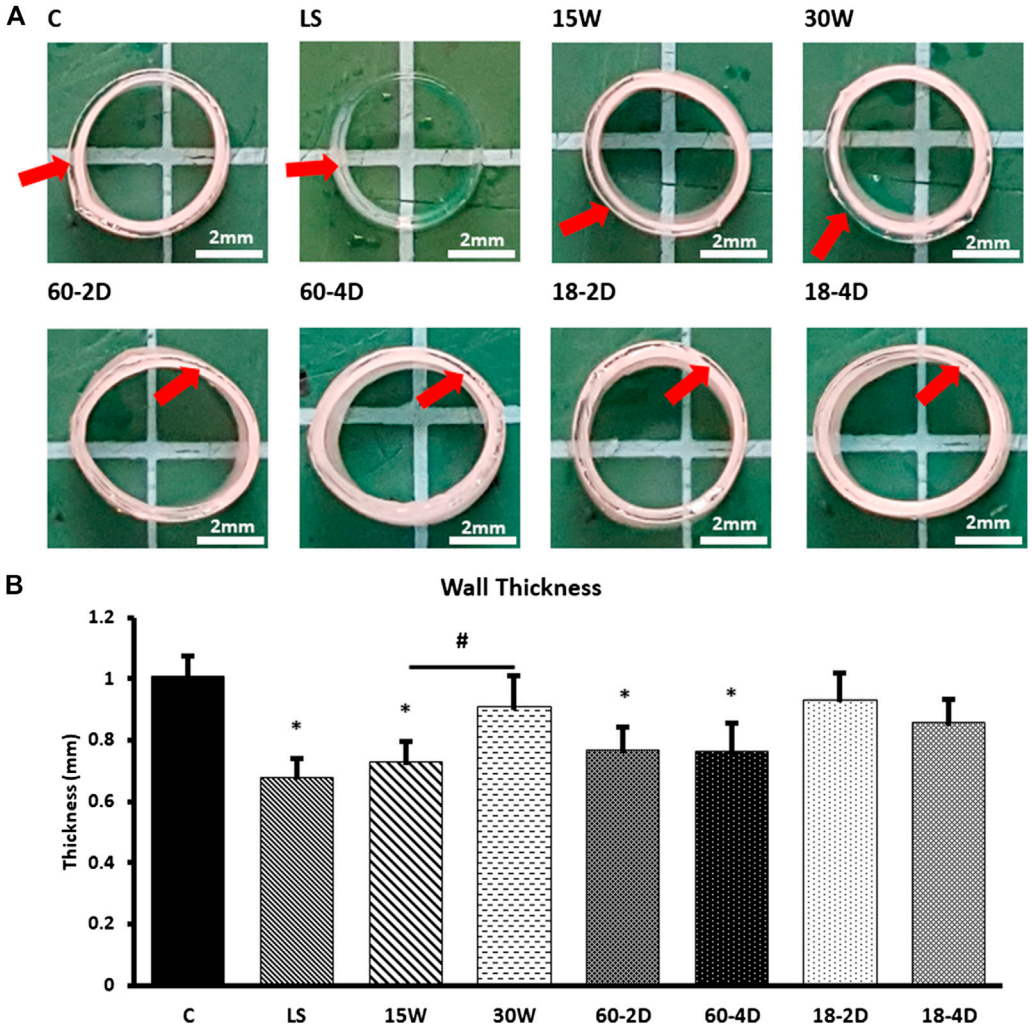

FIGURE 3 | Physical characterization of the experimental groups. **(A)** Cross-sectional images. Red arrows used to identify difference level of transparency between layers within a sample. **(B)** Wall thickness of the samples for different number of layers. **(C)** Wall thickness of the samples. *Indicates $p < 0.05$ with respect to control group. # Indicates $p < 0.05$ between the groups being compared. $n = 9$ for all samples.

Supplementary Figure S3 shows graphs of the different properties measured plotted against either the wall thickness (**Supplementary Figures S1B–S3A**) or compliance (**Supplementary Figures S3C–S3F**). There was no obvious correlation between the measured properties with either the wall thickness or the compliance.

PCA analysis showed that the wall thickness and compliance showed a high positive correlation (**Figure 8A**). Also, it showed that the compliance and burst pressure showed a high negative correlation (**Figure 8B**). All other components did not display significant correlation (**Supplementary Figure S4**).

Additional Analysis on Selected Groups

Figure 9 shows the additional mechanical properties of selected groups. The groups with the highest and lowest compliance were chosen for the additional analysis. There was no statistical difference between all of the groups for all conditions except for the LS for circumferential elastic modulus (**Figures 9A–D**). The suture retention strength of the groups also did not show any statistical difference (**Figure 9E**).

DISCUSSION

Mechanical failure of vascular grafts can result in clinical catastrophe. To ensure the safety of the patients, vascular grafts were traditionally developed to have high mechanical properties matching the native blood vessel properties (**Table 1** (Hansen et al., 1995; Fung, 1998; Kambric et al. 1984; Catanese III et al., 1999; Tai et al., 2000; Krejza et al., 2006; Sarkar, 2006; Konig et al., 2009; Markiewicz et al., 2017; Wise, 2011). Compliance, the elasticity of the blood vessel when exposed to internal pressure, is one of the important parameters that is being studied in vascular graft engineering to understand

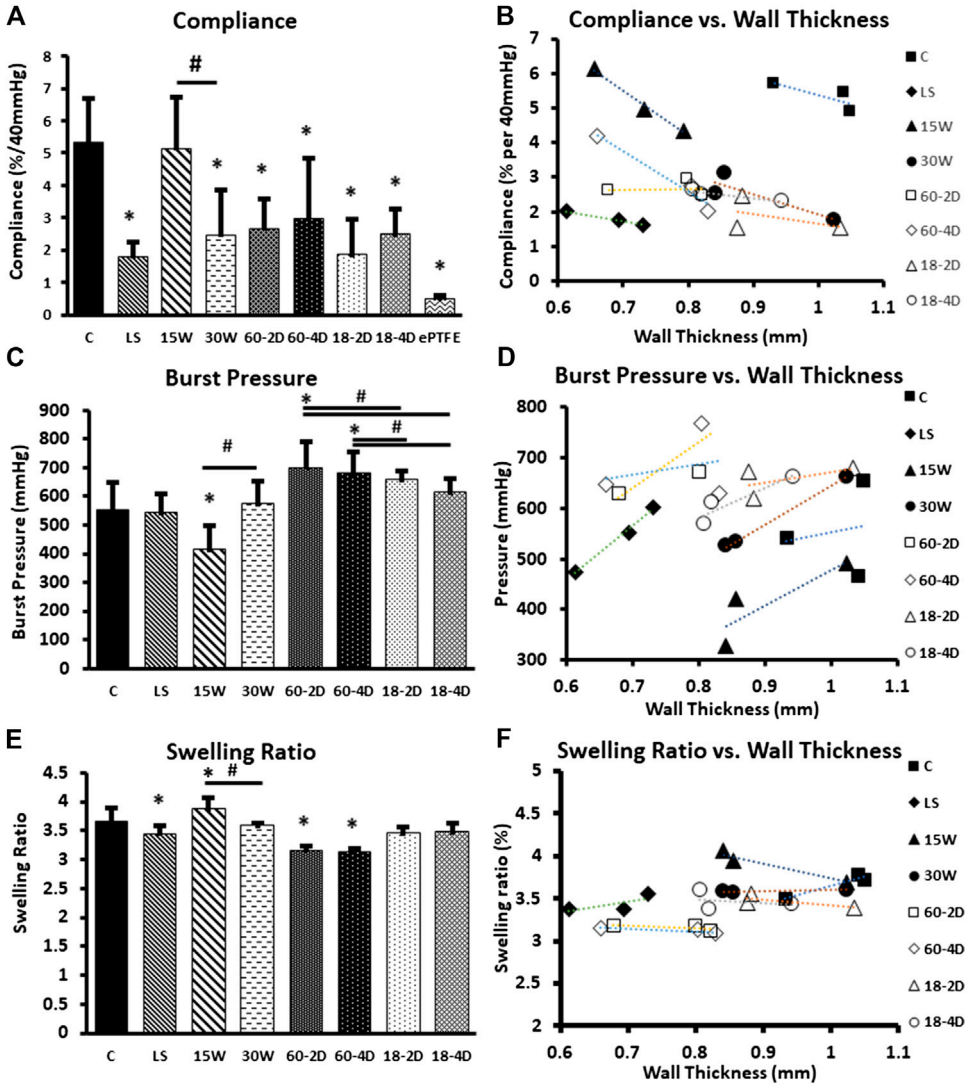

FIGURE 4 | Bulk properties of the samples. **(A)** Compliance of each group. **(B)** Compliance of each group plotted against their respective wall thickness. Average values of compliance and wall thickness of the internal replicates used to plot the graph. **(C)** Burst pressure of each group. **(D)** Burst pressure of each group plotted against their respective wall thickness. Average values of burst pressure and wall thickness of the internal replicates used to plot the graph. **(E)** Swelling ratio of each group, and **(F)** swelling ratio plotted with respect to the wall thickness of each group. *Indicates $p < 0.05$ with respect to control group. # Indicates $p < 0.05$ between the groups being compared. $n = 9$ for all samples.

the current limitations of small diameter vascular grafts (Szafron, 2019; Jeong et al., 2020). There are methods to increase the compliance of a material. One of the methods is to reduce the wall thickness (Biglino, 2013; Nezarati et al., 2015; Gao, 2019). However, reducing the wall thickness can negatively affect the burst pressure (Menon, 2011; Zhu and Leis, 2012). Using vascular

TABLE 1 | Reported values of mechanical properties of native blood vessels and expanded polytetrafluoroethylene (ePTFE).

	Diameter (mm)	Burst pressure (mmHg)	Compliance (% per 100 mmHg)	Elastic modulus (MPa)
Internal mammary artery (human)	1 – 2 (Markiewicz et al., 2017)	2,267 ± 215 (Wise, 2011)	12 (Konig et al., 2009)	0.267 ± 0.046 (Wise, 2011)
Carotid artery (human)	5.11 ± 0.87 (Krejza et al., 2006)	5,000 (Sarkar, 2006)	6.6 ± 1.3 (Hansen et al., 1995)	7 – 11 (Fung, 1998)
Saphenous vein (human)	4.9 ± 0.2 (Tai et al., 2000)	2,295 ± 272 (Wise, 2011)	5.0 ± 6.7 (Tai et al., 2000)	0.683 ± 0.147 (Wise, 2011)
ePTFE	5.4 ± 0.1 (Tai et al., 2000)	2,590 – 3,626 (Kambric et al. 1984)	1.2 ± 0.3 (Tai et al., 2000)	42.9 ± 2.6 (Catanese III et al., 1999)

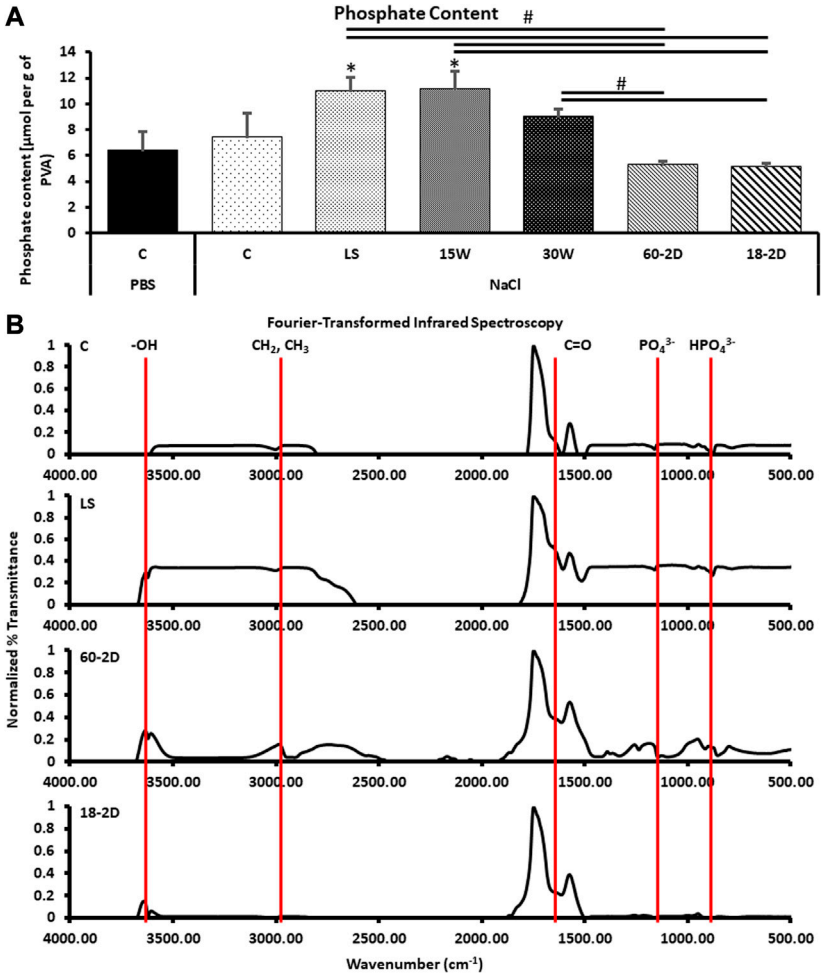

FIGURE 5 | Functional groups and STMP crosslinking density in PVA films. **(A)** Quantification of phosphate content for the samples to characterize covalent crosslinking by STMP. *Indicates $p < 0.05$ between the indicated groups. $n = 6$ for all groups. C PBS was control sample rehydrated in NaCl solution. *Indicates $p < 0.05$ with respect to the control groups. #Indicates $p < 0.05$ between the groups being compared. **(B)** Fourier-transform infrared spectroscopy data. Data was normalized to PVA films. $n = 3$ for all samples.

grafts with low burst pressure could become a critical problem for the patients with the vascular graft implants. Therefore, it is important to understand the effects different parameters have on the burst pressure when increasing the compliance of the vascular grafts. Two parameters that have been found to affect the mechanical properties of hydrogels are interlayer adhesion and crosslinking density (Leone, 2010).

Crosslinking of PVA has been extensively studied. A well-established physical crosslinking method of PVA is freeze-thawing. PVA grafts with freeze-thawing crosslinking are mainly fabricated by bulk molding fabrication. PVA hydrogels crosslinked using freeze-thawing have been shown to have tailored mechanical properties by varying the number of freeze-thawing cycles (Peppas, 1975; Gupta et al., 2012; Holloway et al., 2013). The freeze-thawing crosslinking of PVA involves phase separation and crystalline formation. Hydrogen bonds form in the aqueous solution of PVA. During the freezing of PVA solution, ice forms. The formation of ice induces the growth of polymer crystallinity. The growth of polymer crystallinity acts as physical crosslinking points. Subsequently, water-insoluble hydrogels are formed in the later thermal cycles. The abundant hydroxyl groups in the backbones of PVA polymer chains also provide reactive sites for hydrogen bonding for chemical crosslinking of PVA (Otsuka and Suzuki, 2009). One of the most commonly used crosslinking agent for PVA is glutaraldehyde. It reacts with hydroxyl groups to form an ester bond. Chaouat 2008) found that the hydroxyl groups on PVA can also react with STMP to crosslink PVA hydrogels by phosphoesterification. The PVA hydrogels chemically crosslinked with STMP were shown to be capable of achieving a wide range of mechanical properties by altering the fabrication parameters such as humidity and water evaporation (Cutiongco et al., 2016b). A recent study comparing the hemocompatibility of PVA hydrogels crosslinked by STMP, glutaraldehyde, and freeze-thawing found that crosslinking methods also affect the biological performance of PVA (Bates et al., 2020).

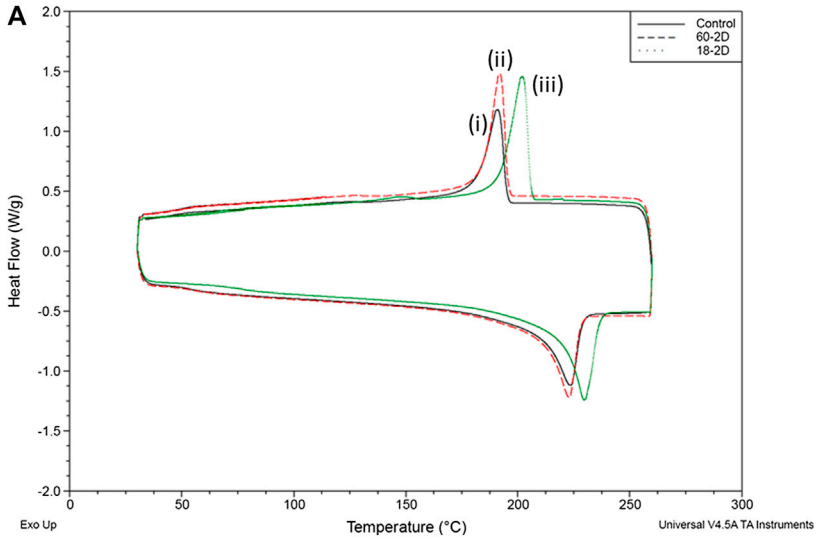

B	Heat of Fusion (J/g)	Fractional Crystallinity (%)
Control	50.27	36.3
60-2D	52.24	37.7
18-2D	57.13	41.2

FIGURE 6 | Degree or crosslinking. Differential Scanning Calorimetry (DSC) data. **(A)** DSC of (i) control, (ii) 60-2D, and (iii) 18-2D. Data is shown for the second heating and cooling cycle. **(B)** Heat of fusion and fractional crystallinity of the samples. $n = 1$ for all groups.

PVA vascular grafts are fabricated using dip-casting with cylindrical molds (Cutiongco et al., 2016a). Different mechanical properties of the PVA vascular grafts can be achieved by altering the number of layers and fabrication parameters. We have observed heterogeneity in transparency between the layers (**Figure 2A**, red arrows) in PVA vascular grafts. The observed heterogeneity can be the result of inconsistencies in crosslinking between the layers (Peacock and Calhoun, 2012). The heterogeneity can also be an indication of a weak interlayer adhesion. A potential method of overcoming the weak interlayer adhesion would be increasing the interlayer crosslinking (Yu et al., 2013). With PVA hydrogels, the interlayer crosslinking could occur by having hydrogen bonding between the residual –OH groups of the PVA layers. It was hypothesized that through increasing the interlayer adhesion, the resulting grafts can have high compliance while maintaining burst pressure. Moreover, the heterogeneity suggests that the crosslinking density can be further fine-tuned. We hypothesized that a decrease in the chemical crosslinking density will result in higher compliance while causing a decrease in burst pressure. Furthermore, we hypothesize that post-fabrication processing can affect physical crosslinking, and impact the compliance and burst pressure.

Compliance and Burst Pressure of the Grafts With Varying Wall Thickness

Most often, tensile measurements are made to assess the mechanical properties of the polymers (Abraham et al., 1998; Peiffer and Nielsen, 1979). Additional properties, such as residual stress, rheology, Izod impact measurement, etc. (Peiffer and Nielsen, 1979; Abraham et al., 1998), are also tested depending on the application of the polymers. For vascular grafts, burst pressure and compliance are important parameters to measure. Although PVA vascular grafts have been studied previously (Elshazly, 2004; Chaouat, 2008), the relationship between the wall thickness and burst pressure and compliance have not been characterized. Thorough characterization of the compliance and burst pressure of the grafts with different wall thickness was performed first to identify the compliance and burst pressure achieved by different wall thickness. The relationship between the wall thickness and burst pressure (**Figure 2C**) was expected as the structural integrity of tubes is dependent on the wall thickness (Menon, 2011; Zhu and Leis, 2012). The grafts with 6 layers displayed high compliance, but its burst pressure was only 232.7 ± 22.8 mmHg. As systolic blood pressure can rise to 220 mmHg during exercises, PVA grafts with 6 layers were deemed too weak. Grafts with 9 layers have a burst pressure of 485.5 ± 17.9 mmHg, which is at least double the systolic pressure of 220 mmHg. However, the compliance of the grafts with 9 layers was 2.6 ± 0.54% per 40 mmHg. Furthermore, compliance of the PVA grafts with more than 9 layers had compliance < 2% per 40 mmHg. As shown in **Table 1** (Kambric et al. 1984; Hansen et al., 1995; Fung, 1998; Catanese III et al., 1999; Tai et al., 2000; Krejza et al., 2006; Sarkar, 2006; Konig et al., 2009; Wise, 2011; Markiewicz et al., 2017) and **Figure 4A**, the compliances of the PVA grafts with 9 layers and ePTFE are lower than the native

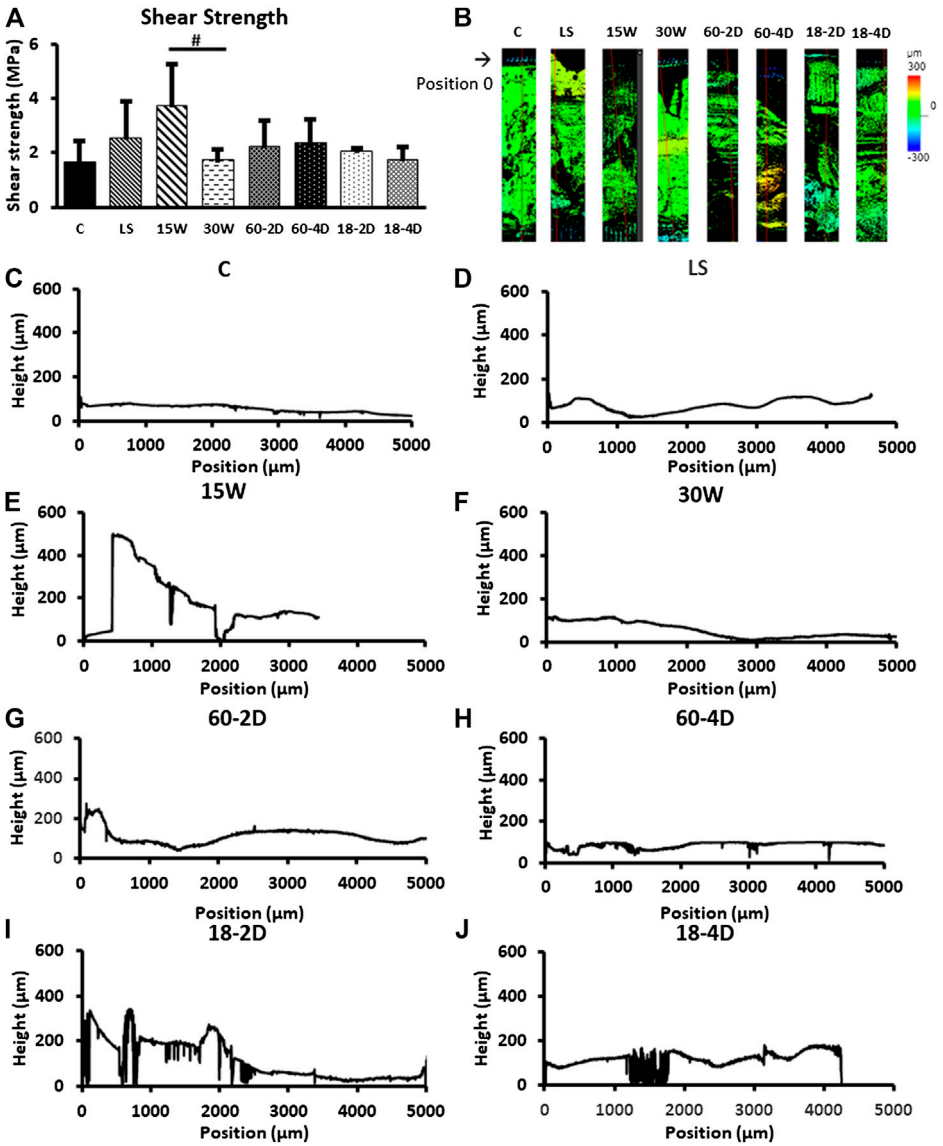

FIGURE 7 | Interfacial energy. **(A)** The adhesive strength of groups. 15 W had $p = 0.0571$ with respect to the control group, and $p = 0.0495$ with respect to the 30 W. **(B)** Height map of the samples after adhesive shear test. **(C)–(J)** Height profile of the samples. *Indicates $p < 0.05$ with respect to control group. # Indicates $p < 0.05$ between the groups being compared. $n = 3$ for all samples.

blood vessels. After assessing the compliance and burst pressure of the groups, the PVA vascular grafts with 9 layers was chosen for further investigation as they had the highest compliance with good burst pressure. Using the PVA grafts with 9 layers, the effect of crosslinking density and interlayer adhesion on the compliance and burst pressure were assessed.

PVA Grafts Fabricated Using Different Fabrication Conditions

The standard fabrication method is described in **Figure 1A** in detail. The crosslinking of PVA using crosslinker STMP in NaOH solution has been described in the literature numerous times (Elshazly, 2004; Chaouat, 2008; Leone, 2010; Ino et al., 2013). In brief, the -OH groups on PVA loses the hydrogen atom in the highly basic solution created by NaOH, and becomes reactive. This reactive site then reacts with the STMP. Subsequently, another PVA molecule reacts with the STMP and results in a crosslinked polymer. This process can be modified via changing the PVA concentration, STMP concentration, NaOH concentration, temperature, humidity, and waiting time between the dips (Chaouat, 2008). The fabrication conditions were varied to achieve different level of interlayer adhesion and crosslinking density.

The interlayer adhesion occurs when there are crosslinks that spans multiple layers of polymers. The mechanical properties of PVA vascular grafts can be affected by the interlayer adhesion as

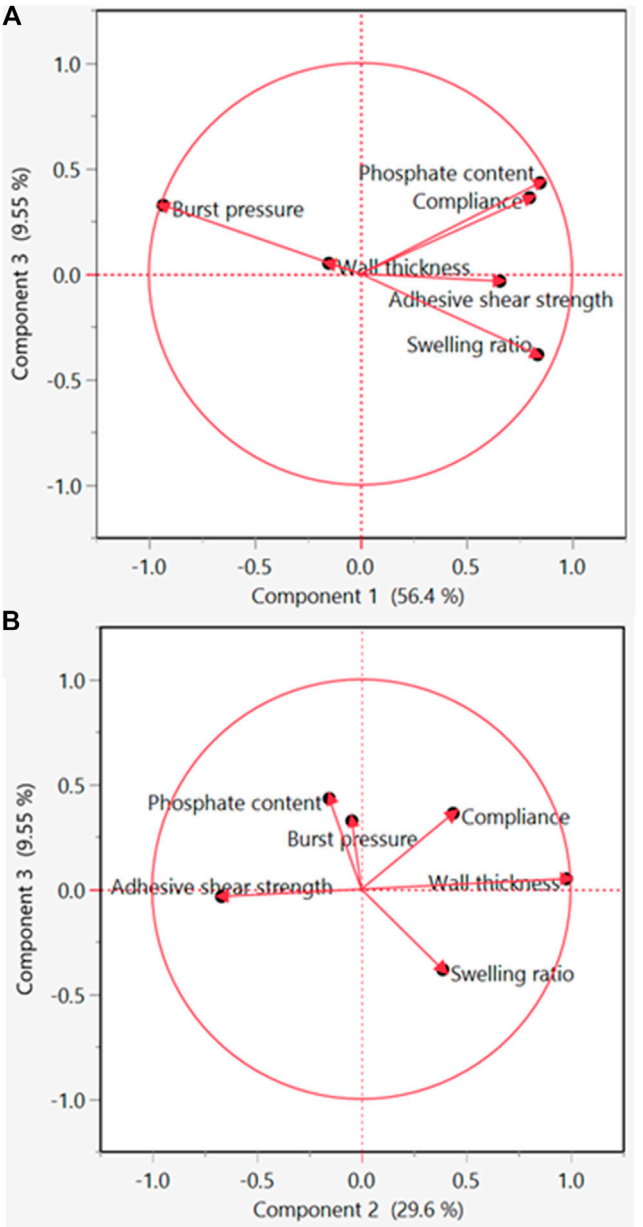

FIGURE 8 | Principle component analysis (PCA) for the identification of significant components. **(A)** PCA plot of component 1 vs. component 3. **(B)** PCA plot of component 2 vs. component 3.

PVA graft fabrication method is a dip-casting process with waiting periods between dips. The dip-casting process is a type of polymer fabrication method where the mold is dipped multiple times to achieve the desired thickness (Abraham et al., 1998; Nautiyal et al., 2017; Srinivasan et al. 2020). Due to the process requiring crosslinking of the layers after each dip, the drying condition of the layers is important to prevent delamination for this fabrication method (Abraham et al., 1998). One of the easiest parameters to control for dip-casting process is the waiting time between the dips. Waiting time is required to allow for the chemical reactions that crosslinks PVA molecules to occur (Chaouat, 2008). Shorter wait time between each dip prevents completion of the reactions, allowing for more partially crosslinked sites for each dip. These partial crosslinking sites can react with the newly applied layer, increasing the interlayer adhesion (Yu et al., 2013). Therefore, the drying time should be kept short for the subsequent layers to be applied before crosslinking of the previous layer is completed to increase the interlayer adhesion.

For the control, the waiting time between the dips is 15 min in the first 4 dips, 25 min in the fifth to seventh dips, and 30 min for the eighth dip and beyond (**Figure 1A**). Instead of increasing the dipping time throughout the fabrication process, the waiting times between dips were kept consistent for the groups comparing the effects of the interlayer adhesion. 15 W was fabricated with a flat 15-min waiting time for all waiting steps instead of the standard protocol. 30 W was made using a flat 30-min waiting time for all waiting steps. The waiting times for 15 and 30 W were kept constant so that interlayer adhesion throughout the grafts would remain consistent. There are many methods to make measurements to assess the adhesion between layers (Awaja et al., 2009). The most standard method of measuring the interlayer adhesion is the adhesive shear test (which is also known as lap shear test) (Awaja et al., 2009).

The crosslinking density and concentration of STMP are positively correlated to the stiffness of the material (Leone, 2010). As decrease in crosslinking agent can result in lowered crosslinking density, STMP concentration was decreased for one of the experimental groups (LS samples). Also, the concentration of NaOH was reported to be positively related to the crosslinking density (Lack, 2004). Therefore, 15% w/v NaOH concentration was explored to achieve decreased crosslinking density to assess the effect of low crosslinking density. However, the graft could not be fabricated using the low concentration of NaOH (**Supplementary Table S1**). We also speculate post-fabrication thermal drying may induce additional physical crosslinking, resulting in higher crosslinking density. To create the PVA grafts with higher crosslinking density, additional groups (60-2D, 60-4D, 18-2D, and 18-4D) were made with extra drying step post-fabrication to encourage additional physical crosslinking.

Effects of Interlayer Adhesion on PVA Graft Compliance and Burst Pressure

As shown in **Figure 3B**, 15 W had significantly thinner wall than the control group. However, the wall thickness of 30 W was not significantly different from the control group. While the 15 and 30 W had consistent waiting times between the dips, control group had 15-min waiting time for the first four dips, 25-min waiting time for the 5th–7th dips, then 30-min waiting time for 8th or more dips. The data showed that the longer waiting time is needed and waiting time of the outer layer was related to wall thickness in the outer layer. When the waiting time of the outer later was decreased in 15 W, the thickness was decreased, compared to 30 W and control. However, it appears that increasing the early dip waiting time did not significantly affect the thickness.

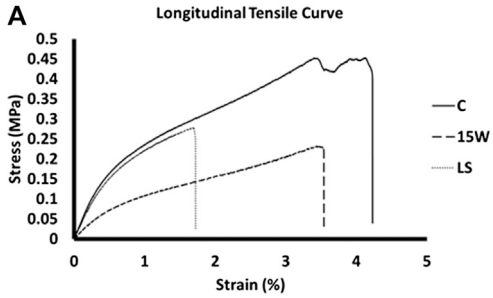

C Longitudinal Tensile Data

	Ultimate Tensile Stress (MPa)	Elastic Modulus (MPa)
C	0.494 ± 0.132	0.571 ± 0.100
15W	0.511 ± 0.051	0.584 ± 0.119
LS	0.584 ± 0.086	0.802 ± 0.456

D Circumferential Tensile Data

	Ultimate Tensile Stress (MPa)	Elastic Modulus (MPa)
C	0.306 ± 0.124	0.690 ± 0.136
15W	0.313 ± 0.067	0.674 ± 0.098
LS	0.326 ± 0.105	1.048 ± 0.126*

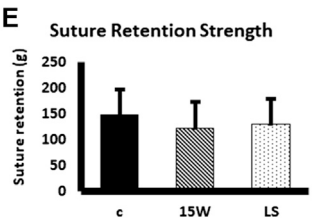

FIGURE 9 | Additional bulk mechanical properties of the selected groups. **(A)** Longitudinal tensile curve. **(B)** Circumferential tensile curve. **(C)** Longitudinal ultimate tensile strength and elastic modulus for each groups. **(D)** Circumferential ultimate tensile stress and elastic modulus. **(E)** Suture retention strength. $n = 6$ for tensile test results, and $n = 9$ for suture retention strength for all groups. *Indicates $p < 0.05$ with respect to the control group.

15 W had higher adhesive shear strength than all of the other groups. While not statistically significant against the control group, 15 W showed a trend toward significantly higher adhesive shear strength than the control group ($p = 0.057$), and a significantly higher adhesive shear strength than 30 W ($p < 0.05$). This indicates that the 15 W had higher adhesion between layers than the other groups, which is in agreement with the height profiles shown in **Figures 5C–J**. As 15 and 30 W were fabricated with a flat 15 and 30-min waiting time, respectively, the significant higher shear strength in 15 W further demonstrated that the shorter waiting time would increase the interlayer adhesive strength. This could be the result of a larger quantity of partial crosslinking sites available for a shorter waiting time in 15 W. The partial crosslinking sites can then work as a bridge between the layers to allow for a larger number of interpenetrating crosslinks (Awaja et al., 2009). With longer waiting time between layers, the partial crosslinking sites can become crosslinked. This can reduce the crosslinking between the layers. Except for 15 and 30W, all of the samples had variable drying time. For the control group, LS, 60-2D, 60-4D, 18-2D, and 18-4D, the last two layers were applied with 30-min waiting intervals. This could be the reason these groups did not show statistical difference in the adhesive shear strength.

Effects of Chemical Crosslinking Density on PVA Graft Compliance and Burst Pressure

15 W had a higher swelling ratio compared to the control group. The partial crosslinking sites could also attribute to the higher swelling ratio. This partial crosslinking sites may have resulted in lower crosslinking density, which could account for the lower burst pressure. However, it is also important to note that the wall thickness of 15 W was significantly thinner than the control, indicating that the decrease in burst pressure could also be due to the thinner walls (Menon, 2011). When the burst pressures were normalized to the wall thickness of the samples, 15 W did not show significant difference from the control group (**Supplementary Figure S1**). This suggests that the affect from partial crosslinking on burst pressure was less significant than the influence from wall thickness.

The crosslinking of PVA was achieved by phosphoesterification, thus the content of phosphate also reflects the number of chemical crosslinking bonds formed during the fabrication. With lower concentration of STMP added in the reaction solution, it was expected that the resulting PVA grafts would display lower concentration of phosphate to indicate a lower chemical crosslinking density. However, LS showed lower phosphate content than the control group (**Supplementary Figure S1**). The lower phosphate content in conjunction with the lower swelling ratio, LS displayed higher crosslinking density compared to the control group. This is in agreement with the burst pressure normalized to wall thickness (**Supplementary Figure S1**). The burst pressure should increase with increase in crosslinking density. A potential explanation for higher crosslinking density is the presence of tighter network due to the multifunctional nature of STMP. As phosphate groups from STMP has 4 potential reactive sites, more than two reactions can occur on a single phosphate group. When less phosphate groups

are available, hydroxyl groups have less phosphate groups to react with. Phosphate groups become the limiting reagents, causing multiple phosphoesterification to occur on one phosphate. This results in tighter mesh formation, and therefore tighter crosslinking density. For the PVA crosslinked in abundance of phosphate, more phosphate could react with the hydroxyl groups. The abundance could result in phosphate population that did not react with multiple hydroxyl groups in the polymer network. These unbound phosphate groups then get washed away during the rehydration and storage, effectively resulted in a lower phosphate content in the hydrogels.

The difference in the crosslinking density among 15W, 30 W and the control, observed from the phosphate assay (**Figure 5A**), indicated that the waiting time in between different layers affected the chemical crosslinking density. 15 W had a significantly higher swelling ratio and significantly lower wall thickness than 30 W. Comparing the mechanical properties of 15 and 30W, 30 W had significantly lower compliance and significantly higher burst pressure. With a decrease in waiting time from 30 to 15 min between each dip, more interpenetrating crosslink occurs. The interpenetrating crosslinks contribute to the observation of increased chemical crosslinking density observed from the phosphate assay. Similar to LS, 30 W had longer waiting time between each dip, allowing more time for polymer chain to get aligned for hydrogen bonding, which may have contributed to the decreased compliance and increased burst pressure.

Effects of Physical Crosslinking Density on PVA Graft Compliance and Burst Pressure

Although the chemical crosslinking density should not change during the additional drying due to extensive washing steps, physical crosslinking may have occurred during 60°C drying. After the STMP crosslinking of PVA, residual hydroxyl groups remain available for hydrogen bonding formation. PVA polymer chains display increased mobility at high temperature. The mobile polymer chains have a higher chance to get aligned, bringing the hydroxyl groups close to form hydrogen bonding. This process was achieved through subjecting the fabricated control groups to additional drying.

The extra-drying groups were 60-2D, 60-4D, 18-2D, and 18-4D. 60-2WD and 60-4WD are the two groups that were dried in the 60°C for 2 and 4 weeks, respectively. These two groups had thinner wall thickness than the control groups. 18-2D and 18-4D were the two groups that were dried in the 18°C for 2 and 4 weeks, respectively. The wall thickness of these groups did not differ from that of the control group. The two groups dried at 60°C had lower swelling ratio than the control group regardless of the length of drying, indicating that they may have higher crosslinking density than the control group. Drying in the 18°C did not alter the swelling ratio of the samples, suggesting that the crosslinking density of the groups dried post-fabrication at 18°C was not different from that of the control group. The compliance of the 18-2D and 18-4D were comparable to the compliance of 60-2D and 60-4D. All of the post-fabrication drying groups had lower compliance than the control group. 18-2D and 18-4D had similar burst pressure compared to the control group. However, 60-2D and 60-4D had higher burst pressure than the control group. There was no difference observed based on the length of extra drying (2 vs. 4 weeks) for both temperatures. This suggests that the additional physical crosslinking occurred during dehydration rather than the storage.

As the length of drying (2 vs. 4 weeks) did not affect the performance of the grafts, further analysis was performed using 18-2D and 60-2D only. According to the phosphate quantification assay (**Figure 5A**), 60-2D and 18-2D did not display any difference in total phosphate content within the polymers. FTIR did not also display any difference between the control group and the extra-drying groups (**Figure 5B**). DSC analysis was performed in addition to assess the degree of crystallinity and overall crosslinking (**Figure 6** and **Supplementary Figure S2**). The DSC results suggested that 18-2D had higher crystallinity and crystallization temperature than the control group, while 60-2D showed a slightly higher fractional crystallinity than the control group. The higher crystallinity, suggesting a higher physical crosslinking, may explain the lower compliance and slight increase in the burst pressure from the post-fabrication drying step. However, while physical crosslinking density can be used to influence compliance and burst pressure, its effect might not be as significant as chemical crosslinking.

Additional Mechanical Analysis of Selected Groups

The group that had the highest compliance (15W) and the group that had the lowest compliance (LS) were used to perform additional mechanical property analysis. Both the longitudinal and circumferential tensile data (**Figures 9A–D**) agreed with the compliance data in that the 15W and control group did not show a statistical difference in mechanical behavior. LS had lower compliance than the control group, therefore it was as expected that the group is less elastic than the control group (**Figure 9D**). Suture retention was not affected by the different fabrication conditions. To reiterate, 15W had higher interlayer adhesion but lower crosslinking density than the control group. Therefore, it could be that the increased interlayer adhesion can also increase the suture retention strength. LS also had a thinner wall thickness than the control group. LS had not significantly different interlayer adhesion and higher crosslinking density compared to the control group. This could indicate that higher crosslinking density can increase the suture retention strength as well.

CONCLUSION

We investigated the effects of interlayer adhesion and crosslinking density on the compliance of PVA vascular grafts. We found that the higher crosslinking density resulted in higher burst pressure, but resulted in lower compliance. Also, we have found that the increase in interlayer adhesion could increase the burst pressure without sacrificing the compliance. While the findings in this

article sheds light on how to improve the performance of the PVA vascular grafts, there are still shortcomings of the PVA crosslinking method utilized here. PVA-STMP crosslinking method using dip-casting is a slow process. This limits the shapes, and therefore applications, of the grafts such fabrication method can produce. Furthermore, PVA tubular grafts are prone to kinking. Kinking could potentially affect the blood flow when the graft is implanted in the patients, resulting in negative clinical outcome. Further research should be performed to improve the fabrication process of PVA-STMP vascular grafts to increase the potential application. Also, the kink resistance of the grafts should be improved to result in better clinical outcome.

DATA AVAILABILITY STATEMENT

The original contributions presented in the study are included in the article/**Supplementary Material**, further inquiries can be directed to the corresponding author.

AUTHOR CONTRIBUTIONS

YJ performed the experiments, performed data analysis, and contributed to writing and editing of the article. EY performed data analysis, and contributed to writing and editing of the article. TM performed data analysis, and contributed to writing and editing of the paper. Lastly, YY performed data analysis, and contributed to writing and editing of the article.

FUNDING

The authors would like to thank the National Institute of Health (NIH RO1 HL130274-01A1), NSERC-CREATE Training in Global Biomedical Technology Research and Innovation at the University of Waterloo (CREATE-509950-2018), NSERC Canada Discovery Grant (RGPIN-2016-04043), John R. Evans Leaders Fund - Canada Foundation for Innovation (35573), and Mitacs Research Training Award for Financial Support.

ACKNOWLEDGMENTS

The authors would like to thank Clyde Overby for editing the work.

SUPPLEMENTARY MATERIAL

The Supplementary Material for this article can be found online at: https://www.frontiersin.org/articles/10.3389/fmats.2020.595295/full#supplementary-material.

REFERENCES

Abbott, W. M., Megerman, J., Hasson, J. E., L'Italien, G., and Warnock, D. F. (1987). Effect of compliance mismatch on vascular graft patency. *J. Vasc. Surg.* 5 (2), 376–382. doi:10.1016/0741-5214(87)90148-0

Abraham, G., Frontini, P., and Cuadrado, T. (1998). Molding of biomedical segmented polyurethane delamination events and stretching behavior. *J. Appl. Polym. Sci.* 69 (11), 2159–2167. doi:10.1002/(sici)1097-4628(19980912)69:11<2159::aid-app7>3.0.co;2-f

Ahmed, A. A., Stella, G., Leinweber, P., Freese, D., and Kühn, O. (2019). Infrared spectroscopic characterization of phosphate binding at the goethite–water interface. *Phys. Chem. Chem. Phys.* 21 (8), 4421–4434. doi:10.26434/chemrxiv.7370048.v2

Awaja, F., Gilbert, M., Kelly, G., Fox, B., and Pigram, P. J. (2009). Adhesion of polymers. *Prog. Polym. Sci.* 34 (9), 948–968. doi:10.1016/j.progpolymsci.2009.04.007

Bates, N. M., Maugis, D., and Barquins, M. (2020). Evaluation of the effect of crosslinking method of poly (vinyl alcohol) hydrogels on thrombogenicity. *Cardiovasc. Eng. Technol.* 12, 1–8. doi:10.1007/978-1-4899-3454-3_5

Biglino, G. (2013). Rapid prototyping compliant arterial phantoms for in-vitro studies and device testing. *J. Cardiovasc. Magn. Reson.* 15 (1), 2. doi:10.1007/978-1-4899-3454-3

Catanese, J., III, Gilbert, M., and Kelly, G. (1999). Mechanical properties of medical grade expanded polytetrafluoroethylene: the effects of internodal distance, density, and displacement rate. *Jpn. Soc. Biomater.* 48, 187–192. doi:10.1007/978-1-4899-3454-3_7

Chaouat, M. (2008). A novel cross-linked poly (vinyl alcohol)(PVA) for vascular grafts. *Adv. Funct. Mater.* 18 (19), 2855–2861. doi:10.1016/j.polymer.2016.05.043

Chen, H., Stella, G., Leinweber, P., and Freese, D. (2016). Thermo-and water-induced shape memory poly (vinyl alcohol) supramolecular networks crosslinked by self-complementary quadruple hydrogen bonding. *Polym. Chem.* 7 (43), 6637–6644. doi:10.1039/c6py01302c

Court, R., Sutcliffe, M., and Tavakoli, S. (2001). Ageing of adhesively bonded joints—fracture and failure analysis using video imaging techniques. *Int. J. Adhesion Adhes.* 21 (6), 455–463. doi:10.1002/macp.201100149

Cutiongco, M. F. A., Frontini, P., and Cuadrado, T., (2015). Composite scaffold of poly (vinyl alcohol) and interfacial polyelectrolyte complexation fibers for controlled biomolecule delivery. *Front. Bioeng. Biotechnol.* 3, 3. doi:10.1021/acsmacrolett.7b00275.s001

Cutiongco, M. F., Sutcliffe, M., Chen, H., and Stella, G. (2016a). Planar and tubular patterning of micro and nano-topographies on poly (vinyl alcohol) hydrogel for improved endothelial cell responses. *Biomaterials* 84, 184–195. doi:10.1021/acsami.6b11476.s001

Cutiongco, M. F., Gilbert, M., and Kelly, G. (2016b). Submillimeter diameter poly (vinyl alcohol) vascular graft patency in rabbit model. *Frontiers in bioengineering and biotechnology.* 4, 44. doi:10.1021/acsami.6b11476.s003

Elshazly, T. H. (2004). *Characterization of PVA hydrogels with regards to vascular graft development*. Georgia: Georgia Institute of Technology.

Fung, Y.-C. (1998). Biomechanics: circulation. *Shock.* 9, 155.

Gao, J. (2019). Effect of wall structures on mechanical properties of small caliber PHBHHx vascular grafts. *Fibers Polym.* 20 (11), 2261–2267. doi:10.1021/acsami.6b11476.s002

Gupta, S., Goswami, S., and Sinha, A. (2012). A combined effect of freeze–haw cycles and polymer concentration on the structure and mechanical properties of transparent PVA gels. *Biomed. Mater.* 7 (1), 015006. doi:10.1021/acsami.6b11476.s004

Hansen, F., Kelly, G., Fox, B., and Pigram, P. J. (1995). Diameter and compliance in the human common carotid artery—variations with age and sex. *Ultrasound Med. Biol.* 21 (1), 1–9. doi:10.1021/acsami.6b11476.s005

Holloway, J. L., Lowman, A. M., and Palmese, G. R. (2013). The role of crystallization and phase separation in the formation of physically cross-linked PVA hydrogels. *Soft Matter.* 9 (3), 826–833. doi:10.1039/c2sm26763b

Ino, J. M., Fox, B., and Pigram, P. J. (2013). Evaluation of hemocompatibility and endothelialization of hybrid poly (vinyl alcohol)(PVA)/gelatin polymer films. *J. Biomed. Mater. Res. B Appl. Biomater.* 101 (8), 1549–1559. doi:10.1021/acs.iecr.9b01796.s001

Jeong, Y., Yao, Y., and Yim, E. K. (2020). Current understanding of intimal hyperplasia and effect of compliance in synthetic small diameter vascular grafts. *Biomater. Sci.* 24, 93–124. doi:10.1021/acs.macromol.6b00584.s001

Kambric, H., Kantrowitz, A., and Sung, P. (1984). *Vascular graft update*. Philadelphia:ASTM.

Kim, H., Han, S., and Seo, Y. (2020). Novel dual curing process for a stereolithographically printed Part Triggers A remarkably improved interlayer adhesion and excellent mechanical properties. *Langmuir*. 14, 33–39. doi:10.1021/acs.jpcb.6b06009.s001

Konig, G., Gupta, S., Goswami, S., and Sinha, A. (2009). Mechanical properties of completely autologous human tissue engineered blood vessels compared to human saphenous vein and mammary artery. *Biomaterials* 30 (8), 1542–1550. doi:10.1016/j.biomaterials.2008.11.011

Krejza, J., Chen, H., Stella, G., Leinweber, P., and Freese, D. (2006). Carotid artery diameter in men and women and the relation to body and neck size. *Stroke* 37 (4), 1103–1105. doi:10.4149/bll_2019_147

Lack, S., (2004). Hydrogels based on pullulan crosslinked with sodium trimetaphosphate (STMP): rheological study. *Polym. Bull.* 52 (6), 429–436. doi:10.1111/j.1476-5381.2011.01264.x

Leone, G., (2010). PVA/STMP based hydrogels as potential substitutes of human vitreous. *J. Mater. Sci. Mater. Med.* 21 (8), 2491–2500. doi:10.1136/heartjnl-2019-bcs.189

Markiewicz, M. R., Ord, R., and Fernandes, R. P. (2017). Local and regional flap reconstruction of maxillofacial defects. *Maxillofac. Surg.* 29, 616–635. doi:10.1016/b978-0-7020-6056-4.00044-7

Menon, E. S. (2011). "Chapter 7—Pipe strength and wall thickness," in *Pipeline planning and construction field manual*. Editor E. S. Menon (Houston, TX: Gulf Professional Publishing), 105–121.

Nautiyal, P., Boesl, B., and Agarwal, A. (2017). Harnessing three dimensional anatomy of graphene foam to induce superior damping in hierarchical polyimide nanostructures. *Small*. 13 (10), 1603473. doi:10.1002/smll.201603473

Nezarati, R. M., Boesl, B., and Agarwal, A. (2015). Electrospun vascular grafts with improved compliance matching to native vessels. *J. Biomed. Mater. Res. B Appl. Biomater.* 103 (2), 313–323. doi:10.1021/acsami.6b06024.s001

Otsuka, E., and Suzuki, A. (2009). A simple method to obtain a swollen PVA gel crosslinked by hydrogen bonds. *J. Appl. Polym. Sci.* 114 (1), 10–16. doi:10.1021/jacs.8b04119.s001

Peacock, A. J., and Calhoun, A. (2012). *Polymer chemistry: properties and application*. Berlin: Carl Hanser Verlag GmbH Co KG.

Peiffer, D. G., and Nielsen, L. E. (1979). Preparation and mechanical properties of thick interlayer composites. *J. Appl. Polym. Sci.* 23 (8), 2253–2264. doi:10.1021/acsami.9b19656.s001

Peppas, N. A., Stella, G., Leinweber, P., and Freese, D. (2006). Hydrogels in biology and medicine: from molecular principles to bionanotechnology. *Adv. Mater.* 18 (11), 1345–1360. doi:10.1021/acs.langmuir.6b01864.s002

Peppas, N. A., and Merrill, E. W. (1976). Differential scanning calorimetry of crystallized PVA hydrogels. *J. Appl. Polym. Sci.* 20 (6), 1457–1465. doi:10.1021/acsbiomaterials.6b00139.s003

Peppas, N. A. (1975). Turbidimetric studies of aqueous poly (vinyl alcohol) solutions. *Makromol. Chem.: Macromol. Chem. Phys.* 176 (11), 3433–3440. doi:10.1021/acsbiomaterials.6b00139.s001

Pohan, G., Lowman, A. M., and Palmese, G. R. (2020). Effect of ethylene oxide sterilization on polyvinyl alcohol hydrogel compared with gamma radiation. *Tissue Eng. A.* 6, 1077–1090. doi:10.1089/ten.tea.2020.0002

Pohan, G., Stella, G., and Leinweber, P. (2019). Luminal plasma treatment for small diameter polyvinyl alcohol tubular scaffolds. *Front. Bioeng. Biotechnol.* 7, 117. doi:10.1016/0146-5724(85)90031-7

Puy, N. M. B. C., McCarty, O., and Hinds, M. (2019). "Thrombogenicity of poly (Vinyl) alcohol hydrogels is dependent on the crosslinking agent," in 42nd Society for biomaterials annual meeting and ExpositionThe pinnacle of biomaterials innovation and excellence. London: Society for Biomaterials.

Sarkar, S. (2006). The mechanical properties of infrainguinal vascular bypass grafts: their role in influencing patency. *Eur. J. Vasc. Endovasc. Surg.* 31 (6), 627–636. doi:10.1063/1.5018937

Srinivasan, E., Vanchinathan, T., and Siva Kumar, G. (2020). *Fabrication of microcontroller based dip-casting for thin films depositions*. Berlin: Springer.

Szafron, J. M. (2019). Optimization of tissue-engineered vascular graft design using computational modeling. *Tissue Eng. C Methods* 25 (10), 561–570. doi:10.1016/s0969-806x(01)00427-3

Tai, N., Merrill, E. W., and Szafron, J. M. (2000). Compliance properties of conduits used in vascular reconstruction. *Br. J. Surg.* 87 (11), 1516–1524. doi:10.3403/00343577u

Wise, S. G. (2011). A multilayered synthetic human elastin/polycaprolactone hybrid vascular graft with tailored mechanical properties. *Acta Biomaterialia.* 7 (1), 295–303. doi:10.1016/j.actbio.2010.11.009

Xiong, D.-S. (2008). Synthesis and properties of physically crosslinked poly (vinyl alcohol) hydrogels. *J. China Univ. Min. Technol.* 18 (2), 271–274. doi:10.1016/j.actbio.2010.07.022

Yao, Y. (2020). Fucoidan functionalization on poly (vinyl alcohol) hydrogels for improved endothelialization and hemocompatibility. *Biomaterials* 18 (2), 271–274. doi:10.1016/j.jmbbm.2012.02.026

Yu, L. Y., Daugaard, A. E., and Skov, A. L. (2013). Adhesion between polydimethylsiloxane layers by crosslinking. *Adv. Sci. Technol. Trans. Tech. Publ.* 17, 23. doi:10.1177/0885328220907775

Zhu, X.-K., and Leis, B. N. (2012). Evaluation of burst pressure prediction models for line pipes. *Int. J. Pres. Ves. Pip.* 89, 85–97. doi:10.1016/j.jvir.2007.11.027

Conflict of Interest: The authors declare that the research was conducted in the absence of any commercial or financial relationships that could be construed as a potential conflict of interest.

Polymeric and Composite Materials

Françoise Berzin

Prof. Françoise Berzin currently works at the Fractionnement des Agroressources et Environnement (FARE), Université de Reims Champagne-Ardenne. Françoise is a specialist of composite materials and polymer extrusion. She achieved her doctorate in 1998 at École des Mines de Paris (MINES ParisTech), followed by two postdoctorate positions at École Polytechnique de Montréal, Canada, and École des Mines de Paris (MINES ParisTech) and Arkema Partnership, respectively. From 2000 to 2017, she was an Associate Professor at the University of Reims Champagne-Ardenne, and she has been a Full Professor there since 2017.

Jayashree Bijwe

Prof. Jayashree Bijwe has worked as a Professor at the Indian Institute of Technology, Delhi, India, for the past 25 years. Her current major research areas include the development of high-performance polymer composites/nanocomposites for tribological applications, such as Non-asbestos-Non-Copper- organic brake pads, dry bearings, and high-temperature adhesives, and the development of oils/nano-oils, greases for engines, gears, etc. She has published 200 research papers in international journals, 100 conference papers, and 12 book chapters. Her h Index (google scholar) is 48, she has an i10-index of 142, and she has over 8000 citations. She has been on the editorial/advisory boards of various journals like Wear, Tribology International, STMP, Industrial Lubrication and Tribology, IOP SciNotes, etc.

Valentina Brunella

Prof. Valentina Brunella received her Ph.D. in Chemistry, and, since 2002, she has been serving the Department of Chemistry at the University of Torino, first as Assistant Professor and now as Associate Professor in Industrial Chemistry. She has proven experience in the polymeric and composite material field. Her research interests are focused on the characterization of polymeric materials from different points of view: (i) structure-property relationships in polymers, copolymers, and composites; (ii) the study of different degradation processes of polymeric matrices under the effect of temperature, radiation, and so on; and (iii) chemical and mechanical characterization and modification of polymeric adhesive joints.

Valerie Desauziers

Prof. Valérie Desauziers, Ph.D. in analytical chemistry, is a Professor at IMT Mines Ales, a French school for engineering and applied science. She is the head of the research group RIME (research for material/environment interactions) located in Pau, France. Their objective is to study the impact of materials and associated processes (manufacturing, use, aging, recycling, etc.) on the environment, health, and sensory properties. Valerie Desauziers's research concerns the development of sampling and analytical methods for VOCs and SVOCs traces in air and at the material/air interface to study transfers of emerging pollutants and assess their impact on indoor air quality and health.

Patricia Maria Frontini

Prof. Patricia Maria Frontini is a Full Professor at the University of Mar del Plata and a Superior Researcher of the National Research Council of Argentina. Her scientific activities concern the deformation and fracture of polymers and composites, performance under high-rate loading, yield behavior under multiaxial loading, the performance of injection molded parts, nanoindentation, and constitutive modeling. She has participated in numerous international scientific collaboration projects and technological developments for the productive sector. She has published more than 120 papers for international indexed journals and more the 200 conference papers. She has also received several scientific awards in Argentina (Houssay 2005; Ing. Santiago 2015, and Ing. Huergo 2019).

Carla Martins

Dr. Carla I Martins is an Assistant Professor at the University of Minho and a researcher at the Institute for Polymer and Composites (IPC), Portugal. She holds a degree in Polymer Engineering (1998), a Master's in Math Applied to Mechanics (2001) from the University of Minho, and a Ph.D. in Polymer Engineering (2004) from the University of Akron, USA. She has participated in National and European industrial-oriented projects as both an investigator and principal investigator. She has supervised a number of Master's and Ph.D. students in the field of processing structure properties of polymeric materials, filled systems, and recycled/reused materials. She has (co-)authored 40 publications in national and international journals or conferences.

Véronique Michaud

Prof. Véronique Michaud is currently an Associate Professor, Head of the Laboratory for Processing of Advanced Composites, and an Associate Dean of Engineering for Education at the Ecole Polytechnique Fédérale de Lausanne, Switzerland. She graduated in 1987 from Ecole des Mines in Paris with an engineering degree and in 1991 from MIT with a Ph.D. in Materials Engineering. She also obtained a Research Habilitation from INPG in France in 1994. After a post-doctoral research stay at MIT, she spent 3 years at Ecole Centrale in Paris to teach and research at the Laboratory for Materials, Structures, and Soils Mechanics before joining EPFL in 1997. Her fields of research address fundamental aspects of composite materials processing as well as the development of smart materials and structures, including self-healing, shape and vibration control, and tailored damping. She is also the co-founder of CompPair Technologies SA, which was created in 2020.

Hamideh Mirbaha

Dr. Hamideh Mirbaha is currently a post-doctoral researcher at the laboratory of Bio-inspired, Bionic, Nano, Meta Materials & Mechanics at the University of Trento, Italy. She received her Ph.D. from Amirkabir University of Technology, Iran, where she studied the structure formation of PAN/CNT composite fibers during the solution spinning process. She was a visiting researcher at the University of Trento, Italy, during her Ph.D. research, characterizing the mechanical and structural properties of nanocomposite fibers produced under different shear and elongation conditions. Her main research areas also include the actuation behavior of polyacrylonitrile gel fibers, the stabilization process of PAN fibers, and conductive electrospun nanofibers.

Amulya Raj

Dr. Amulya Raj received her Ph.D. in Material Engineering from IMT Lille-Douai, France, in 2019, prior to which she received a Master's degree in Polymer Science and Technology from VTU, India, in 2013. She is currently working as a Polymer Engineer at Eden Tech, Paris, with a focus on polymers in microfluidic applications. Her research interests include polymer chemistry, processing, and blending with a special emphasis on bio-based polymers. She has worked extensively on PLA blends for high-performance and durable applications.

Florence Saffar

Dr. Florence Saffar is a Postdoctoral Research Assistant at the University of Edinburgh in Advanced Materials for Renewable Energy Applications. She currently works on Fiber Metal Laminate (FML) development. She achieved her Ph.D. at ONERA – The French Aerospace Lab on the topic of the consolidation of thermoplastics in low-pressure situations.

frontiers in Materials

ORIGINAL RESEARCH
published: 24 July 2020
doi: 10.3389/fmats.2020.00218

Use of Flow Modeling to Optimize the Twin-Screw Extrusion Process for the Preparation of Lignocellulosic Fiber-Based Composites

Françoise Berzin[1]*, *Chantal David*[2] *and Bruno Vergnes*[3]*

[1] FARE, University of Reims Champagne Ardenne, INRAE, Reims, France, [2] Sciences Computers Consultants, Saint-Étienne, France, [3] MINES ParisTech, PSL Research University, Sophia Antipolis, France

Thermoplastic polymers reinforced by lignocellulosic fibers are increasingly used to replace conventional composites based on carbon or glass fibers. These materials are generally prepared by dispersing the fibers into the polymer matrix by melt mixing in a twin-screw extrusion process. However, during the process, a significant breakage occurs, leading to a reduction in the length, and diameter of the bundles and/or individual fibers. As the mechanical properties of the composite depend, among other, on the fiber morphology, it is important to understand and control the breakage mechanisms during the compounding process. In this paper, we show how the use of a thermomechanical model of twin-screw extrusion coupled with evolution laws of the fiber dimensions makes it possible to calculate the variation in the length and the diameter of the fibers, according to the local values of the flow parameters (shear rate, residence time, temperature, etc.). It is thus possible to define the best processing conditions (screw speed, feed rate, and barrel temperature) or the best screw profile to limit fiber degradation and prepare composites with optimal properties.

Keywords: lignocellulosic fibers, extrusion, modeling, breakage, optimization

OPEN ACCESS

Edited by:
Patricia Krawczak, IMT Lille Douai, France

Reviewed by:
Jose Antonio Covas, University of Minho, Portugal
Margaret J. Sobkowicz, University of Massachusetts Lowell, United States

***Correspondence:**
Françoise Berzin
francoise.berzin@univ-reims.fr
Bruno Vergnes
bruno.vergnes@mines-paristech.fr

Specialty section:
This article was submitted to Polymeric and Composite Materials, a section of the journal Frontiers in Materials

Received: *15 May 2020*
Accepted: *15 June 2020*
Published: *24 July 2020*

Citation:
Berzin F, David C and Vergnes B (2020) Use of Flow Modeling to Optimize the Twin-Screw Extrusion Process for the Preparation of Lignocellulosic Fiber-Based Composites. Front. Mater. 7:218. doi: 10.3389/fmats.2020.00218

INTRODUCTION

Due to their interesting properties, such as lightness, low cost, biobased origin, and satisfactory mechanical properties, lignocellulosic fibers are increasingly used for the preparation of thermoplastic matrix composites (Mohanty and Drzal, 2005; Hodzic and Shanks, 2014; Campilho, 2015). For short fibers (a few mm long) and thermoplastic matrices, the preferred process is melt mixing, i.e., compounding followed by extrusion or injection molding. In a first step, the fibers are mixed with the polymer matrix to obtain composite pellets, generally using a twin-screw extruder. In a second step, these pellets are processed by extrusion or injection molding to obtain the desired final shape. During the compounding step, many problems arise: first, when subjected to high stresses and strains, the fibers break. Not only the length, but also the diameter, of the initial bundles or the individual fibers can be considerably reduced. Second, the dispersion of the fibers into the matrix may be heterogeneous, with the existence of agglomerates. Third, if the temperature rises above about 200°C, thermal degradation can occur (Tajvidi and Takemura, 2010). Therefore, it is clear that the control of the extrusion conditions (screw profile, screw rotation speed, feed rate, etc.) is essential to prepare composites with optimal properties.

The role of the processing conditions on the fiber state and on the final properties of composites has been studied by many authors (Iannace et al., 2001; Le Baillif and Oksman, 2009; Quijano-Solis et al., 2009; Barkoula et al., 2010; Mano et al., 2010; Beaugrand and Berzin, 2012; El Sabbagh et al., 2014; Gonzalez-Sanchez and Gonzalez-Quesada, 2015; Feldmann et al., 2016). In recent years, we have developed a systematic study of the breakage of lignocellulosic fibers under thermomechanical stresses, based on rheo-optical observations (Le Duc et al., 2011; Castellani et al., 2016), and experiments carried out in internal mixers (Di Giuseppe et al., 2017) and twin-screw extruders (Berzin et al., 2017, 2018, 2019, 2020). These studies were conducted with different thermoplastic matrices (polypropylene and polybutylene succinate) and various lignocellulosic fibers (flax, hemp, sisal, miscanthus, and pineapple leaf fibers). The main result is that fiber breakage (i.e., reduction in the length and diameter of bundles and individual fibers) occurs primarily by fatigue, after numerous bends, unlike glass fibers which, due to their rigidity, break when a critical stress is reached (Durin et al., 2013). Consequently, the parameter which controls the kinetics of breakage is the strain accumulated by the fiber during the flow along the twin-screw extruder. This mechanism depends obviously on the properties of the fiber (plant origin, composition, water content, etc.) but also on its dimensions (longer fibers break more easily than short ones) and on the properties of the matrix (viscosity, affinity with fiber, etc.).

As the reinforcing properties of the fibers in the composite are among other controlled by their length (or their aspect ratio), it is necessary to limit breakage during compounding by twin-screw extrusion. However, it remains long and difficult by trial and error to find the optimal conditions, providing the maximum output while preserving the fiber length. In this paper, we will show how the use of flow modeling may allow to solve this delicate problem and to rapidly test many different solutions to select the most interesting.

MATERIALS AND METHODS

Composite Preparation

As noted in the introduction, we focus on the compounding step, where the fibers are dispersed into the matrix by using a co-rotating twin-screw extruder. The laboratory scale extruder used by Berzin et al. (2017) (Clextral BC21, Firminy, France) was selected as an example of application. It has a diameter of 25 mm and a length of 900 mm. The screw profile is shown in **Figure 1**. It comprises nine barrel elements (numbered from 1 to 9, from the hopper to the screw end) and, in addition to the screw conveying elements, it includes a left-handed element in zone 3 to melt the polymer matrix and two mixing blocks in zones 6 and 8, to disperse the fibers. The first one has five kneading discs, staggered by 90°, while the second one is more restrictive, with five kneading discs staggered by −45°. The matrix is introduced in zone 1, melted in the left-handed element (zone 3), then the fibers are added in zone 4.

The matrix is that used in the paper by Berzin et al. (2017). It is a mix of polypropylene (PP) and maleic anhydride grafted polypropylene (PP-g-MA) used as compatibilizer. Indeed, PP-g-MA is commonly used to improve the affinity between the hydrophilic fibers and the hydrophobic matrix (Feng et al., 2001; Bos et al., 2006). The PP-g-MA/fiber ratio is 1/10 by weight, as recommended in the literature (Le Moigne et al., 2011). Among the various fibers studied by Berzin et al. (2017), we have selected flax fibers for this paper. They were provided by FRD© company (Fibres Recherche Développement, Troyes, France) and have the following average dimensions: length $L = 4$ mm, diameter $D = 242\,\mu$m, aspect ratio $L/D = 18.8$. They contain 86.5 wt% of cellulose, 8.6 wt% of hemicellulose and 4.9 wt% of lignin.

Breakage Mechanisms

As indicated in the Introduction, the breakage mechanisms of flax fibers have been characterized and quantified in previous studies (Berzin et al., 2017; Di Giuseppe et al., 2017). For a fixed composition (type of fiber and matrix), it has been shown that the length L and the diameter D vary with the cumulated strain Γ, according to exponential functions. Local strain (without dimension) is the product of the local shear rate by the corresponding local residence time. It is then cumulated from the introduction of the fibers into the extruder up to the sampling point considered. The following expressions have been proposed and validated for various types of fibers and matrices (Berzin et al., 2017, 2018, 2019, 2020):

$$L = L_\infty + (L_0 - L_\infty)\exp(-k_L\,\Gamma) \quad (1)$$

$$D = D_\infty + (D_0 - D_\infty)\exp(-k_D\,\Gamma) \quad (2)$$

where L_0 (respectively, D_0) is the initial fiber length (respectively, diameter), L_∞ (respectively, D_∞) is its ultimate length (respectively, diameter), Γ is the cumulated strain and k_L (respectively, k_D) is a constant, quantifying the breakage kinetics. These constants depend on the properties of the fiber and the matrix. In the case of selected 4 mm flax fibers, the following values were obtained by Berzin et al. (2017): $L_0 = 4$ mm, $L_\infty = 1.2$ mm and $k_L = 1.1 \times 10^{-3}$, and $D_0 = 242\,\mu$m, $D_\infty = 100\,\mu$m, and $k_D = 2.8 \times 10^{-3}$. The corresponding experimental data and the theoretical curves provided by Equations (1) and (2) are illustrated in **Figure 2**.

Flow Modeling

The strain cannot be measured experimentally on a twin-screw extruder. Therefore, it is mandatory to use a model to calculate it and to assess changes in length and diameter of the fibers during the process. In this paper, the Ludovic® software developed by Vergnes et al. (1998) and marketed by SCC company (Saint Etienne, France) was used. Ludovic® is a model based on continuum mechanics, which solves the Stokes and energy equations within the framework of simplified geometry and kinematics. It simulates the whole extrusion process, from the introduction of solid polymer pellets in the hopper to the die exit, and calculates the variations along the screws of the main flow parameters, such as pressure, temperature, residence time, shear rate, stress, strain, etc. The simulation is based on a one-dimensional analysis. The screws are divided into elementary

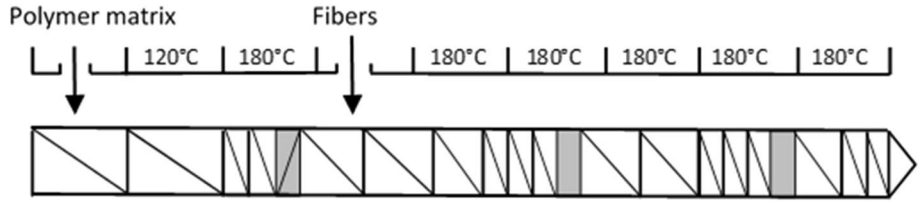

FIGURE 1 | Screw profile. The restrictive elements are in gray.

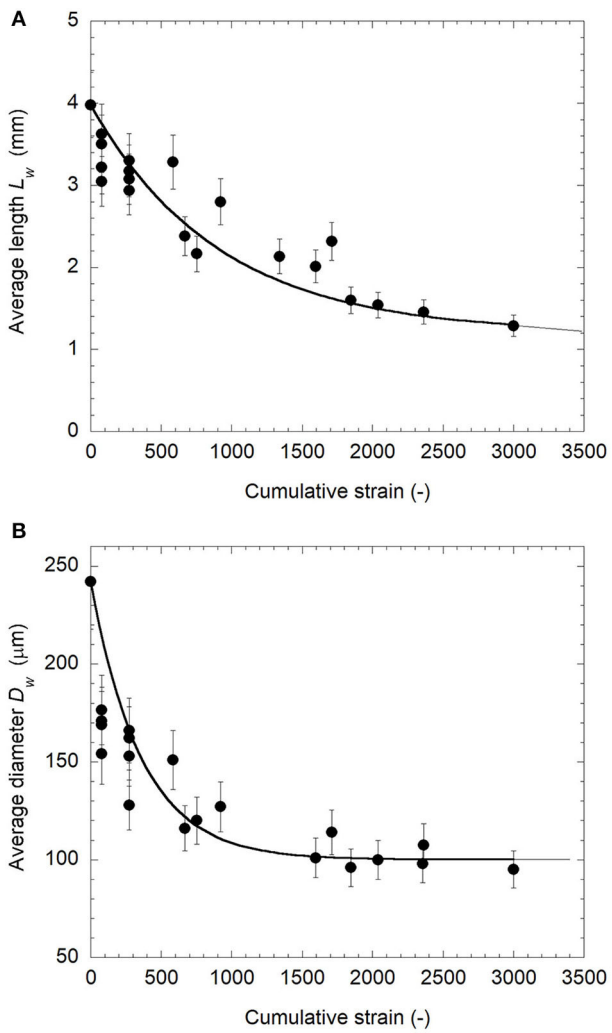

FIGURE 2 | Changes in length **(A)** and diameter **(B)** of 4 mm flax fibers as a function of cumulative strain. Symbols are experimental points, the lines are fits using (Equations 1, 2). Reprinted from Berzin et al. (2017) with permission.

sub-elements in which mass and thermal balances are written. In each type of element (left- and right-handed screw elements, blocks of kneading discs, etc.), average values of flow parameters are computed. The computation starts at the die exit and, element by element, temperature, and pressure are computed by an iterative backward procedure. We refer to the previous publication by Vergnes et al. (1998) for more details. For 20 years, the Ludovic® software has been extensively validated, experimentally (Carneiro et al., 2000) and by comparisons with more elaborate 3D models (Durin et al., 2014).

Optimization Procedure

The objective is to define the best processing conditions to prepare composites with the screw profile presented in **Figure 1**, based on the products defined in section Composite Preparation, i.e., a PP/PP-g-MA matrix reinforced by 20 wt% of flax fibers. The best conditions mean reaching the maximum flow rate while keeping the fibers as long as a possible, i.e., at the lowest cumulated strain. However, other constraints must be taken into account.

As explained in the Introduction, the fibers must be correctly distributed into the matrix. There are many indices to characterize the distributive mixing, but the simplest is to consider the variance σ^2 of the residence time distribution (RTD) (Manas-Zloczower, 2009). The RTD is usually represented by a function $E(t)$ which gives the extruder response to an input pulse (Danckwerts, 1953). By definition, $E(t)dt$ is the fraction of material leaving the extruder with a residence time between t and $t + dt$. It is such as:

$$\int_0^\infty E(t)dt = 1 \tag{3}$$

The mean residence time $\bar{t}$ is the first moment of the distribution:

$$\bar{t} = \int_0^\infty tE(t)dt \tag{4}$$

The variance σ^2 is the second moment centered on the mean:

$$\sigma^2 = \int_0^\infty (t - \bar{t})^2 E(t)dt \tag{5}$$

σ^2 represents the width of the RTD. In extrusion, it is directly linked to the intensity of the back-mixing. As an example for the application illustrated below, an arbitrary value has been chosen, i.e., a variance >200 s^2 will be requested.

To avoid thermal degradation, the maximum temperature encountered during the process should not exceed 200°C (Gassan

and Bledzki, 2001). As for the strain, this maximum value cannot be measured as it can be reached somewhere inside the extruder, typically in a block of kneading disc. Again, modeling is necessary to obtain this information.

Finally, the last constraint is the maximum loading that can be fed to the extruder. In practice, the fiber feeding is a real challenge because of their very low apparent density, close to 0.1, leading to a large volume to introduce. The maximum feeding capacity can be estimated as follows. The free cross section of the extruder S in the feeding zone can be written:

$$S = S_B - 2S_S \tag{6}$$

where S_B is the cross section of the eight-shaped barrel and S_S that of the screw. S_B and S_S can be easily calculated using the expressions proposed by Booy (1978):

$$S_B = 2(\pi - \psi)R_e^2 + C_l R_e \sin\psi \tag{7}$$

$$S_S = n\left[\psi C_1^2 - C_1 R_e \sin\psi\right] + \frac{n\alpha}{2}\left[R_e^2 + (C_l - R_e)^2\right] \tag{8}$$

where R_e is the screw radius, C_l is the centerline distance, n is the number of flights, and ψ and α are two angles, respectively, defined as:

$$\cos\psi = \frac{C_l}{2R_e} \tag{9}$$

$$\alpha = \frac{\pi}{n} - 2\psi \tag{10}$$

The free cross section S moves downstream at a velocity V equal to:

$$V = \frac{NB}{60} \tag{11}$$

where N is the screw speed (expressed in rpm) and B the screw pitch.

The theoretical free volume by time unit is then $Vol = S\frac{NB}{60}$. However, as the fibers fall out of the hopper, not all of this volume is directly accessible. Only the upper part of the cross section of the channel can be reached by the fibers. Moreover, part of the channel is already filled by the molten polymer. We can thus estimate that the real free volume is only about a third of the theoretical one. This approximation is sufficient because we are simply looking for an order of magnitude, not an exact value. It was checked that this order of magnitude agreed with the experimental observations. The maximum mass flow rate of the fibers will then be approximated as:

$$Q_{f\,\max} \approx \rho_a S\frac{NB}{180} \tag{12}$$

where ρ_a is the apparent density of the fibers, typically close to 0.1.

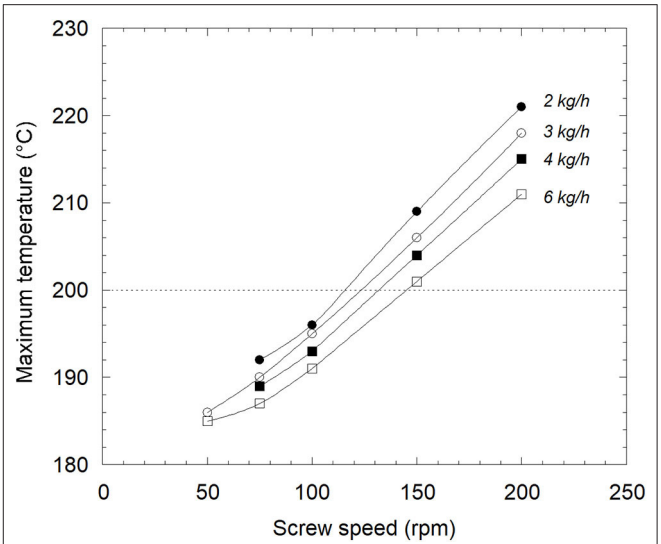

FIGURE 3 | Changes in maximum temperature with screw speed for different feed rates.

To summarize, the following constraints have to be respected for the optimization:

- maximum flow rate;
- minimum cumulated strain Γ;
- variance of RTD higher than 200 s^2;
- maximum temperature <200°C;
- fiber flow rate lower than $Q_{f\ \max}$.

RESULTS AND DISCUSSION

The optimization we propose is not a formal optimization, using specific algorithms, as we have done in other publications (Gaspar-Cunha et al., 2005, 2011), but a practical one, allowing to quickly define an optimal processing window. It will be conducted in two steps. First, the best processing conditions will be defined for the screw in **Figure 1**, according to the constraints defined in section Optimization Procedure. Second, we will show how changing the screw profile can help to improve the first results.

Optimization of Processing Conditions

To define the best processing conditions, simulations with Ludovic® software are performed by varying the total flow rate (PP/PP-g-MA + 20 wt% flax fibers) from 2 to 6 kg/h and the screw speed from 50 to 200 rpm. For each simulation, the values of the cumulated strain Γ, the RTD variance σ^2 and the maximum temperature $T_{\max}$ are recorded. The results are presented in **Figures 3–5**.

The maximum temperature $T_{\max}$ increases a lot with the screw speed, due to viscous dissipation (**Figure 3**). It can reach values of 30–40°C above the barrel temperature (180°C), capable of degrading not only the fibers but also the matrix. At a fixed screw speed, $T_{\max}$ decreases slowly with the feed rate. In order to

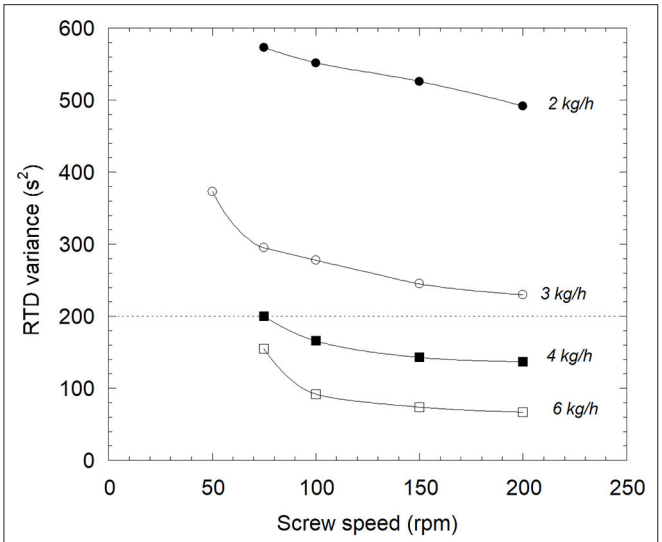

FIGURE 4 | Changes in RTD variance with screw speed for different feed rates.

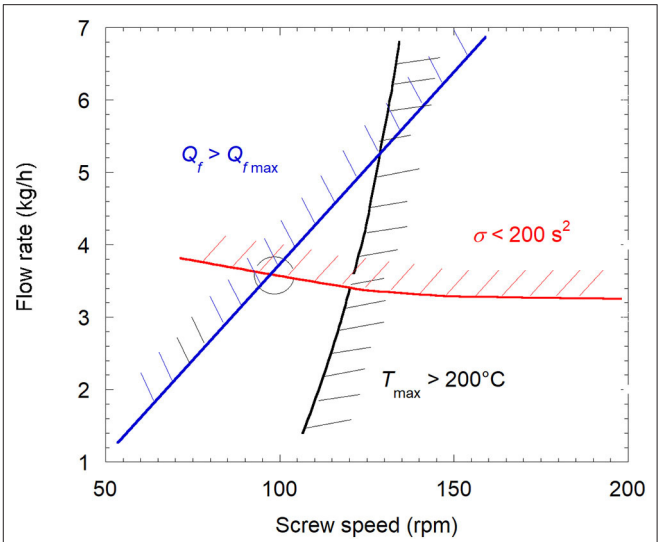

FIGURE 6 | Processing window on a screw speed/feed rate map. Hatched regions are forbidden by the various criteria.

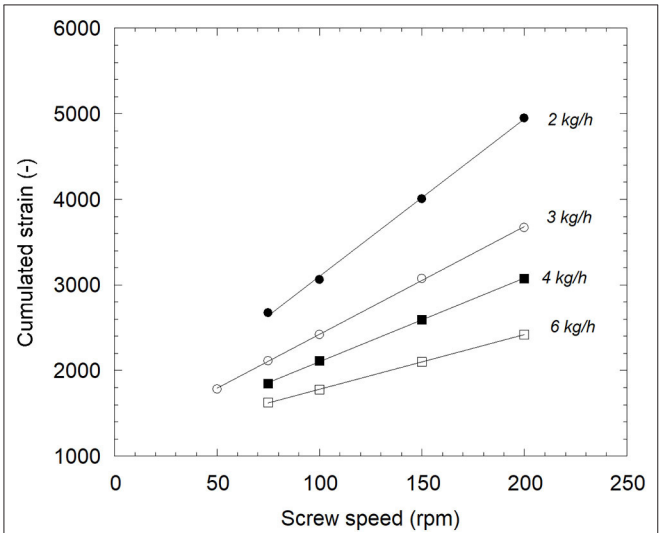

FIGURE 5 | Changes in cumulated strain with screw speed for different feed rates.

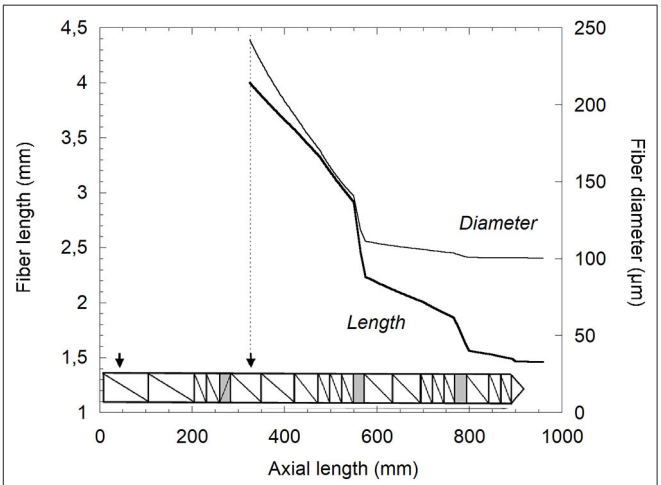

FIGURE 7 | Calculated changes in fiber length and diameter along the screw profile in the optimized conditions.

keep the temperature below the maximum value of 200°C, low screw speeds (in the range 110–150 rpm) are necessary.

The variance of the RTD σ^2, selected as the distributive mixing index, is shown in **Figure 4**. It decreases slightly with the screw speed, but is mainly affected by the flow rate. These effects of screw speed and feed rate on the RTD are well-known in twin-screw extrusion (Poulesquen and Vergnes, 2003): an increase in screw speed shifts the RTD toward shorter times, without affecting its shape, while an increase in feed rate also shifts the RTD toward shorter times, but mainly narrows its width. To comply with the constraint of RTD variance >200 s^2, low flow rates are mandatory: the limit appears between 3 and 4 kg/h.

Finally, the values of the cumulated strain Γ are presented in **Figure 5**. Γ increases linearly with the screw speed and decreases with the feed rate. Indeed, it can be shown that Γ is proportional to the ratio N/Q (Lafleur and Vergnes, 2014). Therefore, to limit the breakage of the fibers, it is necessary to favor low speeds and high feed rates.

If we consider these different results, it is clear that certain conditions appear to be contradictory. To have a clearer view of the situation, plots of isovalues of the limiting parameters T_{max}, σ^2, and $Q_{f\,max}$ are plotted on a flow rate/screw speed map (**Figure 6**). This shows that the processing windows is quite narrow: the screw speed is limited at 100–110 rpm by the maximum temperature and the flow rate below 4 kg/h by the RTD variance. Moreover, another limit is added by the

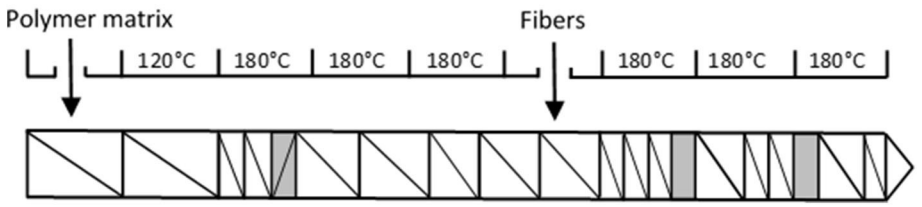

FIGURE 8 | Modified screw profile. The restrictive elements are in gray.

maximum feeding rate of the fibers. In conclusion, it appears that the optimal conditions (circle in **Figure 6**) are $Q = 3.6$ kg/h at $N = 95$ rpm. These values provide a maximum temperature of 194°C, reached in the second block of kneading discs, a RTD variance of 200 s^2, and a cumulated strain of 2,157. For these processing conditions, it is now possible to use (Equations 1, 2) to calculate the variations of the fiber dimensions along the screws. For example, **Figure 7** shows the change in fiber length and diameter under the optimized conditions. Fibers of 1.46 mm in length and 100 μm in diameter are obtained at the die exit.

Optimization of Screw Geometry

It can be seen in **Figure 7** that the fibers undergo a significant reduction in both the length and the diameter, even though the processing conditions have been optimized. Degradation occurs rapidly, along the first screw conveying elements, as soon as the fibers are introduced into the extruder. Therefore, to limit this problem and reduce the fiber attrition, the simplest way is to move the fiber introduction and the two blocks of kneading discs downstream, as shown in **Figure 8**. However, a certain distance along the screws remains necessary to ensure a good distribution of the fibers into the matrix. By repeating the same procedure as in the previous paragraph (different flow simulations under various conditions of screw speed and feed rate) and with the same constraints (on T_{max}, σ^2, and Q_{fmax}), the processing window for this new configuration can be established. The optimal conditions are very close to those of the first profile, with a flow rate of 3.6 kg/h and a screw speed of 100 rpm. However, as the fibers are introduced later, the cumulated strain is lower, here 1,820, and, as expected, the fibers are a little longer: 1.58 mm (i.e., a gain of 8%). Nevertheless, the improvement is not really significant and further modifications to the geometry would be necessary for better results. As the main limitation of the flow rate is the RTD variance, we can imagine to increase this parameter by increasing the length of the first block of kneading discs, staggered at 90° (50 mm instead of 25 mm). In doing so, the numerical simulation shows that at 120 rpm and always with the same constraints, the feed rate can be increased up to 4.8 kg/h, i.e., a gain of 33%. However, the cumulated strain remains around 2,000, indicating no further improvement in the fiber length. Based on the previous results of Berzin et al. (2017), starting from initial longer fibers could be a solution: indeed, for flax fibers 12 mm long, the same processing conditions (4.8 kg/h, 120 rpm) would lead to final fibers about 3 mm in length.

CONCLUSION

In this paper, it has been shown that the use of a model of the flow along a twin-screw extruder coupled with evolution laws for the dimensions of lignocellulosic fibers can be a very useful tool for optimizing the preparation of natural fiber composites. In a very short time (each calculation requires only a few seconds on a PC), it allows one to test many possible conditions and, according to certain constraints, to optimize the processing conditions and the screw profile. Similarly, flow modeling could also be a privileged tool for solving the often difficult problem of scale-up, from laboratory to industrial scale.

DATA AVAILABILITY STATEMENT

The raw data supporting the conclusions of this article will be made available by the authors, without undue reservation.

AUTHOR CONTRIBUTIONS

FB, CD, and BV contributed equally to the paper, by performing the simulations, discussing the results, and writing the text. All authors contributed to the article and approved the submitted version.

REFERENCES

Barkoula, N. M., Garkhail, S. K., and Peijs, T. (2010). Effect of compounding and injections molding on the mechanical properties of flax fiber polypropylene composites. *J. Reinf. Plast. Comp.* 29, 1366–1385. doi: 10.1177/0731684409104465

Beaugrand, J., and Berzin, F. (2012). Lignocellulosic fiber reinforced composites: influence of compounding conditions on defibrization and mechanical properties. *J. Appl. Polym. Sci.* 128, 1227–1238. doi: 10.1002/app.38468

Berzin, F., Amornsakchai, T., Lemaitre, A., Castellani, R., and Vergnes, B. (2019). Influence of fiber content on rheological and mechanical properties of pineapple leaf fibers-polypropylene composites prepared by twin-screw extrusion. *Polym. Comp.* 40, 4519–4529. doi: 10.1002/pc.25308

Berzin, F., Amornsakchai, T., Lemaitre, A., Di Giuseppe, E., and Vergnes, B. (2018). Processing and properties of pineapple leaf fibers-polypropylene composites prepared by twin-screw extrusion. *Polym. Comp.* 39, 3817–4223. doi: 10.1002/pc.24475

Berzin, F., Beaugrand, J., Dobosz, S., Budtova, T., and Vergnes, B. (2017). Lignocellulosic fiber breakage in a molten polymer. Part 3. Modelling of the dimensional evolution of the fibers during compounding by twin screw extrusion. *Comp. Part A* 101, 422–431. doi: 10.1016/j.compositesa.2017.07.009

Berzin, F., Lemkhanter, L., Marcuello-Angles, C., Molinari, M., Chabbert, B., Aguié, V., et al. (2020). Influence of the polarity of the matrix on the breakage mechanisms of lignocellulosic fibers during twin-screw extrusion. *Polym. Comp.* 41, 1106–1117. doi: 10.1002/pc.25442

Booy, M. L. (1978). Geometry of fully wiped twin-screw equipment. *Polym. Eng. Sci.* 18, 973–984. doi: 10.1002/pen.760181212

Bos, H. L., Müssig, J., and van den Oever, M. J. A. (2006). Mechanical properties of short-flax-fibre reinforced compounds. *Comp. Part A* 37, 1591–1604. doi: 10.1016/j.compositesa.2005.10.011

Campilho, R. D. S. G. (2015). *Natural Fibers Composites.* Boca Raton, FL: CRC Press, 368. doi: 10.1201/b19062

Carneiro, O. S., Covas, J. A., and Vergnes, B. (2000). Experimental and theoretical study of the twin screw extrusion of polypropylene. *J. Appl. Polym. Sci.* 78, 1419–1430. doi: 10.1002/1097-4628(20001114)78:7<1419::AID-APP130>3.0.CO;2-B

Castellani, R., Di Giuseppe, E., Beaugrand, J., Dobosz, S., Berzin, F., Vergnes, B., et al. (2016). Lignocellulosic fiber breakage in a molten polymer. Part 1. Quantitative analysis using rheo-optical observations. *Comp. Part A* 91, 229–237. doi: 10.1016/j.compositesa.2016.10.015

Danckwerts, P. V. (1953). Continuous flow systems: distribution of residence times. *Chem. Eng. Sci.* 2, 1–13. doi: 10.1016/0009-2509(53)80001-1

Di Giuseppe, E., Castellani, R., Budtova, T., and Vergnes, B. (2017). Lignocellulosic fiber breakage in a molten polymer. Part 2. Quantitative analysis of the breakage mechanisms during compounding. *Comp. Part A* 95, 31–39. doi: 10.1016/j.compositesa.2016.12.011

Durin, A., De Micheli, P., Nguyen, H. C., David, C., Valette, R., and Vergnes, B. (2014). Comparison between 1D and 3D approaches for twin-screw extrusion simulation. *Intern. Polym. Proc.* 29, 641–648. doi: 10.3139/217.2951

Durin, A., De Micheli, P., Ville, J., Inceoglu, F., Valette, R., and Vergnes, B. (2013). A matricial approach of fibre breakage in twin-screw extrusion of glass fibres reinforced thermoplastics. *Comp. Part A* 48, 47–56. doi: 10.1016/j.compositesa.2012.12.011

El Sabbagh, A. M. M., Steuernagel, L., Meiners, D., and Ziegmann, D. (2014). Effect of extruder elements on fiber dimensions and mechanical properties of bast natural fiber polypropylene composites. *J. Appl. Polym. Sci.* 131:40435. doi: 10.1002/app.40435

Feldmann, M., Heim, H. P., and Zarges, J. C. (2016). Influence of the process parameters on the mechanical properties of engineering biocomposites using a twin-screw extruder. *Comp. Part A* 83, 113–119. doi: 10.1016/j.compositesa.2015.03.028

Feng, D., Caulfield, D. F., and Sanadi, A. R. (2001). Effect of compatibilizer on the structure-property relationships of kenaf-fiber/polypropylene composites. *Polym. Comp.* 22, 506–517. doi: 10.1002/pc.10555

Gaspar-Cunha, A., Covas, J. A., and Vergnes, B. (2005). Defining the configuration of co-rotating twin-screw extruders with multiobjective evolutionary algorithms. *Polym. Eng. Sci.* 45, 1159–1173. doi: 10.1002/pen.20391

Gaspar-Cunha, A., Covas, J. A., Vergnes, B., and Berzin, F. (2011). "Reactive extrusion - optimization of representative processes," in *Optimization of Polymer Processing*, eds A. Gaspar-Cunha and J. A. Covas (New York, NY: Nova Science Publishers), 115–143.

Gassan, J., and Bledzki, A. K. (2001). Thermal degradation of flax and jute fibers. *J. Appl. Polym. Sci.* 82, 1417–1422. doi: 10.1002/app.1979

Gonzalez-Sanchez, C., and Gonzalez-Quesada, M. (2015). Novel automated method for evaluating the morphological changes of cellulose fibres during extrusion-compounding of plastic-matrix composites. *Comp. Part A* 69, 1–9. doi: 10.1016/j.compositesa.2014.10.026

Hodzic, A., and Shanks, R. (2014). *Natural Fibre Composites, Material, Processes and Properties.* Cambridge: Woodhead Publishing, 408.

Iannace, S., Ali, R., and Nicolai, L. (2001). Effect of processing conditions on dimensions of sisal fibers in thermoplastic biodegradable composites. *J. Appl. Polym. Sci.* 79, 1084–1091. doi: 10.1002/1097-4628(20010207)79:6<1084::AID-APP120>3.0.CO;2-J

Lafleur, P. G., and Vergnes, B. (2014). *Polymer Extrusion*. London: ISTE-Wiley, 337. doi: 10.1002/9781118827123

Le Baillif, M., and Oksman, K. (2009). The effect of processing on fiber dispersion, fiber length, and thermal degradation of bleached sulfite cellulose fiber polypropylene composites. *J. Therm. Comp. Mat.* 22, 115–133. doi: 10.1177/0892705708091608

Le Duc, A., Budtova, T., and Vergnes, B. (2011). Polypropylene/natural fibres composites: analysis of fibre dimensions after compounding and observations of fibre rupture by rheo-optics. *Comp. Part A* 42, 1727–1737. doi: 10.1016/j.compositesa.2011.07.027

Le Moigne, N., van den Oever, M., and Budtova, T. (2011). A statistical analysis of fibre size and shape distribution after compounding in composites reinforced by natural fibres. *Comp. Part A* 42, 1542–1550. doi: 10.1016/j.compositesa.2011.07.012

Manas-Zloczower, I. (2009). *Mixing and Compounding of Polymers – Theory and Practice.* Munich: Hanser, 1158. doi: 10.3139/97834464 33717

Mano, B., Araujo, J. R., Spinace, M. A. S., and De Paoli, M. A. (2010). Polyolefin composites with curaua fibres: effect of the processing conditions on mechanical properties, morphology and fibres dimensions. *Comp. Sci. Tech.* 70, 29–35. doi: 10.1016/j.compscitech.2009.09.002

Mohanty, A. K., and Drzal, L. T. (2005). *Natural Fibres, Biopolymers and Biocomposites*. Boca Raton, FL: CRC Press, 896. doi: 10.1201/9780203508206.ch1

Poulesquen, A., and Vergnes, B. (2003). A study of residence time distribution in co-rotating twin screw extruders. Part I: theoretical modelling. *Polym. Eng. Sci.* 43, 1841–1848. doi: 10.1002/pen.10156

Quijano-Solis, C., Yan, N., and Zhang, S. Y. (2009). Effect of mixing conditions and initial fiber morphology on fiber dimensions after processing. *Comp. Part A* 40, 351–358. doi: 10.1016/j.compositesa.2008.12.014

Tajvidi, M., and Takemura, A. (2010). Thermal degradation of natural fiber-reinforced polypropylene composites. *J. Therm. Comp. Mat.* 23, 281–298. doi: 10.1177/0892705709347063

Vergnes, B., Della Valle, G., and Delamare, L. (1998). A global computer software for polymer flows in corotating twin screw extruders. *Polym. Eng. Sci.* 38, 1781–1792. doi: 10.1002/pen.10348

Conflict of Interest: CD was employed by the company SCC.

The remaining authors declare that the research was conducted in the absence of any commercial or financial relationships that could be construed as a potential conflict of interest.

frontiers in Materials

ORIGINAL RESEARCH
published: 28 July 2020
doi: 10.3389/fmats.2020.00205

Roles of Size, Shape, Amount, and Functionalization of Nanoparticles of Titania in Controlling the Tribo-Performance of UHMWPE Composites

*Meghashree Padhan, Gourab Paul and Jayashree Bijwe**

Centre for Automotive Research and Tribology (Formerly ITMMEC), Indian Institute of Technology Delhi, Hauz Khas, India

The present research is based on development and performance evaluation of ultra-high molecular weight polyethylene composites with Titania particles in various amounts and of two sizes, including nano-size. It also included functionalization of nanoparticles (NPs) with a siloxane group to enhance adhesion with the matrix, which would help to reduce wear. Thus, the work had several objectives such as to investigate the effect of size (nano vs. micro) and determine the amount that delivers the best performance from among a series of composites with different Titania particle amounts [0–8% in the case of microcomposites (MCs) and 0–4% in the case of nanocomposites (NCs)]. It was also of interest to examine the effect of siloxane-functionalization of NPs [since they performed significantly better than microparticles (MPs)] on the performance of NCs. It was observed that for adhesive and erosive wear modes, both types of particles (MPs and NPs) proved detrimental in spite of the enhanced hardness of the composites, essentially because of the irregular shape of particles, which altered the wear mechanisms adversely. Nanoparticles proved less detrimental, while F-NPs (functionalized NPs) proved marginally detrimental. In abrasive wear mode, both proved beneficial, NPs being more effective than MPs, and F-NPs proved the best. The studies revealed how the shape of particles influences the performance of composites in various wear modes.

Keywords: UHMWPE, TiO_2, siloxane treatment, abrasive and adhesive wear, erosion

OPEN ACCESS

Edited by:
Patricia Krawczak, IMT Lille Douai, France

Reviewed by:
Sergey Panin, Institute of Strength Physics and Materials Science (ISPMS SB RAS), Russia
Abdul Samad Mohammed, King Fahd University of Petroleum and Minerals, Saudi Arabia
Z. Peng, University of New South Wales, Australia

***Correspondence:**
Jayashree Bijwe
jbijwe@gmail.com

Specialty section:
This article was submitted to Polymeric and Composite Materials, a section of the journal Frontiers in Materials

Received: *27 March 2020*
Accepted: *04 June 2020*
Published: *28 July 2020*

Citation:
Padhan M, Paul G and Bijwe J (2020) Roles of Size, Shape, Amount, and Functionalization of Nanoparticles of Titania in Controlling the Tribo-Performance of UHMWPE Composites. Front. Mater. 7:205. doi: 10.3389/fmats.2020.00205

INTRODUCTION

Ultra-high molecular weight polyethylene (UHMWPE) and its composites are being widely used for applications like producing bottles for runners, chain guides, and lining for coal chutes and also as bearing material in agricultural and mining equipment due to their excellent wear resistance coupled with their low coefficient of friction (μ), along with ease of availability and cost viability. Moreover, UHMWPE is extensively used in a composite form as a bearing material for implants (joint replacements for the hip, knee, and ankle) (Wang et al., 2007; Ge et al., 2009; Holland et al., 2018; Gao et al., 2019; Ortiz-Hernández et al., 2019). It shows excellent wear resistance (W_R) in almost all wear modes (Lee, 1985) along with ultra-low μ, high specific strength and modulus,

toughness, very good dampening capability, excellent resistance to chemicals, etc. Efforts are being made to maximize its W_R, especially by selecting biocompatible fillers like titania, zirconia, etc., and their use as nanoparticles (NPs). The final performance of nanocomposites (NCs) depends on the type of matrix and NPs, their amount, size, shape, filler-matrix adhesion, etc. A lot has been reported on the exploration of various types and amounts of hard NPs (non-bio-compatible) to enhance the W_R of UHMWPE (Chang et al., 2013; Xu and Tangpong, 2013; Chukov et al., 2014; Sharma et al., 2015, 2016; Kumar et al., 2017).

Xu and Tangpong (2013) presented the current trends of research in the tribology of polyethylene-based NCs along with the type of nano-fillers used and the processing approaches. It was stated that agglomeration takes place in a higher concentration of NPs, resulting in deterioration of wear performance.

Few papers have reported on the surface treatment/functionalization of fillers/fibers to improve the performance with UHMWPE. Chukov et al. (2014) studied the effect of nitric acid treatment of carbon fibers leading to enhanced adhesion with the matrix and hence improved mechanical properties. Tribo-properties, however, were not studied. Chang et al. (2011) reported improvement in mechanical and antibacterial properties of UHMWPE due to reinforcement with silane-treated zinc oxide particles (<1 μm) compared to untreated ones. However, no tribo-studies were reported. Kandeva et al. (2018) reported the effect of multi-walled carbon nano-tubes (CNTs) untreated and modified with electro-less nickel plating. Tribo-studies were done in a thumb disk tribo-setup in abrasive wear mode. Modified CNTs showed higher W_R as compared to the unmodified ones.

A lot of patents are available on the applications of UHMWPE in composite form for the biomedical area (Senatov et al., 2014; Coker, 2019; Gopanna et al., 2019; Salari et al., 2019; Saravanan and Devaraju, 2019; Duan et al., 2020)[1,2]. Several researchers have recommended their composites for such applications. Duan et al. (2020) studied the thermal stability and mechanical properties of irradiation-cross-linked graphene oxide/UHMWPE composites with vitamin E. The crystallinity, thermal stability, hardness and scratch resistance, and oxidation resistance of the composites improved as compared to UHMWPE, but at the cost of a slight deterioration in mechanical properties. The fatigue strength, compressive and tensile properties, and wear resistance of the modified composites were not investigated. These composites were claimed to have bright application prospects in the field of artificial joint replacement owing to some further investigations. Senatov et al. (2020) prepared a novel biomimetic highly porous UHMWPE/Hydroxyapatite (HA) (40 wt.%) scaffold for reconstructive surgery with a porosity of 85 vol.%. This biocompatible highly porous UHMWPE/HA scaffold, used separately or in combination with proteins for the reconstruction of non-load bearing parts of bones, was reported to solve the problems associated with differences between implant architecture and trabecular bone, low osteointegration, and bio-inertness. Saravanan and Devaraju (2019) tribo-investigated an γ-irradiated composite of UHMWPE (80 wt.%), alumina (3 wt.%), HA (5 wt.%), and Chitosan (12 wt.%) and reported a 1.3 times increase in tribo-performance due to irradiation. The composites were targeted at biomedical applications. Salari et al. (2019) studied the effect of nano-zirconia (2, 6, and 10 wt.%) in HP (10 wt.%)-reinforced UHMWPE composites and reported significantly improved mechanical properties and wear resistance in comparison with HAp alone and furthermore eliminated the concern of wear debris and adverse biological responses caused by osteolysis. Zirconia also demonstrated exceptional biological responses in the presence of MG-63 osteoblast cell cultures, showing no cytotoxicity and high alkaline phosphatase activity along with fully spread osteo-cells. Hence, the authors claimed it as a promising material for overcoming the shortcomings of the conventionally used UHMWPE as an implant liner. Gopanna et al. (2019), in their overview of polyethylene and polypropylene composites for biomedical applications, suggested that UHMWPE composites reinforced with NPs, nanotubes, and nanofibers should be used in orthopedic bearing applications. Chemically cross-linked UHMWPE filled with particles of Al, Cu Fe, and reinforced with quartz particles of micron size have been developed for orthopedic applications.

Titanium dioxide (TiO_2)/Titania is a hard filler with excellent resistance to UV and chemicals and is also known for bio-compatibility (Hashimoto et al., 2003; Gutwein and Webster, 2004; Lei et al., 2010; Sabetrasekh et al., 2011; You et al., 2014; Celebi Efe et al., 2019). **Supplementary Appendix A** gives details on various available papers on UHMWPE-TiO_2 composites with special reference to NPs and their functionalization (Hu et al., 2016; Celebi Efe et al., 2017; Yu et al., 2017). It seems that only two papers dealt with NPs, and these did not look into tribo-effects (Ortiz-Hernández et al., 2019; Duan et al., 2020). Some papers (Duan et al., 2020; see footnote 1) reported on the functionalization of microparticles (MPs) but not in detail by reporting tribology. Thus, it was concluded that in-depth studies of UHMWPE-Titania composites (MCs and NCs) are required with the following aims, since they are not met in the literature.

- Assess the potential of NPs vs. MPs to improve the tribo-performance in various wear modes.
- Determine the influence of increasing amounts of NPs (realistic amount) and MPs as a means to find the optimum amount for the best W_R value.
- Determine the effect of functionalization of NPs with siloxane treatment on tribo-performance in various wear modes.

With these aims in view, three series of UHMWPE-Titania composites – the first with MPs (0–8%), the second with NPs (0–4%), and the third with functionalized NPs (0–4%) – were developed and characterized for tribo-performance in three wear modes, viz., adhesive, abrasive, and erosive, and the findings are presented in subsequent sections.

[1]https://ryortho.com/breaking/b-one-total-hip-cleared-by-fda/

[2]https://www.materialsforengineering.co.uk/engineering-materials-news/researchers-create-radiopaque-polyethylene-for-the-visualisation-of-medical-implants/110699/

MATERIALS AND METHODS

Materials and Characterization of Particles

Ultra-high molecular weight polyethylene was procured in a particulate form (≈40 μm) from Bhilwara Polymers Ltd., Rajasthan; details of its properties are given in **Table 1**.

Titania (TiO_2) nano (10–25 nm)- and MPs (30–40 μm) were procured from Nano Shell LLC United States. The size was verified with SEM (scanning electron micrograph; Zeiss EVO MA 10) and TEM (transmission electron micrograph; JEOL JEM-1400 Plus), as shown in **Figures 1a,b**, respectively. It seems that MPs were of highly irregular shape and NPs were of 40–50 nm size and also of irregular shape. **Figure 1-II** shows the SEM and EDAX micrographs of selected specimens (V_{8M}, V_{2M},V_{2N}, and F_{2N}) cut to expose the inside transverse section. This was done to determine whether particles are uniformly distributed in the bulk of the composites. Dot maps of Ti represent the distribution of TiO_2 particles irrespective of size. For F_{2N}, additional dot mapping was done for Si element to ensure the presence of siloxane treatment on the particles.

The XRD-X-ray diffraction spectrum (Phillips XPERT-PRO) of NPs was collected to verify the size, and the data are shown in **Figure 1-III**.

The crystallite size of NPs was determined using the Debye–Scherrer method using the following equation (Holzwarth and Gibson, 2011).

$$t = \frac{0.9\lambda}{B\ \cos\theta} \tag{1}$$

where λ is the characteristic wavelength, B is the full width at half maximum, and θ is the midpoint of the peak. The XRD shows coherent diffraction regions that imply the size of the crystallites for the respective diffraction peak. A particle may be made up of several different crystallites or just one crystallite. Sometimes, it also corresponds to the size of the grain s of an analyte sample, or the thickness of a polycrystalline thin film or bulk material. **Supplementary Appendix A** collects the data from XRD.

Overall, it was confirmed that the approximate crystallite size of the particles was in the range of 23–27 nm as observed from the first three peaks.

Experimental Work

Surface Modification of Nanoparticles

For siloxane treatment of NPs, Amino propyl tri-ethoxy silane (APTES) was used (procured from Alpha Aesar). The basic aim of the surface modification of TiO_2 NPs was to impart siloxane functional groups to the surface of particles, which would bridge with matrix, resulting in enhanced filler-matrix adhesion in the composites. It was anticipated that this might lead to improved tribological properties (less wear). Surface modification of TiO_2 with APTES was done as per a reported process as shown in **Figure 2** (Chukov et al., 2014) using reflux reaction and mechanical stirring, with xylene as a medium and at 50°C in a silicon oil bath for varying durations, as shown by **Table 2**.

The particles were washed using xylene, followed by ethanol two times, and finally with acetone. They were then filtered using a REMI PR-24 centrifuge followed by drying under vacuum. Fourier Transform Infrared (FTIR) Spectroscopy was done in attenuated transmission reflectance (ATR) mode in a Nicolet IS 50 for confirmation of the presence of siloxane treatment on the particles as well as for optimization of the time duration of the treatment. The analysis was performed for an iteration of 32 scans for accuracy of results (**Table 2**).

TABLE 1 | Properties of UHMWPE as per the supplier's data.

Property	Value
Density (g/cm^3)	0.93
Tensile strength at yield (MPa)	21
Tensile strength at break (MPa)	48
Hardness, Shore D	62–66
Crystalline melting range, powder, °C	138–142

Development of UHMWPE Composites

Uniform dispersion of micro- and nano-TiO_2 particles is extremely important. De-agglomeration of NPs was performed using a Crome Tech Probe Sonicator (UP-800 ultrasonic processor). An accurately weighed amount of NPs was added to double-distilled water in installments, followed by sonication for two minutes (pulse time 2 s, and pulse off for 5 s, at 800 W) after each installment, the total time of sonication being 30 min. A weighed amount of UHMWPE was then added to this suspension in installments followed by sonication to achieve homogeneous dispersion of NPs and UHMWPE in double-distilled water. A similar procedure was employed in the case of microcomposites (MCs) to maintain uniformity.

Nano- and microcomposites of UHMWPE with TiO_2 were developed by using a compression molding technique under temperature (180°C) and pressure (12–15 bar). The mold was fast cooled using water cooling. The compositions of the composites developed are shown in **Table 3**.

Characterization of Composites

Density

The density of the composites was measured to characterize them, since density is the first basic property. It also helped to gain an overall view of the void content in the composites and also to calculate the specific wear rate.

(a) Density was measured by the standard Archimedes principle following ASTM D792 using a Mettler Toledo weighing balance as per Eq (2). Acetone was used as the liquid, having a density of 0.79 g/cm^3 at 20°C.

$$\rho = \left(\rho_{\text{liquid}} \times W_{\text{air}}\right) / \left(W_{\text{air}} - W_{\text{liquid}}\right) \tag{2}$$

where ρ is the density of the composite, ρ_{liquid} is the density of the liquid used, and W_{air} and W_{liquid} are the weights of the composite in air and liquid.

The rule of mixtures was used to calculate the theoretical density of the composites using the following equation:

$$\rho_t = 1/\left(W_f/\rho_f + W_m/\rho_m\right) \tag{3}$$

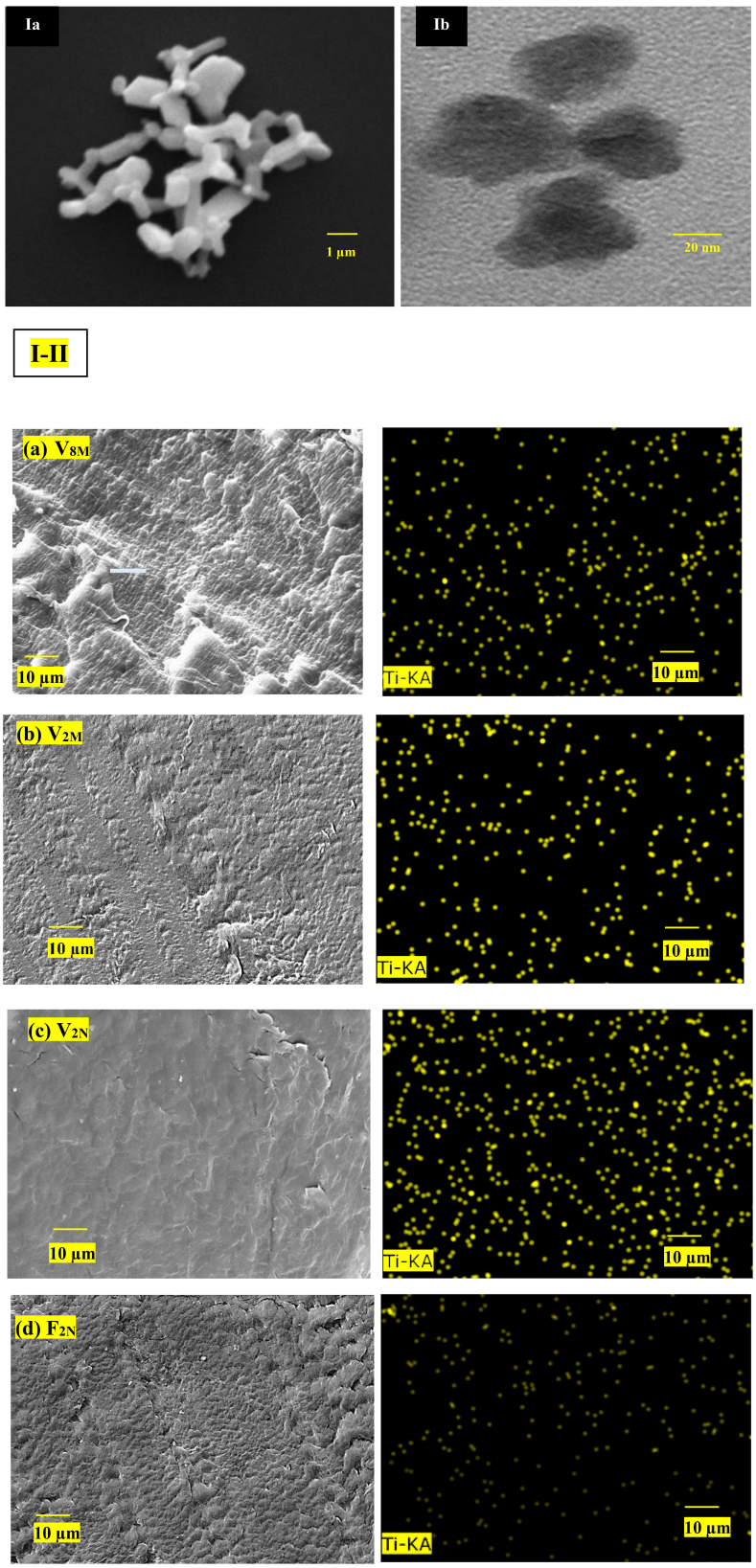

FIGURE 1 | Continued

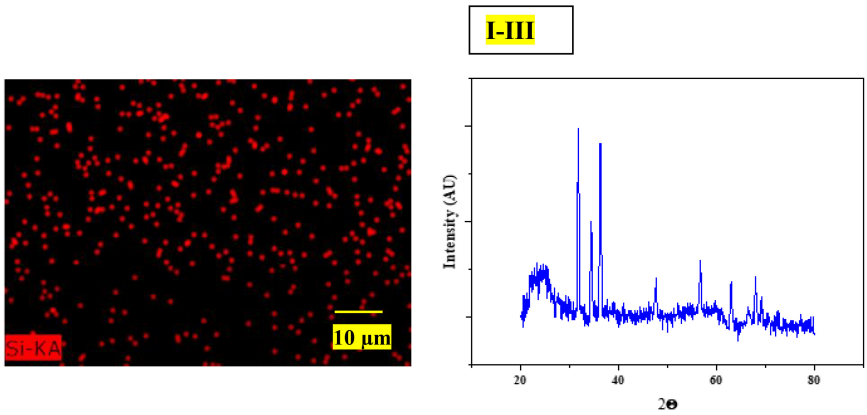

FIGURE 1 | Micrographs of TiO_2 particles; **(1a)** SEM of microparticles and **(1b)** TEM of nanoparticles; 1-II – SEM and EDAX micrographs of representative composites showing uniform distribution of filler particles; 1-III – X-ray diffraction pattern for nano-TiO_2 particles.

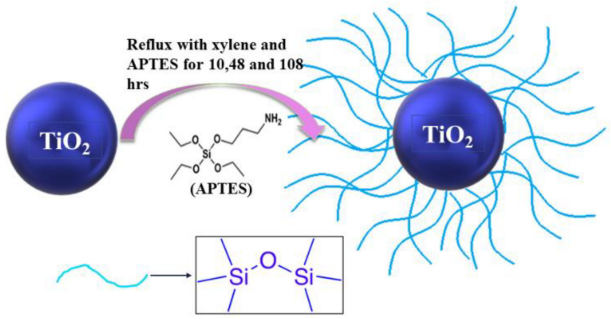

FIGURE 2 | Schematic of treatment of TiO_2 NPs with APTES.

TABLE 2 | Treatment of NPs of TiO_2 (1.5 g) with APTES (1.5 ml) in xylene as a medium (50 ml) at 50°C for various durations and the chemical changes confirmed from FTIR studies.

Treatment	Heating time (h)	Observation
Scheme 1	10	No change
Scheme 2	48	Low-intensity peak of –Si–O–; –O–Ti–O- peak
Scheme 3	108	Sharp and intense –Si–O– peak; –Ti–O–Si– peak

where ρ_m and ρ_f are the theoretical density of the matrix (UHMWPE; 0.93 g/cc) and the filler (Ti; 3.9 g/cc), respectively. W_m and W_f are the respective weight fractions.

(b) Void content.

The void content of the composites was calculated from the following equation:

$$Void\ content\ (\%) = \frac{\rho_{th} - \rho_c}{\rho_{th}} \times 100 \quad (4)$$

where ρ_{th} and ρ_c are the calculated and theoretical densities of the composite as obtained using Eqs 2 and 3.

Vickers Micro-Hardness

TiO_2, being a ceramic material, has an entirely different set of properties, especially hardness, as compared to the softer polymeric phase. It was necessary to examine the extent of its implications for the hardness properties of UHMWPE since hardness is generally well-correlated with abrasive wear performance. The Vickers hardness of the composites was measured as per ASTM E92-82. The composites were polished against 1000 grade *SiC* abrasive paper. A square-based pyramidal diamond indenter with included face angles of 136° was penetrated into the material with a force of 20 N. The Vickers hardness number (HV) is related to the applied force and surface area of the resultant permanent impression according to the following equation:

$$HV = 1.8544 \times \frac{F}{d^2} \quad (5)$$

where F is the force applied and d is the mean diagonal diameter of the impression.

Scanning Electron Microscopy and Energy Dispersive X-ray Spectroscopy

Microscopic worn surface analysis, generally performed with SEM, furnishes a lot of information about the surface topography, damage, and deterioration level of matrix and filler-matrix adhesion, dominating wear mechanisms, etc. An SEM (Zeiss, EVO-MA 10) was used to study the worn surfaces of the composites. The samples were gold-coated to make them conducting using a Cressington Sputter Coater 108.

Wettability Analysis

The wettability of matrix and its composites differ based on the type and amount of filler and also filler-matrix bonding. Generally, this property is evaluated by water drop (the sessile drop method), and reduction in the contact angle is an indication of a higher ceramic content and higher filler-matrix adhesion. The contact angle on the surface of selected composites (V, V_{2N}, and F_{2N}) was measured using a KRUSS GmbH DSA

TABLE 3 | Composition and coding of composites.

(A) Micro-Series with untreated Titania microparticles						
Micro-Series	**TiO_2 (wt.%) Untreated**	**0**	**2**	**4**	**6**	**8**
Codes		**V_0**	**V_{2M}**	**V_{4M}**	**V_{6M}**	**V_{8M}**
Theoretical density (g/cc)		0.930	0.985	1.0416	1.09	1.153
Practical density (g/cc)		0.930	0.952	0.967	0.972	0.996
Void content (%)		0	3.3	7	10	13.61
Vickers Hardness (MPa)		6.621	6.968	7.05	7.15	7.26
(B) Nano-Series with untreated Titania nanoparticles						
Nano-Series	**TiO_2 (wt.%) Untreated**	**0**	**1**	**2**	**3**	**4**
Codes		**V_0**	**V_{1N}**	**V_{2N}**	**V_{3N}**	**V_{4N}**
Theoretical density (g/cc)		0.930	0.965	0.98	1.01	1.04
Practical density (g/cc)		0.930	0.963	0.967	0.971	0.975
Void content (%)		0	0.2	1.32	3.8	6.25
Vickers Hardness (MPa)		6.621	7.56	8.14	9.42	9.876
(C) Nano-Series with treated Titania nanoparticles						
Nano-Series with treated particles	**TiO_2 (wt.%) Treated**	**0**	**1**	**2**	**3**	**4**
Codes		**V_0**	**F_{1N}**	**F_{2N}**	**F_{3N}**	**F_{4N}**
Theoretical density (g/cc)		0.93	0.963	0.967	0.971	0.975
Practical density (g/cc)		0.93	0.964	0.969	0.974	0.979
Void content (%)		0	0	0	0	0
Vickers Hardness (MPa)		6.621	7.85	8.21	9.45	9.88

25S. The surfaces were cleaned by sonication in acetone prior to the experiment. A 2-μl drop of deionized water was placed on the surface. The contact angles at different positions were averaged out.

Roughness Measurement

The surface roughness of composites is a tool with which to quantify the texture/topography of the worn surfaces and is correlated with the extent of wear-damage. The surface roughness of the wear track was measured using a Micro-Xam 100 stylus-type profiler manufactured by KLA-Tencor. The roughness data are the average of three points across various areas on the wear track.

Tribological Characterization

Tribological studies were performed to evaluate the performance of the developed composites in various wear modes, viz., adhesive (sliding against a smooth counterface), abrasive (sliding against a rougher and harder counterface), and erosive (impingement of harder abrasive particles at different angles) wear modes.

Adhesive wear

The adhesive wear performance of the composites was evaluated on a UMT-3MT Tribometer supplied by CETR/Bruker, United States. During initial studies on a pin (polymeric) on metallic disk configuration, hardly any loss in weight of the pin was observed, even after running the test for 4 h, because of the exceptionally high wear resistance of UHMWPE. Hence, a ball (AISI 52100 steel – R_a – ≈50 nm) on disk (polymer) configuration was selected to increase the pressure and also the dissipativity of frictional heat, since point contact has these advantages. A 10-mm ball rotated on a polymeric disk in a wear track, as shown in **Figure 3A**. The tests were conducted under 200 N (P 73 MPa), keeping other parameters such as v (0.15 m/s), rpm (100), sliding distance (4220 m), and duration (4 h) constant.

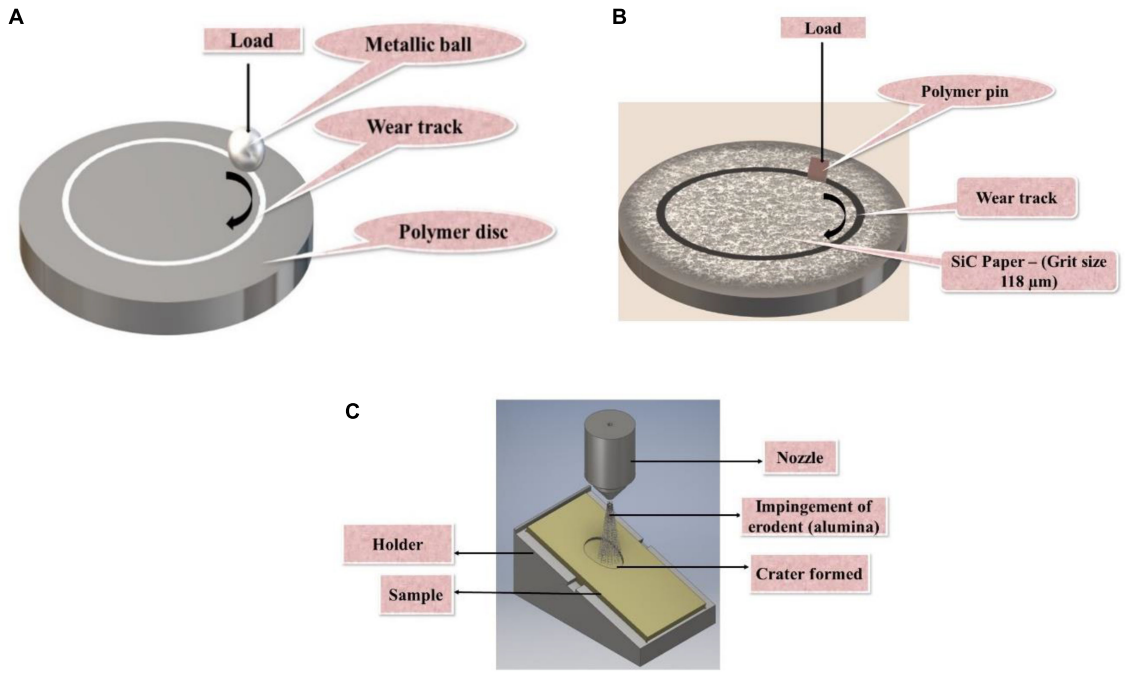

FIGURE 3 | Configurations in **(A)** adhesive wear, **(B)** abrasive wear, and **(C)** erosive wear.

The specific wear of the disk (K_0) (m^3/Nm) was calculated as follows.

$$K_0 = \frac{\Delta W}{\rho \times L \times D} \left(\mathrm{m}^3/\mathrm{Nm}\right) \quad (6)$$

where ΔW – weight loss in kg; ρ – density in kg/cm^3, L – load in N; D – sliding distance completed in 4 h in meters.

The maximum Hertzian Pressure (P) was calculated as

$$P = \frac{F}{\pi a^2} \quad (7)$$

where F is the applied load (N) and a is the radius of the contact area (mm), calculated as

$$a = \left(\frac{3Fr}{4E^*}\right)^{1/3} \quad (8)$$

where r is the radius of the steel ball and E^* is the calculated modulus at contact.

Abrasive wear

Abrasive wear studies were conducted in the UMT-3MT Tribometer supplied by CETR/Brucker, United States in a pin on disk (POD) configuration (**Figure 3B**). Silicon carbide (*SiC*) abrasive paper of 1000 grade was used to achieve a uniform contact, while for testing purposes, 120 grade (118 μm grit size) was used for a single pass rotary motion. A 10-mm × 10-mm × 4-mm polymer pin was abraded at a constant speed of 0.025 m/s. The sliding distance of 1 m was achieved by changing four papers and was kept constant. In each experiment, all parameters except load were kept constant. Load was selected as a variable parameter and was varied between 25, 50, 75, and 100 N. After completion of the experiment, the pin was cleaned ultrasonically in acetone, dried, and weighed. The specific wear rate was calculated from the recorded weight loss using Eq. 6.

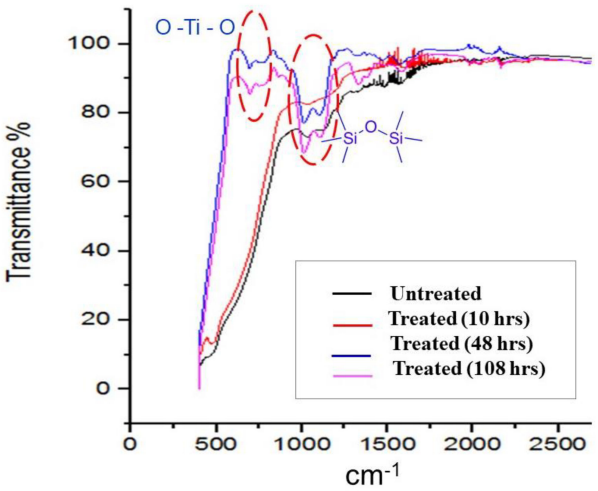

FIGURE 4 | FTIR analysis of siloxane-treated particles for varying treatment durations.

Erosive wear

The erosive wear tests on the UHMWPE composites were carried out on a TR-471-400 air jet erosion tester (Ducom Instruments Ltd., Bangalore). Ultra-high molecular weight polyethylene,

being a ductile material, shows high erosion at lower angles (Hutchings, 1992), and hence 15° and 30° were the two angles chosen for the studies. Alumina particles 60 μm in size were selected as the erodent, and the discharge rate was kept at 4 g/min and the velocity at 58 m/s using a 3-mm diameter Tungsten Carbide nozzle (**Figure 3C**). The tests were performed at 25°C, and the total mass of erodent was 240 g. Amount of wear was quantified by erosion (E), which was calculated by Eq. 9 (Chahar and Pun, 2018).

$$E = \frac{\text{Weight loss}}{\text{Mass of Erodent}}\ \text{g/g} \tag{9}$$

RESULTS AND DISCUSSION

Characterization Studies

FTIR Studies

The FTIR spectra for TiO_2 particles (treated and untreated) are shown in **Figure 4**.

The broad band observed in the region 600–400 cm^{-1} corresponded to the –Ti–O–Ti– stretching vibration peak (Ukaji et al., 2007; Mallakpour and Nikkhoo, 2013). In-plane O–H bending vibration corresponds to peaks at 1399 and 1630 cm^{-1} on the surface of TiO_2. The band at 1088 cm^{-1} attributed to the bending vibration of Ti–OH is shifted to a lower wavenumber (at 993 cm^{-1}) due to the creation of Ti–O–Si in the spectrum of APTES-TiO_2. The formation of the Ti–O–Si group was confirmed from the FTIR spectrum. Such linkage enables better interaction with the polymeric matrix as compared to the non-functionalized particles. It is expected that the enhanced filler-matrix adhesion would lead to less debonding of particles when stressed during sliding and hence less wear.

Density

The densities of the composites are given in **Table 3**. The density of the composite increased with an increase in TiO_2% since it is heavier (4.23 g/cc) than UHMWPE (0.93 g/cc). When comparing the densities of V_{2M} (0.952 g/cc), V_{2N} (0.967 g/cc), and F_{2N} (0.969 g/cc), which contained 2 wt.% Titania particles, it was observed that density was highest where functionalized NPs were used and lowest where untreated MPs were used.

Vickers Hardness

It can be observed from **Table 3** that:

- TiO_2, being a harder filler, increased the micro-hardness of the softer polymeric matrix.
- The hardness of composites increased significantly with increasing content of TiO_2 for MCs and NCs with functionalized particles (F-NCs), indicating good homogeneity of the filler dispersed in the composites. Improvement was highest for F-NCs, ≈60%.
- If the hardnesses of MCs, NCs, and F-NCs with the same amount of particles is compared, they showed the trend V_{2M} (6.967) < V_{2N} (8.14) < F_{2N} (8.20).

Void Contents

The void contents of the composites showed the following trends.

F-NCs

- Showed no void contents, indicating ideal composites.
- With increasing contents of MPs and NPs, void contents increased, though not proportionally.
- Void content was highest for MCs followed by NCs, and it was lowest for F-NCs, as follows: V_{2M} (3.3%) > V_{2N} (1.32%) > F_{2N} (0%)

Wettability Analysis of the Surfaces of Composites

Titania particles, being ceramic, have higher surface energy (72 dynes/cm) than the polymers, UHMWPE (30 dynes/cm) in this case (Travis Curtis, 2013; www.tstar.com, 2020). Hence, it was expected that the inclusion of NPs of Titania in UHMWPE would increase the surface energy of a composite. Their functionalization should do this to a still greater extent. Hence, surface energy or hydrophilicity was evaluated indirectly by wettability studies using a water drop. The UHMWPE showed an angle of around 91°, while those for V_{2N} and F_{2N} were 85° and 82°, respectively, indicating increased hydrophilicity.

Tribo-Properties of Composites

Adhesive Wear

Adhesive wear tests were conducted initially for 100 N, which resulted in non-measurable wear. Results on adhesive wear at 200 N (73 MPa) are shown in **Figure 5**. At 300 N, the composites failed at varying sliding durations, mostly due to melting of polymer.

Figure 5A1 shows the effect of inclusion of MPs, NPs, and F-NPs (all 2%) on adhesive wear of UHMWPE. V_0 (virgin UHMWPE) showed the lowest wear rate ($5 \times 10^{-15} m^3/Nm$). Inclusion of Titania particles (irrespective of size and functionalization) led to an increase in friction (**Figure 5A2**) and wear rate in spite of an increase in the hardness of all of the composites. This was mainly because of the irregular shape of both types of Titania paticles (MPs and NPs). Inclusion of particles of solid lubricants such as PTFE and graphite facilitates beneficial film transfer on the counterface, leading to a reduction in metal asperity-contacts and hence reducing friction and wear. Titania particles do not have a layered lattice structure, and hence, beneficial film formation was not expected. An increase in hardness does not ensure an increase in performance in adhesive wear. If the hard particles are spherical, they may act as load-bearing elements and convert area contact to more of a point contact, thereby reducing the probability of metallic asperities penetrating in the polymer composite. This may lead to performance improvement. In the present case, however, irregularly shaped particles with sharp edges posed the severe problem of third-body abrasion. These particles, especially MPs, were debonded easily during initial sliding because of their weaker bonding with the matrix. Once they appear in the debris, they start abrading both the parent surfaces, and adhesive wear is changed to three-body abrasive wear, showing higher friction and wear. MPs were so dominant in third-body

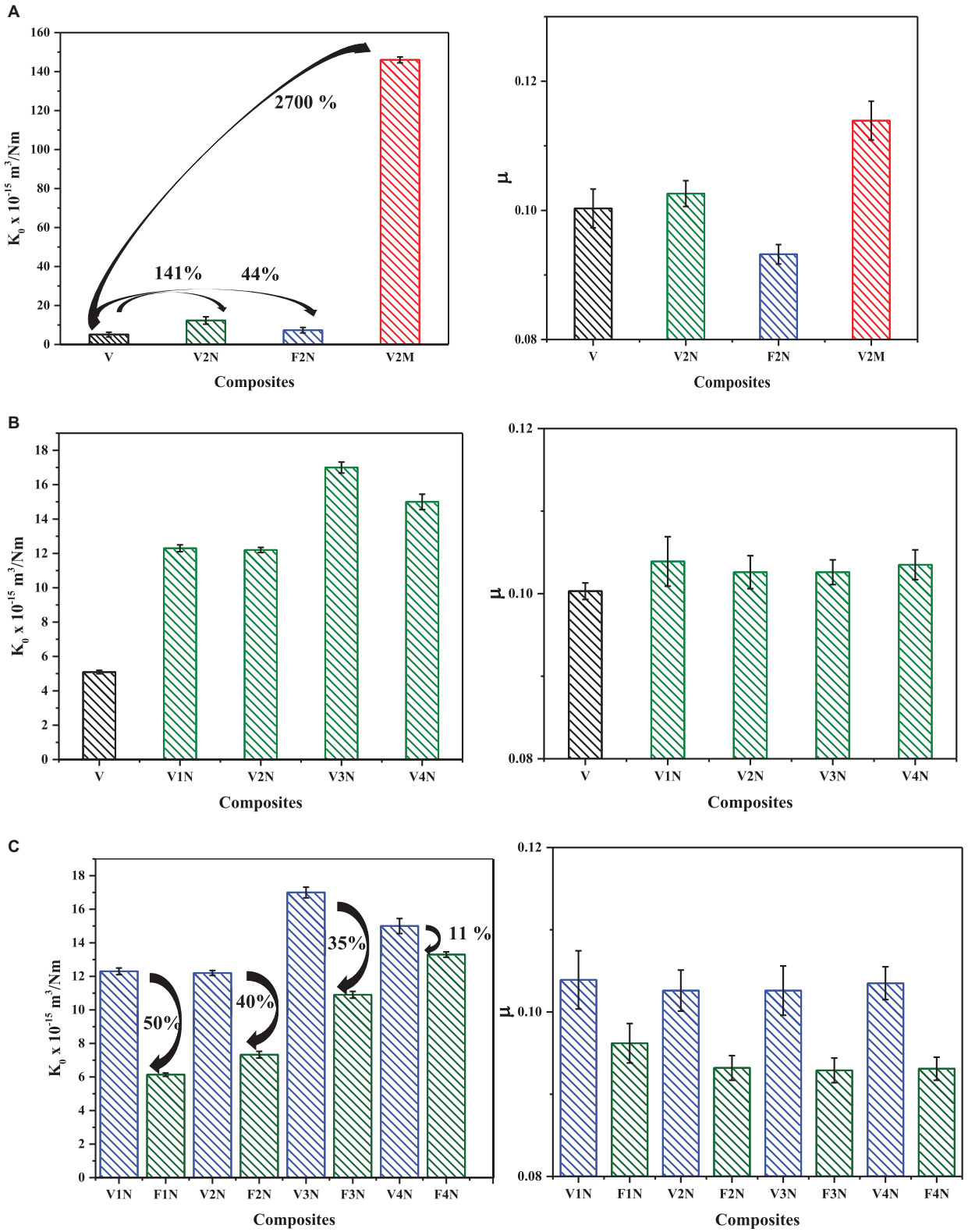

FIGURE 5 | Specific wear rate (K_0) **(a_1,b_1,c_1)** and μ **(a_2,b_2,c_2)** of composite disks against a ball (P – 73 MPa, speed – 0.014 m/s, sliding duration – 4 h). **(A)** Comparison of MC, NC, and F-NC (all with 2% particles) with UHMWPE; **(B)** Influence of increasing amount of NPs, and **(C)** benefits of functionalization of NPs.

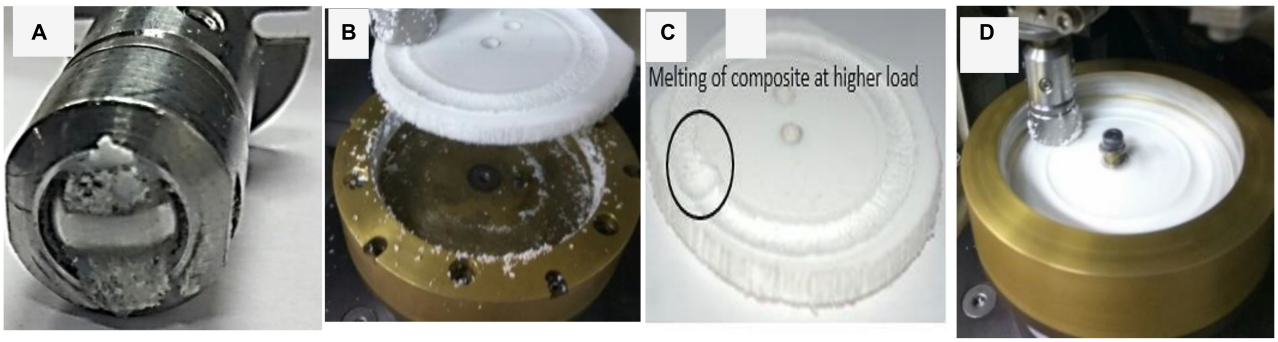

FIGURE 6 | Failed ball **(A)** against disks of a microcomposite **(B,C)** at 300 N and **(D)** disk of UHMWPE at 300 N.

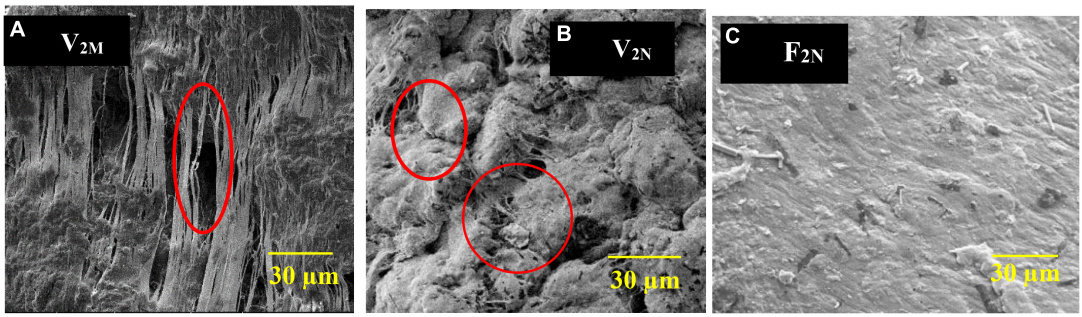

FIGURE 7 | Worn surfaces of composites disks **(A)** V_{2M}, **(B)** V_{2N}, and **(C)** F_{2N} tested at 200 N, 0.15 m/s.

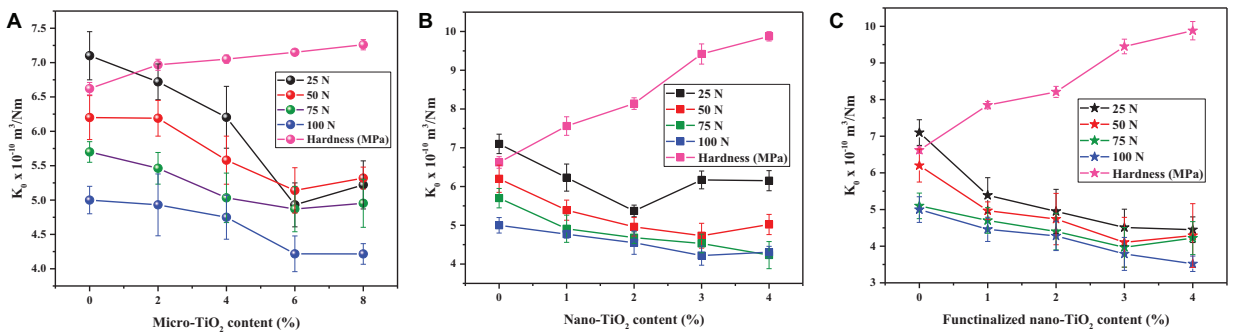

FIGURE 8 | Effect of contents of Titania particles on the abrasive wear of UHMWPE as a function of load for **(A)** microcomposites (MCs), **(B)** nanocomposites (NCs), and **(C)** functionalized nanocomposites (F-NCs).

abrasion that during interaction with the steel ball surface, μ was quite high, which led to an excessive increase in frictional torque and hence heat. The polymer disk, having low thermal conductivity (TC), could not dissipate this heat so efficiently, leading to the removal of softened matrix and debonded MPs, easily accounting for the very high wear of this MC (2700% higher than UHMWPE).

In the case of NPs and F-NPs, wear rates increased by 141 and 44% for V_{2N} and F_{2N}, respectively. The influence of NPs in composites on performance depends on their type (abrasive or solid lubricant), amount, size, shape, etc. Harder particles, if spherical or cylindrical, can act as ball/roller bearings, reducing friction and wear in adhesive wear mode, although not much is reported on the influence of the shape of NPs on the adhesive wear of composites (Jia et al., 2006; Shi et al., 2007). In the current case, harder particles were of irregular shape and hence deteriorated the tribo-performance of UHMWPE. For NPs, the digging out process was not so dominant since they had more interaction with the matrix because of their nano size. Hence, debris contained a smaller number of NPs, and third-body abrasion was not so prominent and detrimental. In the case of functionalized NPs, the process of digging out of particles was still more reduced because of stronger filler-matrix adhesion, and the extent of deterioration to the performance also decreased.

TABLE 4 | Average roughness of worn composite disks.

Composites	R_a(μm)	Composites	R_a(μm)	Composites	R_a(μm)
V	1.45	1.45	1.45	1.45	1.45
V_{1M}	1.75	V_{1N}	1.54	F_{1N}	1.53
V_{2M}	1.74	V_{2N}	1.76	F_{2N}	1.45
V_{3M}	1.89	V_{3N}	1.77	F_{3N}	1.57
V_{4M}	2.2	V_{4N}	1.84	F_{4N}	1.79

As seen in **Figure 5B1**, an effect whereby an increasing amount of NPs leads to increased friction and wear can be seen, although it is not strictly linear. **Figures 5C1,5C2** show how treatment of particles improved the performance of NCs.

Failed Surfaces and SEM Studies

Table 4 shows the average roughness (R_a) of the wear tracks of composites worn at 200 N. With increasing contents of particles, disk surface roughness increased in almost all composites, which is indirect evidence of third-body abrasion of the disk because of more particles being released in the debris. Interestingly, if R_a values are compared row-wise, they were highest for MPs followed by NPs and lowest for F-NPs, in general, indicating that the severity of third-body abrasion was at a maximum in the case of MPs and at a minimum for F-NPs.

Figures 6A,D show photographs of failed ball and disk surfaces of MC when slid under 300 N. The failure was characterized by excessive wear of the disk and adherence of the softened wear debris to the ball surfaces. It also shows localized melting of the wear track at a particular location (**Figure 6C**). An UHMWPE disk (**Figure 6D**) with excessive wear can also be seen.

SEM of Worn Surfaces of Disks

Although the experiments could run for 4 h, the surfaces show some marks of melting (**Figure 7A**) in the case of MC since frictional heat was very high. The shearing forces on the high-temperature surfaces elongated/fibrillated the UHMWPE. In the case of NC (**Figure 7B**), such marks are negligible (marked), and surface is very rough. In the case of F-NC (**Figure 7C**), fibrillation marks are not evident since the melting phenomenon was milder due to lower frictional heat. However, the entire surface of composite disc shows evidence of softening and then solidifying after the test.

Abrasive Wear

Incorporation of particles proved beneficial for UHMWPE in the case of abrasion resistance, as seen in **Figure 8** for MCs, NCs, and F-NCs (K_0 as a function of contents of Titania particles) and **Figure 9** in comparisons of MCs vs. NCs and NCs vs. F-NCs (K_0 as a function of load). It was observed that:

- K_0 was in the range of 3–7 × 10^{-10} m^3/Nm for the composites.
- With increase in load, K_0 decreased, which is in line with Lhymn's equation (Lhymn, 1987),

$$K_0 = K\frac{v_s}{EH\varepsilon\mu}V_c\frac{1}{F_N^{\delta}} \quad (10)$$

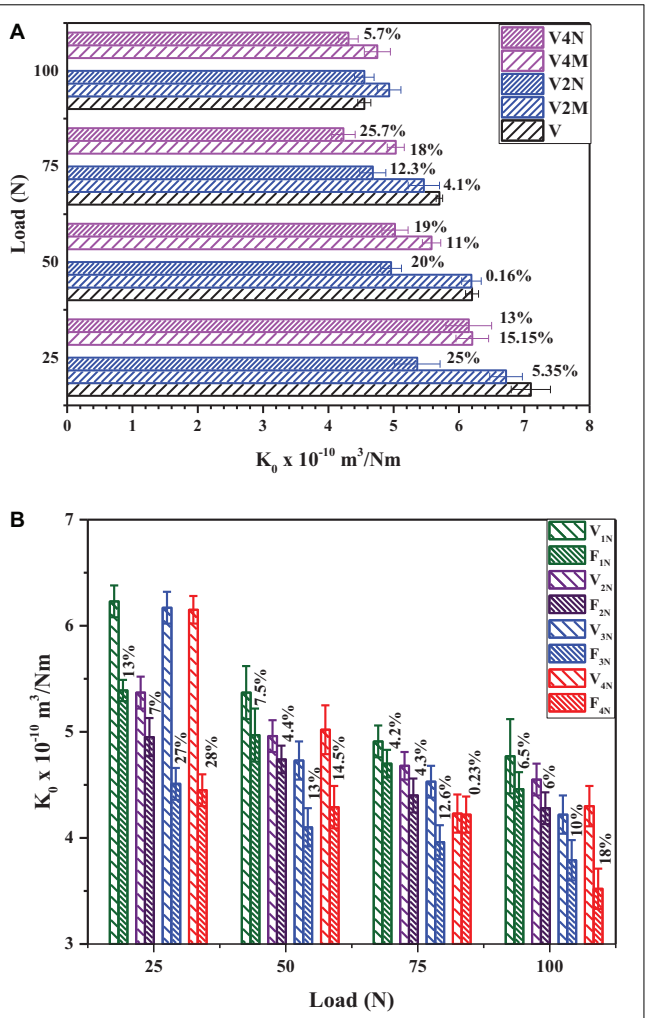

FIGURE 9 | Comparative abrasive wear performance at various loads for **(A)** nanocomposites (NCs) and microcomposites (MCs) (% indicates the% improvement in wear resistance as compared to neat UHMWPE) and **(B)** NCs and functionalized nanocomposites (F-NCs) (% indicates the% improvement in wear resistance as compared to non-functionalized NCs).

where K_0 is the specific wear rate, V_s is the sliding speed, E is the elastic modulus, H is the hardness, ε is the critical wear strain, μ is the friction coefficient, V_c is the crack growth velocity, and F_N is the normal load. At lower loads, variation was higher. It also shows that wear is inversely propotional to hardness.

- With increase in the amount of MCs (0–8 wt.%), K_0 was lowest for 6% followed by a slight rise for 8% (**Figure 8A**). The highest reduction (29%) in K_0 was for V_{6M} at 25 N.
- For NCs, the optimum contents for the lowest K_0 were in the range of 3%, barring 25 N, where it was 2% (**Figure 8B**), and the highest reduction in K_0 was for 2% (22%) at 25N.
- For F-NCs, the optimum contents for the lowest K_0 were in the range of 3%, barring 25 N, where it was 2% (**Figure 8C**), and the highest reduction in K_0 was for 2% (33%) at 25N.

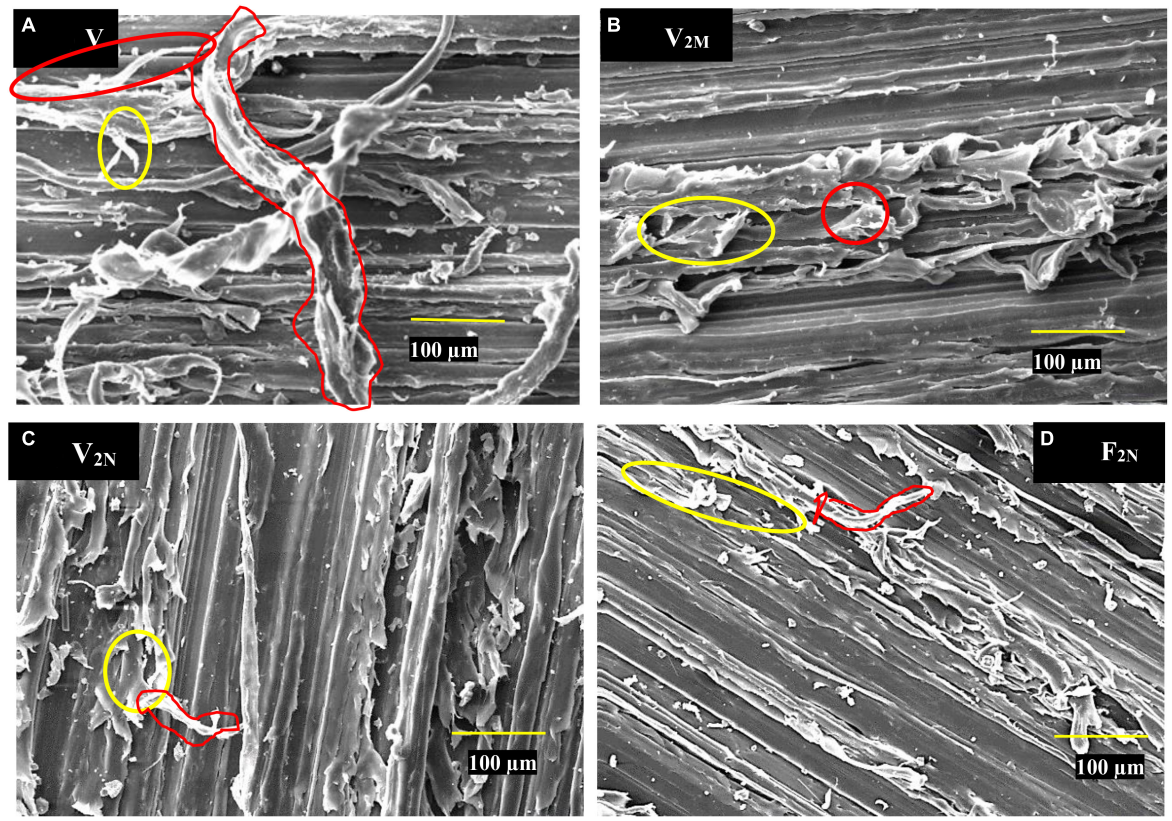

FIGURE 10 | Worn surfaces of composite pins abraded by *SiC* paper at 75 N, 25 mm/s for **(A)** V_0, **(B)** V_{2M}, **(C)** V_{2N}, and **(D)** F_{2N} (secondary micro-cutting indicated by yellow ellipses).

- In general, NCs exhibited superior performance to MCs (**Figure 9A**).

The reasons for wear resistance enhancement are explained in the section below on worn surface analysis.

Worn Surface Analysis by SEM

SEM micrographs of composite pins abraded by *SiC* paper at 75 N are shown in **Figures 10A–D**. The hardness of composites was in the order UHMWPE (6.621 MPa) < V_{2M} (6.968 MPa) < V_{2N} (8.14 MPa) < F_{2N} (8.21 MPa), and wear rate also followed the same order. In abrasive wear, micro-cutting and microplowing are the two major wear mechanisms. Micro-cutting, which is indicated by ribbon-shaped elongated debris and further fibrillation (secondary micro-cutting) due to abrasion by successive grits, and microplowing are the most prominent mechanisms in abrasion for ductile polymers like UHMWPE and PTFE (Hutchings, 1992). Indeed, microplowing occurs in both ductile and brittle polymers. It has a direct correlation with hardness: harder polymers are more resistant to microplowing. In the case of composites with hard fillers like Titania, an additional mechanism of digging out of particles during microplowing also plays an important role. Ease of digging out depends on the size and shape of particles and their bonding with the polymer. Rounded particles can be easily dug out while being abraded by the *SiC* grits, while irregularly shaped particles resist to a greater extent. After being dug out, the particles appear in wear debris. These then start damaging the *SiC* grits and their abrasivity. The higher the hardness, the higher is the damaging power, and the higher is the protection to the polymer composite from the grits during further abrasion.

As seen in Micrograph 10a, excessive micro-cutting and secondary micro-cutting were reponsible for the highest wear of UHMWPE. The depth of grooves due to microplowing is also highest, since UHMWPE has the lowest hardness. Moving from UHMWPE to V_{2M}, hardness increased, and both microplowing and micro-cutting were abruptly reduced. Drastically decreased ductility of the composite can be seen from the edges of ribbons (marked). The depth of grooves is also reduced, indicating reduced extents of both phenomena, supporting the lower wear of this MC.

For NC (**Figure 10C**) and then F-NC (**Figure 10D**), increased ductility (due to their being NCs) can be observed along with secondary micro-cutting. The microplowing is drastically reduced, especially for F-NC, where it is reduced to the extent that the surface topography appears to be quite smooth. This supports the lowest wear occurring in this composite.

Supplementary Appendix A elaborates on the difference in adhesive and abrasive wear and the reasons behind it.

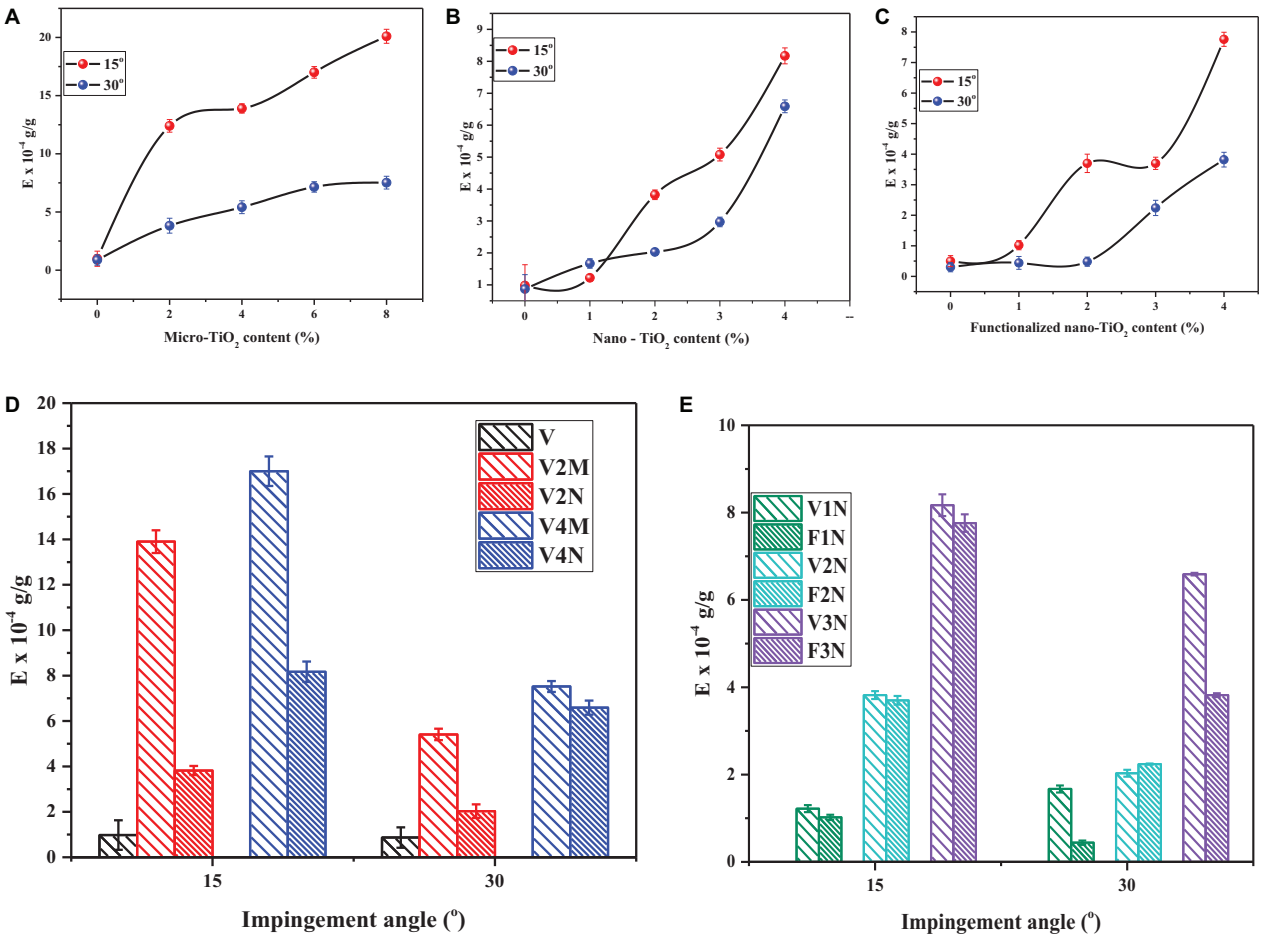

FIGURE 11 | Erosion as a function of amount of particles for two angles; **(A)** microcomposites (MCs), **(B)** nanocomposites (NCs), and **(C)** functionalized nanocomposites (F-NCs); comparative erosion performance for **(D)** MCs and NCs, and **(E)** NCs and F-NCs.

Erosive Wear

Erosive wear is a complex wear mode, and in case of particulate composites, wear resistance is always deteriorated, mainly due to the ease with which particles are detached and thrown off. The literature reports that in spite of increasing hardness, wear performance always decreases (Suh, 1986). An enhancement of performance has only been reported for Aramid and Zylon fabric reinforced composites (Sharma et al., 2019). **Figure 11** shows the erosion performance of composites eroded at two angles. In all cases, erosion of composites was higher at 15°, indicating super-ductile failure (Hutchings, 1992).

It was observed that the virgin UHMWPE was the best performer. Inclusion of Titania particles deteriorated the performance significantly in spite of an increase in hardness. The extent of deterioration increased with increase in Titania particle content, being at a maximum for MPs and a minimum for F-NPs. Erosion definitely depends on the hardness of the analyte material. In the case of composite, which is a heterogeneous material, however, hardness does not help. It depends on the ease with which particles are dislodged from the matrix during bombardment. NPs definitely lead to more homogeneity of the composite and have many-times superior particle–matrix adhesion because of the increased surface activity of NPs. It is not so easy to dislodge NPs, and hence wear of NCs was significantly less severe than that of MCs. Interestingly NC with 1% Titania showed quite similar behavior to UHMWPE. For functionalized NCs, adhesion was still stronger, and hence erosion performance was the best among all of the particulate composites. **Figures 11D,E** demonstrates this comparative behavior more clearly.

CONCLUSION

In this study, composites of UHMWPE and Titania were developed with three objectives, viz, to investigate the size effect (nano vs. micro), the amount effect, and the particle-functionalization effect.

It was worth pointing out that the testing conditions in this work were not in tune with testing for biomedical applications, although UHMWPE composites are being researched for the same. There is scope to extend this work in that direction. This

work is instead an indication of how abrasive wear resistance of UHMWPE can be increased by incorporating functionalized Titania NPs of irregular shape. The same theme may possibly work to enhance adhesive wear resistance if spherical NPs with functionalization could be used.

Based on the investigations on the three series of composites, the following conclusions are drawn.

- Functionalization of NPs led to increased adhesion with the matrix, as evident from the increased density (compactness) and lowering of contact angle (increased hydrophilicity).
- Inclusion of particles increased the hardness of composites. The higher the amount, the higher was the hardness. For composites with the same amount of particles (2%), functionalized nanocomposite (F-NC) showed the highest hardness, followed by NC, and then MC.
- Based on the abrasive wear studies, the optimum% of MPs for the highest improvement (20%) in wear resistance was 6%, while for nano-series, it was 3% for attaining a 28% improvement. Functionalized NPs proved most effective, and a 35% improvement in wear resistance was observed for 3 wt% of F-NPs. Increase in hardness was found to be the major reason for this, as it was responsible for reducing the severity of dominating wear mechanisms viz micro-cutting and microplowing significantly, as confirmed from the SEM studies.
- In the case of adhesive and erosive wear modes, however, the inclusion of particles led to a deterioration in performance, which depended on the size, amount, and functionalization of NPs. It was concluded that the increase in hardness did not help to increase the wear performance in these two wear modes. The irregular shape of MPs and NPs was the main controlling parameter. Including 2% MPs deteriorated the performance of UHMWPE excessively (2400%) in adhesive wear mode, while NPs reduced it by 140%. F-NCs were least detrimental (40% deterioration). Third-body abrasion appeared to be the dominating wear mechanism due to released particles from the composites accumulating as wear debris in adhesive wear mode. An increase in the roughness of worn surfaces supported this phenomenon.
- In the case of erosive wear, UHMWPE again proved best, followed by F-NCs and then NCs. MCs proved worst, and the higher the amount of particles, the more severe was the deterioration. It was concluded that the ease with which particles are dislodged from the composites during bombardment was the key factor controlling the erosion of composites. F-NCs proved best in this respect since particle–matrix bonding was the best. The composites showed failure in super-ductile mode by exhibiting the highest erosion at 15°.

The most important conclusions regarding the selection of particles to improve the hardness and wear resistance of UHMWPE are as follows.

The type, size, amount, shape, and filler–matrix adhesion are the most important aspects. Nano-sized particles worked best, and a content of around 3% proved optimum. Siloxane treatment proved very effective in improving all performance properties. However, the shape of particles controlled adhesive wear performance in an adverse way. For abrasive wear mode, it was appropriate.

DATA AVAILABILITY STATEMENT

The raw data supporting the conclusions of this article will be made available by the authors, without undue reservation.

AUTHOR CONTRIBUTIONS

MP conducted and repeated many experiments and performed the manuscript writing and data analysis. GP developed composites, conducted several experiments, and helped in data compilation along with figures and tables. JB performed to identifying and conceptualizing of the problem and supervision during implementation, analysis of the data, helped in writing the draft of the manuscript, and contributed extensively for the depiction of the ideas for the present. All authors contributed to the article and approved the submitted version.

ACKNOWLEDGMENTS

The authors are thankful to Mr. Bhaskaranand Bhatt (Research Scholar, Indian Institute of Technology Delhi) for providing help in SEM work.

SUPPLEMENTARY MATERIAL

The Supplementary Material for this article can be found online at: https://www.frontiersin.org/articles/10.3389/fmats.2020.00205/full#supplementary-material

REFERENCES

Coker, R. (2019). *Parx Plastics Granted Antimicrobial Vitamin e-blended UHWMPE patent*. Available online at: https://www.eppm.com/materials/parx-plastics-granted-antimicrobial-vitamin-e-blended-uhwmpe/ (accessed May 1, 2020).

Celebi Efe, G., Altinsoy, I., Türk, S., Bindal, C., and Ucisik, A. H. (2019). Effect of particle size on microstructural and mechanical properties of UHMWPE–TiO2 composites produced by gelation and crystallization method. *J. Appl. Polym. Sci.* 136, 15–18. doi: 10.1002/app.47402

Celebi Efe, G., Bindal, C., and Ucisik, A. H. (2017). Characterization of UHWPE-TiO2 composites produced by gelation/crystallization method. *Acta Phys. Pol. A* 132, 767–769. doi: 10.12693/APhysPolA.132.767

Chahar, B. S., and Pun, A. K. (2018). Erosion wear of ductile materials: a review. *ELK Asia Pacific J.* ISBN: 978-81-930411-8-5.

Chang, B. P., Akil, H. M., and Nasir, R. M. (2013). Mechanical and tribological properties of zeolite-reinforced UHMWPE composite for implant application. *Proc. Eng.* 68, 88–94. doi: 10.1016/j.proeng.2013.12.152

Chang, B. P., Akil, H. M., Nasir, R. M., and Nurdijati, S. (2011). Mechanical and antibacterial properties of treated and untreated zinc oxide filled UHMWPE composites. *J. Thermoplast. Compos. Mater.* 24, 653–667. doi: 10.1177/0892705711399848

Chukov, D. I., Stepashkin, A. A., Gorshenkov, M. V., Tcherdyntsev, V. V., and Kaloshkin, S. D. (2014). Surface modification of carbon fibers and its effect on the fiber-matrix interaction of UHMWPE based composites. *J. Alloys Compd.* 586, S459–S463. doi: 10.1016/j.jallcom.2012.11.048

Duan, W., Wu, M., Han, J., and Ni, Z. (2020). Research into the thermal stability and mechanical properties of vitamin e diffusion modified irradiation cross-linked graphene oxide/ultra-high molecular weight polyethylene composites. *RSC Adv.* 10, 4175–4188. doi: 10.1039/c9ra09893c

Gao, Y., Feng, X., Liu, J., Fu, H., Li, S., and He, C. (2019). Design and ballistic penetration of "SiC/Ti6Al4V/UHMWPE" composite armor. *IOP Conf. Ser. Mater. Sci. Eng.* 563:042043. doi: 10.1088/1757-899X/563/4/042043

Ge, S., Wang, S., and Huang, X. (2009). Increasing the wear resistance of UHMWPE acetabular cups by adding natural biocompatible particles. *Wear* 267, 770–776. doi: 10.1016/j.wear.2009.01.057

Gopanna, A., Rajan, K. P., Thomas, S. P., and Chavali, M. (2019). *Polyethylene and Polypropylene Matrix Composites for Biomedical Applications*. Amsterdam: Elsevier Inc, doi: 10.1016/B978-0-12-816874-5.00006-2

Gutwein, L. G., and Webster, T. J. (2004). Increased viable osteoblast density in the presence of nanophase compared to conventional alumina and titania particles. *Biomaterials* 25, 4175–4183. doi: 10.1016/j.biomaterials.2003.10.090

Hashimoto, M., Takadama, H., Mizuno, M., Yasutomi, Y., and Kokubo, T. (2003). Titanium dioxide/ultra high molecular weight polyethylene composite for bone-repairing applications: preparation and Biocompatibility. *Key Eng. Mater.* 242, 415–418. doi: 10.4028/www.scientific.net/KEM.240-242.415

Holland, M., Fleming, L., Walton, K., Cerquiglini, A., Hothi, H., Hart, A., et al. (2018). Characterisation of wear areas on UHMWPE total knee replacement prostheses through study of their areal surface topographical parameters. *Surf. Topogr. Metrol. Prop.* 6:034006. doi: 10.1088/2051-672X/aac071

Holzwarth, U., and Gibson, N. (2011). The Scherrer equation versus the "Debye-Scherrer equation,". *Nat. Nanotechnol.* 6:534. doi: 10.1038/nnano.2011.145

Hu, J., Gao, Q., Xu, L., Zhang, M., Xing, Z., Guo, X., et al. (2016). Significant improvement in thermal and UV resistances of UHMWPE fabric through in situ formation of polysiloxane-TiO_2 hybrid layers. *ACS Appl. Mater. Interf.* 8, doi: 10.1021/acsami.6b04914

Hutchings, I. M. (1992). *Tribology: Friction and Wear of Engineering Materials*. Oxford: Butterworth-Heinemann.

Jia, Q. M., Zheng, M., Xu, C. Z., and Chen, H. X. (2006). The mechanical properties and tribological behavior of epoxy resin composites modified by different shape nanofillers. *Polym. Adv. Technol.* 17, 168–173. doi: 10.1002/pat.710

Kandeva, M., Kamburov, V., Nikolov, K., and Dimitrov, L. (2018). Abrasive wear of Ultra-High-Molecular-Weight Polyethylene (UHMWPE) modified with Carbon Nanotubes (CNTs). *Tribol. J. Bultrib* 7, doi: 10.13140/RG.2.2.28527.28327

Kumar, A., Bijwe, J., and Sharma, S. (2017). Hard metal nitrides: role in enhancing the abrasive wear resistance of UHMWPE. *Wear* 378–379, 35–42. doi: 10.1016/j.wear.2017.02.010

Lee, L. H. (1985). *Polymer Wear and Its Control*. Washington, DC: American Chemical Society. doi: 10.1016/0142-9612(86)90076-1

Lei, Y., Guo, J. L., and Zhang, Y. X. (2010). Tribological behaviour of nano-TiO_2 filled ultra high molecular weight polyethylene composites. *Polym. Mater. Sci. Eng.* 26, 48–51.

Lhymn, C. (1987). Effect of normal load on the specific wear rate of fibrous composites. *Wear* 120, 1–27. doi: 10.1016/0043-1648(87)90130-X

Mallakpour, S., and Nikkhoo, E. (2013). Production and characterization of nanocomposites based on poly(amide-imide) containing 4,4′-methylenebis(3-chloro-2,6- diethylaniline) using nano-TiO_2 surface-coupled by 3-aminopropyltriethoxysilane. *Prog. Org. Coatings.* 76, 231–237. doi: 10.1016/j.porgcoat.2012.09.022

Ortiz-Hernández, R., Ulloa-Castillo, N. A., Diabb-Zavala, J. M., La Vega, A. E. D., Islas-Urbano, J., Villela-Castrejón, J., et al. (2019). Advances in the processing of UHMWPE-TiO2 to manufacture medical prostheses via SPIF. *Polymers* 11:2022. doi: 10.3390/polym11122022

Sabetrasekh, R., Tiainen, H., Lyngstadaas, S. P., Reseland, J., and Haugen, H. (2011). A novel ultra-porous titanium dioxide ceramic with excellent biocompatibility. *J. Biomater. Appl.* 25, 559–580. doi: 10.1177/0885328209354925

Salari, M., Mohseni Taromsari, S., Bagheri, R., and Faghihi Sani, M. A. (2019). Improved wear, mechanical, and biological behavior of UHMWPE-HAp-zirconia hybrid nanocomposites with a prospective application in total hip joint replacement. *J. Mater. Sci.* 54, 4259–4276. doi: 10.1007/s10853-018-3146-y

Saravanan, I., and Devaraju, A. (2019). Wear mechanism of UHMWPE polymer composites for bio medical applications. *Mater. Res. Express* 6, 0–11. doi: 10.1088/2053-1591/ab3ed9

Senatov, F., Amanbek, G., Orlova, P., Bartov, M., Grunina, T., Kolesnikov, E., et al. (2020). Biomimetic UHMWPE/HA scaffolds with rhBMP-2 and erythropoietin for reconstructive surgery. *Mater. Sci. Eng. C* 111:110750. doi: 10.1016/j.msec.2020.110750

Senatov, F. S., Gorshenkov, M. V., Kaloshkin, S. D., Tcherdyntsev, V. V., Anisimova, N. Y., Kopylov, A. N., et al. (2014). Biocompatible polymer composites based on ultrahigh molecular weight polyethylene perspective for cartilage defects replacement. *J. Alloys Compd.* 586, S544–S547. doi: 10.1016/j.jallcom.2012.10.014

Sharma, S., Bijwe, J., and Panier, S. (2016). Assessment of potential of nano and micro-sized boron carbide particles to enhance the abrasive wear resistance of UHMWPE. *Compos. Part B Eng.* 99, 312–320. doi: 10.1016/J.COMPOSITESB.2016.06.003

Sharma, S., Bijwe, J., and Panier, S. (2019). Exploration of potential of Zylon and Aramid fibers to enhance the abrasive wear performance of polymers. *Wear* 422–423, 180–190. doi: 10.1016/j.wear.2019.01.068

Sharma, S., Bijwe, J., Panier, S., and Sharma, M. (2015). Abrasive wear performance of SiC-UHMWPE nanocomposites - Influence of amount and size. *Wear* 332–333, 863–871. doi: 10.1016/j.wear.2015.01.012

Shi, Y. J., Feng, X., Wang, H. Y., Liu, C., and Lu, X. H. (2007). Effects of filler crystal structure and shape on the tribological properties of PTFE composites. *Tribology Int.* 40, 1195–1203.

Suh, N. P. (1986). *Tribophysics, First Edition*. Upper Saddle River, NJ: Prentice Hall.

Travis Curtis (2013). *Surface Characterization of an Organized Titanium Dioxide Layer*. Master's Thesis, University of Arizona, Tucson. doi: 10.1017/CBO9781107415324.004

Ukaji, E., Furusawa, T., Sato, M., and Suzuki, N. (2007). The effect of surface modification with silane coupling agent on suppressing the photo-catalytic activity of fine TiO_2 particles as inorganic UV filter. *Appl. Surf. Sci.* 254, 563–569. doi: 10.1016/j.apsusc.2007.06.061

Wang, Q., Zhang, D., and Ge, S. (2007). Biotribological behaviour of ultra-high molecular weight polyethylene composites containing Ti in a hip joint simulator. *Proc. Inst. Mech. Eng. Part J: J. Eng. Tribol.* 221, 307–313. doi: 10.1243/13506501JET232

www.tstar.com (2020). Available online at: https://www.tstar.com/blog/bid/33845/surface-energy-of-plastics (accessed March 25, 2020).

Xu, S., and Tangpong, X. W. (2013). Review: tribological behavior of polyethylene-based nanocomposites. *J. Mater. Sci.* 48, 578–597. doi: 10.1007/s10853-012-6844-x

You, Y. L., Li, D. X., Si, G. J., and Deng, X. (2014). Investigation of the influence of solid lubricants on the tribological properties of polyamide 6 nanocomposite. *Wear* 311, 57–64. doi: 10.1016/j.wear.2013.12.018

Yu, W. W., Shi, J. G., Wang, L., Liu, Y. L., and Chen, X. X. (2017). Structure and mechanical properties of TiO_2/UHMWPE nanocomposite monofilaments. *MATEC Web. Conf.* 128, 2–4. doi: 10.1051/matecconf/201712803007

Conflict of Interest: The authors declare that the research was conducted in the absence of any commercial or financial relationships that could be construed as a potential conflict of interest.

frontiers in Materials

ORIGINAL RESEARCH
published: 04 August 2020
doi: 10.3389/fmats.2020.00243

Hollow Section Fibers Characterization for Seats Covers Fabric Application

Valentina Brunella[1], Giulia Albini[1,2], Vito Guido Lambertini[2] and Bartolomeo Placenza[2]*

[1] Dipartimento di Chimica e NIS Research Centre, University of Turin, Turin, Italy, [2] Group Materials Labs, Polymers Group, Centro Ricerche Fiat, Turin, Italy

This research is focused on hollow polyethylene terephthalate (PET) fibers and fabrics. The aim of hollow section fibers application is a textile contribution to weight reduction of the whole vehicle. CO_2 emissions consequences and awareness of companies to environmental issues are driving studies on the direction of vehicle weight reduction, according to recent European regulations. For this purpose, fabrics composed of hollow fibers have been produced and characterized. In order to be applied as seats covers for the automotive sector, they have been compared to current production woven fabrics. Tensile, tear strength tests and aesthetic and structural abrasion have been carried out. The performance of hollow fibers PET fabrics is slightly lower than full section fabrics, but completely acceptable according to automotive requirements. Its specific application can be evaluated.

Keywords: hollow fibers, PET fibers, automotive fabric, technical textile, weight reduction, emission reduction

OPEN ACCESS

Edited by:
Emilia Morallon,
University of Alicante, Spain

Reviewed by:
Antonio Greco,
University of Salento, Italy
Philippe Boisse,
Institut National des Sciences Appliquées de Lyon (INSA Lyon), France
Kadir Bilisik,
Erciyes University, Turkey

****Correspondence:***
Valentina Brunella
valentina.brunella@unito.it

Specialty section:
This article was submitted to Polymeric and Composite Materials, a section of the journal Frontiers in Materials

Received: *18 February 2020*
Accepted: *03 July 2020*
Published: *04 August 2020*

Citation:
Brunella V, Albini G, Lambertini VG and Placenza B (2020) Hollow Section Fibers Characterization for Seats Covers Fabric Application. Front. Mater. 7:243. doi: 10.3389/fmats.2020.00243

INTRODUCTION

Due to recent European regulations and Companies' awareness to environmental issues, CO_2 emissions need to decrease and more recycled materials need to be used. Recycling involves reducing waste and production of new materials, recovering and transforming of refuse. PET and other plastics affect the amount of waste for disposal, but they can be recycled, as an economical way to reduce plastic waste for automotive application (Cole and Sherman, 1995; Jambor and Beyer, 1997; Koch, 2005). Apart from Companies' responsibility, Customers' awareness in reducing fuel consumption and using fuels from renewable resources are important (Official Journal of the European Union, 2009). In fact, CO_2 production is directly related to type and fuel consumption quantity. European legislation has set 95 g/km maximum limit of CO_2 emission within 2020 (Official Journal of the European Union, 2009; Poyant, 2013).

Carmakers have been looking for new ways for reducing CO_2 emissions, focusing on increasing the use of recycled materials and vehicle total weight reduction. The technology of new engines is related to innovation with an increased efficiency, trying to reduce fuel consumption in conventional engines or using renewable resources origin fuels together with new kinds of engines. Emissions reducing is related to whole vehicle weight reduction, and similarly, vehicle weight reduction affects fuel consumption for 75% (Fredriksson and Veitl, 2011; Poyant, 2013).

In the recent years, the average weight of vehicles has been increasing from 800 kg of 1970s to its climax, 1300 kg of 2012. The increase is approximately 32% (Koch, 2005). 100 kg vehicle weight reduction can cause fuel consumption decreasing of 0.3–0.8 L per 100 km (Fredriksson and Veitl, 2011).

In the textile field for automotive application, awareness of environmental issues is related both to the use of green materials from recycled sources and to weight reduction. To continue in the eco-friendly direction for the automotive area, in this work our attention will be driven to the last objective.

A study (Albini et al., 2019), about recycled PET fabrics for automotive application has already proved that post-consumer PET fibers can be used to make yarns and fabrics, which withstand all high technical requirements. Instead, in order to reduce the weight of the whole vehicle, a collaboration among automotive sectors is essential and a contribution of all areas can be decisive. These areas are car body development, engine manufacturing departments and design. The goal of reducing total weight of vehicle can be achieved using lightweight materials (Cole and Sherman, 1995; Jambor and Beyer, 1997). Among these, plastics, composites and light alloys (Lyu and Choi, 2015). Reducing weight in every kind of component affects vehicle final weight (Cole and Sherman, 1995; Jambor and Beyer, 1997). Textile covering also conditions the whole weight of about 20 kg and this could be a significant part if related with all other improvements in weight (Fredriksson and Veitl, 2011). Textile materials cover seats, floor, door panels, ceiling and they are used in functional roles, as for seat belts, pipes, airbags, and tires.

Textile weight reduction is demanding. First, fabrics have to meet automotive requirements to satisfy applications with high technical-mechanical performances. High wear resistance, fastness to light, comfort and safety features are fundamental characteristics to ensure durability of the vehicle (Fung and Hardcastle, 2001; Hearle and Morton, 2008). Different papers tell about possible applications of hollow fibers in the automotive sector. For example, hollow fibers fabrics for interiors insulation applications or composing technical non-woven (Mahmoud et al., 2011; Ki-Young et al., 2013).

The objective of this research is to examine hollow section PET fibers and hollow PET fibers fabric. These fabric properties need to be equivalent to current production fabrics for seats covers application. Hollow fibers are polymeric fibers with a continuous hole running down the middle (Eichhorn et al., 2009). This particular section affects fabric mechanical, structural and after wearing aesthetical final properties (Matsudaira et al., 1993; Khoddami et al., 2009). Hollow fibers fabrics have been compared to current production fabrics in order to evaluate their possible application. Fabrics characteristics and hollow section fibers fabrics final weight reduction will be evaluated. Assessing different mechanical properties, this research can contribute increasing knowledge about hollow fibers production and fabrics characteristics and, above all, their possible applications.

For *Original Research Articles, Clinical Trial Articles*, and *Technology Reports* the introduction should be succinct, with no subheadings. For *Case Reports* the Introduction should include symptoms at presentation, physical exams, and lab results.

MATERIALS AND METHODS

An Italian manufacturer supplied fibers. PET hollow section fibers and full section fibers were produced. The production of the two different fibers is substantially equivalent in order to obtain two final products comparable. Fibers production starts from PET chips, which are crystallized at 100–170°C before the spinning process, in order to decrease the humidity content. After that, PET chips are melted, extruded and sent to the dosing pumps. They were mass dyed in black. The parameters of the first step of fibers production are:

- Entry air temperature (drying) 170°C; exit air temperature (drying) 100°C;
- Enter temperature (extrusion) 270°C; exit temperature (extrusion) 280°C;
- Rotating pumps speed is 21,6 rpm for hollow ones and 25,7 rpm for full ones;
- Spinneret pack holes number is 56 for hollow ones and 48 for full ones;
- Cooling temperature is 30°C;
- Yarn collecting speed is 3000 m/min for hollow ones and 3050 m/min for full ones;
- Yarn count (for each yarn end) is 235 dtex for hollow ones and 257 dtex for full ones;
- Finish is texturing for both fibers type.

Main differences between hollow and full section fibers production are rotating speed and number of holes of the spinneret pack (**Figure 1**). Melted material is sent to the spinneret pack, composed of 48 and 56 holes for full and hollow section fibers production, respectively.

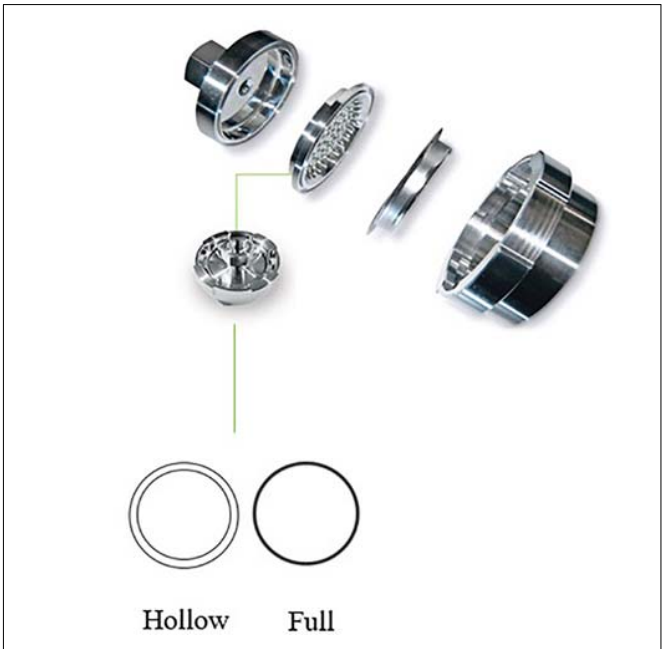

FIGURE 1 | Part of the spinneret pack (Lukay Nonwoven Solutions, 2019) and hollow (left) and full (right) section of spinneret pack holes.

Because of lower covering capability of hollow section fibers yarns compared to full section fibers yarns, the holes number of the spinneret pack has been increased to give them better covering capability and volume and make them comparable to full section fibers.

As regards hollow fibers production, the hole is usually shaped with the introduction of air or other gas (nitrogen) in the polymeric solution (wet spinning process) or melt spinning through specially designed spinnerets. For this research, the method is the last. Hollow fibers provide greater bulk with less weight. Exiting the spinneret pack, yarns are POY (partially oriented yarn) and they progressively are cooled, stretched and textured with "Taslan" process. The last process allows the yarn to be structurally modified with a air flow bending some areas of the yarn and creating curled fibers on the yarn itself, giving the yarn specific characteristics (Andreoli and Freti, 2004).

The two kinds of fiber sections have been structurally analyzed by a metallographic microscope Reichert MeF3A, to understand their section. The preparation of the samples for microscope analysis includes yarns insertion into a thermosetting resin. These samples are 40 mm wide. The upper side of the sample is polished with abradents and diamond paste to better evaluate its surface.

Yarns and fabrics properties are summarized in **Table 1**. Yarns are composed of 6 yarn ends for warp yarns direction and 4 yarn ends for weft yarns direction. The final yarn count is reported in the table below, with a reduction of 19.6% for hollow fibers warp yarns and 19% for hollow fibers weft yarns. The setting parameters for fibers production have conducted to an acceptable reduction in weight of the yarns (equal length). A major Italian company produced flat woven fabrics with a Jacquard loom, using hollow and full section fibers yarns. Woven fabric is the most used for seat cover application (Pamuk, 2008) and consists of two sets of yarns interlaced at right angles to each other. Its strength and durability can be varied and depend on the yarn type and the thread spacing (Horrocks and Arnand, 2016). For this research, woven fabric structure type is twill weave. Three samples with different number of weft yarns/cm have been considered to notice the influence of yarns density on the results and to better evaluate global fabrics characteristics.

Fabrics were subjected to further processes: dry cleaning with C_2Cl_4, thermo-fix process at 140°C and calender process to optimize dimensional stability. As some authors tell (Becerir et al., 2007), hollow fibers can compromise wear resistance of the final product. For this reason, double washing during the production process was done, to better eliminate impurities and weaving oils. The last production step is a lamination process. It is applied to almost every kind of fabric in the automotive sector and it impart a soft touch to the fabric and ease the sewing process of cover manufacturing. During this step, a flame lamination step, the polyurethane is the adhesive, melted with a gas flame. The fabric manufacturer laminated fabrics to one side of a polyurethane foam layer and a scrim fabric to the other side of the polyurethane layer (Fung and Hardcastle, 2001). In **Table 1**, values of fabrics total thickness and fabrics total weight are referred to laminated fabrics with polyurethane layer foam and the scrim fabric, instead fabric weight and thickness refers to the fabric itself, without lamination.

As visible in **Table 1**, hollow and full fibers fabrics weight is different and we can evaluate a 20% average reduction in weight for the fabric without lamination. This reduction reflects reduction of the yarn weight with the yarn count, as mentioned above with data reported in **Table 1**. Each hollow section fibers sample has been compared to its respective full section fiber sample. The evaluation has been done on five samples for each kind of fabric. In particular, the reduction in weight is 20.1% for 13 weft yarns/cm sample, 20.7 and 20.9% for 14 and 15 weft yarns/cm samples, respectively. Instead, total laminated weight can change depending on the variability of polyurethane and scrim fabric weight and thickness and on the variability of the sampling.

Tensile and tear resistance tests were performed to evaluate fabrics mechanical characteristics. Fabrics need to bear seat cover manufacturing processes and to perform highly when exposed to mechanical stress throughout the lifetime of the vehicle. Tensile strength test was performed on Acquati AG/7E/306 electronic dynamometer according to ISO 13934-1 (Iso 13934-1:2013, 2013). For each type of fabric, five samples for warp and five for weft direction were tested. This is necessary because fabric properties are affected by the loading direction. Tear strength test was carried out to measure the force to propagate a tear in fabric. This test is useful to evaluate the textile material stress suffered during the process of cover production. The test was

TABLE 1 | Yarns and fabrics characteristics.

Fabrics characteristics	Sample 1		Sample 2		Sample 3	
	Hollow s.	Full s.	Hollow s.	Full s.	Hollow s.	Full s.
Number of warp yarns/cm	24 ± 1	24 ± 1	24 ± 1	24 ± 1	24 ± 1	24 ± 1
Number of weft yarns/cm	13 ± 1	13 ± 1	14 ± 1	14 ± 1	15 ± 1	15 ± 1
Fabric total weight (g/m^2)	444 ± 3	520 ± 5	444 ± 4	534 ± 6	455 ± 3	541 ± 6
Fabric weight (g/m^2)	345 ± 3	432 ± 2	343 ± 1	433 ± 2	354 ± 2	448 ± 1
Fabric total thickness (mm)	3 ± 0.2	3 ± 0.2	3.1 ± 0.2	3 ± 0.2	3 ± 0.2	3 ± 0.2
Fabric thickness (mm)	0.5 ± 0.1	0.5 ± 0.1	0.6 ± 0.1	0.5 ± 0.1	0.5 ± 0.1	0.6 ± 0.1
Warp yarn count (dtex)	905 ± 45	1125 ± 56	905 ± 45	1125 ± 56	905 ± 45	1125 ± 56
Weft yarn count (dtex)	610 ± 30	753 ± 36	610 ± 30	753 ± 36	610 ± 30	753 ± 36

The values are reported for each characteristic with standard deviation.

performed according to ISO 9073 (ISO 9073:1999, 1999). Samples were prepared in the format as in **Figure 2** and tore on one side ("cut" in **Figure 2**). The dashed lines point out where the clamps of the dynamometer grab the sample.

According to internal automotive validation test, perforation resistance test has been evaluated. This test reproduce the stress suffered from the fabric of seat cover when a foreign body accidentally perforates it, during the lifetime of the vehicle. The test was performed with the dynamometer and the particular device as in **Figure 3**, placed instead of the clamps, made up of a metallic sphere of 12.7 mm diameter. With the help of the dynamometer, the sphere moves at 80 mm/min and produce a perforation of the round sample.

Structural wear resistance was evaluated to define the resistance of the yarns composing the fabric. The test was performed on a Taber (Rotary Platform Double Head Tester) abrasimeter, according to ASTM D3884/09 (ASTM D3884/09:2013, 2013). The analyzed fabric was worn against two Calibrase 10 abrasive wheels, moving in opposite directions on its surface, as schematized in **Figure 4**. Three samples for each type of fabric were examined. According to internal automobile specification, 600 cycles of wheels rotation were set for woven fabrics. Flat woven fabrics require a longer period of testing because of their inherently more resistant structure, compared to other kinds of fabric structure, such as knitted ones.

Furthermore, worn surfaces were visually examined and graded by setting values from 3, best result with no yarns breakage, to 1, worse result, with at least a yarn breakage.

Aesthetic wear resistance of all type of fabrics was evaluated with a Cesconi Abrasive tester, comparable to Martindale Abrasimeter, according to ISO 12947/1-2-3-4 (ISO 12947/1-2-3-4:1998, 1998). This test reproduces the mechanical stress suffered by seat cover fabrics during their

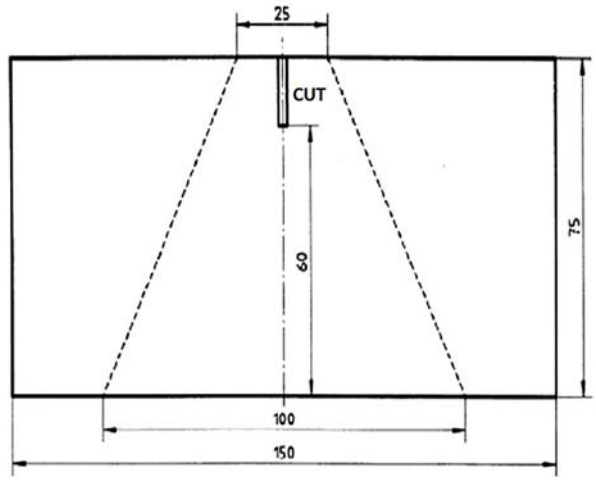

FIGURE 2 | Sample template for tear strength test. The dimensions are in mm.

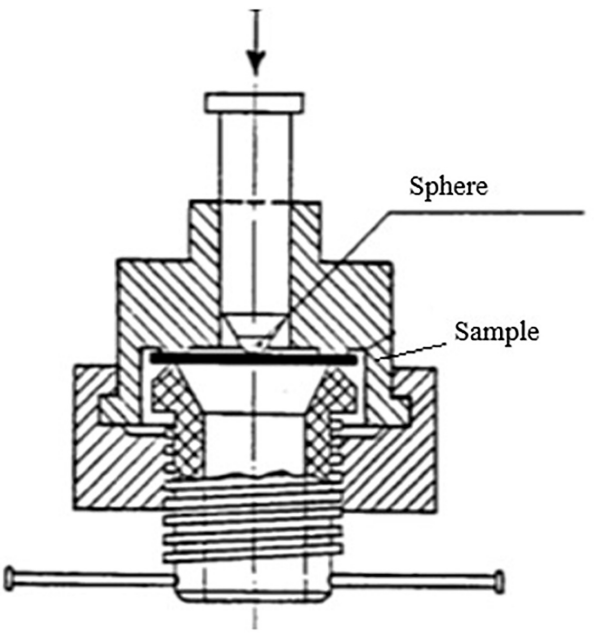

FIGURE 3 | Device for perforation resistance test.

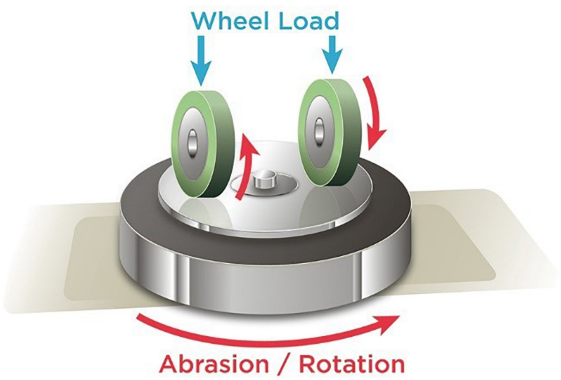

FIGURE 4 | Scheme of the structural wearing test apparatus.

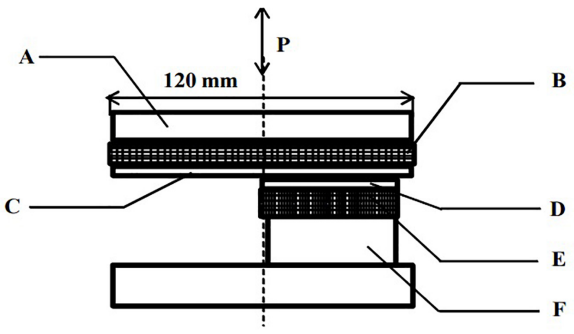

FIGURE 5 | Scheme of wear resistance test apparatus. The substrate to test (D) is placed on the rotating plate (F), through a substrate holder (E). The abrasive fabric, instead, is placed on the fixed plate (A), using an appropriate substrate holder (B), on which a load is applied (P).

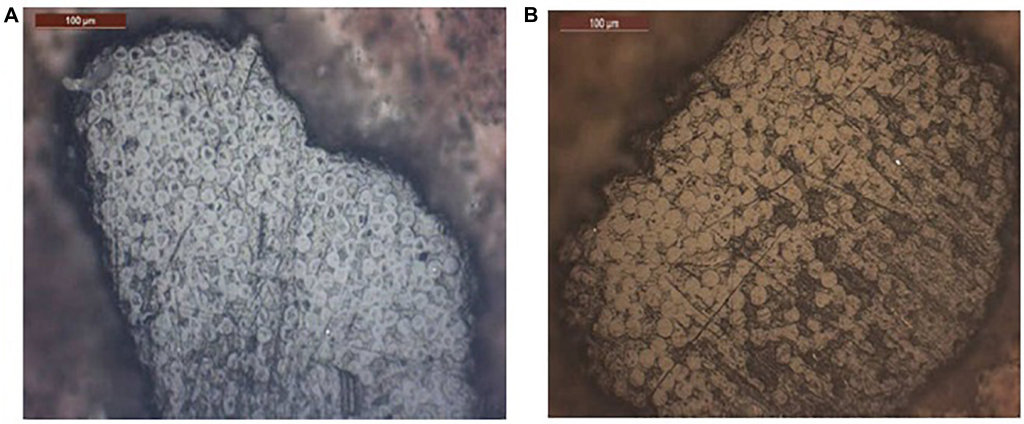

FIGURE 6 | (A) Hollow fibers section image and **(B)** full fibers section image.

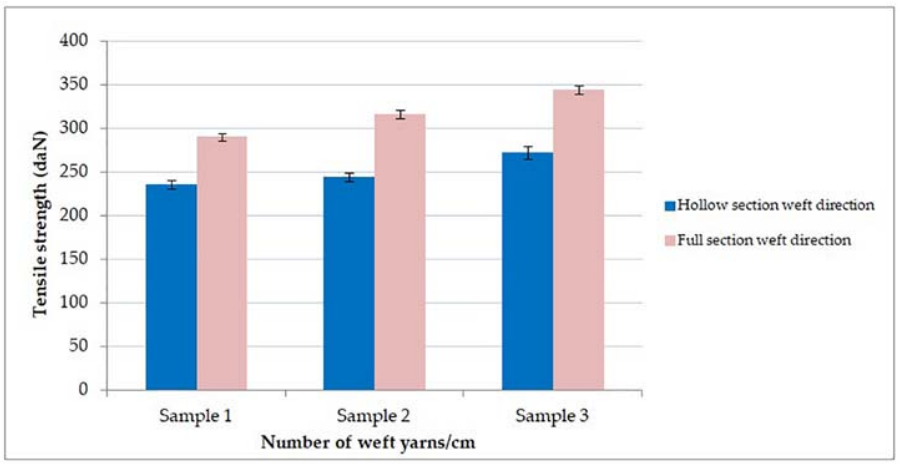

FIGURE 7 | Tensile strength results. Hollow and full section and different number of weft yarns/cm have been evaluated.

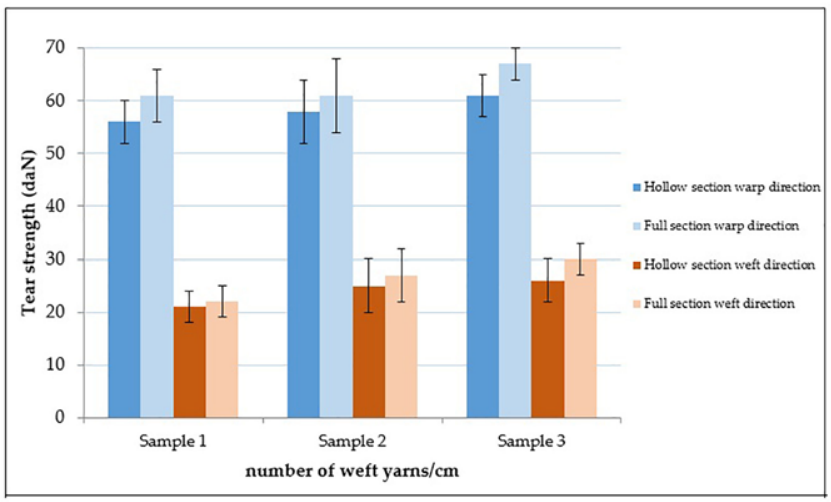

FIGURE 8 | Tear strength results for warp and weft direction samples. Hollow and full section and different number of warp yarns/cm have been evaluated.

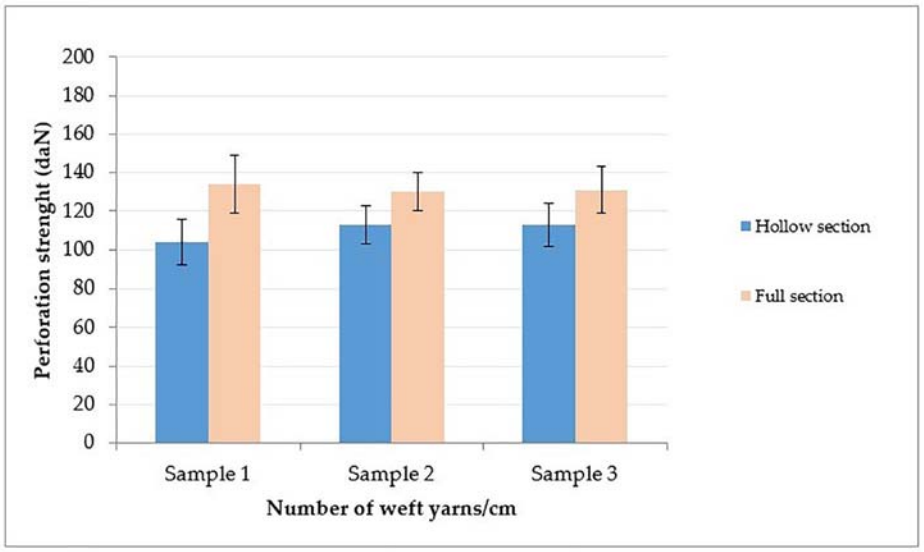

FIGURE 9 | Perforation strength results. Hollow and full sections and different number of warp yarns/cm have been evaluated.

use for an average lifetime of the vehicle. The abrasion tester is generally used for testing textile materials. The apparatus is schematized in **Figure 5**. The abrading standard fabric is made of woolen fibers and fixed on a given plate (point A in **Figure 5**). The tested surface is placed on a rotating disk located under the fixed plate. The rotating plate moves with a revolution movement in order to ensure a complete wear of the fabric sample. 3000 and 6000 cycles were performed with a load of 3 kg, according to internal automobile validation test.

For aesthetic wear resistance test three samples for each kind of fabric were examined and evaluated according to gray scale. The scale quantifies changes in color compared to the reference. It includes a range of shade of gray, from 1, worse result, evident modification of the surface to 5, better result, almost no superficial changes on fabric, with a step of 0.5. Minolta CM-3610 spectrophotometer provided gray scale measurements, under a D65 illuminant using a 10° standard observer with specular component excluded (SCE) mode. Not worn surfaces were taken as standards and worn fabrics as samples. Surfaces pictures were recorded with LEICA M205C optical microscope. Before the tests, all specimens were conditioned for 72 h in a standard atmosphere at 20 ± 2°C with 65 ± 2% relative humidity, according to ISO 139 (ISO 139:2005, 2005).

RESULTS

Hollow and full sections have been compared in **Figure 6**, which shows fibers transversal section.

On the left, the hollow section of the fibers is visible.

The average diameter of the fibers is 17 μm for hollow section and 19 μm for full section. The inner average diameter of hollow section is 8 μm.

TABLE 2 | Structural wear resistance test results.

Sample	Grade values	
	Hollow fibers	Full fibers
Sample 1 600 cycles	2	3
Sample 2 600 cycles	3	3
Sample 3 600 cycles	3	3

TABLE 3 | Aesthetical wear resistance test results.

Sample	Gray scale values	
	Hollow fibers	Full fibers
Sample 1 3000 cycles	2.5	4.5
Sample 1 6000 cycles	2.5	4
Sample 2 3000 cycles	2	4
Sample 2 6000 cycles	2	4
Sample 3 3000 cycles	2	4.5
Sample 3 6000 cycles	2	4

Tensile Strength Test

Figure 7 shows strength resistance test for all kind of fabrics. Three samples (**Table 1**) have been tested: sample 1 (13 weft yarns/cm); sample 2 (14 weft yarns/cm) and sample 3 (15 weft yarns/cm).

Considering warp direction samples, they are all above automotive requirements (≥100 daN) and they don't break under a force of 500 daN, the maximum load detectable for the dynamometer cell. High loads are required during fabric manufacturing and covers assembling steps. These results depend on the particular flat woven structure of the fabric and on the high number of warp yarns/cm. During the test, all warp yarns

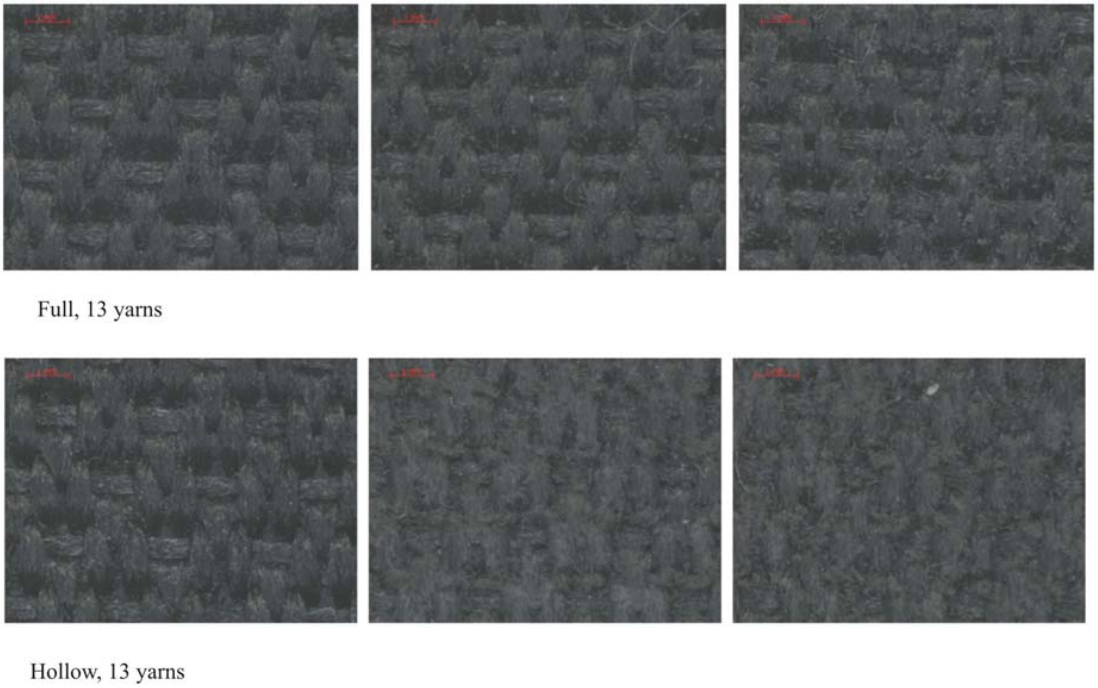

FIGURE 10 | Pictures under the microscope of full and hollow section 13 weft yarns/cm PET fabric surfaces before wear resistance test and after 3000 and 6000 cycles of wearing (from left to right).

are stressed simultaneously and contribute to the result. There is no significant difference between hollow and full section fibers fabrics, and hollow section fibers do not seem less strong than full section fibers. Instead, considering weft direction samples, for both hollow and full sections, the load increase with the number of weft yarns/cm, as expected.

Tear Strength Resistance

In order to evaluate hollow section fibers fabrics performance tear strength test has been performed. **Figure 8** shows the results with a comparison between hollow and full section fibers fabrics with different number of yarns/cm.

Tear strength resistance of hollow fibers fabrics is slightly lower than full fibers fabric, but almost comparable to them. This difference is kept for weft direction samples (**Figure 8**). Maximum load values are higher for warp direction samples, compared to weft direction samples. This is due to higher number of yarns/cm, 24, compared to 13, 14, and 15 for weft direction samples. Among three different yarns density sample there are not significant differences, considering standard deviation, so they are all considered comply with automotive standards.

Perforation Strength

Figure 9 shows perforation strength results for hollow and full section fabrics. Different number of warp yarns/cm have been evaluated. Current production fabrics are perforation resistant, with high average values included between 130 and 134 daN. Hollow section fibers fabrics show slightly lower values of perforation strength, due to the particular fiber section, but acceptable according to automotive standards, for which 25 daN minimum is required.

Abrasion Resistance

For all kinds of fabrics, structural wear resistance results are summarized in **Table 2**. Not worn fabrics were taken as standard fabrics, and they are evaluated grade 3. After Taber test, full section fibers fabric does not show any yarn breakage, nor structural changes. The worn surface presents a slight shadow, hence it's evaluated grade 3. This result is positive according to automobile standard, for which there must be no yarns breakage.

Sample 1 surface, composed of hollow section fibers, shows some fibers/yarns breakage after structural wear resistance test, compared to sample 2 and 3. The abrasive wheels stress their surface several times and cause the damage of the most superficial fibers. Sample 1 has lower weft yarns density and this can have influence on the result. Furthermore, the hollow structure of the fiber and the less number of weft yarns/cm compared to sample 2 and 3 affect the result.

Afterward, fabrics surface was examined after aesthetic wear resistance test. Values of gray scale have been registered with the spectrophotometer and they are represented in **Table 3**.

For a more accurate analysis, pictures of the surfaces have been taken at different magnification with an optical microscope (**Figures 10–12**). Worn surfaces of full section fibers fabrics do not present broken yarns nor structural modifications. Hollow section fiber fabrics (sample 1, 2, and 3) show evident modification of the surface after 3000 cycles, fibers lifting and breakage and clear whitening of the surface. After 6000 cycles,

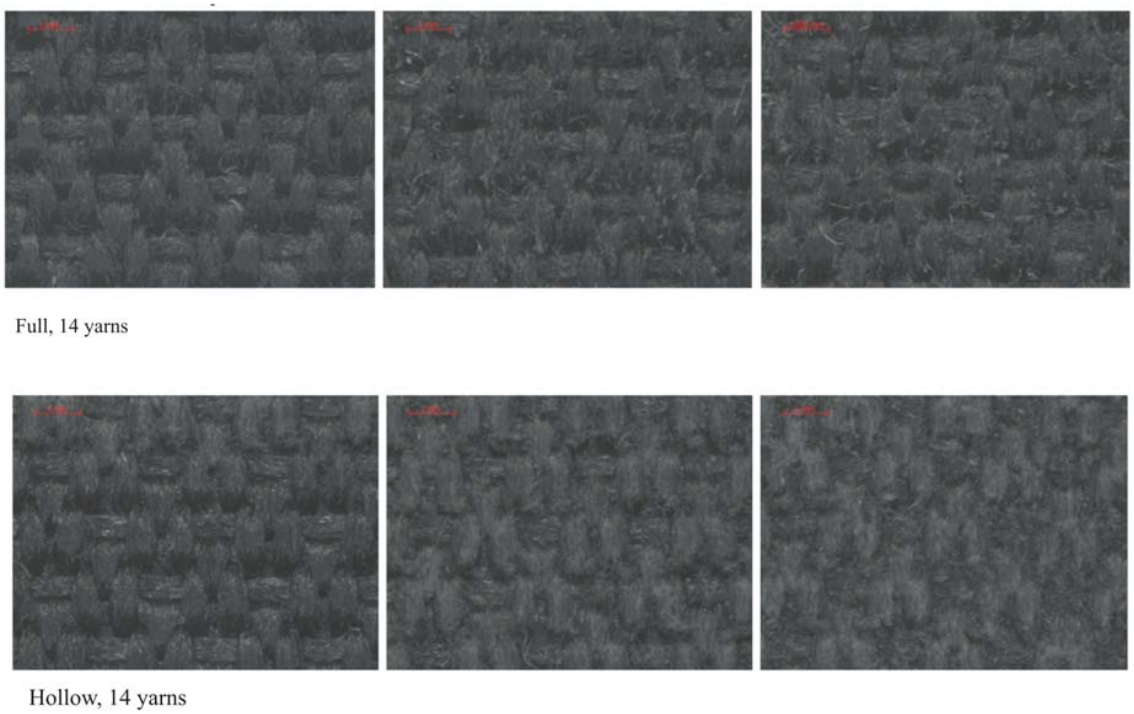

FIGURE 11 | Pictures under the microscope of full and hollow section 14 weft yarns/cm PET fabric surfaces before wear resistance test and after 3000 and 6000 cycles of wearing (from left to right).

FIGURE 12 | Pictures under the microscope of full and hollow section 15 weft yarns/cm PET fabric surfaces before wear resistance test and after 3000 and 6000 cycles of wearing (from left to right).

the surface has lifted fibers and disappearing of fabric structure but it is not worse compared to 3000 cycles results. This is confirmed by gray scale values: their surfaces are evaluated 2 of gray scale after 3000 and 6000 cycles (**Table 3**), unacceptable according to automotive standards. Despite the slightly better gray scale evaluation (**Table 3**), sample 1 (hollow section) surface appearance is visually the worst compared to sample 2 and 3, because of lifting and damaging of the fibers. This is a consequence of a difference in yarns density and structural weakness, as observable also after Taber abrasion test (**Table 2**). Full fiber fabrics bear the abrasive wheels stress of surface and they are evaluated 4.5 of gray scale after 3000 cycles and 4 after 6000 cycles.

For both structural and aesthetical, wear resistance depends on a combination of fiber structure, yarn, and fabric construction characteristics.

CONCLUSION

In this paper, structural and mechanical characteristics of PET fabrics composed of hollow section fibers were evaluated. They were compared to current production full section fibers PET fabrics. Mechanical tests were performed to evaluate their matching with specific automotive requirements.

Despite good mechanical results, hollow section fibers fabrics can't be applied as cover of very contactable areas, for example sittings areas and back seats. In fact, structural and aesthetic wear resistance test results showed fibers breakages and lifting and structure disappearing. For this reason, they are not in compliance with automotive regulations. Otherwise, hollow section fibers fabric is suitable as "covering textile" for less contactable areas, lateral zones, ceiling, door panels, etc. With these specific applications, negative effects of aesthetic abrasion may be avoided. Hollow fibers fabric reaches the elevated mechanical performance of current production PET textile materials, and it can replace them where aesthetic abrasion cannot compromise its use. A slight difference has been found among the three hollow section fiber samples tested, regarding abrasion resistance test result for 13 warp yarns/cm density fabric (sample 1). This result can direct fabric choice toward sample 2 and 3, to gain a durability for the lifetime of the vehicle.

Hollow section fiber fabrics can contribute to benefits as reducing vehicle weight of approximately 20% compared to current production textiles materials, being applied as covering of specific parts of car interior. In this way, these fabrics can be environmentally friendly.

DATA AVAILABILITY STATEMENT

All datasets generated for this study are included in the article/supplementary material.

AUTHOR CONTRIBUTIONS

VB and BP designed the experiments. GA performed the experiments. GA and VB analyzed the data. VL revised the manuscript. All the authors reviewed and approved the manuscript.

ACKNOWLEDGMENTS

The authors wish to thank AUNDE for fabrics production.

REFERENCES

Albini, G., Brunella, V., Lambertini, V. G., Placenza, B., and Martorana, B. (2019). Comparative study of mechanical characteristics of recycled PET fabrics for automotive application. *J. Ind. Text.* 48, 992–1008. doi: 10.1177/1528083717750887

Andreoli, C., and Freti, F. (2004). *Man-Made Fibres – Reference Book of Textile Technologies*, 1st Edn. Milano: Fondazione Acimit, 37–48.

ASTM D3884/09:2013 (2013). *Standard Guide for Abrasion Resistance for Textile Fabrics - Taber Method*. West Conshohocken, PA: ASTM.

Becerir, B., Karaca, E., and Omeroglu, S. (2007). Assessing colour values of polyester fabric produced from fibres having different cross-sectional shapes after abrasion. *Color. Technol.* 123, 252–259. doi: 10.1111/J.1478-4408.2007.00092.X

Cole, G. S., and Sherman, A. M. (1995). Light-weight materials for automotive applications. *Mater. Charact.* 1995, 3–9. doi: 10.1016/1044-5803(95)00063-1

Eichhorn, S., Hearle, J. W. S., Jaffe, M., and Kikutani, T. (2009). *Handbook of Textile Fibres Structure*, 1st Edn, Vol. 2. Cambridge, MA: Woodhead Publishing, 328–391.

Fredriksson, L., and Veitl, A. (2011). *Automotive Development: All Eyes on CAE Weight Managemen*. Avaliable at: http://blog.altair.co.kr/4251 Presentation of Altair (accessed December 23, 2011).

Fung, W., and Hardcastle, M. (2001). "Introduction survey," in *Textile in Automotive Engineering*, 1st Edn, ed Woodhead Publishing (Cambridge, MA: Woodhead Publishing), 1–23.

Hearle, W., and Morton, W. (2008). "An introduction to fibres structure," in *Physical Properties of Textile Fibres*, 1st Edn, ed Woodhead Publishing (Cambridge, MA: Woodhead Publishing), 1–81. doi: 10.1533/9781845694425.1

Horrocks, A. R., and Arnand, S. C. (2016). "Technical fabrics structures-woven fabrics," In *Handbook of Technical Textile*, 2nd Edn, Eds A. R. Horrocks, S. Anand, and S. C. Anand, Vol. 2. Duxford: Woodhead Publishing, 62–94. doi: 10.1533/9781855738966.62

ISO 12947/1-2-3-4:1998 (1998). *Determination of Abrasion Resistance - Martindale Method*. Geneva: ISO.

ISO 139 2005 (2005). *Standard Atmospheres for Conditioning and Testing*. Geneva: ISO.

ISO 13934-1:2013 (2013). *Tensile Properties of Fabrics*. Geneva: ISO.

ISO 9073:1999 (1999). *Determination of Laceration Resistance*. Geneva: ISO.

Jambor, A., and Beyer, M. (1997). New cars, new materials. *Mater. Design.* 1997, 203–209. doi: 10.1016/s0261-3069(97)00049-6

Khoddami, A., Carr, C. M., and Gong, R. H. (2009). Effect of hollow polyester fibres on mechanical properties of knitted wool/polyester fabrics. *Fibre Polym.* 10, 452–460. doi: 10.1007/s12221-009-0452-7

Ki-Young, K., Song, J. D., and Jung, N. I. (2013). Effects of binder fibres and bonding processes on PET hollow fibre nonwovens for automotive cushion materials. *Fibre Polym.* 2013, 639–646. doi: 10.1007/s12221-013-0639-9

Koch, H. J. (2005). *Reducing CO2 Emissions from Cars*. Dessau-Roßlau: German Advisory Council on the Environment.

Lukay Nonwoven Solutions (2019). *Lukay Nonwoven Solutions*. Available online at: http://www.lnws.eu/it/prodotti/pacchifiliere/ (accessed February 18, 2019).

Lyu, M. Y., and Choi, T. G. (2015). Research trends in polymer materials for use in lightweight vehicles Int. *J. Precis. Eng. Man.* 2015, 213–220. doi: 10.1007/s12541-015-0029-x

Mahmoud, A., El-Shenawy, G., and Ramadan, E. (2011). Using nonwoven hollow fibres to improve cars interior acoustic properties. *Life Sci. J.* 8, 344–351.

Matsudaira, M., Tan, Y., and Kondo, Y. (1993). The Effect of fibre cross-sectional shape on fabric mechanical properties and handle. *J. Text. I.* 84, 376–386. doi: 10.1080/00405009308658970

Official Journal of the European Union (2009). *Regulation (EC) 443/2009 of the European Parliament and of the Council Setting Emission Performance Standards for new Passenger Cars, as Part of the Community's Integrated Approach To Reduce CO2 Emissions From Light-Duty Vehicles*. Brussels: Official Journal of the European Union.

Pamuk, G. (2008). Comparative study of the abrasion resistance of automobile seat covers. *Fibres Text. East. Eur.* 16, 57–61.

Poyant, M. (2013). "Automotive interior trends and their impact on component weight reduction," in *Automotive Interiors Expo Conference*, Stuttgard.

Conflict of Interest: The authors declare that AUNDE provided materials analyzed in this work. AUNDE did not provide funding and was not involved in the study design, collection, analysis, interpretation of data, the writing of this article or the decision to submit it for publication.

frontiers in Materials

ORIGINAL RESEARCH
published: 18 June 2020
doi: 10.3389/fmats.2020.00162

Under Glass Weathering of Hemp Fibers Reinforced Polypropylene Biocomposites: Degradation Mechanisms Based on Emitted Volatile Organic Compounds

*Célia Badji[1,2], Jean-Marc Sotiropoulos[3], Joana Beigbeder[1], Hélène Garay[1], Anne Bergeret[2], Jean-Charles Bénézet[2] and Valérie Desauziers[1]**

[1] IPREM, IMT Mines Ales, Universite de Pau et des Pays de l'Adour, E2S UPPA, CNRS, Pau, France, [2] PCH, IMT Mines Ales, Ales, France, [3] IPREM, Universite de Pau et des Pays de l'Adour, E2S UPPA, CNRS, Pau, France

OPEN ACCESS

Edited by:
Patricia Krawczak,
IMT Lille Douai, France

Reviewed by:
Xavier Colin,
École Nationale Supérieure d'Arts et Métiers, ParisTech, France
Dan Maskell,
University of Bath, United Kingdom
Asim Shahzad,
National University of Sciences and Technology (NUST), Pakistan

***Correspondence:**
Valérie Desauziers
Valerie.Desauziers@mines-ales.fr

Specialty section:
This article was submitted to Polymeric and Composite Materials, a section of the journal Frontiers in Materials

Received: 09 March 2020
Accepted: 04 May 2020
Published: 18 June 2020

Citation:
Badji C, Sotiropoulos J-M, Beigbeder J, Garay H, Bergeret A, Bénézet J-C and Desauziers V (2020) Under Glass Weathering of Hemp Fibers Reinforced Polypropylene Biocomposites: Degradation Mechanisms Based on Emitted Volatile Organic Compounds. Front. Mater. 7:162. doi: 10.3389/fmats.2020.00162

The durability of hemp fibers reinforced polypropylene biocomposites was investigated after one year under glass exposure. Volatile organic compounds emissions were assessed using a new passive sampling method. Degradation pathways were examined in order to understand the weathering mechanisms. The polymer matrix was decomposed into oxygenated products due to UV rays and high temperatures. As regards hemp fibers, different degradation steps of the carbohydrates were highlighted according to the nature of the detected furans. At a non-weathered state, dehydrations preceded the ring-opening mechanism, often catalyzed by Maillard reactions. The further cyclization induced the formation of 2- or 5-substituted furans emitted by non-weathered materials. Reactions between identified products after weathering which were not yet found in literature were proposed in this paper. They often implied a keto-enol tautomerism but also dehydrations that induced the formation of 3- and 4-substituted furanones. These differences can be explained by a primary decomposition of carbohydrates favored at a non-weathered state and a secondary one occurring at a weathered state.

Keywords: hemp fiber, ageing, VOCs, oxidation, dehydration

INTRODUCTION

Recently, bio-fillers have emerged as an attractive alternative to inorganic fillers in the reinforcement of thermoplastics in response to growing awareness of environmental issues and increasing global waste problems (Liu and Hu, 2008). The main application areas of vegetal filler reinforced composites are the automotive and building industries (John and Thomas, 2008; Azwa et al., 2013). The natural fibers improve the mechanical properties of the composites (Saba et al., 2016; Kumre et al., 2017). Recently, lignin in a lignin–polyethylene (PE) biocomposite showed some antioxidant properties that protect the PE matrix (Van Schoors et al., 2018). Otherwise, with increasing concerns about indoor air quality, volatile organic compounds (VOCs) emissions

behavior in interior materials used as automotive parts has become widely recognized as an important topic for indoor environment air quality (Yu and Crump, 1998; Air quality sciences Inc., 2006; Badji et al., 2018).

During the melt mixing process of biocomposites through extrusion and injection molding, the high manufacturing temperatures exceed the bio-fillers degradation temperature (Dorez et al., 2013; Khazaeian et al., 2015). Also, during their use, climatic conditions weaken their chemical stability because of their high sensitivity (Zou et al., 2008; Ahmad et al., 2011; Badji et al., 2017). Temperature variations induce carbonization and odors emanating from the heated matter. Also, a press molding temperature increase induces biocomposites color turning from brown to close to black (Shibata, 2016). This was thought to be the result of vegetal fibers caramelization. Some solutions for reducing the odors and the amount of VOCs produced by biocomposites have been studied (Kim et al., 2006, 2011). But molecules responsible for the worsening air quality, color changes, and odors must be assessed.

Volatile organic compounds emitted by plastics are generally due to polymer degradation. Studies on thermal and photochemical oxidation of polypropylene (PP) showed that radical processes are responsible for chain scission, leading to low molecular weight products migrating from the polymeric matrix to the atmosphere (François-Heude et al., 2014; Rouillon et al., 2016). It is widely accepted that Norrish type I and II photochemical reactions occur involving C–C cleavage, leading to the formation of oxygenated compounds (Rabek, 1990; Muasher and Sain, 2006). Those generally result from the oxidation of tertiary carbon atoms of the polymer chains, leading to methyl ketones, along with alcohols, aldehydes, and aliphatic hydrocarbons formation.

The pyrolysis of lignocellulosic biomass was widely studied and further identification of the volatile compounds issued from the natural fibers' thermal degradation was sometimes performed. Some products, originating from pyrolysis of cellulose [molecular formula: $(C_6H_{10}O_5)_n$], are identified as low molecular weight compounds. They are formed by ring-opening reactions, while pyrans and furans are obtained from dehydration reactions (Sanders et al., 2003; Nowakowski and Jones, 2008). These molecules are generally stable aromatic compounds and hardly decompose into lower molecular weight compounds (Katō and Komorita, 1968). Their decomposition accounts for the major reactions occurring in the secondary reaction stage of cellulose. Hemicelluloses consist of saccharides such as glucose, mannose, xylose, and arabinose (Nowakowski and Jones, 2008; Binder et al., 2010). Once pyrolyzed, the derivatives of these pentose sugars, such as cyclopentanes and cyclopentenones, are detected in large quantities in addition to furan molecules (Peng and Wu, 2011; Carrier et al., 2012). Lignin component, a highly complex aromatic structure, breaks down into phenolic structures (Wittkowski et al., 1992; Brzonova et al., 2014). It mainly consists of three basic building blocks: guaiacyl, syringyl, and *p*-hydroxyphenyl units. However, non-cellulosic polysaccharides, such as proteins, are also found in lower proportions under amino acid forms (Sari, 2015). Each component proportion present in the vegetal fibers depends on several parameters such as their nature, retting time, and geographic origin.

Maillard reactions are mainly responsible for the formation of flavor compounds like the 2-furanones with similar structures, unlike those of volatile substances issued from biofillers degradation. Besides the flavoring of food, the interest in Maillard mechanism has grown in fields concerned with the physico-chemical properties of proteins and polysaccharides (Mitsuo, 1988; He et al., 2014). This reaction implies the interaction between the amino group from an amino acid, a protein, or an amine and the carbonyl functional group from the carbohydrate part (glucose, fructose) under heating conditions (Zhang et al., 2008). It produces an unstable N-substituted glycosylamino compound. This first step is reversible but the generated glycosylamine is immediately converted into an Amadori compound (Newton et al., 2012). Amadori intermediate compounds belonging to the 1-amino-1-deoxy-2-ketoses family are important precursors in the formation of flavor compounds from Maillard reactions (Hodge et al., 1972; Zhang et al., 2008). Caramelized sugar aromas furanones, such as furfural and 5-methylfurfural, or pyranones such as maltol, evolving from holocellulose, are generated through sugar-amine condensation. Then, the formed Amadori compound can react along multiple pathways to form Maillard reaction products at lower temperatures than those found in pyrolysis studies of natural fibers, since the presence of nitrogen containing compounds catalyzes the reaction (Newton et al., 2012). For instance, maltol, a well-known carbohydrate derivative, and 4-hydroxy-2,5-dimethyl-3(2H)-furanone, derives from a common intermediate arising by sugar-amine condensation and Amadori rearrangement. 2,3-enolization of the 1-amino-1-deoxy-2-ketose and elimination of the 1-amino group occur at the final step (Hodge et al., 1972). Then, dehydrations and cyclization lead to furans generation (Wang et al., 2012) and ene-diol scissions and retroaldolization to short products (Belitz et al., 2004).

However, formations of the substances found in literature dealing with biomass and their controlled decomposition (pyrolysis)were not explained to be due to this mechanism. Indeed, the reactions involved require the presence of artificial catalysts (chromium, copper) facilitating the conversion (Binder et al., 2010; Perez and Fraga, 2014). Otherwise, when decomposition products are obtained from the pyrolysis process, this includes energetic conditions favorable enough (temperature reaching 800°C) that ring-opening, dehydrogenation, and cracking can occur (Sanders et al., 2003; Peng and Wu, 2011). Moreover, formation of other methylfurans that could issue from thermal decomposition and reactions between volatile chemicals emitted by natural fibers were not reported.

A one-year natural under-glass weathering of hemp fibers reinforced PP biocomposites was investigated to simulate a car interior environment. Volatile organic compounds emissions were assessed throughout the process. The objective was to use the identification of emitted VOCs to understand the components' method of degradation by firstly studying the neat polymer ageing and secondly the aging of the hemp fibers load

in the polymer matrix. The well-known Maillard mechanism for the holocellulose part decomposition has been examined thanks to VOCs identification. Reactions between identified VOCs and their concentration evolution were proposed. Finally, the lignin degradation was also investigated.

MATERIALS AND METHODS

Materials

Polypropylene grade H733-07 with a melt flow rate of 7.5 g/10 min (230°C, 2.16 kg) (Braskem, Brazil) was used as a polymer matrix. Hemp fibers were provided by AgroChanvre (France). Two hemp fibers loading, 10 wt% (PP10) and 30 wt% (PP30), were tested. Maleic anhydride grafted polypropylene (MA-g-PP), under the trademark Orevac CA100 (Arkema, France), was added at 3.1 wt% of PP as a coupling agent.

Process Conditions

Hemp fibers and MA-g-PP were dried for 15 h at 60°C. Then, granules of PP and MA-g-PP were mixed with hemp fibers in a BC21 Clextral twin-screw extruder (L/D = 36 with D = 25 mm) (Clextral, France) with the temperature profile 190-190-190-180-175-175-175°C and a screw speed of 220 rpm. Once dried for 3 days at 60°C, extruded pellets were injection molded into specimens in a Krauss Maffei machine (Krauss Maffei, Germany) at 210°C with an injection speed of 30 $cm^3 \cdot s^{-1}$. Square samples of 100 mm × 100 mm × 2 mm were obtained.

Weathering Conditions

Samples were exposed from September 2015 to September 2016 in the south west of France under windshield glass to simulate a car interior environment according to ISO 877-2:2011 (**Figure 1**). The exposition panels were oriented toward the south at 45° with the ground. The interior environment was naturally ventilated thanks to holes located on stainless steel boxes 2 h per day. Temperature T(°C) and relative humidity RH(%) were monitored and PP, PP10, and PP30 materials were sampled after 1, 2, 3, 6, 9, and 12 months. Temperatures ranged from −5°C in February to 91°C in August and relative humidity fluctuated between 3% in September and 95% in November.

FIGURE 1 | Under windshield glass exposure racks.

Sampling and Analytical Methodology

At each weathering step, three samples of each material were brought from the racks to the laboratory where VOCs emission analysis was carried out through a passive sampling method developed at the laboratory (Bourdin et al., 2014; Badji et al., 2018). It consists of two steps: firstly, a glass cell is placed on the material in order to isolate a part of its surface, and the VOCs are left to diffuse from the material to the air enclosed in the cell. When the VOCs concentration stabilizes, i.e., when material/air equilibrium is reached (Bourdin et al., 2014), a solid phase microextraction (SPME) fiber is introduced in the glass cell through a septum to sample emitted VOCs. Then, the SPME fiber is desorbed in the injector of a gas chromatograph (GC) coupled with mass spectrometer (MS) and flame ionization detector (FID; Varian, France) for identification and quantification of VOCs. The analytical procedure is detailed elsewhere (Bourdin and Desauziers, 2014). Both VOCs screening and specific analysis of formaldehyde and acetaldehyde, which are classified as carcinogen mutagenic and reprotoxic (CMR) substances, were performed (Chemical Risk Prevention Unit [CNRS], 2015). A polydimethylsiloxane–divinylbenzene–Carboxen fiber (PDMS/DVB/CAR, 50/30 μm) was selected for VOCs screening whereas a polydimethylsiloxane–divinylbenzene (PDMS/DVB, 65 μm) fiber impregnated with *O*-(2,3,4,5,6-pentafluorobenzyl)hydroxylamine hydrochloride (PFBHA) (Fluka, Switzerland) was used for formaldehyde and acetaldehyde (Koziel et al., 2001; Bourdin and Desauziers, 2014). The SPME fibers were purchased from Supelco (United States). A sampling temperature of 80°C was tested to simulate extreme car interior conditions. The extraction time was fixed at 5 min.

Quantitative Analysis

The methodology described above allows for determining the concentration (in $\mu g \cdot m^{-3}$) of VOCs at the material/air interface. That concentration is related to the emission rate of the considered substance by the first Fick law of diffusion under steady state conditions (Wittkowski et al., 1992). For the screening analysis using a PDMS–DVB–CAR fiber, VOCs were quantified as toluene equivalent using an FID response since it is proportional to the effective carbon atoms number in the molecule (Fedoruk and Kerger, 2003). Furfural and 2-furanmethanol, compounds specific to hemp fibers and listed as CMR substances (Chemical Risk Prevention Unit [CNRS], 2015), as well as formaldehyde and acetaldehyde, were specifically quantified as described in a previous paper (Badji et al., 2018). Standard gases of formaldehyde and acetaldehyde were generated by a permeation device (Badji et al., 2018). For the other standard VOCs (toluene, furfural, and 2-furanmethanol), a continuous syringe injection method was used, as described elsewhere (Nicolle et al., 2008; Desauziers, 2004). The detection limit and quantification limit are around 8 and 23 $\mu g \cdot m^{-3}$, respectively for

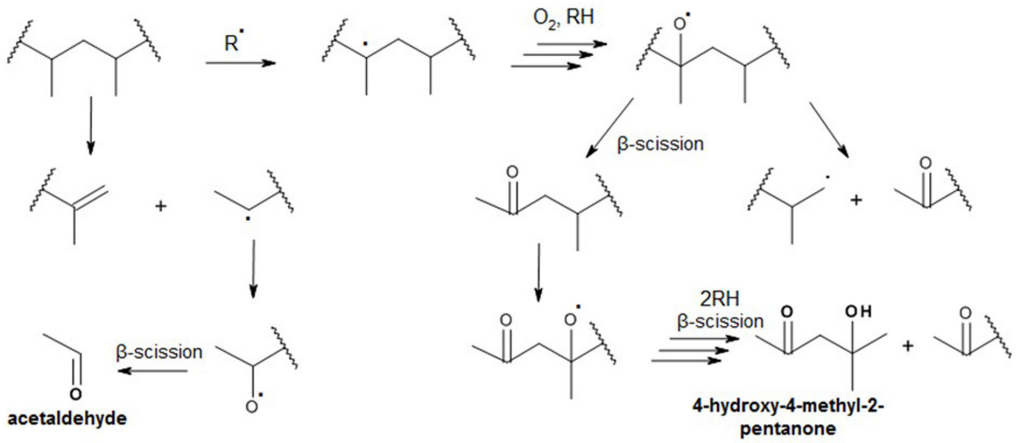

FIGURE 2 | PP degradation global scheme [Badji, 2017; from Bernstein et al. (2008)].

all compounds and the repeatability (relative standard deviation) is about 3% for three replicates.

RESULTS AND DISCUSSION

Polypropylene Oxidation

Some emitted VOCs were issued from the polymer degradation: long-chain aliphatic hydrocarbons and oxygenated products (linear ketones, aldehydes, and carboxylic acids). Acetic acid, acetone, and 2,4-pentanedione were the main compounds emitted by weathered PP. Some pathways are proposed in the literature to explain the formation of molecules containing a carbonyl functional group. Their mechanistic formation is found in literature (François-Heude et al., 2013; François-Heude et al., 2015). Mainly radical reactions lead to intermediate tertiary alkoxy radicals and their β-scission induces the previously identified carbonyl products (**Figure 2**). 2,4-pentanedione can result from the oxidation of methylketone issued from polymer chain reaction with unstable hydroperoxide. Moreover, 4-hydroxy-4-methyl-2-pentanone was also detected as high-level ketone (65 ± 13 and 82 ± 25 $\mu g \cdot m^{-3}$ for non-weathered and for one-year weathered PP, respectively (Badji et al., 2018). It has been proposed that it originates from the same methyl ketone precursor. Indeed, the hydroxyl formation resulting from the alkoxy radical reaction with hydrogen followed by scission could form 4-hydroxy-4-methyl-2-pentanone.

Formaldehyde and acetaldehyde were also released by the polymer and biocomposites. Their levels increased with the time of exposure. A polymer degradation way, similar to previous oxygenated chemicals pathway, could explain acetaldehyde generation with secondary alkoxy radical initiator responsible for this low molecular compound formation. Moreover, formaldehyde generation is reported according to the mechanism of Hoff and Jacobsson, which consists of the oxidation of primary alkyl radicals (Hoff and Jacobsson, 1982).

Alcohols, resulting from polymer degradation, could arise from intermediate alkoxy radicals. However, abstracts of a hydrogen from another molecule yields an hydroxyl group in tertiary carbon rather than a carbonyl group (Bernstein et al., 2008).

Cellulose and Hemicelluloses Degradation

Primary Decomposition

Two specifically quantified furan derivatives, furfural and 2-furanmethanol, were emitted at 1611 ± 20 and 2319 ± 176 $\mu g \cdot m^{-3}$, respectively by non-weathered PP30. Also, 5-methylfurfural (660 ± 30 $\mu g \cdot m^{-3}$), 5-methyl-2(3H)-furanone (40 ± 14 $\mu g \cdot m^{-3}$), furfuryl formate (38 ± 4 $\mu g \cdot m^{-3}$), and furfuryl acetate (43 ± 4 $\mu g \cdot m^{-3}$) evolved from biocomposites at the initial state. Apart from the last two compounds, these low molecular weight products were evidenced to be generated by holocellulose sequential degradation (Shen and Gu, 2009; Binder et al., 2010; Mäki-Arvela et al., 2012; Al-Shaal et al., 2015). **Figure 3** shows the formation pathways of degradation products identified in this study and issued from the carbohydrate part of hemp fibers. The nominated products were those identified as VOCs issued from biocomposites. The carbohydrates' degradation under high temperature involves the depolymerization of polysaccharides by the glycosidic bonds cleavage between D-glucose units (Wang et al., 2012). This process is followed by dehydrations, leading to D-glucopyranose and D-xylofuranose formation. The formation of 2- or 5-substituted furans is generally explained to occur via glucopyranose ring-opening pathway with acyclic forms such as hexoses and pentoses intermediates (Sanders et al., 2003; Binder et al., 2010). The further cyclization of these oses leads to the furans formation. Primary subsequent dehydration steps produced specifically followed furfural and 2-furanmethanol emitted at high concentrations by non-weathered biocomposites. In this mechanistic scheme, other cyclic molecules were derived from hydroxymethylfurfural, which was not detected in the conditions of this study. Otherwise, the generation of

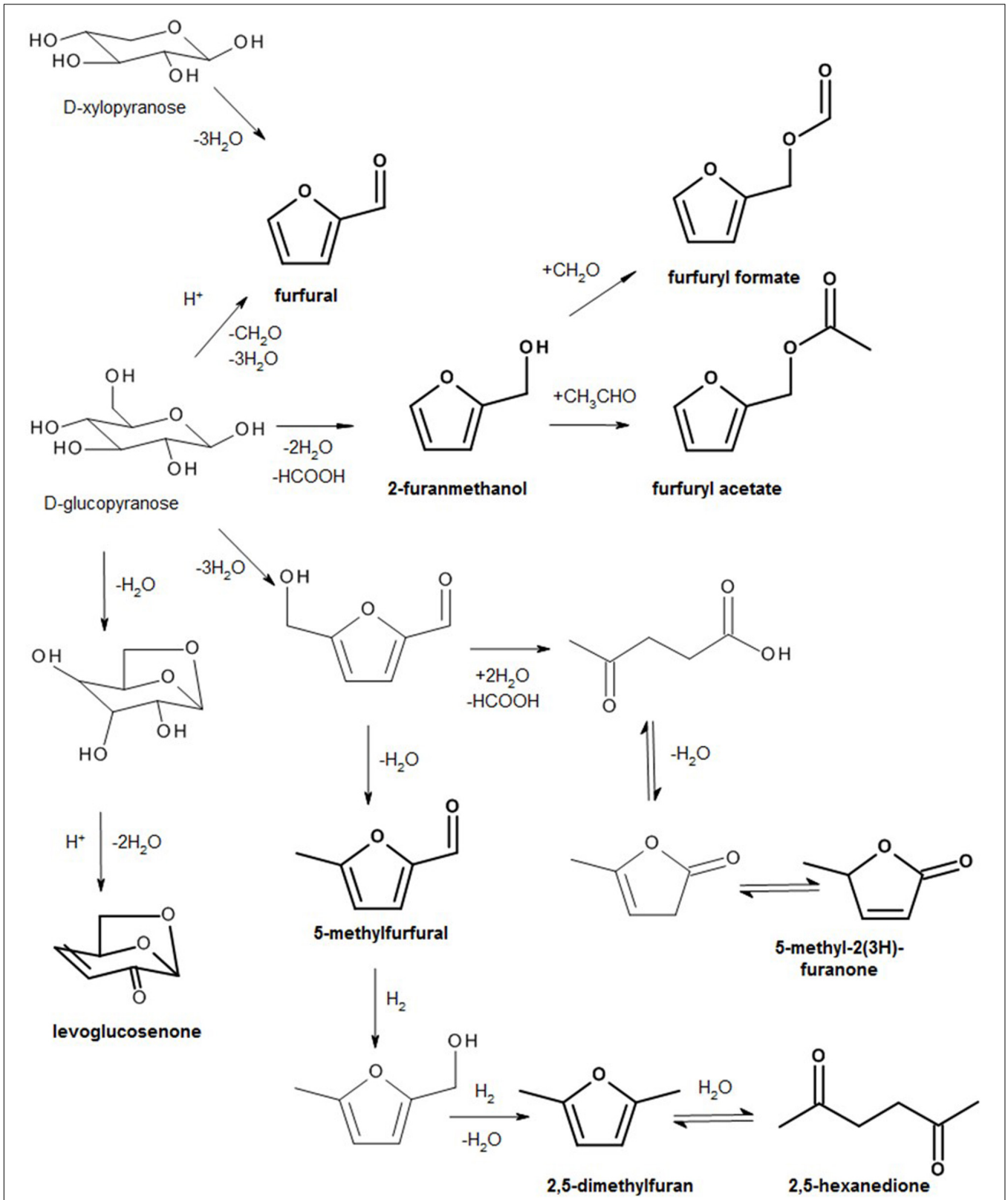

FIGURE 3 | Primary holocellulose decomposition products and their dehydrated derivatives through funneling pathways (Shen and Gu, 2009; Binder et al., 2010; Mäki-Arvela et al., 2012; Al-Shaal et al., 2015; Badji, 2017).

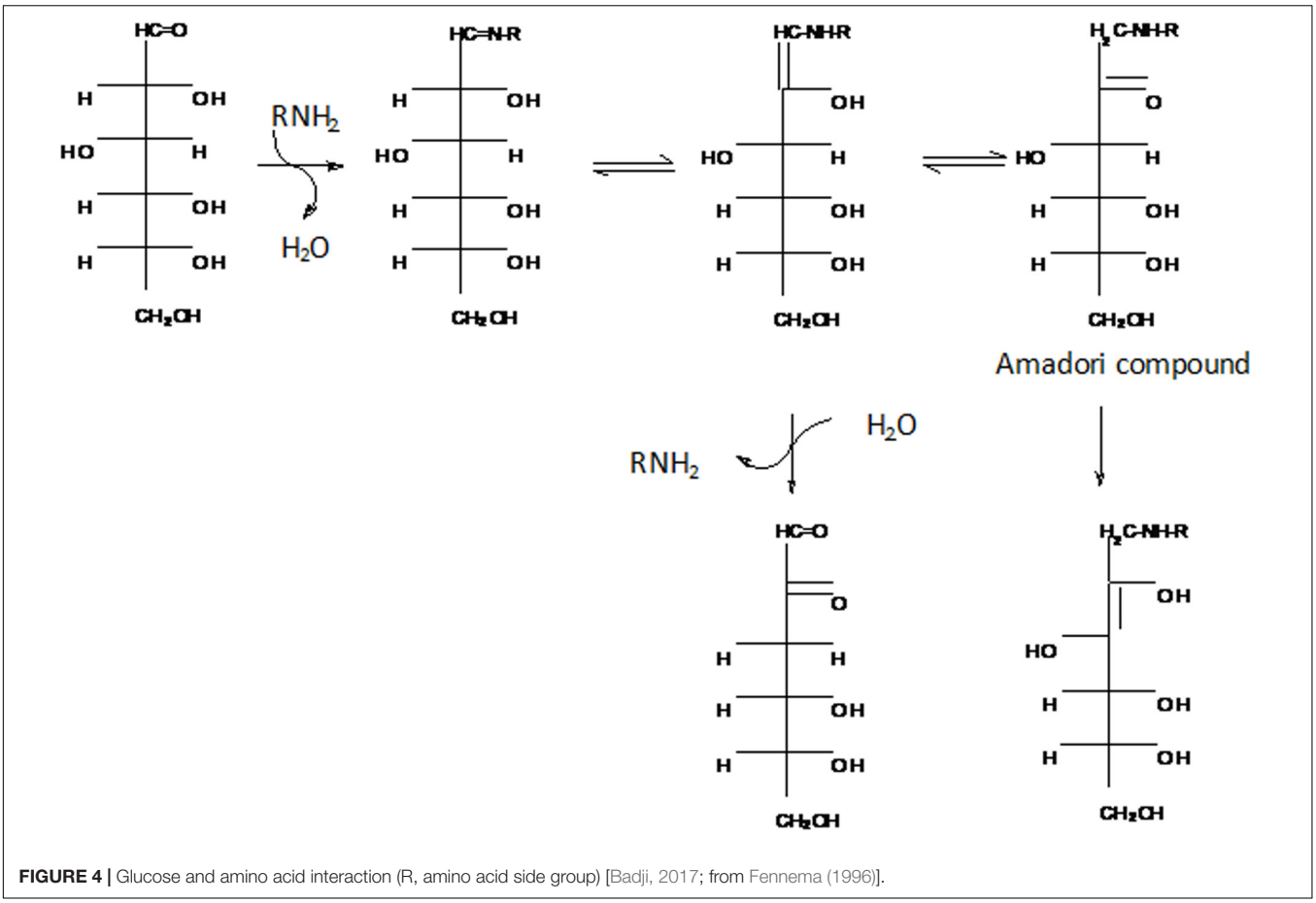

FIGURE 4 | Glucose and amino acid interaction (R, amino acid side group) [Badji, 2017; from Fennema (1996)].

levoglucosenone (97 ± 4 $\mu g \cdot m^{-3}$) derivative does not need the sugar ring-opening.

The products issued from the carbohydrate primary decomposition were mainly emitted by biocomposites at a non-weathered state. It has been supposed that generation could also be favored by Maillard reactions for which non-elevated temperatures (almost 100°C) are required (Newton et al., 2012) (chosen sampling temperature and those found in exposure racks do not exceed 91°C), contrary to the pyrolysis method. Indeed, until now, Maillard reactions have not supported the degradation pathways of vegetal fibers. However, either 1,2- or 2,3-enolization of the Amadori compound, previously mentioned in the introductory part, rising from aldoses such as glucose could effectively lead to furfural and hydroxymethylfurfural. Indeed, these compounds were already explained to originate from sugar-containing food, such as lactose, through Maillard reactions (Newton et al., 2012). But the same mechanism could justify the formation of the products detected here. Also, further intermediate dicarbonyls (reductones) formed after intra-rearrangement (enolization) are responsible for the autocatalytic character of the Maillard reaction (**Figure 4**). Moreover, as mentioned in the introductory part, proteins present in fibers could allow the glycosylamine precursor formation required for obtaining advanced Maillard reaction products. Otherwise, their presence is demonstrated by the detection of pyrazines emitted by biocomposites (methylpyrazine and N-acetyl-4(H)-pyridine at 25 ± 2 and 38 ± 4 $\mu g \cdot m^{-3}$, respectively for PP30). These secondary products of Strecker degradation are due to aminoketones condensation.

Contrary to other compounds, the formation of furfuryl formate and furfuryl acetate (total concentration of 81 ± 8 $\mu g \cdot m^{-3}$) aroused from non-weathered PP30 composite has not been reported in the literature. Here, it is suggested that they result from the interaction between the hydroxy functional groups of 2-furanmethanol and formaldehyde and acetaldehyde, respectively (**Figure 3**). Formaldehyde and acetaldehyde could also evolve from the Strecker degradation (Hodge et al., 1972; Newton et al., 2012) by β-scission. Indeed, for biocomposites, lots of aliphatic ketones and aldehydes such as 1-hydroxy-2-propanone, 1-acetyloxy-2-propanone, and nonanal are emitted at the highest levels of their chemical family: 420 ± 81, 366 ± 11, and 160 ± 28 $\mu g \cdot m^{-3}$, respectively, for unaged PP30. They were identified as hemp fibers by-products at a non-weathered state. These by-products could be linked to the reaction between amino acids and two-carbonyl compounds.

Secondary Decomposition

After weathering, mainly methyl substituted furanones deriving from carbohydrates were formed. They represented 13% of the level of ketones released by PP30 after one year of weathering,

whereas they only accounted for 8% of ketones by-products emitted by non-weathered PP30. Moreover, contrary to a non-weathered state, only furans compounds containing at least one substitution in 3 and 4 positions were identified after weathering. In addition, contrary to 2- and 5-substituted furanones presented in **Figure 3**, the explanation of 3- or 4-substituted furanones issued from vegetal fibers decomposition has not yet been reported in the literature. The proposed reactions featured in **Figure 5** involve the interaction between functional groups of identified volatile products. Substances that are designed by their names in **Figure 5** correspond to substances detected in this work. The first reaction (1) implies a radical attack in α position of

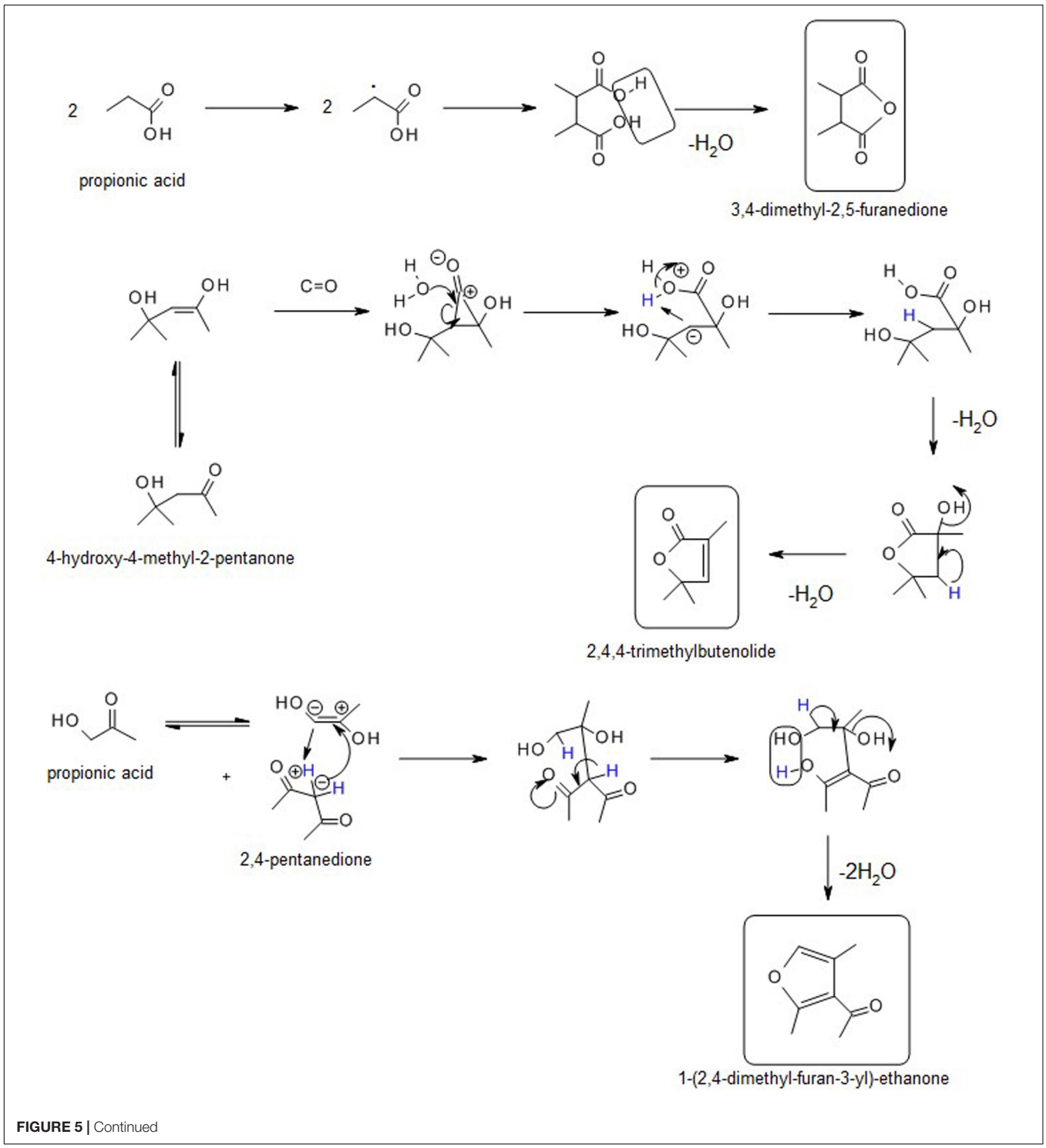

FIGURE 5 | Continued

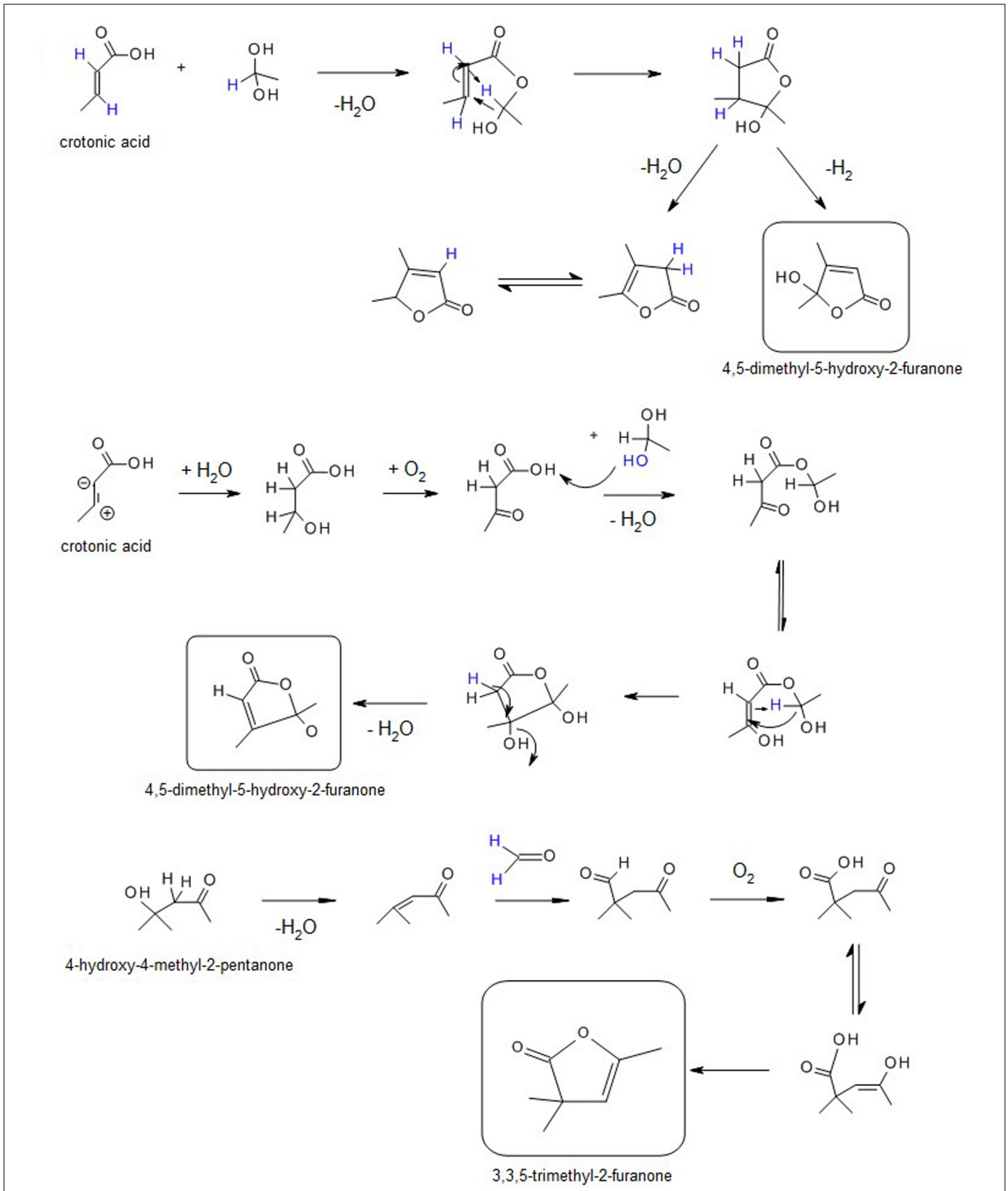

FIGURE 5 | Proposed reaction pathways of furan derivatives.

two identical propionic acid by-products, whose levels increased from 39 ± 4 to 839 ± 75 $\mu g \cdot m^{-3}$ and 56 ± 16 to 1403 ± 3 $\mu g \cdot m^{-3}$ for PP10 and PP30, respectively, via a photo-chemical method caused by ultraviolet (UV) rays. It is followed by the dehydration of the generated intermediate symmetrical molecule leading to an intramolecular cyclization giving 3,4-dimethyl-2,5-furanedione (118 ± 32 $\mu g \cdot m^{-3}$ for weathered PP30).

The reaction (2) occurs through the establishment of a keto-enolization equilibrium thermodynamically driven between the keto and enol forms of 4-hydroxy-4-methyl-2-pentanone (**Figure 5**). Moreover, this ketone was detected at an extremely high concentration after weathering (until almost 3000 $\mu g \cdot m^{-3}$ for PP30 after 12 months), especially for biocomposites. Then, the attack of the enone form via C=C hydroformylation by carbon monoxide leads to an instable compound formation. Its further hydrolysis induces a cyclopropane ring-opening. Thus, these two previous steps lead to the functionalization of a formic acid group. Then, two successive dehydrations firstly induce a cyclization into 2-furanone structure. After, the dehydroxylation in the 3-position induces a double bond formation to generate 2,4,4-trimethylbut-2-enolide. This volatile compound was emitted at the highest concentration of the 2-furanones group after one year of weathering. Indeed, since the group of 2-furanones products was emitted at 3285 ± 666 $\mu g \cdot m^{-3}$ by PP30 weathered for one year, 2,4,4-trimethylbut-2-enolide accounted for almost 40% (1314 ± 30 $\mu g \cdot m^{-3}$) for PP30 weathered for one year. This can be explained by the extremely high concentration of the 4-hydroxy-4-methyl-2-pentanone reactant previously mentioned, giving way to the formation of 2,4,4-trimethylbut-2-enolide.

1-(2,4-dimethyl-furan-3-yl)-ethanone, whose generation (1063 ± 243 $\mu g \cdot m^{-3}$ for PP30 and 1807 ± 149 $\mu g \cdot m^{-3}$ for PP10) is explained in pathway (3) of **Figure 5**, implies the reaction between propionic acid and 2,4-pentanedione, two volatile compounds emitted in high quantities. Indeed, propionic acid was emitted at almost 800 and 1400 $\mu g \cdot m^{-3}$ for PP10 and PP30, respectively, and a concentration of almost 7300 $\mu g \cdot m^{-3}$ of the 2,4-pentanedione was recorded for the two biocomposites after one year. The highly reactive C = C formed through keto-enolization tautomerism of propionic acid is opened by C3 of the diketone. Then, a further keto-enolization of the intermediate compound hydroxydiketone derivative is established and precedes dehydrations occurring in the final stage.

As regards reaction (4.1) shown in **Figure 5**, the esterification of crotonic acid favored by the condensation of ethanol hydrate hydroxyl group, a molecule easily generated from acetaldehyde hydration on crotonic acid, is followed by the removal of a water molecule. The C–C double bond initially present is opened after cyclization. This produces a 4-hydroxy-4,5-dimethyl-2-furanone. However, as it is difficult for the possible further dehydrogenation process to occur, the reaction (4.2) is an alternative to (4.1) that requires more energy than (4.2). This generates the previously explained structure (4-hydroxy-4,5-dimethyl-2-furanone) at the final stage. A similar esterification way of the diketone intermediate product, followed by a cyclization and dehydration, could explain its formation.

The same precursors as found in reaction (2) may be responsible for the 5-hydroxy-3,3,5-trimethyl-2-furanone formation [pathway (5) of **Figure 5**]. Indeed, the dehydration and hydroformylation of the methylpentanone due to its reactions with CO and O_2 lead to methyl substituted levulinic acid generation, a well-known biomass derivative (Al-Shaal et al., 2015), that finally cyclizes after its keto-enolization.

Some of these reactions may require high energy conditions to occur. However, the biomass inorganic part contains metals which could catalyze these reactions (Nowakowski and Jones, 2008).

Lignin Degradation

Primary Decomposition

Two methoxy-substituted phenols, vanillin and 4-vinylguaiacol, were emitted by non-weathered biocomposites. These two compounds are thought to originate from a primary decomposition of lignin favored in the heating conditions of ferulic acid, a well-known by-product evolving from lignin degradation, but not identified in this study (Coghe et al., 2004; Peleg et al., 1992).

Firstly, decarboxylation of ferulic acid may cause the formation of vinylguaiacol through (1.1) pathway (**Figure 6**; Coghe et al., 2004). Indeed, it is reported that temperatures ranging from 100 to 250°C (including the process temperature) cause severe damage to natural fibers' chemical structure through depolymerization, dehydration, or decarboxylation (Gassan and Bledzki, 2001). Vanillin is known to originate from the oxidation of 4-vinylguaiacol issued from lignin (1.2). The literature also proposed vanillin arises through the hydrolysis of the ferulic acid by-product (2.1) (Peleg et al., 1992). A further deacetylation could induce the formation of vanillin (2.2). This pathway could occur more easily than the vinylguaiacol or eugenol oxidation. Indeed, even if the decarboxylation consists in a naturally occurring step, the oxidation of carbon-carbon double bond must be catalyzed. Moreover, it has been shown that (2) pathways preferentially

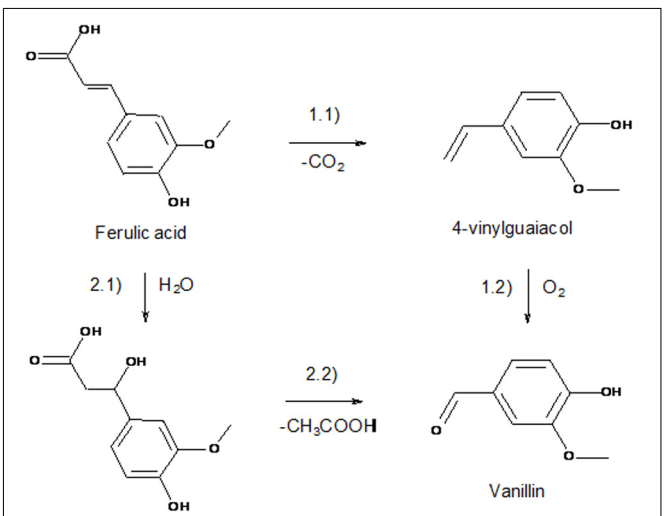

FIGURE 6 | Lignin primary by-products decomposition.

occur for obtaining vanillin than (1) ones (Peleg et al., 1992). Otherwise, the presence of metalloproteins containing iron, copper, and manganese might catalyze the by-products formation (Pollegioni et al., 2015).

Secondary Decomposition

3,5-dimethylphenol (3,5-xylenol) was continuously emitted by biocomposites during the weathering. It rose from 94 ± 30 $\mu g \cdot m^{-3}$ after 1 month to 471 ± 75 $\mu g \cdot m^{-3}$ (PP30) after 12 months of exposition for PP30. At high temperatures, these alkylated phenols are formed by C–O radical cleavage of the methoxy group and further coupling of phenolic radical with the methyl radical group (Wittkowski et al., 1992). However, alkylphenols can appear easily only under pyrolysis conditions of lignin allowing alkylation. In our study, the temperature conditions are not favorable enough to trigger methylation. Nevertheless, as discussed previously, several factors could still contribute to alkylphenols sourcing. Indeed, brown and white-root fungi are recognized to be able to demethoxylize lignin (Lopretti et al., 1998). Moreover, UV radiation leading to demethoxylation (Hon and Chang, 1984; Srinivas and Pandey, 2012) may explain the formation of xylenol emitted only once biocomposites were exposed to climatic conditions. In this work, it has been assumed that this abstraction can give way to combinations between methyl radicals issued from the demethylation of lignin allowed by *O*-demethylase enzymes active before the hemp fibers process (Peng et al., 2002) and phenol radical. Moreover, enzymes present in lignin and included in proteins could play the role of natural biocatalysts of these reactions before the process of biocomposites (Pollegioni et al., 2015). In addition, the retting process could favor micro-organisms formation, thereby accelerating by-products generation.

CONCLUSION

Since biocomposites are becoming more and more integrated in vehicles, knowledge about their aging and related mechanisms is needed. Therefore, the aim of this work was to rely on the structure of VOCs issued from non-weathered and under-glass-weathered PP and hemp fibers reinforced biocomposites to understand their degradation pathways. Reaction schemes were proposed according to volatile products that were identified in this study accordingly to an original and non-destructive sampling method.

Firstly, it was assumed that the primary decomposition of holocellulose and lignin in hemp fibers occurred at a non-weathered state whereas secondary decomposition was favored at a weathered state. Mainly 2- and 5-substituted furans were emitted by non-weathered biocomposites. Since the same precursors and the same nitrogen-containing chemicals evolved from non-weathered vegetal fibers decomposition as food thermal degradation, Maillard mechanism could be extrapolated to this study. 3-, 4-, and 5-substituted furanones were preferentially emitted after weathering. Some reactions between volatile products were proposed: they mainly involved keto-enolization, dehydration, and cyclization mechanisms. As regards lignin decomposition, methoxyphenols, detected at a non-weathered state, were explained by hydration and oxidation whereas dimethylphenol, evolved from weathered biocomposites, could originate from radical reactions.

However, the reactions implying dehydrogenation that produce 4,5-dimethyl-5-hydroxy-2-furanone (cellulose) and oxidation of vinyl specie to give vanillin (lignin) need highly favorable conditions to occur. Thus, activation energy calculation of the proposed reactions could be further modeled to check their occurrence feasibility. Also, the precise role of proteins and enzymes in carbohydrates and lignin degradation must be more deeply investigated. Additives such as light stabilizers or antioxidants incorporated in the materials can be used to limit dehydrations inducing sugar ring-opening and the impact of exposition to UV rays and high temperatures.

DATA AVAILABILITY STATEMENT

The datasets generated for this study are available on request to the corresponding author.

AUTHOR CONTRIBUTIONS

CB was the head of the whole project and drafted the manuscript. J-MS gave his expertise on the chemical pathways determination. HG helped for the weathering experiments. JB helped for VOCs measurements. AB and J-CB supervised the hemp fiber composite design and fabrication. VD was expert for the whole projet, designing it and supervising the COVs measurements. All the authors read and approved the manuscript.

REFERENCES

Ahmad, T., Maa, Z., Mohd Ishak, Z. A., Mat Taib, R., Rahim, S., and Jani, S. M. (2011). Natural Weathering of Kenaf Bast Fibre-Filled Poly(Butylene Succinate) Composites: effect of Fibre Loading and Compatibiliser Addition. *J. Polym. Environ.* 19, 263–273. doi: 10.1007/s10924-010-0272-2

Air quality sciences Inc. (2006). *Indoor Air Quality Hazards of New Cars*. Marietta, GA: Air quality sciences Inc, 47–51.

Al-Shaal, M. G., Ciptonugroho, W., Holzhäuser, F. J., Mensah, J. B., Hausoul, P. J. C., and Palkovits, R. (2015). Catalytic Upgrading of α-Angelica Lactone to Levulinic Acid Esters under Mild Conditions over Heterogeneous Catalysts. *Catal. Sci. Technol.* 5, 5168–5173. doi: 10.1039/C5CY00446B

Azwa, Z. N., Yousif, B. F., Manalo, A. C., and Karunasena, W. (2013). A Review on the Degradability of Polymeric Composites Based on Natural Fibres. *Mater. Design* 47, 424–442. doi: 10.1016/j.matdes.2012.11.025

Badji, C. (2017). *Vieillissement de Matériaux Composites Renforcés de Fibres Naturelles: Étude de l'impact Sur Les Propriétés d'aspect et Sur Les Émissions Dans l'air Intérieur*. France: Université de Pau et des Pays de l'Adour.

Badji, C., Beigbeder, J., Garay, H., Bergeret, A., Bénézet, J. C., and Desauziers, V. (2018). Under Glass Weathering of Hemp Fibers reinforced polypropylene biocomposites: impact of volatile organic compounds emissions on indoor air

quality. *Polym. Degrad. Stabil.* 149, 85–95. doi: 10.1016/j.polymdegradstab.2018.01.020

Badji, C., Soccalingame, L., Garay, H., Bergeret, A., and Bénézet, J.-C. (2017). Influence of weathering on visual and surface aspect of wood plastic composites: correlation approach with mechanical properties and microstructure. *Polym. Degrad. Stabil.* 137, 162–172. doi: 10.1016/j.polymdegradstab.2017.01.010

Belitz, H.-D., Grosch, W., and Schieberle, P. (2004). "Aroma compounds," in *Food Chemistry*, ed. M. Dekker (Boca Raton, FL: CRC Press), 340–402. doi: 10.1007/978-3-662-07279-0

Bernstein, R., Thornberg, S. M., Irwin, A. N., Hochrein, J. M., Derzon, D. K., Klamo, S. B., et al. (2008). Radiation-oxidation mechanisms: volatile organic degradation products from polypropylene having selective C-13 labeling studied by GC/MS. *Polym. Degrad. Stabil.* 93, 854–870. doi: 10.1016/j.polymdegradstab.2008.01.020

Binder, J. B., Blank, J. J., Cefali, A. V., and Raines, R. T. (2010). Synthesis of Furfural from Xylose and Xylan. *ChemSusChem* 3, 1268–1272. doi: 10.1002/cssc.201000181

Bourdin, D., and Desauziers, V. (2014). Development of SPME On-Fiber Derivatization for the Sampling of Formaldehyde and Other Carbonyl Compounds in Indoor Air. *Anal. Bioanal. Chem.* 406, 317–328. doi: 10.1007/s00216-013-7460-6

Bourdin, D., Mocho, P., Desauziers, V., and Plaisance, H. (2014). Formaldehyde emission behavior of building materials: on-site measurements and modeling approach to predict indoor air pollution. *J. Hazard. Mater.* 280, 164–173. doi: 10.1016/j.jhazmat.2014.07.065

Brzonova, I., Kozliak, E., Kubátová, A., Chebeir, M., Qin, W., Christopher, L., et al. (2014). "Kenaf Biomass Biodecomposition by Basidiomycetes and Actinobacteria in Submerged Fermentation for Production of Carbohydrates and Phenolic Compounds. *Bioresour. Technol.* 173, 352–360. doi: 10.1016/j.biortech.2014.09.057

Carrier, M., Loppinet-Serani, A., Absalon, C., Aymonier, C., and Mench, M. (2012). Degradation Pathways of Holocellulose, Lignin and Alpha-Cellulose from *Pteris Vittata* fronds in sub- and super critical conditions. *Biomass Bioenergy* 43, 65–71. doi: 10.1016/j.biombioe.2012.03.035

Chemical Risk Prevention Unit [CNRS] (2015). *European Harmonised Classification and Labelling of Carcinogenic, Mutagenic and Toxic for Reproduction (CMR) Substances According to the Criteria of the CLP Regulation*. Paris: CNRS.

Coghe, S., Benoot, K., Delvaux, F., Vanderhaegen, B., and Delvaux, F. R. (2004). "Ferulic Acid Release and 4-Vinylguaiacol formation during brewing and fermentation: indications for Feruloyl esterase activity in *Saccharomyces cerevisiae*. *J. Agric. Food Chem.* 52, 602–608. doi: 10.1021/jf0346556

Desauziers, V. (2004). Traceability of Pollutant Measurements for Ambient Air Monitoring. *Trends Anal. Chem.* 23, 252–260. doi: 10.1016/S0165-9936(04)00310-3

Dorez, G., Taguet, A., Ferry, L., and Lopez-Cuesta, J. M. (2013). Thermal and fire behavior of natural Fibers/PBS biocomposites. *Polym. Degrad. Stabil.* 98, 87–95. doi: 10.1016/j.polymdegradstab.2012.10.026

Fedoruk, M. J., and Kerger, B. D. (2003). Measurement of volatile organic compounds inside automobiles. *J. Expo. Anal. Environ. Epidemiol.* 13, 31–41. doi: 10.1038/sj.jea.7500250

Fennema, O. R. (1996). *Food Chemistry*, 3rd Edn, ed. M. Dekker (Boca Raton, FL: CRC Press).

François-Heude, A., Richaud, E., Desnoux, E., and Colin, X. (2014). Influence of Temperature, UV-Light wavelength and intensity on polypropylene photothermal oxidation. *Polym. Degrad. Stabil.* 100, 10–20. doi: 10.1016/j.polymdegradstab.2013.12.038

François-Heude, A., Richaud, E., Desnoux, E., and Colin, X. (2015). A general kinetic model for the Photothermal Oxidation of polypropylene. *J. Photochem. Photobiol. A* 296, 48–65. doi: 10.1016/J.JPHOTOCHEM.2014.08.015

François-Heude, A., Richaud, E., Leprovost, J., Heninger, M., Mestdagh, H., Desnoux, E., et al. (2013). Real-Time quantitative analysis of volatile products generated during solid-state Polypropylene thermal oxidation. *Polym. Testing* 32, 907–917. doi: 10.1016/j.polymertesting.2013.04.008

Gassan, J., and Bledzki, A. K. (2001). Thermal Degradation of Flax and Jute Fibers. *J. Appl. Polym. Sci.* 82, 1417–1422. doi: 10.1002/app.1979

He, C., Chen, C. L., Giannis, A., Yang, Y., and Wang, J. Y. (2014). Hydrothermal Gasification of Sewage Sludge and Model Compounds for Renewable Hydrogen Production: a Review. *Renew. Sustain. Energy Rev.* 39, 1127–1142. doi: 10.1016/j.rser.2014.07.141

Hodge, J. E., Mills, F. D., and Fisher, B. E. (1972). Compounds of browned flavor derived from sugar-amine reactions. *Am. Assoc. Cereal Chem.* 17, 34–40.

Hoff, A., and Jacobsson, S. (1982). Thermal oxidation of Polypropylene close to industrial processing conditions. *J. Appl. Polym. Sci.* 27, 2539–2551. doi: 10.1002/app.1982.070270723

Hon, D. N.-S., and Chang, S.-T. (1984). Surface degradation of wood by ultraviolet light. *J. Polym. Sci.* 22, 2227–2241. doi: 10.1002/pol.1984.170220923

John, M., and Thomas, S. (2008). Biofibres and biocomposites. *Carbohydr. Polym.* 71, 343–364. doi: 10.1016/j.carbpol.2007.05.040

Katō, K., and Komorita, H. (1968). Pyrolysis of cellulose. *Agricult. Biol. Chem.* 32, 21–26. doi: 10.1080/00021369.1968.10859016

Khazaeian, A., Ashori, A., and Dizaj, M. Y. (2015). Suitability of Sorghum stalk fibers for production of particleboard. *Carbohydr. Polym.* 120, 15–21. doi: 10.1016/j.carbpol.2014.12.001

Kim, H.-S., Kim, S., Kim, H.-J., and Kim, H.-G. (2006). Physico-Mechanical Properties, Odor and VOC Emission of Bio-Flour-Filled Poly(Propylene) Bio-Composites with Different Volcanic Pozzolan contents. *Macromol. Mater. Eng.* 291, 1255–1264. doi: 10.1002/mame.200600212

Kim, H.-S., Lee, B.-H., Kim, H.-J., and Yang, H.-S. (2011). Mechanical–Thermal Properties and VOC emissions of natural-flour-filled biodegradable polymer hybrid bio-composites. *J. Polym. Environ.* 19:628. doi: 10.1007/s10924-011-0313-5

Koziel, J. A., Noah, J., and Pawliszyn, J. (2001). Field sampling and determination of Formaldehyde in indoor air with solid-phase Microextraction and on-Fiber Derivatization. *Environ. Sci. Technol.* 35, 1481–1486. doi: 10.1021/es001653i

Kumre, A., Rana, R. S., and Purohit, R. (2017). A review on mechanical property of sisal glass Fiber Reinforced polymer composites. *Mater. Today* 4, 3466–3476. doi: 10.1016/J.MATPR.2017.02.236

Liu, Y., and Hu, H. (2008). X-Ray Diffraction Study of Bamboo Fibers Treated with NaOH. *Fibers Polym.* 9, 735–739. doi: 10.1007/s12221-008-0115-0

Lopretti, M., Cabella, D., Morais, J., and Rodrigues, A. (1998). Demethoxylation of Lignin-Model Compounds with Enzyme Extracts from Gloeophilum Trabeum. *Process Biochem.* 33, 657–661. doi: 10.1016/S0032-9592(98)00028-4

Mäki-Arvela, P., Salminen, E., Riittonen, T., Virtanen, P., Kumar, N., and Mikkola, J. P. (2012). The Challenge of Efficient Synthesis of Biofuels from Lignocellulose for future renewable transportation fuels. *Int. J. Chem. Eng.* 2012:674761. doi: 10.1155/2012/674761

Mitsuo, N. (1988). "Chemistry of Maillard reactions: recent studies on the browning reaction mechanism and the development of antioxydants and mutagens," in *Advances in Food Research*, Vol. 32, eds C. O. Chichester and B. S. Schweigert (Amsterdam: Elsevier Inc), 116–143.

Muasher, M., and Sain, M. (2006). The efficacy of photostabilizers on the color change of wood filled plastic composites. *Polymer Degrad. Stabil.* 91, 1156–1165. doi: 10.1016/j.polymdegradstab.2005.06.024

Newton, A. E., Fairbanks, A. J., Golding, M., Andrewes, P., and Gerrard, J. A. (2012). The Role of the Maillard Reaction in the formation of flavour compounds in dairy products - not only a deleterious reaction but also a rich source of flavour compounds. *Food Funct.* 3, 1231–1241. doi: 10.1039/c2fo30089c

Nicolle, J., Desauziers, V., and Mocho, P. (2008). Solid Phase Microextraction sampling for a rapid and simple on-site evaluation of volatile organic compounds emitted from building materials. *J. Chromatogr. A* 1208, 10–15. doi: 10.1016/j.chroma.2008.08.061

Nowakowski, D. J., and Jones, J. M. (2008). Uncatalysed and Potassium-catalysed pyrolysis of the cell-wall constituents of biomass and their model compounds. *J. Anal. Appl. Pyroly.* 83, 12–25. doi: 10.1016/j.jaap.2008.05.007

Peleg, H., Naim, M., Zehavi, U., Rouseff, R. L., and Nagy, S. (1992). Pathways of 4-Vinylguaiacol Formation from Ferulic Acid in Model Solutions of Orange Juice. *J. Agric. Food Chem.* 40, 764–767. doi: 10.1021/jf00017a011

Peng, X., Masai, E., Kitayama, H., Harada, K., Katayama, Y., and Fukuda, M. (2002). Characterization of the 5-Carboxyvanillate Decarboxylase Gene and Its Role in Lignin-Related Biphenyl Catabolism in Sphingomonas Paucimobilis SYK-6. *Appl. Environ. Microbiol.* 68, 4407–4415. doi: 10.1128/AEM.68.9.4407

Peng, Y., and Wu, S. (2011). Fast pyrolysis characterisctics of sugarcane bagasse hemicellulose. *Cell. Chem. Technol.* 45, 605–612.

Perez, R. F., and Fraga, M. A. (2014). Hemicellulose-derived chemicals: one-step production of furfuryl alcohol from Xylose. *Green Chem.* 16:3942. doi: 10.1039/C4GC00398E

Pollegioni, L., Tonin, F., and Rosini, E. (2015). Lignin-degrading enzymes. *FEBS J.* 282, 1190–1213. doi: 10.1111/febs.13224

Rabek, J. F. (1990). *Photostabilization of Polymers: Principles and Applications*. Amsterdam: Elsevier, doi: 10.1007/978-94-009-07-47-8

Rouillon, C., Bussiere, P. O., Desnoux, E., Collin, S., Vial, C., Therias, S., et al. (2016). Is Carbonyl Index a Quantitative Probe to Monitor Polypropylene Photodegradation? *Polym. Degrad. Stabil.* 128, 200–208. doi: 10.1016/j.polymdegradstab.2015.12.011

Saba, N., Jawaid, M., Alothman, O. Y., and Paridah, M. T. (2016). A review on dynamic mechanical properties of natural fibre reinforced polymer composites. *Construct. Build. Mater.* 106, 149–159. doi: 10.1016/J.CONBUILDMAT.2015.12.075

Sanders, E. B., Goldsmith, A. I., and Seeman, J. I. (2003). A Model That Distinguishes the Pyrolysis of D-Glucose, d-Fructose, and sucrose from that of cellulose. application to the understanding of cigarette smoke formation. *J. Anal. Appl. Pyrolys.* 66, 29–50. doi: 10.1016/S0165-2370(02)00104-3

Sari, Y. W. (2015). *Biomass and Its Potential for Protein and Amino Acids; Valorizing Agricultural by-Products*. PhD thesis, Wageningen University, Wageningen.

Shen, D. K., and Gu, S. (2009). The mechanism for thermal decomposition of cellulose and its main products. *Bioresour. Technol.* 100, 6496–6504. doi: 10.1016/j.biortech.2009.06.095

Shibata, S. (2016). *Natural Fiber Composites*. Amsterdam: Elsevier, 157–173.

Srinivas, K., and Pandey, K. K. (2012). Photodegradation of Thermally Modified Wood. *J. Photochem. Photobiol. B* 117, 140–145. doi: 10.1016/j.jphotobiol.2012.09.013

Van Schoors, L., Gueguen, M. M., Moscardelli, S., Rabii, H., and Davies, P. (2018). Antioxidant Properties of Flax Fibers in Polyethylene matrix composites. *Indus. Crops Products* 126, 333–339. doi: 10.1016/J.INDCROP.2018.09.047

Wang, S., Guo, X., Liang, X. T., Zhou, Y., and Luo, Z. (2012). Mechanism research on cellulose Pyrolysis by Py-GC/MS and subsequent density functional theory studies. *Bioresour. Technol.* 104, 722–728. doi: 10.1016/j.biortech.2011.10.078

Wittkowski, R., Ruther, J., Drinda, H., and Rafiei-Taghanaki, F. (1992). Formation of Smoke Flavor Compounds by Thermal Lignin Degradation. *ACS Symposium Series* 490, 232–243. doi: 10.1021/bk-1992-0490.ch018

Yu, C., and Crump, D. (1998). A review of the emission of VOCs from Polymeric materials used in buildings. *Build. Environ.* 33, 357–374. doi: 10.1016/S0360-1323(97)00055-3

Zhang, Q., Ames, J. M., Smith, R. D., Baynes, J. W., and Metz, T. O. (2008). A perspective on the Maillard reaction and the analysis of protein Glycation by mass spectrometry: probing the pathogenesis of Chronic disease. *J. Proteome Res.* 8, 754–769. doi: 10.1021/pr800858h

Zou, P., Xiong, H., and Tang, S. (2008). Natural Weathering of Rape Straw Flour (RSF)/HDPE and Nano-SiO2/RSF/HDPE composites. *Carbohydr. Polymers* 73, 378–383. doi: 10.1016/j.carbpol.2007.12.002

Conflict of Interest: The authors declare that the research was conducted in the absence of any commercial or financial relationships that could be construed as a potential conflict of interest.

frontiers in Materials

CORRECTION
published: 06 November 2020
doi: 10.3389/fmats.2020.00266

Corrigendum: Under Glass Weathering of Hemp Fibers Reinforced Polypropylene Biocomposites: Degradation Mechanisms Based on Emitted Volatile Organic Compounds

*Célia Badji[1,2], Jean-Marc Sotiropoulos[3], Joana Beigbeder[1], Hélène Garay[1], Anne Bergeret[2], Jean-Charles Bénézet[2] and Valérie Desauziers[1]**

[1] IPREM, IMT Mines Ales, Universite de Pau et des Pays de l'Adour, E2S UPPA, CNRS, Pau, France, [2] PCH, IMT Mines Ales, Ales, France, [3] IPREM, Universite de Pau et des Pays de l'Adour, E2S UPPA, CNRS, Pau, France

Keywords: hemp fiber, ageing, VOCs, oxidation, dehydration

OPEN ACCESS

Approved by:
Frontiers Editorial Office, Frontiers Media SA, Switzerland

****Correspondence:***
Valérie Desauziers
valerie.desauziers@mines-ales.fr

Specialty section:
This article was submitted to Polymeric and Composite Materials, a section of the journal Frontiers in Materials

Received: *16 July 2020*
Accepted: *17 July 2020*
Published: *06 November 2020*

Citation:
Badji C, Sotiropoulos J-M, Beigbeder J, Garay H, Bergeret A, Bénézet J-C and Desauziers V (2020) Corrigendum: Under Glass Weathering of Hemp Fibers Reinforced Polypropylene Biocomposites: Degradation Mechanisms Based on Emitted Volatile Organic Compounds. Front. Mater. 7:266. doi: 10.3389/fmats.2020.00266

A Corrigendum on

Under Glass Weathering of Hemp Fibers Reinforced Polypropylene Biocomposites: Degradation Mechanisms Based on Emitted Volatile Organic Compounds
by Badji, C., Sotiropoulos, J.-M., Beigbeder, J., Garay, H., Bergeret, A., Bénézet, J.-C., et al. (2020). Front. Mater. 7:162. doi: 10.3389/fmats.2020.00162

In the published article, there was an error in affiliations 2 and 3.

Affiliation 2: Instead of "IPREM, Universite de Pau et des Pays de l'Adour, E2S UPPA, CNRS, Pau, France," it should be "**PCH, IMT Mines Ales, Ales, France**."

Affiliation 3: Instead of "PCH, IMT Mines Ales, Ales, France," it should be "**IPREM, Universite de Pau et des Pays de l'Adour, E2S UPPA, CNRS, Pau, France**."

The authors apologize for this error and state that this does not change the scientific conclusions of the article in any way. The original article has been updated

frontiers in Materials

ORIGINAL RESEARCH
published: 16 July 2020
doi: 10.3389/fmats.2020.00169

Fiber Orientation Distribution Predictions for an Injection Molded Venturi-Shaped Part Validated Against Experimental Micro-Computed Tomography Characterization

María C. Quintana[1], Patricia M. Frontini[1], Aitor Arriaga[2], Bernhard Plank[3] and Zoltan Major[4]*

[1] Instituto de Investigaciones en Ciencia y Tecnología de Materiales (INTEMA), Universidad Nacional de Mar del Plata, Mar del Plata, Argentina, [2] Leartiker-Lea Artibai Ikastetxea, Markina-Xemein, Spain, [3] Technology & Environmental Sciences Department, University of Applied Sciences Upper Austria, Wels, Austria, [4] Institut für Polymer Product Engineering (IPPE), Johannes Kepler Universität Linz, Linz, Austria

OPEN ACCESS

Edited by:
Emilia Morallon, University of Alicante, Spain

Reviewed by:
Jyrki Vuorinen, Tampere University of Technology, Finland
Antonio Greco, University of Salento, Italy

***Correspondence:**
María C. Quintana
cquintana@fi.mdp.edu.ar

Specialty section:
This article was submitted to Polymeric and Composite Materials, a section of the journal Frontiers in Materials

Received: *23 March 2020*
Accepted: *07 May 2020*
Published: *16 July 2020*

Citation:
Quintana MC, Frontini PM, Arriaga A, Plank B and Major Z (2020) Fiber Orientation Distribution Predictions for an Injection Molded Venturi-Shaped Part Validated Against Experimental Micro-Computed Tomography Characterization. Front. Mater. 7:169. doi: 10.3389/fmats.2020.00169

This work evaluates and compares the accuracy of different fiber orientation prediction models for a short fiber reinforced injection molded Venturi-shaped part which displays variable thickness. The experimental characterization of the specimen fiber orientation distribution (FOD) was carried out by the micro computed tomography technique (micro-CT). The computational study of fiber orientation predictions was performed using Moldex3D. All the possible combinations of the Folgar-Tucker (FT) and improved Anisotropic Rotary Diffusion (iARD) rotary diffusion models and the Hybrid (Hyb), Orthotropic (ORE), and Invariant Based Optimal Fitting (IBOF) closure approximations were considered. The relevance of the Retardant Principal Rate (RPR) model on predictions results was also evaluated. The values of the fiber-fiber (Ci), matrix-fiber (Cm) interaction coefficients and the alpha-RPR parameter were varied in a significant range in order to find the set of parameters that better fits the experimental fiber orientation data. The parameters' sensitivity effect over the second order orientation tensor components was quantified via the Analysis of Variance (ANOVA) statistical method. The experimental micro-CT results show an increase in the fiber orientation degree at the specimen constriction region due to the narrowed cavity and the Venturi effect. The comparison of the experimental and predicted orientation profiles demonstrates that the predictions of the iARD model, in combination with the IBOF closure approximation, are the most accurate for the case studied. However, simulations fail to estimate the change in orientation caused by variable thickness and section. ANOVA results prove that the orientation tensor component in the flow direction (a_{11}) is more sensitive to changes in alpha-RPR and Ci coefficient, while the perpendicular components (a_{22}, a_{33}) are also

significantly affected by Cm. From the predictive error analysis it is seen that the optimal parameters set to capture the orientation state of the specimen is: (i) for the FT model, Ci = 0.005, alpha-RPR = 0.7 and (ii) for the iARD model, Ci = 0.005, Cm = 0.2, and alpha-RPR = 0.7.

Keywords: short-fiber composites, micro-CT characterization, injection molding simulation, rotary diffusion models, closure approximations, experimental validation

INTRODUCTION

Fiber orientation distribution (FOD) prediction consists of determining the degree of fiber alignment as a function of the location through the part. The state of fiber orientation depends upon a molten polymer fluid dynamic coupled with the movement of the fibers in polymer suspension. Thus, both fiber-fiber and polymer-fiber interactions must be taken into account in a pertinent analysis. The models that predict fiber orientation state in concentrated suspensions incorporate the effect of the interaction between fibers as a rotary diffusion term. The Folgar-Tucker model (FT) (Folgar and Tucker, 1984) considers an isotropic rotary diffusion term. The Anisotropic Rotary Diffusion (ARD) models and their improvements (iARD) (Wang et al., 2008; Phelps and Tucker, 2009; Tseng et al., 2016) define an anisotropic rotary diffusion term. On the other hand, the Retardant principal Rate model (RPR) (Tseng et al., 2016) and the Reduced Strain Closure (RSC) (Wang et al., 2008) account for the quick evolution of the FT model and correct it.

Another aspect concerning prediction approaches arises from the use of tensors to describe fiber orientation states (Advani and Tucker, 1987). The evolution equation of the fiber orientation models involves a fourth-order orientation tensor which must be approximated in a mathematically closed expression in order to compute fiber orientation data. A complete summary of existing closure approximations can be found in Zheng et al. (2011). The most commonly used closure approximations are the Hybrid (Hyb) (Advani and Tucker, 1990), the Orthotropic family or Eigenvalue Based Optimal Fitting (EBOF) (Cintra and Tucker, 1995)–among them the denominated ORE–and the Invariant Based Optimal Fitting (IBOF) (Chung and Kwon, 2002).

Most fiber orientation experimental validation works available in the literature mainly focus on the use of two analytical geometries: the center-gated disk and the end-gated plate, which are uniform and display well-known flow patterns (Bay and Tucker, 1992; Gupta and Wang, 1993; Greene and Wilkes, 1997; Papathanasiou, 1997; Larsen, 2000). Two exceptions are found in Kleindel et al. (2015) and Tseng et al. (2018), which use a complex thick-walled piece and a traction bar with a welding line, respectively. Besides, in the past few years, some valuable efforts have been made to develop new closure approximations for the fourth order orientation tensor (Montgomery-Smith et al., 2011; Kuzmin, 2018) as well as to compare the accuracy of the existing mathematically closed expressions (Chung and Kwon, 2000; Wang and Jin, 2010). In these articles, the mentioned typical analytical geometries are also chosen for validation purposes.

Regarding the experimental characterization of the fiber orientation, the typical method used to determine their distribution is a two-dimensional technique based on optical microscopy, which is called the method of ellipses (MoE). The MoE implies the sectioning and polishing of the samples, i.e., it is a destructive technique, followed by optical microscopy or scanning electron microscopy (SEM) in order to determine the in-plane and out-of-plane angles of the projected fibers from the surface characterization. This method has certain limitations, such as the ambiguity in determining the 3D fiber orientation and the difficulty in achieving a proper FOD characterization over a representative area/volume of the material (McGee and McCullough, 1984; Vélez-Garcia, 2012; Sharma et al., 2018; Hanhan et al., 2019). Alternatively, in recent years the application of three-dimensional techniques, such as micro-CT scanning, have become really appealing for non-destructively characterizing composites' microstructural features (Salaberger et al., 2011; Emerson et al., 2017; Hanhan et al., 2019). However, there are few studies using these techniques to validate predictions given by simulation (Kleindel et al., 2015; Tseng et al., 2018).

Taking into account the scope of the previous contributions, the objective of this work is to validate the most relevant fiber orientation models and closure approximations in a specimen different from those already studied–but with characteristics that can be extrapolated to many injected parts—using the novel experimental micro-CT technique to test the accuracy of the predictions. Specifically, the injected part studied here consists of a Venturi-shaped tube that displays variable thickness. The specimen is made of polyamide and it is reinforced with short glass fiber (40 wt%).

This work presents: (i) a brief overview of the fiber orientation prediction models and closure approximations deemed to be evaluated (these being the FT, iARD, and RPR models, and the Hyb, ORE and IBOF closures); (ii) a description of the experimentally measured fiber orientation distribution; (iii) a computational study performed using the injection molding simulation software Moldex3D R.13 to explore the effect of the models and closures on fiber orientation predictions; (iv) a statistical study via the Analysis of Variance (ANOVA) technique to investigate the effect of the models parameters (fiber-fiber Ci and matrix-fiber Cm interaction coefficients and alpha-RPR parameter) on the predicted components of the second order orientation tensor; and (v) a quantitative determination of the FT and iARD prediction errors.

BACKGROUND

The hydrodynamic effect of the fluid flow over the motion of an infinite aspect ratio particle was first described by Jeffery (2012). This theory applies to dilute suspensions but it has been shown to provide practical qualitative agreement with simple shear flow experiments under certain conditions. Folgar and Tucker (1984) have considered the evolution of the fiber orientation state of non-dilute fiber suspensions as a diffusive process, adding to the theoretical model of Jeffery's Hydrodynamic an isotropic rotary diffusion term to model the randomizing effect of the interaction between fibers. The isotropic rotary diffusion is proportional to the scalar rate of deformation, being the constant of proportionality to a scalar parameter named the interaction coefficient (Ci), adjusted to fit with experimental data. Due to its acceptable accuracy for the prediction of the fiber orientation state in semi-concentrated suspensions, the Folgar-Tucker model (FT) has been the most frequently used for the estimation of the local fiber orientation distribution in the simulation of SFRC so far.

However, the FT model does not match all of the aspects of experimental discontinuous fiber orientation data. For instance, in concentrated suspensions fibers tend to align more slowly with respect to the strain rate than the models based on the Jeffery's equation predict, especially for composites with long discontinuous fibers (Wang et al., 2008; Phelps and Tucker, 2009; Tseng et al., 2016). Wang et al. (2008) introduced the reduced-strain closure (RSC) model, which slows the orientation kinetics in order to achieve better agreement between the experiments and predictions. Phelps and Tucker (2009) developed a fiber orientation model that incorporates an anisotropic rotary diffusion term, namely the Anisotropic Rotary diffusion model (ARD). In the ARD model, the diffusivity is assumed to depend on a second-order space tensor which in turn is a function of the orientation state and the deformation rate. Nowadays, the FT and ARD-RSC models are available in most commercial injection molding simulation software. Some years ago, Tseng et al. (2016) proposed and implemented on Moldex3D an approach named the improved Anisotropic Rotary diffusion (iARD), which also considers anisotropic fiber diffusion and incorporates the effect of the fiber-matrix interaction (like the ARD model) and the slowing down of the orientation through the Retardant Principal Rate model (RPR). The iARD-RPR model has been proved to be suitable for both short and long fiber reinforced composites (Tseng et al., 2016).

When using the tensor description of the fiber orientation state proposed by Advani and Tucker (1987) instead of the probability distribution function (DFC), all the information regarding fiber orientation is represented by the components of a second-order momentum tensor, named the orientation tensor. The mathematical expression for the advection of the second-order orientation tensor involves a fourth-order orientation tensor that has to be defined in a closed form in order to compute fiber data. Then, a closure approximation is defined as an expression of the fourth-order orientation tensor as a function of the second-order orientation tensor. Advani and Tucker (1990) proposed the so-called Hybrid closure approximation (Hyb), which has been proven to be exact when the fibers are in both random and perfect aligned states, but that accelerates the orientation in transient shearing flows (Zheng et al., 2011). A family of closure approximations called orthotropic or Eigenvalue Based Optimal Fitting closures (EBOF) was developed by Cintra and Tucker (1995). Among them, the version called Orthotropic Fitted Closure Approximation (ORE) improved the non-physical oscillations for low interaction coefficients. Although the EBOF closures adequately predict fiber orientation in most simple flows, its implementation demands much computational time. Later, Chung and Kwon (2000) developed the Invariant Based Optimal Fitting closure approximation (IBOF) whose accuracy is as good as EBOF but requires less computational time to obtain a solution. The Hyb, ORE, and IBOF closure approximations are already implemented in Moldex3D.

Fiber Orientation and Rotary Diffusion Models

The orientation of a single fiber is determinate by a unit vector named p, which is defined by the in-plane (ϕ) and out-of-plane (θ) fiber angles. The most general way to describe the orientation state of a group of fibers is given by the probability density distribution function (ψ). The function ψ represents the probability of finding a fiber over the space between (ϕ, θ) and (ϕ+dϕ, θ+dθ).

Given that the time variation of ψ requires much computational time for its calculation, the tensor description of fiber orientation proposed in Advani and Tucker (1987) is generally implemented in simulations. The second-order orientation tensor (A) is defined so that the probability of a fiber being oriented within an angular range dp of the direction p is equal to ψ(p)dp, Equation 1.

$$A = \int \psi(\mathrm{p}) pp d\mathrm{p} \tag{1}$$

The second order orientation tensor can be expressed with a matrix that meets the following conditions: it is symmetric, and the sum of its diagonal components are 1.

The Folgar-Tucker Model

The evolution equation of the 2nd order orientation tensor can be expressed as the contribution of a hydrodynamic (h) and a diffusive term (d), Equation 2. In the so-called standard Folgar-Tucker model, the first term is represented by the Jeffery's Hydrodynamic (H) model, Equation 3 and the second by the Folgar-Tucker isotropic rotary diffusion (IRD) model, Equation 4.

$$\dot{A} = \dot{A}^{h} + \dot{A}^{d} \tag{2}$$

$$\dot{A}^{H} = (W \cdot A - A \cdot W) + \lambda (D \cdot A + A \cdot D - 2A_4 : D) \tag{3}$$

$$\dot{A}^{IRD} = 2\dot{\gamma} C_i (I - 3A) \tag{4}$$

Where, $\dot{A}$ is the material derivative of the second order orientation tensor; λ is a constant that depends on the geometry

of the fiber. In this work, λ is the value corresponding to slender particles and is equal to 1; I is the unit tensor, and Ci is the fiber-fiber interaction coefficient.

W is the vorticity tensor and D is the rate of deformation tensor. They are defined from the velocity gradient tensor L:

$$L = \nabla v = W + D \tag{5}$$

$$W = \frac{1}{2}(L - L^T) \tag{6}$$

$$D = \frac{1}{2}(L + L^T) \tag{7}$$

A_4 is the fourth-order orientation tensor, also symmetric, defined as:

$$A_4 = \oint \psi(p) pppdp \tag{8}$$

The iARD Model

The iARD model is formed by the contribution of the Jeffery Hydrodynamics model (H), Equation 3, the improved anisotropic rotary diffusion term (iARD), Equation 10 and the Retardant Principal Rate (RPR) model, Equation 13.]

$$\dot{A} = \dot{A}^{H} + \dot{A}^{iARD}(Ci, Cm) + \dot{A}^{RPR}(\alpha) \tag{9}$$

Where Ci and Cm are the fiber-fiber and matrix-fiber interaction coefficients and alpha is the RPR model parameter that indicates the slow-down fiber rotation behavior.

The iARD term is:

$$\dot{A}^{iARD} = \dot{\gamma}\left[2D_r - 2tr(D_r)A - 5D_r \cdot A - 5A \cdot D_r + 10A_4 : D_r\right] \tag{10}$$

Where

$$D_r = C_i(I - C_m \frac{D^2}{\|D^2\|}) \tag{11}$$

$$\|D^2\| = \sqrt{\frac{1}{2}D^2 : D^2} \tag{12}$$

The RPR term is:

$$\dot{A}^{RPR} = -R \cdot \dot{\Lambda}^{IOK} \cdot R^T \tag{13}$$

$$\dot{\Lambda}^{IOK}_{ii} = \alpha\lambda_i i, j, k = 1, 2, 3 \tag{14}$$

Where $R = [e_1, e_2, e_3]$ is the rotation matrix; R^T is its transpose; $\lambda_i(\lambda_1 \geq \lambda_2 \geq \lambda_3)$ are the eigenvalues of Λ and $\dot{A}^{IOK}$ is the material derivative of a particular diagonal tensor (IOK is for intrinsic orientation kinetics).

Closure Approximations

Hybrid Closure Approximation (Hyb)

Hyb approximation (Advani and Tucker, 1990), Equation 15, is the hybrid from the Linear, Equation 16, and Quadratic, Equation 17, closures. In index notation, Aij and Aijkl represent the second- and fourth-order orientation tensors, respectively, and Iij is the unit matrix.

$$\begin{aligned} \tilde{A}^{hybrid}_{ijkl} &\approx (1-f)\tilde{A}^{linear}_{ijkl} + f\tilde{A}^{quadratic}_{ijkl} \\ f &= 1 - 27\det(A_{ij}), \text{ for three dimensional orientation} \\ f &= 1 - 4\det(A_{ij}), \text{ for planar orientation} \end{aligned} \tag{15}$$

$$\tilde{A}^{linear}_{ijkl} = -\frac{1}{35}(I_{ij}I_{kl} + I_{ik}I_{jl} + I_{il}I_{jk}) + \frac{1}{7}(A_{ij}I_{kl} + A_{ik}I_{jl} + A_{il}I_{jk} + A_{kl}I_{ij} + A_{jl}I_{ik} + A_{jk}I_{il}) \tag{16}$$

$$\tilde{A}^{quadratic}_{ijkl} \approx A_{ij}A_{kl} \tag{17}$$

Since the Linear approximation has been proved to be exact for random orientations and the Quadratic closure is exact when the fibers are perfectly aligned, it is deduced that the hybrid closure will be exact when the fibers are in both random and perfect alignment states (Chung and Kwon, 2000; Wang and Jin, 2010). This model, however, tends to accelerate the orientation transients in transient shearing flows (Advani and Tucker, 1990). It has been demonstrated that Hyb closure approximation predictions are in a good agreement with experimental fiber orientation data when the value of the interaction coefficient is taken as 0.01 (Advani and Tucker, 1990; Wang and Jin, 2010).

Orthotropic or Eigenvalue Based Optimal Fitting Closures Family (EBOF)

EBOF approximations assume that only three components of the fourth-order tensor are independent, based on the fact that in the second-order tensor only two of the diagonal components are independent variables (the sum of diagonal components is 1). The directional information of Aijkl is obtained from Aij, both tensors having the same principal axis (Zheng et al., 2011). Then, the three principal components of the fourth-order tensor are expressed as functions of the independent principal components of the second-order tensor, Equation 18. Here aij and aijkl represent the components of the second- and fourth-order tensors, respectively. The superscript p indicates that the components are principal.

$$\tilde{A}^{orthotropic}_{ijkl} = \begin{Bmatrix} \tilde{a}^p_{1111} \\ \tilde{a}^p_{2222} \\ \tilde{a}^p_{3333} \end{Bmatrix} = \begin{Bmatrix} f_1(a^p_{11}, a^p_{22}) \\ f_2(a^p_{11}, a^p_{22}) \\ f_3(a^p_{11}, a^p_{22}) \end{Bmatrix} \tag{18}$$

In Equation 18, the functions f1, f2, and f3 are determinate by matching predicted values of the second-order components with experimental ones in well-defined flow conditions. These coefficient functions will be different for the different orthotropic approximations.

Among the orthotropic approaches, the so-called ORF provides good results for a range of interaction coefficient values from 0.01 to 0.1. The ORL closure is used in a range of Ci from 0.001 to 0.01, while the Orthotropic fitted closure approximation named ORE corrects the non-physical oscillations for low interaction coefficients (Cintra and Tucker, 1995).

Invariant Based Optimal Fitting Closure (IBOF)

IBOF closure approximates the Aijkl tensor as a function of the second-order orientation tensor and its invariants (Chung and Kwon, 2002). The IBOF approach is the same as the natural approximation (Zheng et al., 2011) and is expressed in Equation 19.

$$\begin{aligned}\tilde{A}_{ijkl}^{IBOF} &= \beta_1 S(\delta_{ij}\delta_{kl}) + \beta_2 S(\delta_{ij}a_{kl}) + \beta_3 S(a_{ij}a_{kl}) \\ &+\beta_4 S(\delta_{ij}a_{km}a_{ml}) + \beta_5 S(a_{ij}a_{km}a_{ml}) \\ &+\beta_6 S(a_{im}a_{mj}a_{kn}a_{nl}) \end{aligned} \quad (19)$$

Where S is the symmetric operator that applied to a general fourth-order tensor T will give, Equation 20:

$$\begin{aligned}S(T_{ijkl}) = \frac{1}{24}(&T_{ijkl} + T_{ijkl} + T_{ijkl} + T_{ijkl} + T_{ijkl} + T_{ijkl} + T_{ijkl} \\ &+T_{ijkl} + T_{ijkl} + T_{ijkl} + T_{ijkl} + T_{ijkl} + T_{ijkl} \\ &+T_{ijkl} + T_{ijkl} + T_{ijkl} + T_{ijkl} + T_{ijkl} + T_{ijkl} + T_{ijkl} \\ &+T_{ijkl} + T_{ijkl} + T_{ijkl}) \end{aligned} \quad (20)$$

The coefficients βj (with j = 1 to 6) are polynomial expansions of the second and third invariants of Aij. The difference between Natural and IBOF closures is that in the latter only three of the six β coefficients are considered linear independent. The computational cost of this approximation is much lower compared to the orthotropic one and gives results without non-physical oscillations for a wide range of interaction coefficients. It has been proven that this approximation provides good results with Ci = 0.0001 at the steady flow zones and with Ci = 0.001 at the transient flow zones (at the entrance, for instance). But, in a general way, IBOF results are close to experimental fiber orientation data when a Ci = 0.001 applies.

EXPERIMENTAL

Material and Processing Conditions

The specimen is made of short glass fiber filled (40 wt%) polyamide 6 (PA6), grade name Akulon K224-G8, produced by DSM Engineering Plastics. Average extracted fiber length measured through the CT experiment is around 150 μm (from around 1 million extracted fibers); real fiber length is expected to be higher due to the virtual fiber breakage influence of the high fiber content (>30 wt%). Maximum extracted fiber length is ∼1,000 μm. Average fiber aspect ratio, from the material datasheet provided by the PA6 manufacturer, is ranged from 20 to 25. Specimen's molding parameters are melt temperature, 280°C; mold temperature, 90°C; injection time, 1.13 s; holding time, 8 s; cooling time, 32 s; injection pressure, 11 MPa, and holding pressure, 10 MPa.

Flow behavior of the PA6 matrix was described by the Modified Cross Viscosity Model to account for the viscosity dependence on the shear rate and temperature, Equation 21 and 22.

$$\eta = \frac{\eta_0}{1 + \left(\frac{\eta_0 \dot{\gamma}}{\tau^*}\right)^{1-n}} \quad (21)$$

Where

$$\begin{aligned}\eta_0 &= D_1 \exp\left(\frac{-A_1(T - T_c)}{A_2 + (T - T_c)}\right) \\ T_c &= D_2 + D_3 P \\ A_2 &= \tilde{A}_2 + D_3 P \end{aligned} \quad (22)$$

The parameters of the viscosity model for the PA6 grade used in the study are available in the Moldex3D database. These are $n = 0.223$; $\tau = 407$ MPa; $D_1 = 5.0222$ Kg/(m.s); $D_2 = 323.606$ K; $D_3 = 0$ K.MPa^{-1}; $A_1 = 39.958$; and $A_2 = 51.6$ K.

Geometry Description

The Venturi-shaped specimen, the three regions of interest to the study and the experimental micro-CT samples, are shown in **Figure 1**. The regions are defined as: (R1) the entrance region, where the molten polymer enters the cavity; (R2) the central region, i.e., the constricted section or choke of the Venturi part, and (R3) the filling completion region which is, as the name implies, the last to fill. Dimensions of the specimen are total length L = 195 mm; thickness and diameter at R2, H = 1 mm and ϕ = 30 mm, and thickness and diameter at R1 and R3, H = 2.4 mm and ϕ = 45 mm.

The specimen was manufactured using a single screw injection molding machine. The injection of the molten polymer into the mold cavity occurs through an annular runner located at one end of the part, see the computational model at **Figure 2**; the characteristics of the inlet are similar to those of the film-gated strip. In **Figure 2**, X corresponds to the Main Flow Direction (MFD) or filling coordinate; Y corresponds to the Cross Flow Direction (CFD), and Z corresponds to the Through-Thickness Direction (TTD). Z and Y are both gap-wise coordinates (since Moldex3D results are displayed in a Cartesian reference system), with the difference that Y forms a plane with X (X and Y are the in-plane components) and Z is the out-of-plane component. When the index notation is used, 1, 2 and 3 are equivalent to X, Y, and Z, respectively.

The part has two distinctive features: (i) the wall thickness of the central region is less than half that of the entry and filling completion regions, 1 and 2.4 mm, respectively, i.e., it has variable thickness; and (ii) its geometric shape gives rise to the Venturi effect, which implies that the fluid velocity increases as it passes through the constriction in accord with the principle of mass continuity, while its static pressure decrease0073 in accord with the principle of conservation of mechanical energy.

Micro-CT Measurements

The experimental fiber orientation characterization was done via the micro-CT technique. Three 5 × 5 mm^2 area samples, one from each region of interest, were extracted and subjected to the CT-scan, see **Figure 1**. A GE phönix X-ray Nanotom 180 NF was used for the measurements. This equipment reaches a minimal voxel size of 0.5 μm. Parameters of the scans were: maximum sample size, ∼4 × 4 × 2.5 mm^3; voltage, 80 kV; current, 74 μA; number of projections, 1,900; exposure time 0.9 s; voxel size 2.75 μm. The single fiber characterization method was used to obtain the components of the orientation tensor from

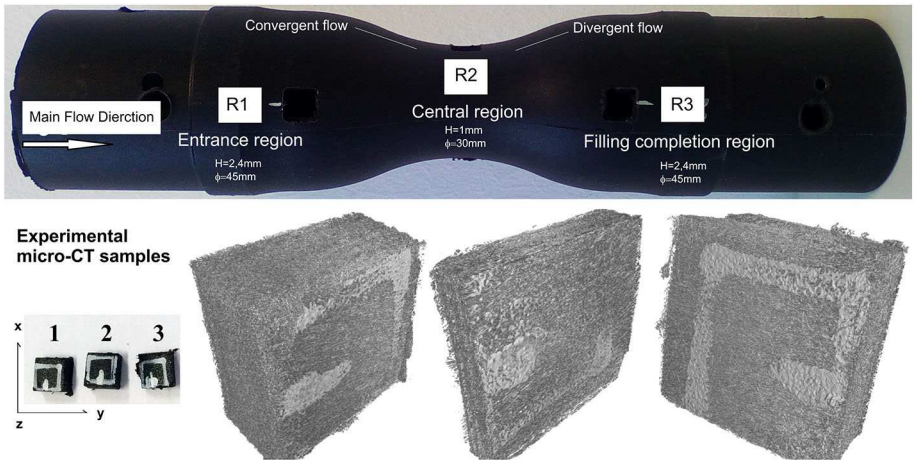

FIGURE 1 | Specimen, regions of interest and micro-CT samples.

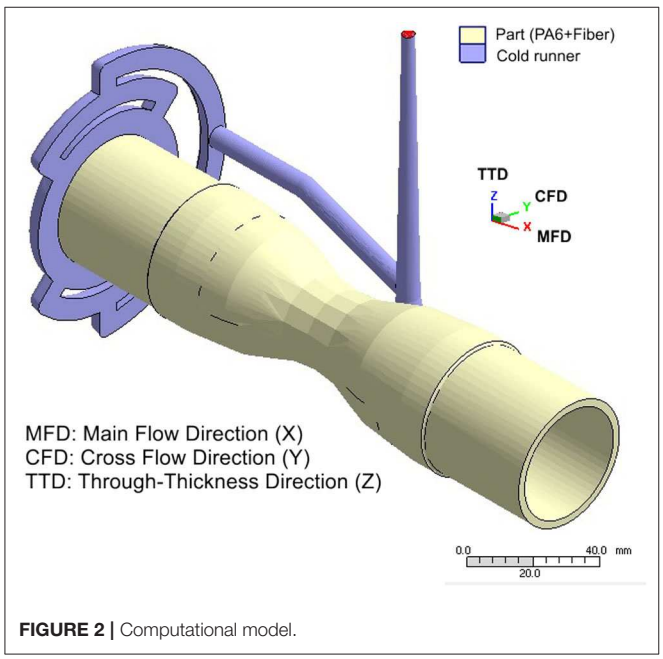

FIGURE 2 | Computational model.

the measured CT-data. A complete description of the micro-CT technique and the calculation scheme is presented in Salaberger et al. (2011), Emerson et al. (2017), and Salaberger (2019).

SIMULATION AND STATISTICAL CALCULATION

Simulation Details

The mold filling and fiber orientation simulations were performed using Moldex3D R.13, see **Figure 2**. For this case, a 3D analysis was preferable over a 2.5D to capture the potential influence of variable thickness and the Venturi effect over the FOD. Auto tetrahedral 3-dimensional meshing of the model was performed using the Moldex3D Designer. This method is widely used by commercial simulation codes users due to tetrahedral meshes' ability to fit almost any complex geometry. Despite this, tetrahedral meshes possess some drawbacks, such as the large number of elements and the difficulty in controlling the element layer count of the whole part (it is not constant). To overcome this limitation, the highest meshing reliability level of the Moldex3D Designer with a small enough size of element was chosen to ensure a minimum of 5 elements in the thickness direction.

TABLE 1 | Simulation trials for the evaluation of orientation models and closure approximations.

Orientation model	Closure	Parameter		
		Ci	Cm	alpha-RPR
FT	Hyb-ORE-IBOF	0.01	–	0
iARD	Hyb-ORE-IBOF	0.01	0.99	0

Computational Study Details

The computational study was divided into two parts. The first part is the comparison of the experimental profiles with those obtained from all the possible combinations of the rotary diffusion models (FT and iARD) and the closure approximations (Hyb, ORE, and IBOF). The FOD was examined throughout the specimen (regions of interest) and through its thickness. The default values of the model parameters were set for these simulations (Ci = 0.01, Cm = 0.99, and α-RPR = 0). The summary is in **Table 1**. For the comparison, the optimal closure approximation was selected in terms of adjustment to the experimental results and the shorter time consumed. In the second part, the models parameters were varied to establish, via ANOVA, their influence over the fiber orientation tensor components and to calculate predictive errors. The summary is in **Table 2**.

Statistical and Error Calculation Details

The sensitivity of the principal components of the 2nd-order orientation tensor (responses) as a function of the fiber model parameters listed in **Table 2** (factors) was evaluated via the Analysis of Variance (ANOVA) method. The operation of the ANOVA technique broadly follows this scheme: in order to compare the means of the factors associated with their different levels, a measure of the response variation due to their different levels (Mean Square factor, MS-factor) is compared with a measurement of the response variation due to the error (Mean Square error, MS-error). If the MS-factor is significantly larger than the MS-error, it is concluded that the means associated with different levels of the factor are different. That factor then has an important influence over the response. In the ANOVA analysis, the P (%) represents the percentage of contribution of each term (factors and error) to the variation of the dependent variables.

The predictive errors of the FT and iARD models as functions of the parameters levels listed in **Table 2** were calculated according to Equation 23.

$$\mathrm{RMSE} = \sqrt{\left(a_i^{\mathrm{prediction}} - a_i^{\mathrm{experimental}}\right)^2} \tag{23}$$

This is the Root Mean Squared Error (RMSE) computed from the difference in the predicted and experimental values of the principal components of the orientation tensor. From these results, the combination of parameters per model that lead to the lower prediction error was determined.

TABLE 2 | Simulation trials for ANOVA analysis.

Orientation model	Closure	Parameter								
		Ci			Cm			alpha-RPR		
FT-RPR	IBOF	0.001	0.005	0.01	–	–	0	0.2	0.7	0.95
iARD-RPR	IBOF	0.001	0.005	0.01	0.2	0.99	0	0.2	0.7	0.95

RESULTS AND DISCUSSION

Experimental Fiber Orientation Description

Fiber Orientation in the Thickness Direction

Figure 3 shows the experimentally determined through-thickness fiber orientation distributions for the regions of interest along the specimen. The degree of fiber alignment in the MFD is indicated by the value of a_{11}, whereas a_{22} and a_{33} corresponds to the cross-flow and through-thickness fiber orientations, respectively.

It is observed that the part exhibits a gap-wise three-layered laminated structure which corresponds to the so-called shell-core-shell structure. The fibers in the shell layers are mainly aligned in the MFD, this implies high a_{11} values and low a_{22} values. The core layer, located approximately at the specimen mid-plane ($z/H = 0.5$) and between the shell layers, is characterized by a high cross-flow fiber orientation with high a_{22} values and low a_{11} values. Also, a fraction of the fibers aligned in the thickness direction can be observed in the core layer (a_{33} value different from zero).

Fiber Orientation Along the Specimen

The experimental results in **Figure 3** reveal that, at the entrance and central regions, the distributions are essentially flat (the fibers remain parallel to the XY plane). Whereas, at the filling completion region, the portion of fibers aligned in the thickness direction is larger.

Furthermore, it can be seen from **Figure 3** that the fiber alignment degree in the MFD changes after the fluid experiences the convergent and divergent transitions between R1 and R2 and between R2 and R3, respectively (**Figure 1**). In the convergent transition an increase in the a_{11} component occurs, both in the shell and core layers (through-thickness averaged values from 0.74 to 0.85), while the remaining components decrease. Since the orientation in the MFD is governed by the shear flow, the increase in a_{11} is associated with the increase of the fluid velocity caused by the Venturi effect and the increase in the shear rate due to the narrower cavity. On the contrary, in the divergent transition, a_{11} decreases (through-thickness averaged values from 0.85 to 0.7) and the remaining components increase, specially a_{33} (through-thickness averaged values from 0.03 to 0.1). This

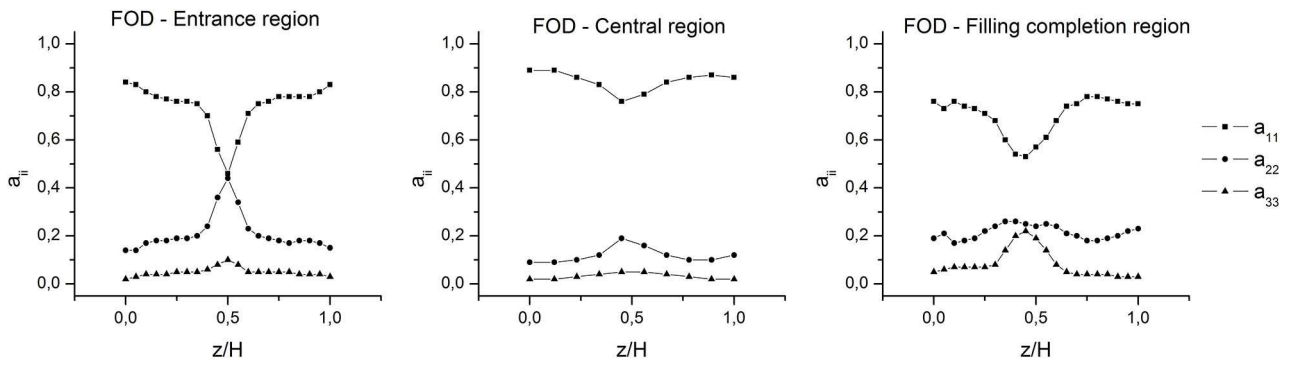

FIGURE 3 | Experimental a_{11}, a_{22}, and a_{33} orientation profiles at the regions of interest.

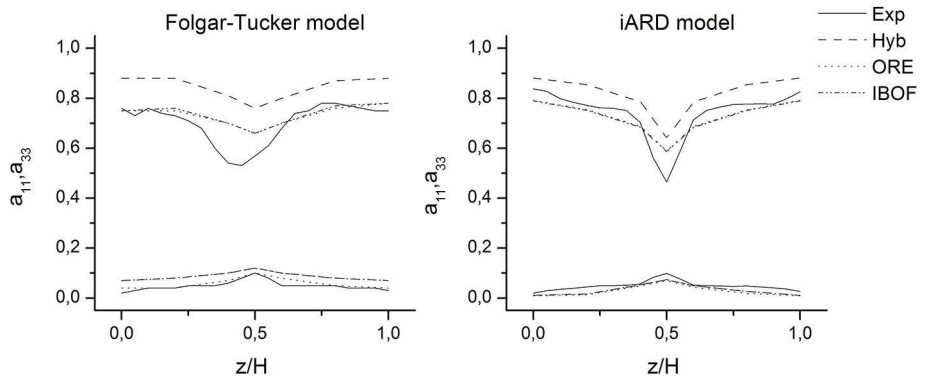

FIGURE 4 | Experimental and predicted a_{11} and a_{33} profiles at the entrance region (R1).

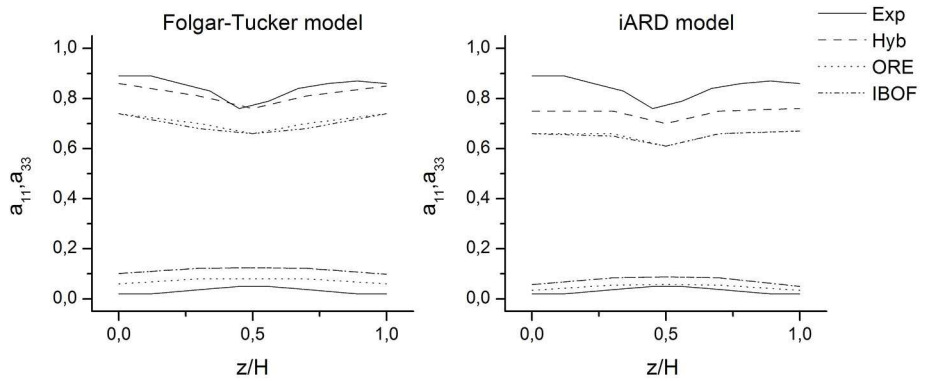

FIGURE 5 | Experimental and predicted a_{11} and a_{33} profiles at the central region (R2).

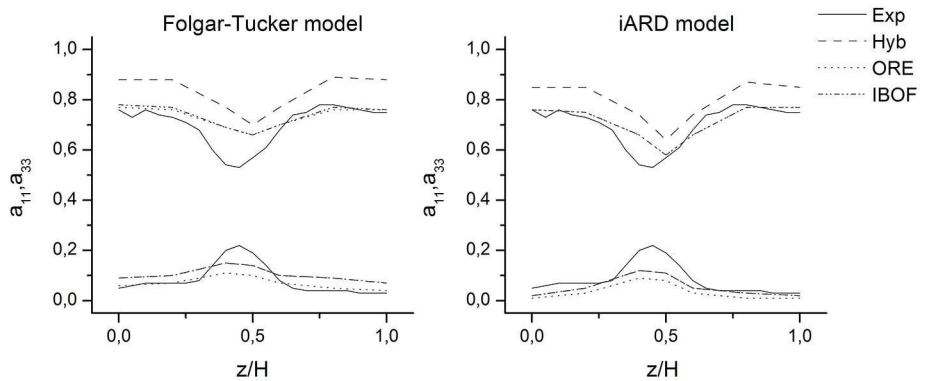

FIGURE 6 | Experimental and predicted a_{11} and a_{33} profiles at the filling completion region (R2).

last can be attributed to the rotation of the fibers being located completely outside the XY plane at the cavity enlargement.

Computational Study Results

Comparisons Between Experimental and Predicted FODs

Figures 4–6 show the comparison between the experimental and predicted orientation components along the flow and through-thickness directions, i.e., a_{11} and a_{33}, for each region of interest, respectively. Results are reported in terms of these components since they contain most of the qualitative information about the layered microstructure and, as it was demonstrated by the experimental results, they are more sensitive to flow and geometrical changes. Predicted profiles correspond to the combinations of rotary diffusion models, closure approximations and models parameters listed in

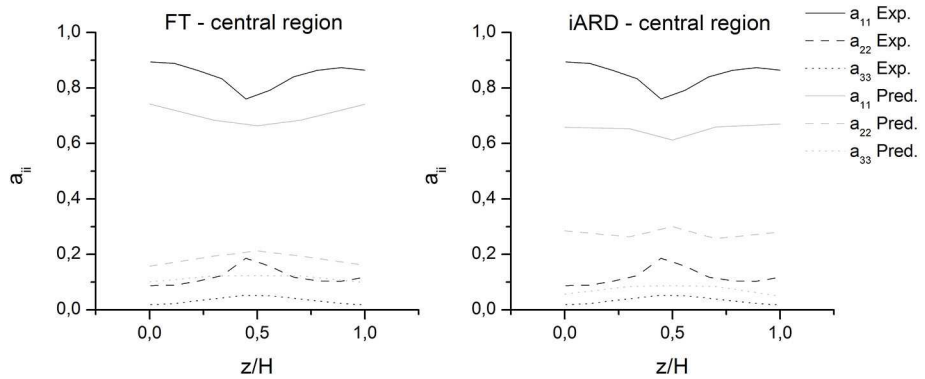

FIGURE 7 | Experimental and predicted a_{11}, a_{22}, and a_{33} orientation profiles at the central region.

Table 1. The following observations arise from the analysis of the results.

Comparison of fiber orientation in the thickness direction

The Hyb approximation leads to an over-estimation of the orientation in the flow direction. When using the Hyb closure, the a_{11} predicted value is higher than the experimental one with respect to the prediction using ORE and IBOF closures for all the through-thickness profiles. The ORE and IBOF approximations estimate the orientation of the shell layers fairly closely to the experimental one; however, they over-predict the orientation of the core layer. The results provided by these closures are essentially the same, but the computational time consumed by the IBOF closure calculation is approximately half of the ORE closure. Due to its higher accuracy and computational efficiency, the IBOF has been selected as the optimum closure.

Comparison of fiber orientation along the specimen

At the entrance and filling completion regions (**Figures 4**, **6**), it is observed that, using the IBOF closure with the iARD model, there is a reasonably good correlation between the predicted and experimental values of all the principal orientation components. While using the IBOF closure in combination with the FT model, the results of a_{11} correlate well, but a_{22} is under-predicted and a_{33} is over-predicted.

On the other hand, at the central region (**Figure 5**), although the simulations predict an increase of fluid velocity and an increase of the shear rate caused by the convergent transition, none of the orientation models predict the expected increase of the fiber alignment (a_{11}) that was observed experimentally. This discrepancy is more likely attributable to the estimation error of the remaining components, see **Figure 7**. As explained in the experimental section, when the wall thickness is narrowed, the fibers tend to align in the MFD; hence, the central region is characterized by a high value of a_{11} and a very low a_{22}. However, simulation results for this region evidence that a_{22} and a_{33} are highly overestimated for both orientation models. So then, considering that the sum of the principal components is equal to 1 ($a_{11}+a_{22}+a_{33} = 1$), a_{11} is consequently underestimated.

Taking into account the degree of adjustment to the experimental results, it follows that the iARD model in combination with the IBOF closure approximation are the most accurate for the case studied.

ANOVA Analysis

The results of the ANOVA analysis are described in terms of the P(%), i.e., the percentage of contribution of each parameter (varied according to **Table 2**) and of the error to the variation of the principal components of the orientation tensor. These are: (i) FT model: P(%) over a_{11}, Ci = 10.35%, alpha-RPR = 88.01% and error = 1.64%; P(%) over a_{22}, Ci = 8.27%, alpha-RPR = 91.03% and error = 0.7%, and P(%) over a_{33}, Ci = 12.39%, alpha-RPR = 84.84% and error = 2.77%. (ii) iARD model: P(%) over a_{11}, Ci = 11.8%, Cm = 1.89%, alpha-RPR = 82.88%, and error = 3.42%; P(%) over a_{22}, Ci = 1.3%, Cm = 3.76%, alpha-RPR = 93.11%, and error = 1.84% and P(%) over a_{33}, Ci = 23.02%, Cm = 16.15%, alpha-RPR = 47.88%, and error = 12.95%.

Additionally, **Figures 8**, **9** show the principal effects and interactions of the same parameters over the component in the MFD. From the P(%) results, it is observed that for both models, the alpha-RPR parameter has the higher impact on the value of a_{11}, a_{22}, and a_{33}. However, in light of the results shown in the figures, it can be noted that this behavior is not valid for all the factors' levels; an abrupt change in the trend occurs from alpha-RPR = 0.7 due to a stronger interaction of the factors. Below this point, the effect of Ci and Cm can be considered practically independent of each other and of alpha-RPR. While above it, the interaction between the factors become significant and the orientation prediction is dominated by alpha-RPR.

With this in mind, a new ANOVA analysis was performed taking the alpha-RPR parameter up to 0.7, i.e., in the levels range in which the population means are not considerably different. The results are: (i) FT model: P(%) over a_{11}, Ci = 85.44%, alpha-RPR = 13.59%, and error = 0.97%; P(%) over a_{22}, Ci = 79.49%, alpha-RPR = 20.01%, and error = 0.5%, and P(%) over a_{33}, Ci = 88.92%, alpha-RPR = 9.47%, and error = 1.61%. (ii) iARD model: P(%) over a_{11}, Ci = 77.38%, Cm = 15.35%, alpha-RPR = 3.64%, and error = 3.62%; P(%) over a_{22}, Ci = 13.29%,

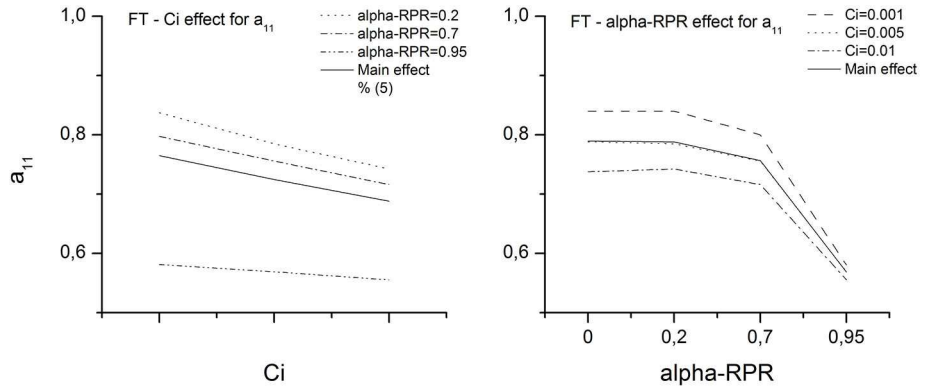

FIGURE 8 | Main effects and interaction of the FT-RPR model parameters.

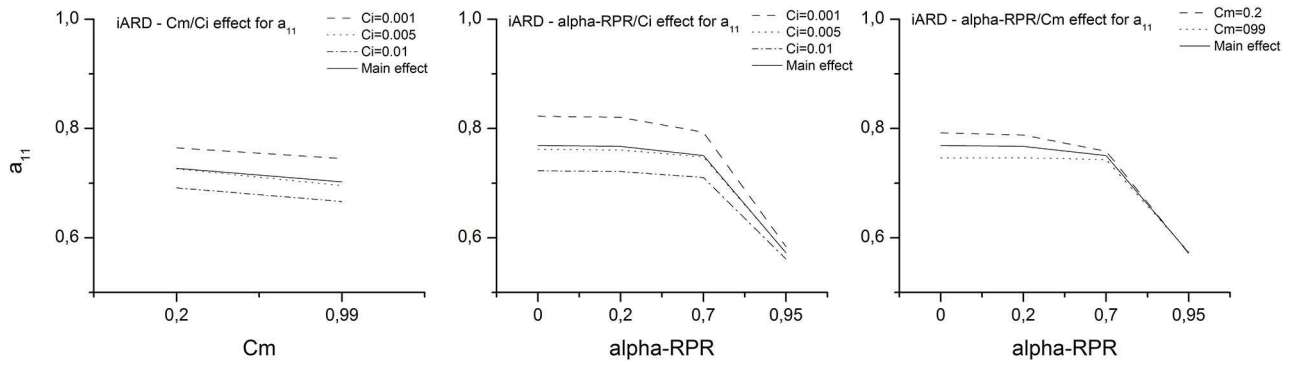

FIGURE 9 | Main effects and interaction of the iARD-RPR model parameters.

Cm = 44.46%, alpha-RPR = 29.07%, and error = 13.17%; and P(%) over a_{33}, Ci = 52.88%, Cm = 39.85%, alpha-RPR = 0.03%, and error = 7.24%.

It is observed now that: (i) for the FT model, the fiber-fiber interaction coefficient Ci is the one that has the higher effect on all the principal orientation components; (ii) for the iARD model, as Ci is the one with the higher impact on a_{11}, the matrix-fiber interaction coefficient Cm significantly impacts the perpendicular components (a_{22} and a_{33}) and (iii) the error on the estimation of a_{22} and a_{33} is confirmed to be considerable.

Finally, the effect of the factors is summarized as follows: (i) increasing alpha-RPR produces a decrease in a_{11} and an increase in a_{22} and a_{33}. Above alpha-RPR = 0.7 these variations become very pronounced; (ii) increasing Ci produces a decrease in a_{11} and an increase in a_{22} and $a_{33;}$ (iii) increasing Cm produces a decrease in a_{11} and a_{22} and an increase in a_{33}. The amount (%) of these variations will depend upon the level of alpha-RPR considered, being below alpha-RPR = 0.7 those corresponding to the first ANOVA, and above alpha-RPR = 0.7 those corresponding to the second ANOVA.

Prediction Error Analysis

Figures 10, **11** show the prediction error of the FT and iARD models, respectively (computed from Equation 23) as functions of the different model parameters. Based on the fact that there are certain deficiencies of the models in predicting the orientation changes that occur due to the specimen geometrical variations, and that the model parameters affected the principal orientation tensor components in a different way, the criterion used to find the optimal parameters set was that of trying to capture the best the global orientation state of the specimen. For this reason, a_{11}, $a_{22,}$ and a_{33} were analyzed by averaging their values across the thickness and the three regions of interest of the specimen. It should be noted that this analysis will not tell much about the precision of each model (best determined by comparison with the experimental profiles), since information from the predictions is lost locally.

Parameter values were chosen to minimize the error of each component without maximizing the error of the others. The optimal sets are as follows: (i) FT model, Ci = 0.005, alpha-RPR = 0.7, and (ii) iARD model, Ci = 0.005, Cm = 0.2, and alpha-RPR = 0.7.

These results show that the alpha-RPR parameter must be chosen carefully, since after a certain value (coincident with that obtained from the ANOVA above which its effect is predominant) it induces a significant error in the predictions. The same is valid for the interaction coefficients (Ci and Cm) regarding the prediction of the components perpendicular to the

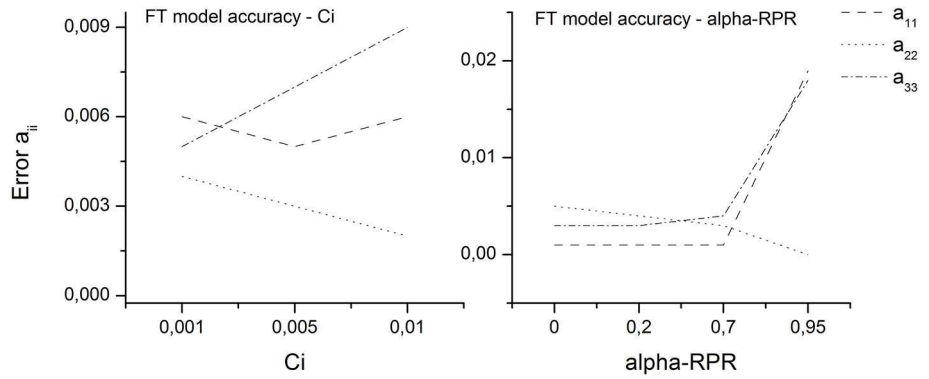

FIGURE 10 | Prediction error of the FT-RPR model.

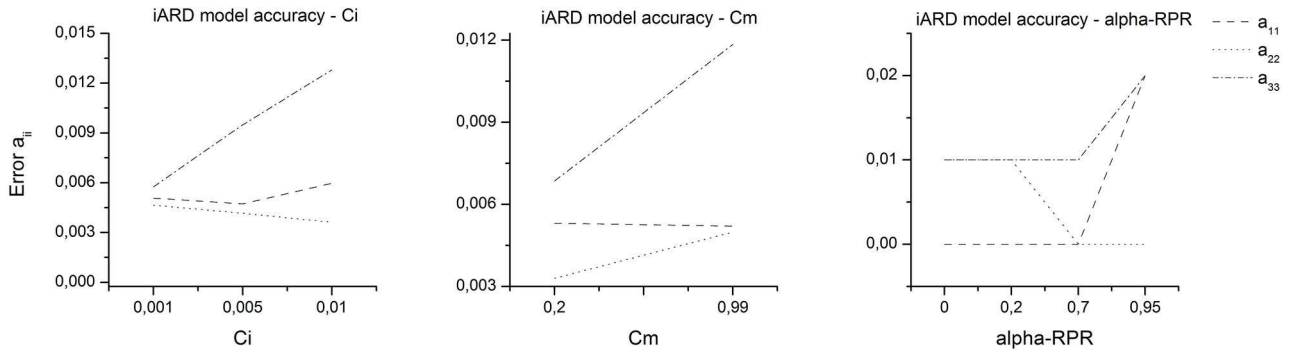

FIGURE 11 | Prediction error of the iARD-RPR model.

flow (a_{22} and a_{33}), due to these parameters' variation strongly influencing their respective prediction errors.

SUMMARY AND CONCLUSIONS

This paper evaluates the predictions of the fiber orientation distribution (FOD) of an injected Venturi-shaped specimen. The choice of the specimen was made in order to study a different case from the specimens traditionally used for validation purposes (usually the center gated-disk and the film-gated strip), which in turn presents characteristics common to many injected parts, such as variable thickness, section changes, convergent, and divergent transitions among others. The experimental characterization was performed using the novel micro computed tomography technique.

The experimental results describe the physical phenomenon to be modeled by the simulation. The orientation pattern measured through the CT technique is in accordance with the expectations arisen from previous knowledge and from the patterns measured by the standard method of optical microscopy (the ellipse method). These are broadly: the presence of a shell-core-shell layered structure across the part thickness, with the fibers aligned in the main flow direction in the shell layers and the fibers aligned in the cross flow direction in the layer core. It is also demonstrated that the convergent and divergent transitions that the flow experiences through this specimen and the variations of its thickness induce changes in the fibers' alignment degree. In this way, in the convergent transition that occurs at the specimen constriction, characterized by an increase in the flow rate caused by the Venturi effect and an increase in the shear rate due to the narrower cavity, there is an increase in orientation in the main flow direction in both the shell and core layers. Whereas, at the divergent transition that occurs after the constriction there is a decrease in orientation in the main flow direction and an increase in orientation perpendicular to flow.

The computational study evaluates the ability of present theories to predict fiber orientation, revealing certain deficiencies in both the orientation models and the second-order orientation tensor closure approximations. Specifically, it is observed that the hybrid (Hyb) closure overestimates the orientation with respect to the experimental orientation and that obtained when using the ORE and IBOF closures. For their part, it is observed that the results obtained from ORE and IBOF closures are closer to the experimental ones, being essentially the same. However, the computational time consumed by the IBOF closure is approximately half that of the ORE. Due to its higher accuracy and computational efficiency, the IBOF

approximation is selected as the optimum. Moreover, at the entrance and filling completion regions of specimen, using the IBOF closure, it is observed that the iARD model fairly estimates the orientation components, while the FT model underestimates the a_{22} component and overestimates the a_{33} component. Then, from the comparison of experimental and predicted profiles it follows that the predictions of the iARD model in combination with the IBOF closure approximation are the most accurate for the case studied.

On the other hand, from the analysis of the predictions corresponding to the central region (thinner gap), a very important result of this work emerges: it is the demonstration that both orientation models fail to predict the increase in orientation that occurs in the specimen constriction. The a_{11} component depends on the flow in the main direction, and simulations effectively predict the increase in the flow velocity and shear rate that should cause the increase of a_{11}. Then, this discrepancy may be attributed to the error in estimating the components in the directions perpendicular to the flow rather than to the estimation of a_{11}.

The ANOVA technique is used in order to objectively explore and quantify the effect of model parameters on predicting second-order tensor components. In strictly statistical terms, it is possible to demonstrate that after a certain level of the alpha-RPR parameter, the interaction between the different factors become significant, and alpha-RPR dominates the orientation prediction regardless the value taken by the rest of the parameters. However, for values below this alpha-RPR level, it is shown that for both the FT and iARD models, the fiber-fiber interaction coefficient (Ci) is the one that most influences the component in the main flow direction (a_{11}); whereas for the iARD model, the fiber-matrix interaction coefficient (Cm) has a significant impact on the prediction of the components perpendicular to the main flow direction (a_{22} and a_{33}). The effect of the factors is as follows: (i) increasing alpha-RPR produces a decrease in a_{11} and an increase in a_{22} and a_{33}; (ii) increasing Ci produces a decrease in a_{11} and an increase in a_{22} and $a_{33;}$ and (iii) increasing Cm produces a decrease in a_{11} and a_{22} and an increase in a_{33}. These results suggest that since Ci, Cm and alpha-RPR are fitting parameters, which affect the orientation components differently, the adjustment to the experimental results will never be entirely accurate.

Finally, and taking into account the described limitations of the models and the adjustment of their parameters, predictive error analysis is used to find the optimal parameter that better captures the global orientation state of the component. The optimal set for this case, recommended for application in similar cases, is as follows: (i) for the FT model, Ci = 0.005, alpha-RPR = 0.7, and (ii) for the iARD model, Ci = 0.005, Cm = 0.2, and alpha-RPR = 0.7. It can be concluded that it is of fundamental importance to carefully define the models' parameters values (especially alpha-RPR) because their variation is closely related to the prediction error.

DATA AVAILABILITY STATEMENT

The raw data supporting the conclusions of this article will be made available by the authors, without undue reservation.

AUTHOR CONTRIBUTIONS

AA provided the injected part which was injected in the installations of the Leartiker group. BP performed the characterization of the samples via micro-CT and provided the experimental curves. MQ performed the simulations and the statistical calculations, performed the analysis of the results, and wrote the manuscript. PF and ZM has given significant intellectual inputs and supervised the work. ZM coordinated the working groups. All authors contributed to the article and approved the submitted version.

ACKNOWLEDGMENTS

The authors want to thank all the institutions involved in the elaboration of this work. Particularly to the Institute of Polymer Product Engineering directed by Dr. ZM—Johannes Kepler University at Linz (Austria)—for kindly inviting MQ to carry out a research stay at its facilities, from which this work emerged, to the National Research Council of Argentina (CONICET) and the MINCyT (Argentina). Micro-CT results were gained within the projects DigiCT-Sim (project number: 862015) and pore3D (project number: 868735). Both micro-CT projects were funded by the State Government of Upper Austria and Austrian Research Promotion Agency (FFG).

REFERENCES

Advani, S. G., and Tucker, C. L. (1987). The use of tensors to describe and predict fiber orientation in short fiber composites. *J. Rheol.* 31, 751–784. doi: 10.1122/1.549945

Advani, S. G., and Tucker, C. L. (1990). Closure approximations for three-dimensional structure tensors. *J. Rheol.* 34, 367–386. doi: 10.1122/1.550133

Bay, R. S., and Tucker, C. L. (1992). Fiber orientation in simple injection moldings. Part I: theory and numerical methods. *Polym. Compos.* 13, 317–331. doi: 10.1002/pc.750130409

Chung, D.-H., and Kwon, T.-H. (2000). Applications of recently proposed closure approximations to injection molding filling simulation of short-fiber reinforced plastics. *Korea-Aust. Rheol. J.* 12, 125–133.

Chung, D. H., and Kwon, T. H. (2002). Invariant-based optimal fitting closure approximation for the numerical prediction of flow-induced fiber orientation. *J. Rheol.* 46, 169–194. doi: 10.1122/1.1423312

Cintra, J. S., and Tucker, C. L. (1995). Orthotropic closure approximations for flow-induced fiber orientation. *J. Rheol.* 39, 1095–1122. doi: 10.1122/1.550630

Emerson, M. J., Jespersen, K. M., Dahl, A. B., Conradsen, K., and Mikkelsen, L. P. (2017). Individual fibre segmentation from 3D X-ray computed tomography for characterising the fibre orientation in unidirectional composite materials. *Compos. Part A Appl. Sci. Manuf.* 97, 83–92. doi: 10.1016/j.compositesa.2016.12.028

Folgar, F., and Tucker, C. L. (1984). Orientation behavior of fibers in concentrated suspensions. *J. Reinf. Plast. Compos.* 3, 98–119. doi: 10.1177/073168448400300201

Greene, J. P., and Wilkes, J. O. (1997). Numerical analysis of injection molding of glass fiber reinforced thermoplastics. Part 2: fiber orientation. *Polym. Eng. Sci.* 37, 1019–1035. doi: 10.1002/pen.11747

Gupta, M., and Wang, K. K. (1993). Fiber orientation and mechanical properties of short-fiber-reinforced injection-molded composites: simulated and experimental results. *Polym. Compos.* 14, 367–382. doi: 10.1002/pc.750140503

Hanhan, I., Agyei, R., Xiao, X., and Sangid, M. D. (2019). Comparing non-destructive 3D X-ray computed tomography with destructive optical microscopy for microstructural characterization of fiber reinforced composites. *Compos. Sci. Technol.* 184:107843. doi: 10.1016/j.compscitech.2019.107843

Jeffery, A. G. B. (2012). The motion of ellipsoidal particles imnmersed in a viscous fluid. *Proc. R. Soc. Lond. Ser A*. 102, 161–179. doi: 10.1098/rspa.1922.0078

Kleindel, S., Salaberger, D., Eder, R., Schretter, H., and Hochenauer, C. (2015). Prediction and validation of short fiber orientation in a complex injection molded part with chunky geometry. *Int. Polym. Process.* 30, 366–380. doi: 10.3139/217.3047

Kuzmin, D. (2018). Planar and orthotropic closures for orientation tensors in fiber suspension flow models. *SIAM J. Appl. Math.* 78, 3040–3059. doi: 10.1137/18M1175665

Larsen, Å. (2000). Injection molding of short fiber reinforced thermoplastics in a center-gated mold. *Polym. Compos.* 21, 51–64. doi: 10.1002/pc.10164

McGee, S. H., and McCullough, R. L. (1984). Characterization of fiber orientation in short-fiber composites. *J. Appl. Phys.* 55, 1394–1403. doi: 10.1063/1.333230

Montgomery-Smith, S., Jack, D., and Smith, D. E. (2011). The fast exact closure for Jeffery's equation with diffusion. *J. Nonnewton. Fluid Mech.* 166, 343–353. doi: 10.1016/j.jnnfm.2010.12.010

Papathanasiou, T. D. (1997). *Flow-Induced Alignment in Injection Molding of Fiber-Reinforced Polymer Composites*. Sawston: Woodhead Publishing Ltd.

Phelps, J. H., and Tucker, C. L. (2009). An anisotropic rotary diffusion model for fiber orientation in short- and long-fiber thermoplastics. *J. Nonnewton. Fluid Mech.* 156, 165–176. doi: 10.1016/j.jnnfm.2008.08.002

Salaberger, D. (2019). *Micro structure of discontinuous fibre polymer matrix composites determined by X ray Computed Tomography* [Ph.D. Thesis]. Technical University Vienna, Vienna, Austria.

Salaberger, D., Kannappan, K. A., Kastner, J., Reussner, J., and Auinger, T. (2011). Evaluation of computed tomography data from fibre reinforced polymers to determine fibre length distribution. *Int. Polym. Process* 26, 283–291. doi: 10.3139/217.2441

Sharma, B. N., Naragani, D., Nguyen, B. N., Tucker, C. L., and Sangid, M. D. (2018). Uncertainty quantification of fiber orientation distribution measurements for long-fiber-reinforced thermoplastic composites. *J. Compos. Mater.* 52, 1781–1797. doi: 10.1177/00219983177 33533

Tseng, H.-C., Chang, R.-Y., and Hsu, C.-H. (2016). An objective tensor to predict anisotropic fiber orientation in concentrated suspensions. *J. Rheol.* 60, 215–224. doi: 10.1122/1.4939098

Tseng, H. C., Chang, R. Y., and Hsu, C. H. (2018). Numerical predictions of fiber orientation for injection molded rectangle plate and tensile bar with experimental validations. *Int. Polym. Process.* 33, 96–105. doi: 10.3139/21 7.3404

Vélez-Garcia, G. M. (2012). *Experimental Evaluation and Simulations of Fiber Orientation in Injection Molding of Polymers Containing Short Glass Fibers*. Virginia Tech.

Wang, J., and Jin, X. (2010). "Comparison of recent fiber orientation models in autodesk moldflow insight simulations with measured fiber orientation data," in *Proceedings of the Polymer Processing Society 26th Annual Meeting PPS-26* (Banff, AB).

Wang, J., O'Gara, J. F., and Tucker, C. L. (2008). An objective model for slow orientation kinetics in concentrated fiber suspensions: theory and rheological evidence. *J. Rheol.* 52, 1179–1200. doi: 10.1122/1.29 46437

Zheng, R., Tanner, R. I., and Fan, X. J. (2011). "Flow-induced alignment in short-fiber reinforced polymers," in *Injection Molding* (Berlin; Heidelberg: Springer). doi: 10.1007/978-3-642-21263-5_5

Conflict of Interest: The authors declare that the research was conducted in the absence of any commercial or financial relationships that could be construed as a potential conflict of interest.

frontiers in Materials

ORIGINAL RESEARCH
published: 25 September 2020
doi: 10.3389/fmats.2020.00297

Processing–Structure–Properties of Cork Polymer Composites

Carla I. Martins and Vitória Gil*

Institute for Polymers and Composites (IPC), University of Minho, Guimarães, Portugal

This work aims at presenting a new strategy for the use of cork by-products on the development of sustainable composites with potential applications in rotational molding. In this study, different cork granulometries (0.15–3 mm) and matrix/cork ratios (90/10, 85/15, 80/20) are analyzed to access the processability of medium-density polyethylene (MDPE) with cork by rotational molding. The influence of processing parameters, such as the mold peak internal air temperature (PIAT) (200–240°C), is analyzed and correlated with the aesthetics, morphological and mechanical properties of the parts. The aim is to obtain a complete understanding of the processing–structure–property relationships. Defect-free parts are obtained with thin granulometric cork powders at a maximum of 10% by weight in PE/cork composites. The increase in cork content reduces the sintering capability and increases the porosity, wall thickness, and surface defects, simultaneously weakening the mechanical properties. The increase in PIAT favors a more compact structure and reveals better impact properties. All the parts are soft on touch and transmit the comfort and sensation of warm feeling of the cork. Moreover, lightweight parts and hydrophobic surfaces are achieved from the cork intrinsic properties. As a natural material, cork darkens its color with temperature, which is attributed to the reactions of the extractives within the components of cork, with no degradation associated. The work shows that polymer cork composites (CPC) are suitable for rotational molding within the processing window characteristic of PE, to achieve innovative and sustainable products with unique aesthetics and functionalities given by the cork material.

Keywords: rotational molding, cork-polymer-composites, cork, polyethylene, thermal properties, morphology, mechanical properties

OPEN ACCESS

Edited by:
Jacqueline Anne Johnson, University of Tennessee Space Institute (UTSI), United States

Reviewed by:
Veronique Michaud, École Polytechnique Fédérale de Lausanne, Switzerland
Liqing Wei, United States Forest Service (USDA), United States

****Correspondence:***
Carla I. Martins
cmartins@dep.uminho.pt

Specialty section:
This article was submitted to Polymeric and Composite Materials, a section of the journal Frontiers in Materials

Received: *13 June 2020*
Accepted: *10 August 2020*
Published: *25 September 2020*

Citation:
Martins CI and Gil V (2020) Processing–Structure–Properties of Cork Polymer Composites. Front. Mater. 7:297. doi: 10.3389/fmats.2020.00297

INTRODUCTION

Cork is a natural product obtained from the outer bark of an oak tree known botanically as Quercus suber L (Gibson et al., 1981). This material has a unique combination of properties such as low density, excellent acoustic and thermal properties, impermeability to liquids and gases, a high coefficient of friction, resilience, high energy absorption, excellent insulation properties, and a near-zero Poisson coefficient, which makes it an optimum material for a variety of applications (Fortes and Nogueira, 1989; Mano, 2002; Gibson, 2003). In addition, it is a natural, reusable, and renewable product and offers a unique look and touch which makes it difficult to be replaced by synthetic materials (Silva et al., 2005).

In terms of morphology, cork can be described as anisotropic material with thin-walled cells, regularly arranged without intercellular space. The cells are rectangular prisms like an alveolar structure and similar to a honeycomb, with their axes along the tree's radial direction, stacked in columns (Pereira, 2007).

In cork, the structural components of cell wall are as follows: suberin, an aliphatic polyester (42%); lignin, an aromatic polymer (21,5%); polysaccharides, including cellulose and hemicelluloses (16%); extractives (13%); and ashes (7%) (Pereira, 1988). The cell wall of cork is chemically made up of two types of components: the structural components (suberin, lignin, and polysaccharides) build up the cell wall and define its structure; they are insoluble and cannot be removed from the cell wall without profoundly affecting the cell structure and properties; and the nonstructural components (extractives or inorganic minerals), either low-molecular organic compounds that may be solubilized by appropriate solvents (Pereira, 2007).

This cellular configuration has a strong influence on the mechanical properties of cork-based materials (Gibson, 2005). Castro et al. (2010) presented a compilation of the main mechanical properties of natural cork obtained from different experimental tests. They concluded that natural cork has a poor mechanical behavior when compared with other types of core materials for sandwich components of lightweight structures, such as synthetic foams. However, its low thermal conductivity combined with a reasonable compressive strength makes it an excellent material for thermal insulation purposes as well as for applications in which compressive loads are present.

From the reuse of by-products resulting from the transformation of cork, composites were created. Cork was incorporated into polymeric matrices, which allowed the combination of the ecological properties with the good mechanical performance of polymeric materials (Fernandes et al., 2011; Soares et al., 2011). The combination of cork with polymers through melt-based technologies brought added value to cork-based materials, promoting the development of a wide range of innovative applications.

Studies can be found on the combination of cork and cork by-products with polyolefins such as polyethylene (PE) and polypropylene (PP) (Fernandes et al., 2010) as well as biodegradable matrices such as PLA (Vilela et al., 2013). The effect of adding a coupling agent (Fernandes and Correlo, 2014) and chemical surface modification (Pereira and Velez Marques, 1988; Abenojar et al., 2014) was also studied to improve the compatibility and the mechanical properties. Fernandes et al. (2010) concluded that the mechanical performance of the composites decreased with the increase in cork content but increased with the introduction of coupling agents that promoted the adhesion between cork–polymer phases.

The structural properties of cork were found to be strongly dependent on temperature and may affect its color. A darkening effect was observed in samples treated at lower temperatures (150°C). The thermal decomposition of cork studied by thermogravimetry analysis has shown a mass decrease of about 30% upon heating at 300°C and less than 10% at 200°C (Rosa and Fortes, 1988a,b; Rosa and Fortes, 1988a,b; Şen et al., 2014). Therefore, the color changes observed at 150 and 200°C, when cork did not undergo significant chemical decomposition, were originated from extractives and hydrolyzed carbohydrates and their reactions with cork cell wall components particularly with cork lignin, while above 200°C it resulted from decomposition of hemicelluloses and formation of oxidation products. According to Pereira (2007), the cork extractives were the first to be volatized, hemicelluloses were the first structural components to be degraded, and lignin and suberin were the most stable components, therefore degraded at last.

Most of these studies were based on injection molding and extrusion processes for the production of cork-polymer materials and applications. There is no knowledge in the processing of this material by rotational molding. This technique is used to produce hollow parts for various applications like liquid storage tanks, containers, toys, indoor and outdoor furniture, and playgrounds, among other applications. The advantages are the production of stress-free parts; the low costs for tooling's and molds; the little or no waste production; and the low restriction on mold design allowing the production of multilayer materials, especially when different compositions and thicknesses are required (Jansri and O-charoen, 2018; Fletes et al., 2020). This process is based on the rotation of polymeric powder material in an externally heated and cooled mold. Therefore, larger cycle times are involved compared to other plastic processing techniques such as injection molding or extrusion blow molding used to process similar parts (Crawford and Throne, 2002; Crawford and Kearns, 2003; Crawford and Gibson, 2012; Pereira, 2015; Nugent, 2017). Moreover, rotomolding is a challenge for several materials due to the possibility of thermo-oxidative degradation during processing, as a result of high temperature and large cycle time applied with impact on morphological and mechanical properties (Oliveira et al., 1996, 2007; Cramez et al., 2001). Due to that, this paper focuses on the processability of PE/cork by rotational molding and the relationship between material, processing, and product characteristics. The parts are characterized by aesthetic (color), chemical (evaluation of chemical composition), thermal (mass loss with temperature), physical (contact angles and density), morphological (microscopy), and mechanical (impact resistance) tests. The aim is to explore and characterize new materials to be used on the rotational molding process to produce differentiated new products with high value, sustainability, aesthetics, and functionality. This study is in line with other recently published articles in the finding of new materials for rotational molding (Greco et al., 2019; Vignali et al., 2019; Fletes et al., 2020).

MATERIALS AND METHODS

Cork and Polymer Materials

Different cork powders and granules, from cork processing stages, were kindly supplied by Amorim Cork Composites, SA (Portugal). The polymer used in the preparation of the cork-based composites was medium-density polyethylene (MDPE) (Advancene EM-3405-UVH) with MFI of 5 g/10 min

(190°C/2.16 kg) obtained from Ethydco (Egypt). The bulk density, particle size, and visual aspect of the cork are shown in **Table 1** and **Figure 1**, respectively.

Compounding and Processing

Different cork powders were dry blended with MDPE in the proportions of 90/10, 85/15, and 80/20 wt% and processed by rotational molding. For each sample, 150 g of material was used. The oven was heated by electrical resistances and its temperature was set to 290°C. The peak internal air temperature inside the mold (PIAT) was set to 210°C, and it was monitored by a thermocouple placed inside the mold through the vent conduct during processing. Cooling by air was applied until the temperature inside the mold dropped to 60°C before demolding the parts.

In a second part of the study, there was a need to understand the influence of the processing conditions applied on the aesthetics and morphological and mechanical characteristics of the parts. Therefore, parts of MDPE with 10 wt% MF8 cork were produced with PIAT ranging from 185 to 235°C.

For the processing of the parts, a laboratory rotational molding equipment with characteristics of a Rock and Roll and Shuttle machine was used, with an aluminum mold with parallelepipedic dimensions of 140 × 90 × 90 mm and 5 mm of mold wall thickness. This is a prototype machine developed at the Department of Polymer Engineering at the University of Minho (Pontes et al., 2014). In this type of machine, the mold rotates 360° through the axis of the support arm and the oven performs a swinging motion (from 45° to 45° to the right to the left) perpendicular to the support arm, allowing the spreading of the material for the ends of the part. The rotation speed of the mold and the pendulum swing were 7 rpm and 1.5 rpm, respectively.

TABLE 1 | Bulk density and maximum particle size of MDPE and cork powders.

Sample code	Type	Bulk density (kg/m^3)	Max. particle size (mm)
MDPE	Powder	330–390	0.50
MF5	Powder	50–70	<0.60
MF8	Powder	75–95	<0.15
BD-0.5/1	Granules	50–60	0.5/1
BD-2/3	Granules	55–65	2/3

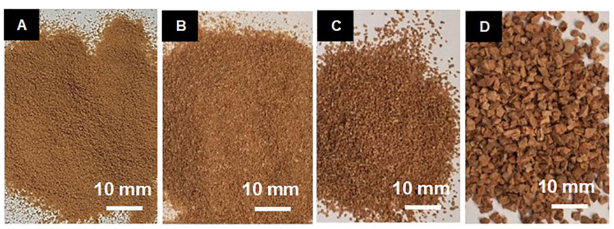

FIGURE 1 | Cork powders **(A)** MF8 and **(B)** MF5 and cork granules **(C)** BD-0.5/1 and **(D)** BD-2/3.

Color Determination

The aesthetic characteristics of the MDPE/cork parts were evaluated by visual inspection and by color measurements using a Spetro-Guide BYK portable colorimeter and a Shimadzu UV-2401PC reflectance spectrophotometer operating in the range of visible light between 380 to 740 nm with a 2 nm spectral resolution. The color parameters L, a, and b were determined according to the CIELab method. The system is based on the measurement of three coordinates: lightness L* between 0 (black) and 100 (white), a* representing red–green levels (+60 red, -60 green), and b* representing yellow–blue levels (+60 yellow, -60 blue). The color of a material is a mixture of these three parameters. The color variation was calculated according to the following formula (Bekhta and Niemz, 2003), where ΔL, Δa, and Δb correspond, respectively, to the variation of the coordinates L*, a*, and b* relative to the reference sample of a virgin cork powder.

$$\Delta E = \sqrt{\Delta L^2 + \Delta a^2 + \Delta b^2}$$

Thermal Properties

The thermal stability studies determined by thermogravimetric analysis (TGA) were performed to understand the degradation characteristics of the cork powder and the CPCs using a TGA Q500 series thermogravimetric analyzer from TA Instruments. Experiments were performed in platinum pans, at a heating rate of 10°C/min from 40 to 800°C under air atmosphere with an air flow rate of 40 mL/min. This atmosphere was used to replicate the atmosphere condition inside the mold during the rotational molding process.

FTIR Analysis

To evaluate changes in the functional groups on the CPC after heating treatment, FTIR-ATR spectra were recorded using a MKII Golden Gate Single Reflection ATR System equipped with an ATR Golden Gate cell. Each spectrum was an average of 64 scans taken with 8 cm^{-1} resolution in the 4000–600 cm^{-1} range.

Contact Angles

Contact angle measurements of the parts were determined according to the standard D7334-08 using a DataPhysics Contact Angle System OCA-20. Distilled water was used for sample analysis, and the volume of the sessile drop on the top surface was maintained at 2 μL in all cases, using a micro-syringe. For accuracy, all measurements were performed right after deposition of the droplet and repeated 10 times on different pieces of the same sample.

Density

To determine the density of the parts, the samples were weighted in air and propanol according to the standard ISO 1183-1, Method A, using an OHAUS Pioneer^{TM} analytical balance equipped with a stationary support for the immersion vessel. The tested specimens were rectangular bars with 20 mm length and 10 mm width. Five specimens were tested for each sample.

Scanning Electron Microscopy

The morphology of the cork structure and the fracture of the CPC parts were analyzed using an ultra-high-resolution field-emission gun scanning electron microscope (FEG-SEM) (Nova 200 NanoSEM, FEI Company, at SEMAT, Guimarães, Portugal). Secondary electron images were performed with an acceleration voltage of 10 kV.

Prior to the morphological analyses, the samples were covered with a very thin film (20 nm) of Au–Pd (80–20 wt%), in a high-resolution sputter coater (208HR Cressington Company), coupled to a MTM-20 Cressington High Resolution Thickness Controller.

Mechanical Tests

The mechanical properties of the parts were determined by Izod and puncture impact tests. The Izod impact tests were performed according to the standard ISO 180 on a Ceast Resil Impactor instrument falling-weight impact tester with a pendulum energy of 7.5 J. The notched specimens were rectangular bars with 80 mm length and 10 mm width. Ten specimens were tested for each sample.

The puncture impact tests were performed according the standard ISO 6603-1:2000 and ISO 6603-2:2000 on a Ceast Fractovis Plus instrument falling-weight impact tester. All the specimens were subjected to the same energy level (147.5 J), with an impact velocity of 4.4 m/s resulting from a drop height of 1 m of a carriage of total mass of 3 kg. The tested specimens were squared with a 60 mm side. Ten specimens were tested for each sample.

RESULTS AND DISCUSSION

Effect of Cork Powder Granulometry on Part Quality

Figure 2 and **Table 2** depict the appearance of rotomolded parts produced with different granulometries and compositions of cork powders. The parts are soft on touch and transmit the sensation of comfort and warm feeling of the cork. This unique characteristic of natural cork material is maintained when CPC are processed by rotational molding. Parts processed by other plastic processing techniques like extrusion or injection molding lose this property as plastic shiny look and plastic touch are obtained.

Several difficulties were encountered in the attempt to process good-quality parts when using MDPE/cork of big particle size (0.5/1 and 2/3 mm) (**Figure 2**). The apparent density of these materials prevents their easy fitting on the mold cavity and facilitates the appearance of defects such as incomplete parts at the corner and heterogeneous surfaces due to the poor mixing, phase separation of polymer/cork, and lack of polymer wetting.

Parts of good quality were obtained using fine cork powders (**Table 2**). However, the increase in cork percentage resulted in the reduction of the sintering capability of the composite material increasing its porosity, wall thickness, and surface defects. These effects were more pronounced for MF5 than for MF8, given its difference in the powder size and powder characteristics as revealed by SEM images (**Figure 3**). MF5 powder particles are larger in size (<0.6 mm) and form a well-defined honeycomb cellular structure, whereas MF8 was grinded to a much smaller particle size (<0.15 mm) resulting in almost individual cells.

In terms of processing, rotational molding is defined by the rotation of the material inside the mold that is only subjected to a thermal environment and free coalescence of the particles; therefore, sintering is favored for MDPE/MF8. This result reveals that MF8 cork powder has the preferred material characteristics for the production of CPC by this processing technique.

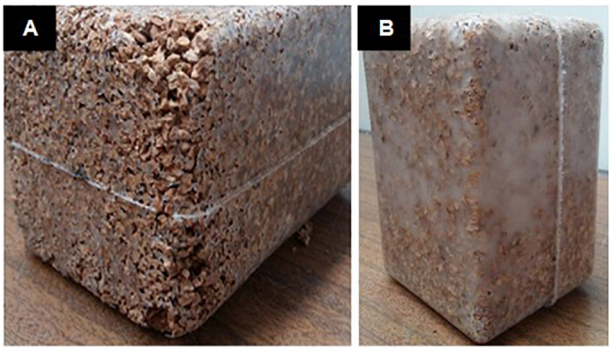

FIGURE 2 | Main defects obtained for parts produced by MDPE with 20% of BD-0.5/1 **(A)** and BD-2/3 **(B)**.

TABLE 2 | Images of parts produced by MDPE with different compositions of MF5 and MF8 cork.

Cork type	10%	15%	20%
	Whole parts		
MF5			
MF8			
	Cross section		
MF5			
MF8	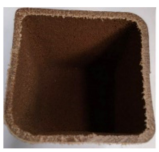	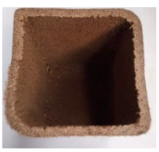	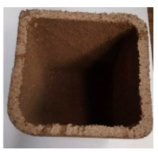

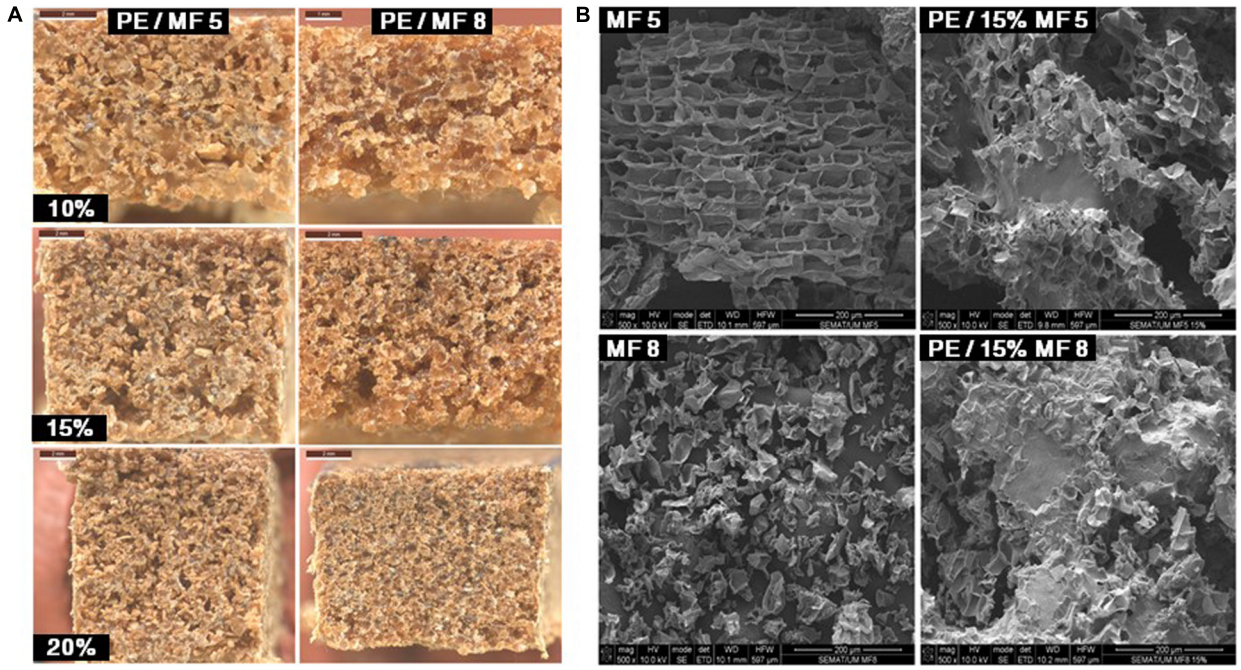

FIGURE 3 | Effect of MDPE/cork composition on the structure of the parts. **(A)** Images obtained by optical magnification of the cross section along the wall thickness. **(B)** Images obtained by SEM analysis of MF5 and MF8 cork powder and its MDPE/cork composites.

Effect of Mold Internal Air Temperature

Rotomolding is a challenge for several materials due to the possibility of thermo-oxidative degradation during processing. Since cork is prone to color and structural changes at high temperatures, a study was carried out on the effect of mold internal air temperature (IAT) on the properties of MDPE/10 wt% MF8.

The processing cycle, generally monitored by the changes in the internal air temperature of the mold with time, is shown in **Figure 4A**. The incorporation of cork material has an important influence on the processing cycle when compared to MDPE. The difference starts at the moment of melting and adhesion of the PE particles to the mold surface (plateau observed between 110 and 150°C). In the case of PE/cork, there is a significant delay on that process, which also delays the rapid increase in the temperature inside the mold observed when all the material reaches the molten state and adheres completely to the mold surface (cooking stage of the material). Once the setup PIAT is reached, the mold is transferred to the cooling chamber. The temperature drops, and a small plateau occurs due to the crystallization process. It follows the solidification of the material until the part is demolded. The difference in the processing cycle of both materials is justified by the lower thermal conductivity of cork material (0.039–0.045 W/mK) as compared to PE (0.32–0.40 W/mK) (Hansen and Bernier, 1972; Silva et al., 2005; Gil, 2007). Therefore, the heat transferred from the mold to the particles is delayed by the presence of cork that affects not only the melt of the material (observed by the delay on reaching the PIAT) but also the transferring of the heat trapped inside the mold during cooling, leading to an overshooting of temperature and longer cycle times. It is important to note that both samples were transferred to the cooling chamber at the same time, corresponding to the abrupt drop of the oven temperature. While MDPE starts the cooling phase, MDPE/cork temperature is still rising, delaying for some minutes the cooling of the material.

The effect of mold temperature, namely, the PIAT, on the cycle time is depicted in **Figure 4B**. As observed, the higher the temperature at which the parts are processed, the longer it takes to reach PIAT and the longer is the cycle time. The shortest cycle time recorded for PIAT of 185°C (real PIAT of 201°C due to overshooting) was about 38 min, whereas the longest cycle time recorded for PIAT of 235°C (real PIAT of 238°C) was about 43 min. The variations in the mold internal air temperature can be directly related to the materials and processing conditions and are very sensitive to differentiate between the samples as reported in other studies (Cramez et al., 2002; Ramkumar et al., 2014).

Table 3 depicts the image of parts obtained at each PIAT and its effect on the color parameters in comparison to natural cork. The repeatability of part production is observed most of the time, with the darkening of the color with the increase in PIAT being clear. This is observed by the lightness parameter, ΔL, whose values change from 22.4 to 35.1. The total color difference, ΔE, follows this trend by increasing steadily with the increase in PIAT (22.5–37.6).

The effect caused by the processing at high temperatures is a decrease in lightness, which means the parts are darker than the parts processed at the lowest temperatures. These results are in agreement with the findings obtained using Q.

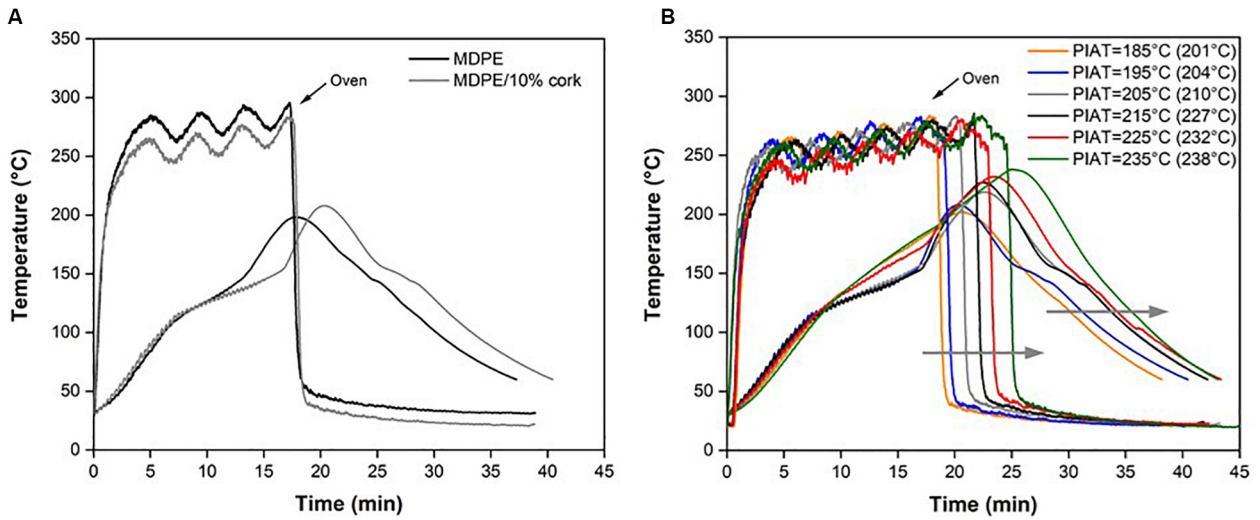

FIGURE 4 | Mold internal air temperature profiles during the rotational molding process of **(A)** MDPE and MDPE/10% cork parts and **(B)** MDPE/10% cork parts processed at different IAT. The arrow indicates the direction of increase in the IAT setup used for processing the parts.

TABLE 3 | Repeatability studies of MDPE/10% MF8 cork parts at different processing temperatures and CIELab color parameter variations in relation to the neat cork powder.

PIAT (°C) Setup (Real)	Rotomolded parts	CIELab parameters variation			
		ΔL	Δa	Δb	ΔE
185°C (201°C)		22.38	2.13	1.38	22.52
195°C (204°C)		22.08	1.54	3.37	22.39
205°C (210°C)		25.41	1.53	3.64	25.71
215°C (227°C)		28.89	0.23	8.57	30.13
225°C (232°C)		31.62	1.60	9.79	33.14
235°C (238°C)		35.05	3.52	13.42	37.69

cerris cork (Şen et al., 2012). The authors found that the change in color at low temperatures (150°C) can occur even if there is no significant chemical decomposition of cork as a result of the reactions between extractives and hydrolyzed carbohydrates with cork cell wall components particularly with lignin. Above 200°C, decomposition of hemicelluloses may occur and the formation of oxidation products contributes to the color change of the cork. Further details are given in the following sections.

From now on the real PIAT is described on the figures and tables, and the data discussed according to real PIAT.

Evaluation of Cork by Thermal Analysis

Thermogravimetry analysis (TGA) of neat cork material was carried out to understand the thermodegradation behavior of cork and to identify the temperatures at which the main chemical processes occur. TGA was carried under air atmosphere to evaluate the thermal stability of cork at high temperature and to have a similar environment as that occurring inside the mold during processing. The TGA/DTG curves for cork are presented in **Figure 5**.

Four regions can be identified in the thermogravimetric curves. The cork powder shows an initial region of mass loss between room temperature and 100°C corresponding to the elimination of water. However, water is only completely eliminated at 200°C, corresponding to 1% of mass loss. The second region of the curve, between 200 and 350°C and about 500°C, is characterized by a rapid mass loss. The first peak (351.8°C) corresponds to polysaccharides composed of cellulose and hemicellulose that have degradation temperatures in the range between 300 and 400°C (Silva et al., 2005; Kim et al., 2006; Wei et al., 2013). Suberin and lignin also contribute to this reaction but with smaller magnitudes. It is at this peak that the greatest loss of mass is found, which indicates that the reactions that contribute to the first exothermal peak are those that induce the darkening of the samples and that there is no further color change with the subsequent reactions (Şen et al., 2014). Lignin and suberin are relatively more thermal stable components when compared to polysaccharides and extractives, which means these components contribute mainly to the second reaction (455.5°C) in cork. Hence, the color changes in cork are the result of hemicellulose decomposition and formation of

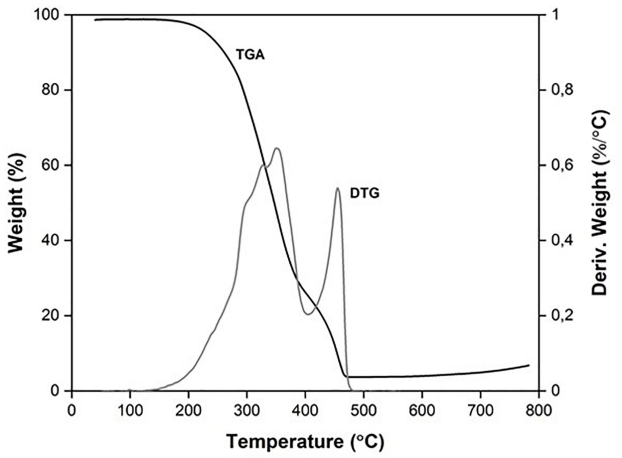

FIGURE 5 | TGA and DTG curves of cork powder under air atmosphere.

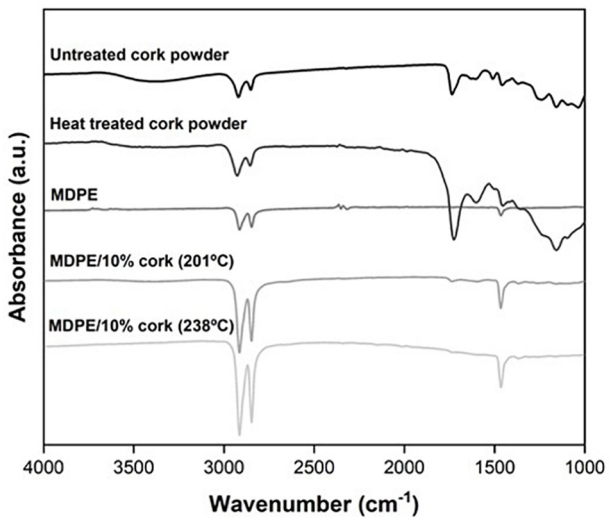

FIGURE 6 | FTIR spectrum for untreated cork powder, heat-treated cork powder for 48 h in the oven at 255°C, virgin MDPE and MDPE/10% cork part processed at 238°C.

oxidation products. In the final region, above about 500°C, the rate of mass loss is lower until the cork reduces to ashes (about 3.79% by weight).

Furthermore, the loss mass at 250°C was 6% and at 300°C was less than 30%. The thermal degradation of cork, in air atmosphere, starts at 258.4°C. This suggests that the cork powder can be processed at temperatures lower than 250°C without induced irreversible changes in cork chemical composition, and it can also be processed with polymers having processing temperatures lower than this value, such as the case of polyethylene.

Evaluation of Cork Structural Changes by FTIR Analysis

Figure 6 shows the FTIR spectrum of cork powder, MDPE powder, and MDPE/10% cork produced at 238°C. Natural cork powder was subjected to a heat treatment of 48 h at 255°C in an oven prior to FTIR so that color and possible structural changes could be identified and compared to the material changes occurring during the rotational molding process.

The FTIR spectrum of cork powder before heat treatment shows a band between 3600 and 3200 cm^{-1}, assigned to the O–H vibration from carbohydrates and lignin (Şen et al., 2012). The spectrum is dominated by the absorbance bands of suberin: two peaks at 2920 and 2847 cm^{-1}, corresponding to the asymmetric and symmetric vibration, respectively, of C–H in the olefinic chains and an intense band at 1732 cm^{-1} corresponding to the carbonyl C = O in aliphatic acids and esters (Pereira, 2007). The band at 1128 cm^{-1} can also be attributed to the C–O–C of the ester group in suberin. Suberin also contributes to the 1242 cm^{-1} peak corresponding to the C–O stretch, through the epoxide group (Fernandes et al., 2014). The band at approximately 1466 cm^{-1} is typical for lignin, and the peaks at 1087 and 1035 cm^{-1} correspond to the C–O bond and are characteristic of polysaccharides (cellulose and hemicelluloses) (Abenojar et al., 2014).

The comparison of the FTIR spectrum of cork powder, before and after heat treatment, confirmed the occurrence of chemical modifications. The largest modification in the chemical composition of cork observed in the FTIR spectrum was the substantial intensity reduction in the O–H (3600–3200 cm^{-1}) with temperature and treatment time. This means that carbohydrate content reduced substantially with temperature, and carbohydrate is the most heat-sensitive component of cork. Thus, temperature-induced alterations in the chemical composition of the components are condensation of carbohydrate products with suberin in the lower temperature range and heavy condensation of all remaining components at higher temperatures.

The FTIR spectrum of a CPC sample produced at 238°C and the pure materials (cork and MDPE) show significant differences in the absorption patterns. The absorption of the C–O band between 1030 and 1000 cm^{-1} and the O–H band between 3600 and 3200 cm^{-1}, corresponding to O–H stretching, decreased after heating, indicating the loss of polysaccharides and condensation of lignin side chains with phenyl nuclei. The bands at 3000 and 2800 cm^{-1} did not decrease by heating, indicating the stability of suberin in these conditions. In addition, these bands are more pronounced in the CPC sample because MDPE is composed of long chains of C–H and due to the presence of C–H in cork from suberin. The band at 1466 cm^{-1}, corresponding to the vibration of aromatic ring of lignin increased by heating, indicating the stability of lignin in these conditions (Dekier, 2012). The results are in agreement with findings by Pereira (1992, 2007), Şen et al. (2012), and Fernandes et al. (2014).

Effect of PIAT on the Contact Angles of Parts

The purpose of the contact angle tests was to study the wettability of MDPE as compared to MDPE/cork parts.

Figure 7 shows the measurement of the contact angles and the drop plain view digital image taken right after the sessile drop test.

The MDPE part has a contact angle of 86°, which is close to the value reported in the literature (Subedi, 2011). The incorporation of cork results in the increase in the contact angle to values above 100°. This proves that the liquid does not wet the surface, and therefore, there is a more pronounced hydrophobic and impermeable behavior of the parts with the incorporation of cork. In fact, cork is impermeable to liquids and gases, because its cell walls are closed and essentially composed of suberin, which is a hydrophobic component (Abenojar et al., 2014).

With the increase in PIAT, there is a decrease in the contact angle between the drop and the surface of the parts. At 201°C, the contact angle was 118.9° and at the highest temperature of 238°C was 109°, however, the parts still have a hydrophobic character. This result reveals that the surface of the part changes with the processing cycle applied, namely, the PIAT. The increase in PIAT leads to a slight decrease in the contact angle, which may indicate a better wettability of the cork powder by the polymer with the increase in temperature and a transition of parts with a touch of cork to a more plastic touch. This characteristic allows the liquid to have a better tendency to wet the surface, and consequently, there is a decrease in the contact angle.

Morphology of CPC Parts

The morphology of the impact-fracture surface of MDPE/10%MF8 at different processing temperatures was evaluated by SEM (**Figure 8**). The first observation is that all the parts are very porous, but there seems to be evidence of good interfacial adhesion between the two components, as cork powder particles are embedded in the thermoplastic matrix. According to the micrographs, the peculiar morphology of the cork was maintained after compounding and processing (compare to **Figure 3B** – MF8). The increase in processing

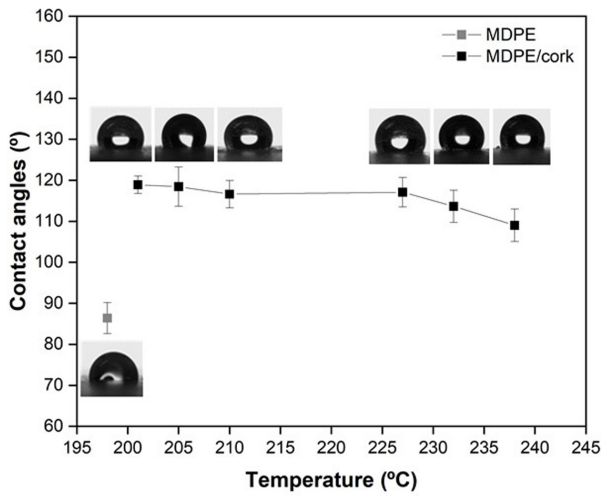

	MDPE	MDPE/10% cork					
PIAT (°C)	198	201	204	210	227	232	238
Contact angles (°)	86.4 ±3.8	118.9 ±2.1	118.5 ±4.8	116.6 ±3.3	117.1 ±3.6	113.6 ±3.9	109.0 ±4.0

FIGURE 7 | Contact angles between a drop of water and the surface of virgin MDPE and MDPE/10% cork parts.

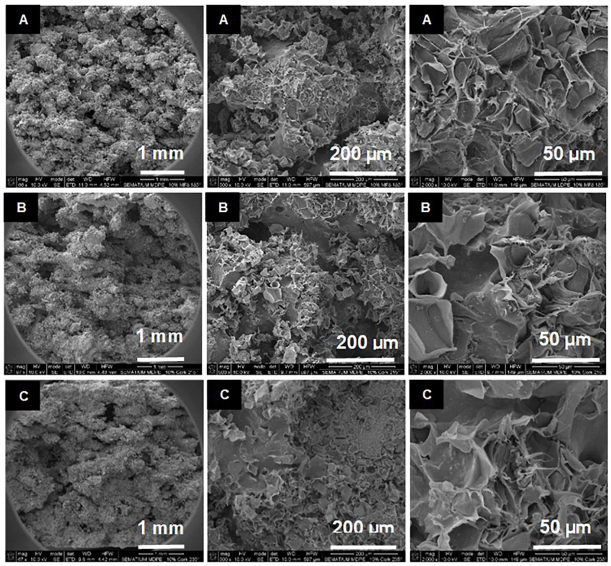

FIGURE 8 | Morphology of the impact–fracture surface of MDPE/10% cork produced at **(A)** 201°C, **(B)** 227°C, and **(C)** 238°C.

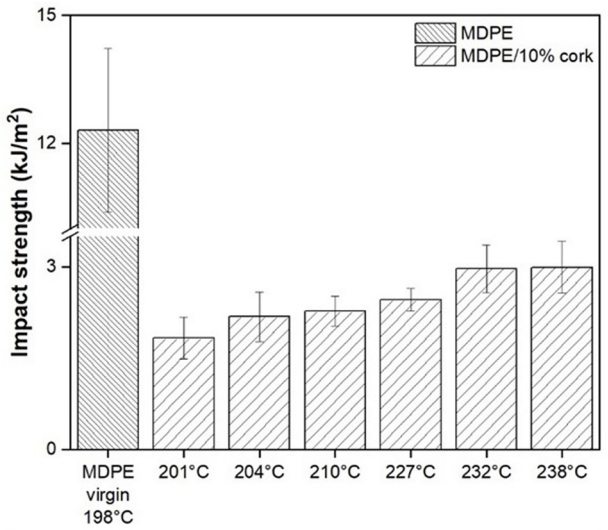

	MDPE	MDPE/10% cork					
PIAT (°C)	198	201	204	210	227	232	238
Impact strength (kJ/m²)	12.3 ±1.9	1.8 ±0.3	2.2 ±0.4	2.3 ±0.2	2.5 ±0.2	3.0 ±0.4	3.0 ±0.4

FIGURE 9 | Effect of PIAT on the impact strength of MDPE and MDPE/10 wt% cork parts.

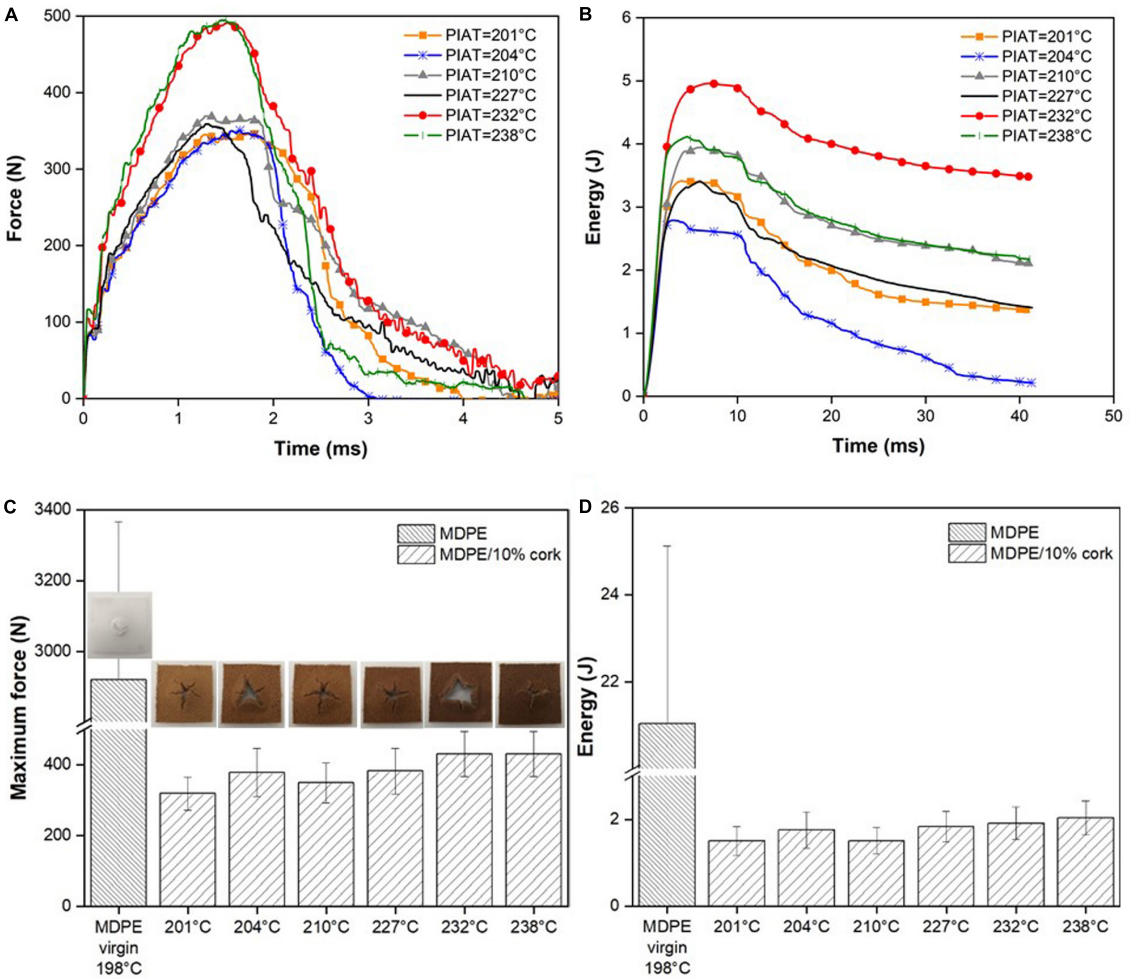

	MDPE	MDPE/10% cork					
PIAT (°C)	198	201	204	210	227	232	238
Maximum force (N)	2920.0± 446.9	318.7± 46.2	377.6± 68.6	349.1± 56.5	382.3± 64.1	430.9± 79.9	431.0± 63.7
Energy (J)	21.0 ± 4.1	1.51 ± 0.3	1.76 ± 0.4	1.50 ± 0.3	1.83 ± 0.4	1.91 ± 0.4	2.03 ± 0.4

FIGURE 10 | Effect of PIAT on the impact behavior of MDPE and MDPE/10% cork parts. **(A)** Force over time; **(B)** Energy over time; **(C)** Maximum force as a function of PIAT and related samples fracture surfaces; **(D)** Energy at maximum force as a function of PIAT.

TABLE 4 | Density of the parts.

	MDPE	MDPE/10% cork					
PIAT (°C)	198	201	204	210	227	232	238
Density (g/cm^3)	0.924 ± 0.001	0.909 ± 0.009	0.913 ± 0.007	0.887 ± 0.006	0.885 ± 0.019	0.0897 ± 0.015	0.889 ± 0.012

temperature favors a better sintering of materials reducing the porosity level of the part.

Mechanical Properties of Parts

Impact strength results are shown in **Figure 9**. It can be seen that the impact strength decreased greatly with the addition of 10% of cork powder (1.83 kJ/m^2) compared with neat MDPE (12.30 kJ/m^2). This tendency is mostly related to the presence of voids and porous structure observed (see **Figure 3**), which contributes to stress concentration points and a weak ability to transfer energy between materials. Previous studies (Xu and Crawford, 1993; Oliveira et al., 1996, 2007; Pick and Harkin-Jones, 2004) reported a correlation between the number of voids and the impact strength in rotational molded parts; the

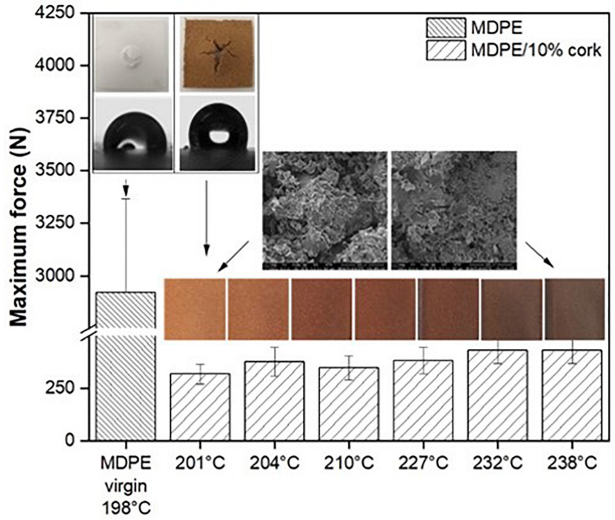

FIGURE 11 | Relationship between processing and properties of parts.

greater the number of voids, the lower the impact resistance. Moreover, according to Oliveira et al. (2007) and Ramkumar et al. (2016), there is a processing window that maximizes the mechanical properties as a result of better sintering (reduction of voids) and the absence of thermal degradation of the polymer matrix. In the present study, cork hinders the formation of a well-compacted structure, as observed previously by SEM. Nevertheless, CPC parts increase their impact strength from PIAT at 201 to 238°C. This result can be attributed to the diminishing of voids and the building up of a more compact structure at higher PIATs. This means that the composites can absorb more energy and, consequently, their mechanical properties are improved.

Puncture impact tests are depicted in **Figure 10**. The results indicate that MDPE and MDPE/10% cork parts exhibit a quite different failure and deformation behavior. While MDPE suffers a ductile fracture, the CPC parts fracture in a fragile way, as observed by the images of the fracture surfaces presented in **Figure 10C**.

The maximum contact force between the impactor and specimen and the absorbed energy in the crushing process were determined for all the impact tests carried (**Figures 10C,D**). The reduction in the puncture impact behavior of the CPC compared to MDPE is clear. In the force–time curves, MDPE samples got to a maximum load peak around 2900 N, while all the samples with cork present values between 300 and 450 N (decrease up to 84%). Thus, the use of cork affects the maximum allowed loads related to impact. These values (in terms of percentage) are similar to those obtained by other authors working with fibers in rotomolding, where reductions up to 90% in impact properties were reported (Torres and Aragon, 2006; Yuan et al., 2007; Ortega et al., 2013; Cisneros-López et al., 2017).

With the increase in temperature (PIAT), there is a tendency for the maximum force to be higher and the curve to be more extensive over time, which indicates that energy absorption is achieved in a longer period of time. This can prevent the appearance of undesirable fracture accelerations resulting from the impact.

Regarding the energy curves, it can also be seen that upon CPC reaching the maximum of absorbed energy, the curve tends to show a negative slope. Thus, in CPC parts there is a slight tendency to increase the strength supported by the sample before fracture and the absorbed energy with the increase in PIAT. Due to the heterogeneity of the samples, the fluctuations in the force and energy absorbed from the materials are expected.

Density of Parts

The density of the parts is shown in **Table 4** and reveals a significant decrease with the addition of 10% of cork powder (0.909 g/cm^3) as compared to neat MDPE (0.924 g/cm^3). This result is expected given the difference in the density of both materials, namely, cork (0.11–0.25 g/cm^3) (Anjos et al., 2014) and MDPE (0.934 g/cm^3) (Datasheet of Medium Density Polyethylene, 2016), and the fact that the amount of polymer in the composite was reduced.

Cork is composed of closed cells with a gas similar to the air inside, which promotes a decrease in the density of the parts in which the cork is incorporated (Gul et al., 2013). With the increase in PIAT, it seems to have a slight decrease in density of the parts. The values may vary due to the heterogeneity of the samples.

Relationship Between Processing–Morphological–Properties of Parts

Figure 11 summarizes the relationship between processing, morphology, and properties of the PE/cork parts obtained by rotational molding. The mechanical properties of CPC parts are greatly affected when compared to pure PE, because the sintering ability of PE material becomes more difficult in the presence of cork, resulting in a high level of porosity and voids. This changes the fracture behavior of PE from ductile to fragile behavior. The increase in processing temperature (seen by the PIAT) results in a more compact structure, improving the mechanical properties of the composite. It also influences the appearance of the final parts, by the darkening of the color with the increase in PIAT. No significant chemical degradation of the cork structural components occurs during processing at these temperatures; therefore, the hydrophobic character of the surface of the parts is achieved and maintained during processing. It is important to notice that the parts preserve the texture and soft touch of the cork natural material, although its color depends greatly on the processing conditions used.

Despite the decrease in the mechanical properties of the PE/cork composite parts produced by rotational molding, there are some benefits to be pointed out, namely, the aesthetics of cork, touch (soft and warm feeling), the hydrophobicity of the surface, and the lightness of the final part. Therefore, different functionalities can be achieved by using PE/cork composites on the production of parts by rotational molding.

CONCLUSION

The rotational molding of PE/cork composites was investigated to understand the relationship between processing, morphology, and characteristics of the parts. The effect of cork powder granulometry (0.15–2/3 mm), the composition of MDPE/cork (10–15–20 wt% cork), and processing window (200–240°C) were analyzed. Good-quality parts were obtained by rotomolding using fine cork powders (<0.6 mm particle size) and a maximum of 10 of cork by weight. The increase of cork reduced the sintering capability of the materials, increasing part porosity, wall thickness, and surface defects. These effects were more pronounced in MF5 (<0.6 mm, honeycomb cellular structure) than for MF8 (<0.15 mm, individual cells), given its difference in size and morphological characteristics. Part defects such as incomplete parts at the corns and heterogeneous surfaces due to poor mixing and lack of polymer wetting were observed for large particle sizes. These results allow the selection of MF8 cork as the preferred material for the composition of PE/cork composites.

Cork characteristics such as soft touch and warm feeling were obtained regardless of the processing conditions applied. However, the brownish tone, typical of cork, gradually became darker with the increase in processing temperature. The color change was due to the reaction of the extractives within the components of the cork cell wall, and not by degradation of cork, indicating that a typical processing window for rotomolding of PE can be adopted for MDPE/cork composites. Higher temperatures favor the sintering of the PE material and the construction of a more compact structure, which in turn results in the improvement of the impact properties (from 318.69 N at 201°C to 430.98 N at 238°C). Nevertheless, virgin PE parts have a ductile behavior and absorb seven times more energy than PE/cork parts.

This work presents a different strategy for the upgrading of cork by-product (cork powder) and simultaneously the development of sustainable composites with potential applications in rotational molding. This processing technique allows the cork characteristics to be preserved in the processing window typical for PE, giving rise to products with lightweight, unique visual appearance, soft touch, sensation of comfort, and warm feeling of cork.

DATA AVAILABILITY STATEMENT

The datasets generated for this study are available on request to the corresponding author.

AUTHOR CONTRIBUTIONS

CM was the scientific mentor of the work, conceiving and designing the experiments. VG performed the experimental work and analyses of results. CM and VG analyzed the data and wrote the manuscript. Both authors have read and agreed to the published version of the manuscript.

FUNDING

The authors acknowledge the financial support of the Project RoTMI-Rotomolding Technology and Materials Innovations (POCI-01-0247-FEDER-33095), cofinanced by the European Regional Development Fund (FEDER) through the Operational Program for Competitiveness and Internationalization (POCI) under the "Portugal 2020" framework. IPC acknowledges the support of the Portuguese Foundation for Science and Technology (FCT) through the National Funds References UIDB/05256/2020 and UIDP/05256/2020.

REFERENCES

Abenojar, J., Barbosa, A. Q., Ballesteros, Y., Del Real, J. C., Da Silva, L. F. M., and Martínez, M. A. (2014). Effect of surface treatments on natural cork: surface energy, adhesion, and acoustic insulation. *Wood Sci. Technol.* 48, 207–224. doi: 10.1007/s00226-013-0599-7

Anjos, O., Rodrigues, C., Morais, J., and Pereira, H. (2014). Effect of density on the compression behaviour of cork. *Mater. Des.* 53, 1089–1096. doi: 10.1016/j.matdes.2013.07.038

Bekhta, P., and Niemz, P. (2003). Effect of high temperature on the change in color, dimensional stability and mechanical properties of spruce wood. *Holzforschung* 57, 539–546. doi: 10.1515/HF.2003.080

Castro, O., Silva, J. M., Devezas, T., Silva, A., and Gil, L. (2010). Cork agglomerates as an ideal core material in lightweight structures. *Mater. Des.* 31, 425–432. doi: 10.1016/j.matdes.2009.05.039

Cisneros-López, E. O., González-López, M. E., Pérez-Fonseca, A. A., González-Núñez, R., Rodrigue, D., and Robledo-Ortíz, J. R. (2017). Effect of fiber content and surface treatment on the mechanical properties of natural fiber composites produced by rotomolding. *Compos. Interfaces* 24, 35–53. doi: 10.1080/09276440.2016.1184556

Cramez, M. C., Oliveira, M. J., and Crawford, R. J. (2001). Effect of nucleating agents and cooling rate on the microstructure and properties of a rotational moulding grade of polypropylene. *J. Mater. Sci.* 36, 2151–2161. doi: 10.1023/A:1017583731513

Cramez, M. C., Oliveira, M. J., and Crawford, R. J. (2002). Optimisation of rotational moulding of polyethylene by predicting antioxidant consumption. *Polym. Degrad. Stab.* 75, 321–327. doi: 10.1016/S0141-3910(01)00234-8

Crawford, R. J., and Gibson, S. (2012). Rotational molding: some basics. *Pop. Plast. Packag.* 10, 26–28.

Crawford, R. J., and Kearns, M. P. (2003). *Practical Guide to Rotational Moulding*. Akron: Rapra Technology Ltd.

Crawford, R. J., and Throne, J. L. (2002). *Rotational Molding Technology*. New York, NY: William Andrew Publishing.

Datasheet of Medium Density Polyethylene (2016). *Datasheet of Advancene EM-3405-UVH Medium Density Polyethylene (MDPE)*. Alexandria: Unipol Pe Technology.

Dekier, Ł (2012). The origins and evolution of lean management system. *J. Int. Stud.* 5, 46–51. doi: 10.14254/2071-8330.2012/5-1/6

Fernandes, E. M., Aroso, I. M., Mano, J. F., Covas, J. A., and Reis, R. L. (2014). Functionalized cork-polymer composites (CPC) by reactive extrusion using suberin and lignin from cork as coupling agents. *Compos. Part B Eng.* 67, 371–380. doi: 10.1016/j.compositesb.2014.07.028

Fernandes, E. M., and Correlo, V. M. (2014). Polypropylene-based cork-polymer composites: processing parameters and properties. *Compos. Part B Eng.* 66, 210–223. doi: 10.1016/j.compositesb.2014.05.019

Fernandes, E. M., Correlo, V. M., Chagas, J. A. M., Mano, J. F., and Reis, R. L. (2010). Cork based composites using polyolefin's as matrix: morphology and mechanical performance. *Compos. Sci. Technol.* 70, 2310–2318. doi: 10.1016/j.compscitech.2010.09.010

Fernandes, E. M., Correlo, V. M., Chagas, J. A. M., Mano, J. F., and Reis, R. L. (2011). Properties of new cork-polymer composites: advantages and drawbacks as compared with commercially available fibreboard materials. *Compos. Struct.* 93, 3120–3129. doi: 10.1016/j.compstruct.2011.06.020

Fletes, R. C. V., López, E. O. C., Sánchez, F. J. M., Mendizábal, E., Núñez, R. G., Rodrigue, D., et al. (2020). Morphological and mechanical properties of bilayers wood-plastic composites and foams obtained by rotational molding. *Polymers* 12, 1–19. doi: 10.3390/polym12030503

Fortes, M. A., and Nogueira, M. T. (1989). The poisson efect in cork. *Mater. Sci. Eng. A* 122, 227–232.

Gibson, L., Easterling, K., and Ashby, M. (1981). The structure and mechanics of cork. *Proc. R. Soc. London A* 377, 99–117. doi: 10.1007/s10853-011-5914-9

Gibson, L. J. (2005). Biomechanics of cellular solids. *J. Biomech.* 38, 377–399. doi: 10.1016/j.jbiomech.2004.09.027

Gibson, L. J. (2003). Cellular solids. *MRS Bull.* 28, 270–274.

Gil, L. (2007). *Cork as a building material Technical Manual*. Santa Maria de Lamas: APCOR-Associação Portuguesa de Cortiça.

Greco, A., Ferrari, F., Buccoliero, M. G., and Trono, G. (2019). Thermal and mechanical analysis of polyethylene homo-composites processed by rotational molding. *Polymers* 11:528. doi: 10.3390/polym11030528

Gul, J., Saleemi, A. R., Mirza, S., Feroze, N., Mansha, M., Gul, J., et al. (2013). Thermal and mechanical characteristics of cork filled insulation for aerospace applications. *Plast. Rubber Compos.* 39, 28–32. doi: 10.1179/174328910X12608851832010

Hansen, D., and Bernier, G. A. (1972). Thermal conductivity of polyethylene: the effects of crystal size, density and orientation on the thermal conductivity. *Polym. Eng. Sci.* 12, 204–208. doi: 10.1002/pen.760120308

Jansri, E., and O-charoen, N. (2018). Polypropylene / polyethylene two-layered by one-step rotational molding. *J. Polym. Eng.* 38, 685–694. doi: 10.1515/polyeng-2017-0367

Kim, H. S., Kim, S., Kim, H. J., and Yang, H. S. (2006). Thermal properties of bio-flour-filled polyolefin composites with different compatibilizing agent type and content. *Thermochim. Acta* 451, 181–188. doi: 10.1016/j.tca.2006.09.013

Mano, J. F. (2002). The viscoelastic properties of cork. *J. Mater. Sci.* 37, 257–263. doi: 10.1023/A:1013635809035

Nugent, P. (2017). "Rotational Molding," in *Applied Plastics Engineering Handbook: Processing, Materials, and Applications*, ed. M. Kutz (Reading, PA: Elsevier).

Oliveira, M. J., Cramez, M. C., and Crawford, R. J. (1996). Structure-property relationships in rotationally moulded polyethylene. *J. Eng. Appl. Sci.* 2, 2096–2099. doi: 10.1007/BF01152932

Oliveira, M. J., Cramez, M. C., Oliveira, M. J., and Cramez, M. C. (2007). Rotational molding of polyolefins: processing, morphology and properties. *J. Macromol. Sci. Part B* 40, 457–471. doi: 10.1081/MB-100106170

Ortega, Z., Monzón, M. D., Benítez, A. N., Kearns, M., McCourt, M., and Hornsby, P. R. (2013). Banana and abaca fiber-reinforced plastic composites obtained by rotational molding process. *Mater. Manuf. Process.* 28, 879–883. doi: 10.1080/10426914.2013.792431

Pereira, H. (1988). Chemical composition and variability of cork from *Quercus suber* L. *Wood Sci.Technol.* 218, 211–218. doi: 10.1007/bf00386015

Pereira, H. (1992). The thermochemical degradation of cork. *Wood Sci.Technol.* 269, 259–269.

Pereira, H. (2007). *Cork: Biology, Prodution and Uses*. Lisboa: Elsevier.

Pereira, H. (2015). Rotational molding: some basics. *Pop. Plast. Packag.* 10, 26–28.

Pereira, H., and Velez Marques, A. (1988). The effect of chemical treatments on the cellular structure of cork. *IAWA J.* 9, 337–345. doi: 10.1163/22941932-90001093

Pick, L. T., and Harkin-Jones, E. (2006). Effect of mould pressurisation on impact strength of rotationally moulded polyethylenes. *Plast. Rubber Compos.* 35, 324–330. doi: 10.1179/174328906X143868

Pontes, A. J., Ferreira, E. C., Mendes, J., Fonseca, J., Cramez, M. C., and Pouzada, A. S. (2014). Inovação na moldação por injeção. *Rev. da Cefanol Assoc. Nac. da Indúst. Moldes* 103, 23–29.

Ramkumar, P. L., Kulkarni, D. M., and Chaudhari, V. V. (2014). Parametric and mechanical characterization of linear low density polyethylene (LLDPE) using rotational moulding technology. *Sadhana* 39, 625–635. doi: 10.1007/s12046-013-0223-4

Ramkumar, P. L., Waigaonkar, S. D., and Kulkarni, D. M. (2016). Effect of oven residence time on mechanical properties in rotomoulding of LLDPE. *Sadhana* 41, 571–582. doi: 10.1007/s12046-016-0489-4

Rosa, M. E., and Fortes, M. A. (1988a). Temperature-induced alterations of the structure and mechanical properties of cork. *Mater. Sci. Eng.* 100, 69–78. doi: 10.1016/0025-5416(88)90240-6

Rosa, M. E., and Fortes, M. A. (1988b). Termogravimetric analysis of cork. *J. Mater. Sci. Lett.* 7, 1064–1065. doi: 10.1007/BF00720828

Şen, A., Marques, A. V., Gominho, J., and Pereira, H. (2012). Study of thermochemical treatments of cork in the 150-400°C range using colour analysis and FTIR spectroscopy. *Ind. Crops Prod.* 38, 132–138. doi: 10.1016/j.indcrop.2012.01.018

Şen, A., Van Den Bulcke, J., Defoirdt, N., Van Acker, J., and Pereira, H. (2014). Thermal behaviour of cork and cork components. *Thermochim. Acta* 582, 94–100. doi: 10.1016/j.tca.2014.03.007

Silva, M. D., Oleskovicz, M., and Coury, D. V. (2005). Cork: properties, capabilities and applications. *Control. y Autom.* 16, 345–358. doi: 10.1179/174328005X41168

Soares, B., Reis, L., and Sousa, L. (2011). Cork composites and their role in sustainable development. *Procedia Eng.* 10, 3214–3329. doi: 10.1016/j.proeng.2011.04.531

Subedi, D. P. (2011). Contact angle measurement for the surface characterization of solids. *Himal. Phys.* 2, 1–4. doi: 10.3126/hj.v2i2.5201

Torres, F. G., and Aragon, C. L. (2006). Final product testing of rotational moulded natural fibre-reinforced polyethylene. *Polym. Test.* 25, 568–577. doi: 10.1016/j.polymertesting.2006.03.010

Vignali, A., Iannace, S., Falcone, G., Utzeri, R., Stagnaro, P., and Bertini, F. (2019). Lightweight poly(ε-caprolactone) composites with surface modified hollow glass microspheres for use in rotational molding: thermal, rheological and mechanical properties. *Polymers* 11:624. doi: 10.3390/polym11040624

Vilela, C., Sousa, A. F., Freire, C. S. R., Silvestre, A. J. D., and Pascoal Neto, C. (2013). Novel sustainable composites prepared from cork residues and biopolymers. *Biomass Bioenergy* 55, 148–155. doi: 10.1016/j.biombioe.2013.01.029

Wei, L., McDonald, A. G., Freitag, C., and Morrell, J. J. (2013). Effects of wood fiber esterification on properties, weatherability and biodurability of wood plastic composites. *Polym. Degrad. Stab.* 98, 1348–1361. doi: 10.1016/j.polymdegradstab.2013.03.027

Xu, L., and Crawford, R. J. (1993). Analysis of the formation and removal of gas bubbles in rotationally moulded thermoplastics. *J. Mater. Sci.* 28, 2067–2074. doi: 10.1007/BF00367563

Yuan, X., Easteal, A. J., and Bhattacharyya, D. (2007). Mechanical performance of rotomoulded wollastonite-reinforced polyethylene composites. *Int. J. Mod. Phys. B* 21, 1059–1066. doi: 10.1142/S0217979207036916

Conflict of Interest: The authors declare that the research was conducted in the absence of any commercial or financial relationships that could be construed as a potential conflict of interest.

frontiers in Materials

ORIGINAL RESEARCH
published: 14 September 2020
doi: 10.3389/fmats.2020.561852

Statistical Fatigue Investigation and Failure Prediction of a Healable Composite System

*Nathan Hostettler, Amaël Cohades and Véronique Michaud**

Laboratory for Processing of Advanced Composites (LPAC), Institute of Materials, Ecole Polytechnique Fédérale de Lausanne (EPFL), Lausanne, Switzerland

Fiber reinforced polymers are massively used as an alternative to metals in structural applications. The brittle nature of their matrix, however, makes them more susceptible to crack formation and propagation resulting in costly repair operations and increased environmental impact. Intrinsic healable composites provide a good alternative to these conventional composite materials, whereas their mechanical properties in static solicitation or impact testing are well documented, only few studies address fatigue testing. This research focuses on 3-point bending fatigue tests of polymer-blend based healable E-glass composite materials. The S–N curve was first built to compare the fatigue behavior of the healable system to a conventional epoxy composite. A statistical approach based on Weibull statistics was developed to predict the failure probability as a function of the applied stress amplitude, to compare both systems at equivalent probability of failure. The healable system showed a higher fatigue resistance at high cycle fatigue. Furthermore, a full stiffness recovery was obtained and a life extension of at least five times compared to the reference system when healed after reaching a 90% chance of survival. The healable system thus opens new perspectives for more sustainable load-bearing composites.

Keywords: self-healing, composites, fatigue, failure prediction, Weibull statistics

OPEN ACCESS

Edited by:
Patricia Krawczak, IMT Lille Douai, France

Reviewed by:
Ming Qiu Zhang, Sun Yat-sen University, China
Nancy Sottos, University of Illinois at Urbana-Champaign, United States
Ruben Dirk Sevenois, Ghent University, Belgium

****Correspondence:***
Véronique Michaud
veronique.michaud@epfl.ch

Specialty section:
This article was submitted to Polymeric and Composite Materials, a section of the journal Frontiers in Materials

Received: *13 May 2020*
Accepted: *24 August 2020*
Published: *14 September 2020*

Citation:
Hostettler N, Cohades A and Michaud V (2020) Statistical Fatigue Investigation and Failure Prediction of a Healable Composite System. Front. Mater. 7:561852. doi: 10.3389/fmats.2020.561852

INTRODUCTION

The use of fiber reinforced polymers as a stiff and lightweight alternative to metal in structural applications enables to reach higher performance especially in transport, energy, and aerospace industry. However, the brittle nature of these materials makes them more prone to damage during manufacturing, handling, maintenance activities or during operation. Repair is not straightforward and often requires to remove part of the damaged zone and adhesively bond composite patches (Bond et al., 2008; Katnam et al., 2015; Préau et al., 2016). The overall budget for composite materials repair is thus significant and expected to reach not less than 22 Bn$ worldwide by 2026 (MarketsAndMarkets, 2017); in parallel, tons of unrecycled composite waste are produced due to unrepaired damaged structures, reaching 40,000 tons in France for the year 2015 (JEC-GROUP, 2017). Self-healing and more especially healable composites are a promising alternative to conventional composites to reduce repair costs and waste because of their ease of repair, demanding no additional material, which sometimes goes along with increased recyclability using moderate manpower and energy.

Healable polymer systems have been under investigation in the recent years, in particular integrating healing functionalities into thermoset polymers for the autonomous repair of subcritical damage in composite materials (Cohades et al., 2018). Two approaches are usually identified: a) extrinsic healable systems, where an extrinsic healing agent is integrated in the matrix through loaded microcapsules or vascules, and is released after damage events so as to flow, fill, and heal the crack after polymerization (Blaiszik, et al., 2010; Kling and Czigàny 2014), b) intrinsic healable systems, based on a modification of the matrix chemistry itself providing autonomous healing capabilities to the system (Garcia, 2014). Extrinsic systems generally show a reduction in composite mechanical properties by the integration of a large amount of capsules or vascules necessary to reach good healing capabilities; alternatively, the volume fraction of structural fibers is reduced, and the textile structure modified to make sufficient space for the healing agent containers; finally, these are limited to one healing cycle, and/or require the use of external pumping systems to circulate the healing fluids (Kessler and White, 2001; Patel et al., 2010; Norris et al., 2013; Patrick et al., 2014; Manfredi et al., 2015; Zhu et al., 2016). The intrinsic healing approach solves most of these issues providing the initial matrix with healable capabilities through reversible covalent (Park et al., 2009; Heo and Sodano 2015) bonds (Post et al., 2017; Shabani et al., 2020), supramolecular chemistries (Sordo and Michaud, 2016) or polymer blends (Pingkarawat et al., 2013; Cohades and Michaud 2017). Even if these intrinsic systems demonstrate good healing capabilities, and allow composites with a high load of reinforcing fibers, their mechanical properties are usually below those of conventional epoxy in term of stiffness, strength and damage tolerance. This is particularly true for composites based on matrices that heal at room temperature, which tend to show high mobility of bonds, and thus low mechanical properties (Deng et al., 2015; Sordo and Michaud 2016).

Healing efficiency is generally determined in composite materials through static fracture mechanics tests, in mode I or II, bending tests or compression after impact (Tsangouri et al., 2015); however, few studies are carried out on cyclic damage progression, as found in fatigue, although this case is one where small matrix cracks initially develop, that may be healed if caught at an early stage. Several studies were conducted on the fatigue resistance of extrinsic self-healing systems showing a retardation of failure due to the increased tortuosity of the crack path (Brown et al., 2005; Hamilton et al., 2012; Luterbacher et al., 2016; Ye, et al. 2017; Kim et al., 2019); however, little work is reported on the fatigue performance of intrinsically healable composites, although it is a key parameter for their long term integration as a structural material. To the best of our knowledge, only Pingkarawat and co-workers (Pingkarawat et al., 2012; Pingkarawat et al., 2013; Pingkarawat et al., 2014; Ladani et al., 2019) investigated the fatigue behavior of carbon-epoxy composites, using thermoplastic additives and only in double cantilever beam forced crack propagation mode, under cyclic loading. They found that thermoplastic additives in general helped retard the fatigue crack growth in mode I due to the presence of bridging thermoplastic ligaments formed in the healing operation at the crack location. Polyethylene-co-methacrylic acid (EMAA) was found to be the most effective, and was shown to also delay crack growth under cyclic loading when under the form of stitches, provided the quantity was high enough, or when they were combined with carbon fiber tows (Pingkarawat et al. 2014; Ladani et al., 2019). In this research, a commercial healable system based on epoxy/thermoplastic polymer blends was tested in 3-point bending fatigue to investigate its performance compared to a conventional epoxy-based composite. This loading method was chosen to concentrate the damage at the center of the specimen and to mimic potential applications where the part is loaded in flexural mode. Furthermore, a statistical approach based on Weibull statistics was developed to predict the probability of failure of the samples as a function of any applied stress amplitude. This approach was used as a damage criterion to reach a similar extent of damage in the two systems before healing, and re-testing to assess the healing efficiency.

MATERIALS AND METHODS

Materials and Samples Preparation

Two types of resin were used to produce the samples. A first set of plates was produced with the healable system from CompPair Technologies Ltd. This novel resin system is based on epoxy/thermoplastic blends capable of autonomous healing by heat treatment at 150°C for 30 min. The second set was produced with the EPIKOTE™ MGS RIMR 135 from Hexion, a difunctional bisphenol A/epichlorohydrin derived liquid epoxy resin commonly used in rotor blades industry for wind turbines or boat building and cured with EPIKURE™ Curing Agent MGS™ RIMH 137 with a 100:30 weight mixing ratio and used as reference. The reinforcement was a woven twill 2 × 2 E-glass fabric with a nominal areal weight of 390 g/m^2, 6 end/cm for wrap fibers and 6.7 picks/cm for weft fibers, with a diameter of 9 μm, a yarn thickness of 0.45 mm, warp tex of 68 × 5 and weft tex of 272, from Suter-Kunststoffe AG.

Both systems were produced by vacuum assisted resin infusion molding. Sixteen layers of reinforcements were cut in 350 mm × 250 mm rectangles and stacked following a quasi-isotropic stacking sequence of $[(+45/-45);(0/90)]_{4s}$. The stack was infused at room temperature through the long edge with the resin systems and then cured at 60°C for 6 h. A post-cure treatment was then performed for 4 h at 80°C and 1 h at 100°C to reach the infinite glass transition temperature of the system ($T_{g,\mathrm{inf}}$ = 97°C). The resulting composite had a target fiber volume fraction (V_f) of 50 vol% with a thickness of ~5 mm.

Fractured samples from each system were transversally cut, embedded in EPOFIX resin (Struers, Inc., Cleveland, United States) and polished to a 1 μm diamond paste finish. The crack profiles were then observed with an optical microscope (Olympus BH-2).

Three-Point Bending Fatigue Testing

Rectangular samples were cut from the infused plates with dimensions following 3-point bending ASTM D7264 (ASTM

International, 2015) with a length, width and span-to-thickness ratio of respectively, 120, 13 mm and 16:1 (80 mm for 5 mm thick samples). The analysis method following this norm implies treating the material as homogeneous which is incorrect for a stack of laminates. In the special case of the symmetrical quasi-isotropic layup studied here, a preliminary static stress analysis with Altair ESAcompTM, using a woven 2–2 Twill glass and an equivalent epoxy resin, showed that it can be approximated as a homogeneous material in 3-point bending, allowing the use of this simple approach for comparison purposes. Nonetheless, the values provided in this work are thus an apparent maximal stress, apparent maximal strain, and apparent flexural secant modulus as defined in the norm, and are also based on a small strain approximation. The tests were performed at a frequency of 5 Hz on a 100 kN servo-hydraulic Schenk testing machine. Preliminary tests were performed at 0.1, 2, and 5 Hz to confirm that the heat generation due to micro-friction in the crack regions was negligible up to 5 Hz, in order to ensure that no healing could take place due to local heating during fatigue testing (Herman et al., 1990; Gagel et al., 2006; Adam and Horst 2017; Movahedi-Rad et al., 2018). These preliminary tests at 0.1 and 2 Hz were also integrated in the final S–N curve.

The tests were conducted at room temperature under load control with a loading ratio of $R = 0.1$ in compression. At least three ($N_{cycle} > 106$) and usually five ($N_{cycle} < 106$) replicates were carried out for each stress conditions to establish the S–N curve of the two systems. Note that because of the difference in volume fraction of fibers (V_f) between the healable and reference systems (**Table 1**), all the results are presented normalized to an equivalent volume fraction of $V_f = 50\%$ (which was the theoretical target volume fraction) for better comparison. This difference is due to the higher viscosity of the healable system that leads to a lower fiber compaction during infusion.

To investigate the healing efficiency of the system, a damage criterion was defined through Weibull statistical analysis of the fatigue experiments allowing direct access to a survival probability of the sample at a specific stress amplitude as a function of the number of cycles. This approach was necessary to take into account any difference in thickness and stiffness between the two systems and be able to compare and reach a similar amount of damage prior healing, since there is not direct access to damage levels in these bulk fatigue experiments, as compared to forced crack growth as performed in the literature.

The healing performance tests were performed at the stress amplitude of 220 MPa ($V_f = 50\%$ equivalent) at 5 Hz. Once the sample had reached a number of cycles corresponding to a survival probability of 90% (determined from the Weibull statistical study), the tests were stopped, the samples were healed at 150°C for 30 min in an oven, but under no applied pressure, then cooled down for an additional 30 min at room temperature (approximately 20 min from 150°C to ambient plus an additional 10 min for temperature equilibration) and again tested in fatigue at the exact same stress amplitude. This test-healing procedure was repeated several times, and at each step the change of the apparent flexural secant modulus calculated from the estimated maximal strain value at the maximal load of each cycle to determine the lifetime extension of the materials.

TABLE 1 | Volume fraction of fiber for the healable and reference system.

System	V_f	SD
Healable	0.39	0.0206
Reference	0.48	0.0052

RESULTS AND DISCUSSION

S–N Curve Determination

The results of the fatigue tests, in the form of conventional S–N curves (stress amplitude vs. number of cycles to failure), are given in **Figure 1** for the two studied systems, along with a standard power law fit. The stress amplitude was corrected to an equivalent volume fraction of $V_f = 50\%$ to take into account the large difference in thickness due to the processing of the healable system. This correction was carried out simply multiplying the stress amplitude by the ratio $0.5/V_f$ explaining the scattering of the point regarding the applied stress. The ultimate strength in static mode of the reference system (437 ± 20 MPa) is slightly higher than that of the healable systems (361 ± 23 MPa) due to the presence of the thermoplastic phase accordingly reducing the flexural strength. Note that this diminution follows a rule of mixture considering the amount of thermoplastic present in the healable system, confirming the good quality of the composites. Damage, however, progresses faster in the pure epoxy system with a fatigue curve decreasing faster and even crossing the healable systems endurance curve at a stress amplitude of ~200 MPa. The healable system is thus more durable than the reference one in particular for a stress amplitude lower than 200 MPa, i.e., for high cycle fatigue. This case of fatigue is typically the solicitation observed in structural parts during their lifetime. In both systems, damage mainly occurred by interlaminar crack propagation through the fiber tows and at the resin/fiber interface

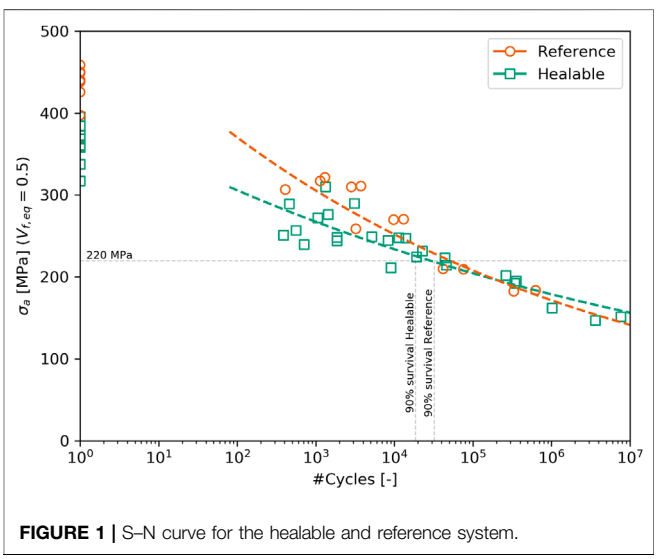

FIGURE 1 | S–N curve for the healable and reference system.

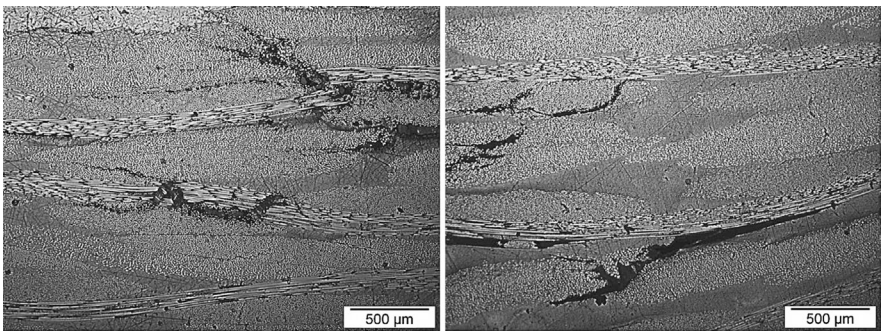

FIGURE 2 | (Left) Micrograph of a reference sample after failure (σ_a = 191.8 MPa). **(Right)** Micrograph of a healable sample after failure (σ_a = 204.9 MPa).

(see **Figure 2**). Whereas the crack path in the reference system clearly follows the tows outer boundary or directly progresses through the tows, the healable system shows a similar crack path location, but with a greater tortuosity which is expected since the system is tougher than pure epoxy. Note that the lower fiber volume fraction in the healable samples probably led to resin pockets known to affect the local stress concentration and reduce the fatigue performance of the material (Silva et al., 2005). However, as the damage mostly propagated through the fiber tows, we assumed that this effect can be neglected when comparing our two types of samples. Nevertheless, the overall fatigue resistance of the healable systems might therefore be underestimated here, keeping a conservative approach in the conclusions drawn.

Damage Criterion Determination—Weibull Statistics

To evaluate the healing efficiency of the healable systems in fatigue, a damage criterion had to be established, so as to determine when to stop the test for each sample at the same amount of damage. Indeed, simply fixing a stress amplitude and stopping the test at an arbitrary number of cycles would not affect the two systems identically because of their different intrinsic fatigue response. The same conclusion is reached when considering the reduction in flexural secant modulus because of the statistical nature of the tests. Damage was thus considered as a probability of failure based on a two parameters Weibull distribution characterized by a probability density function $f(x)$ (Khashaba, 2003; Sakin and Ay, 2008):

$$f(x) = \frac{\beta}{\alpha}\left(\frac{x}{\alpha}\right)^{\beta-1} e^{-\left(\frac{x}{\alpha}\right)^{\beta}} \quad (1)$$

where α and β are the shape and the scale parameter, respectively. Following the methods described in Sakin and Ay (2008), the cumulative density function is obtained by integrating the probability density function, obtaining a probability of failure F_f and a probability of survival F_s for a number of cycles x:

$$F_f = 1 - F_s = 1 - e^{-\left(\frac{x}{\alpha}\right)^{\beta}}. \quad (2)$$

By taking the natural logarithm and rearranging, the following linear regression model is obtained:

$$Y = mX + c, \quad (3)$$

With $X = \ln(x)$, $m = \beta$, $c = -\beta(\ln(\alpha))$.

To determine the Weibull parameters, the unreliability of each fatigue tests must be determined. The median ranks, the true

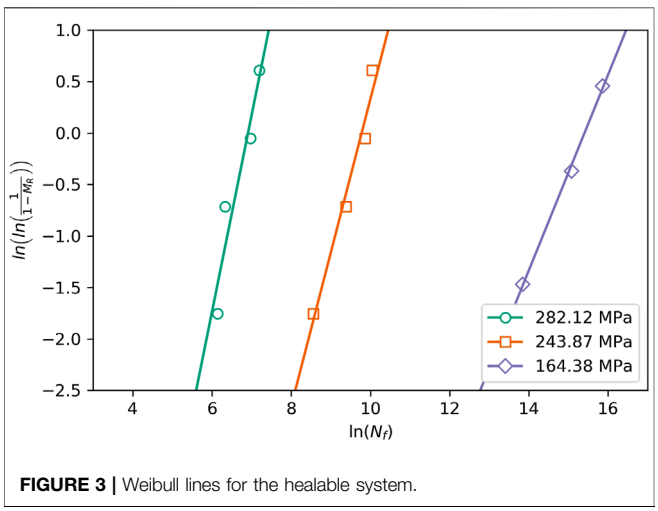

FIGURE 3 | Weibull lines for the healable system.

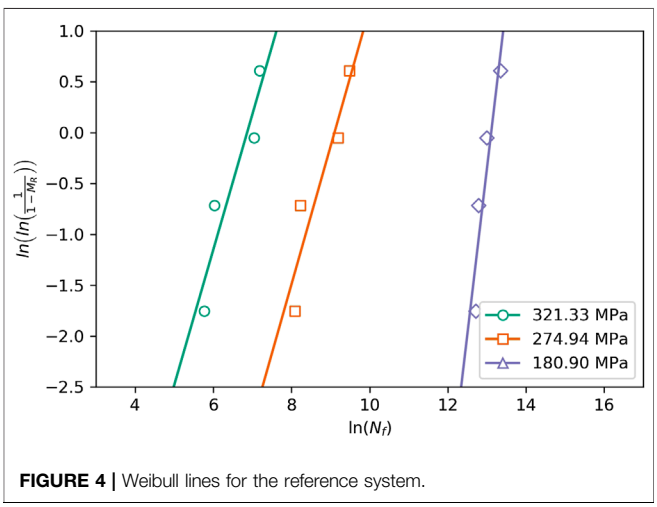

FIGURE 4 | Weibull lines for the reference system.

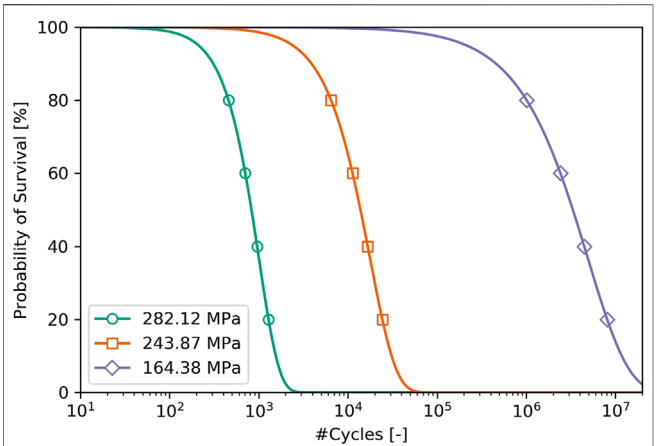

FIGURE 5 | Weibull curves for the healable system.

probability of failure that the *i*th sample of a group should have in a group of n samples at a 50% confidence level, can be used to estimate this value. In this study, Bernard's median rank approximation was used:

$$\mathrm{MR} = \frac{i - 0.3}{n + 0.4} \tag{4}$$

By grouping the fatigue tests of similar stress amplitude in groups of n samples, the median rank of each sample with a rank i = 1, 2, 3, ..., n could be determined. From the Weibull lines obtained by plotting $\ln(\ln(1/(1-\mathrm{MR})))$ against $\ln(N_f)$ as plotted in **Figures 3** and **4**, the parameters of linear regressions $Y(X)$ could be obtained for each stress level. This approach was carried out for both the healable and reference system allowing to draw survival curves as a function of the test's stress amplitude, **Figures 5** and **6**. The detailed values for each stress conditions and systems as well as the obtained Weibull parameters are shown in **Tables 2** and **3**.

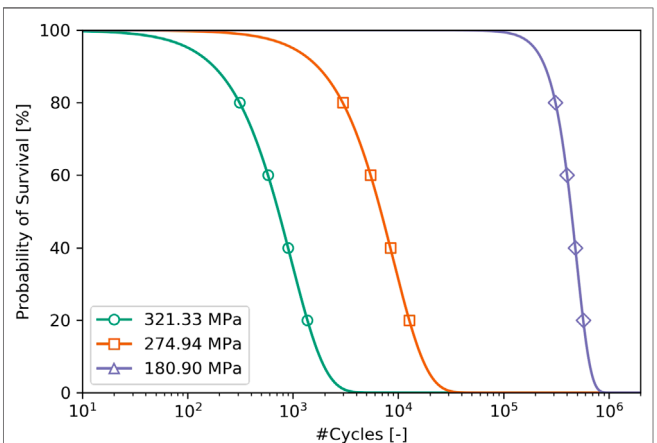

FIGURE 6 | Survival curves for the reference system.

TABLE 2 | Weibull's parameter and parameters used to draw the Weibull lines for the healable system.

σ_a (MPa)	# Cycles	Rank	α	β
282.13	466	1	1,004	1.910
	562	2		
	1,069	3		
	1,335	4		
243.87	5,198	1	17,574	1.492
	11,840	2		
	19,187	3		
	22,970	4		
164.38	1,026,365	1	4,900,399	0.950
	3,500,000	2		
	7,698,653	3		
	–	–		

The curves obtained from the median rank analysis only provide a survival probability for a determined stress amplitude; there is no direct generalization. To extend this analysis to the full range of possible stress values, the dependence of the Weibull parameters with respect to the stress amplitude must be quantified. From the definition of the survival probability and assuming that the number of cycles x generally follows a power law behavior with respect to the applied stress σ:

$$F_S = e^{-\left(\frac{x}{\alpha}\right)^{\beta}} = e^{-\left(\frac{\sigma^b}{\alpha}\right)^{\beta}} \tag{5}$$

The stress can now be directly linked to the first Weibull parameter α as:

$$\alpha(-\ln(F_S))^{1/\beta} = \sigma^b \tag{6}$$

As β is usually much smaller than α and assuming a constant value for F_S the expression would reduce to:

$$C\alpha \approx \sigma^b. \tag{7}$$

From this simple analysis, α seems to be linked by a power law to σ. However, fitting the experimental data shows that the relation is closer to:

TABLE 3 | Weibull's parameter and the parameters used to draw the Weibull lines for the reference system.

σ_a (MPa)	# Cycles	Rank	α	β
321.33	320	1	959	1.332
	417	2		
	1,149	3		
	1,314	4		
274.94	3,248	1	8961	1.357
	3,763	2		
	9,819	3		
	13,140	4		
180.91	332,004	1	493,527	3.256
	358,002	2		
	441,561	3		
	628,491	4		

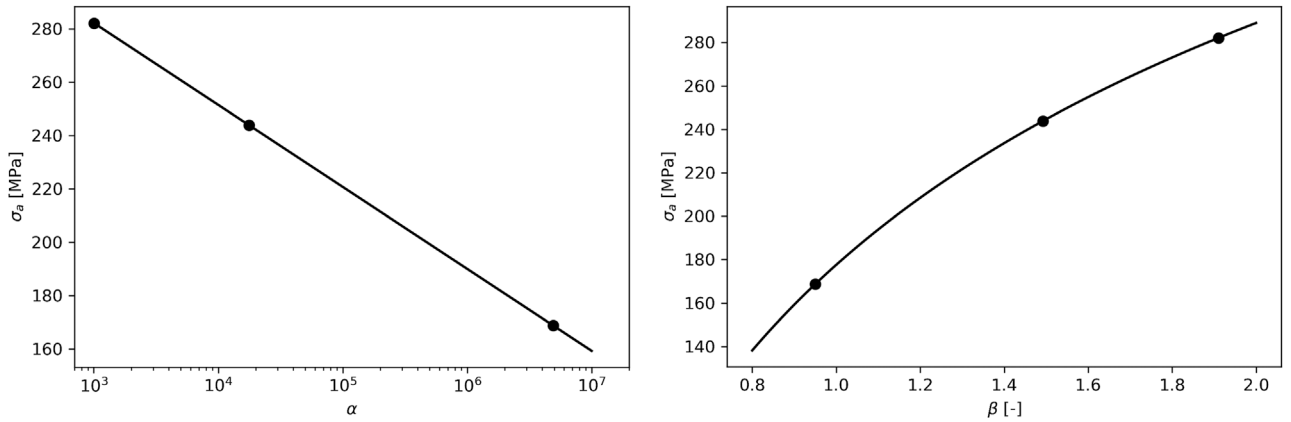

FIGURE 7 | Determination of Weibull parameters as a function of the stress amplitude.

$$C\alpha \approx \ln\left(\sigma^b\right). \tag{8}$$

From this, it is then possible to find an expression for α as a function of the stress amplitude fitting the experimental results as:

$$\alpha(\sigma) = e^{\left(\frac{\sigma - C_2}{C_1}\right)^{\frac{1}{C_3}}}. \tag{9}$$

The same approach was performed with the second Weibull parameter β. Starting from the last expression of the previous analysis:

$$\alpha\left(-\ln\left(F_S\right)\right)^{\frac{1}{\beta}} = \sigma^b \leftrightarrow \frac{1}{\beta}\ln\left(\alpha\ln\left(-\ln\left(F_S\right)\right)\right) = b\ln\left(\sigma\right) \tag{10}$$

Assuming again a constant value for F_s and taking the exponential on the expression gives:

$$\sigma = \alpha C e^{\left(\frac{1}{\beta b}\right)} \approx e^{\left(\frac{1}{\beta b}\right)}$$

The stress amplitude is then exponentially linked to β. It is finally possible to find an expression for β as a function of the stress amplitude fitting the experimental results as:

$$\beta(\sigma) = \left(\ln\left(\frac{\sigma - C_2}{C_1}\right)\right)^{\frac{1}{C_3}}$$

These fitting approaches were successfully applied to both Weibull parameters on the two studied systems. An example of the obtained fits is shown for the healable system in **Figure 7** as well as the detailed fitting parameters in **Table 4**.

Now that an expression for the Weibull parameters as a function of the applied stress was found, it is possible to determine the survival curve at any stress amplitude. A comparison of the experimental values and the fitted survival curves as well as additional new ones obtained from the fitting approach at intermediate values are shown for the healable and reference system in **Figures 8** and **9**.

The obtained fits closely follow the experimental data giving a good approximation of the survival probability of the

TABLE 4 | Detailed fitting parameters to determine the Weibull parameters as a function of the stress amplitude.

Equation	System	Parameters
$\alpha(\sigma) = e^{\left(\frac{\sigma - C_2}{C_1}\right)^{\frac{1}{C_3}}}$	Healable	$C_1 = -13.189$ $C_2 = 1.004$ $C_3 = 373.918$
	Reference	$C_1 = -6.998$ $C_2 = 1.372$ $C_3 = 419.663$
$\beta(\sigma) = \left(\ln\left(\frac{\sigma - C_2}{C_1}\right)\right)^{\frac{1}{C_3}}$	Healable	$C_1 = -611.26$ $C_2 = 1{,}839.149$ $C_3 = -0.104$
	Reference	$C_1 = -165.104$ $C_2 = 0$ $C_3 = -1.805$

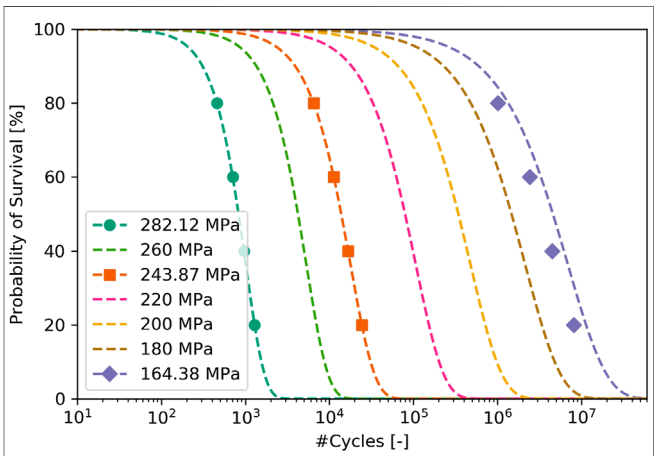

FIGURE 8 | Survival curves of the healable system obtained from the fitted Weibull parameters (dashed lines) as well as the initial experimental data (solid dots).

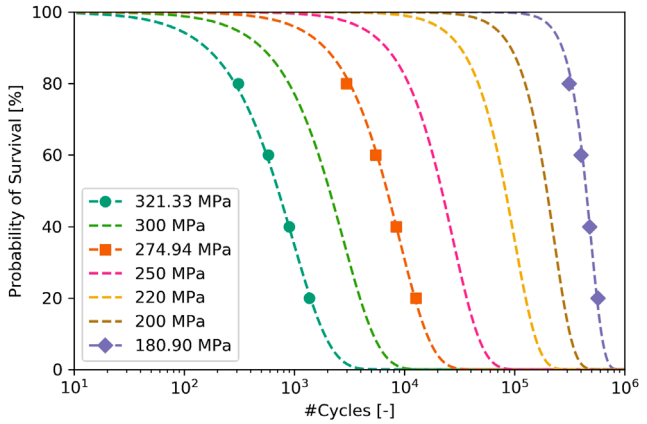

FIGURE 9 | Survival curves of the reference obtained from the fitted Weibull parameters (dashed lines) as well as the initial experimental data (solid dots).

samples as a function of the stress amplitude. It is interesting to note on **Figure 8** that the curve at 164 MPa slightly diverges from the prediction. This can be linked to the reduced number of tested samples at this low stress amplitude because of the time scale of the experiments (sometimes extending up to 17 days of tests).

Healing Efficiency

The healing efficiencies of each system were tested at 220 MPa ($V_f = 50\%$ equivalent) until a probability of survival of 90% was reached. This probability corresponds to 18,401 cycles for the healable system and 32,205 cycles for the reference system (see **Table 5**). This difference is justified by the chosen stress amplitude that corresponds to a region before the crossing

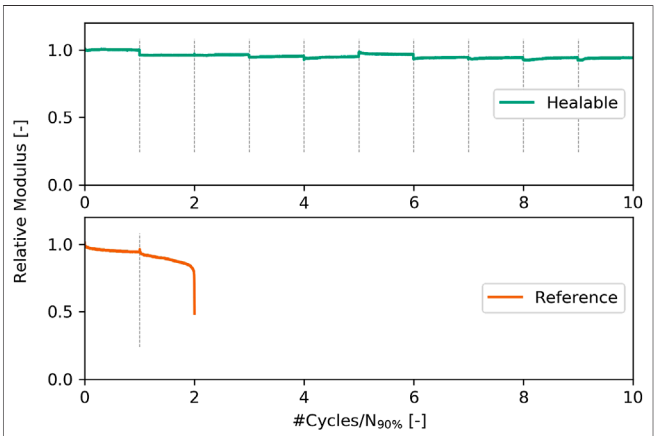

FIGURE 10 | Relative secant modulus as a function of the number of cycles normalized by the number of cycles corresponding to a probability of 90% of survival for the healable and reference system. The vertical dashed lines correspond to each healing cycle.

TABLE 5 | Summary of the stop criteria for the fatigue/healing tests.

System	σ_a^{eq} (MPa)	σ_a^{record} (MPa)	Stop crit. (# cycles)	Prob. survival (%)
Healable	220	172	18,401	90
Reference	220	210	32,205	90

of the two S–N curves (see **Figure 1**). The change of the relative flexural secant modulus of each system as a function of the number of cycles is shown in **Figure 10**. The efficiency of the healing procedure is clearly observed for the healable system: when stopping the test at a 90% probability of survival, the sample could sustain 10 test/heal repetitions. Note however, that the healable system could not be tested in a row because of the extended testing time. The tests were stopped for 12 h after the 5th healing cycle, explaining the sudden peak of the relative modulus because of the longer time allowed for stress relaxation. The reference system on the other hand shows no improvement in durability from the healing cycle. Only a small regain of properties was observed after the first (and only) healing which was attributed to the relaxation of internal stresses barely affecting its durability. The secant modulus decrease of the reference sample is more marked after healing, indicating that the healing step did not increase the fatigue resistance of the reference system. Interesting to notice as well is the increase in relative modulus for the healable system just after healing, which is especially visible after the 6th healing cycle. This different behavior compared to the reference system can be attributed to the increased toughness of the healable system, artificially increasing the relative modulus by friction. These observations confirm the excellent efficiency of the healable system to recover its mechanical properties in fatigue.

CONCLUSION

The potential of healable composites as an alternative to conventional composites was confirmed through 3-point bending fatigue tests. The tested healable system showed enhanced fatigue resistance compared to the reference system at high cycle fatigue, opening a door to the use of these materials in highly solicited structural parts. A damage criterion based on Weibull statistics was successfully derived and used to work out a probability of failure. Following this method, the life of the healable system could be extended by at least five times compared to that of the reference system by consecutive testing/healing cycles. Note that this approach could also be used to predict the failure of composite parts during their operation, or to organize the maintenance schedule for parts submitted to cyclic loading during their service. Even if the mechanical properties of this healable system show promising results, its processing under the present form led to a reduced fiber volume fraction compared to conventional systems. This study nonetheless demonstrates the high potential of this material system at equivalent volume fraction.

DATA AVAILABILITY STATEMENT

The raw data supporting the conclusions of this article will be made available by the authors, without undue reservation.

AUTHOR CONTRIBUTIONS

NH, AC, and VM conceived the experiments, discussed the methods and results, and prepared the manuscript. NH and AC manufactured the test coupons and performed the experimental test and analysis.

FUNDING

The initial research for this work was supported by the Swiss National Fund (project no. 20020-15007-1) and later by the EPFL Enable grants program.

ACKNOWLEDGMENTS

We would like to thank Hexion for providing the reference epoxy resin.

REFERENCES

Adam, T. J., and Horst, P. (2017). Fatigue damage and fatigue limits of a GFRP angle-ply laminate tested under very high cycle fatigue loading. *Int. J. Fatigue* 99, 202–214. doi:10.1016/j.ijfatigue.2017.01.045

ASTM International (2015). ASTM D7264. Standard test method for flexural properties of polymer matrix composite materials.

Blaiszik, B. J., Kramer, S. L. B., Olugebefola, S. C., Moore, J. S., Sottos, N. R., and White, S. R. (2010). Self-healing polymers and composites. *Annu. Rev. Mater. Res.* 40, 179–211. doi:10.1146/annurev-matsci-070909-104532

Bond, I. P., Trask, R. S., and Williams, H. R. (2008). Self-healing fiber-reinforced polymer composites. *MRS Bull.* 33, 770–774. doi:10.1557/mrs2008.164

Brown, E., White, S., and Sottos, N. (2005). Retardation and repair of fatigue cracks in a microcapsule toughened epoxy composite-part II: in situ self-healing. *Compos. Sci. Technol.* 65, 2474–2480. doi:10.1016/j.compscitech.2005.04.053

Cohades, A., Branfoot, C., Rae, S., Bond, I., and Michaud, V. (2018). Progress in self-healing fiber-reinforced polymer composites. *Adv. Mater. Interfaces* 5, 17. doi:10.1002/admi.201870084

Cohades, A., and Michaud, V. (2017). Thermal mending in E-glass reinforced poly(ε-caprolactone)/epoxy blends. *Compos. Part A Appl. Sci. Manuf.* 99, 129–138. doi:10.1016/j.compositesa.2017.04.013

Deng, W., You, Y., and Zhang, A. (2015). "7-Supramolecular network-based self-healing polymer materials," in *Recent advances in smart self-healing polymers and composites. Woodhead Publishing Series in Composites Science and Engineering*. Sawston, United Kingdom: Wodhead Publishing, 181–210. doi:10.1016/B978-1-78242-280-8.00007-8

Gagel, A., Lange, D., and Schulte, K. (2006). On the relation between crack densities, stiffness degradation, and surface temperature distribution of tensile fatigue loaded glass-fibre non-crimp-fabric reinforced epoxy. *Compos. Part A Appl. Sci. Manuf.* 37, 222–228. doi:10.1016/j.compositesa.2005.03.028

Garcia, S. J. (2014). Effect of polymer architecture on the intrinsic self-healing character of polymers. *Eur. Polym. J.* 53, 118–125. doi:10.1016/j.eurpolymj.2014.01.026

Hamilton, A. R., Sottos, N. R., and White, S. R. (2012). Mitigation of fatigue damage in self-healing vascular materials. *Polymer* 53, 5575–5581. doi:10.1016/j.polymer.2012.09.050

Heo, Y., and Sodano, H. A. (2015). Thermally responsive self-healing composites with continuous carbon fiber reinforcement. *Compos. Sci. Technol.* 118, 244–250. doi:10.1016/j.compscitech.2015.08.015

Herman, W. A., Hertzberg, R. W., and Manson, J. A. (1990). The influence of loading history on fatigue in engineering plastics. *J. Mater. Sci.* 25, 434–440. doi:10.1007/bf00714052

JEC-GROUP (2017). *Overview of the global composites market: at the crossroads*. France: Frédérique Mutel, JEC Group.

Katnam, K. B., Comer, A. J., Roy, D., Da Silva, L. F. M., and Young, T. M. (2015). Composite repair in wind turbine blades: an overview. *J. Adhes.* 91, 113–139. doi:10.1080/00218464.2014.900449

Kessler, M. R., and White, S. R. (2001). Self-activated healing of delamination damage in woven composites. *Compos. Part A Appl. Sci. Manuf.* 32, 638–699. doi:10.1016/s1359-835x(00)00149-4

Khashaba, U. A. (2003). Fatigue and reliability analysis of unidirectional GFRP composites under rotating bending loads. *J. Compos. Mater.* 37 (4), 317–331. doi:10.1177/0021998303037004680

Kim, S. Y., Sottos, N. R., and White, S. R. (2019). Self-healing of fatigue damage in cross-ply glass/epoxy laminates. *Compos. Sci. Technol.* 175, 122–127. doi:10.1016/j.compscitech.2019.03.016

Kling, S., and Czigány, T. (2014). Damage detection and self-repair in hollow glass fiber fabric-reinforced epoxy composites via fiber filling. *Compos. Sci. Technol.* 99, 82–88. doi:10.1016/j.compscitech.2014.05.020

Ladani, R. B., Wang, C. H., and Mouritz, A. P. (2019). Delamination fatigue resistant three-dimensional textile self-healing composites. *Compos. Part A Appl. Sci. Manuf.* 127, 105626. doi:10.1016/j.compositesa.2019.105626

Luterbacher, R., Trask, R. S., and Bond, I. P. (2016). Static and fatigue tensil properties of crossply laminates containing vascules for self-healing applications. *Smart Mater. Struct.* 25, 015003. doi:10.1088/0964-1726/25/1/015003

Manfredi, E., Cohades, A., Richard, I., and Michaud, V. (2015). Assessment of solvent capsule-based self-healing for woven E-glass fibre-reinforced polymers. *Smart Mater. Struct.* 24, 1–11. doi:10.1088/0964-1726/24/1/015019

MarketsAndMarkets (2017). Report code CH 4906. Composite repairs market by type (structural, semi-structural, cosmetic), process (hand lay-up, vacuum infusion, autoclave), end-use industry (aerospace and defense, wind energy, automotive and transportation), and region—global forecast to 2026.

Movahedi-Rad, A. V., Keller, T., and Vassilopoulos, A. P. (2018). Fatigue damage in angle-ply GFRP laminates under tension-tension fatigue. *Int. J. Fatigue* 109, 60–69. doi:10.1016/j.ijfatigue.2017.12.015

Norris, C. J., Bond, I. P., and Trask, R. S. (2013). Healing of low-velocity impact damage in vascularised composites. *Compos. Part A Appl. Sci. Manuf.* 44, 78–85. doi:10.1016/j.compositesa.2012.08.022

Park, J. S., Kim, H. S., and Thomas Hahn, H. (2009). Healing behavior of a matrix crack on a carbon fiber/mendomer composite. *Compos. Sci. Technol.* 69, 1082–1087. doi:10.1016/j.compscitech.2009.01.031

Patel, A. J., Sottos, N. R., Wetzel, E. D., and White, S. R. (2010). Autonomic healing of low-velocity impact damage in fiber-reinforced composites. *Compos. Part A Appl. Sci. Manuf.* 41, 360–368. doi:10.1016/j.compositesa.2009.11.002

Patrick, J. F., Hart, K. R., Krull, B. P., Diesendruck, C. E., Moore, J. S., and White, S. R. (2014). Continuous self-healing life cycle in vascularized structural composites. *Adv. Mater.* 26, 4302–4308. doi:10.1002/adma.201400248

Pingkarawat, K., Bhat, T., Craze, D. A., Wang, C. H., Varley, R. J., and Mouritz, A. P. (2013). Healing of carbon fibre-epoxy composites using thermoplastic additives. *Polym. Chem.* 4, 5007. doi:10.1039/c3py00459g

Pingkarawat, K., Wang, C. H., Varley, R. J., and Mouritz, A. P. (2012). Self-healing of delamination fatigue cracks in carbon fibre–epoxy laminate using mendable thermoplastic. *J. Mater. Sci.* 47, 4449–4456. doi:10.1007/s10853-012-6303-8

Pingkarawat, K., Wang, C. H., Varley, R. J., and Mouritz, A. P. (2014). Healing of fatigue delamination cracks in carbon–epoxy composite using mendable polymer stitching. *J. Intell. Mater. Syst. Struct.* 25, 75–86. doi:10.1177/1045389X13505005

Post, W., Cohades, A., Michaud, V., van der Zwaag, S., and Garcia, S. J. (2017). Healing of a glass fibre reinforced composite with a disulphide containing organic-inorganic epoxy matrix. *Compos. Sci. Technol.* 152, 85–93. doi:10.1016/j.compscitech.2017.09.017

Préau, M., and Hubert, P. (2016). Processing of co-bonded scarf repairs: void reduction strategies and influence on strength recovery. *Compos. Part A Appl. Sci. Manuf.* 84, 236–245. doi:10.1016/j.compositesa.2016.01.016

Sakin, R., and Ay, İ. (2008). Statistical analysis of bending fatigue life data using Weibull distribution in glass-fiber reinforced polyester composites. *Mater. Design* 29, 1170–1181. doi:10.1016/j.matdes.2007.05.005

Shabani, P., Shokrieh, M. M., and Saeedi, A. (2020). A novel model to simulate the formation and healing of cracks in self-healing cross-ply composites under flexural loading. *Compos. Struct.* 235, 111750. doi:10.1016/j.compstruct.2019.111750

Silva, J. M. A., Devezas, T. C., Silva, A. P., and Ferreira, J. A. M. (2005). Mechanical characterization of composites with embedded optical fibers. *J. Compos. Mater.* 39 (14), 1261–1281. doi:10.1177/0021998305050423

Sordo, F., and Michaud, V. (2016). Processing and damage recovery of intrinsic self-healing glass fiber reinforced composites. *Smart Mater. Struct.* 25, 084012. doi:10.1088/0964-1726/25/8/084012

Tsangouri, E., Aggelis, D., and Van Hemelrijck, D. (2015). Quantifying thermoset polymers healing efficiency: a systematic review of mechanical testing. *Prog. Polym. Sci.* 49–50, 154–174. doi:10.1016/j.progpolymsci.2015.06.002

Ye, X. J., Zhu, Y., Yuan, Y. C., Song, Y. X., Yang, G. C., and Rong, M. Z. (2017). Improvement of fatigue resistance of epoxy composite with microencapsulated epoxy-SbF5 self-healing system. *Express Polym. Lett.* 11, 853–862. doi:10.3144/expresspolymlett.2017.82

Zhu, Y., Ye, X. J., Rong, M. Z., and Zhang, M. Q. (2016). Self-healing glass fiber/epoxy composites with polypropylene tubes containing self-pressurized epoxy and mercaptan healing agents. *Compos. Sci. Technol.* 135, 146–152. doi:10.1016/j.compscitech.2016.09.020

Conflict of Interest: The authors declare that the research was conducted in the absence of any commercial or financial relationships that could be construed as a potential conflict of interest.

frontiers in Materials

ORIGINAL RESEARCH
published: 24 July 2020
doi: 10.3389/fmats.2020.00226

Supramolecular Structure and Mechanical Properties of Wet-Spun Polyacrylonitrile/Carbon Nanotube Composite Fibers Influenced by Stretching Forces

Hamideh Mirbaha[1,2], Paolo Scardi[3], Mirco D'Incau[3], Shahram Arbab[4], Parviz Nourpanah[2] and Nicola M. Pugno[1,5]**

[1] Laboratory of Bio-Inspired, Bionic, Nano, Meta Materials & Mechanics, Department of Civil, Environmental and Mechanical Engineering, University of Trento, Trento, Italy, [2] Department of Textile Engineering, Amirkabir University of Technology, Tehran, Iran, [3] Department of Civil, Environmental and Mechanical Engineering, University of Trento, Trento, Italy, [4] Advanced Textile Materials and Technology Research Institute, Department of Textile Engineering, Amirkabir University of Technology, Tehran, Iran, [5] School of Engineering and Materials Science, Queen Mary University of London, London, United Kingdom

OPEN ACCESS

Edited by:
Patricia Krawczak, IMT Lille Douai, France

Reviewed by:
Yaodong Liu, Institute of Coal Chemistry (CAS), China
Wei Xu, IMDEA Nanociencia, Spain

***Correspondence:**
Hamideh Mirbaha
hamideh.mirbaha@unitn.it
Nicola M. Pugno
nicola.pugno@unitn.it

Specialty section:
This article was submitted to Polymeric and Composite Materials, a section of the journal Frontiers in Materials

Received: *29 April 2020*
Accepted: *22 June 2020*
Published: *24 July 2020*

Citation:
Mirbaha H, Scardi P, D'Incau M, Arbab S, Nourpanah P and Pugno NM (2020) Supramolecular Structure and Mechanical Properties of Wet-Spun Polyacrylonitrile/Carbon Nanotube Composite Fibers Influenced by Stretching Forces. Front. Mater. 7:226. doi: 10.3389/fmats.2020.00226

The effect of different elongation conditions on the crystalline structure and physical and mechanical properties of polyacrylonitrile/carbon nanotube (PAN/CNT) microfibers during the wet spinning process was studied. It turns out that the response of polymer chains in PAN/CNT and in PAN fibers to the stretching forces from jet stretching and steam drawing is different. The X-ray diffraction (XRD) results showed that the crystalline domain size in steam-drawn PAN/CNT fibers is 1.5 times larger than in PAN fibers. CNTs alter the optimum stretching conditions, as they improve the crystalline structure of the PAN/CNT fibers at lower steam drawing ratios than PAN fibers, through nucleation of crystals on their surface. Synchrotron-radiation XRD studies revealed that the presence of CNTs improves the crystal orientation of PAN/CNT fibers significantly. In addition, steam drawing is more effective in improving the crystal orientation than jet stretching. The mechanical properties of PAN/CNT fibers have also been affected by steam drawing more than jet stretching. Multiwalled CNTs have the biggest impact on Young's modulus. The Young's modulus of PAN/CNT fibers could increase up to 19% higher than PAN fibers at specific stretching conditions, i.e., steam drawing ratio of 2.5. Better orientation of polymers and crystals in the fiber direction is the reason for the enhancement of Young's modulus. To our knowledge, the differences between the response of PAN/CNT and PAN fibers to stretching forces inside coagulation bath and after fiber coagulation as well as the difference in evolution of crystalline structure at different stretching stages has not been reported elsewhere.

Keywords: PAN/CNT composite fibers, wet spinning, jet stretch, steam drawing, crystalline structure, mechanical properties

INTRODUCTION

Incorporation of CNTs in PAN microfibers has the potential to improve the physical, mechanical, electrical, and thermal properties of PAN fibers. This can be achieved without any significant weight change and or need to use different production equipment (Brown et al., 2014; Sahin et al., 2014; Li et al., 2018; Mirbaha et al., 2019). These fibers have the potential to be used as a carbon fiber precursor (Mikolajczyk et al., 2010; Sahin et al., 2014). By addition of CNTs, Li et al. (2015) obtained 35 and 17% improvement in tensile strength and tensile modulus of PAN fibers, respectively. To have PAN/CNT fibers with better mechanical properties, the internal structure of fibers needs to be controlled and designed (Ji et al., 2007). The formation of a fiber structure in the wet spinning process is a very important step in determining the properties of produced fibers (Wilms et al., 2013; Wei et al., 2020). Since there are many effective parameters on the evolution of a fiber structure in the wet spinning stage, the favored production of PAN/CNT composite fibers with promising properties involves thorough research on the spinning process, which is also the main aim of this work.

PAN/CNT composite fibers can be produced by the wet spinning method (Mirbaha et al., 2019). During the wet spinning process, shear and elongational forces are applied on filaments, affecting the alignment of polymer chains (Mai et al., 2011; Dintcheva et al., 2011). Shear stress is applied on the spinning dope while it flows inside the spinneret (Mikolajczyk et al., 2010). According to Cao et al. (2004), a strong enough shear force can align polymer chains in the flow direction. The melt spinning process of polypropylene/CNT composite fibers was studied by Kang and Ryu (2013). They observed that shear stress applied to the spinning dope can also be transferred to CNTs, resulting in their orientation in the flow direction. Minus et al. (2012) observed that CNTs can act as nucleating agents for the crystallization of polyethylene. A small amount of CNT dispersed within a polymer can influence its orientation and crystallinity.

Stretching is one of the most necessary steps in fiber production, leading to improvement in molecular orientation along the fiber direction as well as fineness, tensile strength, and modulus (Zeng et al., 2007; Arbab et al., 2011a). The study on the effect of elongational forces on the initial structure of the PAN fibers in the presence of CNTs can help control the alignment of polymers and CNTs, and the formation of an interphase between them, subsequently playing an important role on the final properties of the fiber (Lin et al., 2019). Fiber stretching can be done at different production stages including jet stretching inside the coagulation bath and hot drawing of coagulated fibers in different environments (Arbab et al., 2011a; Lian et al., 2012). Jet stretching reduces the residence time of filaments in the coagulation bath, decreasing the available time for formation and growth of voids (Arbab et al., 2011b). Arbab et al. (2011b) obtained a denser structure with smaller voids, when they increased the jet stretch inside the coagulation bath of the wet spinning process of PAN fibers. Li et al. (2015) observed that drawing has two opposite effects on the crystallization of PAN fibers. Applying stretch results in orientation assisted crystallization and crystallinity improvement. On the other hand, increasing the stretch ratio shortens the crystallization step and reduces the crystallinity. According to Cao et al. (2004), the stretching force inside the coagulation bath is able to unwind the random coils inside fiber filaments, stretch the chains, improve the chain orientation, and increase the compactness of the structure. While shear forces inside the spinneret can cause the alignment and orientation of polymer chains, the coexistence of shear and elongational forces results in stretching and orientation of polymer chains and opening of random coils (Cao et al., 2004). According to Mai et al. (2011), polymer chains and CNTs are likely to change from an entangled shape to a stretched form under elongational force. Polymer chains and CNTs have a greater chance of interaction in their stretched form. Polymer chains can crystallize around CNTs, thus producing a better interface interaction. Mai et al. (2011) reported better dispersion of CNTs at higher stretch ratios during melt spinning of PA66 as well as better orientation of fibers in the presence of CNTs.

After formation of a fiber structure in the coagulation bath, it is possible to improve the orientation and fiber properties by hot drawing the as-spun fibers (Zeng et al., 2007). The time scale of the reaction of polymer chains to hot drawing of coagulated fibers is different from the jet stretching of the polymer fluid (Zeng et al., 2007). During the hot drawing stage, the orientation of a fibrillar network and polymer chains in amorphous and crystalline regions increases, improving the mechanical strength (Arbab et al., 2011b).

Most of the researches in the field of PAN/CNT composite fiber production have focused on the structure and properties of the final products, while studies on the evolution of the structure during the production phases are still limited. The coexistence of shear and elongation in the wet spinning stage alters the orientation and placement of the polymer chains and CNTs and determines the initial fiber structure that can be developed during the next production stages. In a previous work, we reported the different effects of shear rates and jet stretching ratios inside the coagulation bath – where the filaments are still not fully solidified – on the morphology, crystalline structure, and physical and mechanical properties of as-spun PAN/CNT fibers (Mirbaha et al., 2019). In this work, we kept the shear rate constant, while applying a new stretching step in water vapor after full fiber coagulation. The objective of this research is the exploration of the effect of elongational forces at different stretching conditions on the formation and evolution of the PAN/CNT fiber structure and properties affected by the presence of CNTs. Understanding the effect of the mentioned variables can be regarded as a scheme part to control the spinning process and improve the physical and mechanical properties of the final PAN/CNT fibers. For this reason, the effect of jet stretching and hot drawing on the structure and properties of PAN/CNT composite fibers is studied using physical and mechanical measurements, X-ray diffraction, and FESEM microscopy. The impact of the existence of CNTs inside fibers on structural development is also explored in comparison with PAN reference fibers.

EXPERIMENTAL

Materials

PAN powder with methyl acrylate and sodium methallyl sulfonate comonomers was obtained from Polyacryl Corp., Iran. The viscosity molecular weight was 112,000 g/mole. Analysis-grade dimethyl formamide (DMF) solvent was obtained from Merck Co., Germany, and was used as received. Multiwalled CNTs were obtained from the Research Institute of Petroleum Industry, Iran. The average length and diameter of nanotubes are 10 micron and 10–30 nanometers, respectively. The purity was over 95%.

Methods

Preparation of the Spinning Dope

The spinning dope for reference PAN fibers was prepared from dissolving PAN powder in DMF solvent at a concentration of 20% w/v. The spinning dope for PAN/CNT composite fibers was prepared by dissolving PAN powder in DMF solvent at a concentration of 20% w/v, as in the spinning dope for PAN fibers. Based upon the literature review and optimization tests, the CNT concentration of 0.75% wt. proportional to the weight of the PAN polymer was chosen. For production of 35 cc of polymer solution, 0.0525 g CNT was added to 400 mL of DMF solvent. CNTs were dispersed for 30 min in DMF solvent using a UP200S ultrasonic homogenizer (Hielscher Ultrasonics GmbH, Germany). Then, a mechanical stirrer was placed in the CNT/DMF dispersion and polymer solution was continuously added to the dispersion under shear force until a homogenous solution was attained. The composite solution was further homogenized for 30 min using a ultrasonic homogenizer. An optical image of the final state of composite solution after ultrasonication is shown in **Figure 1**. Using mild heating and shear force, the extra solvent was evaporated and the final PAN/CNT/DMF solution with PAN and CNT concentrations of 20 and 0.75%, respectively, was attained. For determination of the end point of solvent evaporation, a finely scaled narrow glass container was used and the volume reduction during evaporation was closely observed until the final volume of the spinning solution was achieved.

FIGURE 1 | An optical image of the composite solution after sonication and mechanical stirring.

Wet Spinning

A laboratory wet spinning machine was used to produce composite PAN/CNT and reference PAN fibers. A schematic diagram of this wet spinning machine is reported in our previous paper (Mirbaha et al., 2019). A metering pump was used to pump the spinning dope at the constant shear rate of 8,000 s^{-1} to the coagulation bath through a one-hole spinneret with a diameter of 200 microns. The coagulation bath contained water as non-solvent and the temperature was kept at 20°C to reduce the phase separation speed. The freely spun fibers were produced without any stretching force applied on the filaments. These fibers were collected from the coagulation bath and then were thoroughly washed and dried at room temperature. Jet-stretched fibers were picked up at take-up rollers. The take-up velocity to the extrusion velocity of the spinning dope is defined as the jet stretch ratio. Jet stretch ratios of 2 and 2.5 were applied on fibers by changing the take-up speed in relation to the extrusion velocity. Jet-stretched fibers were washed thoroughly with water, and they were dried naturally in air. The hot drawing stage was performed in water vapor at 100°C in a laboratory-designed drawing machine (**Figure 2**). Fibers were fixed between two steel grips inside the hot steam chamber and were drawn up to different drawing ratios with constant speed of 1.3 mm/sec. The drawn fibers were then dried at room temperature.

The sample names and production conditions of PAN/CNT and PAN fibers are listed in **Table 1**. The letters of P and PC in sample names represent PAN and PAN/CNT, respectively. The numbers coming after the letters of S and D are jet-stretch ratios inside the coagulation bath and steam-draw ratios, respectively. The fiber codes without these numbers are freely spun fibers. Steam-draw ratios are defined as the final length of fibers after drawing in hot water vapor at 100°C to the initial length of fibers before drawing. The freely spun and jet-stretched fibers are similar to those reported in our previous work (Mirbaha et al., 2019). They are reported in this work for comparison to steam-drawn fibers.

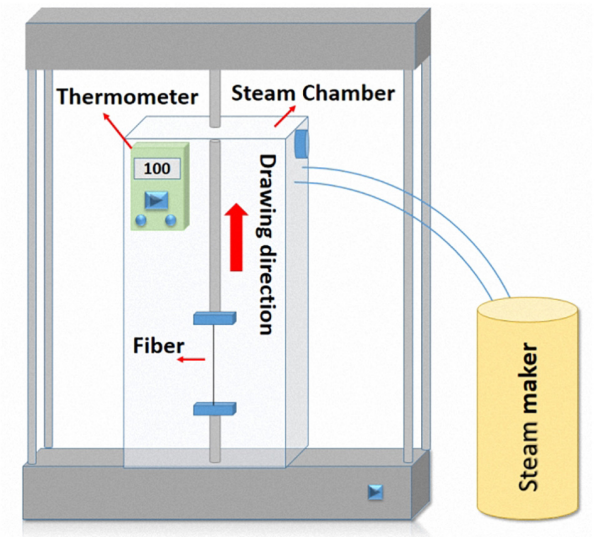

FIGURE 2 | Schematic diagram of the steam drawing chamber used in this research.

TABLE 1 | Denotation and production conditions of PAN/CNT and PAN fibers.

Condition	Sample names		Jet stretch ratio	Jet stretch ratio
	PAN/CNT	PAN		
Freely spun	PC	P	–	–
Jet stretched	PC-S2	P-S2	2	–
	PC-S2.5	P-S2.5	2.5	–
Steam srawn	PC-D2.5	P-D2.5	–	2.5
	PC-D5	P-D5	–	5
	PC-S2-D5	P-S2-D5	2	5

Characterization

In order to evaluate the dispersion of CNTs and determine the optimum dispersion conditions, UV-visible analysis was utilized. For this purpose, the PAN/DMF solution with a concentration of 20% and the CNT/DMF suspension with a CNT concentration of 0.75% proportional to the weight of the PAN polymer were prepared. Similar to preparation of the spinning dope, the CNT/DMF solution was first ultrasonicated for 30 min. Then, by the help of a mechanical stirrer, the polymer solution was added to the CNT/DMF dispersion under shear force. The dispersion process was again continued for 15, 30, 60, and 75 min. At each of these times, a sample was collected, diluted, and tested in a Cary 100 UV-visible spectrophotometer (Agilent, United States) in a wave number ranging from 200 to 700 nm.

A Microphot FXA optical microscope (Nikon, Japan) at a magnification of 50× was used to measure the fiber diameter at several points along the fiber. The average values of different replicates are reported here. A GR-200 balance (A and D Balance, Japan) was used to measure the mass of different fibers at various lengths, and the average value of linear density was calculated and reported in unit of tex as the mass in grams of 1,000 meters of fibers. The overall porosity of fibers was approximately calculated as follows (Arbab et al., 2008):

$$Overall\ porosity\ (\%) = \frac{\pi R^2 L - m\rho^{-1}}{\pi R^2 L} \times 100 \quad (1)$$

where R, L, and m are the radius, length, and mass of fibers, respectively, and ρ is the polymer density.

The microscopic images of fiber cross sections at magnifications of 500×, 7,000×, and 35,000× were obtained using a MIRA3 FESEM (Tescan, Czech Republic). The operation voltage was 15 kV. The samples were coated by gold, and the intact cross sections were cut in liquid nitrogen.

A Panalytical X'Pert MRD X-ray diffractometer (United Kingdom) was utilized to study the crystalline parameters of PAN/CNT and PAN fibers. The diffractometer worked at an operation voltage of 40 kV and current of 40 mA. Co Kα radiation at wavelength of 1.790 Å was used. Fibers were placed as bundles on the sample holder. The scanning range was 10°–48° (2θ), the scanning step was 0.15°, and the counting time was 25 s/step. To extract data from X-ray patterns, the diffraction peaks were resolved using Origin 2017 software (OriginLab, United States) based on three Lorentzian functions. The crystalline parameters were calculated from the intense peak at 2θ∼17°. Bragg law was used to calculate the plane spacing (d), and lateral crystallite size (L_c) was estimated using the Scherrer equation (Ji et al., 2007; Gong et al., 2014):

$$L_C = \frac{K\lambda}{\beta cos\theta} \quad (2)$$

where K is a constant with a value of 0.89 and β is the full width at half maximum (FWHM) intensity of the peak.

The degree of crystallinity was assessed using Gupta–Singhal's method (Ouyang et al., 2015):

$$Crystallinity = \frac{A_{crystal}}{A_{total}} \times 100 \quad (3)$$

where $A_{crystal}$ is the area of crystalline peaks and A_{total} is the total area of diffraction after subtracting the background.

Synchrotron X-ray patterns were collected at the MCX beamline of Elettra synchrotron in Trieste, Italy (Rebuffi et al., 2014). A beamline energy of 17.5 keV was used. The single fiber was placed horizontally with its axis perpendicular to X-ray radiation beam. Therefore, the vertical and horizontal directions in two-dimensional (2D) patterns are related to equatorial and meridional directions of fibers, respectively. 2D X-ray diffraction patterns were integrated to two one-dimensional (1D) equatorial and meridional scans. The intensity and area under the peak were calculated by modeling with a Python script. The modeling is made using a decaying exponential background and a pseudo-Voigt peak profile.

A universal testing machine MIDI 10 (Messphysik Materials Testing GmbH, Austria) was used to measure the mechanical properties of single threads of PAN and PAN/CNT fibers. A 10-N load cell was utilized. The initial distance between two steel grips was 1 cm. An elongation rate of 0.1 mm/s based on Standard D3822 was chosen. The mechanical properties reported in this paper are the average values of at least 10 test replicates. The

coefficient of variation (% CV) was calculated for each set of tests. The breaking tenacity was measured from the load at break divided by the linear density of fibers in tex. Young's modulus was measured from the slope of the initial linear section of a specific stress–strain curve. The mechanical properties are reported in cN/tex (force divided by mass per unit length) instead of MPa, as the cross section of some fibers cannot be easily defined. Considering 1 tex = 0.001 g/m, tensile data in cN/tex (force per unit linear density) can be converted to Pa (force per unit area of cross section) by multiplying by the density of the fiber in proper units (Ward, 1997).

RESULTS AND DISCUSSION

Determination of Optimum Dispersion Time

CNTs tend to form aggregates in solution due to Van der Waals forces. Therefore, one of the challenges for producing PAN/CNT composite fibers is dispersion of CNTs in the form of individual tubes or in small bundles inside the viscous polymer matrix (Basu-Dutt et al., 2012). At these conditions, the interface area between CNT and polymer increases, leading to improvement in fiber mechanical properties.

The addition of polymer to dispersion solution after 30 min of sonication is due to the fact that polymer chains can be adsorbed on the surface of CNTs and penetrate to their bundles with the help of ultrasonic force (Bakhtiary Davijani and Kumar, 2015). Therefore, CNT bundles can become smaller. As the dispersion time increases, the PAN/CNT/DMF dilute solution becomes darker, while the aggregations that can be recognized with the naked eye decrease. These aggregations completely disappear at dispersion times of 60 min or longer (**Figure 3A**).

UV-visible spectra of PAN/CNT/DMF solutions contain one absorption peak at a wavelength of about 265 nm (**Figure 3B**). Since only individual CNTs can absorb UV and visible lights, the maximum absorbance during dispersion can be used as a method to evaluate the dispersion state of CNTs (Sapalidis et al., 2018). The maximum UV-visible absorbance increases with an increase in dispersion time (**Figure 3B**). At dispersion time of 60 min or longer, the maximum absorbance stays constant, revealing that maximum possible dispersion of CNTs is achieved. Increasing the dispersion time to longer than 60 min not only does not improve the dispersion state of CNTs in the solution but also increases the energy consumption as well as the possibility of undesired damages to the CNTs. As a result, dispersion period of 60 min was used in this research.

Physical Properties

The existence of CNTs among PAN polymer chains causes a decrease in the fiber diameter in all spinning and stretching conditions, i.e., freely spun, jet-stretched, and steam-drawn fibers (**Table 2**). The diameter decrease is attributed to the smaller die swell as a result of the effect of CNTs on lowering the elastic recovery of polymer chains (Mirbaha et al., 2019). CNTs decrease the elastic recovery of polymer chains by reducing the chain mobility and formation of the interphase between polymers and CNTs. Consequently, polymer chains can preserve their orientation better in the presence of CNTs.

At identical stretch ratios, the reduction in diameter and linear density after steam drawing is less than that of jet stretch inside the coagulation bath (**Table 2**). For example, the diameter of steam-drawn PAN/CNT fibers at the ratio of 2.5 is about 1.5 times larger than that of jet-stretched PAN/CNT fibers at the ratio of 2.5.

The porosity of PAN fibers increases when CNT exists in the structure. The high porosity of fiber samples shows that the spinning conditions need further optimization. The overall fiber porosity is attributed to macrovoids (finger-like voids between fibrillar parts) as well as nanovoids (among fibrils) (Arbab et al., 2008). The more voids are present in the structure, the more random and disordered will be the arrangement of molecular chains, leading to less fiber orientation (Ji et al., 2007). The biggest difference between porosity of PAN/CNT and PAN fibers is observed when fibers are jet stretched (**Table 2**). For PAN reference fibers, jet stretch has brought structural elements close to each other reducing the voids, whereas for PAN/CNT fibers the void volume has increased by application of jet stretch. In addition, the presence of CNTs among polymer chains and formation of interphase with polymers has probably prevented from free movement of chains, intensifying the formation of voids under stretching forces inside coagulation bath. The higher porosity of PAN/CNT fibers compared to PAN fibers could also possibly be due to increased solution elasticity. The smallest difference between porosity of PAN/CNT and PAN fibers is observed when fibers are spun under steam drawing. Steam drawing has increased the porosity of PAN fibers sharply compared to jet-stretched fibers, whereas the difference between porosity of jet-stretched and steam-drawn PAN/CNT fibers is negligible. These results show the different response of PAN/CNT and PAN fibers to jet stretch and steam drawing. The lowest porosity of PAN/CNT fibers is obtained when fibers are jet stretched at the ratio of 2 and then steam drawn at the ratio of 5. The combination of jet stretch and steam drawing results in diameter reduction, formation of smaller voids during coagulation, and narrowing and healing of the voids in water steam, leading to a more compact structure.

The porosity of P-S2-D5 has increased compared to P-S2 fibers, whereas the opposite trend is observed in PC fibers. Jet stretching has brought the structural parameters in PAN fibers close to each other, reducing the voids and porosity of structure. However, jet stretching at high ratios used in this research, which turned out to be higher than optimum values for PAN/CNT fibers, has increased the porosity of PAN/CNT fiber structure. Steam drawing at temperatures higher than glass transition temperatures has been more successful in healing the pores and voids in the structure of PAN/CNT fibers. This may be due to lower crystallinity of the structure of jet-stretched PAN/CNT fibers (as it will be discussed in section "Laboratory X-Ray Diffraction"), which makes the structural arrangement and orientation easier than PAN fibers. In PAN fibers, however, steam drawing at the temperature and rate used in this research has not reduced the porosity of structure. This might result from chain breakage during steam drawing and/or slippage of

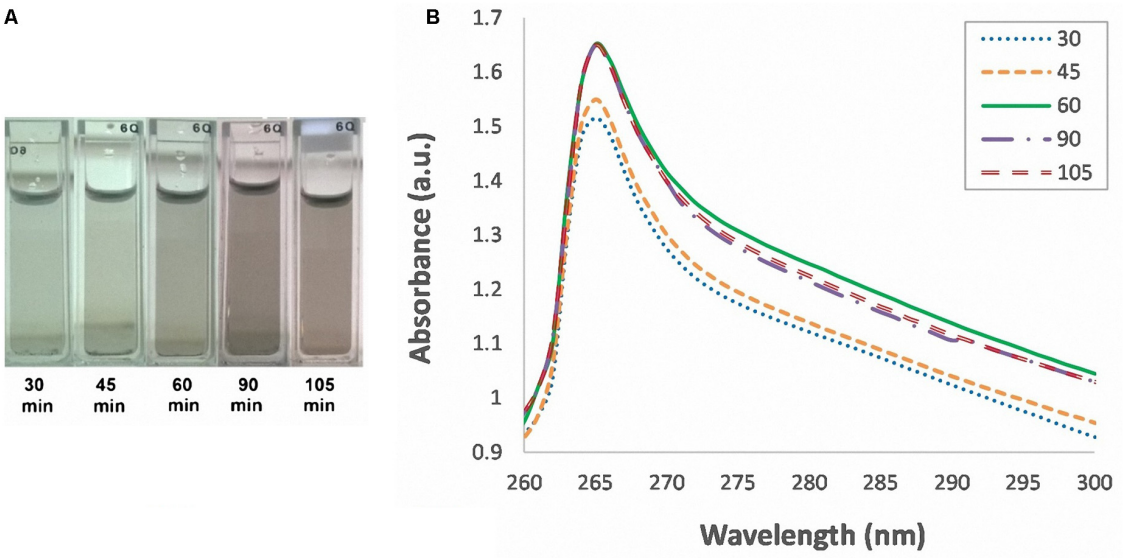

FIGURE 3 | (A) Dilute PAN/CNT/DMF solutions after ultrasonication at different times. **(B)** UV-visible spectrum of PAN/CNT/DMF solutions at different ultrasonication times.

some fibrils and crystalline domains to rearrange and reorganize new domains, introducing new voids in the structure. Liu et al. (2015) also observed an increase in porosity at some hot drawing ratios and lower drawing temperatures during the production of ultra-high molecular weight polyethylene fibers.

Fiber Morphology

During the coagulation process of PAN fibers, a structure consisting of loose fibrils and finger-like voids along the radius of the fiber is formed. This structure is formed because of counter diffusion of solvent/non-solvent and rapid phase separation (Ouyang et al., 2011). Finger-like voids reduce the mechanical properties of the fibers (Arbab et al., 2008). Application of jet-stretch ratios of 2 and 2.5 to PAN/CNT fibers makes the cross section irregular with deep surface grooves (**Figure 4** in Mirbaha et al., 2019). On the other hand, application of steam drawing with the ratio of 5 to jet-stretched PAN/CNT fibers heals the surface grooves to a large extent, **Figure 4A**. The cross section of these fibers is also more regular compared to jet-stretched PAN/CNT fibers (Mirbaha et al., 2019). The discrepancy of the shape of the cross section from a circular form affects the mechanical properties of the fibers (Chen et al., 2010). PAN reference fibers at jet stretch ratios of 2 and 2.5 have a circular cross section (**Figure 4** in Mirbaha et al., 2019). Application of a steam drawing ratio of 5 to these fibers also does not change the cross section shape significantly (**Figure 4B**). This difference suggests that the tolerability of PAN/CNT fibers to jet stretch is less than that of PAN fibers. The voids in the cross section of steam-drawn fibers are shrunk as a result of elongational forces. In addition, the fibrils are more oriented and compact after steam drawing. Fibrillar compactness of PAN/CNT fibers is more than that of PAN fibers. This is attributed to the smaller die swell in PAN/CNT fibers (Mirbaha et al., 2019). As it was reported in our previous paper (Mirbaha et al., 2019), we could not identify aggregations of CNTs in fiber cross sections even at magnifications of 150,000×. This can possibly show the good state of dispersion of CNT in the matrix and wrapping individual CNTs with polymer chains (Mirbaha et al., 2019).

TABLE 2 | Physical properties of PAN/CNT and PAN fibers at different spinning conditions.

Condition	Sample name	Diameter (μm)	% CV	Linear density (tex)	% CV	Porosity (%)
PAN/CNT						
Freely spun	PC	275.0	0.04	15.1	0.05	78.5
Jet stretched	PC-S2	147.9	0.07	4.0	0.09	80.3
	PC-S2.5	138	0.13	2.8	0.16	84.1
Steam Drawn	PC-D2.5	197.6	0.04	6.3	0.07	82.6
	PC-D5	157	0.06	3.3	0.08	85.5
	PC-S2-D5	77.4	0.15	1.1	0.19	79.1
PAN						
Freely spun	P	335.4	0.05	28.2	0.06	73.1
Jet stretched	P-S2	185.5	0.06	10.0	0.05	68.7
	P-S2.5	164.2	0.11	7.3	0.05	70.7
Steam Drawn	P-D2.5	241.4	0.05	12.4	0.06	77.2
	P-D5	196.2	0.05	6.8	0.07	81.1
	P-S2-D5	102	0.04	2.1	0.06	76.1

Crystalline Structure

Laboratory X-Ray Diffraction

A sharp peak at 2θ∼17° exists in the X-ray pattern of PAN/CNT fibers, which is attributed to the diffraction peak from the (100) planes (Ouyang et al., 2015). A broad diffuse scattering appearing around 2θ∼20–30° is attributed to the contribution of amorphous regions of fibers (**Figure 5**). These peaks in freely spun fibers are wide and weak. Application

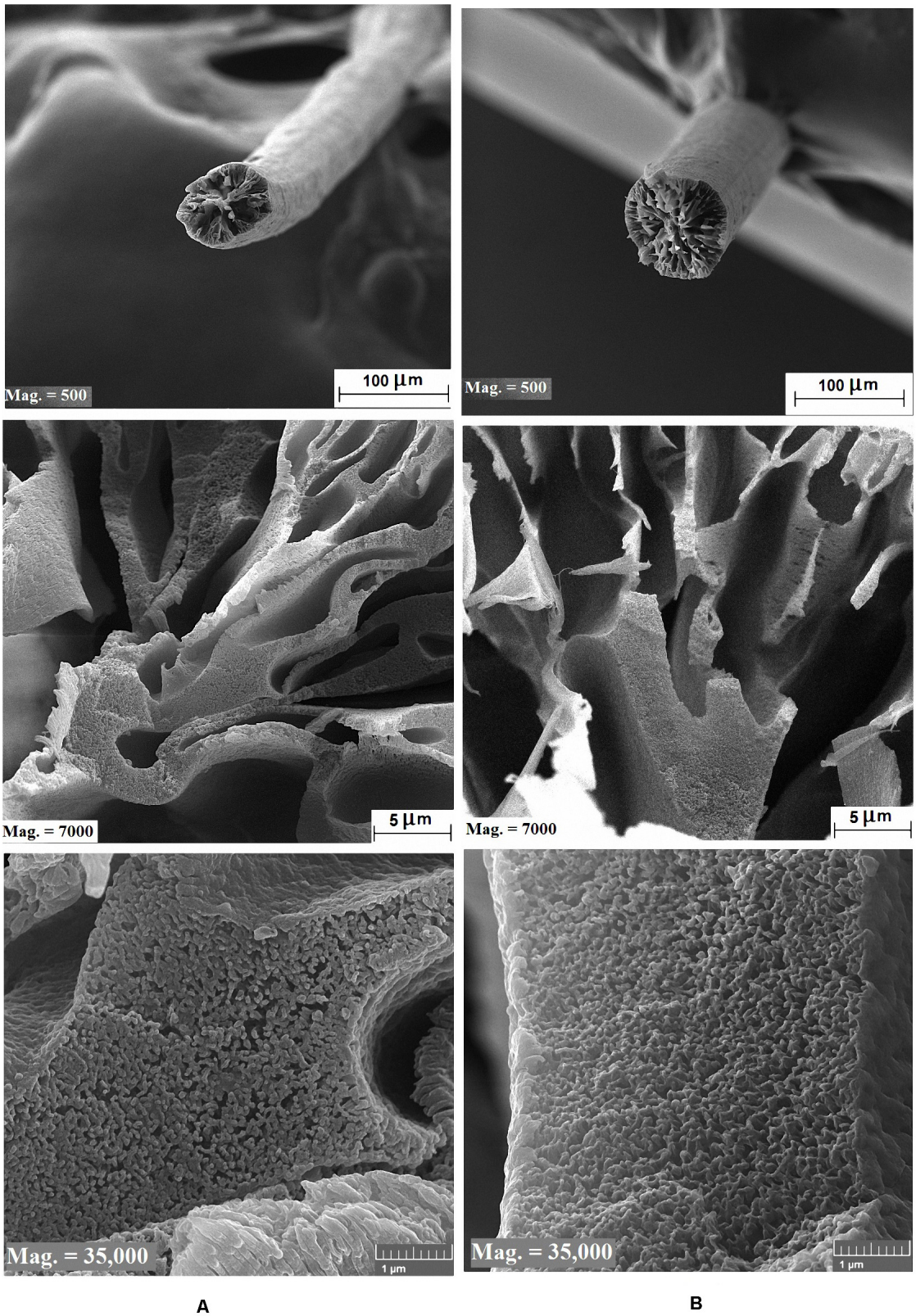

FIGURE 4 | FESEM images of the cross section and morphology of PAN/CNT and PAN fibers at magnifications of 500×, 7,000×, and 35,000×. **(A)** PC-S2-D5, and **(B)** P-S2-D5.

of jet stretch increases the peak intensity to some extent, whereas steam drawing sharpens the diffraction peak at 2θ∼17° and increases its intensity significantly. In addition, a small crystalline peak appears at 2θ∼30°, showing an improvement in the crystalline structure of PAN/CNT fibers with steam drawing.

During steam drawing, polymer chains are oriented and packed in a way that orientation-induced crystallization can take place. As a result, the crystallinity and crystallite size increase sharply (**Table 3**). Application of steam drawing at the ratio of 2.5 has better efficiency in improving the crystalline structure of the freely spun PAN/CNT fibers compared to a total draw ratio of 10 (**Table 3**), whereas the improvement in the crystalline structure of PAN reference fibers at a steam drawing ratio of 2.5 is negligible. For improving the crystalline structure of PAN fibers and increasing their crystallite size in the absence of CNTs, application of both jet stretch and steam drawing at higher drawing ratios is necessary. To our knowledge, the difference between the response of polymer chains in the composite PAN/CNT and reference PAN fibers to the stretching force inside the coagulation bath and after fiber coagulation as well as the difference in evolution of the crystalline structure at different stretching steps has not been reported elsewhere. This information can help optimize the stretching stages of PAN/CNT fibers to obtain better fiber properties.

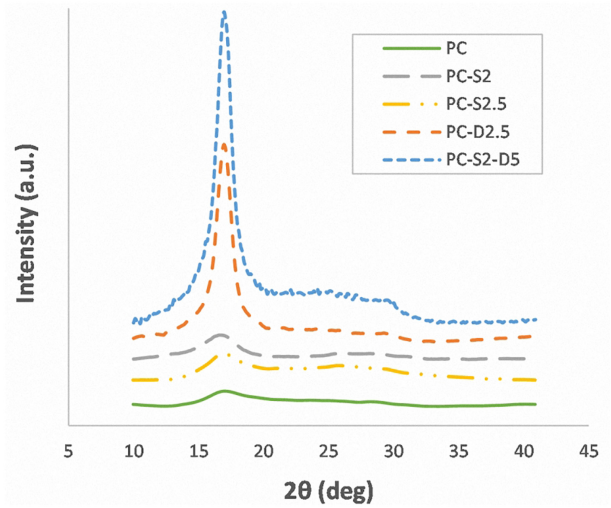

FIGURE 5 | XRD patterns of PAN/CNT fibers at different stretching conditions.

Comparison of crystalline parameters of PC-S2.5 and PC-D2.5 shows the larger influence of steam drawing on the crystalline structure of PAN/CNT fibers compared to jet stretching (**Table 3**). Steam drawing has resulted in the growth of crystals and significant improvement in fiber crystallinity. As reported by Gissinger et al. (2018), this can improve the interfacial shear strength of CNTs in the matrix and result in stronger cohesion.

In the presence of the water vapor molecules at the temperature of 100°C, polymer chains have more freedom for mobility and alignment. In addition, there is more intense nucleation and growth of crystals in the presence of CNTs, whereas PAN reference fibers show a different behavior.

Crystallite size and average crystallite layers of PAN/CNT fibers are larger than those of corresponding PAN fibers at most spinning conditions (**Figure 6A**). The presence of CNTs among the polymer chains facilitates the growth of crystallites by joining smaller crystallites together and joining more chains from the amorphous and transition phases to the crystal phase. We propose that nucleation and growth of PAN crystals on the surface of CNTs has resulted in improvement in the crystalline domain size. Other researchers also reported the growth of crystals in the vicinity of CNTs (Mai et al., 2011; Zhang et al., 2013).

Despite larger crystallites, the crystallinity of PAN/CNT fibers is less than that of PAN reference fibers at most spinning conditions (**Figure 6B**). It shows the presence of larger crystals at fewer numbers in PAN/CNT composite fibers. Jet-stretched PAN/CNT fibers have significantly lower crystallinity than corresponding PAN fibers, whereas the crystallinity of PAN/CNT fibers increases sharply with steam drawing, bringing it close to or even higher than that of PAN fibers. This shows the larger

TABLE 3 | Parameters of crystalline structure of PAN/CNT and PAN fibers at different stretching conditions.

Condition	Sample name	Angle (2θ)	FWHM (2θ)	d (A)	L_c (nm)	L_c/d	C (%)
PAN/CNT fibers							
Freely spun	PC	17.09	3.07	5.185	2.6	5.0	13.0
Jet stretched	PC-S2	16.93	2.19	5.233	3.6	6.9	34.1
	PC-S2.5	16.76	2.10	5.286	3.8	7.1	36.5
Steam drawn	PC-D2.5	16.98	1.29	5.218	6.1	11.8	54.5
	PC-S2-D5	16.98	1.15	5.216	6.9	13.3	58.4
PAN fibers							
Freely spun	P	17.02	3.10	5.206	2.6	4.9	13.5
Jet stretched	P-S2	16.91	2.32	5.240	3.4	6.5	53.9
	P-S2.5	16.82	2.29	5.266	3.5	6.6	54.6
Steam Drawn	P-D2.5	16.86	2.16	5.255	3.7	7.0	53.2
	P-S2-D5	16.97	1.03	5.222	7.7	14.7	60.5

FWHM, Full width at half maximum; d, interplanar spacing; L_c, crystalline domain size; L_c/d, average crystallite layers; C, crystallinity.

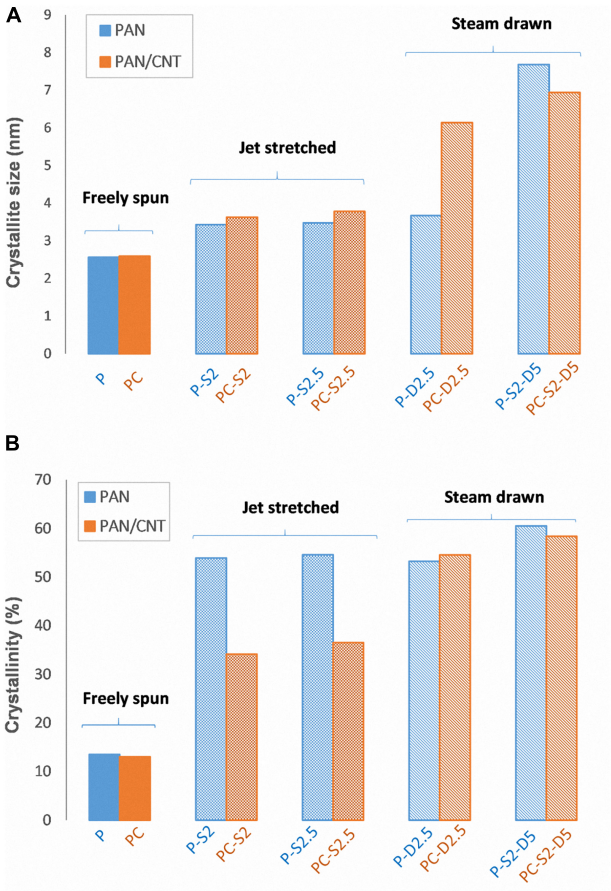

FIGURE 6 | Comparison of crystalline parameters of PAN/CNT and PAN fibers at different st retching conditions: **(A)** Crystallite size, **(B)** Crystallinity.

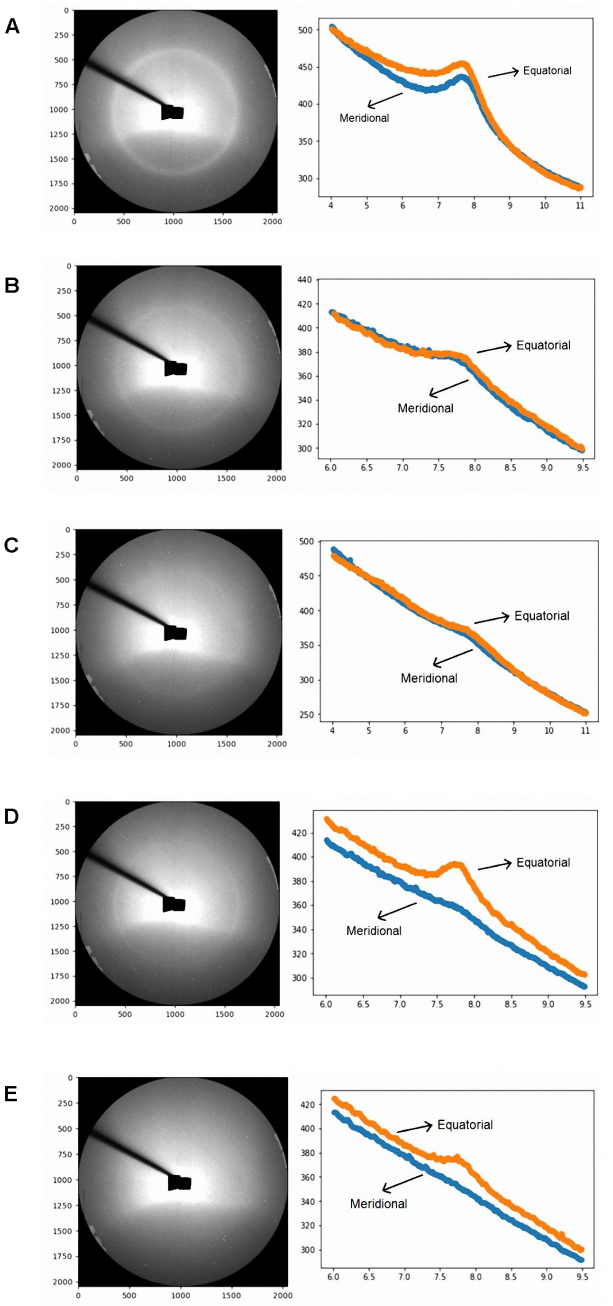

FIGURE 7 | Synchrotron radiation 2D X-ray diffraction patterns of PAN/CNT fibers at different stretching conditions and their 1D equatorial and meridional cross section profiles. **(A)** PC, **(B)** PC-S2, **(C)** PC-S2.5, **(D)** PC-D5, **(E)** PC-S2-D5.

influence of steam drawing on crystalline evolution of PAN/CNT fibers compared to PAN fibers.

Synchrotron X-Ray Diffraction

Synchrotron radiation 2D X-ray diffraction patterns of PAN/CNT fibers and their 1D equatorial and meridional cross section profiles are shown in **Figure 7**. Freely spun fibers exhibited broad reflections with similar equatorial and meridional profiles, resulting from low crystallinity and irregular placement of crystals inside fibers. Application of jet stretch sharpens the peak slightly with small differences in diffraction area in equatorial and meridional directions. After steam drawing, the reflections become sharper and their intensity on the equator increases due to increased crystal perfection. Since single fibers were used for synchrotron X-ray diffraction, the intensity of diffraction ring decreases with increasing the stretching ratio and diameter reduction.

The difference between intensity (I) and area (A) under the peak in equatorial (*eq.*) and meridional (*mer.*) profiles can be used as a measure of crystal orientation along the fiber direction (**Table 4**). $I_{eq.}/I_{mer}$, and $A_{eq.}/A_{mer}$. ratios of jet-stretched PAN/CNT fibers have been increased slightly compared to freely spun fibers. Application of steam drawing with the ratio of 5 to the jet-stretched fibers increases these ratios significantly, revealing the remarkable improvement in the crystal orientation.

When PAN/CNT fibers are stretched, CNTs can also orient along the fiber direction (Dintcheva et al., 2011; Mai et al., 2011). Since crystals can nucleate in the vicinity of CNTs, increasing the orientation of CNTs improves the crystal

TABLE 4 | Parameters extracted from equatorial ad meridional scans of synchrotron radiation X-ray diffraction patterns of PAN/CNT and PAN fibers spun at different stretching conditions.

Sample name	Spinning condition	$I_{eq.}/I_{mer.}$	$A_{eq.}/A_{mer.}$
PC	Freely spun	1.4	1.49
PC-S2	Jet stretched	1.51	1.58
PC-S2.5	Jet stretched	1.78	1.81
PC-D5	Steam drawn	4.44	4.76
PC-S2-D5	Jet stretched and steam drawn	18.44	15.65
P	Freely spun	0.81	0.53
P-D5	Steam drawn	4.05	4.09
P-S2-D5	Jet stretched and steam drawn	7.91	10.38

I, diffraction intensity; A, area under the peak; eq, equatorial; mer, meridional.

orientation at polymer/CNT interface, which leads to higher crystal orientation compared to the structures without CNTs (**Table 4**). It confirms the possibility of crystal growth in the vicinity of CNTs.

Mechanical Properties

Young's Modulus

The Young's modulus of PAN and PAN/CNT fibers increases with jet stretch (**Table 5**). Even with the lower crystallinity of jet-stretched PAN/CNT fibers in comparison with the corresponding PAN reference fibers (**Table 3**), Young's modulus of PC-S2 is still 9% higher than that of P-S2, and Young's modulus of PC-S2.5 and P-S2.5 are almost identical. It seems that better orientation of the polymer chains and CNTs by application of jet stretch can result in the growth of crystals on CNTs and in increasing the crystal orientation along the fiber axis. Hence, the jet-stretched PAN/CNT fibers have higher Young's modulus despite high porosity and low crystallinity compared to the corresponding PAN fibers.

When steam drawing is applied to coagulated fibers, Young's modulus has increased significantly due to improved polymer and crystal orientation as well as larger crystalline domain size and crystallinity even at high porosity (**Table 5** and **Figure 8A**). Comparison of Young's modulus of the steam-drawn fibers at the ratio of 2.5 with the jet-stretched fibers at the ratio of 2.5 shows the larger impact of steam drawing on Young's modulus. It should be noted that steam drawing has larger impact on Young's modulus of PAN/CNT fibers than that of PAN reference fibers. For example, Young's modulus of PC-D2.5 fibers is 100% higher than that of PC-S2.5, whereas Young's modulus of P-D2.5 is 67% higher than that of P-S2.5. In addition, Young's modulus of PC-D2.5 is 20% higher than that of P-D2.5. It is evident that the presence of multiwalled CNTs inside the fiber structure has improved Young's modulus. The improvement in orientation of polymer chains and crystals in the fiber direction is the reason for the improvement of Young's modulus in PAN/CNT fibers.

Tenacity

The mechanical properties of fibers increase with application of elongational forces inside the coagulation bath through alignment of bonds of the chain backbone in the fiber direction and crystallinity enhancement. Jet stretch has increased the tenacity of PAN/CNT and PAN reference fibers up to 21 and 24%, respectively (**Table 5**).

Steam drawing increases the tenacity of PAN/CNT and PAN fibers significantly (**Table 5** and **Figure 8B**). For example, application of steam drawing at the ratio of 5 results in 320–350% increase in tenacity of PAN/CNT and PAN fibers. Steam drawing is more effective in improving the structure and mechanical properties than jet stretching. The tenacity of steam-drawn PAN/CNT composite fibers at the ratio of 2.5 is 65% higher than that of jet-stretched PAN/CNT fibers at the ratio of 2.5. Steam drawing at temperatures above the glass transition temperature of PAN has increased the freedom of movement of polymer chains and CNTs in PAN/CNT fibers. Crystalline domain size, crystallinity, and crystal orientation have also been improved as a result of better orientation of polymer chains in the fiber direction (**Tables 3**, **4**). However, steam drawing has mostly increased the

TABLE 5 | Mechanical properties of PAN/CNT and PAN reference fibers at different stretching conditions.

Condition	Sample name	Tenacity (cN/tex)	% CV	Strain at break (%)	% CV	Young's modulus (cN/tex)	% CV
PAN/CNT							
Freely spun	PC	2.4	11.6	40	16.2	50.1	16.4
Jet stretched	PC-S2	2.6	4.9	19	18.1	73.0	8.8
	PC-S2.5	2.9	5.7	18	16.2	77.6	17.0
Steam Drawn	PC-D2.5	4.7	15.5	15	21.3	154.2	4.6
	PC-D5	9.9	6.9	28	6.3	156.2	16.6
	PC-S2-D5	6.8	7.6	13	8.9	166.1	11.4
PAN							
Freely spun	P	2.4	8.9	33	14.0	48.1	11.6
Jet stretched	P-S2	2.7	7.5	36	7.0	67.2	7.0
	P-S2.5	3.2	2.8	34	7.2	78.1	8.2
Steam drawn	P-D2.5	6.8	5.9	25	13.2	130.2	15.0
	P-D5	10.8	7.0	35	6.9	153.8	16.4
	P-S2-D5	13.1	2.3	24	5.4	263.7	6.1

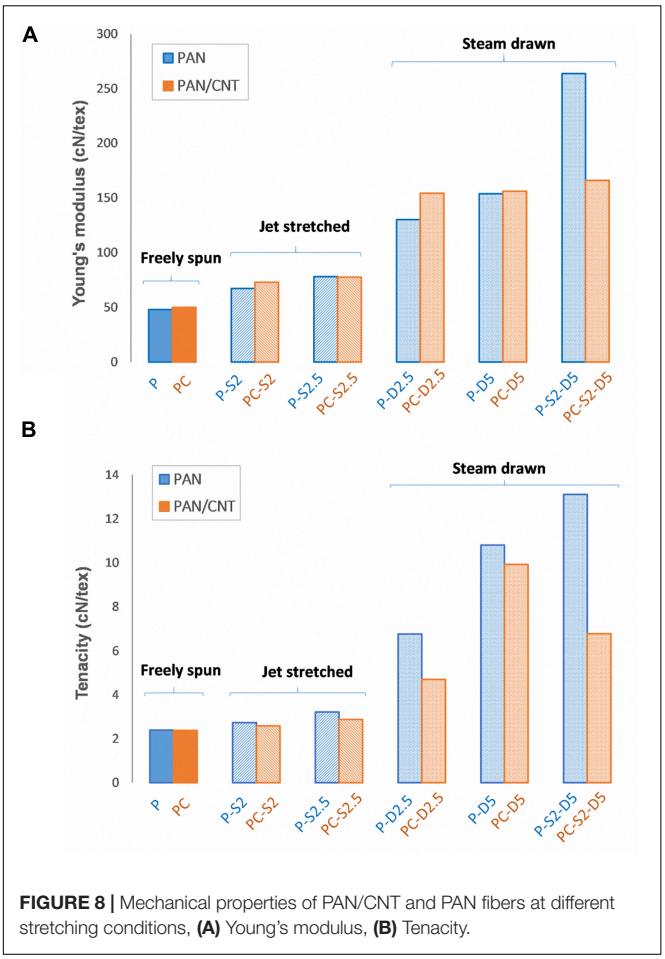

FIGURE 8 | Mechanical properties of PAN/CNT and PAN fibers at different stretching conditions, **(A)** Young's modulus, **(B)** Tenacity.

chain orientation of PAN reference fibers without increasing its crystallinity.

The highest tenacity of PAN/CNT fibers was achieved at steam drawing ratio of 5 (9.928 cN/tex), whereas PAN fibers had the highest tenacity when they were jet stretched at the ratio of 2 and then steam drawn at the ratio of 5 (13.112 cN/tex). Carbon nanotubes alter the optimum stretching conditions by affecting the orientation and crystallinity of structure. At similar steam drawing conditions, the tenacity of PAN fibers is higher than that of PAN/CNT fibers. Supposedly, CNTs have reduced the structure integrity, increasing the porosity. Not only does the polymer orientation affect the fiber strength, but also defects and voids in the molecular structure have an important role in mechanical properties of fibers (Ouyang et al., 2015). Macrovoids act as breaking points during stretching. To increase the tenacity of PAN/CNT fibers, it is necessary to control the coagulation and drying stage during the wet-spinning process to lower the porosity of the structure. Comparing the influence of various types of CNTs on the properties of PAN/CNT fibers, Chae et al. (2005) reported that multiwalled CNTs have a larger effect on tenacity and strain at break. However, the results of our work show that Young's modulus of fibers is more affected by the presence of multiwalled CNTs than tenacity.

When a combination of jet stretch at the ratio of 2 and steam drawing at the ratio of 5 is applied on fibers, the mechanical properties of PAN fibers exceeds that of PAN/CNT fibers. This can possibly be due to the negative effect of the high jet stretch ratio on porosity, morphology, crystalline structure, and mechanical properties of PAN/CNT fibers. Taking into account the outcomes of our previous paper (Mirbaha et al., 2019) as well as the observations in the current work, it is clear that for production of PAN/CNT fibers, lower jet-stretch ratios should be applied on fibers. In addition, controlling the porosity of structure by optimization of spinning conditions (i.e., coagulation, stretching and drying conditions) can lead to improvement in mechanical properties of PAN/CNT fibers compared to PAN fibers.

CONCLUSION

The present research on the impact of different stretching conditions on the crystalline structure and properties of wet-spun PAN/CNT microfibers led to the following outcomes:

(1) Steam drawing has a larger effect on crystalline structure and Young's modulus of PAN/CNT fibers than jet stretching, whereas jet stretching and steam drawing have a comparable effect on the crystalline structure of PAN fibers. Application of the steam draw ratio of 2.5 has improved Young's modulus of PAN/CNT fibers by a maximum of 100% in comparison to corresponding PAN/CNT fibers jet-stretched at the ratio of 2.5.

(2) The effect of steam drawing on the crystalline structure and Young's modulus of PAN/CNT fibers is larger than its effect on PAN fibers. Young's modulus of PAN/CNT fibers could increase up to 19% higher than that of PAN fibers at a steam drawing ratio of 2.5. The existence of multiwalled CNTs inside the fibers has provided better crystalline structure of PAN/CNT fibers at lower steam drawing ratios compared to PAN fibers via nucleation of crystals around the CNTs. Improvement in the orientation of polymer chains and crystals in the fiber direction is the reason for the enhancement Young's modulus.

The results of this research can help to understand how different stretching stages in wet spinning (i.e., jet stretching inside coagulation bath and steam drawing after fiber coagulation) affect the structure and properties of composite PAN/CNT fibers in comparison to PAN fibers.

DATA AVAILABILITY STATEMENT

The raw data supporting the conclusions of this article will be made available by the authors, without undue reservation, to any qualified researcher.

AUTHOR CONTRIBUTIONS

HM contributed to the conceptualization, doing the experiments, original draft preparation, writing, and editing the manuscript. PS contributed to editing the manuscript. MD'I contributed to the data acquiring. PS and MD'I contributed to the methodology. PS, MD'I, and HM contributed to the data analysis. PS, NP, and SA contributed to the providing resources. PN and NP contributed to the supervision and project administration. NP contributed to the original draft preparation and editing. All authors contributed to the article and approved the submitted version.

FUNDING

NP was supported by the European Commission under the FET Proactive ("Neurofibres") Grant No. 732344. NP and HM were also supported by the PRIN-2017 7TTP3S.

ACKNOWLEDGMENTS

We thank MCX beamline and the technical staff of the Italian synchrotron Elettra for collaboration.

REFERENCES

Arbab, S., Noorpanah, P., Mohammadi, N., and Soleimani, M. (2008). Designing index of void structure and tensile properties in wet-spun polyacrylonitrile (PAN) Fiber. I. Effect of dope polymer or nonsolvent concentration. *J. Appl. Polym. Sci.* 109, 3461–3469. doi: 10.1002/app.28458

Arbab, S., Noorpanah, P., Mohammadi, N., and Zeinolebadi, A. (2011a). Exploring the effects of non-solvent concentration, jet-stretching and hot-drawing on microstructure formation of poly(acrylonitrile) fibers during wet-spinning. *J. Polym. Res.* 18, 1343–1351. doi: 10.1007/s10965-010-9537-7

Arbab, S., Noorpanah, P., Mohammadi, N., and Zeinolebadi, A. (2011b). Simultaneous effects of polymer concentration, jet-stretching, and hot-drawing on microstructural development of wet-spun poly(acrylonitrile) fibers. *Polym. Bull.* 66, 1267–1280. doi: 10.1007/s00289-010-0422-7

Bakhtiary Davijani, A. A., and Kumar, S. (2015). Ordered wrapping of poly(methyl methacrylate) on single wall carbon nanotubes. *Polymer* 70, 278–281. doi: 10.1016/j.polymer.2015.06.018

Basu-Dutt, S., Minus, M. L., Jain, R., Nepal, D., and Kumar, S. (2012). Chemistry of carbon nanotubes for everyone. *J. Chem. Educ.* 89, 221–229. doi: 10.1021/ed1005163

Brown, T. R., Choudhury, R. P., Meree, C. E., Beckham, H. W., Kumar, S., and Shofner, M. L. (2014). Viscoelastic properties and structure of poly(acrylonitrile-co-methacrylic acid) polymer solutions for gel spinning at long aging times. *J. Appl. Polym. Sci.* 131:39821.

Cao, C., Chung, T., Chen, S., Dong, Z., and Jiang, S. (2004). The study of elongation and shear rates in spinning process and its effect on gas separation performance of poly(ether sulfone) (PES) hollow fiber membrane. *Chem. Eng. Sci.* 59:1053. doi: 10.1016/j.ces.2003.10.023

Chae, H. G., Sreekumar, T. V., Uchida, T., and Kumar, S. (2005). A comparison of reinforcement efficiency of various types of carbon nanotubes in polyacrylonitrile fiber. *Polymer* 46, 10925–10935. doi: 10.1016/j.polymer.2005.08.092

Chen, J., Ge, H., Liu, H., Li, G., and Wang, C. (2010). The coagulation process of nascent fibers in PAN Wet spinning. *J. Wuhan Uni. Technol.* 25, 200–205. doi: 10.1007/s11595-010-2200-7

Dintcheva, N. T., Arrigo, R., Nasillo, G., Caponetti, E., and Mantia, F. P. L. (2011). On the role of extensional flow in morphology and property modifications of MWCNT/polyamide-based fibers. *Macromol. Mater. Eng.* 296, 645–657. doi: 10.1002/mame.201000355

Gissinger, J. R., Pramanik, C., Newcomb, B., Kumar, S., and Heinz, H. (2018). Nanoscale structure-property relationships of polyacrylonitrile/CNT composites as a function of polymer crystallinity and CNT diameter. *ACS Appl. Mater. Interfaces* 10, 1017–1027. doi: 10.1021/acsami.7b09739

Gong, Y., Du, R., Mo, G., Xing, X., Lu, C. X., and Wu, Z. (2014). In-situ Microstructural changes of polyacrylonitrile based fibers with stretching deformation. *Polymer* 55, 4270–4280. doi: 10.1016/j.polymer.2014.06.073

Ji, B., Wang, C., and Wang, Y. (2007). Effect of jet stretch on polyacrylonitrile as-spun fiber formation. *J. Appl. Polym. Sci.* 103, 3348–3352. doi: 10.1002/app.25490

Kang, D. W., and Ryu, S. H. (2013). Orientation of carbon nanotubes in polypropylene melt. *Polym. Int.* 62, 152–157. doi: 10.1002/pi.4270

Li, X., Qin, A., Zhao, X., Liu, D., Wang, H., and He, C. (2015). Drawing dependent structures, mechanical properties and cyclization behaviors of polyacrylonitrile and polyacrylonitrile/carbon nanotube composite fibers prepared by plasticized spinning. *Phys. Chem. Chem. Phys.* 17, 21856–21865. doi: 10.1039/c5cp02498f

Li, Y., Yu, Y., Liu, Y., and Lu, C. (2018). Interphase Development in Polyacrylonitrile/SWNT Nano-composite and its Effect on Cyclization and Carbonization for Tuning Carbon Structures. *ACS Appl. Nano Mater.* 1, 3105–3113. doi: 10.1021/acsanm.8b00125

Lian, F., Liu, J., Ma, Z., and Liang, J. (2012). Stretching-induced deformation of polyacrylonitrile chains both in quasicrystals and in amorphous regions during the in situ thermal modification of fibers prior to oxidative stabilization. *Carbon* 50, 488–499. doi: 10.1016/j.carbon.2011.09.003

Lin, Y., Che, J., Pu, S., and Wang, K. (2019). Structural origins of mechanical strengthening in poly(phenylene sulfide)multiwalled carbon nanotube nanocomposites obtained via hot-stretching. *Polym. Comp.* 40, E589–E598.

Liu, H., Lv, F., Li, J., Cao, T., Wan, C., Zhang, W., et al. (2015). Two-stage drawing process to prepare high-strength and porous ultrahigh-molecular-weight polyethylene fibers: cold drawing and hot drawing. *J. Appl. Polym. Sci.* 132:42823. doi: 10.1002/app.42823

Mai, F., Pan, D., Gao, X., Yao, M., Deng, H., Wang, K., et al. (2011). Extension-induced mechanical reinforcement in melt-spun fibers of polyamide 66/multiwalled carbon nanotube composites. *Polym. Int.* 60, 1646–1654. doi: 10.1002/pi.3144

Mikolajczyk, T., Szparaga, G., Bogun, M., Fraczek-Szczypta, A., and Blazewicz, S. (2010). Effect of spinning conditions on the mechanical properties of polyacrylonitrile fibers modified with carbon nanotubes. *J. Appl. Polym. Sci.* 115, 3628–3635. doi: 10.1002/app.31414

Minus, M. L., Chae, H. G., and Kumar, S. (2012). Polyethylene crystallization nucleated by carbon nanotubes under shear. *ACS Appl. Mater. Interface* 4, 326–330. doi: 10.1021/am2013757

Mirbaha, H., Nourpanah, P., Scardi, P., D'incau, M., Greco, G., Valentini, L., et al. (2019). The impact of shear and elongational forces on structural formation of polyacrylonitrile/carbon nanotubes composite fibers during wet spinning process. *Materials* 12:2797. doi: 10.3390/ma12172797

Ouyang, Q., Chen, Y., Wang, X., Ma, H., Li, D., and Yang, J. (2015). Supramolecular structure of highly oriented wet-spun polyacrylonitrile fibers used in the preparation of high-performance carbon fibers. *J. Polym. Res.* 22:229.

Ouyang, Q., Chen, Y. S., Zhang, N., Mo, G. M., Li, D. H., and Yan, Q. (2011). Effect of jet swell and jet stretch on the structure of wet-spun polyacrylonitrile fiber. *J. Macromol. Sci. B Phys.* 50, 2417–2427. doi: 10.1080/00222348.2011.564104

Rebuffi, L., Plaisier, J. R., Abdellatief, M., Lausi, A., and Scardi, P. (2014). MCX: a synchrotron radiation beamline form X-ray diffraction line profile analysis. *Z. Anorg. Allg. Chem.* 640, 3100–3106. doi: 10.1002/zaac.201400163

Sahin, K., Fasanella, N. A., Chasiotis, I., Lyons, K. M., Newcomb, B. A., Kamath, M. G., et al. (2014). High strength micron size carbon fibers from polyacrylonitrile–carbon nanotube precursors. *Carbon* 77, 442–453. doi: 10.1016/j.carbon.2014.05.049

Sapalidis, A., Sideratou, Z., Panagiotaki, K. N., Sakellis, E., Kouvelos, E. P., Papageorgiou, S., et al. (2018). Fabrication of antibacterial poly(Vinyl Alcohol) nanocomposite films containing dendritic polymer functionalized multi-walled carbon nanotubes. *Front. Mater.* 5:11. doi: 10.3389/fmats.2018.00011

Ward, I. M. (1997). *Structure and Properties of Oriented Polymers*. Netherlands: Springer.

Wei, H., Suo, X., Lu, C., and Liu, Y. (2020). A comparison of coagulation and gelation on the structures and stabilization behaviors of polyacrylonitrile fibers. *J. Appl. Polym. Sci.* 137:48671. doi: 10.1002/app.48671

Wilms, C., Seide, G., and Gries, T. (2013). The relationship between process technology, structure development and fibre properties in modern carbon fibre production. *Chem. Eng. Trans.* 32, 1609–1614.

Zeng, X., Hu, J., Zhao, J., Zhang, Y., and Pan, D. (2007). Investigating the jet stretch in the wet spinning of PAN fiber. *J. Appl. Polym. Sci.* 106, 2267–2273. doi: 10.1002/app.26929

Zhang, Y., Song, K., Meng, J., and Minus, M. L. (2013). Tailoring polyacrylonitrile interfacial morphological structure by crystallization in the presence of single-wall carbon nanotubes. *ACS Appl. Mater. Interface* 5, 807–814. doi: 10.1021/am302382m

Conflict of Interest: The authors declare that the research was conducted in the absence of any commercial or financial relationships that could be construed as a potential conflict of interest.

frontiers in Materials

ORIGINAL RESEARCH
published: 17 July 2020
doi: 10.3389/fmats.2020.00193

Role of Compatibilizer in Improving the Properties of PLA/PA12 Blends

Amulya Raj[1,2]*, *Cedric Samuel*[1,2] *and Kalappa Prashantha*[1,2,3]

[1] Ecole Nationale Supérieure Mines Telecom Lille Douai, Institut Mines Telecom Lille Douai (IMT Lille Douai), Département Technologie des Polymères et Composites & Ingénierie Mécanique (TPCIM), Douai, France, [2] Université de Lille, Lille, France, [3] ACU-Centre for Research and Innovation, Faculty of Natural Science, Adichunchanagiri University, Mandya, India

Engineering properties of partially-biobased poly(L-Lactide)/poly(amide-12) (PLA/PA12) blends are here addressed using a functional compatibilizer, namely poly(L-Lactide) grafted maleic anhydride (PLA-*g*-MA). PLA/PA12 blends with compatibilizers are processed using twin-screw extrusion, and the amount of PLA-*g*-PMA is here optimized with respect to final blend properties such as ductility, impact toughness, and thermal resistance. Blend morphologies depict the enhanced PA12 dispersion into PLA-*g*-MA with strong interfacial adhesion, in accordance with a compatibilization effect of PLA-*g*-MA in PLA/PA12 blends. Ductility of the compatibilized blends shows remarkable improvements with the highest ductility close to 290% for an optimized PLA/PA12/PLA-g-MA weight composition (respectively, 69/30/1). The impact strength of compatibilized blends showed a similar two-fold improvement for compatibilized blends. Morphology of injection molded samples revealed finer dispersion and stronger interfaces. The morphology of the transversal section displayed fibrillation of PA12 for PLA-g-MA content up to 2 wt.%. Fibrillation and lower droplet size seemed to play a key role in the improvement of ductility in compatibilized blends. Considerable synergy was detected in the dynamic mechanic analysis of the compatibilized blends. The thermal resistance of the PLA/PA12 blends showed improvement, and this behavior could be due to the formation of copolymer leading to additional interfacial crystallization. This study consequently indicates that PLA-g-MA is an efficient compatibilizer for partially biobased PLA/PA12 blends with potential applications in the automotive and electronic industry.

Keywords: biobased polymers, poly(lactic acid), polymer blends, compatilibization, morphologies, engineering properties

OPEN ACCESS

Edited by:
Jacqueline Anne Johnson, University of Tennessee Space Institute (UTSI), United States

Reviewed by:
M. E. Ali Mohsin, University of Technology Malaysia, Malaysia
Debora Puglia, University of Perugia, Italy

***Correspondence:**
Amulya Raj
amulya.raj@imt-lille-douai.fr

Specialty section:
This article was submitted to Polymeric and Composite Materials, a section of the journal Frontiers in Materials

Received: *17 March 2020*
Accepted: *25 May 2020*
Published: *17 July 2020*

Citation:
Raj A, Samuel C and Prashantha K (2020) Role of Compatibilizer in Improving the Properties of PLA/PA12 Blends. Front. Mater. 7:193. doi: 10.3389/fmats.2020.00193

INTRODUCTION

The replacement of petroleum-based polymers to biobased polymers is an immediate need due to the detrimental effects of the former on the environment (Mecking, 2004; Gandini et al., 2011; Mülhaupt, 2013; Harmsen et al., 2014). Among the various biobased polymers, Poly(Lactide) (PLA), also known as Poly(Lactic acid), has gained special attention in the past years owing to its remarkable properties such as renewability (Drumright et al., 2000), biocompatibility (Madhavan Nampoothiri et al., 2010; Farah and Anderson, 2016), transparency (Farah and Anderson, 2016), high modulus (Pang et al., 2010), and biodegradability (Pang et al., 2010; Saeidlou et al., 2012; Hamad et al., 2018; Nofar et al., 2019). These properties led to the commercialization of PLA, thereby making it suitable for various applications such as resorbable sutures

(Pawar et al., 2014), food and beverage packaging (Auras et al., 2004; Ahmed and Varshney, 2011), surgical implants (Pawar et al., 2014), scaffolds (Lasprilla et al., 2012; Lopes et al., 2012), and textiles (Gupta et al., 2007). Despite its propitious properties and applications, the intricacy of implementing PLA in high value or durable applications is restricted due to limitations arising from low melt strength (Nofar et al., 2019), inherent brittleness (Madhavan Nampoothiri et al., 2010; Farah and Anderson, 2016; Hamad et al., 2018), poor impact strength (Farah and Anderson, 2016; Nagarajan et al., 2016), and low heat resistance (Madhavan Nampoothiri et al., 2010; Hamad et al., 2018). Various strategies have been investigated to overcome the drawbacks of PLA, such as toughening mechanisms (Nagarajan et al., 2016; Anderson et al., 2018), copolymerization (Liu and Zhang, 2011; Nagarajan et al., 2016), stereocomplexation of PLA (Li et al., 2016; Tan et al., 2016), addition of nanoparticles and nucleating agents (Shi et al., 2015; Krishnan et al., 2016), and polymer blending (Hamad et al., 2018; Nofar et al., 2019). Among all of the strategies, polymer blending stands out owing to its feasible way to develop new material with versatile and tailor-made properties with the additional benefit of being cost-effective (Utracki and Wilkie, 2014; Mishra et al., 2017; Hamad et al., 2018; Nofar et al., 2019). Blending PLA with engineering polymers is an efficient way to overcome a majority of the limitations of PLA. Over recent years, intensive research is being carried on PLA based blends with engineering polymers such as polycarbonates (Bouzouita et al., 2016), poly(methylmethacrylate) (Samuel and Jean-Marie Raquez, 2013), polyesters (Jiang et al., 2014), and polyamides (Stoclet et al., 2011; Raj et al., 2019). Among the engineering polymers, polyamides stand out, as the blending would enhance the targeted properties of PLA such as low ductility, poor impact strength, and low heat resistance. The improvement in these properties would help in the market penetration of PLA to high-end or durable applications.

Polyamides are engineering polymers with propitious properties such as high ductility, impact strength, stiffness, and higher thermal resistance. In general, PLA/PA blends are immiscible but compatible in nature. Different types of polyamides have been blended with PLA including PA6 (Wang et al., 2010), PA11 (Stoclet et al., 2011), PA6-10 (Pai et al., 2013), PA10-10 (Cailloux et al., 2018), PA10-12 (Raj et al., 2019), and PA12 (Raj et al., 2019). In order to achieve better final properties, it is necessary to improve the compatibility further. One of the classic methods to improve the compatibility is by incorporation of compatibilizers (Utracki and Wilkie, 2014; Zeng et al., 2015). Multifarious compatibilization strategies have been employed in PLA/PA blends by addition of compatibilizers such as polyalkenyl-poly-maleic-anhydride-imide/amide agents, maleic anhydride fraction grafted on polyethylene-octene elastomer, epoxy based compounds, and poly(ethylene-co-glycidyl methacrylate-graft-styrene-co-acrylonitrile) (Wang et al., 2010; Kucharczyk et al., 2012; Dong et al., 2014; Walha et al., 2016; Cailloux et al., 2018; Pai et al., 2019; Rasselet et al., 2019). Walha F et al. studied the effect of multifunctional epoxide (Joncryl ADR®-4368) on PLA and PA11 blends, and two routes of compatibilization were investigated: (i) one step mixing of adding all the components at once to the extruder, (ii) two-step process where initially PLA and Joncryl are premixed and PA11 is introduced later (Walha et al., 2016). Rheological studies revealed good compatibility between the phases and formation of PLA-joncryl-PA11 copolymer was also confirmed. It was observed that both the processes improved the interfacial adhesion, thus reducing droplet size ($<1\,\mu m$). Significant improvement in ductility was also observed with the highest being for PLA/PA11(80/20) and 0.7 wt.% of Joncryl ADR®-4368 ($\sim$355%) (Rasselet et al., 2019). In another interesting study, maleic anhydride grafted on polyethylene octene elastomer was utilized as a compatibilizer in PLA/PA6 (Wang et al., 2010). The blends showed good dispersion with lower domain size, good ductility, and impact strength. This is due to the formation of POE-co-PA6 and POE-co-PLA copolymers, thereby improving the compatibility between the blend components (Wang et al., 2010). There have been some recent studies about reactive compatibilization of PLA/PA11; catalysts such as p-toluenesulfonic acid and titanium isopropoxide have been incorporated to induce ester amide interchange reactions between the blend components (Patel et al., 2014; Gug and Sobkowicz, 2016). Patel et al. observed that the mechanical properties such as ductility, tensile modulus, and toughness of the PLA/PA11 blends were in between the pure polymer's values, suggesting that although the catalyst titanium ispropoxide induced interchange reactions between the polymers, this did not improve the mechanical properties significantly (Patel et al., 2014).

PLA grafted maleic anhydride (PLA-g-MA) has shown to be a potential compatibilizer for PLA blends. It has been incorporated in PLA based starch, poly(ethylene terephthalate glycol) (PETG), and Poly(butylene adipate terephthalate) (PBAT) blends (Zeng et al., 2015). In PLA/starch blends the addition of PLA-g-MA has brought about an improvement in the interface by decreasing the droplet size of the dispersed phase. Significant improvement in tensile strength and ductility were also observed (Huneault and Li, 2007; Wang et al., 2007; Zeng et al., 2015). Additional improvement in morphology, tensile properties, and ductility were found in PLA/PBAT and PLA/PETG blends in the presence of PLA-g-MA as the compatibilizer (Zeng et al., 2015). Maleic anhydride based coupling agents have been previously utilized in PLA/PA blends as mentioned above (Wang et al., 2010; Kucharczyk et al., 2012). However, there are no significant studies of PLA-g-MA as a compatibilizer in the PLA/PA blend system. It would be interesting to observe the effect of PLA-g-MA as a compatibilizer on PLA/PA12 blend properties and investigate if similar improvement in morphology and ductility can be obtained.

In our previous work, we have reported various PLA blends with long-chain aliphatic polyamides. It was found that PA12 showed the best compatibility with PLA with low interfacial tensions, good dispersion, and exceptional mechanical properties (ductility>170% for 40 wt.% PA12), good impact properties, and thermal resistance (Raj et al., 2019). Hence, in an attempt to obtain further improvement thermal resistance and mechanical properties we present the effect of PLA-g-MA as a compatibilizer on the properties of PLA/PA12 blends.

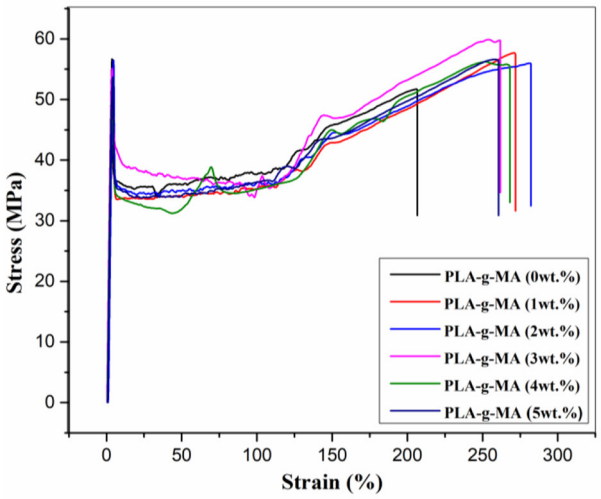

FIGURE 1 | Stress-strain curves of PLA/PA12 blends with varying concentrations of compatibilizer (PLA-g-MA).

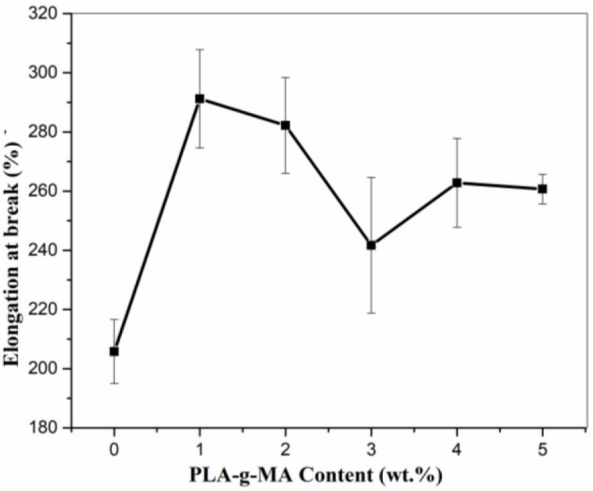

FIGURE 2 | Ductility of PLA/PA12 blends with varying PLA-g-MA content.

TABLE 1 | Stress at yield, strain at break, and impact strength for as-produced PLA/PA12/PLA-g-MA blends.

PLA/PA12/ PLA-g-MA compositions	Stress at yield (MPa)	Strain at break (%)	Young's Modulus modulus (GPa)	Impact strength (un-notched) (kJ/m^2)
100/0/0	66.6 (1.8)	3.4 (1.5)	2.9 (0.06)	18.1 (0.6)
0/100/0	39.5 (1.2)	138.3 (2.3)	1.4 (0.05)	No break
70/30/0	56.5 (1.6)	153.0 (3.3)	2.2 (0.06)	28.3 (0.7)
69/30/1	55.3 (1)	291.2 (16.6)	2.1 (0.05)	45.4 (0.8)
68/30/2	53.9 (2.4)	282.2 (16.2)	2.1 (0.04)	46.8 (0.8)
67/30/3	52.8 (3.1)	268.7 (22.9)	2.1 (0.09)	40.5 (0.2)
66/30/4	52.4 (4.5)	268.2 (15)	2.1 (0.1)	40.4 (0.2)
65/30/5	53.7 (0.9)	260.7 (5.04)	2.0 (0.3)	32.1 (2.4)

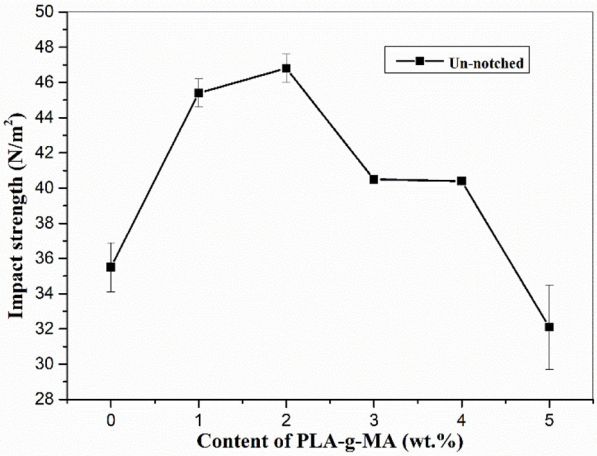

FIGURE 3 | Impact strength of the PLA/PA12 blends with varying concentration of PLA-g-MA.

MATERIALS AND METHODS

Materials

Poly(L-lactide) (PLA, grade 4032D, biobased content 100%, density 1.24 g/cm^3, melting temperature 171°C, melt volume index 6.5 cm^3/10 min at 210°C, according to manufacturer data) was procured from NatureWorks®, USA. Poly(amide-12) (PA12, grade Rilsamid AESNO, density 1.01 g/cm^3, melting temperature 179°C, melt volume index 2.1 cm^3/10 min at 235°C, according to manufacturer data) was supplied by Arkema, France. PLA and PA12 were used as received in the pellet form. PLA grafted maleic anhydride (PLA-g-MA) was kindly provided to us by the University of Mons and the preparation method can be referred in the research work published by Quintana et al. (2016). It has a maleic anhydride content of 0.45%.

Processing of PLA/PA12 Blends

Before compounding, the polymers were dried thoroughly under vacuum at 80°C for 8 h to remove any traces of moisture in the materials. PLA/PA12/PLA-g-MA (wt.% 70/30/0, 69/30/1, 68/30/2, 67/30/3, 66/30/4, 65/30/5) were processed by twin-screw extrusion using a Haake Rheomex PTW 16 OS twin-screw extruder (Thermoscientific, Germany, screw diameter 16 mm, L/D 40). The average speed maintained during extrusion was 80 rpm, with a total mass flow rate close to 500 g/h and a mean residence time of ∼2 min. The barrel temperature regulation is carried out on 10 zones and the temperature profile was maintained constant for all experiments (200–205–210–210–210–210–210–210–200–185°C), from the hopper to the die. The extrudates were cooled in a water bath and pelletized. The

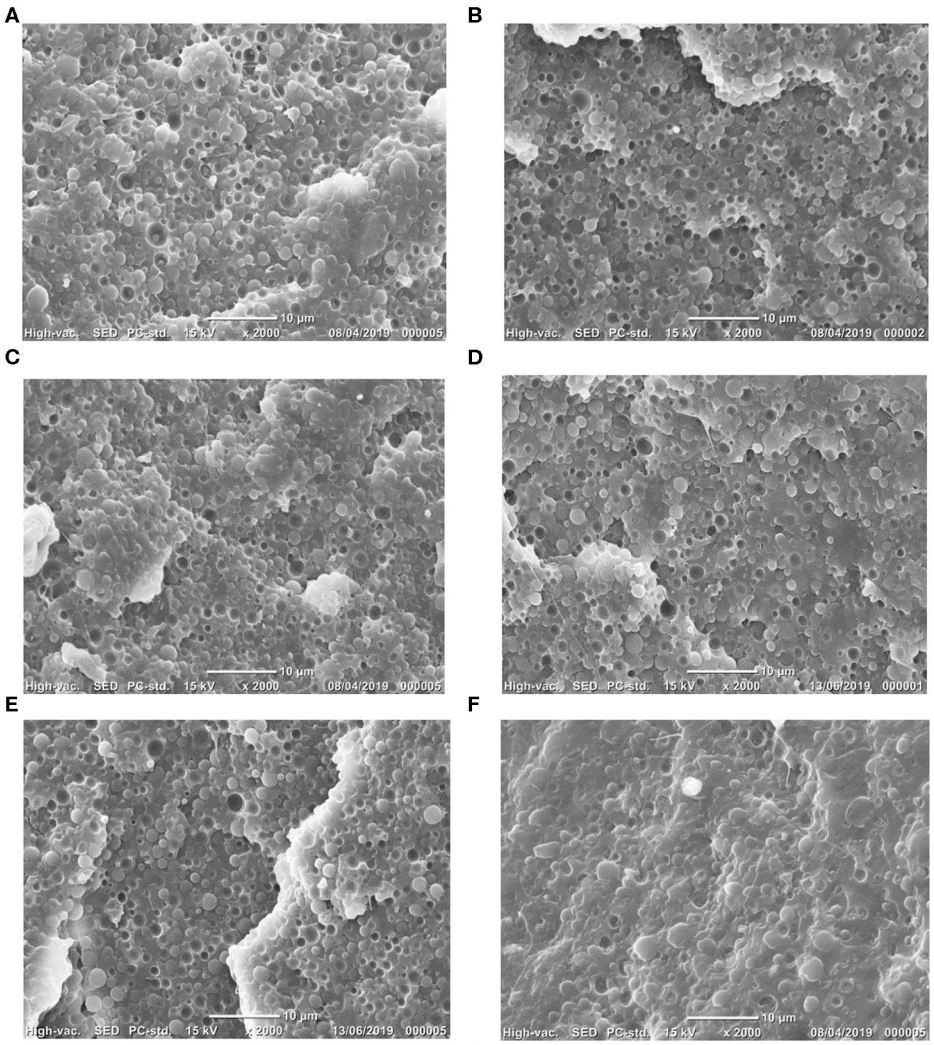

FIGURE 4 | Morphology of PLA/PA/PLA-g-MA of various compositions **(A)** 70/30/0, **(B)** 69/30/1, **(C)** 68/30/2, **(D)** 67/30/3, **(E)** 66/30/4, and **(F)** 65/30/5.

pellets were dried at 80°C under vacuum overnight. After thorough drying pellets were used for the following molding processes. Pristine polymers were also extruded through a similar procedure.

Tensile test specimens were prepared by following the ISO-527-1 standards. The dimensions of the specimens are as follows: gauge length 50 mm, width of 5 mm, and thickness of 1.5 mm. They were processed by injection-molding using a Haake Minijet II molding machine. The following processing conditions were used for the preparation of injection-molded specimens: mold temperature 45°C, chamber temperature 215°C, injection pressure 550 bar, cooling time 5 s. Impact specimens were prepared by injection molding (Babyplast 6/10P, Spain). The processing parameters maintained during the preparation of samples were as follows: the temperature ranged from 200 to 210°C and the mold temperature was around 35–50°C. The injection and the consecutive pressure were 60 and 80 bars, respectively, with a cooling time of 10 s. Specimens for morphological characterization were processed by compression-molding, and Dolouet molding press was utilized for this process. The parameters and conditions were used for all compression-molded specimens (melt temperature: 205°C, melting time and low-pressure cycle: 8 min, high pressure cycle: 5 min).

Methods

Scanning Electron Microscopy (SEM)

The morphology of the compression-molded PLA/PA blends was examined using a scanning electron microscope (SEM, Neoscope II, JEOL, magnification ×60,000). Prior to the observation of morphologies, the specimens were cryo-fractured in liquid nitrogen. These fractured samples were then metallized by gold sputtering under vacuum in order to make them conductive. Droplet sizes of the dispersed phase were measured

TABLE 2 | Number-average and volume-average PA12 droplet diameters (D_n and D_v), PA droplet size polydispersity (I_p) with standard deviation in brackets of PLA/PA12/PLA-g-MA blends (compression molded samples).

Blend	D_n (μm)	D_v (μm)	I_p
70/30/0	1.1 (0.1)	1.4 (0.03)	1.2
69/30/1	1 (0.06)	1.2 (0.05)	1.2
68/30/2	1 (0.04)	1.2 (0.06)	1.2
67/30/3	1.3 (0.1)	1.5 (0.09)	1.1
66/30/4	1.3 (0.1)	1.6 (0.06)	1.2
65/30/5	1.5 (0.07)	1.8 (0.05)	1.2

by image analysis using Image J software. The analysis was done on 50 droplets at least followed by size classification into 7/8 classes. The volume and number average droplet radius diameters (D_v, D_n) with the droplet diameter polydispersity (I_D) were calculated using Equations 1–3. The standard deviations of the size of the droplets were presented by measuring two samples.

$$D_n = 2 \times \frac{\sum n_i \times R_i}{\sum n_i} \quad (1)$$

$$D_v = 2 \times \frac{\sum n_i \times R_i^4}{\sum n_i \times R_i^3} \quad (2)$$

$$I_D = \frac{D_v}{D_n} \quad (3)$$

with D_n the droplet number-average diameter, D_v the droplet volume-average diameter, R_i the average droplet radius of the *i*-class, and n_i the number of droplets into the *i*-class.

Tensile and Impact Tests

Tensile tests were carried out on PLA/PA blends and neat polymers in a tensile test machine (Instron 3110, U.K) and a 1 kN force cell to obtain stress–strain curves. Tensile properties were determined in accordance with ISO 527-1 (pre-load of 0.5 N, strain rate 1 mm/min for Young's modulus, and 10 mm/min for general properties). Five dumbbell specimens were tested at the least. Charpy un-notched impact tests were carried out as per ISO 179-1 standard by using a pendulum impact machine (Model 5101, Zwick, Germany) at 25°C and 50% RH and impact energy of 7.1 J. The reported values were evaluated as averages of seven specimens.

Dynamic Mechanical Analysis (DMA)

The dynamic mechanical analysis of the specimens was carried out on dual cantilever beam in the flexion mode (DMA+150, MetraviB, France). The samples were heated over a temperature range (25–130°C) at a heating rate of 2°C/min and frequency of 10 Hz. Two rectangular specimens were tested at the least. The cold crystallization peak of PLA was avoided by annealing the specimens at 110°C for 6 h. The approximate thermal resistance of blends which could correspond to heat deflection temperature (HDTa and HDTb) at two different storage moduli

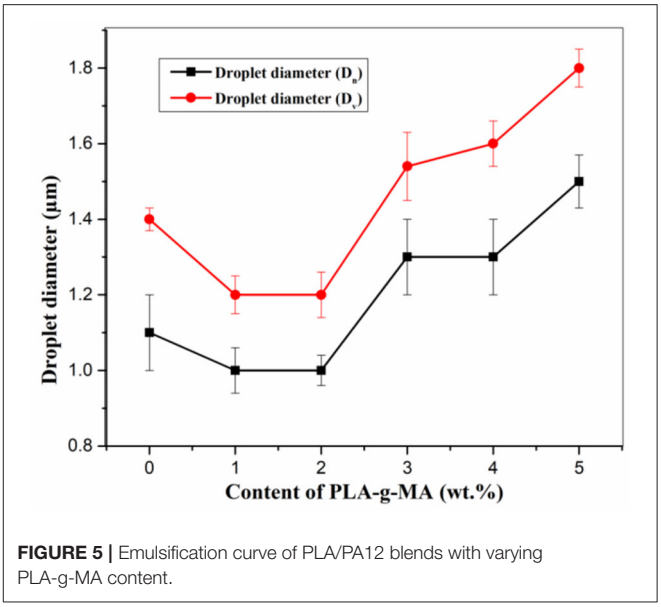

FIGURE 5 | Emulsification curve of PLA/PA12 blends with varying PLA-g-MA content.

(400 and 250 MPa), respectively, were evaluated by the DMA graphs. A method was partially implemented in several studies (Takemori, 1979; Spinella et al., 2016). These storage modulus values were first calibrated using known values on polyamides and temperatures where storage modulus drops down to 400 and 250 MPa were named $T_{400MPa-HDTa}$ and $T_{250MPa-HDTb}$, respectively (Battegazzore et al., 2016).

Differential Scanning Calorimetry (DSC)

Differential scanning calorimetry (DSC Mettler Toledo) was utilized to measure the PLA crystallinity of pristine PLA and PLA/PA12/PLA-g-MA blends. The evaluation was performed on injection-molded specimens following an annealing step. The DSC evaluation was carried out under nitrogen atmosphere and a single heating scan at 10°C/min was used for this purpose. PLA melting temperatures and associated enthalpy of fusion (Tm and ΔHm) were obtained and the PLA crystallinity index (Xc-PLA) was assessed according to Equation 4. It should be noted that PLA crystallinities were normalized to the amount of PLA in PLA/PA blends

$$X_{c-PLA} = \frac{\Delta H_{m-PLA} - \Delta H_{cc-PLA}}{\Delta H_m^0} \times 100 \quad (4)$$

with X_c is the degree of crystallinity, ΔH_{m-PLA} the melting enthalpy of PLA, ΔH_{cc-PLA} the cold crystallization enthalpy of PLA during heating, and ΔH_m^0 the melting enthalpy of fusion for 100% crystalline PLA (93 J/g) (Jia et al., 2017).

Extraction/Separation Experiments by Centrifugation

The PLA matrix and the PA12 dispersed phase of PLA/PA12/PLA-g-MA blends were selectively extracted/separated by PLA dissolution followed by centrifugation in centrifugal rotary machine (Hettich D7200, Germany). Predetermined weights (~1 g) of extruded pellets of PLA/PA12 blends were dissolved in dichloromethane (1 mL)

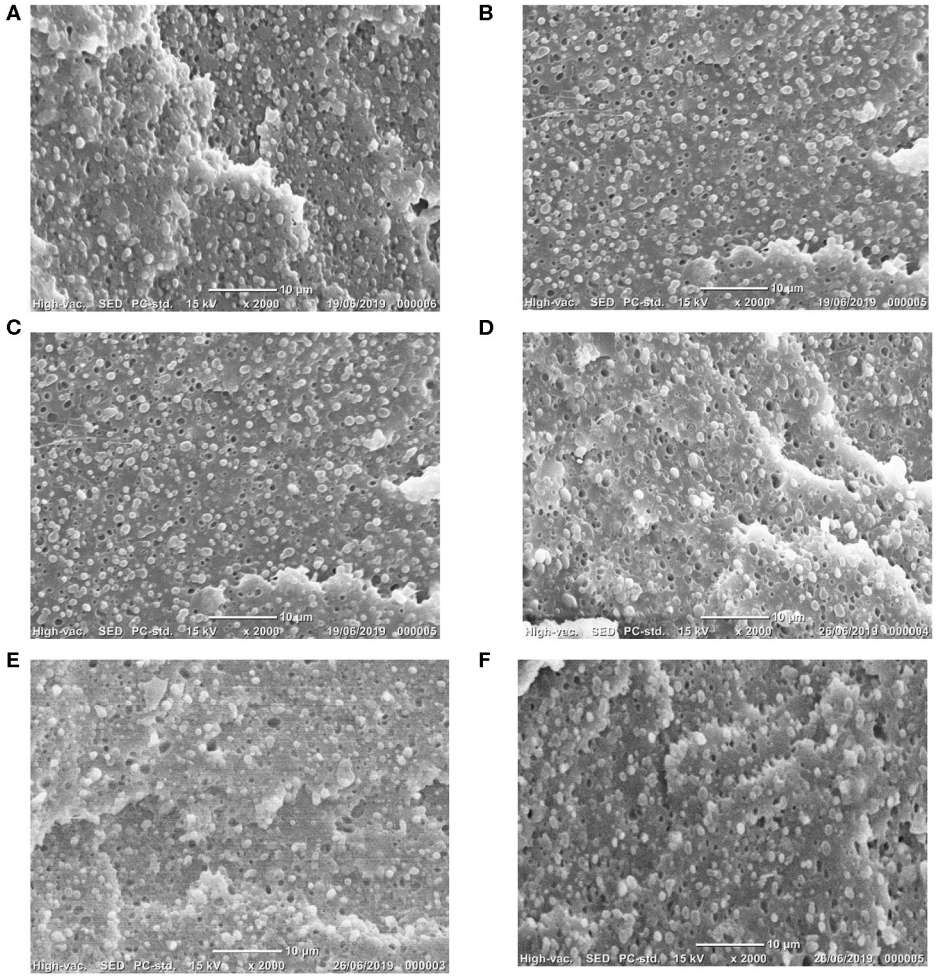

FIGURE 6 | Cross-sectional SEM analysis of injection-molded PLA/PA12/PLA-g-MA blends **(A)** 70/30/0, **(B)** 69/30/1, **(C)** 68/30/2, **(D)** 67/30/3, **(E)** 66/30/4, and **(F)** 65/30/5.

and acetone (9 mL). The solution was then submitted to centrifugation. Centrifugation time was set 1 h at a rotation speed of 4,000 rpm. After every centrifugation cycle, the dissolved phase was carefully transferred in a beaker and a fresh solvent system (dichloromethane/acetone 1:9) was added to the centrifugation tube containing the insoluble PA12 fraction. The dissolution–centrifugation was repeated 5–6 times. The PLA solution and settled PA12 particle were dried for 48 h prior to further characterizations.

Fourier Transform Infrared Studies

The chemical structure of the neat PLA, PA12, and extracted PA12 phase was evaluated by Fourier transform infrared (FTIR) spectroscopy (Nicolet 380 FTIR, ThermoScientific, France). The analysis was carried out on the extracted PA12 phase in reflection mode. The absorption spectra were logged utlising a microscope in reflection or transmission mode. The range of spectra employed is 4,000–800 cm^{-1} by the resolution of 16 cm^{-1} and utilizing 62 scans.

RESULTS AND DISCUSSIONS

Mechanical Properties

The major emphasis of this study was to investigate the effect of compatibilizer on engineering properties such as mechanical and the same under dynamic load. The blends were processed by injection molding and subjected to tensile testing; the related stress-strain curves are plotted in **Figure 1**. The values of stress at yield, elongation at break, and Young's modulus evaluated by tensile tests are tabulated in **Table 1**. The poor ductility of PLA (3.4%) drastically improved by the addition of 30 wt.% PA12 (153%), indicating good compatibility as confirmed in our previous studies (Raj et al., 2019). PLA-g-MA was incorporated in the blends to observe the potential evolution of compatibility and its effect on mechanical properties.

There was a significant improvement in the ductility with the addition of PLA-g-MA as a compatibilizer in PLA/PA12 blends as can be seen in **Figure 1**. Even at low concentrations of PLA-g-MA (1 wt.%), the improvement in ductility (≈291%)

TABLE 3 | Number-average and volume-average PA12 droplet diameters (D_n and D_v), PA droplet size polydispersity (I_p) with standard deviation in brackets of PLA/PA12/PLA-g-MA blends.

Blend	D_n (μm)	D_v (μm)	I_p
70/30/0	1.1 (0.09)	1.3 (0.09)	1.2
69/30/1	0.94 (0.07)	1.06 (0.04)	1.1
68/30/2	0.83 (0.04)	0.9 (0.03)	1.1
67/30/3	0.9 (0.05)	1 (0.03)	1.1
66/30/4	0.9 (0.03)	1.02 (0.04)	1.1
65/30/5	0.96 (0.06)	1.04 (0.09)	1.1

is noteworthy. Hence, it could be said that very little amount of PLA-g-MA is adequate to further improve the compatibility, leading to higher ductility.

However, with further increase in content of PLA-g-MA, a minor decrease in the ductility is observed, the lowest ductility obtained for 5 wt.% of PLA-g-MA (260%). The decrease in ductility is linear with PLA-g-MA content, and it should be noted that the decrease in ductility is not drastic, suggesting that even at higher concentrations there is no interfacial debonding leading to poor ductility.

The values of Young's modulus and stress at yield are in the range of 2.0–2.1 GPa and 54–55 MPa, respectively for all the compositions. These values are intermediate of PLA (2.9 GPa, 67 MPa) and PA12 (1.4 GPa, 39.5 MPa) in accordance with previous studies of PLA and PA (Stoclet et al., 2011; Nuzzo et al., 2014; Rashmi et al., 2015).

The evolution of ductility with varying content of PLA-g-MA in PLA/PA12 blends is plotted in **Figure 2**. The content of PLA-g-MA required to improve the ductility remarkably (291%) is as low as 1 wt.%, and a further increase in the content does not have an incremental effect on ductility.

The impact strength of the injection molded blend samples was evaluated. The Charpy un-notched impact strength of the PLA/PA12/PLA-g-MA blends are tabulated in **Table 1**. The variation of impact strength with different concentrations of PLA-g-MA is plotted in **Figure 3** for a clear depiction of the influence of compatibilizer on PLA/PA blends. The toughening effect of PA12 can be clearly seen in the PLA/PA12 (70/30, 28.3 kJ/m^2) blends without compatibilizer. It is noteworthy to observe that with the incorporation of PLA-g-MA there is further increase in impact strength, suggesting the positive effect of compatibility in blends. The maximum impact strength (45 kJ/m^2) achieved was for the blends containing 2 wt.% of PLA-g-MA. Further addition of PLA-g-MA in blends showed a slight linear decrease in impact strength and the least value (32.1 kJ/m^2) being for 5 wt.% of PLA-g-MA. Ductility and toughness are considered important properties for durable applications. The addition of compatibilizer (PLA-g-MA) in PLA/PA12 blends has a positive effect on ductility and toughness. Hence, it can be said that these blends could be suitable for high value applications with high ductility requirements.

The SEM images of the blends with various amounts of compatibilizer could give us a better understanding of the improvement in properties. The morphologies of compressed and injection molded samples of blends and their correlation with mechanical properties are discussed in the following section.

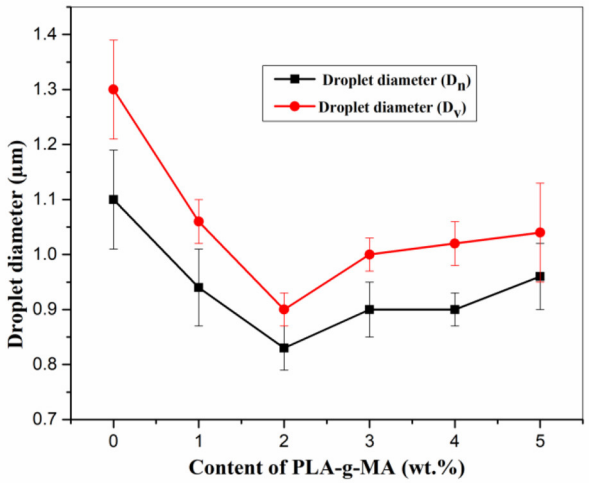

FIGURE 7 | Droplet diameter of PLA/PA12 blends with varying concentration of PLA-g-MA.

Morphology

PLA/PA12/PLA-g-MA blend samples were compressed and cryogenically fractured; the SEM images of the same are represented in **Figure 4**. The continuous phase is represented by PLA, and PA12 droplets are dispersed in the PLA matrix (**Figure 4**). The blends displayed good dispersion and the dispersion seems to improve with the addition of PLA-g-MA. The D_n, D_v, and I_p are tabulated in **Table 2**, where it can be observed that the polydispersity index remains constant (≈1.2) for all compositions.

The domain size of PA12 decreased with the addition of PLA-g-MA (≈1 μm) until 2 wt.%; further addition increased the droplet size of PA12. The droplet size of PA12 in blends with the highest concentration of PLA-g-MA (5 wt.%) is ≈1.5 μm, and it could be said that the blends reached saturation at 2 wt.% of PLA-g-Ma as further increase in the content results in the bigger droplet size of dispersed phase (PA12) (**Figure 5**). The reduction in the droplet size could be related to compatibilization effect of PLA-g-MA on PLA/PA12 blends at the interface, resulting in decrease of coalescence of droplets. However, the interfacial adhesion is strong between the blend components and remains unaltered with the increase in concentration of PLA-g-MA, suggesting no interfacial debonding occurs even at higher concentrations of PLA-g-MA.

Morphology of Injection Molded Samples-Correlation With Mechanical Properties

Morphology of injection-molded samples was observed to get an in-depth knowledge of the effect of compatibilizer on the

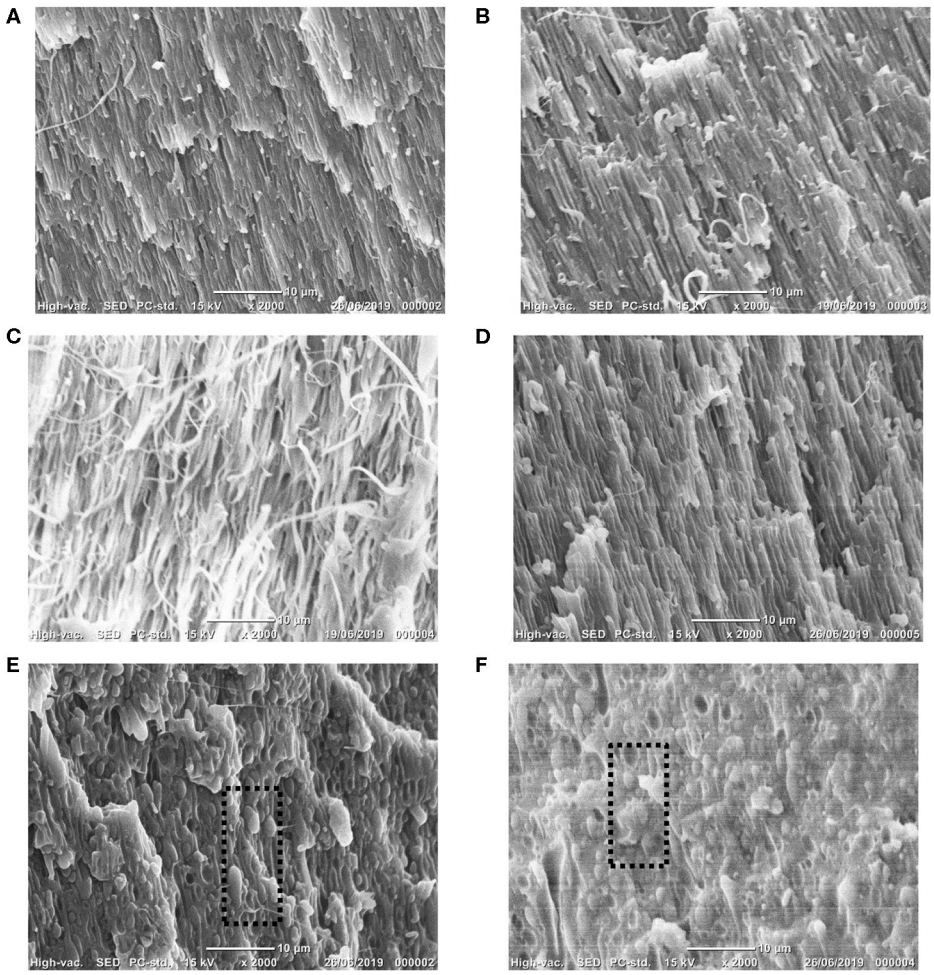

FIGURE 8 | Transversal section SEM analysis of injection-molded PLA/PA12/PLA-g-MA blends **(A)** 70/30/0, **(B)** 69/30/1, **(C)** 68/30/2, **(D)** 67/30/3, **(E)** 66/30/4, and **(F)** 65/30/5.

mechanical properties of the blends. The SEM images of the transversal and cross-sectional part of the injection-molded samples are depicted in **Figures 6**, **8**. The blends display a fine dispersion of PA12 droplets in PLA matrix. D_n, D_v, and I_p of the PLA/PA12/PLA-g-MA blends are tabulated in **Table 3**. The droplet diameter of PA12 ranges from micronic to submicronic with lowest being for 2 wt.% of PLA-g-MA (0.8 μm), and the polydispersity index is ≈1.1 for all the blend compositions.

The evolution of droplet diameter as a function of PLA-g-MA content has been plotted in **Figure 7**. It can be clearly seen that the droplet diameter decreases linearly up to 2 wt.% and an increment in the droplet size was noticed with a further increase in PLA-g-MA concentration. The lower droplet diameters, better interfacial adhesion, and stronger interface between the blend components of injection molded samples (**Figure 6**) when compared to compression molded samples (**Figure 4**) could be the reason for higher ductility in blends (Stoclet et al., 2011; Walha et al., 2016; Raj et al., 2019). It is interesting to observe that for injection molded samples, the droplet size of 5 wt.% PLA-g-MA (0.96 μm) is lower than PLA/PA12 (70/30) (1.1 μm); this fine dispersion of PA12 droplets even at higher concentration of PLA-g-MA could be the reason for the ductility behavior of the blends at 5 wt.% of PLA-g-MA (260%). The fibrillation of PA12 can be observed in the **Figures 8A–D**.

At higher concentrations of PLA-g-MA the fibrillation of PA12 appears to be hindered as can be observed in the highlighted area in **Figures 8E,F**. This could be due to higher concentration of compatibilizer at the interface limiting the formation of elongated PA12 in the injection molded samples (Mantia et al., 2017; Kuzmanović et al., 2018). This behavior of hindered elongation of PA12 could be related to the slightly lower ductility and impact strength values (260%, 32 kJ/m^2) obtained for the blends containing a higher concentration of PLA-g-MA (5 wt.%). To further study the interactions between the compatibilizers and the polymers, FTIR was performed.

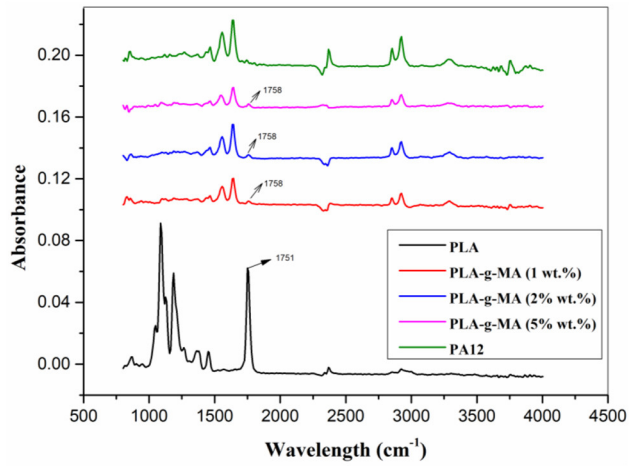

FIGURE 9 | FTIR studies of PLA/PA12 blends with varying content of compatibilizers.

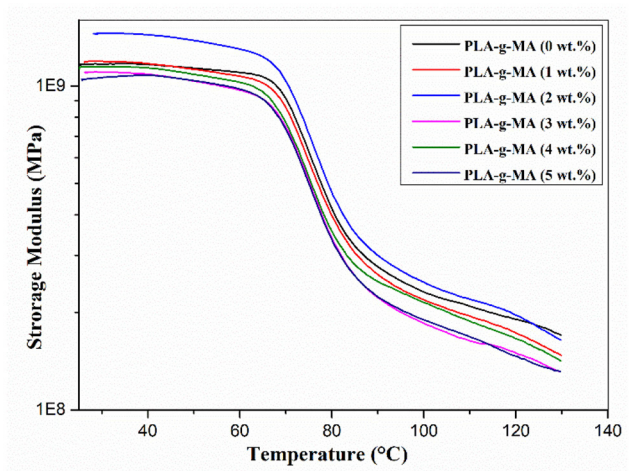

FIGURE 10 | Storage modulus as a function of the temperature of PLA/PA12 blends with varying content of PLA-g-MA(wt.%).

FTIR Studies

FTIR was performed to study the possible grafting or copolymer formation between PLA and PA due to the presence of compatibilizer. FTIR was done on the extracted PA12 phase from centrifugation. The relative absorptions at 3,286 and 1,751 cm^{-1} correspond to characteristic stretching vibration absorptions of NH amide groups and C=O ester groups of PA12 and PLA, respectively, (**Figure 9**) (Feng and Ye, 2010; Ogunniran et al., 2012). The existence of the absorption peak corresponding to the carbonyl group of PLA in the extracted phase of PA12 could be considered as evidence to grafting/copolymer formation in low amounts.

Additionally, the absorption peak of the carbonyl group appears to have shifted from 1,751 to 1,758 cm^{-1} for the blend (**Figure 9**), suggesting hydrogen bonding interaction between the molecules of PLA and PA12 resulting from the grafting/copolymer formation of PLA and PA12 (Feng and Ye, 2010). Overall the enhancement of mechanical properties could be due to the combined effects of grafting, PA12 droplet size, and PA12 fibrillation. However, PA12 fibrillation and PA12 droplet size could be a predominant factor for the improvement in ductility and toughness. The amount of PLA grafting could represent a key parameter to control in order to avoid losing PA12 fibrillated structures.

TABLE 4 | Thermal properties of PLA/PA12 blends with varying content of PLA-g-MA.

PLA/PA12/ PLA-g-MA compositions	T_{400Mpa} HDT_A (°C)	T_{250Mpa} HDT_B (°C)	Melting point (°C)		T_g (°C)
			(PLA)	(PA12)	
100/0/0	78 (0.5)	84 (1)	168.0	-	61.0
70/30/0	81 (2.5)	95 (3.7)	169.4	177.8	64.7
69/30/1	80 (0.5)	92 (0.0)	168.6	176.7	64.7
68/30/2	84 (1)	99 (0.5)	168.3	176.4	64.2
67/30/3	80.5 (1)	86 (1)	168.1	176.4	64.2
66/30/4	81 (1.5)	89 (1.5)	169.3	176.7	64.2
65/30/5	79 (1)	86 (0.8)	169.8	177.2	64.0

(Thermo)mechanical Properties

Thermomechanical properties including thermal resistance or heat deflection temperature (HDT) are prominent for high value applications. Thermomechanical properties were evaluated using DMA to obtain the evolution of the storage modulus/loss factor with temperature.

The HDT ($T_{400MPa-HDTa}$ and $T_{250MPa-HDTb}$) were subsequently extracted from storage modulus with a specific experimental procedure previously reported (Raj et al., 2019). The HDT of PLA/PA12 blends under load was evaluated by dynamic mechanical analysis. The influence of varying concentrations of compatibilizer on the HDT of blends was investigated through these tests. The variation of storage modulus with temperature has been plotted in **Figure 10**. It is important to note that the blends were annealed at 110°C to eliminate the cold crystallization of PLA. The storage modulus (E′) gradually decreases with temperature with a classical drop for temperatures higher than 70°C associated with the glass transition/α-relaxation of PLA (**Figure 10**). The α-relaxation temperature of PLA/PA12(70/30) blends is noticed close to 70°C. Higher storage modulus is observed for 2 wt.% of PLA-g-MA blends in comparison with the other compositions. This behavior is still indeterminate but an additional PLA crystallization at PLA/PA12 interface could induce a significant increase in PLA crystallinity (Zhang and Thomas, 2011; Srithep et al., 2013; Raj et al., 2019). The impact of the concentration of compatibilizer on storage modulus is not significant in the glassy state. However, in rubbery state ($T > 70–80$°C), a prominent influence of 2 wt.% of PLA-g-MA is observed. The other concentrations did not show this synergism.

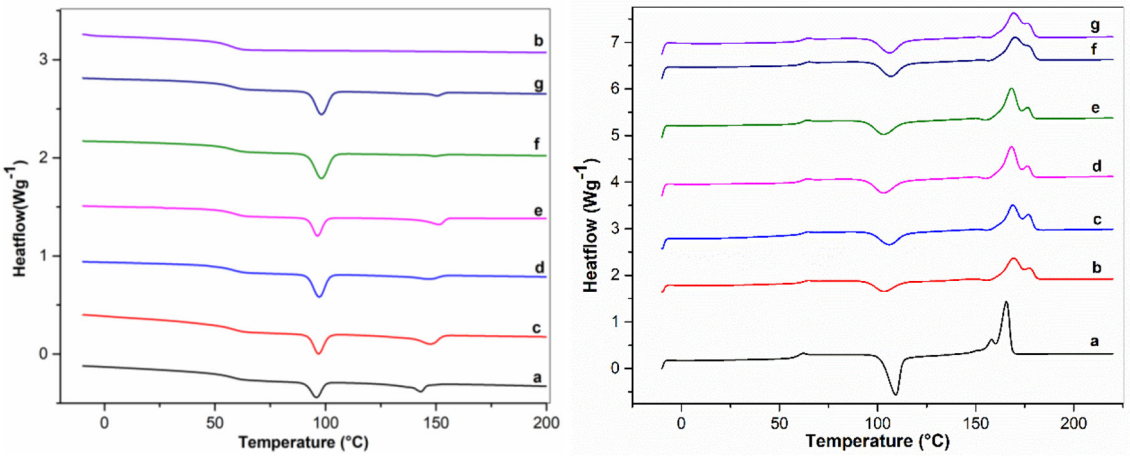

FIGURE 11 | DSC cooling (left) and heating (right) thermogram of PLA/PA12 blends with PLA-g-MA.

Such thermomechanical modifications in the glassy/rubbery state can be correlated with HDT/thermal resistance improvements. Heat deflection temperature ($T_{400MPa-HDTa}$ and $T_{250MPa-HDTb}$) of blends were subsequently evaluated from DMA graphs and tabulated in **Table 4**. PLA/PA12/PLA-g-MA blends exhibited similar HDT values as uncompatibilized blends with an exception of PLA-g-MA 2wt.%. Significant improvement of HDT was observed for 2wt.% of PLA-g-MA (84°C-$T_{400MPa-HDTA}$ and 99°C-$T_{250MPa-HDTB}$). The HDT values do not display similar trends that were observed in mechanical properties. However, above 2 wt.% of PLA-g-MA, decrease in HDT values was observed with the least being for 5 wt.% (79°C-$T_{400MPa-HDTA}$, 86°C-$T_{250MPa-HDTB}$).

In conclusion, the addition of compatibilizer to the PLA/PA12 blends is beneficial to improve thermal resistance with a considerable increase in the thermal resistance for 2 wt.% of PLA-g-MA. Similar to tensile and impact properties, the optimum content of PLA-g-MA to enhance thermal resistance of PLA/PA12 blends is found to be at 2 wt.%.

Differential scanning calorimetry was performed on PLA/PA12 blends to investigate several thermal properties such as glass transition temperature, melting temperature, and cold crystallization behavior. The T_g of all the blends is around 64°C, which is an intermediate value between PLA and PA12. This is a typical additive rule behavior and it could be said that the compatibilizer does not affect T_g of the blend. It can be observed in heating thermograms (**Figure 11**) that the melting point of the blends with compatibilizer is slightly lower than that of uncompatibilized blends, the reaction of anhydride group of PLA-g-MA and amino group PA12 could be the reason, thereby suggesting a formation of copolymer at the interface. This copolymer could be a hindrance to the motion of segments causing difficulty in polymer chain arrangement (Wang et al., 2010). However, there is a minor increase in the melting point at 4 and 5 wt.% of PLA-g-MA. The cooling thermograms of the blends show a typical droplet and bulk crystallization behavior of PLA/PA blends (Stoclet et al., 2011; Rashmi et al., 2015; Raj et al., 2019). The temperature at which droplet crystallization occurs remains almost unaltered (97°C) for uncompatibilized and compatibilized blends. However, the bulk crystallization behavior shows an effect of compatibilizer (PLA-g-MA), with an increase in temperature of bulk crystallization as the content of PLA-g-MA increases. This might be due to larger droplets or the copolymer at interface delaying the bulk crystallization of the blends.

CONCLUSIONS

The major emphasis of this study is to examine the compatibilization effects of PLA-g-MA on PLA/PA12(70/30) blends in a twin-screw extruder. Various concentrations of PLA-g-MA were incorporated in the blends to assess the optimum content of compatibilizer required to achieve properties. The positive effect of PLA-g-MA is evident in morphology, mechanical properties, and thermal resistance. Concerning the mechanical properties, remarkable improvement in ductility was observed in the blends with varying content of PLA-g-MA. The impact properties of the compatibilized blends showed similar trends, and the toughening behavior of PA12 is observed. Based on this study the content of PLA-g-MA required to improve the mechanical properties (ductility and impact strength) is 1–2 wt.%. Morphology of the compression molded blend samples with different concentrations of PLA-g-MA revealed fine dispersion of PA12 in the PLA matrix with a strong interface and good interfacial adhesion. To get a better in-depth understanding of the improvement in mechanical properties, the morphology of injection molded specimens was examined. The cross-sectional SEM images revealed finer dispersion, stronger interface, and better interfacial adhesion when compared to compression molded samples. This could be the reason for the improvement in ductility and toughness of the blends.

Transversal sections of injection molded samples were also examined to assess the relation between fibrillation of PA12 and mechanical properties of the blends; the fibrillation of PA12 is evident in the SEM images. However, for higher content of PLA-g-MA hindrance in the fibrillation might be due to the higher concentration of PLA-g-MA at the interface, impeding the elongation of PA12. FTIR studies were also done to study the probable grafting and its correlation with mechanical properties. The absorption peak corresponding to carbonyl group of PLA in the extracted phase of PA12 could be considered an indication of grafting/copolymer formation. This could be considered as a contributing factor for the improvement in ductility. The influence of compatibilizer on PLA/PA12 blends on the thermal resistance of the blends (HDT) was not as significant as mechanical properties. In conclusion, PLA-g-MA is a suitable compatibilizer for PLA/PA12 blends. Remarkable improvement in ductility was observed and considerable improvement in toughness and heat resistance was attained. These blends could be well suited for durable applications which require high ductility and toughness. Further studies related to particular applications are required to discover the apt application for these blends.

DATA AVAILABILITY STATEMENT

All datasets generated for this study are included in the article/supplementary material.

AUTHOR CONTRIBUTIONS

AR, CS, and KP planned the conceptualization and design of the study. AR carried out the experiments and characterizations of the materials and wrote the first draft of the manuscript. All authors contributed to manuscript revision and read and approved the submitted version.

ACKNOWLEDGMENTS

We are gratefully acknowledge the International Campus on Safety and Intermodality in Transportation (CISIT, France), the European Community (FEDER funds), as well as the Hauts-de-France Region (France) for their contributions to funding extrusion equipment and characterization tools (dynamic rheometers, microscopes, goniometers, calorimeters, and tensile benches).

REFERENCES

Ahmed, J., and Varshney, S. K. (2011). Polylactides—chemistry, properties and green packaging technology: a review. *Int. J. Food Prop.* 14, 37–58. doi: 10.1080/10942910903125284

Anderson, K. S., Schreck, K. M., Hillmyer, M. A., and Schreck, K. M. (2018). Toughening polylactide. *Polym. Rev.* 48, 85–108. doi: 10.1080/15583720701834216

Auras, R., Harte, B., and Selke, S. (2004). An overview of polylactides as packaging materials. *Macromol. Biosci.* 4, 835–864. doi: 10.1002/mabi.200400043

Battegazzore, D., Salvetti, O., Frache, A., Peduto, N., De Sio, A., and Marino, F. (2016). Thermo-mechanical properties enhancement of bio-polyamides (PA10.10 and PA6.10) by using rice husk ash and nanoclay. *Compos. A Appl. Sci. Manuf.* 81, 193–201. doi: 10.1016/j.compositesa.2015.11.022

Bouzouita, A., Samuel, C., Notta-Cuvier, D., Odent, J., Lauro, F., Dubois, P., et al. (2016). Design of highly tough poly (l -lactide)-based ternary blends for automotive applications. *J. Appl. Polym. Sci.* 133:n/a–n/a. doi: 10.1002/app.43402

Cailloux, J., Abt, T., Santana, O., and Carrasco, F. (2018). Effect of the viscosity ratio on the PLA / PA10. *10* bioblends morphology and mechanical properties. *exPRESS Polym. Lett.* 12, 569–582. doi: 10.3144/expresspolymlett.2018.47

Dong, W., Cao, X., and Li, Y. (2014). High-performance biosourced poly(lactic acid)/polyamide 11 blends with controlled salami structure. *Polym. Int.* 63, 1094–1100. doi: 10.1002/pi.4618

Drumright, R. E., Gruber, P. R., and Henton, D. E. (2000). Polylactic acid technology. *Adv. Mater.* 12, 1841–1846. doi: 10.1002/1521-4095(200012)12:23<1841::AID-ADMA1841>3.0.CO;2-E

Farah, S., and Anderson, D. G. (2016). Physical and mechanical properties of PLA, and their functions in widespread applications — a comprehensive review. *Adv. Drug Deliv. Rev.* 107, 367–392. doi: 10.1016/j.addr.2016.06.012

Feng, F., and Ye, L. (2010). Structure and property of polylactide/polyamide blends. *J. Macromol. Sci. B* 49, 1117–1127. doi: 10.1080/00222341003609179

Gandini, A., Rodríguez, H., Rahman, M., Rogers, R. D., Labidi, J., Hedenqvist, M. S., et al. (2011). The irruption of polymers from renewable resources on the scene of macromolecular science and technology. *Green Chem.* 13, 1061–1083. doi: 10.1039/c0gc00789g

Gug, J., and Sobkowicz, M. J. (2016). Improvement of the mechanical behavior of bioplastic poly(lactic acid)/polyamide blends by reactive compatibilization. *J. Appl. Polym. Sci.* 133:n/a–n/a. doi: 10.1002/app.43350

Gupta, B., Revagade, N., and Hilborn, J. (2007). Poly(lactic acid) fiber: an overview. *Prog. Polym. Sci.* 32, 455–482. doi: 10.1016/j.progpolymsci.2007.01.005

Hamad, K., Kaseem, M., Ayyoob, M., Joo, J., and Deri, F. (2018). Polylactic acid blends: the future of green, light and tough. *Prog. Polym. Sci.* 85, 83–127. doi: 10.1016/j.progpolymsci.2018.07.001

Harmsen, P. F. H., Hackmann, M. M., and Bos, H. L. (2014). Green building blocks for bio-based plastics. *Biofuel. Bioprod Bior.* 8, 306–324. doi: 10.1002/bbb.1468

Huneault, M. A., and Li, H. (2007). Morphology and properties of compatibilized polylactide/thermoplastic starch blends. *Polymer (Guildf).* 48, 270–280. doi: 10.1016/j.polymer.2006.11.023

Jia, S., Yu, D., Zhu, Y., Wang, Z., Chen, L., Fu, L., et al. (2017). Morphology, crystallization and thermal behaviors of PLA-based composites: wonderful effects of hybrid GO/PEG via dynamic impregnating. *Polymers (Basel).* 9:528. doi: 10.3390/polym9100528

Jiang, W.-R., Bao, R.-Y., Yang, W., Liu, Z.-Y., Xie, B.-H., and Yang, M.-B. (2014). Morphology, interfacial and mechanical properties of polylactide/poly(ethylene terephthalate glycol) blends compatibilized by polylactide-g-maleic anhydride. *Mater. Des.* 59, 524–531. doi: 10.1016/j.matdes.2014.03.016

Krishnan, S., Pandey, P., Mohanty, S., and Nayak, S. K. (2016). Toughening of polylactic acid: an overview of research progress. *Polym. Plast. Technol. Eng.* 55, 1623–1652. doi: 10.1080/03602559.2015.1098698

Kucharczyk, P., Sedlarik, V., Miskolczi, N., Szakacs, H., and Kitano, T. (2012). Properties enhancement of partially biodegradable polyamide/polylactide blends through compatibilization with novel polyalkenyl-poly-maleic-anhydride-amide/imide-based additives. *J. Reinf. Plast. Compos.* 31, 189–202. doi: 10.1177/0731684411434150

Kuzmanović, M., Delva, L., Mi, D., Martins, C., Cardon, L., and Ragaert, K. (2018). Development of crystalline morphology and its relationship with mechanical properties of PP/PET microfibrillar composites containing POE and POE-g-MA. *Polymers (Basel).* 10:291. doi: 10.3390/polym10030291

Lasprilla, A. J. R., Martinez, G. A. R., Lunelli, B. H., Jardini, A. L., and Filho, R. M. (2012). Poly-lactic acid synthesis for application in biomedical devices — a review. *Biotechnol. Adv.* 30, 321–8. doi: 10.1016/j.biotechadv.2011.06.019

Li, Z., Tan, B. H., Lin, T., and He, C. (2016). Recent advances in stereocomplexation of enantiomeric PLA-based copolymers and applications. *Prog. Polym. Sci.* 62, 22–72. doi: 10.1016/j.progpolymsci.2016.05.003

Liu, H., and Zhang, J. (2011). Research progress in toughening modification of poly(lactic acid). *J. Polym. Sci. B Polym. Phys.* 49, 1051–1083. doi: 10.1002/polb.22283

Lopes, M. S., Jardini, A. L., and Filho, R. M. (2012). Poly (lactic acid) production for tissue engineering applications. *Procedia Eng.* 42, 1402–1413. doi: 10.1016/j.proeng.2012.07.534

Madhavan Nampoothiri, K., Nair, N. R., and John, R. P. (2010). An overview of the recent developments in polylactide (PLA) research. *Bioresour. Technol.* 101, 8493–8501. doi: 10.1016/j.biortech.2010.05.092

Mantia, F., Ceraulo, M., Giacchi, G., Mistretta, M., and Botta, L. (2017). Effect of a compatibilizer on the morphology and properties of polypropylene/polyethylentherephthalate spun fibers. *Polymers (Basel).* 9:47. doi: 10.3390/polym9020047

Mecking, S. (2004). Nature or petrochemistry?—biologically degradable materials. *Angew. Chemie Int. Ed.* 43, 1078–1085. doi: 10.1002/anie.200301655

Mishra, J., Tiwari, S. K., Abolhasani, M. M., Azimi, S., and Nayak, G. C. (2017). "Fundamental of polymer blends and its thermodynamics," in *Micro and Nano Fibrillar Composites (MFCs and NFCs) From Polymer Blends*, eds S. Thomas, R. Mishra, and N. Kalarikkal (Dhanbad: Elsevier), 27–55. doi: 10.1016/B978-0-08-101991-7.00002-9

Mülhaupt, R. (2013). Green polymer chemistry and bio-based plastics: dreams and reality. *Macromol. Chem. Phys.* 214, 159–174. doi: 10.1002/macp.201200439

Nagarajan, V., Mohanty, A. K., and Misra, M. (2016). Perspective on polylactic acid (PLA) based sustainable materials for durable applications: focus on toughness and heat resistance. *ACS Sustain. Chem. Eng.* 4, 2899–2916. doi: 10.1021/acssuschemeng.6b00321

Nofar, M., Sacligil, D., Carreau, P. J., Kamal, M. R., and Heuzey, M.-C. (2019). Poly (lactic acid) blends: processing, properties and applications. *Int. J. Biol. Macromol.* 125, 307–360. doi: 10.1016/j.ijbiomac.2018.12.002

Nuzzo, A., Coiai, S., Carroccio, S. C., Dintcheva, N. T., Gambarotti, C., and Filippone, G. (2014). Heat-resistant fully bio-based nanocomposite blends based on poly(lactic acid). *Macromol. Mater. Eng.* 299, 31–40. doi: 10.1002/mame.201300051

Ogunniran, E. S., Sadiku, R., Sinha Ray, S., and Luruli, N. (2012). Morphology and thermal properties of compatibilized PA12/PP blends with boehmite alumina nanofiller inclusions. *Macromol. Mater. Eng.* 297, 627–638. doi: 10.1002/mame.201100254

Pai, F.-C., Chu, H.-H., and Lai, S.-M. (2019). Preparation and properties of thermally conductive PLA/PA 610 biomass composites. *J. Elastomers Plast.* 52:0095244318825286. doi: 10.1177/0095244318825286

Pai, F.-C., Lai, S.-M., and Chu, H.-H. (2013). Characterization and properties of reactive poly(lactic acid)/polyamide 610 biomass blends. *J. Appl. Polym. Sci.* 130, 2563–2571. doi: 10.1002/app.39473

Pang, X., Zhuang, X., Tang, Z., and Chen, X. (2010). Polylactic acid (PLA): research, development and industrialization. *Biotechnol. J.* 5, 1125–1136. doi: 10.1002/biot.201000135

Patel, R., Ruehle, D. A., Dorgan, J. R., Halley, P., and Martin, D. (2014). Biorenewable blends of polyamide-11 and polylactide. *Polym. Eng. Sci.* 54, 1523–1532. doi: 10.1002/pen.23692

Pawar, R. P., Tekale, S. U., Shisodia, S. U., Totre, J. T., and Domb, A. J. (2014). Biomedical applications of poly(lactic acid). *Recent Pat. Regen. Med.* 4, 40–51. doi: 10.2174/22102965046661404022350 24

Quintana, R., Persenaire, O., Lemmouchi, Y., Bonnaud, L., and Dubois, P. (2016). Compatibilization of co-plasticized cellulose acetate/water soluble polymers blends by reactive extrusion. *Polym. Degrad. Stab.* 126, 31–38. doi: 10.1016/j.polymdegradstab.2015.12.023

Raj, A., Prashantha, K., and Samuel, C. (2019). Compatibility in biobased poly(L-lactide)/polyamide binary blends: from melt-state interfacial tensions to (thermo)mechanical properties. *J. Appl. Polym. Sci.* 137:48440. doi: 10.1002/app.48440

Rashmi, B. J., Prashantha, K., Lacrampe, M.-F., and Krawczak, P. (2015). Toughening of poly(lactic acid) without sacrificing stiffness and strength by melt-blending with polyamide 11 and selective localization of halloysite nanotubes. *Express Polym. Lett.* 9, 721–735. doi: 10.3144/expresspolymlett.2015.67

Rasselet, D., Caro-Bretelle, A.-S., Taguet, A., and Lopez-Cuesta, J.-M. (2019). Reactive compatibilization of PLA/PA11 blends and their application in additive manufacturing. *Materials (Basel).* 12:485. doi: 10.3390/ma12030485

Saeidlou, S., Huneault, M. A., Li, H., and Park, C. B. (2012). Poly(lactic acid) crystallization. *Prog. Polym. Sci.* 37, 1657–1677. doi: 10.1016/j.progpolymsci.2012.07.005

Samuel, C., Jean-Marie Raquez, P. D. (2013). PLLA/PMMA blends: a shear-induced miscibility with tunable morphologies and properties? *Polymer (Guildf).* 54, 3931–3939. doi: 10.1016/j.polymer.2013.05.021

Shi, X., Zhang, G., Phuong, T., and Lazzeri, A. (2015). Synergistic effects of nucleating agents and plasticizers on the crystallization behavior of poly(lactic acid). *Molecules* 20, 1579–1593. doi: 10.3390/molecules 20011579

Spinella, S., Samuel, C., Raquez, J.-M., McCallum, S. A., Gross, R., and Dubois, P. (2016). Green and efficient synthesis of dispersible cellulose nanocrystals in biobased polyesters for engineering applications. *ACS Sustain. Chem. Eng.* 4, 2517–2527. doi: 10.1021/acssuschemeng.5b01611

Srithep, Y., Nealey, P., and Turng, L.-S. (2013). Effects of annealing time and temperature on the crystallinity and heat resistance behavior of injection-molded poly(lactic acid). *Polym. Eng. Sci.* 53, 580–588. doi: 10.1002/pen.23304

Stoclet, G., Seguela, R., and Lefebvre, J.-M. (2011). Morphology, thermal behavior and mechanical properties of binary blends of compatible biosourced polymers: polylactide/polyamide11. *Polymer (Guildf).* 52, 1417–1425. doi: 10.1016/j.polymer.2011.02.002

Takemori, M. T. (1979). Towards an understanding of the heat distortion temperature of thermoplastics. *Polym. Eng. Sci.* 19, 1104–1109. doi: 10.1002/pen.760191507

Tan, B. H., Muiruri, J. K., Li, Z., and He, C. (2016). Recent progress in using stereocomplexation for enhancement of thermal and mechanical property of polylactide. *ACS Sustain. Chem. Eng.* 4, 5370–5391. doi: 10.1021/acssuschemeng.6b01713

Utracki, L. A., and Wilkie, C. A. (2014). *Polymer Blends Handbook*. Dordrecht: Springer. doi: 10.1007/978-94-007-6064-6

Walha, F., Lamnawar, K., Maazouz, A., Jaziri, M., Walha, F., Lamnawar, K., et al. (2016). Rheological, morphological and mechanical studies of sustainably sourced polymer blends based on poly(lactic acid) and polyamide 11. *Polymers (Basel).* 8:61. doi: 10.3390/polym8030061

Wang, N., Yu, J., and Ma, X. (2007). Preparation and characterization of thermoplastic starch/PLA blends by one-step reactive extrusion. *Polym. Int.* 56, 1440–1447. doi: 10.1002/pi.2302

Wang, Y.-L., Hu, X., Li, H., Ji, X., and Li, Z.-M. (2010). Polyamide-6/poly(lactic acid) blends compatibilized by the maleic anhydride grafted polyethylene-octene elastomer. *Polym. Plast. Technol. Eng.* 49, 1241–1246. doi: 10.1080/03602559.2010.496418

Zeng, J.-B., Li, K.-A., and Du, A.-K. (2015). Compatibilization strategies in poly(lactic acid)-based blends. *RSC Adv.* 5, 32546–32565. doi: 10.1039/C5RA01655J

Zhang, M., and Thomas, N. L. (2011). Blending polylactic acid with polyhydroxybutyrate: the effect on thermal, mechanical, and biodegradation properties. *Adv. Polym. Technol.* 30, 67–79. doi: 10.1002/adv.20235

Conflict of Interest: The authors declare that the research was conducted in the absence of any commercial or financial relationships that could be construed as a potential conflict of interest.

frontiers in Materials

ORIGINAL RESEARCH
published: 25 June 2020
doi: 10.3389/fmats.2020.00195

In-situ Monitoring of the Out-Of-Autoclave Consolidation of Carbon/Poly-Ether-Ketone-Ketone Prepreg Laminate

Florence Saffar[1,2,3]*, *Camille Sonnenfeld*[1], *Pierre Beauchêne*[1] and *Chung Hae Park*[2,3]

[1] DMAS, ONERA, Université Paris Saclay, Châtillon, France, [2] Technology of Polymers and Composites & Mechanical Engineering Department, IMT Lille Douai, Institut Mines-Télécom, Douai, France, [3] Université de Lille, Lille, France

The main objectives of this article were to examine the feasibility of high quality laminate (carbon PEKK—Poly-Ether-Ketone-Ketone) manufacturing under low pressure and to analyze the principal phenomena governing the consolidation quality. The quality of laminate was evaluated in terms of the interlaminar shear strength measured by short-beam shear test and the residual voids observed by micrographic images. This work underlined the possibility to obtain a good interlaminar consolidation quality, i.e., interlaminar shear strength of 100 MPa under a low pressure of 7.0×10^4 Pa even for prepregs which were not designed for out-of-autoclave processes. To better understand the interlaminar consolidation phenomena, we developed an experimental set-up for the *in-situ* monitoring of the laminate consolidation to measure the change of laminate thickness and the temperature gradient in the thickness direction during the manufacturing process. In particular, we identified two major phenomena, the establishment of intimate contact between the adjacent layers at the glass transition temperature and the molten matrix flow at the melting temperature. The assumption on the intimate contact establishment at the glass transition temperature was confirmed by the heat transfer simulation considering the change of thermal contact resistance at the interlaminar interface.

Keywords: polymer-matrix-composites (PMCs), interfacial strength, thermal properties, out-of-autoclave (OOA) consolidation, *in-situ* monitoring

OPEN ACCESS

Edited by:
Maria Chiara Bignozzi, University of Bologna, Italy

Reviewed by:
Liqing Wei, United States Forest Service (USDA), United States
Veronique Michaud, École Polytechnique Fédérale de Lausanne, Switzerland

***Correspondence:**
Florence Saffar
florence.saffar@onera.fr

Specialty section:
This article was submitted to Polymeric and Composite Materials, a section of the journal Frontiers in Materials

Received: *29 March 2020*
Accepted: *25 May 2020*
Published: *25 June 2020*

Citation:
Saffar F, Sonnenfeld C, Beauchêne P and Park CH (2020) In-situ Monitoring of the Out-Of-Autoclave Consolidation of Carbon/Poly-Ether-Ketone-Ketone Prepreg Laminate. Front. Mater. 7:195. doi: 10.3389/fmats.2020.00195

INTRODUCTION

In the aircraft design and manufacturing, thermoplastic composites have many technical advantages over carbon/epoxy composites, such as high impact resistance, a short process cycle time, favorable storage conditions, and ease of patch repair. Among a wide spectrum of thermoplastic matrices for high performance composites are Poly-Aryl-Ether-Ketone (PAEK) matrices which have attracted great attention owing to high environmental resistance at elevated temperature. For example, unidirectional carbon fiber reinforced Poly-Ether-Ether-Ketone (PEEK) prepreg is a representative thermoplastic composite material used in the aircraft design (Bishop, 1985; Carlile et al., 1989; Denault and Dumouchel, 1998; El Kadi and Denault, 2001). Recently, more attention is being paid to Poly-Ether-Ketone-Ketone (PEKK) as a promising matrix material for

carbon fiber reinforced composites (Chang, 1988). PEKK has a higher glass transition temperature (155°C) than PEEK (145°C) and offers a better high temperature resistance, whereas it has a similar melting temperature (335–340°C) which leads to almost the same manufacturing condition as PEEK. In spite of its advantages, the data on the carbon/PEKK consolidation is seldom found in the literature, however, whereas the characterization of carbon/PEEK prepreg systems has been extensively reported (Blundell et al., 1989; Yang and Colton, 1995; Phillips et al., 1997; Ageorges et al., 1998; Gao and Kim, 2000, 2001; Wang et al., 2001; Stokes-Griffin and Compston, 2016a; Talbott et al., 2016). Only a small number of articles about the degradation and isothermal crystallization of PEKK have been published by Choupin et al. and other authors (Hsiao et al., 1991; Krishnaswamy and Kalika, 1996; Choupin, 2017; Tadini et al., 2017; Choupin et al., 2018; Li and Strachan, 2019).

Moreover, a critical drawback in the use of such materials is the high manufacturing cost. In general, the price of those materials is very high. To reduce the labor cost due to the manual lay-up, automated tape placement (ATP) is widely considered (Khan et al., 2010; Comer et al., 2015; Stokes-Griffin and Compston, 2016a,b). Nevertheless, the high consolidation quality cannot be achieved only by ATP and a post-consolidation process is required. For this post-consolidation step, an expensive manufacturing equipment such as autoclave is generally used because high temperature and pressure are needed to consolidate laminates. Indeed, all the commercial grades of carbon/PEKK prepreg available in the current market are designed for the autoclave manufacturing.

Nowadays, there is a growing interest in out-of-autoclave consolidation processes where low compaction pressure is employed to reduce the manufacturing cost (Witik et al., 2012; Centea et al., 2015). For example, laminates can be consolidated under vacuum condition in a heated oven.

About the high pressure consolidation of thermoplastic composites, different phenomena have already been identified such as intimate contact, autohesion, and crystallization.

The phenomenon of intimate contact has been described by different models. In the literature, the principal mechanism of the intimate contact establishment has been assumed to be the flattening of surface roughness which has been modeled by the squeeze flow of the material under compaction pressure (Lee and Springer, 1987; Loos and Dara, 1987; Mantell and Springer, 1992; Butler et al., 1998; Yang and Pitchumani, 2001). In the early work, the main focus was on the description of the geometric pattern on the rough surface of prepreg. For example, Dara and Loos proposed a model where the surface roughness of the prepreg was represented by a series of rectangles with different dimensions (Loos and Dara, 1987). Lee and Springer simplified this model by representing the prepreg surface roughness by a series of rectangles with the same dimensions (Lee and Springer, 1987). Nevertheless, the limits of this model have also been underlined. Butler et al., and Yang and Pitchumani explained that the identification of the geometric parameters in the models was very complex (Butler et al., 1998; Yang and Pitchumani, 2001). The results of profilometric and micrographic studies showed that the prepreg surface roughness could not necessarily be described by rectangles. Butler et al. highlighted that according to the geometric parameters, the time for the intimate contact establishment could vary between 1 and 10^5 s (Butler et al., 1998). Hence, Yang and Pitchumani introduced Cantor fractals to represent the surface roughness of prepreg ply (Yang and Pitchumani, 2001). By this method, the estimation of intimate contact establishment time could be close to a real value. Yet, the complexity to determine the geometric parameters still remains as a critical issue to address in this approach.

In another approach, the evolution of the intimate contact during the consolidation was assessed by the change of the thermal contact resistance between the adjacent plies of a laminate. To monitor the evolution of this thermal contact resistance, Schaefer et al. installed thermocouples between the adjacent layers in the middle of composite laminate (Schaefer et al., 2016, 2017). With the temperature values measured by the thermocouples, the thermal diffusivities of initial prepreg and of final consolidated laminate were estimated. Subsequently, they determined the thermal contact resistance at the interface between the adjacent layers and found that it decreased during the consolidation process. The relation between the thermal contact resistance and the intimate contact has also been studied by Levy et al. (2014) and Cassidy and Monaghan (1994). It should be noted that in all the aforementioned works, the composite material was considered to be viscous fluid and the intimate contact was assumed to take place at high temperature (i.e., around the melting point of the matrix) and under high compaction pressure (i.e., over 3.0×10^5 Pa). Moreover, all the works have focused on the PEEK, Polyimide, and PIXA-M matrix composites, whereas PEKK matrix composites have not been investigated (Lee and Springer, 1987; Butler et al., 1998; Yang and Pitchumani, 2001). Finally, the intimate contact phenomenon of carbon fibers/PEKK laminates began to be investigated in a recent work by Çelik et al. (2020). This last study focuses on the intimate contact phenomenon during laser assisted automated fiber placement manufacturing, and so under high pressure conditions.

Therefore, the main subject of this paper is the low pressure consolidation of carbon fibers/PEKK laminates. In particular, the influence of pressure level on the consolidation is experimentally investigated. Moreover, an *in-situ* monitoring set-up to study the consolidation phenomena in terms of the temperature differential in the thickness direction and the change of the total thickness of laminates is presented. Finally, thermal modeling of the intimate contact phenomenon under low pressure is proposed.

EXPERIMENTAL METHODS AND NUMERICAL SIMULATION

Material

We used unidirectional carbon fiber reinforced PEKK prepreg. The weight fraction of fibers was 66 %, the areal weight was 145 g/m^2 and the thickness of a single ply before the consolidation was 0.15 mm. A microscopic image of the prepreg ply is presented in **Figure 1**. The prepreg was placed in an oven

at 120°C for 80 min before the consolidation process to dry the samples.

Thermal Expansion Characterization

The thermal expansion of the prepreg in the thickness direction was evaluated by dilatometer (TGA-TDA Setsys Evolution 16/18). The chosen temperature cycle was a 5 K/min heating rate from 40 to 300°C and an inert gas (argon) was used in order to obtain the conditions close to the vacuum manufacturing conditions. Tested samples were laminates with a thickness of 4.3mm consolidated using a press. The prepregs were placed in an oven at 120°C for 80 min before the measurement of thermal expansion coefficient.

Two Set-Ups for Out-Of-Autoclave Manufacturing

Two different heating methods were employed for out-of-autoclave consolidation, namely, oven and heating plate.

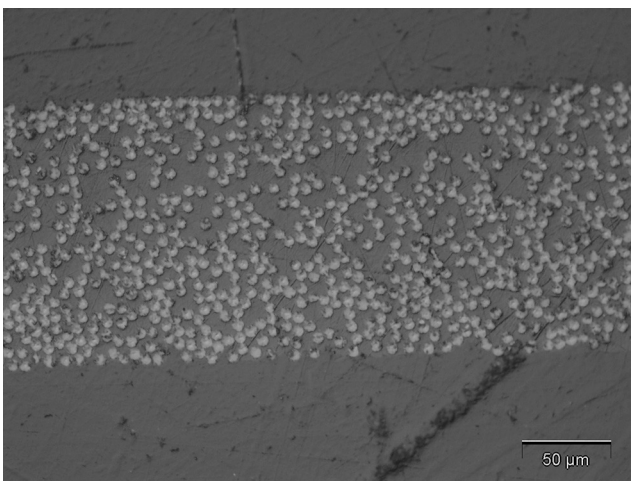

FIGURE 1 | Microscopic image of the prepreg ply.

Oven Heating

In order to study the feasibility of out-of-autoclave manufacturing, laminate consolidation in a heated oven was used. Using this experimental set-up, only the temperature was measured whereas the thickness of laminate was not monitored. A laminate lay-up of 16 UD plies was chosen. The planar dimensions of the laminates were 115 × 115 mm^2. Three thermocouples of K type were installed on the planar surfaces of laminate to monitor the temperature evolution as shown in **Figure 2A**. Because the laminate stack was heated in an oven, relatively uniform heating of laminates could be obtained. The temperature cycle of the oven was controlled by Eurotherm system. The vacuum pressure applied to the laminate stack was controlled and recorded by a pressure gauge (Pfeiffer APR250).

One-Side Heating Plate

The second method which has been developed is a heating plate set-up in order to monitor both the temperature difference and the laminate thickness change. A stack of 16 UD prepreg plies with planar dimensions of 60 × 60 mm^2 was placed on a stainless steel plate which was heated. The prepreg stack was subsequently covered by a speckled vacuum bag as shown in **Figure 2B**. Two thermocouples of K type with a diameter of 0.25 mm were installed beneath and on the laminate. It should be noted that the laminate was heated only from the bottom side which induced a non-uniform temperature distribution through the thickness direction. As previously done for the oven heating method, the temperature cycle of the stainless steel plate was controlled by Eurotherm system and the vacuum pressure was controlled and recorded by a pressure gauge.

To monitor the change of the laminate thickness during the consolidation, speckles were applied on the upper face of the vacuum bag and two optical cameras (AVT Pike-421, 4/80 lens and 41 mm extension ring) were placed 1,000 mm above the laminate stack. The angle between the two cameras was around 33° to measure the change of the out-of-plane displacement. The data acquisition interval was 30 s. Vis-Snap 8 was used as a data acquisition system and the data processing was performed by Vic-3D. For each time step, the mean value of laminate thickness

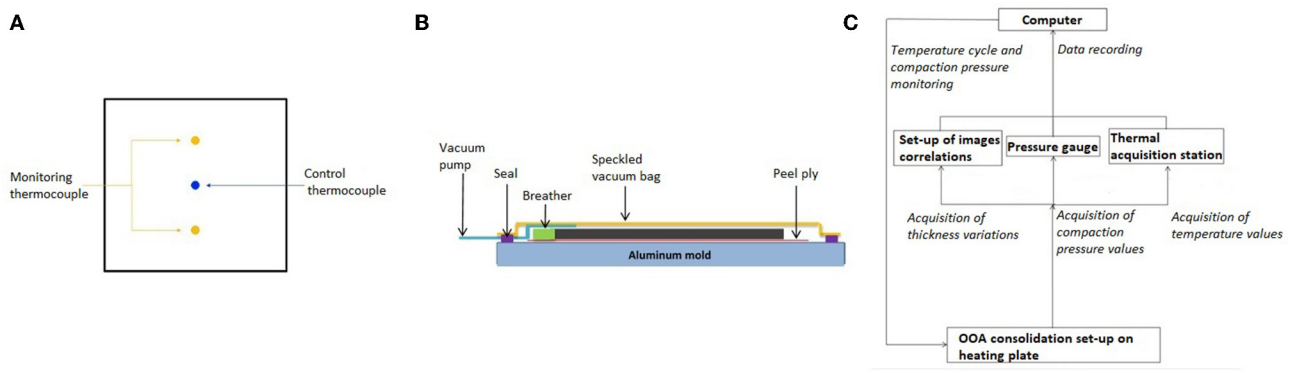

FIGURE 2 | *In-situ* monitoring system for out-of-autoclave consolidation of thermoplastic composites. **(A)** Scheme of thermocouples monitoring for oven manufacturing. **(B)** Schematic of prepreg lay-up. **(C)** Schematic diagram of *in-situ* monitoring system.

was calculated from around 35 data on the sampling surface of 5 × 5 cm^2 which was located in the center of the laminate surface of 6 × 6 cm^2 in order to avoid the edges effects. During the consolidation, the pressure, the temperatures at the top and at the bottom of the laminate and the laminate thickness were recorded. The whole *in-situ* monitoring system is represented by a schematic drawing in **Figure 2C**.

Manufacturing Conditions

Temperature Cycle

Two different temperature cycles were applied in the heating plate method, to investigate the influence of temperature on the interlaminar consolidation.

In the first case, a classic temperature cycle was used for manufacturing with the heating plate. A prepreg stack was heated from room temperature at a heating rate of 5 K/min. Once the temperature reached 360°C (=Melting temperature of PEKK + 25°C), this temperature was maintained for 15 min. Then, the prepreg stack was cooled down at a free cooling rate (see **Figure 3A**).

To better understand the consolidation phenomena, another identical successive consolidation cycle was applied again on the laminate which had already been consolidated.

In the second case, a stack of prepreg which had not been consolidated was submitted to the peak temperature of 230°C which was maintained for 15 min, while employing the same heating and cooling rates (see **Figure 3B**), to observe the interlaminar microstructure of laminate consolidated at the intermediate temperature (i.e., 230°C) between the glass transition temperature (T_g) and the melting temperature (T_m).

Finally, for the manufacturing in an oven, the same temperature cycle as shown in **Figure 3A** was applied, while employing a different cooling rate of 5 K/min.

Vacuum Pressure

The compaction pressure applied on the prepreg stack was determined by the difference between the atmospheric pressure and the vacuum pressure. During the manufacturing cycles, a steady vacuum pressure was applied. The used reference value was −995 × 10^2 Pa. In order to determine the minimum compaction pressure to obtain a good consolidation quality, different compaction pressure values (i.e., −995 × 10^2, −973 × 10^2, −915 × 10^2, −825 × 10^2,−740 × 10^2, −511 × 10^2, −253 × 10^2,−209 × 10^2, −185 × 10^2, −93 × 10^2, −24 × 10^2) were tested in the oven manufacturing method. Moreover, two different vacuum pressures (−995 × 10^2 Pa, −325 × 10^2 Pa) were used for heating plate method to better understand the influence of vacuum pressure on interlaminar consolidation phenomena.

Assessment of Consolidation Quality: Interlaminar Shear Strength and Void Content

Despite the drawbacks of interlaminar shear strength (ILSS) test related to the multiple failure modes which can occur for thermoplastic composites (Kadlec et al., 2014), ILSS test is widely accepted because the interlaminar shear strength of laminate is a representative parameter which is sensitive to interlaminar properties in shear, and in addition it is easy and fast to perform. Furthermore, their results are reproducible from a test to another and enough discriminating. Three rectangular specimens were cut from each laminate according to the same orientation in the laminate to conduct short-beam shear three-point bending. The dimensions of the specimens were 25 × 12 × 2.35 mm^3. For the three-point short-beam shear test, the radius of the loading pin was 5 mm and the radius of the two supporting pins was 2 mm. The distance between the two supporting pins was 12 mm and the displacement speed of the loading pin was 0.5 mm/min. The tests were performed on Zwick/Roell Z010 with a load cell of 10 kN.

Reference laminate samples were fabricated by the compression molding with a high compaction pressure (i.e., 10 × 10^5 Pa), while applying the same temperature cycle as shown in **Figure 3A**. The corresponding ILSS value was regarded as the reference ILSS of the present prepreg samples.

The void content was evaluated by image analysis. The transverse cross-section of laminates was observed using an optical microscope and the void content was determined by thresholding method on (Image J software, 2020). The observations were made at the zone around the interlaminar interfaces and the observation window size was 1,740 × 60 μm^2.

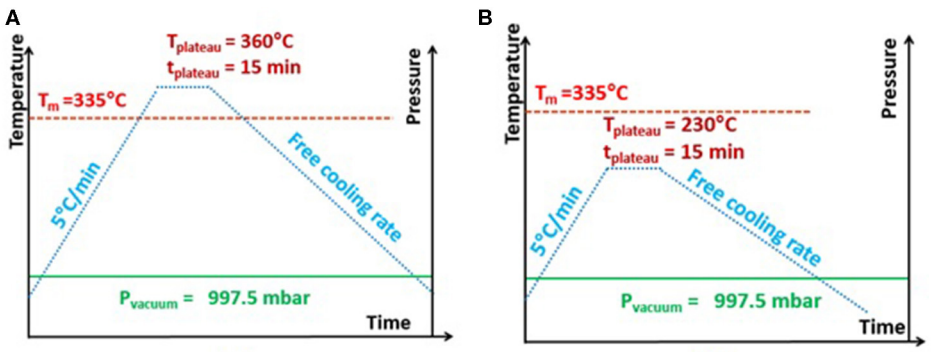

FIGURE 3 | Manufacturing cycles. **(A)** First cycle. **(B)** Third cycle.

TABLE 1 | Thermal properties of the prepreg.

	T = 50°C	T = 100°C	T = 150°C	T = 200°C	T = 250°C	T = 300°C
Cp (J/g.°C)	0.6681	0.8481	1.025	1.269	1.454	1.639
δ (m^2/s)	4.28×10^{-7}	3.99×10^{-7}	3.71×10^{-7}	3.24×10^{-7}	3.06×10^{-7}	2.80×10^{-7}

Characterization of the Thermal Properties and Numerical Simulation of Heat Transfer

One dimensional finite element model was used for the numerical simulation of heat transfer during the heating plate manufacturing method. The computational domain for heat conduction was composed of 16 layers of composite prepreg with a thickness of 0.15 mm and 15 interlaminar interface layers with a thickness of 8 μm which corresponded to the mean height of the prepreg surface roughness. For the heat transfer simulation, the heat transfer module of COMSOL was used. As the boundary conditions, a convective heat transfer coefficient of 15 $W{\cdot}m^{-2}{\cdot}K^{-1}$ was applied on the top surface and a preassigned temperature profile was given at the bottom surface. The density of prepreg was 1,400 kg/m^3. The thermal diffusivity (δ) has been measured for temperatures between room temperature and 300°C at every 50°C by flash method on the consolidated laminate with a thickness of 2.3 mm. Finally, the specific heat capacity (Cp) of prepreg was evaluated by DSC tests. All the material properties which were used in this model are summarized in **Table 1**. For the interface layers, the thermal properties were assumed to change, as the intimate contact was established according to the increase of temperature. The thermal conductivity of the interface layers was represented by a sigmoid temperature dependent function. This function was defined by four parameters, viz. the initial conductivity (k_{init}), the final conductivity (k_{fin}), the inflection temperature (T_r), and the temperature range (dT) (see **Figure 4**). These four parameters were determined by an inverse identification using Levenberg-Marquardt method (Marquardt, 1963).

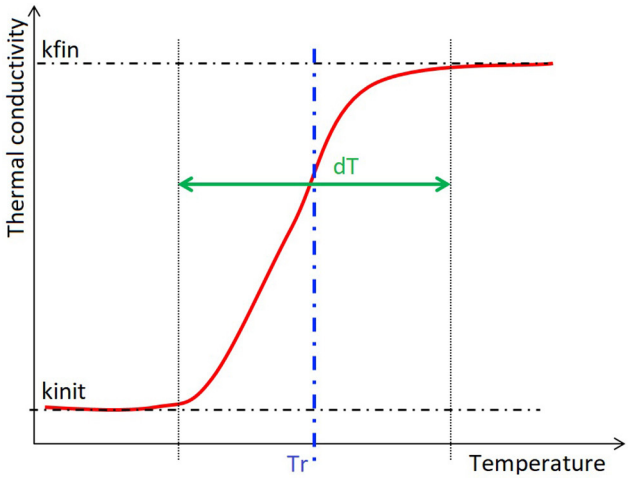

FIGURE 4 | Evolution of thermal conductivity of interlaminar interfaces with temperature.

RESULTS AND DISCUSSION

In-situ Monitoring Data: Temperature Difference and Laminate Thickness

From the *in-situ* monitoring of thermoplastic laminates manufacturing on the heating plate, the data for the thickness of the laminate and the average temperature gradient through the thickness during the whole consolidation cycle were obtained. **Figure 5** shows the time-dependent change of the laminate thickness obtained by the two optical cameras and the change of the average temperature gradient.

The temperature gradient was greatly increased from "$T_g - 30$°C" and reached its maximum value when the temperature of the bottom layer was T_g(see **Figure 5**). Afterwards, the temperature gradient dropped fast as the temperature increased further from T_g. At the same time, an increase of the laminate thickness was observed as the temperature increased above T_g. Both the laminate thickness and the temperature differential were decreased again around the melting temperature of the matrix, even if the temperature of the bottom layer continued to increase. We could verify the reproducibility of these observations from the repeated experiments under the same condition. This speculation can be verified by the successive consolidation experiment.

In **Figure 6**, the evolution of the temperature difference between top and bottom layers is shown during the two identical successive consolidation steps. We can see two sudden decreases of temperature difference at the glass transition temperature and the melting temperature, respectively, during the first consolidation. During the second consolidation of the same laminate, however, such sudden decrease of temperature is not observed at the glass transition temperature. Thus, we can assume that the intimate contact was totally established during the first consolidation and there was no more change of thermal contact resistance at the interlaminar interfaces during the second consolidation.

The change of the laminate thickness can be explained by the competition between the thermal expansion effect and the intimate contact establishment which tends to decrease the thickness due to the flattening of prepreg surface roughness. Until the melting temperature of the matrix, the increase of the laminate thickness according to the increase of temperature can be correlated with the coefficient of thermal expansion (CTE) in the thickness direction of laminate which had been experimentally measured (see **Figure 7**).

Conversely, it is assumed that the molten matrix flow at the interlaminar interfaces accounts for the decreases of the laminate

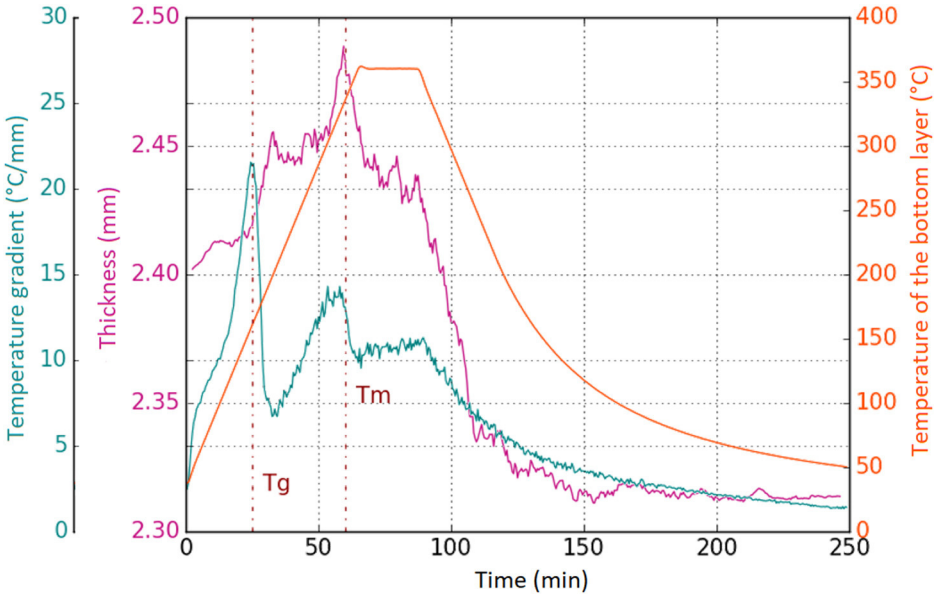

FIGURE 5 | Results of average temperature gradient and thickness against time.

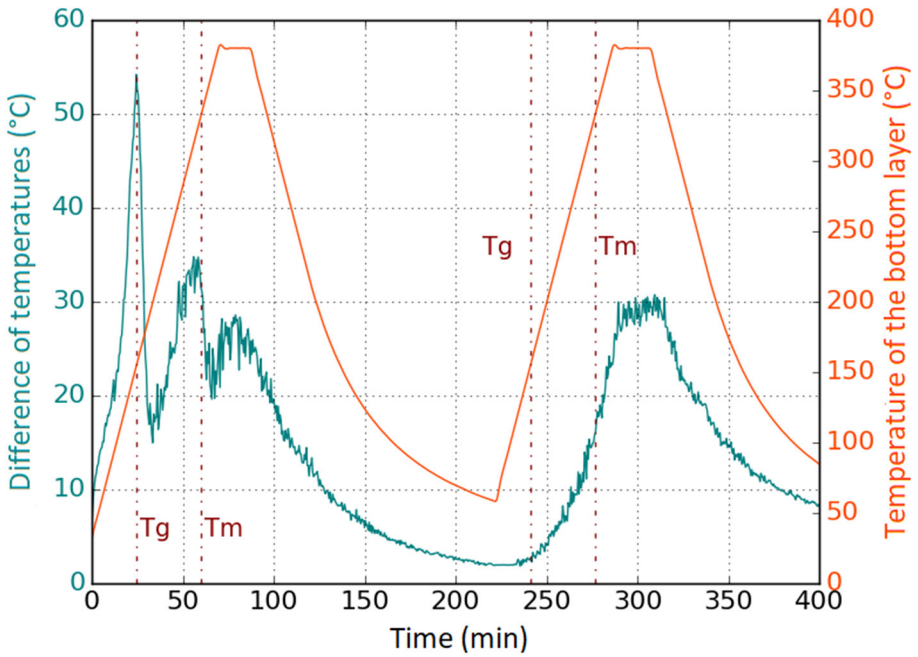

FIGURE 6 | Result of temperature difference for two successive consolidation cycles.

thickness at the melting temperature. Thus, it can be assumed that the intimate contact is not totally complete between the glass transition temperature and the melting temperature, however and there are still some voids at the interlaminar interfaces. The perfect contact between adjacent layers is only obtained around the melting temperature (see **Figure 8**). Microscopic observations of laminates highlight a relatively low void content which shows the establishment of intimate contact at the interlaminar interfaces (see **Figure 9**). The most of voids are concentrated at the three or four top interlaminar interfaces close to the vacuum bag and the approximate void content at these zones is 5%. At the other zones, it is not easy to identify the interfaces between two adjacent layers and the void content is lower than 2%. This difference between the upper

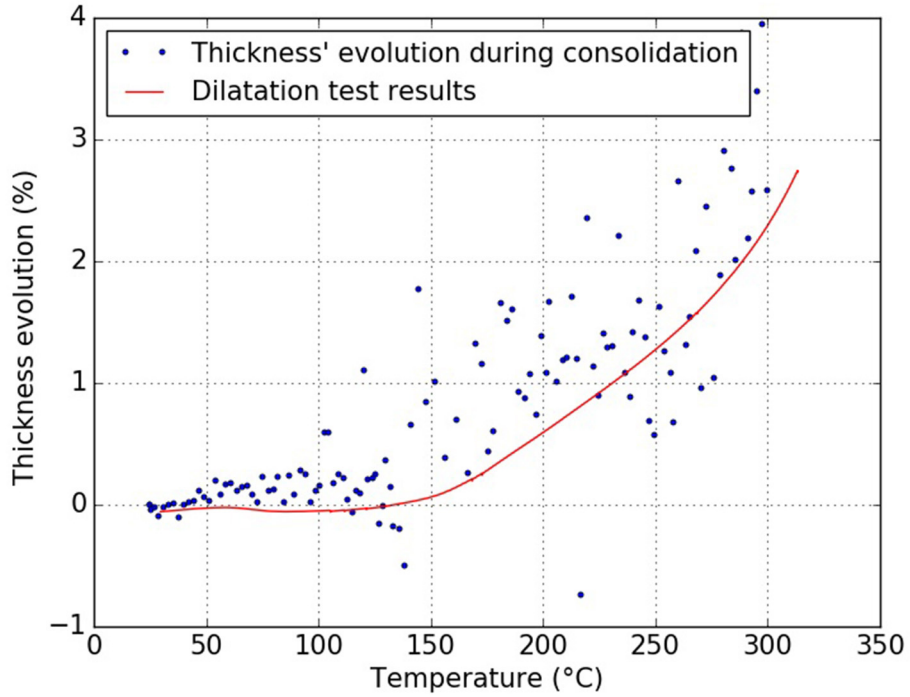

FIGURE 7 | Comparison between thermal expansion and laminate thickness results.

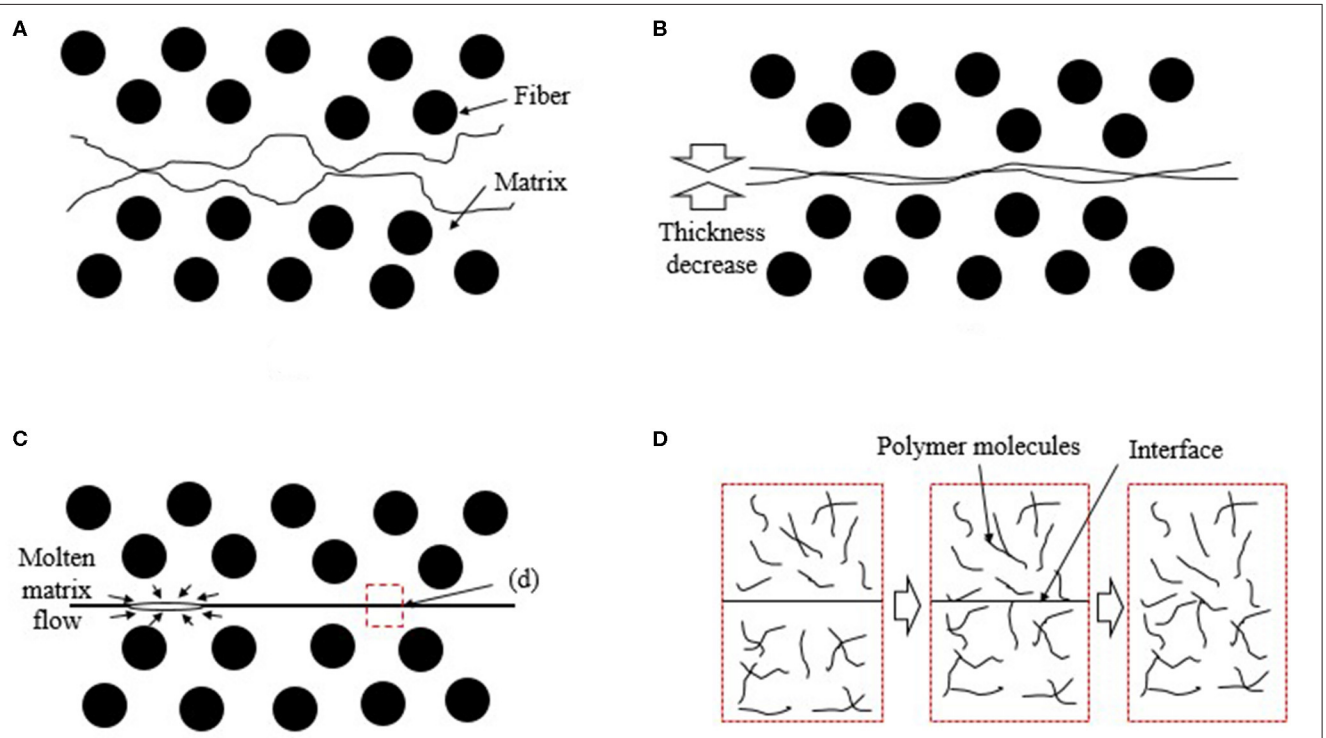

FIGURE 8 | Schematic of the interlaminar consolidation phenomena. **(A)** Below T_g. **(B)** At T_g (Establishment of intimate contact). **(C)** At T_m (Molten matrix flow). **(D)** Above T_m (Interdiffusion of polymer molecules).

and bottom zones in the laminate can be explained by the delay in the temperature rise due to one side heating from the bottom heating plate. The maximum temperature in the upper part near the vacuum bag just reached the melting temperature of the PEKK when that in the bottom part near the heating plate was sufficiently above the melting temperature. Thus, we can suppose that some portion of matrix in the upper layers was not sufficiently melted and therefore the matrix could not flow to fill the interlaminar gaps in these zones. Otherwise, voids could migrate from the bottom zone to the upper zone of the laminate because they might move along the negative temperature gradient according to the phenomenon described by Lu et al. (2004).

Laminate Consolidated at the Low Temperature

Figure 10 shows a micrographic image of the laminate obtained by low temperature consolidation (i.e., 230°C). Because the laminate was consolidated above the glass transition temperature, the intimate contact began to be established even if it was not totally complete. The surface roughness was reduced and the adjacent layers became in contact with each other. Nevertheless, there was still a high average content (e.g. ∼11%) of interlaminar voids. It was more difficult to assess the gradient of void content in the thickness direction in a partially consolidated laminate (consolidated at the low temperature, i.e., 230°C) than in a fully consolidated laminate (consolidate at the high temperature, i.e., 360°C). It could be noticed only that the void content at the interlaminar interfaces was higher at the outer layers (>10%) than at the middle layers (<6%) of the laminate.

The final laminate quality was also evaluated by ILSS tests. The interlaminar shear strength of the laminate consolidated at 230°C was around 1 MPa. We can conclude that the intimate contact establishment at the glass transition temperature is not enough to build the interlaminar bonding strength. Once the matrix temperature reaches at the melting temperature, the matrix is melted and flows to fill the small gaps between the adjacent layers (see **Figure 8C**). As the temperature rises further above the melting point, there is an interdiffusion of polymer molecules across the interlaminar interfaces to erase the interface between the adjacent layers which establishes the interlaminar bonding strength (see **Figure 8D**). Thus, the phenomena at the melting temperature, viz. molten matrix flow and molecule interdiffusion play the principal role in the laminate consolidation process.

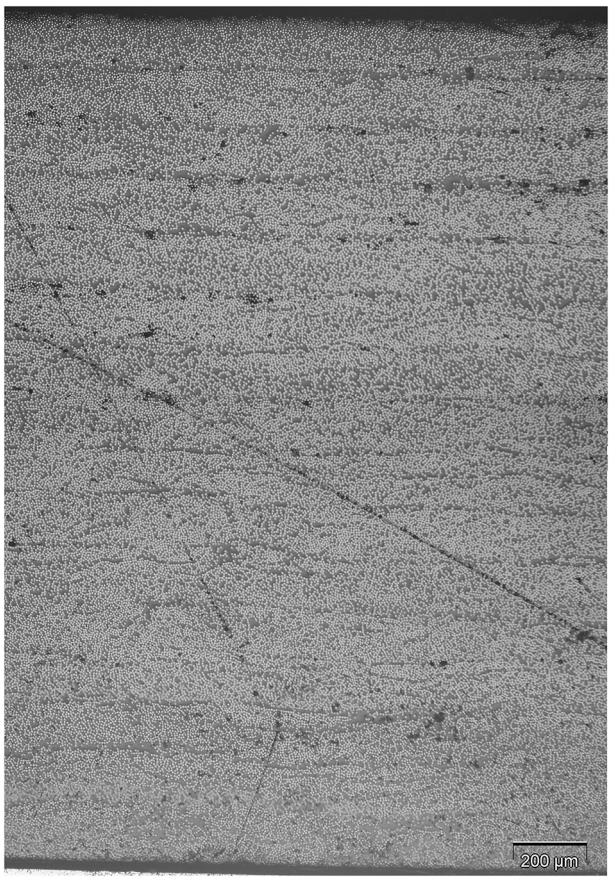

FIGURE 9 | Micrographic image of laminate consolidated by one side heating plate.

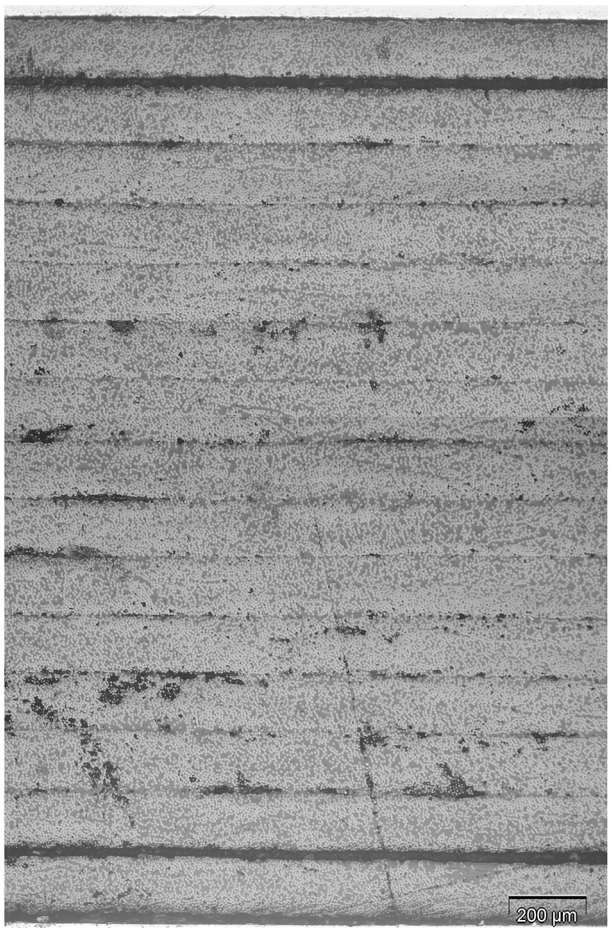

FIGURE 10 | Micrographic image of the laminate consolidated at 230°C.

It should be emphasized that the intimate contact begins to be established at a low temperature, viz. around the glass transition temperature, whereas in the literature it has been assumed to occur at a high temperature, i.e., around the melting temperature of the matrix. Hence, the initial surface roughness of prepreg ply is changed above the glass transition temperature, which improves the intimate contact between adjacent layers. This phenomenon can be correlated with the reduction of thermal contact resistance at the interlaminar interfaces. We can see in **Figure 5** that the decrease of the average temperature gradient took place around the glass transition temperature. As the intimate contact is established, the heat conduction path is enlarged and the thermal resistance is decreased at the interlaminar interfaces.

Influence of Compaction Pressure

The influence of the compaction pressure on the interlaminar consolidation of laminate was investigated for both heating methods, i.e., heating plate and oven.

For the heating plate method, two levels of compaction pressure were tested, viz. 995×10^2 Pa and 325×10^2 Pa. **Figure 11** presents the *in-situ* monitoring results of the evolution of the average temperature gradient, which is the temperature difference divided by the laminate thickness (**Figure 11A**) and the evolution of the laminate thickness (**Figure 11B**). It should be noticed that the laminate thickness was not uniform on the surface of the laminate. The final thickness of laminate was greater in the zones far from the pressure pump than near the pressure pump. This difference is assumed to be come from the non-uniform distribution of compaction pressure. Moreover, the standard deviation of the laminate thickness was increased with the decreasing of compaction pressure applied during the consolidation cycle. Thus, the maximum value for standard deviation was obtained for the compaction pressure of 325×10^2 Pa which is presented in **Figure 11C**.

The average temperature gradient and the laminate thickness were highly dependent on the compaction pressure. In the case of low compaction pressure (i.e., 325×10^2 Pa), there was no remarkable change of the average temperature gradient and the laminate thickness at the glass transition temperature. Moreover, it should be noted that the average temperature gradient at the plateau of peak temperature was the highest for the lowest value of compaction pressure (i.e., 325×10^2 Pa). This high average temperature gradient implies a weak interlaminar consolidation because of the too low compaction pressure.

In the same manner, the result of the laminate thickness evolution shows that the lowest compaction pressure led to a higher laminate thickness during the whole consolidation cycle. This implies the presence of air layers at the interlaminar interfaces which are likely to swell during the heating phase. Finally, the sudden change of the average temperature gradient at the glass transition temperature is also related with the change of the thermal conductivity of the air layers at the interlaminar interfaces, which can be correlated with the compaction pressure according to Equation 1 adopted by Wu et al. (Cassidy and Monaghan, 1994).

$$k_{air} = \frac{k_0}{1 + \frac{7.6.10^{-5} T}{PD}} \quad (1)$$

where k_{air} is the thermal conductivity of air, k_o is the thermal conductivity of air at the room temperature and pressure, T is the temperature (in K), P is the air pressure and D is the air gap height.

When the compaction pressure was important, the pressure in vacuum bag was below 5.0×10^2 Pa and the corresponding thermal conductivity of air was around 1 mW/(m·K). This low value increased the magnitude of the average temperature gradient. On the contrary, when the compaction pressure was around 325×10^2 Pa, the thermal conductivity of air in the vacuum bag and in the gaps at the interlaminar interfaces was around 25 mW/(m·K) at room temperature. The difference of the thermal conductivity between the prepreg plies and the interlaminar zones was not big enough to highlight the intimate contact phenomenon.

As a result, it has been found that thermoplastic laminates can be consolidated under low pressure ($< 1.0 \times 10^5$ Pa) and that under these conditions the *in-situ* monitoring is helpful to improve the understanding of the interlaminar consolidation.

In the oven heating method, the temperature distribution is more uniform than in the heating plate method. Hence, the

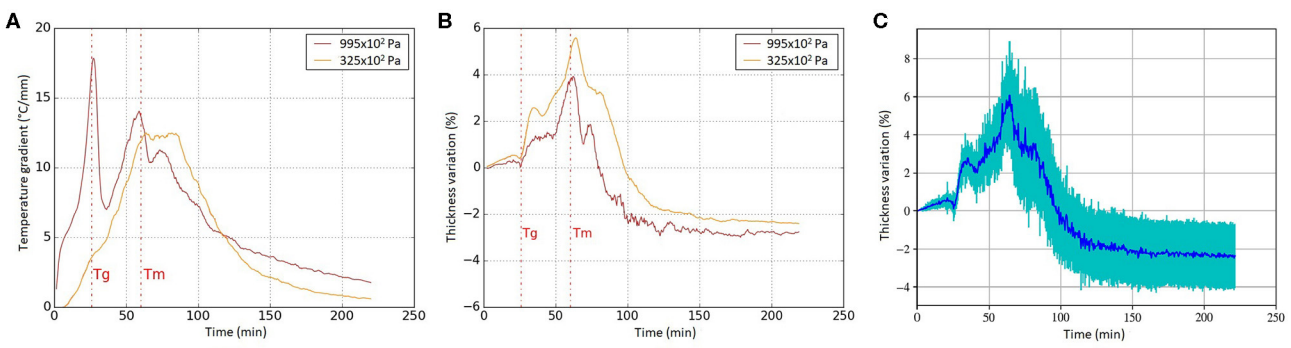

FIGURE 11 | Compaction pressure influence on the consolidation phenomena. **(A)** Temperature gradient evolution. **(B)** Thickness evolution. **(C)** Maximal standard deviation of laminate thickness variations for 3.25×10^4 Pa.

influence from the non-uniform heating on the interlaminar consolidation can be minimized and eventually ruled out. The interlaminar consolidation quality was assessed by ILSS tests. **Figure 12** shows the results of the interlaminar shear strength of the laminates against the compaction pressure which was applied during the consolidation. The compaction pressure has a huge influence on the final consolidation quality of the material. The ILSS changes from 21 MPa to 107 MPa when the compaction pressure increases from25 $\times$ 10^2 Pa to 980 $\times$ 10^2 Pa. Moreover, above 700 $\times$ 10^2 Pa the ILSS values are superior to 100 MPa which is so close to the reference value, viz. 110 MPa (from the compression molded samples). The failure modes of the laminates were more complex to identify. Indeed, the delamination mostly occurred at very low compaction pressure (-10 $\times$ 10^2 Pa) whereas it could also take place for the laminates consolidated at-825 $\times$ 10^2 Pa (see **Figure 13A**). However, this failure mode was relatively rarely observed. Most of samples showed large plastic deformation with or without a small drop of stress after the elastic region (see **Figure 13B**) which can reveal the presence of crack propagation (van Rijswijk et al., 2009; Vieille et al., 2011; See et al., 2015; Obande et al., 2019). According to these results the failure mode cannot be directly related with the pressure level of the consolidation.

These results highlight that high interlaminar consolidation quality can be achieved by Out-Of-Autoclave (OOA) or Vacuum-Bag-Only (VBO) manufacturing techniques.

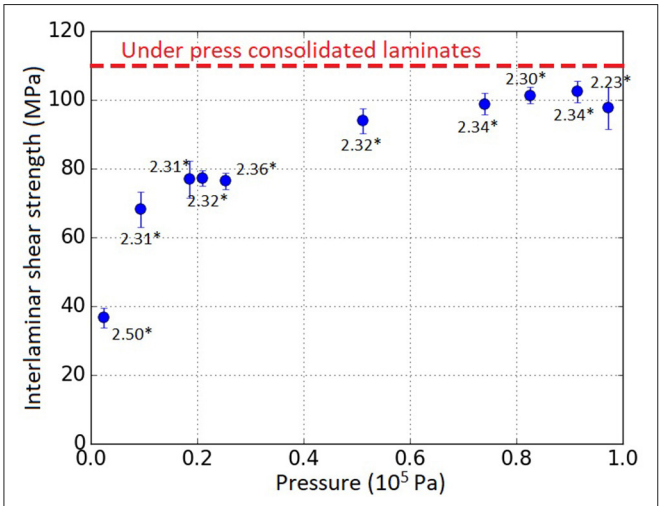

FIGURE 12 | Results of ILSS measurements for different compaction pressure levels in the heated oven (*: average thickness of the laminate in *mm*).

Heat Transfer Simulation Result

The four parameters of the sigmoid function for the thermal conductivity of interface layers (see **Figure 4**) have been identified. The temperature range (dT) was 22 K. The inflection temperature (T_r = 440 K) corresponded to the glass transition temperature and the improvement of conductivity is associated with the matrix phase change. The initial conductivity (k_{init}) was 0.003 $W{\cdot}m^{-1}{\cdot}K^{-1}$ which corresponded to the air conductivity under very low pressure (1–5 $\times$ 10^2 Pa). The final conductivity (k_{fin}) was 0.032 $W{\cdot}m^{-1}{\cdot}K^{-1}$ which was still lower than the matrix conductivity, because the intimate contact was not complete under the melting point. **Figure 14** presents the experimental result and the simulation result for the temperature evolution at the top layer during the consolidation process. We can see that the fast increase of the temperature at the top layer above the glass transition temperature was well-reproduced by the numerical simulation considering the change of thermal contact resistance at the interlaminar interfaces. As the amorphous zones of the matrix softened above the glass transition temperature, the surface roughness was deformed and flattened out to increase the contact area between the adjacent layers. Subsequently, the heat conduction path was enlarged and the thermal contact resistance was decreased. As a result, the heat transfer was enhanced and the temperature at the top layer was fast increased.

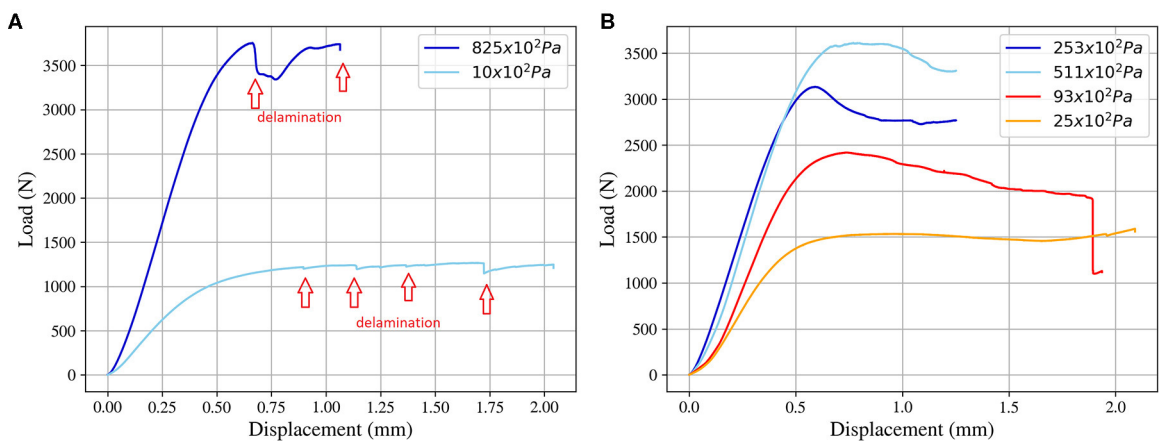

FIGURE 13 | ILSS failure profiles. **(A)** Failure by delamination profiles. **(B)** Plastic deformation profiles.

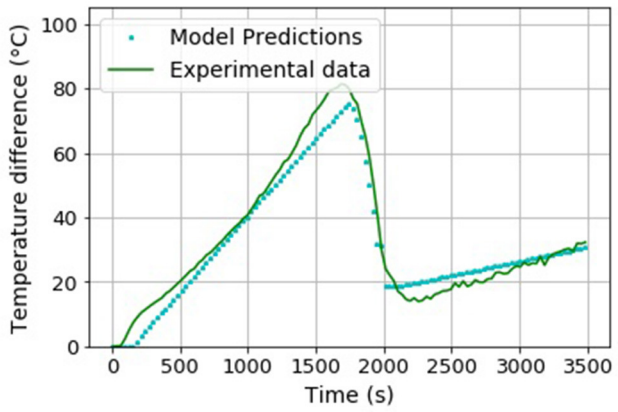

FIGURE 14 | Experimental and numerical results of the temperature at the top layer.

CONCLUSION

The OOA or VBO manufacturing of high performance thermoplastic composite laminate was investigated by *in-situ* monitoring method. Two kinds of experimental set-up were developed, viz. the oven heating method where more uniform heating could be obtained and the heating plate method coupled with the *in-situ* monitoring system. For this second set-up, carbon/PEKK prepreg laminates were fabricated by the one-side heating mold while the laminate thickness and the temperature differential along the thickness direction were monitored during the consolidation cycle. This method was very effective to produce laminates which were unaltered by the *in-situ* monitoring (no thermocouples placed inside the laminates) and to analyze the interlaminar consolidation phenomena during the manufacturing process.

Moreover, this work proved the feasibility to consolidate thermoplastic laminate with high interlaminar shear strength by VBO set-up, according to ILSS results and microscopic observations. A high ILSS value (around 100 MPa) can be reached for compaction pressure above700×10^2 Pa.

Finally, from the *in-situ* monitoring experiments, the two major phenomena were identified. At the glass transition temperature of the matrix, the laminate thickness and the temperature differential are decreased. It is assumed that the amorphous zone of the matrix softens at the glass transition temperature and the surface roughness of prepreg can be flattened out to establish the intimate contact even under low compaction pressure, i.e., below1.00×10^5 Pa. This establishment of intimate contact reduces the thermal contact resistance at the interlaminar interfaces and subsequently decreases the temperature differential. In particular, it has been found that the intimate contact begins to be established at the glass transition temperature whereas, in the literature, it has been assumed to take place around the melting temperature. At the melting temperature, the matrix becomes totally in a molten state to flow into small gaps at the interlaminar interfaces and the polymer molecules can get across the interfaces to build the interlaminar bonding strength.

DATA AVAILABILITY STATEMENT

The raw data supporting the conclusions of this article will be made available by the authors, without undue reservation.

AUTHOR CONTRIBUTIONS

FS, CS, and PB contributed to the design of experimental works and realized them. All the authors contributed to the development of the model, the interpretation of the results, the statistical analysis, and contributed to conception of the study.

REFERENCES

Ageorges, C., Ye, L. Y., Mai, W., and Hou, M. (1998). Characteristics of resistance welding of lap shear coupons.: Part IConsolidation. *Compos. Part Appl. Sci. Manuf.* 29, 911–919. doi: 10.1016/S1359-835X(98)00023-2

Bishop, S. M. (1985). The mechanical performance and impact behaviour of carbon-fibre reinforced PEEK. *Compos. Struct.* 3, 295–318. doi: 10.1016/0263-8223(85)90059-5

Blundell, D. J., Crick, R. A., Fife, B., Peacock, J., Keller, A., and Waddon, A. (1989). Spherulitic morphology of the matrix of thermoplastic PEEK/carbon fibre aromatic polymer composites. *J. Mater. Sci.* 24, 2057–2064. doi: 10.1007/BF02385421

Butler, C. A., McCullough, R. L., Pitchumani, R., and Gillepsie, J. W. J. (1998). An analysis of mechanisms governing fusion bondinf of thermoplastic composites. *J. Thermoplast. Compos. Mater.* 11, 338–363. doi: 10.1177/089270579801100404

Carlile, D. R., Leach, D. C., Moore, D. R., and Zahlan, N. (1989). "Mechanical Properties of the Carbon Fiber/PEEK Composite APC-2/AS-4 for Structural Applications," in *Advances in Thermoplastic Matrix Composite Materials*, ed. G. Newaz (West Conshohocken, PA: ASTM International), 199–212. doi: 10.1520/STP24603S

Cassidy, S. F., and Monaghan, P. F. (1994). Effect of contact resistances on the thermal conductivity of an unconsolidated fibre-reinforced thermoplastic prepreg stack, *Compos. Manuf.* 5, 225–230. doi: 10.1016/0956-7143(94)90137-6

Çelik, O., Peeters, D., Dransfeld, C., and Teuwen, J. (2020). Intimate contact development during laser assisted fiber placement: microstructure and effect of process parameters. *Compos. Part Appl. Sci. Manuf.* 134:105888. doi: 10.1016/j.compositesa.2020.105888

Centea, T., Grunenfelder, L. K., and Nutt, S. R. (2015). A review of out-of-autoclave prepregs – material properties, process phenomena, and manufacturing considerations. *Compos. Part Appl. Sci. Manuf.* 70, 132–154. doi: 10.1016/j.compositesa.2014.09.029

Chang, I. Y. (1988). PEKK as a new thermoplastic matrix for high-performance composites. *Sampe Q U. S.* 19.

Choupin, T. (2017). *Mechanical Performances of PEKK Thermoplastic Composites Linked to Their Processing Parameters*. Paris: Ecole Nationale Supérieure d'Arts et Métiers.

Choupin, T., Fayolle, B., Régnier, G., Paris, C., Cinquin, J., and Brul,é, B. (2018). A more reliable DSC-based methodology to study crystallization kinetics: Application to poly(ether ketone ketone) (PEKK) copolymers. *Polymer* 155, 109–115. doi: 10.1016/j.polymer.2018.08.060

Comer, A. J., Ray, D., Obande, W. O., Jones, D., Lyons, J., Rosca, I., O' Higgins, R. M., et al. (2015). Mechanical characterisation of carbon fibre–PEEK manufactured by laser-assisted automated-tape-placement and autoclave. *Compos. Part Appl. Sci. Manuf.* 69, 10–20. doi: 10.1016/j.compositesa.2014.10.003

Denault, J., and Dumouchel, M. (1998). Consolidation process of PEEK/carbon composite for aerospace applications. *Adv. Perform. Mater.* 5, 83–96. doi: 10.1023/A:1008638105370

El Kadi, H., and Denault, J. (2001). Effects of processing conditions on the mechanical behavior of carbon-fiber-reinforced PEEK. *J. Thermoplast. Compos. Mater.* 14, 34–53. doi: 10.1106/XDX9-U8K4-E0PM-70MX

Gao, L.-S., and Kim, K.-J. (2000). Cooling rate influences in carbon fibre/PEEK composites. Part 1. Crystallinity and interface adhesion. *Compos. Part Appl. Sci. Manuf.* 31, 517–530. doi: 10.1016/S1359-835X(00)00009-9

Gao, L.-S., and Kim, K-J. (2001). Cooling rate influences in carbon fibre/PEEK composites. Part II: interlaminar fracture toughness. *Compos. Part Appl. Sci. Manuf.* 32, 763–774. doi: 10.1016/S1359-835X(00)00188-3

Hsiao, B. S., Chang, I. Y., and Sauer, B. B. (1991). Isothermal crystallization kinetics of poly(ether ketone ketone) and its carbon-fibre-reinforced composites, *Polymer* 32, 2799–2805. doi: 10.1016/0032-3861(91)90111-U

Image J software (2020). Availabvle online at: https://imagej.nih.gov/ij/

Kadlec, M., Nováková, L., and RuŽek, R. (2014). An experimental investigation of factors considered for the short beam shear strength evaluation of carbon fiber–reinforced thermoplastic laminates. *J. Test. Eval.* 42, 581–592. doi: 10.1520/JTE20120043

Khan, M. A., Mitschang, P., and Schledjewski, R. (2010). Identification of some optimal parameters to achieve higher laminate quality through tape placement process. *Adv. Polym. Technol.* 29, 98–111. doi: 10.1002/adv.20177

Krishnaswamy, R. K., and Kalika, D. S. (1996). Glass transition characteristics of poly(aryl ether ketone ketone) and its copolymers. *Polymer* 37, 1915–1923. doi: 10.1016/0032-3861(96)87309-5

Lee, W. I., and Springer, G. S. (1987). A model of the manufacturing process of thermoplastic matrix composites. *J. Compos. Mater.* 21, 1017–1055. doi: 10.1177/002199838702101103

Levy, A., Heider, D., Tierney, J., and Gillespie, J. W. (2014). Inter-layer thermal contact resistance evolution with the degree of intimate contact in the processing of thermoplastic composite laminates. *J. Compos. Mater.* 48, 491–503. doi: 10.1177/0021998313476318

Li, C., and Strachan, A. (2019). Prediction of PEKK properties related to crystallization by molecular dynamics simulations with a united-atom model. *Polymer* 174, 25–32. doi: 10.1016/j.polymer.2019.04.053

Loos, A. C., and Dara, P. H. (1987). Processing of thermoplastic matrix composites. *Rev. Progress Q. Nondestr. Eval.* 1257–1265. doi: 10.1007/978-1-4613-1893-4_143

Lu, M., Ye, L., and Mai, W.-Y. (2004). Thermal de-consolidation of thermoplastic matrix composites—II. 'Migration' of voids and 're-consolidation.' *Compos. Sci. Technol.* 64, 191–202. doi: 10.1016/S0266-3538(03)00233-1

Mantell, S. C., and Springer, G. S. (1992). Manufacturing process models for thermoplastic composites. *J. Compos. Mater.* 26, 2348–2377. doi: 10.1177/002199839202601602

Marquardt, D. (1963). An algorithm for least-squares estimation of nonlinear parameters. *SIAM J Appl Math* 11, 431–441. doi: 10.1137/0111030

Obande, W., Mamalis, D., Ray, D., Yang, L., and Ó., Brádaigh, C. M. (2019). Mechanical and thermomechanical characterisation of vacuum-infused thermoplastic- and thermoset-based composites. *Mater. Des.* 175:107828. doi: 10.1016/j.matdes.2019.107828

Phillips, R., Glauser, T., and Månson, A. E.-J. (1997). Thermal stability of PEEK/carbon fiber in air and its influence on consolidation. *Polym. Compos.* 18, 500–508. doi: 10.1002/pc.10302

Schaefer, P., Guglhoer, T., Sause, M., and Drechsler, K. (2017). Development of intimate contact during processing of carbon fiber reinforced Polyamide-6 tapes. *J. Reinf. Plast. Compos.* 36, 593–607. doi: 10.1177/0731684416687041

Schaefer, P., Kreuzhage, S., Zaremba, S., and Drechsler, K. (2016). *Experimental Investigation of Inter-Layer Thermal Contact Resistance and Its Relevance for Consolidation of Thermoplastic Composites, ECCM17*, München.

See, S., Hana, S. H., Jeong, K. U., Bae, I. J., Hong, I. P., Choi, S. K., et al. (2015). Effect of crystal morphology transition of polypropylene on interfacial properties of carbon fiber-reinforced composites through AlOOH surface treatment, *Compos. Part Appl. Sci. Manuf.* 78, 362–370. doi: 10.1016/j.compositesa.2015.08.036

Stokes-Griffin, C. M., and Compston, P. (2016a). Investigation of sub-melt temperature bonding of carbon-fibre/PEEK in an automated laser tape placement process. *Compos. Part Appl. Sci. Manuf.* 84, 17–25. doi: 10.1016/j.compositesa.2015.12.019

Stokes-Griffin, C. M., and Compston, P. (2016b). An inverse model for optimisation of laser heat flux distributions in an automated laser tape placement process for carbon-fibre/PEEK. *Compos. Part Appl. Sci. Manuf.* 88, 190–197. doi: 10.1016/j.compositesa.2016.05.034

Tadini, P., Grange, N., Chetehouna, K., Gascoin, N., Senave, S., and Reynaud, I. (2017). Thermal degradation analysis of innovative PEKK-based carbon composites for high-temperature aeronautical components. *Aerosp. Sci. Technol.* 65, 106–116. doi: 10.1016/j.ast.2017.02.011

Talbott, M. F., Springer, G. S., and Berglund, L. A. (2016). The effects of crystallinity on the mechanical properties of PEEK polymer and graphite fiber reinforced PEEK. *J. Compos. Mater.* 21:1987. doi: 10.1177/002199838702101104

van Rijswijk, K., van Geenen, A. A., and Bersee, H. E. N. (2009). Textile fiber-reinforced anionic polyamide-6 composites. Part II: Investigation on interfacial bond formation by short beam shear test. *Compos. Part Appl. Sci. Manuf.* 40, 1033–1043. doi: 10.1016/j.compositesa.2009.02.018

Vieille, B., Aucher, J., and Taleb, L. (2011). Carbon fiber fabric reinforced PPS laminates: influence of temperature on mechanical properties and behavior. *Adv. Polym. Technol.* 30, 80–95. doi: 10.1002/adv.20239

Wang, J., Yang, X., Li, G., and Zhou, E. (2001). Isothermal and nonisothermal crystallization of poly(aryl ether ketone ketone) with all-para phenylene linkage. *J. Appl. Polym. Sci.* 82, 3431–3438. doi: 10.1002/app.2204

Witik, R. A., Gaille, F., Teuscher, R., Ringwald, H., Michaud, V., and J.-,Månson, A. E. (2012). Economic and environmental assessment of alternative production methods for composite aircraft components. *J. Clean. Prod.* 29–30, 91–102. doi: 10.1016/j.jclepro.2012.02.028

Yang, F., and Pitchumani, R. (2001). A fractal Cantor set based description of interlaminar contact evolution during thermoplastic composites processing. *J. Mater. Sci.* 36, 4661–4671. doi: 10.1023/A:1017950215945

Yang, H., and Colton, J. S. (1995). Thermal analysis of thermoplastic composites during processing, *Polym. Compos.* 16, 198–203. doi: 10.1002/pc.750160303

Conflict of Interest: The authors declare that the research was conducted in the absence of any commercial or financial relationships that could be construed as a potential conflict of interest.

Smart Materials

Caroline Duc

Dr. Caroline Duc received her M.Eng. in Material Sciences from Institut National de Science Appliquée, Lyon (France) and her Ph.D. degree in Micro/Nanosystems and Sensors from Lille University, France, in 2017. In 2019, she joined the Department of Energy and Environment of the Institut Mines Telecom Lille Douai as an Assistant Professor. Her research interests focus on the behavior of nanocomposites based on conductive polymers and their uses in biomedical and environmental applications.

frontiers in Materials

REVIEW
published: 30 September 2020
doi: 10.3389/fmats.2020.00215

Hydrogen Sulfide Detection by Sensors Based on Conductive Polymers: A Review

Caroline Duc, Mohamed-Lamine Boukhenane, Jean-Luc Wojkiewicz and Nathalie Redon*

IMT Lille Douai, Institut Mines-Télécom, University of Lille, Energy and Environment Centre, Lille, France

Coming from natural and anthropogenic sources, hydrogen sulfide gas (H_2S) is a smelly hazardous substance at the sub-ppm level, which can lead to poisoning deaths at higher concentrations. Researchers have been working for decades to design sensors with sufficient/good/robust metrological properties and good stability in order to monitor and control in real time the risk associated with this gas. Among the devices proposed, chemiresistive sensors based on conductive polymer appear as a good alternative to the most common solutions such as electrochemical and optical sensors. They present various advantages in terms of design (easy fabrication, easy tuning of physical and chemical properties, low cost, etc.) and performances (good sensitivity, good reproducibility, room temperature operation, short response time, etc.). In this review, we summarize the progresses made on conductive polymer sensors dedicated to H_2S detection, including the performance of the different materials and sensing mechanisms. Finally, we identify the limitations of these sensors and highlight the most promising approaches to enable the use of these technologies in real-world applications.

Keywords: hybrid polymer, conductive polymer, chemiresistive sensor, hydrogen sulfide detection, H_2S sensors, gas sensing

OPEN ACCESS

Edited by:
Emilia Morallon,
University of Alicante, Spain

Reviewed by:
Peter Kruse,
McMaster University, Canada
Haibao Lu,
Harbin Institute of Technology, China

****Correspondence:***
Caroline Duc
caroline.duc@imt-lille-douai.fr

Specialty section:
This article was submitted to Smart Materials, a section of the journal Frontiers in Materials

Received: *27 April 2020*
Accepted: *12 June 2020*
Published: *30 September 2020*

Citation:
Duc C, Boukhenane M-L, Wojkiewicz J-L and Redon N (2020) Hydrogen Sulfide Detection by Sensors Based on Conductive Polymers: A Review. Front. Mater. 7:215. doi: 10.3389/fmats.2020.00215

INTRODUCTION

Corrosive, colorless, water-soluble, and flammable in ambient conditions, hydrogen sulfide (H_2S) is a smelly hazardous substance at the sub-ppm level, which can lead to poisoning deaths at higher concentrations (Malone Rubright et al., 2017). The exposure toward this gas is mainly linked to geothermal activity (e.g., crude petroleum, natural gas, hot spring) and organic decomposition from sewers, wastewater treatment plants, landfills, Sargasse seaweeds, etc. It is also produced by the industry as a by-product of paper manufacturing and tanneries or synthetized intentionally for its use as an agricultural disinfectant and an intermediate in sulfuric acid production [(National Research Council (US) Committee on Acute Exposure Guideline Levels, 2010)]. According to the Occupational Safety and Health Administration and the Bureau of Labor Statistics, H_2S is one of the most dangerous gases in the workplace (Malone Rubright et al., 2017; Occupational Safety Health Administration, 2020). International public safety organizations have established several exposure limits from 1 ppb to 100 ppm in order to (i) limit the olfactory disturbance from the natural and industrial production of H_2S and to (ii) protect the workers from acute and chronic exposures (Malone Rubright et al., 2017). Humans can smell H_2S at low concentrations (0.5 to 300 ppb) (Beauchamp et al., 1984), and the gas can produce severe damages such as possible nausea (∼2 ppm), loss of smell (∼20 ppm), severe lung/nose/throat irritation (∼100 ppm), and death (>250 ppm) (Habeeb et al., 2018). Moreover, H_2S is present in various and complex

environments, in which the humidity as well as the concentration in co-pollutants (e.g., SO_2, CO in geothermal activity) are continuously changing (Malone Rubright et al., 2017). Therefore, monitoring equipment working in different ranges of concentration and environmental conditions is needed.

Analytical methods such as gas chromatography and/or spectrometry are commonly used to quantify H_2S concentration in air. Possessing high sensitivity toward low concentration, they present many drawbacks such as complex sampling and analyzing processes, high cost, and low temporal resolution or a posteriori measurements (Tranchida et al., 2016; Zoccali et al., 2019). Odor monitoring and safety control demand cost-effective, user-friendly, and continuous real-time measurements. As standardized methods are not fully fulfilling those requirements, many researches have been done to develop fast, portable, and low-cost devices (Llobet et al., 2017). Among the devices developed, chemiresistive, electrochemical, and optical sensors are the most popular in H_2S sensing (Pandey et al., 2012; Serban et al., 2014). Even if few sensors have been commercialized, their sensitivity and stability need to be optimized.

Among the H_2S sensors in vogue, the chemiresistive sensor is the simplest transducing system (Wong et al., 2020). Translating chemical information in an electrical signal, this device is based on a two-point contact measurement of the resistance of a sensitive material. Metal oxides (MOx) appear as a model sensitive material in gas sensing (Korotcenkov and Cho, 2017; Joshi et al., 2018) and more specifically in H_2S sensing (Guo et al., 2015; Mirzaei et al., 2018) given their high sensitivity, fast response, and easy integration in compact electronic devices. Nevertheless, MOx-based sensors present a limited selectivity and a high dependence on relative humidity and generally require a high operating temperature ($>100°C$).

An alternative to MOx is the use of conductive polymer (CP) as a sensitizing surface. Showing electronic properties of metals and semiconductors while retaining mechanical properties and processing advantages of polymers, CPs have appeared as promising materials in the field of gas sensor in early 1980s (Nylabder et al., 1983). Since then, many works have been done to increase their metrological performances (Bai and Shi, 2007; Fratoddi et al., 2015; Park et al., 2017). Indeed, CPs present the advantages of being easily synthetized and modified through chemical or electrochemical processes, being easily included in low-cost and miniaturized devices, and being gas sensitive at room temperature, but their selectivity toward H_2S and their long-term stability need to be enhanced.

The aim of this paper is to give an overview of the roles played by CPs in chemiresistive sensors dedicated to H_2S. After a presentation of the mechanism of detection and sensing performances of pure CPs, the discussion focuses on their hybridization with inorganic fillers. Indeed, these materials trying to combine the advantages of CPs and inorganic nano-objects have awakened extensive interest in the last decade (Hangarter et al., 2013; Kaushik et al., 2015; Park et al., 2017; Iqbal and Ahmad, 2018). Mechanisms and performances are addressed for each type of inorganic fillers (i.e., noble metal, MOx, metal chloride, and carbon-based nanostructures). Finally, a cross-comparison of the sensing properties and the potential for future application of the different sensitive surfaces is done in order to highlight the promising approaches and the investigation needed for achieving those technologies employed in the field. The discussion is based on comparative tables (**Supplementary Material**) ordered by class of material (e.g., pure CPs, noble metal composites, etc.), where the sensing performance of the materials (i.e., limit of detection and response time) and properties allowing their access to real-field application (i.e., selectivity, stability, reversibility, operating temperature, behavior under humidity changes, etc.) are presented.

SENSORS BASED ON INTRINSIC CONDUCTIVE POLYMERS

Intrinsic CPs are π-conjugated systems presenting a multilevel structure at the scale of the monomers, the chains, and the bulk of the material. This chemical organization makes their properties highly tunable at different scales from combination of different monomers and chain conformation modification by additive to formation of various morphologies at nanoscale/microscale (Skotheim and Reynolds, 2007).

The π-conjugation along the polymer chain allows the formation of delocalized electrons at the origin of the electric conduction of CPs. Actually, electrons in double bonds are free to move along the carbon skeleton given the overlap of the p_z orbitals (Dongmin Kang and Jeffrey Snyder, 2017). Due to the presence of imperfections [e.g., localization of charges induced by Peierls distortion (Anderson and Roth, 1994), short conjugation length, weak degree of crystallinity (Le et al., 2017)], this phenomenon provides low conductivity to CPs in neutral state. Dopants are often used to remove or add electrons from the chain to increase conductivity and form p-type and n-type doped CPs, respectively. In p-type doping, the electrons move from the polymer to the dopant (oxidation process), creating holes along the polymer chain. Conversely, the electron density increases in the n-type doped polymer by the movement of the electron from the dopant to the polymer (reduction process) (Le et al., 2017). Thereby, CPs display conductivity which can be modulated by redox reaction or protonation from near-insulator to metallic conductor (Bai and Shi, 2007).

As a nucleophilic (i.e., reducing) gas, H_2S is expected to decrease the conductivity of p-type CPs and conversely increase the conductivity of n-type CPs (Wong et al., 2020). However, this classical behavior is observed only in few studies concerning polyaniline (PANI) deposited by thermal evaporation (Agbor et al., 1995), PANI doped in maleic acid with dodecyl hydrogen sulfate studied under nitrogen (Palaniappan and Saravanan, 2010), polycarbazole (Joshi et al., 2014), and polyazomethines studied in air (Patil et al., 2019). Those p-type materials show effectively a decrease in conductivity under H_2S (**Figure 1A**). On the contrary, the other sensors based on pristine CPs display an increasing conductivity in the presence of H_2S. In fact, in the presence of water at room temperature, H_2S tends to dissociate into H^+ and HS^- (Agbor et al., 1995). H^+ protonates the nitrogen atoms from PANI (Agbor et al., 1995; Dong et al., 2016), polypyrrole (PPy) (Kriván et al., 2000; Garg et al., 2015), or poly(N-propylaniline) (PNPA) (Chabukswar et al., 2013) and

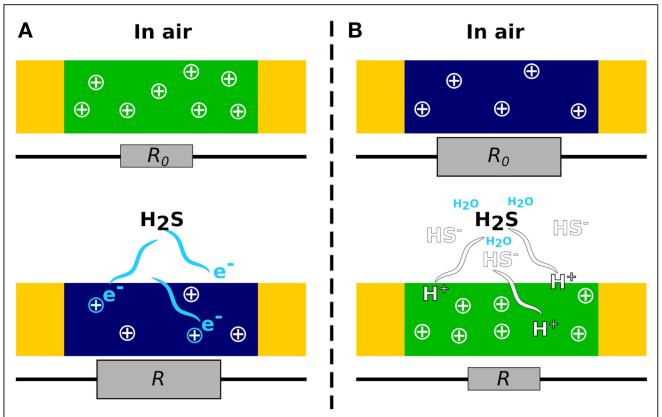

FIGURE 1 | Mechanisms of H_2S detection by CPs. **(A)** The reducing gas H_2S induces a reduction of the major charge carrier (holes, +) resulting in an increase in CP resistance ($R_0 < R$). **(B)** In the presence of water, H_2S releases protons, which increase the charge carrier in the polymer and thus decrease the resistivity ($R_0 > R$).

leads to an increase in conductivity toward H_2S (**Figure 1B**). The reducing effect of H_2S and the dissociation of the gas followed by the protonation of CPs are the two mechanisms at the origin of the resistance modulation of the H_2S sensors based on CPs exclusively.

In chemiresistive sensors, the presence of gaseous analyte induces changes in electronic conductivity of a sensitive surface. Therefore, the sensing performance depends on (i) the interaction between the gas and the sensitive material and on (ii) the charge transport (i.e., capacity to transmit the changes to the electrodes) (Park et al., 2017). Each property of the material affecting one of these two parameters will alter the sensing performance of the device.

Given the mechanism of action of H_2S, the interactions of gas/polymer are mainly driven by the number of active sites (i.e., redox groups or atoms able to receive proton) capable of interacting with the gas. Beside the molecular structure of the polymer chain, which delimits the total number of active sites, the morphology controls the accessibility to the sites. This parameter can influence the sensitivity as well as the response time of the sensor. Indeed, an open structure (e.g., a porous material) facilitates the adsorption/desorption of the gas in the polymer. For example, the porous agglomerate of nanoparticles (50–100 nm) of PNPA insures a high surface-to-volume ratio leading to the best response from pure-CP sensor toward H_2S, with a modulation of −25% of the resistance at 500 ppb and a response time lower than 60 s at 100 ppm (Chabukswar et al., 2013).

Then, the charge transport in CPs is achieved by two mechanisms, the intra-chain transport (i.e., along the chain) and the inter-chain transport, which are both influenced by many factors. The intra-chain transport is fast and localized along the conjugated backbone. It depends mainly on the charge carrier and the conjugation length (Kivelson and Heeger, 1988; Phillips and Wu, 1991). The inter-chain is based on hopping or tunneling of the charge carrier and depends mainly on the conformation of the chain and their organization, which can influence the distance between chains and the degree of crystallinity (Hangarter et al., 2013). Therefore, the disorder of the structure of the polymer can affect its sensing performance.

In the case of H_2S detection by CPs, two parameters have shown a large impact on the performance of the sensor: the dopant and the process. The dopant is known to affect the charge transport and the morphology (Krukiewicz and Katunin, 2016). Thus, the size and nature of the dopant can influence the sensing performance of the CPs and their stability. For example, PANI doped with hydrochloride acid (HCl) has a response five times higher than the same material doped with sulfosalicylic acid (SSA) tested toward 100 ppm of H_2S (Dong et al., 2016). SSA anions being bigger, they lead to larger chain spacing. The inter-chain transport is less effective, resulting in a lower activity. Moreover, PANI–HCl is less stable over 50 days. Small anions (as HCl) are known to be less stable (Li and Wan, 1999). They are more likely to migrate and volatilize from the CPs, leading to a drift of the resistance with time. Moreover, functional groups, such as the presence of both polar and non-polar groups on SSA, can increase the decomposition temperature (Dong et al., 2016). Those two parameters influence directly the stability of CPs.

Besides influencing the morphology of the sensitive surface, the process of fabrication can affect even the mechanism of variation of the conductivity of CPs. As illustration, PANI in emeraldine base form deposited on Au-IDE by spin-coating (1 µm thick) or thermal evaporation (210 nm) shows, respectively, an reversible increase or an irreversible decrease in the conductivity in the presence of H_2S under dry nitrogen (Agbor et al., 1995). The increase in the conductivity from the spin-coated film is due to the protonation of PANI when H_2S dissociates into H^+ and HS^- in contact with water from the film, whereas in the case of thermal evaporation, the film does not contain water and H_2S acts as a reducing gas decreasing the conductivity of the film.

CPs have shown their ability to detect H_2S from 0.5 to 1,000 ppm. They present the advantage of having a good sensitivity at room temperature and of being highly tunable chemically and physically, giving rise to many optimization approaches. However, as reported in **Supplementary Table 1**, intrinsic CPs dedicated to H_2S sensing are often instable and present a low selectivity. Each reducing or oxidizing gas can affect differently their resistance depending on their mutual affinities. For example, PPy nanowires present an interesting 53% resistance decrease in contact with 200 ppm H_2S but they also suffer a larger increase in resistance (143%) in the presence of ammonia (Garg et al., 2015). In order to overcome those main drawbacks, many works dedicated to H_2S sensing by CPs are a focus on the hybridization of those materials with inorganic fillers.

HYBRIDS CONDUCTIVE POLYMER SENSORS: ORGANIC-INORGANIC COMPOSITES

Noble Metal Composites

Noble metals are often used in MOx sensors as sensitizing agent (Ramgir et al., 2013). Indeed, they provide additional absorption sites, promoting a chemical reaction occurring on

the surface (chemisorption, redox). This strategy has been applied to CPs hybridized by surface functionalization or bulk inclusion of noble metal nanoparticles (NPs) or clusters in order to increase the sensitivity and/or selectivity toward H_2S gas. PANI, PPy, polycarbazole, and polyimide have been used as a matrix when Ag and Au have been used as metallic additives (**Supplementary Table 2**).

The mechanisms at the origin of the sensing performance of polymer/metal hybrids are not perfectly understood. As shown in **Figure 2**, the metallic particles can have two effects on the response of CPs toward H_2S. Firstly, they present high affinity with analytes carrying sulfur atoms, which facilitates the interaction gas/material (Joshi et al., 2014). Indeed, by reacting with the gas, the metallic items release protons, which dope the CP and induce an increase in conductivity. For example, in the PANI-AuNP system, the gas reacts with gold to form AuS and H^+, leading to an enhancement in the doping level of PANI (Shirsat et al., 2009; Liu et al., 2012). Secondly, the presence of metallic particles in p-type CPs induces the formation of nano-Schottky junctions. At the interface between the two components of the material, the difference in work function between the metal and the organic semiconductor prevents the transfer of electron, resulting in an excess of negative charge at the surface of the particles and the formation of a depletion region (Joshi et al., 2014; Kaushik et al., 2015). Changes in the width of the depletion region modulate the conductivity of the sensing material by changing the resistance but also the capacitance of the material (Joshi et al., 2014; Mekki et al., 2014). The properties of the Schottky junctions are highly sensitive to adsorption phenomena, and their presence amplifies the response toward gas adsorbed, resulting in enhanced sensitivity.

Given the sensing mechanism, the efficiency of the metallic fillers is highly dependent on their nature, geometry, and distribution. The role of sensitizing agents endorsed by metallic nanoparticles has been demonstrated on PANI nanowires decorated by Au-NPs (Shirsat et al., 2009). Electropolymerization followed by electrofunctionalization of the material leads to the formation of polymeric fibers with a diameter of 250–320 nm and well-dispersed NPs (70–120 nm). This system shows an extraordinarily high response at sub-ppb level (−20% at 0.1 ppb) when the unfunctionalized nanofibers have a limit of detection four orders of magnitude higher (>50 ppm). The high performance of the system is mainly attributed to its morphology (i.e., nanofibers decorated by nanoparticles) and the good dispersion of the metallic particles.

Moreover, the addition of metal can enhance the selectivity toward H_2S. Compared to the pristine polymer, electropolymerized polycarbazole covered by a 1-nm layer of gold shows a response toward 40 ppm H_2S doubled when its response toward 40 ppm NH_3 is divided by a factor of 7.5 (Joshi et al., 2014). The slower response and recovery of the functionalized surface endorse the authors' assumption, i.e., this specific behavior is due to the enhanced interaction between H_2S and the material.

Briefly, metal/CP composites have shown their ability to detect H_2S from 0.1 ppb to 800 ppm. PANI nanofibers decorated with gold particles provide the lowest detection limit

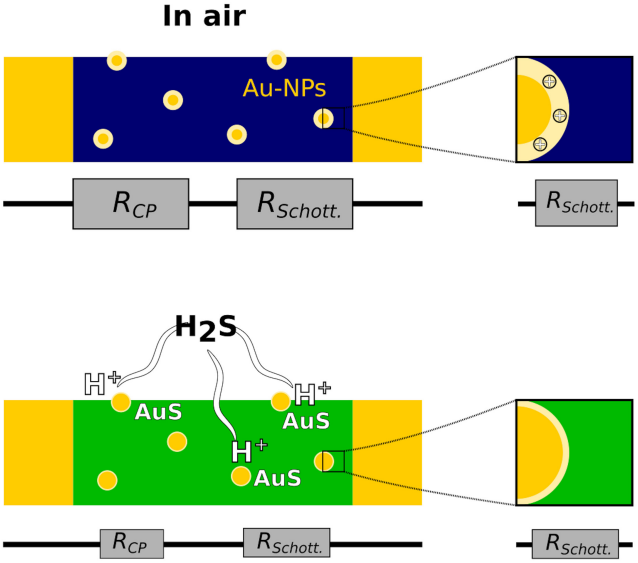

FIGURE 2 | Mechanisms of H_2S detection by CPs hybridized with metallic nanoparticles (Au-NPs). R_{CP} and R_{Schott} represent the resistance contribution of the polymer and depletion layer (in pale yellow) at the interface with the metal (Schottky junction), respectively. Those resistances tend to decrease in contact with H_2S gas.

from the literature dedicated to organic chemiresistive sensors for H_2S detection (Shirsat et al., 2009). The origin of this good performance can be attributed to three factors: (i) the morphology insures the accessibility to a high number of active sites, (ii) the presence of gold leads to the release of protons by reacting with H_2S, and (iii) the formation of Schottky junction in the bulk of material leads to the amplification of the response toward H_2S. In order to optimize the sensitive materials, the exact role of the metallic items in hybridized CPs needs to be clarified and, most importantly, the effects of environmental parameters such as humidity need to be considered. Indeed, those parameters have never been investigated on the hybridized metal/CPs when they are crucial for the end-use of gas sensors.

Metal Oxide and Sulfide Composites

Metal oxides (MOx) are the most commonly employed material in chemiresistive gas sensors in the academic and industrial field (Korotcenkov and Cho, 2017; Llobet et al., 2017; Joshi et al., 2018). The hybridization of such material with CPs often aims to overcome some of their drawbacks, e.g., their low selectivity and high operating temperature, and to optimize their sensing performances (Hangarter et al., 2013). For H_2S detection, mechanical mixing and *in situ* polymerization have been used to prepare MOx/CPs hybrids based on PPy, PANI, or polythiophene and WO_3, SnO_2, or the metal sulfide CdS (**Supplementary Table 3**).

The presence of H_2S can induce a decrease in the resistance of both CPs and n-type semiconductors. This fact tends to support the assumption that the conjoint effect of gas on the different moieties of the material is at the origin of the increased sensitivity

of hybrids (Geng et al., 2006). However, it is not the lonely mechanism involved.

In composites based on organic and inorganic semiconductors, the inorganic moieties are often the main sensitizing agents when the polymer plays the role of amplifier (Hangarter et al., 2013). Indeed, the adsorption of reducing/oxidizing gas modulates easily the resistance of inorganic semiconductors by affecting the properties of the depletion layer at the interface gas/solid. In air, adsorbed oxygen traps electrons from n-type MOx (which are classically used in H_2S sensing), resulting in a lower concentration of electron at the surface than in the bulk of the material (i.e., appearance of a depletion layer). Upon exposure to H_2S, the gas reacts with adsorbed oxygen ions (O_2^{n-}), leading to the release of the trapped electrons and the decrease in the resistance, as shown in the following equations (Moseley et al., 1991; Mirzaei et al., 2018):

$$O_{2(g)} + ne^- \longrightarrow O^{n-}_{2(ads)} \quad (1)$$

$$2H_2S_{(g)} + 3O^{n-}_{2(ads)} \longrightarrow 2H_2O + 2SO_2 + 3n\,e^- \quad (2)$$

This mechanism of sensing often insures toward MOx a higher sensitivity than CPs. For example, polythiophene shows a response four times lower than WO_3 and nine times lower than the composite loading WO_3 and 10% of polythiophene toward 100 ppm H_2S at 70°C (Bai et al., 2014).

As illustrated in **Figure 3**, the mechanism of amplification is based on the appearance of p–n junctions at the interface of p-type CPs and n-type MOx. The inclusion of CPs increases the width of the depletion layer of MOx (Su and Peng, 2014). As seen for noble metal/CP hybrids, the presence of heterojunctions produces a new potential barrier in material, which are highly sensitive toward gas absorption (Bärtsch and Niederberger, 2017; Walker et al., 2019). When H_2S is adsorbed on the composite, more electrons migrate from the polymer to MOx, decreasing the potential barrier at the interface CPs/MOx. The induced resistance change is extreme and makes easier the detection of the gas.

Thereby, the presence of a heterojunction in the material leads to an increase in the sensitivity and decrease in the limit of detection. For example, WO_3 NPs decorated with PPy by *in situ* photopolymerization show a response around −80% toward 1 ppm H_2S when pure WO_3 and PPy present a response of −10 and −25%, respectively. Noticeable changes in resistance (−8.9%) are still visible on the hybrid sensor at 100 ppb in contrast to the sensors based on pure material (Su and Peng, 2014). Moreover, hybridizing CPs with MOx can also shorten the response and recovery times. As illustration, in comparison to pure inorganic material, the oxidative polymerization of PPy around SnO_2 nanograins results in a response time and a recovery time at 50 ppm divided by more than six and three, respectively (Shu et al., 2017). Additionally, among the enhancements allowed by hybridization is the decrease in the operating temperature. Indeed, the hybrid composites dedicated to H_2S present a generally lower operating temperature than the pure MOx sensor does. As shown in the **Supplementary Table 3**, most of the systems work at room temperature when the others present an optimal response at 70 or 90°C.

However, the improvement in the performances of hybrids is not always easy to capture given the high sensitivity of this strategy to the quality of CPs, metal oxide, and interfaces as well as the ratio of CPs/MOx and the resultant morphology (Hangarter et al., 2013). As shown on polythiophene/WO_3, the composite with 10% of polymer shows a response 2.3 times higher than that of pure WO_3. However, above this content, the sensing performance decreases to reach a lower performance than pure WO_3 at 30% (Bai et al., 2014). With a high amount of polymer, the organic layer is too thick to allow the gas to contact the inorganic sensitizing agent, affecting the sensing properties of the system. A compromise is necessary between the extent of the heterojunction (i.e., the extent of the interface CPs/MOx) and the accessibility to MOx.

Finally, a promising approach to optimizing the properties of hybrid CPs/MOx sensors is the inclusion of the doping agent in the MOx lattice in order to create new active sites. In the PPy/SnO_2 composite, substituting Cu for Sn atoms by doping SnO_2 with Cu^{2+} ions promotes the generation of oxygen vacancies acting as reaction sites (i.e., where adsorbed gas easily traps electrons from SnO_2). Thereby, the response (defined *as* $S = (I_g - I_a)/I_a$, where I_g and I_a correspond, respectively to the steady-state current of the sensor in H_2S and air) of the doped-hybrid material is about 4 at 50 ppb when the response of undoped PPy/SnO_2 is not appreciable at 10 ppm (Shu et al., 2017). The synergetic effect from the doping providing an extra active site and the polymer creating a heterojunction gives rise to sensors having high sensitivity, fast response and recovery rate, satisfactory selectivity, and long-term stability over 1 month.

Concisely, MOx/CP composites have shown their ability to detect H_2S from 0.05 to 1,000 ppm. The hybridization with MOx can enhance drastically the performance of the H_2S sensor by improving the quality of the response (i.e., the sensitivity, limit of detection, response and recovery time) and the operating condition of the sensor by decreasing the temperature. Given the entanglement of the sensing mechanisms in the material (i.e., sensing from CP, MOx and p–n heterojunction), the synergetic effect between MOx and CPs can be found delicate and the parameters controlling their efficiency are numerous (e.g., synthesis, process of deposition, morphology). Further investigation is needed to understand better the impact of each sensing mechanism and their controlling parameter. Moreover, the impact of environmental conditions and long-term stability (>1 month) are too rarely investigated once they become crucial for sensor application.

Metal-Chloride Composites

The addition of metal chlorides to CPs has been done directly in solution or by alternate deposition (i.e., deposition of a polymeric layer covered by a metallic layer, etc.). In the literature dedicated to H_2S sensing, only PANI has been hybridized with metallic chlorides (**Supplementary Table 4**). Commonly, $CuCl_2$ is used for this purpose given its higher sensing performances (Virji et al., 2005).

Metal chlorides are used to overcome the fact that H_2S is a weak acid, which cannot directly induce high changes in the conductivity of CPs. Indeed, hydrogen sulfide is known to react

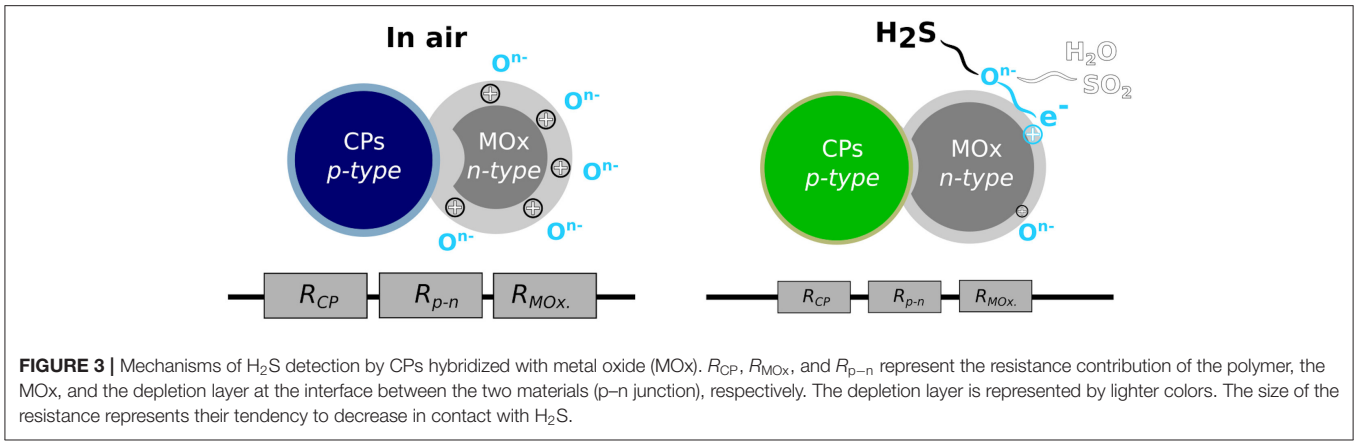

FIGURE 3 | Mechanisms of H_2S detection by CPs hybridized with metal oxide (MOx). R_{CP}, R_{MOx}, and R_{p-n} represent the resistance contribution of the polymer, the MOx, and the depletion layer at the interface between the two materials (p–n junction), respectively. The depletion layer is represented by lighter colors. The size of the resistance represents their tendency to decrease in contact with H_2S.

with metal salts (MCl_2) in solution to form a metal sulfide (MS) and a strong acid (HCl) (Skoog and West, 1963), as illustrated in the following Equation:

$$H_2S + MCl_2 \longrightarrow MS + 2\,HCl \quad (3)$$

n air, metal and chloride ions are strongly bound, making the reaction with H_2S unfavorable. The association with PANI by coordination of metal ions facilitates the reaction with gas. Therefore, the presence of the two components is necessary for the detection of H_2S gas. In contact with metal salts lightly coordinated to nitrogen atoms from the polymer, H_2S releases a strong acid, which dopes PANI resulting in a drastic increase in polymer conductivity (Virji et al., 2005).

Given the mechanisms of action, the hybrids based on metal chloride present two specificities. Showing a variation of resistance of a few orders of magnitude at 10 ppm, they have the highest response from literature but their responses are quasi-systematically irreversible. For example, screen-printed PANI–$CuCl_2$ from an aqueous solution shows a resistance divided by 10^5 toward 15 ppm H_2S at room temperature but the signal presents no recovery during the ventilation of the sample even after 20 h (Sarfraz et al., 2013). The enhanced response is attributed to the doping effect from HCl released, associated with a favorable morphology, facilitating the diffusion of the analyte in the bulk of the material. Unlike the doping of PANI, the reaction of metal chloride with H_2S is irreversible, resulting in the formation of stable copper sulfides (CuS and/or Cu_2S), which are good conductors at room temperature (Silvester et al., 1991).

The unique hybrid material based on metal chloride showing recovery are surface-printed layer-by-layer alternating PANI NPs and $CuCl_2$ deposited on silver electrodes (Crowley et al., 2010). The reversibility of the signal depends on the nature of the electrode. Indeed, the signal is irreversible on carbon electrodes and completely reversible on silver for several exposures at a high concentration (100 ppm). The presence of silver postpones the end of the stock of reactants able to form strong acid. Silver chlorides (AgCl) can be formed in the presence of copper chlorides ($CuCl_2$), leading to the formation of copper (Cu) and/or copper(I) chloride (CuCl). Under exposition to H_2S, both chlorides and metal can react, resulting in the release of proton, electron, and HCl according to the following equations:

$$H_2S + 2Cu_{(s)} \longrightarrow Cu_2S + H_2S + H^+ + e^- \quad (4)$$

$$H_2S + 2AgCl \longrightarrow Ag_2S + 2HCl \quad (5)$$

The release of electrons is assumed to be at the origin of the reversibility of the signal. However, due to the finite reservoir of free copper, the sensor response results to be irreversible over time.

Shortly, CPs hybridized with metal chloride have shown their ability to detect H_2S from 2.5 to 15 ppm. The use of metal chloride insures a high response toward H_2S. However, due to the irreversible reaction at the origin of the enhanced response, those hybrid materials can be used only for short-time applications.

Graphitic Composites (CNT/Graphene)

Due to their good transducing properties, efficient adsorption of gas molecules, and high aspect ratio (Joshi et al., 2018), carbon nanotubes (CNT) and graphene are the most explored additives for the hybridization of CPs in gas sensing (Hangarter et al., 2013; Varghese et al., 2015). However, only few carbon-based composites are dedicated to H_2S sensing (**Supplementary Table 5**). Graphitic hybrid CPs are exclusively composed of PANI decorated by single-wall nanotubes (SWNT), graphene oxide (GO), or reduced graphene oxide (rGO).

In the literature dedicated to H_2S, carbon fillers have never been employed as sensitizing agent. Firstly, they are used to enhance analyte and/or charge transport. For example, in PSS-doped PANI hybridized with GO, H_2S is not detected by pristine graphene sheets when the response of the composites is −20% toward 1 ppm of gas (Cho et al., 2014). Moreover, the conductivity is changing from 11.2 to 168.4 S/cm with the addition of 30 wt% of graphene.

Secondly, carbon fillers can be used as an amplifier in a ternary system based on the p–n junction by adding new p–n interfaces and thus increasing the effect of the depletion region on the signal. In the SnO_2/RGO/PANI nanocomposite, the heterojunction is the main contributor to sensing enhancement (Zhang et al., 2019). The band gaps of SnO_2, RGO, and PANI are 3.5, 4.39, and 4.49 eV, respectively, resulting in the formation of

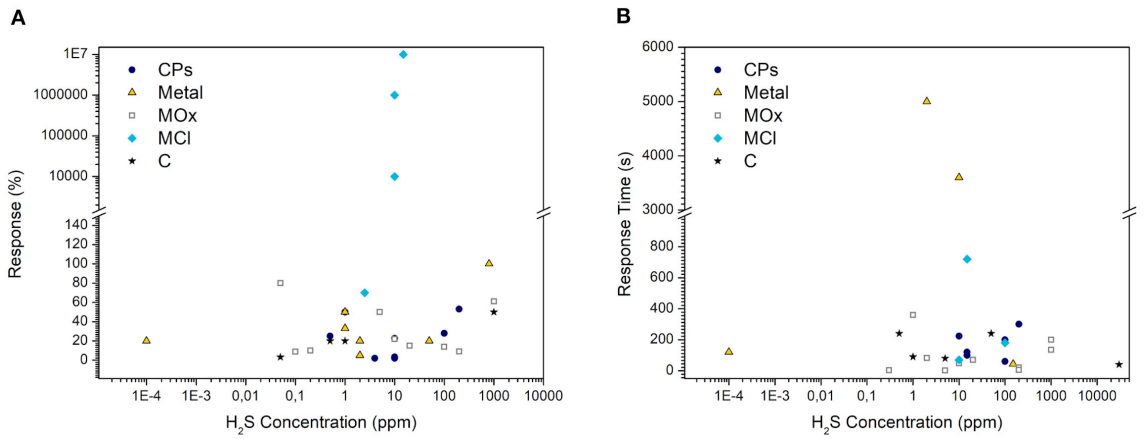

FIGURE 4 | (A) Relative responses of different materials at the lowest H_2S concentration tested. The relative response is defined as $(R_g\text{-}R_0)*100/R_0$, where R_g and R_0 correspond to the resistance of the sensor in H_2S and in the reference medium (air or nitrogen). It has been directly extracted or calculated from the papers presented in **Supplementary Tables 1–4**. **(B)** Response times of different materials directly extracted from the literature. Metal, MOx, MCl, and C refer to hybrid composites based on conductive polymers (CPs) mixed with noble metal particles and metal-oxide, metal-chloride, and carbon-based items, respectively.

a p–n junction between the two p-type materials (i.e., RGO and PANI) and the metal oxide (SnO_2).

Finally, carbon-based hybrids have shown their ability to detect H_2S from 50 ppb to 30 000 ppm. However, the graphitic composites often result in low selectivity toward H_2S with a higher response toward NH_3, as shown for PANI hybridized with SWNT (Lim et al., 2010) or GO (Gaikwad et al., 2017).

SENSING PERFORMANCES

The first characteristics of sensing performance are the amplitude and rate of the response. **Figure 4** summarizes the relative response of the materials discussed previously as a function of the lowest concentration tested and the response time at different concentrations (the values and references are detailed in **Supplementary Tables 1–5**).

Considering the relative response (**Figure 4A**), the hybrids filled with metal chloride present an extraordinarily high amplitude of response about several orders of magnitude. This performance can be explained by the sensing mechanism, resulting in the release of a strong acid in the presence of H_2S jointly to the increase in filler conductivity. Tested between 2.5 and 15 ppm, those sensors show the highest relative response, but the contact with the target gas induces irreversible changes in the material giving rise to devices with a short lifetime.

In contrast, odor disturbance is felt below 1.5 ppm (Malone Rubright et al., 2017), and the guideline value likely to protect the public from H_2S odor nuisance established by the World Health Organization is 7 $\mu g/m^3$ (i.e., 4 ppb for an averaging time of 30 min) (World Health Organization, 2000); only few studies characterize the sensors at the sub-ppm level. The lack of characterization at lower concentrations is not specific to CP-based sensors. Indeed, a similar trend is observed on MOx sensors (Mirzaei et al., 2018). According to **Figure 4A**, PANI-nanofibers decorated with gold nanoparticles are the lonely CP-based material characterized below 50 ppb (Shirsat et al., 2009). Presenting a good response even at a lower concentration (−20% at 0.1 ppb), this nanostructured hybrid material highlights the high potential of CP-based sensors. Indeed, it largely outperforms chemiresistive sensors based on metal oxide nanostructures, whose best combination (i.e., highest response at the lowest concentration) is −33% at 10 ppb for CuO nanowires (Mirzaei et al., 2018).

Given the necessity of real-time measurement, the rapidity of the sensor is also an important parameter to consider. This parameter is often characterized by the response time and less systematically by the recovery time, which are the times to reach 90% of the resistance change upon injection of the target gas and reference gas (air or nitrogen), respectively. As shown in **Figure 4B**, the response time of pure CPs comprised the range 100–300 s. In general, the addition of MOx allows reducing the response time, to values lower than 120 s. The lowest response time (2.5 s at 5 ppm) is observed on nanostructured WO_3 functionalized with polythiophene. Despite the increase in the response time with the concentration of H_2S, it is still lower than 35 s even at 200 ppm (Bai et al., 2014). In addition, this material shows a fast recovery (<15 s). The hierarchical structure of the material can be one reason for this high rapidity. Here, the hybridization of CPs and the fabrication of an open hierarchical structure appear as functional approaches to enhancing the velocity of CP-based devices.

Beyond the sensitivity and velocity, selectivity needs to be considered in order to evaluate the performance of a device. Ammonia is the interfering species most frequently investigated on CP-based chemiresistive sensors dedicated to H_2S sensing (**Supplementary Tables 1–5**). Commonly inducing an opposite change of resistance than H_2S, ammonia can induce high response, which can disturb the ability of the sensor to quantify the target gas as seen on carbon-based hybrids and some of

pure CPs. The hybridization with metal, MOx, or metal chloride seems to enhance the selectivity toward H_2S. However, the exact benefit of the fillers on the selectivity is difficult to prove given the fact that the interfering studies are most of the time only conducted on the best composite and not on its different components. Further investigations are necessary to clarify the origin of increased selectivity in order to rationalize the research on sensitive material.

Then, the stability of the material under different environmental conditions is crucial to turning those CP-based sensors effective on the field. This pre-requisite encompasses two main capacities of the devices: (i) the preservation of its behavior under different humidities and temperatures and (ii) the conservation of its performance over time. Those two parameters undergo a lack of consideration in the literature. Indeed, <25% of the studies address the impact of humidity or time. When the increase in humidity can induce an increase or a decrease in response depending on the material, the mechanisms at the origin of this changing behavior are rarely explicated. Moreover, only short-term aging is considered. CP-based sensors seem stable for a few weeks. For example, WO_3 nanoparticles decorated by PPy maintain 83% of its response toward 1 ppm of H_2S after 54 days (Su and Peng, 2014), which corresponds to the longest aging test.

CONCLUSION AND PERSPECTIVES

Finally, working at room temperature, easily tuned by changing monomers or dopants, easily processed, and integrated into low-cost and miniaturized devices, CPs present a large potential in H_2S sensing applications. The common approach to enhancing their sensing performance while retaining the advantages from their polymeric nature is to hybridize them with inorganic fillers (e.g., noble metal particles, metal oxide or chloride items, and carbon-based nano-objects). The addition of those fillers allows decreasing the limit of detection and the response time, leading to composites competing with MOx sensors. However, more investigation is needed to be able to establish a clear link between the material properties (chemical nature and morphology) and its sensing performance. Moreover, none of the sensors developed have been employed in realistic situations. Indeed, the impact of interfering species (other reducing/oxidizing gas), environmental conditions (humidity and temperature), and time should be examined more systematically. While field measurement can be complicated to implement, experiments with continuous changes in H_2S concentration, using gas mixture as reference and controlled humidity/temperature, can easily be done in laboratory in order to validate the applicative potential of the materials under investigation.

AUTHOR CONTRIBUTIONS

CD made the illustrations and the main part of the bibliographic, analytic, and writing work. M-LB participated in the bibliographic research. J-LW and NR participated in the reflection and correction. All authors contributed to the article and approved the submitted version.

FUNDING

The study has been funded by Institut Mines-Télécom Lille Douai (IMT Lille Douai).

ACKNOWLEDGMENTS

The authors gratefully acknowledge Alexis Vlandas (CNRS, IEMN) and Sabine Crunaire (IMT Lille Douai) for their corrections and fruitful discussions and Patricia Krawczak (IMT Lille Douai) for the opportunity to participate in the article collection Women in Science: Materials.

SUPPLEMENTARY MATERIAL

The Supplementary Material for this article can be found online at: https://www.frontiersin.org/articles/10.3389/fmats.2020.00215/full#supplementary-material

REFERENCES

Agbor, N. E., Petty, M. C., and Monkman, A. P. (1995). Polyaniline thin films for gas sensing. *Sensors Actuators B. Chem.* 28, 173–179. doi: 10.1016/0925-4005(95)01725-9

Anderson, T., and Roth, S. (1994). Conducting polymers: electrical transport and current applications. *Braz. J. Phys.* 24, 746–754.

Bai, H., and Shi, G. (2007). Gas sensors based on conducting polymers. *Sensors* 7, 267–307. doi: 10.3390/s7030267

Bai, S., Zhang, K., Sun, J., Zhang, D., Luo, R., Li, D., et al. (2014). Polythiophene-WO_3 hybrid architectures for low-temperature H2S detection. *Sensors Actuators B. Chem.* 197, 142–148. doi: 10.1016/j.snb.2014.02.038

Bärtsch, M., and Niederberger, M. (2017). The role of interfaces in heterostructures. *ChemPlusChem* 82, 42–59. doi: 10.1002/cplu.201600519

Beauchamp, R. O., Bus, J. S., Popp, J. A., Boreiko, C. J., Andjelkovich, D. A., and Leber, P. (1984). A critical review of the literature on hydrogen sulfide toxicity. *Crit. Rev. Toxicol.* 13, 25–97. doi: 10.3109/10408448409029321

Chabukswar, V. V., Bhavsar, S. V., Horne, A. S., Handore, K., Gaikwad, V. B., and Mohite, K. C. (2013). Conducting poly(N-propylaniline) nanoparticles for hydrogen sulfide gas detection. *Macromol. Symp.* 327, 39–44. doi: 10.1002/masy.201350504

Cho, S., Lee, J. S., Jun, J., Kim, S. G., and Jang, J. (2014). Fabrication of water-dispersible and highly conductive PSS-doped PANI/graphene nanocomposites using a high-molecular weight PSS dopant and their application in H_2S detection. *Nanoscale* 6, 15181–15195. doi: 10.1039/C4NR04413D

Crowley, K., Morrin, A., Shepherd, R. L., In Het Panhuis, M., Wallace, G. G., Smyth, M. R., et al. (2010). Fabrication of polyaniline-based gas sensors using piezoelectric inkjet and screen printing for the detection of hydrogen sulfide. *IEEE Sens. J.* 10, 1419–1426. doi: 10.1109/JSEN.2010.2044996

Dong, X., Zhang, X., Wu, X., Cui, H., and Chen, D. (2016). Investigation of gas-sensing property of acid-deposited polyaniline thin-film sensors for detecting H_2S and SO_2. *Sensors* 16:1889. doi: 10.3390/s16111889

Dongmin Kang, S., and Jeffrey Snyder, G. (2017). Charge-transport model for conducting polymers. *Nat. Mater.* 16, 252–257. doi: 10.1038/nmat4784

Fratoddi, I., Venditti, I., Cametti, C., and Russo, M. V. (2015). Chemiresistive polyaniline-based gas sensors: a mini review. *Sensors Actuators B. Chem.* 220, 534–548. doi: 10.1016/j.snb.2015.05.107

Gaikwad, G., Patil, P., Patil, D., and Naik, J. (2017). Synthesis and evaluation of gas sensing properties of PANI based graphene oxide nanocomposites. *Mater. Sci. Eng. B Solid State Mater. Adv. Technol.* 218, 14–22. doi: 10.1016/j.mseb.2017.01.008

Garg, R., Kumar, V., Kumar, D., and Chakarvarti, S. K. (2015). Polypyrrole microwires as toxic gas sensors for ammonia and hydrogen sulphide. *J. Sensors Instrum.* 3, 1–13. doi: 10.7726/jsi.2015.1001

Geng, L., Huang, X., Zhao, Y., Li, P., Wang, S., Zhang, S., et al. (2006). H_2S sensitivity study of polypyrrole/WO_3 materials. *Solid. State. Electron.* 50, 723–726. doi: 10.1016/j.sse.2006.04.024

Guo, Z., Chen, G., Zeng, G., Liu, L., and Zhang, C. (2015). Metal oxides and metal salt nanostructures for hydrogen sulfide sensing: mechanism and sensing performance. *RSC Adv.* 5, 54793–54805. doi: 10.1039/C5RA10394K

Habeeb, O. A., Kanthasamy, R., Ali, G. A. M., Sethupathi, S., and Yunus, R. B. M. (2018). Hydrogen sulfide emission sources, regulations, and removal techniques: a review. *Rev. Chem. Eng.* 34, 837–854. doi: 10.1515/revce-2017-0004

Hangarter, C. M., Chartuprayoon, N., Hernández, S. C., Choa, Y., and Myung, N. V. (2013). Hybridized conducting polymer chemiresistive nano-sensors. *Nano Today* 8, 39–55. doi: 10.1016/j.nantod.2012.12.005

Iqbal, S., and Ahmad, S. (2018). Recent development in hybrid conducting polymers: synthesis, applications and future prospects. *J. Ind. Eng. Chem.* 60, 53–84. doi: 10.1016/j.jiec.2017.09.038

Joshi, N., Hayasaka, T., Liu, Y., Liu, H., Oliveira, O. N., and Lin, L. (2018). A review on chemiresistive room temperature gas sensors based on metal oxide nanostructures, graphene and 2D transition metal dichalcogenides. *Microchim. Acta* 185:213. doi: 10.1007/s00604-018-2750-5

Joshi, N., Saxena, V., Singh, A., Koiry, S. P., Debnath, A. K., Chehimi, M. M., et al. (2014). Flexible H_2S sensor based on gold modified polycarbazole films. *Sensors Actuators B. Chem.* 200, 227–234. doi: 10.1016/j.snb.2014.04.041

Kaushik, A., Kumar, R., Arya, S. K., Nair, M., Malhotra, B. D., and Bhansali, S. (2015). Organic-inorganic hybrid nanocomposite-based gas sensors for environmental monitoring. *Chem. Rev.* 115, 4571–4606. doi: 10.1021/cr400659h

Kivelson, S., and Heeger, A. J. (1988). Intrinsic conductivity of conducting polymers. *Synth. Met.* 22, 371–384. doi: 10.1016/0379-6779(88)90108-7

Korotcenkov, G., and Cho, B. K. (2017). Metal oxide composites in conductometric gas sensors: achievements and challenges. *Sensors Actuators B. Chem.* 244, 182–210. doi: 10.1016/j.snb.2016.12.117

Kriván, E., Visy, C., Dobay, R., Harsányi, G., and Berkesi, O. (2000). Irregular response of the polypyrrole films to H_2S. *Electroanalysis* 12, 1195–1200. doi: 10.1002/1521-4109(200010)12:15andlt;1195::AID-ELAN1195andgt;3.0.CO;2-1

Krukiewicz, K., and Katunin, A. (2016). The effect of reaction medium on the conductivity and morphology of polyaniline doped with camphorsulfonic acid. *Synth. Met.* 214, 45–49. doi: 10.1016/j.synthmet.2016.01.017

Le, T.-H., Kim, Y., and Yoon, H. (2017). Electrical and electrochemical properties of conducting polymers. *Polymers.* 9:150. doi: 10.3390/polym9040150

Li, W., and Wan, M. (1999). Stability of polyaniline synthesized by a doping-dedoping-redoping method. *J. Appl. Polym. Sci.* 71, 615–621. doi: 10.1002/(SICI)1097-4628(19990124)71:4andlt;615::AID-APP13andgt;3.0.CO;2-O

Lim, J. H., Phiboolsirichit, N., Mubeen, S., Deshusses, M. A., Mulchandani, A., and Myung, N. V. (2010). Electrical and gas sensing properties of polyaniline functionalized single-walled carbon nanotubes. *Nanotechnology* 21:75502. doi: 10.1088/0957-4484/21/7/075502

Liu, C., Hayashi, K., and Toko, K. (2012). Au nanoparticles decorated polyaniline nanofiber sensor for detecting volatile sulfur compounds in expired breath. *Sensors Actuators B. Chem.* 161, 504–509. doi: 10.1016/j.snb.2011.10.068

Llobet, E., Brunet, J., Pauly, A., Ndiaye, A., and Varenne, C. (2017). Nanomaterials for the selective detection of hydrogen sulfide in air. *Sensors* 17, 1–19. doi: 10.3390/s17020391

Malone Rubright, S. L., Pearce, L. L., and Peterson, J. (2017). Environmental toxicology of hydrogen sulfide. *Nitric Oxide.* 71, 1–13. doi: 10.1016/j.niox.2017.09.011

Mekki, A., Joshi, N., Singh, A., Salmi, Z., Jha, P., Decorse, P., et al. (2014). H_2S sensing using *in situ* photo-polymerized polyaniline-silver nanocomposite films on flexible substrates. *Org. Electron.* 15, 71–81. doi: 10.1016/j.orgel.2013.10.012

Mirzaei, A., Kim, S. S., and Kim, H. W. (2018). Resistance-based H_2S gas sensors using metal oxide nanostructures: a review of recent advances. *J. Hazard. Mater.* 357, 314–331. doi: 10.1016/j.jhazmat.2018.06.015

Moseley, P. T., Norris, J. O. W., and Williams, D. E. (1991). *Technique and Mechanism in Gas Sensing*, ed A. Hilger. Bristol: Taylor & Francis.

National Research Council (US) Committee on Acute Exposure Guideline Levels (2010). "4 hydrogen sulfide acute exposure guideline levels," in *Acute Exposure Guideline Levels for Selected Airborne Chemicals* (Washington, DC: National Academies Press), 173–218.

Nylabder, C., Armgrath, M., and Lundstrom, I. (1983). "An ammonia detector based on a conducting polymer," in *International Meeting on Chemical Sensors* (Fukuoka), 203–207.

Occupational Safety and Health Administration, USA (2020). *OSHA Standards: Hydrogen Sulfide Exposure*. OSHA. Available online at: https://www.osha.gov/SLTC/hydrogensulfide/hazards.html (accessed Sepetember 17, 2020).

Palaniappan, S., and Saravanan, C. (2010). Polyaniline–maleicacid–dodecylhydrogensulfate salt as sensor material for toxic gases. *J. Appl. Polym. Sci.* 118, 518–524. doi: 10.1002/app.32347

Pandey, S. K., Kim, K. H., and Tang, K. T. (2012). A review of sensor-based methods for monitoring hydrogen sulfide. *TrAC Trends Anal. Chem.* 32, 87–99. doi: 10.1016/j.trac.2011.08.008

Park, S. J., Park, C. S., and Yoon, H. (2017). Chemo-electrical gas sensors based on conducting polymer hybrids. *Polymers.* 9:155. doi: 10.3390/polym9050155

Patil, Y. S., Salunkhe, P. H., Navale, Y. H., Patil, V. B., Ubale, V. P., and Ghanwat, A. A. (2019). Tetraphenylthiophene–thiazole-based π-conjugated polyazomethines: synthesis, characterization and gas sensing application. *Polym. Bull.* 77, 2205–2226. doi: 10.1007/s00289-019-02856-2

Phillips, P., and Wu, H. L. (1991). Localization and its absence: a new metallic state for conducting polymers. *Science.* 252, 1805–1812. doi: 10.1126/science.252.5014.1805

Ramgir, N. S., Sharma, P. K., Datta, N., Kaur, M., Debnath, A. K., Aswal, D. K., et al. (2013). Room temperature H_2S sensor based on Au modified ZnO nanowires. *Sensors Actuators B. Chem.* 186, 718–726. doi: 10.1016/j.snb.2013.06.070

Sarfraz, J., Ihalainen, P., Määttänen, A., Peltonen, J., and Lindén, M. (2013). Printed hydrogen sulfide gas sensor on paper substrate based on polyaniline composite. *Thin Solid Films* 534, 621–628. doi: 10.1016/j.tsf.2013.02.055

Serban, B., Cobianu, C., and Brezeanu, M. (2014). Hydrogen sulphide sensing review. *Ann. Acad. Romanian Sci. Ser. Sci. Technol. Inf.* 7, 55–67.

Shirsat, M. D., Bangar, M. A., Deshusses, M. A., Myung, N. V., and Mulchandani, A. (2009). Polyaniline nanowires-gold nanoparticles hybrid network based chemiresistive hydrogen sulfide sensor. *Appl. Phys. Lett.* 94, 2012–2015. doi: 10.1063/1.3070237

Shu, J., Qiu, Z., Lv, S., Zhang, K., and Tang, D. (2017). Cu^{2+}-doped SnO_2 nanograin/polypyrrole nanospheres with synergic enhanced properties for ultrasensitive room-temperature H_2S gas sensing. *Anal. Chem.* 89, 11135–11142. doi: 10.1021/acs.analchem.7b03491

Silvester, E. J., Grieser, F., Sexton, B. A., and Healy, T. W. (1991). Spectroscopic studies on copper sulfide sols. *Langmuir* 7, 2917–2922. doi: 10.1021/la00060a009

Skoog, D. A., and West, D. M. (Eds.) (1963). *Fundamentals of Analytical Chemistry, 3rd Edn*. New York, NY: Holt, Rinehart, and Winston.

Skotheim, T. A., and Reynolds, J. R. (Eds.). (2007). *Handbook of Conducting Polymers - Conjugated Polymers Processing and Applications*, *3rd Edn*. Boca Raton, FL: CRC Press Taylor and Francis Group.

Su, P. G., and Peng, Y. T. (2014). Fabrication of a room-temperature H_2S gas sensor based on PPy/WO_3 nanocomposite films by *in-situ* photopolymerization. *Sensors Actuators B. Chem.* 193, 637–643. doi: 10.1016/j.snb.2013.12.027

Tranchida, P. Q., Franchina, F. A., Dugo, P., and Mondello, L. (2016). Comprehensive two-dimensional gas chromatography- mass spectrometry: recent evolution and current trends. *Mass Spectrom. Rev.* 35, 524–534. doi: 10.1002/mas.21443

Varghese, S. S., Lonkar, S., Singh, K. K., Swaminathan, S., and Abdala, A. (2015). Recent advances in graphene based gas sensors. *Sensors Actuators B. Chem.* 218, 160–183. doi: 10.1016/j.snb.2015.04.062

Virji, S., Fowler, J. D., Baker, C. O., Huang, J., Kaner, R. B., and Weiller, B. H. (2005). Polyaniline nanofiber composites with metal salts: chemical sensors for hydrogen sulfide. *Small* 1, 624–627. doi: 10.1002/smll.200400155

Walker, J. M., Akbar, S. A., and Morris, P. A. (2019). Synergistic effects in gas sensing semiconducting oxide nano-heterostructures: a review. *Sensors Actuators B. Chem.* 286, 624–640. doi: 10.1016/j.snb.2019.01.049

Wong, Y. C. Y. H., Ang, B. C., Haseeb, A. S. M. A., Baharuddin, A. A., and Wong, Y. C. Y. H. (2020). Review—conducting polymers as chemiresistive gas sensing materials: a review. *J. Electrochem. Soc.* 167:037503. doi: 10.1149/2.0032003JES

World Health Organization (2000). *Air Quality Guidelines for Europe. Second*. Copenhagen: WHO.

Zhang, D., Wu, Z., and Zong, X. (2019). Flexible and highly sensitive H_2S gas sensor based on *in-situ* polymerized SnO_2/rGO/PANI ternary nanocomposite with application in halitosis diagnosis. *Sensors Actuators B. Chem.* 289, 32–41. doi: 10.1016/j.snb.2019.03.055

Zoccali, M., Tranchida, P. Q., and Mondello, L. (2019). Fast gas chromatography-mass spectrometry: a review of the last decade. *TrAC Trends Anal. Chem.* 118, 444–452. doi: 10.1016/j.trac.2019.06.006

Conflict of Interest: The authors declare that the research was conducted in the absence of any commercial or financial relationships that could be construed as a potential conflict of interest.

Structural Materials

Maria Chiara Bignozzi

Prof. Maria Chiara Bignozzi (MCB) is an associate professor in Materials Science and Technology at the School of Engineering and Architecture, Alma Mater Studiorum University of Bologna, Italy, and director of Centro Ceramico (www.centroceramico.it). She is also involved in European and international standards, being a Convener of WG1 "Test methods" for ISO TC 189 and CEN TC 67 "Ceramic tiles". Her research activity is mainly concerned with building materials (ceramic tiles, geopolymers/alkali-activated materials, concrete, cement, etc.) and their physical-mechanical performances, durability, and sustainability features.

Chiara Magrini

Chiara Magrini is a Ph.D. candidate in the Department of Civil, Chemical, Environmental, and Materials Engineering (DICAM), University of Bologna, Italy, under the supervision of Professor Alessandra Bonoli. Her research focuses on waste prevention and management, both at the European and regional levels (Emilia-Romagna region, Italy). She has worked on projects co-funded by the European Institute of Innovation and Technology-EIT, Climate-KIC.

Alessandra Bonoli

Prof. Alessandra Bonoli is an associate professor at the University of Bologna. Her main research topics are in Environmental Engineering with particular regard to treatment, recovery, and recycling of raw materials and solid waste; the life cycle assessment and circular economy; and the dissemination of urban green technologies and unconventional building materials for climate change resilience in urban areas. She founded and currently coordinates the research group of Transition Engineering whose activities are aimed at building a sustainable future, from an environmental, social, and economical point of view, through conservation and valorization of natural resources, raw materials, water, and energy. She is a delegate of UNIBO at the UN Sustainable Development Solutions Network (UN, New York) and UE Commission Operational Groups of the European Innovation Partnership on Raw Materials (EIP Raw Materials).

Severine A. E. Boyer

Dr. Séverine A.E. Boyer is a CNRS Research Officer at MINES-Paris/PSL – CEMEF-CNRS 7635 (Sophia Antipolis, France), and she wrote her Ph.D. Dissertation in 2003 with IFPEN. She conducts fundamental and finalized studies on the mechanisms of the poly-morphogenesis/deformation of structural synthetic and natural organic systems to develop or recycle functional and original materials and predict their use. She has developed chains of original experimental and numerical models connecting the multi-scale structure from a chemical-molecular size to a macroscopic size in complex and extreme environments (species diffusion, thermodynamic, or not equilibrium). Her international recognitions include the following: Thesis - 'William F. Giauque Student Award, CALCON 2003 (USA)'; Young Researcher - "ICTAC Young Scientific Award, ICTAC 2012 (Japan)" (first time awarded to a French researcher); 'First Place Best Poster, PPS 2019 (South Africa)'; and awards given to her collaborative colleagues.

Vilma Ducman

Dr. Vilma Ducman, head of the Laboratory for Cements, Mortars, and Ceramics at ZAG, has been involved in the research of ceramic building products and the development of recycled (lightweight) aggregate and composites. In the last 10 years, she has also been actively involved in the research and development of alkali-activated materials. She has led or been involved in many projects (both national and international) on recycling and the development of new building materials or products. She has published over 50 articles in scientific journals and over 100 in professional magazines and conference proceedings, and she has also acquired four SI patents on recycling.

Stefania Manzi

Prof. Stefania Manzi is an Associate Professor in Materials Science and Technology at the School of Engineering and Architecture, University of Bologna, Italy. She has a Master's degree cum laude in Building Engineering and a Ph.D. in Materials Engineering. Her research activity mainly concerns materials for civil and building engineering, architectural restoration, and the most innovative production and setting processes. She has taught various courses in the field of Materials Science and Technology to students of Building Engineering, Building Engineering/Architecture, Civil Engineering, Industrial Design, Chemical and Process Engineering, and Environmental Engineering at the University of Bologna.

frontiers in Materials

ORIGINAL RESEARCH
published: 17 September 2020
doi: 10.3389/fmats.2020.572514

Gender Balance in Construction Material Research: The Analysis of Alkali-Activated Materials by a Bibliometric Study Using Scopus Database

*Giulia Masi, Stefania Manzi and Maria Chiara Bignozzi**

Department of Civil, Chemical, Environmental and Materials Engineering, University of Bologna, Bologna, Italy

Research in alkali-activated materials (AAMs) is an innovative and dynamic material science topic. This is due to the relevant performances in terms of physico-mechanical properties comparable to traditional construction materials (e.g., ordinary Portland cement). The sustainability of AAMs is often highlighted since they can be developed by using many natural or industrial by-products–based precursors. This leads to challenges with the optimization of AAM production due to their different performances, availability, and costs. However, they are flexible and locally adapted materials. The research interest in AAMs has rapidly increased in the early 2000s. In recent years, about 1,000 international articles have been published each year. This study aims at assessing the gender balance of this specific research topic to investigate the relevance of women's participation. Author lists of the published articles were analyzed throughout the Scopus database, applying "alkali-activated material" and "geopolymers" as keywords in the titles, abstracts, and keywords search. The last 10 years (2009–2019) were taken into account. The gender of the most prolific authors was analyzed, and a focus of European authors on this topic was considered, as more than 25% of the research in AAMs have been carried out in Europe. The analysis of 5,900 publications in the last decade shows that there is currently a shift toward men in the gender balance in this specific research, and female authors only covered 22% of the most productive authors worldwide. Considering European authors, a more equal gender distribution is reached, when the first author is considered, with a concentration of women in the range of 36–56%, recorded over 1,396 articles.

Keywords: geopolymers, gender balance, bibliometry, alkali activation, Scopus database, alkali activated materials

OPEN ACCESS

Edited by:
Claire Emily White,
Princeton University, United States

Reviewed by:
Ailar Hajimohammadi,
University of New South Wales, Australia
Francisca Puertas Maroto,
Eduardo Torroja Institute for Construction Sciences (IETcc-CSIC), Spain

****Correspondence:***
Maria Chiara Bignozzi
maria.bignozzi@unibo.it

Specialty section:
This article was submitted to Structural Materials, a section of the journal Frontiers in Materials.

Received: *23 June 2020*
Accepted: *26 August 2020*
Published: *17 September 2020*

Citation:
Masi G, Manzi S and Bignozzi MC (2020) Gender Balance in Construction Material Research: The Analysis of Alkali-Activated Materials by a Bibliometric Study Using Scopus Database. Front. Mater. 7:572514. doi: 10.3389/fmats.2020.572514

INTRODUCTION

Literature Review on Alkali-Activated Materials and Geopolymers

Nowadays, all around the world concrete is the main widely employed construction material. Moreover, its consumption is constantly increasing, due to its rising demand in developing countries. On the other hand, the production of cement has a huge impact on the environment. Worldwide, it has been estimated that the cement sector is responsible for nearly 8% of all carbon dioxide (CO_2) emissions caused by anthropic actions. Indeed, it is well known that the manufacturing of 1 ton of Portland cement implies the emission of almost the same amount of CO_2 in atmosphere, although

during its entire life cycle, carbonation of cement allows for CO_2 sequestration (for a cumulative amount of 4.5 GtC measured between 1930 and 2013) and determines an adjustment of CO_2 emissions (43% calculated considering the same period) related to cement production (Xi et al., 2016). Moreover, taking into account the period of time from 1990 to 2050, a rise in cement manufacturing of nearly 250% is expected (Imbabi et al., 2012; Scrivener et al., 2018), even if economic crisis due to external factors (e.g., COVID emergency) may locally modify this scenario.

The first use of the term "alkali activation" dates back to 1908, but only in the 1930s–1950s Purdon carried out some work on this technology in Belgium (Palomo et al., 2014; Provis, 2014). The real development of alkali activation was due to an extensive research program by Glukhovsky starting from the 1950s (Provis, 2014). The term "geopolymer" was introduced in the 1970s by Davidovits, indicating the alkali activation of metakaolinite, limestone, and dolomite (Palomo et al., 2014).

Especially in the last two decades, alkali-activated materials (AAMs), including geopolymers, have quickly caught people's interest, in order to reduce CO_2 emissions due to cement and ceramic material productions (Provis, 2014; Pacheco-Torgal et al., 2017; Sandanayake et al., 2018; Asim et al., 2019; Rakhimova and Rakhimov, 2019b; Shi et al., 2019; Singh and Middendorf, 2020). Alkali activation is the general expression used for the reaction of a precursor (i.e., a solid aluminosilicate) in an alkaline environment sourced by alkali activators to obtain a hardened binder mainly based on hydrous alkali aluminosilicate. This explanation can even include low amount of traditional cement together with elevated combinations of blast furnace slag or pozzolans. However, when cement is the principal origin of alkalinity, these kinds of binders are not considered in the alkali activation nomenclature (Bignozzi and Bonduà, 2011). Moreover, the term geopolymer is largely used, sometimes also in a quite indiscriminate way, to account for low calcium AAMs. Finally, hybrid binders containing both cement and a source of alkalis together with aluminosilicate elements have also been developed. Nevertheless, in general, all these systems may be considered as part of the wider field of alkali activation (Provis and Bernal, 2014; Provis et al., 2015; Provis, 2018; Provis and van Deventer, 2019; Shi et al., 2019).

AAMs can be synthetized by two main routes: i) a one-part mix (dry precursors and activators activated by water) and ii) a two-part mix (dry powder combined with activating solutions) procedure. Alkali activation by the two-part mix approach has been for sure the most investigated and used in the first applications of alkali activation–based products introduced in the market. The two-part mixture is used in the precast production, where packaging and transporting of chemical substances, together with curing conditions, can be managed at a close range (Provis, 2018; Singh and Middendorf, 2020). On the other hand, studies are being carried out to improve the one-part methodology and to develop products suitable for the market, so this methodology would be widely employed henceforth (Luukkonen et al., 2018).

As solid precursors for the production of AAMs, typical aluminosilicate supplementary cementitious precursors can be used (Rakhimova and Rakhimov, 2019a), including blast furnace slag, coal fly ash (Zhuang et al., 2016), calcined clays, and natural pozzolans (Robayo-Salazar and Mejía de Gutiérrez, 2018) that have shown high-quality outcomes. Blast furnace slags used in alkali activation need to be granulated and ground. Additions exhibiting pozzolanic behavior, generally utilized in cement blends only to a lower extent, can be suitable for alkali activation as well. Various types of slags (cooled until a reactive condition and finely ground), sludges coming from industrial processing, ashes of different nature and origin (Hertel and Pontikes, 2020), etc., can also be employed in alkali activation, ensuring their safe use in terms of leachability of potentially toxic elements (Provis, 2018; Singh and Middendorf, 2020). As alkali activators, $M_2O{\cdot}rSiO_2$ and MOH (with M = Na or K) are the most utilized chemicals (Silva et al., 2017; Provis, 2018; Rakhimova and Rakhimov, 2019a).

Inter-grinding or co-calcination of different aluminosilicate powder precursors and solid activators have been demonstrated to be effective in the synthesis of one-part AAMs, thus promoting their development (Luukkonen et al., 2018; Provis, 2018).

The great variability of precursors and activators available worldwide does not allow one to design one or more model mixes that are always applicable; thus, studying fundamental rules to properly set up *ad hoc* mix designs together with a precise quality control and characterization of the starting materials is a challenge that needs to be addressed. The control of setting time, the choice of suitable admixtures, and the curing conditions are some of the features under investigation. For example, when a low quantity of calcium was present in the fly ash used as precursor, alkali activation at room temperature obtaining outstanding mechanical properties was demonstrated (Bignozzi et al., 2014). At the same time, also clay-based binders can harden quickly at room temperature; however, the amount of water added, as function of particle size, can strongly influence the setting time and workability. Generally speaking, sealed curing is highly indicated for AAMs.

A large number of AAMs and geopolymers have been studied so far, from the point of view of chemical, microstructural, physical, mechanical, and durability performances of precursors and hardened products (Bignozzi et al., 2013; Masi et al., 2014; Singh et al., 2015; Ma et al., 2018; Zhang et al., 2018; Hassan et al., 2019; Li et al., 2019; Tang et al., 2019; Wu et al., 2019; Saccani et al., 2020; Mugahed Amran et al., 2020); however, it is still difficult to think that alkali-activated binders will soon be ready for complete substitution of cement in all the applications where it is normally involved. AAMs are surely attractive for their potentially high degree of sustainability, especially when they are obtained with raw materials and/or waste locally available, without requiring thermal and/or specific separation treatments (Pacheco-Torgal et al., 2017; Rakhimova and Rakhimov, 2019b; Shi et al., 2019; Singh and Middendorf, 2020).

The field of application of AAMs is broad (Wu et al., 2019), and is still increasing, with exploitations in renders, grouts, mortars, lightweight and foamed concrete (Carabba et al., 2019a), precast concrete elements, plain and reinforced concrete (Kamseu et al., 2014; Monticelli et al., 2016a;

Monticelli et al., 2016b; Mo et al., 2016; Carabba et al., 2017b; Tittarelli et al., 2018; Hassan et al., 2019), pipes, or matrix for nuclear or toxic waste immobilization (Rasaki et al., 2019; Singh and Middendorf, 2020). Moreover, features such as high temperatures and chemical attack resistance make AAMs particularly attractive for specific applications such as refractory blocks, passive fire protection systems, and sewer pipes (Pacheco-Torgal et al., 2012; Masi et al., 2015; Carabba et al., 2017a; Carabba et al., 2019b; Rashidian-Dezfouli and Rangaraju, 2017; Zhang et al., 2017; Ameri et al., 2019; Carabba et al., 2019b; Lahoti et al., 2019; Wang et al., 2020).

Gender Equality in Material Science

Gender equality represents a major issue in all science, technology, engineering, and mathematics (STEM) fields. Traditionally, women are underrepresented in these sectors. Among the others, women underrepresentation in material science and engineering is an historical problem (The University Materials Council, 2008; Larivière et al., 2013). In addition, the trend related to the presence of women decreases especially at the highest level of academic careers or when high responsibility positions are considered within scientific decision-making bodies (European Commission, 2008; European Commission, 2010).

Considering all the fields of life, in the last 5 years in Europe, some improvements have been achieved (European Commission, 2015): women's employment reached 64% (the highest rate ever recorded) and an improvement in the presence of women was recorded in decision-making positions in many spheres of life (+9% of women as board members in the biggest listed companies). These results are related to some of the policies sponsored by the European Commission in the first years of the 2000s. In particular, the Commission's 2010–2015 strategies for bridging the gender gap consisted in the following principles: equal economic independence for women and men; work of equal value shall be equally paid; decision-making, dignity, integrity, and ending gender-based violence are equally assessed; and last, gender equality is promoted beyond European Union (EU) (European Commission, 2015). It was demonstrated that major improvements were achieved in those countries where introduced legislative measures were properly addressed (European Commission, 2015). In addition, in the early 2000s, a group of women scientists was involved in a European Technology Assessment Network group to explore and make recommendations on the issue of women in science in Europe. The European Technology Assessment Network group proposed three models to promote gender equality, which consisted of equal treatment between men and women, positive action, and mainstreaming (Rees, 2001). In particular, they identified gender mainstreaming as the most positive action for a long-term strategy, in order to contribute to bridging the gender balance. This was because equal treatment refers to individuals' rights with the aim of equality, and a positive action can partly improve the gender gap. On the contrary, gender mainstreaming can recast the systems and structures themselves that currently advantage men. In addition, several recommendations, mainly focused on the science, engineering, and medicine sectors, have been proposed to promote gender equity, in terms of direct economic support, strategies related to psychology and culture, and major collaborative and international motivations (Smith et al., 2015).

However, gender inequalities are still present in education and in occupations, especially in STEM and related careers in the EU and worldwide (Shen, 2013; European commission, 2015; Kang et al., 2019; Stoet and Geary, 2018). Many factors influence these differences. First, gender inequalities in education still persist, in terms of study subject preferences, performance, and participation (Kang et al., 2019; Stoet and Geary, 2018). At the age of 11 or 12 years, students begin their career aspirations which will be developed on the basis of their studies during the secondary school. In particular, the perception of STEM careers by females is generally stereotyped, as it is perceived with less time for oneself and as an obstacle for achieving the traditional life goals (family, children, etc.). For these reasons, higher involvement in scientific subjects in schools could help bridge the gender gap in the selection of future careers (Kang et al., 2019). In addition, women are more likely to have a higher education (even, if according to the United States National Science Foundation, grants for women are about half of the grants for men during their doctorates in the United States), but female scientists still face major challenges [e.g., in United States, women represent only 21 and 5% of full science and full engineering professors, respectively (Shen, 2013); in Italy, female full professors in the scientific sector of "materials science and technology" are only 26% (https://cercauniversita.cineca.it/)]. One of the most persistent issues is that a large part of qualified female researchers quit in the early stages of their science careers. This is mainly linked to several aspects, such as family values (women in postdoc positions drop out of research careers when they become parents or plan to have children, up to twice as often as men with families), life issues and discriminations, and pay problems (in the EU public sector, women in science earned 25–40% less than male scientists in 2006) (Shen, 2013).

One of the tools to investigate gender distribution in any field of science and engineering is the study of journal authorship, journal editorial boards, and the extent of collaborations, due to the fact that generally journal publications are the main outcomes indicating scientific and technological productivity, as well as the main channel for communicating new knowledge (Larivière et al., 2013; Mauleón et al., 2013; West et al., 2013). A cross-disciplinary bibliometric study on the relationship between gender and research outputs by Larivière et al. highlighted that men dominated in scientific production in nearly every country worldwide and women were underrepresented, especially when first authorship was considered (Larivière et al., 2013). Moreover, another research analyzed the gender distribution in paper authorship, as well as the compositions of editorial boards of Spanish journals in the years between 1998 and 2009 (Mauleón et al., 2013). They found that female presence was lower that of men, but the gender gap was narrowing in the last period of the analysis, indicating a higher participation and recognition of women. Finally, a bibliometric study based in the United States using JSTOR corpus highlighted an increase of women

in the authorships (27% in 1990–2012 vs. 15% in 1665–1989) and in obtaining higher education degrees (64% of PhD recipients are women in 2004), especially in the first years of the 2000s (West et al., 2013). However, women were still underrepresented in tenure track and research university faculty positions (only 39% in full-time positions). Finally, West et al. demonstrated that whereas, historically, women were underrepresented in the first author positions in journal-article author lists, the situation was more equal in terms of first author, while a gender gap remained when last author positions and single-author articles were considered (West et al., 2013).

Aim of the Study

As previously mentioned, research in AAMs is nowadays a proficient and very active research sector of material science, which is a very broad research field. In addition, this specific topic has recently seen a quick increase in terms of scientific interest and number of published articles and involves many aspects, applications, and research backgrounds (chemistry, material and civil engineering, etc.). AAMs exhibited strong development as a possible replacement of ordinary Portland cement in the construction sector, due to the sustainability features of the production of these materials (Provis, 2018). Traditionally, construction and construction material production are a male-dominated sector. A study by Paul et al. (2020) on gender balance in the European cement industry showed that female authors gain some achievement in terms of presence in scientific publications. Especially it was found that women are very active and involved in the development of strategies to increase sustainability features in cement production. However, women are still underrepresented in this specific sector, and only 33% of contributions are from female authors. Last, due to the relatively recent sensitivity to the gender balance issue and to the increasing involvement of women in research, a quick increase in the selection of a topic such as AAMs in the last two decades may represent a very good opportunity for monitoring the growing presence of female researchers in material science, specifically in the building sector. For all these reasons, the analysis of gender distribution based on a bibliometric study was performed using the Scopus database, including indexed articles on peer-reviewed journals, conference proceedings, and books. This shall be a representative scenario describing gender balance in one specific field of material science. Beyond numerical and geographical distribution of the research outputs, analysis of the gender of the most prolific authors (first 100) in the last decade, between 2009 and 2019, was reported. Last, the European scenario was also discussed in detail, analyzing gender equity in terms of first and last positioned authors in the author lists. This choice was because usually the most important contributors to articles are found in the first and last positions (with one usually overlapping with the name of the corresponding author), especially when some scientific areas (including material science) are considered (Kosmulski, 2012; Simoes and Crespo, 2020). Accordingly, in this study, the corresponding author role was excluded in the analysis as it often coincides with the first author. In addition, the first author is generally the most involved researcher in a specific study, i.e., performing laboratory testing (if any) and writing the main body of the paper, while the last author is usually the one who conceptualizes the research study and/or the director of the research laboratory. Moreover, even if different author orders can be also applied, for example, the alphabetic order when all authors provide the same contribution to the study, this represents more the exception rather than the rule in article publishing. Finally, the impact of the research based in Europe was considered through analysis of the citations of the research outputs, as well as the correlation with gender distribution.

MATERIALS AND METHODS

The bibliometric study was carried out using the Scopus database (https://www.scopus.com). This database indexes content from 24,600 titles and 5,000 publishers which are selected by an independent review board. Scopus generates precise citation results and detailed researcher profiles. Moreover, the selected database takes into consideration only indexed research products; thus, non–peer-reviewed papers published in conference proceedings and articles published in non-indexed journals are not considered in this study.

The keywords used for the bibliometric research were "alkali activated materials" or "geopolymers." In order to refine the results and be sure that all the documents were related to the specific topic, a first refinement of the results was carried out selecting only English language articles, reviews, and conference papers in order to analyze international research studies. A second refinement was based on selecting further keywords with the aim of a more precise delimitation of the topic. In particular, the following keywords were considered: "inorganic polymer," "geopolymer(s)," "alkali activated," "geopolymer concrete," "geopolymer composites," "geopolymer binders," "alkali-activated binder," "alkali-activated cement," "geopolymerization," "alkali-activated slag," "geopolymer mortars," "alkaline activation," "geopolymer materials," "geopolymer matrix," "geopolymer cement," and "alkali-activated fly ash." These refinements allowed us to bring down the number of documents to be analyzed from more than 8,000 to 5,900 documents.

The analysis was carried out as follows: i) the trend of the published articles and the geographical distribution of the authors were processed by the "Analyze search results" tool available in Scopus. ii) The analysis of gender balance was carried out for the first 100 most prolific authors for each year. In order to correctly define the gender of the authors, each author profile was checked using the Scopus database and/or ResearchGate web page (https://www.researchgate.net/) and/or Google Scholar database (https://scholar.google.com/), in which author profile pictures are also usually reported, thus making gender recognition easier. When no information about the author profile (e.g., first name and picture) was available, the specific author was categorized as "undefined." iii) Only for European authors, gender analysis of the first and last authors was carried out considering each author profile. As previously reported, first and last positioned authors usually play the most important roles in manuscript writing and in research development. Moreover, a

correlation with the number of citations was also considered to analyze the impact of the publications related to gender distribution. Number of citations for each article was recorded on May 6th, 2020, on the Scopus database web page.

RESULTS AND DISCUSSION

The following section reports the results of the bibliometric study on gender balance in the field of AAMs, including geopolymers. First, numerical and geographical distribution of published articles is reported. Then, gender analysis of the most prolific authors worldwide is discussed. Last, analysis of the gender balance of European authors is shown, considering first and last authors in the author list, as well as the correlation between author gender and number of citations.

Numerical and Geographical Distribution of Published Articles

The first publication on geopolymers dates back to 1979 by Davidovits. However, only in the first years of the 2000s, this specific research topic started attracting research interests, as depicted in **Figure 1**, probably due to an increasing attention to environmental pollution problems and the consequent need to reduce CO_2 emission in building material production. Especially in the last decade, there has been an exceptional increase in research interest about AAMs (including geopolymers), as demonstrated by the increasing linear trend of published articles between 2009 and 2019 (inlay of **Figure 1**). Specifically, in 2019 almost 1,000 articles were published in scientific peer-reviewed journals and international conference proceedings, highlighting that research on this topic is still strongly active all over the world. Due to this trend in the last 10 years, further analyses about geographical distribution and gender balance were carried out considering only the period between 2009 and 2019.

Geographical distribution of the articles on AAMs published between 2009 and 2019 is shown in **Figure 2**. Most of the articles were published by Chinese (13%), Australian (10%), and Indian (8%) researchers. In detail, about half of the publications on AAMs were based in Asia (47%), mainly in China, India, Malaysia, Thailand, and Indonesia. In addition, 26% of the publications were based in Europe, most of them in Italy, United Kingdom, France, the Czech Republic, and Spain, while 12% were publications from America and Oceania. Finally, only 3% of the publications were from African researchers, mainly based in Egypt, Cameroon, Tunisia, Nigeria, and South Africa.

Gender Balance of Most Prolific Authors

A record of about 5,900 publications was analyzed to investigate the gender balance of the most prolific authors with a focus on each year in the last decade (2009–2019). The analysis took into account 595 authors, and among them, only 144 authors were females (24%), against 434 male authors (73%) (for 17 authors (about 3%), the gender was not identified). The distribution of author gender of the most productive researchers for each year is reported in **Figure 3**. No specific trend was observed. The gender

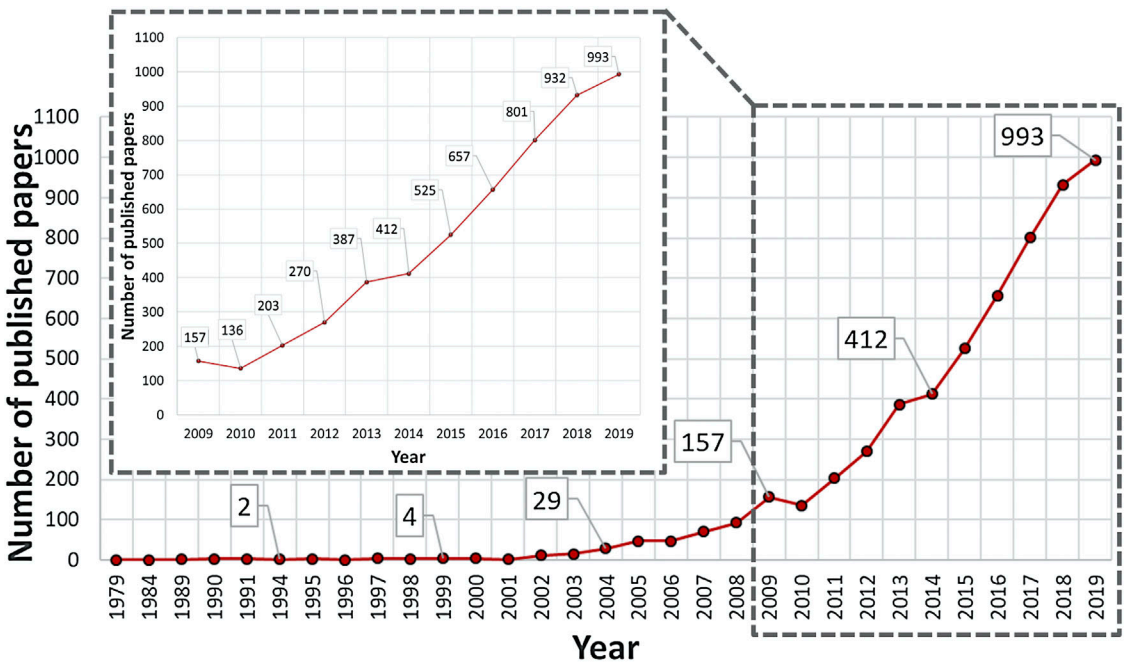

FIGURE 1 | Distribution of the published works on the topic of alkali-activated materials (including geopolymers). In the inlay, distribution of publications in the last 10 years is reported (2009–2019).

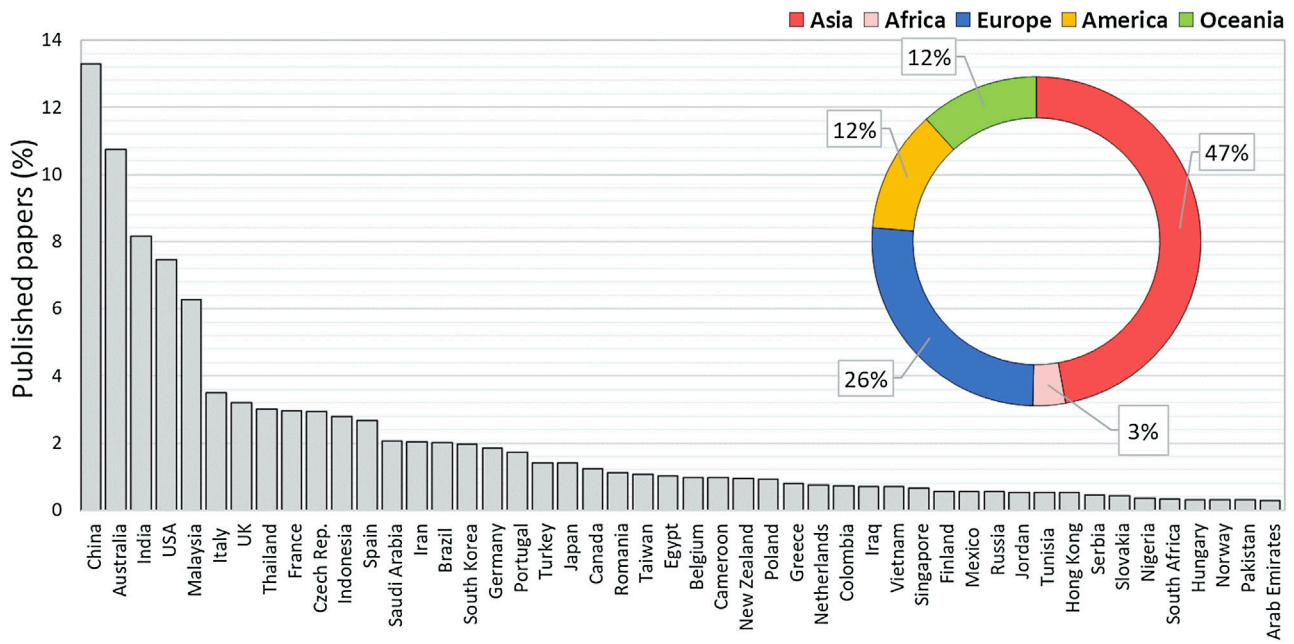

FIGURE 2 | Geographical distribution of the published works (2009–2019) on the specific topic of alkali-activated materials and geopolymers: representation of country-based and continent-based distribution.

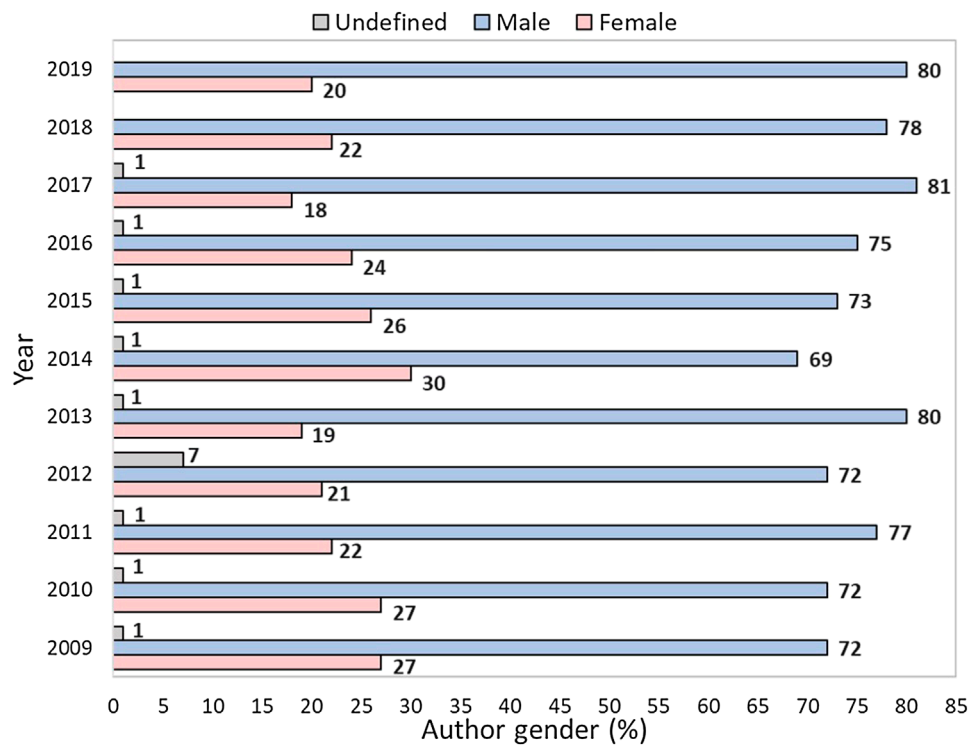

FIGURE 3 | Gender distribution of the first 100 most prolific authors publishing on alkali-activated materials in the years 2009–2019.

distribution is similar to the one determined for the 5,900 publications, showing a female author rate ranging between 19% in 2013 and 30% in 2014. Surprisingly, in the last 5 years, an increase in women as most prolific authors was not observed, thus indicating that women have less opportunity or interest in publishing the results of their research or, alternatively, the number of women involved in building material science is still rather limited. Moreover, the fact that no specific trend of gender distribution was observed can be ascribed to the limited range of time considered in this study, due to the recent development of the research topic taken into account. Even if this specific topic has been mainly prolific in the last decade, the analyzed situation exhibited only one generation of researchers. Thus, this kind of analysis should be repeated for the next decades in order to monitor the gender distribution, and hopefully a significant increase in female authors among the most prolific researchers could be recorded. This result would be significant to reach a more equal gender distribution in this specific field of material science.

The Case Study of Publications by European Authors

In order to deeply examine the gender distribution of authors involved in AAM research, a case study of publications with at least one European author was considered. In this specific case, a total record of 1,386 publications in the period 2009–2019 was analyzed: **Table 1** reports the type and distribution of the considered publications. In particular, most of the outputs are articles published in international peer-reviewed journals (74%). The remaining part is split as follows: 23% publications in international conference proceedings and only 3% of the publications are reviews.

Generally speaking, the number of all the publication types increased from 2009 to 2019, except for conference proceedings where a more alternate trend is detected. This peculiar behavior can be ascribed to the fact that international conferences are rarely scheduled every year, with biennial frequency being the most popular solution for many important congresses in the material sector (e.g., International Conferences on Modern Materials and Technologies, conferences organized by the European Ceramic Society and the American Ceramic Society, American Concrete Institute conventions, and International Conference on Advanced Ceramics and Composites). Moreover, at the moment, AAMs (including geopolymers) are usually included in one-day specific sessions inside conferences covering broader topics (such as ceramics, cement, and concrete) and specific congresses on these are only a few (e.g., Engineering Conference International on AAMs, the Geopolymer Camp organized by the Geopolymer Institute, and International Conference on Non-Traditional Cement and Concrete at BRNO in Czech Republic).

It is further highlighted that open access (OA) publications represent 18% of publications by European authors, with an increasing trend in the last decade. In particular, from 2013, the number of OA publications continuously increased up to 26% in 2018 and 2019. OA publications provide free online access of scientific information, thus following European recommendations. Nowadays, in fact it is recognized that more accessible research results have the positive impact to produce better and more efficient science. Especially the EU Commission policies have encouraged and supported OA publications at the international level as demonstrated in the framework of its Research and Innovation Programmes, such as Horizon 2020 (European Commission, 2017).

Finally, only 1.4% of the total publication by European authors are by single authors, highlighting the interdisciplinary and collaboration research aspects characteristic of the material science sector.

Regarding the gender distribution of the European authors in 2009–2019, analysis of the record was carried out considering both first and last author positions in the author lists. These are key roles in research, as previously explained, usually representative of the active and responsible figure and the manager of the specific research, respectively. For this reason, generally speaking, it is possible that most of the first authors are researchers in an early-stage career, while expert researchers and professors are usually located in the last author position.

Figure 4 reports the gender distribution regarding the European authorships of the first (**Figure 4A**) and last authors (**Figure 4B**) in articles published in 2009–2019. Unlike that reported for most productive authors publishing on AAMs worldwide (**Figure 3**), the case of European authors shows a higher participation of women in publications. In particular, for first authors in the author lists, a concentration of women in the range 36–56% was recorded (**Figure 4A**). Even if no specific trend was exhibited in the last decade, these results are encouraging as they are almost double of those observed worldwide and can be considered an interesting result of the policies of EU only recently strongly addressed to promote gender balance. As previously mentioned, first authors generally correspond to researchers in an early-stage career; thus, the actual and future European policies for enhancing excellence in research would help and encourage

TABLE 1 | Type of publications based in Europe on alkali-activated materials (including geopolymers) in the last decade (2009–2019).

	2009	2010	2011	2012	2013	2014	2015	2016	2017	2018	2019	Total
Total publications	30	31	48	51	110	111	128	165	205	273	234	1,386
Journal articles	17	20	30	39	86	74	104	123	148	193	194	1,028
Conference proceedings	13	11	14	7	24	31	21	38	50	72	34	315
Review	—	—	4	5	—	6	3	4	7	8	6	43
Open access	1	—	—	—	11	12	17	38	41	70	62	252
Single author	—	—	2	2	3	2	3	—	6	5	6	19

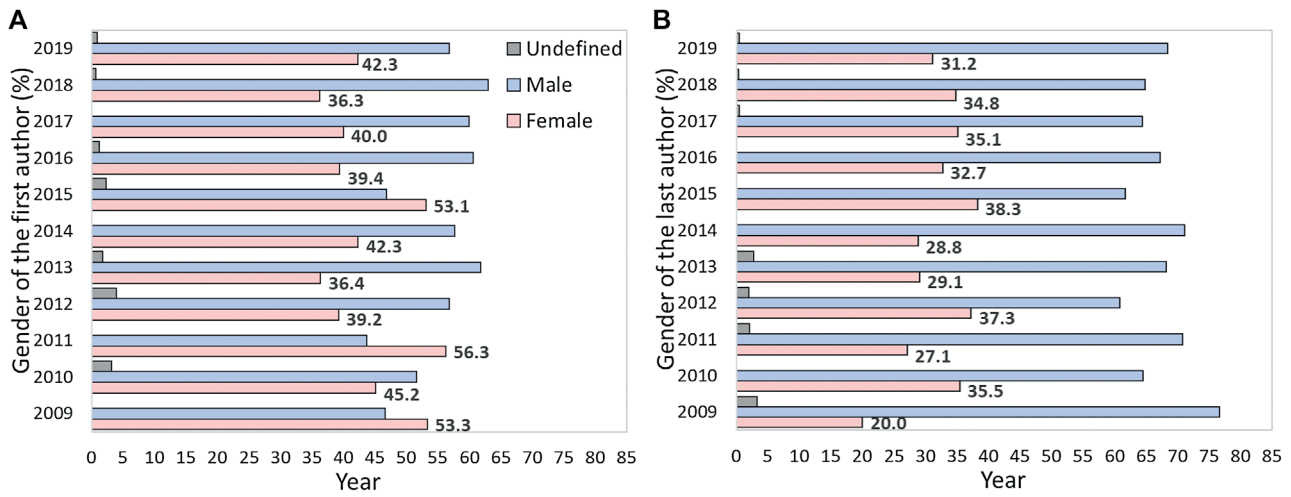

FIGURE 4 | Gender distribution of publications with European authors in the last decade (2009–2019): **(A)** first author and **(B)** last author in the publication author lists.

the most valued researchers to continue in their careers. On the other hand, analysis of the gender distribution of the last authors (**Figure 4B**) shows a lower concentration of women in the last author position than in the first author one, thus confirming that women in high positions (full professor, manager of laboratory, etc.) are still a minority. This situation is, however, better than that reported for most prolific authors worldwide, being the range between 20 and 38% (**Figure 3**). The trends in **Figures 4A, B** (showing near equity in the first author position and the low amount of women in the last author position) agree with those reported in a previous study developed in the United States regarding several research fields (West et al., 2013).

Moreover, an analysis of the citations of publications about AAMs in which the first or last European authors were represented by women was carried out to highlight the impact of the publications. Results are reported in **Table 2** considering the last decade (2009–2019). Generally speaking, higher percentages of women are found for number of citations lower

TABLE 2 | Correlation between female authors and the number of publication citations (data refer to papers published in 2009–2019).

Year	Author list position	Number of citations									
		>100		50–100		10–50		<10		None	
		Publications	Women (%)	Publications	Women (%)	Publications	Women (%)	Publications	Women (%)	Publications	Women (%)
2009	First author	4	25.0	5	60.0	10	50.0	8	87.5	3	0.0
	Last author		25.0		20.0		30.0		12.5		0.0
2010	First author	5	20.0	6	66.7	7	28.6	11	54.5	2	50.0
	Last author		40.0		16.7		28.6		45.5		50.0
2011	First author	8	50.0	7	71.4	17	58.8	12	58.3	4	25.0
	Last author		0.0		42.9		23.5		25.0		50.0
2012	First author	2	0.0	10	20.0	24	41.7	14	57.1	1	0.0
	Last author		0.0		10.0		37.5		57.1		100.0
2013	First author	4	100.0	23	39.1	56	30.4	23	30.4	7	42.9
	Last author		0.0		21.7		39.3		13.0		28.6
2014	First author	9	44.4	8	37.5	48	47.9	40	32.5	7	57.1
	Last author		22.2		50		27.1		27.5		28.6
2015	First author	3	0.0	15	46.7	69	53.6	36	58.3	5	60
	Last author		33.3		33.3		37.7		44.4		40
2016	First author	—	—	15	26.7	86	37.2	51	43.1	13	53.8
	Last author		—		33.3		33.7		29.4		38.5
2017	First author	—	—	2	50.0	109	31.2	50	44.0	13	53.8
	Last author		—		50.0		29.4		30.0		38.5
2018	First author	1	0.0	1	0.0	91	38.5	134	36.6	36	41.7
	Last author		0.0		0.0		34.1		33.6		44.4
2019	First author	—	—	1	0.0	18	27.8	138	41.3	76	48.7
	Last author		—		0.0		27.8		31.2		31.6

than 100 and female author in the first position. However, in the years 2011, 2013, and 2014, noteworthy percentages of European women as first authors are found in publications with more than 100 citations. Less relevant is the percentage related to women in the last author position with a high number of citations, even if some exceptions are observed (e.g., 2017: 50% of European female last authors with number of citations in the range of 50–100; 2015: 33.3% of European female last authors with number of citations >100). These results agree with previous results indicating that researchers in the early-stage careers, represented by first authors, are more equally gender distributed also in highly cited publications.

CONCLUSIONS

The following conclusions can be drawn from this study:

- AAMs, including geopolymers, is a new material science field in which the research is prolific and innovative. Especially in the last decade, a continuous growth in publications in international peer-reviewed journals and in international conference proceedings was detected;
- publications on AAMs are mainly based in Asia (about 50%), even if Europe (about 26%) is largely involved in this specific topic;
- the analysis of gender distribution of the most productive authors worldwide showed that only 22% of the total authors are women;
- considering European authors, a more equal gender distribution is reached when the first author is considered. This trend is also highlighted when citations are related to the gender: a significant concentration of women, especially in the first author positions, with citations >50, was found.

The analysis of the gender distribution reported in this study takes into consideration only indexed research products (articles published in peer-reviewed journals and conference proceedings) reported in the Scopus database. Moreover, it is representative of just one relative recent field of material science, so further gender-based bibliometric researches should be carried out to have a broader scenario for the material science sector. Results from this specific study can be used as the basis for future studies to bridge the gender gap and may contribute to enhancing the sensitivity toward gender issues. Finally, a continuous increase in the participation of female researchers is constantly registered in national and international conferences on AAMs and more in general in the construction material sector, thus showing an encouraging signal for narrowing the still existing gender gap.

DATA AVAILABILITY STATEMENT

All datasets presented in this study are included in the article.

AUTHOR CONTRIBUTIONS

MB conceptualized the topic of the study. GM elaborated the statistical data. GM, SM, and MB drafted the manuscript. All authors contributed to the article and approved the submitted version.

REFERENCES

Ameri, F., Shoaei, P., Zareei, S. A., and Behforouz, B. (2019). Geopolymers vs. alkali-activated materials (AAMs): a comparative study on durability, microstructure, and resistance to elevated temperatures of lightweight mortars. *Constr. Build. Mater.* 222, 49–63. doi:10.1016/j.conbuildmat.2019.06.079

Asim, N., Alghoul, M., Mohammad, M., Amin, M. H., Akhtaruzzaman, M., Amin, N., et al. (2019). Emerging sustainable solutions for depollution: geopolymers. *Constr. Build. Mater.* 199, 540–548. doi:10.1016/j.conbuildmat.2018.12.043

Bignozzi, M. C., and Bonduà, S. (2011). Alternative blended cement with ceramic residues: corrosion resistance investigation on reinforced mortar. *Cem. Concr. Res.* 41, 947–954. doi:10.1016/j.cemconres.2011.05.001

Bignozzi, M. C., Manzi, S., Lancellotti, I., Kamseu, E., Barbieri, L., and Leonelli, C. (2013). Mix-design and characterization of alkali activated materials based on metakaolin and ladle slag. *Appl. Clay Sci.* 73, 78–85. doi:10.1016/j.clay.2012.09.015

Bignozzi, M. C., Manzi, S., Natali, M. E., Rickard, W. D. A., and Van Riessen, A. (2014). Room temperature alkali activation of fly ash: the effect of Na2O/SiO2 ratio. *Constr. Build. Mater.* 69, 262–270. doi:10.1016/j.conbuildmat.2014.07.062

Carabba, L., Manzi, S., Rambaldi, E., Ridolfi, G., and Bignozzi, M. C. (2017a). High-temperature behaviour of alkali-activated composites based on fly ash and recycled refractory particles. *J. Ceram. Sci. Technol.* 8, 377–387. doi:10.4416/JCST2017-00047

Carabba, L., Santandrea, M., Carloni, C., Manzi, S., and Bignozzi, M. C. (2017b). Steel fiber reinforced geopolymer matrix (S-FRGM) composites applied to reinforced concrete structures for strengthening applications: a preliminary study. *Compos. B Eng.* 128, 83–90. doi:10.1016/j.compositesb.2017.07.007

Carabba, L., Moricone, R., Scarponi, G. E., Tugnoli, A., and Bignozzi, M. C. (2019a). Alkali activated lightweight mortars for passive fire protection: a preliminary study. *Constr. Build. Mater.* 195, 75–84. doi:10.1016/j.conbuildmat.2018.11.005

Carabba, L., Pirskawetz, S., Krüger, S., Gluth, G. J. G., and Bignozzi, M. C. (2019b). Acoustic emission study of heat-induced cracking in fly ash-based alkali-activated pastes and lightweight mortars. *Cem. Concr. Compos.* 102, 145–156. doi:10.1016/j.cemconcomp.2019.04.013

Davidovits, J. (1979). Synthesis of new high-temperature geo-polymers for reinforced plastics composites. *Spe Pactec.* 79, 151–154. Elsevier and Scopus. Available at: https://www.scopus.com/ (Accessed March 2020)

European Commission (2017). "H2020 Programme - guidelines to the rules on open access to scientific publications and open access to research data" in *Horizon 2020*.

European Commission (2008). "Mapping the maze: getting more women to the top in research", in *European commission. Directorate-general for research. Directorate L-science, economy and society. Unit L.4. Scientific culture and gender issues*. EUR23311EN.

European Commission (2015). *Strategic engagement for gender equality 2016-2019*. Publications Office of the European Union.

European Commission (2010). "Stocktaking 10 years of women in science policy by the European commission 1999–2009", in *Publications Office of the European Union*. Directorate-General for Research.

Hassan, A., Arif, M., and Shariq, M. (2019). Use of geopolymer concrete for a cleaner and sustainable environment – a review of mechanical properties and microstructure. *J. Clean. Prod.* 223, 704–728. doi:10.1016/j.jclepro.2019.03.051

Hertel, T., and Pontikes, Y. (2020). Geopolymers, inorganic polymers, alkali-activated materials and hybrid binders from bauxite residue (red mud) – putting things in perspective. *J. Clean. Prod.* 258, 120610. doi:10.1016/j.jclepro.2020.120610

Imbabi, M. S., Carrigan, C., and McKenna, S. (2012). Trends and developments in green cement and concrete technology. *Int. J. Sustain. Built Environ.* 1, 194–216. doi:10.1016/j.ijsbe.2013.05.001

Kamseu, E., Cannio, M., Obonyo, E. A., Tobias, F., Bignozzi, M. C., Sglavo, V. M., et al. (2014). Metakaolin-based inorganic polymer composite: effects of fine aggregate composition and structure on porosity evolution, microstructure and mechanical properties. *Cem. Concr. Compos.* 53, 258–269. doi:10.1016/j.cemconcomp.2014.07.008

Kang, J., Hense, J., Scheersoi, A., and Keinonen, T. (2019). Gender study on the relationships between science interest and future career perspectives. *Int. J. Sci. Educ.* 41, 80–101. doi:10.1080/09500693.2018.1534021

Kosmulski, M. (2012). The order in the lists of authors in multi-author papers revisited. *J. Informetr.* 6, 639–644. doi:10.1016/j.joi.2012.06.006

Lahoti, M., Tan, K. H., and Yang, E.-H. (2019). A critical review of geopolymer properties for structural fire-resistance applications. *Constr. Build. Mater.* 221, 514–526. doi:10.1016/j.conbuildmat.2019.06.076

Larivière, V., Ni, C., Gingras, Y., Cronin, B., and Sugimoto, C. R. (2013). Global gender disparities in science. *Nature* 504, 211–213. doi:10.1038/504211a

Li, N., Shi, C., Zhang, Z., Wang, H., and Liu, Y. (2019). A review on mixture design methods for geopolymer concrete. *Compos. B Eng.* 178, 107490. doi:10.1016/j.compositesb.2019.107490

Luukkonen, T., Abdollahnejad, Z., Yliniemi, J., Kinnunen, P., and Illikainen, M. (2018). One-part alkali-activated materials: a review. *Cem. Concr. Res.* 103, 21–34. doi:10.1016/j.cemconres.2017.10.001

Ma, C.-K., Awang, A. Z., and Omar, W. (2018). Structural and material performance of geopolymer concrete: a review. *Constr. Build. Mater.* 186, 90–102. doi:10.1016/j.conbuildmat.2018.07.111

Masi, G., Rickard, W. D. A., Bignozzi, M. C., and Van Riessen, A. (2015). The effect of organic and inorganic fibres on the mechanical and thermal properties of aluminate activated geopolymers. *Compos. B Eng.* 76, 218–228. doi:10.1016/j.compositesb.2015.02.023

Masi, G., Rickard, W. D. A., Vickers, L., Bignozzi, M. C., and Van Riessen, A. (2014). A comparison between different foaming methods for the synthesis of light weight geopolymers. *Ceram. Int.* 40, 13891–13902. doi:10.1016/j.ceramint.2014.05.108

Mauleón, E., Hillán, L., Moreno, L., Gómez, I., and Bordons, M. (2013). Assessing gender balance among journal authors and editorial board members. *Scientometrics* 95, 87–114. doi:10.1007/s11192-012-0824-4. Ministero dell'Istruzione, dell'Università e della Ricerca in collaboration with CINECA. Available at: https://cercauniversita.cineca.it/ (Accessed May 2020)

Mo, K. H., Alengaram, U. J., and Jumaat, M. Z. (2016). Structural performance of reinforced geopolymer concrete members: a review. *Constr. Build. Mater.* 120, 251–264. doi:10.1016/j.conbuildmat.2016.05.088

Monticelli, C., Natali, M. E., Balbo, A., Chiavari, C., Zanotto, F., Manzi, S., et al. (2016a). A study on the corrosion of reinforcing bars in alkali-activated fly ash mortars under wet and dry exposures to chloride solutions. *Cem. Concr. Res.* 87, 53–63. doi:10.1016/J.CEMCONRES.2016.05.010

Monticelli, C., Natali, M. E., Balbo, A., Chiavari, C., Zanotto, F., Manzi, S., et al. (2016b). Corrosion behavior of steel in alkali-activated fly ash mortars in the light of their microstructural, mechanical and chemical characterization. *Cem. Concr. Res.* 80, 60–68. doi:10.1016/J.CEMCONRES.2015.11.001

Mugahed Amran, Y. H., Alyousef, R., Alabduljabbar, H., and El-Zeadani, M. (2020). Clean production and properties of geopolymer concrete; A review. *J. Clean. Prod.* 251, 119679. doi:10.1016/j.jclepro.2019.119679

Pacheco-Torgal, F., Abdollahnejad, Z., Camões, A. F., Jamshidi, M., and Ding, Y. (2012). Durability of alkali-activated binders: a clear advantage over Portland cement or an unproven issue? *Constr. Build. Mater.* 30, 400–405. doi:10.1016/j.conbuildmat.2011.12.017

Pacheco-Torgal, F., Abdollahnejad, Z., Miraldo, S., and Kheradmand, M. (2017). "Alkali-activated cement-based binders (AACB) as durable and cost-competitive low-CO 2 binder materials: some shortcomings that need to be addressed," in *Handbook of low carbon concrete*. Waltham, US: Elsevier Science and Tech, 195–216.

Palomo, A., Krivenko, P., Garcia-Lodeiro, I., Kavalerova, E., Maltseva, O., and Fernández-Jiménez, A. (2014). A review on alkaline activation: new analytical perspectives. *Mater. Constr.* 64, e022. doi:10.3989/mc.2014.00314

Paul, G., Boccaleri, E., Braschi, I., and Marchese, L. (2020). "On the pursuit of gender balance in European cement industries: a bibliometric study using Scopus database." in Plotina conference - the inclusion of the sex/gender variables in research: gender-inclusive material sciences and engineering, Bologna, Italy, January 27–28, 2020, 138–140.

Provis, J. L. (2018). Alkali-activated materials. *Cem. Concr. Res.* 114, 40–48. doi:10.1016/j.cemconres.2017.02.009

Provis, J. L. (2014). Geopolymers and other alkali activated materials: why, how, and what? *Mater. Struct. Constr.* 47, 11–25. doi:10.1617/s11527-013-0211-5

Provis, J. L., and Bernal, S. A. (2014). Geopolymers and related alkali-activated materials. *Annu. Rev. Mater. Res.* 44, 299–327. doi:10.1146/annurev-matsci-070813-113515

Provis, J. L., Palomo, A., and Shi, C. (2015). Advances in understanding alkali-activated materials. *Cem. Concr. Res.* 78, 110–125. doi:10.1016/j.cemconres.2015.04.013

Provis, J. L., and van Deventer, J. S. J. (2019). "Geopolymers and other alkali-activated materials," in *Lea's chemistry of cement and concrete*. 5th Edn, Netherlands: Elsevier, 779–805.

Rakhimova, N. R., and Rakhimov, R. Z. (2019a). Reaction products, structure and properties of alkali-activated metakaolin cements incorporated with supplementary materials - a review. *J. Mater. Res. Technol.* 8, 1522–1531. doi:10.1016/j.jmrt.2018.07.006

Rakhimova, N. R., and Rakhimov, R. Z. (2019b). Toward clean cement technologies: a review on alkali-activated fly-ash cements incorporated with supplementary materials. *J. Non Cryst. Solids.* 509, 31–41. doi:10.1016/j.jnoncrysol.2019.01.025

Rasaki, S. A., Bingxue, Z., Guarecuco, R., Thomas, T., and Minghui, Y. (2019). Geopolymer for use in heavy metals adsorption, and advanced oxidative processes: a critical review. *J. Clean. Prod.* 213, 42–58. doi:10.1016/j.jclepro.2018.12.145

Rashidian-Dezfouli, H., and Rangaraju, P. R. (2017). A comparative study on the durability of geopolymers produced with ground glass fiber, fly ash, and glass-powder in sodium sulfate solution. *Constr. Build. Mater.* 153, 996–1009. doi:10.1016/j.conbuildmat.2017.07.139

Rees, T. (2001). Mainstreaming gender equality in science in the European union: the 'ETAN report'. *Gend. Educ.* 13, 243–260. doi:10.1080/09540250120063544

Robayo-Salazar, R. A., and Mejía de Gutiérrez, R. (2018). Natural volcanic pozzolans as an available raw material for alkali-activated materials in the foreseeable future: a review. *Constr. Build. Mater.* 189, 109–118. doi:10.1016/j.conbuildmat.2018.08.174

Saccani, A., Manzi, S., Lancellotti, I., and Barbieri, L. (2020). Manufacturing and durability of alkali activated mortars containing different types of glass waste as aggregates valorisation. *Constr. Build. Mater.* 237, 117733. doi:10.1016/j.conbuildmat.2019.117733

Sandanayake, M., Gunasekara, C., Law, D., Zhang, G., and Setunge, S. (2018). Greenhouse gas emissions of different fly ash based geopolymer concretes in building construction. *J. Clean. Prod.* 204, 399–408. doi:10.1016/j.jclepro.2018.08.311

Scrivener, K. L., John, V. M., and Gartner, E. M. (2018). Eco-efficient cements: potential economically viable solutions for a low-CO_2 cement-based materials industry. *Cem. Concr. Res.* 114, 2–26. doi:10.1016/j.cemconres.2018.03.015

Shen, H. (2013). Inequality quantified: mind the gender gap. *Nature* 495, 22–24. doi:10.1038/495022a

Shi, C., Qu, B., and Provis, J. L. (2019). Recent progress in low-carbon binders. *Cem. Concr. Res.* 122, 227–250. doi:10.1016/j.cemconres.2019.05.009

Silva, R. V., de Brito, J., Lynn, C. J., and Dhir, R. K. (2017). Use of municipal solid waste incineration bottom ashes in alkali-activated materials, ceramics and granular applications: a review. *Waste Manag.* 68, 207–220. doi:10.1016/j.wasman.2017.06.043

Simoes, N., and Crespo, N. (2020). Self-citations and scientific evaluation: leadership, influence, and performance. *J. Informetr* 14, 100990. doi:10.1016/j.joi.2019.100990

Singh, B., Ishwarya, G., Gupta, M., and Bhattacharyya, S. K. (2015). Geopolymer concrete: a review of some recent developments. *Constr. Build. Mater.* 85, 78–90. doi:10.1016/j.conbuildmat.2015.03.036

Singh, N. B., and Middendorf, B. (2020). Geopolymers as an alternative to Portland cement: an overview. *Constr. Build. Mater.* 237, 117455. doi:10.1016/j.conbuildmat.2019.117455

Smith, K. A., Arlotta, P., and Watt, F. M., Initiative on Women in Science and Engineering Working Group, Solomon, S. L. (2015). Seven actionable strategies

for advancing women in science, engineering, and medicine. *Cell Stem Cell* 16, 221–224. doi:10.1016/j.stem.2015.02.012

Stoet, G., and Geary, D. C. (2018). The gender-equality paradox in Science, Technology, Engineering, and Mathematics Education, *Psychol. Sci,* 29 (4), 581–593. doi:10.1177/0956797617741719

Tang, Z., Li, W., Hu, Y., Zhou, J. L., and Tam, V. W. Y. (2019). Review on designs and properties of multifunctional alkali-activated materials (AAMs). *Constr. Build. Mater.* 200, 474–489. doi:10.1016/j.conbuildmat.2018.12.157

The University Materials Council (2008). "Gender equity in material science and engineering,"in A report on the Workshop on gender equity in Materials Science and Engineering, College Park, Maryland, May 18–20, 2008.

Tittarelli, F., Mobili, A., Giosuè, C., Belli, A., and Bellezze, T. (2018). Corrosion behaviour of bare and galvanized steel in geopolymer and ordinary Portland Cement based mortars with the same strength class exposed to chlorides. *Corros. Sci.* 134, 64–77. doi:10.1016/J.CORSCI.2018.02.014

Wang, A., Zheng, Y., Zhang, Z., Liu, K., Li, Y., Shi, L., et al. (2020). The durability of alkali-activated materials in comparison with ordinary portland cements and concretes: a review. *Engineering* 6, 695. doi:10.1016/j.eng.2019.08.019

West, J. D., Jacquet, J., King, M. M., Correll, S. J., and Bergstrom, C. T. (2013). The role of gender in scholarly authorship. *PloS One* 8, e66212. doi:10.1371/journal.pone.0066212

Wu, Y., Lu, B., Bai, T., Wang, H., Du, F., Zhang, Y., et al. (2019). Geopolymer, green alkali activated cementitious material: synthesis, applications and challenges. *Constr. Build. Mater.* 224, 930–949. doi:10.1016/j.conbuildmat.2019.07.112

Xi, F., Davis, S. J., Ciais, P., Crawford-Brown, D., Guan, D., Pade, C., et al. (2016). Substantial global carbon uptake by cement carbonation. *Nat. Geosci.* 9, 880–883. doi:10.1038/ngeo2840

Zhang, J., Shi, C., Zhang, Z., and Ou, Z. (2017). Durability of alkali-activated materials in aggressive environments: a review on recent studies. *Constr. Build. Mater.* 152, 598–613. doi:10.1016/j.conbuildmat.2017.07.027

Zhang, P., Zheng, Y., Wang, K., and Zhang, J. (2018). A review on properties of fresh and hardened geopolymer mortar. *Compos. B Eng.* 152, 79–95. doi:10.1016/j.compositesb.2018.06.031

Zhuang, X. Y., Chen, L., Komarneni, S., Zhou, C. H., Tong, D. S., Yang, H. M., et al. (2016). Fly ash-based geopolymer: clean production, properties and applications. *J. Clean. Prod.* 125, 253–267. doi:10.1016/j.jclepro.2016.03.019

Conflict of Interest: The authors declare that the research was conducted in the absence of any commercial or financial relationships that could be construed as a potential conflict of interest.

frontiers in Materials

ORIGINAL RESEARCH
published: 10 December 2020
doi: 10.3389/fmats.2020.572955

A Case Study of Industrial Symbiosis to Reduce GHG Emissions: Performance Analysis and LCA of Asphalt Concretes Made With RAP Aggregates and Steel Slags

Alessandra Bonoli, Anna Degli Esposti and Chiara Magrini**

Department of Civil, Chemical, Environmental and Materials Engineering (DICAM), University of Bologna, Bologna, Italy

The concept of sustainability in the road construction sector is a complex issue because of the various steps that contribute to the production and release of greenhouse gas (GHG) emissions. Addressing this issue, the European Commission has put various policy initiatives in place to encourage the construction industry to adopt circular economy (CE) and industrial symbiosis (IS) principles e.g., the use of recycled materials. *Cooperativa Trasporti Imola* (CTI), a company located in the Emilia-Romagna region (Italy), has been chosen for the current case study to examine practices, management, and the industrial symbiosis network among various companies in the road construction and rehabilitation sector. In this regard, the use of steel slags, obtained by an electric arc furnace (EAF), and reclaimed asphalt pavement (RAP), obtained by the deconstruction and milling of old asphalt pavement have been investigated. Two mixtures of recycled hot Mix Asphalt (HMA) i) were prepared incorporating different recycled material percentages for the wearing and binder course, respectively, ii) were characterized in terms of size distribution, strength modulus and volumetric properties, iii) and finally were compared to the performances of two mixtures entirely designed by virgin materials for the wearing and binder course, respectively. Therefore, the Life Cycle Assessment (LCA) tool was chosen to evaluate the environmental impacts that affect the designed road life cycle. The results show that recycling RAP and EAF slags in a CTI batch plant provides benefits by reducing the consumption of virgin bitumen and aggregates and by reducing CO_{2eq} emissions. Finally, practical implications on the use of recycled materials in new asphalt mixtures from a life cycle and industrial symbiosis perspective are provided.

Keywords: life cycle assessement, circular economy, industrial symbiosis, road construction, electric arc furnace steel slags, reclaimed asphalt pavement, recycled aggregates, standard characterization

OPEN ACCESS

Edited by:
Emilia Morallon,
University of Alicante, Spain

Reviewed by:
Luigi Coppola,
University of Bergamo, Italy
Marco Pasetto,
University of Padua, Italy

****Correspondence:***
Alessandra Bonoli
alessandra.bonoli@unibo.it
Chiara Magrini
chiara.magrini7@unibo.it

Specialty section:
This article was submitted to Structural Materials, a section of the journal Frontiers in Materials.

Received: *09 July 2020*
Accepted: *09 November 2020*
Published: *10 December 2020*

Citation:
Bonoli A, Degli Esposti A and Magrini C (2020) A Case Study of Industrial Symbiosis to Reduce GHG Emissions: Performance Analysis and LCA of Asphalt Concretes Made With RAP Aggregates and Steel Slags. Front. Mater. 7:572955. doi: 10.3389/fmats.2020.572955

INTRODUCTION

Greenhouse gas (GHG) emissions in infrastructure projects are a key indicator when sustainability is being assessed (Gasparatos et al., 2008; Fernández-Sánchez and Rodríguez-López, 2010). The road sector, due to its characteristics (high energy consumption; use of resources, raw material, and surface; generation of high volumes of waste; quantity of linked transports and long service life) is

one of the main sectors that contributes to global warming (GW) (Cass and Mukherjee, 2011). Significant GHG emissions result from many stages of the road life cycle. Santero and Horvath (2009) stated that GHG emissions could range from negligibly small values to 60,000 tons of equivalent carbon dioxide (CO_{2eq}) per lane-kilometer over a service life of 50 years. Similarly, the emission factor per meter per year associated with the construction of road infrastructure has been estimated at 14.7 kg of CO_{2eq} (Hill et al., 2012). In this sense, regarding road construction and maintenance, several steps contribute to the production and release of GHG emissions, i.e., site clearing, preparation of the sub-grade, production of construction materials (i.e., granular sub-base, base course, surfacing), site delivery, construction works, ongoing supervision, and maintenance activities. As European road infrastructure includes a growing network, with 4.8 million km at the end of 2013 (European Union Road Federation, 2017) and 5.5 million km at the end of 2016 (European Union Road Federation, 2019), this sector has broad margins for environmental improvement (Santero et al., 2011a; Santero et al., 2011b; JRC, 2016). For these reasons, this study is of particular interest.

Road construction is one of three main drivers of resource use in the European Union (Steger and Bleischwitz, 2011). Road construction not only requires large quantities of materials, but also their maintenance is highly material intensive. Construction works and regular maintenance of roads require materials that are produced through highly carbon-intensive and energy-demanding processes (Santos et al., 2015; Jiang and Wu, 2019). Previous studies have suggested that the life-cycle of GHG emissions associated with building roads can account for 10–20% of the emissions associated with the lifetime usage of the road by vehicles (Chester and Horvath, 2009; Hanson and Noland, 2015; Noland and Hanson, 2015). Previous research has also shown that the bulk of the emissions related to road construction and maintenance activities is often associated with the upstream emissions embodied in the materials used (Hanson and Noland, 2015; Huang et al., 2015; Noland and Hanson, 2015). Hence, the choice of materials impacts local pollution and environmental degradation. These materials primarily include asphalt, concrete, and steel (Hanson and Noland, 2015). Therefore, also considering the increase of landfilling restrictions on CDW, the use of alternative materials such as industrial by-products has gained greater significance and attention from academia and industrial sectors (Jamshidi et al., 2017).

The European Commission (EC) has put various policy initiatives in place to encourage the construction industry toward circular economy (CE) principles. The overall idea is to reconsider the whole life cycle of resources, to make the European Union (EU) a "circular economy" based on recycling, and the use of waste as a resource (EC, 2011).

The use of alternative materials for the construction and rehabilitation of roads would therefore be a strategy to be boosted, establishing regional industrial symbiosis (IS) agreements which can support companies to gain competitiveness and reduce the environmental impact associated to their day to day business activities (Martin-Portugues Montoliu et al., 2019). For that reason, the EC has recently launched an industry-led IS reporting and certification system (EC, 2020). In this sense, symbiotic activities can be applied at different levels. According to Roberts (Roberts, 2004), they can involve a single firm or organization (micro level); companies co-located in the same area (meso level); and finally the entire regional or national production system (macro level). The greatest benefits are achieved at the meso level, where the clustering of complementary companies provides a complexity of functions (Roberts, 2004; Taddeo, 2016).

Background of Hot Mix Asphalt, Recycling of Reclaimed Asphalt Pavement and Electric Arc Furnace Steel Slags

Roads are built in layers and three main types of road pavements can be identified: flexible, semi-rigid, and rigid pavements. In Europe, the main pavement type is flexible (asphalt) (Sherwood, 2001; Garbarino et al., 2016). As shown in **Figure 1**, the main road layers for flexible pavement are:

- surface, binder, and base courses, which consist of bituminous mixtures;
- road base and sub-base courses, which consist of cement bound or unbound aggregates.

Asphalt mixtures are typically composed of approximately 95% of mineral aggregates mixed with about 5% paving bitumen, with bitumen functioning as the glue that binds the mineral aggregates in a cohesive mix (EAPA, 2011). In general, three types of asphalt mixtures can be used: hot mix asphalt (HMA), warm mix asphalt (WMA), and cold mix asphalt (CMA).

Some aggregates can, usefully, be created by recycling processes.

In this study, the use of steel slags obtained by an electric arc furnace (EAF), and reclaimed asphalt pavement (RAP) obtained by the deconstruction and milling of old asphalt pavement have been investigated. The HMA technology was used in the production process.

While recycling HMA results in a reusable mixture of aggregates and aged asphalt binders known as RAP (Al-Qadi et al., 2007; Noferini et al., 2018), recycling steel slags produces artificial aggregates, containing 90% iron oxide and smaller quantities of other oxides (calcium, magnesium, silicon, etc.), derived from additives used in steel production. Moreover, on the basis of production technology, steel slags can be classified as basic oxygen furnace (BOF), electric arc furnace (EAF), and ladle refining (LF) slags (Meng and Liu, 2000; Gu et al., 2018).

As is widely known, steel slags, produced during the separation of molten steel from impurities in a steel-making furnace, are one of the most common industrial wastes and they can be used for several applications. Thanks to their high hardness and cementing properties, they are commonly used in the road sector (Rashad, 2019). In steel plants, high-grade steel

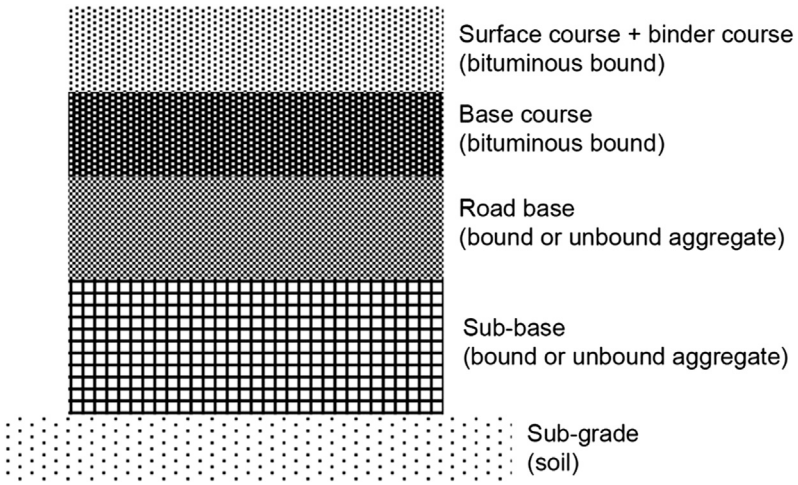

FIGURE 1 | Flexible pavement layer system (Garbarino et al., 2016). The sizes of each course represented in the figure do not necessarily correspond to the actual ones.

is melted, obtaining a sinking heavy liquid metal fraction, which agglomerates into a metal phase, separating metals from some light fractions such as chromium by reducing agents and liberating chromium from its compounds. Slag composition can be optimized in relation with application requirements and then it can be cast. In some processes (i.e., RecArc project, http://www.recarc.bam.de) the high-grade steel slags can be converted into a chromium-rich metal phase, which can be used as a raw material in high-grade steel production.

As far as the recycling of RAP and of EAF steel slags are concerned, several studies have shown that the use of these materials is common in pavement construction because of their technical performances and economic value. Miliutenko et al. (2013) have shown that HMA mixes with RAP content have the same technical characteristics (stiffness, fatigue, and deformation resistance) as virgin ones. Thanks to the incorporation of RAP in new asphalt mixtures, the need of neat bitumen is reduced, making RAP recycling economically attractive (Noferini et al., 2018; Pantini et al., 2018).

Similarly, other studies have demonstrated that steel slags with proper pre-processing and sufficient in-place quality control procedures can perform credibly well as asphalt aggregates (Del Fabbro et al., 2001; Ahmedzade and Sengoz, 2009; Gu et al., 2018). In particular, EAF slags have been frequently used as pavement aggregates due to their excellent mechanical properties, which make them suitable for asphalt layers with any kind of traffic load (Santos et al., 2015).

Moreover, Pasetto and Baldo (2017) studied the stiffness and the fatigue performance of five different base-binder bituminous mixtures, made with RAP and EAF steel slag, up to 70% by weight of the aggregate. They reported that the resulting mixes with RAP and EAF slag were characterized by improved stiffness and fatigue performance compared to the control asphalt concrete, made exclusively with natural aggregate.

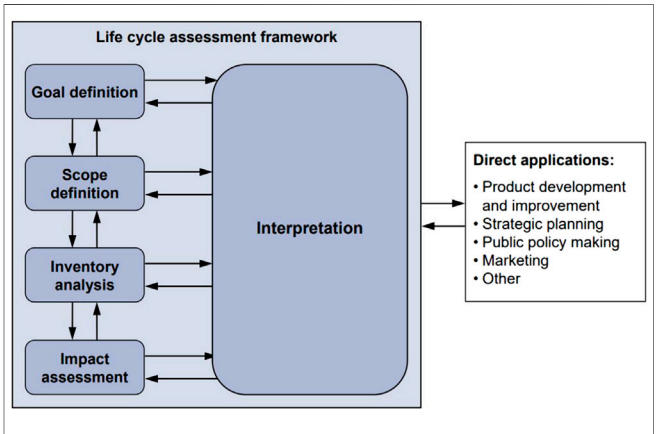

FIGURE 2 | LCA phases (EC et al., 2010).

The Life Cycle Assessment and the Circularity Approach

The Life Cycle Assessment (LCA) is a considerable method to evaluate the environmental impacts of a system, a product, or a process. All the inputs (such as energy and resources) are identified, with the aim of quantifying the relevant emissions, the consumed resources, and the related environmental impacts. Considering a product, the impacts do not only arise during the manufacturing stage, but along its entire life cycle, including the extraction and transportation of raw materials, use and maintenance, possible reuse, and end of life. Therefore, the approach encompasses the whole life cycle of a product, "from cradle to grave," as the first definition stated (SETAC, 1993): from "cradle," where raw materials are extracted, put into production, and used, to "grave," i.e., waste disposal, with the aim to provide a comprehensive picture of the environmental impacts of the system.

According to a circularity perspective, a new philosophy, referred to as "from cradle to cradle", is taking hold: at their end of life, materials are not considered as waste to be discarded, but as secondary raw material, thanks to an appropriate recycling process. In this way, a cradle-to-cradle closed loop is outlined.

According to the ISO14040 standard, the four steps to perform a Life Cycle Assessment (LCA) are: the definition of the goal and scope of the analysis, the inventory analysis, the impact assessment, and finally, the interpretation of the results (**Figure 2**).

Goal and Scope Definition

The context of the study and its purpose are set. The goal of the LCA states the intended application and the reasons for carrying out the study, the intended audience, and whether the results are to be used for internal purpose or for disclosure to the public. The scope includes the following items: functional unit, system boundary, allocation procedure, data requirements, impact assessment method, assumption, and data quality. In particular, the functional unit, that defines the quantification of the identified function of the product, has the primary purpose to provide a reference to which the inputs and outputs are related, ensuring the comparability of the LCA results. The system boundary defines the unit processes to be included in the system. Criterions for the choice of the system boundaries are physical (description of the productive cycle), geographical (reference area), and temporal (reference period).

Inventory Analysis or Life Cycle Inventory

It lists all the inputs (materials and energy) and outputs (products, co-products, and emissions) to be used to compare standards and processes. Inventory analysis involves data collection and calculation procedures, aiming at quantifying the relevant inputs and outputs of a product system. The life cycle inventory uses both primary and specific as well as literature and secondary data from international databases.

Impact Assessment

The life cycle impact assessment (LCIA) includes the following mandatory elements: the selection of impact categories and characterization models; the assignment of LCI results to the selected impact categories (classification); and the calculation of category indicator results (characterization).

Interpretation

Finally, the life cycle interpretation aims at the identification of substantial issues, based on the results of the previous steps. The evaluation includes considerations about the completeness and the consistency of the study, conclusions, limitations, and recommendations.

In **Figure 2**, the two-way arrows highlight the iterative approach of an LCA. During the analysis, the results and the assumptions in subsequent stages might lead to the revision of what has been done in previous stages, in a process of continuous improvement. Information which was not available during the compilation of the previous phases can be added afterward.

The Life Cycle Assessment in the Road Construction Sector

Due to the high amount of GHG emissions generated during road construction, rehabilitation, and operation, the evaluation and reduction of the environmental impact related to the road sector have become an international challenge (Espinoza et al., 2019). In this sense, a systematic approach has emerged to assess the environmental impact of pavements. LCA is considered a relevant methodology to evaluate the environmental impacts that affect the road life-cycle (Espinoza et al., 2019) and the International Organization for Standardization (ISO) has established the principles, requirements, and guidelines to regulate the LCA analysis (ISO 14040, ISO 14044, ISO 14020, ISO 14024, and ISO 14025). Moreover, the Joint Research Centre (JRC) in 2016 proposed an LCA as an assessment methodology of road environmental performance, with reference to ISO 14067 or equivalents and ISO 14040/14044. Finally, according to Espinoza et al., (2019), the use of an LCA for evaluating the environmental performance of the construction of road projects allows construction companies to obtain information that can be used to predict the performance of their projects and to evaluate compliance with environmental requirements. Similarly, it allows the selection of optimal materials and construction processes, reducing the GHG emissions and permitting a more sustainable approach.

Therefore, LCA analysis performed by Espinoza et al., (2019) highlighted that HMA production generates the greatest environmental impact, considering the extraction of raw material and the construction of the HMA layers. Previous research has shown that HMA emits up to 18–22 $kgCO_2/t$ (Agentschap Wegen en Verkeer, 2012; JRC, 2016) and a recent LCA literature review for roads, carried out by JRC (2016), shows that the second largest source of environmental impact after the use phase is the production of construction materials. In addition, in low traffic roads, this can in fact be the most significant source of environmental impact (JRC, 2016). Moreover, the durability of road materials is a key factor that will influence the requirement for maintenance. The impacts of maintenance activities themselves are dominated by impacts from material production and transportation. Consequently, special attention to HMA production and construction materials is required in order to minimize GHG emissions. For these reasons, several studies have pointed out the environmental benefits of using recycled materials, such as RAP and EAF steel slags. Hasan et al. (2020) argued that RAP obtained after milling and screening existing asphalt pavements is a viable alternative to mitigate the high GHG burdens of bitumen and aggregates (Praticò et al., 2015; Guo et al., 2018) and transport agencies (AASHTO, 2012; Hasan et al., 2020). In particular, the use of steel slags in asphalt mixtures saves natural resources, by reducing the consumption of natural and non-renewable aggregates and the quantity of slag deposited on landfill sites (Ferreira et al., 2016) and the reduction of the landfill space requirements associated with the need to landfill industrial

wastes and by-products (Carpenter et al., 2007; Huang et al., 2009; Miliutenko, et al., 2013, Mladenovic et al., 2015). The EAF is a less energy intensive process where electricity is used to melt steel into the end product. This could be a promising alternative that may have close to zero CO_2 emissions, theoretically (Ferreira et al., 2016; Morfeldt et al., 2015). Finally, Giani et al. (2015) explored the replacement of virgin asphalt by 10% RAP in a HMA surface course and by 20% RAP in a HMA binder course of a 1 km asphalt pavement section in Italy. They found that the HMA RAP alternative exhibited 688 tons of CO_2eq (6.8%) GHG emissions reductions, considering that the environmental burdens of asphalt significantly depend on the bitumen content (Häkkinen and Mäkelä, 1996).

Description of Context: Recycling Asphalt Pavement in "Cooperativa Trasporti Imola Scrl" Company

The "Cooperativa trasporti Imola Scrl" (CTI) company has four plants for the production of asphalt mixes, three batch plants and one drum plant. In both the typologies, the mineral aggregates are dried and heated in a rotating drum. Nowadays, the predominant plant type in the U.S. and New Zealand is the drum-mix plant, while batch plants prevail in Europe, South Africa, and Australia (EAPA, 2018). While in batch plants aggregates are stored in hot bins to mix them with bitumen in discrete batches, in drum plants the mixing of aggregates with bitumen takes place in the same drum. After those processes, the mixtures are stored in silos or loaded into trucks for delivery. Afterwards, aggregates, temporarily stored in a silo, are transported by mechanical shovels, and loaded on hoppers for pre-dosage. The CTI plants have seven hoppers, five for aggregates and two for milled materials, with the possibility of introducing RAP. In the drum plant, the drum acts both as a dryer and a mixer, whereas in the batch plant the mixing of aggregates with bitumen takes place in different machines. The bitumen, heated to 130–150°C by an oil-fired oleothermal boiler, is kept at a constant temperature in the storage tanks. Considering hot in plant recycling, while the most conventional drum plants can accommodate up to 50% RAP, and the percentage of reusable RAP in batch plants ranges from 10 to 30% (Kandhal and Mallick, 1997; Noferini et al., 2018), nowadays multiple readily available for production technologies can accommodate up to 100% of recycled hot mix asphalt (Zaumanis et al., 2014; Noferini et al., 2018). The CTI batch plants might accommodate up to 45–50% RAP, while the percentage of reusable RAP in drum plants is approximately 50%. Hence, nowadays there is no technical limit on RAP content in new asphalt mixtures, as long as an adequate performance is achieved. However, it is a common practice to set a maximum value, to guarantee the durability of asphalt mixes in the long term (JRC, 2016), due to the possible compromising effect of the aged bitumen in RAP on the final mix. Moreover, the defined optimum content of RAP in asphalt mixtures varies widely from country to country, from 7 to 50% (up to 66%) by mass (Kalman et al., 2013; Garbarino et al., 2016). On average, western European countries have 40% RAP content in HMA and WMA mixtures, while Eastern European countries have 6% (BIOIS and EC, 2011; Blankendaal et al., 2014; Garbarino et al., 2016).

Moreover, according to the European Commission, steel slags can be used in road construction, meeting the requirements of European and national legislations and standards, although a specific recycling target is not set (JRC, 2016).

In Italy, the steel slags resulting from steelmaking are considered by-products, whereas RAP, as a result of the milling operations of existing road pavements at their end of life stage, is not considered to be waste, as long it is re-used within the domain of the asphalt sector (Italian M.D. 69/2018). Due to the fact that in Italy the use of steel slags and RAP for road construction is allowed, in this study, the content of RAP and EAF slags in the mixtures was designed to allow for the production of the mixtures in the CTI batch plant and to achieve acceptable values of physical and mechanical properties, in compliance with national legislations and technical standards.

Objectives and Research Approach

This study aims at testing the use of EAF steel slags and RAP in two mixtures, for wearing and binder courses, respectively. The physical and mechanical properties and the environmental performances have been evaluated. The objectives of the research study are summarized below:

- define a standard characterization of mixtures in order to evaluate the physical and mechanical performances related to the use of virgin and recycled materials;
- assess the environmental impacts associated with the mixtures and model a best-case scenario for the CTI batch plant with the maximum percentages of steel slags and RAP;
- identify practical implications of the use of recycled materials in new asphalt mixtures, from a life cycle and industrial symbiosis perspective.

The research study is divided into two phases: in the first phase, the effects of recycled materials on asphalt mixture proprieties are investigated. Two specific types of asphalt mixtures are produced with different compositions:

(1) 35% RAP and 16% steel slags for the wearing course, by weight;
(2) 40% RAP and 15% steel slags for the binder course, by weight.

Asphalt materials are characterized in terms of size distribution, strength modulus (indirect tensile strength), and volumetric properties (air voids content).

The second phase aims at evaluating environmental impacts by applying LCA methodology to the geographical context of the CTI company. The novelty of this study is the integration of the technical analysis of material characterization, assessed by laboratory experiments, with the analysis of the environmental impacts.

TABLE 1 | Composition of asphalt mixtures, percentages of aggregates by weight.

Material	Fraction (mm)	MixW0 (control)	MixW1 (35% RAP, 15% EAF steel slags)	MixB0 (control)	MixB1 (40% RAP, 16% EAF steel slags)
Gravel	14/20		—	15	6
Gravel	10/16	—	—	20	—
Gravel	8/12	—	—	10	—
Gravel	4/8	19	10	7	—
Gravel	3/6	30	9	12	10
Sand	0/4	45	30	32	25
Filler	—	6	1	4	3
RAP	0/8	—	35	—	—
RAP	8/12	—	—	—	40
EAF slag	4/8	—	15	—	16

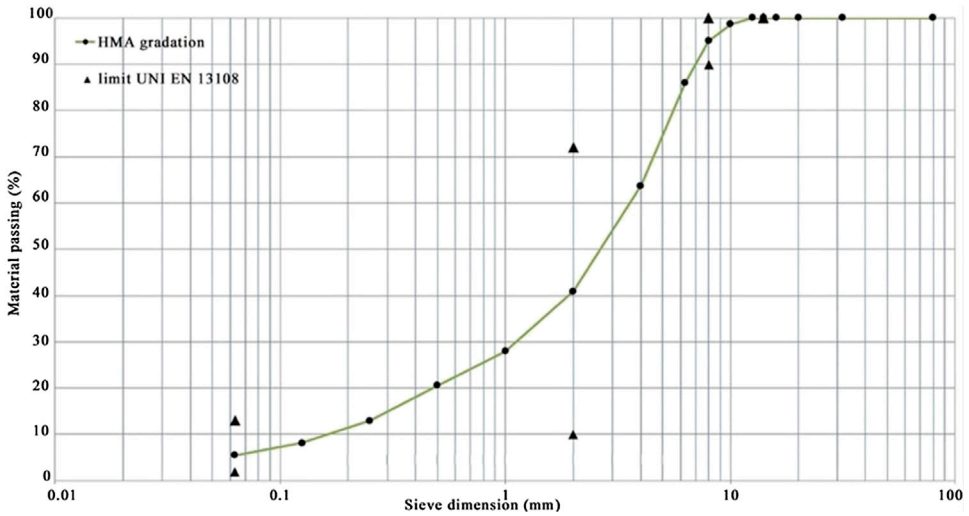

FIGURE 3 | MixW1 gradation and limits.

MATERIALS AND METHOD

Performance Analysis of Asphalt Mixtures

Four mixtures were analyzed:

- A control mixture for the wearing course (MixW0)
- An experimental mixture for the wearing course (MixW1)
- A control mixture for the binder course (MixB0)
- An experimental mixture for the binder course (MixB1)

A description of the four mixtures can be found in **Table 1**.

The design of the aggregate distribution was based on gradation limits specified in the UNI 13108 Italian technical specification for bituminous layers, as shown in **Figures 3**, **4**, with cumulative percentage passing on the *y* axis and logarithmic sieve size on the *x* axis. On the graphs, the sieve size scale (*x* axis) is logarithmic.

The experimental program can be divided into three different phases. In order to evaluate the physical and mechanical performances of the designed mixtures, MixW1 and MixB1 were characterized in terms of particle size distribution (1), volumetric properties (2), and strength modulus (3) according to the standard UNI EN 933-1 (2012), UNI EN 12697-12 (2018), UNI EN 12697-23 (2003), and UNI EN 12697-26 (2012). Asphalt mixtures were manufactured in a laboratory with design neat bitumen content of 6% for the wearing course and 5% for the binder course (these percentages include aged bitumen contained in RAP, 3.85% for the wearing course and 3.30% for the binder course, respectively). A neat binder was incorporated into the mixes, taking into account the presence of the aged binder in the RAP fractions. At the same time, the inclusion of recycled materials in the mixtures requires the addition of rejuvenating agents (ACF) to improve the adhesion properties, thermal susceptibility, viscosity, and workability of the mixes. The ACF

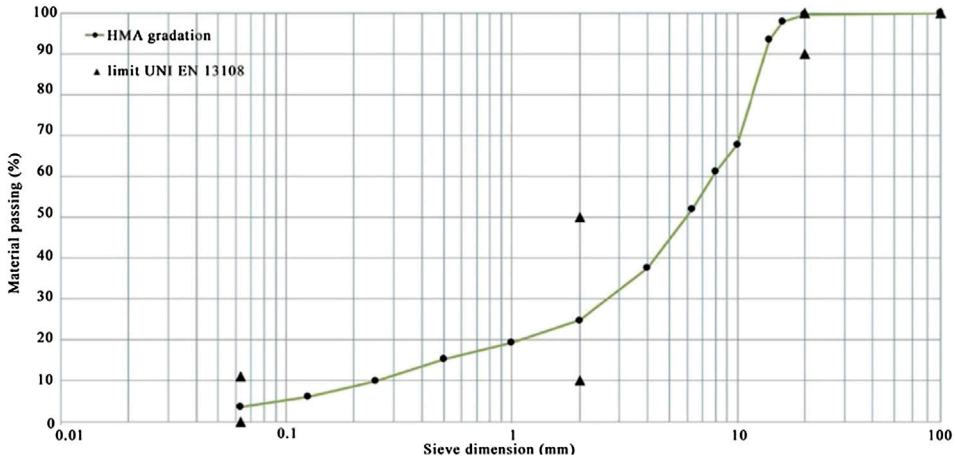

FIGURE 4 | MixB1 gradation and limits.

is incorporated in the commercial bitumen. Both aggregates and bitumen can directly replace their equivalent virgin products in the new mixtures (MixW1 and MixB1) at a ratio of 1:1. Aggregates were heated at 160°C. The physical and mechanical characterizations were then carried out. Asphalt mixes were tested for particle size distribution (EN 933 – 1), air void content (EN 12697-8), and indirect tensile strength (EN 12697 – 23).

Determination of Particle Size Distribution (EN 933 – 1)

The sieve analysis was carried out in a laboratory to define the particle size distribution of MixW1 and MixB1. According to the EN 933-1 standard, a representative weighed sample for each mixture was separated on sieves of different sizes (Series 2). To find the percentage of the aggregate passing through each sieve, **Eq. 1** was used:

$$\% \text{ retained} = \frac{W_{\text{Sieve}}}{W_{\text{Total}}} \times 100\% \quad (1)$$

where: W_{Sieve} is the mass of the aggregate in the sieve; W_{Total} is the total mass of the aggregate.

In order to find the cumulative percentage of the aggregate retained in each sieve, **Eq. 2** was used. The total amount of the aggregate retained in each sieve and the amount in the previous sieves were added up. Then, the cumulative percentage passing of the aggregate was found by subtracting the percentage retained from 100%.

$$\% \text{ cumulative passing} = 100\% - \% \text{ cumulative retained} \quad (2)$$

The % cumulative retained (P_i) used was calculated using **Eq. 3**:

$$P_{c1,i} \cdot \alpha_{C1} + P_{c2,i} \cdot \alpha_{C2} + \ldots P_{cj,i} \cdot \alpha_{Cj} + \ldots + P_{cm,j} \cdot \alpha_{Cm,j} = P_i \quad (3)$$

where: $P_{cj,i}$ is the passing at sieve j; α_{Cj} is the percentage by weight of the total of the sieve j.

To solve **Eq. 3**, **Eq. 4** was provided:

$$\sum_{j=1}^{m} \alpha_{Cj} = \alpha_{C1} + \alpha_{C2} + \ldots + \alpha_{Cj} + \ldots + \alpha_{Cm} = 1 \quad (4)$$

Determination of Air Voids Content (EN 12697-8)

Once the mix design for MixW1 and MixB1 was defined, the following step in the research program considered their physical analysis. The compactability and workability properties of the HMAs were evaluated against gyratory compactor samples (EN 12697-31). For both mixtures, three specimens per MixW1 were compacted up to 180 times more than the gyratory compactor, and three specimens per MixB1 were compacted up to 210 times more than the gyratory compactor. The air voids content (v) of each specimen was evaluated according to the EN 12697-8 standard.

Determination of Indirect Tensile Strength (EN 12697–23)

Finally, for each mixture, according to the EN 12697-23 standard, the indirect tensile strength (ITS) was performed at 25°C.

Life Cycle Assessment Study

The present study has assessed the impacts arising from the hot-mix batch plant by applying an LCA methodology to the geographical context of the CTI plant, located in the Emilia-Romagna region. As previously described, an LCA study consists of four stages: 1) goal and scope definition, 2) inventory analysis, 3) impact assessment, and 4) results and interpretation.

Goal and Scope Definition

Quantitative and comparative life cycle assessment results on road construction materials are essential first steps toward making informed decisions and toward more sustainable practices in road construction (Chowdhury et al., 2010). The present LCA study aims at evaluating the potential environmental impacts related to asphalt mixtures: 1) MixW0 compared to MixW1 and 2) MixB0 compared to MixB1. The final aim is to

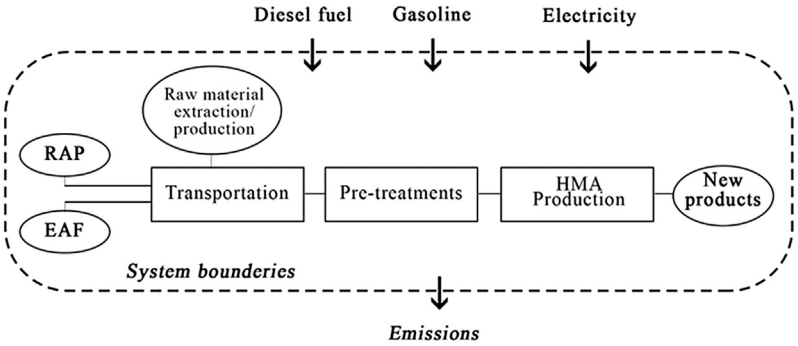

FIGURE 5 | Diagram flow of recycling reclaimed asphalt pavement (RAP) and electric arc furnace (EAF) in the CTI batch plant.

provide recommendations to the CTI for the improvement of technologies and regulations, based on environmental considerations. The functional unit (FU) of LCA is 1 km of secondary suburban road (with a width of 10.5 m, and a thickness of 4 cm for the wearing course, and 6 cm for the binder course). The system boundary includes all the treatment processes, starting from virgin material mining, and secondary and virgin materials entering the CTI batch plant (diesel, electricity), until when they leave the plant as an (solid, liquid, or gaseous) emission or as a new material. The final disposal or recycling processes are out of the boundary. Hence, this LCA is a cradle-to-gate analysis. As depicted in **Figure 5**, the system and processes involved in the present study are:

- The raw material transportation from the mining site/quarry to the CTI plant;
- The RAP transportation from road worksites to the CTI plant;
- The RAP pre-processing, which includes crushing and screening;
- The avoided production and transportation of natural aggregates (replaced by recycled aggregates), including extraction, processing, and transportation to the CTI batch plant;
- The avoided production and transportation of virgin bitumen (replaced by recycled bitumen).

The geographical scope is local. The study focuses on the conditions and CTI technologies used in 2018. The potential environmental impacts were evaluated using the software SimaPro®. This analytical tool works in accordance with the ISO 14040 standard (ISO, 2006a). The impact assessment baseline, performed by the Institute of Environmental Sciences of the Leiden University (CML) in version 3.05, was selected as a method for the environmental impact assessment, using the LCI "Ecoinvent 3.5" and "Europe & Denmark input output" databases. The following impact categories were evaluated: abiotic depletion, acidification, eutrophication, global warming potential, ozone layer depletion, and photochemical oxidation.

Inventory Analysis

Data regarding the core processes, i.e., transportation, hot recycling, and energy consumption, are primary data. For analyzing the CTI HMA batch plant, data were collected directly from the CTI company. Data related to other foreground processes, i.e., bitumen production, extraction of natural mineral resources, and pre-processes of waste asphalt, were instead taken from the LCA software SimaPro databases (Ecoinvent and Europe & Denmark databases). Therefore, the avoided impacts, due to the avoided consumption of natural virgin aggregates because of the EAF steel slags and RAP addition into hot mixes, are modelled using secondary data on quarry activities in Europe.

Inventory data about the transportation of the raw materials, asphalt waste, and bitumen are modelled using the primary data on CTI transports, as shown in **Table 2**. **Table 3** shows the inventory data on energy consumption in the CTI batch plant.

Impact Assessment

In the LCIA, the CML impact assessment baseline calculation method was adopted. The consumption of materials and energy as well as the emissions to air, water, and soil were gathered according to the effects they can have on the environment. According to ISO 14044 (2006b), the LCIA consists of classifications into impact categories, normalization, and the weighting of impacts. In this standard, a distinction between mandatory elements (classification and characterization) and optional elements (normalization, grouping, ranking, and weighting) was pointed out. In the current LCA study, classification and characterization were performed to assess the environmental impacts of MixW1 compared to MixW0 and of MixB1 compared to MixB0. No optional elements were evaluated.

Therefore, this methodology aims to assess the environmental impacts of the processes identified in the inventory analysis. Hence, all substances were measured and assigned to an impact category. The results are represented by single midpoints.

TABLE 2 | Inventory data about the transportation of the asphalt waste, the by-products, and the primary materials to the plant.

Material	Transport distance (km)	Description	Lorry type	Source
EAF slags	150	Road distance between company – CTI batch plant	32 metric tons, EURO 6	Ecoinvent 3.5
Asphalt waste	40	Road distance between RAP site – CTI batch plant	32 metric tons, EURO 6	Ecoinvent 3.5
Natural aggregates	190	Road distances between quarry site – CTI batch plant	32 metric tons, EURO 6	Ecoinvent 3.5
Virgin bitumen	230	Road distances between bitumen plants – CTI batch plant	28 metric tons, EURO 6	Ecoinvent 3.5

TABLE 3 | Inventory data about the energy consumption in the CTI batch plant.

Processes	Energy type	Energy consumption/ton (kWh/ton)	Methane (m^3)	Source
Line 0	Electricity	6131	8.5	Ecoinvent 3.5
Line 1	Electricity	273	8.5	Ecoinvent 3.5

TABLE 4 | Environmental impacts related to MixW1 and MixB1.

Impact categories	Unit	Total	
		MixW1	MixB1
Global warming potential	kg CO_2 eq.	4.60E + 04	5.80E + 04
Human toxicity	kg 1.4 - DB eq.	1.82E + 04	2.62E + 04
Acidification	kg. SO_2 eq.	3.09E + 02	3.35E + 02
Eutrophication	kg PO_4 eq.	8.31E + 01	1.09E + 02
Ecotoxicity	kg 1.4 - DB eq.	1.53E + 03	1.55E + 03
Photochemical oxidation	kg C_2H_4	1.53E + 01	1.72E + 01
Ozone layer depletion	kg CFC - 11 eq.	3.18E – 02	3.39E – 02
Abiotic depletion	kg Sb eq.	1.45E – 01	1.49E – 01
Abiotic depletion fossil fuels	MJ	2.52E + 06	2.73E + 06

TABLE 5 | Mechanical and volumetric properties of MixW1 and MixW0.

Specimen	Avg. ITS (MPa)	Avg. void (%)		
		10	120	210 (v)
MixW1	2.68	11.2	2.7	1.8
MixW0	1.19	13.2	4.0	2.5

TABLE 6 | Mechanical and volumetric properties of MixB1 and MixB0.

Specimen	ITS (MPa)	Void (%)		
		10	100	180
MixB1	1.88	9.6	4.6	1.6
MixB0	1.35	13.6	4.9	2.9

RESULTS

Standard Characterization Test Results: Performances of the MixW1 and MixB1 Mixtures

In order to evaluate the physical and mechanical performances of the mixtures incorporating different recycled aggregate percentages for the wearing and binder courses, MixW1 and MixB1 were characterized in terms of air void content (v), indirect tensile strength (ITS), indirect tensile stiffness modulus (ITSM), and indirect tensile strength ratio (ITSR).

The determination of the air void content of MixW1 and MixB1 can be found in the **Supplementary Material** as well as the results of the determination of ITS, ITSR, and ITSM of MixW1 and of MixB1, respectively. According to the UNI EN 12 697 – 12 standard, the ITSR value represents the ratio of the indirect tensile strength of wet (water conditioned) specimens to that of dry specimens expressed as percentages, calculated by using the following equation (**Eq. 5**):

$$ITSR = 100 \cdot \frac{ITS_w}{ITS_d} \quad (5)$$

Where: ITS_w is the indirect tensile strength of wet (water conditioned) specimens; ITS_d is the indirect tensile strength of dry specimens.

Life Cycle Assessment Results: Performances of the MixW1 and MixB1 Mixtures

The LCA was chosen to evaluate the environmental impacts that affect the designed road life cycle (production and treatment processes and transportation of the involved materials). The overall environmental impacts related to the production of asphalt mixtures MixW1 and MixB1 in the CTI batch plant are shown in **Table 4**. The analysis was supported by the LCA in compliance with the ISO 14040 standard and the ISO 14044 standard.

DISCUSSION OF STANDARD CHARACTERIZATION OF MIXTURES AND LIFE CYCLE ASSESSMENT

To discuss the results of the standard characterization of the designed mixtures, a comparison of the performances of the designed mixtures and control mixtures was first performed.

Tables 5, **6** show the results for the four mixtures, in terms of average indirect tensile strength (ITS) and average air void percentages.

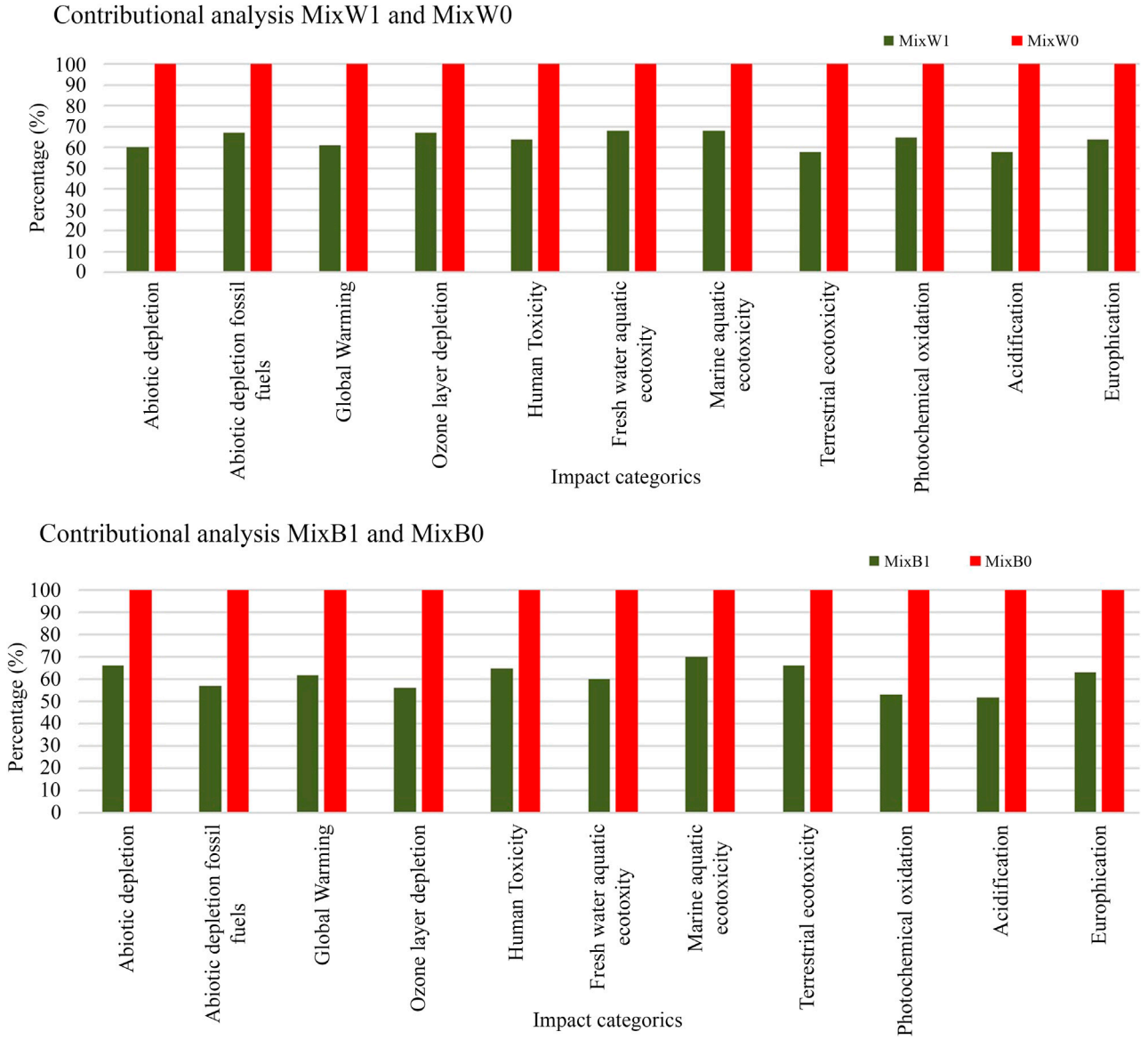

FIGURE 6 | Contribution analysis related to recycling of RAP and EAF slags in CTI batch plant for wearing course **(above)** and for binder course **(below)**.

The mechanical analysis was supported by the ITS test in compliance with the EN 12697-23 standard. For each mixture, three samples were prepared with a gyratory compactor (180 and 210 times) and then conditioned at 25°C for 4 h before testing. According to the scientific literature, an ITS test is generally used to assess the level of tenacity of the aggregate-filler-bitumen bond (Sangiorgi et al., 2019) and the ITS value strongly depends on the medium-high amount of aggregates, bitumen, and recycled materials. From the analysis of data, there was a difference in terms of indirect tensile resistance between the two experimental mixtures (MixW1 and MixB1) compared to the control ones (MixW0 and MixB0). It could be argued that the results indicate a hardening of the composite blend caused by the presence of the aged bitumen. Therefore, the two mixtures show different air void contents.

To note, the average value of ITS recorded for both experimental mixtures was considerably higher than the limit suggested by the Italian technical specifications (ANAS, 2019), which ranges between 0.72 and 1.60 MPa per wearing course, and between 0.72 and 1.40 MPa per binder course.

Similarly, if the Italian technical specification is taken into account, the air void content (v) was lower than the suggested one, which ranges between 3 and 8%.

The standard characterization of the mixtures evaluated the hardening effect of the old bitumen on the content blend. According to Noferini et al. (2018), the hardening effect becomes relevant when the RAP binder content is above 20% by weight of the mixture. In particular, the new bituminous mixtures per binder and wearing course (MixB1 and MixW1)

TABLE 7 | Environmental impacts related to MixW0 and MixW1, MixB0 and MixB1.

Impact categories	Unit	Total			
		MixW0	MixW1	MixB0	MixB1
Global warming potential	kg CO_2 eq.	7.51E + 04	4.60E + 04	9.37E + 04	5.80E + 04
Human toxicity	kg 1.4 - DB eq.	2.86E + 04	1.82E + 04	4.02E + 04	2.62E + 04
Acidification	kg. SO_2 eq.	5.30E + 02	3.09E + 02	6.36E + 02	3.35E + 02
Eutrophication	kg PO_4 eq.	1.30E + 02	8.31E + 01	1.73E + 02	1.09E + 02
Ecotoxicity	kg 1.4 - DB eq.	2.30E + 03	1.53E + 03	2.33E + 03	1.55E + 03
Photochemical oxidation	kg C_2H_4	2.61E + 01	1.53E + 01	3.25E + 01	1.72E + 01
Ozone layer depletion	kg CFC - 11 eq.	4.74E – 02	3.18E – 02	5.97E – 02	3.39E – 02
Abiotic depletion	kg Sb eq.	2.44E – 01	1.45E – 01	2.23E – 01	1.49E – 01
Abiotic depletion fossil fuels	MJ	3.74E + 06	2.52E + 06	4.73E + 06	2.73E + 06

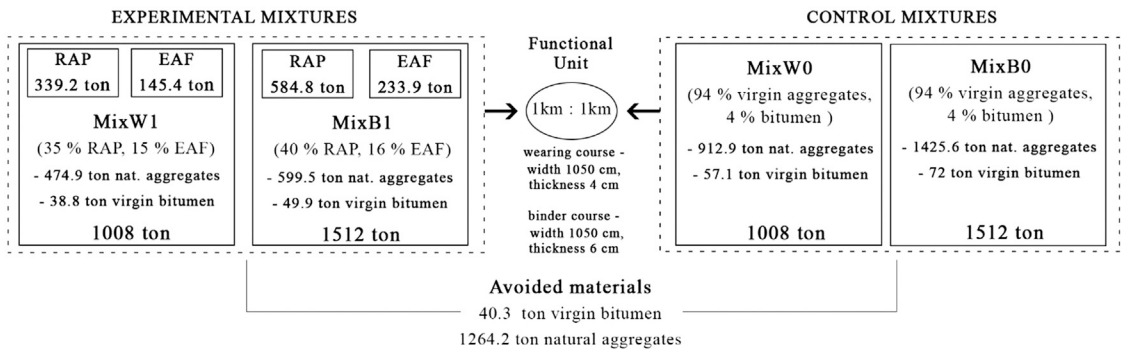

FIGURE 7 | Diagram flow of recycling RAP and EAF in the CTI batch plant for hot-mix asphalt, with the inclusion of the avoided products for wearing course (MixW0 and MixW1) and binder course (MixB0 and MixB1).

were more rigid than the traditional ones (MixB0 and MixW0), but they were not excessively thickened because the final void value was less than 2%. Hence, the final void content of the two new mixtures was optimal.

Moreover, as the stiffness and the fatigue performance were not tested, further research might investigate these aspects.

Secondly, a comparison of LCA results between the two mixtures for the wearing course (MixW0 and MixW1) and the two mixtures for the binder course (MixB0 and MixB1) was performed. Hence, **Figure 6** and **Table 7** show the results of the contribution analysis related to the recycling of RAP and EAF slags in the CTI batch plant. Interestingly, significant differences were found between MixW0 and MixW1, and between MixB0 and MixB1. LCA allows the authors to evaluate the environmental benefits related to the use of recycled aggregates. Due to the reduction of emissions and natural resources used, MixW1 and MixB1 provide environmental benefits in all impact categories (abiotic depletion, abiotic depletion fossil fuels, global warming potential, ozone layer depletion, human toxicity, terrestrial ecotoxicity, photochemical oxidation, acidification, and eutrophication). The avoided impacts associated with the use of recycled material and with the reduction in the consumption of bitumen and aggregates overcome the impacts related to the waste transportation and the pre-treatment processes, resulting in a total reduction in environmental impact. Hence, it can be argued that recycling RAP and EAF steel slags in the CTI batch plant provides environmental benefits, besides reducing the consumption of virgin bitumen and natural aggregates.

These results are supported by the ones obtained in a preliminary and more general study, previously undertaken (Degli Esposti et al., 2020), showing that the experimental mixtures have fewer environmental impacts than the control ones. According to the LCA results, a reduction in all impact categories occurred, and mainly in human toxicity (−30.5%) and eutrophication (−24%), related to the intensive energy consumption and the utilization of non-renewable sources, during both the extraction and transportation phases. In particular, a robust reduction in CO_{2eq} emissions was demonstrated by the better performance of the category global warming potential (−21%), as it was estimated at 46 tons of CO_{2eq} for the experimental mixtures (MixW1 and MixB1) and at 58 tons of CO_{2eq} for the control mixtures (Mix W0 and MixB0). To summarize, the use of RAP and EAF steel slags in 1 km of suburban road allows the CTI to reduce the content of virgin bitumen by weight of the total mixture by 2.15% (by total weight) for the wearing course and by 1.70% (by total weight) for the binder course. Moreover, the use of recycled materials in 1 km of suburban road allows the company to save 438.0 tons of natural aggregates and 18.2 tons of virgin bitumen for the

wearing course, 826.2 tons of natural aggregates and 22.1 tons of virgin bitumen for the binder course, as shown in **Figure 7**.

CONCLUSION

The inert nature of RAP, and the excellent mechanical properties of the EAF slags make them two potentially useful materials in a wide variety of applications, including re-use or recycling in new asphalt pavements. This case study demonstrates the high potential for recycling RAP and EAF steel slags in the road construction sector, as a secondary raw material and a by-product, respectively.

As a result of testing the use of EAF steel slags and RAP in new bituminous mixtures, the physical and mechanical properties as well as the environmental performances of the two mixtures have been evaluated for wearing and binder courses, respectively. In order to maximize the environmental sustainability of the road pavement, the use of RAP and EAF steel slags can be recommended.

Moreover, the authors believe that LCA results and indicators are appropriate tools to compare and communicate the environmental performances of different asphalt mixtures in road construction.

By reducing the global environmental impact and recycling by-products, the CTI and the co-located companies are a real case study of industrial symbiosis at the meso-level.

The authors believe that the development of industrial symbiosis projects provides the opportunity to promote waste reduction, reuse, and recycling, while reducing the environmental impacts, as well as increasing companies' competitiveness, in particular in countries like Italy, where there are already several large industrial clusters. Moreover, information sharing among stakeholders would facilitate the development of industrial symbiosis networks.

Future research efforts could focus on investigating other recycled materials, for the same applications as virgin ones, with the purpose of reaching the same quality level and performances. In this issue, no economic evaluation was carried out. As a future research direction, the economic sustainability will be evaluated.

DATA AVAILABILITY STATEMENT

The original contributions presented in the study are included in the article/**Supplementary Material**, further inquiries can be directed to the corresponding authors.

AUTHOR CONTRIBUTIONS

AB and AE designed the study. AE collected information and materials from the company. AB and AE conceived and planned the experiments for the characterization of asphalt mixtures. AE carried out the experiment. All the authors contributed to the interpretation of the results. AE and CM designed the LCA model and analysed the data. All the authors contributed to the interpretation of the LCA results. AB took the lead in writing the manuscript. All authors provided critical feedback and helped shape the research, analysis and manuscript.

ACKNOWLEDGMENTS

The authors gratefully acknowledge contributions from the CTI company (Imola, Italy).

SUPPLEMENTARY MATERIAL

The Supplementary Material for this article can be found online at: https://www.frontiersin.org/articles/10.3389/fmats.2020.572955/full#supplementary-material.

REFERENCES

AASHTO (2012). *Standard specification for use of reclaimed asphalt shingles (RAS) as an additive in hot mix asphalt (HMA)*. Washington, DC: American Association of State Highway Transportation Officials. https://www.sciencedirect.com/science/article/pii/S0959652620305783#bib.

Agentschap Wegen en Verkeer (2012). *Carbon free-ways*. http://www.wegenenverkeer.be/parallelle-sessies/sessies-pm/carbon-free-ways/item/carbon-free-ways.html

Ahmedzade, P., and Sengoz, B. (2009). Evaluation of steel slag coarse aggregate in hot mix asphalt concrete. *J. Hazard Mater.*,165, 1–3, 300–305. doi:10.1016/j.jhazmat.2008.09.105

Al-Qadi, I. L., Elseifi, M., and Carpenter, S. H. (2007). Report No. FHWA-ICT-07-001. Reclaimed asphalt pavement–a literature review. Rantoul, IL: Illinois Center for Transportation. http://hdl.handle.net/2142/46007

ANAS (2019). I quaderni tecnici per la salvaguardia delle infrastrutture, Vol. V. https://www.stradeanas.it/sites/default/files/pdf/1.3.3/Quaderni_tecnici_volume_5.PDF.

BIOIS and EC (2011). Service contract on management of construction and demolition waste – SR1. Final report task 2. http://ec.europa.eu/environment/waste/pdf/2011_CDW_Report.pdf.

Blankendaal, T., Schuur, P., and Voordijk, H. (2014). Reducing the environmental impact of concrete and asphalt: a scenario approach. *J. Clean. Prod.* 66, 27–36. doi:10.1016/j.jclepro.2013.10.012

Carpenter, A. C., Gardner, K. H., Fopiano, J., Benson, C. H., and Edil, T. B. (2007). Life cycle based risk assessment of recycled materials in roadway construction. *Waste Manag.* 27 (10), 1458–1464. doi:10.1016/j.wasman.2007.03.007

Cass, D., and Mukherjee, A. (2011). Calculation of greenhouse gas emissions for highway construction operations using a hybrid life cycle assessment approach: a case study for pavement operations. *J. Construct. Eng. Manag.* 137 (11), 1015–1025. doi:10.1061/(ASCE)CO.1943-7862.0000349

Chester, M. V., and Horvath, A., (2009). Environmental assessment of passenger transportation should include infrastructure and supply chains. *Environ. Res. Lett.* 4 (2). 024008. doi:10.1088/1748-9326/4/2/024008

Chowdhury, R. D. A., and Fry, T. (2010). A life cycle based environmental impacts assessment of construction materials used in road construction. *Resour. Conserv. Recycl.* 54. 250–255. doi:10.1016/j.resconrec.2009.08.007

Degli Esposti, A., Magrini, C., and Bonoli, A. (2020). Industrial symbiosis and strategies to enhance pavement sustainability, in Proceedings of the third SUN Conference of the Best practices on industrial symbiosis in Italy and the contribution of regional policies, Rimini, Italy. November 7, 2019. https://www.enea.it/en/publications/abstract/industrial-symbiosis-in-italy.

Del Fabbro, M., Stefanutti, M., and Ceschia, C. (2001). Impiego di derivati delle scorie di forno ad arco elettrico come materiale eco-compatibile nella sovrastruttura stradale, Quarry & Construction, Prince Edward Island C1N 4K5: PEI.

EAPA (2018). Asphalt in figures 2018. Available at: https://eapa.org/asphalt-in-figures/.

Espinoza, M., Campos, N., Yang, R., Ozer, H., Aguiar-Moya, J. P., Baldi Sevilla, A., et al. (2019). Carbon footprint estimation in road construction: La Abundancia–Florencia case study. *Sustainability* 11, 2276. doi:10.3390/su11082276

European Asphalt Pavement Association (EAPA) (2011). *The asphalt pavement industry. A global perspective*. 2nd Edn. Global series 101.

European Commission - Joint Research Centre - Institute for Environment and Sustainability (2010). *International reference life cycle data system (ILCD) handbook - general guide for life cycle assessment - detailed guidance*. 1st Edn (2010). EUR 24708 EN. Luxembourg: Publications Office of the European Union.

European Commission (2011). COM (2011) 21, Communication from the commission to the European parliament, the council, the European economic and social committee and the committee of the regions, a resource-efficient Europe–flagship initiative under the Europe 2020 strategy. Available at: https://eur-lex.europa.eu/LexUriServ/LexUriServ.do?uri=COM:2011:0021:FIN:EN:PDF

European Commission (2020). COM (2020) 98, Final communication from the commission to the European parliament, the council, the European economic and social committee and the committee of the regions. A new circular economy action plan- for a cleaner and more competitive Europe.

European Union Road Federation (2017). Road statistics. Available at: http://www.erf.be/wp-content/uploads/2018/01/Road_statistics_2017.pdf.

European Union Road Federation (2019). Road statistics. Available at: https://erf.be/statistics/road-network-2019/

Fernández-Sánchez, G., and Rodríguez-López, F. (2010). A methodology to identify sustainability indicators in construction project management-application to infrastructure projects in Spain. *Ecol. Indicat.*, 10 (6), 1193–1201. doi:10.1016/j.ecolind.2010.04.009

Ferreira, V. J., Sáez-De-Guinoa Vilaplana, A., García-Armingol, T., Aranda-Usón, A., Lausín-González, C., López-Sabirón, A. M., et al. (2016). Evaluation of the steel slag incorporation as coarse aggregate for road construction: technical requirements and environmental impact assessment, *J. Clean. Prod.*,130, 175–186. doi:10.1016/j.jclepro.2015.08.094

Garbarino, E., Rodriguez Quintero, R., Donatello, S., Gama Caldas, M., and Wolf, O. (2016). EUR 28013 EN. Revision of green public procurement criteria for road design, construction and maintenance. Technical report and criteria proposal. doi:10.2791/683567

Gasparatos, A., El-Haram, M., and Horner, M. (2008). A critical review of reductionist approaches for assessing the progress towards sustainability *Environ. Impact Assess. Rev.* 28, 286–311. doi:10.1016/j.eiar.2007.09.002

Giani, M. I., Dotelli, G., Brandini, N., and Zampori, L. (2015). Comparative life cycle assessment of asphalt pavements using reclaimed asphalt, warm mix technology and cold in-place recycling. *Resour. Conserv. Recycl.* 104, 224–238. doi:10.1016/j.resconrec.2015.08.006

Gu, X., Yu, B., Dong, Q., and Deng, Y. (2018). Application of secondary steel slag in subgrade: performance evaluation and enhancement, *J. Clean. Prod.* 181, 102–108. doi:10.1016/j.jclepro.2018.01.172

Guo, S., Hu, J., and Dai, Q. (2018). A critical review on the performance of portland cement concrete with recycled organic components. *J. Clean. Prod.*, 188, 92–112. doi:10.1016/j.jclepro.2018.03.244

Häkkinen, T., and Mäkelä, K. (1996). Environmental adaption of concrete: environmental impact of concrete and asphalt pavements. Espoo: VTT Technical Research Centre of Finland. VTT Tiedotteita - Meddelanden - Research Notes, No. 1752.

Hanson, C. S., and Noland, R. B. (2015). Greenhouse gas emissions from road construction: an assessment of alternative staging approaches. *Transport. Res. Transport Environ.* 40, 97–103. doi:10.1016/j.trd.2015.08.002

Hasan, U., Whyte, A., and Al Jassmi, H. (2020). Life cycle assessment of roadworks in United Arab Emirates: recycled construction waste, reclaimed asphalt pavement, warm-mix asphalt and blast furnace slag use against traditional approach, *J. Clean. Prod.* 257, doi:10.1016/j.jclepro.2020.120531

Hill, N., Brannigan, C., Wynn, D., Milnes, R., van Essen, H., den Boer, E., an Grinsven, A., Ligthart, T., and van Gijlswijk, R. (2012). The role of GHG emissions from infrastructure construction, vehicle manufacturing, and ELVs in overall transport sector emissions. Task 2 paper produced as part of a contract between European Commission Directorate-General Climate Action and AEA Technology plc. http://eutransportghg2050.eu/cms/assets/Uploads/Reports/EU-Transport-GHG-2050-II-Task-2-draftfinal1Mar12.pdf.

Huang, L., Bohne, R. A., Bruland, A., Jakobsen, P. D., and Lohne, J. (2015). Life cycle assessment of Norwegian road tunnel. *Int. J. Life Cycle Assess.* 20, 174–184. doi:10.1007/s11367-014-0823-1

Huang, Y., Bird, R. N., and Heidrich, O. (2009). Development of life cycle assessment tool for construction and maintenance of asphalt pavements. *J. Clean. Prod.* 17, 283–296. doi:10.1016/j.jclepro.2008.06.005

ISO (2006a). Environmental management–life cycle assessment–principles and framework (ISO 14040: 2006), European Standard EN ISO 14040, Geneva, Switzerland: The International Organization for Standardization.

ISO (2006b). Environmental management–life cycle assessment–requirements and guidelines (ISO 14044: 2006), European Standard EN ISO 14044, Geneva, Switzerland: The International Organization for Standardization.

Italian Ministerial Decree Number 69 (2018). Available at: https://www.gazzettaufficiale.it/eli/id/2018/06/18/18G00093/sg

Jamshidi, A., Kurumisawa, K., Nawa, T., Jize, M., and White, G. (2017). Performance of pavements incorporating industrial byproducts: a state-of-the-art study, *J. Clean. Prod.* 164, 367–388. doi:10.1016/j.jclepro.2017.06.223

Jiang, R., and Wu, P. (2019). Estimation of environmental impacts of roads through life cycle assessment: a critical review and future directions, *Transport. Res. Transport Environ.* 77, 148–163. doi:10.1016/j.trd.2019.10.010

JRC (2016). EUR 28013 EN. Revision of green public procurement criteria for road design, Construction and Maintenance. doi:10.2791/201271

Kalman, B., et al. (2013). Final report Re-road – summary report. Available online at http://re-road.fehrl.org/?m=48&id_directory=7325

Kandhal, P., and Mallick, R. (1997). Pavement recycling guidelines for state and local governments. https://rosap.ntl.bts.gov/view/dot/33835.

Martin-Portugues Montoliu, C., Casado Barrada, R., and Guedella Bustamante, E. (2019). Generation of circular economy models and use of renewable materials for a more sustainable pavement construction. *Carreteras.* 4 (223), 62–70.

Meng, H. D. and Liu, L. (2000). Stability processing technology and application prospect of steel slag. *Steelmaking (in Chinese)*, 25 (6), 74–78.

Miliutenko, S., Björklund, A., and Carlsson, A. (2013). Opportunities from environmentally improved asphalt recycling: the example from Sweden. *J. Clean. Prod.* 43, 156–165. doi:10.1016/j.jclepro.2012.12.040

Mladenovic, A., Turk, J., Kovac, J., Mauko, A., and Cotic, Z. (2015). Environmental evaluation of two scenarios for the selection of materials for asphalt wearing courses. *J. Clean. Prod.* 87, 683–691. doi:10.1016/j.jclepro.2014.10.013

Morfeldt, J., Nijs, W., and Silveira, S. (2015). The impact of climate targets on future steel production–an analysis based on a global energy system model, *J. Clean. Prod.* 103, 469–482. doi:10.1016/j.jclepro.2014.04.045

Noferini, L., Simone, A., Sangiorgi, C., and Mazzotta, F. (2018). Investigation on performances of asphalt mixtures made with Reclaimed Asphalt Pavement: effects of interaction between virgin and RAP bitumen. *International Journal of Pavement Research and Technology*.10, 322–332. doi:10.1016/j.ijprt.2017.03.011

Noland, R. B., and Hanson, C. S., (2015). Life-cycle greenhouse gas emissions associated with a highway reconstruction: a New Jersey case study. *J. Clean. Prod.* 107, 731–740. doi:10.1016/j.jclepro.2015.05.064

Pantini, S., Borghi, G., and Rigamonti, L. (2018). Towards resource-efficient management of asphalt waste in Lombardy region (Italy): identification of effective strategies based on the LCA methodology. *Waste Manag.* 80, 423–434. doi:10.1016/j.wasman.2018.09.035

Pasetto, M., and Baldo, N., (2017). Dissipated energy analysis of four-point bending test on asphalt concretes made with steel slag and RAP. *Int. J. Pavement Res. Technol.* 10 (5), 446–453, doi:10.1016/j.ijprt.2017.07.004

Praticò, F. G., Vaiana, R., and Iuele, T., (2015). Permeable wearing courses from recycling reclaimed asphalt pavement for low-volume roads. Transportation research record. *J. Transp. Res. Board*, 2474 (1), 65–72. doi:10.3141/2474-08

Rashad, A. M. (2019). A synopsis manual about recycling steel slag as a cementitious material. *J. Mater. Res.* 8 (5), 4940–4955. doi:10.1016/j.jmrt.2019.06.038

Roberts, B. H. (2004). The application of industrial ecology principles and planning guidelines for the development of eco-industrial parks: an Australian case study. *J. Clean. Prod.* 12, 997–1010. doi:10.1016/j.jclepro.2012.12.040

Sangiorgi, C., Tataranni, P., Lantieri, C., and Mazzotta, F. (2019). Application of mining waste powder as filler in hot mix asphalt. *MATEC Web of Conferences* 274, 04002. doi:10.1051/matecconf/201927404002

Santero, N. J. and Horvath, A. (2009). Global warming potential of pavements. *Environ. Res. Lett.* 4, 3. doi:10.1088/1748-9326/4/3/034011

Santero, N. J., Masanet, E., and Horvath, A. (2011a). Life-cycle assessment of pavements. Part I: critical review. *Resour. Conserv. Recycl.* 55 (9-10), 801–809. doi:10.1016/j.resconrec.2011.03.010

Santero, N. J., Masanet, E., and Horvath, A. (2011b). Life-cycle assessment of pavements Part II: filling the research gaps. *Resour. Conserv. Recycl.* 55 (9-10), 810–818. doi:10.1016/j.resconrec.2011.03.009

Santos, J., Ferreira, A., and Flintsch, G. (2015). A life cycle assessment model for pavement management: road pavement construction and management in Portugal, *Int. J. Pavement Eng.* 16 (4), 315–336. doi:10.1080/10298436.2014.942862

SETAC, SETAC (Society of Environmental Toxicology and Chemistry) (1993). *Definition, "code of practice"*, Bruxelles.

Sherwood, P. (2001). Alternative materials in road construction- A guide to the use of recycled and secondary aggregates. 2nd Edn. London, United Kingdom: ICE Publishing.

Steger, S., and Bleischwitz, R. (2011). Drivers for the use of materials across countries, *J. Clean. Prod.* 19 (8), 816–826. doi:10.1016/j.jclepro.2010.08.016

Taddeo, R. (2016). Local industrial systems towards the eco-industrial parks: the model of the ecologically equipped industrial areas. *J. Clean. Prod.* 131, 189–197. doi:10.1016/j.jclepro.2016.05.051

UNI EN 12697-12 (2018). Bituminous mixtures - Test methods for hot mix asphalt – Part 12: Determination of the water sensitivity of bituminous specimen.

UNI EN 12697-23 (2003). Bituminous mixtures - test methods for hot mix asphalt - Part 23: determination of the indirect tensile strength of bituminous specimens.

UNI EN 12697-26 (2012). Bituminous mixtures - Test methods for hot mix asphalt - Part 26: Stiffness.

UNI EN 933-1 (2012). Tests for geometrical properties of aggregates - Part 1: determination of particle size distribution - sieving method.

Zaumanis, M., Mallick, R. B., and Frank, R. (2014). 100 % recycled hot mix asphalt: a review and analysis. *Resour. Conserv. Recycl.*, 92, 230–245, doi:10.1016/j.resconrec.2014.07.007

Conflict of Interest: The authors declare that the research was conducted in the absence of any commercial or financial relationships that could be construed as a potential conflict of interest.

frontiers in Materials

ORIGINAL RESEARCH
published: 21 April 2021
doi: 10.3389/fmats.2021.582885

3D-Extrusion Manufacturing of a Kaolinite Dough Taken in Its Pristine State

Séverine A. E. Boyer[1]*, *Lucie Jandet*[2] *and Alain Burr*[1]*

[1]MINES Paris, CEMEF-Centre de Mise en Forme des Matériaux, PSL Research University, Sophia Antipolis Cedex, France, [2]MINES Paris Engineering School, PSL Research University, Paris Cedex, France

Ceramic is among the complicated materials to use in the design of fine objects. Complex shapes without any major defect are not easy to produce. In most of the cases, the production of ceramic parts is the results of three steps. Firstly, the "sculpture" of the raw piece by adding raw materials to lead to the final object. Secondly, the "drying" and finally the "high temperature oven-dry" of the dried raw object to transform the granular dough into a nice consistent compact material. Exploiting the special characteristics of ceramic is not only a thing of the past. Nowadays new possibilities, i.e., shapes and styles, can be offered in the use of ceramics, and especially where it concerns the application of the Additive Manufacturing (AM) concept. The combination of Computer Aided Design (CAD) to AM opens a completely new means of finding novel ways of processing final objects. By choosing to use kaolin clay without any chemical additions (or improvers) as "a model material," the ability to produce controlled structures with freedom in design by additive deposition modeling is exposed. Discussions relate to the concomitant control of the process parameters, the kaolin hydration and the complexity of printed structures. The optimization of process parameters (nozzle speed, layer thickness, wall thickness) were defined with the calibration of the material flow. Both windows adjusting water content in dough (%wt) and imposing pressure in the tank of the 3D printer have been defined accordingly. The role of layer impression support was also found to be important. This study credits to use the state-of-the art technique (3D printing) to explore sustainable manufacturing of potteries.

Keywords: ceramics, 3D dough printing, metastable state, kaolin hydration, artistic pottery

OPEN ACCESS

Edited by:
Patricia Krawczak,
IMT Lille Douai, France

Reviewed by:
David Olubiyi Obada,
Ahmadu Bello University, Nigeria
Mohd Mustafa Al Bakri Abdullah,
Universiti Malaysia Perlis, Malaysia

***Correspondence:**
Séverine A. E. Boyer
severine.boyer@mines-paristech.fr
Alain Burr
alain.burr@mines-paristech.fr

Specialty section:
This article was submitted to Structural Materials, a section of the journal Frontiers in Materials

Received: *13 July 2020*
Accepted: *10 February 2021*
Published: *21 April 2021*

Citation:
Boyer SAE, Jandet L and Burr A (2021) 3D-Extrusion Manufacturing of a Kaolinite Dough Taken in Its Pristine State. Front. Mater. 8:582885. doi: 10.3389/fmats.2021.582885

INTRODUCTION

The three-dimensional (3D) printing is transforming the manufacturing technology space. It brings original concepts and promotes the emergence of native materials (and taken in their pristine state), such as biomaterials, within new possibilities of CAD engineering (Guvendiren et al., 2016; Bourell et al., 2017; Bose et al., 2018; Gutierrez-Heredia et al., 2018; Ngo et al., 2018; Harris et al., 2019; Jovic et al., 2019; Wasti and Adhikari, 2020). As example, Bose et al., in 2018 classified selected Addititive Manufacturing (AM) (binder jetting, direct energy deposition techniques, material extrusion and jetting, powder bed fusion and vat polymerization) and presented some combination of AM and biomaterials (ceramics, metallic biomaterials, polymers) to finally focus on applications of AM in biomaterials and biomedical devices (metallic implants to improve osteointegration, hard tissue engineering, soft tissue engineering). Gutierrez-Heredia et al., in 2018 presented a method for

printing 3D models of coral colonies; they generated accurate 3D models suitable for research and education. Ngo et al., in 2018 discussed the revolutionary applications of AM (fused deposition modelling, powder bed fusion, inkjet printing, and contour crafting, stereolithography, direct energy deposition, laminated object manufacturing) in trending applications, i.e. biomedical, aerospace, buildings and protective structures. Materials of survey were metal alloys, polymer composites, ceramics, and concrete. They identified few drawbacks as defaults (voids), inferior and anisotropic microstructure and mechanical properties, divergent from design to execution, layer-by-layer appearance. Additional information can be found in the indexed work of Bourell et al., in 2017. Harris et al., in 2019 reported multimaterial 3D printing by fused filament fabrication and showed the ability of Thermoplastic PolyUrethane (TPU) to adhere to Acrylonitrile Butadiene Styrene (ABS) and acrylonitrile styrene acrylate (ASA). More recently, Jovic et al., in 2019 outlined the most widely used biomaterials derived from land plants and marine algae (nanocellulose, pectin, starch, alginate, agarose, fucoidan, and carrageenan) with an in-depth focus on nanocellulose and alginate. They discussed their potential in 3D bioprinting for tissue engineering, drug delivery, wound healing, and implantable medical devices. And Wasti and Adhikari in 2020 reviewed biomaterials (Poly-Lactid Acid (PLA), PolyHydroxy-Alkanoate (PHA) and blends used in fused deposition modeling technique.

Various ranges of applications are concerned, for instance aerospace, electronics, aeronautics, automobile, art, biomedical, healthcare (Azad et al., 2020; Fan et al., 2020), architecture, and building (Shakor et al., 2019), fashionable food industries (Godoi et al., 2016). Since the pioneer works reported in 2013, 4D printing is introduced and proposes a new strategy that involves the design of a 3D printed part able to undergo a controllable shape change with time as described by (Ge et al., 2013; Tibbits, 2014; González-Henríquez et al., 2019).

The Rapid Prototyping (RP) is based on the local deposition of small volumes of material to directly form as a solderlike shape. The available technologies have been improving constantly since the first French artist Willeme's photosculpture in 1860. The history and evolution of AM technologies are comprehensively discussed by Bourell et al. (Bourell et al., 2009). Among the AM technology, the concept of continuous microextrusion printing is used. The material is selectively dispensed through a nozzle over a movable platform (build stage). When using extrusion, two primary approaches are found. *i.* First, the commonly FDM (Fused Deposition Modeling) where the material is molten (heat) inside the channel of the liquefier. This step allows flow out through the nozzle and bonding before complete solidification. And *ii.* second, the revisited use of a supersaturated fluid slurry, as a material for extrusion, is usually carried out without heating. The later includes pressure-assisted methods such as pneumatic (air, compressed gas) and piston methods (Godoi et al., 2016), as both presented in micro-extrusion bioprinters (Bose et al., 2018; Kumar et al., 2019).

Continuous efforts have made possible the use of geo-materials in 3D printing technologies. Issues, potentialities and opportunities are illustrated in works such as (Travitzky et al., 2014; Zocca et al., 2015; Gosselin et al., 2016; Zhong et al., 2017; Buswell et al., 2018; Lin et al., 2019; Shahsavari and Hwang, 2020; Wang et al., 2020). However, progress is still needed in this geo-materials domain. Indeed, as introduced by (Nair et al., 2020; Shakor et al., 2020a; Shakor et al., 2020b), the printing procedures and dimensional accuracies of printed objects lack details. These details call for a large crossing of knowledge, i.e. interdependent factors of geo-based matrix/control of the process/functional properties.

For this reason, the present research has evaluated kaolin clays in its pristine state. Kaolinite is one of the widely used aluminosilicate minerals, encountered in the manufacturing of traditional ceramics, paper, pottery, paintings and cosmetics. Generally speaking, chemical additions (or improvers) are brought together to propose the best formulation to meet a specific clay-based material; the improvement requiring to answer diverse features as thermal and mechanical properties, rheology, inter-particle interactions, stable phase (Revelo and Colorado, 2018; Revelo and Colorado, 2019).

The regular fused deposition modeling apparatus (FDM) was adapting with a pressure-assisted piston connected to a single screw extruder before the regular nozzle used for printing thermoplastics. For a fundamental approach, the clay-water mixture was selected as a model system, without any chemical additions (or improvers). Concomitant control of the tested process parameters, the kaolin hydration and the complexity of printed structures permitted to understand the effect of the printing conditions on the green mixture. A like-pottery part was fabricated, illustrating the ability, and feasibility of this technology. Post-processed temperature curing, i.e. sintering or as called "high temperature oven-dry," validated the structural stability of the pottery.

MATERIALS AND METHODS

Material Properties

Kaolin Clay and Slurries

Kaolin clay was chosen due to its availability worldwide as minerals found in the Earth's crust, particularly in South of France with its pottery. The porcelain powder (PT010B: composition of kaolin clay 50–100% and quartz 10–25%, density of 2.6 g/cm^3) was supplied by Imerys (France).

The eco-responsible character and the low cost of kaolin clays is also an important factor for scaling up and promoting the results, for individual artists to big traditional ceramics industry and specific use. The single clay was used throughout all slurries, without purification. Only the amount of water was varied from one formulation to the other to, in the end, work with a single formulation optimized for processing. Therefore, the chemical composition and the solid particle characteristics (network microstructure, size distribution and shape of particles) may be deemed as constant and practically without any effect on the final printed parts.

From Atomic Composition to Hexagonal Sheets

The crystallographic structure of kaolin is made of two layers. One is formed by octahedral meshes sharing their oxygen atoms

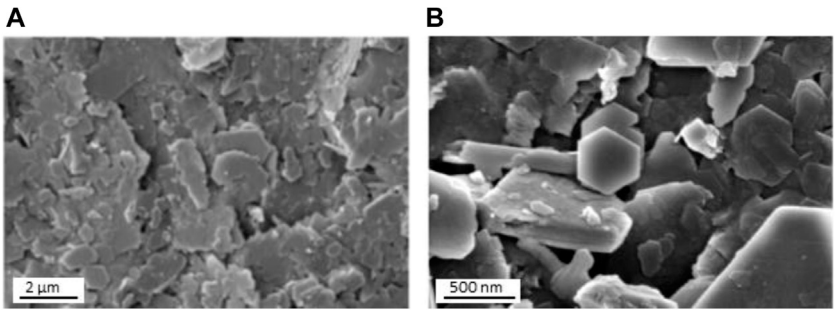

FIGURE 1 | Hexagonal booklet-like sheets of native (powder) kaolin clay **(A)** scale of 2 µm, **(B)** scale of 500 nm. Hexagonal structure forms of steps which reveal successive layers of sheets.

at their corners with other neighbour octahedral meshes. The second one is an assembly of tetrahedral meshes connected to the octahedral layer with hydroxide groups. Aluminum is in the center of the octahedra and silicon in the center of the tetrahedra. Kaolinite is a widely used hydrated alumino-silicate minerals, mainly composed by kaolin clay with a theoretical molecular formula of Al_2O_3 $2SiO_2$ $2H_2O$ (Bergaya et al., 2006; Loginov et al., 2008). In the observable morphology scale, the assembly of a layer formed of octahedra to a layer formed of tetrahedra forms is called a leaflet. The surfaces of these single sheets have hydroxide and oxygen atoms which allow water molecules to be inserted between the sheets (Awad et al., 2017; Awad et al., 2019). **Figure 1** displays the hexagonal sheets, on native kaolin clay.

Hydration

The suspensions of kaolin clay were prepared from dry kaolinite powder. These suspensions were conducted by mechanically mixing the clay powder with water (or dispersant solution) at appropriate quantities. Water to clay ratios (in % wt) was of 23 and 27% (see Results part). The water content was checked for each test, by collecting a certain mass of the suspensions and measuring it before and after drying at 37°C. This temperature of 37°C was selected to follow the kaolin clay loss of water mass over time and to avoid any deformation of objects. For a standard consideration, recent work by Shakor et al. (Shakor et al., 2020a) post-processed the objects in an oven for 3 h at 60°C.

Viscosity and Filament Size

The rheological behavior of the green slurries was directly verified with the 3D printer. The flow rate was determined using a capillarity test (controlled directly by the 3D printer). Appropriate G-code files with different "extrusion screw speed rates" were tested to perform a single linear path with the printer. The nozzle speed was varied while the nozzle diameter stayed constant (1.0 mm). Then a visual appreciation was made to maintain the optimal print flow. This is necessary to calibrate the throughput, which is unique to each individual printer.

The real flow and the flow programmed from a test code in which the printing time was set (and so only the flow was changed) were compared (see Results part, **Figure 2**). Then single line objects were printed to determine the optimal speed of the nozzle. Again a visual inspection of the surface of the filament was made to verify the homogeneity of the printed lines. A slow speed of 1 mm/s was chosen to produce a very good surface definition of the pottery, with a thickness of 1 mm for all layers (see **Table 1**).

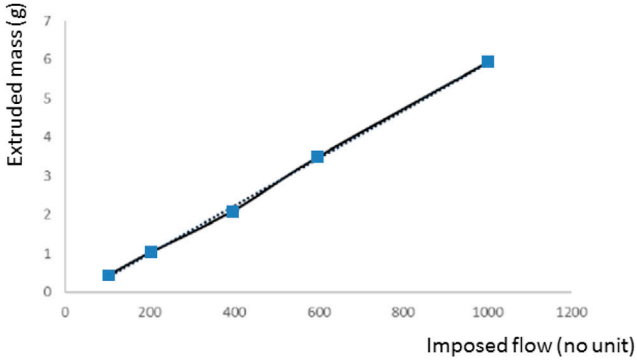

FIGURE 2 | Collected data of extruded mass with imposed flow. Flow is without unit, taken as in the hardware. It corresponds to an activation of the stepper motor of the extruder, and it is compatible with the G-code which controls it.

TABLE 1 | Key parameters in 3D printer, constant flow of 1 mm/s, nozzle diameter of 1.0 mm.

Material flow	Printing speed	Layer thickness	Wall thickness	Infill
60%[a]	1 mm/s[b]	1 mm	1 mm	Concentric

[a] *Proper to our software controller.*
[b] *To be tested directly on the printer with the clay extruder.*

Methodology and Approach

As identified in the spectrum of works of (Buswell et al., 2018), the clay in all its forms is surrounded: properties of wet materials prior to solidification (i.e. pumpability and extrudability); hardened properties of 3D parts, achievement of geometric conformity.

Pressure-Assisted Deposition Modelling

A commercial Delta WASP 2040 TURBO Printer (Italy) was employed to produce prints of the kaolinite parts. The Delta printer is composed of three mechanical arms powered by three independent motors. In the present work, the 3D printer is a modification of a regular Delta fused deposition modeling (FDM) machine in which the thermo-mechanical system for carrying out the extrusion process was adapted to the clay configuration. In clay configuration, no more temperature control is possible.

The machine extrusion unit is connected to a piston tank (3 L), which contains the clay dough, and a nozzle for filament layer deposition. The material is directly transported in its paste (i.e. slurries) form with a pressure-assisted piston system (2.5–3.5 bar) just before it is extruded (see Results part). The whole system works at ambient temperature (nozzle, print with tray).

The Delta printer can produce parts of 400 mm in height and 200 mm in diameter. The advantage of such a printer is its aptitude to print large parts in height unlike other printers. The minimum thickness of a layer is about 50 μm and the maximum thickness is 330 μm. The maximum speed at which the paste can be deposited is 300 mm/s just as the speed of moving the print head.

The modelled-parts (digital one) were scaled and orientated in an upright position. They were printed with the amount of infill for all prints set at 100%, without any scaffold support material, i.e. only walls.

Printed parts were developed layer by layer at a thickness of h = 1 mm per layer. The thickness was optimized by reporting a study with thickness variation from 0.3, 0.6 and 1.0 mm respectively. Simultaneously, the speed of the moving of the print head was taken to be 1 mm/s. The speed of 1 mm/s is in adequacy with the flow speed that was used in the Gcode "capillary" test, directly on the 3D machine.

The basement orientation layers, that is, the first layers of the support surface or foundation of the modeled part, have been defined by the printer specifications (concentric or square). No effect was evidenced in the quality of the successive building layers, even if a concentric or squared foundation was chosen.

But it could and can find its importance when looking at drying, sintering and mechanical behavior.

Skin overlap was set to 1, which indicates full overlap between the outer perimeter and the infill.

To ensure good adhesions of the first deposit layer (which supports the rest of the structure), different support surfaces for impression were tested, i.e. aluminum foil, paper, and polishing paper (see Results part).

Specimen Replication, Software vs. Hardware

Each trial PAM files (gmesh, version 4.1.4) were imported into Cura 3D, an open source slicing software for 3D printers (version 4.4.1) to generate the individual printing slices, paths, or patterns (software). These slices were then compiled and exported as a G-code file ready to be printed on the printer. The file transfer is made via an SD card to the printer (hardware).

Thermal Stabilization, Sintering

Selected printed parts were open-air dried at 37°C for 24 h. They were then sintered in a furnace (Carbolite type, United Kingdom) at 500°C (campaign 1) or 700°C (campaign 2) for 1 h, and then at 1,200°C for 1 h, respectively in air atmosphere. The conditions were selected by following a pottery process and to control the evolution of the metastable states encountered in clay. The heating and cooling temperature ramps were 10°C/min.

Structural Characterization and Mechanical Tests

Nano-Micro-Meso-Scales Structure

The morphology of nano-micro scales structure was evaluated for the raw and in-transition materials. Scanning Electron Microscopy with a high resolution Field Emission in high vacuum mode (MAIA3 Triglav FESEM, TESCAN type, Czech Republic) was used. Samples were mounted on carbon tape and coated with a 7 nm platinum film controlled by a quart crystal nano-balance using a Quorum Q150TES to 30 mA AC. The meso-scale structure was characterized with a binocular microscope (Olympus SZH10, Japan) and an optical microscope (Olympus PMG3, Japan) in reflexion mode.

Compression

Bulk compression test on sintered parts were performed at 1 mm/min, total deformation of 25%, at 23°C (Dartec HA250 type, United States).

Hardness

Bulk hardness was tested using a single lap joint specimen (on a sanded surface of sintered parts), by Knoop indentation tests done for 10 s in force loading 1 Kgf, at 23°C (Buehler type, Switzerland) (Ghorbal et al., 2017).

RESULTS AND DISCUSSIONS

To ensure reproducibility, a methodology has been developed. Itemized protocols concern first the slurries and second the adaptation of the thermoplastic 3D printer to clay configuration.

Slurries

Hydration

In this step, our g-code calibration test maintains two process parameters constant: the flow of 1 mm/s and the nozzle diameter of 1.0 mm. Different hydration %, in H_2O wt, have been tested. The conditions to allow the identification of as named "good printing" slurries are summarized in **Table 2**. The filament diameter and the collapse between filaments were checked post process after the g-code calibration test. The viscosity can play an important role in ensuring defect-free products (Chan et al., 2020). The best solution of the g-code test depends on the conjunction with a suitable combination of printing pressures and speeds. Indeed, at first kaolinite dough should present viscoelastic characteristic to allow extrusion through the fine

TABLE 2 | Percentage of water in printing paste, constant flow of 1 mm/s, nozzle diameter of 1.0 mm.

Water, %wt	Aspect with illustration		Consequence
<23	Too solid		-Poor merger between filaments -Irregular flow
24.5–26	Fine line between too solid-too fluid	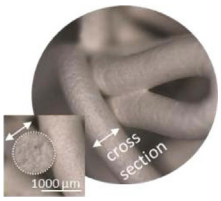	-Good performance of the piece -Homogeneous filaments -Regular flow
>27	Too fluid		-Bad behavior of the printed part (slumping) -Non-homogeneous filaments -No regular flow, in the form of drops

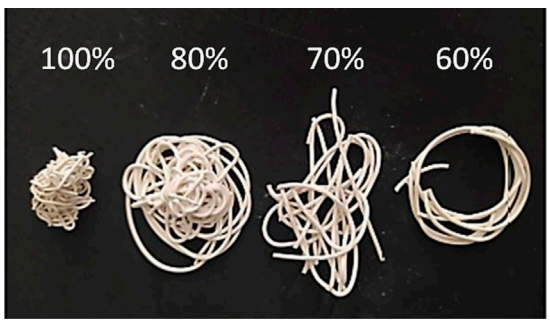

FIGURE 3 | Shear-thinning kaolinite dough suspension behaviors, for highest to lowest speed (%).

nozzle, and then turn into self-supporting clay prior post-deposition of the consecutive layers.

Nonplastic Dry Kaolin Clay

As water is added, the kaolin clay becomes plastic (**Table 2A**). The water (<27 %wt H_2O) acts as a lubricant, surrounding the clay platelets and allowing them to glide over each other. Surface tension forces acting both on the water and the clay bind them weakly together and allow a printed object to retain its shape (24.5–26 %wt H_2O) (**Table 2B**). The diameter of filament of kaolinite dough (950 µm checked) respected the nozzle one (1.0 mm). When excess water is added (>27 %wt H_2O), more than the needed minimum to maintain surface tension, water and mass will start to flow (**Table 2C**). Kaolin clay becomes too fluid to retain the original shape of the object as it was formed from the CAD part.

The development of plasticity in clay is critical to the manufacture of ceramics. Depending on the composition of the clay, plasticity will develop over a narrow range of water content. The hydration window for processing is identified between 24.5 and 26 %wt H_2O; that shows all the importance in preparing valuable slurries.

Real Flow Rate

In our g-code calibration the flow is saying constant. The flow rate is set on the Cura software as a percentage. It is per default equal to 100%. Data translation between software to hardware jobs needed to make a correction of 60% in hardware flow rate. The average extruder mass as a function of the programmed flow rate was then checked, as collected in **Figure 2**. The real flow and the programmed flow are perfectly equivalent. The correlation coefficient of 0.999 allows us to validate the adaptation of the throughput in hardware when it is modified in software.

In addition, it can be visually noticed (**Figure 3**) that for the same movement speed, the flow rate changes the behavior of the kaolinite dough: the higher its speed, the less viscous the fluid. In fact, the supersaturated suspensions of kaolin clay display a shear-thinning (non-Newtonian thixotropic) behaviour (Coussot, 1995; Loginov et al., 2008; Ordonez et al., 2019). The difference in viscosity behavior gives evidence that suspensions of kaolin clay can flow much easier during a print. Thus, the flow of the slurries does not depend merely on its water content but also on the printing speed, and temperature around. This behavior would allow kaolin clay to settle more easily into the n-1 layer, meaning that the cold adhesion would be inherently stronger. The addition of water to raw kaolinite produces a plastic mixture which can be

TABLE 3 | Tank inlet pressure adjustment, constant flow of 1 mm/s, nozzle diameter of 1.0 mm.

Pressure, bar	Water content, %wt	Consequence
<2.5	24.5–26	-No dough flow even when an impression is launched (clogging)
2.5–3.5	24.5–26	-Good flow, dough only came out when the print is launched, setting validated
>3.5	24.5–26	-Dough flowed alone, without the printing being launched

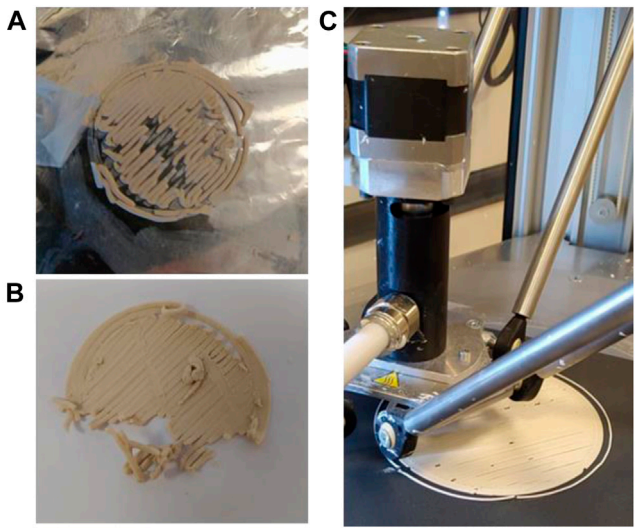

FIGURE 4 | First layer of a cylinder printing of kaolinite dough with different substrates **(A)** aluminium, **(B)** paper, and **(C)** polishing paper (mesh size P320).

shaped without rupture. Kaolinite exhibits plastic properties for primary reasons: kaolin clay particles themselves are crystalline platelet-like structure; with small size of particles; and the presence of water called "water of formation" between the crystalline clay particles. The water acts as a lubricant and allows the clay particles to slide across each other rather than rupture when a shear force is applied.

Adaptation of Thermoplastic 3D Printer to Clay Configuration

The Effect of Print Order on Pressure

Two parameters are used to modify the print throughput: the throughput imposed by the software and the pressure imposed in the pressurized tank. To have a total control of the flow, a window for adjusting the imposed pressure in the tank was kept constant, (<2.5; 2.5–3.5, and >3.5) bar, only the software parameter has been changed. It was possible then to fix the following pressure window as given in **Table 3**, the data are collected on the optimized water content given in **Table 2**.

The Effect of Print Order on First Layer Impression Support

The very first layer was printed and only the optimal condition was tested (24.5–26 wt% H_2O, nozzle diameter of 1.0 mm, nozzle speed of 1 mm/s, software rate 100% (60% in hardware), thickness layer 1 mm, skin overlap set at 1). **Figure 4** illustrates the first layer (foundation) of a cylinder printing of kaolin clay with different substrates A aluminium, B paper, and C polishing paper (mesh size P320, which corresponds to a grain size of 46.2 μm). Aluminum adhesion is the worst; the material slides over the surface and gives heterogeneous dimensional control. For the paper, the adhesion in the early stages of printing is correct, but after a while the adhesion becomes of poor quality. In fact, it has been observed that the surface of the paper does not stay dry but absorbs water (moisture) from the slurry of kaolinite; the surface curls. The best compromise is found for the polishing paper (P320 mesh size). It is mainly due to the surface roughness and probably to its impermeable surface or poor water absorbing character, giving a better anchorage to the deposited material. A P1200 mesh size (equivalent to 15.3 μm) was also tested and did not give better adhesion. Generally speaking, on one hand, the adhesion must be sufficient to allow the slurries to follow the required printing conditions. On the other hand, the adhesion must leave certain freedom to the layer of slurries to avoid any cracking as the slurries start to dry during printing. Indeed, once printed, water can evaporate freely and the slurries will contract (see *To Access to the Effect of Print Order on Structural 3D Making and Sintering*).

To Access to the Effect of Print Order on Structural 3D Making and Sintering

Kaolin needs post "high temperature oven-dry" treatment to produce solid ceramic objects. This additional processing should be carefully checked and carried out to prevent further defects in the part such as its explosion or change of dimension during sintering (such as an unwanted deformation) and to ensure controlled phase change of the hydrated kaolin (Njoya et al., 2017). The sintering profile is illustrated in **Figure 5A** with morphology in **Figure 5B**. The chemical changes can be summarized as here after:

Step 1: heating ramps 10°C/min

Step 2: annealing 500°C (or 700°C), 1h

$Al_2(OH)_4Si_2O \rightarrow Al_2O_3\ 2SiO_2 + 2H_2O$

(hydrated kaolin) (metakaolin) (water)

Step 3: heating ramps 10°C/min

350-750°C, $Al_2O_3\ 2SiO_2 \rightarrow Al_2O_3 + SiO_2$

(metakaolin) (alumina) (silica)

950-1050°C, $Al_2O_3\ 2SiO_2 \rightarrow MgAl_2O_4 + SiO_2$

(metakaolin) (spinel) (amorphous silica)

Step 4: annealing 1200°C, 1h

$Al_2O_3\ 2SiO_2 \rightarrow 2(3Al_2O_3\ 2SiO_2) + 5SiO_2$

(metakaolin) (mullite) (amorphous silica)

Step 5: cooling ramp 10°C/min

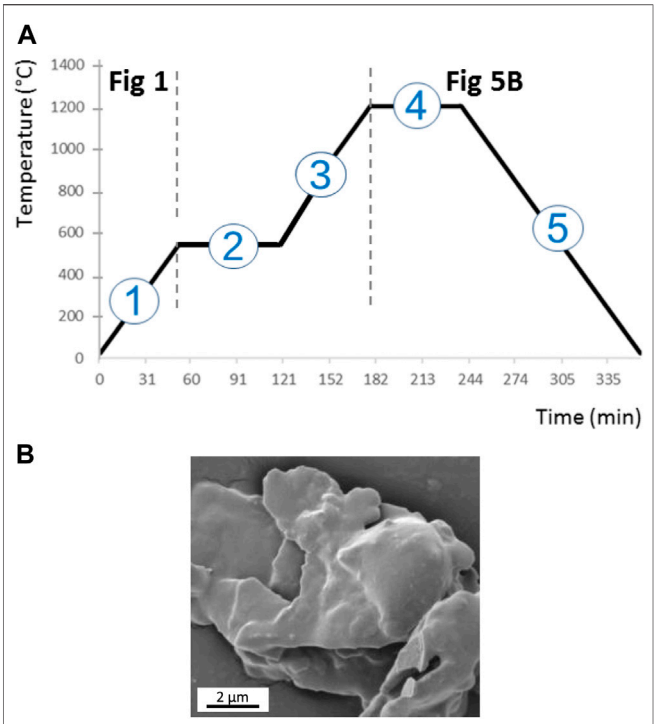

FIGURE 5 | From hydrated kaolin to pseudo-ceramic: **(A)** thermal history, **(B)** morphology after thermal sintering. Depending of the nature of the system, variety of higher temperature mineral phases may crystallize.

Chemical Reaction-Scale

Before sintering process of ceramics, the first stage is the "air drying" (**Figure 5A**). It is generally carried out at temperature around 150°C, but in our case 24 h at 37°C (see Material part, Material Properties). At this stage of "air drying," the water is in the form of films surrounding the kaolin sheets; the mechanically admixed water is lost. The kaolin mixture shrinks and loses its plasticity. The solid to solid transition gives specific results, here the kaolin sheets draw closer together, until they may eventually come into contact and start to adhere. The next water loss takes place more slowly, coming from the pore spaces between the clay particles. Induced-stresses may later lead to structural damage (cracking or warping) of the printed part. The printed layers experience maximum shrinkage while exhibiting maximum of water loss. Water first evaporates from the surface of the printed part, then by capillary action, water rises from the interior to the surface and in turn evaporates. One can notice that this property makes clay a candidate for environmental remediation applications (Garrisson, 2016; Awad et al., 2019).

When the temperature rises to 200–400°C①, any mechanically bound or interstitial water, still present after the ambient drying, is vaporized and driven off.

In addition to water, as the temperature rises to over 200°C, any carbon or organic matter in the clay will start to oxidize, migrate to the surface and finally escape as CO or CO_2. The oxidation rate and completeness depend on the temperature scan (rate), the time hold at the maximum annealing temperature, the size (wall width) of the parts, the clay and paste nature.

Two plateaus then follow the "air drying" stage. Indeed, when the clay is sintering at temperatures over 600°C②, and in particular at higher temperatures of ~1,200°C④, the clay undergoes major structural and chemical changes due to dehydroxylation (i.e. hydroxyl ions (OH^-) lost which are chemically bound within the clay lattice) (Johnson and Kessler, 1969). Chemically bound water is lost. These changes dictate the conversion of clay into a useful ceramic. High temperatures dislodge ions from original positions held in the clay structure into more favorable sites, thus converting the clay into chemically stable and structurally stronger material.

Plateau at 450–500°C② permits a complete evaporation of the water contained between the sheets of the kaolin structure. The water loss occurs abruptly during the structural transformation of hydrated kaolin to metakaolin with minor shrinkage but with increased porosity. Heating kaolinite above about 500°C results in a disordered crystalline form which is still reversible by rehydration back to its ordered kaolin structure. At 550°C, the organic matter is fully oxidized. At 750–850°C③, mineral water was successfully expelled from the clay. Clay starts to lose its characteristic crystalline structure, the crystal lattice itself will break down. At 950–1,100°C, the structure of kaolin is irreversibly lost, but some illite may persist. With the breakdown in clays, high-temperature alteration and reaction products can appear, generally accompanied by pronounced shrinkage. Si-Al kaolin chain collapses on sintering into metakaolin, followed by the rejection of amorphous SiO_2 during spinel formation. Above 1,000°C④, high temperature new mineral mullite phase ($3Al_2O_3$ $2SiO_2$) is expected to form (Yamuna et al., 2002); >1,100°C is the glassy phase of the ceramic where porosity diminishes rapidly. Notice that starting about 600°C, vitrification or "sintering" can start in the more fusible impurities. At the plateau of 1,200°C, the microstructural arrangements take place during the processing transformation of kaolin to ceramics. In theory, the piece should be cooked over 1,400°C to be completely transformed, but we only had at our disposal an oven reaching 1,200°C (Revelo and Colorado, 2018).

Morphology-Scale

Morphology of kaolin particles after sintering at 1,200°C for 1 h is illustrated in **Figure 5B**. Compared to the morphology of native kaolin (**Figure 1**), the hexagonal shapes have given way to more rounded shapes with a densification (**Figure 5B**). The densification would be done by two mechanisms, the volume distribution or/and the grain boundaries diffusion (Johnson, 1969). At this stage (it is not the scope of the works to discuss the processus that will require further analysis) diffusion in volume therefore in the solid state is a time dependent processus sensitive to the sintering speed. Secondly, the diffusion at interfaces (grain boundaries) would be plausible since observations with Scanning Electron Microscopy shows that the pseudo-hexagonal plate structure seems to be retained during densification and after transformation of metakaolin. This morphology as well as small size (about 2 µm) would favor obtaining a large specific surface of solid-solid contacts necessary for efficient diffusion at grain boundaries. It is also necessary to consider the simultaneous existence of a mechanism of densification by viscous flux which has been demonstrated in the literature during the sintering of compacts or kaolinite-based

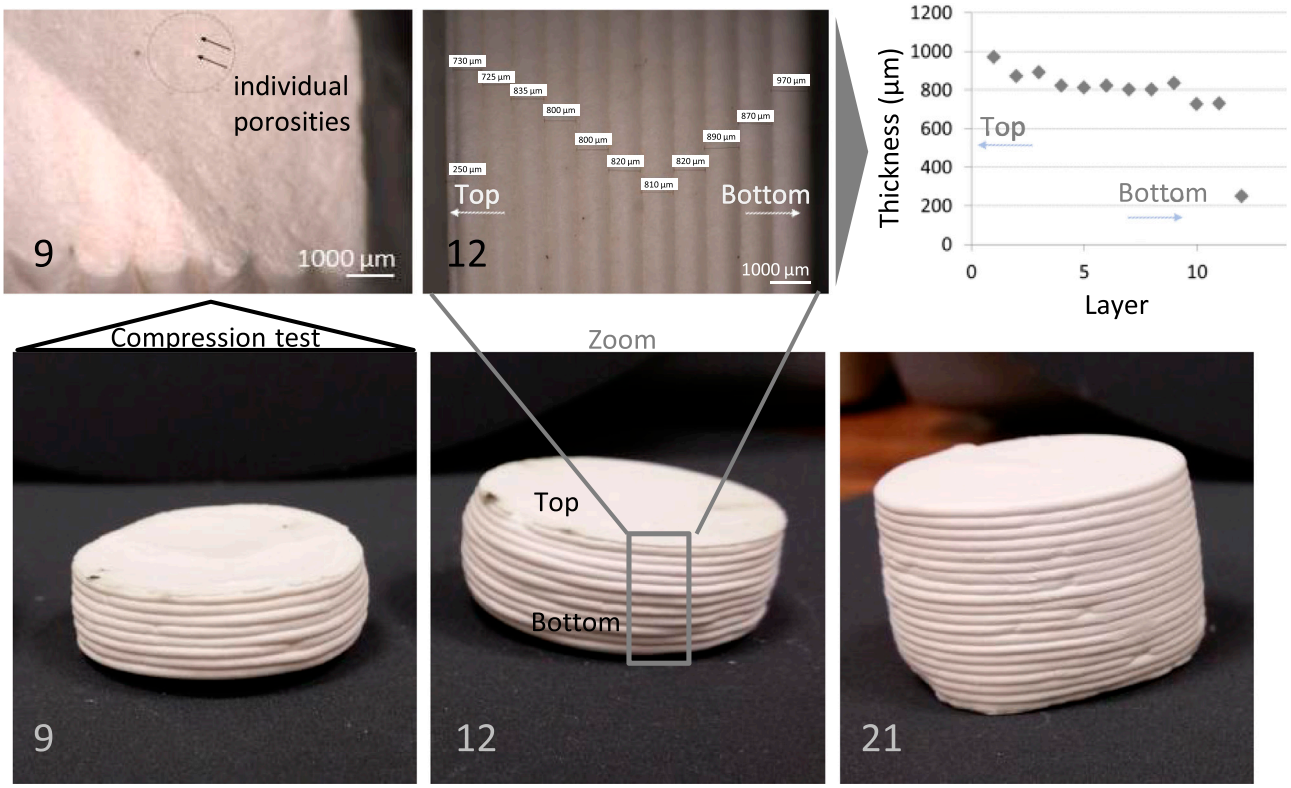

FIGURE 6 | Printed pawns after sintering, first campaign with Step 2: annealing at 500°C, 1 h. The illustrations (9, 12, and 21 mm) show the dimensional stability of the parts. Right side: facies of rupture after compression test (1 mm/min 25% deformation, T 23°C) on 9 mm pawn. Medium side: size of the inter-filament on 12 mm pawn. Printed-layer thickness of 1 mm. Cylinders of 20 mm in diameter.

ceramics (Cambier et al., 1984). This point considers additional open questions, the application of the speed method, the constant annealing, the growth of primary mullite above 1,150°C and, but around 1,250°C the crystallization of new phases (cristobalite and secondary mullite).

3D Printed Part-Scale

Printed pawns of different size (3, 9, 12, 15, 18, and 21 mm corresponding to the superposition of the number of layers) after sintering were observed. Bearing at Step 2: 500°C② (campaign 1) was of interest because the pawns did not break during sintering, whatever their size, with dimension stability and conformity. **Figure 6** shows 9, 12, 21-layered pieces fabricated using kaolin clay, after the first sintering campaign. The inter-layers coexist with one another much more smoothly than the top adhesion layer does (**Figure 6**, 12-pawn Top and Bottom and graph), thickness variation 970–730 µm. The layer on the top adhesion is flush, thickness of 250 µm.

While observing the pawns, their difference to the touch clearly shows that the microstructural arrangement expected during baking has taken place, even with a color change from beige to light pink. The kaolin is then supposed to be found in a frozen metakaolin-mullite transient state (**Figure 5B**).

To examine the dimensional stability idea more closely, optical microscopy was used to look at the cross-section of a rupture facies of a pawn after a compression test (1 mm/min, 25% deformation, 23°C) (**Figure 6**, 9-facies of rupture). The facies of rupture revealed that kaolin clay indeed well settled, in the bulk and outer shell. The interlayer connection shows no defaults, only few small individual porosities are found within layer thickness itself. The hardness of the bulk material has been checked, by indentation Knoop test (10°s in force loading 1 Kgf, 23°C); a HK of [300–350] was revealed, typical values for hard materials. Enough vitrification has taken place to give a moderate degree of hardness, the clay is considered baked.

Nota, a second sintering campaign, with a Step 2: annealing at 700°C②, 1 h was also experimented. This second campaign confirmed that the first level annealing step at 500°C is essential to allow the water to fully evaporate. At 700°C, some water would still be confined and blocked before processing the kaolin. The pressure exerted by the water during heating would cause the fissuration or even the explosion of the object with temperature increasing. It also allowed studying the influence of the thickness of the pawn on the quality of sintering. The 3 mm high pawn became curled after sintering, no crack is visible showing strong inter-layer contact (**Figure 7**, 3-pawn). The pawns of 9, 12, 15, and 18 mm exhibit slight cracks. This clearly evinces concentric failure along the filament interfaces and inter-layer distortion of the outer shell (**Figure 7**, 18-pawn Top and Bottom and graph), thickness variation range of 800–700 µm. The layer on the top adhesion is very flush, thickness

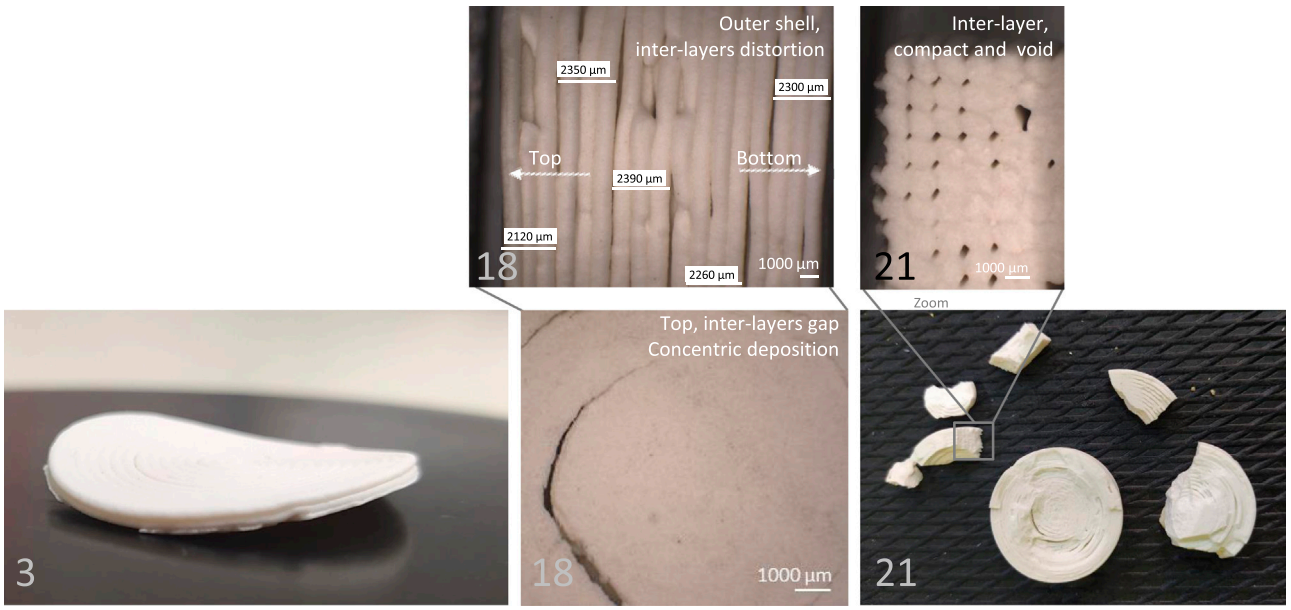

FIGURE 7 | Printed pawns after sintering, second campaign with Step 2: annealing at 700°C, 1 h. The illustrations (3, 18, and 21 mm) show the three tendencies of dimensional loss: 3 mm with curled deformation, 18 mm with cracks formation and inter-layer delamination batches, and 21 mm broken parts with a zoom showing voids between inter-filament inside the bulk part due to the printing 3D process. Printed-layer thickness of 1 mm. Cylinders of 20 mm in diameter.

less than 250 µm. We can speak about anisotropic shrinkage considering that the border effect or inter-layer discontinuity makes these areas the weakest points of the printed paste, where local constraints are concentrated while water evaporates. The thickest pawn of 21 mm completely exploded (**Figure 7**, 21-pawn and facies of rupture). The facies of rupture revealed additional weakest mesoscale points between inter-layers with rectangular sometimes accentuated air gaps in the printed-bulk; sometimes compact area. Noting that these cohesive peel failures resulted from each individual pass of the printer. Internal stresses are set up in the ceramic if it loses water too fast according to the kinetics of vitrification of the kaolin. This information is very useful. The quality of the print depends on the type of structure you want to print.

A 3D-PADM CERAMIC AS A PROOF OF CONCEPT

From a CAD Idea and Using Hydrated Kaolin

Of these observations, an artistic pottery sculpture was designed, printed, dried and sintered. The main steps of the AM process are combined in **Figure 8**. Step 1. Software—3D model is designed by using the specialized computer-aided gmesh (version 4.1.4) modeling software. It is digitized and sliced into a number of consecutive layers (Cura 3D version 4.4.1). Step 2. Software to Hardware—The file is subsequently converted to an appropriate format for printing and exported as a G-code file to be transferred to the PADM set up. Step 3. Optimal process parameters—the printing conditions are adjusted depending on the printing methodology, i.e. slurries, pressure, air temperature, and nozzle material flow.

To an Artistic Pottery

Step 4. 3D printing—The designed structure is processed. Step 5. Drying and sintering—The structure is dried and sintered at 500 and 1,200°C (campaign 1, **Figure 5A**, Steps 2 and 4). Successfully a pottery part was fully designed. Kaolinite of low plasticity undergoes no shrinkage upon drying, the printed sculpture did not show deformation. This method permits the fabrication of fully customized and personalized products with a geometrical complex structure in an economical manner (mostly for limited productions). It is worth mentioning that ceramics PADM offers environmental responsible implications, kaolinite slurries can be recycled before complete sintering.

SUMMARY AND OUTLOOK

Manufacturing industries are being forced to create and deliver quality products while decreasing their environmental impact. Kaolinite dough taken in its pristine state is offered to bring insight to help frame and direct future research around the technology.

Specifically:

- Applying PADM technology to print complex structures in geo-materials does not rely on the concentration of manufacturing processes of the product in a single step. It is associated with the synergetic combination of the states of the materials:
  - properties of wet materials prior to solidification (i.e. pumpability and extrudability), i.e. the essential constituents of ceramics (design of slurries with enhanced formulation value),

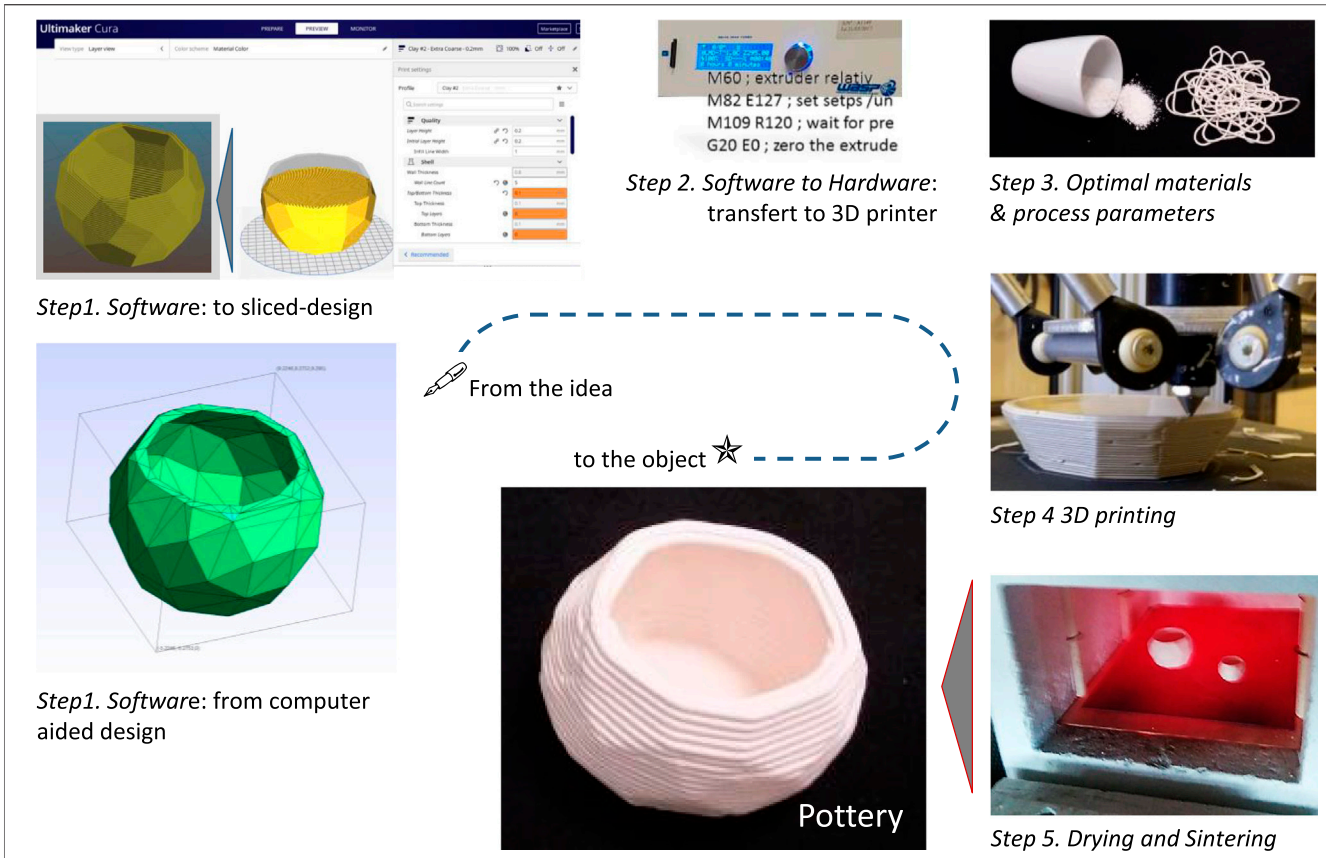

FIGURE 8 | From a CAD idea and using hydrated kaolinite to an artistic pottery.

- binding mechanisms and hardened properties of parts during 3D deposition of layers
- dehydration
- "high temperature oven-dry";

- together with the set of PADM parameters such as:
  - material flow
  - printing speed
  - layer thickness.
- Achievement of geometric conformity is demonstrated. Ceramic parts have no cracks nor shape-instability (warping) before and after sintering.

There are still research gaps to be explored in the optimization and sustainability of AM processes. Challenges in the 3D printing of ceramics are not only attributed to controlling slurries properties to have sufficient workability and open time for extrusion but also the metrics to improve the precision and reliability of the manufacturing process, the efficient post-processing structural properties e.g. strength, inter-layer adhesion, deformation, build-ability.

Finally the non-toxic and reusable materials with the development of new innovative materials are nowadays a fundamental consideration. Future works will concern the formulation of geo-materials especially applying for 3D-printing.

DATA AVAILABILITY STATEMENT

The original contributions presented in the study are included in the article/Supplementary Material, further inquiries can be directed to the corresponding authors.

AUTHOR CONTRIBUTIONS

SAEB: literature review, designing and drafting the content of the manuscript. AB: reading the content of the manuscript. LJ with SAEB and AB: study's work.

FUNDING

Delta WASP 2040 TURBO Printer was bought through the ANR project 'Western Mediterranean Impressed Wares: An interdisciplinary research on Early Neolithic–CIMO' (ANR-14-CE31-0009).

ACKNOWLEDGMENTS

The authors would like to acknowledge the MINES Paris Engineering School of PSL Research University, and especially Michel Bellet, Professor in charge of the Specialty "Materials" for

graduate students, for giving us the nice opportunity to propose and work on this exploratory subject. The authors would also thank Suzanne Jacomet, Gilbert Fiorucci, Thierry Colin and Cyrille Collin, respectively for SEM, sintering with compression, and hardness technical support. CNRS institution is also acknowledged.

REFERENCES

Awad, A. M., Shaikh, S. M. R., Jalab, R., Gulied, M. H., Nasser, M. S., Benamor, A., et al. (2019). Adsorption of organic pollutants by natural and modified clays: a comprehensive review. *Sep. Purif. Technol.* 228, 115719–115739. doi:10.1016/j.seppur.2019.115719

Awad, M. E., López-Galindo, A., Setti, M., El-Rahmany, M. M., and Iborra, C. (2017). Kaolinite in pharmaceutics and biomedicine. *Int. J. Pharm.* 533 (1), 34–48. doi:10.1016/j.ijpharm.2017.09.056

Azad, M. A., Olawuni, D., Kimbell, G., Badruddoza, A. Z. M., Hossain, M. S., and Sultana, T. (2020). Polymers for extrusion-based 3D printing of pharmaceuticals: a holistic materials-process perspective. *Pharmaceutics* 12, 124. doi:10.3390/pharmaceutics12020124

Bergaya, F., Theng, B. K. G., and Lagaly, G. (2006). *Handbook of clay science*. Amsterdam, Netherlands: Elsevier, 1572–4352.

Bose, S., Ke, D., Sahasrabudhe, H., and Bandyopadhyay, A. (2018). Additive manufacturing of biomaterials. *Prog. Mater. Sci.* 93, 45–111. doi:10.1016/j.pmatsci.2017.08.003

Bourell, D., Kruth, J. P., Leu, M., Levy, G., Rosen, D., Beese, A. M., et al. (2017). Materials for additive manufacturing. *CIRP Ann.* 66, 659–681. doi:10.1016/j.cirp.2017.05.009

Bourell, D. L., Beaman, J. J., Leu, M. C., and Rosen, D. W. (2009). "A brief history of additive manufacturing and the 2009 roadmap for additive manufacturing: looking back and looking ahead," in Proceedings of RapidTech 2009: US-Turkey workshop on Rapid technologies, Istanbul, Turkey, September, 2009, 1–8.

Buswell, R. A., Leal de Silva, W. R., Jones, S. Z., and Dirrenberger, J. (2018). 3D printing using concrete extrusion: a roadmap for research. *Cem. Con. Res.* 112, 37–49. doi:10.1016/j.cemconres.2018.05.006

Cambier, F., N'Dala, I., Deletter, M., and Anseau, M. R. (1984). Analysis of the influence of additives on the sintering of kaolinite based ceramics. *Silic. Ind.* 11-12, 219–225.

Chan, S. S. L., Pennings, R. M., Edwards, L., and Franks, G. V. (2020). 3D printing of clay for decorative architectural applications: effect of solids volume fraction on rheology and printability. *Addit. Manuf.* 35, 101335–101338. doi:10.1016/j.addma.2020.101335

Coussot, P. (1995). Structural similarity and transition from Newtonian to non-Newtonian behavior for clay-water suspensions. *Phys. Rev. Lett.* 74 (20), 3971–3974. doi:10.1103/PhysRevLett.74.3971

Fan, D., Li, Y., Wang, X., Zhu, T., Wang, Q., Cai, H., et al. (2020). Progressive 3D printing technology and its application in medical materials. *Front. Pharmacol.* 11, 122. doi:10.3389/fphar.2020.00122

Garrisson, E. (2016). *Techniques in archaeological geology*. 2nd Edn. Berlin, Germany: Springer, 179–207.

Ge, Q., Qi, H. J., and Dunn, M. L. (2013). Active materials by four-dimension printing. *Appl. Phys. Lett.* 103, 131901. doi:10.1063/1.4819837

Ghorbal, G. B., Tricoteaux, A., Thuault, A., Louis, G., and Chicot, D. (2017). Comparison of conventional Knoop and Vickers hardness of ceramic materials. *J. Eur. Ceram. Soc.* 37 (6), 2531–2535. doi:10.1016/j.eurceramsoc.2017.02.014

Godoi, F. C., Prakash, S., and Bhandari, B. R. (2016). 3D printing technologies applied for food design: status and prospects. *J. Food Eng.* 179, 44–54. doi:10.1016/j.jfoodeng.2016.01.025

González-Henríquez, C. M., Sarabia-Vallejos, M. A., and Rodriguez-Hernandez, J. (2019). Polymers for additive manufacturing and 4D-printing: materials, methodologies, and biomedical applications. *Prog. Polym. Sci.* 94, 57–116. doi:10.1016/j.progpolymsci.2019.03.001

Gosselin, C., Duballet, R., Roux, P., Gaudillière, N., Dirrenberger, J., and Morel, P. (2016). Large-scale 3D printing of ultra-high performance concrete—a new processing route for architects and builders. *Mater. Des.* 100, 102–109. doi:10.1016/j.matdes.2016.03.097

Gutierrez-Heredia, L., Keogh, C., and Reynaud, E. G. (2018). Assessing the capabilities of additive manufacturing technologies for coral studies, education, and monitoring. *Front. Mar. Sci.* 5, 1–12. doi:10.3389/fmars.2018.00278

Guvendiren, M., Molde, J., Soares, R. M., and Kohn, J. (2016). Designing biomaterials for 3D printing. *ACS Biomater. Sci. Eng.* 2 (10), 1679–1693. doi:10.1021/acsbiomaterials.6b00121

Harris, C. G., Jursik, N. J., Rochefort, W. E., and Walker, T. W. (2019). Additive manufacturing with soft TPU—adhesion strength in multimaterial flexible joints. *Front. Mech. Eng.* 5, 1–6. doi:10.3389/fmech.2019.00037

Johnson, D. L. (1969). New method of obtaining volume, grain-boundary, and surface diffusion coefficients from sintering data. *J. Appl. Phys.* 40 (1), 192–200. doi:10.1063/1.1657030

Johnson, H. B., and Kessler, F. (1969). Kaolinite dehydroxylation kinetics. *J. Am. Ceram. Soc.* 52 (4), 199–203. doi:10.1111/j.1151-2916.1969.tb13365.x

Jovic, T. H., Kungwengwe, G., Mills, A. C., and Whitaker, I. S. (2019). Plant-derived biomaterials: a review of 3D bioprinting and biomedical applications. *Front. Mech. Eng.* 5, 1–18. doi:10.3389/fmech.2019.00019

Kumar, A., Kargozar, S., Baino, F., and Han, S. S. (2019). Additive manufacturing methods for producing hydroxyapatite and hydroxyapatite-based composite scaffolds: a review. *Front. Mater.* 6, 313. doi:10.3389/fmats.2019.00313

Lin, K., Sheikh, R., Romanazzo, S., and Roohani, I. (2019). 3D printing of bioceramic scaffolds-barriers to the clinical translation: from promise to reality, and future perspectives. *Materials* 12, 2660. doi:10.3390/ma1217266010.3390/ma12172660

Loginov, M., Larue, O., Lebovka, N., and Vorobiev, E. (2008). Fluidity of highly concentrated kaolin suspensions: influence of particle concentration and presence of dispersant. *Colloids Surf, A Physicochem. Eng. Asp.* 325 (1–2), 64–71. doi:10.1016/j.colsurfa.2008.04.040

Nair, S. A. O., Panda, S., Santhanam, M., Sant, G., and Neithalath, N. (2020). A critical examination of the influence of material characteristics and extruder geometry on 3D printing of cementitious binders. *Cem. Concr. Compos.* 112, 103671. doi:10.1016/j.cemconcomp.2020.103671

Ngo, T. D., Kashani, A., Imbalzano, G., Nguyen, K. T. Q., and Hui, D. (2018). Additive manufacturing (3D printing): a review of materials, methods, applications and challenges. *Compos. B. Eng.* 143, 172–196. doi:10.1016/j.compositesb.2018.02.012

Njoya, D., Tadjuidje, F. S., Ndzana, E. J. A., Pountouonchi, A., Tessier-Doyen, N., and Lecomte-Nana, G. (2017). Effect of flux content and heating rate on the microstructure and technological properties of Mayouom (Western-Cameroon) kaolinite clay based ceramics. *J. Asian Ceram. Soc.* 5 (4), 422–426. doi:10.1016/j.jascer.2017.09.004

Ordoñez, E., Gallego, J. M., and Colorado, H. A. (2019). 3D printing via the direct ink writing technique of ceramic pastes from typical formulations used in traditional ceramics industry. *Appl. Clay Sci.* 182, 105285. doi:10.1016/j.clay.2019.105285

Revelo, C., and Colorado, H. (2019). 3D printing of kaolinite clay with small additions of lime, fly ash and talc ceramic powders. *Process. Appl. Ceram.* 13 (3), 287–299. doi:10.2298/PAC1903287R

Revelo, C. F., and Colorado, H. A. (2018). 3D printing of kaolinite clay ceramics using the Direct Ink Writing (DIW) technique. *Ceramics Int.* 44 (5), 5673–5682. doi:10.1016/j.ceramint.2017.12.219

Shahsavari, R., and Hwang, S. H. (2020). Bioinspired cementitious materials: main strategies, progress, and applications. *Front. Mater.* 7, 1–12. doi:10.3389/fmats.2020.00062

Shakor, P., Nejadi, S., and Paul, G. (2020a). Investigation into the effect of delays between printed layers on the mechanical strength of inkjet 3DP mortar. *Manuf. Lett.* 23, 19–22. doi:10.1016/j.mfglet.2019.11.004

Shakor, P., Nejadi, S., Paul, G., and Malek, S. (2019). Review of emerging additive manufacturing technologies in 3D printing of cementitious materials in the construction industry. *Front. Built Environ.* 4, 85. doi:10.3389/fbuil.2018.00085

Shakor, P., Nejadi, S., Paul, G., and Sanjayan, J. (2020b). Dimensional accuracy, flowability, wettability, and porosity in inkjet 3DP for gypsum and cement

mortar materials. *Autom. Constr.* 110, 102964. doi:10.1016/j.autcon.2019.102964

Tibbits, S. (2014). 4D printing: multi-material shape change. *Archit Des.* 84, 116–121. doi:10.1002/ad.1710

Travitzky, N., Bonet, A., Dermeik, B., Fey, T., Filbert-Demut, I., Schlier, L., et al. (2014). Additive manufacturing of ceramic-based materials. *Adv. Eng. Mater.* 16 (6), 729–754. doi:10.1002/adem.201400097

Wang, Z., Yuan, X., Yang, J., Haun, Y., Gao, X., Li, Z., et al. (2020). 3D-printed flexible, Ag-coated PNN-PZT ceramic-polymer grid-composite for electromechanical energy conversion. *Nano Energy* 73, 104737. doi:10.1016/j.nanoen.2020.104737

Wasti, S., and Adhikari, S. (2020). Use of biomaterials for 3D printing by fused deposition modeling technique: a review. *Front. Chem.* 8, 315. doi:10.3389/fchem.2020.00315

Yamuna, A., Devanarayanan, S., and Lalithambika, M. (2002). Phase-pure mullite from kaolinite. *J. Am. Ceram. Soc.* 85 (6), 1409–1413. doi:10.1111/j.1151-2916.2002.tb00289.x

Zhong, G., Vaezi, M., Liu, P., Pan, L., and Yang, S. (2017). Characterization approach on the extrusion process of bioceramics for the 3D printing of bone tissue engineering scaffolds. *Ceramics Int.* 43 (16), 13860–13868. doi:10.1016/j.ceramint.2017.07.109

Zocca, A., Colombo, P., Gomes, C. M., and Günster, J. (2015). Additive manufacturing of ceramics: issues, potentialities, and opportunities. *J. Am. Ceram. Soc.* 98 (7), 1983–2001. doi:10.1111/jace.13700

Conflict of Interest: The authors declare that the research was conducted in the absence of any commercial or financial relationships that could be construed as a potential conflict of interest.

frontiers in Materials

ORIGINAL RESEARCH
published: 03 September 2020
doi: 10.3389/fmats.2020.572347

Characterization of Fly Ash Alkali Activated Foams Obtained Using Sodium Perborate Monohydrate as a Foaming Agent at Room and Elevated Temperatures

*Lidija Korat and Vilma Ducman**

Slovenian National Building and Civil Engineering Institute (ZAG), Ljubljana, Slovenia

Alkali activated foams have been extensively studied in recent years, due to their high performance and low environmental footprint compared to foams produced *via* other methods. Three types of fly ash differing in chemical and mineralogical composition and specific surface were used to synthesize alkali activated foams. Sodium perborate monohydrate was added as a foaming agent and sodium dodecyl sulphate as a stabilizing agent. Foams were characterized at room temperature and after exposure to an elevated temperature (1,000°C). Densities from 1.2 down to 0.3 g/cm^3 were obtained, depending on the type of fly ash and quantity of foaming agent added. Correspondingly, compressive strength ranged from 1 to 6 MPa. Comparing all three fly ashes the most favorable results, in terms of density and corresponding compressive strength, were achieved from the fly ash with the highest amounts of SiO_2 and Al_2O_3, as well as the highest amorphous phase content i.e., RI fly ash. Furthermore, after firing to 1,000°C, the density of samples prepared using fly ash RI remained approximately the same, while the compressive strength increased on average by 50%. In the other two types of fly ash the density increased slightly after firing, due to significant shrinkage, and compressive strength increased by as much as 800%. X-ray powder diffraction analysis confirmed the occurrence of a crystallization process after firing to 1,000°C, which resulted in newly formed crystal phases, including nepheline, sodalite, tridymite, and gehlenite.

Keywords: alkali activated foams, fly ash, sodium perborate monohydrate, microstructural evaluation, mechanical properties

OPEN ACCESS

Edited by:
Jacqueline Anne Johnson, University of Tennessee Space Institute (UTSI), United States

Reviewed by:
Ping Duan, China University of Geosciences, Wuhan, China
Sriramya Duddukuri Nair, Cornell University, United States

****Correspondence:***
Vilma Ducman
vilma.ducman@zag.si

Specialty section:
This article was submitted to Structural Materials, a section of the journal Frontiers in Materials

Received: *15 June 2020*
Accepted: *18 August 2020*
Published: *03 September 2020*

Citation:
Korat L and Ducman V (2020) Characterization of Fly Ash Alkali Activated Foams Obtained Using Sodium Perborate Monohydrate as a Foaming Agent at Room and Elevated Temperatures. Front. Mater. 7:572347. doi: 10.3389/fmats.2020.572347

INTRODUCTION

Alkali-activated (AA) materials have been widely investigated in recent years (Provis and Bernal, 2014; Provis et al., 2015; Luukkonen et al., 2018; Provis, 2018) within the context of the construction and building industry. More specifically, research in the area of sintered and non-sintered foam materials, based on the process of alkali activation, is currently extremely active (Zhao et al., 2010; Chen et al., 2011; Hajimohammadi et al., 2017a; Rabelo Monich et al., 2018; Rincon, 2019). The aforementioned foams present one of the most promising types of AA materials, given their high performance and low environmental footprint in comparison to foams produced by other methods (Dal Pozzo et al., 2019). They are known to offer relatively high strength and good insulation, as well

as being non-combustible up to high temperatures (Bajare et al., 2019). The key element likely to influence the use of alkali-activation is the local availability of appropriate raw materials (precursors and activators) (Provis, 2018), typically metakaolinite, slags and ashes. The wide availability of fly ash has forced researchers to find novel applications suitable for larger-scale production, one option being lightweight foams with a bulk density of <1 g/cm^3. The mechanical properties, i.e., compressive strength of such lightweight materials depends on the density of the foamed AA materials, and is found to range between 1 and 10 MPa for densities from 0.36 to 1.4 g/cm^3 (Zhao et al., 2010; Masi et al., 2014a; Sanjayan, 2015). Foaming agents for producing AA foams are selected from various compounds, especially hydrogen peroxide (Masi et al., 2014; Abdollahnejad et al., 2015; Palmero et al., 2015; Hajimohammadi et al., 2017b; Szabo, 2017), NaOCl (Nyale et al., 2013; Boke, 2015; Łach et al., 2018), metal powders (e.g., elemental aluminum or zinc) (Masi et al., 2014a; Hlaváček et al., 2015; Kamseu et al., 2015; Hajimohammadi et al., 2017c), perborate (Abdollahnejad et al., 2015; Davidovits, 2015), as well as silica fume and some others (Zhao et al., 2010; Henon et al., 2013; Guo et al., 2016; Kioupis et al., 2018). Foaming agents react or decompose in alkaline conditions and form gas which remains trapped inside the structure, thus expanding the material, increasing its volume and forming a cellular structure (Masi et al., 2014a; Sanjayan, 2015). Dried AA foams (already successfully stabilized at room or slightly elevated temperature) (Masi et al., 2014b; Sanjayan, 2015; Kioupis et al., 2018) can also be subjected to heat treatment at higher temperatures, for example in a furnace at temperatures between 800 and 1,000°C, in order to improve mechanical properties (Chen et al., 2011; Badanoiu et al., 2015; Carabba et al., 2017; Bajare et al., 2019; Rincon Romero, 2019). Rincon Romero et al. (2019) presented glass-ceramic foams, based on soda lime glass and coal fly ash, where dried foams were later subjected to heat treatment at 700–900°C. The glass-ceramic foams produced had a high porosity (58–78%), a thermal conductivity of 0.163 ± 0.005 W m^{-1} K^{-1} (measured at 25°C, samples treated at 800°C), and reasonable compressive strength (1.8–8.7 MPa). The results of Abdollahnejad et al. (2015) show that sodium perborate outperforms hydrogen peroxide, leading to a lower overall thermal conductivity of foam materials (approximately 0.1 W m^{-1} K^{-1}) and a compressive strength of approximately 6 MPa. Zhao et al. (2010) fabricated foams with coal fly ash and 13 wt% foaming agent (sodium dodecyl benzene sulfonate and gluten) sintered at 1,050°C for 2 h after alkali-activation. The resulting foams exhibited values for water absorption, apparent density, and compressive strength of approximately 126.5%, 0.414 g/cm^3, and 6.76 MPa, respectively. Results from other researchers to date have nevertheless shown that the stability of foams at high temperatures (especially with regard to shrinkage) is strongly affected by the composition of raw materials, not only when fly ash is used (Martin et al., 2015) but also when other additives such as metakaolin and slag are present in the AA material (Mierzwinski et al., 2019; Tran et al., 2019). Some of the authors concluded that shrinkage occurs due to the increased density or change in volume induced by the crystallization of new phases, rather than due to a melting point or viscous creep (Martin et al., 2015). In 2006, Bakharev wrote that fly ash activated with activators containing sodium exhibited shrinkage cracking and a rapid decline in strength at 800°C (but an increase in average pore size), where the loss of strength on firing may have been associated with the deterioration of the aluminosilicate gel and feldspar crystallization. Martin et al. (2015) studied AA material (fly ash with 15% sodium silicate + 85% 10-M NaOH) from 25 to 600°C and their findings showed that the increase in temperature led to an increased compressive strength (with the specimens exhibiting elastic behavior and brittle failure), increased pore size distribution, and the presence of hydroxysodalite (nepheline at 800°C), and that the dimensional stability of the material was affected at temperatures over 1,000°C. According to Chen-Yong et al. (2017), the mechanical strength of foamed AA materials (class F fly ash with hydrogen peroxide) deteriorated to 3 MPa at 400°C but increased up to 11 MPa at 800°C, due to the formation of crystalline phases (nepheline, anorthite, and cristobalite) at higher temperatures, which potentially act as fillers to reinforce the matrix.

The aim of the present research was to evaluate the usability of sodium perborate monohydrate (SPM), which is inexpensive and widely available, as a foaming agent in AA systems. Three different types of fly ash were used, the main difference being their chemical composition, i.e., the content of SiO_2 and Al_2O_3, which might subsequently influence the properties of the foams produced. The performance of foams was determined after curing at 70°C but also assessed after exposure to an elevated temperature (1,000°C), in order to verify their mechanical properties and dimensional stability at an elevated temperature and thus expand the potential applications of inorganic AA foams to areas where resistance to high temperatures is required, such as for the insulation of furnaces, chimneys, and heat resistant doors.

MATERIALS AND METHODS

Materials

Three types of fly ash (designated as RI, TS, and TT) originating from different sources were investigated, including two types (RI, TS) originating from coal thermal power plants, and one (TT) derived from the co-combustion of coal and biomass material at a heat and power station. RI fly ash is F type, while the other two are C type fly ash. The Brunauer-Emmet-Teller (BET) specific surface areas and chemical compositions (determined by X-ray fluorescence) of the investigated fly ashes are shown in **Table 1**. Sodium silicate solution (sodium silicate crystal 0112; produced by Tennants Distribution, Ltd., SiO_2:Na_2O = 1.97, 54.2 mass% aqueous solution) and NaOH (produced by Donau Chemie, 41.7 mass% aqueous solution) were used as activating agents. The foaming agent was SPM (Sodium Perborate Monohydrate produced by Belinka) and the stabilizing agent was sodium dodecyl sulphate (SDS) (produced by Acros Organics).

Preparation of Alkali-Activated Foams

The investigated AA foams were synthesized from sodium silicate solution, NaOH, and the selected fly ash, to which

TABLE 1 | BET specific surface area and chemical composition of the different types of fly ash (wt%) which were used in the study of alkali-activated foams.

Fly ash	BET specific surface area (cm^2/g)	Loss on ignition (at 950°C)	SiO_2	Al_2O_3	Fe_2O_3	CaO	MgO	Na_2O	K_2O	SO_3
RI	1.7	2.3	52.5	23.3	7.5	6.1	2.5	0.8	2.2	0.7
TS	16.7	5.0	39.4	17.0	8.6	18.6	3.9	0.8	1.8	2.7
TT	33.4	10.2	27.3	10.1	16.7	19.7	11.1	0.2	0.9	1.5

SPM (as the selected foaming agent) and SDS (as the stabilizing agent) were then added. SDS has already been confirmed as a suitable stabilizing agent in a previous study (Korat and Ducman, 2017). Samples were prepared with varying compositions, the sample designations and sample compositions of the various mixtures of the AA foams are presented in **Table 2**. Three mixtures were prepared for each selected fly ash, with designations 1, 2, and 3 representing the amount of SPM and/or SDS added. The amount of SPM and SDS is equal, determined according to the mixture of water glass, NaOH, and fly ash being investigated. First NaOH was dissolved in the water glass solution, and then this solution was added to the fly ash. Components were then mixed together. Samples were mixed for 5 min in a laboratory mixer. At the end of mixing process the SPM and SDS were added and the foaming process started. The mixture was then placed in molds with dimensions of 20 mm × 20 mm × 80 mm and the samples expanded further. The molds were then placed in an oven for 24 h at a temperature of 70°C. The resulting hardened test specimens were demolded and stored for a further 3 days at a controlled temperature of 20 ± 2°C.

Thermal Treatment of Alkali-Activated Foams

The investigated AA foams were subjected to thermal treatment using a Porotherm furnace fired to 1,000°C at a heating rate of 600°C/h.

Methods

The density of the AA foams were calculated by dividing the measured weight of the samples by their dimensions, firstly at the age of 4 days and later after firing. The dimensions, which were also used to determine shrinkage, were measured using digital Vernier calipers (Mitutoyo, Japan), and the sample mass was measured using a laboratory scale (Sartorious, Germany). Reported density values were obtained from the average of three separate measures per sample.

The compressive strength of the test specimens was determined at the age of 4 days and later on after firing, by means of a Toninorm testing machine (Toni Technik, Germany), using a force application rate of 0.005 kN/s. The reported values of mechanical strength were obtained from the average of 10 sample measures per mixture.

The back-scattered electrons image mode of a low vacuum Scanning Electron Microscope (JEOL 5500 LV equipment) was then used to examine the microstructure of selected cross-sections of the hardened foams.

X-ray diffraction analysis was performed using an Empyrean (PANalytical) X-ray diffractometer equipped with Cu Kα radiation. The data was collected at room temperature at an acceleration voltage of 45 kV using a current of 40 mA, from 4 to 70° 2θ in steps of 0.031° 2θ.

For the porosity analysis X-ray micro-computed tomographic imaging was conducted using an Xradia μCT-400″ tomograph (XRadia, Concord, CA, United States). The 3D images were produced using a working voltage of 80 kV and an energy of 125 μA, with a spatial resolution of 29 μm, using a ×0.39 magnification optical objective. Regions of interest (ROIs) were selected from the center of the sample, at a size of 15 mm × 15 mm × 15 mm. The projection data for each tomographic scan consisted of 2,000 projection images, which were taken from different view-points with an exposure time of 1 s per projection. These images were reconstructed into 3D tomographic volumes using Avizo Fire 3D-image analysis software. The segmentation procedure and quantification, for the determination of overall porosity and pore size distribution of the hardened foams, was performed using the procedure previously described (Korat et al., 2013).

Thermal conductivity tests on the samples were performed using a Hot Disk TPS 2500S instrument with a Kapton sensor 7577 at a temperature of 22–23°C. The measure was tested on square samples (20 mm × 20 mm × 80 mm), with 10 measurements performed on each samples.

TABLE 2 | The sample designation and sample compositions of the different mixtures prepared for the investigation (in wt%).

Sample designation	Fly ash	Water glass	NaOH	Addition of sodium perborate monohydrate	Addition of sodium dodecyl sulfate
RI1	64.9	9.2	24.0	1.0	1.0
RI2	63.6	9.0	23.5	1.9	1.9
RI3	62.4	8.8	23.1	2.8	2.8
TS1	51.7	15.5	31.0	0.9	0.9
TS2	50.8	15.3	30.5	1.7	1.7
TS3	50.0	15.0	30.0	2.5	2.5
TT1	46.8	14.2	37.1	0.9	0.9
TT2	45.9	13.9	36.4	1.9	1.9
TT3	45.1	13.7	35.8	2.7	2.7

RESULTS AND DISCUSSION

Analysis of Samples Cured at 70 and 1,000°C

Figure 1 shows the AA foams from three types of fly ash (designated as RI, TS, and TT), prepared using a foaming agent and stabilizing agent in the range 0.9–2.8 wt% (designated as 1, 2, and 3). **Figure 1A** depicts cured samples at 70°C and **Figure 1B** shows samples after being thermally treated at 1,000°C. The change in color observed in the thermally treated samples can be explained by oxidation of the iron present in the raw fly ash, presenting from greyish to brownish color at higher temperatures. This explains why samples with TT fly ash are darker and have a more intense brown color (see **Table 1**).

Table 3 shows the density and compressive strength of the AA foams investigated, after curing at 70°C and when thermally treated to 1,000°C. Sample RI1 exhibits the highest density of all the samples prepared with RI fly ash when cured at 70°C (0.67 g/cm^3). As the amount of foaming agent and stabilizing agent added increased, the density of the RI1 sample decreased by more than half, to 0.3 g/cm^3. A similar trend is observed for samples from the TS and TT fly ash, but both have a higher density than the samples produced from RI fly ash. Nevertheless, even with the highest amount of foaming and stabilizing agents added, their densities remain above 0.5 g/cm^3. Compressive test results for samples from RI, TS, and TT fly ash (cured at 70°C) are also shown in **Table 3** and **Figure 2**. Values are the highest for samples from RI fly ash (around 6 MPa) and begin to decline as the amount of foaming and stabilizing agent added increased, which decreases density. Values for the samples from TT fly ash are slightly higher than for the sample from TS.

Compressive test results for samples from RI, TS, and TT fly ash exposed to temperatures of 1,000°C are also shown in **Table 3**. A tendency to increase compressive strength upon thermal treatment was observed in all samples. After heat treatment, sample RI1 still has the highest density among all three samples from RI fly ash and the lowest amongst all the samples when compared to those produced from the other two types of fly ash. Compressive strength values for RI fly ash began to decline (from 10 to 2 MPa) as the amount of foaming and stabilizing agent added increased, and the density decreased. A similar trend is observed for samples from TS and TT fly ash. There are no significant differences in density between cured and thermally treated samples for samples from RI fly ash (only a few percent), or for samples from TS fly ash, but there is a big difference for samples from TT fly ash (from 10 to 50%), which can be attributed to the increased density resulting from the significant shrinkage.

Dimensional changes, i.e., shrinkage, occurred in samples after exposure to high temperatures of 1,000°C. For samples with the most foaming agent added, the biggest changes were detected in the direction of length, as shown in **Figure 3**. The results show that the difference in dimensional changes (percentage change in length) is approximately 4% for sample RI3, 9% for sample TS3, and 19% for sample TT3. Lin's work (Lin et al., 2009) revealed thermal shrinkage values of 45% for geopolymer and 30% for geopolymer with the addition of 10 vol% alumina filler, when heated to 1,000°C. Shrinkage could be attributed to the presence of alkaline earth flux and other oxides in the fly ash and activators, which enter the glassy phase, decreasing the viscosity of these samples resulting in higher shrinkage (Dana et al., 2004), or, as suggested by Martin, to volume changes caused by the formation of new crystalline phases (Martin et al., 2015). Weight loss after exposure to temperatures at 1,000°C is approximately 10% for sample RI3, 14% for sample TS3, and 20% for sample TT3, as shown in **Figure 3**.

Thermal conductivity tests were conducted on AA foams cured at 70°C, the results of which are listed in **Table 4**. Thermal conductivity properties relative to density are given in **Figure 4**.

The results show the thermal conductivity of RI samples to be 0.205 W/m K for the least porous sample (RI1), falling to 0.123 W/m K for the most porous one (RI3; **Table 4**), where the range of apparent densities for the corresponding samples obtained is 0.67–0.33 g/cm^3. The results for TS samples show that thermal conductivity ranges from 0.151 W/m K for the most

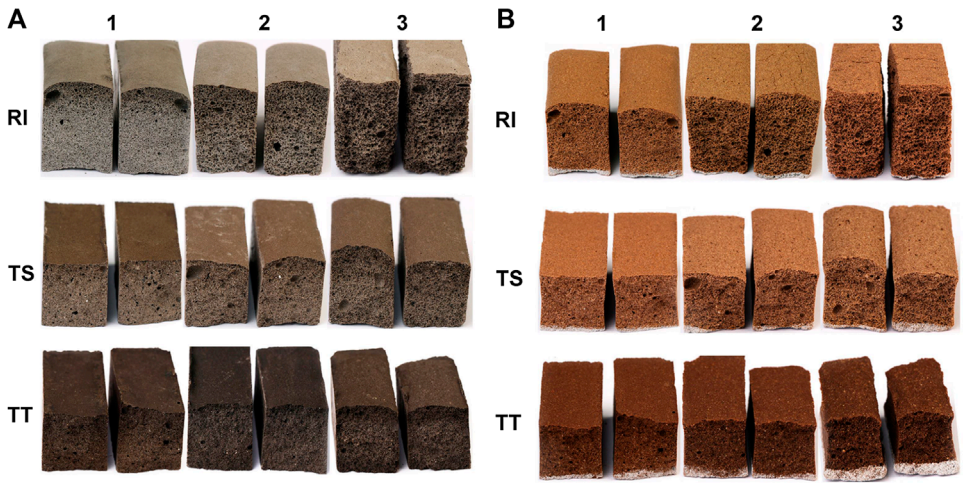

FIGURE 1 | Alkali-activated foams **(A)** cured at 70°C and **(B)** thermally treated to 1,000°C (two samples per mixture).

TABLE 3 | Density and compressive strength of the alkali-activated foams investigated when cured at 70°C and thermally treated at 1,000°C (the measured standard deviations are shown in brackets).

	Density (g/cm^3)		Compressive strength (MPa)	
	Cured samples	Thermally treated	Cured samples	Thermally treated
RI1	0.67 (0.01)	0.68 (0.01)	6.33 (0.79)	9.73 (0.28)
RI2	0.43 (0.02)	0.43 (0.01)	1.93 (0.26)	3.02 (1.25)
RI3	0.33 (0.03)	0.34 (0.02)	1.02 (0.12)	2.17 (0.04)
TS1	1.02 (0.02)	0.95 (0.01)	3.61 (0.46)	12.89 (0.51)
TS2	0.75 (0.01)	0.75 (0.01)	1.81 (0.44)	8.15 (0.69)
TS3	0.57 (0.01)	0.63 (0.01)	1.20 (0.31)	4.98 (0.52)
TT1	1.18 (0.02)	1.03 (0.03)	4.12 (0.33)	9.21 (0.42)
TT2	0.87 (0.01)	0.97 (0.03)	2.31 (0.35)	7.19 (0.96)
TT3	0.71 (0.02)	1.07 (0.02)	2.23 (0.39)	15.51 (2.84)

porous sample (TS3) to 0.262 W/m K for the least porous one (TS1), with the range of apparent densities being 0.57–1.02 g/cm^3. The thermal conductivity measured in the TT samples treated at 70°C ranges from 0.232 to 0.363 W/m K, with a density of 0.71 g/cm^3 in the least porous sample (TT3). As expected, the higher the density, the higher the thermal conductivity (**Figure 4**). The overall behavior of the thermal conductivity is generally controlled by the pore volume, as the most porous sample exhibits the lowest thermal conductivity, as has been found by other researchers (Henon et al., 2013).

Microstructural Examination of Samples Cured at 70°C

Microstructural characteristics have a significant influence on material characteristics, especially thermal and mechanical properties, and because the pore structure inside the material strongly affects the cell (solid) structure, tests by scanning electron microscope (SEM) and X-ray micro-computed tomography (XCT) were performed to gain a more detailed understanding. Firstly, **Figure 5** shows the microstructural evolution of AA foam samples attained through SEM before exposure to higher temperatures. It is evident that samples from RI fly ash have a porous structure with evenly distributed round pores, clearly developed and connected to each other. No micro-cracks are observed within and nearly all of them are cell pores with no mineral crystallization observed inside or on the walls. Contrarily, samples from TS and TT fly ash have a different pore distribution, especially TT foamed samples, which exhibit high structural heterogeneity and contain hardly any rounded pores. These differences in the type of porosity are most probably a reflection of the previously mentioned thermal conductivity—for example TS2 samples have a higher density than RI1 (0.75 and 0.67 g/cm^3, respectively) and exhibited slightly lower thermal conductivity (0.200 vs. 0.205 W/m K), and sample TT3, with a density of 0.71 g/cm^3, showed a thermal conductivity of 0.232 W/m K.

SEM images can only, however, provide the pore characteristics on a single cross section of the specimen, meaning representative shapes or the number of pores cannot be appropriately characterized. More detailed microstructural 3D data can be obtained from high resolution 3D images achieved through X-ray microcomputed tomography. 3D data is displayed on the basis of threshold segmentation and 3D reconstructions, and where the pore structure quantitative visualization and characterization of pore structure of AA foams cured at 70°C are presented on **Figure 6**. **Figure 6** illustrates the ROI (Region Of Interest) of the analyzed AA foams cured at 70°C, including the grayscale image and the biggest pores (by volume), and after the watershed algorithm, where the labeled images show distinct colors for similar pores (purple, green, and yellow pores, as determined according to the EqDiameter). The overall porosity of samples is presented in **Table 5**.

Overall porosity, the local volume ration of the cell (solid) in the ROI, is the highest for samples with RI fly ash. The higher percentages for the RI2 and RI3 samples are illustrated by the porous nature of the AA foams analyzed, due to the addition of the largest amount of agents. RI2 and RI3 both consist of a defined connected pore network with larger individual pores, some of which are even larger than 1 mm. A similar effect is observed in samples from the TS fly ash, but with a smaller pore size and porosity up to approximately 40% in TS3. In the case of TT, the effect of poor porosity development is more notably pronounced. The differences between TT1 and TT3 can be seen from the SEM images (**Figure 5**), which is coherent to the structure detected by XCT scanning, revealing deficient pore development. The structure of samples is similar to one another, with the porosity ranging from 10 to 20%.

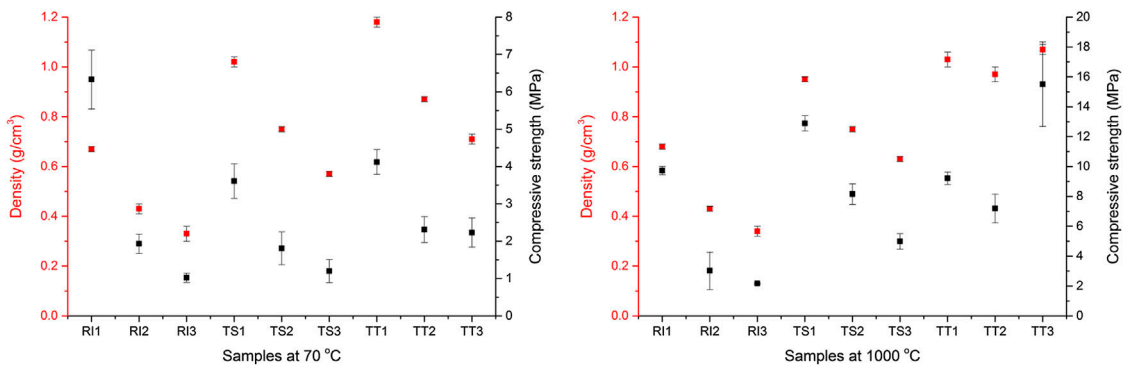

FIGURE 2 | Density and compressive strength of the alkali-activated foams investigated when cured at 70°C and thermally treated at 1,000°C.

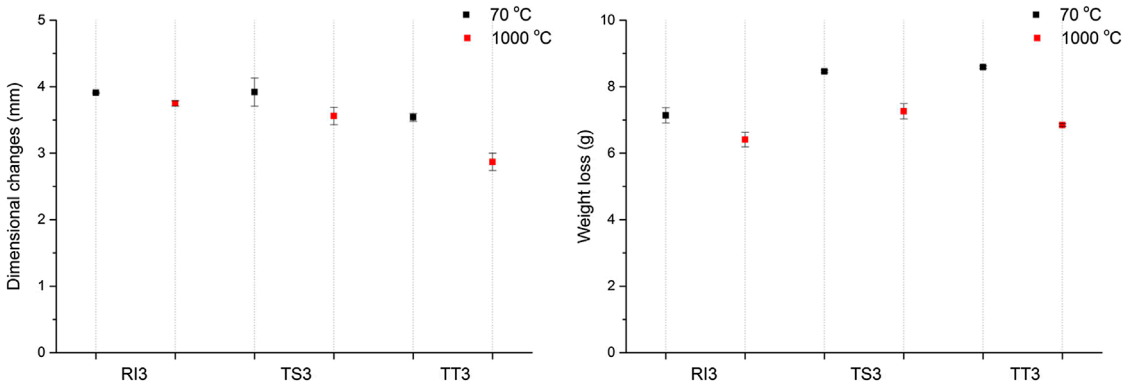

FIGURE 3 | Changes in sample dimensions of the alkali-activated foams investigated, expressed in length and weight loss.

3D geometrical parameters (especially equivalent diameter) are relevant for the determination of pore morphology and can indicate the thickness of the asymmetric and/or elongated pore structures. Equivalent diameter is reported as the diameter of a sphere having the same volume as the feature (**Figure 7**), showing the percentage of pores (as well as number and volume) distributed in each sample.

As shown in **Figure 7A**, the highest number of pores in the RI samples is in the 100–850 μm pore diameter range, where RI1 has the larger number of pores ranging in diameter from 100 to 500 μm, due to the addition of the least amount of foaming agent. The number of pores with a diameter below 100 μm is similar across all three RI samples, with the RI1 sample containing the highest number of pores in this category. In TS samples, the greatest number of pores fall in the pore diameter range below 500 μm (**Figure 7D**), where TS1 has the largest number of pores with a pore diameter less than 100 μm, due to the addition of a smaller amount of foaming agent. Despite the larger percentage of foaming agent added to samples TS2 and TS3, the number of pores in the 100–500 μm pore diameter range is still high in sample TS1. TT samples (**Figure 7G**) have the highest number of pores with a diameter less than 500 μm, compared to other types of fly ash, where sample TT1 having the largest number of pores with a diameter less than 100 μm.

In the R1 sample, most pores are in the 100–850 μm pore diameter range (**Figure 7B**), where RI1 has the largest amount/percentage of pores in the pore diameter range 100–500 μm, reaching almost 70%. Due to the addition of a greater amount of foaming agent, the percentage of number of pores in the range 500–850 μm is higher for samples RI2 and RI3, with approximately 38% of pores in sample RI2 falling in this range. Sample RI3 has a larger percentage of pores with a diameter above 500 μm, approximately 60%. The percentage of pores with a diameter below 100 μm is about 10% for all three RI samples. In TS samples most pores are below 500 μm in diameter, with sample TS1 having the largest percentage of pores with a diameter less than 100 μm, reaching almost 70% (**Figure 7E**). Due to the addition of a greater amount of foaming agent, the percentage of number of pores in the diameter range 100–500 μm is higher (above 60%) for samples TS2 and TS3. Only sample TS3 has a larger percentage of pores in the pore diameter range above 500 μm (about 35%) and the least in the pore diameter range below 100 μm (about 10%). In the TT samples, most pores are in the pore diameter range below 500 μm (**Figure 7H**). Due to the addition of a greater amount of foaming agent, the percentage of number of pores in the range 100–500 μm is higher only for TT2 (almost 60%). The percentage of pores in the pore diameter range below 100 μm is large, especially in the RI3 sample (70%).

The volume of pores in the pore diameter range from 100 to 850 μm is between 40 and almost 90% for all three RI samples (**Figure 7C**), with the greatest volume of pores observed in the RI1 sample, showing the maximum volume of pores for the RI1 sample. In the RI2 sample the volume of pores in this pore diameter range is 60%, with 40% of pores having a diameter greater than 850 μm. In the RI3 sample the largest percentage of pore volume has a pore diameter of greater than 500 μm, almost 95%. TS samples have the greatest volume of pores in the pore diameter range between 100 and 850 μm (**Figure 7F**), whereas sample TS1 has almost 80% in the pore diameter range between 100 and 500 μm, and sample TS2 more than 80%. In the TS3 sample the maximum volume of pores is in the pore diameter range above 500 μm (75%). In samples TT1 more than 70% of the volume of pores lie in the pore diameter range from 100 to 500 μm (**Figure 7I**). A high volume of pores in this pore diameter range is also seen in the TT2 sample (80%), whilst in sample TT3

TABLE 4 | Thermal conductivity of the investigated alkali-activated foams cured at 70°C (the measured standard deviations are shown in brackets).

Sample designation	RI1	RI2	RI3	TS1	TS2	TS3	TT1	TT2	TT3
λ (W/m K)	0.205 (0.006)	0.143 (0.002)	0.123 (0.007)	0.262 (0.008)	0.200 (0.002)	0.151 (0.003)	0.363 (0.006)	0.303 (0.005)	0.232 (0.007)

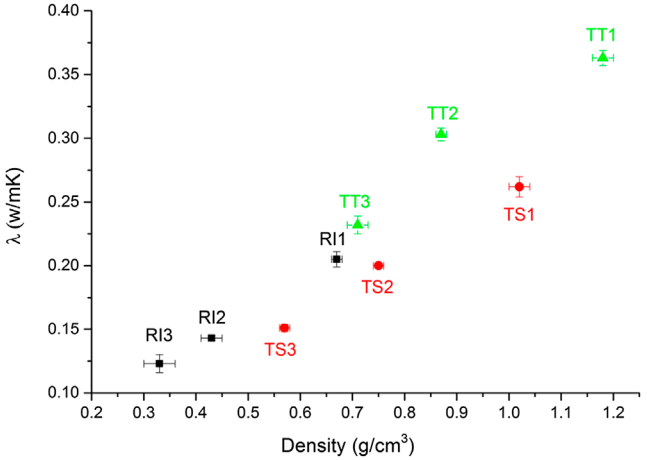

FIGURE 4 | Thermal conductivity properties vs. density in the analyzed alkali-activated foams cured at 70°C (RI, TS, and TT fly ash used, 1, 2, and 3 represent amount of foaming and stabilizing agent used).

the maximum percentage of the volume of pores is in the pore diameter range above 850 μm, due to poor porosity development.

Another 3D geometrical parameter relevant for the determination of pore morphology is sphericity, which describes how spherical an object is, or how rounded it is. Sphericity is a measure of the degree to which an object approximates the shape of a sphere, where the sphericity of 1 represents a perfect spherical shape. X-ray computer micro-tomography has given the possibility of evaluating the results and the calculated sphericity values, as a function of pore size, are shown in **Figure 8**. The sphericity of the samples cured at 70°C is also given in **Table 5** and represents the quantitative statistical data measured from the reconstructed images. The average value, and minimal and maximal sphericity of the tested samples, are also written in **Table 5**. This analysis was conducted on pores larger than 850 μm diameter, as presented in **Figure 8**.

The results for RI samples thermally treated at 70°C show that the majority of pores were close to spherical in shape as their sphericity values are above 0.50, between 0.55 and 0.95, with no huge difference between mixtures (**Figure 8A**). There are less spherical pores, i.e., with a sphericity smaller than 0.65, in the TS1 samples and more spherical pores in TS2 and TS3 (up to 0.85). The sphericity of the pores in TT samples thermally treated at 70°C is relatively low (0.25–0.75), confirming their irregular shape, especially for sample TT3, which has the lowest sphericity due to poor pore shape (**Figure 8C**). It is also observed that the sphericity is equal between mixtures in R1 samples, whereas sphericity is seen to slightly change between the mixtures in TS samples (mixtures with a higher addition of foaming agent have higher sphericity values) and in TT samples there are huge changes between the mixtures. Notably, no large differences in the sphericity of samples occur due to an increase in the equivalent diameter of pores.

Phase Changes by X-Ray Powder Diffraction

X-ray powder diffraction (XRD) (**Figure 9**) revealed the variable phase composition of the studied ashes and AA foams cured at 70 and 1,000°C (results only for samples with the smallest and largest addition of agents). Based on the height of the background presenting the amorphous phase it can be seen the RI fly ash contains the highest amount of amorphous phase of all three precursors, followed by the TT fly ash, and then the TS. The amount of amorphous phase was determined in a previous study (Kramar and Ducman, 2018), as 84.4% for RI, 71.7% for TT, and 70.0 for TS (designated in the previous research as K3, K1, and K2, respectively). The main crystalline phases identified in the designed geopolymers were similar to those found in the raw precursor, such as quartz and hematite, which were also present in all samples cured at 70°C. Lime, anhydrite, and gehlenite were

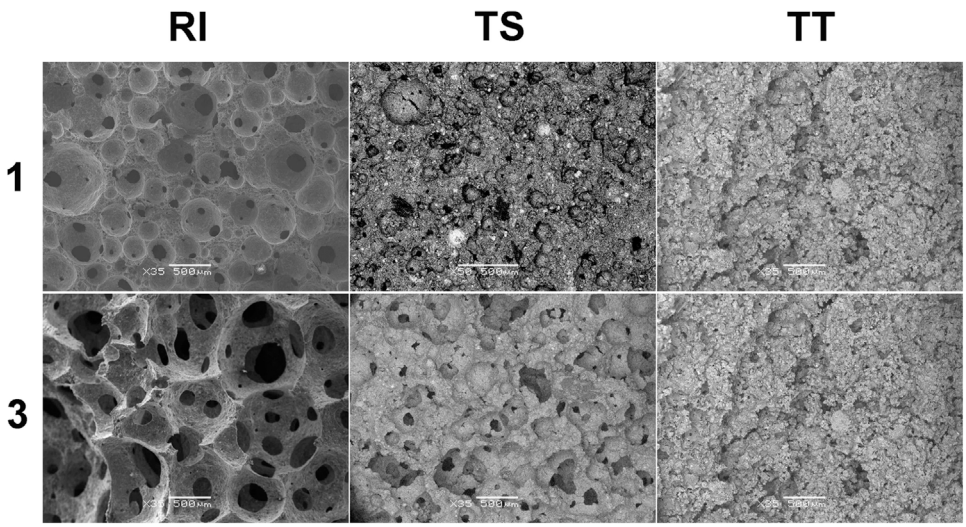

FIGURE 5 | Representative SEM image of alkali-activated foams cured at 70°C (RI, TS, and TT fly ash, 1 and 3 represent the amount of foaming and stabilizing agents used).

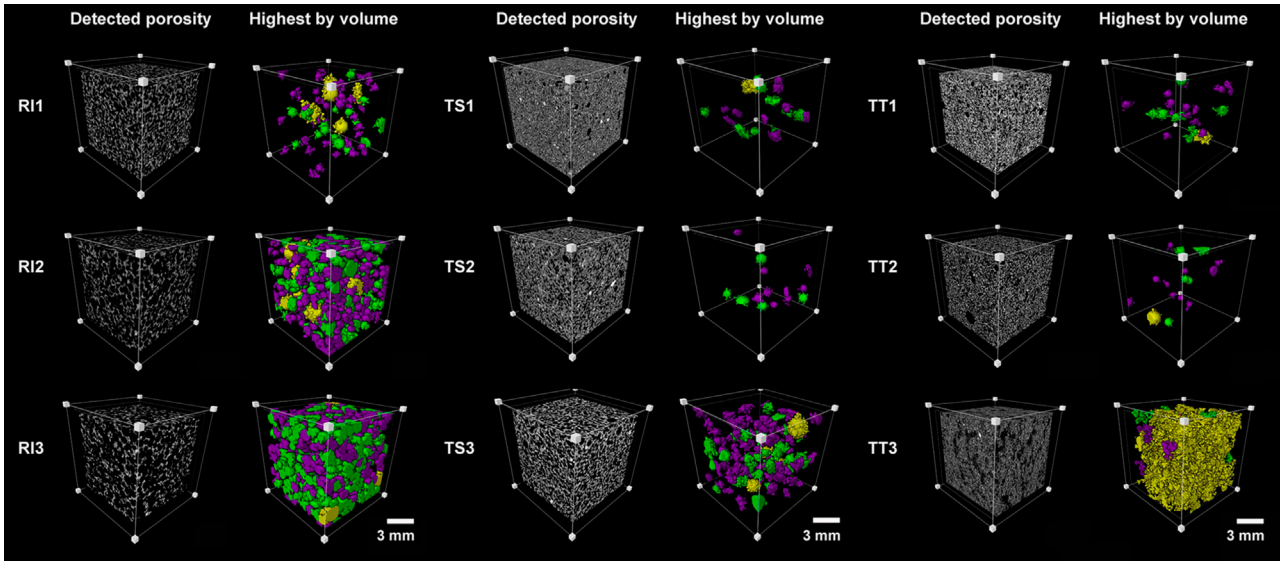

FIGURE 6 | Region of interest of the analyzed alkali-activated foams cured at 70°C (RI, TS, and TT fly ash, 1, 2, and 3 represent the amount of foaming and stabilizing agents used) presenting grayscale images and the biggest main pores. Colors denote a range of size classes with respect to EqDiameter: purple (0.85–1 mm), green (1–1.6 mm), and yellow (more than 1.6 mm).

found in all samples, with the exception of one from RI ash (**Figure 9**). It is known that an increase in quartz concentration positively influences mechanical properties, due to the capacity of its particles to create barriers for crack propagation (Nergis et al., 2020). Brownmillerite, a hydraulic phase, which could contribute to the increase in strength, was present in the samples with TT ash derived from the co-combustion of coal and biomass, while feldspar was identified in samples with TS ash, periclase in RI and TT ashes and mullite in RI samples. Mullite is a less commonly encountered compound formed from aluminum, silicon, and oxygen, which increases the refractivity of a geopolymer due to its very high melting temperature of 1,840°C (Nergis et al., 2020). As written by Diaz et al. (2010), amorphous compounds are easier to dissolve than crystalline compounds during the first step of geopolymerization (dissolution of species), yielding higher amounts of reactive SiO_2 and Al_2O_3 to combine during the transportation/coagulation phase of the geopolymeric reaction, therefore resulting in a higher degree of geopolymerization and consequently higher mechanical strength. When the sodium based alkalis are used with fly ash, the reaction product in the system is associated with the formation of sodium aluminosilicate gel (Bhagath Singh and Subramaniam, 2016).

TABLE 5 | Porosity by XCT of the investigated alkali-activated foams cured at 70°C and thermally treated at 1,000°C.

	Porosity by XCT (%)		Sphericity by XCT (due to sample diameter range above 850 μm)					
	Cured samples	Thermal treated	Cured samples			Thermal treated		
			Average	Min	Max	Average	Min	Max
RI1	39.7	32.2	0.71	0.50	0.94	0.70	0.54	0.90
RI2	66.4	56.5	0.81	0.54	0.96	0.78	0.57	0.95
RI3	76.5	72.4	0.83	0.60	0.95	0.83	0.58	0.95
TS1	18.3	15.7	0.50	0.28	0.65	0.47	0.33	0.56
TS2	19.8	18.7	0.72	0.56	0.90	0.58	0.40	0.80
TS3	38.9	38.0	0.63	0.46	0.83	0.56	0.38	0.74
TT1	16.4	12.7	0.53	0.32	0.76	0.64	0.53	0.75
TT2	15.5	17.9	0.76	0.57	0.88	0.67	0.51	0.86
TT3	15.9	15.0	0.32	0.20	0.51	0.29	0.20	0.41

Microstructural Evolution of Samples Heat Treated at 1,000°C

Figure 10 shows the microstructural evolution of AA foam samples after exposure to higher temperatures at 1,000°C, attained through SEM. Samples with RI fly ash still have a nice porous structure with evenly distributed round pores, connected and with no micro-cracks, whereas samples with TT fly ash exhibit poor microstructural evolution. **Figure 10** shows that no noticeable changes were observed in samples after exposure to higher temperatures. The more detailed results of X-ray microcomputed tomography further confirm the findings obtained by SEM, as presented in **Figure 10**.

Overall porosity determined by XCT is still the highest for samples with RI fly ash, followed by TS samples and TT with poor porosity development (**Table 5**). The difference in overall porosity between cured samples and samples exposed to higher temperatures is noticeable, varying between samples from 1 to 10%.

Porosity determined by XCT is visually presented in **Figure 11**, depicting a range of size classes above 0.85 mm, and pore size distribution of the samples is shown in **Figure 12**. The pore diameter ranges and the number of pores observed in RI samples show a similar trend to the same samples cured at 70°C, but the number of pores in the 100–850 μm pore diameter range, as well as below 100 μm, is smaller in samples cured at 1,000°C (**Figure 12A**). TS samples cured at 1,000°C also

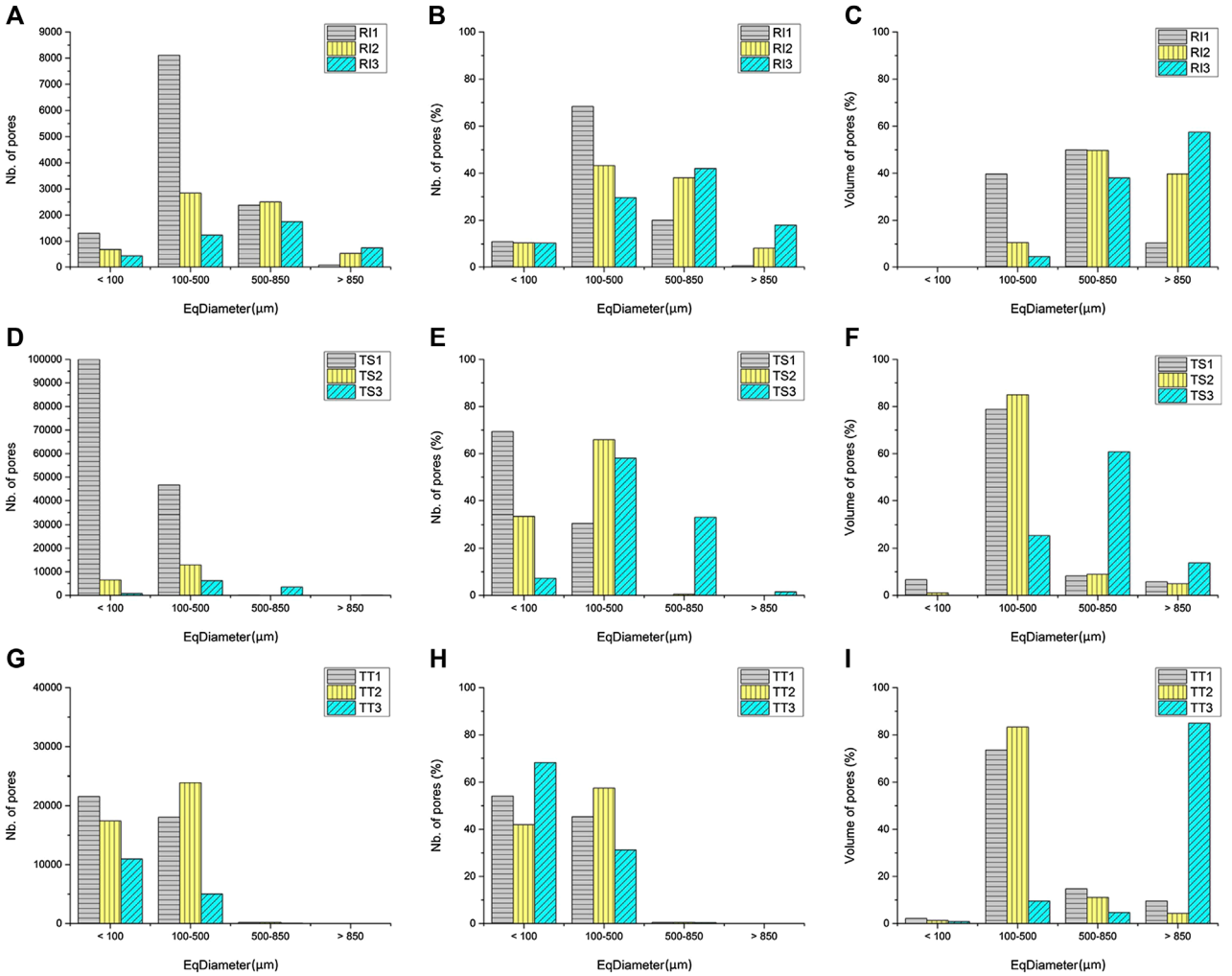

FIGURE 7 | Graphical representation of the pore size distribution of the analyzed alkali-activated foams cured at 70°C (RI, TS, and TT fly ash used, 1, 2, and 3 represent the amount of foaming and stabilizing agents used; **(A)**–**(C)** RI fly ash, **(D)**–**(F)** TS fly ash, **(G)**–**(I)** TT fly ash), determined by means of X-ray micro-tomography. The results present the number, percentage and volume of pores with respect to pore size diameter (EqDiameter).

show similar porosity development to samples cured at 70°C, where sample TS1 cured at 1,000°C has large amount of pores in the pore diameter range below 100 µm (**Figure 12D**), although still less than samples cured at 70°C. Despite the greater percentage of foaming agent added to samples TS2 and TS3, the number of pores in sample TS3 (in the 100–500 µm pore diameter range) is still high, unlike in sample TS3 cured at 70°C. The highest number of pores for TT samples is in the pore diameter range below 500 µm (**Figure 12G**), where sample TT1 still has the largest number of pores in the pore diameter range below 100 µm, due to the addition of a smaller amount of foaming agent. A similar trend to in samples cured at 70°C can be seen, although a smaller number of pores with a pore diameter below 100 µm are present in sample TT1 when cured at 1,000°C. Despite the larger percentage of foaming agent added to samples TT2 and TT3, TT1 has the highest number of pores in the pore diameter range between 100 and 500 µm, unlike in the sample cured at 70°C.

In R1 samples cured at 1,000°C the majority of pores are in the pore diameter range 100–850 µm (**Figure 12B**), where RI1 has the largest percentage of pores in the pore diameter range 100–500 µm, reaching almost 74%, which is more than in those samples cured at 70°C. Due to the higher amount of foaming agent, the percentage of pores in the range 500–850 µm is higher in RI2 and RI3 samples, about 33 and 10%, respectively, which is slightly lower than in those samples cured at 70°C. The percentage of pores in the pore diameter range below 100 µm is approximately 10% for all three RI samples. In TS samples cured at 1,000°C (**Figure 12E**) the majority of pores have a diameter below 500 µm, with samples TS1 and TS2 having a large percentage of pores in the pore diameter range below 100 µm, approximately 54 and 35%, respectively. A similar trend as in TS samples cured at 70°C was observed, but with a smaller amount of pores. Due to the higher addition of foaming agent in samples TS2 and TS3, the percentage of pores in the 100–500 µm range is higher (above 60%) when cured at 1,000°C compared to when

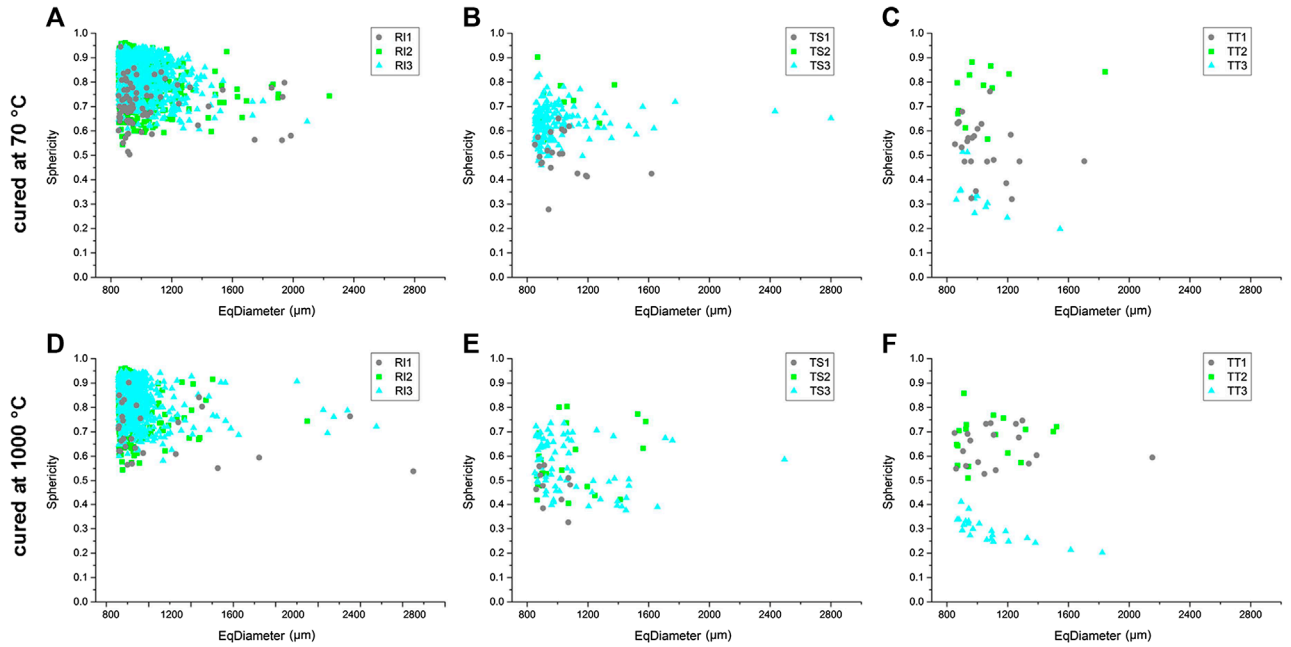

FIGURE 8 | Graphical representation of the sphericity values as a function of pore size of the analyzed alkali-activated foams cured at 70 **(A)**–**(C)** and 1,000°C **(D)**–**(F)**, determined by means of X-ray micro-tomography.

cured at 70°C. Sample TS3 has a larger percentage of pore sizes both in the pore diameter range 100–500 µm about (approximately 60%) and in the pore diameter range below 100 µm (approximately 30%), unlike the samples cured at 70°C. In TT samples cured at 1,000°C (**Figure 12H**), the majority of pores have a diameter below 500 µm. Due to the higher addition of foaming agent, the percentage of pores between 100 and 500 µm is higher only for TT1, similar to in samples cured at 70°C. Sample TT3 cured at 1,000°C has a large percentage of pores in the pore diameter range below 100 µm (70%).

When compared to other RI samples cured at 1,000°C, sample RI1 has the highest volume of pores in the pore diameter range 100–850 µm (approximately 80%; **Figure 12C**), which is slightly less than in the samples cured at 70°C. In the RI2 samples almost 60% of the volume of pores lies in the 500–850 µm pore diameter range, while 25% of pores have a diameter larger than 850 µm. In the RI3 sample the largest percentage of the volume of pores is above a diameter of 500 µm (almost 92%), slightly less than in the samples cured at 70°C. At least 75% of the volume of pores in samples TS1 cured at 1,000°C have a pore diameter ranging between 100 and 500 µm (**Figure 12F**), which is less than in the TS1 sample cured at 70°C. Sample TS2 cured at 1,000°C has 70% in the same pore diameter range and sample TS3 almost 88% volume in the pore diameter range from 100–850 µm. Sample TT1 cured at 1,000°C has more than 60% of the volume of pores in the pore diameter range from 100 to 500 µm (**Figure 12I**), less than in the same sample cured at 70°C. A high volume of pores in this pore diameter range is also seen in the TT2 sample, reaching 70% (less than the sample cured at 70°C) while sample TT3 has poor porosity development.

The results for RI samples thermally treated at 1,000°C show that the majority of pores were close to spherical in shape, as their sphericity values are above 0.50 (between 0.55 and 0.95) with no huge difference between mixtures (**Figure 8D**). The same trend is evident as in RI samples thermally treated at 70°C. The same trend also occurs in TS samples thermally treated at 1,000°C, where TS1 samples have a sphericity smaller than 0.6, while more spherical pores occur in TS2 and TS3 (up to 0.8; **Figure 8E**). The sphericity of the pores in TT samples thermally treated at 1,000°C is relatively low, similar to as in TT samples thermally treated at 70°C, confirming their irregular shape, especially for sample TT3, which has the lowest sphericity due to poor pore shape (**Figure 8F**). The results for RI samples thermally treated at 1,000°C also show that sphericity is equal between mixtures, whereas it can be seen that sphericity slightly changes according to the mixture in TS samples (mixtures with higher addition of foaming agent have higher sphericity values), and in TT samples huge changes are observed between the mixtures, similar to in samples thermally treated at 70°C.

Phase Changes by X-Ray Powder Diffraction

The XRD patterns of the studied ashes and AA foams cured at 1,000°C are shown in **Figure 9**. The results show multiple peaks specific to quartz and hematite, and in some cases mullite in the RI samples, and gehlenite in TS and TT samples. The aforementioned crystalline phases detected in the initial material remain apparently unaltered with heating, as it was not expected that the mullite would melt or dissolve during firing to 1,000°C (given their melting point of approximately 1,830°C). It is believed that the presence of free sodium in the matrix causes the dissolution/melting of the mullite into the geopolymer at

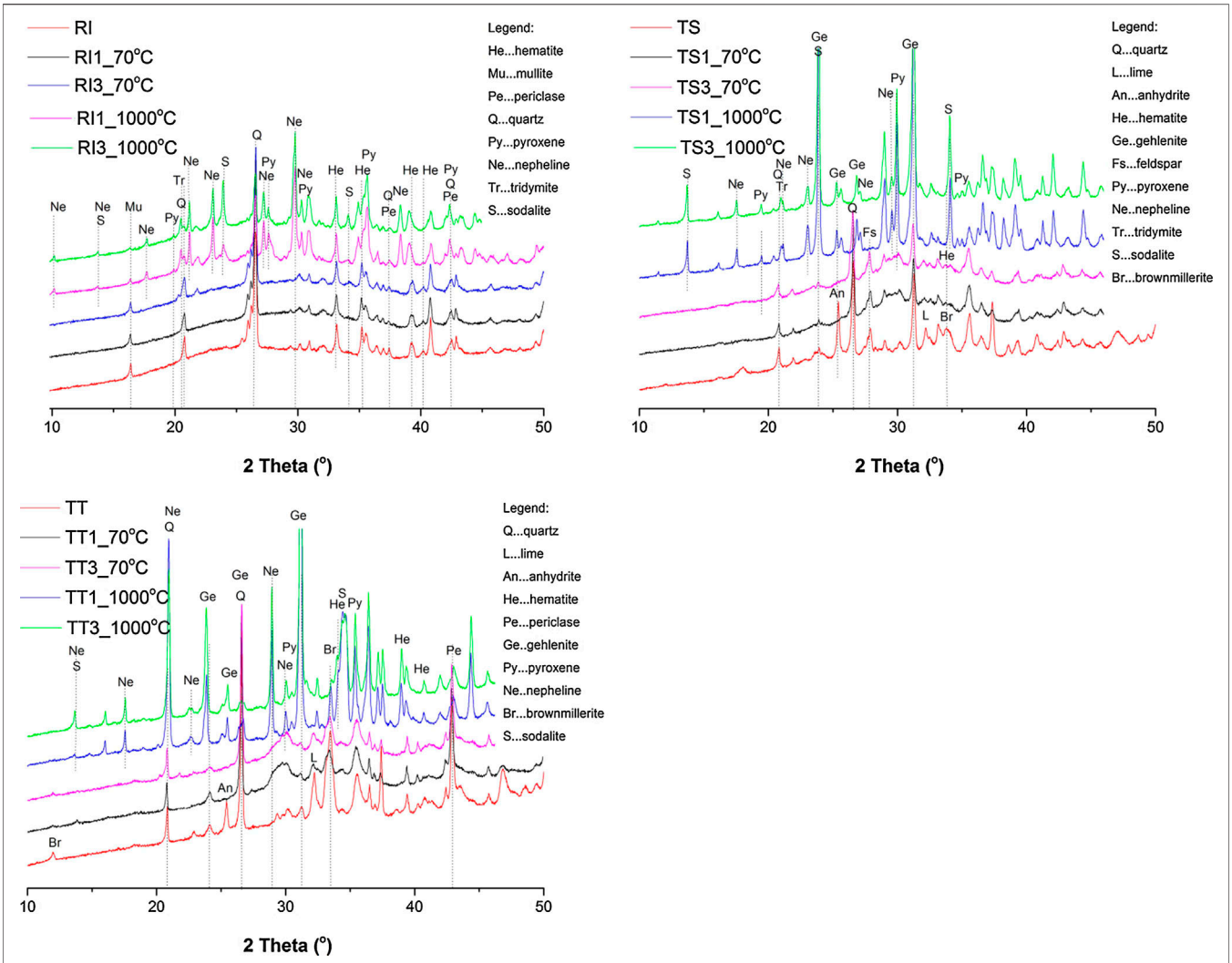

FIGURE 9 | Phase composition of the analyzed alkali-activated foams cured at 70 and 1,000°C (RI, TS, and TT fly ash used, 1, 2, and 3 represent amount of foaming and stabilizing agents used), as determined by means of X-ray powder diffraction.

lower temperature, as alkali's are known to be excellent sintering agents (Rickard et al., 2012). Hematite, however, exhibited an increased peak intensity, especially in the TT samples (due to their higher concentration of iron). Rickard et al. (2012) reported that hematite is likely to have crystallized from the amorphous iron in the fly ash.

When the temperature is increased to 1,000°C, the diffraction peaks of the aforementioned phases become weak, and new phases start to crystalize into pyroxene, nepheline, tridymite, sodalite, brownmillerite, and gehlenite as response to the thermal treatment. The reduction of quartz peak intensity is likely due to a partial phase change to tridymite. In the presence of alkali oxides, quartz converted to tridymite, depending on the temperature. It has been reported that tridymite starts to form above 872°C with Na_2O and above 883°C with K_2O (Holmquist, 1961). These high temperature phases, tridymite (SiO_2) and nepheline ($NaAlSiO_4$), are reported to improve the thermal resistance of the geopolymers due to their high melting points (tridymite 1,670°C and nepheline 1,257°C) (Rickard et al., 2012). In general, if silicon dioxide is available at such a high temperature, nepheline is no longer stable and feldspar will form. The amount of calcium available causes different types of feldspar to form (Dombrowski et al., 2007). It seems that the matrix decomposes, then the aluminosilicate species react with the released alkalis and calcium to form crystalline phases (nepheline and gehlenite, respectively) (Gyekenyesi et al., 2011). One reason to explain this could be that the mullite and quartz were needed to form the large amount of gehlenite ($Ca_2(Al(AlSi)O_7)$), (Dombrowski et al., 2007), as seen in the samples (especially TS and TT) treated at 1,000°C. In addition, at 1,000°C, a phase belonging to the pyroxene group (diopside) is additionally formed due to sufficient Al_2O_3 content, which has been reported to have a positive role in its crystallization (Qian et al., 2006). Yang et al. (2017) also reported that the Mg-silicate crystalline phases of diopside may work as compensation for the thermal shrinkage of the geopolymer gel phase, in order to

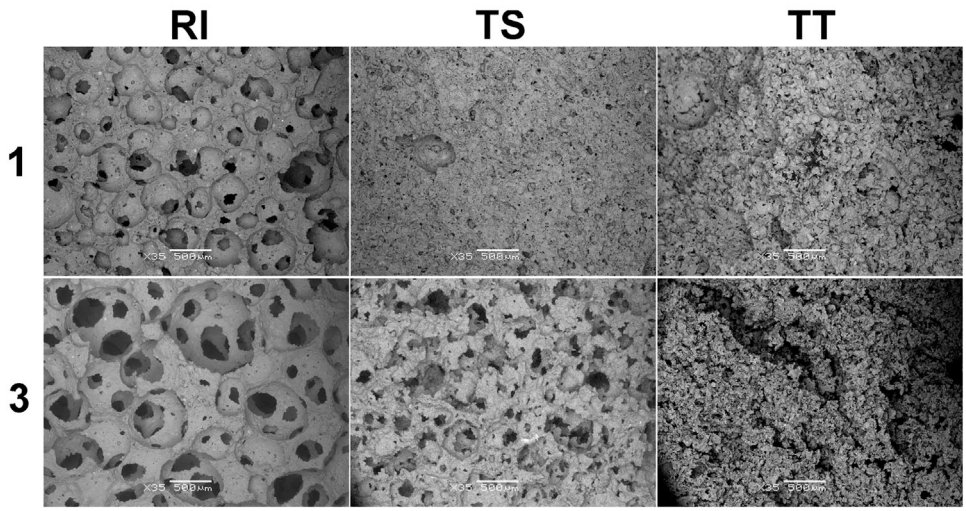

FIGURE 10 | Representative SEM image of alkali-activated foams thermally treated at 1,000°C (RI, TS, and TT fly ash used, 1 and 3 represent the amount of foaming and stabilizing agent added). The bars on all SEM photos represent 500 μm (×35 magnification).

improve the volume stability. The intensities of peaks and small amounts of already crystallized aluminosilicate detected corresponded to sodalite ($Na_8(Al_6Si_6O_{24})Cl_2$), which has been observed to increase in fly ash samples activated by NaOH solution when exposed to temperatures of 1,000°C. Sodalite crystallizes in the cubic system as a mineral complex, formed by the reaction of sodium and chlorine with the main elements of the raw material (aluminum, silicon, and oxygen). The natural sodalite consists of an Al–O–Si network that encompasses Cl^+ cations, but the one resulting from geopolymerization shows inter-structural Na^+ cations, similar to zeolites (Nergis et al., 2020).

Based on the properties of all three precursors, it can be seen that the fly ash which contains the highest amounts of SiO_2 and Al_2O_3, and the highest amorphous phase content, i.e., RI, is also the most reactive, both in terms of pozzolanic activity (Kramar and Ducman, 2018), and the alkali activation process. By adding foaming and stabilizing agents, the density can be tailored to one's needs, but the initial precursor should provide sufficient reactivity and consequently result in good mechanical properties. In our

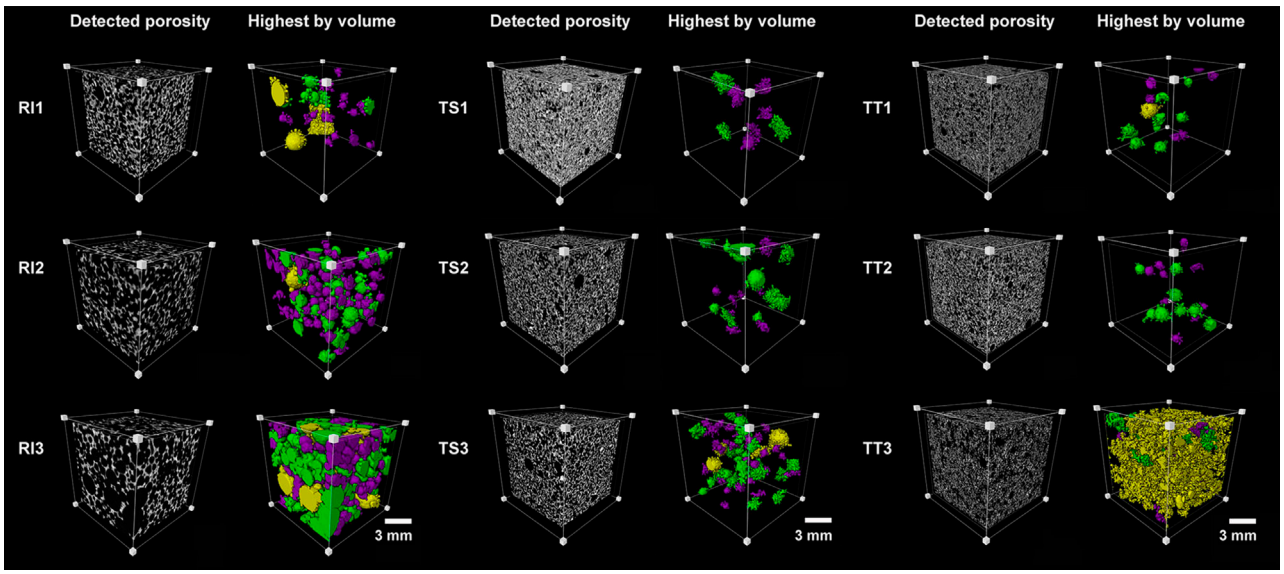

FIGURE 11 | Region of interest of the analyzed alkali-activated foams cured at 1,000°C (RI, TS, and TT fly ash used, 1, 2, and 3 represent the amount of foaming and stabilizing agent added) presenting grayscale image and the biggest main pores. Colors correspond to a range of size classes with respect to EqDiameter, purple (0.85–1 mm), green (1–1.6 mm), and yellow (more than 1.6 mm).

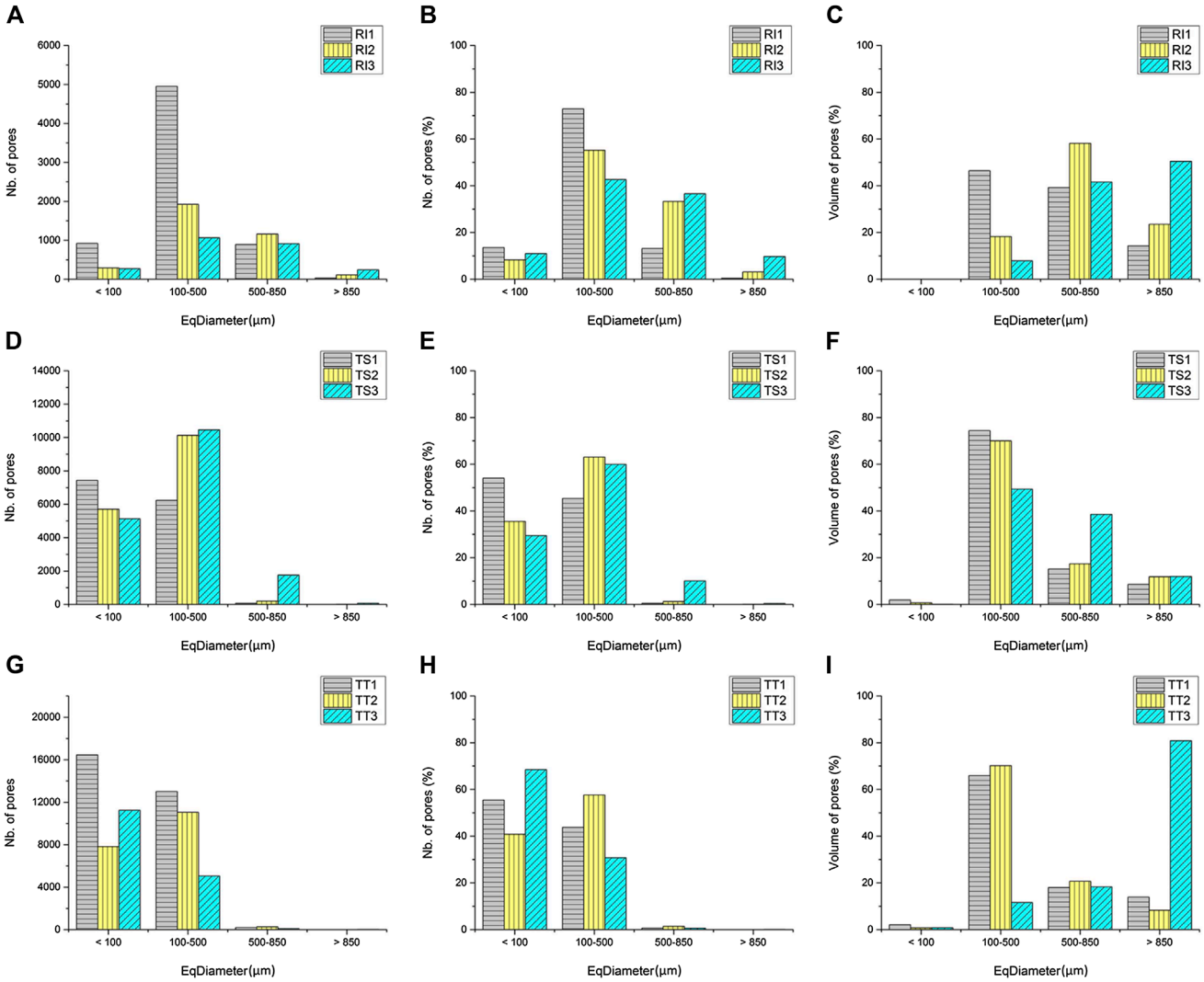

FIGURE 12 | Graphic representation of the pore size distribution of the analyzed alkali-activated foams cured at 1,000°C (RI, TS, and TT fly ash used, 1, 2, and 3 represent the amount of foaming and stabilizing agents added; **(A)**–**(C)** RI fly ash, **(D)**–**(F)** TS fly ash, **(G)**–**(I)** TT fly ash), determined by means of X-ray micro-tomography. The results show the number, percentage, and volume of pores with regard to pore size diameter (EqDiameter).

study the RI fly ash exhibited the lowest density and when densities were comparable to those obtained from the other two fly ashes the compressive strength was significantly higher, which can be ascribed to the higher reactivity. Contrary to the expectation that BET specific surface would play an important role in the alkali activation process, by providing a surface available for reaction, in our case the BET specific surface area was not recognized as an important parameter.

CONCLUSIONS

Three types of fly ash were tested as precursors for the preparation of AA foams. SPM was used as the foaming agent and SDS as the stabilizing agent. Foam properties were determined after curing at 70°C and after exposure to 1,000°C. In all three systems the foaming process was successfully implemented, resulting in foams of density down to 0.3 g/cm. Compressive strength is highly dependent on density, and for the densities from 1.2 down to 0.3 g/cm^3, compressive strength ranged from 1 to 6 MPa. Comparing all three fly ashes the favorable results in terms of performance (density vs. mechanical properties) were achieved from the fly ash with the highest SiO_2 and Al_2O_3 content, and the highest amorphous phase content, i.e., RI fly ash. Also compressive strength is influenced by the type of fly ash; the sample from RI fly ash exhibited the highest compressive strength at a comparable (or even lower) density than the other two fly ashes. With the high amount of SiO_2 and Al_2O_3, and high amorphous phase content, the alkali activation reaction is completed to a greater extent, resulting in better mechanical properties. In the case of the fly ash with the highest SiO_2 and Al_2O_3 content, i.e., RI fly ash, the density remained virtually the

same after firing to 1,000°C, but the compressive strength increased on average by 50%. In the case of the other two types of fly ash the density increased slightly after firing, but significant shrinkage occurred. Density did not increase, as would be expected due to the high shrinkage. Even though density did not increase, compressive strength increased hugely, by as much as 800% in the case of the TT fly ash, which contains the lowest amount of SiO_2 and Al_2O_3.

XRD analysis also confirmed that the lime contained in the TS and TT fly ash disappeared after firing to 1,000°C, which could have contributed to the loss in mass and consequent reduction in density (in spite of significant shrinkage on firing). The crystallization process also took place during firing, resulting in newly formed crystal phases, including nepheline, sodalite, tridymite, and gehlenite, which could contribute to the increased compressive strength. SEM and microtomography analysis showed differences in the microstructure of foams, whereby pores are more uniform and spherical in foams based on RI fly ash compared to the other two fly ashes, which may also influence properties of thermal insulation and compressive strength. Improvements in the performance of foams in terms of density and mechanical properties, especially after exposure to elevated temperature when their structure remains stable after firing up to 1,000°C, could expand the potential use of inorganic AAM foams into areas where resistance to elevated temperature is required.

DATA AVAILABILITY STATEMENT

All datasets presented in this study are included in the article.

AUTHOR CONTRIBUTIONS

Conceptualization, VD; data curation, VD and LK; formal analysis, VD and LK; funding cquisition, VD and LK; methodology, VD, LK; supervision, VD; writing—original draft, LK; writing—review and editing, VD and LK.

ACKNOWLEDGMENTS

We acknowledge financial support from the Slovenian Research Agency through the project No. J2-9197 (VD) and post-doctoral project No. Z2-1861 (LK).

REFERENCES

Abdollahnejad, Z., Pacheco-Torgal, F., Félix, T., Tahri, W., and Barroso Aguiar, J. (2015). Mix design, properties and cost analysis of fly ash-based geopolymer foam. *Construct. Build. Mater.* 80, 18–30. doi:10.1016/j.conbuildmat.2015.01.063

Badanoiu, A. I., Al Saadi, T. H. A., Stoleriu, S., Voicu, G., and Voicu, G. (2015). Preparation and characterization of foamed geopolymers from waste glass and red mud. *Construct. Build. Mater.* 84, 284–293. doi:10.1016/j.conbuildmat.2015.03.004

Bajare, D., Vitola, L., Dembovska, L., and Bumanis, G. (2019). Waste stream porous alkali activated materials for high temperature application. *Front. Mater.* 6, 92. doi:10.3389/fmats.2019.00092/full

Bakharev, T. (2006). Thermal behaviour of geopolymers prepared using class F fly ash and elevated temperature curing. *Cem. Concr. Res.* 36 (6), 1134–1147. doi:10.1016/j.cemconres.2006.03.022

Bhagath Singh, G. V. P., and Subramaniam, K. V. L. (2016). Quantitative XRD study of amorphous phase in alkali activated low calcium siliceous fly ash. *Construct. Build. Mater.* 124, 139–147. doi:10.1016/j.conbuildmat.2016.07.081

Böke, N., Birch, G. D., Nyale, S. M., and Petrik, L. F. (2015). New synthesis method for the production of coal fly ash-based foamed geopolymers. *Construct. Build. Mater.* 75, 189–199. doi:10.1016/j.conbuildmat.2014.07.041

Carabba, L., Manzi, S., Rambaldi, E., Ridolfi, G., and Bignozzi, M. C. (2017). High-temperature behaviour of alkali-activated composites based on fly ash and recycled refractory particles. *J. Ceram. Sci. Technol.* 08 (3), 377–388.

Chen, B., Luo, Z., and Lu, A. (2011). Preparation of sintered foam glass with high fly ash content. *Mater. Lett.* 65 (23–24), 3555–3558. doi:10.1016/j.matlet.2011.07.042

Cheng-Yong, H., Yun-Ming, L., Mustafa Al Bakri Abdullah, M., and Hussin, K. (2017). Thermal resistance variations of fly ash geopolymers: foaming responses. *Sci. Rep.* 27 (7), 45355.

Dal Pozzo, A., Carabba, L., Bignozzi, M. C., and Tugnoli, A. (2019). Life cycle assessment of a geopolymer mixture for fireproofing applications. *Int. J. Cycle Assess.* 10, 1743–1757.

Davidovits, J. (2015). *Geopolymer: chemistry and applications*. 4th Edn. Saint-Quentin, France: J. Davidovits.

Diaz, E. I., Allouche, E. N., and Eklund, S. (2010). Factors affecting the suitability of fly ash as source material for geopolymers. *Fuel* 89, 992–996. doi:10.1016/j.fuel.2009.09.012

Dombrowski, K., Buchwald, A., and Weil, M. (2007). The influence of calcium content on the structure and thermal performance of fly ash based geopolymers. *J. Mater. Sci.* 42, 3033–3043. doi:10.1007/s10853-006-0532-7

Guo, Y., Zhang, Y., Huang, H., Meng, K., Hu, K., Hu, P., et al. (2014). Novel glass ceramic foams materials based on red mud. *Ceram. Int.* 40 (5), 6677–6683. doi:10.1016/j.ceramint.2013.11.128

Gyekenyesi, A., Kriven, W. M., and Wang, J. (2011). *Developments in Strategic materials and computational design II*. New York, NY: Wiley, Vol. 32, Issue 10, 24.

Hajimohammadi, A., Ngo, T., and Mendis, P. (2017a). How does aluminium foaming agent impact the geopolymer formation mechanism? *Cem. Concr. Compos.* 80, 277–286. doi:10.1016/j.cemconcomp.2017.03.022

Hajimohammadi, A., Ngo, T., Mendis, P., Nguyen, T., Kashani, A., and van Deventer, J. S. J. (2017b). Pore characteristics in one-part mix geopolymers foamed by H_2O_2: the impact of mix design. *Mater. Des.* 130, 381–391. doi:10.1016/j.matdes.2017.05.084

Hajimohammadi, A., Ngo, T., Mendis, P., Kashani, A., and van Deventer, J. S. J. (2017c). Alkali activated slag foams: the effect of the alkali reaction on foam characteristics. *J. Clean. Prod.* 147, 330–339. doi:10.1016/j.jclepro.2017.01.134

Henon, J., Alzina, A., Absi, J., Smith, D. S., and Rossignol, S. (2013). Potassium geopolymer foams made with silica fume pore forming agent for thermal insulation. *J. Porous Mater.* 20, 37–46. doi:10.1007/s10934-012-9572-3

Hlaváček, P., Šmilauera, V., Škvárab, F., Kopeckya, L., and Šulc, R. (2015). Inorganic foams made from alkali-activated fly ash: mechanical. *Chem. Phys. Prop.* 35 (2), 703–709.

Holmquist, S. B. (1961). Conversion of quartz to tridymite. *J. Am. Ceram. Soc.* 44 (2), 82–86. doi:10.1111/j.1151-2916.1961.tb15355.x

Kamseu, E., Ngouloure, Z. N. M., Ali, B. N., Zekeng, S., Melo, U. C., Rossignol, S., et al. (2015). Cumulative pore volume, pore size distribution and phases percolation in porous inorganic polymer composites: relation microstructure and effective thermal conductivity. *Energy Build.* 88 (1), 45–56. doi:10.1016/j.enbuild.2014.11.066

Kioupis, D., Kavakakis, C., Tsivilis, S., and Kakali, G. (2018). Synthesis and characterization of porous fly ash-based geopolymers using Si as foaming agent. *Adv. Mater. Sci. Eng.* 2018, 11.

Korat, L., and Ducman, V. (2017). The influence of the stabilizing agent SDS on porosity development in alkali-activated fly-ash based foams. *Cem. Concr. Compos.* 80, 168–174. doi:10.1016/j.cemconcomp.2017.03.010

Korat, L., Ducman, V., Legat, A., and Mirtič, B. (2017). Characterisation of the pore-forming process in lightweight aggregate based on silica sludge by means of X-ray micro-tomography (micro-CT) and mercury intrusion porosimetry (MIP). *Ceram. Int.* 39 (6), 6997–7005. doi:10.1016/j.ceramint.2013.02.037

Kramar, S., and Ducman, V. (2018). Evaluation of ash pozzolanic activity by means of the strength activity index test, Frattini test and DTA/TG analysis. *Tech. Gaz.* 25 (6), 1746–1752.

Łach, M., Mierzwiński, D., Korniejenko, K., and Mikuła, J. (2010). Geopolymer foam as a passive fire protection. *MATEC Web Conf.* 247, 00031.

Lin, T. S., Jia, D. C., He, P. G., and Wang, M. R. (2009). Thermo-mechanical and microstructural characterization of geopolymers with α-Al2O3 particle filler. *Int. J. Thermophys.* 30, 1568–1577. doi:10.1007/s10765-009-0636-9

Luukkonen, T., Abdollahnejad, Z., Yliniemi, J., Kinnunen, P., and Illikainen, M. (2018). One-part alkali-activated materials: a review. *Cem. Concr. Res.* 103, 21–34. doi:10.1016/j.cemconres.2017.10.001

Martin, A., Pastor, J. Y., Palomo, A., and Fernández Jiménez, A. (2015). Mechanical behaviour at high temperature of alkali-activated aluminosilicates (geopolymers). *Construct. Build. Mater.* 93, 1188–1196. doi:10.1016/j.conbuildmat.2015.04.044

Masi, G., Rickard, W. D. A., Bignozzi, M. C., and van Riessen, A. (2014a). The influence of short fibres and foaming agents on the physical and thermal behaviour of geopolymer composites. *Adv. Sci. Tech.* 92, 56–61. doi:10.4028/www.scientific.net/ast.92.56

Masi, G., Rickard, W. D. A., Vickers, L., Bignozzi, M. C., and van Riessen, A. (2014b). A comparison between different foaming methods for the synthesis of light weight geopolymers. *Ceram. Int.* 40, 13891–13902. doi:10.1016/j.ceramint.2014.05.108

Mierzwinski, D., Łach, M., Hebda, M., Walter, J., Szechynska-Hebda, M., and Mikuła, J. (2019). Thermal phenomena of alkali-activated metakaolin studied with a negative temperature coefficient system. *J. Therm. Anal. Calorim.* 138, 4167–4175.

Nergis, D. D. B., Al Bakri Abdullah, M. M., Sandu, A. V., and Vizureanu, P. (2020). XRD and TG–DTA study of new alkali activated materials based on fly ash with sand and glass powder. *Materials* 13 (2), 343.

Nyale, S. M., Babajide, O. O., Birch, G. D., Böke, N., and Petrik, L. F. (2013). Synthesis and characterization of coal fly ash-based foamed geopolymer. *Proc. Environ. Sci.* 18, 722–730. doi:10.1016/j.proenv.2013.04.098

Palmero, P., Formi, A., Antonaci, P., Brini, S., and Tulliani, J. M. (2015). Geopolymer technology for application-oriented dense and lightened materials. Elaboration and characterization. *Ceram. Int.* 41 (10), 12967–12979.

Provis, J. L. (2018). Alkali-activated materials. *Cem. Concr. Res.* 114, 40–48. doi:10.1016/j.cemconres.2017.02.009

Provis, J. L., and Bernal, S. A. (2014). Milestones in the analysis of alkali-activated binders. *J. Sustain. Cem.-Based Mater.* 4 (2), 74–84. doi:10.1080/21650373.2014.958599

Provis, J. L., Palomo, A., and Shi, C. (2015). Advances in understanding alkali-activated materials. *Cem. Concr. Res.* 78, 110–125. doi:10.1016/j.cemconres.2015.04.013

Qian, G., Song, Y., Song, Y., Zhang, C., Xia, Y., Zhang, H., et al. (2006). Diopside-based glass-ceramics from MSW fly ash and bottom ash. *Waste Manag.* 26, 1462–1467. doi:10.1016/j.wasman.2005.12.009

RabeloMonich, P. R., Romero, A. R., Höllen, D., and Bernardo, E. (2018). Porous glass–ceramics from alkali activation and sinter-crystallization of mixtures of waste glass and residues from plasma processing of municipal solid waste. *J. Clean. Prod.* 188, 871–878. doi:10.1016/j.jclepro.2018.03.167

Rickard, W. D. A., Temuujin, J., Riessen, A., and van Riessen, A. (2012). Thermal analysis of geopolymer pastes synthesised from five fly ashes of variable composition. *J. Non-Cryst. Solids* 358, 1830–1839. doi:10.1016/j.jnoncrysol.2012.05.032

Rincón, A., Giacomello, G., Pasetto, M., and Bernardo, E. (2017). Novel 'inorganic gel casting' process for the manufacturing of glass foams. *J. Eur. Ceram. Soc.* 37, 2227–2234. doi:10.1016/j.jeurceramsoc.2017.01.012

Sanyan, J. G., Nazari, A., Chen, L., and Nguyen, H. (2015). Physical and mechanical properties of lightweight aerated geopolymer. *Constr. Build. Mater.* 79, 236–244.

Szabó, R., Gombkötő, I., Svéda, M., and Mucsi, G. (2017). Effect of grinding fineness of fly ash on the properties of geopolymer foam. *Arch. Metall. Mater.* 62, 1257–1261.

Tran, T. T., Kang, H., and Kwon, H.-M. (2019). Effect of heat curing method on the mechanical strength of alkali-activated slag mortar after high-temperature exposure. *Materials* 12, 1789. doi:10.3390/ma12111789

Yang, T., Wu, Q., Zhu, H., and Zhang, Z. (2017). Geopolymer with improved thermal stability by incorporating high-magnesium nickel slag. *Construct. Build. Mater.* 155, 475–484. doi:10.1016/j.conbuildmat.2017.08.081

Zhao, Y., Ye, J., Lu, X., Liu, M., Lin, Y., Gong, W., et al. (2010). Preparation of sintered foam materials by alkali-activated coal fly ash. *J. Hazard Mater.* 174, 108–112. doi:10.1016/j.jhazmat.2009.09.023

Conflict of Interest: The authors declare that the research was conducted in the absence of any commercial or financial relationships that could be construed as a potential conflict of interest.

frontiers in Materials

ORIGINAL RESEARCH
published: 12 November 2020
doi: 10.3389/fmats.2020.583400

Alkali-Activated Binders From Waste Incinerator Bottom Ashes and Metakaolin Reinforced by Recycled Carbon Fiber Composites

Stefania Manzi[1]*, *Isabella Lancellotti*[2], *Giulia Masi*[1] and *Andrea Saccani*[1]

[1]Department of Civil, Chemical, Environmental and Materials Engineering, University of Bologna, Bologna, Italy, [2]Department of Engineering "Enzo Ferrari", University of Modena and Reggio Emilia, Modena, Italy

In view of creating low-impact materials for the building industry, the fostering of alkali-activated binder gains high importance. Metakaolin can successfully be activated with alkalis at room temperature, but the contemporary use of wastes to create mixed binders can further increase the environmental benefits. Bottom ashes obtained from the incineration of municipal solid wastes have been tentatively mixed in different amounts to develop matrix with acceptable mechanical properties, which still can be cured at room temperature. Moreover, scraps obtained from the production of epoxy/carbon fiber composites are employed as a reinforcing phase. No chemical or physical treatments have been used to modify the epoxy/carbon fiber wastes, apart from size reduction, thus minimizing the overall economic and energy impact of the process. The workability, physical and mechanical properties, microstructure, and porosity of the obtained materials are investigated. Up to a 50 weight percent of bottom ashes from municipal solid waste incineration can be mixed with metakaolin. Fibers still embedded in the epoxy matrix disclose a fair interaction with the matrix, thus managing to increase flexural strength, toughness, and dimensional stability without decreasing the compressive strength.

Keywords: building materials, carbon fibers composites wastes, bottom ashes, recycling, alkali-activated materials

OPEN ACCESS

Edited by:
Patricia Krawczak,
IMT Lille Douai, France

Reviewed by:
Nassim Sebaibi,
École Supérieure d'Ingénieurs des Travaux de la Construction, France
Girts Bumanis,
Riga Technical University, Latvia

***Correspondence:**
Stefania Manzi
stefania.manzi4@unibo.it

Specialty section:
This article was submitted to Structural Materials, a section of the journal Frontiers in Materials

Received: *15 July 2020*
Accepted: *06 October 2020*
Published: *12 November 2020*

Citation:
Manzi S, Lancellotti I, Masi G and Saccani A (2020) Alkali-Activated Binders From Waste Incinerator Bottom Ashes and Metakaolin Reinforced by Recycled Carbon Fiber Composites. Front. Mater. 7:583400. doi: 10.3389/fmats.2020.583400

INTRODUCTION

Municipal waste incineration can be used as a waste handling solution. This process can recover energy, exploiting the heat of combustion of the organic fraction of the waste and allows the overall reduction of the volume of wastes, consequently decreasing landfilling depletion. As a drawback, the process itself generates solid wastes, defined as fly ash and bottom ash. Bottom ashes from municipal solid waste incineration have some remarkable characteristics. They contain negligible amounts of toxic elements, have high amorphous fraction, and are largely composed of silica and aluminium oxides. These characteristics have already attracted interest for their use in producing new glass compositions (Saccani et al., 2001) or building materials, especially their pozzolanic activity in traditional Portland cement composites (Saccani et al., 2005; Li et al., 2012; Kuo et al., 2013; Tang et al., 2016; Chen and Yang, 2017; Chen et al., 2019). In recent years, a new class of binders has been investigated, characterized by a lower carbon dioxide footprint than Portland cement, that is, alkali-activated materials (De Vargas et al., 2011; Sun and Vollpracht, 2019). There are a set of inorganic

phases showing amorphous or semicrystalline structure formed by a three-dimensional network of AlO_4 and SiO_4 tetrahedra. They are obtained from a chemical reaction between a binding component (the source of aluminosilicates) and an alkaline activator, usually a blend of caustic alkalis or alkaline salts. For their synthesis, raw materials such as metakaolin, calcined clays, or industrial wastes, such as fly ash or slags, have been used (Boca Santa et al., 2016; Borges et al., 2016; Logesh Kumar and Revathi, 2016; Boca Santa et al., 2017; Bai et al., 2019). Bottom ashes from municipal solid waste incineration can also have an application in these materials because they can be alkali activated when mixed with metakaolin (Lancellotti et al., 2013; Lancellotti et al., 2014; Lancellotti et al., 2015; Silva et al., 2017; Wongsa et al., 2017; Huang et al., 2018). They cannot be used alone as precursor because the amount of Al_2O_3 is too low and the higher amount of calcium can change the chemistry of the polymerized network that is formed from alkali activation with the creation of C-A-S-H gels (Borges et al., 2016; Zhu et al., 2018). The alkali activation of this class of materials can take place at different temperatures (Rovnaník, 2010). The most interesting results are obtained from the activation at room temperature (Aredes et al., 2015). Other wastes can be activated only at high temperatures (Sha et al., 2020). It is thus important to verify the mechanical properties of the mixed binders when cured at room temperature.

However, the main problems concerning alkali-activated materials are their complete brittleness and their low dimensional stability. Both defects can be mitigated by modifying the composites through fibers addition, as reported in the literature (Uddin and Shaikh, 2013; Vilaplana et al., 2016; Al-Mashhadani et al., 2018; Bhutta et al., 2018; Luna-Galiano et al., 2018; Akono et al., 2019; Farooq et al., 2019). Waste carbon fibers (CF), embedded in a thermosetting polymer matrix, virtually have high mechanical properties. Either they can be derived from post-user dismissed items or they can be the pre-preg offcuts derived from the manufacturing process. Bare fibers can be recovered, eliminating the thermosetting matrix by means of high thermal treatments or selective chemical dissolution. Both the processes imply energy consumption and waste production. The direct use of scraps has been proposed in different matrixes, such as Portland cement, alkali-activated fly ashes, and pure metakaolin. Positive results have been obtained in terms of increased flexural strength and toughness, implying that the presence of a polymeric interphase (epoxy resin) between the fiber and the ceramic matrix still enables a positive interaction between fiber and matrix (Saccani et al., 2019). It seems thus interesting to evaluate the effect of CF/epoxy scraps also in the alkali-activated systems where metakaolin is partially substituted by bottom ashes from municipal solid waste incineration. The mix design has been investigated focusing on the workability of fresh mixtures, microstructure (i.e., fibers dispersion and porosity), flexural strength, and toughness. A room temperature curing has been studied, being the lowest energy-consuming treatment. In case these materials should prove to have acceptable mechanical properties, which is the main scope of the research, they could provide potentially high environmental benefit because they could enable the simultaneous recycling of different wastes, reducing the amount of metakaolin and virgin carbon fibers to be used. The first issue eliminates the thermal treatments of aluminosilicate precursor that are necessary, thus avoiding CO_2 emissions, and the second one would prevent scrap damping and avoid virgin fiber production. Indeed, the complete life cycle assessment of the derived material should be carried out, a process that is however beyond the aims of this study that merely faces the technical problems related to the material performance upon modification.

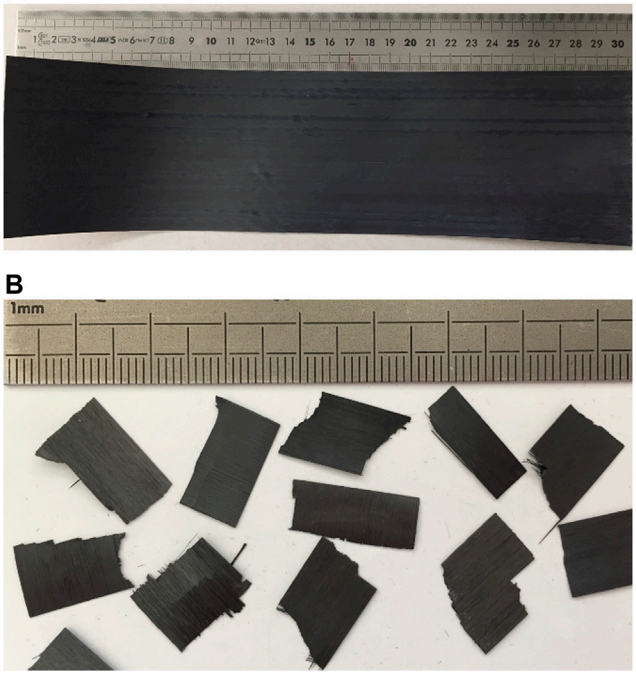

FIGURE 1 | (A) Full view of composite pre-pregs scraps. **(B)** Micrograph of the shredded multi layers.

TABLE 1 | Composition of the raw materials (wt%).

Material	SiO_2	Al_2O_3	Na_2O	K_2O	CaO	MgO	Fe_2O_3	TiO_2	MnO	LOI
Metakaolin	53.5	41.9	0.0	2.6	0.0	0.0	1.4	0.6	0.0	0.0
Bottom ash	49.5	9.4	5.7	1.4	17.5	2.9	4.9	0.9	0.2	4.9

EXPERIMENTAL

Composites Waste Scraps

Pre-preg offcuts derived from the production of CF/epoxy (hereafter defined as W_CF/EP) composites have been used. The as-received scraps had an almost rectangular shape with side dimension ranging from 10 to 40 cm (**Figure 1A** shows an example). They were made of multiple CF/epoxy impregnated layers with an average thickness ranging from 150 to 450 μm.

TABLE 2 | Formulation of composites.

Sample	Metakaolin (g)	BA (g)	NaOH 8M (ml)	Na_2SiO_3 (ml)	W_CF/EP (g)	w/b ratio
BA25-W_CF/EP0	75	25	25	60	0	0.36
BA25-W_CF/EP3	75	25	25	60	3	0.36
BA25-W_CF/EP6	75	25	25	60	6	0.36
BA25-W_CF/EP9	75	25	25	60	9	0.36
BA25-W_CF/EP12	75	25	25	60	12	0.36
BA50-W_CF/EP0	50	50	16	40	0	0.28
BA50-W_CF/EP3	50	50	16	40	3	0.28
BA50-W_CF/EP6	50	50	16	40	6	0.28
BA50-W_CF/EP9	50	50	16	40	9	0.28
BA50-W_CF/EP12	50	50	16	40	12	0.28

BA, bottom ash; CF, waste carbon fibers; W_CF/EP, pre-preg offcuts derived from the production of CF/epoxy; w/b ratio: water/binder ratio.

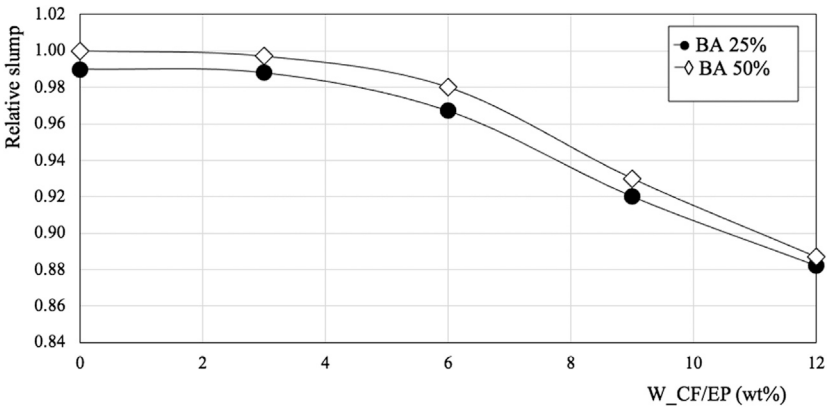

FIGURE 2 | Relative workability of the investigated composites.

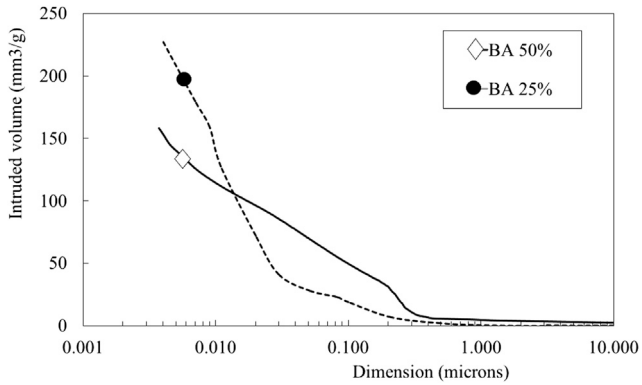

FIGURE 3 | Cumulative intruded volume in the plain matrices.

The original multiple layer sheets were treated for 1 h at 130°C to complete the cross-linking reactions and then cut to obtain fibers bundles with the length of 13 ± 2 mm and lateral size ranging from 5 to 10 mm (**Figure 1B**). The amount of resin that surrounds the carbon fibers was evaluated by weight loss through the use of a TGA instrument (Thermogravimetric Analysis, Q50 Model TA Instruments) and was estimated as a 30 ± 8 wt%.

Binders

Metakaolin with a dimension lower than 75 μm was used as binder. Bottom ashes from municipal waste incineration, hereafter simply defined as BA, once collected by the company managing the disposal of ashes from different incinerator plants are submitted to beneficiation. The process involves ageing, grinding, and Fe and Al separation by means of magnetic and eddy current systems. After these treatments, BA are no more classified as waste according to the European Waste Code, but as secondary raw materials (end of waste). Final product was ball-milled and sieved through a 100 μm sieve to favor their homogeneous mixing with metakaolin and subsequent reactions. In details, metakaolin powders show the following parameters: D_{10} = 1.40, D_{50} = 11.08, and D_{90} = 50.98. For BA the values are as follows: D_{10} = 1.81, D_{50} = 21.53, and D_{90} = 61.71. Data have been derived by laser particle sizer Fritsch, Analysette 22. **Table 1** reports the chemical composition of both metakaolin and BA as derived by X-ray fluorescence (Philips PW 2004). Other detected elements, such as sulphur, phosphor, and chlorine, are not reported. Loss on ignition was determined after a 2 h treatment at 1,100°C. X-ray analysis was performed in order to evaluate the amorphous or crystalline nature of BA and to identify the crystalline phases present. From the analysis (not reported for briefness sake), the typical amorphous/

TABLE 3 | Classification of porosity in the investigated samples according to IUPAC.

Designation	Porosity range (nm)	BA 25% (mm^3Hg/g) (%)	BA 50% (mm^3Hg/g) (%)
Micropores	<1.25	n.d.	n.d.
Mesopores	1.25–25	156.0 **(68.4)**	67.0 **(42.4)**
Macropores	25–5,000	71.9 **(31.5)**	88.0 **(55.7)**
Directly accessible large pores	5,000–50,000	0.1 **(0.0)**	3.0 **(1.9)**
Total porosity	—	228.0 **(100)**	158.0 **(100)**

Pore size classification (percentage of porosity over the total specific volume of Hg is reported in brackets).

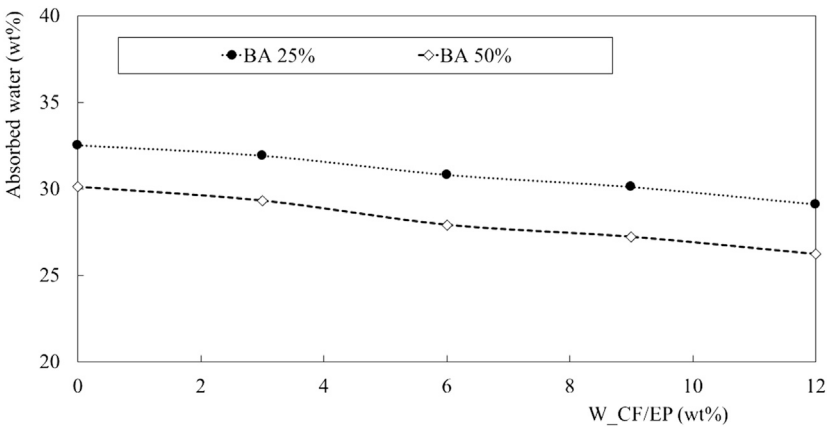

FIGURE 4 | Water absorption of all the investigated samples.

crystalline nature of the material is determined. Among the crystalline fraction, the main detected phase is α-quartz (α-SiO_2, JCPDF file 33-1161) followed by calcite (CaCO3 JCPDF file 5-586), and aluminosilicates as albite ($NaAlSi_3O_8$ JCPDF file 10-393) and ghelenite ($Ca_2Al(Al,Si)O_7$ JCPDF file 35-755), thus reflecting the chemical analysis of a typical ash rich in calcium and sodium.

Activators

Sodium hydroxide reagent grade and sodium silicate solution, a viscous liquid produced for the cement industry with a water content of 57 wt% and a SiO_2/Na_2O ratio of 3, were used as alkaline activators.

Mixing Procedures and Compositions

Sodium hydroxide 8M solution and sodium silicate have been first mixed according to the quantities determined in previous experiments (Lancellotti et al., 2013; Lancellotti et al., 2014). The quantities added aimed primarily to obtain equal workability. Moreover, due to the higher content of Na in BA, less amount of sodium hydroxide and silicate are added. On account of the higher ratio of SiO_2/Al_2O_3 in BA, less silicate is added (**Table 1**). Afterward, metakaolin mixed with the different quantity of BA (25 or 50 wt%) was added. The workability was determined through the minislump test proposed by EN-ETC. No additional water has been added to the fiber-modified materials and consequently workability decreased as the amount of W_ CF/EP increased. However, up to the highest investigated quantity, it was still possible to effectively fill the moulds without creating macro-voids. W_CF/EP amounts were 3, 6, 9, and 12 wt% on the powders. **Table 2** reports the mix design of the investigated materials. The dimension of the prepared samples during casting procedures was different on the basis of further characterizations. Prisms of 100 mm × 20 mm × 20 mm size were cast (nine for each composite composition) and cured for 28 days at 25 ± 1°C and 98 ± 1% relative humidity. Prisms of 250 mm × 25 mm × 25 mm were used to investigate the free-drying shrinkage *vs* time when samples were cured at 25°C and 35 ± 5% relative humidity.

Tests and Procedures

Water Absorption and Porosity

Water absorption has been evaluated according to the UNI 7699 Standard (UNI 7699, 2005) on three samples (100 mm × 20 mm × 20 mm) cured for 28 days. The cumulative open porosity and the size distribution of the porosities in samples without fibers (i.e., the plain matrixes formulated with 25 and 50 wt% of BA but without the fibers) have been evaluated by mercury intrusion porosimetry (MIP) equipped with a macropore unit (Thermo Scientific, Pascal 140 and 240). Measurements were conducted at 28 days of curing. MIP measurements performed on composite samples were not reliable or reproducible because of the small dimension of the tested specimens allowed and the unavoidable damage induced by specimen size reduction. Accordingly, they will not be reported.

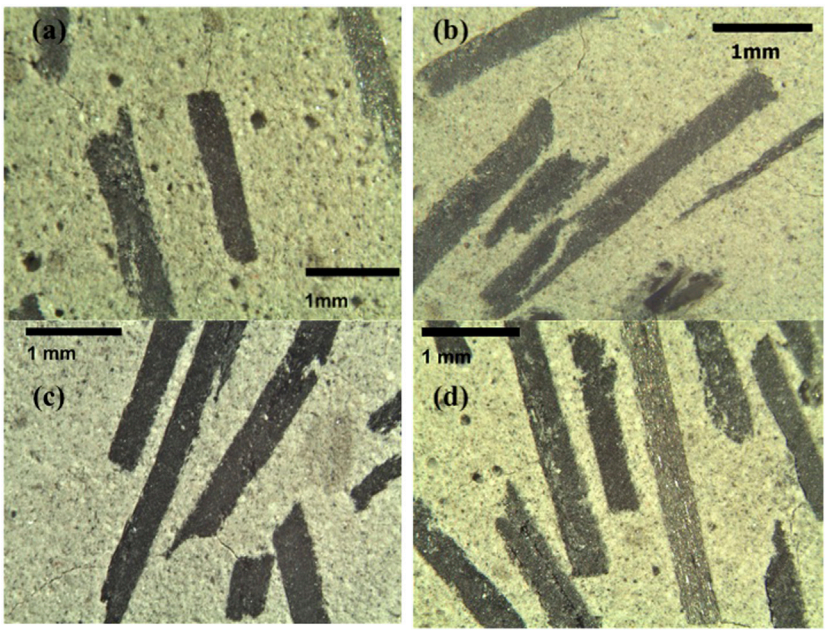

FIGURE 5 | Optical micrograph of BA25-W_CF/EP samples cross sections at 3 **(A)**, 6 **(B)**, 9 **(C)**, and 12 **(D)** wt. amount of fibers at 20×.

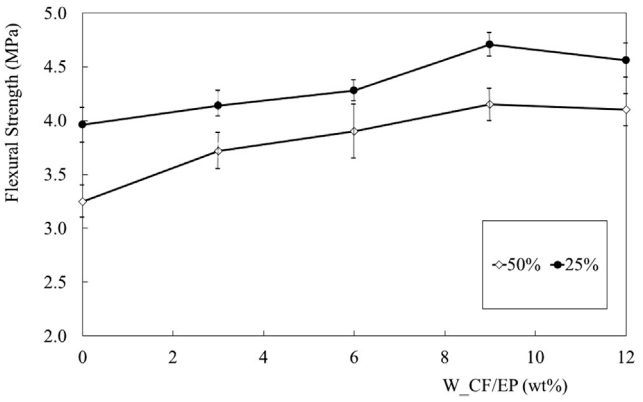

FIGURE 6 | Flexural strength of the investigated materials.

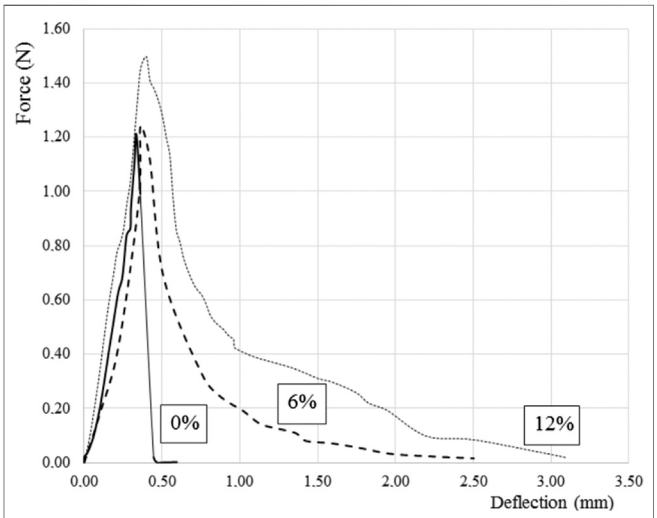

FIGURE 7 | Force *vs* deflection plot of specimens containing 50% of BA at different amounts of W_CF/EP.

Mechanical Tests

Mechanical tests (three-point bending) were performed at room temperature with a relative humidity of 50 ± 10% by means of 100 kN Amsler Wolpert equipment, with a 5 mm/min displacement rate. Flexural strength values are reported as the average of six measurements. Compressive strength measurement was performed on both the prisms derived from the previous flexural test (12 measurements).

SEM Analysis

Morphological investigations were carried out on fractured surfaces of mortar samples sputtered by graphite by means of electron scanning microscopy (ESEM, Quanta-200, FEI Co.), exploiting the signal collected by secondary electrons detectors. An accelerating voltage of 20 kV was applied.

Dimensional Stability

Dimensional stability has been evaluated according to the ASTM C1012/C1012M standards (ASTM C1012/C1012M, 2015) on three prismatic specimens of 250 mm × 25 mm × 25 mm cured at 25°C and 35 ± 5% relative humidity.

RESULTS

Figure 2 shows the relative workability of samples containing the different amounts of recycled composites, as well as the different amounts of BA. Standard deviations are not included for the sake of clearness because they almost coincide with the dimension of the symbols. While the effect of the different amounts of BA is negligible as desired, W_CF/EP addition progressively decreases this property. However, as underlined before, all mixtures could be easily cast without the formation of macrovoids. The decrease is partially related to the amount of water requested to wet the reinforcement surfaces. Although the composites scraps are no more flexible after the full–cross-linking reaction, their small dimension prevents buckling phenomena.

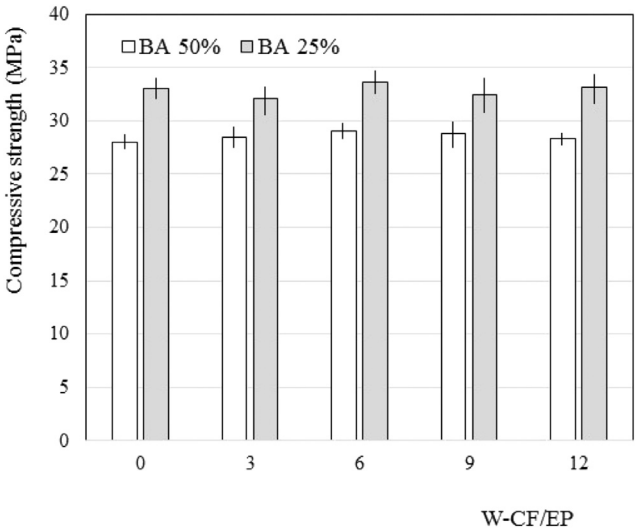

FIGURE 8 | Compressive strength of the investigated materials *vs* amount of recycled composite.

Figure 3 shows the results of MIP analysis: the total intruded volume in the two different plain matrices is reported *vs* the pore dimension. The sample containing the lower amount of BA (25%) shows the highest overall porosity (228 mm^3/g of intruded volume), with almost half of the pores having dimensions lower than 0.01 μm. BA 50% matrix shows a lower overall porosity (158 mm^3/g of intruded volume), but the dimension of the pores is larger than that in the previous sample, mainly falling in the range from 0.4 to 0.01 μm. To get a detailed analysis of the results, **Table 3** reports the amount of pores divided in different ranges proposed by the IUPAC classification. The main differences are related to the mesopores and macropores that suggest similar observations as those previously proposed. In the BA 25% sample, no large pores (>5,000 nm) are detected, and the amount is quite limited in the BA 50% sample.

This can be explained by assuming that, in the applied curing conditions, the reactions involving the BA fraction are slower than those involving metakaolin, thus producing a lower amount of binding products or polymerized network only partially filling the larger voids, as found in other researches (Guo et al., 2017; Sha et al., 2020). Moreover, the presence of C-S-A-H product can change the porosity of the products. Consequently, although the w/b ratio in the BA 50% sample is lower, the capillary porosity is increased.

Figure 4 reports the water absorption of all the samples after 28 days of curing. The higher amount of BA slightly decreases the amount of absorbed water. Moreover, as the amount of recycled composite increases, values tend to decrease slightly at both the BA amounts. The percentage of absorbed water is usually linked to the overall volume of open porosity in the material. This result is also in accordance with the previous observation on the absence of large voids caused by the workability reduction. Moreover, as the amount of absorbed water progressively decreases, there is absence of a discontinuity

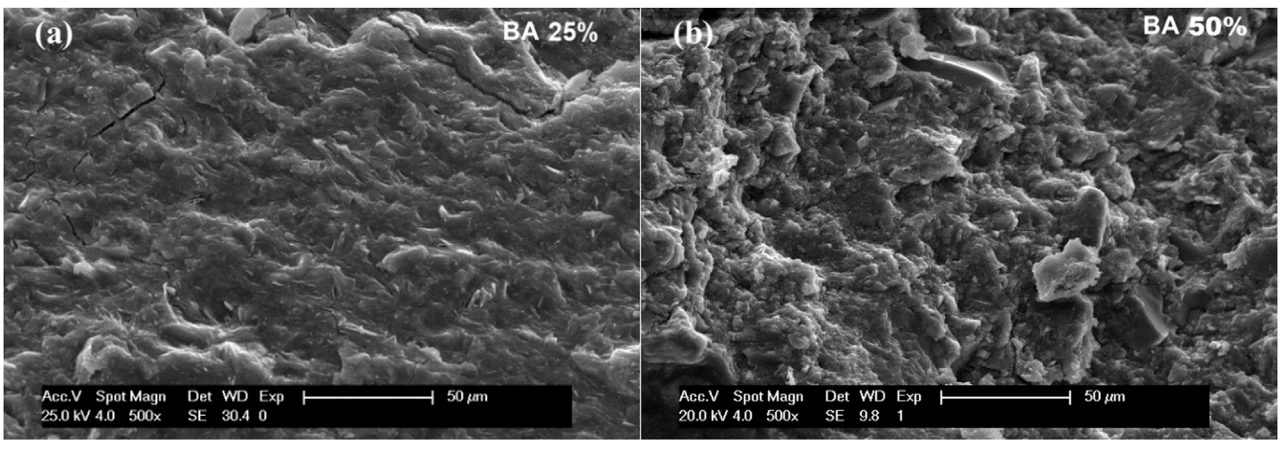

FIGURE 9 | Microstructure of **(A)** BA25-W_CF/EP0 and **(B)** BA50-W_CF/EP0 (fracture surfaces).

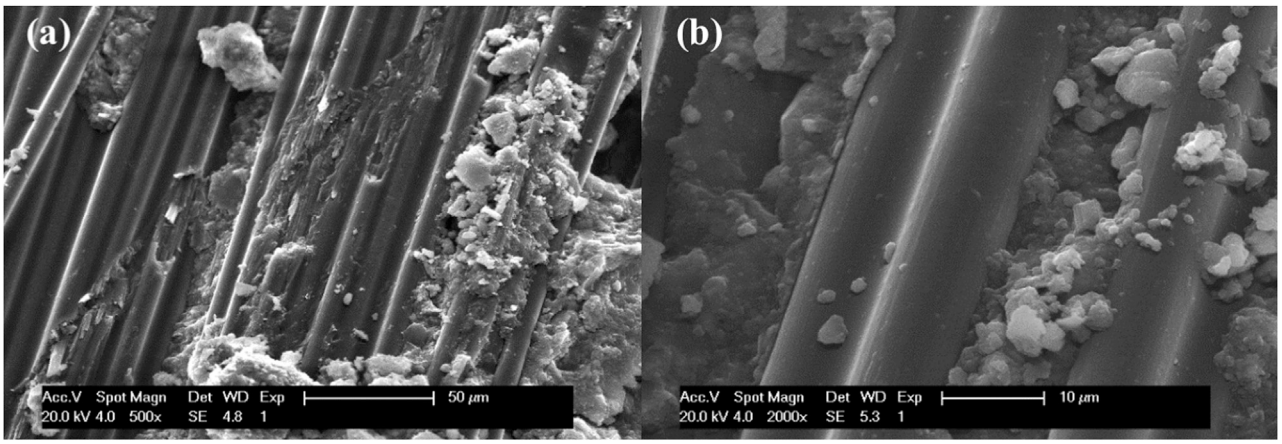

FIGURE 10 | Fracture surface of **(A)** BA25-W_CF/EP6 and **(B)** BA50-W_CF/EP6.

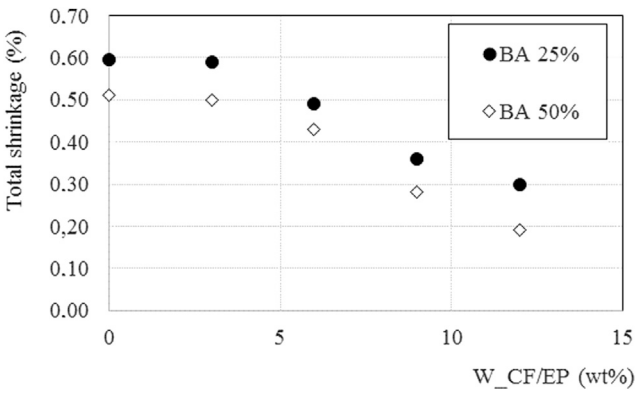

FIGURE 11 | Dimensional changes for samples cured at 35 ± 5% relative humidity.

between the waste and the matrix, suggesting an efficient adhesion between the different phases and the creation of a continuous interface transition zone between the cured epoxy and the ceramic matrix that can promote the increase in mechanical properties. The positive interaction is related to the presence of dipoles formed by C-O bonds in the resin interacting with ceramic matrix. The slight decrease in BA 50% compared with BA 25% can be explained considering the different total porosity of the two matrixes found by MIP analysis as observed in **Figure 3**. The same observation can explain the progressive reduction in the absorbed water as the amount of W_CF/EP increases. Indeed, a partial substitution of the porous phase, the matrix, with a non-porous fraction, the organic composite, takes place, decreasing the overall fraction of porosities.

The severed surfaces obtained by diamond sawing of the different samples (**Figures 5A–D**) again underline the absence of large voids (>1 mm) derived from insufficient workability, as was expected by visual inspection during casting operations. No differences at this magnification were found between the different amounts of BA and consequently only 25 wt% BA loading is reported. No clusters of fibers were also visible from the Figures, implying that an efficient dispersion is obtained.

Figure 6 shows the flexural strength of the composites at 28 days of curing. As it can be observed, the increase in the amount of BA, from 25 to 50 wt%, decreases the mechanical properties of the composites. This is probably related to the presence, in the 50% samples, of a higher amount of porosities in the range from 0.02 to 0.4 μm with respect to the 25% BA composition as observed from the MIP measurements. This difference is possibly derived, as explained before, from the different reaction products generated (i.e., from the presence of C-A-S-H products) and also from the different kinetics of the binding reactions involving metakaolin and BA. However, the addition of W_CF/EP almost linearly increases the flexural strength of all the samples, confirming the positive effect of the fibers.

Figure 7 shows the plots reporting the force *vs* the deflection of all samples containing 50% of BA. For sake of brevity, only this set of specimens is reported. Along with the increase in flexural strength already discussed, a progressive increase in toughness takes place. In fiber-modified samples instead of one crack leading to the almost instantaneous overall fracture, a web of small cracks is formed leading to a postponed failure. Consequently, as the fully brittle behavior of the unmodified matrix is changed, higher amounts of energy can be absorbed as the amount of recycled composite increases. The mechanism supporting this effect is related to the progressive pull-out of the fibers from the matrix. The toughening effect of the fibers is reflected by the increase in the area beneath the plot.

Figure 8 reports the values of compressive strength of the investigated materials. This property is almost unaffected by the waste addition, both W_CP/EP and BA. Only at the highest amount of fibers, a slight reduction is found in samples, whereas at the lowest amounts, compressive strength slightly increases. Larger increases in compressive strength were found in other

researches, although with different conditions (Uddin and Shaikh, 2013; Bhutta et al., 2018).

The SEM analysis of mortars without W_CF/EP at different BA amounts is reported in **Figure 9**. Both the matrixes appear as compact without porosities. In the 50% BA matrix, some unreacted BA particles still showing sharp edges are visible. This confirms that at room temperature, the reactions leading to the geopolymerization of at least one fraction of BA are rather slow as previously observed (Uddin and Shaikh, 2013; Bhutta et al., 2018). **Figure 10** reports the morphology of the fractured surfaces derived from the flexural tests of samples modified with W_CF/EP. Some matrix particles adhere to the fibers, and no porosities are present at the interphase between matrix and wastes. This implies a fair interaction of the filler with the matrix, supporting the previous observations related to the amounts of absorbed water.

Indeed, it should also be underlined that no remarkable qualitative differences can be observed on changing the amount of BA in the matrix. Eventually, **Figure 11** reports the dimensional changes at 14 days for samples cured at 35 ± 5% relative humidity. A slight increase in the dimensional shrinkage of sample BA25-W_CF/EP can be observed when compared with BA50-W_CF/EP, probably on account of the overall higher porosity. Samples containing 3% of W_CF/EP show almost the same behavior as the unmodified matrixes, but further additions progressively increase the dimensional stability of the composites, an effect that has been found in conventional Portland cement materials by adding recycled carbon fibers (Wang et al., 2019).

It is important to underline from the results so far obtained that wastes derived from composite manufacturing can be recycled in the production of building materials without previous chemical or thermal treatments. The scraps can improve the mechanical behavior of metakaolin materials geopolymerized at low temperature. In this way, the use of low-energy consuming, low-impact products, where an economical value-added benefit is also achieved, can be successfully promoted.

CONCLUSIONS

The results of this research can thus be summarized as follows:

- Metakaolin can be mixed with BA up to an amount of 50 wt %. The binder can still be activated at room temperature still showing even at the highest amount of BA, acceptable mechanical strengths.
- Untreated wastes derived from the production of carbon fiber epoxy composites have been homogeneously dispersed to formulate composites up to 12 weight %. Although the workability of the fresh mixtures decreases as the amount of waste increases, it is possible to cast mortars without high-dimension porosities. Microstructural analysis discloses a fair interaction between the fibers still surrounded by the epoxy coating and the matrix.
- CF/epoxy wastes increase the flexural strength of all the composites and drive their fracture from a brittle behaviour to a semiductile one. The compressive strength is practically unaffected by carbon fibers addition. Moreover, the addition of the fibrous wastes increases the dimensional stability of the composites.

DATA AVAILABILITY STATEMENT

All datasets presented in this study are included in the article.

AUTHOR CONTRIBUTIONS

SM: conceptualization, methodology, validation, investigation, resources, data curation, visualization, writing original draft preparation, and editing. IL: methodology, validation, and resources. GM: investigation, data curation, and visualization. AS: conceptualization, methodology, validation, investigation, resources, data curation, visualization, writing original draft preparation and editing, and supervision.

ACKNOWLEDGMENTS

The authors acknowledge the support of Lorenzo Lipparini (REGLASS) for providing CF/EP composites.

REFERENCES

Akono, A. T., Koric, S., and Kriven, W. M. (2019). Influence of pore structure on the strength behavior of particle and fiber-reinforced metakaolin-based geopolymer composites. *Cem. Concr. Comp.* 104, 103361. doi:10.1016/j.cemconcomp.2019.103361

Al-Mashhadani, M., Canpolat, O., Aygörmez, Y., Uysal, M., and Erdem, S. (2018). Mechanical and microstructural characterization of fiber reinforced fly ash based geopolymer composites. *Constr. Build. Mater.* 167, 505–513. doi:10.1016/j.conbuildmat.2018.02.061

Aredes, F. G. M., Campos, T. M. B., Machado, J. P. B., Sakane, K. K., Thim, G. P., and Brunelli, D. D. (2015). Effect of cure temperature on the formation of metakaolinite-based geopolymer. *Ceram. Int.* 41, 7302–7311. doi:10.1016/j.ceramint.2015.02.022

ASTM C1012/C1012M (2015). Standard test method for length change of hydraulic-cement mortars exposed to a sulfate solution, West Conshohocken, PA: ASTM International, 19428–2959.

Bai, T., Song, Z., Wang, H., Wu, Y., and Huang, W. (2019). Performance evaluation of metakaolin geopolymer modified by different solid wastes. *J. Clean. Prod.* 226, 114–121. doi:10.1016/j.jclepro.2019.04.093

Bhutta, A., Farooq, M., and Banthia, N. (2018). Matrix hybridization using waste fuel ash and slag in alkali-activated composites and its influence on maturity of fibre-matrix bond. *J. Clean. Prod.* 177, 857–867. doi:10.1016/j.jclepro.2018.01.001

Boca Santa, R. A. A., Soares, C., and Gracher Riella, H. (2016). Geopolymers with a high percentage of bottom ash for solidification/immobilization of different toxic metals. *J. Hazard. Mater.* 318, 145–153. doi:10.1016/j.jhazmat.2016.06.059

Boca Santa, R. A. A., Soares, C., and Gracher Riella, H. (2017). Geopolymers obtained from bottom ash as source of aluminosilicate cured at room temperature. *Constr. Build. Mat.* 157, 459–466. doi:10.1016/j.conbuildmat.2017.09.111

Borges, P. H. R., Banthia, N., Alcamand, H. A., Vasconcelos, W. L., and Nunes, E. H. M. (2016). Performance of blended metakaolin/blastfurnace slag alkali-activated mortars. *Cem. Concr. Comp.* 71, 42–52. doi:10.1016/j.cemconcomp.2016.04.008

Chen, P., Feng, B., Lin, Y., and Lin, C. (2019). Solidification and stabilization of sewage sludge and MSWI bottom ash for beneficial use as construction materials. *J. Mater. Civ. Eng.* 31(1), 04018351. doi:10.1061/(ASCE)MT.1943-5533.0002572

Chen, Z., and Yang, E. (2017). Early age hydration of blended cement with different size fractions of municipal solid waste incineration bottom ash. *Constr. Build. Mater.* 15, 880–890. doi:10.1016/j.conbuildmat.2017.09.063

De Vargas, A. S., Dal Molin, D. C. C., Vilela, A. C. F., da Silva, F. J., Pavão, B., and Veit, H. (2011). The effects of Na_2O/SiO_2 molar ratio, curing temperature and age on compressive strength, morphology and microstructure of alkali-activated fly ash-based geopolymers. *Cem. Concr. Comp.* 33(6), 653–660. doi:10.1016/j.cemconcomp.2011.03.006

Farooq, M., Bhutta, A., and Banthia, N. (2019). Tensile performance of eco-friendly ductile geopolymer composites (EDGC) incorporating different micro-fibers. *Cem. Concr. Comp.* 103, 183–192. doi:10.1016/j.cemconcomp.2019.05.004

Guo, X., Shi, H., and Wei, X. (2017). Pore properties, inner chemical environment, and microstructure of nano-modified CFA-WBP (class C fly ash-waste brick powder) based geopolymers. *Cem. Concr. Comp.* 79, 53–61. doi:10.1016/j.cemconcomp.2017.01.007

Huang, G., Ji, Y., Li, J., Hou, Z., and Jin, C. (2018). Use of slaked lime and Portland cement to improve the resistance of MSWI bottom ash-GBFS geopolymer concrete against carbonation. *Constr. Build. Mater.* 166, 290–300. doi:10.1016/j.conbuildmat.2018.01.089

Kuo, W. T., Liu, C. C., and Su, D. S. (2013). Use of washed municipal solid waste incinerator bottom ash in pervious concrete. *Cem. Concr. Comp.* 37 (1), 328–335. doi:10.1016/j.cemconcomp.2013.01.001

Lancellotti, I., Cannio, M., Bollino, F., Catauro, M., and Leonelli, C. (2015). Geopolymers: an option for the valorization of incinerator bottom ash derived "end of waste". *Ceram. Int.* 41, 2116–2123. doi:10.1016/j.ceramint.2014.10.008

Lancellotti, I., Ponzoni, C., Barbieri, L., and Leonelli, C. (2013). Alkali activation processes for incinerator residues management. *Waste Manag.* 33, 1740–1749. doi:10.1016/j.wasman.2013.04.013

Lancellotti, I., Ponzoni, C., Bignozzi, M., Barbieri, L., and Leonelli, C. (2014). Incinerator BA and Ladle slag for geopolymers preparation. *Waste Bio.Valor.* 5, 393–401. doi:10.1007/s12649-014-9299-2

Li, X., Lv, Y., Ma, B., Chen, Q., Yin, X., and Jian, S. (2012). Utilization of municipal solid waste incineration bottom ash in blended cement. *J. Clean. Prod.* 32, 96–100. doi:10.1016/j.jclepro.2012.03.038

Logesh Kumar, M., and Revathi, V. (2016). Metakaolin bottom ash blend geopolymer mortar – a feasibility study. *Constr. Build. Mater.* 114, 1–5. doi:10.1016/j.conbuildmat.2016.03.149

Luna-Galiano, Y., Leiva, C., Villegas, R., Arroyo, F., Vilches, L., and Fernández-Pereira, C. (2018). Carbon fiber waste incorporation in blast furnace slag geopolymer-composites. *Mater. Lett.* 233, 1–3. doi:10.1016/j.matlet.2018.08.099

Rovnaník, P. (2010). Effect of curing temperature on the development of hard structure of metakaolin-based geopolymer. *Constr. Build. Mater.* 24, 1176–1183. doi:10.1016/j.conbuildmat.2009.12.023

Saccani, A., Manzi, S., Lancellotti, I., and Lipparini, L. (2019). Composites obtained by recycling carbon fibre/epoxy composite wastes in building materials. *Constr. Build. Mater.* 204, 296–302. doi:10.1016/j.conbuildmat.2019.01.216

Saccani, A., Sandrolini, F., Andreola, F., Lancellotti, I., Barbieri, L., and Corradi, A. (2005). Influence of the pozzolanic fraction obtained from vitrified bottom ashes from MSWI on the properties of cementitiuos composites. *Mater. Struct.* 38, 367–371. doi:10.1007/BF02479303

Saccani, A., Sandrolini, F., Barbieri, L., and Lancellotti, I. (2001). Structural studies and electrical properties of re-cycled glasses from glass and incinerator wastes. *J. Mater. Sci.* 36, 2173–2177. doi:10.1023/A:1017539932421

Sha, D., Pan, B., and Sun, Y. (2020). A novel raw material for geopolymers: coal-based synthetic natural gas slag. *J. Clean. Prod.* 262, 121238. doi:10.1016/j.jclepro.2020.121238

Silva, R. V., de Brito, J., Lynn, C. J., and Dhir, R. K. (2017). Use of municipal solid waste incineration bottom ashes in alkali-activated materials, ceramics and granular applications: a review. *Waste Manag.* 68, 207–220. doi:10.1016/j.wasman.2017.06.043

Sun, Z., and Vollpracht, A. (2019). One year geopolymerisation of sodium silicate activated fly ash and metakaolin geopolymers. *Cem. Concr. Comp.* 95, 98–110. doi:10.1016/j.cemconcomp.2018.10.014

Tang, P., Florea, M., Spiesz, P., and Brouwers, H. (2016). Application of thermally activated municipal solid waste incineration (MSWI) bottom ash fines as binder substitute. *Cem. Concr. Comp.* 70, 194–205. doi:10.1016/j.cemconcomp.2016.03.015

Uddin, F., and Shaikh, A. (2013). Review of mechanical properties of short fibre reinforced geopolymer composites. *Constr. Build. Mater.* 43, 37–49. doi:10.1016/j.conbuildmat.

UNI 7699 (2005). *Testing hardened concrete. Determination of water absorption at atmospheric pressure*, Milano, Italy: Ente Nazionale Italiano di Unificazione.

Vilaplana, J. L., Baeza, F. J., Galao, O., Alcocel, E. G., Zornoza, E., and Garces, P. (2016). Mechanical properties of alkali activated blast furnace slag pastes reinforced with carbon fibers. *Constr. Build. Mater.* 116, 63–71. doi:10.1016/j.conbuildmat.2016.04.066

Wang, Y., Zhang, S., Li, G., and Shi, X. (2019). Effects of alkali treated recycled carbon fiber on the strength and free drying shrinkage of cementitious mortar. *J. Clean. Prod.* 228, 1187–1195. doi:10.1016/j.jclepro.2019.04.295

Wongsa, A., Boonserm, K., Waisurasingha, C., Sata, V., and Chindaprasirt, P. (2017). Use of municipal solid waste incinerator (MSWI) bottom ash in high calcium fly ash geopolymer *J. Clean. Prod.* 148, 49–59. doi:10.1016/j.jclepro.2017.01.147

Zhu, W., Chen, X., Struble, L. J., and Yang, E.-H. (2018). Characterization of calcium containing phases in alkali-activated municipal solid waste incineration bottom ash binder through chemical extraction and deconvoluted Fourier transform infrared spectra. *J. Clean. Prod.* 192, 782–789. doi:10.1016/j.jclepro.2018.05.049

Conflict of Interest: The authors declare that the research was conducted in the absence of any commercial or financial relationships that could be construed as a potential conflict of interest.

Advantages of publishing in Frontiers

OPEN ACCESS
Articles are free to read for greatest visibility and readership

FAST PUBLICATION
Around 90 days from submission to decision

HIGH QUALITY PEER-REVIEW
Rigorous, collaborative, and constructive peer-review

TRANSPARENT PEER-REVIEW
Editors and reviewers acknowledged by name on published articles

Frontiers
Avenue du Tribunal-Fédéral 34
1005 Lausanne | Switzerland

Visit us: www.frontiersin.org
Contact us: frontiersin.org/about/contact

REPRODUCIBILITY OF RESEARCH
Support open data and methods to enhance research reproducibility

DIGITAL PUBLISHING
Articles designed for optimal readership across devices

FOLLOW US
@frontiersin

IMPACT METRICS
Advanced article metrics track visibility across digital media

EXTENSIVE PROMOTION
Marketing and promotion of impactful research

LOOP RESEARCH NETWORK
Our network increases your article's readership